ENHANCED BISMUTH-BASED PHOTOCATALYSIS APPLIED TO ENVIRONMENTAL REMEDIATION

Xiangchao Meng

Thesis submitted to the

Faculty of Graduate and Postdoctoral Studies

in partial fulfillment of the requirements for

the Doctorate in Philosophy degree in Chemical Engineering



uOttawa

Department of Chemical and Biological Engineering

Faculty of Engineering

University of Ottawa

© Xiangchao Meng, Ottawa, Canada, 2018

Abstract

The basis of prosperity of 20^{th} centrury is oil. As oil is going to be used up, people need to find alternatives to meet the earth's energy demand in 21^{st} centrury. For each second, there are about 1.2×10^{17} J energy hitting the earth. The energy in 1 hour of sunlight is about 4.32×10^{20} J, which almost meets the energy consumed on earth in 2016. It determines solar energy may be a potential candidate to solve the energy crisis. As for techniques to utilize solar energy, the most popular one is using photovoltaic (PV) cells. PV cell is a device to convert solar energy into electricity. There are also some other techniques trying to utilize solar energy. Photocatalysis is one of them, which is to convert solar energy into chemical energy. Applications of photocatalysis have extended from hydrogen evolution via water splitting to environemtnal remediation, CO_2/ N_2 reduction and so on.

Photocatalysis, as an advanced oxidation process, has been extensively studied and applied to the purification and remediation of contaminated water and wastewater, and exhibits advantages over conventional treatment technologies. When considering solar energy as an energy source for photocatalysis, it is key to prepare visible light-responsive materials. Bismuth-based semiconductors are promising materials as visible light-responsive photocatalysts primarily due to their suitable band gaps, well-dispersed valence bands, and commercial availabilities at reasonable costs, as well as the possibility of preparing them under mild conditions. Recent work focusing on the preparation, characterization and activity testing of bismuth-based photo-active materials as well as their associated photoreactor designs are introduced herein. In order to enhance the photocatalytic activities of the new materials, different precursors, additives, preparation procedures and process parameters, as well as surface treatments were explored to obtain binary and ternary heterostructures, with different doping, surface modification, nanoparticle sizes and morphologies. It was found that formation of heterojunction and loading metal nanoparticle on the surface are very effective to imrove the photocatalytic activity of the support. In this work, we found that palladium nanoparticles modified $BiVO_4$ exhibited excellent activity in the decomposition of phenol, which was even higher than TiO_2. To facilitate the separation process of catalysis particels from a slurry system, magnetically separable composites were also prepared, and it was found that it is very effective to remove the

particles from the slurry system using external magnets. To further scale up this process, two different types of immbolized photoreactors (flat-plate and packed beads photoreactor) were also developed. Suggestions were made for further work in this research area.

Resúmé

Le pétrole est devenu la base de la prospérité du 20^{e} siècle et au fur et à mesure que cette ressource sera utilisée, les gens devront trouver des alternatives pour rencontrer les exigences de la planète. À chaque seconde, on estime que $1.2x10^{17}$ J d'énergie frappent la surface de la terre. L'énergie approximative d'une heure d'ensoleillement équivaut à $4.32x10^{20}$ J, ce qui constitue de près, l'énergie consommée sur la terre en 2016. L'énergie solaire pourrait s'avérer la solution à la crise d'énergie! Pour ce qui en est des techniques pour utiliser l'énergie solaire, la plus populaire utilise l'énergie solaire photovoltaïque. Grâce à des panneaux ou des centrales solaires photovoltaïques, l'énergie solaire est convertie en électricité. Depuis quelques années, l'efficacité de cette technique s'est beaucoup améliorée. Mais il existe aussi d'autres techniques pour utiliser l'énergie solaire. Des applications de photocatalyse se sont étendues à partir de l'évolution de l'hydrogène via le fractionnement de l'eau jusqu'à la dépollution environnementale, réduction de CO_2 / N_2 et davantage.

La photocatalyse est un processus d'oxydation avancé, hautement étudié et appliqué à la purification et à la remédiation des eaux contaminées et des eaux usées qui démontre ses avantages sur les technologies de traitement conventionnels. Dans la considération d'énergie solaire comme source énergétique pour la photocatalyse, on doit prévoir des matériaux sensibles à la lumière visible. Grâce à l'écart de leur bandes d'énergie, leur bandes de valence bien dispersées, leur disponibilité commerciale a cout raisonnable et la possibilité de les préparer dans des conditions douces, les semi-conducteurs à base de bismuth sont des matériaux sensibles à la lumière visible prometteurs a la photocatalyse. Vous trouverez ci-dedans, de récents travaux mettant l'emphase sur la préparation, la caractérisation et l'évaluation de l'activité des matériaux sensibles à la lumière visible à base de bismuth et, leurs modèles de photoréacteurs associés. Afin de rehausser les activités photocatalytiques des nouveaux matériaux, différents précurseurs, additifs, procédures de préparation, paramètre de processus et, traitements de surface ont été explorés afin d'obtenir des hétérostuctures binaires et ternaires démontrant différents dopages, modifications de surface, tailles de nanoparticules et morphologies. On a déterminé que la formation d'hétérojonctions et le chargement de nanoparticules de métal sont effectifs à

l'amélioration de l'activité photocatalytique. Dans cet ouvrage, nous avons trouvé que les nanoparticules de palladium $BiVO_4$ modifiées exhibent des activités excellentes de décomposition de phénol, plus élevé que le TiO_2. Afin de faciliter le processus de séparation de particules de catalyse d'un système de lisier, des composites magnétiquement séparables ont aussi été préparées et on démontrait qu'on pouvait efficacement soustraire les particules du lisier avec des aimants. Pour augmenter l'échelle de ce processus, deux types différents de photoréacteurs immobilisés (à écran plan et à billes compressées) ont aussi été développés. On suggère plus de travaux en cette recherche.

Copyright Statement

All material contained in this thesis that has previously been published has been published in journals that allow their use in graduate theses. Full references for the original publication are provided where required.

Statement of Contributions of Collaborators

I hereby declare that I am the sole author of this thesis. I independently designed all experimental studies, performed all data analyses, and wrote all of the chapters and appendices presented in this thesis. I also conducted all of the experimental work, with the exceptions of Chapters / Appendices under my supervision. Further details are summarized below. All collaborators were listed as co-authors in their related publications. I have also acknowledged sources of assistance in analysis where applicable. Dr. Z. (Jason) Zhang supervised this thesis project, provided guidance throughout and made editorial contributions to the written work presented. All material presented in this thesis are with their full knowledge and consent, and in accordance with the rules established by the University of Ottawa.

Chapter/ Appendix	Collaborator(s) and affiliation	Details
3	H. Qin, University of Ottawa	H. Q. provided guidance contribution.
4	Z. Li, University of Ottawa J. Chen, University of Ottawa H. Xie, Taiyuan University of Technology	Z. L. and J. C. conducted all of the degradation tests, and Prof. Xie, as a visiting scholar, conducted the materials simulations.
5	Z. Li, University of Ottawa	Z. L. conducted all of the degradation tests and analysis.
6	Z. Li, University of Ottawa H. Zeng, University of Ottawa J. Chen, University of Ottawa	H. Z. and J. C. (M.Eng. students) conducted all of the degradation tests and materials preparation. Z. L. conducted all the disinfection experiments.
C	Z. Li, University of Ottawa	Z. L. prepared materials and conducted the degradation experiments.
D	Z. Li, University of Ottawa N. Yun, University of Ottawa	Z. L. prepared materials, and N. Y. conducted materials simulations and analysis.
E	L. Jiang, University of Ottawa W. Wang, Qingdao University of Science and Technology	L. J. (a M.Eng. student) and Prof. W. Wang (a visiting scholar) conducted all of the experiments.
H	Z. Li, University of Ottawa	Z. L. prepared materials and conducted the degradation experiments.
I	X. Li, Tianjin University	Prof. Li guided and proof read the comprehensive review.
M	N. Yun	Dr. Yun (PDF) wrote the part of materials simulation in the review.

Acknowledgements

Thanks must first be extended to my supervisor Dr. Jason Zhang for his knowledgeable guidance, encouragement and staunch support over the duration of my doctoral studies.

I would like to acknowledge the Natural Sciences and Engineering Research Council of Canada (NSERC), the China Scholarship Council (CSC) and University of Ottawa for their generous financial support.

I would like to express my gratitude to technical support staff, especially Louis Tremblay, for their help to maintain the lab equipment. I am grateful to Dr. Yun Liu (SEM&TEM), Dr. Alexander Mommers (XPS), Dr. Yong Yang (BET), Dr. Tara Kell (PXRD), Dr. Bulat Gabidullin (PXRD), and Dr. Rebeca Rondon Belandria (Raman) at the Centre for Catalysis Research and Innovation (CCRI, University of Ottawa), Dr. Sebastian Schaefer (Lamp spectra measurements) at SUNLAB (University of Ottawa), Dr. Patrick M. D'Aoust (TOC) at the Department of Civil Engineering (University of Ottawa), and Dr. Paul Dubé (SQUAD) at the Brockhouse Institute for Materials Research (McMaster University) for their help with materials characterizations. Thanks are also extended to Scott Proulx and Fahad Chowdhury for their assistance in English language editing of the document.

Thanks should also be extended to graduate and undergraduate students who have been involved in this project, Jie Chen, Haoming Zeng, Lingyun Jiang, Huiqiang Bao, David Schlachter and Fahad Chowdhury.

Finally, it remains that I should thank my family and friends, too numerous to enumerate, whose unwavering support always encouraged me, and without their support none of this work would have been completed.

To my family

Table of Contents

Abstract ..... **ii**

Resúmé ..... **iv**

Copyright Statement ..... **vi**

Statement of Contributions of Collaborators ..... **vi**

Acknowledgements ..... **viii**

Table of Contents ..... **x**

List of Figures ..... **xxii**

List of Tables ..... **xliv**

Nomenclature, Abbreviations and symbols ..... **xlviii**

SECTION I: INTRODUCTION **1**

CHAPTER 1 INTRODUCTION 2

CHAPTER 2 BACKGROUND AND LITERATURE REVIEW 5

2.1 Introduction *5*

2.2 Bismuth-based photocatalytic materials *6*

2.2.1 Bi_2O_3 and Bi_2S_3 6

2.2.2 Bi_2MO_6 (M = Cr, Mo, W) 8

2.2.3 $BiVO_4$ 12

2.2.4 BiOX (X = F, Cl, Br, I) 13

2.2.5 $BiPO_4$ 15

2.2.6 $(BiO)_2CO_3$ 16

2.2.7 $M(BiO_3)_n$ (n = 1, M = Li, Na, K and Ag; n = 2, M = Mg, Zn, Sr, Ba, and Pb) 17

2.3 Main challenges and possible approaches *17*

2.3.1 Energy band engineering analysis 17

2.3.2 Development of visible-light sensitivity 20

2.3.3 Implementation in water splitting 28

2.3.4 Improvement of electrons/holes separate efficiency 30

2.3.5 Stabilities 33

2.4 Future work and concluding remarks *34*

References *35*

SECTION II: SURFACE PLASMON RESONANCE ENHANCED BISMUTH-BASED PHOTOCATALYSIS..... 52

CHAPTER 3 NEW INSIGHT INTO THE ENHANCED VISIBLE LIGHT-DRIVEN PHOTOCATALYTIC ACTIVITY OF $Pd/PdCl_2$-doped Bi_2WO_6 PHOTOCATALYSTS..... 53

Abstract..... *53*

3.1 Introduction..... *53*

3.2 Experimental..... *55*

3.2.1 Synthesis of Bi_2WO_6..... 55

3.2.2 Synthesis of $Pd/PdCl_2$-Bi_2WO_6 composites..... 56

3.2.3 Characterization..... 56

3.2.4 Photocatalytic activity tests..... 57

3.3 Results and discussions..... *59*

3.3.1 XRD and XPS..... 59

3.3.2 FT-IR..... 62

3.3.3 N_2 sorption analysis..... 63

3.3.4 Photoabsorption properties..... 65

3.3.5 Proposed formation mechanisms of Pd-Bi_2WO_6..... 67

3.3.6 Photocatalytic activity..... 69

3.3.7 Mechanisms..... 81

3.4 Conclusions..... *85*

References..... *85*

CHAPTER 4 ENHANCED VISIBLE LIGHT-INDUCED PHOTOCATALYTIC ACTIVITY OF SURFACE-MODIFIED BIOBR WITH PD NANOPARTICLES..... 95

Abstract..... *95*

4.1 Introduction..... *95*

4.2 Experimental..... *97*

4.2.1 Preparation of BiOBr..... 97

4.2.2 Preparation of Pd-BiOBr composites..... 98

4.2.3 Characterization..... 98

4.2.4 Photocatalytic activity tests..... 99

4.2.5 Electronic structure calculation..... 100

4.3 Results and discussions..... *100*

4.3.1 Morphologies..... 100

4.3.2 Crystal structure and surface chemical states 103
4.3.3 Possible formation process 106
4.3.4 Optical properties 108
4.3.5 Adsorption properties 110
4.3.6 Photocatalytic activity tests 112
4.3.7 Photoluminescence spectra analysis 116
4.3.8 Electrochemical properties 116
4.3.9 Proposed mechanism 119
4.4 Conclusions *120*
References *120*
CHAPTER 5 Pd NANOPARTICLES DECORATED PEANUT-SHAPED $BiVO_4$ WITH IMPROVED VISIBLE LIGHT-DRIVEN PHOTOCATALYTIC ACTIVITY COMPARABLE TO TiO_2 UNDER UV LIGHT 128
Abstract *128*
5.1 Introduction *129*
5.2 Experimental *131*
5.2.1 Preparation of peanut-shaped $BiVO_4$ 131
5.2.2 Preparation of palladium modified-$BiVO_4$ composites 131
5.2.3 Characterization 131
5.2.4 Photocatalytic activity tests 132
5.2.5 Electronic structure calculation 133
5.3 Results and discussions *133*
5.3.1 Crystal structures and surface chemical components 133
5.3.2 Morphologies 137
5.3.3 Proposed formation process 139
5.3.4 Energy band structure analysis 140
5.3.5 Optical properties 142
5.3.6 Photocatalytic activity testing 143
5.3.7 Proposed mechanism discussions 145
5.4 Conclusions *155*
References *156*
SECTION III: HETEROSTRUCTURE ENHANCED BISMUTH-BASED PHOTOCATALYSIS 163

CHAPTER 6 MoS_2 QUANTUM DOTS-INTERSPERSED Bi_2WO_6 HETEROSTRUCTURES FOR VISIBLE LIGHT-INDUCED DETOXIFICATION AND DISINFECTION 164
Abstract *164*
6.1 Introduction *164*
6.2 Experimental *166*
6.2.1 Chemicals 166
6.2.2 Synthesis of layered MoS_2 nanoflowers 166
6.2.3 Synthesis of hierarchical Bi_2WO_6 166
6.2.4 Synthesis of MoS_2 QDs interspersed-Bi_2WO_6 composites 167
6.2.5 Characterization 167
6.2.6 Photocatalytic activity tests 168
6.2.7 Electronic structure calculation 170
6.3 Results and discussions 170
6.3.1 Crystal structure and surface composition analysis 170
6.3.2 Morphologies 174
6.3.3 UV-Vis diffuse reflectance spectra 176
6.3.4 N_2 sorption isotherms 177
6.3.5 Adsorption analysis 178
6.3.6 Photocatalytic activity test 181
6.3.7 Electrochemical exploration 188
6.3.8 Energy band engineering analysis 190
6.4 Conclusions *193*
References *193*
SECTION IV: TERNARY BISMUTH-BASED STRUCTURE WITH ENHANCED PHOTOCATALYTIC ACTIVITY 200
CHAPTER 7 PLASMONIC TERNARY Ag-rGO-Bi_2MoO_6 COMPOSITES WITH ENHANCED VISIBLE LIGHT-DRIVEN PHOTOCATALYTIC ACTIVITY 201
Abstract *201*
7.1 Introduction *201*
7.2 Experimental *203*
7.2.1 Preparation of GO- and rGO-Bi_2MoO_6 203
7.2.2 Preparation of Ag-rGO-Bi_2MoO_6 204
7.2.3 Characterization 204

7.2.4 Photocatalytic activity tests 205
7.3 Results and discussion *206*
7.3.1 Crystal structure analysis 206
7.3.2 Spectroscopic analysis 209
7.3.3 FT-IR 213
7.3.4 Morphologies and possible formation processes 214
7.3.5 BET surface areas 218
7.3.6 Optical properties 220
7.3.7 Photocatalytic activity test 221
7.3.8 Possible mechanisms 224
7.4 Conclusions *229*
References *230*

SECTION V: MAGNETICALLY SEPARABLE BISMUTH-BASED PHOTOCATALYST 237

CHAPTER 8 SYNTHESIS AND CHARACTERIZATION OF PLASMONIC AND MAGNETICALLY SEPARABLE Ag/AgCl-Bi_2WO_6@ Fe_3O_4@SiO_2 CORE-SHELL COMPOSITES FOR VISIBLE LIGHT-INDUCED WATER DETOXIFICATION 238

Abstract *238*
8.1 Introduction *238*
8.2 Experimental *240*
8.2.1 Preparation of magnetic Bi_2WO_6 ((M) Bi_2WO_6) 240
8.2.2 Preparation of Ag/AgCl-(M) Bi_2WO_6 241
8.2.3 Characterization 242
8.2.4 Photocatalytic activity test 242
8.3 Results and discussions *244*
8.3.1 XRD and XPS analysis 244
8.3.2 FT-IR 248
8.3.3 Morphologies and proposed formation process 249
8.3.4 Optical properties 251
8.3.5 SQUID magnetometry and magnetic separation 252
8.3.6 Photocatalytic activity test 254
8.3.7 Proposed mechanism for photocatalytic degradation of organic compounds 261
8.4 Conclusions *262*

References *262*

SECTION VI: PHOTOREACTOR DESIGN **269**

CHAPTER 9 EXPERIMENTAL ANALYSIS OF A PHOTOREACTOR PACKED WITH Pd-$BiVO_4$-COATED GLASS BEADS 270

Abstract *270*

Nomenclature *270*

9.1 Introduction *271*

9.2 Experimental methods and materials *273*

9.2.1 Chemical and catalyst 273

9.2.2 Coating procedures 274

9.2.3 Photoreactor and system setup 274

9.2.4 Testing procedure and analysis methods 276

9.2.5 Mass transfer measurement 277

9.3 Results and discussion *277*

9.3.1 System validation 277

9.3.2 Experimental results 280

9.4 Conclusion *291*

References *292*

SECTION VII: CONCLUSIONS **296**

CHAPTER 10 GENERAL DISCUSSION AND CONCLUSIONS 297

SECTION VIII: APPENDICES **299**

APPENDIX A Ag/AgCl LOADED Bi_2WO_6 COMPOSITE: A PLASMONIC Z-SCHEME VISIBLE LIGHT-RESPONSIVE PHOTOCATALYST 300

Abstract *300*

A.1 Introduction *300*

A.2 Experimental *302*

A.2.1 Preparation of Bi_2WO_6 and Ag/AgCl-Bi_2WO_6 composites 302

A.2.2 Characterization 302

A.2.3 Photocatalytic activity test 303

A.3 Results and discussions *304*

A.3.1 XRD and XPS 304

A.3.2 SEM, EDS and TEM 308

A.3.3 UV-Vis diffused reflectance spectra (DRS) 311
A.3.4 Photocatalytic activity test under visible light 313
A.3.5 Roles of radical species 317
A.3.6 Reusability 318
A.3.7 Proposed mechanism of photocatalytic degradation 320
A.4 Conclusion *321*
References *321*
APPENDIX B Pd-DOPED Bi_2MoO_6 PLASMONIC PHOTOCATALYSTS WITH ENHANCED VISIBLE LIGHT PHOTOCATALYTIC PERFORMANCE 326
Abstract *326*
B.1 Introduction *326*
B.2 Experimental *328*
B.2.1 Synthesis of Bi_2MoO_6 328
B.2.2 Synthesis of $Pd/PdCl_2$-Bi_2MoO_6 328
B.2.3 Characterization 329
B.2.4 Photocatalytic activity tests 329
B.2.5 Electronic structure calculation 330
B.3 Results and discussions *331*
B.3.1 XRD and XPS 331
B.3.2 FT-IR 333
B.3.3 Morphologies 334
B.3.4 Optical properties 337
B.3.5 Photocatalytic activity test 339
B.3.6 Pathways for the photocatalytic degradation of phenol 342
B.3.7 Reusability 343
B.3.8 Mechanisms 344
B.4 Conclusions *346*
References *347*
APPENDIX C HIGHLY EFFICIENT DEGRADATION OF PHENOL OVER A Pd-BiOBr MOTT-SCHOTTKY PLASMONIC PHOTOCATALYST 354
Abstract *354*
C.1 Introduction *354*
C.2 Experimental *356*
C.2.1 Preparation of palladium particles 356
C.2.2 Preparation of BiOBr 356

C.2.3 Preparation of Pd -BiOBr composites 357
C.2.4 Characterization 357
C.2.5 Photocatalytic activity tests 358
C.3 Results and discussions *359*
C.3.1 Crystal structures analysis 359
C.3.2 Morphologies 360
C.3.3 Optical properties 361
C.3.4 Photocatalytic activity evaluation 362
C.3.5 Electrochemical properties 366
C.3.6 Proposed mechanism 369
C.4 Conclusions *370*
References *370*
APPENDIX D A COMPARISON OF Pd^0 NANOPARTICLES AND Pd^{2+} MODIFIED $Bi_2O_2CO_3$ FOR VISIBLE LIGHT-DRIVEN PHOTOCATALYSIS 377
Abstract *377*
D.1 Introduction *377*
D.2 Experimental *379*
D.2.1 Preparation 379
D.2.2 Characterization 379
D.2.3 Photocatalytic activity tests 380
D.3 Results and discussions *381*
D.3.1 Crystal structures and compositions analysis 381
D.3.2 Morphologies, optical properties and photocatalytic activity tests 383
D.3.3 Mechanism exploration 388
D.4 Conclusions *390*
References *391*
APPENDIX E ENHANCED PHOTOCATALYTIC ACTIVITY OF BiOBr/ZnO HETEROJUNCTION SEMICONDUCTORS PREPARED BY FACILE HYDROTHERMAL METHOD 396
Abstract *396*
E.1 Introduction *397*
E.2 Experiment *398*
E.2.1 Synthesis 398
E.2.2 Characterization 398

E.2.3 Photocatalytic Activity Test....399
E.3 Results and discussions.... *401*
E.3.1 XRD analysis....401
E.3.2 SEM analysis....402
E.3.3 UV-Vis diffuse reflection spectra (DRS)....405
E.3.4 Photocatalytic activity....407
E.4 Discussions and conclusions.... *411*
E.4.1 Mechanism of the enhancement effect....411
E.4.2 Conclusion....413
References.... *413*
APPENDIX F PLASMONIC Z-SCHEME Ag_2O-Bi_2MoO_6 p-n HETEROJUNCTION PHOTOCATALYSTS WITH GREATLY ENHANCED VISIBLE-LIGHT RESPONSIVE ACTIVITIES 417
Abstract.... *417*
F.1 Introduction.... *417*
F.2 Experimental.... *418*
F.2.1 Preparation of Bi_2MoO_6 and Ag_2O-Bi_2MoO_6....418
F.2.2 Characterization....419
F.2.3 Photocatalytic activity tests....419
F.3 Results and discussions.... *420*
F.4 Conclusions.... *424*
References.... *424*
APPENDIX G Bi_2MoO_6 CO-MODIFIED BY REDUCED GRAPHENE OXIDE AND PALLADIUM (Pd^{2+} AND Pd^0) WITH ENHANCED PHOTOCATALYTIC DECOMPOSITION OF PHENOL 426
Abstract.... *426*
G.1 Introduction.... *427*
G.2 Experimental.... *429*
G.2.1 Preparation of rGO-Bi_2MoO_6....429
G.2.2 Preparation of Pd-rGO-Bi_2MoO_6....429
G.2.3 Characterization....430
G.2.4 Photocatalytic activity tests....431
G.2.5 Electronic structure calculation....432
G.3 Results and discussions.... *432*

G.3.1 XRD and XPS 432
G.3.2 FT-IR 436
G.3.3 Morphologies and possible formation processes 437
G.3.4 N_2 sorption isotherms 439
G.3.5 Optical properties 441
G.3.6 Photocatalytic activity test 443
G.3.7 Reusability 445
G.3.8 Mechanism exploration 446
G.4 Conclusions *449*
References *449*
APPENDIX H PALLADIUM NANOPARTICLES AND rGO CO-MODIFIED $BiVO_4$ WITH GREATLY IMPROVED VISIBLE LIGHT-INDUCED PHOTOCATALYTIC ACTIVITY 458
Abstract *458*
H.1 Introduction *459*
H.2 Experimental *460*
H.2.1 Preparation of $BiVO_4$, rGO-$BiVO_4$ and Pd-rGO-$BiVO_4$ 460
H.2.2 Characterization 461
H.2.3 Photocatalytic activity tests 462
H.2.4 Electronic structure calculation 463
H.3 Results and discussions *464*
H.3.1 Crystal structure and surface components analysis 464
H.3.2 Morphologies and possible formation processes 467
H.3.3 Band structure analysis and optical properties 472
H.3.4 Photocatalytic activity tests 475
H.3.5 Mechanism exploration 480
H.4 Conclusions *487*
References *488*
APPENDIX I SYNERGETIC PHOTOELECTROCATALYTIC REACTORS FOR ENVIRONMENTAL REMEDIATION: A REVIEW 497
Abstract *497*
I.1 Introduction *497*
I.2 Mechanism of heterogeneous photoelectrocatalysis *499*
I.2.1 Photocatalysis 500

I.2.2 Photoelectrocatalysis....502
I.2.3 Affecting factors in designing PEC reactor....503
I.3 Types of photoelectrocatalytic reactor configuration....506
I.3.1 Slurry photoelectocatalytic reactor with three-dimensional electrodes....506
I.3.2 Immobilized photoelectrocatalytic reactor....511
I.4 Cost-effective composite system....532
I.5 Conclusions and future work for PEC reactor designs....538
References....539
APPENDIX J ACETIC ACID ASSISTED TO PREPARE Bi_2MoO_6 WITH VISIBLE-LIGHT-INDUCED ACTIVITY....560
Abstract....560
J.1 Introduction....560
J.2 Experimental....561
J.2.1 Preparation of Bi_2MoO_6....561
J.2.2 Characterizations....562
J.2.3 Photocatalytic activity testing....562
J.2.4 Electronic structure calculation....563
J.3 Results and Discussion....563
J.3.1 Morphology....563
J.3.2 XRD analysis....564
J.3.3 FT-IR....566
J.3.4 Optical properties....568
J.3.5 Photocatalytic activity test....570
J.4 Conclusions....573
References....573
APPENDIX K TWO DIMENSIONAL GRAPHITIC MATERIALS FOR PHOTOELECTROCATALYSIS: A SHORT REVIEW....579
Abstract:....579
K.1 Introduction....579
K.2 Graphitic materials implemented in photoelectrocatalysis....582
K.2.1 Graphene/reduced graphene oxide....582
K.2.2 Layered Transition Metal Dichalcogenides (TMDs)....586
K.2.3 Graphite-like carbon nitride (g-C_3N_4)....589
K.3 Concluding remarks and prospects....590

References *591*

APPENDIX L NEW INSIGHT INTO BiOX (X = Cl, Br, and I) HIERARCHICAL MICROSPHERES IN PHOTOCATALYSIS 599

Abstract: *599*

L.1 Introduction *599*

L.2 Experimental *600*

L.2.1 Preparation of BiOX microspheres 600

L.2.2 Characterizations 600

L.2.3 Adsorption tests 601

L.3 Results and discussions *601*

L.3.1 Morphologies and crystal structures 601

L.3.2 Adsorption 604

L.3.3 Optical properties 607

L.4 Conclusion *609*

References *609*

APPENDIX M RECENT ADVANCES OF COMPUTATIONAL PHOTOCATALYSIS: A REVIEW 611

Abstract *611*

M.1 Introduction *611*

M.2 Modelling of light absorption in photoreactors *612*

M.3 Mass transfer and reaction kinetics *618*

M.4 Computational methods for photocatalyst design *621*

M.4.1 Principles 621

M.4.2 Applications 627

M.4.3 Limitations 639

M.5 Evaluation of photocatalytic activity *639*

M.6 Concluding remarks *642*

Nomenclature *643*

References: *646*

APPENDIX N RESUME 660

List of Figures

Figure 2.1 Phase transfer of Bi_2O_3. 7

Figure 2.2 Bi_2S_3 (a) nanorods, (b) nanosheets, and (c) naonospheres. 8

Figure 2.3 Band structures of (a) Bi_2CrO_6, (b) Bi_2MoO_6, and (c) Bi_2WO_6. 9

Figure 2.4 (a) Diffused reflectance spectra and (b) photocatalytic kinetics of Bi_2WO_6 prepared by hydrothermal and SSR methods..... 10

Figure 2.5 SEM images of Bi_2WO_6 samples prepared by hydrothermal method (a) without surfactant, with (b) triblock poly(ethylene oxide)-block-poly(propylene oxide)-block-poly(ethylene oxide) copolymer ($EO_{20}PO_{70}EO_{20}$, Pluronic P123), (c) sodium dodecyl sulfate (SDS) and (d) polyvinyl pyrrolidone (PVP), and by solvothermal method with (e) nitric acid and (f) ethylene glycol (EG) as solvent. SEM images of Bi_2MoO_6 prepared by (g) hydrothermal and (h) solvothermal method..... 11

Figure 2.6 Two crystal structures of $BiVO_4$: tetragonal (left) and monoclinic (right). 12

Figure 2.7 Band structures of (a) BiOF, (b) BiOCl, (c) BiOBr, and (d) BiOI. 14

Figure 2.8 (a) Nanofibers of BiOCl, (b) nanosheets, and (c) microspheres of BiOI. 15

Figure 2.9 Comparison of photocatalytic kinetic constants in the presence of $BiPO_4$ and P25 on degradation of MO, RhB and 4-CP. 16

Figure 2.10 SEM images of $(BiO)_2CO_3$ prepared at 180°C for (a) 12h and (b) 24 h by hydrothermal method. 16

Figure 2.11 Flat band-edge positions of Bi-based semiconductor photocatalysts. 20

Figure 2.12 (a)Total density of states (TDOS) of the 3d-transition metal-doped TiO_2 (Gray solid line: TDOS; black solid line: DOS of dopants, (b) XPS valence band spectra of (a) $BiVO_4$ and (b) Ag-$BiVO_4$, and (c) TDOS of non-metal doped TiO_2. (Calculated by FLAPW, arb. Unit: arbitrary unit..... 23

Figure 2.13 (a) Mechanism of plasmon-induced charge transfer: (i) SPR-induced electrons transfer, (ii) electrons transfer to conduction band of nearby semiconductor, (iii)

electrons participate in the photocatalytic process. (b) Normalized extinction spectra of spherical Ag, Au, and Cu nanoparticles. 27

Figure 2.14 Mechanism of degradation of organic pollutants in presence of Ag/AgCl/$BiPO_4$. 27

Figure 2.15 Schematic processes of water splitting on photocatalytic semiconductors: (a) one photon process, (b) two photon process (Z scheme), and (c) process with an electron acceptor. 29

Figure 2.16 Schemes of (a) $(BiO)_2CO_3$-Bi_2S_3 n-n heterojunction and (b) BiOBr-Bi_2WO_6 p-n heterojunction. 32

Figure 2.17 Mechanism of photoelectrocatalysis in the improvement of electrons-holes separation by an external circuit. (a. recombination in bulk, b. recombination on the surface) 33

Figure 3.1 Spectra for the lamp (Ushio, USA) with and without the UV cut-off. 57

Figure 3.2 XRD patterns and lattice parameters of pure Bi_2WO_6, and Bi_2WO_6 composites with different quantities of doped Pd in the range of (a) 10° - 80° and (b) 27.5 – 29.0°. 59

Figure 3.3 XPS spectra of 4% Pd-Bi_2WO_6 composite: (a) survey spectra, and high-resolution orbital scans of (b) O1s, Pd3d for composites illuminated for 120 min (c), 60 min (d), and 30 min (e), and Cl2p for composites illuminated for 120 min (f), 60 min (g), and 30 min (h). 62

Figure 3.4 FT-IR spectra of pure Bi_2WO_6 (a) and those of Pd-Bi_2WO_6 composites with 0.5% (b), 1.0% (c), 2.0% (d), 4.0% (e), and 8.0% (f) Pd. 63

Figure 3.5 N_2 sorption isotherms for Bi_2WO_6 and Pd-Bi_2WO_6 composites. 64

Figure 3.6 UV-Vis diffuse reflectance spectra of pure Bi_2WO_6 and 4% Pd-Bi_2WO_6 powder samples, with $(\alpha E_{photon})^{1/2}$ vs E_{photon} curves shown in inset. 66

Figure 3.7 UV-Vis spectrum of palladium nanoparticles. 67

Figure 3.8 Low-resolution and high-resolution TEM images of pure Bi_2WO_6 (a, b) and 4%Pd-Bi_2WO_6 composite (c, d); EDS of 4%Pd-Bi_2WO_6 composite (f) at the point indicated in (e), and elemental mapping (g, h). 69

Figure 3.9 Photocatalytic degradation of phenol with pure Bi_2WO_6 and Pd-Bi_2WO_6 composites..... 70

Figure 3.10 Kinetic analysis of photocatalytic degradations with different photocatalysts 72

Figure 3.11 Concentrations of phenol and intermediates (hydroquinone, catechol, and benzoquinone) during the visible light-driven photocatalytic degradation process..... 74

Figure 3.12 Possible pathways for the photocatalytic degradation of phenol. 75

Figure 3.13 Phenol profiles during photocatalytic degradation with 4%Pd-Bi_2WO_6 composite and TiO_2 under UV light irradiation..... 77

Figure 3.14 Concentration profiles of intermediates hydroquinone, catechol and benzoquinone during photocatalytic degradation of phenol with TiO_2 and 4% Pd-Bi_2WO_6 under UV light irradiation. 78

Figure 3.15 Relative amount of benzene ring during the degradation process in presence of TiO_2 and 4% Pd-Bi_2WO_6 under UV light irradiation. 78

Figure 3.16 Phenol removal efficiency of recycled 4% Pd-Bi_2WO_6. 79

Figure 3.17 XPS high-resolution orbits scan of Pd3d and Cl2p for Pd/$PdCl_2$-Bi_2WO_6 after degradation of phenol under irradiation for 300 min. 80

Figure 3.18 XRD patterns for Pd/$PdCl_2$-Bi_2WO_6 prepared under illumination for 1h and 2h, and after degradation of phenol over 300 min. 81

Figure 3.19 EIS Nyquist plots of the Bi_2WO_6 and 4%Pd-Bi_2WO_6 photocatalysts..... 82

Figure 3.20 PL spectra for Bi_2WO_6 and Pd-Bi_2WO_6 composites at an excitation wavelength of 300 nm. 83

Figure 3.21 Photocatalytic degradation of phenol by 4%Pd-Bi_2WO_6 with and without quenchers (EDTA-2Na, 1-butanol and N_2 bubbling)..... 84

Figure 3.22 Proposed mechanism for the degradation of phenol with photocatalyst Pd-Bi_2WO_6..... 85

Figure 4.1 SEM photos of BiOBr at (a) low and (b) high magnification, 0.5 Pd-Bi at (c) low and (d) high magnification, and EDS spectra for pure BiOBr and 0.5 Pd-Bi. 102

Figure 4.2 TEM images of BiOBr at (a) low and (b) high magnification, and 0.5 Pd-Bi at (c) low and (d) high magnification; Inset of (d): size distribution of Pd nanoparticles on the surface. 103

Figure 4.3 XRD patterns for pure BiOBr and Pd-BiOBr composites..... 104

Figure 4.4 Survey spectra for pure BiOBr and 0.5 Pd-Bi samples. 106

Figure 4.5 High-resolution XPS orbital scan for Pd 3d orbits of 0.5 Pd-Bi sample. 106

Figure 4.6 Possible formation process of Pd NP-decorated BiOBr composites. 107

Figure 4.7 Flat-band structure as well as total/partial density of states calculated for pure BiOBr (the top of valence band is fixed at 0 eV)..... 109

Figure 4.8 UV-Vis diffused reflectance spectra (DRS) for pure BiOBr and Pd-BiOBr composites..... 110

Figure 4.9 pH_{pzc} plot of BiOBr and 0.5 Pd-Bi samples. 111

Figure 4.10 N_2 sorption isotherms and pore size distributions for (a) BiOBr and (b) 0.5 Pd-Bi, respectively..... 112

Figure 4.11 (a) Photocatalytic degradation of phenol in the presence of prepared samples under visible light irradiation (c_o = 10 mg/L; photocatalysts dosage amount = 1 g/L; T = 20°C); and (b) Chromatogram of the separation in a C18 column of phenol (t_R = 9.1 min). Samples taken from the suspension containing 0.5 Pd-Bi composites. 115

Figure 4.12 PL spectra of BiOBr, 0.5 Pd-Bi and 0.8 Pd-Bi composites (excitation wavelength = 300 nm)..... 116

Figure 4.13 (a) EIS Nyquist plots and (b) transient photocurrent responses of the BiOBr and Pd-BiOBr electrodes. 118

Figure 4.14 Schematic of charge separation for photocatalysis over Pd-BiOBr composite under visible light irradiation. 120

Figure 5.1 XRD patterns of prepared $BiVO_4$ and Pd-$BiVO_4$ composites, as well as standard XRD patterns for $BiVO_4$. 134

Figure 5.2 XPS spectra of prepared $BiVO_4$ and Pd-$BiVO_4$: (a) survey, (b) Bi 4f and (c) V 2p, as well as (d) Pd 3d and (e) Cl 2p for Pd-$BiVO_4$. 137

Figure 5.3 Low- and high-magnification SEM images of pure $BiVO_4$ (a, b) and Pd-$BiVO_4$ composites (c, d); TEM images for pure $BiVO_4$ in low (e) and high (f) magnification, and Pd-$BiVO_4$ composites in low (g) and high (h) magnification. 138

Figure 5.4 Possible formation process of Pd nanoparticles decorated $BiVO_4$ composites. 140

Figure 5.5 Band structure and density of states for $BiVO_4$ calculated by the DFT method (Fermi level fixed at band energy of 0 eV). 141

Figure 5.6 UV-Vis diffused reflectance spectra for prepared $BiVO_4$ and Pd-$BiVO_4$ composites..... 143

Figure 5.7 Concentration profiles of phenol in the presence of different photocatalysts under visible light irradiation (c_o = 10 mg/L, catalysts dosage: 1 g/L and temperature: 20°C). 144

Figure 5.8 (a) Possible reactions in the presence of $BiVO_4$ under visible light irradiation, (b) Possible oxidation of phenol through photo-generated oxidants including holes and OH radicals. 146

Figure 5.9 Concentrations of phenol in the presence of 8% Pd-$BiVO_4$ with or without addition of scavengers..... 146

Figure 5.10 Photocatalytic degradation of pCBA with TiO_2 under UV irradiation as well as $BiVO_4$ and 8%Pd-$BiVO_4$ composites under visible light irradiation. 148

Figure 5.11 Chromatogram of the separation in a C18 column of: benzoquinone (BQ, t_R = 6.5 min), hydroquinone (HQ, t_R = 8.3 min), catechol (CA, t_R = 9.0 min) and phenol (t_R = 10.2 min). Samples taken from the suspension containing 8% Pd-$BiVO_4$ composites (left) and TiO_2 (right). 150

Figure 5.12 Concentrations of benzoquinone, hydroquinone, catechol and phenol during the photolysis processes in the presence of 8%Pd-$BiVO_4$ under visible light irradiation and TiO_2 under UV irradiation. 150

Figure 5.13 Relative TOC and phenol concentrations in the photocatalysis processes with pure $BiVO_4$ and 8% Pd-$BiVO_4$ under visible light irradiation, as well as TiO_2 under UV irradiation, respectively. 151

Figure 5.14 Possible pathways for the photocatalytic degradation of phenol in the presence of Pd-$BiVO_4$ under visible light irradiation. 151

Figure 6.1 Schematic preparation of MoS_2 QDs-interspersed Bi_2WO_6 composites via a bath sonication method. 167

Figure 6.2 XRD patterns of prepared samples, and standard XRD patterns for pure Bi_2WO_6 (PDF card # 39-0256) and MoS_2 (PDF card # 24-0513). 171

Figure 6.3 XPS spectra of MoS_2-Bi_2WO_6 composites: (a) survey, (b) Mo 3d and (c) S 2p. 173

Figure 6.4 SEM images of (a) pure Bi_2WO_6, (b) pure MoS_2 and (c) MoS_2-Bi_2WO_6 composites; and TEM images of (d) pure Bi_2WO_6 and (e, f) MoS_2-Bi_2WO_6 composites. 175

Figure 6.5 UV-Vis Diffuse Reflectance spectra and the plots of $(\alpha \times E_{photon})^{1/2}$ vs. E_{photon} (inset) of pure Bi_2WO_6, MoS_2 and MoS_2-Bi_2WO_6 composites. 177

Figure 6.6 N_2 sorption isotherms for Bi_2WO_6, MoS_2-Bi_2WO_6 and MoS_2. 178

Figure 6.7 (a) RhB adsorption isotherms (b) Pseudo second-order modelling for pure Bi_2WO_6, MoS_2 and MoS_2-Bi_2WO_6 composites, where dash lines in (a) and (b)

represent Pseudo second-order modelling results and fitting lines, respectively. 180

Figure 6.8 Photocatalytic degradation of RhB in the presence of prepared samples under visible light irradiation. (Catalyst dosages: 1g/L, initial concentration of RhB: 10 mg/L, Temperature: 20°C)..... 182

Figure 6.9 UV-Vis spectra of RhB samples taken during the photocatalytic process in the presence of 1.0% MoS_2-Bi_2WO_6. 184

Figure 6.10 Changes in TOC concentration during the course of photocatalytic degradation of RhB in the presence of prepared samples under visible light irradiation. (Catalyst dosages: 1g/L, initial concentration of RhB: 10 mg/L, Temperature: 20°C)..... 185

Figure 6.11 Recycling 1.0% MoS_2-Bi_2WO_6 composites for four runs in the degradation of RhB under visible light irradiation..... 186

Figure 6.12 (a) Inactivation curves for dark control, photolysis and irradiated composite; (b) photos of E. coli colonies on an agar plate for samples taken and spread at different time during the photocatalytic disinfection in the presence of 1%MoS_2-Bi_2WO_6..... 188

Figure 6.13 EIS Nyquist plots of the Bi_2WO_6 and MoS_2-Bi_2WO_6 photocatalysts. 189

Figure 6.14 (a, b) Band structure for Bi_2WO_6 and MoS_2. (c, d) Partial and total density of states (PDOS and TDOS) for Bi_2WO_6 and MoS_2. (Simulated by Quantum Espresso 191

Figure 6.15 Proposed mechanism of photogenerated electrons and holes transfer for MoS_2-Bi_2WO_6 composite under visible light irradiation. 193

Figure 7.1 Photoreactor geometry and positioning. 206

Figure 7.2 (a) XRD patterns of prepared samples; (b) fragments of enlarged XRD patterns for pure Bi_2MoO_6, GO-Bi_2MoO_6, rGO-Bi_2MoO_6 and 16% Ag-rGO-Bi_2MoO_6. 208

Figure 7.3 XPS survey spectra of pure Bi_2MoO_6, GO-Bi_2MoO_6 and Ag-rGO-Bi_2MoO_6. 211

Figure 7.4 High-resolution orbits scan of (a) Bi 4f, (b) Mo 3d, (c) C 1s, (d) O 1s, (e) Ag 3d and (f) Cl 2p in prepared samples. 213

Figure 7.5 FT-IR of prepared samples: Bi_2MoO_6, GO-Bi_2MoO_6, rGO-Bi_2MoO_6 and Ag-rGO-Bi_2MoO_6. 214

Figure 7.6 SEM images of (a) Bi_2MoO_6, (b) rGO-Bi_2MoO_6 and (c, d) Ag-rGO-Bi_2MoO_6 in low- and high-magnification, STEM images of (e) Ag-rGO-Bi_2MoO_6, and high-resolution TEM image of Ag-rGO-Bi_2MoO_6. 217

Figure 7.7 EDS of Bi_2MoO_6 and Ag-rGO-Bi_2MoO_6. 217

Figure 7.8 Proposed formation process for Ag (Ag^0 and AgCl)-, rGO-comodified Bi_2MoO_6. 218

Figure 7.9 Nitrogen adsorption-desorption isotherms and the corresponding pore size distribution curves (insets) of (a) Bi_2MoO_6, (b) GO-Bi_2MoO_6, (c) rGO-Bi_2MoO_6, and (d) 8 wt%Ag-rGO-Bi_2MoO_6. 219

Figure 7.10 DRS of prepared samples: Bi_2MoO_6, Ag/AgCl, GO-Bi_2MoO_6, rGO-Bi_2MoO_6 and Ag-rGO-Bi_2MoO_6 composites. 221

Figure 7.11 Concentration profiles of phenol during the photocatalytic degradation tests in the presence of different photocatalyst composites under visible light irradiation. 223

Figure 7.12 Adsorption profiles of phenol on samples: GO, rGO, Bi_2MoO_6, GO-Bi_2MoO_6 and rGO-Bi_2MoO_6..... 225

Figure 7.13 EIS Nyquist plots of the Bi_2MoO_6, Ag-Bi_2MoO_6, rGO-Bi_2MoO_6, and Ag-rGO-Bi_2MoO_6 photocatalysts. 226

Figure 7.14 (a) Relative concentration of phenol with different scavengers added, and (b) concentrations of phenol and possible intermediates (hydroquinone, catechol and benzoquinone) in the presence of Ag-rGO-Bi_2MoO_6 composites under visible light irradiation. 228

Figure 7.15 Proposed photocatalytic degradation of organics in the presence of Ag-rGO-Bi_2MoO_6 composites under visible light irradiation. 229

Figure 8.1 Schematic of photocatalytic reactor 243

Figure 8.2 XRD patterns of prepared samples. 245

Figure 8.3 XPS survey spectrum of Ag/AgCl-(M) Bi_2WO_6. 247

Figure 8.4 High-resolution orbital scan of Ag 3d in Ag/AgCl-(M) Bi_2WO_6 composite. 247

Figure 8.5 FTIR of prepared samples. 248

Figure 8.6 TEM photos of (a) Bi_2WO_6, (b) Ag/AgCl-Bi_2WO_6, (c) Fe_3O_4, (d) SiO_2-Fe_3O_4, (e) magnetic Bi_2WO_6, and (f) Ag/AgCl-(M) Bi_2WO_6. 250

Figure 8.7 Possible process for formation of Ag/AgCl-(M) Bi_2WO_6. 251

Figure 8.8 DRS of prepared samples. 252

Figure 8.9 Room temperature magnetization hysteresis loops of (M) Bi_2WO_6 and Ag/AgCl-(M) Bi_2WO_6. (Inset: magnetic separation using Ag/AgCl-(M) Bi_2WO_6 exposed to cubic NdFeB magnets) 253

Figure 8.10 Photocatalytic degradation of RhB in the presence of prepared samples under visible light irradiation. (c_o = 10 mg/L, catalyst dosage = 1 g/L, T = 20°C) 256

Figure 8.11 Photocatalytic kinetics of each process in the degradation of RhB under visible light irradiation. 257

Figure 8.12 UV-Vis spectra of samples taken from reactor in the presence of Ag/AgCl-(M) Bi_2WO_6 (left) and Ag/AgCl-Bi_2WO_6 (right) with regards to RhB. 257

Figure 8.13 Concentration of phenol in the solution with prepared samples under visible light irradiation. (Catalysts dosage = 1 g/L, T = 20 °C) 259

Figure 8.14 Photocatalytic kinetics of each process in the degradation of phenol under visible light irradiation. 260

Figure 8.15 (a) Chromatograms of samples taken at different time and (b) calculated concentration profiles of phenol and possible intermediates (hydroquinone,

catechol and benzoquinone) in the presence of Ag/AgCl-(M) Bi_2WO_6 under visible light irradiation. 260

Figure 8.16 Possible pathways for the photocatalytic degradation of phenol. 261

Figure 8.17 Proposed mechanism for the photocatalytic degradation of organic compounds in the presence of Ag/AgCl-(M) Bi_2WO_6. 262

Figure 9.1 Schematic of the experimental packed beads reactor with dimensions. 275

Figure 9.2. Schematic of the experimental system setup. 276

Figure 9.3. Photos of coated beads and stainless steel plates: (a) bare glass beads (d = 5 mm); (b) $BiVO_4$, (c) Pd-$BiVO_4$ (0.1 g/ 100 mL glass beads), (d) Pd-$BiVO_4$ (0.5 g/ 100 mL glass beads), and (e) TiO_2 (0.5 g/ 100 mL glass beads) coated glass beads (d = 5 mm); (f) Pd-$BiVO_4$ and (g) TiO_2 coated stainless steel plates. 279

Figure 9.4. SEM images of (a) Pd-$BiVO_4$ coated glass beads and (b) Pd-$BiVO_4$, and TEM image of Pd-$BiVO_4$ (size distribution of palladium nanoparticles). 280

Figure 9.5. Light distribution at different thickness of beads (diameter: 5 mm) 282

Figure 9.6. Effect of volume of coated beads on degradation kinetics (c_o = 5 mg/L; f = 5 GPH; T = 25°C, lines: fittings). 283

Figure 9.7. Geometry of the cross-section of a bead. 286

Figure 9.8. Energy distribution for a glass bead. 287

Figure 9.9. Effect of diameter of coated beads on degradation kinetics (c_o = 5 mg/L; f = 5 GPH; T = 25°C, lines: fittings). 288

Figure 9.10. Effect of concentration of photocatalysts on coated beads (diameter: 5 mm) on degradation kinetics (c_o = 5 mg/L; f = 5 GPH; T = 25°C, lines: fittings). 289

Figure 9.11. Photocatalytic degradation of phenol in different systems (For the systems with flat plate and glass beads: c_o = 5 mg/L; f = 5 GPH; T = 25°C, lines: fittings). 290

Figure A.1 XRD patterns of as-prepared samples: pure Bi_2WO_6, Ag/AgCl and Ag/AgCl-Bi_2WO_6 composites. 305

Figure A.2 XRD pattern of Ag/AgCl (10 wt%)-Bi_2WO_6 306

Figure A.3 XPS spectra of Ag/AgCl (10 wt%)-Bi_2WO_6 composite: (a) survey spectra, and high-resolution orbits scan of (b) Bi 4f, (c) W4f, (d) O 1s, (e) Ag 3d and (f) Cl 2p. 308

Figure A.4 SEM images of pure Bi_2WO_6 (a) and Ag/AgCl (10 wt%)-Bi_2WO_6 composite (b), and TEM images of Ag/AgCl (10 wt%)-Bi_2WO_6 composite (c). 309

Figure A.5 EDS of Ag/AgCl (10 wt%)-Bi_2WO_6 composite. 309

Figure A.6 Potential mechanism of forming the hierarchical flower-like superstructure of Bi_2WO_6 310

Figure A.7 (a) UV-Vis diffused reflectance spectra and (b) $(\alpha E_{photon})^{1/2}$-$E_{photon}$ curves of as-prepared pure Bi_2WO_6, Ag/AgCl and Ag/AgCl (10 wt%)-Bi_2WO_6. 312

Figure A.8 Band gap of Bi_2WO_6. (Simulated by Quantum Espresso) 313

Figure A.9 Photocatalytic degradation of RhB (10 mg/L) under visible light with as-prepared pure Bi_2WO_6, Ag/AgCl and Ag/AgCl-Bi_2WO_6 composites. 315

Figure A.10 Photocatalytic kinetics of each process. 316

Figure A.11 UV-Vis spectra of solutions taken during the photocatalytic process in the presence of Ag/AgCl (10 wt%)-Bi_2WO_6 (inset table shows characteristic wavelength for each intermediate species in water). 316

Figure A.12 Degradation of Phenol (10 mg/L) by using Ag/AgCl-Bi_2WO_6 composite. 317

Figure A.13 Photocatalytic activity in presences of Ag/AgCl/-Bi_2WO_6 and quenchers. 318

Figure A.14 Removal efficiencies for 4 runs of 45 min. 319

Figure A.15 XRD patterns of Ag/AgCl (10 wt%)-Bi_2WO_6 before and after 4 runs. 320

Figure A.16 Schematic of possible mechanism of degrading RhB in the presence of Ag/AgCl-Bi_2WO_6 321

Figure B.1 Photoreactor geometry and positioning. 330

Figure B.2 XRD patterns of pure Bi_2MoO_6, and Bi_2MoO_6 composites with different quantities of doped Pd. 331

Figure B.3 XPS spectra of 2% Pd-Bi_2MoO_6 composite: (a) survey, and high-resolution orbital scan of (b) O 1s, (c) Pd 3d and (d) Cl 2p. 333

Figure B.4 FT-IR spectra of pure Bi_2MoO_6 and those of Pd-Bi_2MoO_6 composites with different quantities of Pd. 334

Figure B.5 SEM images of (a) pure Bi_2MoO_6 and (b) Pd-Bi_2MoO_6, and (c) TEM/HRTEM images of Pd-Bi_2MoO_6. 336

Figure B.6 DRS of pure Bi_2MoO_6 and Pd-Bi_2MoO_6 composites. 338

Figure B.7 Total and partial densities of states (DOS) of relaxed Bi_2MoO_6 and Pd-Bi_2MoO_6. 338

Figure B.8 Photocatalytic degradation of phenol in the presence of pure Bi_2MoO_6 and Pd-Bi_2MoO_6 composites. 340

Figure B.9 Photocatalytic kinetic analysis of processes in the presence of pure Bi_2MoO_6 and Pd-Bi_2MoO_6 composites. 341

Figure B.10 Concentrations of phenol, hydroquinone, catechol and benzoquinone during the degradation process in the presence of 2% Pd-Bi_2MoO_6 under visible light irradiation. 343

Figure B.11 Possible pathways for the photocatalytic degradation of phenol in the presence of Pd-Bi_2MoO_6 under visible light irradiation. 343

Figure B.12 Removal efficiencies of phenol with recycled 2% Pd-Bi_2MoO_6. 344

Figure B.13 EIS Nyquist plots of the Bi_2MoO_6 and 2% Pd-Bi_2MoO_6 photocatalysts. .. 345

Figure B.14 Photocatalytic mechanism of Pd-Bi_2MoO_6 composite under visible light. 346

Figure C.1 Spectra for the lamp (Ushio, USA) with and without the UV cut-off. 358

Figure C.2 XRD patterns of prepared samples. 360

Figure C.3 TEM images of (a) Pd particles, (b) BiOBr, (c) Pd-Bi composites, and (d) EDS spectra of BiOBr and Pd-Bi composites. 361

Figure C.4 DRS spectra of BiOBr as well as Pd-Bi composites. (Inset: UV-Vis-Infrared spectroscopy Pd particles dispersed in ethanol)..... 362

Figure C.5 (a) Phenol concentration profiles of systems in the presence of various prepared samples under visible light irradiation; (b) pseudo first-order reaction constants and TOC removal fraction of different systems..... 364

Figure C.6 (a) Photocatalytic degradation of phenol in the presence of Pd-BiOBr composites prepared with different methods; and TEM images for Pd-BiOBr prepared by one-pot (b) and photodeposition (c) methods, respectively. 365

Figure C.7 Removal efficiencies of phenol with recycled 1.0 Pd-Bi composites. 366

Figure C.8 (a) EIS Nyquist plots, (b) Bode plot curves, (c) transient photocurrent response and (d) Mott-Schottky plots of BiOBr and Pd-Bi electrodes. 368

Figure C.9 Proposed mechanism of the enhancement in photocatalysis of loading palladium cubic on the surface of BiOBr..... 370

Figure D.1 XRD patterns for pure $Bi_2O_2CO_3$, Pd(0)-Bi and Pd(II)-Bi composites..... 382

Figure D.2 FTIR for pure $Bi_2O_2CO_3$, Pd(0)-Bi and Pd(II)-Bi composites. 382

Figure D.3 High-resolution orbital scans of (a) Pd 3d and (b) Cl 2p for Pd(0)-Bi and Pd(II)-Bi composites. 383

Figure D.4 TEM image of Pd(0)-Bi composite. 384

Figure D.5 N_2 adsorption-desorption isotherm of for pure $Bi_2O_2CO_3$, Pd(0)-Bi and Pd(II)-Bi composites (the inset shows the enlarged isotherm at p/p_0 = 0.80-1.00). 385

Figure D.6 (a) DRS for pure $Bi_2O_2CO_3$, Pd(0)-Bi and Pd(II)-Bi composites, and (b) UV-Visible spectrum for palladium nanoparticles. 386

Figure D.7 Photocatalytic degradation of RhB in the presence of various prepared samples. 387

Figure D.8 TOC removal ratio for photocatalytic degradation of RhB in presence of various photocatalysts. 387

Figure D.9 EIS Nyquist plots of prepared samples (inset: equivalent circuit). 388

Figure D.10 (a) Crystal structures, and (b) total density of states of $Bi_2O_2CO_3$ with and without Pd(II) doping 389

Figure D.11 Proposed mechanism for the photocatalytic degradation process in the presence of (a) Pd(0)-Bi and (b) Pd(II)-Bi. 390

Figure E.1 Calibration curve of plotting absorption intensities at various concentration of RhB. 400

Figure E.2 XRD patterns of pure ZnO, BiOBr, and 5 wt.% BiOBr-ZnO, 10 wt.%-ZnO, 15 wt.% BiOBr-ZnO, 25 wt.% BiOBr-ZnO, 50 wt.% BiOBr-ZnO and 75 wt.% BiOBr-ZnO composites synthesized by hydrothermal method. 402

Figure E.3 SEM images of pure ZnO at low (a) and high (b) magnification, 50 wt. % BiOBr-ZnO composites at low (c) and high (d) magnification, and pure BiOBr from different direction (e, f). 404

Figure E.4 Possible formation processes of hourglass-like ZnO, flake-like microspheres, and the SEM image of final BiOBr-ZnO composite. 405

Figure E.5 (a) Diffused reflectance spectra (DRS) and (b) $(\alpha * E_{photon})^n$-E_{photon} curves of pure ZnO and 50 wt.% BiOBr-ZnO composites. 406

Figure E.6 Band structure of ZnO (left) and BiOBr (right). (simulated by using Quantum Espresso). 407

Figure E.7 Photocatalytic degradation efficiencies of RhB as a function of time by loading various photocatalysts. (Dosage amount of photocatalysts: 0.5 g/L, initial concentration of RhB: 10 mg/L and temperature of the system: 25 °C) 408

Figure E.8 Kinetics for each photocatalytic process by plotting $\ln(c_o/c)$ vs time. 409

Figure E.9 Photocatalytic degradation efficiencies of RhB with or without cut-off. (Dosage amount of photocatalysts: 0.5 g/L, initial concentration of RhB: 10 mg/L and temperature of the system: 25 °C) 410

Figure E.10 Removal efficiencies in degrading RhB by using 50 wt.% BiOBr-ZnO synthesized by hydrothermal method and mixed mechanically. 411

Figure E.11 Diagram of band structure for BiOBr/ZnO composite and the possible photocatalytic degradation process. 412

Figure F.1 (a) XRD patterns, (b) XPS survey spectrum, (c) O 1s orbits scan and (d) Ag 3d orbits scan of prepared samples. 421

Figure F.2 (a) DRS of prepared samples, (b) RhB and (d) phenol removal profiles during photocatalytic degradation process, and (c) UV-Vis spectra of RhB samples taken during the degradation process. 422

Figure F.3 (a) SEM image of 15%Ag_2O-Bi_2MoO_6, (b) EIS Nyquist plot of pure Bi_2MoO_6 and 15%Ag_2O-Bi_2MoO_6, (c) study of active species for 15% Ag_2O-Bi_2MoO_6 in photocatalysis and (d) proposed mechanism of the enhancement. 423

Figure G.1 Scheme of preparation processes of Pd-rGO-Bi_2MoO_6. 430

Figure G.2 XRD patterns of as-prepared composites: (a) pure Bi_2MoO_6, (b) GO-Bi_2MoO_6, (c) rGO-Bi_2MoO_6 and (d) Pd-rGO-Bi_2MoO_6..... 433

Figure G.3 (a) XPS survey spectra, and high –resolution orbits scan of (b) C 1s, (c) O 1s, (d) Pd 3d and (e) Cl 2p for GO- and Pd-rGO-Bi_2MoO_6 composites, respectively. 436

Figure G.4 FTIR spectra for (a) pure Bi_2MoO_6 and (b) GO-, (c) rGO-, (d) Pd-rGO-Bi_2MoO_6 composites. 437

Figure G.5 SEM images for (a) pure Bi_2MoO_6 and (b) Pd-rGO-Bi_2MoO_6 composites, STEM image for Pd-rGO-Bi_2MoO_6 composites, and TEM image for Pd-rGO-Bi_2MoO_6 composites. 438

Figure G.6 EDS spectra for (a) pure Bi_2MoO_6 and (b) Pd-rGO-Bi_2MoO_6 composites. . 439

Figure G.7 N_2 sorption isotherms and pore size distributions for (a) Bi_2MoO_6, (b) GO-Bi_2MoO_6, (c) rGO-Bi_2MoO_6, and (d) Pd-rGO-Bi_2MoO_6, respectively. 440

Figure G.8 UV-Vis spectra for as-prepared samples. 442

Figure G.9 Calculated band structure, and Density of states (DOS) and partial density of states (PDOS) for pure Bi_2MoO_6 (Fermi level fixed at band energy of 0 eV). 442

Figure G.10 Concentration profiles of phenol during the photocatalytic degradation tests in the presence different as-prepared photocatalysts under visible light irradiation. 444

Figure G.11 Reusability of 2% Pd-rGO-Bi_2MoO_6 composites with regard to phenol under visible light irradiation. 446

Figure G.12 EIS Nyquist plots of the Bi_2MoO_6, rGO-Bi_2MoO_6 and Pd-rGO-Bi_2MoO_6 samples. 447

Figure G.13 Proposed mechanism of photocatalytic degradation of phenol in the presence of Pd-rGO-Bi_2MoO_6 composites. 449

Figure H.1 XRD patterns of as-prepared samples. 464

Figure H.2 (a) XPS survey spectra for $BiVO_4$ and Pd(G)-Bi, and high-resolution orbital scans of (b) Pd 3d for Pd(G)-Bi, (c) C 1s for $BiVO_4$, GO-Bi and rGO-Bi and (d)Bi 4f for $BiVO_4$, rGO-Bi and Pd(G)-Bi. 467

Figure H.3 SEM images of (a) $BiVO_4$, (b) rGO-Bi and (c) Pd(G)-Bi, and (d) EDS spectra for pure $BiVO_4$ and Pd(G)-Bi. 468

Figure H.4 TEM images of (a) GO, (b) $BiVO_4$, (c) rGO-Bi and (d) Pd(G)-Bi (inset: particle sizes distribution). 469

Figure H.5 TEM images of Pd(G)-Bi composites. 470

Figure H.6 Schematic illustration of preparation of Pd(G)-Bi composites and photos for prepared samples. 472

Figure H.7 Band configuration of $BiVO_4$ simulated using the Quantum Espresso code [43], and pathways of electrons recombined with holes. 473

Figure H.8 UV-Vis diffused reflectance spectra (DRS) for prepared samples. 475

Figure H.9 Plots of $(\alpha E_{photon})^{1/2}$ vs E_{photon} for prepared samples. 475

Figure H.10 Photocatalytic degradation of phenol in the presences of prepared samples under visible light irradiation. 477

Figure H.11 Five cycles for degradation of phenol over 1.0 Pd(G)-Bi photocatalysts. . 478

Figure H.12 Possible pathways of phenol in the photocatalytic degradation process in the presence of 1.0 Pd(G)-Bi composites. 481

Figure H.13 Concentrations of phenol as well as produced intermediates: benzoquinone (BQ), hydroquinone (HQ) and catechol (CA) along with the photocatalytic process in the presence of 1.0 Pd(G)-Bi composites under visible light irradiation (Inset: TOC change before and after the photocatalysis). 482

Figure H.14 (a) Photocatalytic degradation phenol in the presence of 1.0 Pd(G)-Bi composites with or without adding scavengers; (b) Photocatalytic degradation of p-CBA in the presence of TiO_2 under UV light as well as $BiVO_4$ and 1.0 Pd(G)-Bi under visible light irradiation. 484

Figure H.15 (a) EIS Nyquist plots and (b) the Bode plot curves of $BiVO_4$, rGO-Bi, Pd(G)-Bi and Pd-Bi. 486

Figure H.16 Proposed processes of photocatalytic degradation of phenol in the presence of Pd(G)-Bi composites. 487

Figure I.1 Schematic processes of photocatalysis when combined with an external circuit (a) recombination in bulk (b) recombination on the surface. 503

Figure I.2 Line source geometry. 505

Figure I.3 Scheme of (a) parabolic trough reactor (PTR) and (b) compound parabolic collector (CPC). 506

Figure I.4 Diagram of cell with three-dimensional 507

Figure I.5 Diagram of three-dimensional electrode slurry PEC reactor (1. Stainless steel cathode 2. Recycled water outlet 3. Granulated activated carbon layer 4. Microporous plate 5. Pressured air inlet 6. Recycled water inlet 7. TiO_2 particle layer 8. Stainless steel anode 9. UV lamp). 507

Figure I.6 Diagram of three-dimensional electrode packed bed PEC reactor (1, 5. Recycled water in/out 2. Purified solution 3. Packed TiO_2 particle 4. Microporous plate 6. UV lamp 7. Solution inlet 8. Pressured air inlet) 508

Figure I.7 Scheme of Three-dimensional reactor, and two-dimentional reactor when without the particle electrode 510

Figure I.8 Diagram of cylinder groove PEC reactor with the external light source. 512

Figure I.9 Diagram of cylindrical PEC reactor (1. Lamp 2. Photoanode 3. Counter electrode 4. Outer glass tube) 514

Figure I.10 Top view of the PEC reactor. 515

Figure I.11 Cylindrical PEC reactor with bar-type electrode fixed by Teflon support (a) 1. Liquid outlet 2. Cathode 3. Anode 4. Liquid inlet 5. Telflon support 6. UV-vis lamp (b) Teflon support. 515

Figure I.12 Schematic diagram of the TNAs based thin-layer PEC reactor (a) front view and (b) side view. 518

Figure I.13 Diagram of dual slant-placed electrodes thin-film PEC reactor. 519

Figure I.14 Diagram of vortex reactor. 521

Figure I.15 Diagram of rotating disk PEC reactor. 523

Figure I.16 Schematic cross section of cylindrical PEC reactor. 525

Figure I.17 PEC reactors in operation: (a) left, Helioman module (b) right, CPCs..... 525

Figure I.18 Thin-layer reactor used in PECOD analysis. 527

Figure I.19 (a) overview and (b) illustration of hybrid system (electrolysis and photocatalysis). 529

Figure I.20 (a) Schematic of the flat-plate PEC reactor (b) photoelectrocatalytic unit (c) photoelectrocatalytic electrodes. 531

Figure I.21 Schematic diagram of the composite system. 533

Figure J.1 SEM images of Bi_2MoO_6 prepared at 120°C for (a) 6h, (b) 12h, (c) 24h and (d) 48h. 564

Figure J.2 XRD patterns of Bi_2MoO_6 synthesized under different hydrothermal temperature for 24 hours. 565

Figure J.3 XRD patterns of Bi_2MoO_6 synthesized at 120 °C for different duration..... 566

Figure J.4 Proposed crystal growth in the directions of plane (060) and (062)..... 566

Figure J. 5 FT-IR spectra of Bi_2MoO_6 samples prepared (a) at different temperature for 24h and (b) at 120°C for different hydrothermal duration time..... 568

Figure J.6 Band structure of Bi_2MoO_6. (The red dash line represents the Fermi level) . 569

Figure J.7 Total and partial DOS of relaxed Bi_2MoO_6. 570

Figure J.8 DRS of as-prepared Bi_2MoO_6 (red line) with corresponding $(\alpha E_{photon})^{1/2}$ vs E_{photon} curves shown in inset, and simulated UV-Vis absorption properties of relaxed Bi_2MoO_6 (blue dash line). 570

Figure J.9 Photocatalytic degradation RhB in the presences of Bi_2MoO_6 prepared at different temperature for 24 h under visible light irradiation. 572

Figure J.10 Photocatalytic degradation RhB in the presences of Bi_2MoO_6 prepared at 120°C for different time under visible light irradiation. 572

Figure J.11 Photocatalytic degradation of RhB in the presence of Bi_2MoO_6 samples prepared with and without acetic acid in the precursor (inset: photocatalytic degradation of phenol in the presence of Bi_2MoO_6 prepared assisted with acetic acid)..... 573

Figure K.1 Number of yearly publications with topic keywords of (a) 'photocatalysis', (b) 'photocatalysis' + 'graphene', (c) 'photoelectrocatalysis' and (d) 'photoelectrocatalysis' + 'graphene'. (Searched on November 19, 2017, using the SCOPUS database)..... 581

Figure K.2 Schematic processes of photoelectrocatalysis when combined with an external circuit. 581

Figure K.3 Electronic structure of a single layer of graphene. 583

Figure K.4 Photoelectrocatalytic mechanism for Er^{3+}:$YAlO_3$/rGO/TiO_2 electrode under visible light. 584

Figure K.5 Schematic diagram of Schematic diagram of the smart "umbrella" Bi_2S_3/rGO-modified TiO_2 NRs structure. The Bi_2S_3 nanostructures act as the "canopy" and can efficiently harvest sunlight. The rGO sheet layers and 1D TiO_2 NRs act as the "ribs" and "stretchers", respectively, and can quickly transport electrons. The FTO conductive layer acts as the "shaft". The Pt counter electrode serves as the "handle". 585

Figure K.6 Schematic illustration for the fabrication of the electrode in photoelectrocatalysis. 586

Figure K.7 Summary of stability analysis and semiconducting properties of 44 different MX_2 compounds and binary compounds of group-IV elements and group III–V. 587

Figure K.8 Band structure of MoS_2 and WS_2 with the form of bulk, bilayer and mono layer 588

Figure K.9 The redox potentials of the relevant reactions with respect to the estimated position of the g-C_3N_4 band edges at pH 7. 590

Figure L.1 SEM images of (a) BiOCl-S, (b) BiOCl-H, (c) BiOBr-S, (d) BiOBr-H, (e) BiOI-S and (f) BiOI-H. 602

Figure L.2 XRD patterns of prepared samples. 603

Figure L.3 N_2 sorption isotherms (a), and adsorption isotherms for RhB adsorption over BiOCl-S (b), BiOBr-S (c) and BiOI-S (d). 605

Figure L.4 Pore size distribution of BiOX samples 606

Figure L.5 (a) DRS spectra for BiOX samples, (b) scheme for the light propagation on plate and slit-like morphologies, (c) DRS spectra for BiOX after illumination under visible light (a 300-W halide tungsten projector bulb) for 1h, and (d) color of BiOX-S samples before and after illumination. 608

Figure M.1 Sample detector system for measurement of the absorption coefficient. 614

Figure M.2 (a) Geometry of the annular photoreactor, and simulated profiles of incident radiation with high optical density: (a) diactinic medium ($\kappa = \sigma = 0$ m^{-1}), and catalysts dosage amount = 0.10 ($\kappa = 28$ m^{-1}, $\sigma = 360$ m^{-1}), 0.50 ($\kappa = 140$ m^{-1}, $\sigma = 1800$ m^{-1}), and 1.0 ($\kappa = 280$ m^{-1}, $\sigma = 3600$ m^{-1}) g/L in (b), (c) and (d), respectively 616

Figure M.3 Geometry of the flat plate photocatalytic reactor 617

Figure M.4 Geometric profile of (a)a parabolic trough reactor (PTR) and (b) a compound parabolic collecting reactor. 617

Figure M.5 Mass transfer of a photocatalytic process. 618

Figure M.6 Band electronic structure of BiOBr, simulated using a DFT method with LDA+GGA as implemented in the Quantum Espresso code. 630

Figure M.7 Comparison of recombination processes of photogenerated charge carriers within (a) indirect and (b) direct band gaps 630

Figure M.8 Total DOSs of TiO_2 as well as doped TiO_2. 632

Figure M.9 (a) Bands of BiOI including the bottom of conduction band and top of valence band; (b) Calculated D for different bismuth oxyhalides (x: composition fraction). 633

Figure M.10 Optical absorption curves of pure (a, a'), Si-doped (b, b'), Fe-doped (c, c') and Si, Fe-codoped (d, d') TiO_2 (Left: obtained by simulation; Right: obtained by experiments) 635

Figure M.11 Band alignment with three types. 636

Figure M.12 (a) The charge density difference (0.0004 eÅ-3) for g-C_3N_4/TiO_2; (b) Planar-averaged electron density difference $\Delta\rho(Z)$ for g-C_3N_4/TiO_2. (The yellow and cyan areas represent the electron accumulation and depletion, respectively). 637

Figure M.13 Potential energy profiles for adsorption mechanism of CO_2 on TiO_2 surface (CO_2/[TiO_2]-P: physical adsorption, CO_2/[TiO_2]-NC: non-dissociative

chemical adsorption, CO_2/[TiO_2]-DC and CO_2/[TiO_2]-DC': two dissociative chemical adsorptions) 638

Figure M.14 (a) Photocatalytic degradation of RhB, and (b) Inactivation curves for dark control, photolysis and irradiated composite. 641

List of Tables

Table 2.1 Band gaps for $M(BiO_3)_n$ 17

Table 2.2 Electro negativities of Bi-based semiconductors..... 19

Table 2.3 Approaches to narrow band gap by modulation of valence band. ($\Delta E_g=E_g$(doped)-E_g(pure)) 21

Table 2.4 Different morphologies of prepared Bi-Based compounds. 25

Table 2.5 Water splitting using Z-scheme photocatalysis systems. (light source: 300-W Xe-arc lamp; weight ratio: H_2-photocatalyst/O_2-photocatalysts (g/g); aqueous H_2SO_4 solution: pH 3.5.) 30

Table 2.6 Bismuth based heterojunctions. 31

Table 3.1 Lattice parameters and volume of a lattice cell for prepared samples..... 60

Table 3.2 Specific surface area, pore volume, and average pore size of prepared composites. 65

Table 3.3 Pseudo first-order kinetic constants of systems with Bi_2WO_6 doped with different quantities of Pd. 72

Table 3.4 Photonic efficiency ζ ($\mu g\ W^{-1}\ min^{-1}\ g^{-1}$) for systems in this work and other reported systems..... 73

Table 3.5 Fitting results for equivalent circuits of different prepared samples. 83

Table 4.1 Lattice parameters for prepared samples including pure BiOBr and Pd-BiOBr composites. 105

Table 4.2 Band gap and flat-band edge position of BiOBr. 108

Table 4.3 Specific surface area, pore volume, and average pore size of BiOBr and 0.5 Pd-Bi composites..... 112

Table 4.4 Photocatalytic reaction kinetics constants and photonic efficiency for systems with pure BiOBr and BiOBr composites with different quantities of palladium. 115

Table 4.5 Fitting results for equivalent circuits of different prepared samples. 119

Table 5.1 Lattice parameters of prepared samples. 134

Table 5.2 Parameter values for Equation 4 and 5. 142

Table 5.3 Kinetic constants for systems in the presence of different photocatalysts. 145

Table 5.4 Fitting results for equivalent circuits of different prepared samples. 154

Table 6.1Crystal size and lattice parameters of prepared samples. 172

Table 6.2 Specific surface area and pore volume of Bi_2WO_6, MoS_2-Bi_2WO_6 and MoS_2. 178

Table 6.3 Apparent reaction kinetic constants of photocatalytic processes with different samples. 183

Table 6.4 Fitting results for equivalent circuits of different prepared samples. 189

Table 6.5 Band gap and flat-band edge position of Bi_2WO_6 and MoS_2. 192

Table 7.1 Lattice parameters of Bi_2MoO_6 and Ag/AgCl-rGO-Bi_2MoO_6 composites 207

Table 7.2 Surface composition of Bi_2MoO_6, GO-Bi_2MoO_6, and Ag-rGO-Bi_2MoO_6 composites according to XPS analysis. 211

Table 7.3 Specific surface area, pore volume, and average pore size of Bi_2MoO_6, GO-Bi_2MoO_6, rGO-Bi_2MoO_6, and Ag-rGO-Bi_2MoO_6 composites. 220

Table 7.4 Photocatalytic kinetics constants for systems with various photocatalyst composites. 224

Table 7.5 Fitting results for equivalent circuits of different prepared samples. 227

Table 8.1 Compositions of the prepared photocatalysts 241

Table 8.2 Magnetic properties of (M) Bi_2WO_6 and Ag/AgCl-(M) Bi_2WO_6. 253

Table 9.1. Properties of Pd-$BiVO_4$ used in the work. 278

Table 9.2. Attenuation factor for glass beads without and with coating. 282

Table 9.3. Exposed area for flat plat and glass beads with different diameters. 284

Table 9.4. Calculated $t_{1/2}$ and EEO for slurry, PBR and flat-plate reactor systems. 291

Table A.1 Lattice parameters of Bi_2WO_6 and Ag/AgCl-Bi_2WO_6 composites 304

Table A.2 Pseudo-first order reaction rate constants for various processes. 315

Table B.1 Pseudo first-order kinetic constants of systems with Bi_2MoO_6 doped with different quantities of Pd. 342

Table B.2 Fitting results for equivalent circuits of different prepared samples. 345

Table C.1 Lattice parameters derived from the XRD patterns 360

Table C.2 Electrochemical impedance results of $BiVO_4$, rGO-Bi, Pd(G)-Bi and Pd-Bi. 368

Table E.1 Pseudo-first order reaction rate constant (k) for various processes, respectively. 409

Table G.1 Specific surface area, pore volume, and average pore size of Bi_2MoO_6, GO-Bi_2MoO_6, rGO-Bi_2MoO_6, and Pd-rGO-Bi_2MoO_6 composites. 440

Table G.2 Photocatalytic kinetic constants for the photocatalytic process of degradation of phenol with various photocatalysts under visible light irradiation. 445

Table G. 3 Fitting results for equivalent circuits of different prepared samples. 447

Table H.1 Parameter values for Equation 4 and 5. 474

Table H.2 Photocatalytic kinetic constants and average photonic efficiencies for the photocatalytic process of degradation of phenol with various photocatalysts under visible light irradiation. 480

Table H.3 Electrochemical impedance results of $BiVO_4$, rGO-Bi, Pd(G)-Bi and Pd-Bi. 486

Table I.1 Band gaps (E_g), and measured or estimated pH_{ZPC} for semiconducting metal oxides 501

Table I.2 Standard electrode potential (E^o) of general oxidant..... 502

Table I.3 Overview of photoelectrocatalytic reactor types, application and electrode materials. 534

Table L.1 Crystal parameters calculated from XRD patterns and specific surface area for prepared samples. 603

Table L.2 Pore volume, and average pore size of BiOX samples. 606

Table L.3 Fitting results for adsorption isotherms of RhB over BiOX samples. 607

Table M.1 Absorption and Scattering coefficients of TiO_2 614

Table M.2 Approaches to estimate the exchange-correlation energy in KS equation..... 626

Table M.3 Band gaps for TiO_2 (anatase) using different DFT methods and Hartree-Fock calculation compared with experimental result. 629

Nomenclature, Abbreviations and symbols

Nomenclature and Abbreviation

AFM	Atomic force microscopy
AOP	Advanced oxidation process
AVS	Absolute vacuum energy system
BET	Brunauer, Emmett and Teller
BJH	Barrett-Joyner-Halenda
CB	Conduction band
CC	Coupled-Cluster
CI	Configuration Interaction
DDW	Deionized distilled water
DFT	Density Function Theory
DOS	Density of states
DRS	Diffused reflectance spectra
EDS	Energy-dispersive X-ray spectroscopy
EG	Ethylene glycol
EIS	Electrochemical impedance spectroscopy
FT-IR	Fourier transform infrared spectrometer
GGA	Generalized Gradient Approximation
HF	Hartree-Fock
HK	Hohenberg-Kohn
HPLC	High-performance liquid chromatograph
ITO	Indium-tin oxide
KS	Kohn-Sham
LDA	Local Density Approximation
LEED	Low-energy electron diffraction
L-H	Langmuir-Hinshelwood
LVREA	Local volumetric rate of energy absorption
MB	Methylene blue
MF	Methyl format

MPMS	Magnetic properties measurement system
MPx	Møller-Plesset perturbation theory
MW	Molecular weight
NHE	Normal hydrogen electrode
NP	Nanoparticles
NXES	Normal x-ray emission spectroscopy
pCBA	*p*-chlorobenzoic acid
PL	Photoluminescence
PZC	Ponit of zero charge
QD	Quantum dot
RhB	Rhodanmine B
RTE	Radiation transport equation
SCF	Self-consistent field
SEM	Scanning electron microscopy
SM	Scheelite with a monoclinic structure
SPR	Surface plasmon resonance
SQUID	Superconducting quantum interference device
SSR	Solid-state reaction
ST	Scheelite with a tetragonal structure
STM	Scanning tunneling microscopy
SXRD	Surface X-ray diffraction
TEM	Transmission electron microscopy
TF	Thoms-Fermi
TFD	Thomas-Fermi-Dirac
UV	Ultraviolet
VB	Valence band
XPS	X-ray photoelectron spectroscopy
XRD	X-ray diffraction
ZT	Zircon with a tetragonal structure

Symbols

E_g	Band gap (eV)
A	Coated area (m^2)
a	Length of reactive area (m)
b	Width of reactive area (m)
c	Concentration (mg/L)
c^*	Concentration at the interface (mol L^{-1})
c_{bulk}	Concentration in the bulk (mol L^{-1})
c_f	Final concentration (mg/L)
c_o	Initial concentration (mol L^{-1})
c_s	Concentration on the surface (mol L^{-1})
c_t	Concentration at time of t (mol L^{-1})
d	Diameter of beads (mm)
D	Diffusion coefficient (m^2 s^{-1})
d_L	Characteristic dimension of the deposit (m)
E	Energy state of the wave function (eV)
$E[\rho]$	Total energy (eV)
E_{CB}	Bottom position of the conduction band (eV)
E^e	energy of free electrons on the hydrogen scale (~ 4.5 eV)
EEO	Electricity energy per order (kW h/m^3)
E_g	Band gap value (eV)
E_{photon}	Energy of photons (eV)
E_{VB}	top position of the valence band (eV)
$E_{xc}[\rho]$	Exchange-correlation energy (eV)
f	Flowrate (mL min^{-1})
$\hat{H}$	Hamiltonian operator
$\hbar$	Reduced Planck constant (eV-s)
I	Intensity of irradiation (W m^{-2})
$I(\omega)$	Optical absorption intensity at the angular frequency (ω)
I_v	Monochromatic radiation intensity (einsteins m^{-2} s^{-1} sr^{-1})
K	Adsorption constant
k'	Pseudo first-order reaction constant (s^{-1})

$k_{external}$	External mass transfer coefficient (m s^{-1})
k_L	Average mass transfer coefficient (m/s)
m^*	Effective mass
N	Number of beads layer
P	Lamp power (W)
p	Phase function of the in-scattering of incident radiation to an element
q_{photon}	Wave vector of the assisted photon
R	Coordinate of nuclei (m)
r'	Reaction rate per unit of catalyst (mol L^{-1} s^{-1} g^{-1})
$r_{external}$	Rate of external mass transfer (mol m^{-2} s^{-1})
s	Spin coordinates (m)
T	Temperature (°C)
t	Time (s, min, h)
$T[\rho]$	Kinetic energy (eV)
$t_{1/2}$	Half-life of reaction (h)
V	Volume (m^3)
$V[\rho]$	Potential energy (eV)
x	Coordinate of electron (m)
α	Absorption coefficient
ε	Attenuation factor
E_κ	Energy corresponding to the wave vector κ
ζ	Photonic effieciency (µg W-1 min-1 g-1)
η	Quantum yield (%)
θ	Ratio of adsorbed molecules
κ	Wave vector (m^{-1})
κ_v	Coefficient of absorption (m^{-1})
λ	Wavelength (nm)
λ_{min}	Minimum wavelength (nm)
ρ	Density (g m^{-3})
σ_v	Coefficient of out-scattering (m^{-1})
τ	Tortuosity of the catalyst (dimensionless)

φ	Scattering angle (°)
χ_p	electronegativity of the semiconductor (eV)
Ψ	A wave function where Hamiltonian operator acts ($m^{-3/2}$)

SECTION I: INTRODUCTION

Chapter 1 Introduction

One of the most prevalent environmental problems facing us today is the persistent and toxic organic pollutants which contaminate surface and ground water bodies all over the world. These pollutants are potential threats to humans, as they may be accumulated in the food chain. Therefore, effective approaches are required to mineralize these organic pollutants. As an advanced oxidation process (AOP), heterogeneous photocatalysis exhibits superiorities to conventional treatment technologies, such as the nonselective decomposition of all of emerging organic pollutants and a capability to inactivate bacteria. Photocatalysis is also a technique to convert light energy to chemical energy, which is significantly promising when solar energy can be utilized as the energy source. A semiconductor is being applied as the catalyst, and the band gap of the semiconductor determines the range of wavelengths of an irradiation that can be used.

As one of the first developed photocatalysts, TiO_2 has been widely studied and developed. However, one of the intrinsic properties for TiO_2, the band gap, is too wide (~3.2 eV), which allows only ultraviolet (UV) light to activate the process. It should be noted that UV light accounts for only ~5% of energy in the solar spectrum. If a more cost-effective energy source such as sunlight was to be used, it would be requisite that the applied photocatalyst is visible light-responsive. One effective approach to this solution is to prepare novel materials with more narrow band gaps and visible light-responsivities. Bismuth-based semiconductors have narrow band gaps and thus have the potential to be applied as photocatalysts. In this work, visible light-responsive, bismuth-based photocatalysts were prepared, modified, tested, analysed and discussed. In addition, to overcome the difficulty in separation of catalyst particles from slurry, magnetically separable composites as well as immobilized systems were developed and explored.

This document is divided into ten chapters and fourteen appendices. Chapter 1 provides an introduction of this document. Chapter 2 and Appendices I, K and M provide in-depth literature review of the relevant fields. Chapters 3-7, as well as Appendices A-H, J and L discuss work performed to improve the photocatalytic activities of bismuth-based photocatalysts. Chapters 8 and 9 are focused on overcoming the separation difficulty in the separation of catalyst particles from slurry. Chapter 10 and Appendix N are conclusions, outlooks and scholarly contributions.

Background and literature review

Chapter 2 comprehensively reviewed most of the bismuth-based materials in the literature. The main challenges and possible approaches on the basis of reported works were highlighted here. Future work as well as concluding remarks were suggested and summarized.

Appendix I focuses on the development of photoelectrocatalytic reactors applied to environmental remediation. Various reported designs of photoreactors and cost-effective photoreactor systems were introduced, and future work in this area was also suggested.

Appendix K introduced a developing area in photocatalysis, which is two-dimensional materials applied to photocatalysis. Primary photocatalytic materials were introduced, and possible prospects of this area were also identified.

Appendix M introduced a review about computational methods that have been applied to photocatalytic systems. All of the relevant computational methods including modelling of light, mass transfer and reaction kinetics, material simulations as well as methods applied to evaluate a photocatalytic system were included.

Modification methods

1. Plasmonic photocatalysis

Chapters 3, 4 and 5, as well as Appendices B and C discuss palladium nanoparticle-modified, bismuth-based semiconductors. It was found that the photocatalytic activity for the decomposition of organics in water under visible light irradiation was greatly improved, which may be due to the surface plasmonic resonance effect. Appendix D provides evidence that doping may be more effective for a bismuth-based semiconductor with a

wide band gap. Silver nanoparticle-modified Bi_2WO_6 constructs were also prepared and are discussed in Appendix A.

A ternary plasmonic photocatalyst structure was also formed via the introduction of a graphene layer between the metal nanoparticles and bismuth-based photocatalysts. Chapter 7 and Appendices G and H are sample works.

2. Heterostructure

Chapter 6 and Appendices E and F are focusing on the preparation of heterostructures between bismuth-based semiconductors and other materials. It was found that heterostructures facilitated the separation of photogenerated charge carriers, and further improved photocatalytic activity.

3. Morphology control

Appendices J and L discuss the effect of morphology on the photocatalytic activity of Bi_2MoO_6 and BiOX.

Scale up

To address the difficulty in separation of photocatalyst particles, especially those on the nanoscale from slurry, magnetically separable composites were reported in Chapter 8, which can effectively separate the photocatalyst particles from the suspension. In Chapter 9, bismuth-based semiconductors were coated onto glass beads and embedded in a packed bead reactor, exhibiting the potential to be implemented on a large scale.

Chapter 2 Background and Literature Review

2.1 Introduction

Photocatalysis is an advanced oxidation process (AOPs) involving the participation of photons that has been widely extended into areas such as the generation of hydrogen by splitting water and the protection of the environment. Unique properties such as an inexpensive energy source and a wide range of applications make it attractive for further research. Photocatalytic materials as the basis are also extensively developed. When compared to early photocatalytic materials, namely TiO_2 [1], recently developed materials possess several advantageous properties such as visible-light responses, controllable structures, and higher photo-quantum yields. The intrinsic electronic band structure of TiO_2 is a well-known shortcoming of the material, and results in a large band gap of about 3.2 eV. Given that only UV light possesses enough energy to activate TiO_2 and trigger a photocatalytic process, use of this material is uneconomical. Approaches to overcome this barrier usually include either modification of TiO_2 to narrow the band gap (such as doping [2]) or development of other novel visible-light-responsive materials.

Bismuth-based semiconductors are a promising new candidate for visible-light-responsive photocatalysts. Their electronic structure results in a valence band consisting of hybrid orbitals of O *2p* and Bi *6s*, while that of TiO_2 is composed solely of O *2p* orbitals. It has been reported that the well-dispersed Bi *6s* orbital increases mobility of photogenerated charge carriers and decreases the band gap [3, 4]. As a result, bismuth-based compounds usually possess band gaps less than 3.0 eV. A variety of bismuth-based substances have been prepared and tested as photocatalysts, e.g. Bi_2O_3, Bi_2MO_6 (M = Cr, Mo and W), $BiVO_4$, BiOX (X = Cl, Br and I), $BiPO_4$, $(BiO)_2CO_3$, and pentavalent bismuthates. In terms of environmental protection applications, bismuth-based semiconductors have been used for degradation of organics in wastewater such as dye pollutants [5-8], oxidation of gaseous

pollutants such as NO [9], and photo reduction of CO_2 [10]. Studies on photocatalytic water splitting to generate H_2 and O_2 have also been reported [11-15].

In this review, current bismuth-based photocatalysts and their applications are summarized. Next, main challenges in their application are presented along with possible approaches for overcoming them. Finally, future work in this area is proposed.

2.2 Bismuth-based photocatalytic materials

2.2.1 Bi_2O_3 and Bi_2S_3

Bismuth trioxide (Bi_2O_3) is the simplest and most significant bismuth compound. It has potential applications, among others, in a wide range of gas sensors and ceramic glass solid oxide fuel cells[16]. It has also been implemented as a photocatalyst in both the splitting of water and in the decomposition of organic pollutants [17]. Bi_2O_3 as a semiconductor has a band gap that varies from 2.1 eV to 2.8 eV, making it a viable visible-light-responsive photocatalyst. Polymorphs of Bi_2O_3 include the alpha (monoclinic), beta (tetragonal), gamma (body-centered cubic), delta (face-centered cubic), and omega (triclinic) phases. These metastable phases can be easily transformed to α phase at low temperatures and δ phase at high temperatures (Fig. 2.1). Further transformation to $(BiO)_2CO_3$ [18] has also been observed, and this chemical instability represents the main obstacle for further applications of Bi_2O_3 as a photocatalyst. Approaches including metal doping, ion doping, and establishing composites have been attempted, but have yet to overcome this intrinsic disadvantage.

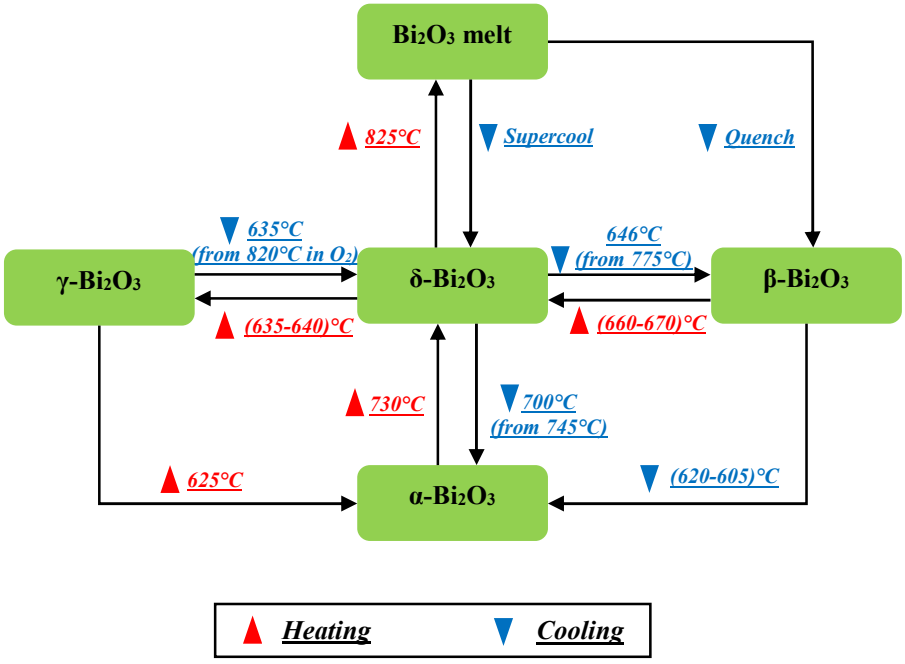


Figure 2.1 Phase transfer of Bi_2O_3.

Bi_2S_3 has a bulk band gap of 1.7 eV and is an ideal light-harvesting photocatalytic material due to its activation by visible and near-IR light. A variety of Bi_2S_3 nanocrystals have been prepared, ranging from 1D nanorods and 2D nanosheets (Fig. 2.2a, b) by standard oxygen-free and hot injection techniques [19, 20], to 3D urchin-like spheres (Fig. 2.2c) by solvothermal method [10]. The photogenerated holes on the valence band of Bi_2S_3 with a flat potential of 1.62 eV, as well as the production of hydroxyl radicals (•OH) may be the oxidants for decomposing most dye pollutants [19]. Photocatalytic reduction of CO_2 to methyl formate (MF) in the presence of Bi_2S_3 [10] has also been reported. Bi_2S_3 has a narrow band gap and if combined with other photocatalysts such as TiO_2 [21], Bi_2WO_6 [22] and CdS [23], the recombination rate of e^-/h^+ pairs could be decreased resulting in further improvements to photocatalytic performance under visible light irradiation.

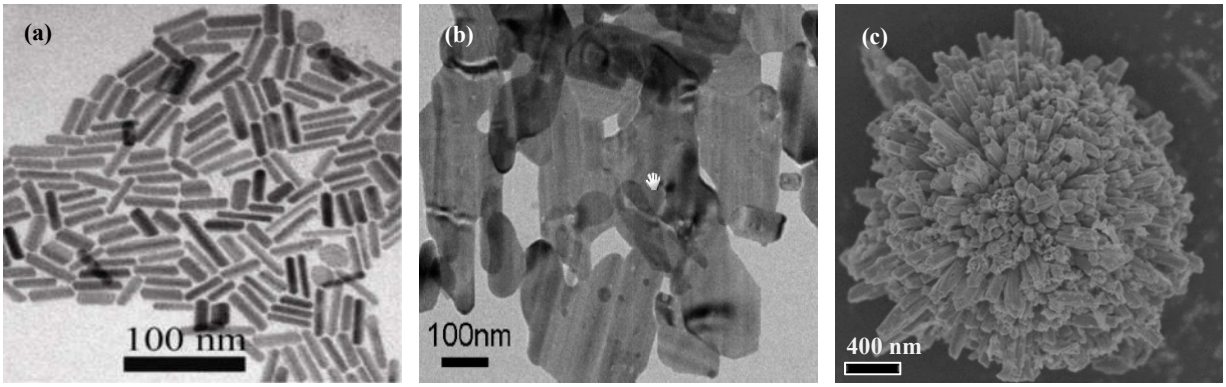


Figure 2.2 Bi_2S_3 (a) nanorods (adapted from[19]), (b) nanosheets (adapted from [20]), and (c) spheres (adapted from [10]).

2.2.2 Bi_2MO_6 (M = Cr, Mo, W)

Bi_2MO_6 (M = Cr, Mo, W) is the simplest member in the Aurivillius family, the general formula for which is $Bi_2A_{n-1}B_nO_{3n+3}$ (A = Ca, Sr, Ba, Pb, Bi, Na, K; B=Ti, Nb, Ta, Mo, W, Fe). Theoretically, the electronic structure of Bi_2MO_6 can be simulated based on density functional theory (DFT) [24]. The crystal structure of Bi_2MO_6 falls under the orthorhombic space group *Pca2(1)*. Simulated results suggest that both the valence band and conduction band of Bi_2MO_6 are composed of hybridized Bi *6p*, O *2p* and M *nd* (n = 3, 4, and 5 for Bi_2CrO_6, Bi_2MoO_6 and Bi_2WO_6, respectively) orbitals. Band structures of Bi_2MO_6 are illustrated in Fig. 2.3, and the predicted bandgaps shown are 1.245 eV, 1.96 eV and 2.2 eV for Bi_2CrO_6, Bi_2MoO_6 and Bi_2WO_6, respectively [24]. These predictions are smaller than experimental results, which determiend the band gaps to be 2.16 eV, 2.63 eV and 2.77 eV for Bi_2CrO_6, Bi_2MoO_6 and Bi_2WO_6 [25, 26]. The discrepancy is due to well-known limitations of GGA. However, both suggest that Bi_2MO_6 compounds are suitable for visible-light-activated photocatalysts. It should also be noted that Bi_2CrO_6, despite having the narrowest band gap in Bi_2MO_6, is not suitable for photocatalysis due to easy recombination of the photogenerated electrons and holes. Therefore, few studies are focused on the implementation of Bi_2CrO_6 in photocatalysis.

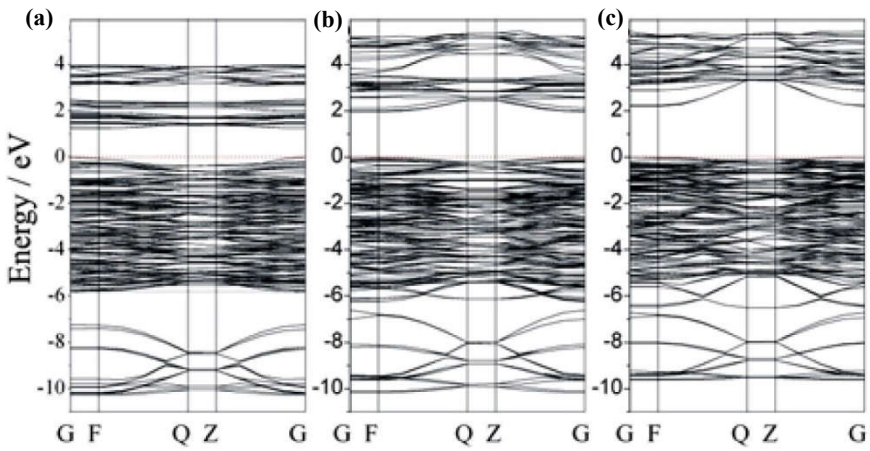


Figure 2.3 Band structures of (a) Bi_2CrO_6, (b) Bi_2MoO_6, and (c) Bi_2WO_6. (Adapted from [24])

The original preparation method for Bi_2WO_6 was a solid-state reaction (SSR) under high temperature (1173 K) [27]. This resulted in prepared samples that were generally of large particle size and low surface area. Hydrothermal methods have gradually become the main synthesis method for preparation of nano-sized Bi_2WO_6, owing to their moderate experimental conditions, simple operation procedures, and controllable sample shapes and sizes [28]. It has also been shown experimentally that Bi_2WO_6 prepared through hydrothermal methods has a narrower band gap and better photocatalytic activity than that prepared through the SSR method (Fig. 2.4) [29]. Additionally, morphologies of Bi_2WO_6 prepared by hydrothermal methods are controllable either by adjusting the pH of the precursor solution or by adding surfactants (Fig. 2.5a-d), both of which directly affect the photocatalytic activity. Due to the low solubility of bismuth precursors (*e.g.* $Bi(NO_3)_3$) in distilled water, hydrothermal methods often require the addition of nitric acid to assist in solvation (Fig. 2.5e) [30]. However, the addition of such a strong acid introduces problems with corrosion of equipment and pollution of the environment. Acetic acid has been employed in place of nitric acid in order to alleviate some of these issues [4]. In addition, it has been found that bismuth nitrate can be dissolved in various alcohols, which has led to the development of solvothermal methods to prepare Bi_2WO_6. Ethylene glycol (EG) is the most commonly used solvent to prepare uniform Bi_2WO_6 through solvothermal methods [31-33]. EG-assisted solvothermally synthesized Bi_2WO_6 with hollow microspheres (Fig. 2.5f) has shown excellent photocatalytic activity with organic pollutants [34]. In an attempt to decrease the preparation time, microwave heating was employed in

place of traditional oven heating and resulted in a subsequent decrease from 10 – 20 h to 7 min [33, 35, 36]. Microwave-assisted hydrothermal and solvothermal processes have successfully prepared Bi_2WO_6 with nanosheets, nanoplates and flower-like nanoflake morphologies. However, microwaves applied in the process may result in a dramatic rise of temperature as well as pressure in the system, increasing risk of the operation.

Similarly, Bi_2MoO_6 has also been prepared through SSR, hydrothermal, and solvothermal methods [37-40]. Hydrothermal and solvothermal methods are effective at preparing Bi_2MoO_6 samples with smaller particle size, larger specific surface area, and higher photocatalytic activities when compared to SSR methods. Various morphologies of Bi_2MoO_6 including nanoplates (Fig. 2.5g, hydrothermal method) and flower-like hollow spheres (Fig. 2.5h, solvothermal method) have been reported. Moreover, microwave heating was also used to prepare Bi_2MoO_6 samples in short periods of time with high photocatalytic activity [41].

Principal applications of Bi_2MO_6 (mainly Bi_2WO_6 and Bi_2MoO_6) photocatalysts involve the degradation of organic pollutants and disinfection of polluted water and air. The primary pollutants that have been studied include dye [42], phenol [43], $CHCl_3$ and CH_3CHO in wastewater [27], as well as NO in polluted air [9]. Microorganisms such as *E.coli* were successfully destroyed by adding Bi_2MoO_6 [44] and Bi_2WO_6 [45] under visible light irradiation.

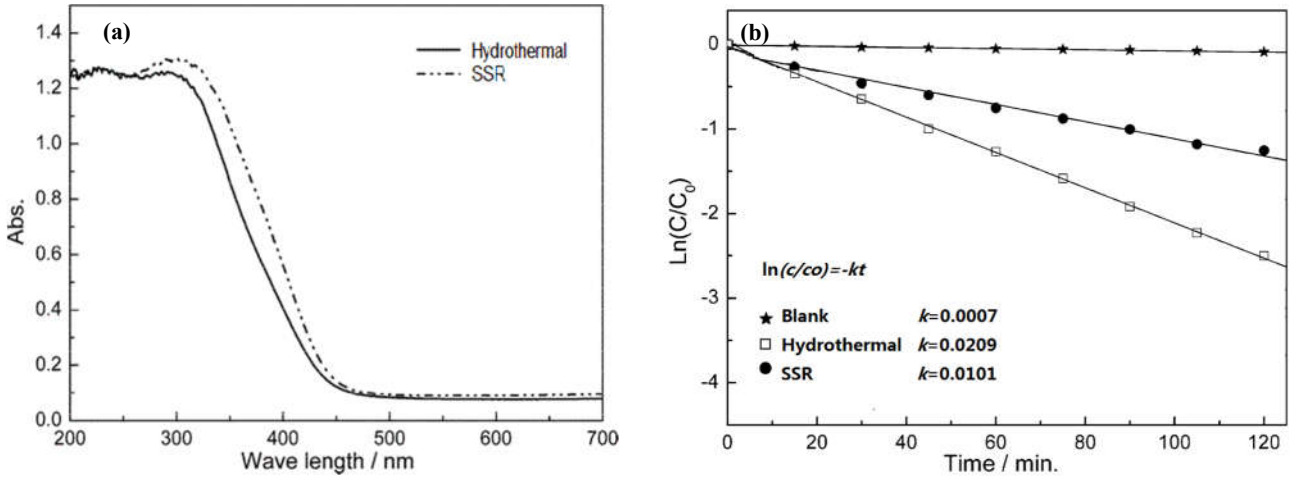


Figure 2.4 (a) Diffused reflectance spectra and (b) photocatalytic kinetics of Bi_2WO_6 prepared by hydrothermal and SSR methods. (Adapted from [29])

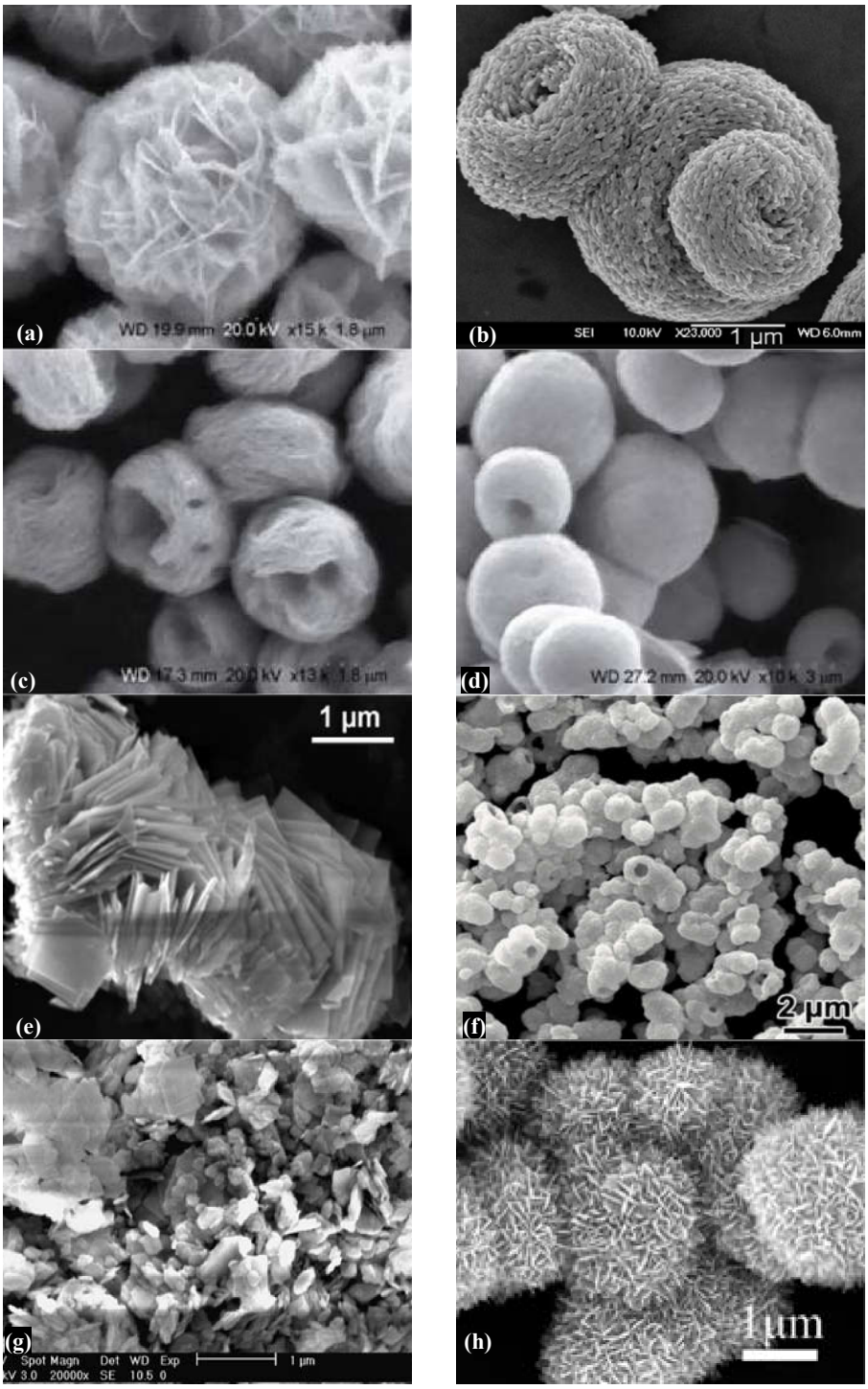


Figure 2.5 SEM images of Bi_2WO_6 samples prepared by hydrothermal method (a) without surfactant, with (b) triblock poly(ethylene oxide)-block-poly(propylene oxide)-block-poly(ethylene oxide) copolymer ($EO_{20}PO_{70}EO_{20}$, Pluronic P123), (c) sodium dodecyl sulfate (SDS) and (d) polyvinyl pyrrolidone (PVP), and by solvothermal method with (e) nitric acid and (f) ethylene glycol (EG) as solvent. SEM images of Bi_2MoO_6 prepared by (g) hydrothermal and (h) solvothermal method. ((a), (c), and (d) adapted from [46], (b) adapted from [47], (e) adapted from [30], (f) adapted from [34], (g) adapted from [37], and (h) adapted from [48])

2.2.3 $BiVO_4$

Bismuth vanadate ($BiVO_4$) exhibits interesting physicochemical properties including ferro-elasticity and ionic conductivity. It has been recently introduced into the field of visible-light-driven photocatalysis and has a theoretical band gap of 2.047 eV, as calculated by the DFT method [49]. The valence band of $BiVO_4$ mainly consists of O *2p* and V *3d* orbitals. There are three observed phases of $BiVO_4$, namely monoclinic fergusonite, tetragonal sheelite and tetragonal zircon (Fig. 2.6). Reversible phase transition between monoclinic fergusonite and tetragonal sheelite occurs at 255°C [50].

Numerous approaches to synthesize $BiVO_4$ have been reported. Monoclinic $BiVO_4$ has been prepared both by solid state reaction (SSR) methods and by melting reactions at high temperatures [51]. Tetragonal $BiVO_4$ has been obtained by a precipitation method at room temperature [52]. The band gaps for monoclinic and tetragonal $BiVO_4$ are 2.4 eV and 2.9 eV, respectively, indicating that selective preparation of monoclinic $BiVO_4$ is beneficial for fabricating more efficient visible-light-driven photocatalyst. An additional approach to preparing both monoclinic and tetragonal crystal $BiVO_4$ through a simple aqueous process has also been reported [53]. More recently, the hydrothermal method was also successfully applied in the preparation of monoclinic $BiVO_4$ [54]. Use of the hydrothermal method has several advantages including mild experimental conditions, simple experimental equipment, and controllable conditions able to produce selective structures of $BiVO_4$.

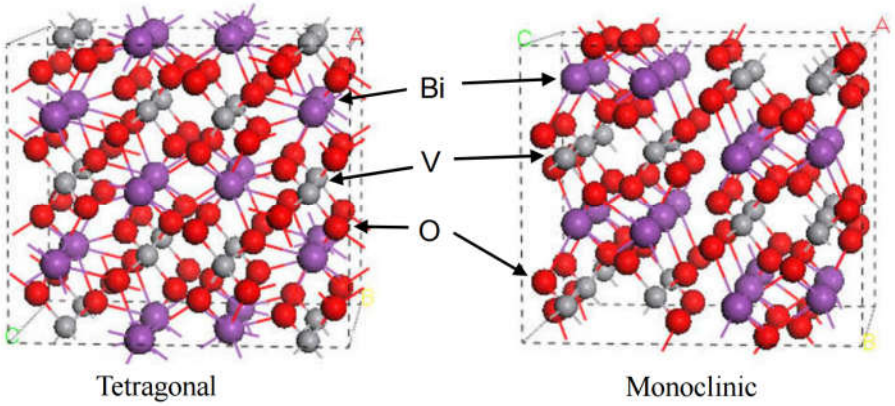


Figure 2.6 Two crystal structures of $BiVO_4$: tetragonal (left) and monoclinic (right) (adapted from [55]).

$BiVO_4$ has been widely applied in the photocatalytic degradation of organic pollutants under visible light (*e.g.* RhB and phenol [56]), and has exhibited higher removal efficiency when compared with N doped-TiO_2 [57]. $BiVO_4$ photocatalyst has also been implemented in water splitting [14, 58]. However, it was found that $BiVO_4$ is an active photocatalyst for O_2 evolution under visible light irradiation, the conduction band potential of which is not high enough for the production of H_2 by H_2O reduction [59]. In a separate study, Liu et al. [60] reported the ability to selectively produce ethanol from photocatalytic reduction of CO_2 in the presence of $BiVO_4$ under visible light irradiation. Booshehri et al. [61] have also found $BiVO_4$ to be a promising candidate for the photocatalytic inactivation of bacteria in water under visble light irradiation.

2.2.4 BiOX (X = F, Cl, Br, I)

Bismuth oxyhalides have potential as photocatalysts as a result of their optical properties. The crystal structure of BiOX consists of a layer structure of $[Bi_2O_2]$ slabs interleaved by double slabs of halogen atoms. Electrical structures of BiOX were simulated based using the DFT method and the results are illustrated in Fig. 2.7 [62]. Both the valence band and conduction band of BiOX consist of X *np* (n = 2, 3, 4 and 5 for X = F, Cl, Br and I, respectively), O *2p*, and Bi *6p* orbitals. The theoretically calculated band gaps of BiOF, BiOCl, BiOBr and BiOI are 2.79 eV, 2.34 eV, 1.99 eV, and 1.38 eV, respectively. Comparatively, their experimentally determined band gaps are 3.64 eV [63], 3.22 eV, 2.64 eV, and 1.77 eV [64], respectively. The differences between the calculated and experimental results of band gaps are due to limitations existing within the GGA method. However, both indicate that band gaps generally decrease with increasing atomic number. Only UV light could be used to activate BiOF as a photocatalyst, while both visible light and near-IR were successful in activating BiOI applied in photocatalysis. As a result, BiOBr and BiOCl are frequently studied due to their suitable band gaps.

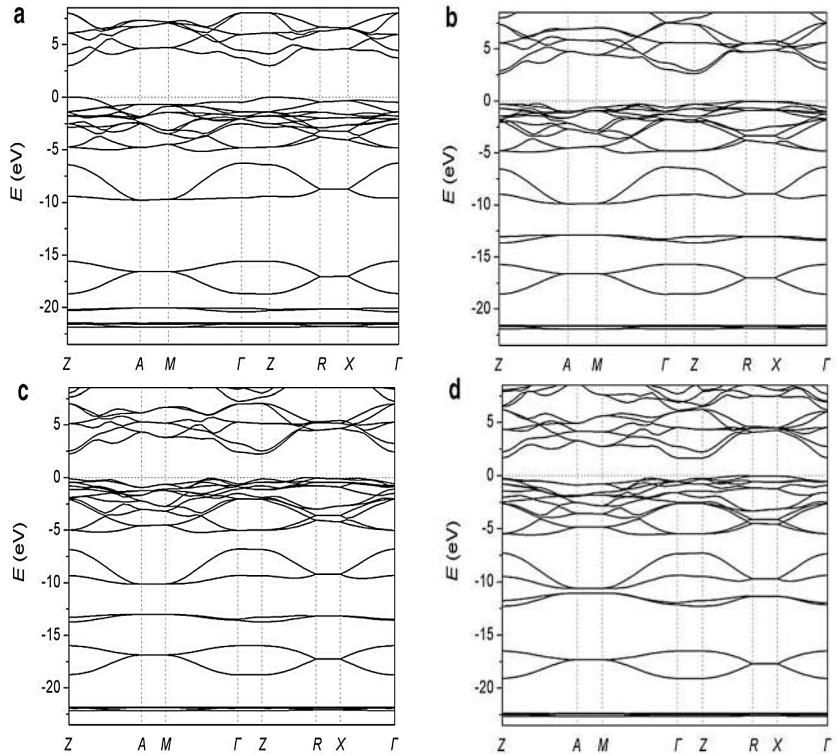


Figure 2.7 Band structures of (a) BiOF, (b) BiOCl, (c) BiOBr, and (d) BiOI. (Adapted from [62])

A number of methods have been successfully implemented for synthesis of BiOX with various morphologies. Except for hydrolysis and direct precipitation methods, hydrothermal and solvothermal methods are the primary approaches used to prepare BiOX with selective nano-/microstructures such as nanofibers, nanosheets and microspheres (Fig. 2.8). By adding a template, adjusting the pH of the precursor, and controlling the hydrothermal temperature and duration time, the structure can be controlled and will have a direct influence the photocatalytic performance. A comprehensive review of BiOX nanostructures was already reported in [65]. To date, most work with BiOX has focused on degradation of organic pollutants, especially dye pollutants in wastewater. Further research should extend its applications to other areas such as photo reduction of CO_2 and photo-generation of organics. The potential of the conduction band of BiOX makes it unsuitable for splitting water for the production of H_2. Work on BiOX is still in its early stages, and more attention must be given to overcome these challenges.

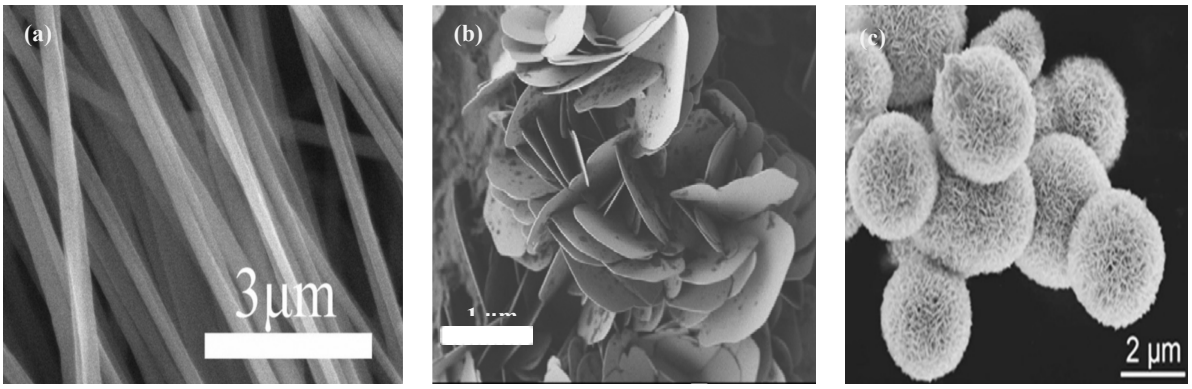


Figure 2.8 (a) Nanofibers of BiOCl (adapted from[66]), (b) nanosheets (adapted from [4]), and (c) microspheres of BiOI (adapted from [67]).

2.2.5 $BiPO_4$

$BiPO_4$ was first reported in [68], and has since been successfully synthesized through hydrothermal methods with high photocatalytic activity shown in the degradation of organics,. A microwave-assisted hydrothermal method to prepare $BiPO_4$ more rapidly has also been reported [69]. The band gap of $BiPO_4$ prepared through hydrothermal methods is about 3.85 eV, which is larger than that of TiO_2 (3.2 eV). It has also been shown that $BiPO_4$ nanocrystals prepared by standard oxygen-free procedures have a band gap of about 4.6 eV [70]. The wide band gap permits only the use of UV light as a photocatalytic light source. Although it has a wider band gap than TiO_2, $BiPO_4$ also has more rapid photocatalytic kinetics in degradation of certain organics (Fig. 2.9). This may be due to the valence band position of $BiPO_4$ being 0.3 eV higher than that of TiO_2, resulting in photogenerated holes in the valence band of $BiPO_4$ that are more oxidative than those of TiO_2. In addition to degradation of organic pollutants in an aqueous phase, photocatalytic conversion of gas phase benzene into CO_2 by $BiPO_4$ has also been reported [71]. However, limitations of $BiPO_4$ in more widespread applications are primarily a due to the wide band gap resulting in visible-light inactivity.

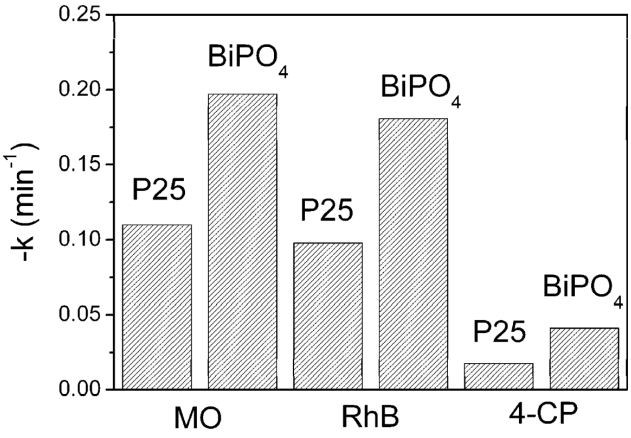


Figure 2.9 Comparison of photocatalytic kinetic constants in the presence of $BiPO_4$ and P25 on degradation of MO, RhB and 4-CP. (Adapted from [68])

2.2.6 $(BiO)_2CO_3$

Bismuth subcarbonate ($(BiO)_2CO_3$ or Bi_2CO_5) is the only well-established solid carbonate in the system Bi_2O_3-CO_2-H_2O [72]. The band gap of $(BiO)_2CO_3$ is 3.4 eV, and as a result only irradiation with wavelengths less than 365 nm can activate the band gap transition [73]. The conduction band of $(BiO)_2CO_3$ mainly consists of hybridized O 2p and Bi 6p orbitals, while the valence band is composed of O 2p, Bi 6p and C 2p orbitals. A template-free hydrothermal method has been successfully used to prepare $(BiO)_2CO_3$ with hierarchical hollow microspheres (Fig. 2.10), the structure of which was time-dependent and followed Ostwald growth properties. In terms of the applications of $(BiO)_2CO_3$, the compound has displayed photocatalytic activity in disinfection and oxidation of pollutants (dye, NO, *etc.*) in wastewater and in polluted air [74-76].

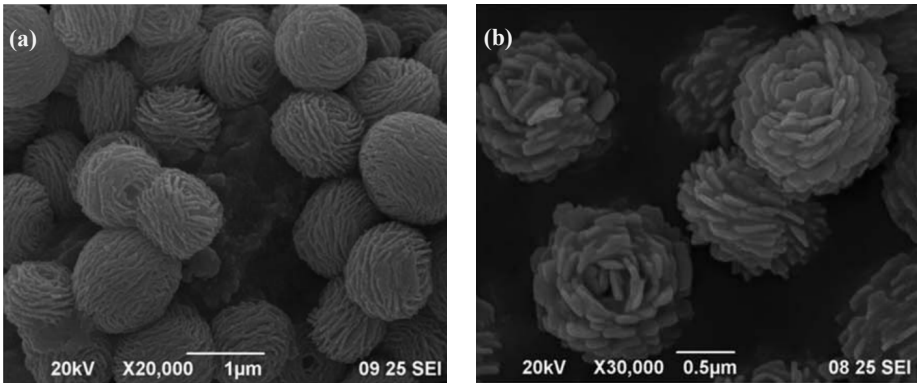


Figure 2.10 SEM images of $(BiO)_2CO_3$ prepared at 180°C for (a) 12h and (b) 24 h by hydrothermal method. (Adapted from [73])

2.2.7 $M(BiO_3)_n$ (n = 1, M = Li, Na, K and Ag; n = 2, M = Mg, Zn, Sr, Ba, and Pb)

Pentavalent bismuthates ($M(BiO_3)_n$) can be directly purchased from commercial companies, and are usually used as a Bi source to prepare other Bi-based compounds such as BiOX [77]. Band gaps of these are shown in Table 2.1. While other Bi-based compounds have a valence of +3, the valence of $M(BiO_3)_n$ is +5. The Bi^{3+} cation consists of two 6s electrons and a d^{10} closed shell, while Bi^{5+} contains an empty 6s orbital. This suggests that pentavalent bismuthates have a different electronic structure. Takei et al. tested the ability of nine pentavalent bismuthates, listed in Table 2.1, in degrading methylene blue and phenol [78]. Only $LiBiO_3$, $NaBiO_3$, $SrBi_2O_6$ and $BaBi_2O_6$ showed high photocatalytic under visible light irradiation. Electronic structures strongly influence catalytic performance: the d electrons of Ag, Zn, and Pb result in a wide conduction band and subsequent poor photocatalytic performance. Excellent visible-light-responsive photocatalytic activity suggests that pentavalent bismuthates could be promising candidates in photocatalytic applications. It was found $M(BiO_3)_n$ can be applied in the photocatalytic degradation of organic pollutants with high efficiency under visible light irradiation [78-81]. However, to the best of the authors' knowledge, other applications of this advanced material were rarely reported.

Table 2.1 Band gaps for $M(BiO_3)_n$

$MBiO_3$	Band gap	Ref.	$M(BiO_3)_2$	Band gap	Ref.
$LiBiO_3$	1.8 eV	[82]	$MgBi_2O_6$	1.61 eV	[78]
$NaBiO_3$	2.6 eV	[83]	$ZnBi_2O_6$	1.53 eV	[78]
$KBiO_3$	2.1 eV	[82]	$SrBi_2O_6$	1.93 eV	[78]
$AgBiO_3$	2.5 eV	[84]	$BaBi_2O_6$	1.93 eV	[78]
			$PbBi_2O_6$	1.92 eV	[78]

2.3 Main challenges and possible approaches

2.3.1 Energy band engineering analysis

The energy band configuration of a semiconductor is crucial to most photocatalytic properties, such as the wavelength range of exciting irradiation, the redox ability of

photogenerated holes and electrons, and the recombination rate of electrons/holes pairs. The flat-band potentials of semiconductors can be calculated by applying the Mulliken electronegativity theory for atoms as follows (equation 1&2) [85]:

$$E_{CB} = \chi_p - E^e - \frac{1}{2}E_g \qquad (1)$$

$$E_{VB} = E_{CB} + E_g \qquad (2)$$

where E_{CB} is the bottom position of the conduction band, E_{VB} is the top position of the valence band, E_g is the band gap value of semiconductor, χ_p is the electronegativity of the semiconductor, and E^e is the energy of free electrons on the hydrogen scale (~ 4.5 eV). The electronegativity of the semiconductor, χ_p, can be estimated by the geometric mean of electro negativities of the constituent atoms [86]. Results of electro negativities of all compounds are summarized in Table 2.2. The flatband-edge position of each Bi-based semiconductor both in a normal hydrogen electrode (NHE) and in an absolute vacuum energy system (AVS) scale are illustrated in Fig. 2.11. The band positions of semiconductors depended on pH with a variation of 0.059V/pH at 25°C and 1 atm (Nernstian relation) [87, 88]. Results shown in Fig. 2.11 are all at zero point of charge (pH_{ZPC}). Redox potentials of H^+/H_2 (0 V vs. NHE) and O_2/H_2O (1.23 V vs. NHE) are also shown in this figure. Band gaps can also be found in electron volts. By using equation (3), the minimum wavelength (λ_{min}) of irradiation that can activate the electron jump from valence band to conduction band can be calculated, as shown in Table 2.2.

$$E_g[eV] = \frac{1240}{\lambda}[nm] \qquad (3)$$

It could be concluded that four compounds (BiOF, BiOCl, $BiPO_4$ and $(BiO)_2CO_3$) are non-responsive to visible light. Some, such as Bi_2WO_6 and BiOBr, are slightly visible-light-responsive. How to efficiently utilize the most of visible light in the spectrum has been increasingly becoming one of the significant challenges for application of bismuth based semiconductors as photocatalysts.

A significant branch of photocatalysis application is in water splitting to produce H_2 and O_2. The reaction requires that both the top valence band of the semiconductor be more positive than the redox potential of O_2/H_2O (1.23 V vs. NHE), and that the bottom of the conduction band of the semiconductor be more negative than the redox potential of H^+/H_2 (0 V vs NHE). In Fig. 2.11, it can be observed that all of the valence band positions satisfy these conditions. However, most of the reducing capacities of electrons on the conduction bands are too weak to reduce H^+ to H_2. This presents an additional challenge for application of bismuth-based materials in photocatalytic water splitting.

Along with the challenges described above, a universal problem for the application of photocatalysts is the rapid recombination of generated electrons and holes, resulting in a severe reduction of photocatalytic activity. Exploration on how to prevent recombination is another important area to further develop semiconductor photocatalysts, including bismuth-based compounds.

Table 2.2 Electro negativities of Bi-based semiconductors.

Compounds	Electronegativity/eV	λ_{min}/nm	Compounds	Electronegativity/eV	λ_{min}/nm
Bi_2O_3	5.92	590.48	$(BiO)_2CO_3$	6.33	364.71
Bi_2S_3	5.27	729.41	$LiBiO_3$	5.56	688.89
Bi_2WO_6	6.20	447.65	$NaBiO_3$	5.50	476.92
Bi_2MoO_6	6.13	471.48	$KBiO_3$	5.32	590.48
Bi_2CrO_6	6.09	574.07	$AgBiO_3$	6.01	496.00
$BiVO_4$	6.04	516.67	$MgBi_2O_6$	6.11	770.19
BiOF	6.86	340.66	$ZnBi_2O_6$	6.25	810.46
BiOCl	6.36	385.09	$SrBi_2O_6$	5.92	642.49
BiOBr	6.17	469.70	$BaBi_2O_6$	5.87	642.49
BiOI	5.94	700.56	$PbBi_2O_6$	6.12	645.83
$BiPO_4$	6.49	322.08			

Notes: *Electronegativity of each constituent element is Mulliken electronegativity, defined as the arithmetic mean of the first ionization energy (I) and the electron affinity (E_{ea}): $\chi=|I+E_{ea}|/2$ [89, 90]. The electronegativity of compounds was estimated by the geometric mean of electronegativities of constituent elements.*

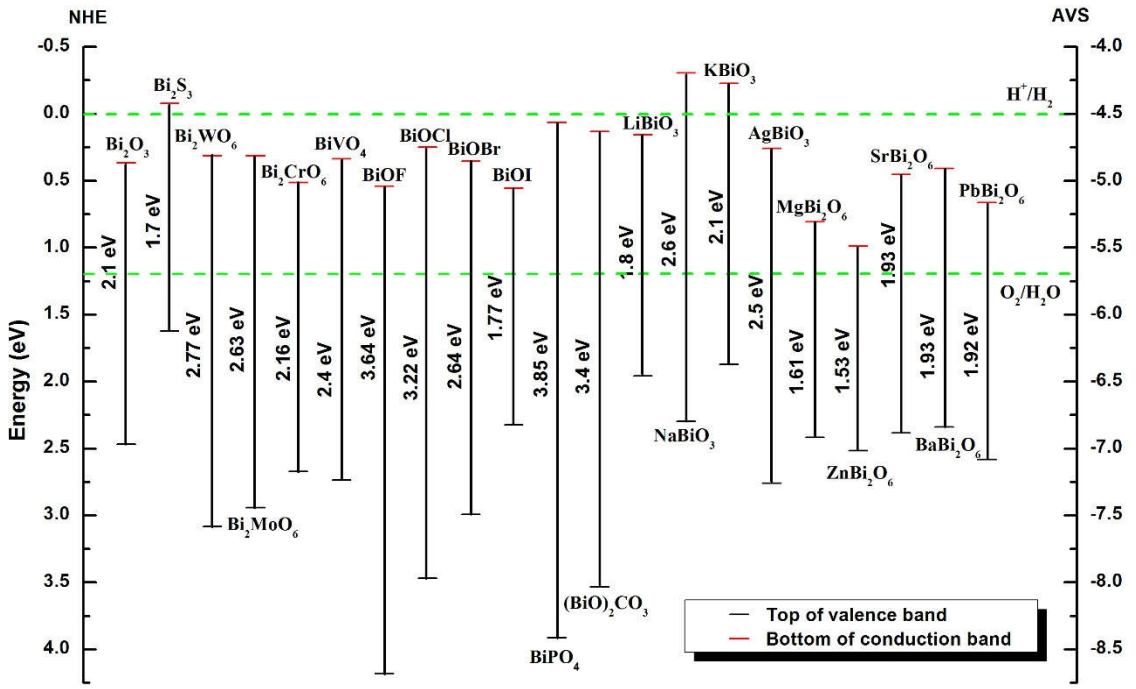


Figure 2.11 Flat band-edge positions of Bi-based semiconductor photocatalysts.

2.3.2 Development of visible-light sensitivity

2.3.2.1 Modulation of energy band

With respect to the band structure, to improve the visible-light sensitivity is to narrow the band gap. In Fig. 2.11, the bottom of the conduction bands are slightly lower or higher than the redox potential of H^+/H_2, while almost all of the tops of the valence bands are significantly more positive than the redox potential of O_2/H_2O. Therefore, modulation of the valence band to narrow the band gap would be preferred, considering the stability of the materials. Main approaches include doping with *3d*-transition elements, with cations having d^{10} or $d^{10}s^2$ configurations, and with non-metal elements, as shown in Table 2.3.

Table 2.3 Approaches to narrow band gap by modulation of valence band. ($\Delta E_g = E_g(doped) - E_g(pure)$)

***3d*-transition elements:** Sc, Ti, V, Cr, Mn, Fe, Co, Ni, Cu, Zn					
Examples	**ΔE_g/eV**	**Ref.**	**Examples**	**ΔE_g/eV**	**Ref.**
Fe-BiOBr	>0	[91]	Cu-Bi_2WO_6	>0	[92]
Co-$BiVO_4$	0.16	[93]	Cu-$BiVO_4$	0.09	[94]
Ni-$BiVO_4$	0.02	[93]	Zn-, Ni-Bi_2O_3	0.11, 0.06	[95, 96]
d^{10} or $d^{10}s^2$ configurations: Pd, Ag^+, Cd^{2+}, Pb^{2+}, Bi^{3+}, etc.					
Examples	**ΔE_g/eV**	**Ref.**	**Examples**	**ΔE_g/eV**	**Ref.**
Pd-$BiVO_4$	0.27	[97, 98]	Ag^+-$BiVO_4$	0.04	[99]
non-metal elements: N, B, F, S, etc.					
Examples	**ΔE_g/eV**	**Ref.**	**Examples**	**ΔE_g/eV**	**Ref.**
N-Bi_2WO_6	0.07	[100]	B-Bi_2WO_6	>0	[101]
N-$BiVO_4$	0.05	[102]	N-$(BiO)_2CO_3$	0.76	[76]
F-Bi_2WO_6	0.21	[42]	F-Bi_2WO_6	0.11	[103]
F-$BiPO_4$	>0	[104]			

By doping with *3d*-transition elements, it has been reported that the states of *3d* dopants insert a new band into the original band gap and shift to lower energy with increase of the atomic numbers of the dopants [105]. The impurity band energy can be regarded as the top of the valence band, so as to narrow the band gap and make it possible to absorb more visible light energy of the doped semiconductor. It has also been extended to applications in modification of bismuth based photocatalysts, aiming to improve visible-light sensitivity. Examples are shown in Table 2.3. Xu et al. reported that for a preparation of Cu-$BiVO_4$, when the ratio of dopants was varied from 0.5 at% to 20 at%, the band gaps were narrowed from 2.40 eV for $BiVO_4$ to 2.31 eV for Cu (20 at%)-$BiVO_4$ [94]. Correspondingly, the visible-light-induced photocatalytic activities were improved in degrading organic pollutants. Enhanced photocatalytic performance by doping Bi_2O_3 with *3d*-transition metal

(Ni and Zn) was also reported by Malathy et al. [96]. The band gaps were changed from 2.8 eV for Bi_2O_3 to 2.69 eV for Ni-Bi2O3 and 2.74 eV for Zn-Bi_2O_3. As a result, the photocatalytic activity in degrading MG (a triphenyl methane dye) were improved 12.5% and 275% under visible light irradiation for 180 min. It should also be mentioned that when doping with *3d*-transition elements, the visible-light sensitivity is improved by inserting *3d*-states in the band gap. However, these impurities may increase the bulk defects, which can be the recombination centers of electrons and holes. Also, the full *3d* orbital hinders electron transfer. These two factors might degrade the final photocatalytic activities and should be considered.

As for doping with d^{10} and $d^{10}s^2$ configurations in the valence band, it was proposed the *d* or *s*-orbital can be hybridized with O *2p* orbital, which would up-shift the top of valence band so as to narrow the band gap [4]. For instance, Shan et al. [99] studied the effect of doping Ag on $BiVO_4$ on photocatalytic performance. In Fig. 2.12b, the XPS spectra of $BiVO_4$ and Ag-$BiVO_4$ showed that the top of the valence band was up-shifted. The top valence band of $BiVO_4$ is mainly composed of Bi $5d^{10}6s^26p^3$ and hybridization of Bi *6s* - O *2p*. By loading Ag with $4d^{10}5s^1$ configuration, the stronger hybridization of *5s*-*2p* can push up the valance band maximum (VBM) energy so as to narrow the band gap. In another study, it was reported [97] that by doping Pd on $BiVO_4$, the visible-light sensitivity was significantly enhanced and the photocatalytic activity in degrading methyl orange was improved 66.7% under visible light for 15 hours.

As discussed above, the anionic metals were doped to improve the photocatalytic activity under visible light irradiation. A problem for using metal as dopants arises when the localized d states often insert into the band gap and result in recombination centers for electrons/holes. It was reported by Asahi and coworkers [106] that doping with non-metals such as C, N, and F could also introduce impurity states into and subsequently narrow the band gap (see Fig. 2.12c). *p* states of the non-metals could mix with O *2p* orbitals and generate the valence band maximum energy of the doped composites. For example, nitrogen doping of Bi_2WO_6 resulted in a narrowing of the band gap from 2.72 eV to 2.69 eV , accompanied by an improvement of the photocatalytic activity by 2-3 times under visible light over 60 min [100]. Dong and coworkers also reported N-$(BiO)_2CO_3$ as efficient visible light driven photocatalysts [76]. The band gap was significantly decreased

from 3.40 eV for $(BiO)_2CO_3$ to 2.66 eV for N-$(BiO)2CO_3$. The photocatalytic activity was investigated in removal of NO, and results showed that the removal efficiency was improved by 90% after doping N on $(BiO)_2CO_3$. F and B doped Bi_2WO_6 and F doped $BiPO_4$ were also reported with improved photocatalytic performance [42, 101, 104]. Compared to doping with metals, doping with non-metals could not only narrow the band gap to improve the visible-light-induced photocatalytic activity, but also inhibit the recombination of photogenerated electrical carriers.

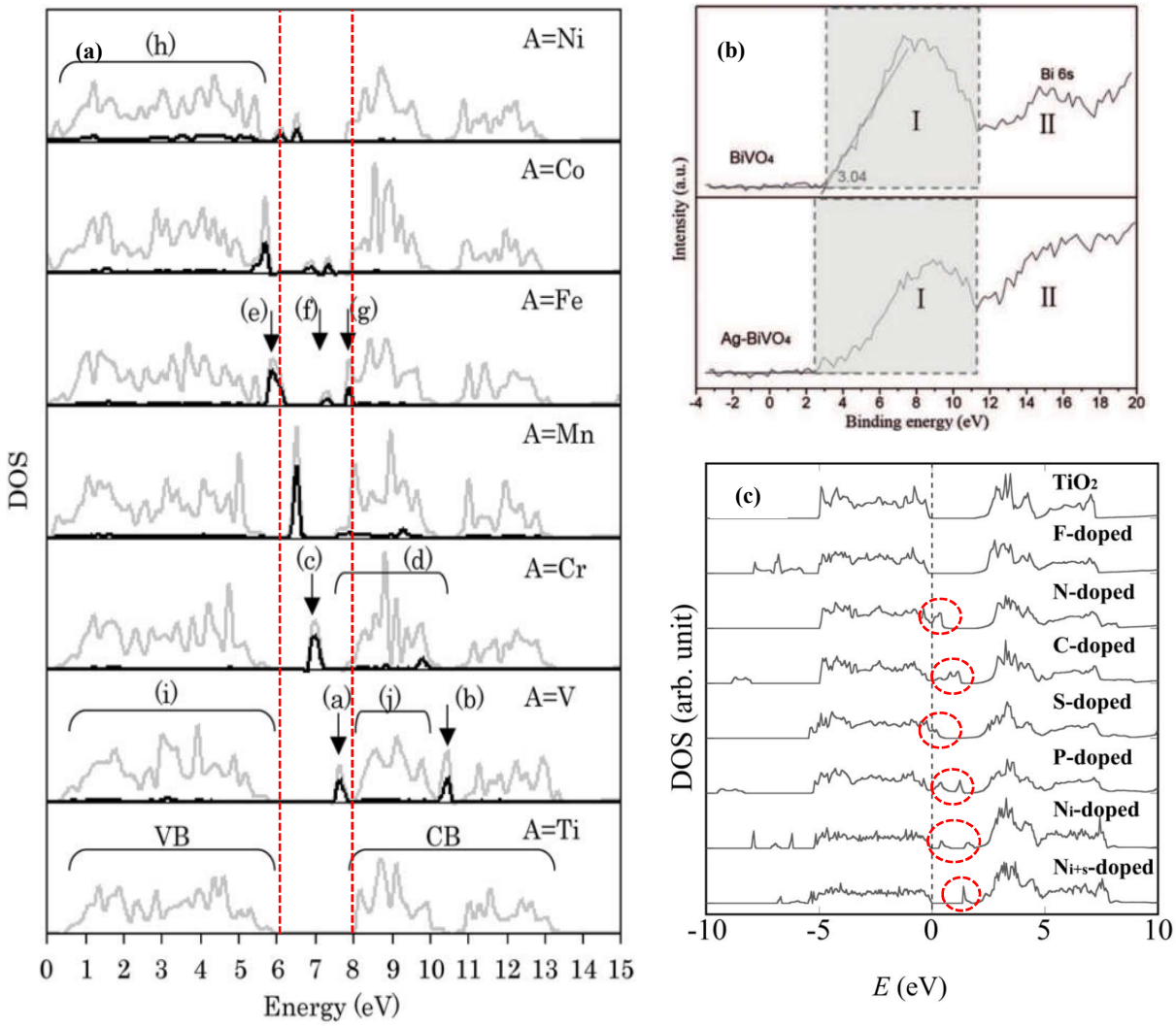


Figure 2.12 (a)Total density of states (TDOS) of the 3d-transition metal-doped TiO_2 (Gray solid line: TDOS; black solid line: DOS of dopants, Adapted from [105]), (b) XPS valence band spectra of (a) $BiVO_4$ and (b) Ag-$BiVO_4$ (Adapted from [99]), and (c) TDOS of non-metal doped TiO_2. (Calculated by FLAPW, arb. Unit: arbitrary unit. Adapted from [106])

2.3.2.2 Morphology control

Bismuth-based compounds can be prepared by various methods such as solid-state reactions, and hydrothermal and solvothermal methods. Samples prepared by different methods exhibit various morphologies and properties, including variable band gap energies. Zhang and coworkers [47] prepared Bi_2WO_6 with various nano- and microstructures by a surfactant-assisted hydrothermal method, including flower-, nanoplate (2D and 3D)-, tyre-, and sphere-like structures. Interestingly, the optical properties were influenced by the shapes of samples, especially their band gaps (ranging from 2.70 eV to 2.85 eV). This indicated that 3D super-structures such as flower-, tyre-like, and spherical structures have a red-shift in the bandgap transition when compared to plate-like structures. Zhao et al. [107] also reported a high-efficiency $(BiO)_2CO_3$ photocatalyst by controlling morphology to improve visible-light-driven photocatalytic activity. By adjusting the carbon source, sponge-, rose-, and plate-like $(BiO)_2CO_3$ were successfully synthesized (Table 2.4), with band gaps of about 2.87 eV, 2.97 eV, and 3.34 eV respectively. Similar results were also reported in [108]. The difference in band gaps for $(BiO)_2CO_3$ samples with different microstructures can be explained by the thinner units increasing the amplitude of the atomic vibrations and the inter-atomic spacing correspondingly enlarging. It also suggests that the 3D structure is of interest to narrow the band gap and improve the visible-light-driven photocatalytic activities. However, when the size of particles is small (in the nano scale), the quantum confinement effect [109] should be considered, as it can widen the band gap . For example, in the work reported on preparation of $BiVO_4$ [110], cubic-, sheet-, and flower-like structure were prepared with band gaps of 2.39 eV, 2.40 eV and 2.46 eV , respectively. The thickness of composed sheets decreased with each structure, and the thickness of the constituent plates for flower-like was in the nanoscale. Owing to the quantum confinement effect, the flower-like $BiVO_4$ had the widest band gap (2.46 eV). In conclusion, adjustment of morphologies of bismuth-based is an effective approach to control the band gap.

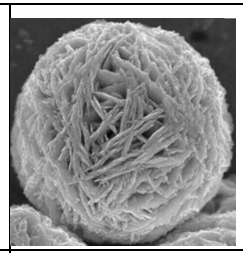
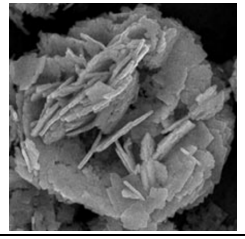
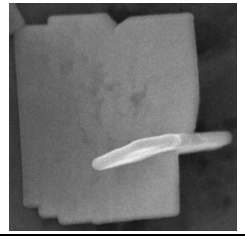
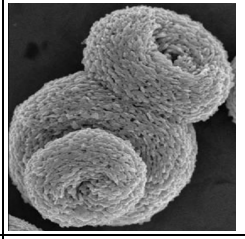
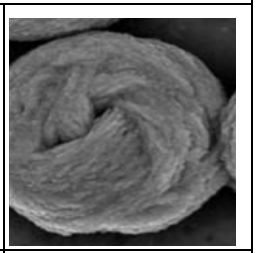
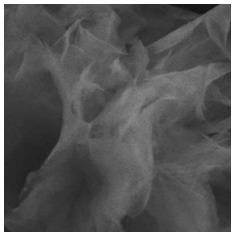
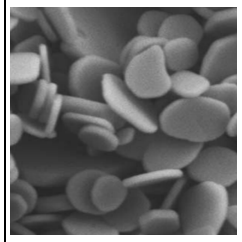
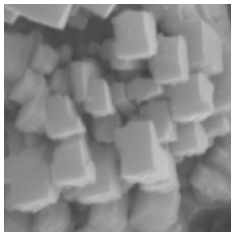
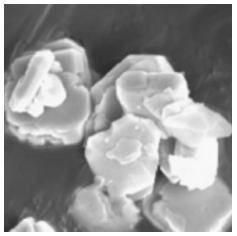
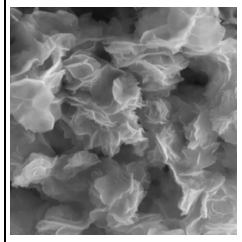
Compounds	Properties					
Bi_2WO_6 (adapted from [47])	SEM image					
	Morphology	Flower-like	Nanoplates (3D)	Nanoplates (2D)	Tyre-like	Spherical
	E_g/eV	2.76	2.85	2.81	2.75	2.70
$(BiO)_2CO_3$ (adapted from [107])	SEM image					
	Morphology	Sponge-like		Rose-like		Plate-like (2D)
	E_g/eV	2.87		2.97		3.34
$BiVO_4$ (adapted from [110])	SEM image					
	Morphology	Cubic-like		Sheet-like		Flower-like
	E_g/eV	2.39		2.40		2.46

Table 2.4 Different morphologies of prepared Bi-Based compounds.

2.3.2.3 Plasmonic-metal/semiconductor photocatalysts

Surface plasmon resonance (SPR) can be described as the resonant photon-induced collective oscillation of valence electrons, which occurs when the frequency of photons matches the natural frequency of surface electrons oscillating against the restoring force of positive nuclei [111]. For nanoparticles of noble metals, the SPR energy is in the range of 1.0~4.0 eV with respect to the Fermi level (Fig. 2.13a). In energetic electrons generated by the SPR effect, excitation can transfer to the conduction band of nearby semiconductors and then participate in the photocatalytic process. The extinction spectra of Au, Ag and Cu nanoparticles are shown in Fig. 2.13b. All can be activated by the SPR effect under visible light irradiation. This indicates that loading noble nanoparticles on bismuth based compounds may be a feasible and efficient approach to improve visible-light-driven photocatalytic performance [112]. Ren et al. [113] and Wang et al. [114] reported on loading Ag nanoparticles on Bi_2WO_6. The Ag-loaded Bi_2WO_6 were then applied in degradation of organic pollutants and disinfection. Both exhibited enhanced photocatalytic activity after loading Ag nanoparticles under visible light. By measuring the photoluminescence (PL) spectra, the electrons/holes recombination rate was also reduced to some extent. Cao and coworkers [115] also prepared Au-$BiVO_4$ applied in solar-driven wastewater treatment and water splitting. After loading Au nanoparticles, band gap energy was decreased by 0.03 eV, and the photocatalytic degradation of MB was improved by 64% under visible light irradiation. Au nanoparticles were also grown on $(BiO)_2CO_3$, aiming to enhance its visible light photocatalysis [116]. The excitation light was extended to the visible light range and photocatalytic performance in oxidization of NO was improved by 33%. Loading Ag/AgX (X=Cl, Br and I) on Bi-based compounds to the heterostructure was also an important approach to improve the visible-light-induced photocatalysis. For example, Shan et al. [117] prepared Ag/AgCl/$BiPO_4$ plasmonic photocatalysts with significantly enhanced visible photocatalytic activity and high stability. The band gap was narrowed from 3.9 eV for $BiPO_4$ to 2.75 eV for Ag/AgCl/$BiPO_4$. The possible degradation process of organic pollutants is shown in Fig. 2.14. AgCl plays a significant role in the process, forming a heterostructure with $BiPO_4$ to improve the electron/hole separation and generating a Cl• radical which can oxidize some of the organic pollutants. By loading Ag/AgCl, the photocatalytic activity of $BiPO_4$ was enhanced. Similarly, Ag/AgCl-BiOCl

[118], Ag/AgCl/Bi_2WO_6 [119] and Ag/AgBr-$(BiO)_2CO_3$[120] were also reported to enhance visible-light-induced photocatalytic activity.

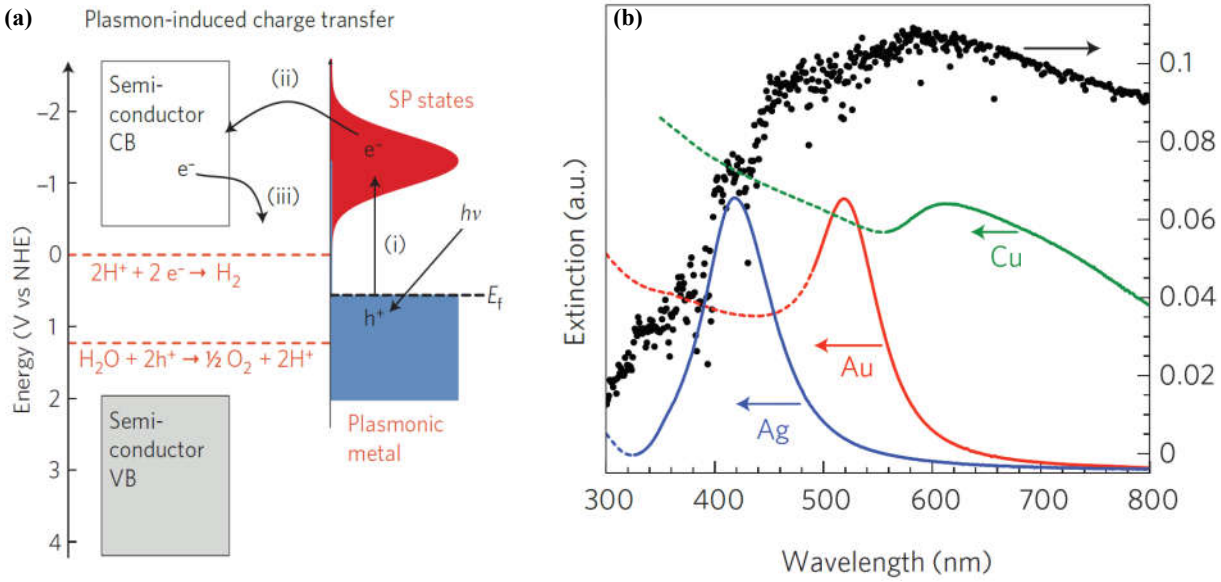


Figure 2.13 (a) Mechanism of plasmon-induced charge transfer: (i) SPR-induced electrons transfer, (ii) electrons transfer to conduction band of nearby semiconductor, (iii) electrons participate in the photocatalytic process. (b) Normalized extinction spectra of spherical Ag, Au, and Cu nanoparticles. (Adapted from [111])

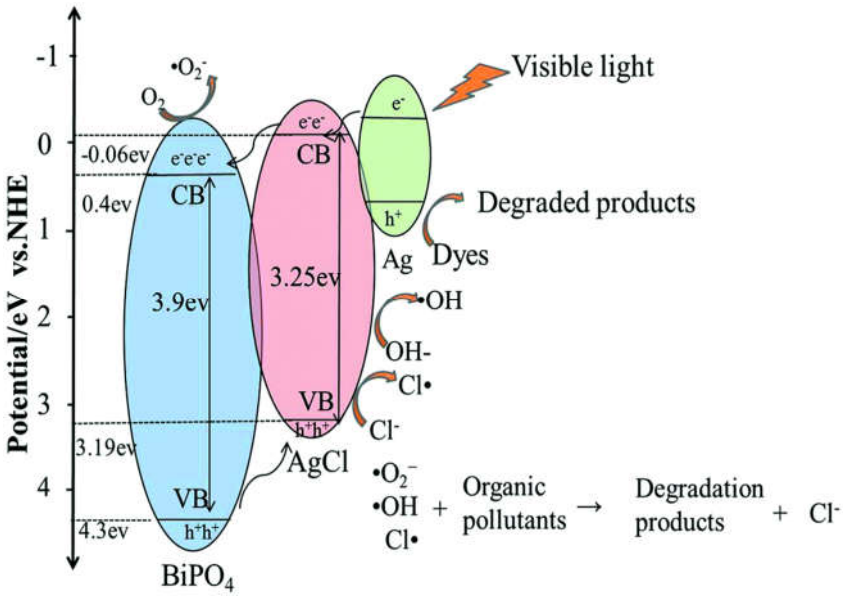


Figure 2.14 Mechanism of degradation of organic pollutants in presence of Ag/AgCl/$BiPO_4$. (Adapted from [117])

2.3.3 Implementation in water splitting

Crucial factors of water splitting to generate both H_2 and O_2 are (1) electrons on the conduction band with stronger reducing capacity to reduce H^+ to H_2, and (2) the potential of a valence band maximum higher than the redox potential of O_2/H_2O. The ideal band gap configuration to efficiently split water to produce H_2 and O_2 by a one photon excitation process is shown in Fig. 2.15a. However, it is rarely found in photocatalytic semiconductors. Only a few novel materials to directly split water to produce H_2 and O_2 have been reported, such as $In_{1-x}Ni_xTaO_4$ (x = 0 – 0.2)[121], Bi_2MNbO_7 (M = Al^{3+}, Ga^{3+} and In^{3+}) and $InMO_4$ (M = Nb^{5+} and Ta^{5+}) [13].

For band structures of most bismuth based semiconductors (as shown in Fig. 2.11), holes on the valence band with strong oxidizing capacity are able to produce O_2, but electrons on the conduction band with weak reducing capacity cannot generate H_2. The two photon excitation process is usually adopted by constructing a Z scheme between bismuth based semiconductors and other semiconductors to simultaneously generate O_2 and H_2 [122]. For example, Sasaki et al. successfully prepared Z-schematic photocatalysis between $BiVO_4$ and $Ru/SrTiO_3$:Rh with efficient water splitting under visible light irradiation (Table 2.5) [15]. $SrTiO_3$:Rh is a photocatalyst with high activity for H_2 evolution. Ru co-catalyst is used to suppress the back reaction from generated H_2 and O_2 to form H_2O. Rh (Cr or Ta), with reversible oxidation states, plays a pivotal role for the electron transfer between particles. When the weight ratio is 0.1/0.1 (g H_2-photocatalyst/g O_2-photocatalyst), the maximum production rates of O_2 and H_2 are 19 and 40 μmol h^{-1}, respectively. Z-scheme photocatalysis systems with Bi_2MoO_6 - $Ru/SrTiO_3$:Rh were also established, with the production rate of O_2 and H_2 being 5.2 and 5.2 μmol h^{-1}, respectively.

Some researchers have reported photocatalytic water splitting using bismuth based semiconductors employing strong oxidative holes to produce O_2 with the help of an additional electron acceptor (Ag^+, Fe^{3+}, etc.). Ke and coworkers [12] reported photocatalytic water splitting for O_2 production under visible light irradiation on $BiVO_4$, with the addition of Ag^+ and Fe^{3+} solutions as the electron acceptors. Production rates of O_2 were 194.6 and 139.7 μmol h^{-1}, respectively, for systems containing either $AgNO_3$ or $Fe(NO_3)_3$ solutions. Using an external electrode to transfer the extra electrons is also an

efficient way to improve photocatalytic water splitting performance. Ng et al. [14] reported on photoelectrochemical water splitting in the presence of BiVO4 connected with an external Pt electrode, resulting in a significant enhancement of water splitting for O_2 evolution.

Even though bismuth based semiconductors are visible-light-responsive, they are limited by their band configurations when applied in photocatalytic splitting, especially for H_2 production. Establishing Z-scheme photocatalysis systems and adding external electron acceptors as conventional approaches, as well as new methods, must be developed.

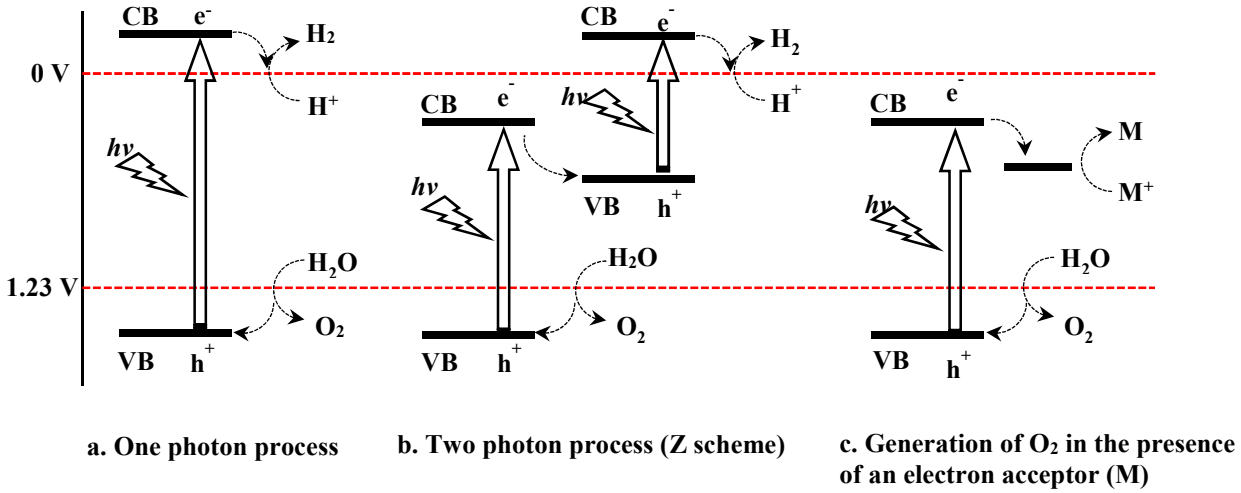


Figure 2.15 Schematic processes of water splitting on photocatalytic semiconductors: (a) one photon process, (b) two photon process (Z scheme), and (c) process with an electron acceptor.

Table 2.5 Water splitting using Z-scheme photocatalysis systems. (light source: 300-W Xe-arc lamp; weight ratio: H_2-photocatalyst/O_2-photocatalysts (g/g); aqueous H_2SO_4 solution: pH 3.5.) (Reproduced from [15])

H_2-photocatalyst	O_2-photocatalyst	Weight ratio	Incident light/nm	Production rate/μmol h^{-1}	
				H_2	O_2
-	$BiVO_4$	-	>420	0	0
Ru/SrTiO3:Rh	$BiVO_4$	0.04/0.1	>420	13	6.0
Ru/SrTiO3:Rh	$BiVO_4$	0.1/0.1	>420	40	19
Ru/SrTiO3:Rh	$BiVO_4$	0.2/0.1	>420	22	9.6
Ru/SrTiO3:Rh	$BiVO_4$	0.4/0.1	>420	14	5.8
Ru/SrTiO3:Cr, Ta	$BiVO_4$	0.1/0.1	>420	0.3	0.1
Ru/SrTiO3:Rh	Bi_2MoO_6	0.1/0.1	>420	12	5.2

2.3.4 Improvement of electrons/holes separate efficiency

The high recombination rate of electrons/holes significantly inhibits photocatalytic performance. Studies on improving photocatalytic activities by supressing their recombination have increasingly drawn researchers' attention. As discussed in section 3.2, metal doping and morphology control can prevent the recombination to some extent. Other than these methods, some other approaches have also been studied and reported on Bi-based semiconductors, *e.g.* forming heterojunctions between semiconductors and constructing external circuits by effect of photoelectrocatalysis.

2.3.4.1 Heterojunction

In recent years, fabrication of heterojunctions has been one of the most ingenious methods to inhibit the recombination of photogenerated electrons and holes. Numerous bismuth based heterostructures have been prepared (Table 2.6), which can be divided into two categories based on their types of constituent semiconductors: n-n heterojunction and p-n heterojunction. The mechanism of improvement in electron/hole separation for n-n and p-n heterojunctions can be explained by Fig. 2.16. Take the $(BiO)_2CO_3$-Bi_2S_3 n-n heterojunction as an example: photogenerated electrons on the conduction band of $(BiO)_2CO_3$ can be recombined with holes accumulated on the valence band of Bi_2S_3 at the interface of the Bi_2S_3/$(BiO)_2CO_3$ heterojunction. The consumption of electrons for

$(BiO)_2CO_3$ and holes for Bi_2S_3 results in an accumulation of holes in the $(BiO)_2CO_3$ side and of electrons in the Bi_2S_3 side. As a result, the n-n type heterojunction facilitates the separation of photogenerated electrons and holes and further improves photocatalytic activity. For p-n heterojunctions (BiOBr-Bi_2WO_6 as an example), a different mechanism explains the improvement in photocatalytic performance. In Fig. 2.16b, under the electrical force by p-n heterojunctions, electrons on the valence band of p-type BiOBr can transfer to that of n- type Bi_2WO_6 while holes move oppositely. The result is that electrons and holes are accumulated in n-type Bi_2WO_6 and p-type BiOBr, which facilitates the separation of electrons and holes and further increases activity. Both n-n heterojunctions and p-n heterojunctions are significant factors in improving the separation efficiency of photogenerated electron-hole pairs and can increase the lifetime of photogenerated carriers, thereby further improving the photocatalytic activity of bismuth based composites.

Table 2.6 Bismuth based heterojunctions.

Heterojunction	**Type**	**Ref.**	**Heterojunction**	**Type**	**Ref.**
Bi_2O_3-Bi_2WO_6	n-n	[123]	BiOI-$BiPO_4$	p-n	[124]
WO_3-Bi_2WO_6	n-n	[125]	$BiVO_4$-Bi_2O_3	n-n	[126]
g-C_3N_4-Bi_2WO_6	n-n	[127]	Ag_2O-$(BiO)_2CO_3$	p-n	[128]
Bi_2S_3-$(BiO)_2CO3$	n-n	[129]	$(BiO)_2CO_3$-BiOI	n-p	[130]
Bi_2WO_6-$BiVO_4$	n-n	[131]	BiOCl-$BiVO_4$	p-n	[132]
Bi_2S_3-BiOCl	n-p	[133]	Bi_2S_3-BiOCl	n-p	[133]
$NaBiO_3$-BiOCl	n-p	[134]	BiOBr-Bi_2WO_6	p-n	[4]

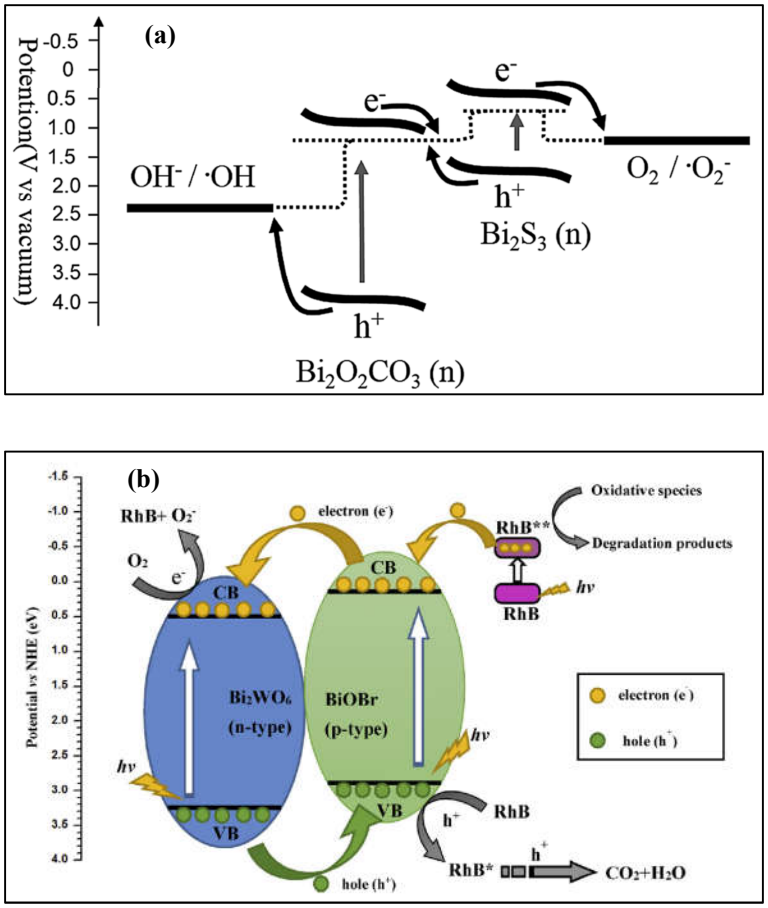


Figure 2.16 Schemes of (a) $(BiO)_2CO_3$-Bi_2S_3 n-n heterojunction (adapted from [129]) and (b) BiOBr-Bi_2WO_6 p-n heterojunction (adapted from [4]).

2.3.4.2 Photoelectrocatalysis

Photoelectrocatalysis is an integrated technique combining photocatalysis with electrochemistry. The purpose of this technique is mainly to improve the utilization efficiency of the electrons accumulated on the conduction band. The process requires an external circuit as shown in Fig. 2.17. Under the force of the electrical potential, photogenerated electrons and holes move directionally, resulting in electrons accumulating at the cathode and holes concentrating on photocatalysts at the anode. As a result, the recombination rate of electrons and holes is decreased, and the utilization rate of electrons and holes is improved. For bismuth based semiconductors applied in photoelectrocatalysis, studies are increasingly reported. For example, Bi_2WO_6 stabilized on Fluorine-doped Tin oxide (FTO) glass [135] and Indium-Tin oxide (ITO) glass [136, 137] showed efficient

removal of contaminants when subjected to visible light irradiation. Zhang *et al.* [138] reported on Ag-doped $BiVO_4$ film applied in photoelectrocatalytic degradation of phenol under visible light irradiation. Kinetic constants for the photocatalytic process in the presence of $BiVO_4$ and Ag-doped $BiVO_4$ were 0.0174 h^{-1} and 0.0280 h^{-1}, respectively. The kinetic constant was improved to 0.743 h^{-1} for the photoelectrocatalytic process in the presence of Ag-doped $BiVO_4$ under applied bias potential. Ag doping and applied bias potential significantly improved the separation of photogenerated carriers and further improved photocatalytic activity. Enhanced photoelectrocatalytic water splitting by electrical promotion of electron migration has also been reported [11, 14].

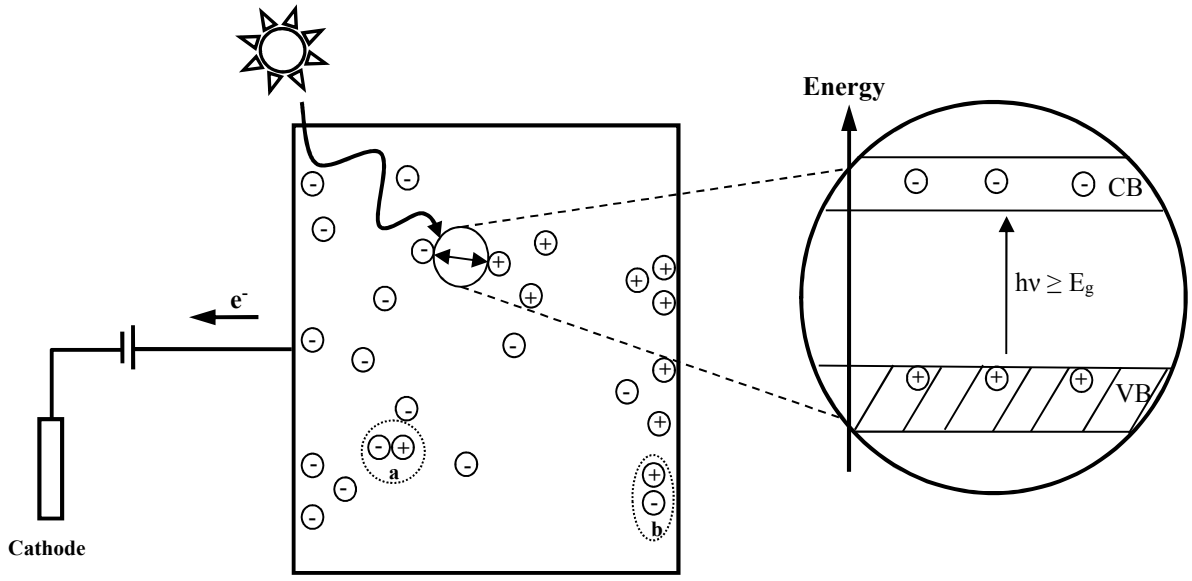


Figure 2.17 Mechanism of photoelectrocatalysis in the improvement of electrons-holes separation by an external circuit. (a. recombination in bulk, b. recombination on the surface)

2.3.5 Stabilities

Stability is an important parameter for a catalyst's performance. Stabilities of bismuth based photocatalyst semiconductors is mainly affected by the intrinsic structure and solubility of the photocatalyst, as well as the pH value and other properties of the substrate [139]. For layered bismuth based semiconductors such as BiOX and Bi_2MO_6, van der Waals, as well as covalent interaction forces, exist between layers. This results in higher stability when compared to other layered semiconductors (e.g. C_3N_4, where only van der

Waals interaction forces exist between layers). Bismuth based photocatalysts have low solubility constants. An example of this phenomenon is BiOCl, which has a small solubility constant of about 1.8×10^{-31}. This suggests that this type of material cannot be easily dissolved onto a substrate. However, some of the bismuth based photocatalysts are instable in an acidic environment. For example, Bi_2WO_6 may be transformed into H_2WO_4 and Bi_2O_3 in an acidic solution which directly deteriorates its photocatalytic performance [140]. Another important factor is photocorrosion associated with Bi releasing, which was rarely studied in the reported work and should be taken into account in future work.

2.4 Future work and concluding remarks

The interesting physiochemical properties of bismuth based semiconductors, especially the highly visible-light-induced photocatalytic activity, have drawn researchers' attention and driven significant research. The most widely studied bismuth based photocatalysts have been described in this review. In addition, main challenges have been summarized, including the high recombination rate of photogenerated carriers, the wide band gap, and the weak reducing capacity of electrons in the conduction band. Feasible approaches to overcome these challenges have also been suggested based on the work reported. Although drawbacks of using bismuth based photocatalysts can be significantly remedied, further efforts are still needed to obtain much more significant progress. Future work should focus on following aspects:

(1) To date, main applications of these prepared materials are to destroy organic pollutants and bacteria in wastewater and to purify polluted air, especially by denitration. The production rate of H_2 in photocatalytic water splitting under visible light should be developed by either modulation of energy bands or by formation of Z-scheme structures. Future work should also extend these advanced materials into other important areas, such as photocatalytic organic synthesis and photocatalytic reduction and recovery of heavy metals.

(2) Practical applications of bismuth based photocatalysts are rarely reported. Photocatalytic reactor design can significantly accelerate the scale-up process. This is a potential area for the industrialization of this advanced material. Additionally,

using a solar simulator instead of a bulb in experiments can test photocatalytic activity under solar irradiation, which gives a better evaluation of the material.

(3) Integrating with other techniques such as electrochemistry, membrane technique and biotechnology, can widen the application areas and prompt further development.

Even though many bismuth based semiconductors with high photocatalytic performance under visible light have been reported, they are still in the early stages in as long run of commercialization of this advanced material. The excellent and promising properties of Bi-based compounds suggest a bright future.

References

1. Akira Fujishima and Kenichi Honda, "Electrochemical photolysis of water at a semiconductor electrode," *nature*, vol. 238, pp. 37-38, 1972.

2. S. Girish Kumar and L. Gomathi Devi, "Review on Modified TiO2 Photocatalysis under UV/Visible Light: Selected Results and Related Mechanisms on Interfacial Charge Carrier Transfer Dynamics," *The Journal of Physical Chemistry A*, vol. 115, no. 46, pp. 13211-13241, 2011.

3. Huizhong An, Yi Du, Tianmin Wang, Cong Wang, Weichang Hao and Junying Zhang, "Photocatalytic properties of BiOX (X = Cl, Br, and I)," *Rare Metals*, vol. 27, no. 3, pp. 243-250, 2008.

4. Xiangchao Meng and Zisheng Zhang, "Facile synthesis of $BiOBr/Bi_2WO_6$ heterojunction semiconductors with high visible-light-driven photocatalytic activity," *Journal of Photochemistry and Photobiology A: Chemistry*, vol. 310, no. 0, pp. 33-44, 2015.

5. Brijesh Pare, S. B. Jonnalagadda, Hitendra Tomar, Pardeep Singh and V. W. Bhagwat, "ZnO assisted photocatalytic degradation of acridine orange in aqueous solution using visible irradiation," *Desalination*, vol. 232, no. 1–3, pp. 80-90, 2008.

6. Manon Vautier, Chantal Guillard and Jean-Marie Herrmann, "Photocatalytic Degradation of Dyes in Water: Case Study of Indigo and of Indigo Carmine," *Journal of Catalysis*, vol. 201, no. 1, pp. 46-59, 2001.

7. Gary A. Epling and Chitsan Lin, "Photoassisted bleaching of dyes utilizing TiO2 and

visible light," *Chemosphere*, vol. 46, no. 4, pp. 561-570, 2002.

8. S. Sakthivel, B. Neppolian, M. V. Shankar, B. Arabindoo, M. Palanichamy and V. Murugesan, "Solar photocatalytic degradation of azo dye: comparison of photocatalytic efficiency of ZnO and TiO2," *Solar Energy Materials and Solar Cells*, vol. 77, no. 1, pp. 65-82, 2003.

9. Yu Huang, Zhihui Ai, Wingkei Ho, Meijuan Chen and Shuncheng Lee, "Ultrasonic Spray Pyrolysis Synthesis of Porous Bi_2WO_6 Microspheres and Their Visible-Light-Induced Photocatalytic Removal of NO," *The Journal of Physical Chemistry C*, vol. 114, no. 14, pp. 6342-6349, 2010.

10. Jingshuai Chen, Shiyue Qin, Guixian Song, Tianyu Xiang, Feng Xin and Xiaohong Yin, "Shape-controlled solvothermal synthesis of Bi2S3 for photocatalytic reduction of CO2 to methyl formate in methanol," *Dalton Transactions*, vol. 42, no. 42, pp. 15133-15138, 2013.

11. Chunzhi Li, Junying Zhang and Kejia Liu, "A new method of enhancing photoelectrochemical characteristics of Bi/Bi2O3 electrode for hydrogen generation via water splitting," *Int. J. Electrochem. Sci*, vol. 7, pp. 5028-5034, 2012.

12. Dingning Ke, Tianyou Peng, Liang Ma, Ping Cai and Ping Jiang, "Photocatalytic water splitting for O2 production under visible-light irradiation on BiVO4 nanoparticles in different sacrificial reagent solutions," *Applied Catalysis A: General*, vol. 350, no. 1, pp. 111-117, 2008.

13. Zhigang Zou, Jinhua Ye and Hironori Arakawa, "Photocatalytic water splitting into H2 and/or O2 under UV and visible light irradiation with a semiconductor photocatalyst," *International Journal of Hydrogen Energy*, vol. 28, no. 6, pp. 663-669, 2003.

14. Yun Hau Ng, Akihide Iwase, Akihiko Kudo and Rose Amal, "Reducing Graphene Oxide on a Visible-Light BiVO4 Photocatalyst for an Enhanced Photoelectrochemical Water Splitting," *The Journal of Physical Chemistry Letters*, vol. 1, no. 17, pp. 2607-2612, 2010.

15. Yasuyoshi Sasaki, Hiroaki Nemoto, Kenji Saito and Akihiko Kudo, "Solar Water Splitting Using Powdered Photocatalysts Driven by Z-Schematic Interparticle Electron Transfer without an Electron Mediator," *The Journal of Physical Chemistry C*, vol. 113,

no. 40, pp. 17536-17542, 2009.

16. Yan Wang, Yanyuan Wen, Hanming Ding and Yongkui Shan, "Improved structural stability of titanium-doped β-Bi2O3 during visible-light-activated photocatalytic processes," *Journal of Materials Science*, vol. 45, no. 5, pp. 1385-1392, 2010.

17. Gangqiang Zhu, Wenxiu Que and Jin Zhang, "Synthesis and photocatalytic performance of Ag-loaded β-Bi2O3 microspheres under visible light irradiation," *Journal of Alloys and Compounds*, vol. 509, no. 39, pp. 9479-9486, 2011.

18. Joachim Eberl and Horst Kisch, "Visible light photo-oxidations in the presence of [small alpha]-Bi2O3," *Photochemical & Photobiological Sciences*, vol. 7, no. 11, pp. 1400-1406, 2008.

19. Tong Wu, Xinggui Zhou, Hua Zhang and Xinhua Zhong, "Bi2S3 nanostructures: A new photocatalyst," *Nano Research*, vol. 3, no. 5, pp. 379-386, 2010.

20. Hua Zhang, Jing Huang, Xinggui Zhou and Xinhua Zhong, "Single-Crystal Bi2S3 Nanosheets Growing via Attachment–Recrystallization of Nanorods," *Inorganic Chemistry*, vol. 50, no. 16, pp. 7729-7734, 2011.

21. Y. Bessekhouad, D. Robert and J. V. Weber, "Bi2S3/TiO2 and CdS/TiO2 heterojunctions as an available configuration for photocatalytic degradation of organic pollutant," *Journal of Photochemistry and Photobiology A: Chemistry*, vol. 163, no. 3, pp. 569-580, 2004.

22. Zhijie Zhang, Wenzhong Wang, Lu Wang and Songmei Sun, "Enhancement of Visible-Light Photocatalysis by Coupling with Narrow-Band-Gap Semiconductor: A Case Study on Bi2S3/Bi2WO6," *ACS Applied Materials & Interfaces*, vol. 4, no. 2, pp. 593-597, 2012.

23. I. M. Kobasa and G. P. Tarasenko, "Photocatalysis of Reduction of the Dye Methylene Blue by Bi2S3/CdS Nanocomposites," *Theoretical and Experimental Chemistry*, vol. 38, no. 4, pp. 255-258, 2002.

24. Kangrong Lai, Wei Wei, Ying Dai, Ruiqin Zhang and Baibiao Huang, "DFT calculations on structural and electronic properties of Bi2MO6 (M = Cr, Mo, W)," *Rare Metals*, vol. 30, no. 1, pp. 166-172, 2011.

25. Qianqian Zhang, Baibiao Huang, Peng Wang, Xiaoyang Zhang, Xiaoyan Qin and zeyan wang, "Synthesis and Photocatalytic Properties of One-Dimensional Composite Bi2O3-Bi2CrO6 Nanowires," *International Journal of Photoenergy*, vol. 2012, pp. 5, 2012.

26. Lin Zhou, Wenzhong Wang and Lisha Zhang, "Ultrasonic-assisted synthesis of visible-light-induced Bi2MO6 (M = W, Mo) photocatalysts," *Journal of Molecular Catalysis A: Chemical*, vol. 268, no. 1–2, pp. 195-200, 2007.

27. Junwang Tang, Zhigang Zou and Jinhua Ye, "Photocatalytic Decomposition of Organic Contaminants by Bi2WO6 Under Visible Light Irradiation," *Catalysis Letters*, vol. 92, no. 1-2, pp. 53-56, 2004.

28. Liwu Zhang and Yongfa Zhu, "A review of controllable synthesis and enhancement of performances of bismuth tungstate visible-light-driven photocatalysts," *Catalysis Science & Technology*, vol. 2, no. 4, pp. 694-706, 2012.

29. Chuan Zhang and Yongfa Zhu, "Synthesis of Square Bi_2WO_6 Nanoplates as High-Activity Visible-Light-Driven Photocatalysts," *Chemistry of Materials*, vol. 17, no. 13, pp. 3537-3545, 2005.

30. Tamar Saison, Nicolas Chemin, Corinne Chanéac, Olivier Durupthy, Valérie Ruaux, Laurence Mariey, Françoise Maugé, Patricia Beaunier and Jean-Pierre Jolivet, "Bi2O3, BiVO4, and Bi2WO6: Impact of Surface Properties on Photocatalytic Activity under Visible Light," *The Journal of Physical Chemistry C*, vol. 115, no. 13, pp. 5657-5666, 2011.

31. Jian Zhu, Jin-Guo Wang, Zhen-Feng Bian, Fen-Glei Cao and He-Xing Li, "Solvothermal synthesis of highly active Bi2WO6 visible photocatalyst," *Research on Chemical Intermediates*, vol. 35, no. 6-7, pp. 799-806, 2009.

32. Chunxiao Xu, Xiao Wei, Zhaohui Ren, Ying Wang, Gang Xu, Ge Shen and Gaorong Han, "Solvothermal preparation of Bi2WO6 nanocrystals with improved visible light photocatalytic activity," *Materials Letters*, vol. 63, no. 26, pp. 2194-2197, 2009.

33. Ling Wu, Jinhong Bi, Zhaohui Li, Xuxu Wang and Xianzhi Fu, "Rapid preparation of Bi2WO6 photocatalyst with nanosheet morphology via microwave-assisted solvothermal synthesis," *Catalysis Today*, vol. 131, no. 1–4, pp. 15-20, 2008.

34. Sheng-Peng Hu, Cheng-Yan Xu and Liang Zhen, "Solvothermal synthesis of Bi2WO6

hollow structures with excellent visible-light photocatalytic properties," *Materials Letters*, vol. 95, pp. 117-120, 2013.

35. Xiao-Feng Cao, Lei Zhang, Xue-Tai Chen and Zi-Ling Xue, "Microwave-assisted solution-phase preparation of flower-like Bi2WO6 and its visible-light-driven photocatalytic properties," *CrystEngComm*, vol. 13, no. 1, pp. 306-311, 2011.

36. Huidong Xie, Dezhong Shen, Xiaoqing Wang and Guangqiu Shen, "Microwave hydrothermal synthesis and visible-light photocatalytic activity of Bi2WO6 nanoplates," *Materials Chemistry and Physics*, vol. 103, no. 2–3, pp. 334-339, 2007.

37. HongHua Li, ChaoYu Liu, KunWei Li and Hao Wang, "Preparation, characterization and photocatalytic properties of nanoplate Bi2MoO6 catalysts," *Journal of Materials Science*, vol. 43, no. 22, pp. 7026-7034, 2008.

38. Yanhui Shi, Shouhua Feng and Changsheng Cao, "Hydrothermal synthesis and characterization of Bi2MoO6 and Bi2WO6," *Materials Letters*, vol. 44, no. 3–4, pp. 215-218, 2000.

39. Liwu Zhang, Tongguang Xu, Xu Zhao and Yongfa Zhu, "Controllable synthesis of Bi2MoO6 and effect of morphology and variation in local structure on photocatalytic activities," *Applied Catalysis B: Environmental*, vol. 98, no. 3–4, pp. 138-146, 2010.

40. Lijin Xie, Junfeng Ma and Gaojie Xu, "Preparation of a novel Bi_2MoO_6 flake-like nanophotocatalyst by molten salt method and evaluation for photocatalytic decomposition of rhodamine B," *Materials Chemistry and Physics*, vol. 110, no. 2–3, pp. 197-200, 2008.

41. Huidong Xie, Dezhong Shen, Xiaoqing Wang and Guangqiu Shen, "Microwave hydrothermal synthesis and visible-light photocatalytic activity of γ-Bi2MoO6 nanoplates," *Materials Chemistry and Physics*, vol. 110, no. 2–3, pp. 332-336, 2008.

42. Hongbo Fu, Shicheng Zhang, Tongguang Xu, Yongfa Zhu and Jianmin Chen, "Photocatalytic Degradation of RhB by Fluorinated Bi2WO6 and Distributions of the Intermediate Products," *Environmental Science & Technology*, vol. 42, no. 6, pp. 2085-2091, 2008.

43. Sebastián Murcia-López, María C. Hidalgo and José A. Navío, "Degradation of Rhodamine B/Phenol Mixtures in Water by Sun-Like Excitation of a Bi2WO6–TiO2

Photocatalyst," *Photochemistry and Photobiology*, vol. 89, no. 4, pp. 832-840, 2013.

44. Yan Zhang, Yukun Zhu, Jianqiang Yu, Dongjiang Yang, Tsz Wai Ng, Po Keung Wong and Jimmy C. Yu, "Enhanced photocatalytic water disinfection properties of Bi2MoO6-RGO nanocomposites under visible light irradiation," *Nanoscale*, vol. 5, no. 14, pp. 6307-6310, 2013.

45. Li-Sha Zhang, Kin-Hang Wong, Ho-Yin Yip, Chun Hu, Jimmy C. Yu, Chiu-Yeung Chan and Po-Keung Wong, "Effective Photocatalytic Disinfection of E. coli K-12 Using AgBr−Ag−Bi2WO6 Nanojunction System Irradiated by Visible Light: The Role of Diffusing Hydroxyl Radicals," *Environmental Science & Technology*, vol. 44, no. 4, pp. 1392-1398, 2010.

46. Yi Huang, JiHuai Wu, MiaoLiang Huang, JianMing Lin and YunFang Huang, "Influence of surfactants on the morphology and photocatalytic activity of Bi2WO6 by hydrothermal synthesis," *Science China Chemistry*, vol. 54, no. 1, pp. 211-216, 2011.

47. Lisha Zhang, Wenzhong Wang, Lin Zhou and Haolan Xu, "Bi_2WO_6 Nano‐ and Microstructures: Shape Control and Associated Visible‐Light‐Driven Photocatalytic Activities," *Small*, vol. 3, no. 9, pp. 1618-1625, 2007.

48. Guohui Tian, Yajie Chen, Wei Zhou, Kai Pan, Youzhen Dong, Chungui Tian and Honggang Fu, "Facile solvothermal synthesis of hierarchical flower-like Bi2MoO6 hollow spheres as high performance visible-light driven photocatalysts," *Journal of Materials Chemistry*, vol. 21, no. 3, pp. 887-892, 2011.

49. Zongyan Zhao, Wenjun Luo, Zhaosheng Li and Zhigang Zou, "Density functional theory study of doping effects in monoclinic clinobisvanite BiVO4," *Physics Letters A*, vol. 374, no. 48, pp. 4919-4927, 2010.

50. J. D. Bierlein and A. W. Sleight, "Ferroelasticity in BiVO4," *Solid State Communications*, vol. 16, no. 1, pp. 69-70.

51. M. Gotic, S. Music, M. Ivanda, M. Soufek and S. Popovic, "Synthesis and characterisation of bismuth(III) vanadate," *Journal of Molecular Structure*, vol. 744-747, pp. 535-540, 2005.

52. Akihiko Kudo, Keiko Omori and Hideki Kato, "A Novel Aqueous Process for Preparation of Crystal Form-Controlled and Highly Crystalline BiVO4 Powder from Layered Vanadates at Room Temperature and Its Photocatalytic and Photophysical Properties," *Journal of the American Chemical Society*, vol. 121, no. 49, pp. 11459-11467, 1999.

53. Xi Zhang, Zhihui Ai, Falong Jia, Lizhi Zhang, Xiaoxing Fan and Zhigang Zou, "Selective synthesis and visible-light photocatalytic activities of BiVO4 with different crystalline phases," *Materials Chemistry and Physics*, vol. 103, no. 1, pp. 162-167, 2007.

54. JingBing Liu, Hao Wang, Shu Wang and Hui Yan, "Hydrothermal preparation of BiVO4 powders," *Materials Science and Engineering: B*, vol. 104, no. 1–2, pp. 36-39, 2003.

55. Rong'an He, Shaowen Cao, Peng Zhou and Jiaguo Yu, "Recent advances in visible light Bi-based photocatalysts," *Chinese Journal of Catalysis*, vol. 35, no. 7, pp. 989-1007, 2014.

56. Zhijie Zhang, Wenzhong Wang, Meng Shang and Wenzong Yin, "Photocatalytic degradation of rhodamine B and phenol by solution combustion synthesized BiVO4 photocatalyst," *Catalysis Communications*, vol. 11, no. 11, pp. 982-986, 2010.

57. Meng Shang, Wenzhong Wang, Jia Ren, Songmei Sun and Ling Zhang, "A novel BiVO4 hierarchical nanostructure: controllable synthesis, growth mechanism, and application in photocatalysis," *CrystEngComm*, vol. 12, no. 6, pp. 1754-1758, 2010.

58. Jinzhan Su, Liejin Guo, Ningzhong Bao and Craig A. Grimes, "Nanostructured WO3/BiVO4 Heterojunction Films for Efficient Photoelectrochemical Water Splitting," *Nano Letters*, vol. 11, no. 5, pp. 1928-1933, 2011.

59. Jingxiu Yang , Donge Wang , Xin Zhou and Can Li, "A Theoretical Study on the Mechanism of Photocatalytic Oxygen Evolution on BiVO4 in Aqueous Solution," *Chemistry – A European Journal*, vol. 19, no. 4, pp. 1320-1326, 2013.

60. Yuanyuan Liu, Baibiao Huang, Ying Dai, Xiaoyang Zhang, Xiaoyan Qin, Minhua Jiang and Myung-Hwan Whangbo, "Selective ethanol formation from photocatalytic reduction of carbon dioxide in water with BiVO4 photocatalyst," *Catalysis Communications*, vol. 11, no. 3, pp. 210-213, 2009.

61. Amin Yoosefi Booshehri, Simon Chun-Kiat Goh, Jindui Hong, Rongrong Jiang and Rong Xu, "Effect of depositing silver nanoparticles on BiVO4 in enhancing visible light photocatalytic inactivation of bacteria in water," *Journal of Materials Chemistry A*, vol. 2, no. 17, pp. 6209-6217, 2014.

62. Wen Lai Huang and Qingshan Zhu, "Electronic structures of relaxed BiOX (X = F, Cl, Br, I) photocatalysts," *Computational Materials Science*, vol. 43, no. 4, pp. 1101-1108, 2008.

63. Wenyue Su, Jian Wang, Yingxing Huang, Wanjun Wang, Ling Wu, XuXu Wang and Ping Liu, "Synthesis and catalytic performances of a novel photocatalyst BiOF," *Scripta Materialia*, vol. 62, no. 6, pp. 345-348, 2010.

64. Xi Zhang, Zhihui Ai, Falong Jia and Lizhi Zhang, "Generalized One-Pot Synthesis, Characterization, and Photocatalytic Activity of Hierarchical BiOX (X = Cl, Br, I) Nanoplate Microspheres," *The Journal of Physical Chemistry C*, vol. 112, no. 3, pp. 747-753, 2008.

65. Hefeng Cheng, Baibiao Huang and Ying Dai, "Engineering BiOX (X = Cl, Br, I) nanostructures for highly efficient photocatalytic applications," *Nanoscale*, vol. 6, no. 4, pp. 2009-2026, 2014.

66. Yuechen Chou, Changlu Shao, Xinghua Li, Chunyan Su, Hongchuan Xu, Mingyi Zhang, Peng Zhang, Xin Zhang and Yichun Liu, "BiOCl nanosheets immobilized on electrospun polyacrylonitrile nanofibers with high photocatalytic activity and reusable property," *Applied Surface Science*, vol. 285, Part B, pp. 509-516, 2013.

67. Xiaoyan Qin, Hefeng Cheng, Wenjun Wang, Baibiao Huang, Xiaoyang Zhang and Ying Dai, "Three dimensional BiOX (X=Cl, Br and I) hierarchical architectures: facile ionic liquid-assisted solvothermal synthesis and photocatalysis towards organic dye degradation," *Materials Letters*, vol. 100, pp. 285-288, 2013.

68. Chengsi Pan and Yongfa Zhu, "New Type of BiPO4 Oxy-Acid Salt Photocatalyst with High Photocatalytic Activity on Degradation of Dye," *Environmental Science & Technology*, vol. 44, no. 14, pp. 5570-5574, 2010.

69. Guangfang Li, Yao Ding, Yafang Zhang, Zhong Lu, Hongzhe Sun and Rong Chen,

"Microwave synthesis of BiPO4 nanostructures and their morphology-dependent photocatalytic performances," *Journal of Colloid and Interface Science*, vol. 363, no. 2, pp. 497-503, 2011.

70. Chengsi Pan and Yongfa Zhu, "Size-controlled synthesis of BiPO4 nanocrystals for enhanced photocatalytic performance," *Journal of Materials Chemistry*, vol. 21, no. 12, pp. 4235-4241, 2011.

71. Baihua Long, Jianhui Huang and Xinchen Wang, "Photocatalytic degradation of benzene in gas phase by nanostructured BiPO4 catalysts," *Progress in Natural Science: Materials International*, vol. 22, no. 6, pp. 644-653, 2012.

72. Peter Taylor, S. Sunder and Vincent J. Lopata, "Structure, spectra, and stability of solid bismuth carbonates," *Canadian Journal of Chemistry*, vol. 62, no. 12, pp. 2863-2873, 1984.

73. Fan Dong, Anmin Zheng, Yanjuan Sun, Min Fu, Boqiong Jiang, Wing-Kei Ho, S. C. Lee and Zhongbiao Wu, "One-pot template-free synthesis, growth mechanism and enhanced photocatalytic activity of monodisperse (BiO)2CO3 hierarchical hollow microspheres self-assembled with single-crystalline nanosheets," *CrystEngComm*, vol. 14, no. 10, pp. 3534-3544, 2012.

74. Rong Chen, Man Ho So, Jun Yang, Feng Deng, Chi-Ming Che and Hongzhe Sun, "Fabrication of bismuth subcarbonate nanotube arrays from bismuth citrate," *Chemical Communications*, no. 21, pp. 2265-2267, 2006.

75. Fan Dong, S. C. Lee, Zhongbiao Wu, Yu Huang, Min Fu, Wing-Kei Ho, Shichun Zou and Bo Wang, "Rose-like monodisperse bismuth subcarbonate hierarchical hollow microspheres: One-pot template-free fabrication and excellent visible light photocatalytic activity and photochemical stability for NO removal in indoor air," *Journal of Hazardous Materials*, vol. 195, pp. 346-354, 2011.

76. Fan Dong, Yanjuan Sun, Min Fu, Wing-Kei Ho, Shun Cheng Lee and Zhongbiao Wu, "Novel in Situ N-Doped (BiO)2CO3 Hierarchical Microspheres Self-Assembled by Nanosheets as Efficient and Durable Visible Light Driven Photocatalyst," *Langmuir*, vol. 28, no. 1, pp. 766-773, 2012.

77. Xiaofeng Chang, Jun Huang, Cheng Cheng, Qian Sui, Wei Sha, Guangbin Ji, Shubo

Deng and Gang Yu, "BiOX (X = Cl, Br, I) photocatalysts prepared using NaBiO3 as the Bi source: Characterization and catalytic performance," *Catalysis Communications*, vol. 11, no. 5, pp. 460-464, 2010.

78. Takahiro Takei, Rie Haramoto, Qiang Dong, Nobuhiro Kumada, Yoshinori Yonesaki, Nobukazu Kinomura, Takayuki Mano, Shunsuke Nishimoto, Yoshikazu Kameshima and Michihiro Miyake, "Photocatalytic activities of various pentavalent bismuthates under visible light irradiation," *Journal of Solid State Chemistry*, vol. 184, no. 8, pp. 2017-2022, 2011.

79. Kai Yu, Shaogui Yang, Huan He, Cheng Sun, Chenggang Gu and Yongming Ju, "Visible Light-Driven Photocatalytic Degradation of Rhodamine B over NaBiO3: Pathways and Mechanism," *The Journal of Physical Chemistry A*, vol. 113, no. 37, pp. 10024-10032, 2009.

80. Naoki Kikugawa, Liqun Yang, Takehiko Matsumoto and Jinhua Ye, "Photoinduced degradation of organic dye over LiBiO3 under illumination of white fluorescent light," *Journal of Materials Research*, vol. 25, no. 01, pp. 177-181, 2010.

81. Xiaofeng Chang, Jun Huang, Cheng Cheng, Wei Sha, Xue Li, Guangbin Ji, Shubo Deng and Gang Yu, "Photocatalytic decomposition of 4-t-octylphenol over NaBiO3 driven by visible light: Catalytic kinetics and corrosion products characterization," *Journal of Hazardous Materials*, vol. 173, no. 1–3, pp. 765-772, 2010.

82. Rajalakshmi Ramachandran, M. Sathiya, K. Ramesha, A. S. Prakash, Giridhar Madras and A. K. Shukla, "Photocatalytic properties of KBiO3 and LiBiO3 with tunnel structures," *Journal of Chemical Sciences*, vol. 123, no. 4, pp. 517-524, 2011.

83. Tetsuya Kako, Zhigang Zou, Masahiko Katagiri and Jinhua Ye, "Decomposition of Organic Compounds over NaBiO3 under Visible Light Irradiation," *Chemistry of Materials*, vol. 19, no. 2, pp. 198-202, 2007.

84. Xiaojuan Yu, Jiangya Zhou, Zhiping Wang and Weimin Cai, "Preparation of visible light-responsive AgBiO3 bactericide and its control effect on the Microcystis aeruginosa," *Journal of Photochemistry and Photobiology B: Biology*, vol. 101, no. 3, pp. 265-270, 2010.

85. Yong Xu and Martin A.A. Schoonen, "The absolute energy positions of conduction and

valence bands of selected semiconducting minerals," *American Mineralogist*, vol. 85, no. 3-4, pp. 543-556, 2000.

86. Robert Thomas Sanderson, *Chemical periodicity*, Reinhold, New York, US, 1961.

87. M. A. Butler and D. S. Ginley, "Prediction of Flatband Potentials at Semiconductor - Electrolyte Interfaces from Atomic Electronegativities," *Journal of The Electrochemical Society*, vol. 125, no. 2, pp. 228-232, 1978.

88. F. El Halouani and A. Deschanvres, "Interfaces semi-conducteur-electrolyte: Correlations entre le potentiel de bande plate et les echelles d'electronegativite," *Materials Research Bulletin*, vol. 17, no. 8, pp. 1045-1052, 1982.

89. Robert S. Mulliken, "A New Electroaffinity Scale; Together with Data on Valence States and on Valence Ionization Potentials and Electron Affinities," *The Journal of Chemical Physics*, vol. 2, no. 11, pp. 782-793, 1934.

90. Robert S. Mulliken, "Electronic Structures of Molecules XI. Electroaffinity, Molecular Orbitals and Dipole Moments," *The Journal of Chemical Physics*, vol. 3, no. 9, pp. 573-585, 1935.

91. Guohua Jiang, Xiaohong Wang, Zhen Wei, Xia Li, Xiaoguang Xi, Ruanbing Hu, Bolin Tang, Rijing Wang, Sheng Wang, Tao Wang and Wenxing Chen, "Photocatalytic properties of hierarchical structures based on Fe-doped BiOBr hollow microspheres," *Journal of Materials Chemistry A*, vol. 1, no. 7, pp. 2406-2410, 2013.

92. Jiehui Xu, Wenzhong Wang, Erping Gao, Jia Ren and Lu Wang, "Bi2WO6/Cu0: A novel coupled system with enhanced photocatalytic activity by Fenton-like synergistic effect," *Catalysis Communications*, vol. 12, no. 9, pp. 834-838, 2011.

93. Bin Zhou, Xu Zhao, Huijuan Liu, Jiuhui Qu and C. P. Huang, "Synthesis of visible-light sensitive M–BiVO4 (M = Ag, Co, and Ni) for the photocatalytic degradation of organic pollutants," *Separation and Purification Technology*, vol. 77, no. 3, pp. 275-282, 2011.

94. Hui Xu, Huaming Li, Chundu Wu, Jinyu Chu, Yongsheng Yan, Huoming Shu and Zheng Gu, "Preparation, characterization and photocatalytic properties of Cu-loaded

BiVO4," *Journal of Hazardous Materials*, vol. 153, no. 1–2, pp. 877-884, 2008.

95. Abdul Hameed, Valentina Gombac, Tiziano Montini, Laura Felisari and Paolo Fornasiero, "Photocatalytic activity of zinc modified Bi2O3," *Chemical Physics Letters*, vol. 483, no. 4–6, pp. 254-261, 2009.

96. P. Malathy, K. Vignesh, M. Rajarajan and A. Suganthi, "Enhanced photocatalytic performance of transition metal doped Bi2O3 nanoparticles under visible light irradiation," *Ceramics International*, vol. 40, no. 1, Part A, pp. 101-107, 2014.

97. Lei Ge, "Novel Pd/BiVO4 composite photocatalysts for efficient degradation of methyl orange under visible light irradiation," *Materials Chemistry and Physics*, vol. 107, no. 2–3, pp. 465-470, 2008.

98. Lei Ge, "Synthesis and characterization of novel visible-light-driven Pd/BiVO4 composite photocatalysts," *Materials Letters*, vol. 62, no. 6–7, pp. 926-928, 2008.

99. Lianwei Shan, Yuteng Liu, Chengguo Ma, Limin Dong, Lizhu Liu and Ze Wu, "Enhanced Photocatalytic Performance in Ag+-Induced BiVO4/β-Bi2O3 Heterojunctions," *European Journal of Inorganic Chemistry*, pp. n/a-n/a, 2015.

100. Meng Shang, Wenzhong Wang, Ling Zhang and Haolan Xu, "Bi_2WO_6 with significantly enhanced photocatalytic activities by nitrogen doping," *Materials Chemistry and Physics*, vol. 120, no. 1, pp. 155-159, 2010.

101. Yu Fu, Chun Chang, Peng Chen, Xiaolong Chu and Lingyan Zhu, "Enhanced photocatalytic performance of boron doped Bi2WO6 nanosheets under simulated solar light irradiation," *Journal of Hazardous Materials*, vol. 254–255, pp. 185-192, 2013.

102. Min Wang, Qiong Liu, Yinsheng Che, Lifang Zhang and Dong Zhang, "Characterization and photocatalytic properties of N-doped BiVO4 synthesized via a sol–gel method," *Journal of Alloys and Compounds*, vol. 548, pp. 70-76, 2013.

103. Rui Shi, Guangli Huang, Jie Lin and Yongfa Zhu, "Photocatalytic Activity Enhancement for Bi2WO6 by Fluorine Substitution," *The Journal of Physical Chemistry C*, vol. 113, no. 45, pp. 19633-19638, 2009.

104. Yanfang Liu, Yanhui Lv, Yanyan Zhu, Di Liu, Ruilong Zong and Yongfa Zhu,

"Fluorine mediated photocatalytic activity of BiPO4," *Applied Catalysis B: Environmental*, vol. 147, pp. 851-857, 2014.

105. Tsutomu Umebayashi, Tetsuya Yamaki, Hisayoshi Itoh and Keisuke Asai, "Analysis of electronic structures of 3d transition metal-doped TiO2 based on band calculations," *Journal of Physics and Chemistry of Solids*, vol. 63, no. 10, pp. 1909-1920, 2002.

106. R. Asahi, T. Morikawa, T. Ohwaki, K. Aoki and Y. Taga, "Visible-Light Photocatalysis in Nitrogen-Doped Titanium Oxides," *Science*, vol. 293, no. 5528, pp. 269-271, 2001.

107. Tianyu Zhao, Jiantao Zai, Miao Xu, Qiong Zou, Yuezeng Su, Kaixue Wang and Xuefeng Qian, "Hierarchical Bi2O2CO3 microspheres with improved visible-light-driven photocatalytic activity," *CrystEngComm*, vol. 13, no. 12, pp. 4010-4017, 2011.

108. Yan Zheng, Fang Duan, Mingqing Chen and Yi Xie, "Synthetic Bi2O2CO3 nanostructures: Novel photocatalyst with controlled special surface exposed," *Journal of Molecular Catalysis A: Chemical*, vol. 317, no. 1–2, pp. 34-40, 2010.

109. Toshihide Takagahara and Kyozaburo Takeda, "Theory of the quantum confinement effect on excitons in quantum dots of indirect-gap materials," *Physical Review B*, vol. 46, no. 23, pp. 15578-15581, 1992.

110. Haibin Li, Guocong Liu and Xuechen Duan, "Monoclinic BiVO4 with regular morphologies: Hydrothermal synthesis, characterization and photocatalytic properties," *Materials Chemistry and Physics*, vol. 115, no. 1, pp. 9-13, 2009.

111. Suljo Linic, Phillip Christopher and David B. Ingram, "Plasmonic-metal nanostructures for efficient conversion of solar to chemical energy," *Nature Materials*, vol. 10, no. 12, pp. 911-921, 2011.

112. Peng Wang, Baibiao Huang, Ying Dai and Myung-Hwan Whangbo, "Plasmonic photocatalysts: harvesting visible light with noble metal nanoparticles," *Physical Chemistry Chemical Physics*, vol. 14, no. 28, pp. 9813-9825, 2012.

113. Jia Ren, Wenzhong Wang, Songmei Sun, Ling Zhang and Jiang Chang, "Enhanced photocatalytic activity of Bi2WO6 loaded with Ag nanoparticles under visible light irradiation," *Applied Catalysis B: Environmental*, vol. 92, no. 1–2, pp. 50-55, 2009.

114. Danjun Wang, Ganglin Xue, Yanzhong Zhen, Feng Fu and Dongsheng Li, "Monodispersed Ag nanoparticles loaded on the surface of spherical Bi2WO6 nanoarchitectures with enhanced photocatalytic activities," *Journal of Materials Chemistry*, vol. 22, no. 11, pp. 4751-4758, 2012.

115. Shao-Wen Cao, Zhen Yin, James Barber, Freddy Y. C. Boey, Say Chye Joachim Loo and Can Xue, "Preparation of Au-BiVO4 Heterogeneous Nanostructures as Highly Efficient Visible-Light Photocatalysts," *ACS Applied Materials & Interfaces*, vol. 4, no. 1, pp. 418-423, 2012.

116. Rui Wang, Xinwei Li, Wen Cui, Yuxin Zhang and Fan Dong, "In situ growth of Au nanoparticles on 3D Bi2O2CO3 for surface plasmon enhanced visible light photocatalysis," *New Journal of Chemistry*, vol. 39, no. 11, pp. 8446-8453, 2015.

117. Pandi Shan, Chenggang Niu, Dawei Huang, Guangming Zeng and Huan Zhang, "Facile synthesis of Ag/AgCl/BiPO4 plasmonic photocatalyst with significantly enhanced visible photocatalytic activity and high stability," *RSC Advances*, vol. 5, no. 108, pp. 89105-89112, 2015.

118. Wei Xiong, Qidong Zhao, Xinyong Li and Dongke Zhang, "One-step synthesis of flower-like Ag/AgCl/BiOCl composite with enhanced visible-light photocatalytic activity," *Catalysis Communications*, vol. 16, no. 1, pp. 229-233, 2011.

119. Yinghua Liang, Shuanglong Lin, Li Liu, Jinshan Hu and Wenquan Cui, "Oil-in-water self-assembled Ag@AgCl QDs sensitized Bi2WO6: Enhanced photocatalytic degradation under visible light irradiation," *Applied Catalysis B: Environmental*, vol. 164, pp. 192-203, 2015.

120. Lei Jin, Gangqiang Zhu, Mirabbos Hojamberdiev, Xiancong Luo, Congwei Tan, Jianhong Peng, Xiumei Wei, Jinping Li and Peng Liu, "A Plasmonic Ag–AgBr/Bi2O2CO3 Composite Photocatalyst with Enhanced Visible-Light Photocatalytic Activity," *Industrial & Engineering Chemistry Research*, vol. 53, no. 35, pp. 13718-13727, 2014.

121. Zhigang Zou, Jinhua Ye, Kazuhiro Sayama and Hironori Arakawa, "Direct splitting of water under visible light irradiation with an oxide semiconductor photocatalyst," *Nature*, vol. 414, no. 6864, pp. 625-627, 2001.

122. Akihiko Kudo, "Z-scheme photocatalyst systems for water splitting under visible light irradiation," *MRS Bulletin*, vol. 36, no. 01, pp. 32-38, 2011.

123. Ming-Sheng Gui, Wei-De Zhang, Qing-Xi Su and Cai-Hong Chen, "Preparation and visible light photocatalytic activity of Bi2O3/Bi2WO6 heterojunction photocatalysts," *Journal of Solid State Chemistry*, vol. 184, no. 8, pp. 1977-1982, 2011.

124. Jing Cao, Benyan Xu, Haili Lin and Shifu Chen, "Highly improved visible light photocatalytic activity of BiPO4 through fabricating a novel p–n heterojunction BiOI/BiPO4 nanocomposite," *Chemical Engineering Journal*, vol. 228, pp. 482-488, 2013.

125. Ming-Sheng Gui, Wei-De Zhang, Ya-Qi Chang and Yu-Xiang Yu, "One-step hydrothermal preparation strategy for nanostructured WO3/Bi2WO6 heterojunction with high visible light photocatalytic activity," *Chemical Engineering Journal*, vol. 197, pp. 283-288, 2012.

126. Lingzhi Li and Bing Yan, "BiVO4/Bi2O3 submicrometer sphere composite: Microstructure and photocatalytic activity under visible-light irradiation," *Journal of Alloys and Compounds*, vol. 476, no. 1–2, pp. 624-628, 2009.

127. Lei Ge, Changcun Han and Jing Liu, "Novel visible light-induced g-C_3N_4/Bi_2WO_6 composite photocatalysts for efficient degradation of methyl orange," *Applied Catalysis B: Environmental*, vol. 108–109, pp. 100-107, 2011.

128. Na Liang, Min Wang, Lun Jin, Shoushuang Huang, Wenlong Chen, Miao Xu, Qingquan He, Jiantao Zai, Nenghu Fang and Xuefeng Qian, "Highly Efficient Ag2O/Bi2O2CO3 p-n Heterojunction Photocatalysts with Improved Visible-Light Responsive Activity," *ACS Applied Materials & Interfaces*, vol. 6, no. 14, pp. 11698-11705, 2014.

129. Na Liang, Jiantao Zai, Miao Xu, Qi Zhu, Xiao Wei and Xuefeng Qian, "Novel Bi2S3/Bi2O2CO3 heterojunction photocatalysts with enhanced visible light responsive activity and wastewater treatment," *Journal of Materials Chemistry A*, vol. 2, no. 12, pp. 4208-4216, 2014.

130. Lang Chen, Shuang-Feng Yin, Sheng-Lian Luo, Rui Huang, Qiang Zhang, Tao Hong and Peter C. T. Au, "Bi2O2CO3/BiOI Photocatalysts with Heterojunctions Highly Efficient

for Visible-Light Treatment of Dye-Containing Wastewater," *Industrial & Engineering Chemistry Research*, vol. 51, no. 19, pp. 6760-6768, 2012.

131. Peng Ju, Ping Wang, Bin Li, Hai Fan, Shiyun Ai, Dun Zhang and Yi Wang, "A novel calcined Bi2WO6/BiVO4 heterojunction photocatalyst with highly enhanced photocatalytic activity," *Chemical Engineering Journal*, vol. 236, pp. 430-437, 2014.

132. Zhiqiao He, Yuanqiao Shi, Chao Gao, Lina Wen, Jianmeng Chen and Shuang Song, "BiOCl/BiVO4 p–n Heterojunction with Enhanced Photocatalytic Activity under Visible-Light Irradiation," *The Journal of Physical Chemistry C*, vol. 118, no. 1, pp. 389-398, 2014.

133. Jing Cao, Benyan Xu, Haili Lin, Bangde Luo and Shifu Chen, "Novel Bi2S3-sensitized BiOCl with highly visible light photocatalytic activity for the removal of rhodamine B," *Catalysis Communications*, vol. 26, pp. 204-208, 2012.

134. Xiaofeng Chang, Gang Yu, Jun Huang, Zheng Li, Shufeng Zhu, Pingfeng Yu, Cheng Cheng, Shubo Deng and Guangbin Ji, "Enhancement of photocatalytic activity over NaBiO3/BiOCl composite prepared by an in situ formation strategy," *Catalysis Today*, vol. 153, no. 3–4, pp. 193-199, 2010.

135. Songmei Sun, Wenzhong Wang and Ling Zhang, "Efficient Contaminant Removal by Bi2WO6 Films with Nanoleaflike Structures through a Photoelectrocatalytic Process," *The Journal of Physical Chemistry C*, vol. 116, no. 36, pp. 19413-19418, 2012.

136. Xu Zhao, Yan Wu, Wenqing Yao and Yongfa Zhu, "Photoelectrochemical properties of thin Bi2WO6 films," *Thin Solid Films*, vol. 515, no. 11, pp. 4753-4757, 2007.

137. Xu Zhao, Tongguang Xu, Wenqing Yao, Chuan Zhang and Yongfa Zhu, "Photoelectrocatalytic degradation of 4-chlorophenol at Bi2WO6 nanoflake film electrode under visible light irradiation," *Applied Catalysis B: Environmental*, vol. 72, no. 1–2, pp. 92-97, 2007.

138. Xiufang Zhang, Yaobin Zhang, Xie Quan and Shuo Chen, "Preparation of Ag doped BiVO4 film and its enhanced photoelectrocatalytic (PEC) ability of phenol degradation under visible light," *Journal of Hazardous Materials*, vol. 167, no. 1–3, pp. 911-914, 2009.

139. Liqun Ye, Yurong Su, Xiaoli Jin, Haiquan Xie and Can Zhang, "Recent advances in BiOX (X = Cl, Br and I) photocatalysts: synthesis, modification, facet effects and

mechanisms," *Environmental Science: Nano*, vol. 1, no. 2, pp. 90-112, 2014.

140. Xiangchao Meng and Zisheng Zhang, "Synthesis, Analysis, and Testing of BiOBr-Bi_2WO_6 Photocatalytic Heterojunction Semiconductors," *International Journal of Photoenergy*, vol. 2015, pp. 12, 2015.

SECTION II: SURFACE PLASMON RESONANCE ENHANCED BISMUTH-BASED PHOTOCATALYSIS

Chapter 3 New Insight into the Enhanced Visible Light-Driven Photocatalytic Activity of Pd/$PdCl_2$-doped Bi_2WO_6 Photocatalysts

Xiangchao Meng, Hanna Qin and Zisheng Zhang

Journal of colloid and interface science 513, 877-890

Abstract

A bismuth-based compound, Bi_2WO_6, was successfully synthesized using a facile hydrothermal method. Aiming to improve its photocatalytic activity under visible light irradiation, Pd/$PdCl_2$ was first doped onto the surface of Bi_2WO_6 via a photo-reduction method. The prepared Pd/$PdCl_2$-Bi_2WO_6 samples were characterized based on crystal structures, chemical states, atomic compositions, and morphologies as well as photoabsorption properties. In the screening tests for photocatalytic activity, the 4% Pd-Bi_2WO_6 sample performed with the highest removal efficiency with respect to the degradation of phenol in wastewater. This sample exhibited better in complete degradation of phenol under visible light irradiation, compared to TiO_2 under ultraviolet irradiation. A possible mechanism for the enhanced visible light-driven photocatalytic activity by means of loading Bi_2WO_6 with Pd was also suggested. This work sheds light on the potential applications of noble metal nanoparticles in visible light-driven photocatalysis.

3.1 Introduction

Photocatalysis is an advanced oxidation process that has been actively implemented in various practical areas [1]. Notable applications include the production of hydrogen by water splitting, the degradation of organic contaminants in wastewater as well as polluted air, disinfection, heavy metal recovery and organic synthesis reactions [2-7].

Photocatalytically generated species have strong oxidative potentials, and most organic compounds may be oxidized to CO_2 and H_2O by these species. Phenol and its derivatives are well known for their toxicities, yet they are widely found in wastewater from many industrial processes. The aromatic rings of phenolic compounds are difficult to destroy without a strong oxidant. Photocatalysis therefore presents itself as an efficient approach for the degradation of phenol.

The most studied UV light-driven, semiconductor-based photocatalyst is TiO_2 [4, 8]. Its high chemical stability, low toxicity and excellent photocatalytic activity (under UV light irradiation) initially made it an attractive photocatalyst. However, shortages of the photocatalyst quickly became a problem in industry. Specifically, TiO_2 makes use of only the UV spectrum (band gap of 3.2 eV), accounting for approximately 5% of the entire solar spectrum [4]. This combination of issues would eventually drive industries to invest in research of alternative photocatalytic materials.

Various materials were prepared with significant promise and attempts were made to apply them to visible light-driven photocatalysis. Among these, bismuth-based composites, including Bi_2O_3 [9], Bi_2MO_6 (M = Cr, Mo, W) [10-15], BiOX (X = Cl, Br, I) [16], $BiPO_4$ [17] and $BiVO_4$ [18], increasingly drew the attention of researchers [19]. This may be attributed to the following explanations: a) the band gaps of bismuth composites are approximately 1.7 to 3.2 eV, which means that a larger proportion of the solar spectrum may be applied; b) the valence band (VB) of a bismuth composite consists not only of O 2p orbitals (commonly the only orbital in a VB for metal oxides), but also Bi 6s orbitals. The O 2p and Bi 6s hybrid orbitals are reported to be beneficial by increasing the mobilities of photogenerated carriers [16], and c) the morphologies of Bi-based composites may be controlled by adjusting the pH or by adding surfactants [17, 20-22]. However, the high recombination rate of electron-hole (e^-/h^+) pairs inhibits the drive to further explore the applications of these materials. Approaches to mitigate this effect mainly include preparing heterojunctions such as BiOBr-Bi_2WO_6 composites [23, 24] and Bi_2WO_6-C_3N_4 [25], as well as doping (metal, ion, *etc.*) of photocatalytic materials, with examples of such composites being Ag/Bi_2WO_6 (BiOBr) [26, 27], Pd-Bi_2MoO_6 [28], or (Rh, Pd, Pt)/BiOX (X = Cl, Br, I) [29]. Metal modification may therefore effectively suppress the recombination of photogenerated electron-hole pairs.

Among bismuth-based semiconductors, Bi_2WO_6 exhibited excellent activity in photocatalytic applications [14, 15, 19, 23, 24, 30, 31]. However, because of the high recombination of photogenerated charge carriers hinders the wide application of Bi_2WO_6. Approaches to overcome this hindrance were explored by our and other groups. We have reported Ag/AgCl modified Bi_2WO_6, which exhibited excellent activity in photocatalytic oxidation of organics in water [15]. Ag/AgCl has been reported as a highly efficient plasmonic photocatalyst. It is strongly suggested to use nanoparticles composed primarily of noble metals due to their ability to absorb visible light, attributable to their surface plasmon resonance (SPR). In this work, Pd/$PdCl_2$ was selected and implemented to improve the photocatalytic activity of Bi_2WO_6. Although no research has been completed on the topic as of yet, Pd/$PdCl_2$ should enhance the effects of visible light-driven photocatalysis [13, 28]. Herein, Bi_2WO_6 was synthesized by a facile hydrothermal method. $PdCl_2$ was dispersed under ultrasonic conditions and then photo-reduced by the photogenerated electrons produced by Bi_2WO_6 under visible light irradiation. Properties such as crystal structures, chemical states and components, morphologies as well as photoabsorption capabilities were investigated and analyzed. Photocatalytic activity of as-prepared samples was conducted with regard to the degradation of phenol as probe molecule, and possible mechanism was also proposed.

3.2 Experimental

3.2.1 Synthesis of Bi_2WO_6

All reagents were purchased from Sigma-Aldrich in analytical purities. Bi_2WO_6 was synthesized by a facile hydrothermal method as described in literature [24]. A quantity of 1.9403 g of $Bi(NO_3)_3 \cdot 5H_2O$ was dissolved in 20 mL of acetic acid under magnetic stirring for 10 min, the resultant solution termed ‘Solution A’. Meanwhile, 0.6597 g of $Na_2WO_4 \cdot 2H_2O$ were dissolved in 40 mL of distilled, de-ionized water (DDW), the resultant solution termed ‘Solution B’. Solution B was added dropwise to Solution A and stirred magnetically for 30 min. The suspension was then transferred to a 100-mL Teflon-lined stainless steel autoclave (Parr Instrument Company), and heated at 180°C for 20 h. After the autoclave was allowed to naturally cool to room temperature, the Bi_2WO_6 precipitates

were filtered out then washed once with ethanol and twice with DDW. The washed Bi_2WO_6 samples were dried at 60°C overnight and collected.

3.2.2 Synthesis of Pd/$PdCl_2$-Bi_2WO_6 composites

The Pd/$PdCl_2$-Bi_2WO_6 composites were prepared using a photo-reduction method. First, 0.0015 g of $PdCl_2$ were dispersed in 40 mL of DDW then treated by ultrasonication for 30 min. A quantity of 0.3 g of Bi_2WO_6 was then added to the suspension which was magnetically stirred for 10 min before exposing the sample to light. The light source was a 300-W halogen tungsten projector lamp (Ushio). The distance between the lamp and the surface of the suspension was 15 cm, and the irradiation intensity was measured by a quantum meter (Biospherical QSL-2100, 400 nm < λ < 700 nm). After 1 h of irradiation, the precipitates were filtered out and dried at 60°C overnight. The cooled sample was collected and labelled as 0.5 wt% Pd-Bi_2WO_6. Similarly, 1.0 wt%, 2.0 wt%, 4.0 wt%, and 8.0 wt% samples of Pd-Bi_2WO_6 were also prepared.

3.2.3 Characterization

X-ray diffraction (XRD) analysis was carried out using a Rigaku Ultima IV Diffractometer with Cu Kα radiation (λ = 0.15418 nm) at 40 kV and 44 mA. XRD patterns were recorded at 2θ from 10° to 80°. Surface elements and chemical states were analyzed by employing XSAM-800 X-ray photoelectron Spectroscopy (XPS). The Fourier Transform Infrared Spectrometer (FT-IR) which was used was a Cary 630 (Agilent Technologies). The Brunauer, Emmett and Teller (BET) surface area of the samples were calculated using multi-point estimation. The pore volumes were calculated using the volumes of adsorbed N_2 at p/p_o = 0.993. Spectra were recorded at room temperature from 4000 cm^{-1} to 400 cm^{-1}. Transmission electron microscopy (TEM) was performed with JEM-2100F FE-TEM (JEOL), the acceleration voltage of which was 200 kV. A Thermo Evolution 300 spectrophotometer was employed to measure the ultraviolet-visible diffuse reflectance spectra (DRS). Electrochemical properties of prepared samples were performed on a CHI 604E electrochemical analyzer (CH Instruments Inc., USA) with a platinum wire as counter electrode, a calomel reference electrode and a working electrode. The working electrode was an indium tin oxide (ITO, 75 × 25 × 1.1 mm, 15 - 25 Ω, Sigma-Aldrich Canada Co.) glass coated with the prepared samples. The electrochemical impedance

spectroscopies (EIS) were recorded with frequency in the range of 0.01 - 1000000 Hz and the sinusoidal wave of 5 mV. The electrolyte was Na_2SO_4 with concentration of 0.25 mol/L. The photoluminescence (PL) spectra were measured using a fluorescence Spectrophotometer (F-4500, Hitachi) under excitation with wavelength of 300 nm.

3.2.4 Photocatalytic activity tests

Photocatalytic activities of prepared samples were tested in a slurry system by degrading organic pollutants. A 500-mL beaker fitted with a cooling jacket which maintained the temperature of the system at 20°C served as the photocatalytic reactor. The source of visible light was a 300-W halogen tungsten projector lamp (Ushio, USA) with a cut-off (Kenko Zeta) to filter out irradiation with a wavelength lower than 400 nm. The irradiation intensity was measured to be 1.1×10^{-2} Einsteins·m^{-2}·s^{-1} by a quantum meter (Biospherical QSL-2100, 400 nm < λ <700 nm). To confirm the light source applied was in visible light region, the spectra of the lamp were measured using a Newport IQE-200 system over wavelengths of 350 to 1000 nm, and results were depicted in Fig. 3.1. It can be observed the light with wavelength below 400 nm was almost completely eliminated when the UV cut-off was applied on the lamp. This result indicates the irradiation through the cut-off was attributed visible light and the UV light was completely filtered out.

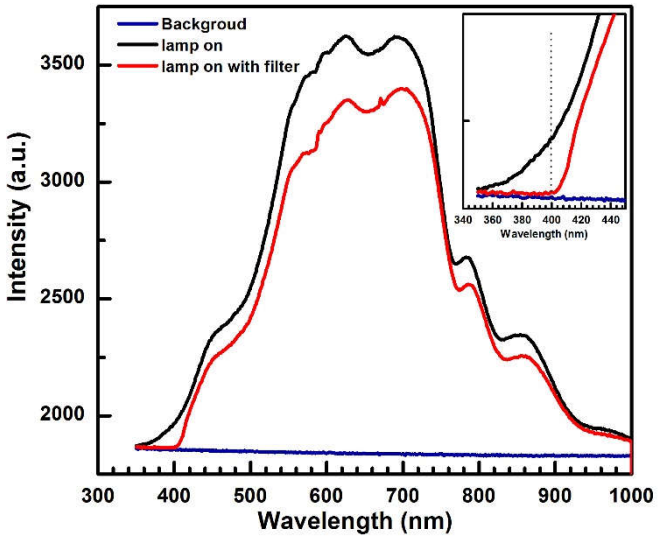


Figure 3.1 Spectra for the lamp (Ushio, USA) with and without the UV cut-off.

In the screening tests used for comparison to TiO_2 (>98%, anatase powder, ACROS Organics), 20 tightly packed 25-W fluorescent black lights (Sylvania, F25T8/350BL/18in/ECO, irradiation wavelength mainly in the range of 300 - 400 nm) were used as the source of UV light. The center-to-center spacing between bulbs was 2.84 ± 0.05 cm, each bulb with a diameter of 2.54 cm and a length of 45.2 cm. The total direct incidence value was determined to be approximately 257.8 W/m^2 by use of a UVX digital UV intensity meter (Cole-Parmer, RK-97651-10) equipped with a 365-nm sensor (Cole-Parmer, RK-97651-22). Additional details regarding the UV light photoreactor may be found in our previously published work [32, 33]. The primary target organic pollutant was selected to be phenol. In each test, 100 mL of solution with an initial concentration of 10 mg/L phenol was added to the reactor. The quantity of catalyst that was subsequently added was 1 g/L of reactor solution (0.10 g in 100 mL of solution). For comparison with TiO_2 under UV light, the optimal catalysts dosages were chosen as 2 g/L for Pd-Bi_2WO_6 and 1g/L for TiO_2.The suspensions were magnetically stirred for 60 min to reach an adsorption-desorption equilibrium between the photocatalysts and organic pollutants, after which irradiation was carried out for 5 h. Aliquots were drawn every 30 min and centrifuged at a rate of 13,000 rpm for 5 min. The supernatant was then analyzed by a high-performance liquid chromatograph (HPLC, Agilent 1100 series) equipped with a UV-Vis detector. A ZORBAX Eclipse Plus C18 (4.6 × 250 mm) was used under 60°C and the wavelength was fixed at 270 nm for the detection of phenol, hydroquinone, catechol and benzoquinone. Eluent was composed of 55% (V/V) methanol and 45% DDW at a flow rate of 0.6 mL/min. The injection volume was 25 μL. Retention time for phenol, hydroquinone, catechol and benzoquinone is at 17.72, 10.53, 13.10 and 9.86 min, respectively. It runs 20 min for each test.

Furthermore, in the quenching experiment, ethylene diamine teraacetic acid disodium (EDTA-2Na) and t-butanol were selected as scavengers for holes and oxidative radicals respectively. The concentrations of these quenching species were each 1 mol/L. N_2 bubbling was applied to purge the dissolved O_2, so as to suppress the production of $\bullet O_2^-$ free radicals. The recyclability of the photocatalysts were analyzed by separating the photocatalysts from suspension following a single run, after which they were mixed with

fresh wastewater to start another run. After four runs, photocatalysts were separated out and dried at 60°C for 12h.

3.3 Results and discussions

3.3.1 XRD and XPS

XRD patterns of pure Bi_2WO_6 and Bi_2WO_6 composites containing various loading quantities of Pd are illustrated in Fig. 3.2a. The diffraction peaks of pure Bi_2WO_6 agree well with an orthorhombic structure (space group: pbca (61), PDF card number 39-0256) [34]. All of the characteristic peaks were identified, which indicates that a well-crystalized Bi_2WO_6 sample was prepared. After loading Pd, characteristic peaks and lattice parameters (shown in Fig. 3.2a and 3.2b, and Table 3.1) of Bi_2WO_6 were found to be negligibly influenced. This indicates that the crystal structure of Bi_2WO_6 was not affected by Pd loading. Additionally, no peaks of Pd were detected in the Pd-Bi_2WO_6 composites, possibly because the amount of Pd in the samples was too low to detect using XRD.

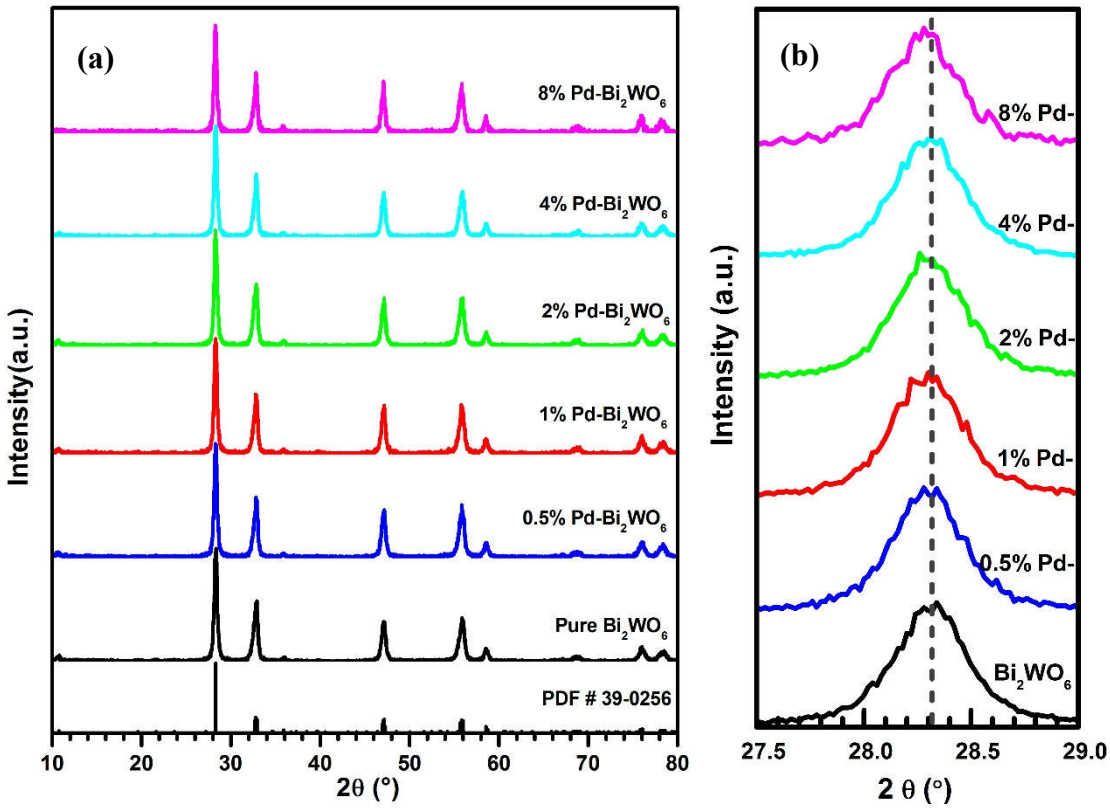


Figure 3.2 XRD patterns and lattice parameters of pure Bi_2WO_6, and Bi_2WO_6 composites with different quantities of doped Pd in the range of (a) 10° - 80° and (b) 27.5 – 29.0°.

Table 3.1 Lattice parameters and volume of a lattice cell for prepared samples.

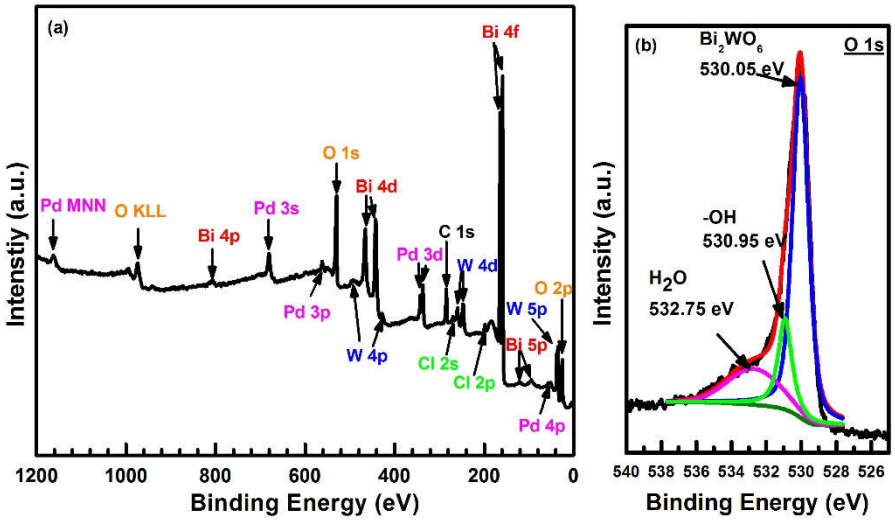
Samples	Lattice parameters (Å)			Volume ($Å^3$)
	a	b	c	
Bi_2WO_6 (PDF card: 39-0256)	5.46	16.46	5.44	487.73
Bi_2WO_6	5.45±0.0054	16.44±0.0193	5.45±0.0083	488.03
0.5% Pd-Bi_2WO_6	5.45±0.0017	16.43±0.0179	5.46±0.0020	488.70
1% Pd-Bi_2WO_6	5.45±0.0017	16.46±0.0068	5.43±0.0039	487.77
2% Pd-Bi_2WO_6	5.45±0.0030	16.44±0.0120	5.43±0.0069	487.14
4% Pd-Bi_2WO_6	5.46±0.0040	16.44±0.0070	5.44±0.0017	488.12
8% Pd-Bi_2WO_6	5.45±0.0026	16.45±0.0106	5.44±0.0061	488.06

XPS was employed to determine the chemical state and elemental composition of 4% Pd-Bi_2WO_6. The survey and high-resolution orbital scan spectra shown in Fig. 3.3 were calibrated with C1s, the binding energy of which is 284.6 eV. The survey spectrum in Fig. 3.3a accounts for each of the elements (*i.e.* Bi, W, O, Pd, and Cl) in the composite, and no peaks from impurities were found, indicating a high sample purity. Quantity of palladium on the surface can be calculated from the survey spectrum as about 8.84 wt% (Pd/Bi_2WO_6). In Fig. 3.3b, the O1s peak includes three single-spin orbitals. The largest peak located at a binding energy of 530.05 eV may be attributed to the oxygen atoms in Bi_2WO_6 in the form of W-O and Bi-O bonds. The other peaks located at binding energies of 530.95 and 532.75 eV agree well with oxygen atoms found in –OH and adsorbed H_2O respectively [35, 36]. To further explore the presence and chemical state of Pd, high-resolution scans of Pd 3d and Cl 2p orbitals were measured. The spectra for Pd 3d, as shown in Fig. 3.3c, d and e, could be resolved to two sets of spin-orbit doublets. Accordingly, as shown in Fig. 3.3d, Pd ($3d_{5/2, 3/2}$) peaks at 335.4 and 340.8 eV as well as at 334.0 and 339.3 eV may be attributed

to Pd^{2+} and Pd^{0} respectively [37-39], suggesting that both bivalent and metallic Pd may be present on the surface of Bi_2WO_6. The relative surface concentrations of Pd^{0} and Pd^{2+} may be calculated using the following equation (Equation 1) [40]:

$$\frac{\eta_{Pd^0}}{\eta_{Pd^{2+}}} = \frac{I_{Pd^0}}{I_{Pd^{2+}}} \times \frac{\sigma_{Pd}\lambda_{Pd}D_E(Pd)}{\sigma_{Pd}\lambda_{Pd}D_E(Pd)} \qquad \textit{Equation 1}$$

where η, I, σ, λ, and D_E are the surface concentration, intensity, photoelectric cross-section, electron free mean path, and geometric factor respectively. The values of σ, λ, and D_E have been calculated by Penn and Scofield, and were obtained from literature [41, 42]. Integrated intensities of Pd^{0} and Pd^{2+} peaks were taken into account to estimate their concentrations. The relative combined surface concentration of Pd^{0} and Pd^{2+} was approximately 23.51%, 19.7% and 20.6% for composites illuminated for 30 min, 60 min and 120 min. It suggested the illumination time in the photoreduction process negligibly influence the relative ratio between Pd^{0} and Pd^{2+}, which was estimated to be 1:5. Furthermore, it is shown in Fig. 3.3f-h that binding energies of 198.0 (±0.1) and 199.6 (±0.1) eV for Cl $2p_{1/2}$ and $2p_{3/2}$ respectively clearly suggest the presence of Cl^{-} [43]. This confirms that only a portion of Pd^{2+} was reduced to metallic Pd in the photocatalytic reduction process.



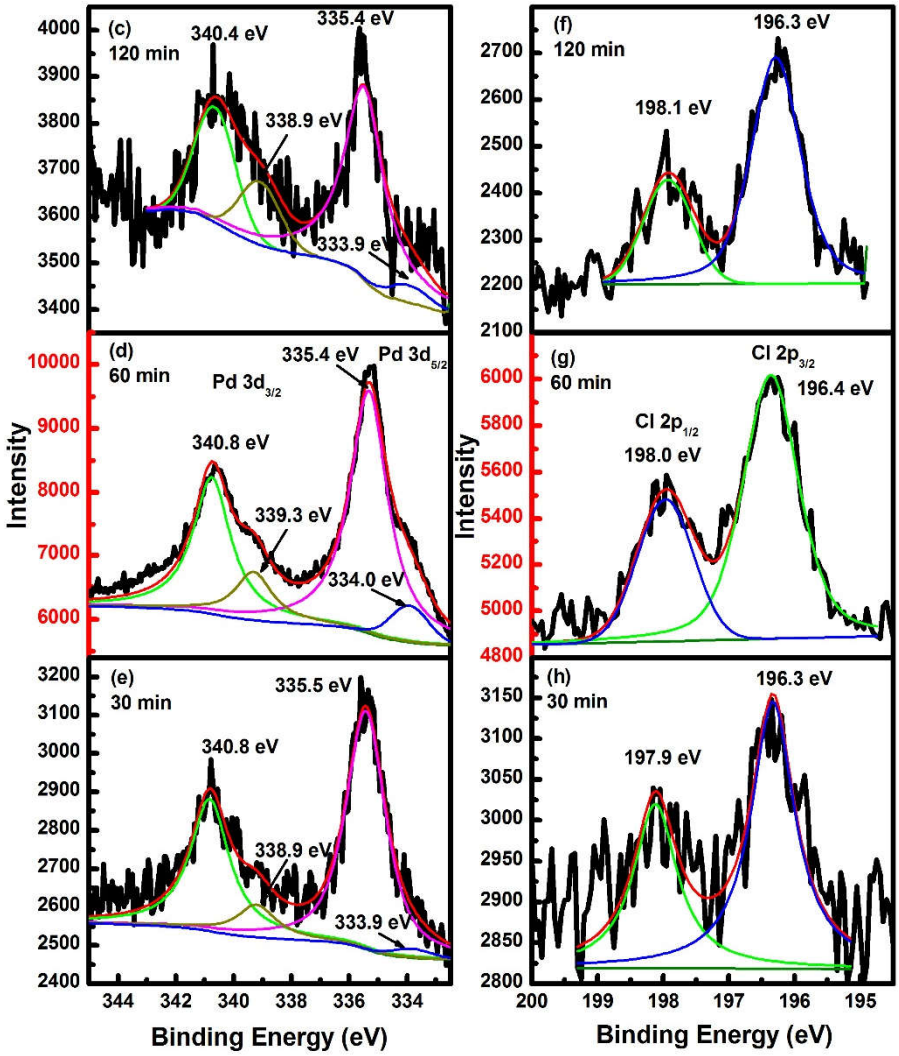


Figure 3.3 XPS spectra of 4% Pd-Bi_2WO_6 composite: (a) survey spectra, and high-resolution orbital scans of (b) O1s, Pd3d for composites illuminated for 120 min (c), 60 min (d), and 30 min (e), and Cl2p for composites illuminated for 120 min (f), 60 min (g), and 30 min (h).

3.3.2 FT-IR

FT-IR spectra of Bi_2WO_6 and x% Pd-Bi_2WO_6 (x = 0.5, 1.0, 2.0, 4.0, 8.0) powder samples are illustrated in Fig. 3.4. For the spectrum of pure Bi_2WO_6, the main absorption bands at wavelength numbers ranging from 600-1000 cm^{-1} may possibly be attributed to Bi-O and W-O stretching as well as W-O-W bridging stretching modes [44, 45]. Small peaks in the wavelength number range of 1300-1600 cm^{-1} may have resulted from adsorbed CH_3COOH, but more specifically, from the δCH vibrations of the $CH_3C{=}O$ moiety as well as from coupled νC-O and δOH vibrations [46, 47]. Similar IR spectra of Bi_2WO_6 were also reported in literature [48, 49]. When Pd is doped onto the surface of Bi_2WO_6, there is a

negligible influence on the main adsorption area of Bi_2WO_6 (600-1000 cm^{-1}). It should also be mentioned that absorption by CH_3COOH was weakened after Pd loading. The reason for this may be that CH_3COOH is diluted and degraded under visible light irradiation during the photo-reduction process.

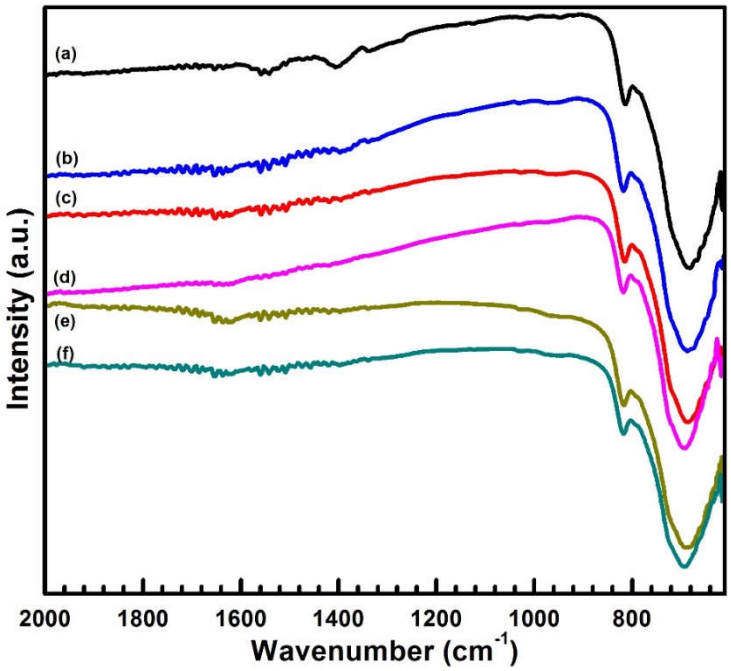


Figure 3.4 FT-IR spectra of pure Bi_2WO_6 (a) and those of Pd-Bi_2WO_6 composites with 0.5% (b), 1.0% (c), 2.0% (d), 4.0% (e), and 8.0% (f) Pd.

3.3.3 N_2 sorption analysis

To investigate the adsorption-desorption property of prepared samples, nitrogen sorption isotherms were tested and depicted in Fig. 3.5. All isotherms are attributed to the type-IV physisorption isotherm [50, 51]. Specifically, type-IV isotherm is primarily resulted mesoporous materials, and a monolayer was firstly formed at low relative pressure, and multilayer adsorption occurred at high relative pressure. As shown in the inset of Fig. 3.5, it can be found there is no plateau observed at high pressure, which may be due to that the capillary condensation did not occur on the surface of macropores [13]. Moreover, a H3-type hysteresis loop was observed for each isotherm. This type hysteresis loop may be resulted from the slit-shaped pores formed by aggregation of plate-like particles, which is typical for plate-like bismuth semiconductors and agrees well with the morphologies as observed in the SEM images. To further quantitively evaluate the specific surface area for Bi_2WO_6 and Pd-Bi_2WO_6 composites, the BET surface area as well as pore volumes were

summarized in Table 3.2. The BET surface area for pure Bi_2WO_6 was estimated as about 28.35 m^2/g, and a slight decrease was observed with the deposition of palladium on the surface. Similar results were observed for the pore volumes. The reduction may be resulted from the palladium nanoparticles blocked the slit-shaped pores. This phenomenon may lead to the reduction in photocatalytic activity via deterioration of the adsorption capacity. However, compared to the improvement of photogenerated charge carriers' separation efficiency with the palladium modification, the influence of reduction in specific surface area is negligible for the overall photocatalytic activity.

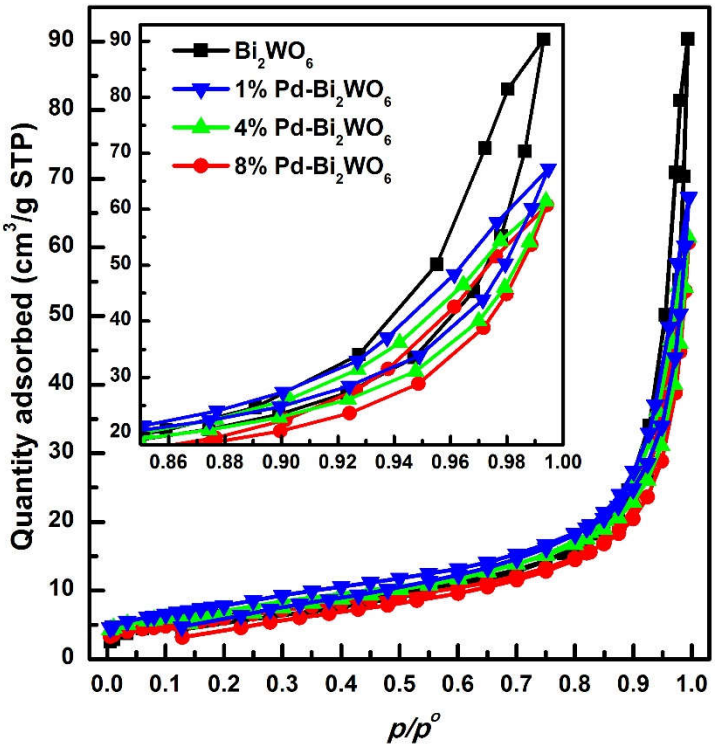


Figure 3.5 N_2 sorption isotherms for Bi_2WO_6 and Pd-Bi_2WO_6 composites.

Table 3.2 Specific surface area, pore volume, and average pore size of prepared composites.

Sample	S_{BET} (m^2/g)	Pore volume (cm^3/g)
Bi_2WO_6	28.35	0.14
1% Pd-Bi_2WO_6	25.22	0.10
4% Pd-Bi_2WO_6	23.75	0.096
8% Pd-Bi_2WO_6	22.00	0.094

3.3.4 Photoabsorption properties

The optical properties of pure Bi_2WO_6 and 4% Pd-Bi_2WO_6 powder samples were evaluated by UV-Vis diffuse reflectance spectroscopy, shown in Fig. 3.6. Bi_2WO_6 exhibited excellent photoabsorption properties in the UV-visible light spectrum with a wavelength lower than 450 nm. There is a steep decrease in the spectrum of Bi_2WO_6, indicating that absorption in the visible light region is due to a band gap transition as opposed to a transition from the impurity level [52]. Specifically, electrons most likely absorb the photo energy and jump from the valence band (hybrid orbital of O 2p and Bi 6s) to the conduction band (W 5d orbital with a small contribution from Bi 6p orbital).

When Pd was loaded on the surface of Bi_2WO_6, a colour change from white to grey was observed, and photoabsorption in the visible light region was greatly improved. This phenomenon may be attributed to electron transfer transitions between the dopant (Pd) and the valence or conduction bands of the support (Bi_2WO_6) [53]. In addition, as shown in Fig. 3.7, palladium nanoparticles are capable of absorbing irradiation with wavelength in the range of 200-1000 nm, which may be attributed to the surface plasmonic effect of Pd nanoparticles on the surface. The band gaps were also calculated by employing the classical Tauc equation (Equation 2):

$$\alpha E_{photon} = K\left(E_{photon} - E_g\right)^{\frac{n}{2}} \qquad (E_{photon} = h\upsilon) \qquad \textbf{Equation 2}$$

Where α, E_{photon}, E_g, h, v and K are the absorption coefficient, energy of irradiation, band gap energy, the Planck constant, the irradiation frequency, and the constant for semiconductors (usually equal to 1), respectively. The constant n depends on the type of band gap, and for the direct transition band gap of Bi_2WO_6, $n = 4$. The inset in Fig. 3.6 is a plot of $(\alpha E_{photon})^{1/2}$ vs E_{photon}. The intercept at the horizontal axis of the tangent line is equal to the band gap energy. It could be deducted that the band gap was narrowed from 2.89 to 2.70 eV. This further proves that the visible light photoabsorption intensity may be improved by loading Pd on the surface of Bi_2WO_6, and that the photocatalytic activity of Pd-Bi_2WO_6 should be increased above levels seen with pure Bi_2WO_6.

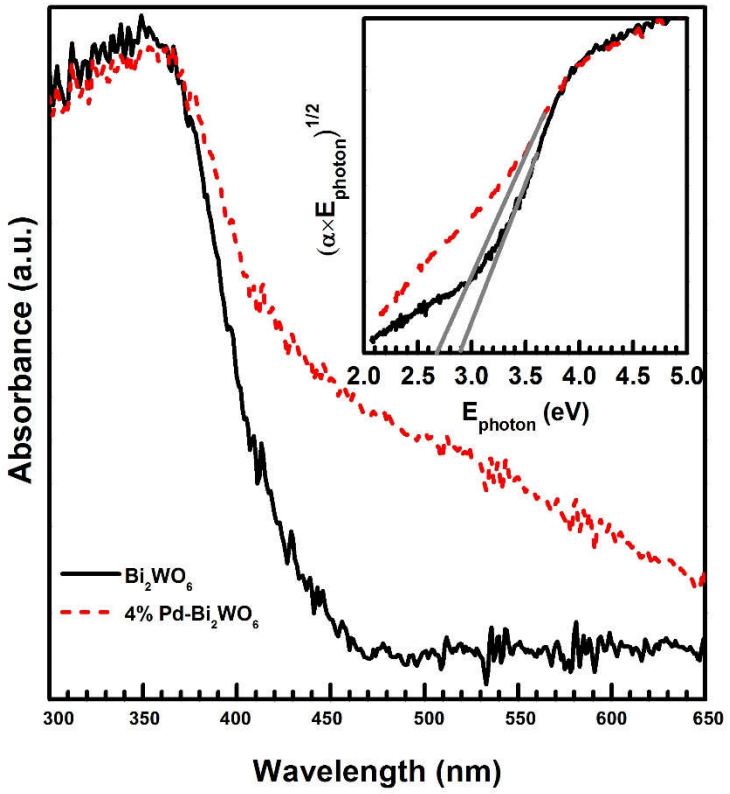


Figure 3.6 UV-Vis diffuse reflectance spectra of pure Bi_2WO_6 and 4% Pd-Bi_2WO_6 powder samples, with $(\alpha E_{photon})^{1/2}$ vs E_{photon} curves shown in inset.

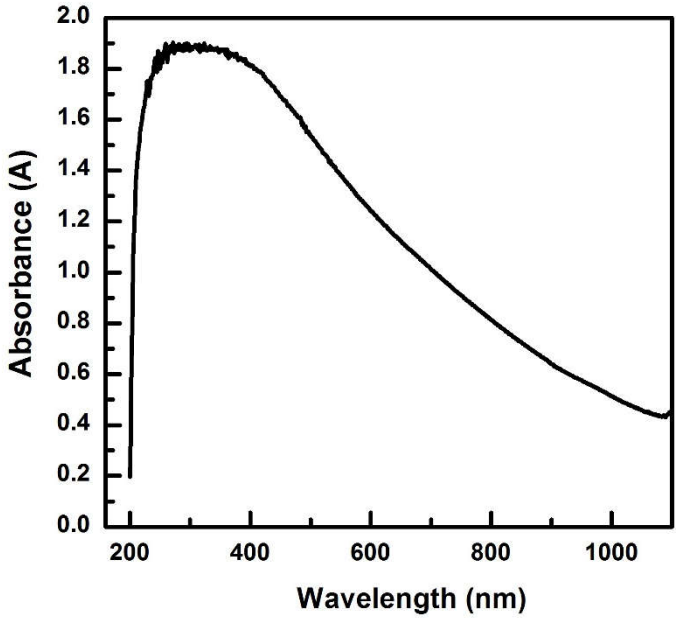


Figure 3.7 UV-Vis spectrum of palladium nanoparticles.

3.3.5 Proposed formation mechanisms of Pd-Bi_2WO_6

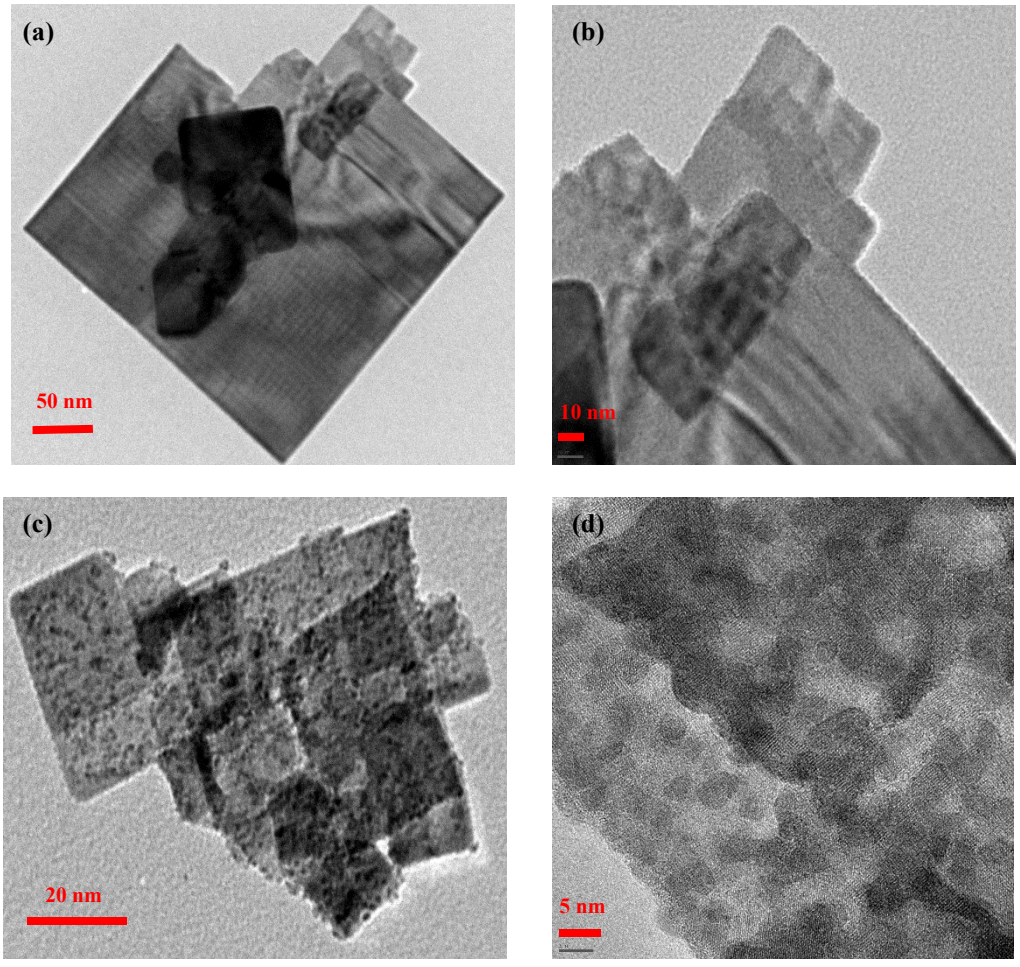
Morphologies of prepared samples were observed by TEM, and are shown in Fig. 3.8. For pure Bi_2WO_6 in Fig. 3.8a and 3.8b, nanosheets of various sizes were stacked together. When Pd was loaded onto their surfaces, as shown in Fig. 3.8c and 3.8d, the nanosheets of Bi_2WO_6 were shown to be covered in quantum dots with diameters between 2 - 3 nm. The identities of these dots could be metallic Pd as well as adsorbed $PdCl_2$. To further confirm the surface composition, EDS was employed to investigate, and results are illustrated in Fig. 3.8d-3.8h. Specifically, elements of Bi, W, O and Pd were observed (peaks for Cu is from the grid used for the test) (Fig. 3.8f). Elemental mapping for Bi and Pd was shown in Fig. 3.8g and 3.8h, respectively. It can be observed Pd were well-dispersed on the support, Bi_2WO_6. Theoretically, the redox potential of Pd^{2+} reduced to Pd^0 is 0.915 V. The bottom potential of the conduction band (E_{CB}) for Bi_2WO_6 was calculated by applying the Mulliken electronegativity theory of atoms (Equation 3):

$$E_{CB,Bi2WO6} = X_{Bi2WO6} - E^e - \frac{1}{2}E_g \qquad \textbf{Equation 3}$$

where X_{Bi2WO6} (6.455 eV), E^e and E_g are the electronegativity, the energy of free electrons on the hydrogen scale (≈4.5eV), and the band gap of Bi_2WO_6 (2.89 eV) [54, 55]. The bottom potential of the conduction band for Bi_2WO_6 was calculated to be 0.51 eV, which is lower than the redox potential of Formula 2. In other words, electrons generated by visible light-activated Bi_2WO_6 in Formula 1 have a reductive potential strong enough to reduce Pd^{2+} to metallic Pd.

$$Bi_2WO_6 \xrightarrow{h\upsilon} e^-_{Bi_2WO_6} + h^+_{Bi_2WO_6} \qquad \textbf{Formula 1}$$

$$Pd^{2+}_{adsorbed} + 2e^-_{Bi_2WO_6} \longrightarrow Pd \qquad \textbf{Formula 2}$$



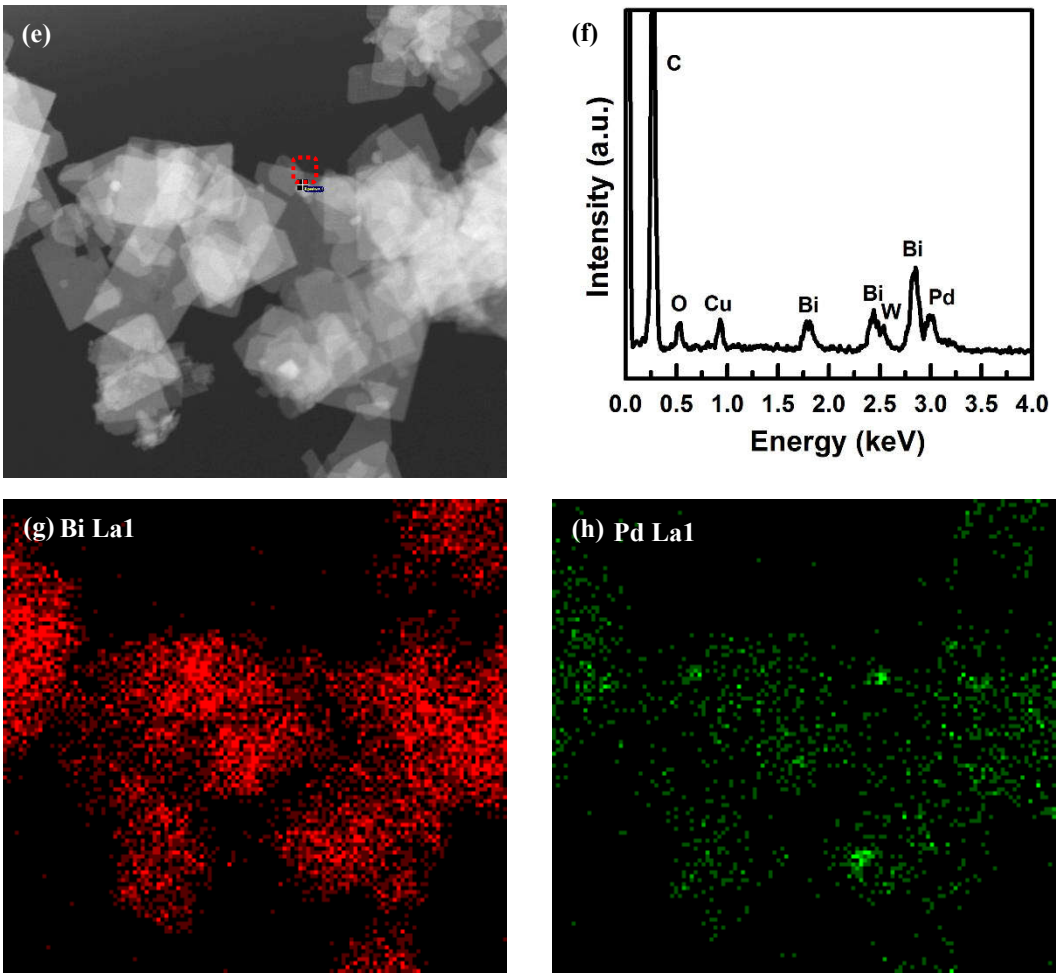


Figure 3.8 Low-resolution and high-resolution TEM images of pure Bi_2WO_6 (a, b) and 4%Pd-Bi_2WO_6 composite (c, d); EDS of 4%Pd-Bi_2WO_6 composite (f) at the point indicated in (e), and elemental mapping (g, h).

3.3.6 Photocatalytic activity

3.3.6.1 Degradation of phenol

Photocatalytic activities were tested by degrading phenol under visible light irradiation, the screening test results of which are plotted in Fig. 3.9. The initial concentration of phenol was 10 mg/L and the photocatalyst dosage was 1.0 g/L in 100 mL of wastewater. The temperature was maintained at 20°C to eliminate its influence in the evaluation of the photocatalytic activities of each photocatalyst sample. It was observed that the removal efficiency of the system using pure Bi_2WO_6 was approximately 60% over 5 h in regards to the degradation of phenol. After introducing the catalyst surface with Pd, photocatalytic

degradation was greatly enhanced. Specifically, the removal efficiencies of systems with 0.5, 1.0, 2.0, 4.0, and 8.0% Pd-Bi_2WO_6 were approximately 62.4%, 69.0%, 88.4%, 95.2%, and 68.9% respectively after 5 h of phenol degradation. The highest photocatalytic activity under visible light irradiation was observed with 4% Pd-Bi_2WO_6. This increase in photocatalytic activity may be attributed to an increase in Pd content, primarily because the recombination rate of photogenerated electrons and holes is gradually reduced with an increasing Pd content. However, Pd contents above 4% were shown to decrease photocatalytic activity. This is thought to be caused by an effective decrease in surface area, resulting in a decrease in the number of reactive sites. Furthermore, Pd can also be regarded as a recombination site for electrons and holes, which would therefore contribute in a reduction in photocatalytic activity. Similar results were also reported in literature [29, 53].

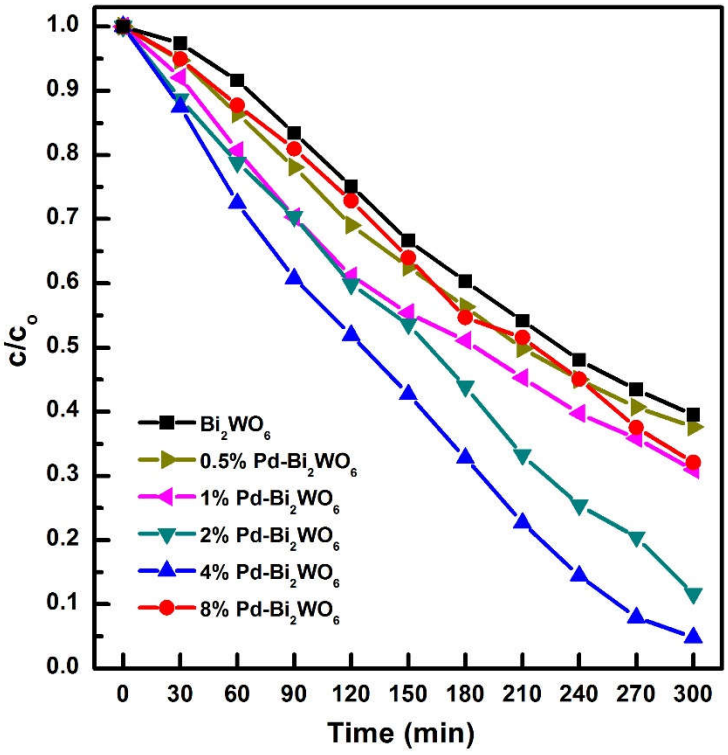


Figure 3.9 Photocatalytic degradation of phenol with pure Bi_2WO_6 and Pd-Bi_2WO_6 composites.

3.3.6.2 Kinetic study

The photocatalytic kinetics of phenol degradation were analyzed with the Langmuir-Hinshelwood (L-H) model, and may be described as follows (Equation 4):

$$r = -\frac{dc}{dt} = k\theta = \frac{kKc}{1+Kc} \qquad \textbf{Equation 4}$$

where r, c, t, k, θ, and K represent reaction rate, concentration of phenol, reaction time, reaction rate constant, ratio of adsorbed phenol, and adsorption constant. When the initial concentration is lower than 10^{-3} mol/L, $Kc << 1$ and $1+Kc \approx 1$, Equation 4 may be expressed in the form of Equation 5 as follows:

$$-\frac{dc}{dt} = kKc = k'c \qquad \textbf{Equation 5}$$

where k' is the pseudo first-order rate constant. Integration of Equation 5, results in the following (Equation 6):

$$\ln(\frac{c_o}{c_t}) = k't \qquad \textbf{Equation 6}$$

A plot of $\ln(c_o/c)$ against t can be seen in Fig. 3.10. The slope and R^2 correlation for a straight line were calculated and are summarized in Table 3.3. All values of R^2 were found to be almost equal to 1, which suggests that the pseudo first-order reaction model is sufficient to describe the Pd-Bi_2WO_6 photocatalytic system for the degradation of phenol. The kinetics for systems using Pd-Bi_2WO_6 as the photocatalyst are stronger than those using pure Bi_2WO_6, indicating that the photocatalytic activity of Bi_2WO_6 is improved after modified by Pd. Specifically, the reaction constant is improved approximately two-fold from that of pure Bi_2WO_6 after depositing Bi_2WO_6 with 4% Pd.

A similar phenomenon further strengthens these results as an optimum loading amount of Pd (4%) was observed with regards to the degradation of phenol.

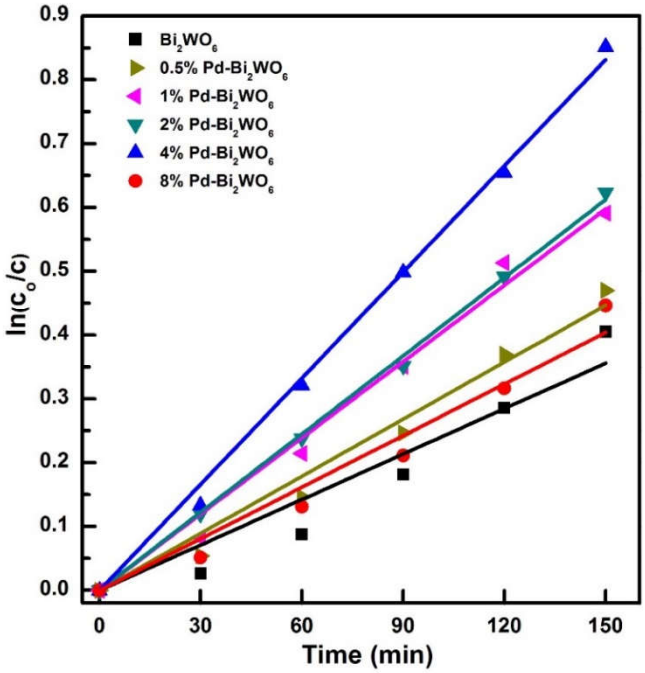


Figure 3.10 Kinetic analysis of photocatalytic degradations with different photocatalysts

Table 3.3 Pseudo first-order kinetic constants of systems with Bi_2WO_6 doped with different quantities of Pd.

Pd content (%)	**0.0**	**0.5**	**1.0**	**2.0**	**4.0**	**8.0**
***k'* ($10^{-2}min^{-1}$)**	0.237	0.298	0.398	0.408	0.554	0.269
R²	0.9745	0.9907	0.9950	0.9994	0.9986	0.9849

3.3.6.3 Photonic efficiency analysis

Photonic efficiency (ζ) for photocatalysis may be evaluated using Equation 7 [56] as follows,

$$\zeta = \frac{V \times \Delta c}{J \times A \times \Delta t \times m_{cat}} \qquad \textit{Equation 7}$$

where V, J, A, Δc, Δt and m_{cat} represent volume of solution, flux of photons, illuminated area, change in concentration, change in time and catalyst dosage amount, respectively. The flux of incoming photons was calculated to be 2.39 kW/m^2 for the mean irradiation wavelength of 550 nm. The solution volume was 100 mL, illuminated area was about

0.0050 m^2 and catalyst dosage amount is 0.1 g. The average photonic efficiency was estimated and summarized in Table 3.4. The highest photonic efficiency was obtained at a value of 2.94 μg W^{-1} min^{-1} g^{-1} when the content of Pd was 4% in the composite. This value is over 1.5 times higher than that for process with pure Bi_2WO_6. Even though the photonic efficiency for the system with Pd-Bi_2WO_6 under visible light irradiation is still about 1.7 times lower than that for TiO_2 under UV light, it is still competitive for other reported systems under visible light irradiation as shown in Table 3.4. Phenol is refractory to decompose due to high stability of the benzene ring. The possible pathways of degradation of phenol were further explored in the next section.

Table 3.4 Photonic efficiency ζ (μg W^{-1} min^{-1} g^{-1}) for systems in this work and other reported systems.

In this work:							
Catalysts	**TiO_2**	**Pd content (%)**					
		0.0	**0.5**	**1.0**	**2.0**	**4.0**	**8.0**
ζ	5.48	2.05	2.07	2.43	2.90	3.16	2.24
Reported systems under visible light:							
Catalysts	N-TiO_2	CoO_x/$BiVO_4$	S, Fe(III)-TiO_2	BiOI	Cu-Bi_2WO_6	Reduced graphene oxide-Bi_2WO_6	Bi_2S_3-Bi_2WO_6
ζ	1.41	0.55	0.5	1.46	1.81	3.33	1.83
Ref.	[57]	[58]	[59]	[60]	[61]	[62]	[63]

4.3.6.4 Possible pathway of phenol degradation

The reaction pathway describing the photocatalytic degradation of phenol implies possible intermediates including hydroquinone, catechol and benzoquinone which were detected (Fig. 3.11). It was found that the concentration of phenol decreased from approximately 11.5 to 0.5 mg/L in 300 min. It was also determined that hydroquinone, catechol and benzoquinone were detected at low concentrations. These smaller concentrations suggest that the direct consumption of phenol is the rate-determining step. To be more specific, hydroquinone was shown to have the highest concentration among these intermediates, followed by catechol and negligibly, benzoquinone. It is possible that benzoquinone easily decomposes in this system, resulting in the formation of smaller organic acids. Based on

other reported work, the final products of the overall reaction are assumedly CO_2 and H_2O [64, 65].

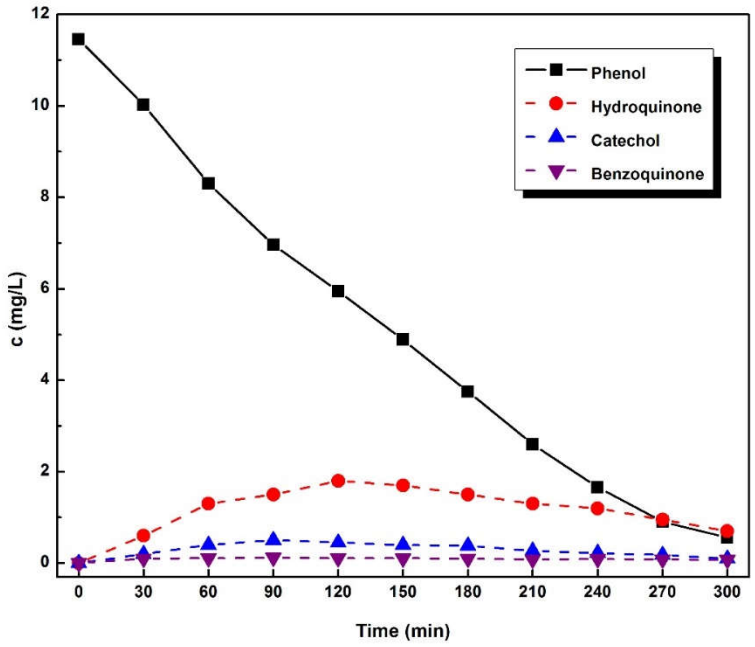


Figure 3.11 Concentrations of phenol and intermediates (hydroquinone, catechol, and benzoquinone) during the visible light-driven photocatalytic degradation process.

The possible pathways of phenol degradation are illustrated in Fig. 3.12. With the effect of oxidative species, phenol is first oxidized to a dihydroxyl cyclohexadienyl radical. In the presence of O_2, benzoquinone, hydroquinone and catechol may then be formed. These compounds degrade much rapidly than phenol, and the aromatic rings may be destroyed to produce carboxylic acids. Finally, these acids may further decompose to CO_2 and H_2O under the influence of photogenerated oxidants.

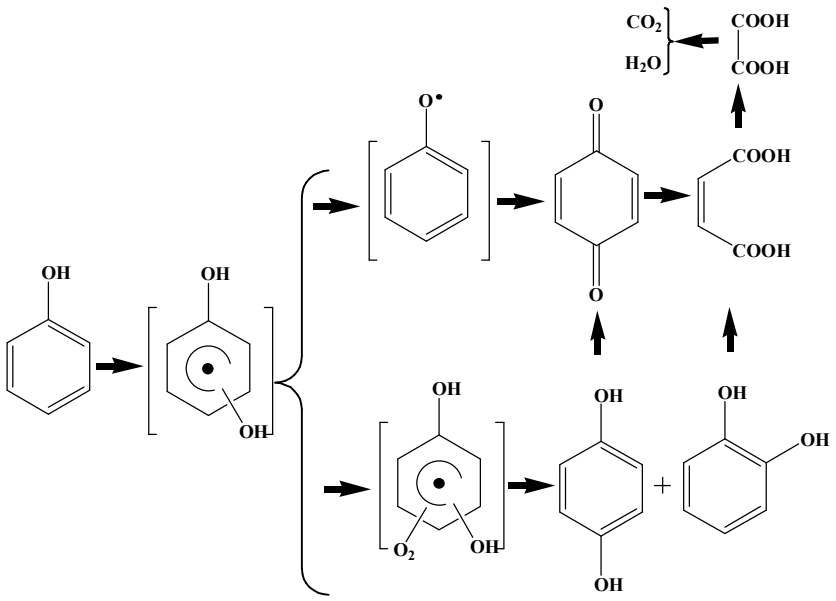


Figure 3.12 Possible pathways for the photocatalytic degradation of phenol.

3.3.6.5 Comparison with TiO_2 under UV light irradiation

As the most thoroughly studied and widely used photocatalyst, TiO_2 is an excellent reference with which to compare the photocatalytic activity of Pd-doped Bi_2WO_6. Under UV light irradiation, the relative concentrations (c/c_o) of phenol in the presence of TiO_2 as well as 4% Pd-Bi_2WO_6 were measured and are illustrated in Fig. 3.13. TiO_2 required 90 min to achieve a removal efficiency of 100% phenol, while 4% Pd-Bi_2WO_6 required 180 min for the same results. This phenomenon indicates that, for the consumption of phenol, the UV-driven photocatalytic activity of TiO_2 is higher than that of Pd-Bi_2WO_6. Absolute concentrations of hydroquinone, catechol and benzoquinone after using TiO_2 and Pd-Bi_2WO_6 are illustrated in Fig. 3.14. It can be seen that a large amount of hydroquinone and benzoquinone accumulated in the system using TiO_2. To be more specific, there were approximately 3 mg/L of benzoquinone and 7 mg/L of hydroquinone detected in the first 30 and 90 min of reaction, respectively. Comparatively, no more than 2 mg/L of hydroquinone was produced in the presence of Pd-Bi_2WO_6. Assuming only phenol and major intermediates (i.e. hydroquinone, catechol and benzoquinone) with aromatic rings, the quantity of benzene rings can be calculated by using the following equation (Equation 8):

$$c_{\text{benzene ring}} = \frac{m_{phenol}}{MW_{phenol}} + \left(\frac{m_{hydroquinone}}{MW_{hydroquinone}} + \frac{m_{catechol}}{MW_{catechol}} + \frac{m_{benzoquinone}}{MW_{benzoquinone}} \right) \quad \textbf{Equation 8}$$

Where $c_{benzene\ ring}$ is the number of benzene rings in mmol/L, m is the mass concentration in mg/L, and MW is the molecular weight of each specie in g/mol. By plotting $c_{benzene\ ring}/c_{0benzene\ ring}$ vs t shown in Fig. 3.15, it can be found more benzene rings left in the solution when using TiO_2 than that when using Pd-Bi_2WO_6. And all the benzene rings were destructed after 270 min when either using TiO_2 or Pd-Bi_2WO_6 under UV- light. This suggests that oxidative species in the system in conjunction with Pd-Bi_2WO_6 are more capable of breaking aromatic rings, which is significant for the purpose of the complete decomposition of phenol as well as other organic pollutants with an aromatic ring. These results may be interpreted by different degradation mechanisms when using TiO_2 and Bi_2WO_6. It is well known that •OH plays the most important role in the degradation of organic pollutants when using TiO_2 as a photocatalyst [66]. As for the presence of •OH, phenol is easily converted to dihydroxyl cyclohexadienyl, then further converted to hydroquinone and benzoquinone. After most of the phenol is converted, hydroquinone and benzoquinone are then oxidized by •OH. The standard electrode potential (E^o) of •OH is 2.80 V, boasting an oxidative strength high enough to break aromatic rings, generating small fragments. However, for bismuth-based photocatalytic semiconductors, the major oxidants in the degradation of organic pollutants are the photogenerated holes on the valence band, reported in literature [24] and also confirmed in section 3.6. The maximum potential of the valence band for Bi_2WO_6 may be calculated using Equation 9:

$$E_{VB} = E_{CB} + E_{\text{g}} \quad \textbf{Equation 9}$$

where E_{CB} and E_g obtained from Equation 3 are 0.51 eV and 2.89 eV. Therefore, E_{VB} is equal to 3.4 eV. This means that holes on the valence band of Bi_2WO_6 have standard electrode potentials of 3.4 V, which is higher than that of •OH. In other words, photogenerated holes on the valence band of Bi_2WO_6 are more oxidative than •OH generated in the presence of TiO_2 under UV light irradiation. As a result, intermediates produced by phenol are easily decomposed and accumulate less in the system when Pd-Bi_2WO_6 is used. Even though the phenol removal efficiency of Pd-Bi_2WO_6 is lower than

that of TiO_2, the intermediates are much more easily removed when using Pd-Bi_2WO_6 than TiO_2. The prepared Pd-Bi_2WO_6 in this work is therefore not inferior to TiO_2.

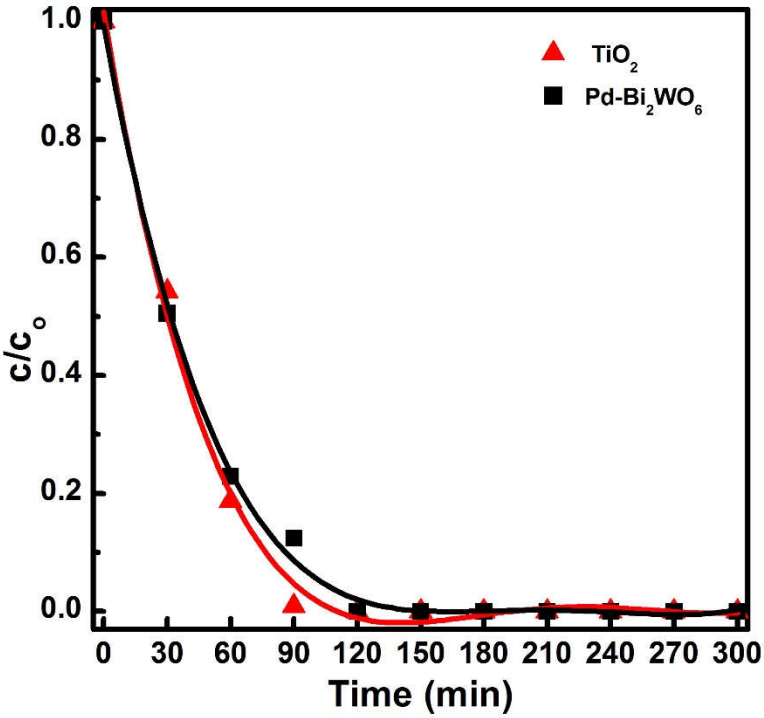


Figure 3.13 Phenol profiles during photocatalytic degradation with 4%Pd-Bi_2WO_6 composite and TiO_2 under UV light irradiation.

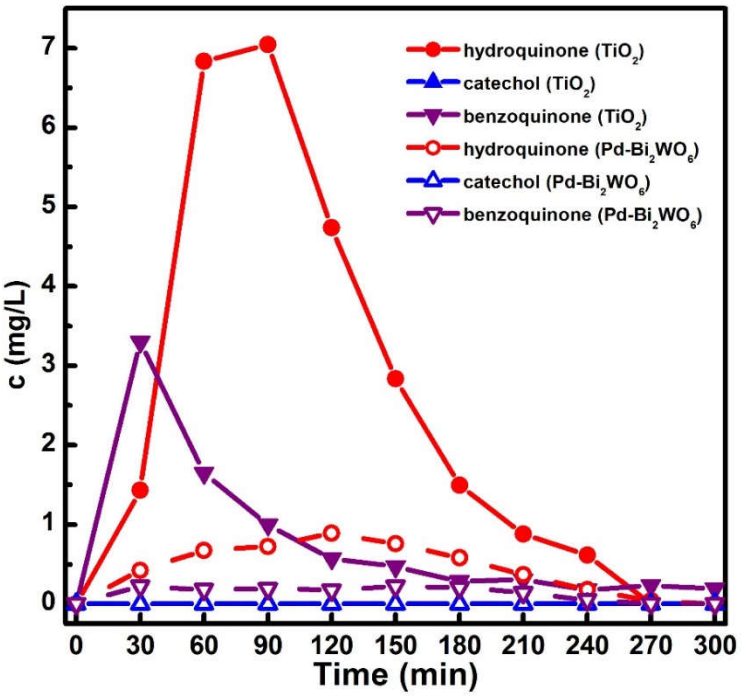


Figure 3.14 Concentration profiles of intermediates hydroquinone, catechol and benzoquinone during photocatalytic degradation of phenol with TiO_2 and 4% Pd-Bi_2WO_6 under UV light irradiation.

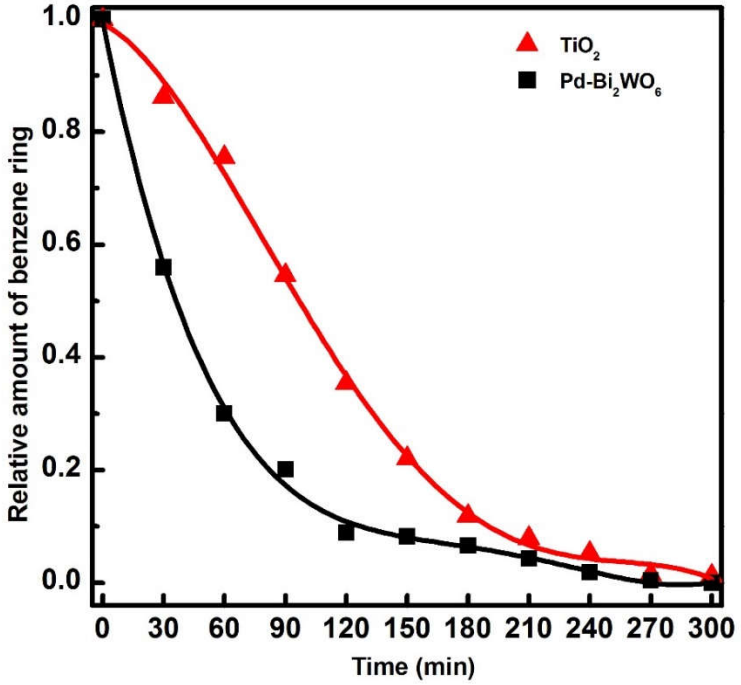


Figure 3.15 Relative amount of benzene ring during the degradation process in presence of TiO_2 and 4% Pd-Bi_2WO_6 under UV light irradiation.

3.3.6.6 Reusability and stability

Reusability, an important consideration from an economic perspective, is determined by recycling the photocatalysts for multiple experiments, the results of which are shown in Fig. 3.16. After four runs, the photocatalysts still exhibited excellent performances with regards to the degradation of phenol. A slight decrease in the removal efficiency over 300 min (95.2% in the first run and 89.2% in the fourth run) may have resulted from the loss of catalyst mass between two runs. Additionally, adsorption of refractory intermediate products on the surface of the photocatalyst decreases the number of exposed reactive sites, resulting in a lower removal efficiency. Despite this slight reduction in removal efficiency, the stability of the reused Pd-Bi_2WO_6 photocatalysts after degradation of phenol is still significant.

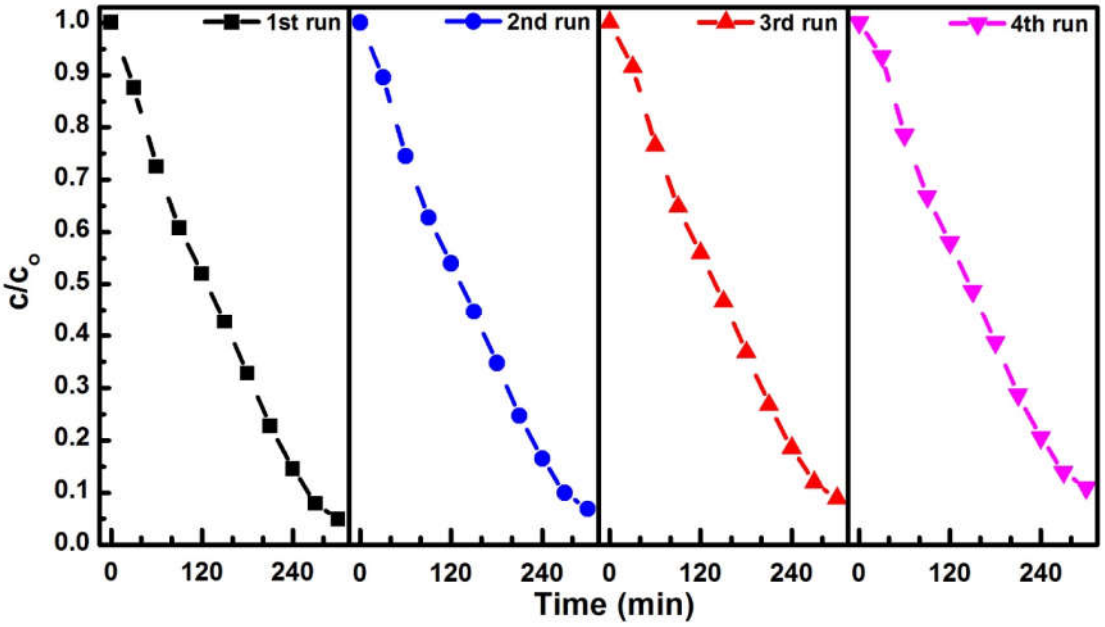


Figure 3.16 Phenol removal efficiency of recycled 4% Pd-Bi_2WO_6.

The stability of Pd-Bi_2WO_6 applied in photocatalysis was also investigated via XPS and XRD testing. As shown in Fig. 3.17, the high-resolution XPS orbit scan for Pd3d and Cl2p indicates that both Pd and Cl were still present on the surface. And the relative molar ratio of Pd^0/Pd^{2+} was about 21.7%, which is almost the same as that before photocatalysis. Also, as shown in Fig. 3.18, the influence of photocatalysis on the crystal structure of Bi_2WO_6

was negligible. These results above further confirm the high chemical stability of Pd-Bi_2WO_6 implemented in photocatalytic oxidation process.

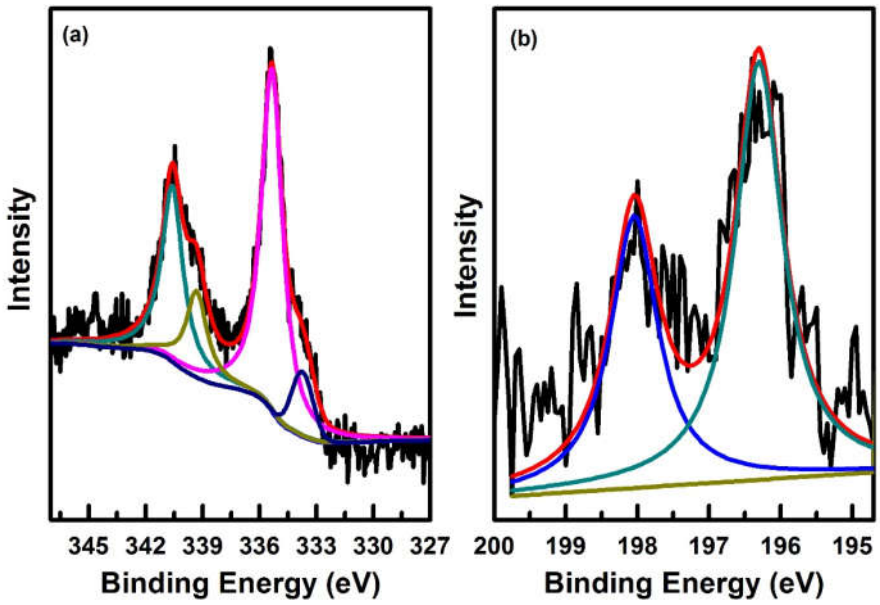


Figure 3.17 XPS high-resolution orbits scan of Pd3d and Cl2p for Pd/$PdCl_2$-Bi_2WO_6 after degradation of phenol under irradiation for 300 min.

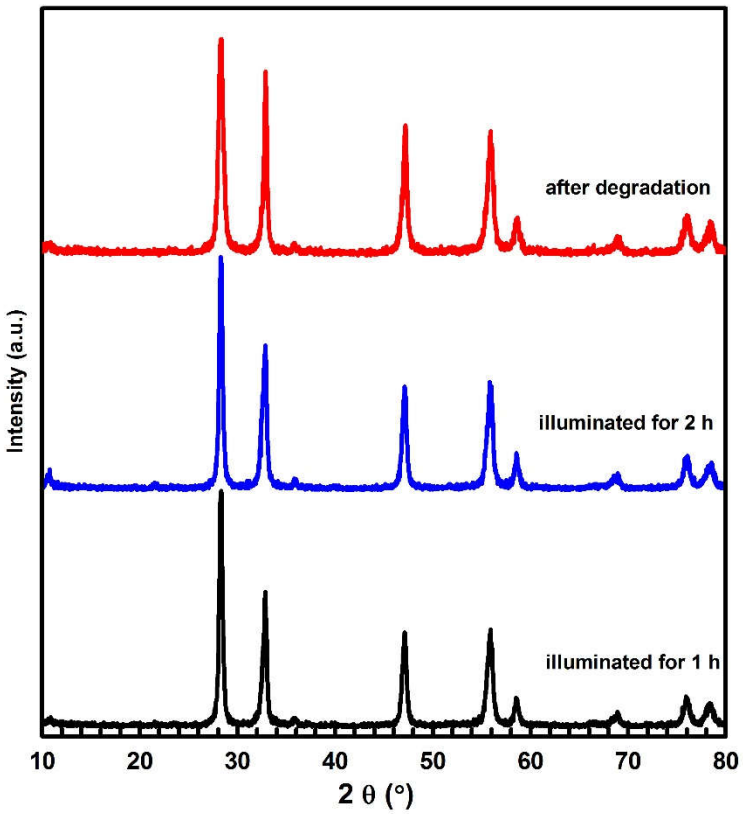


Figure 3.18 XRD patterns for Pd/$PdCl_2$-Bi_2WO_6 prepared under illumination for 1h and 2h, and after degradation of phenol over 300 min.

3.3.7 Mechanisms

4.3.7.1 Evaluation of photogenerated charge carriers' recombination rate

To study the electrons transfer on the prepared photocatalysts under visible light irradiation, electrochemical impedance spectroscopy (EIS) was used, and the EIS Nyquist plots for pure Bi_2WO_6 and Pd-Bi_2WO_6 were shown in Fig. 3.19. It can be found only one semicircle for each plot, which indicates the photocatalytic process may be a simple electrode reaction and electrons transfer and the rate may be determined by the recombination of photogenerated electron/hole pairs [67, 68]. The equivalent circuits of these two processes were shown in Table 3.5, and the fitted values were also obtained. Specifically, R_s, R_{ct} and CPE represent the resistance of solution, resistance of electron transfer on electrode and the constant phase element which can be regarded as a capacity of double layer. R_{ct} is the most important to compare the photocatalytic reaction rate, as it directly determine the rate of electrons transfer on the photocatalysts. The diameter of the arc in the EIS Nyquist plot

is related to the R_{ct}, and the larger the diameter is, the higher the R_{ct} is [69]. It can be found when Pd doped on the surface of Bi_2WO_6, the R_{ct} were significantly decreased from 328.5 to 19.81 kΩ. PL spectra were also measured to evaluate the recombination possibility of photogenerated charge carriers. Theoretically, the generation of photoluminescence may be resulted from the photons released from the recombination of separated electrons and holes. As a result, the higher the PL density is, the higher probability the photogenerated charge carriers' recombination [70]. As shown in Fig. 3.20, it is clear Bi_2WO_6 exhibited the highest PL intensity in the spectrum, and with introduction of palladium, the intensity was greatly reduced, indicating the separation of photogenerated charge carriers was greatly improved. More specifically, the emission intensity for the composite with 4% Pd was the lowest, and further loading of palladium increased the PL intensity. This phenomenon suggests over loading of palladium may increase the recombination of electron and holes pairs, as palladium may serve as recombination sites. EIS and PL results are solid evidences to prove the recombination rate of photogenerated electron and hole was greatly supressed and the photocatalytic activity in oxidation of organic pollutants was significantly improved.

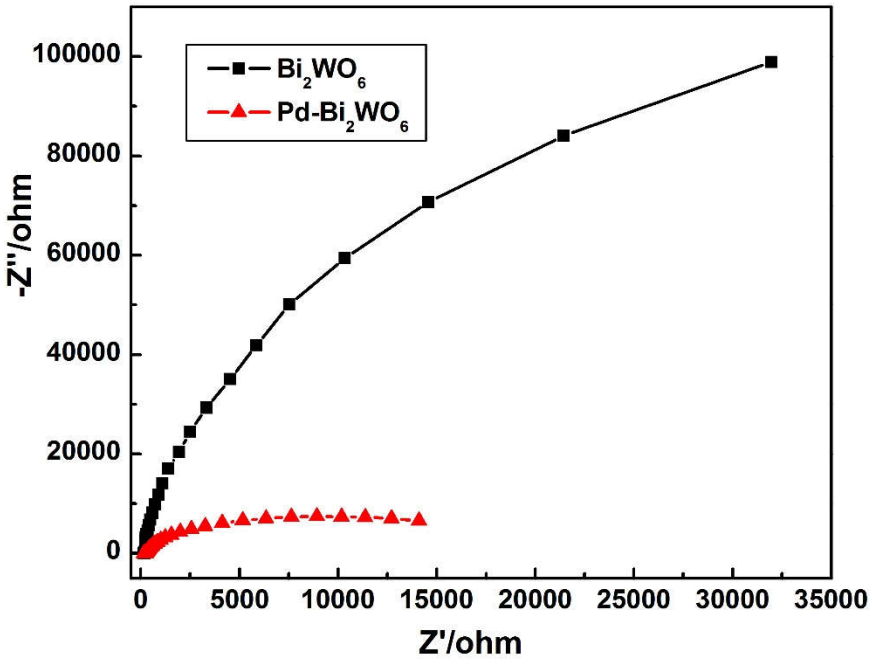
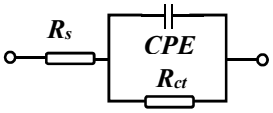


Figure 3.19 EIS Nyquist plots of the Bi_2WO_6 and 4%Pd-Bi_2WO_6 photocatalysts.

Table 3.5 Fitting results for equivalent circuits of different prepared samples.

Samples	R_s (Ω)	R_{ct} (kΩ)	*CPE* (μf)	Equivalent circuits
Bi_2WO_6	165.8	328.5	41.6	
4%Pd-Bi_2WO_6	210.1	19.81	31.01	

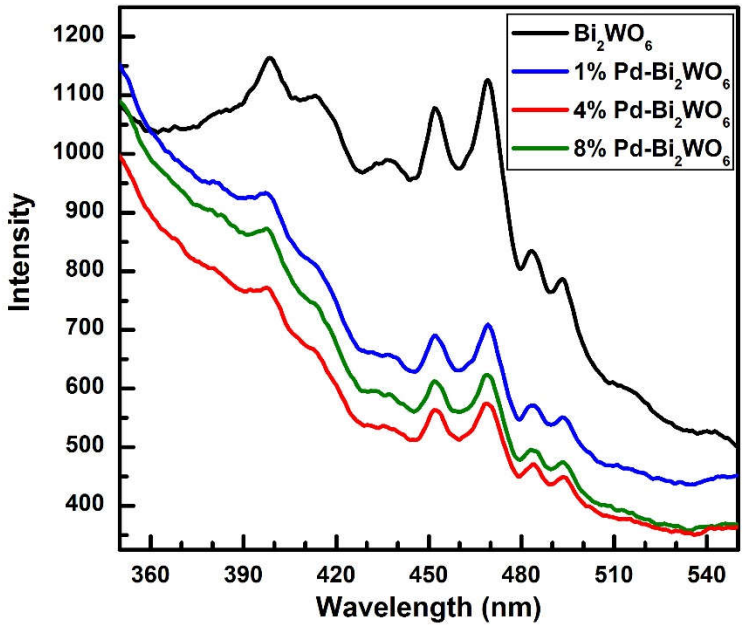


Figure 3.20 PL spectra for Bi_2WO_6 and Pd-Bi_2WO_6 composites at an excitation wavelength of 300 nm.

3.3.7.2 Possible effective oxidative species

Holes and radicals are two primary oxidative species involved in the photocatalytic degradation of organic compounds. EDTA-2Na and 1-butanol were chosen as scavengers for holes and radicals respectively, and N_2 bubbling was applied to purge the dissolved oxygen [39]. The photocatalytic degradation of phenol observed with and without quenchers can be seen in Fig. 3.21. When radicals were quenched with 1-butanol and N_2 bubbling, the removal efficiency was shown to be approximately 71.3% and 68.0%, respectively, after 300 min. However, when the hole scavenger was added to the system,

the removal efficiency decreased to approximately 10.2%. This suggests that holes play significant roles in the photocatalytic oxidation of organic compounds using Pd-Bi_2WO_6.

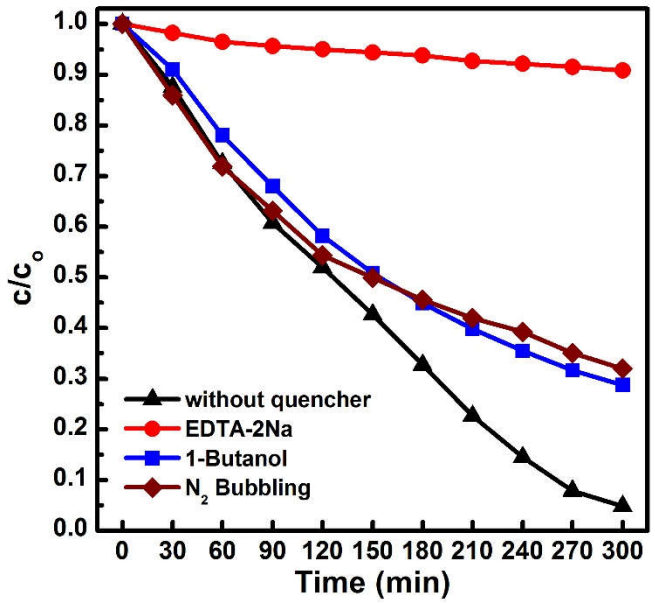


Figure 3.21 Photocatalytic degradation of phenol by 4%Pd-Bi_2WO_6 with and without quenchers (EDTA-2Na, 1-butanol and N_2 bubbling).

3.3.7.3 Proposed mechanism

A mechanism for the photocatalytic action of Pd-Bi_2WO_6 in the degradation of phenol is proposed and illustrated in Fig. 3.22. One possible explanation for this activity may be due to the surface plasmon resonance (SPR) exhibited by Pd nanoparticles on the surface of Bi_2WO_6. Even though there have been no reports on the plasmonic photocatalysis of Pd, similar results have been reported for other noble metals, especially for photocatalysts doped with Ag nanoparticles [71-73]. Specifically, Pd nanoparticles may be activated by visible light, producing electrons which then transfer to the conduction band of Bi_2WO_6. Furthermore, Pd^0 and Pd^{2+} adsorbed on the surface of the photocatalyst could inhibit the recombination of e^-/h^+ pairs, which would efficiently improve the separation rates of photogenerated carriers. Cl^- adsorbed on the surface of Bi_2WO_6 may also be oxidized to Cl^0, which is itself a strong oxidizing agent that may be capable of oxidizing phenol, returning to its reduced, anionic state (Cl^-) [74]. These integrated effects enhance the photocatalytic degradation of phenol in the presence of Pd-Bi_2WO_6.

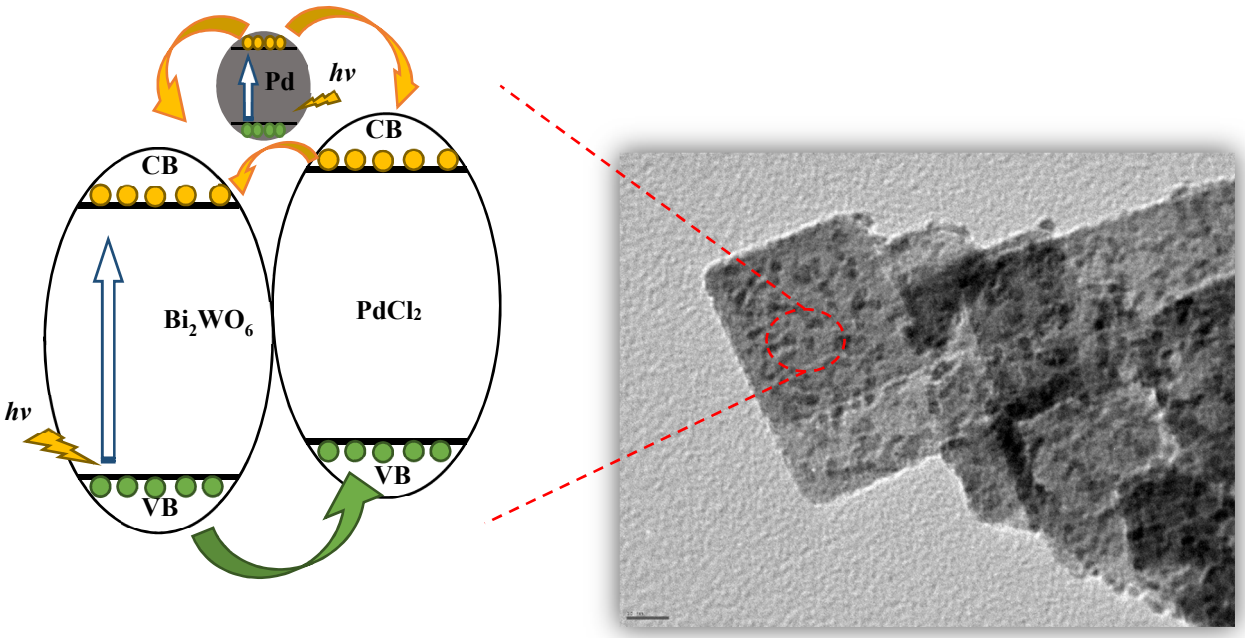


Figure 3.22 Proposed mechanism for the degradation of phenol with photocatalyst Pd-Bi_2WO_6

3.4 Conclusions

Pd-doped Bi_2WO_6 was investigated in this work. It was shown that both Pd^{2+} and metallic Pd^0 are present in the composites. Dopants negligibly influence the crystal structure and simply adsorbed on the surface of Bi_2WO_6. The photoabsorption intensity was enhanced in the visible light region with Pd deposition. As-prepared Pd-Bi_2WO_6 exhibited enhanced photocatalytic activity in the removal of phenol under visible light irradiation. The greatly improvement after palladium modification may be attributed to the surface plasmon resonance effect of palladium nanoparticles on the surface and suppression of photogenerated charge carriers' recombination. A different mechanism was proposed for the Pd-Bi_2WO_6 system, via comparison with TiO_2. The comparable activity of Pd-Bi_2WO_6 in organic decomposition under visible light irradiation to that of TiO_2 under UV light, indicate the significant promise of as-prepared composites in visible light-driven photocatalysis.

References

1. Michael R. Hoffmann, Scot T. Martin, Wonyong Choi and Detlef W. Bahnemann,

"Environmental Applications of Semiconductor Photocatalysis," *Chemical Reviews*, vol. 95, no. 1, pp. 69-96, 1995.

2. Xiaobo Chen, Shaohua Shen, Liejin Guo and Samuel S Mao, "Semiconductor-based photocatalytic hydrogen generation," *Chemical Reviews*, vol. 110, no. 11, pp. 6503-6570, 2010.

3. Meng Ni, Michael K. H. Leung, Dennis Y. C. Leung and K. Sumathy, "A review and recent developments in photocatalytic water-splitting using for hydrogen production," *Renewable and Sustainable Energy Reviews*, vol. 11, no. 3, pp. 401-425, 2007.

4. David F Ollis and Hussain Al-Ekabi, *TiO_2 Photocatalytic Purification and Treatment of Water and Air*, Elsevier Science Ltd, Photocatalytic purification and treatment of water and air: proceedings of the 1st International Conference, 1993.

5. Joanne Gamage McEvoy, Didier Alexandre Bilodeau, Wenquan Cui and Zisheng Zhang, "Visible-light-driven inactivation of Escherichia coli K-12 using an Ag/AgCl–activated carbon composite photocatalyst," *Journal of Photochemistry and Photobiology A: Chemistry*, vol. 267, pp. 25-34, 2013.

6. Xu Zhao, Libao Guo, Baofeng Zhang, Huijuan Liu and Jiuhui Qu, "Photoelectrocatalytic Oxidation of CuII–EDTA at the TiO_2 Electrode and Simultaneous Recovery of CuII by Electrodeposition," *Environmental science & technology*, vol. 47, no. 9, pp. 4480-4488, 2013.

7. Horst Kisch, "Semiconductor Photocatalysis for Organic Synthesis," in *Advances in Photochemistry*, Ed., pp. 93-143, John Wiley & Sons, Inc., 2007.

8. Akira Fujishima, Xintong Zhang and Donald A. Tryk, "TiO_2 photocatalysis and related surface phenomena," *Surface Science Reports*, vol. 63, no. 12, pp. 515-582, 2008.

9. Lin Zhou, Wenzhong Wang, Haolan Xu, Songmei Sun and Meng Shang, "Bi2O3 Hierarchical Nanostructures: Controllable Synthesis, Growth Mechanism, and their Application in Photocatalysis," *Chemistry – A European Journal*, vol. 15, no. 7, pp. 1776-1782, 2009.

10. Kangrong Lai, Wei Wei, Ying Dai, Ruiqin Zhang and Baibiao Huang, "DFT calculations on structural and electronic properties of Bi2MO6 (M = Cr, Mo, W)," *Rare*

Metals, vol. 30, no. 1, pp. 166-172, 2011.

11. Xiangchao Meng and Zisheng Zhang, "Plasmonic Z-scheme Ag_2O-Bi_2MoO_6 p-n heterojunction photocatalysts with greatly enhanced visible-light responsive activities," *Materials Letters*, vol. 189, pp. 267-270, 2017.

12. Xiangchao Meng and Zisheng Zhang, "Plasmonic ternary Ag–rGO–Bi_2MoO_6 composites with enhanced visible light-driven photocatalytic activity," *Journal of Catalysis*, vol. 344, pp. 616-630, 2016.

13. Xiangchao Meng and Zisheng Zhang, "Bi_2MoO_6 co-modified by reduced graphene oxide and palladium (Pd^{2+} and Pd^0) with enhanced photocatalytic decomposition of phenol," *Applied Catalysis B: Environmental*, vol. 209, pp. 383-393, 2017.

14. Xiangchao Meng, Zizhen Li, Haoming Zeng, Jie Chen and Zisheng Zhang, "MoS_2 quantum dots-interspersed Bi_2WO_6 heterostructures for visible light-induced detoxification and disinfection," *Applied Catalysis B: Environmental*, vol. 210, pp. 160-172, 2017.

15. Xiangchao Meng and Zisheng Zhang, "Ag/AgCl Loaded Bi_2WO_6 Composite: A Plasmonic Z-Scheme Visible Light-Responsive Photocatalyst," *International Journal of Photoenergy*, vol. 2016, pp. 11, 2016.

16. Huizhong An, Yi Du, Tianmin Wang, Cong Wang, Weichang Hao and Junying Zhang, "Photocatalytic properties of BiOX (X = Cl, Br, and I)," *Rare Metals*, vol. 27, no. 3, pp. 243-250, 2008.

17. Chengsi Pan and Yongfa Zhu, "Size-controlled synthesis of BiPO4 nanocrystals for enhanced photocatalytic performance," *Journal of Materials Chemistry*, vol. 21, no. 12, pp. 4235-4241, 2011.

18. Jianqiang Yu and Akihiko Kudo, "Effects of structural variation on the photocatalytic performance of hydrothermally synthesized BiVO4," *Advanced Functional Materials*, vol. 16, no. 16, pp. 2163-2169, 2006.

19. Xiangchao Meng and Zisheng Zhang, "Bismuth-based Photocatalytic Semiconductors: Introduction, Challenges and Possible Approaches," *Journal of Molecular Catalysis A: Chemical*, vol. 423, pp. 533-549, 2016.

20. ZhangSheng Liu, BianTao Wu, DongHu Xiang and YaBo Zhu, "Effect of solvents on morphology and photocatalytic activity of BiOBr synthesized by solvothermal method," *Materials Research Bulletin*, vol. 47, no. 11, pp. 3753-3757, 2012.

21. Lisha Zhang, Wenzhong Wang, Lin Zhou and Haolan Xu, "Bi2WO6 Nano‐and Microstructures: Shape Control and Associated Visible‐Light‐Driven Photocatalytic Activities," *Small*, vol. 3, no. 9, pp. 1618-1625, 2007.

22. Xiaojing Shi, Xin Chen, Xiliang Chen, Shaomin Zhou, Shiyun Lou, Yongqiang Wang and Lin Yuan, "PVP assisted hydrothermal synthesis of BiOBr hierarchical nanostructures and high photocatalytic capacity," *Chemical Engineering Journal*, vol. 222, pp. 120-127, 2013.

23. Xiangchao Meng and Zisheng Zhang, "Synthesis, Analysis, and Testing of BiOBr-Bi_2WO_6 Photocatalytic Heterojunction Semiconductors," *International Journal of Photoenergy*, vol. 2015, pp. 12, 2015.

24. Xiangchao Meng and Zisheng Zhang, "Facile synthesis of BiOBr/Bi_2WO_6 heterojunction semiconductors with high visible-light-driven photocatalytic activity," *Journal of Photochemistry and Photobiology A: Chemistry*, vol. 310, no. 0, pp. 33-44, 2015.

25. Yajun Wang, Xiaojuan Bai, Chengsi Pan, Jun He and Yongfa Zhu, "Enhancement of photocatalytic activity of Bi2WO6 hybridized with graphite-like C3N4," *Journal of Materials Chemistry*, vol. 22, no. 23, pp. 11568-11573, 2012.

26. Ying Zhou, Qian Zhang, YuanHua Lin, Elena Antonova, Wolfgang Bensch and GretaR Patzke, "One-step hydrothermal synthesis of hierarchical Ag/Bi2WO6 composites: In situ growth monitoring and photocatalytic activity studies," *Science China Chemistry*, vol. 56, no. 4, pp. 435-442, 2013.

27. Lufeng Lu, Liang Kong, Zheng Jiang, HenryH C. Lai, Tiancun Xiao and PeterP Edwards, "Visible-Light-Driven Photodegradation of Rhodamine B on Ag-Modified BiOBr," *Catalysis Letters*, vol. 142, no. 6, pp. 771-778, 2012.

28. Xiangchao Meng and Zisheng Zhang, "Pd-doped Bi_2MoO_6 Plasmonic Photocatalysts with Enhanced Visible Light Photocatalytic Performance," *Applied Surface Science*, vol. 392, pp. 169-180, 2016.

29. Changlin Yu, Fangfang Cao, Gao Li, Rongfu Wei, Jimmy C. Yu, Rongchao Jin, Qizhe Fan and Chunying Wang, "Novel noble metal (Rh, Pd, Pt)/BiOX(Cl, Br, I) composite photocatalysts with enhanced photocatalytic performance in dye degradation," *Separation and Purification Technology*, vol. 120, pp. 110-122, 2013.

30. Xiaoyue Hu, Xiangchao Meng and Zisheng Zhang, "Synthesis and Characterization of Graphene Oxide-Modified Bi_2WO_6 and Its Use as Photocatalyst," *International Journal of Photoenergy*, vol. 2016, pp. 8, 2016.

31. Xiangchao Meng and Zisheng Zhang, "Synthesis and characterization of plasmonic and magnetically separable Ag/AgCl-Bi_2WO_6@ Fe_3O_4@SiO_2 core-shell composites for visible light-induced water detoxification," *Journal of Colloid and Interface Science*, vol. 485, pp. 296-307, 2017.

32. Adam A. Donaldson, Alice Ye, Joanne Gamage McEvoy and Zisheng Zhang, "Rotating corrugated photoreactor design: Experimental and computational analysis of TiO2-based photocatalysis," *AIChE Journal*, vol. 59, no. 2, pp. 560-570, 2013.

33. Adam A. Donaldson and Zisheng Zhang, "Coupled Transport Phenomena in Corrugated Photocatalytic Reactors," *Chinese Journal of Chemical Engineering*, vol. 19, no. 5, pp. 763-772, 2011.

34. Kevin S Knight, "The crystal structure of russellite; a re-determination using neutron powder diffraction of synthetic Bi_2WO_6," 1992.

35. Jessica Torres, C. C. Perry, Stephen J. Bransfield and D. Howard Fairbrother, "Low-Temperature Oxidation of Nitrided Iron Surfaces," *The Journal of Physical Chemistry B*, vol. 107, no. 23, pp. 5558-5567, 2003.

36. Jan Wielant, Tom Hauffman, Orlin Blajiev, René Hausbrand and Herman Terryn, "Influence of the Iron Oxide Acid−Base Properties on the Chemisorption of Model Epoxy Compounds Studied by XPS," *The Journal of Physical Chemistry C*, vol. 111, no. 35, pp. 13177-13184, 2007.

37. K. R. Priolkar, Parthasarathi Bera, P. R. Sarode, M. S. Hegde, S. Emura, R. Kumashiro and N. P. Lalla, "Formation of Ce1-xPdxO2-δ Solid Solution in Combustion-Synthesized Pd/CeO2 Catalyst: XRD, XPS, and EXAFS Investigation," *Chemistry of Materials*, vol.

14, no. 5, pp. 2120-2128, 2002.

38. Gobind Kumar, J. R. Blackburn, R. G. Albridge, W. E. Moddeman and M. M. Jones, "Photoelectron spectroscopy of coordination compounds. II. Palladium complexes," *Inorganic Chemistry*, vol. 11, no. 2, pp. 296-300, 1972.

39. Xiangchao Meng, Zizhen Li and Zisheng Zhang, "Pd-nanoparticle-decorated peanut-shaped $BiVO_4$ with improved visible light-driven photocatalytic activity comparable to that of TiO_2 under UV light," *Journal of Catalysis*, vol. 356, pp. 53-64, 2017.

40. CD Wagner and GE Muilenberg, *Handbook of X-ray photoelectron spectroscopy*, Perkin-Elmer, 1979.

41. J. H. Scofield, "Hartree-Slater subshell photoionization cross-sections at 1254 and 1487 eV," *Journal of Electron Spectroscopy and Related Phenomena*, vol. 8, no. 2, pp. 129-137, 1976.

42. David R. Penn, "Quantitative chemical analysis by ESCA," *Journal of Electron Spectroscopy and Related Phenomena*, vol. 9, no. 1, pp. 29-40, 1976.

43. R. D. Seals, Robert Alexander, Larry T. Taylor and John G. Dillard, "Core electron binding energy study of group IIb-VIIa compounds," *Inorganic Chemistry*, vol. 12, no. 10, pp. 2485-2487, 1973.

44. M. Lourdes Calzada, Rafael Sirera, Francisco Carmona and Basilio Jiménez, "Investigations of a Diol-based Sol-Gel Process for the Preparation of Lead Titanate Materials," *Journal of the American Ceramic Society*, vol. 78, no. 7, pp. 1802-1808, 1995.

45. M. F. Daniel, B. Desbat, J. C. Lassegues and R. Garie, "Infrared and Raman spectroscopies of rf sputtered tungsten oxide films," *Journal of Solid State Chemistry*, vol. 73, no. 1, pp. 127-139, 1988.

46. M. A. Hasan, M. I. Zaki and L. Pasupulety, "Oxide-catalyzed conversion of acetic acid into acetone: an FTIR spectroscopic investigation," *Applied Catalysis A: General*, vol. 243, no. 1, pp. 81-92, 2003.

47. Li-Fen Liao, Chen-Fu Lien and Jong-Liang Lin, "FTIR study of adsorption and photoreactions of acetic acid on TiO2," *Physical Chemistry Chemical Physics*, vol. 3, no.

17, pp. 3831-3837, 2001.

48. Jiaguo Yu, Jianfeng Xiong, Bei Cheng, Ying Yu and Jianbo Wang, "Hydrothermal preparation and visible-light photocatalytic activity of Bi2WO6 powders," *Journal of Solid State Chemistry*, vol. 178, no. 6, pp. 1968-1972, 2005.

49. Jian Zhu, Jin-Guo Wang, Zhen-Feng Bian, Fen-Glei Cao and He-Xing Li, "Solvothermal synthesis of highly active Bi2WO6 visible photocatalyst," *Research on Chemical Intermediates*, vol. 35, no. 6-7, pp. 799-806, 2009.

50. KSW Sing, DH Everett, RAW Haul, L Moscou, RA Pierotti, J Rouquerol and T Siemieniewska, "Physical and biophysical chemistry division commission on colloid and surface chemistry including catalysis," *Pure Applied Chemistry*, vol. 57, no. 4, pp. 603-619, 1985.

51. Michal Kruk and Mietek Jaroniec, "Gas Adsorption Characterization of Ordered Organic−Inorganic Nanocomposite Materials," *Chemistry of Materials*, vol. 13, no. 10, pp. 3169-3183, 2001.

52. Akihiko Kudo, Issei Tsuji and Hideki Kato, "AgInZn7S9 solid solution photocatalyst for H2 evolution from aqueous solutions under visible light irradiation," *Chemical Communications*, no. 17, pp. 1958-1959, 2002.

53. Fang Duan, Yan Zheng and MingQing Chen, "Flowerlike PtCl4/Bi2WO6 composite photocatalyst with enhanced visible-light-induced photocatalytic activity," *Applied Surface Science*, vol. 257, no. 6, pp. 1972-1978, 2011.

54. M. A. Butler and D. S. Ginley, "Prediction of Flatband Potentials at Semiconductor - Electrolyte Interfaces from Atomic Electronegativities," *Journal of The Electrochemical Society*, vol. 125, no. 2, pp. 228-232, 1978.

55. Arthur H. Nethercot, "Prediction of Fermi Energies and Photoelectric Thresholds Based on Electronegativity Concepts," *Physical Review Letters*, vol. 33, no. 18, pp. 1088-1091, 1974.

56. Clarissa Baumanis and Detlef W. Bahnemann, "TiO_2 Thin Film Electrodes: Correlation between Photocatalytic Activity and Electrochemical Properties," *The Journal of Physical*

Chemistry C, vol. 112, no. 48, pp. 19097-19101, 2008.

57. Zhengpeng Wang, Weimin Cai, Xiaoting Hong, Xiaolian Zhao, Fang Xu and Chuenguang Cai, "Photocatalytic degradation of phenol in aqueous nitrogen-doped TiO2 suspensions with various light sources," *Applied Catalysis B: Environmental*, vol. 57, no. 3, pp. 223-231, 2005.

58. Mingce Long, Weimin Cai, Jun Cai, Baoxue Zhou, Xinye Chai and Yahui Wu, "Efficient Photocatalytic Degradation of Phenol over Co_3O_4/$BiVO_4$ Composite under Visible Light Irradiation," *The Journal of Physical Chemistry B*, vol. 110, no. 41, pp. 20211-20216, 2006.

59. Yuxiao Niu, Mingyang Xing, Jinlong Zhang and Baozhu Tian, "Visible light activated sulfur and iron co-doped TiO_2 photocatalyst for the photocatalytic degradation of phenol," *Catalysis Today*, vol. 201, pp. 159-166, 2013.

60. Xin Xiao and Wei-De Zhang, "Facile synthesis of nanostructured BiOI microspheres with high visible light-induced photocatalytic activity," *Journal of Materials Chemistry*, vol. 20, no. 28, pp. 5866-5870, 2010.

61. Jing Wang, Xiaoming Gao, Feng Fu, Liping Zhang and Yufei Wu, "Photocatalytic Degradation of Phenol-Containing Wastewaterover Cu-Bi_2WO_6 Composite under Visible Light Irradiation," *Journal of Residuals Science & Technology*, vol. 9, no. 3, 2012.

62. Hongwei Ma, Jianfeng Shen, Min Shi, Xin Lu, Zhiqiang Li, Yu Long, Na Li and Mingxin Ye, "Significant enhanced performance for Rhodamine B, phenol and Cr(VI) removal by Bi_2WO_6 nancomposites via reduced graphene oxide modification," *Applied Catalysis B: Environmental*, vol. 121, pp. 198-205, 2012.

63. Zhijie Zhang, Wenzhong Wang, Lu Wang and Songmei Sun, "Enhancement of Visible-Light Photocatalysis by Coupling with Narrow-Band-Gap Semiconductor: A Case Study on Bi_2S_3/Bi_2WO_6," *ACS Applied Materials & Interfaces*, vol. 4, no. 2, pp. 593-597, 2012.

64. Xiao-yan Li, Yu-hong Cui, Yu-jie Feng, Zhao-ming Xie and Ji-Dong Gu, "Reaction pathways and mechanisms of the electrochemical degradation of phenol on different electrodes," *Water Research*, vol. 39, no. 10, pp. 1972-1981, 2005.

65. Chunde Wu, Xinhui Liu, Dongbin Wei, Jinchu Fan and Liansheng Wang,

"Photosonochemical degradation of Phenol in water," *Water Research*, vol. 35, no. 16, pp. 3927-3933, 2001.

66. Z. Ding, G. Q. Lu and P. F. Greenfield, "Role of the Crystallite Phase of TiO2 in Heterogeneous Photocatalysis for Phenol Oxidation in Water," *The Journal of Physical Chemistry B*, vol. 104, no. 19, pp. 4815-4820, 2000.

67. Janet M. Kesselman, Gary A. Shreve, Michael R. Hoffmann and Nathan S. Lewis, "Flux-Matching Conditions at TiO_2 Photoelectrodes: Is Interfacial Electron Transfer to O_2 Rate-Limiting in the TiO_2-Catalyzed Photochemical Degradation of Organics?," *The Journal of Physical Chemistry*, vol. 98, no. 50, pp. 13385-13395, 1994.

68. Baifu Xin, Zhiyu Ren, Haiyuan Hu, Xiangyu Zhang, Chunlei Dong, Keying Shi, Liqiang Jing and Honggang Fu, "Photocatalytic activity and interfacial carrier transfer of Ag–TiO_2 nanoparticle films," *Applied Surface Science*, vol. 252, no. 5, pp. 2050-2055, 2005.

69. Baifu Xin, Zhiyu Ren, Peng Wang, Jia Liu, Liqiang Jing and Honggang Fu, "Study on the mechanisms of photoinduced carriers separation and recombination for Fe^{3+}–TiO_2 photocatalysts," *Applied Surface Science*, vol. 253, no. 9, pp. 4390-4395, 2007.

70. Xiangchao Meng, Zizhen Li, Jie Chen, Hongwei Xie and Zisheng Zhang, "Enhanced visible light-induced photocatalytic activity of surface-modified BiOBr with Pd nanoparticles," *Applied Surface Science*, vol. 433, no. Supplement C, pp. 76-87, 2018.

71. Suljo Linic, Phillip Christopher and David B. Ingram, "Plasmonic-metal nanostructures for efficient conversion of solar to chemical energy," *Nature Materials*, vol. 10, no. 12, pp. 911-921, 2011.

72. Peng Wang, Baibiao Huang, Xiaoyan Qin, Xiaoyang Zhang, Ying Dai, Jiyong Wei and Myung-Hwan Whangbo, "Ag@AgCl: A Highly Efficient and Stable Photocatalyst Active under Visible Light," *Angewandte Chemie International Edition*, vol. 47, no. 41, pp. 7931-7933, 2008.

73. Liqun Ye, Jinyan Liu, Chuqing Gong, Lihong Tian, Tianyou Peng and Ling Zan, "Two Different Roles of Metallic Ag on Ag/AgX/BiOX (X = Cl, Br) Visible Light Photocatalysts: Surface Plasmon Resonance and Z-Scheme Bridge," *ACS Catalysis*, vol. 2, no. 8, pp. 1677-

1683, 2012.

74. Joanne Gamage McEvoy, Wenquan Cui and Zisheng Zhang, "Synthesis and characterization of Ag/AgCl–activated carbon composites for enhanced visible light photocatalysis," *Applied Catalysis B: Environmental*, vol. 144, no. 0, pp. 702-712, 2014.

Chapter 4 Enhanced Visible Light-induced Photocatalytic Activity of Surface-modified BiOBr with Pd Nanoparticles

Xiangchao Meng, Zizhen Li, Jie Chen, Hongwei Xie, Zisheng Zhang

Applied Surface Science 433 (2018), 76-87

Abstract

Palladium nanoparticles well-dispersed on BiOBr surfaces were successfully prepared via a two-step process, namely hydrothermal synthesis of BiOBr followed by photodeposition of palladium. Surface-exposed palladium nanoparticles may improve the harvesting capacity of visible light photons via the surface plasmonic resonance effect to produce extra electrons. Palladium is an excellent electron acceptor, and therefore favours the separation of photogenerated electron/hole pairs. As a result, palladium significantly improves the photocatalytic activity of BiOBr in the removal of organic pollutants (phenol) under visible light irradiation. In addition to as-prepared samples which were comprehensively characterized, the mechanism for the enhancement via the deposition of palladium nanoparticles was also proposed based on results. This work may serve as solid evidence to confirm that surface-deposited palladium nanoparticles are capable of improving photocatalytic activity, and that photodeposition may be an effective approach to load metal nanoparticles onto a surface.

4.1 Introduction

Photocatalysis, as an advanced oxidative process, has been extensively investigated since 1972 [1]. The main applications of photocatalysis involve the generation of hydrogen (H_2) via photocatalytic water splitting and the complete decomposition of organic pollutants in wastewater and polluted air [2-6]. The mechanism as to how photocatalysis works may be

interpreted as electrons on the valence band of a photocatalyst, which are activated by photons from irradiation, jumping to the conduction band, leaving positively charged holes on the valence band. The holes as well as separated electrons may further react with adsorbed species to produce many oxidative species which may degrade some organic pollutants.

As a pioneer material with excellent photocatalytic properties, TiO_2 has been greatly developed to date. Before it may be applied at the pilot scale, hindrances such as a high rate of recombination for photogenerated charge carriers and no activity under visible light irradiation must be overcome. Approaches include modification of TiO_2 and preparation of novel materials aimed to improve the visible light-driven photocatalytic activity [7, 8]. Surface modifications of TiO_2 with non-metal/metal or recombination with other co-catalysts that have narrow band gaps are difficult to change the intrinsic band structure and just tune the band configuration [9].

As an alternative, developing visible light-responsive photocatalysts with suitable band gaps may be more useful. Recently, bismuth-based semiconductor photocatalysis has been reported by researchers including our group [8, 10-18]. The superiority of bismuth-based photocatalysts include a well-dispersed valence band composed of hybrid orbitals Bi *6s* and O *2p*, adjustable morphologies via modular preparation conditions, and a high visible light-driven photocatalytic activity in the removal of organic pollutants. Among these bismuth-based photocatalysts, Bi_2MO_6 (M = Mo and W) and BiOX (X = Cl, Br, I) are the most studied [19-24]. However, the band structures of these photocatalysts are so flat that photogenerated electrons and holes are easily recombined, reducing photocatalytic activity. Methods to improve the separation efficiency of photogenerated charge carriers are still required. As reviewed in [8], modulation of the energy band via doping, morphology control and recombination with other co-catalysts have been reported as effective improvements to visible light sensitivity. Among them, it is an effective approach to deposit rare metal nanoparticles on the surface to improve the visible light harvesting capacity produced by surface plasmonic resonance (SPR), facilitating the separation of photogenerated charge carriers. In addition, photodeposition was reported as an effective approach to load well-dispersed metal nanoparticles (NPs) on the surface of a photocatalyst [25]. Lu *et al.* reported on the preparation of silver NPs loaded on BiOBr with enhanced

photocatalytic activity for the removal of Rhodamine B (RhB) [26]. Moreover, Pd-modified BiOBr was also reported via a facile one-pot process [27, 28]. The drawbacks of a one-pot process to prepare Pd-BiOBr are: 1) most of the palladium is located in the bulk and is difficult to activate by illumination, and 2) divalent palladium may not be completely reduced to Pd NPs. As we reported on Pd-decorated Bi_2MoO_6 produced via the photoreduction process, well-dispersed Pd NPs are distributed on the surface of Bi_2MoO_6, and the photocatalytic activity of Bi_2MoO_6 for the removal of phenol was greatly improved [29]. It was also reported that the SPR peaks of Pd nanostructures may be tuned from 410 to 870 nm [30, 31].

In this work, the fabrication of Pd-modified BiOBr via a photoreduction process is discussed. As-prepared samples were extensively characterized. The photocatalytic activities of the samples were also investigated with regards to phenol consumption under visible light irradiation. It is notable that the photocatalytic activity of BiOBr was greatly improved via photodeposition of palladium NPs, and a mechanism of the improvement is also proposed.

4.2 Experimental

4.2.1 Preparation of BiOBr

All chemicals were purchased from Fisher Scientific Canada and used as received. Pure BiOBr was prepared via a facile hydrothermal method. Typically, 2.00 g of $Bi(NO_3)_3 \cdot 5H_2O$ were dissolved in 10 mL of acetic acid. Next, 30 mL of distilled deionized water (DDW) containing 0.49 g of KBr were added dropwise to the bismuth precursor solution. After stirring magnetically for 30 min, the suspension was transferred to a 50-mL Teflon-lined stainless steel autoclave (Parr Instrument Company). The autoclave was heated at 120°C for 12 hours. After the autoclave was allowed to naturally cool to room temperature, the precipitates were filtered out and washed twice with DDW, then once with ethanol. The precipitates were dried at 60°C overnight before being collected for further use.

4.2.2 Preparation of Pd-BiOBr composites

Palladium was deposited on the as-prepared BiOBr via a photoreduction method [29]. A highly dispersed suspension of $PdCl_2$ was obtained by ultra-sonication for 30 min. Next, 0.30 g of as-prepared BiOBr were suspended in 30 mL of DDW and sonicated for 30 min. After that, a designated amount of $PdCl_2$ suspension was added to the BiOBr suspension. The suspension was then illuminated under a 300-W halogen tungsten projector lamp (Ushio, USA) for 1 h. The particles were then separated out via vacuum filtration and dried at 60°C overnight before being collected and labelled. Following these steps, 0.1, 0.2, 0.5, and 0.8 wt% Pd-BiOBr composites were prepared and designated as 0.1 Pd-Bi, 0.2 Pd-Bi, 0.5 Pd-Bi and 0.8 Pd-Bi, respectively.

4.2.3 Characterization

The morphologies of as-prepared samples were investigated using a scanning electron microscopy (SEM, model: JEOL JSM-7500F) and a transmission electron microscope (TEM, model: JEM-2100F). The SEM was also equipped with an Energy-dispersive X-ray spectroscopy (EDS). Crystal structures of the samples were detected via X-ray diffraction (XRD) on a Rigaku Ultima IV Diffractometer with Cu Kα radiation (λ = 0.15418 nm) at 40 kV and 44 mA. XRD patterns were recorded at 2θ of 5 - 80°. An XSAM-800 X-ray Photoelectron Spectroscope (XPS) was employed to analyze the surface composition and the chemical sates of selected samples. Optical properties of prepared samples were studied by UV-Vis diffused reflectance spectroscopy (DRS). The Brunauer, Emmett and Teller (BET) surface area of the samples were calculated using multi-point estimation. The pore volumes were calculated using the volumes of adsorbed N_2 at $p/p_o = 0.9939$. Pore volume distributions are calculated using N_2 desorption branch, and the Barrett-Joyner-Halenda (BJH) method was used for the desorption branch to calculate the pore size data (d_p) using Equation 1 (where V/A_s is a ratio of volume to surface area of pores) as follows,

$$d_p = 4\left(\frac{V}{A_s}\right)_{BJH} \qquad \textbf{\textit{Equation 1}}$$

The photoluminescence (PL) spectra were measured using a fluorescence Spectrophotometer (F-4500, Hitachi) under excitation with wavelength of 300 nm.

Electrochemical properties of prepared samples were analyzed on a CHI 604E electrochemical analyzer (CH Instruments Inc., USA) with a platinum wire as a counter electrode, a calomel reference electrode and a working electrode. The working electrode composed of indium tin oxide (ITO, 75 × 25 × 1.1 mm, 15 - 25 Ω, Sigma-Aldrich Canada Co.), glass coated with the prepared samples. Electrochemical impedance spectroscopy (EIS) was performed with frequencies in the range of 0 – 8,000 Hz and a sinusoidal wave of 5 mV. Photocurrent was also measured with turning on and off lamp. The electrolyte used was Na_2SO_4 with a concentration of 0.5 mol/L.

Point of zero charge (PZC) of prepared samples was measured using a potentiometric titration method [32]. Typically, 0.1 g of samples were added in 50 mL-NaCl solution (0.01 mol/L). The initial pH of NaCl solution was adjusted using HCl (0.1 mol/L) and NaOH (0.1 mol/L) solutions with a value from 4 to 7. The mixtures shake at 250 rpm for 12 h. Final pH values were measured. PZC is determined when the initial pH equals to the final pH.

4.2.4 Photocatalytic activity tests

Photocatalytic activities of as-prepared samples were measured by degrading a colourless organic pollutant, phenol, in 100-mL water under visible light irradiation. The reactive system was composed of a 500-mL beaker with a cooling jacket. The temperature of the reactive solution was maintained at approximately 20°C for all tests. A 300-W halogen tungsten projector lamp (Ushio, USA) served as the light source, with a UV cut-off (Kenko Zeta, transmittance > 90%) to filter out irradiation with a wavelength below 410 nm so as to ensure the irradiation occurred within the visible light range. The irradiation intensity at the surface of the reactive solution was measured with a quantum meter (Biospherical QSL-2100, $400 < \lambda < 700$ nm), which was measured to be approximately 1.1×10^{-2} Einsteins m^{-2} s^{-1}. Before each test, the samples were stirred magnetically in solution for 60 min in the absence of light in order to reach adsorption-desorption equilibrium between the organic pollutants and the photocatalyst. After that, the photocatalysis process was initiated by turning on the light for 6 hours. During the process, 1-mL aliquots were drawn every 30 min. These samples were centrifuged for 5 min at 13000 rpm, and the supernatant was separated and analyzed on a high-performance liquid chromatograph (HPLC, Agilent 1100

series). The HPLC was equipped with a UV detector and the detecting wavelength was fixed at 270 nm. A ZORBAX Eclipse Plus C18 column (4.6 × 250 mm, Agilent Technology) was used as well, at a temperature of 60°C. The flow phase was composed of 55% methanol and 45% water at a flow rate of 0.6 mL/min. The injection volume was 25 μL for each sample.

4.2.5 Electronic structure calculation

Quantum-mechanical calculations were performed on the basis of the density functional theory (DFT) [33]. The generalized gradient approximation (GGA) was applied to exchange-correlation effects. The open access software Quantum ESPRESSO was used, which utilizes pseudo potentials to describe electron-ion interactions and represents electronic wave functions using a plane-wave basis set [34]. The kinetic energy cut-off was set to 300 eV.

4.3 Results and discussions

4.3.1 Morphologies

Morphologies of prepared samples including pure BiOBr and Pd-modified BiOBr samples were investigated using SEM and TEM as shown in Fig. 4.1 and 4.2, respectively. It was observed that the BiOBr sample is composed of a large quantity of uniform sheets with diameters in the range of 0.5 – 3.0 μm (Fig. 4.1a and b). The average thickness of these sheets is approximately 30 nm. In Fig. 4.1c, BiOBr as the support modified with palladium is observed with a similar structure of uniform sheets stacked together. In the high-magnification SEM image of Pd-BiOBr shown in Fig. 4.1d, coarse surfaces are observed with deposited nanoparticles. These NPs may be attributed to palladium nanoparticles deposited by the photoreduction process. As shown in Fig. 4.1e, the EDS spectra indicate palladium were present on the Pd-BiOBr sample, which confirms these NPs may be attributed to Pd NPs. It should also be noted that in Fig. 4.1 c and 4.1d, particle clusters are found attached to BiOBr sheets. This phenomenon may be due to the $PdCl_2$ suspensions used as the precursor, as trace amounts of $PdCl_2$ are soluble in water. Pd^{2+} dissolved in the suspension is photoreduced on BiOBr to Pd, and Pd^{2+} in $PdCl_2$ particles adsorbed on the BiOBr sheets may also be photoreduced on $PdCl_2$ particles which are the particle clusters observed in the SEM images.

The morphologies of the pure BiOBr as well as of 0.5% Pd-BiOBr samples were further revealed by TEM as shown in Fig. 4.2. For pure BiOBr, a sheet-like structure was observed and a flat surface is shown in Fig. 4.2b. Following the introduction of palladium to BiOBr, rough edges can be seen in the low-magnification TEM image shown in Fig. 4.2c. In the high-magnification TEM image (Fig. 4.2d), it can be seen that small particles are highly dispersed on the sheets. The size distribution of these particles is shown in the inset of Fig. 4.2d, which suggests that these particles are nano-scale in size and may be attributed to Pd NPs. These nanoparticles are coupled well with the support, indicating the successful preparation of Pd modified BiOBr composites via the photoreduction method.

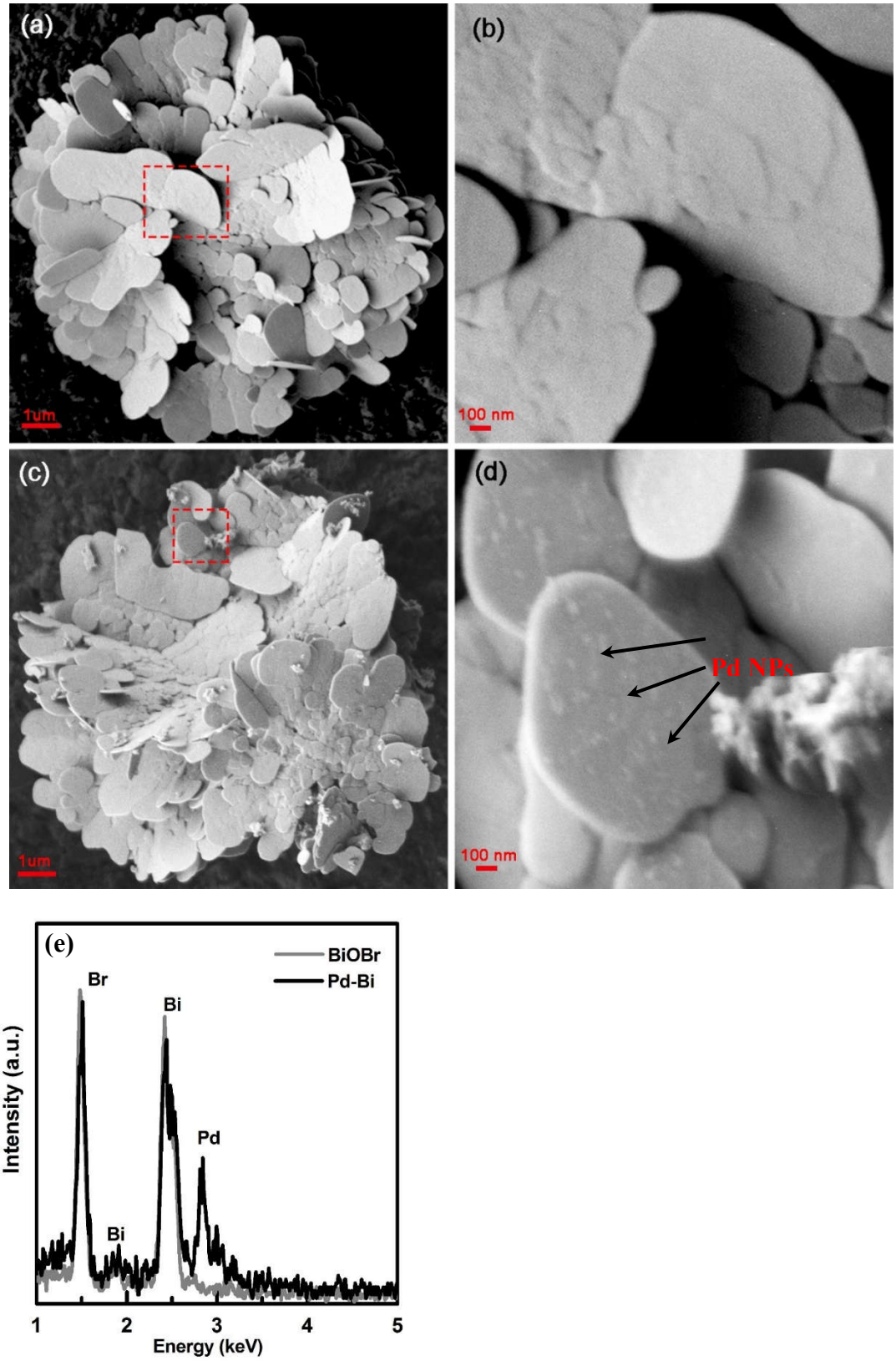


Figure 4.1 SEM photos of BiOBr at (a) low and (b) high magnification, 0.5 Pd-Bi at (c) low and (d) high magnification, and EDS spectra for pure BiOBr and 0.5 Pd-Bi.

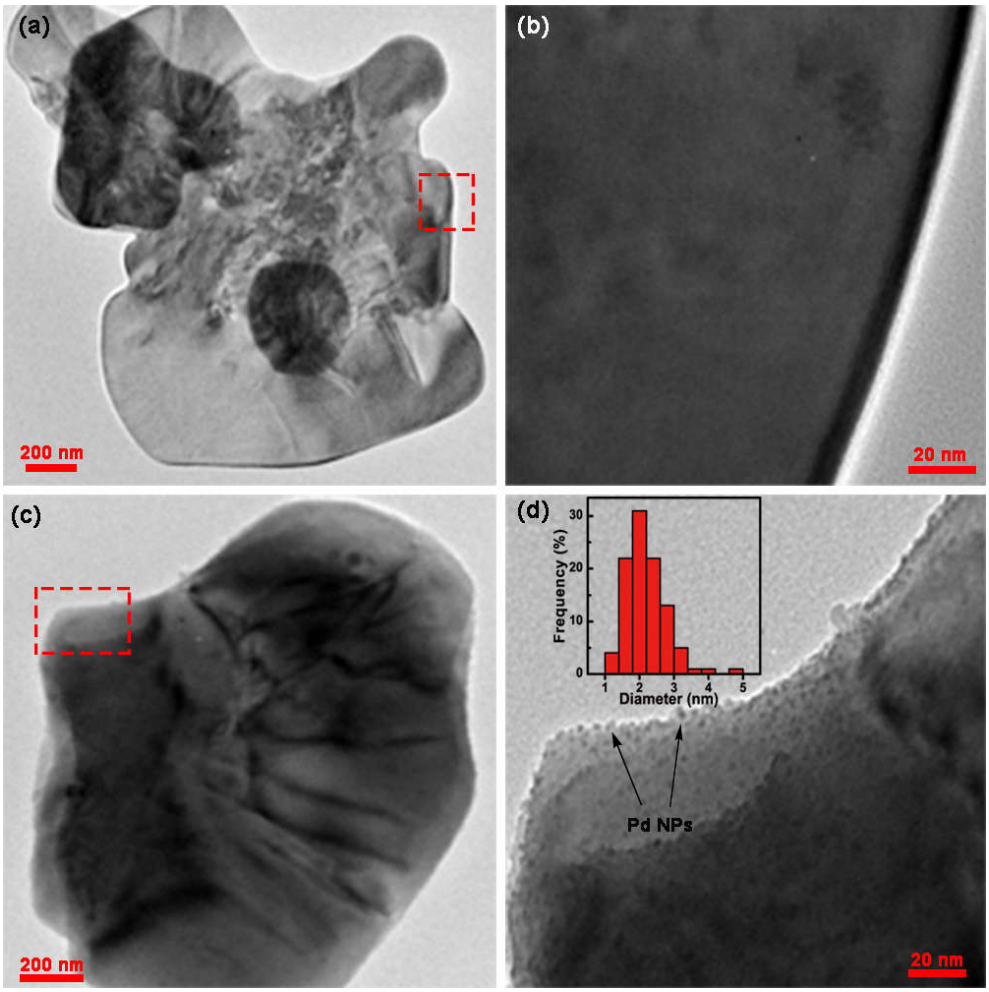


Figure 4.2 TEM images of BiOBr at (a) low and (b) high magnification, and 0.5 Pd-Bi at (c) low and (d) high magnification; Inset of (d): size distribution of Pd nanoparticles on the surface.

4.3.2 Crystal structure and surface chemical states

To further confirm the crystal structures and compositions of prepared samples, XRD patterns as well as XPS were employed. The diffraction patterns of pure BiOBr agree well with the tetragonal BiOBr crystal structure (space group: P4/nmm (129), a = b = 3.92335 Å, c = 8.1052 Å, PDF card number: 78-0348 [35]). Typically, major peaks at 2θ of 10.9°, 25.2°, 31.7°, 32.4°, 46.2° and 57.2° match well with the (001), (101), (102), (110), (200) and (212) crystal planes of BiOBr, respectively. No impurity peaks were observed in XRD patterns for pure BiOBr. In addition, the sharp peaks with widths indicate high crystallinities of as-prepared BiOBr samples. With the introduction of palladium on the

surface of BiOBr at mass percentages from 0.1% to 0.8%, XRD patterns for the Pd-BiOBr composites exhibited negligible differences with those patterns for pure BiOBr. This implies that the main crystal structure of BiOBr was not influenced by the photoreduction process in which palladium was loaded. No apparent peaks for palladium composition were found, which may be due to the loading contents (0.1 – 0.8%) which are too low for detection. Moreover, lattice parameters for pure BiOBr as well as those of Pd-BiOBr composites were obtained from the XRD patterns and are summarized in Table 4.1. It may be concluded that the differences of lattice parameters between pure BiOBr and Pd-BiOBr composites are less than ±0.05%. This further confirms that loading of palladium may not destroy the main crystal structure of the support, and that palladium NPs simply rest on the surface as opposed to covalently anchoring to the lattice [14].

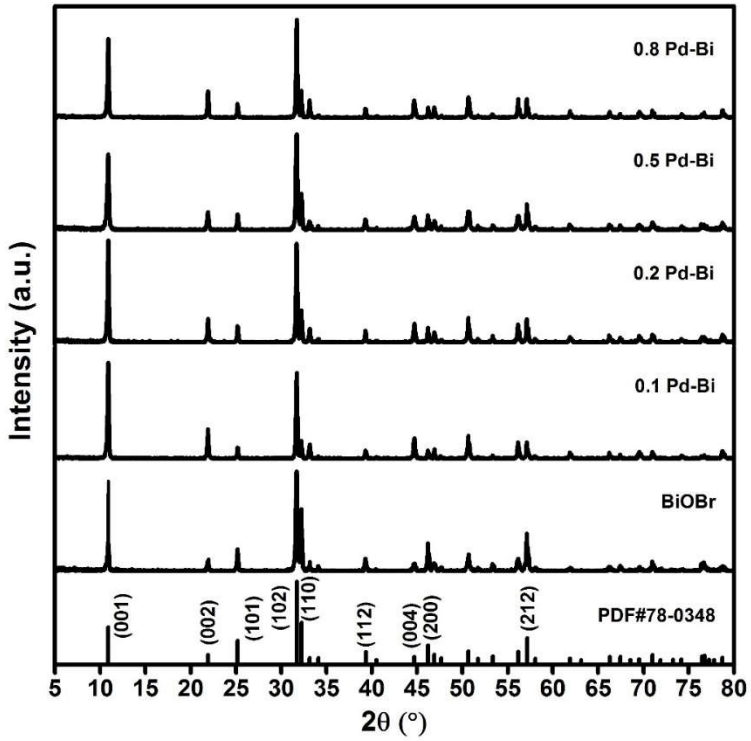


Figure 4.3 XRD patterns for pure BiOBr and Pd-BiOBr composites.

Table 4.1 Lattice parameters for prepared samples including pure BiOBr and Pd-BiOBr composites.

Samples	a = b (Å)	C (Å)
BiOBr	3.92 (0%)	8.10 (0%)
0.1 Pd-Bi	3.92 (+0.041%)	8.10 (-0.014%)
0.2 Pd-Bi	3.92 (+0.028%)	8.10 (-0.008%)
0.5 Pd-Bi	3.92 (+0.008%)	8.10 (-0.017%)
0.8 Pd-Bi	3.92 (+0.020%)	8.10 (+0.006%)

Surface chemical states were investigated using XPS for pure BiOBr and Pd-BiOBr composites. The survey XPS spectra as well as high-resolution Pd 3d orbital scans are depicted in Fig. 4.4 and 4.5, respectively. All spectra were calibrated with C *1s*, the binding energy of which is fixed at 284.6 eV. In the survey spectrum for pure BiOBr, All component elements including Bi, O and Br were detected and identified in Fig. 4.4. No impurities were found, indicating a high purity of as-prepared BiOBr samples. In addition to the composition detected in BiOBr, peaks for palladium were also detected in 0.5 Pd-Bi at binding energies of around 1160.8, 564.8, 342.8 eV as shown in Fig. 4.4. Possible orbits for palladium are also indexed in Fig. 4.4. To further explore the chemical states of palladium, high-resolution XPS orbital scans for characteristic peaks of Pd *3d* were also detected and depicted in Fig. 4.5. A set of spin-orbit doublets was found in the Pd *3d* XPS spectrum. Binding energies at 337.7 and 342.7 eV for Pd $3d_{5/2}$ and Pd $3d_{3/2}$ may be attributed to metallic palladium (Pd^0) species [36]. No Pd^{2+} species were detected, suggesting all of the Pd^{2+} ions were photoreduced to Pd NPs.

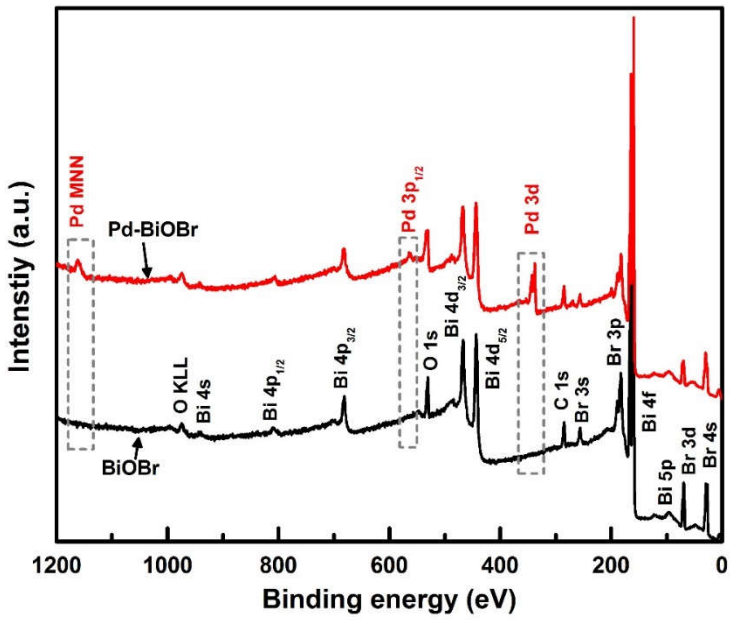


Figure 4.4 Survey spectra for pure BiOBr and 0.5 Pd-Bi samples.

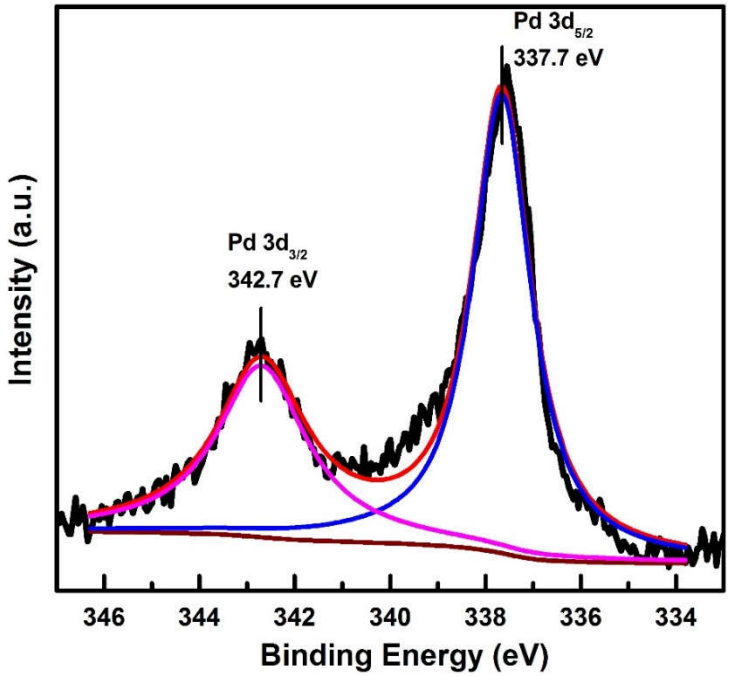


Figure 4.5 High-resolution XPS orbital scan for Pd 3d orbits of 0.5 Pd-Bi sample.

4.3.3 Possible formation process

The possible formation process of Pd-BiOBr composites is proposed and schemed in Fig. 4.6. For crystals of BiOBr, a 'sandwich' layer structure is composed of the tetragonal

[Bi_2O_2] structure on the surface and two bromine slabs on the inside. Different layers are stacked together via van der Waals forces as opposed to bonding interactions. The laminar atomic structure of BiOBr was also reported elsewhere [37]. The flat-band potentials of BiOBr may be calculated by applying the Mulliken electronegativity theory for atoms as follows (equation 2 and 3) [8, 38],

$$E_{CB} = \chi_p - E^e - \frac{1}{2}E_g \qquad \textbf{Equation 2}$$

$$E_{VB} = E_{CB} + E_g \qquad \textbf{Equation 3}$$

where E_{CB} and E_{VB} are the bottom position of the conduction band and the top position of the valence band respectively; χ_p represents the electronegativity which can be estimated by the geometric mean of the electronegativity of the constituent atoms [39-41]; E^e is the energy of free electrons on the hydrogen scale (~ 4.5eV) and E_g is the band gap value. The calculated results for BiOBr are summarized in Table 4.2. The redox potential of Pd^{2+}/Pd^0 is 0.915 V [42]. The conduction band potential for BiOBr is calculated as 0.225 eV, which is lower than the redox potential of Pd^{2+}/Pd^0. This suggests that the photogenerated electrons on the conduction band of BiOBr are capable of reducing Pd^{2+} to Pd^0 via the photoreduction method.

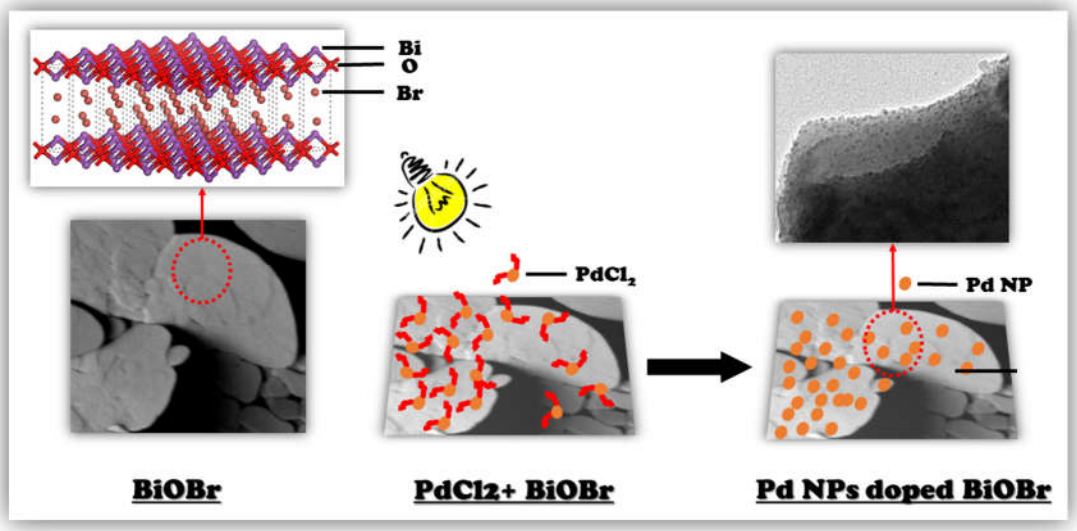


Figure 4.6 Possible formation process of Pd NP-decorated BiOBr composites.

Table 4.2 Band gap and flat-band edge position of BiOBr.

Composites	E_g/eV	χ_p/eV	E^e/eV	E_{CB} *vs* NHE[a]/eV	E_{VB} *vs* NHE[a]/eV
BiOBr	2.89	6.17	4.50	0.225	3.115

a. NHE: Normal Hydrogen Electrode

4.3.4 Optical properties

As one of the most important properties for photocatalysts, optical properties of as-prepared samples were studied by UV-Vis DRS as well as by theoretical calculations based on the DFT method. Flat-band structure and total/partial densities of states for BiOBr were calculated, the results of which are illustrated in Fig. 4.7. The top of the valence band is fixed at 0 eV. The band gap of BiOBr may be obtained from the band structure, which is approximately 2.41 eV. This narrow band gap indicates irradiation with a wavelength below 514.5 nm is capable of activating the photocatalyst in the presence of BiOBr. It may also be seen that BiOBr is an indirect-type semiconductor. The valence band of BiOBr is composed of not only O *2p* orbits but also of Br *4p* and Bi *6s* orbits. The well-dispersed valence bands for bismuth-based photocatalysts can facilitate the transfer of charge carriers [8]. It should also be noted that the relation between the velocity of an electron (v) and the energy of that electron (E) can be expressed as in Equation 4.

$$v = \frac{\Delta_\kappa E(\kappa)}{} \qquad \textit{Equation 4}$$

This means that the flatter the energy band is, the more localized the charge carriers will be [43]. For pure BiOBr, the mobilities of electrons and holes should be low as the band for BiOBr is quite flat, and the efficiency of separation of charge carriers may correspondingly be reduced. Inevitably, even for a 'perfect' bulk BiOBr, its photocatalytic activity may be potentially improved by an increase in separation efficiency.

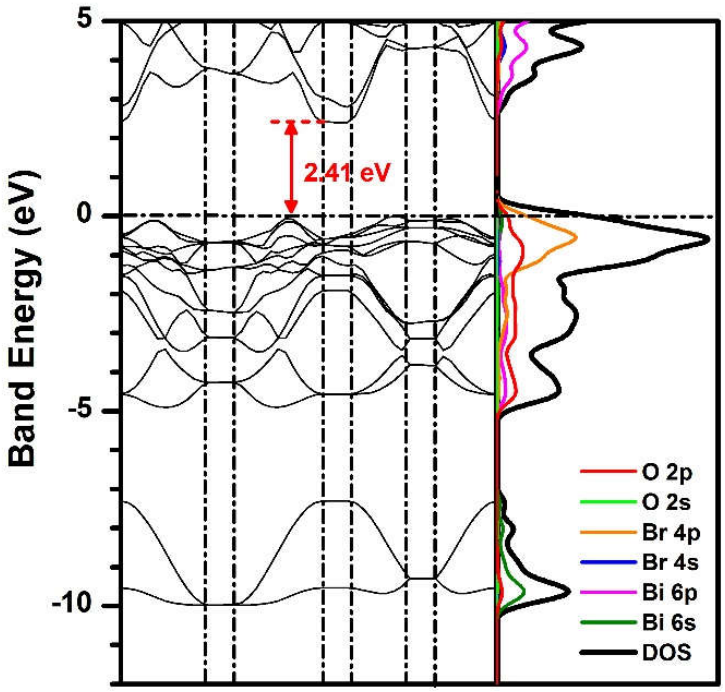


Figure 4.7 Flat-band structure as well as total/partial density of states calculated for pure BiOBr (the top of valence band is fixed at 0 eV).

For as-prepared samples, UV-Vis DRS in the range of 220 – 680 nm are employed, the results of which are illustrated in Fig. 4.8. It can be observed that high absorptive intensities in the UV region and steep decreases in absorbance intensity with an increase in irradiation wavelength for all spectra are shown in Fig. 4.8. The band gap absorption edges for all samples are at approximately 430 nm. The band gap value may be calculated as approximately 2.89 eV, which is higher than what was theoretically calculated (2.41 eV). This phenomenon may be due to the well-known limitations of GGA [44, 45]. A negligible red shift in the band gap edge further confirms that no ions were doped in the lattices of BiOBr. Notably, the absorbance intensity in the visible light region was significantly improved with the decoration of palladium NPs. Furthermore, as the loading amount of palladium was increased from 0.1 to 0.8%, this improvement also gradually increased. This enhancement may be a result of the SPR effect of Pd NPs deposited on the surface [46], and this effect may be improved by increasing the amount Pd NPs.

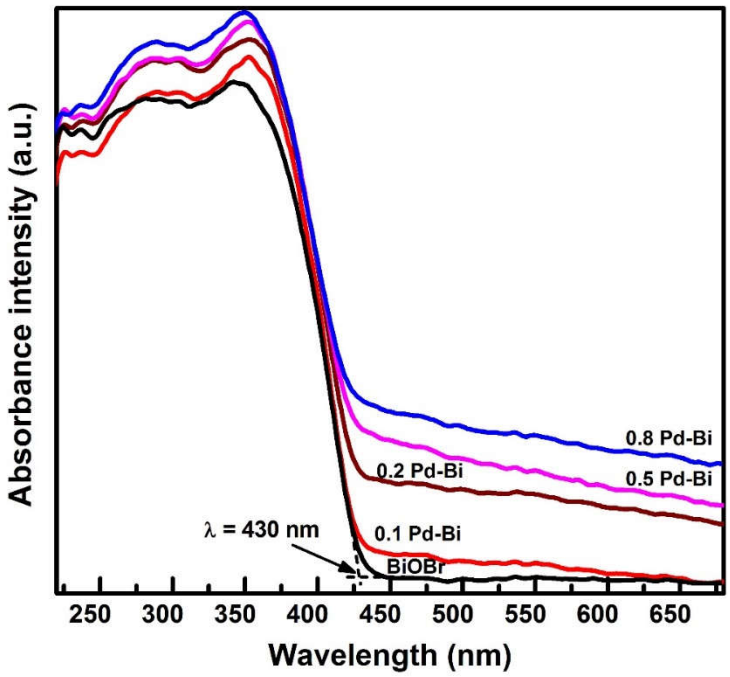


Figure 4.8 UV-Vis diffused reflectance spectra (DRS) for pure BiOBr and Pd-BiOBr composites.

4.3.5 Adsorption properties

Adsorption of phenol on the prepared photocatalysts is significant, which is the first step for photocatalytic process. Phenol is dissociated into phenolate and H^+. The p*Ka* value of phenol is 9.89 at 298K [47]. The ionic ratio ($\Phi_{phenolate}$) of phenolate and anionic ions can be calculated by Equation 5 [48]:

$$\Phi_{phenolate} = \left[1 + 10^{(\mathrm{p}Ka - \mathrm{pH})}\right]^{-1} \qquad \textit{Equation 5}$$

In the photocatalytic activity testing, initial concentration of phenol was 10 mg/L, pH of which was measured as 5.86. The ionic ratio, using Equation 5, was calculated as about 8.13×10^{-5}. It suggests that only the phenol molecules are effectively adsorbed onto the adsorbents through van der Waals interaction. The point of zero charge of the adsorbent surface, namely, PZC, was measured and shown in Fig. 4.9. For BiOBr and 0.5 Pd-Bi, PZC was 4.34 and 4.56, respectively. It should be noted, at a solution pH larger than PZC, the net charge on the surface is negative. This indicates both BiOBr and 0.5 Pd-Bi surfaces were negatively charged. However, only phenol molecules may be adsorbed on the

adsorbent, which limits the adsorption capacity of phenol on the surface of BiOBr and 0.5 Pd-Bi. Only 0.24% and 0.65% of phenol were adsorbed on BiOBr and 0.5 Pd-Bi, respectively, over 60 min in dark as shown in Fig. 4.11a.

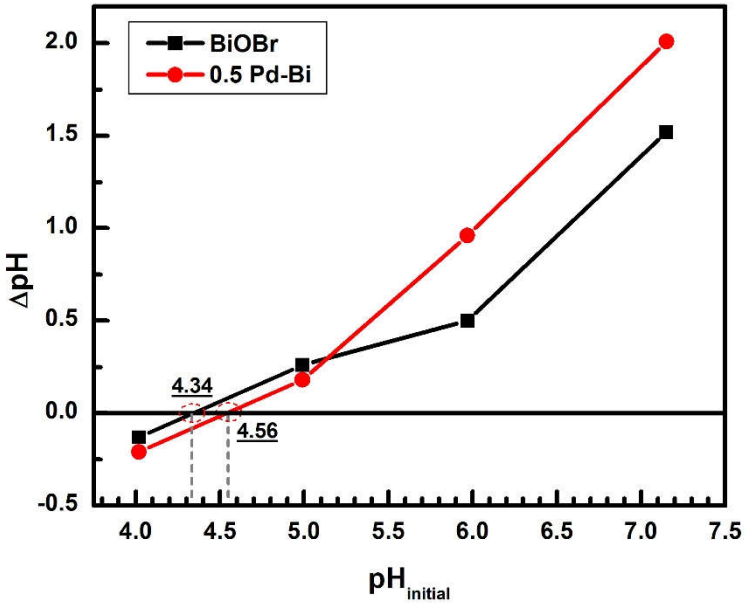


Figure 4.9* pH_{pzc} *plot of BiOBr and 0.5 Pd-Bi samples.

N_2 sorption isotherms were measured at 77K, and results were depicted in Fig. 4.10 for pure BiOBr and 0.5 Pd-Bi composites. Both isotherms fall into Types II and IV, according to the IUPAC classification [49, 50]. For type II isotherm, it may be resulted from unrestricted monolayer-multilayer adsorption up to high p/p^0 [51]. And the adsorbent was nonporous or macroporous. For type IV isotherm, it further confirms both materials were mesoporous material. However, the final saturation plateau was not observed for each isotherm, which is typical for type IV isotherm. This may be due to the capillary condensation does not occur in adsorption on the surface of macropores, resulting in a rapid increase in isotherm as type II isotherms. H3 adsorption-desorption hysteresis loops were also observed for both isotherms. This type loop may be due to the plate-like particles formed slit-shaped pores. This phenomenon agrees well with the morphologies as observed in the SEM images [49, 52, 53]. The mesopores may correspond to the voids between crystals within the two-dimensional layers and interspaces between these stacked layers. Quantitively, the specific surface area, pore volume and average pore size were calculated and summarized in Table 4.3. The specific surface area for BiOBr is as low as 3.3 m^2/g,

pore volume is 0.015 cm^3/g, and the average pore size is 19.8 nm. With deposition of palladium nanoparticles on the surface, all these three parameters are reduced. This may be due to the palladium nanoparticles may block the slit-shaped pores. The decrease in the specific area after loading Pd on the surface of BiOBr may result in the decrease in the adsorption capacity of pollutants on the adsorbents. However, the pretty low specific surface area for pure BiOBr may determine the influence is negligible.

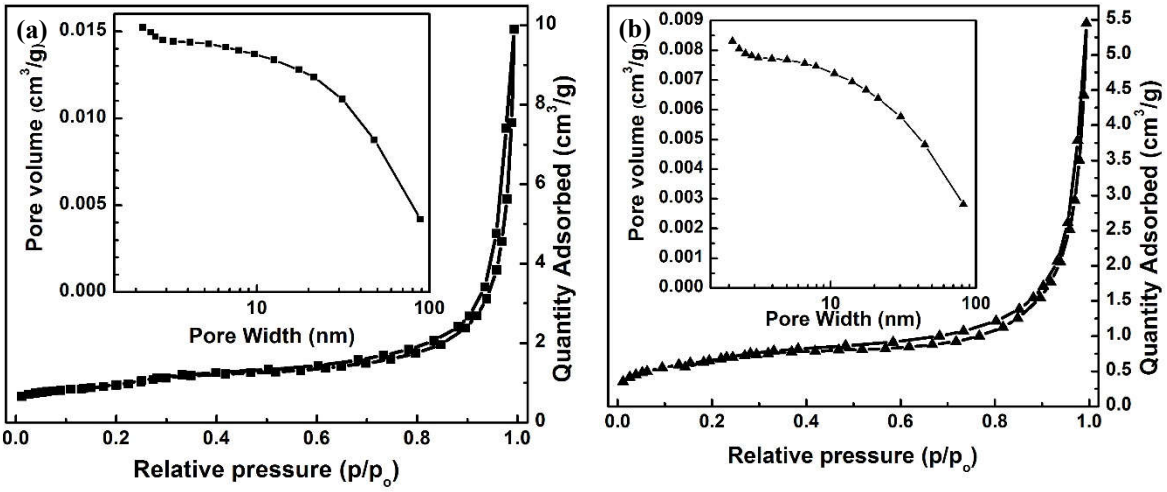


Figure 4.10 N_2 sorption isotherms and pore size distributions for (a) BiOBr and (b) 0.5 Pd-Bi, respectively.

Table 4.3 Specific surface area, pore volume, and average pore size of BiOBr and 0.5 Pd-Bi composites.

Sample	S_{BET} (m^2/g)	Pore volume (cm^3/g)	Average pore size (nm)
BiOBr	3.3	0.015	19.8
0.5 Pd-Bi	2.4	0.008	17.0

4.3.6 Photocatalytic activity tests

The photocatalytic activities of as-prepared samples were studied with regards to a target colourless organic molecule, phenol, under visible light irradiation. Relative concentrations of phenol as a function of time in the presence of as-prepared samples are illustrated in Fig.

4.11a. It was observed that the adsorption capacity for phenol on all samples was negligible. Upon initiating irradiation, the concentration of phenol was observed to immediately decrease, the degree to which is dependent on the composition of the loaded photocatalyst. Specifically, for pure BiOBr, the photocatalytic efficiency of phenol removal was determined to be approximately 67% over 300 min. With decomposition by palladium on the surface of BiOBr, the photocatalytic activity in the removal of phenol was greatly improved. When the palladium content was increased from 0.1% to 0.5%, the photocatalytic efficiency for phenol removal increased from 77% to 100% over 300 min under visible light irradiation. This improvement may be attributed to the following possibilities: 1) the visible light photon harvesting capacity increased with loading quantity of Pd NPs on the surface of BiOBr, and the improvement is a direct result of the SPR effect; 2) Surface-loaded Pd NPs facilitate the separation of photogenerated charger carriers.

Upon further increase of the loading quantity of palladium, the photocatalytic degradation of phenol decreased as shown in Fig. 4.11a. This phenomenon may be attributed to an excess of Pd NPs on the surface which may be regarded as excellent recombination sites for photogenerated electrons and holes [29]. As a result, the increased recombination rate of e^-/h^+ pairs may decrease the photocatalytic activity with respect to the removal of organics. Furthermore, excess Pd NPs on the surface may reduce the number of exposure sites for BiOBr and correspondingly decrease the amount of photogenerated charge carriers.

The concentration of phenol was investigated. Chromatograms of samples taken during the photocatalysis process in the presence of 0.5 Pd-Bi composites under visible light irradiation are shown in Fig. 4.11b. It can be found phenol were removed step-by-step in 240 min, and intermediates, mainly the benzoquinone, hydroquinone as well as catechol [29], were also generated. To obtain a complete mineralization, more time may be required for the photocatalytic treatment.

The Langmuir-Hinshelwood (L-H) model can be applied to describe theses photocatalytic processes as shown in Equation 6. The initial concentration of phenol in this work was 10 mg/L (~ 1×10^{-4} M). The $1 + Kc$ term may be assumed to equal to 1, and so Equation 6 can be simplified to Equation 7. Integration of Equation 7 with respect to concentration from c_o to c_t at time between zero and t, can then produce Equation 8.

$$r = -\frac{dc}{dt} = k\theta = \frac{kKc}{1+Kc} \qquad \textbf{Equation 6}$$

$$-\frac{dc}{dt} = kKc = k'c \qquad \textbf{Equation 7}$$

$$\ln(\frac{c_o}{c_t}) = k't \qquad \textbf{Equation 8}$$

where r, c, t, k, θ, K, and k' represent reaction rate, concentration of phenol (c_o: initial concentration; c_t: concentration at time t), time, reaction rate constant, ratio of adsorbed phenol, adsorption constant and pseudo first-order reaction constant, respectively. By plotting $\ln(c_o/c_t)$ vs t, the pseudo first-order reaction constant (k') can be obtained as the slope from a linear regression with an intercept fixed at the origin. The kinetic constants for each process with respect to the photocatalytic degradation of phenol in the presence of different prepared photocatalysts are summarized in Table 4.4. The excellent linearity is demonstrated through values of R^2 almost equal to 1, indicating that these photocatalytic processes may be described by pseudo first-order kinetics. The photocatalytic kinetic constants are improved from 3.66×10^{-3} to 11.39×10^{-3} min^{-1} comparing processes in the presence of pure BiOBr with 0.5% Pd-BiOBr composites. When the loading content of palladium is further increased to 0.8%, the kinetic constant is slightly reduced. These results further confirm that there is an optimum loading quantity of palladium and that excess Pd may inhibit photocatalytic activity. Moreover, the photonic efficiency for the decomposition of phenol was determined using Equation 9 [54] as follows:

$$\zeta = \frac{V \times \Delta c}{J \times A \times \Delta t} \qquad \textbf{Equation 9}$$

where V, J, A, Δc and Δt represent volume of solution, flux of photons, illuminated area, change in concentration and change in time, respectively. The flux of incoming photons was calculated for the mean irradiation wavelength of 550 nm, which is approximately 2.39 kW/m^2. The volume of solution was 100 mL, and the illuminated area was approximately 0.0050 m^2. The average photonic efficiency for each process was calculated and is summarized in Table 4.4. Among them, the highest photonic efficiency observed was 0.557

μg/m^2/min with the 0.5% Pd-BiOBr composite, which is more than double of that which was observed with pure BiOBr. This further confirms that the loading quantity of palladium in the composite at 0.5% performs the most efficiently in the photocatalytic degradation of phenol.

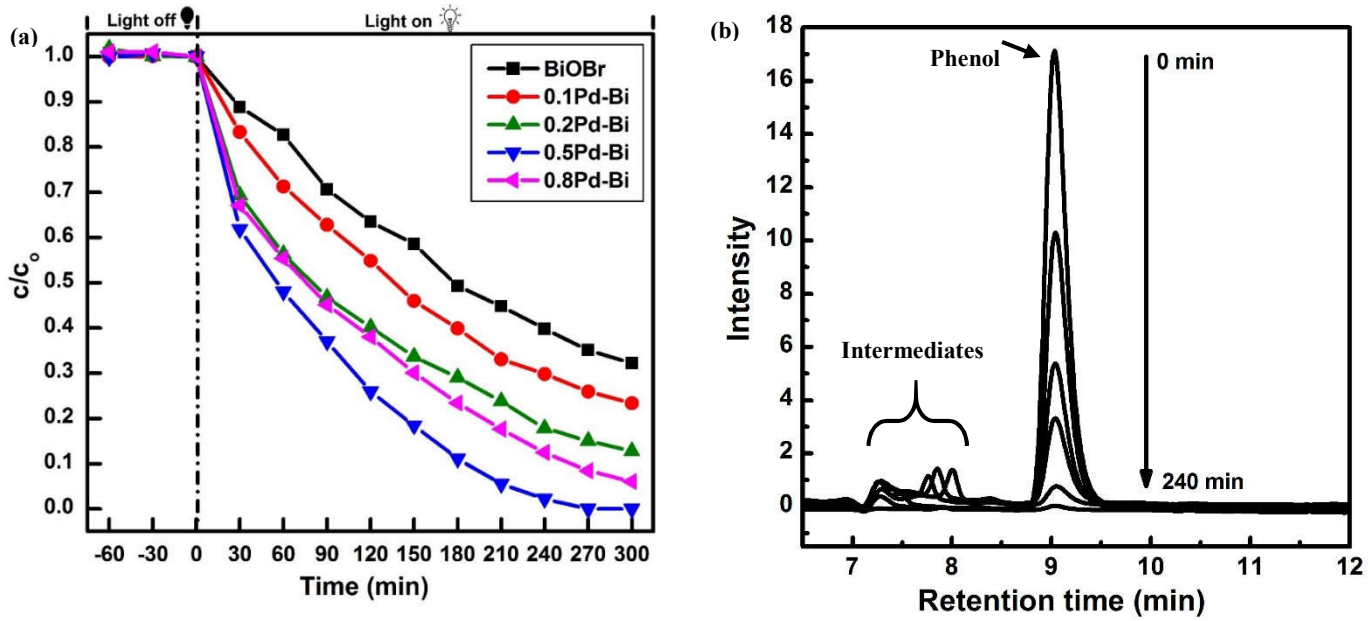


Figure 4.11 (a) Photocatalytic degradation of phenol in the presence of prepared samples under visible light irradiation (c_o = 10 mg/L; photocatalysts dosage amount = 1 g/L; T = 20°C); and (b) Chromatogram of the separation in a C18 column of phenol (t_R = 9.1 min). Samples taken from the suspension containing 0.5 Pd-Bi composites.

Table 4.4 Photocatalytic reaction kinetics constants and photonic efficiency for systems with pure BiOBr and BiOBr composites with different quantities of palladium.

Samples	BiOBr	0.1 Pd-Bi	0.2 Pd-Bi	0.5 Pd-Bi	0.8 Pd-Bi
k (x10^{-3} min^{-1})	3.66	5.17	7.81	11.39	8.39
R^2	0.997	0.998	0.985	0.996	0.988
ζ (μg W^{-1} min^{-1})	0.236	0.305	0.415	0.557	0.439

4.3.7 Photoluminescence spectra analysis

PL spectra were detected to evaluate the separation efficiency of photogenerated charge carriers. Specifically, photoluminescence may be resulted from the photons when photogenerated electrons and holes are recombined. The higher the PL intensity, the higher probability the photogenerated electron-holes pairs' recombination. PL spectra for BiOBr and Pd-Bi composites were depicted in Fig. 4.12. It can be found pure BiOBr exhibited the highest PL intensity in the spectrum, and with modification of palladium, the intensity was reduced, indicating the separation of charge carriers was improved. More specifically, the emission intensity for 0.5 Pd-Bi was the lower than that for 0.8 Pd-Bi. This phenomenon suggests over loading of palladium may increase the recombination probability of electron-holes pairs. It may be an explanation for the photocatalytic activity of 0.5 Pd-Bi was higher than that of 0.8 Pd-Bi.

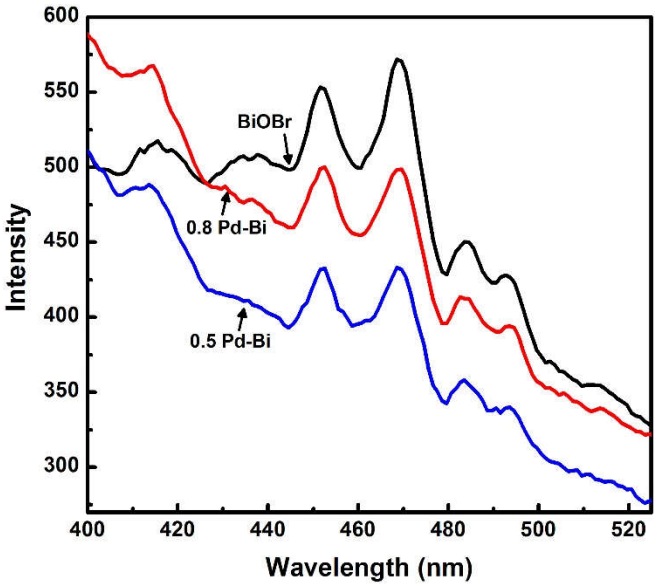


Figure 4.12 PL spectra of BiOBr, 0.5 Pd-Bi and 0.8 Pd-Bi composites (excitation wavelength = 300 nm).

4.3.8 Electrochemical properties

Electrochemical properties, especially the separation efficiency of photogenerated electrons and holes, were investigated via EIS. Fig. 4.13 illustrates the EIS Nyquist plots and photocurrent responses for pure BiOBr as well as for those of Pd-BiOBr composites coated on ITO under visible light irradiation. Only one semicircle was observed for each

curve shown in Fig. 4.13a, indicating that photocatalysis in the presence of as-prepared samples may be a simple electrode reaction. As shown in Fig. 4.13b, fast and uniform photocurrent responses were found for pure BiOBr and Pd-Bi electrodes, and the responses were completely reversible. Specifically, the photocurrent of Pd-Bi electrode was about five times higher than that of BiOBr electrode. The enhancement in photocurrent was attributed to the following reasons: improved separation of photogenerated charge carriers and enhancement of visible light absorbing capacity (SPR effect) after loading palladium nanoparticles on the surface. The radius of the arc on the EIS Nyquist plot reflects the reaction rate occurring at the surface of the electrode [55, 56]. Specifically, an EIS Nyquist plot with a small arc radius reveals a higher efficiency of separation photogenerated charge carriers. The equivalent circuit and the fitted electrical parameters for each process are summarised in Table 4.5. In the equivalent circuit, R_s is the resistance of the solution, R_{ct} is the resistance to electron transfer and CPE represents the constant phase element, which may be considered as a double-layered capacitor. R_{ct} can be determined by the arc radius, and directly reflects the efficiency of separation of photogenerated electron/hole pairs. For pure BiOBr, the resistance to electron transfer was found to be 657.2 kΩ, which is the highest among those of other samples. Upon introduction of palladium, this value decreased to 121.6, 54.3, 50.0, and 52.2 kΩ for composites with 0.1%, 0.2%, 0.5% and 0.8% Pd, respectively. The greatly improved rate of separation of charge carriers brought upon by increasing the Pd content from 0.1% to 0.5% suggests the deposition of palladium on the surface of BiOBr may greatly facilitate the separation of photogenerated electron/hole pairs. However, excess palladium on the surface may reduce the efficiency of separation of charge carriers and further influence the photocatalytic activity in the removal of phenol. Theoretically, the work function of palladium is 0.62 eV (vs. NHE, 5.12 eV in vacuum) [57], and the potential of electrons at the bottom of conduction band of BiOBr 0.225 eV (Table 4.2). This suggests electrons on the conduction band of BiOBr are capable of transferring to the palladium nanoparticles. This phenomenon is beneficial for the separation of photogenerated charge carriers. However, as a p-type semiconductor, the generated holes on the valence band of BiOBr are with high mobility, and are of tending to transfer to the palladium nanoparticles on the surface. With increase of the content of palladium in the Pd-Bi composites, palladium nanoparticles on the surface gradually

become an excellent recombination sites of photogenerated electrons and holes. The discussion above may be also applied to explain the photocatalytic activity of Pd-Bi deteriorate with loading excess of palladium. These results may serve as evidence to confirm that the introduction of palladium on the surface of BiOBr may accelerate the separation of photogenerated charge carriers so as to improve the photocatalytic activity in the removal of organic pollutants.

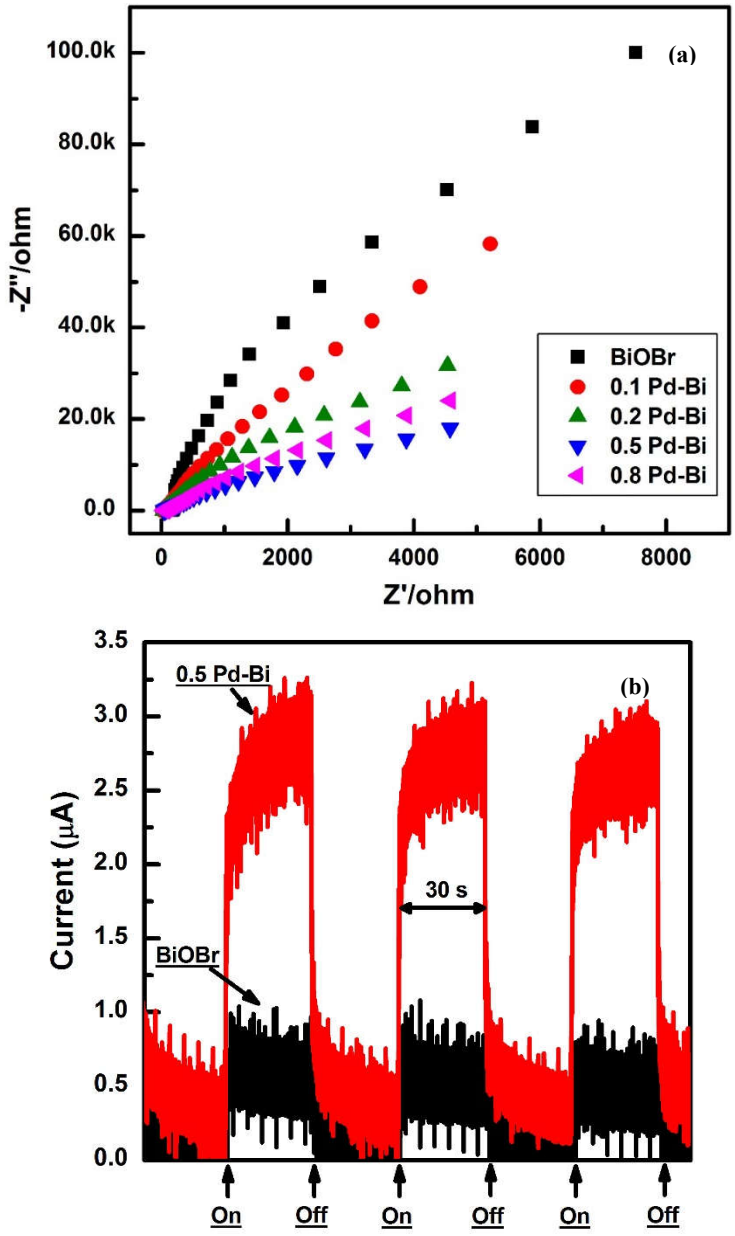
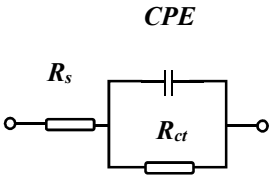


Figure 4.13 (a) EIS Nyquist plots and (b) transient photocurrent responses of the BiOBr and Pd-BiOBr electrodes.

Table 4.5 Fitting results for equivalent circuits of different prepared samples.

Samples	R_s (Ω)	R_{ct} (kΩ)	*CPE* (μf)	Equivalent circuits
BiOBr	175.4	657.2	39.7	
0.1 Pd-Bi	169.2	121.6	62.4	
0.2 Pd-Bi	165.5	54.3	73.2	
0.5 Pd-Bi	161.9	50.0	65.0	
0.8 Pd-Bi	165.7	52.2	66.1	

4.3.9 Proposed mechanism

The mechanism for charge separation by a Pd-BiOBr composite under visible light irradiation is schemed in Fig. 4.14. The band position potentials were calculated and are shown in Table 4.2. Under visible light irradiation, electrons on the valence band of BiOBr may be activated by irradiation with a wavelength below 430 nm. Activated electrons jump to the unoccupied conduction band with positive holes left on valence band. For pure BiOBr, photogenerated electrons and holes may be recombined as for theirs short life time. Otherwise, electrons on the conduction band and holes on the valence band may separately react with adsorbed species on the photocatalyst such as H_2O and O_2, producing oxidative species such as $\bullet O_2^-$ and $\bullet O_2H$. The high recombination rate of photogenerated electron/hole pairs hinders the improvement in photocatalytic activity. Via the introduction of palladium NPs on the surface of BiOBr, photogenerated electrons on the conduction band may be easily transferred to the Pd NPs. This kind of transfer may circumvent electron/hole recombination. Furthermore, surface deposited palladium NPs may be activated by visible light irradiation with a wavelength in the range of 410 to 870 nm, owing to the SPR effect, to generate extra electrons which may participate in photocatalytic reactions [30, 31]. The improvements in the efficiency of separation of charge carriers and in the visible light irradiation harvesting capacity contribute to an enhanced photocatalytic activity towards the removal of phenol under visible light irradiation.

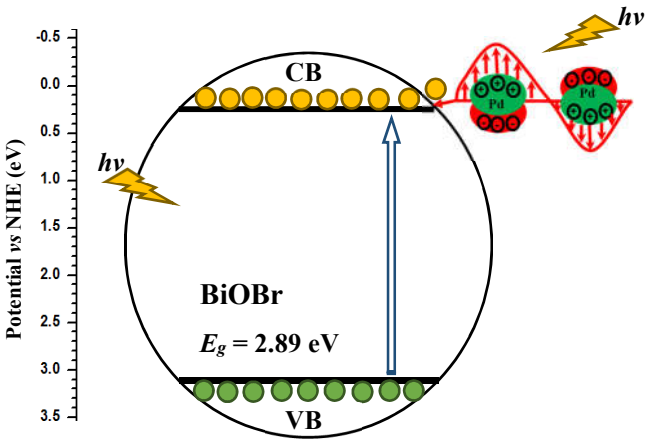


Figure 4.14 Schematic of charge separation for photocatalysis over Pd-BiOBr composite under visible light irradiation.

4.4 Conclusions

Palladium nanoparticles were successfully deposited on the surface of hydrothermally prepared BiOBr via a photoreduction method. Theoretically, photogenerated electrons on the conduction band of BiOBr are capable of reducing divalent palladium to metallic palladium. The photocatalytic activity with respect to the degradation of phenol was significantly improved via the incorporation of palladium nanoparticles with BiOBr under visible light irradiation. Specifically, when the loading quantity of palladium was 0.5 wt%, the Pd-modified BiOBr composite exhibited the highest phenol removal efficiency. The mechanism of the enhancement may be a result of the improvement in the visible light harvesting capacity due to the SPR effect as well as of the suppression of photogenerated charge carrier recombination. This work sheds light on the importance of surface metal nanoparticle deposited via photodeposition which may be used to improve the photocatalytic activity of the support.

References

1. Akira Fujishima and Kenichi Honda, "Electrochemical photolysis of water at a semiconductor electrode," *nature*, vol. 238, pp. 37-38, 1972.

2. Kazuhiko Maeda and Kazunari Domen, "Photocatalytic Water Splitting: Recent Progress and Future Challenges," *The Journal of Physical Chemistry Letters*, vol. 1, no. 18, pp.

2655-2661, 2010.

3. Francesco Montecchio, Don Chinungi, Roberto Lanza and Klas Engvall, "Surface treatments of metal supports for photocatalysis applications," *Applied Surface Science*, vol. 401, pp. 283-296, 2017.

4. Sheng Ye, Rong Wang, Ming-Zai Wu and Yu-Peng Yuan, "A review on g-C_3N_4 for photocatalytic water splitting and CO_2 reduction," *Applied Surface Science*, vol. 358, pp. 15-27, 2015.

5. Raquel Portela and María Dolores Hernández-Alonso, "Environmental Applications of Photocatalysis," in *Design of Advanced Photocatalytic Materials for Energy and Environmental Applications*, Ed., pp. 35-66, Springer, 2013.

6. Xiangchao Meng, Zisheng Zhang and Xingang Li, "Synergetic photoelectrocatalytic reactors for environmental remediation: A review," *Journal of Photochemistry and Photobiology C: Photochemistry Reviews*, vol. 24, pp. 83-101, 2015.

7. S. Girish Kumar and L. Gomathi Devi, "Review on Modified TiO_2 Photocatalysis under UV/Visible Light: Selected Results and Related Mechanisms on Interfacial Charge Carrier Transfer Dynamics," *The Journal of Physical Chemistry A*, vol. 115, no. 46, pp. 13211-13241, 2011.

8. Xiangchao Meng and Zisheng Zhang, "Bismuth-based Photocatalytic Semiconductors: Introduction, Challenges and Possible Approaches," *Journal of Molecular Catalysis A: Chemical*, vol. 423, pp. 533-549, 2016.

9. R. Asahi, T. Morikawa, T. Ohwaki, K. Aoki and Y. Taga, "Visible-Light Photocatalysis in Nitrogen-Doped Titanium Oxides," *Science*, vol. 293, no. 5528, pp. 269-271, 2001.

10. Xiaoyue Hu, Xiangchao Meng and Zisheng Zhang, "Synthesis and Characterization of Graphene Oxide-Modified Bi_2WO_6 and Its Use as Photocatalyst," *International Journal of Photoenergy*, vol. 2016, pp. 8, 2016.

11. Xiangchao Meng, Lingyun Jiang, Weiwen Wang and Zisheng Zhang, "Enhanced Photocatalytic Activity of BiOBr/ZnO Heterojunction Semiconductors Prepared by Facile Hydrothermal Method," *International Journal of Photoenergy*, vol. 2015, pp. 9, 2015.

12. Xiangchao Meng and Zisheng Zhang, "Synthesis, Analysis, and Testing of BiOBr-Bi_2WO_6 Photocatalytic Heterojunction Semiconductors," *International Journal of Photoenergy*, vol. 2015, pp. 12, 2015.

13. Xiangchao Meng and Zisheng Zhang, "Ag/AgCl Loaded Bi_2WO_6 Composite: A Plasmonic Z-Scheme Visible Light-Responsive Photocatalyst," *International Journal of Photoenergy*, vol. 2016, pp. 11, 2016.

14. Xiangchao Meng and Zisheng Zhang, "Plasmonic ternary Ag–rGO–Bi_2MoO_6 composites with enhanced visible light-driven photocatalytic activity," *Journal of Catalysis*, vol. 344, pp. 616-630, 2016.

15. Xiangchao Meng and Zisheng Zhang, "Synthesis and characterization of plasmonic and magnetically separable Ag/AgCl-Bi_2WO_6@ Fe_3O_4@SiO_2 core-shell composites for visible light-induced water detoxification," *Journal of Colloid and Interface Science*, vol. 485, pp. 296-307, 2017.

16. Xiangchao Meng and Zisheng Zhang, "Facile synthesis of BiOBr/Bi_2WO_6 heterojunction semiconductors with high visible-light-driven photocatalytic activity," *Journal of Photochemistry and Photobiology A: Chemistry*, vol. 310, no. 0, pp. 33-44, 2015.

17. Rong'an He, Shaowen Cao, Peng Zhou and Jiaguo Yu, "Recent advances in visible light Bi-based photocatalysts," *Chinese Journal of Catalysis*, vol. 35, no. 7, pp. 989-1007, 2014.

18. Rong-An He, Shao-Wen Cao and Jia-Guo Yu, "Recent Advances in Morphology Control and Surface Modification of Bi-Based Photocatalysts," *Acta Physico-Chimica Sinica*, vol. 32, no. 12, pp. 2841-2870, 2016.

19. Rui Li, Xiaoya Gao, Caimei Fan, Xiaochao Zhang, Yawen Wang and Yunfang Wang, "A facile approach for the tunable fabrication of BiOBr photocatalysts with high activity and stability," *Applied Surface Science*, vol. 355, pp. 1075-1082.

20. Yang Zhao, Xiang Huang, Xin Tan, Tao Yu, Xiangli Li, Libin Yang and Shucong Wang, "Fabrication of BiOBr nanosheets@TiO_2 nanobelts p–n junction photocatalysts for enhanced visible-light activity," *Applied Surface Science*, vol. 365, pp. 209-217, 2016.

21. Xuejun Zou, Yuying Dong, Xiaodong Zhang, Yubo Cui, Xiaoxia Ou and Xiaohui Qi, "The highly enhanced visible light photocatalytic degradation of gaseous o-

dichlorobenzene through fabricating like-flowers BiPO4/BiOBr p-n heterojunction composites," *Applied Surface Science*, vol. 391, pp. 525-534, 2017.

22. Shengyao Wang, Xianglong Yang, Xuehao Zhang, Xing Ding, Zixin Yang, Ke Dai and Hao Chen, "A plate-on-plate sandwiched Z-scheme heterojunction photocatalyst: BiOBr-Bi_2MoO_6 with enhanced photocatalytic performance," *Applied Surface Science*, vol. 391, pp. 194-201, 2017.

23. Xue Yu, Junjie Shi, Lijuan Feng, Chunhu Li and Liang Wang, "A three-dimensional BiOBr/RGO heterostructural aerogel with enhanced and selective photocatalytic properties under visible light," *Applied Surface Science*, vol. 396, pp. 1775-1782, 2017.

24. Xiaowei Li, Li Wang, Lei Zhang and Shuping Zhuo, "A facile route to the synthesis of magnetically separable BiOBr/$NiFe_2O_4$ composites with enhanced photocatalytic performance," *Applied Surface Science*, vol. 419, pp. 586-594, 2017.

25. Kasper Wenderich and Guido Mul, "Methods, Mechanism, and Applications of Photodeposition in Photocatalysis: A Review," *Chemical Reviews*, 2016.

26. Lufeng Lu, Liang Kong, Zheng Jiang, Henry H.-C. Lai, Tiancun Xiao and Peter P. Edwards, "Visible-Light-Driven Photodegradation of Rhodamine B on Ag-Modified BiOBr," *Catalysis Letters*, vol. 142, no. 6, pp. 771-778, 2012.

27. J. Di, J. X. Xia, S. Yin, H. Xu, L. Xu, Y. G. Xu, M. Q. He, H. M. Li and J. G. Wang, "Reactable ionic liquid assisted synthesis of Pd modified BiOBr flower-like microsphere with high dispersion and their enhanced photocatalytic performances," *Materials Technology*, vol. 30, no. 2, pp. 113-121, 2015.

28. Changlin Yu, Fangfang Cao, Gao Li, Rongfu Wei, Jimmy C. Yu, Rongchao Jin, Qizhe Fan and Chunying Wang, "Novel noble metal (Rh, Pd, Pt)/BiOX(Cl, Br, I) composite photocatalysts with enhanced photocatalytic performance in dye degradation," *Separation and Purification Technology*, vol. 120, pp. 110-122, 2013.

29. Xiangchao Meng and Zisheng Zhang, "Pd-doped Bi_2MoO_6 Plasmonic Photocatalysts with Enhanced Visible Light Photocatalytic Performance," *Applied Surface Science*, vol. 392, pp. 169-180, 2016.

30. Yujie Xiong, Benjamin Wiley, Jingyi Chen, Zhi-Yuan Li, Yadong Yin and Younan Xia,

"Corrosion-Based Synthesis of Single-Crystal Pd Nanoboxes and Nanocages and Their Surface Plasmon Properties," *Angewandte Chemie International Edition*, vol. 44, no. 48, pp. 7913-7917, 2005.

31. Yujie Xiong, Jingyi Chen, Benjamin Wiley, Younan Xia, Yadong Yin and Zhi-Yuan Li, "Size-Dependence of Surface Plasmon Resonance and Oxidation for Pd Nanocubes Synthesized via a Seed Etching Process," *Nano Letters*, vol. 5, no. 7, pp. 1237-1242, 2005.

32. Danjun Wang, Huidong Shen, Li Guo, Chan Wang and Feng Fu, "Porous BiOBr/Bi_2MoO_6 Heterostructures for Highly Selective Adsorption of Methylene Blue," *ACS Omega*, vol. 1, no. 4, pp. 566-577, 2016.

33. Walter Kohn and Lu Jeu Sham, "Self-consistent equations including exchange and correlation effects," *Physical Review*, vol. 140, no. 4A, pp. A1133, 1965.

34. Giannozzi Paolo, Baroni Stefano, Bonini Nicola, Calandra Matteo, Car Roberto, Cavazzoni Carlo, Ceresoli Davide, L. Chiarotti Guido, Cococcioni Matteo, Dabo Ismaila, Corso Andrea Dal, Gironcoli Stefano de, Fabris Stefano, Fratesi Guido, Gebauer Ralph, Gerstmann Uwe, Gougoussis Christos, Kokalj Anton, Lazzeri Michele, Martin-Samos Layla, Marzari Nicola, Mauri Francesco, Mazzarello Riccardo, Paolini Stefano, Pasquarello Alfredo, Paulatto Lorenzo, Sbraccia Carlo, Scandolo Sandro, Sclauzero Gabriele, P. Seitsonen Ari, Smogunov Alexander, Umari Paolo and M. Wentzcovitch Renata, "QUANTUM ESPRESSO: a modular and open-source software project for quantum simulations of materials," *Journal of Physics: Condensed Matter*, vol. 21, no. 39, pp. 395502, 2009.

35. J. Ketterer and V. Kramer, "Structure refinement of bismuth oxide bromide, BiOBr," *Acta Crystallographica Section C*, vol. 42, no. 8, pp. 1098-1099, 1986.

36. Ali R. Siamaki, Abd El Rahman S. Khder, Victor Abdelsayed, M. Samy El-Shall and B. Frank Gupton, "Microwave-assisted synthesis of palladium nanoparticles supported on graphene: A highly active and recyclable catalyst for carbon–carbon cross-coupling reactions," *Journal of Catalysis*, vol. 279, no. 1, pp. 1-11, 2011.

37. Da Zhang, Jing Li, Qigang Wang and Qingsheng Wu, "High {001} facets dominated BiOBr lamellas: facile hydrolysis preparation and selective visible-light photocatalytic

activity," *Journal of Materials Chemistry A*, vol. 1, no. 30, pp. 8622-8629, 2013.

38. Yong Xu and Martin A.A. Schoonen, "The absolute energy positions of conduction and valence bands of selected semiconducting minerals," *American Mineralogist*, vol. 85, no. 3-4, pp. 543-556, 2000.

39. Robert Thomas Sanderson, *Chemical periodicity*, Reinhold, New York, US, 1961.

40. Robert S. Mulliken, "A New Electroaffinity Scale; Together with Data on Valence States and on Valence Ionization Potentials and Electron Affinities," *The Journal of Chemical Physics*, vol. 2, no. 11, pp. 782-793, 1934.

41. Robert S. Mulliken, "Electronic Structures of Molecules XI. Electroaffinity, Molecular Orbitals and Dipole Moments," *The Journal of Chemical Physics*, vol. 3, no. 9, pp. 573-585, 1935.

42. Allen J Bard and Larry R Faulkner, "Fundamentals and applications," *Electrochemical Methods, 2nd ed.; Wiley: New York*, 2001.

43. Honglin Li, Ke Yu, Xiang Lei, Bangjun Guo, Hao Fu and Ziqiang Zhu, "Hydrothermal Synthesis of Novel $MoS_2/BiVO_4$ Hetero-Nanoflowers with Enhanced Photocatalytic Activity and a Mechanism Investigation," *The Journal of Physical Chemistry C*, vol. 119, no. 39, pp. 22681-22689, 2015.

44. Kangrong Lai, Wei Wei, Ying Dai, Ruiqin Zhang and Baibiao Huang, "DFT calculations on structural and electronic properties of Bi_2MO_6 (M = Cr, Mo, W)," *Rare Metals*, vol. 30, no. 1, pp. 166-172, 2011.

45. Yanhua Li, Congzhong Cai, Yonghong Gu, Wende Cheng, Wen Xiong and Chengjun Zhao, "Novel electronic properties of a new MoS_2/TiO_2 heterostructure and potential applications in solar cells and photocatalysis," *Applied Surface Science*, vol. 414, pp. 34-40, 2017.

46. Suljo Linic, Phillip Christopher and David B. Ingram, "Plasmonic-metal nanostructures for efficient conversion of solar to chemical energy," *Nature Materials*, vol. 10, no. 12, pp. 911-921, 2011.

47. Ulker Beker, Batchimeg Ganbold, Halil Dertli and Dilek Duranoğlu Gülbayir,

"Adsorption of phenol by activated carbon: Influence of activation methods and solution pH," *Energy Conversion and Management*, vol. 51, no. 2, pp. 235-240, 2010.

48. José C. Lazo-Cannata, Antonio Nieto-Márquez, Andrés Jacoby, Ana L. Paredes-Doig, Amaya Romero, María R. Sun-Kou and José Luis Valverde, "Adsorption of phenol and nitrophenols by carbon nanospheres: Effect of pH and ionic strength," *Separation and Purification Technology*, vol. 80, no. 2, pp. 217-224, 2011.

49. KSW Sing, DH Everett, RAW Haul, L Moscou, RA Pierotti, J Rouquerol and T Siemieniewska, "Physical and biophysical chemistry division commission on colloid and surface chemistry including catalysis," *Pure Applied Chemistry*, vol. 57, no. 4, pp. 603-619, 1985.

50. Michal Kruk and Mietek Jaroniec, "Gas Adsorption Characterization of Ordered Organic−Inorganic Nanocomposite Materials," *Chemistry of Materials*, vol. 13, no. 10, pp. 3169-3183, 2001.

51. Matthias Thommes, Katsumi Kaneko, V. Neimark Alexander, P. Olivier James, Francisco Rodriguez-Reinoso, Jean Rouquerol and S. W. Sing Kenneth, "Physisorption of gases, with special reference to the evaluation of surface area and pore size distribution (IUPAC Technical Report)," in *Pure and Applied Chemistry*, Ed., pp. 1051, 2015.

52. Jinhong Bi, Wei Fang, Li Li, Xiaofen Li, Minghua Liu, Shijing Liang, Zizhong Zhang, Yunhui He, Huaxiang Lin, Ling Wu, Shengwei Liu and Po Keung Wong, "Ternary reduced-graphene-oxide/Bi_2MoO_6/Au nanocomposites with enhanced photocatalytic activity under visible light," *Journal of Alloys and Compounds*, vol. 649, pp. 28-34, 2015.

53. Xiangchao Meng and Zisheng Zhang, "Bi_2MoO_6 co-modified by reduced graphene oxide and palladium (Pd^{2+} and Pd^0) with enhanced photocatalytic decomposition of phenol," *Applied Catalysis B: Environmental*, vol. 209, pp. 383-393, 2017.

54. Clarissa Baumanis and Detlef W. Bahnemann, "TiO_2 Thin Film Electrodes: Correlation between Photocatalytic Activity and Electrochemical Properties," *The Journal of Physical Chemistry C*, vol. 112, no. 48, pp. 19097-19101, 2008.

55. Yajun Wang, Xiaojuan Bai, Chengsi Pan, Jun He and Yongfa Zhu, "Enhancement of photocatalytic activity of Bi_2WO_6 hybridized with graphite-like C_3N_4," *Journal of*

Materials Chemistry, vol. 22, no. 23, pp. 11568-11573, 2012.

56. Joana Ângelo, Pedro Magalhães, Luísa Andrade and Adélio Mendes, "Characterization of TiO_2-based semiconductors for photocatalysis by electrochemical impedance spectroscopy," *Applied Surface Science*, vol. 387, pp. 183-189, 2016.

57. Herbert B. Michaelson, "The work function of the elements and its periodicity," *Journal of Applied Physics*, vol. 48, no. 11, pp. 4729-4733, 1977.

Chapter 5 Pd nanoparticles decorated peanut-shaped $BiVO_4$ with improved visible light-driven photocatalytic activity comparable to TiO_2 under UV light

Xiangchao Meng, Zizhen Li and Zisheng Zhang

Journal of Catalysis 356 (2017), 53-64

Abstract

A porous, peanut-shaped $BiVO_4$ was prepared and further decorated with palladium nanoparticles on its surface using a photodeposition approach. The well-dispersed palladium nanoparticles were found to suppress photogenerated charge carriers, and may also improve the capacity of $BiVO_4$ to harvest visible light photons due to the local surface plasmon resonance effect. The prepared Pd-$BiVO_4$ composites exhibited excellent photocatalytic activities in the degradation of phenol under visible light irradiation. This performance rivaled that of TiO_2 under UV light. However, the active oxidants in these two processes (Pd-$BiVO_4$ and TiO_2- processes) are different: with photogenerated holes in $BiVO_4$ photocatalysis and OH radicals in TiO_2-base photocatalysis, respectively. Furthermore, different mechanisms as well as pathways for the degradation of phenol under the effects of different oxidants were proposed. This work not only opens up a new possibilities for the efficient removal of phenolic compounds in wastewater via visible light-driven photocatalysis in the presence of a Pd-$BiVO_4$ composite, but also suggests that OH radicals may not be the most important oxidants in all photocatalysis processes.

5.1 Introduction

Photocatalysis, as one of the advanced oxidation processes (AOPs), has been extensively studied and implemented in various areas, mainly including hydrogen generation and environmental remediation. Recently developed bismuth-based photocatalysts, compared to the traditional and most widely studied photocatalyst, TiO_2, possess advantages such as a suitable band gap for a visible light-response. This property makes it possible to utilize solar irradiation for photocatalysis, which is economically favourable for the implementation of this advanced technology. In addition, a variety of bismuth-based photocatalysts have been fabricated with high activities, increasing the possibility to be applied in practice [1].

$BiVO_4$ is a ferroelastic and ion conductive material, whose properties significantly depend on its crystal form [2]. There are three primary forms, namely zircon with a tetragonal structure (ZT) as well as scheelite with monoclinic (SM) and tetragonal (ST) structures [3]. It has been reported that the band gaps of $BiVO_4$ (SM) and $BiVO_4$ (ZT) are 2.4 and 2.9 eV, respectively [4], and that $BiVO_4$ (SM) powder exhibits higher photocatalytic activity for O_2 evolution than $BiVO_4$ (ZT) powder. Zhang et al have compared $BiVO_4$ (SM) and $BiVO_4$ (ST) for photocatalytic degradation of organic pollutants in water [5]. $BiVO_4$ (SM) showed higher photocatalytic activity compared to $BiVO_4$ (ST). However, photocatalytic activity of pure $BiVO_4$ within these three crystal forms is relatively low, most likely resulting from its difficult migration of photogenerated charge carriers and its poor adsorptive capacity [6]. It should be noted that the above-mentioned problems are not merely those of $BiVO_4$, but also for most bismuth-based photocatalysts [1, 7-11]. Approaches to overcome these challenges mainly include metal/non-metal doping [12, 13], the formation of heterostructures [14] and morphology adjustments [15].

Interest in the photodeposition of metal nanoparticles has expanded significantly since 1978 [16], and it has increasingly become an effective approach to improve photocatalytic performance under visible light irradiation. Well-dispersed metallic nanoparticles on the surface of a support facilitate the separation of photogenerated electron/hole pairs [17], as well as improve the capacity to harvest photons in the visible light range via the local surface plasmon resonance (SPR) effect [18]. The deposition of silver (Ag) nanoparticles

on $BiVO_4$ has been reported to enhance visible light-induced photocatalytic activity in the degradation of organics [19]. Palladium oxide (PdO) modified $BiVO_4$ was reported to have an enhanced visible light-driven photocatalytic activity for the degradation of Methyl Orange (MO) [20, 21]. In this case, palladium played an important role in supressing the recombination of photogenerated e^-/h^+ pairs. However, it took 9 h to completely remove MO, which is still too low to be used in practice. As reported, the SPR peaks for palladium (Pd) nanoparticles can be tuned from 410 to 870 nm [22, 23]. It can be deduced that depositing palladium nanoparticles on the surface of $BiVO_4$ may be a promising approach to significantly improve photocatalytic activity. We recently reported Bi_2MoO_6 hybrid photocatalysts decorated with Pd nanoparticles which exhibited significantly improved photocatalytic activities in the oxidation of phenol in water [7, 24]. this suggests that surface photodeposition of palladium nanoparticles may be a promising approach to facilitate the uptake of photogenerated electrons so as to improve the photocatalytic activity. In the context of morphology of a photocatalyst, it has been demonstrated that porous materials with tailored pore structures are capable of enhancing the light harvesting via multiple scattering, and facilitating the transfer of organic molecules [25, 26]. Among various morphologies of $BiVO_4$, peanut-shaped porous $BiVO_4$ was successfully prepared by a controlled one-step template-free method [27].

In this work, peanut-shaped $BiVO_4$ constructs decorated by palladium nanoparticles were fabricated via a solvothermal method following a photodeposition method. The photocatalytic activities of as-prepared composites were evaluated with regard to the degradation of a colorless organic model compound, phenol. Phenol is a common pollutant in wastewater from many industrial processes, and refractory to decompose using traditional approaches due to its high chemical stability [28, 29]. A mechanism for photocatalysis in the presence of $BiVO_4$ was proposed and compared to that of TiO_2. This work has shed light on the possibility of applying photo-deposited Pd nanoparticles to improve visible light-driven photocatalysis for the treatment of phenolic compounds in water.

5.2 Experimental

5.2.1 Preparation of peanut-shaped $BiVO_4$

Peanut-shaped $BiVO_4$ was prepared as reported [27]. In a typical process, 2 mmol of $Bi(NO_3)_3$•$5H_2O$ (Fisher Scientific, Certified ACS) were first dissolved in 30 mL of ethylene glycol (EG) (Fisher Scientific, Certified ACS), and 2 mmol of NH_4VO_3 (Fisher Scientific, Certified ACS) were dissolved in 20 mL of hot deionized distilled water (DDW). Next, the NH_4VO_3 solution was dropwise added into the $Bi(NO_3)_3$ solution under magnetic stirring for 30 min. After that, the yellow solution was transferred into a 50 mL Teflon-line autoclave and heated at 100°C for 15h. The yellowish precipitates were filtered out and washed twice with DDW and one time with ethanol. The precipitates were then dried at 60°C for 12h before collected for further use.

5.2.2 Preparation of palladium modified-$BiVO_4$ composites

Palladium (Pd) modified-$BiVO_4$ composites were prepared using a photo-deposition method as previously reported [7, 24]. Specifically, 0.3 g of prepared $BiVO_4$ wasdispersed into 40 mL of DDW with magnetic stirring for 10 min. Then, a designated amount of $PdCl_2$ (Fisher Scientific Canada, ACS certified) suspension was added into the suspension under magnetic stirring for another 10 min. After that, the suspension was illuminated under a 300-W halogen tungsten projector lamp (Ushio, USA) for 1 h. The resultant products were filtered out, washed twice with DDW and dried at 60°C for 12h. Samples of 1, 2, 4, 8 and 10% Pd-$BiVO_4$ were prepared following the above procedures and labelled as 1, 2, 4, 8, and 10% Pd-Bi.

5.2.3 Characterization

A Rigaku Ultima IV diffractometer with Cu Kα radiation (λ = 0.15418 nm) at 40 kV and 44 mA was used for X-ray diffraction (XRD). Surface composition as well as chemical states were measured using a XSAM-800 X-ray Photoelectron Spectroscope (XPS). Morphologies of prepared samples were investigated using a field-emission scanning electron microscope (FE-SEM, JEOL JSM-7500F) and a transmission electron microscope (TEM, JEM-2100F). A Thermo Evolution 300 spectrophotometer was used to study the optical properties of samples through ultraviolet-visible diffuse reflectance spectroscopy

(UV-Vis DRS). The specific surface area was obtained from N_2 sorption isotherms at 77 K, using an automatic adsorption apparatus and measurement systems (ASAP 2020, Micromeritics and Nova 4200E, Quantachrome). The Brunauer, Emmett and Teller (BET) surface area of the samples were calculated using multi-point estimation. Electrochemical properties of prepared samples were performed on a CHI 604E electrochemical analyzer (CH Instruments Inc., USA) with a platinum wire as a counter electrode, a calomel reference electrode and a working electrode. The working electrode was composed of indium tin oxide (ITO, 75 × 25 × 1.1 mm, 15 - 25 Ω, Sigma-Aldrich Canada Co.) glass coated with the prepared samples. The electrolyte was Na_2SO_4 solution with a concentration of 0.1 mol/L.

5.2.4 Photocatalytic activity tests

Photocatalytic activity of as-prepared samples was evaluated through the degradation of a colorless organic pollutant, phenol, in water under visible light irradiation. The photoreactor mainly composed of a 500 mL beaker with a cooling jacket to maintain the system temperature at around 20°C and a 300-W halogen tungsten projector lamp (wavelength mainly in the range of 310 – 800 nm) with a UV cut-off (Kenko Zeta, transmittance > 90%) to filter out irradiation with wavelength below 410 nm. The irradiation intensity at the surface of the solution was measured by a quantum meter (Biospherical QSL-2100, $400 < \lambda < 700$ nm) to be 1.1×10^{-2} Einsteins m^{-2} s^{-1}. For each test, 100 mL of phenol solution with an initial concentration of 10 mg/L was mixed with 0.1 g of photocatalysts. This suspension was first magnetically stirred in the dark for 60 min to ensure an adsorption-desorption equilibrium between the organics and photocatalysts was reached. Photocatalysis started when the light was tuned on, and lasted for 6 h. During the process, aliquots were drawn and centrifuged at 13,000 rpm for 5 min. The supernatant was analyzed using a high-performance liquid chromatograph (HPLC, Agilent 1100 series) equipped with a UV-Vis detector. A ZORBAX Eclipse Plus C18 column (4.6 × 250 mm) was used at a temperature of 60°C. The detecting wavelength was fixed at 270 nm for the detection of phenol and possible intermediates. The flow phase was composed of methanol (55%, V/V) and water (45%, V/V) at a flow rate of 0.6 mL/min. The injection volume was set to 25 μL.

In the quenching experiments, ethylenediaminetetraacetic acid disodium (EDTA-2Na) and isopropanol with a concentration of 1 mol/L were added to the reaction system as scavengers for holes and oxidative free radicals, respectively. The concentration of OH radicals produced during photocatalysis was determined using *p*-chlorobenzoic acid (pCBA) as a probe. The initial concentration of pCBA was aet to 10 mg/L, catalyst dosage amount was equal to 1 g/L and the solution volume was 100 mL. Photocatalytic degradation of pCBA was carried out for 90 min. Aliquots were taken and centrifuged and the supernatant was analyzed using the HPLC with detecting wavelength at 254 nm. All other parameters were kept the same with the detection of phenol mentioned above. For comparison, TiO_2 (anatase powder, Fisher Scientific Canada, ACS certified) was also tested.

5.2.5 Electronic structure calculation

The quantum-mechanical calculations were performed on the basis of the density functional theory (DFT) [30]. The generalized gradient approximation (GGA) was applied to exchange-correlation effects. The open access software Quantum ESPRESSO was used, which utilizes pseudopotentials to describe electron-ion interactions and represents electronic wave functions using a plane-wave basis set [31]. The kinetic energy cut-off was set to 300 eV.

5.3 Results and discussions

5.3.1 Crystal structures and surface chemical components

Crystal structures of prepared samples including pure $BiVO_4$ and Pd decorated $BiVO_4$ composites were investigated via XRD patterns as shown in Fig. 5.1. For pure $BiVO_4$, all peaks may be indexed to the monoclinic phase (space group: I41/a (88), PDF card #: 75-2481 [32]). No peaks for impurities were found, indicating a high crystallinity in $BiVO_4$ in the prepared samples. For XRD patterns for Pd-$BiVO_4$ composites, negligible influence of Pd on the $BiVO_4$ support was observed, suggesting that the $BiVO_4$ crystal structure was not disrupted during the Pd photodeposition process. However, no peaks for palladium were observed for all Pd-$BiVO_4$ composites. This phenomenon may be due to the content of palladium in the composite being too low to be detected by the XRD technique. Furthermore, lattice parameters for all XRD patterns shown in Fig. 5.1 were calculated and

summarized in Table 5.1. Lattice parameters for pure $BiVO_4$ are a = b = 5.1610 Å and c = 11.7117 Å. The introduction of Pd negligibly influenced the lattice parameters for the $BiVO_4$ support. This result further confirmed that the deposition of palladium may not destroy the crystal structure of $BiVO_4$ during the photoreduction process, Instead, it is likely that palladium is resting on the surface as opposed to covalently anchoring to the lattice of $BiVO_4$ [7, 33].

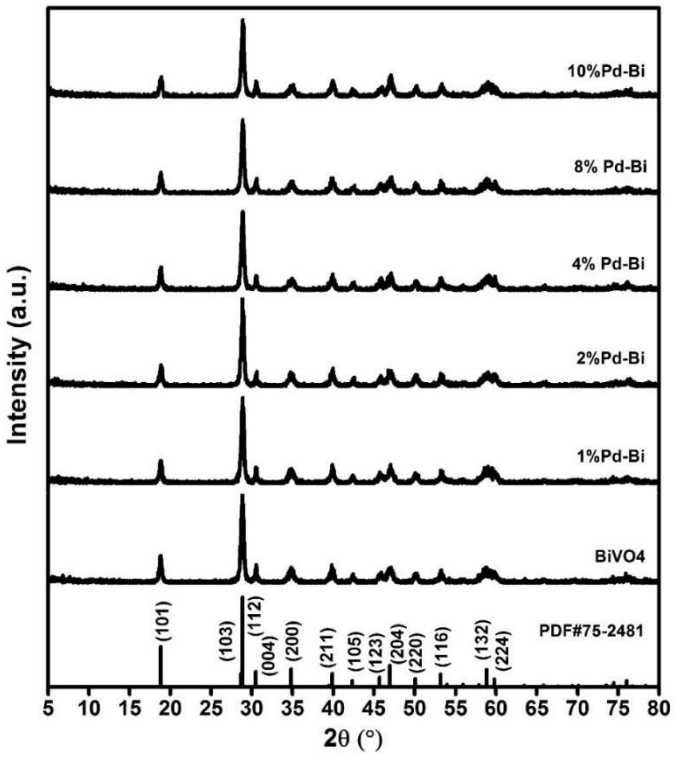


Figure 5.1 XRD patterns of prepared $BiVO_4$ and Pd-$BiVO_4$ composites, as well as standard XRD patterns for $BiVO_4$.

Table 5.1 Lattice parameters of prepared samples.

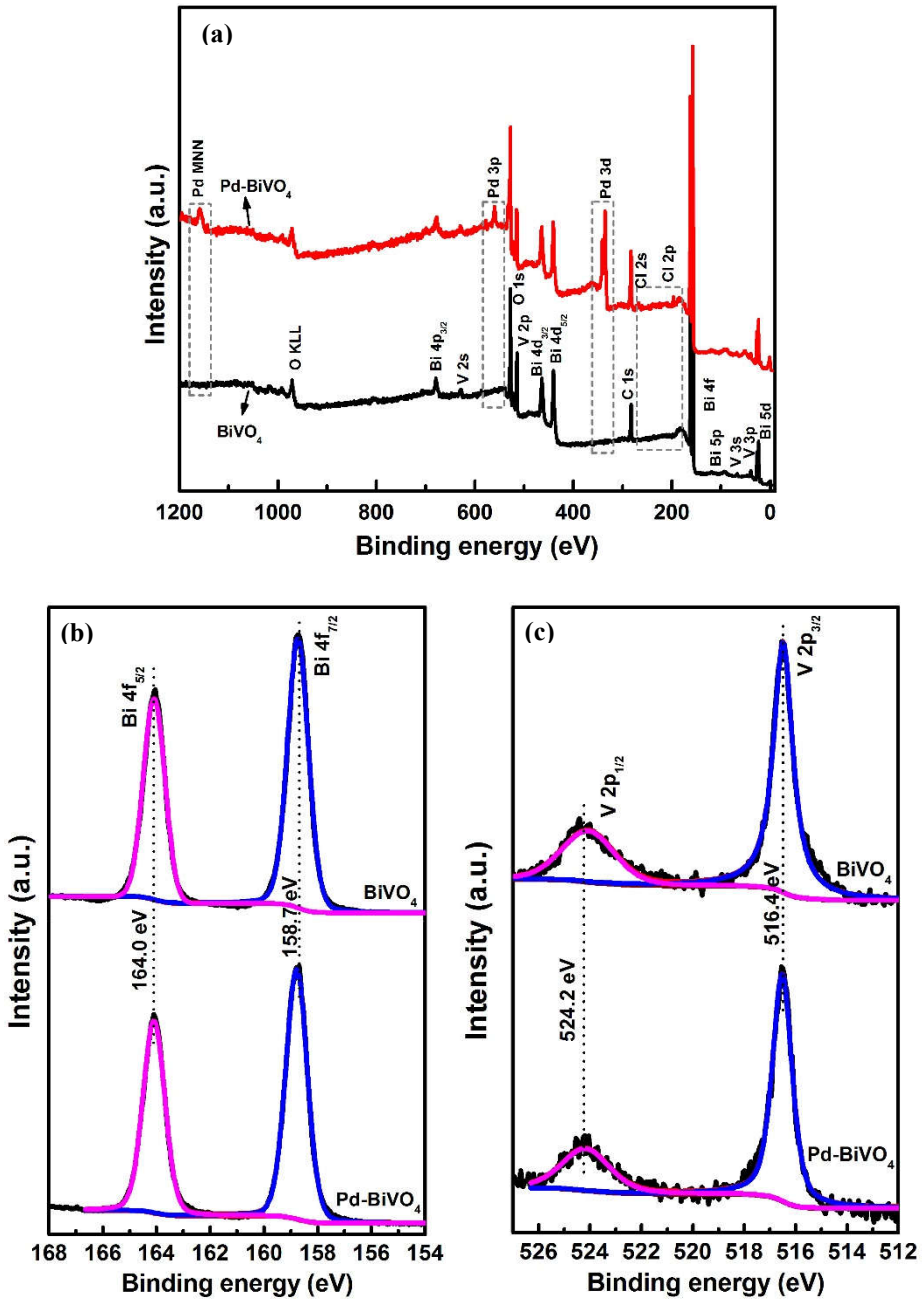
Samples	a = b (Å)	c (Å)
$BiVO_4$	5.1610 (0%)	11.7117 (0%)
1% Pd-Bi	5.1557 (-0.10%)	11.7148 (+0.03%)
2% Pd-Bi	5.1543 (-0.13%)	11.7284 (+0.14%)
4% Pd-Bi	5.1551 (-0.11%)	11.7293 (+0.15%)
8% Pd-Bi	5.1516 (-0.18%)	11.7333 (+0.18%)
10% Pd-Bi	5.1511 (-0.19%)	11.7345 (+0.19%)

To further probe the surface components and chemical states of prepared samples, XPS was employed, the results of which are illustrated in Fig. 5.2. All spectra were calibrated with C 1s, the binding energy of which was fixed at 284.6 eV. In the survey spectra for pure $BiVO_4$ and Pd-$BiVO_4$ (Fig. 5.2a), all components, namely Bi, V, and O, were identified, with peaks for Pd and Cl also detected in the survey spectrum for the Pd-$BiVO_4$ composite. In the high-resolution spectra of Bi 4f orbits (Fig. 5.2b), two major peaks at binding energies of 164.0 and 158.7 eV, corresponding to Bi $4f_{5/2}$ and Bi $4f_{3/2}$ respectively, are indicative of the sole presence of Bi^{5+} ($BiVO_4$) in both samples [34]. It can also be seen that the V 2p spectra consist of two major peaks at 524.2 and 516.4 eV, possibly attributing to V $2p_{1/2}$ and V $2p_{3/2}$ binding energies, being indicative of V^{3+} in $BiVO_4$ [35]. Upon the introduction of Pd on $BiVO_4$, no peak shift was found in both Bi 4f and V 2p spectra as shown in Fig. 5.2b and 5.2c. This result suggests the palladium may not be doped in the lattice of $BiVO_4$. Thus far, considerable studies have been carried out on the structures of Pd and Cl species with XPS. High-resolution XPS orbital scans for Pd 3d and Cl 2p were measured and illustrated in Fig. 5.2d and 5.2e. A set of spin-orbit doublets was found in Pd 3d spectrum. Specifically, peaks at 342.9 and 337.1 eV may be accorded to Pd $3d_{3/2}$ and $3d_{5/2}$ binding energies, respectively, being indicative of Pd^{2+} in the form of $PdCl_2$. Moreover, smaller peaks at binding energies of 339.4 and 335.1 eV may be attributed to the metallic Pd (Pd^0). The relative concentration of bivalent to metallic Pd can be calculated using Equation 1 [36]:

$$\frac{c_{Pd^0}}{c_{Pd^{2+}}} = \frac{I_{Pd^0}}{I_{Pd^{2+}}} \times \frac{\sigma_{Pd}\lambda_{Pd}D_E(Pd)}{\sigma_{Pd}\lambda_{Pd}D_E(Pd)} \qquad \textbf{\textit{Equation 1}}$$

where η, I, σ, λ, and D_E are the surface concentration, integrated intensity, photoelectric cross-section, electron free mean path, and geometric factor, respectively. The values of σ, λ, and D_E have been calculated and were summarized by Penn and Scofield [37, 38]. The areas of Pd^0 and Pd^{2+} peaks were integrated to estimate their concentrations. The relative combined surface concentration ratio of Pd^0 to Pd^{2+} was estimated to be approximately 1:2.8. Similarly to Ag/AgCl system, bivalent palladium was found only partially reduced to metallic palladium nanoparticles, with the presence of Pd^{2+} being beneficial to improve the stability of the palladium loaded system [39, 40]. As shown in Fig. 5.2e, peaks for Cl

2p were detected at binding energies of 199.9 and 198.2 eV for Cl $2p_{1/2}$ and Cl $2p_{3/2}$, which correspond to Cl^-. This further indicates that $PdCl_2$ was partially reduced to Pd nanoparticles during the photoreduction process.



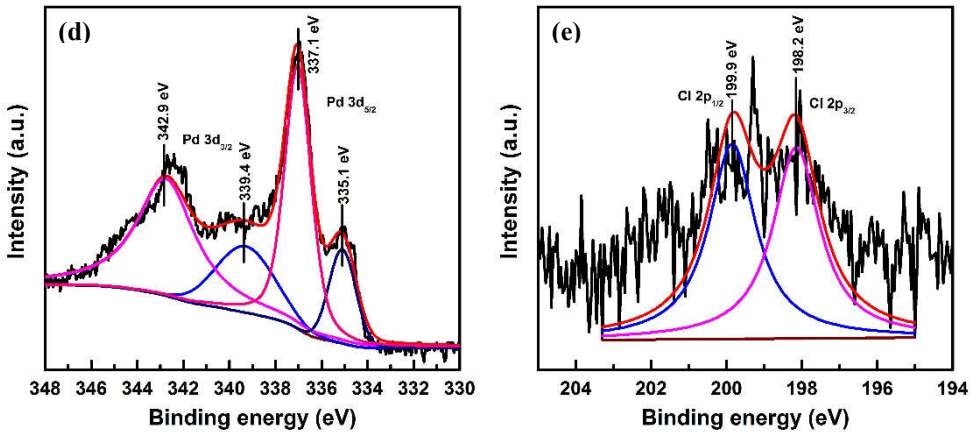


Figure 5.2 XPS spectra of prepared $BiVO_4$ and Pd-$BiVO_4$: (a) survey, (b) Bi 4f and (c) V 2p, as well as (d) Pd 3d and (e) Cl 2p for Pd-$BiVO_4$.

5.3.2 Morphologies

Morphologies of prepared samples were investigated using SEM and TEM. A uniform peanut-shaped morphology for pure $BiVO_4$ was observed in Fig. 5.3a. A close-up view of the composite (Fig. 5.3b) demonstrated a length of about 3.5 µm. Upon introduction of Pd, the morphology of peanut-shaped $BiVO_4$ was negligibly influenced (Fig. 5.3c). The only difference was that the edge for Pd-$BiVO_4$ (Fig. 5.3d) was coarser than that for pure $BiVO_4$. In addition, such peanut-shaped structure was revealed by TEM as depicted in Fig. 5.3e and 5.3g. Comparing the edges of pure $BiVO_4$ (Fig. 5.3f) and Pd-$BiVO_4$ (Fig. 5.3h), nanoparticles were observed at the edge of only the Pd-$BiVO_4$ composite. These nanoparticles may be the photoreduced palladium nanoparticles. Diameter size distribution of the Pd nanoparticles was illustrated in the inset of Fig. 5.3h; 95% of these nanoparticles were found with the width in the range of 3 – 9 nm. The presence of well-dispersed Pd nanoparticles may be an important reason for an enhancement in photocatalytic activity, owing to the surface plasmonic resonance effect.

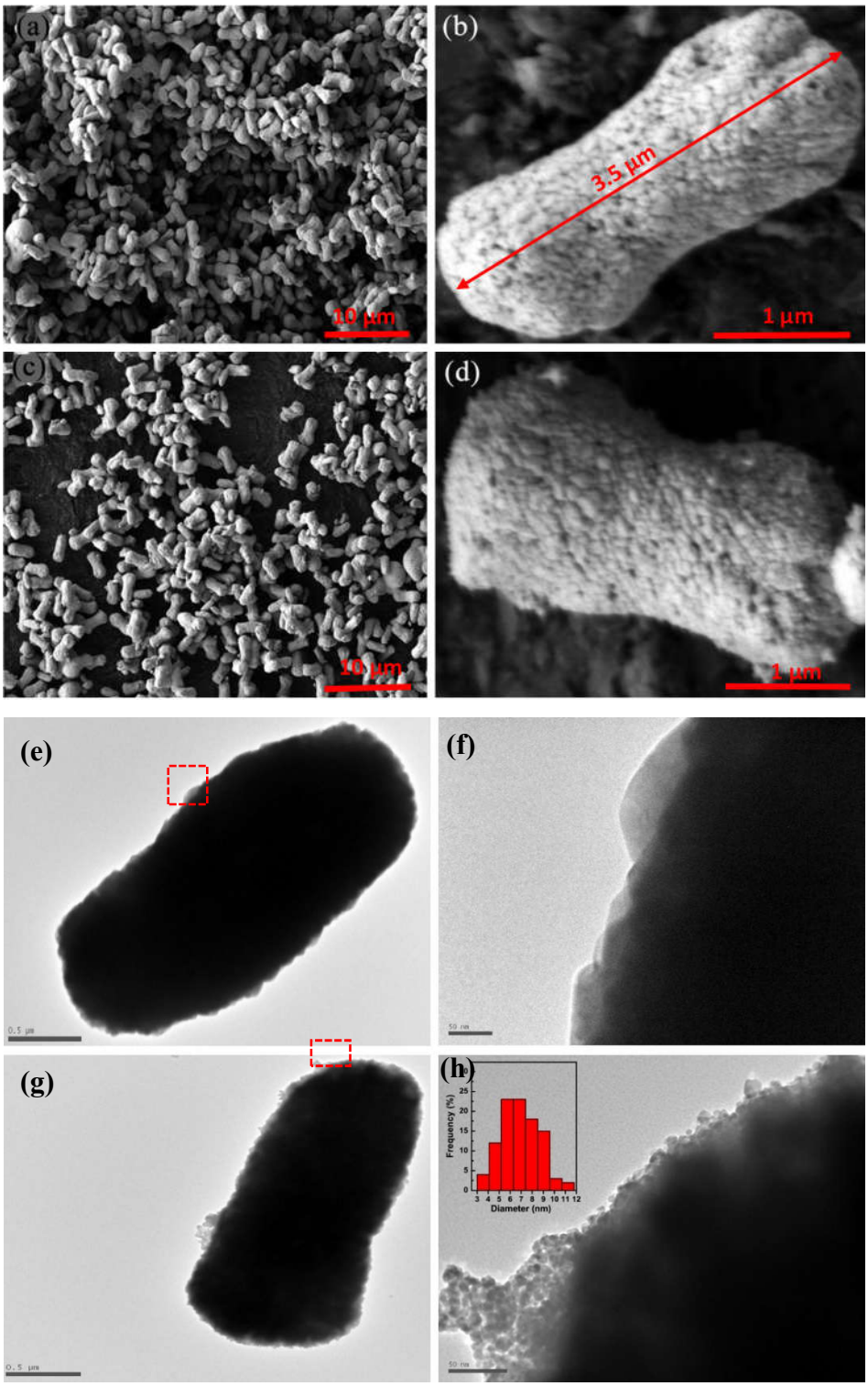


Figure 5.3 Low- and high-magnification SEM images of pure $BiVO_4$ (a, b) and Pd-$BiVO_4$ composites (c, d); TEM images for pure $BiVO_4$ in low (e) and high (f) magnification, and Pd-$BiVO_4$ composites in low (g) and high (h) magnification.

5.3.3 Proposed formation process

The possible formation process of palladium nanoparticle-decorated peanut-shaped $BiVO_4$ is proposed as shown in Fig. 5.4. Typically, when the V precursor was added to the Bi source, the precipitation of $BiVO_4$ was immediately observed. During the solvothermal treatment, $BiVO_4$ precipitation was reformed following the steps of oriented aggregation and self-assembly [41]. The peanut-shaped morphology was self-assembled during the 12-h solvothermal treatment. As for the doping process, $PdCl_2$ was mixed with $BiVO_4$ in a suspension, followed by a photo-reduction process. Theoretically, the redox potential of Pd^{2+}/Pd was 0.987 V (vs NHE). The bottom potential of the conduction band for $BiVO_4$ can be calculated as 0.36 eV using Equation 2:

$$E_{CB,BiVO_4} = \chi_{BiVO_4} - E^e - \frac{1}{2}E_g \qquad \textit{Equation 2}$$

$$E_{VB,BiVO_4} = E_{CB,BiVO_4} + E_g \qquad \textit{Equation 3}$$

where χ_{BiVO4} (6.04 eV) [1], E^e and E_g are the electronegativity, the energy of free electrons on the hydrogen scale (≈ 4.5eV), and the band gap of $BiVO_4$ (2.36 eV, from section 3.4) [42, 43]. This suggests the photogenerated electrons on the conduction band of $BiVO_4$ can reduce Pd^{2+} to Pd^0 during the photo-reduction process. The color of the suspension was changed from dark yellow to black, revealing the Pd^{2+} were successfully reduced to metallic Pd^0 on the peanut-shaped $BiVO_4$.

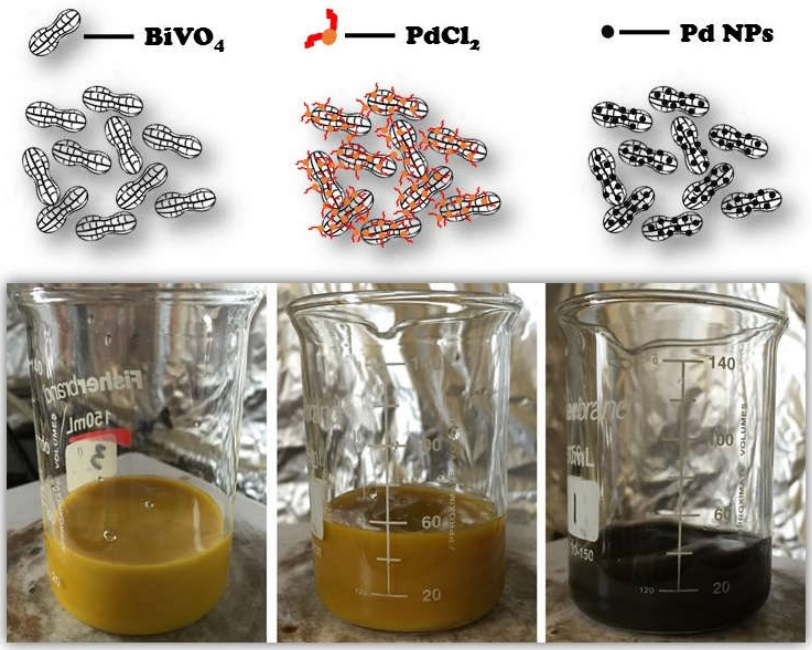


Figure 5.4 Possible formation process of Pd nanoparticles decorated $BiVO_4$ composites.

5.3.4 Energy band structure analysis

The band structure as well as the partial/total density of states of the support, $BiVO_4$, were simulated based on density functional theory (DFT), and are illustrated in Fig. 5.5. The top energy of the valence band was fixed at 0.00 eV. Band gap value for $BiVO_4$ was calculated as about 2.46 eV, indicating $BiVO_4$ may be activated by irradiation with wavelengths lower than 504 nm. The band gap transition for $BiVO_4$ is of the indirect type. The top of the valence band is mainly composed of O 2p and Bi 5s orbitals, while the bottom of the conduction band consists of O 2p, V 3d and Bi 6p orbitals. It should also be noted that the correlation between the effective mass of electrons or holes and the curvature of the bands can be simply described by Equation 4 [44, 45]:

$$m^* = \frac{\hbar^2}{\frac{d^2 E_\kappa}{d\kappa^2}} \qquad \textit{Equation 4}$$

$$\frac{m_e^*}{m_h^*} = \left| \frac{\left. \frac{d^2 E_\kappa}{d\kappa^2} \right|_h}{\left. \frac{d^2 E_\kappa}{d\kappa^2} \right|_e} \right| \qquad \textit{Equation 5}$$

where m^* is the effective mass of the electrons or holes, κ is the wave vector, and $E\kappa$ is the energy corresponding to the wave vector κ. A higher effective mass of the charge carrier implies a lower mobility of the charge carrier. The relative ratio of effective mass between electrons on the conduction band minimum (CBM) and holes on the valence band maximum (VBM) may be obtained via Equation 5. The values of the second-order term of $E\kappa$ for electrons on CBM and holes on VBM, and the absolute ratio are calculated and shown in Table 5.2. It revealed that the mobility of the electron is similar to that of the hole. This characteristic is not desirable in the photogenerated charge carriers' separation, and could possibly result in a lower photocatalytic efficiency. It suggests that in order to improve the photocatalytic activity, the photogenerated charge carriers' separation efficiency of $BiVO_4$ must be increased.

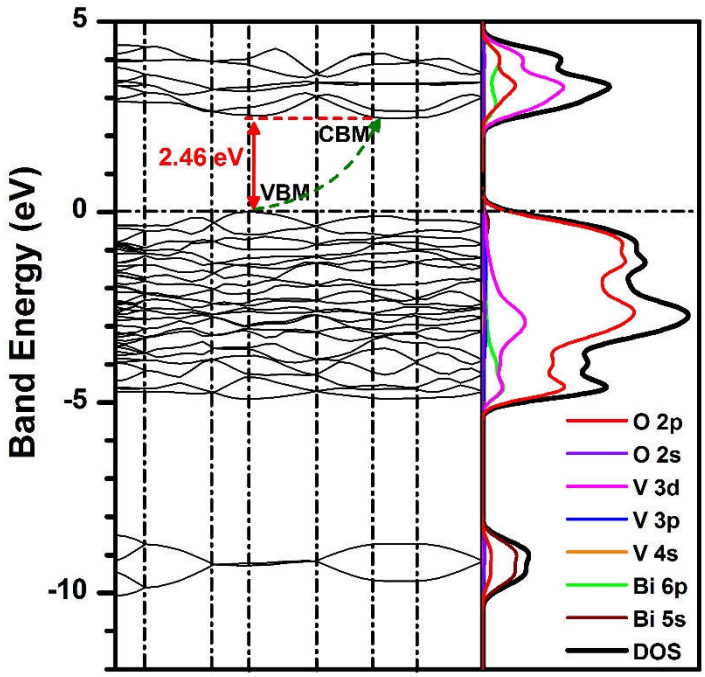


Figure 5.5 Band structure and density of states for $BiVO_4$ calculated by the DFT method (Fermi level fixed at band energy of 0 eV).

Table 5.2 Parameter values for Equation 4 and 5.

Parameter	$\left.\frac{d^2E_\kappa}{d\kappa^2}\right\|_h$	$\left.\frac{d^2E_\kappa}{d\kappa^2}\right\|_e$	$\frac{m_e^*}{m_h^*}$
Value	-27.78	27.22	1.02

5.3.5 Optical properties

Optical properties of prepared samples were investigated using a UV-Vis diffused reflectance spectrometer, the results of which are depicted in Fig. 5.6. For the spectrum of pure $BiVO_4$, a steep increase in the absorbance intensity was observed at wavelengths decrease below 525 nm, indicating that a band gap transition occurs at this wavelength. The corresponding band gap value calculated with the Kubelka-Munk function was about 2.36 eV. The measured band gap is narrower than that of the simulated results as shown in Fig. 5.5, which may be due to the limitations of simulation [46]. Upon the introduction of palladium, the absorbance intensity in the visible light range was greatly improved. With an increase of the loading amount of palladium, the enhancement in visible light absorbance gradually increased. Meanwhile, a negligible red shift of band edge was observed upon introduction of palladium to the surface of $BiVO_4$. This phenomenon further reveals that the palladium nanoparticles were simply loaded onto the surface instead of doped in the lattice of $BiVO_4$. The improvement of absorption in the visible light region may be imparted by the surface plasmonic effect [22, 23].

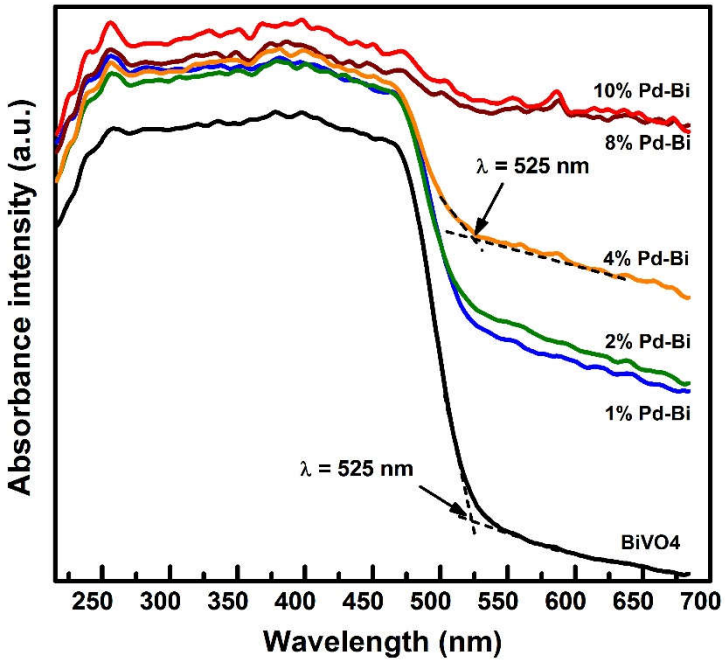


Figure 5.6 UV-Vis diffused reflectance spectra for prepared $BiVO_4$ and Pd-$BiVO_4$ composites.

5.3.6 Photocatalytic activity testing

The photocatalytic activities of prepared samples were tested with regards to the degradation of phenol under visible light irradiation, and results are illustrated in Fig. 5.7. The adsorption of phenol on all prepared samples is no more than 2.5%. The low adsorption capacity of $BiVO_4$ as well as Pd-$BiVO_4$ composites may result from the small specific surface area of as-prepared samples: BET surface areas for pure $BiVO_4$ and 8% Pd-$BiVO_4$ composite are measured as 3.8 m^2/g and 3.2 m^2/g, respectively. The surface coverage for phenol adsorbed on $BiVO_4$ and 8% Pd-$BiVO_4$ was calculated as about 1.7% and 5.1%, respectively. A significant difference was found after turning on the light to start the photocatalysis process. Specifically, only 3.4% of phenol were removed in the presence of pure $BiVO_4$ under visible light irradiation over 360 min. Upon introduction of palladium on the surface of $BiVO_4$, the rate of phenol removal was greatly increased. With increase of the content of palladium, 29.2, 51.8, 88.9 and 100% of phenol were removed for systems with 1%, 2%, 4% and 8% Pd-$BiVO_4$ composites, respectively. It should be noted that, in the presence of 8% Pd-$BiVO_4$ composites, phenol was completely removed after 240 min under irradiation. Further increase of the loading amount of palladium to 10% resulted in

a slight reduction in the phenol removal compared to the system with 8% Pd-$BiVO_4$ composites. This phenomenon may be attributed to the over loading of palladium, resulting in an increase of sites for photogenerated charge carrier recombination, and also a decrease in photoactive sites on $BiVO_4$.

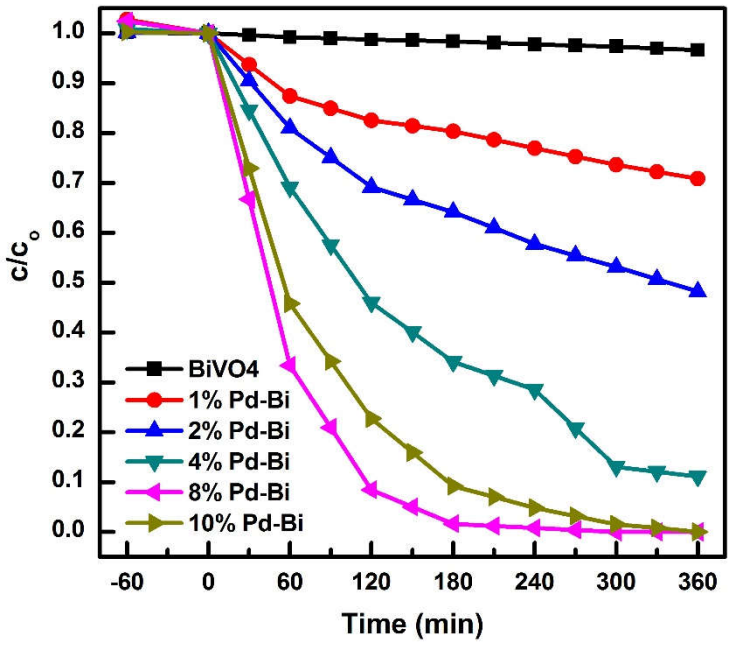


Figure 5.7 Concentration profiles of phenol in the presence of different photocatalysts under visible light irradiation (c_o = 10 mg/L, catalysts dosage: 1 g/L and temperature: 20°C).

Langmuir-Hinshelwood model, as shown in Equation 6, may be applied to describe the photocatalytic oxidation process of decomposition of phenol:

$$r = -\frac{dc}{dt} = k\theta = \frac{kKc}{1+Kc} \qquad \textbf{Equation 6}$$

where r, c, t, k, θ and K represent reaction rate, concentration of phenol, time, reaction rate constant, surface coverage (dimensionless) and adsorption constant, respectively. The initial concentration of phenol for all the tests was 10 mg/L (~ 1×10^{-4} mol/L) and no obvious adsorption of phenol was observed, indicating a low adsorption constant (K) for phenol adsorbed on $BiVO_4$ as well as on Pd-$BiVO_4$ composites. As a result, the $1 + Kc$ term may be assumed to be equal to 1. Equation 6 can be then expressed as Equation 7,

$$-\frac{dc}{dt} = kKc = k'c \qquad \textit{Equation 7}$$

where k' is the pseudo first-order reaction constant. Equation 8 can be obtained by integrating Equation 7 from c_o at a time of 0 min to c_t at time t. The value of k' for each photocatalytic process can be determined by plotting $\ln(c_o/c_t)$ vs t and calculating the slope of the line of best fit.

$$\ln(\frac{c_o}{c_t}) = k't \qquad \textit{Equation 8}$$

The calculated pseudo first-order reaction constants for photocatalytic processes in the presence of different prepared samples are shown in Table 5.3. All values of R^2 are nearly equal to 1, indicating an excellent linearity and a high suitability for this model. The reaction constant for the system with pure $BiVO_4$ was as low as 1.1×10^{-4} min^{-1}. This value was significantly improved for photocatalytic processes with Pd modified $BiVO_4$ composites. When the content of Pd was 8%, the reaction constant was especially large at 19.48×10^{-3} min^{-1} which is 177 times larger than that for the process with pure $BiVO_4$. These results also reveal that over-loading Pd in the composites may decrease their photocatalytic activities in the oxidation of phenol.

Table 5.3 Kinetic constants for systems in the presence of different photocatalysts.

Samples	$BiVO_4$	1% Pd-Bi	2% Pd-Bi	4% Pd-Bi	8% Pd-Bi	10% Pd-Bi
k' ($\times10^{-3}$ min^{-1})	0.11	1.59	2.96	6.21	19.48	12.25
R^2	0.990	0.969	0.991	0.999	0.994	0.999

5.3.7 Proposed mechanism discussions

5.3.7.1 Active species

Photocatalytic oxidation processes occur with the production of strong oxidative species. Possible oxidants produced during the photocatalysis are illustrated in Fig. 5.8a [47]. Among these oxidants, photogenerated holes on the valence band as well as hydroxyl free radicals are considered to be primary oxidants for the decomposition of organic pollutants in water (Fig. 5.8b). Effective oxidative species for $BiVO_4$-based photocatalysis were

detected through trapping experiments using isopropanol as OH radicals' scavenger and EDTA-2Na as holes' scavenger, respectively [48], and the results are shown in Fig. 5.9. With the addition of a scavenger for holes (EDTA-2Na), the photocatalytic activities of Pd-$BiVO_4$ composites were greatly suppressed. However, the addition of isopropanol as a •OH scavenger resulted in a much smaller change in the photocatalytic removal of phenol. These results indicate that photogenerated holes are the primary oxidants in this $BiVO_4$-based photocatalytic system.

$$\text{(a) Photocatalyst} \xrightarrow{+h\nu} \begin{cases} e^-_{CB} \xrightarrow{+O_2} O_2^- \xrightarrow{+H_2O_{adsorbed}} \begin{cases} HO_2 \begin{cases} +HO_2 \rightarrow O_2 + \boxed{H_2O_2} \\ +HO_2 + H^+ + e^- \rightarrow \boxed{H_2O_2} \end{cases} \rightarrow \boxed{\bullet OH} + OH^- \\ OH^- \end{cases} \\ h^+_{VB} \xrightarrow{+H_2O_{adsorbed}} \boxed{\bullet OH} + H^+ \end{cases}$$

$$\text{(b)} \quad \left.\begin{matrix} h^+_{VB} \\ \bullet OH \end{matrix}\right\} + \text{phenol}_{adsorbed} \rightarrow \text{intermediates} \rightarrow\rightarrow CO_2 + H_2O + \ldots$$

Figure 5.8 (a) Possible reactions in the presence of $BiVO_4$ under visible light irradiation, (b) Possible oxidation of phenol through photo-generated oxidants including holes and OH radicals.

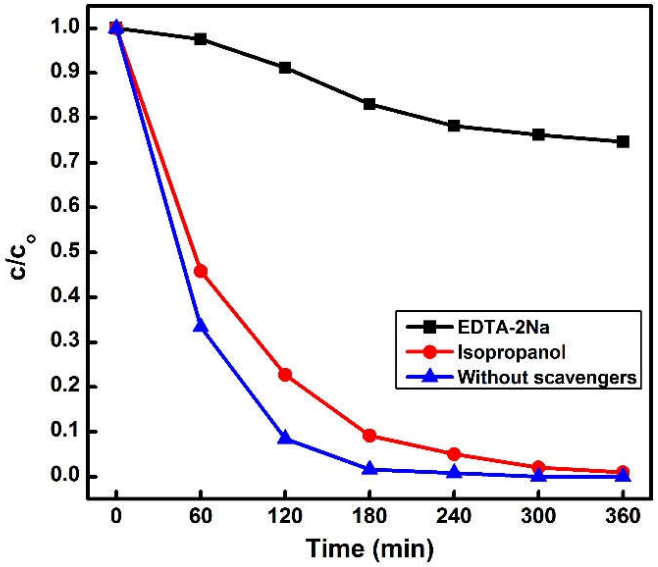


Figure 5.9 Concentrations of phenol in the presence of 8% Pd-$BiVO_4$ with or without addition of scavengers.

To further confirm the minimal contribution from OH radicals in the $BiVO_4$-based photocatalysis system, the concentration of OH radicals was measured indirectly through probe compounds (*p*-chlorobenzoic acid, pCBA) [49, 50]. The rate of reaction between pCBA and OH radicals can be expressed as shown in Equation 10. The reaction rate constant ($k_{\bullet OH\text{-}pCBA}$) is equal to 5×10^9 M^{-1} s^{-1} (3.12×10^{11} M^{-1} min^{-1}). The high reaction rate constant indicates that pCBA selectively react with OH radicals. Profiles for photocatalytic degradation of pCBA in the presences of TiO_2, $BiVO_4$ and Pd-Bi composites are separately depicted in Fig. 5.10. It can be observed that pCBA was rapidly degraded over 90 min with TiO_2 under UV light. In contrast, a negligible amount of pCBA was removed from the system using $BiVO_4$ under visible light irradiation, while about 10% of the initial pCBA was degraded in the system with 8% Pd-Bi composites. These results indicate a large amount of OH radicals were generated in the presence of TiO_2 under UV irradiation., Due to its strong oxidative capacity, •OH has also been confirmed to be one of the most important oxidants for the decomposition of organic species in water [51-54]. However, a negligible amount of •OH was detected in the presence of either pure $BiVO_4$ or Pd-$BiVO_4$ composites under visible light irradiation. It reveals •OH may have not played a determinate role in the decomposition of phenol. It has been widely reported that holes on the valence band play the most significant role in the decomposition of organics in water instead of •OH for $BiVO_4$ as well as other bismuth-based photocatalysts [1, 9, 55]. The oxidative capacity of holes depends on the potential of the valence band top. Equation 3 can be used to calculate the valence band top potential, which is estimated at about 2.72 V for $BiVO_4$. It should be noted the redox potential of $\bullet OH/H_2O$ is 2.27 V at pH 7 and 2.73 at pH 0 (vs SHE) [53]. It may cause the photogenerated holes on the valence band to be incapable of oxidizing the adsorbed water to produce •OH (Fig. 5.8a), while they (holes) are capable of directly reacting with adsorbed organics such as phenol.

$$p-CBA+\bullet OH \rightarrow p-CBA^{*} \qquad \textbf{Equation 9}$$

$$\frac{dc_{p-CBA}}{dt} = -k_{\bullet OH-pCBA} \times c_{p-CBA} \times c_{\bullet OH} \qquad \textbf{Equation 10}$$

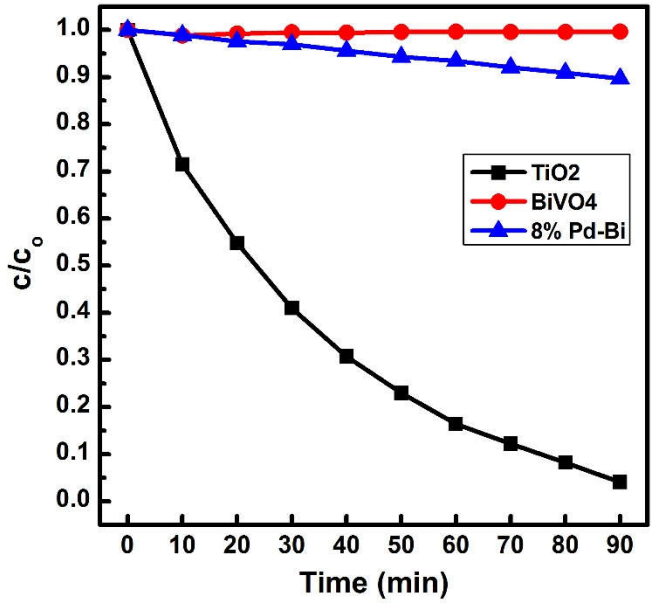


Figure 5.10 Photocatalytic degradation of pCBA with TiO_2 under UV irradiation as well as $BiVO_4$ and 8%Pd-$BiVO_4$ composites under visible light irradiation.

5.3.7.2 Pathways for the degradation of phenol

The concentrations of phenol as well as those of possibly produced intermediates such as benzoquinone (BQ), hydroquinone (HQ) and catechol (CA) were investigated. Chromatograms of samples taken during the photocatalysis in the presence of either 8% Pd-$BiVO_4$ under visible light irradiation or TiO_2 under UV irradiation are shown in Fig. 5.11, and calibrated concentrations for phenol, BQ, HQ and CA were calculated and illustrated in Fig. 5.12. In Fig. 5.11, it can be found that phenol was completely removed after 180 min for system with 8% Pd-$BiVO_4$ and 120 min for system with TiO_2, respectively. However, more intermediates were produced for photocatalysis with TiO_2 compared to that with 8% Pd-$BiVO_4$. These three main intermediates were completely removed at the end of both photocatalysis processes. Quantitively, as shown in Fig. 5.12, around 10 mg/L of phenol were completely removed in 180 min and 120 min in the presence of 8% Pd-$BiVO_4$ and TiO_2, respectively. In the system with TiO_2 as the photocatalyst, 2.72, 0.71 and 0.61 mg/L of HQ, BQ and CA, respectively, were produced over 60 min under UV irradiation. Notably, negligible amount of the three intermediates were detected during the thorough photocatalysis process in the presence of 8% Pd-$BiVO_4$ with regard to the degradation of phenol for 360 min. The total organic carbon (TOC) in

the suspension was also detected to evaluate the mineralization of phenol by $BiVO_4$, Pd-$BiVO_4$ and TiO_2, as illustrated in Fig. 5.13. For pure $BiVO_4$, concentrations of both phenol and TOC were negligibly changed during the photocatalysis for 360 min. Upon introduction of palladium on $BiVO_4$, the TOC rapidly decreased to 45% (of TOC_0) in the first 120 min, and then slightly decreased to 32% (of TOC_0) by 360 min. The decrease in the first stage may be primarily caused by the destruction of phenol, and then the produced organic acids, which were more refractory to degradation, were only slowly destroyed during the following stage. The decrease of TOC in the system with TiO_2 under UV irradiation is similar compared to that with Pd-Bi composites under visible light irradiation, and 27% of TOC were left at the end of photocatalysis at 360 min. For the degradation of phenol with TiO_2, •OH play important role and a large number of phenolic compounds including HQ, BQ and CA were produced from the phenol; these phenolic compounds were degraded into organic acids which were then to be decomposed. Based on the discussions above, possible pathways of degradation of phenol in the presence of Pd-$BiVO_4$ under visible light irradiation were proposed and illustrated in Fig. 5.14. Specifically, OH radicals may react with phenol to form dihydroxycyclohexadienyl radical adducts (Route 1). These adducts may evolve further to form phenoxy radicals by elimination of H_2O (Route 2), which was proven to be a very slow [56]. More likely to occur is that these adducts may react with dissolved oxygen (Route 3), followed by an elimination of HO_2 to form dihydroxy intermediates (Route 4). By contrast, with absence of OH radicals for the Pd-$BiVO_4$ system, Phenol may react with oxygen (Route 5), followed by the formation of phenoxy radicals with the elimination of HO_2 (Route 6) [57]. In the presence of O_2, phenoxy radicals are most probably to form benzoquinone with a small reaction rate (Route 7), which may be a good explanation for the negligible intermediates detected for the system of Pd-$BiVO_4$ [58]. When these three phenolic intermediates formed, OH radicals and dissolved oxygen, and holes and dissolved oxygen may lead to the ring cleavage and fragmentation, respectively for the system of TiO_2 and Pd-$BiVO_4$. The products of the phenolic compounds, once the ring is broken, are different organic acids such as maleic acid, succinic acid, malonic acid oxalic acid and acetic acid (Routes 8 and 9) [59]. Furthermore, these organic acids are probably degraded into CO_2 and H_2O (Route 10).

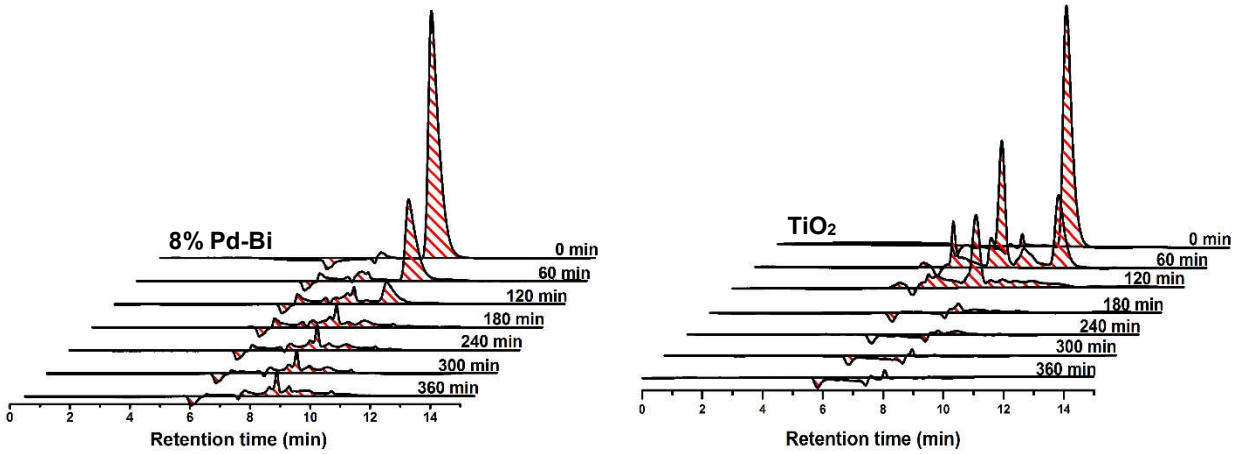


Figure 5.11 Chromatogram of the separation in a C18 column of: benzoquinone (BQ, t_R = 6.5 min), hydroquinone (HQ, t_R = 8.3 min), catechol (CA, t_R = 9.0 min) and phenol (t_R = 10.2 min). Samples taken from the suspension containing 8% Pd-$BiVO_4$ composites (left) and TiO_2 (right).

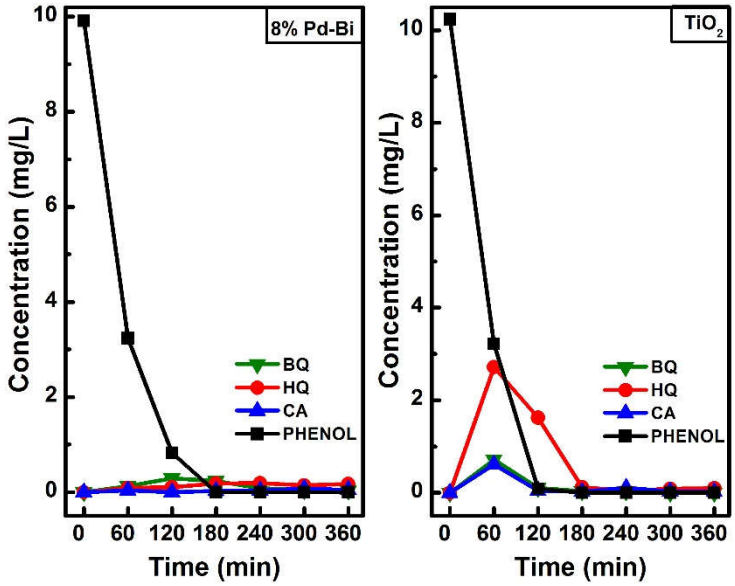


Figure 5.12 Concentrations of benzoquinone, hydroquinone, catechol and phenol during the photolysis processes in the presence of 8%Pd-$BiVO_4$ under visible light irradiation and TiO_2 under UV irradiation.

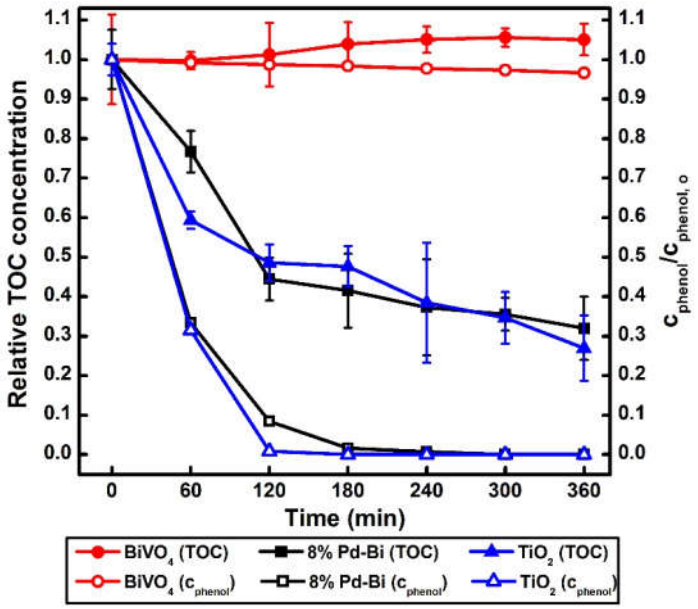


Figure 5.13 Relative TOC and phenol concentrations in the photocatalysis processes with pure $BiVO_4$ and 8% Pd-$BiVO_4$ under visible light irradiation, as well as TiO_2 under UV irradiation, respectively.

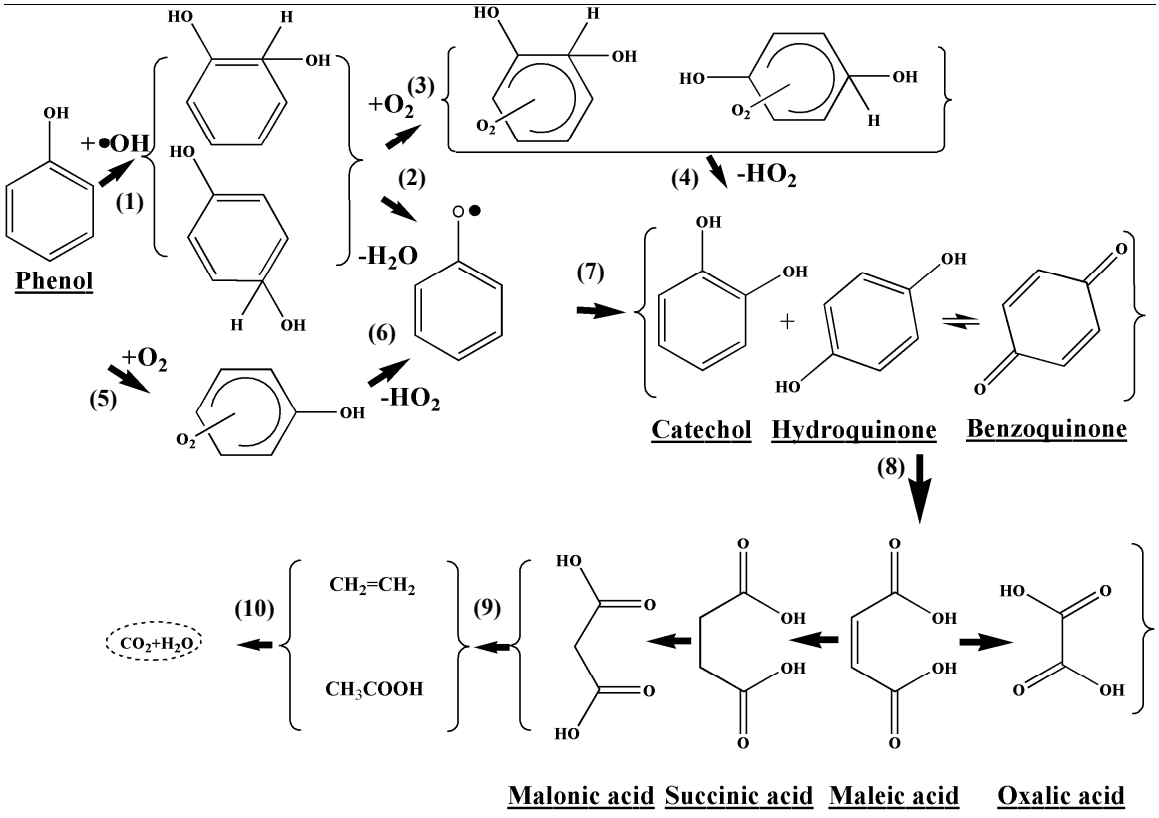


Figure 5.14 Possible pathways for the photocatalytic degradation of phenol in the presence of Pd-$BiVO_4$ under visible light irradiation.

5.3.7.2 Recombination of photogenerated charge carriers

Photocurrents were measured for pure $BiVO_4$ as well as Pd-$BiVO_4$ electrodes to study the electronic interactions between $BiVO_4$ and palladium (Fig. 5.15). For all electrodes, fast and uniform photocurrent responses were observed. In addition, these photocurrent responses were found to be reversible. With the light on, the average photocurrent for pure $BiVO_4$ is as low as 0.16 μA for the first light-on cycle. With palladium loading on its surface, the average photocurrent was increased to 0.41, 1.65 and 0.77 μA, respectively for the first light-on cycle, for 4%, 8% and 10% Pd modified-$BiVO_4$ electrode. Even though some variations are observed both within each 'light-on' cycle and from cycle to cycle. The noticeable enhancement in the photocurrent under visible light irradiation indicates the improved photo-induced electron and hole separation. Also, SPR effect of palladium nanoparticles on the surface of $BiVO_4$ contributes to the improvement of photocurrent. When the loading amount of Pd in the composites was equal to 8%, it exhibited the highest suppression rate of the charge carriers' recombination. However, over loading increased the recombination rate of photogenerated charge carriers, which may be attributed to the excessive number of metallic particles on the surface providing more recombination sites. To further explore this result, electrochemical impedance spectroscopy (EIS) was employed and EIS Nyquist plots for pure $BiVO_4$ and Pd-$BiVO_4$ composites were shown in Fig. 5.16. For each plot, only one semicircle was observed, indicating that the $BiVO_4$-based photocatalysis was a simple electrode reaction. The rate of electron transfer on the electrode may be determined by the recombination rate of photogenerated charge carriers [7, 60, 61]. The equivalent circuits of these processes and the fitted electrical parameters are shown in Table 5.4. The diameter of the arc in the EIS Nyquist plot is in direct proportion to the value of R_{ct} [62]. The semicircle for pure $BiVO_4$ has the largest diameter and the highest resistance at 14.7 kΩ. With palladium loaded on the surface of $BiVO_4$, the semicircle diameters were greatly decreased, resulting in R_{ct} values of 7.61, 1.15 and 2.27 kΩ for 4%, 8% and 10% Pd-$BiVO_4$ electrode, respectively. These results further confirm that palladium loading facilitates the separation of electrons and holes, resulting in an enhanced photocatalytic activity for the degradation of phenol.

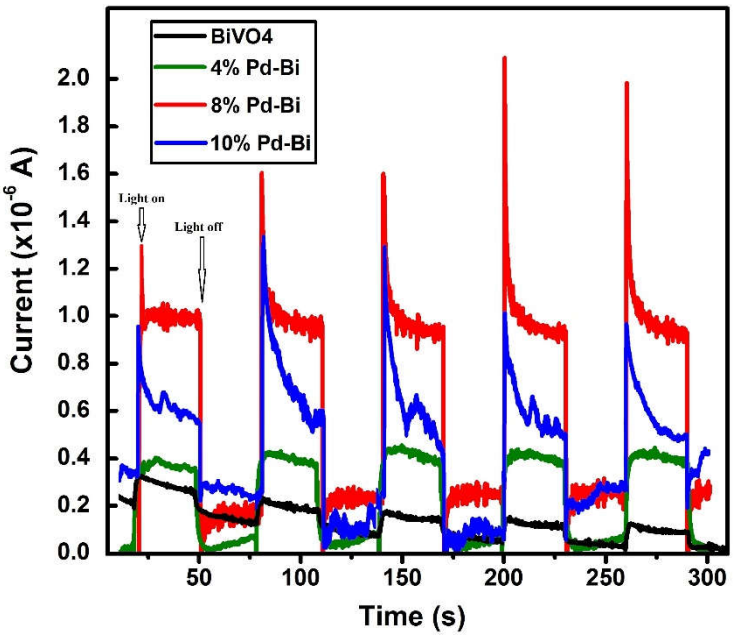


Figure 5.15. Transient photocurrent response of pure $BiVO_4$ and Pd-$BiVO_4$ composites.

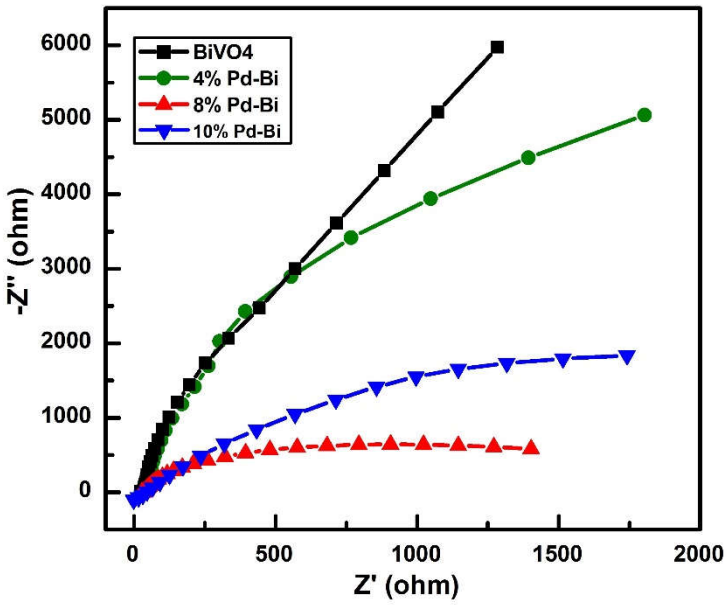
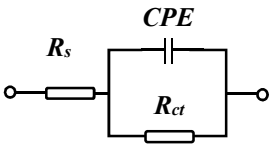


Figure 5.16. EIS Nyquist plots of the pure $BiVO_4$ and Pd-$BiVO_4$ composites.

Table 5.4 Fitting results for equivalent circuits of different prepared samples.

Samples	R_s (Ω)	R_{ct} (kΩ)	*CPE* (mf)	Equivalent circuits
$BiVO_4$	24.85	14.7	175	
4%Pd-Bi	31.49	7.61	230	
8% Pd-Bi	28.69	1.15	223	
10% Pd-Bi	32.49	2.27	351	

Note: R_s: resistance of solution; R_{ct}: resistance of electron transfer on the electrode; CPE: constant phase element which can be regarded as a capacity of double layer.

5.3.7.3 Photocatalytic process

Fig. 5.17 describes possible photocatalytic processes in the presence of palladium nanoparticle-decorated $BiVO_4$ under visible light irradiation. Irradiation at wavelengths below 525 nm can be absorbed by the support, $BiVO_4$. When the electrons on the valence band of $BiVO_4$ are activated, they may jump to the conduction band with positive holes left on the valence band. The photogenerated electrons on the conduction band and holes on the valence band, respectively, may be directly reacted with adsorbed species such as H_2O, O_2 and organic compounds. Activated electrons may also return to the valence band and recombine with positive holes. Upon introducing palladium nanoparticles to the surface, electrons may be activated by irradiation at wavelengths in the range of 410 and 870 nm, due to the SPR effect. As a result, extra electrons may be produced and possibly transferred to the conduction band of $BiVO_4$. Palladium nanoparticles can also act as excellent electron acceptors; the migration of electrons between $BiVO_4$ and Pd is in favor of reducing the recombination rate of photogenerated electron/hole pairs. The improved separation of photogenerated charge carriers may therefore further increase the photocatalytic oxidation activity via production of more oxidative species.

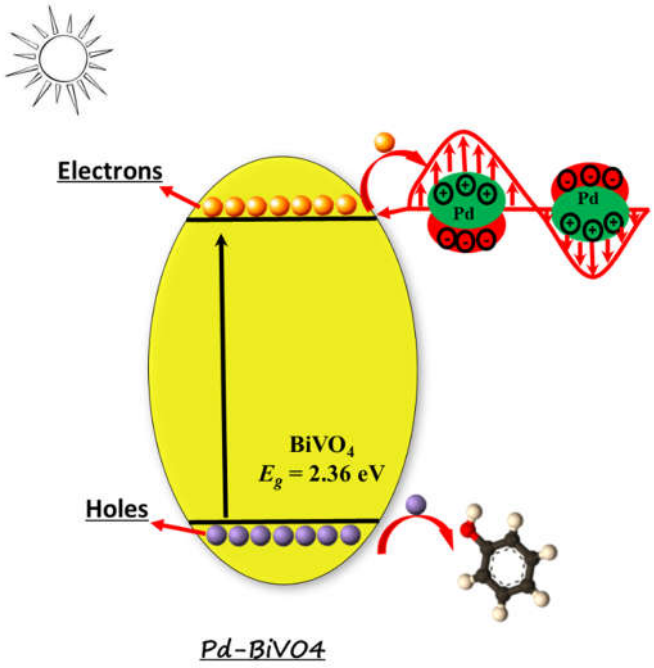


Figure 5.17. Photocatalytic processes of Pd-$BiVO_4$ under visible light irradiation.

5.4 Conclusions

Peanut-shaped porous $BiVO_4$ was successfully prepared using a template-free solvothermal method. Palladium nanoparticles were then well-dispersed on its surface via a photodeposition method. The Pd nanoparticles improved the visible light harvesting capacity, possibly due to the SPR effect. In addition, upon introduction of palladium on the surface of $BiVO_4$, the photocatalytic activity was significantly improved for the degradation of phenol under visible light irradiation. This enhancement may be due to a suppression in recombination of photogenerated charge carriers. In $BiVO_4$-based photocatalysis, photogenerated holes on the valence band play the most important role in the photocatalytic oxidation of organic compounds in water. The possible pathways for the degradation of phenol were proposed by comparison to those in the presence of TiO_2 under UV light. The different degradation mechanisms in the presence of Pd-$BiVO_4$ composites under visible light irradiation as well as those in the presence of TiO_2 under UV light irradiation sheds light on the importance of exploring the active species in photocatalysis. Loading Pd nanoparticles on the surface of $BiVO_4$ makes it a strong rival to TiO_2 for the photocatalytic degradation of phenol.

References

1. Xiangchao Meng and Zisheng Zhang, "Bismuth-based Photocatalytic Semiconductors: Introduction, Challenges and Possible Approaches," *Journal of Molecular Catalysis A: Chemical*, vol. 423, pp. 533-549, 2016.

2. Saimi Tokunaga, Hideki Kato and Akihiko Kudo, "Selective Preparation of Monoclinic and Tetragonal $BiVO_4$ with Scheelite Structure and Their Photocatalytic Properties," *Chemistry of Materials*, vol. 13, no. 12, pp. 4624-4628, 2001.

3. Lim Ae Ran, Choh Sung Ho and Jang Min Su, "Prominent ferroelastic domain walls in $BiVO_4$ crystal," *Journal of Physics: Condensed Matter*, vol. 7, no. 37, pp. 7309, 1995.

4. Akihiko Kudo, Keiko Omori and Hideki Kato, "A Novel Aqueous Process for Preparation of Crystal Form-Controlled and Highly Crystalline $BiVO_4$ Powder from Layered Vanadates at Room Temperature and Its Photocatalytic and Photophysical Properties," *Journal of the American Chemical Society*, vol. 121, no. 49, pp. 11459-11467, 1999.

5. Xi Zhang, Zhihui Ai, Falong Jia, Lizhi Zhang, Xiaoxing Fan and Zhigang Zou, "Selective synthesis and visible-light photocatalytic activities of $BiVO_4$ with different crystalline phases," *Materials Chemistry and Physics*, vol. 103, no. 1, pp. 162-167, 2007.

6. Mingce Long, Weimin Cai, Jun Cai, Baoxue Zhou, Xinye Chai and Yahui Wu, "Efficient Photocatalytic Degradation of Phenol over $Co_3O_4/BiVO_4$ Composite under Visible Light Irradiation," *The Journal of Physical Chemistry B*, vol. 110, no. 41, pp. 20211-20216, 2006.

7. Xiangchao Meng and Zisheng Zhang, "Pd-doped Bi_2MoO_6 Plasmonic Photocatalysts with Enhanced Visible Light Photocatalytic Performance," *Applied Surface Science*, vol. 392, pp. 169-180, 2016.

8. Xiangchao Meng and Zisheng Zhang, "Synthesis, Analysis, and Testing of BiOBr-Bi_2WO_6 Photocatalytic Heterojunction Semiconductors," *International Journal of Photoenergy*, vol. 2015, pp. 12, 2015.

9. Xiangchao Meng and Zisheng Zhang, "Ag/AgCl Loaded Bi_2WO_6 Composite: A Plasmonic Z-Scheme Visible Light-Responsive Photocatalyst," *International Journal of*

Photoenergy, vol. 2016, pp. 11, 2016.

10. Xiangchao Meng and Zisheng Zhang, "Plasmonic Z-scheme Ag_2O-Bi_2MoO_6 p-n heterojunction photocatalysts with greatly enhanced visible-light responsive activities," *Materials Letters*, vol. 189, pp. 267-270, 2017.

11. Xiangchao Meng and Zisheng Zhang, "Plasmonic ternary Ag–rGO–Bi_2MoO_6 composites with enhanced visible light-driven photocatalytic activity," *Journal of Catalysis*, vol. 344, pp. 616-630, 2016.

12. Bin Zhou, Xu Zhao, Huijuan Liu, Jiuhui Qu and C. P. Huang, "Visible-light sensitive cobalt-doped $BiVO_4$ (Co-$BiVO_4$) photocatalytic composites for the degradation of methylene blue dye in dilute aqueous solutions," *Applied Catalysis B: Environmental*, vol. 99, no. 1–2, pp. 214-221, 2010.

13. Min Wang, Qiong Liu, Yinsheng Che, Lifang Zhang and Dong Zhang, "Characterization and photocatalytic properties of N-doped $BiVO_4$ synthesized via a sol–gel method," *Journal of Alloys and Compounds*, vol. 548, pp. 70-76, 2013.

14. Puttaswamy Madhusudan, Jingrun Ran, Jun Zhang, Jiaguo Yu and Gang Liu, "Novel urea assisted hydrothermal synthesis of hierarchical $BiVO_4$/$Bi_2O_2CO_3$ nanocomposites with enhanced visible-light photocatalytic activity," *Applied Catalysis B: Environmental*, vol. 110, pp. 286-295, 2011.

15. S. Obregón, A. Caballero and G. Colón, "Hydrothermal synthesis of $BiVO_4$: Structural and morphological influence on the photocatalytic activity," *Applied Catalysis B: Environmental*, vol. 117–118, pp. 59-66, 2012.

16. Bernhard Kraeutler and Allen J Bard, "Heterogeneous photocatalytic preparation of supported catalysts. Photodeposition of platinum on titanium dioxide powder and other substrates," *Journal of the American Chemical Society*, vol. 100, no. 13, pp. 4317-4318, 1978.

17. Kasper Wenderich and Guido Mul, "Methods, Mechanism, and Applications of Photodeposition in Photocatalysis: A Review," *Chemical Reviews*, 2016.

18. Suljo Linic, Phillip Christopher and David B. Ingram, "Plasmonic-metal nanostructures for efficient conversion of solar to chemical energy," *Nature Materials*, vol. 10, no. 12, pp.

911-921, 2011.

19. Hongyan Li, Yingjuan Sun, Bin Cai, Shiyu Gan, Dongxue Han, Li Niu and Tongshun Wu, "Hierarchically Z-scheme photocatalyst of Ag@AgCl decorated on $BiVO_4$ (0 4 0) with enhancing photoelectrochemical and photocatalytic performance," *Applied Catalysis B: Environmental*, vol. 170–171, pp. 206-214, 2015.

20. Lei Ge, "Novel Pd/$BiVO_4$ composite photocatalysts for efficient degradation of methyl orange under visible light irradiation," *Materials Chemistry and Physics*, vol. 107, no. 2–3, pp. 465-470, 2008.

21. Lei Ge, "Synthesis and characterization of novel visible-light-driven Pd/$BiVO_4$ composite photocatalysts," *Materials Letters*, vol. 62, no. 6–7, pp. 926-928, 2008.

22. Yujie Xiong, Benjamin Wiley, Jingyi Chen, Zhi-Yuan Li, Yadong Yin and Younan Xia, "Corrosion-Based Synthesis of Single-Crystal Pd Nanoboxes and Nanocages and Their Surface Plasmon Properties," *Angewandte Chemie International Edition*, vol. 44, no. 48, pp. 7913-7917, 2005.

23. Yujie Xiong, Jingyi Chen, Benjamin Wiley, Younan Xia, Yadong Yin and Zhi-Yuan Li, "Size-Dependence of Surface Plasmon Resonance and Oxidation for Pd Nanocubes Synthesized via a Seed Etching Process," *Nano Letters*, vol. 5, no. 7, pp. 1237-1242, 2005.

24. Xiangchao Meng and Zisheng Zhang, "Bi_2MoO_6 Co-modified by Reduced Graphene Oxide and Palladium (Pd^{2+} and Pd^0) with Enhanced Photocatalytic Decomposition of Phenol," *Applied Catalysis B: Environmental*.

25. Jimmy C. Yu, Xinchen Wang and Xianzhi Fu, "Pore-Wall Chemistry and Photocatalytic Activity of Mesoporous Titania Molecular Sieve Films," *Chemistry of Materials*, vol. 16, no. 8, pp. 1523-1530, 2004.

26. Changsheng Guo, Ming Ge, Lu Liu, Guandao Gao, Yinchang Feng and Yuqiu Wang, "Directed Synthesis of Mesoporous TiO_2 Microspheres: Catalysts and Their Photocatalysis for Bisphenol A Degradation," *Environmental Science & Technology*, vol. 44, no. 1, pp. 419-425, 2010.

27. Ming Ge, Lu Liu, Wei Chen and Zhen Zhou, "Sunlight-driven degradation of Rhodamine B by peanut-shaped porous $BiVO_4$ nanostructures in the H_2O_2-containing

system," *CrystEngComm*, vol. 14, no. 3, pp. 1038-1044, 2012.

28. I. Oller, S. Malato and J. A. Sánchez-Pérez, "Combination of Advanced Oxidation Processes and biological treatments for wastewater decontamination—A review," *Science of The Total Environment*, vol. 409, no. 20, pp. 4141-4166, 2011.

29. Parag R. Gogate, "Treatment of wastewater streams containing phenolic compounds using hybrid techniques based on cavitation: A review of the current status and the way forward," *Ultrasonics Sonochemistry*, vol. 15, no. 1, pp. 1-15, 2008.

30. Walter Kohn and Lu Jeu Sham, "Self-consistent equations including exchange and correlation effects," *Physical Review*, vol. 140, no. 4A, pp. A1133, 1965.

31. Giannozzi Paolo, Baroni Stefano, Bonini Nicola, Calandra Matteo, Car Roberto, Cavazzoni Carlo, Ceresoli Davide, L. Chiarotti Guido, Cococcioni Matteo, Dabo Ismaila, Corso Andrea Dal, Gironcoli Stefano de, Fabris Stefano, Fratesi Guido, Gebauer Ralph, Gerstmann Uwe, Gougoussis Christos, Kokalj Anton, Lazzeri Michele, Martin-Samos Layla, Marzari Nicola, Mauri Francesco, Mazzarello Riccardo, Paolini Stefano, Pasquarello Alfredo, Paulatto Lorenzo, Sbraccia Carlo, Scandolo Sandro, Sclauzero Gabriele, P. Seitsonen Ari, Smogunov Alexander, Umari Paolo and M. Wentzcovitch Renata, "QUANTUM ESPRESSO: a modular and open-source software project for quantum simulations of materials," *Journal of Physics: Condensed Matter*, vol. 21, no. 39, pp. 395502, 2009.

32. Chen Jia-Ping Liu Jian-Cheng, Li De-Yu, "Crystal Structure and Optical Observations of $BiVO_4$," *Acta Physica Sinica*, vol. 32, no. 8, pp. 1053-1060, 1983.

33. Yuanguo Xu, Hui Xu, Huaming Li, Jiexiang Xia, Chengtang Liu and Ling Liu, "Enhanced photocatalytic activity of new photocatalyst Ag/AgCl/ZnO," *Journal of Alloys and Compounds*, vol. 509, no. 7, pp. 3286-3292, 2011.

34. Ponchio Chatchai, Yoshinori Murakami, Shin-ya Kishioka, Atsuko Y. Nosaka and Yoshio Nosaka, "Efficient photocatalytic activity of water oxidation over $WO_3/BiVO_4$ composite under visible light irradiation," *Electrochimica Acta*, vol. 54, no. 3, pp. 1147-1152, 2009.

35. Aiping Zhang and Jinzhi Zhang, "Synthesis and characterization of $Ag/BiVO_4$

composite photocatalyst," *Applied Surface Science*, vol. 256, no. 10, pp. 3224-3227, 2010.

36. CD Wagner and GE Muilenberg, *Handbook of X-ray photoelectron spectroscopy*, Perkin-Elmer, 1979.

37. J. H. Scofield, "Hartree-Slater subshell photoionization cross-sections at 1254 and 1487 eV," *Journal of Electron Spectroscopy and Related Phenomena*, vol. 8, no. 2, pp. 129-137, 1976.

38. David R. Penn, "Quantitative chemical analysis by ESCA," *Journal of Electron Spectroscopy and Related Phenomena*, vol. 9, no. 1, pp. 29-40, 1976.

39. Peng Wang, Baibiao Huang, Xiaoyan Qin, Xiaoyang Zhang, Ying Dai, Jiyong Wei and Myung-Hwan Whangbo, "Ag@AgCl: A Highly Efficient and Stable Photocatalyst Active under Visible Light," *Angewandte Chemie International Edition*, vol. 47, no. 41, pp. 7931-7933, 2008.

40. Peng Wang, Baibiao Huang, Zaizhu Lou, Xiaoyang Zhang, Xiaoyan Qin, Ying Dai, Zhaoke Zheng and Xiaoning Wang, "Synthesis of highly efficient Ag@ AgCl plasmonic photocatalysts with various structures," *Chemistry-a European Journal*, vol. 16, no. 2, pp. 538-544, 2010.

41. Lang Chen, Shuang-Feng Yin, Rui Huang, Qiang Zhang, Sheng-Lian Luo and Chak-Tong Au, "Hollow peanut-like m-$BiVO_4$: facile synthesis and solar-light-induced photocatalytic property," *CrystEngComm*, vol. 14, no. 12, pp. 4217-4222, 2012.

42. M. A. Butler and D. S. Ginley, "Prediction of Flatband Potentials at Semiconductor - Electrolyte Interfaces from Atomic Electronegativities," *Journal of The Electrochemical Society*, vol. 125, no. 2, pp. 228-232, 1978.

43. Arthur H. Nethercot, "Prediction of Fermi Energies and Photoelectric Thresholds Based on Electronegativity Concepts," *Physical Review Letters*, vol. 33, no. 18, pp. 1088-1091, 1974.

44. Haijun Zhang, Lu Liu and Zhen Zhou, "Towards better photocatalysts: first-principles studies of the alloying effects on the photocatalytic activities of bismuth oxyhalides under visible light," *Physical Chemistry Chemical Physics*, vol. 14, no. 3, pp. 1286-1292, 2012.

45. Xiangchao Ma, Ying Dai, Meng Guo and Baibiao Huang, "The Role of Effective Mass of Carrier in the Photocatalytic Behavior of Silver Halide-Based Ag@AgX (X=Cl, Br, I): A Theoretical Study," *ChemPhysChem*, vol. 13, no. 9, pp. 2304-2309, 2012.

46. Kangrong Lai, Wei Wei, Ying Dai, Ruiqin Zhang and Baibiao Huang, "DFT calculations on structural and electronic properties of Bi_2MO_6 (M = Cr, Mo, W)," *Rare Metals*, vol. 30, no. 1, pp. 166-172, 2011.

47. Michael R. Hoffmann, Scot T. Martin, Wonyong Choi and Detlef W. Bahnemann, "Environmental Applications of Semiconductor Photocatalysis," *Chemical Reviews*, vol. 95, no. 1, pp. 69-96, 1995.

48. Yajun Wang, Rui Shi, Jie Lin and Yongfa Zhu, "Enhancement of photocurrent and photocatalytic activity of ZnO hybridized with graphite-like C_3N_4," *Energy & Environmental Science*, vol. 4, no. 8, pp. 2922-2929, 2011.

49. Michael S. Elovitz and Urs von Gunten, "Hydroxyl Radical/Ozone Ratios During Ozonation Processes. I. The Rct Concept," *Ozone: Science & Engineering*, vol. 21, no. 3, pp. 239-260, 1999.

50. S.-K. Han, S.-N. Nam and J.-W. Kang, "OH radical monitoring technologies for AOP advanced oxidation process," *Water Science and Technology*, vol. 46, no. 11-12, pp. 7-12, 2002.

51. Raquel Portela and María Dolores Hernández-Alonso, "Environmental Applications of Photocatalysis," in *Design of Advanced Photocatalytic Materials for Energy and Environmental Applications*, Ed., pp. 35-66, Springer, 2013.

52. Rimeh Daghrir, Patrick Drogui and Didier Robert, "Modified TiO_2 For Environmental Photocatalytic Applications: A Review," *Industrial & Engineering Chemistry Research*, vol. 52, no. 10, pp. 3581-3599, 2013.

53. Akira Fujishima, Tata N. Rao and Donald A. Tryk, "Titanium dioxide photocatalysis," *Journal of Photochemistry and Photobiology C: Photochemistry Reviews*, vol. 1, no. 1, pp. 1-21, 2000.

54. Akira Fujishima, Xintong Zhang and Donald A. Tryk, "TiO_2 photocatalysis and related surface phenomena," *Surface Science Reports*, vol. 63, no. 12, pp. 515-582, 2008.

55. Zhijun Zhou, Mingce Long, Weimin Cai and Jun Cai, "Synthesis and photocatalytic performance of the efficient visible light photocatalyst Ag–AgCl/$BiVO_4$," *Journal of Molecular Catalysis A: Chemical*, vol. 353–354, pp. 22-28, 2012.

56. Maria J. Lundqvist and Leif A. Eriksson, "Hydroxyl Radical Reactions with Phenol as a Model for Generation of Biologically Reactive Tyrosyl Radicals," *The Journal of Physical Chemistry B*, vol. 104, no. 4, pp. 848-855, 2000.

57. Chunde Wu, Xinhui Liu, Dongbin Wei, Jinchu Fan and Liansheng Wang, "Photosonochemical degradation of Phenol in water," *Water Research*, vol. 35, no. 16, pp. 3927-3933, 2001.

58. Faming Jin, Johannes Leitich and Clemens von Sonntag, "The superoxide radical reacts with tyrosine-derived phenoxyl radicals by addition rather than by electron transfer," *Journal of the Chemical Society, Perkin Transactions 2*, no. 9, pp. 1583-1588, 1993.

59. Xiao-yan Li, Yu-hong Cui, Yu-jie Feng, Zhao-ming Xie and Ji-Dong Gu, "Reaction pathways and mechanisms of the electrochemical degradation of phenol on different electrodes," *Water Research*, vol. 39, no. 10, pp. 1972-1981, 2005.

60. Janet M. Kesselman, Gary A. Shreve, Michael R. Hoffmann and Nathan S. Lewis, "Flux-Matching Conditions at TiO_2 Photoelectrodes: Is Interfacial Electron Transfer to O_2 Rate-Limiting in the TiO_2-Catalyzed Photochemical Degradation of Organics?," *The Journal of Physical Chemistry*, vol. 98, no. 50, pp. 13385-13395, 1994.

61. Baifu Xin, Zhiyu Ren, Haiyuan Hu, Xiangyu Zhang, Chunlei Dong, Keying Shi, Liqiang Jing and Honggang Fu, "Photocatalytic activity and interfacial carrier transfer of Ag–TiO_2 nanoparticle films," *Applied Surface Science*, vol. 252, no. 5, pp. 2050-2055, 2005.

62. Baifu Xin, Zhiyu Ren, Peng Wang, Jia Liu, Liqiang Jing and Honggang Fu, "Study on the mechanisms of photoinduced carriers separation and recombination for Fe^{3+}–TiO_2 photocatalysts," *Applied Surface Science*, vol. 253, no. 9, pp. 4390-4395, 2007.

SECTION III: HETEROSTRUCTURE ENHANCED BISMUTH-BASED PHOTOCATALYSIS

Chapter 6 MoS_2 Quantum Dots-Interspersed Bi_2WO_6 Heterostructures for Visible Light-Induced Detoxification and Disinfection

Xiangchao Meng, Zizhen Li, Haoming Zeng, Jie Chen and Zisheng Zhang

Applied Catalysis B: Environmental 210 (2017), 160-172

Abstract

MoS_2 Quantum dots-interspersed Bi_2WO_6 heterostructure is fabricated for photocatalytic applications for the first time. It exhibits enhanced visible light-driven photocatalytically detoxification and disinfection in wastewater compared to bare Bi_2WO_6 and MoS_2. MoS_2 quantum dots as a co-catalyst applied in photocatalysis oxidation possesses multiple merits: (1) noble-metal-free; (2) high mobility of photogenerated charge carriers; (3) high adsorption capacity and (4) improved capture capacity of visible light photons. Electron-hole separation rate which is a critical step for an efficient photocatalysis is greatly improved via the built-in electric field of p-n heterostructure and the quantum dots interspersed on the surface. This work shed a light on loading MoS_2 quantum dots as a co-catalyst on a support aiming to significantly improve its photocatalytic performance in organic pollutants degradation and bacteria inactivation.

6.1 Introduction

Bismuth-based (Bi-based) semiconductor photocatalysis has been extensively investigated as an advanced oxidative process in environmental remediation [1, 2]. Compared to other metal oxides, the valence bands of Bi-based semiconductors consist of the hybrid orbits of not only O 2p but also the Bi 6s. The well-dispersed Bi 6s orbits facilitate the mobility of photogenerated charge carriers, and decrease the band gap value as well [3, 4]. As a result,

Bi-based semiconductors are usually visible light-responsive owing to the narrow band gap, such as Bi_2O_3, Bi_2S_3, Bi_2MO_6 (M = Cr, Mo and W), $BiVO_4$, and BiOX (X=Cl, Br and I).

Among Bi-based semiconductors, Bi_2WO_6 is reported as an effective photocatalysts for detoxification in wastewater as well as polluted air [5-8]. However, the flat energy band of Bi_2WO_6 implies the low mobility of charge carriers on either valence band or conduction band. And the charge carriers are easily recombined before react with adsorbed species to generate oxidative species. Moreover, the band gap of Bi_2WO_6 is measured as about 2.70 eV, indicating only irradiations with wavelength below 460 nm are able to trigger this photocatalysis process. To improve the capacity of capturing visible light-photons for Bi_2WO_6 will be another issue. Approaches mainly include metal/non-metal doping [9, 10] and coupling co-catalyst with narrow band gap [11, 12]. The synergy effect of establishment of heterostructure between Bi-based semiconductor and other semiconductors may improve the photocatalytic activity through facilitating the separation of photogenerated charge carriers forced by the built-in electric field [4, 13, 14]. Various Bi_2WO_6 based heterostructures were reported, such as BiOBr-Bi_2WO_6 by our group [14], Bi_2O_3-Bi_2WO_6 [12].

Recently, alternative noble-metal-free co-catalysts such graphene, g-C_3N_4 and MoS_2 have been rapidly developed and applied in photocatalysis [15-17]. These conductive two-dimensional (2D) nanosheets not only serve as a support to prevent agglomeration of the photocatalysts, but also provide charge-transfer channels with relatively high mobility to improve the photogenerated charge carriers separation efficiency [18]. Two-dimensional MoS_2 is supposed to be a promising candidate to facilitate organic degradation as a co-catalyst as well. However, it is reported that the active sites for 2D MoS_2 only located along its edges, while the basal surface of MoS_2 is catalytically inert [19]. Moreover, the semiconducting MoS_2 exhibits limited mobility for charge transport [20]. Even though two-dimension MoS_2-Bi_2WO_6 core-shell heterostructure was also reported with enhance photocatalytic activity in degradation of methylene blue[21]. That might be attributed to the enhanced adsorption capacity by introduction of MoS_2 sheets on Bi_2WO_6. The MoS_2-Bi_2WO_6 direct heterojunctions were also fabricated by one-step hydrothermal method and performed enhanced visible-light-driven photocatalytic activity [22]. However, the large size of MoS_2 may not overcome the shortages as mentioned above that the edges of MoS_2

are inactive and the enhancement extent is limited. It is reported that MoS_2 quantum dots (QDs) can be prepared by a bath sonication process [23]. MoS_2 QDs as a co-catalyst may overcome these above mentioned limitations, especially the active sites only located at the edges. Additionally, QDs combined on photocatalysts may provide a convenient approach to direct the flow of the photogenerated charge carriers, so as to improve theirs separation efficiency [24, 25].

In this work, we demonstrate that the fabrication of MoS_2 QDs interspersed Bi_2WO_6 heterostructures via a simple bath sonication method. The MoS_2-Bi_2WO_6 composites exhibited excellent photocatalytic detoxification as well as disinfection in wastewater compared to bare Bi_2WO_6 and MoS_2. As far as we know, this is the first example of using MoS_2 QDs as a co-catalyst for photocatalytic applications.

6.2 Experimental

6.2.1 Chemicals

All chemicals were purchased from Fisher Scientific and used as received of reagent or higher purity, unless otherwise mentioned.

6.2.2 Synthesis of layered MoS_2 nanoflowers

The layered MoS_2 nanoflowers were synthesized via a facile hydrothermal method [26]. Typically, 1.20 g of $Na_2MoO_4 \cdot 2H_2O$ and 1.60 g of NH_2CSNH_2 were mixed together with 0.60 g of oxalic acid in 80 mL Deionized Distilled Water (DDW) termed as solution A. Solution A was magnetically stirred for 30 min, and then it was transferred into a 100-mL Teflon-lined stainless steel autoclave (Parr Instrument Company). The autoclave was heated and maintained at 180°C for 24 h, and then naturally cooled down to room temperature. The black precipitates were separated by vacuum filtration and washed twice with DDW and once with ethanol. At last, the black precipitates were dried at 60°C for 12 h before collected for further use.

6.2.3 Synthesis of hierarchical Bi_2WO_6

Hierarchical Bi_2WO_6 samples were synthesized through a template-free hydrothermal method [4]. In a typical process, 0.97 g of $Bi(NO_3)_3 \cdot 5H_2O$ were dissolved in 30 mL acetic acid, termed as solution B, which was magnetically stirred for 20 min. Then, 0.33 g of

Na_2WO_4•$2H_2O$ were dissolved in 50 mL DDW, termed solution C. Solution C was dropwise added into solution B and magnetically stirred for another 20 min before transferring into a 100-mL Teflon-lined stainless steel autoclave. The autoclave was heated at 180°C for 20 h. After the autoclave was naturally cooled down to room temperature, the precipitates were separated by vacuum filtration and washed twice with DDW then once by ethanol. The precipitate was dried at 60°C for 12 h before collected for further use.

6.2.4 Synthesis of MoS_2 QDs interspersed-Bi_2WO_6 composites

A highly dispersed suspension of MoS_2 QDs interspersed on hierarchical Bi_2WO_6 was synthesised by a simple bath sonication method [23], as schematically depicted in Fig. 6.1. Specifically, 0.30 g of Bi_2WO_6 and a designate amount of MoS_2 were dissolved in 40 mL ethanol. The above suspension was ultrasonicated for 2 h and then magnetically stirred until the solvent was naturally evaporated. The product was dried at 60°C for 12 h before collected. Composites of 0.5, 1.0, 1.5 and 2.0% MoS_2 interspersed-Bi_2WO_6 composites were prepared.

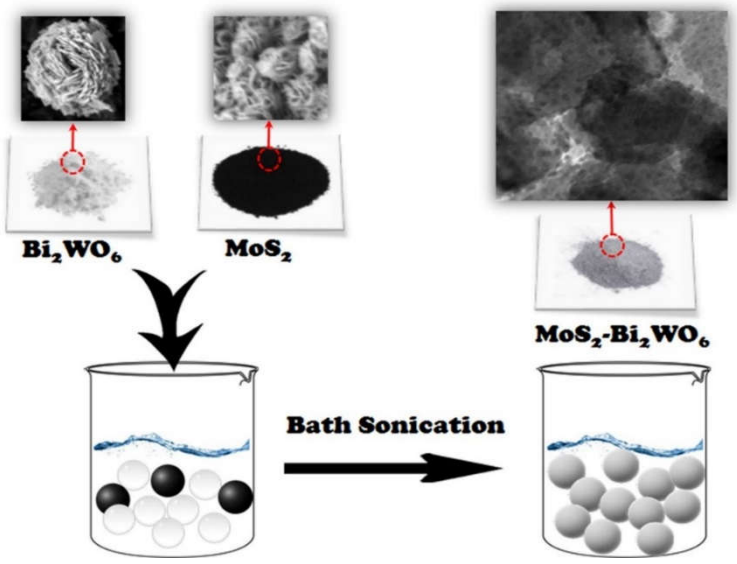


Figure 6.1 Schematic preparation of MoS_2 QDs-interspersed Bi_2WO_6 composites via a bath sonication method.

6.2.5 Characterization

Crystal structures were measured on a Rigaku Ultima IV Diffractometer with Cu Kα radiation (λ = 0.15418 nm) at 40 kV and 44 mA. Surface composition and chemical states

were performed on a XSAM-800 X-ray Photoelectron Spectroscope (XPS). Morphologies were investigated by a field-emission scanning electron microscope (FE-SEM, JEOL JSM-7500F) and a transmission electron microscope (TEM, JEM-2100F). The specific surface area, pore volume and average pore size were obtained from N_2 sorption isotherms at 77 K, using automatic adsorption apparatus and measurement systems (ASAP 2020, Micromeritics and Nova 4200E, Quantachrome). The Brunauer, Emmett and Teller (BET) surface area of the samples were calculated using multi-point estimation. The pore volumes were calculated using the volumes of adsorbed N_2 at p/p_o = 0.977. Ultraviolet-visible diffuse reflectance spectra (DRS) were detected using a Thermo Evolution 300 spectrophotometer. Electrochemical properties of prepared samples were performed on a CHI 604E electrochemical analyzer (CH Instruments Inc., USA) with a platinum wire as a counter electrode, a calomel reference electrode and a working electrode. The working electrode was composed of indium tin oxide (ITO, 75 × 25 × 1.1 mm, 15 - 25 Ω, Sigma-Aldrich Canada Co.), glass coated with the prepared samples. The electrochemical impedance spectroscopies (EIS) were recorded with frequencies in the range of 0.01 – 1000000 Hz and a sinusoidal wave of 5 mV. The electrolyte was Na_2SO_4 with a concentration of 0.50 mol/L.

6.2.6 Photocatalytic activity tests

6.2.6.1 Adsorption and degradation of Rhodamine B (RhB)

The adsorption capacity for Bi_2WO_6, MoS_2 and MoS_2-Bi_2WO_6 composites were measured via adsorbing RhB in dark. In each test, 0.10 g of photocatalysts were mixed with 100 mL of RhB solution with initial concentration of 10 mg/L (catalysts dosage: 1.0 g/L). The suspension was magnetically stirred for 60 min and temperature of the reacting system was kept at 20°C. Aliquots were drawn at every 10 min. After centrifuging at 13,000 rpm for 5 min, the supernatant was analyzed using a spectrometer (Genesys 10 UV) with wavelength fixed at 554 nm which is the characteristic peak location of RhB. The concentration of RhB can be determined based on Beer-Lambert Law. The sorption capacity, q_t [$mg_{RhB}/g_{cat.}$] of the composite powders can be computed by Equation 1 as follows,

$$q_t = \frac{(c_o - c_t) \times V}{m} \qquad \textit{Equation 1}$$

where c_o and c_t [mg/L] are the solution concentrations of RhB at initial and time t (min), respectively; V [L] and m [g] represent the volume and the catalyst weight in the reacting system.

The photocatalytic activity of prepared sample was investigated with regards to RhB under visible light irradiation. Specifically, a 500-mL beaker with a cooling jacket to maintain the temperature at 20°C served as the reactor. The visible light source was a 300-W halogen tungsten projector lamp (Ushio) with a UV cut-off (Kenko Zeta, transmittance > 90%) to filter out the incident irradiation with wavelength below 410 nm. Intensity of irradiation on the surface of the solution was measured to be 1.1×10^{-2} Einsteins m^{-2} s^{-1} through a quantum meter (Biospherical QSL-2100, $400 < \lambda < 700$ nm). In each batch, 0.10 g of photocatalysts were added into 100 mL of RhB solution with concentration of 10 mg/L. The lamp turned on after 30 min, and the test carried out lasted for 90 min. Aliquots were taken and tested with same procedure in the adsorption test. Total organic carbon (TOC) was measured by an Apollo 9000 TOC analyzer equipped with a Non-Dispersive Infra-Red (NDIR) detector. The combustion temperature was fixed at 750 °C. Samples taken at time of 0, 30, 60 and 90 min were investigated.

Reusability of 1.0% MoS_2-Bi_2WO_6 composite was tested with regard to RhB for four runs under visible light irradiation. Typically, photocatalysts were separated out by centrifugation between two runs and then remixed with fresh RhB solution with initial concentration of 10 mg/L in the following experiment without a wash.

6.2.6.2 Temporal course of inactivation

Wild-type *Escherichia coli* (*E. coli*) K-12 (TG1 strain), a non-pathogenic and common model, was used as a standard strain for the bacterial inactivation studies. All inactivation trials were performed in triplicate, and all materials were sterilized for 20 min at 121°C prior to use. Cell culture were prepared by growing *E.coli* K-12 (TG1) aerobically in Luria-Bertani medium (Difco LB broth, Miller; composition: 10 g/L tryptone, 5 g/L yeast extract and 10 g/L NaCl) on a rotary shaker at speed of 250 rpm and temperature of 37°C for 18 h until the stationary phase was reached. The cell concentration was determined by serial

dilution and plating. For the enumeration, 25 μL of cell solution were spread on LB agar plates and incubated at 37°C for 18h. Standard plate counts for viable and cultivable bacteria was used for enumeration [27]. In each temporal course of inactivation, 0.10 g of photocatalysts were dispersed in 100 mL of saline solution containing 10^6 CFU (colony forming units)/mL *E.coli* K-12 (TG1). After magnetically stirring for 30 min in dark, the suspension was illuminated for 60 min. The temperature of the system was kept at 20°C using a water bath. Aliquots were drawn, and serially diluted in saline solution and spread onto LB agar plates. The plates were then incubated at 37°C for 18 h and enumerated. To study the bacterial regrowth after photocatalysis, treated waters are stored for 3 days. The number of bacteria was also enumerated as mentioned above.

6.2.7 Electronic structure calculation

The quantum-mechanical calculations were performed on the basis of density functional theory (DFT) [28]. The generalized gradient approximation (GGA) was applied to exchange-correlation effects. The open access software Quantum ESPRESSO was used, which utilizes pseudopotentials to describe electron-ion interactions and represents electronic wave functions using a plane-wave basis set [29]. The kinetic energy cut-off was set to 300 eV.

6.3 Results and discussions

6.3.1 Crystal structure and surface composition analysis

The XRD patterns (Fig. 6.2) for pure Bi_2WO_6 agree well with an orthorhombic crystal structure (space group: pbca (61), PDF card number 39-0256) [30]. All of the characteristic peaks were identified. For pure MoS_2, all the diffraction peaks can be indexed to the hexagonal phase of MoS_2 (space group: P-6m2 (187), PDF card number: 24-0513) [31]. However, the weak peaks for MoS_2 suggest its poor crystallinity. Major peaks at 2θ of 14.4°, 32.6° and 58.2° may be attributed to the (002), (100) and (110) planes of MoS_2. For MoS_2-Bi_2WO_6 composites, however, no peaks for MoS_2 were found due to its low contents in the composites. And no peaks shift for Bi_2WO_6 were observed, indicating the introduction of MoS_2 has negligibly affected the crystal structure of Bi_2WO_6. The Crystal sizes and lattice parameters were also calculated (Table 6.1). The crystal size for pure Bi_2WO_6 is 211 Å, that for MoS_2 doped Bi_2WO_6 is in the range of 210-214 Å. Lattice

parameters for pure Bi_2WO_6 are a = 5.4499, b = 16.3616, c = 5.4842, and the introduction of MoS_2 negligibly influence the lattice parameters for pure Bi_2WO_6. These results indicate that loading of MoS_2 quantum dots may not destroy the crystal structure of Bi_2WO_6 during the bath sonication process, and MoS_2 were possibly just resting on the surface as opposed to covalently anchoring to the lattice of Bi_2WO_6 [32].

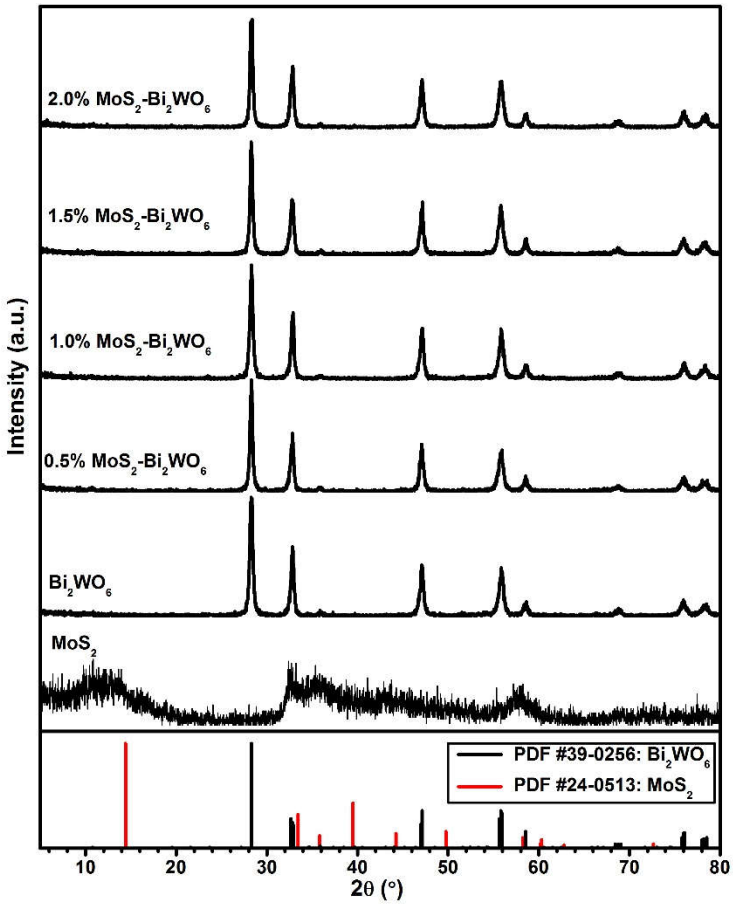


Figure 6.2 XRD patterns of prepared samples, and standard XRD patterns for pure Bi_2WO_6 (PDF card # 39-0256) and MoS_2 (PDF card # 24-0513).

Table 6.1Crystal size and lattice parameters of prepared samples.

Composites	Crystal size (Å)	Lattice parameters (Å)		
		a	b	c
Bi_2WO_6	211	5.45	16.36	5.48
0.5%MoS_2-Bi_2WO_6	212 (+0.47%)	5.45 (+0.07%)	16.40 (+0.22%)	5.47(-0.34%)
1.0%MoS_2-Bi_2WO_6	210 (-0.47%)	5.45 (+0.04%)	16.42 (+0.33%)	5.45 (-0.63%)
1.5%MoS_2-Bi_2WO_6	213 (+0.95%)	5.46 (+0.15%)	16.35 (-0.05%)	5.47 (-0.35%)
2.0%MoS_2-Bi_2WO_6	214 (+1.42%)	5.46 (+0.10%)	16.38 (+0.13%)	5.47 (-0.19%)

To further probe the chemical states and composition of MoS_2-Bi_2WO_6 composites, XPS was employed and results including a survey spectrum and high-resolution orbit scans were shown in Fig. 6.3. All spectra were calibrated with C 1s, the binding energy of which is fixed at 284.6 eV. In the XPS survey spectrum (Fig. 6.3a), all component elements (*i.e.* Bi, W, O, Mo and S) for MoS_2-Bi_2WO_6 composites were detected and identified, no impurity peaks were found. In the high-resolution Mo 3d orbit scan (Fig. 6.3b), two peaks located at binding energies of 226.5 and 230.0 eV may be assigned to Mo 3d doublets, namely $3d_{3/2}$ and $3d_{5/2}$ [33]. A small peak at binding energy of 226.3 eV may be assigned to S 2s. For the high-resolution scan of S 2p orbit, two doublets peaks were observed. Specifically, peaks located at binding energy of 164.1 eV may be attributed to Bi $4f_{5/2}$ with a trivalent oxidation state. Two small doublets adjacent to Bi $4f_{5/2}$ at binding energy of 167.0 and 165.8 eV can be assigned to S $2p_{1/2}$ and S $2p_{3/2}$ respectively [34]. The Mo 3d and S 2p peaks are located the characteristic of MoS_2 with no detectable indication of Mo oxidation states other than Mo^{4+} or of any sulfur species other than sulfide [35]. With increase the content of MoS_2 in the composite, the peak intensities for Mo and S are increased. The [S]/[Mo] ratio can be estimated via Equation 2 as about 2.4, which is close to the stoichiometric value for MoS_2. It can concluded the presence of MoS_2 on the surface of Bi_2WO_6 with the formula of MoS_2.

$$c_i = \frac{\frac{A_i}{q_i}}{\left[\sum_{i=1}^{n} \frac{A_i}{q_i}\right]} \qquad \textit{Equation 2}$$

where c_i are concentrations of specie i, A_i are XPS peak areas and q_i are experimental photoionization cross sections as given by Wagner [36] for various elements present on the surface.

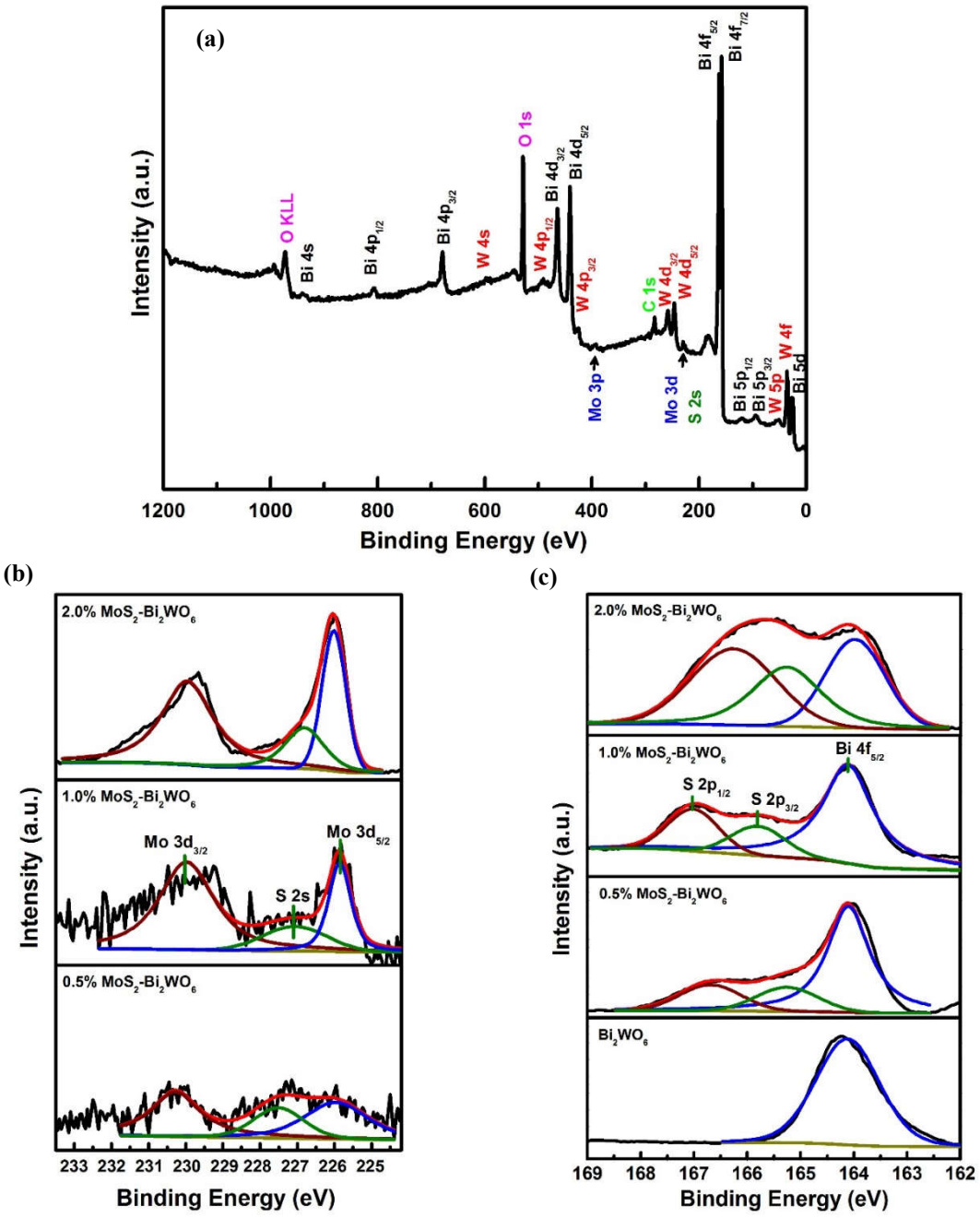


Figure 6.3 XPS spectra of MoS_2-Bi_2WO_6 composites: (a) survey, (b) Mo 3d and (c) S 2p.

6.3.2 Morphologies

The morphologies and microstructure of pure Bi_2WO_6, MoS_2 and MoS_2-Bi_2WO_6 composites were investigated by SEM and TEM. The SEM image of pure Bi_2WO_6 shows hierarchical microsphere microstructures with diameters in the range of 1 - 3 μm (Fig. 6.4a). The thickness of the square plates (Fig. 6.4d) composed of the microsphere in the nano scale. The SEM image of pristine MoS_2 (Fig. 6.4b) exhibits microflower morphology. However, for MoS_2-Bi_2WO_6 (Fig. 6.4c), nanoplates were randomly stacked together. The destruction of the microflower may be resulted from the effect of sonication during the bath sonication treatment. In the TEM image of MoS_2-Bi_2WO_6 composite (Fig. 6.4e), two-dimension nanoplates were also observed with side length of 100 – 400 nm. In the magnified TEM image of MoS_2-Bi_2WO_6 in Fig. 6.4f, well-dispersed quantum dots (QDs) can be found on the nanoplates. Diameter size distribution of the QDs was illustrated in the inset of Fig. 6.4f, they are in the range 1 - 9 nm and 90% of them with diameter of 1.8 – 5.6 nm. The lattice can be observed (Fig. 6.4f). Distance between two planes was measured as about 0.37 nm, which may be assigned to the (111) direction of Bi_2WO_6 based on the PDF card (#39-0256) [4].

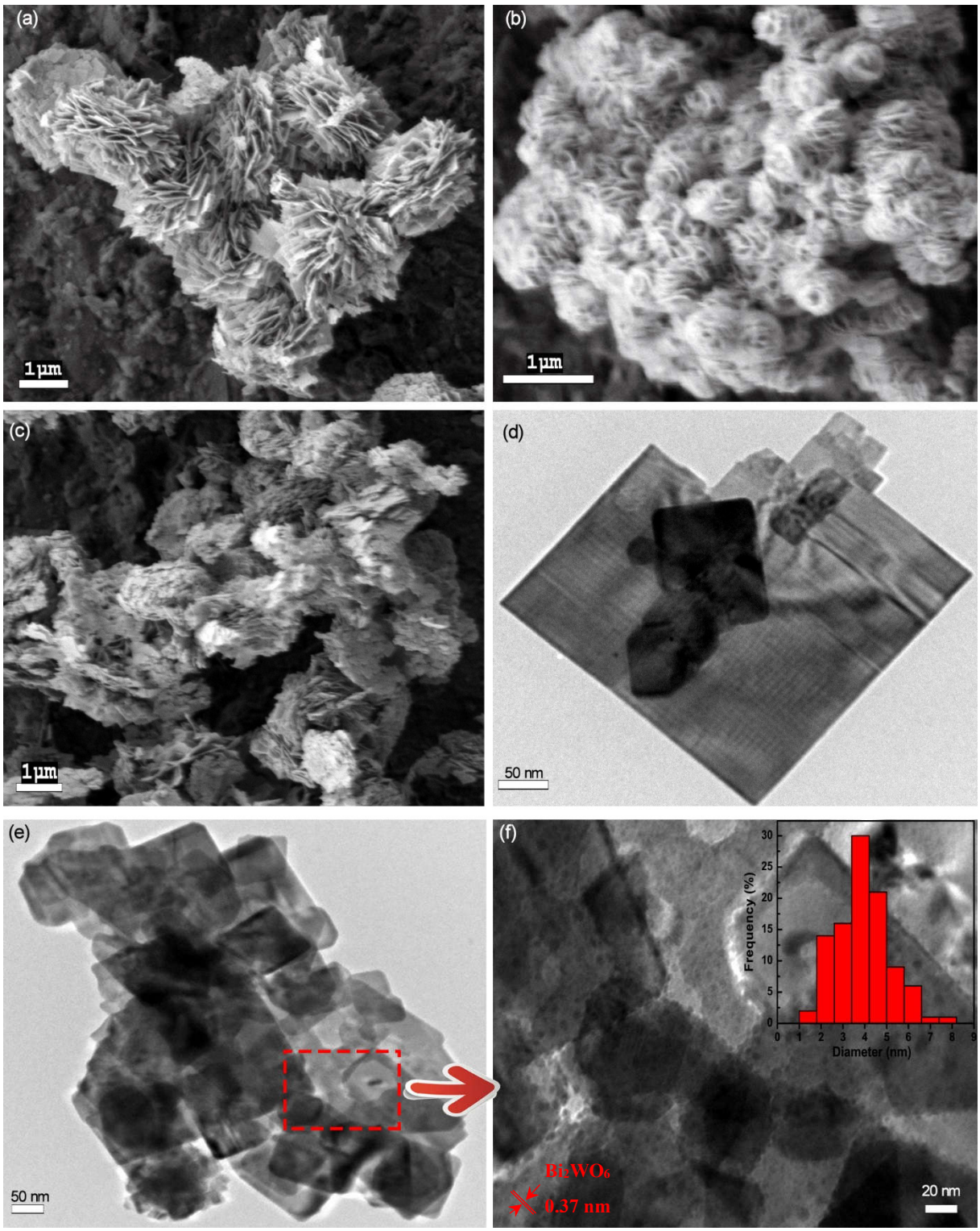


Figure 6.4 SEM images of (a) pure Bi_2WO_6, (b) pure MoS_2 and (c) MoS_2-Bi_2WO_6 composites; and TEM images of (d) pure Bi_2WO_6 and (e, f) MoS_2-Bi_2WO_6 composites.

6.3.3 UV-Vis diffuse reflectance spectra

Optical properties of Bi_2WO_6, MoS_2 as well as MoS_2-Bi_2WO_6 composites, were characterized by DRS in the range of 200 – 700 nm. In Fig. 6.5, the band gap absorption edge of Bi_2WO_6 is around 450 nm, suggesting Bi_2WO_6 is visible light-responsive. MoS_2 almost exhibits complete adsorption in both UV and visible light region, owing for its narrow band gap. Notably, with introduction of MoS_2, the absorption intensity in the visible light region was boosted. Upon increasing the loading amount of MoS_2 in the composite, the absorption intensity in the visible light region was gradually improved compared to the bare Bi_2WO_6. The bandgap (E_g) of the semiconductors can be calculated by the classical Tauc approach as shown in Equation 3:

$$\alpha E_{photon} = K(E_{photon} - E_g)^{\frac{n}{2}} \qquad \textbf{\textit{Equation 3}}$$

where $E_{photon} = hv$; α, K, E_g, n, h and v respectively represent the absorption coefficient, constant for semiconductor (usually equal to 1), bandgap energy, constant for semiconductor depending on the type of the band gap (direct transition: n = 1; indirect transition: n = 4, for Bi_2WO_6, n = 1), Planck constant, and irradiation frequency [37]. Plots of αE_{photon} *vs* E_{photon} were illustrated in the inset of Fig. 6.5. Band gap for pure Bi_2WO_6 was about 2.70 eV. Comparatively, Band gaps for 0.5, 1.0, 1.5, and 2.0% MoS_2-Bi_2WO_6 composites were 2.62, 2.60, 2.52 and 2.50 eV, respectively. This result indicates the band gap of MoS_2-Bi_2WO_6 was slightly narrowed compared to bare Bi_2WO_6. The red-shift in the DRS spectra for MoS_2-Bi_2WO_6 may also be resulted from the narrowed band gap.

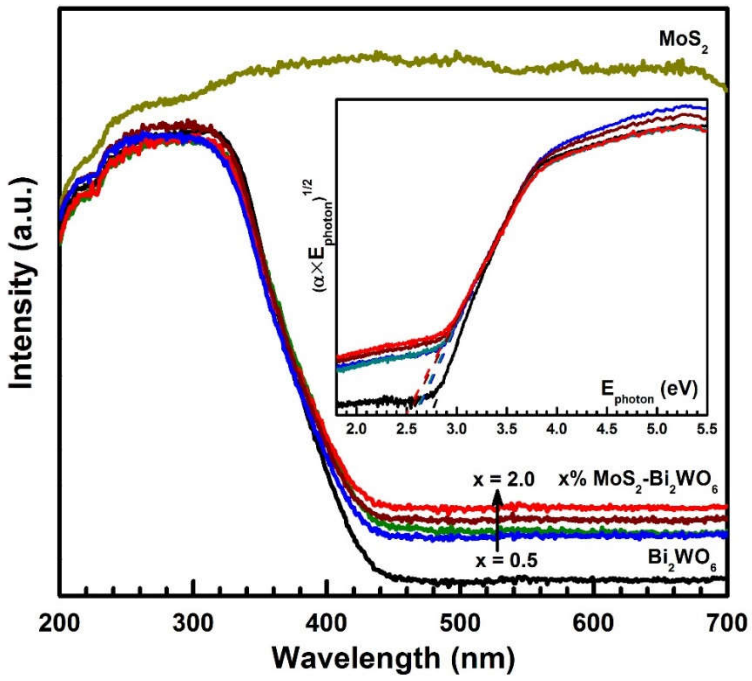


Figure 6.5 UV-Vis Diffuse Reflectance spectra and the plots of $(\alpha \times E_{photon})^{1/2}$ vs. E_{photon} (inset) of pure Bi_2WO_6, MoS_2 and MoS_2-Bi_2WO_6 composites.

6.3.4 N_2 sorption isotherms

N_2 sorption isotherms are measured for pure Bi_2WO_6, MoS_2-Bi_2WO_6 and MoS_2 and depicted in Fig. 6.6. All three isotherms are attributed to type IV physisorption isotherms [38, 39]. Characteristic features of this type isotherm are its hysteresis loop associated with capillary condensation occurring in mesopores, and the limiting uptake in the range of high relative pressure. Hysteresis loop is a H3 loop, which mainly resulted from plate-like particles giving rise to slit-shaped pores [38-40]. This result reveals the hierarchical microsphere microstructures were observed in the SEM images. The specific surface area as well as pore volume calculated from the isotherms are summarized in Table 6.2. The specific surface area of pure Bi_2WO_6 is as small as 9.4 m^2/g. Pure MoS_2 possess high specific surface area of 72.0 m^2/g, which results in the high adsorption capacity of pure MoS_2. Upon introduction of MoS_2, the specific surface was slightly increased, while the pore volume was slightly decreased. The decrease in pore volume via loading MoS_2 on Bi_2WO_6 may be caused by the MoS_2 quantum dots blocked the slit-like pores. The

improvement of specific surface area via loading MoS_2 on Bi_2WO_6 may increase the adsorption capacity of organic pollutants in water.

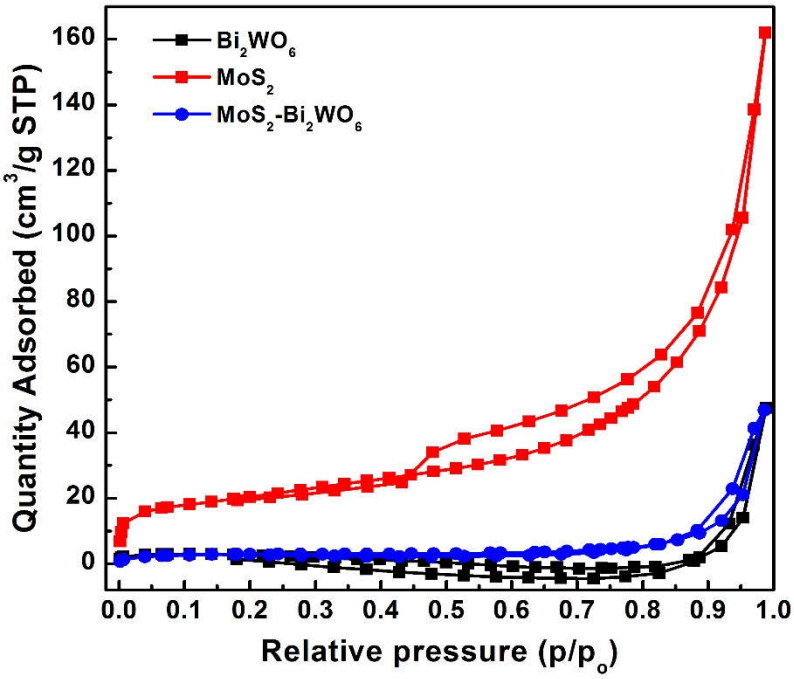


Figure 6.6 N_2 sorption isotherms for Bi_2WO_6, MoS_2-Bi_2WO_6 and MoS_2.

Table 6.2 Specific surface area and pore volume of Bi_2WO_6, MoS_2-Bi_2WO_6 and MoS_2.

Sample	S_{BET} (m^2/g)	Pore volume (cm^3/g)
Bi_2WO_6	9.4	0.074
MoS_2-Bi_2WO_6	10.5	0.073
MoS_2	72.0	0.253

6.3.5 Adsorption analysis

Adsorption kinetics are important for the description of solute uptake rate and for understanding dynamic sorption behavior of the system, and are strongly dependent on adsorbate-adsorbent interactions [41]. Adsorption equilibrium can describe the adsorption capacity of a material when a dynamic balance reached. The adsorption equilibrium and

kinetics modelling for prepared samples were plotted in Fig. 6.7. In Fig. 6.7a, the equilibrium sorption capacity (q_e) for MoS_2 is 82.6 mg/g. Even though this value is lower than that for activated carbon (Darco G60, 100 mesh, Sigma-Aldrich) which is 219.8 mg/g, it is still undoubtedly very impressive. When MoS_2 doped on Bi_2WO_6, q_e is gradually increased from 0.87 mg/g for pure Bi_2WO_6 to 2.25 mg/g for 2.0% MoS_2-Bi_2WO_6 composites. The improvement for Bi_2WO_6 in adsorption capacity when MoS_2 doped may be attributed to the high adsorption capacity of MoS_2. The adsorption kinetics can be described by a pseudo second-order model (Equation 4) [42]

$$\frac{dq_t}{dt} = k_2(q_e - q_t)^2$$
$$\Rightarrow \frac{t}{q_t} = \frac{1}{k_2 q_e^2} + \frac{1}{q_e} t \qquad \textit{Equation 4}$$

where k_2 is the equilibrium rate constant of pseudo second-order adsorption ($g_{adsorbent}$ $mg_{adsorbate}^{-1}$ min^{-1}). It should be notable that the fast adsorption process with high rate constant (k_2). k_2 for these three processes with pure Bi_2WO_6 and MoS_2 and MoS_2-Bi_2WO_6 were calculated via fitting the plots of t/q_t vs t (shown in Fig. 6.7b). All the R^2 are almost close to 1, indicating the high appropriateness of this model to describe this process. Specifically, in presence of Bi_2WO_6, MoS_2-Bi_2WO_6 and MoS_2, the k_2 for each process is shown in Fig. 6.7b. The adsorption rate Bi_2WO_6 is greatly improved when MoS_2 QDs loaded on its surface. The enhanced adsorption capacity and improved adsorption rate constant may be regarded as one of the reasons in the enhanced photocatalytic degradation process.

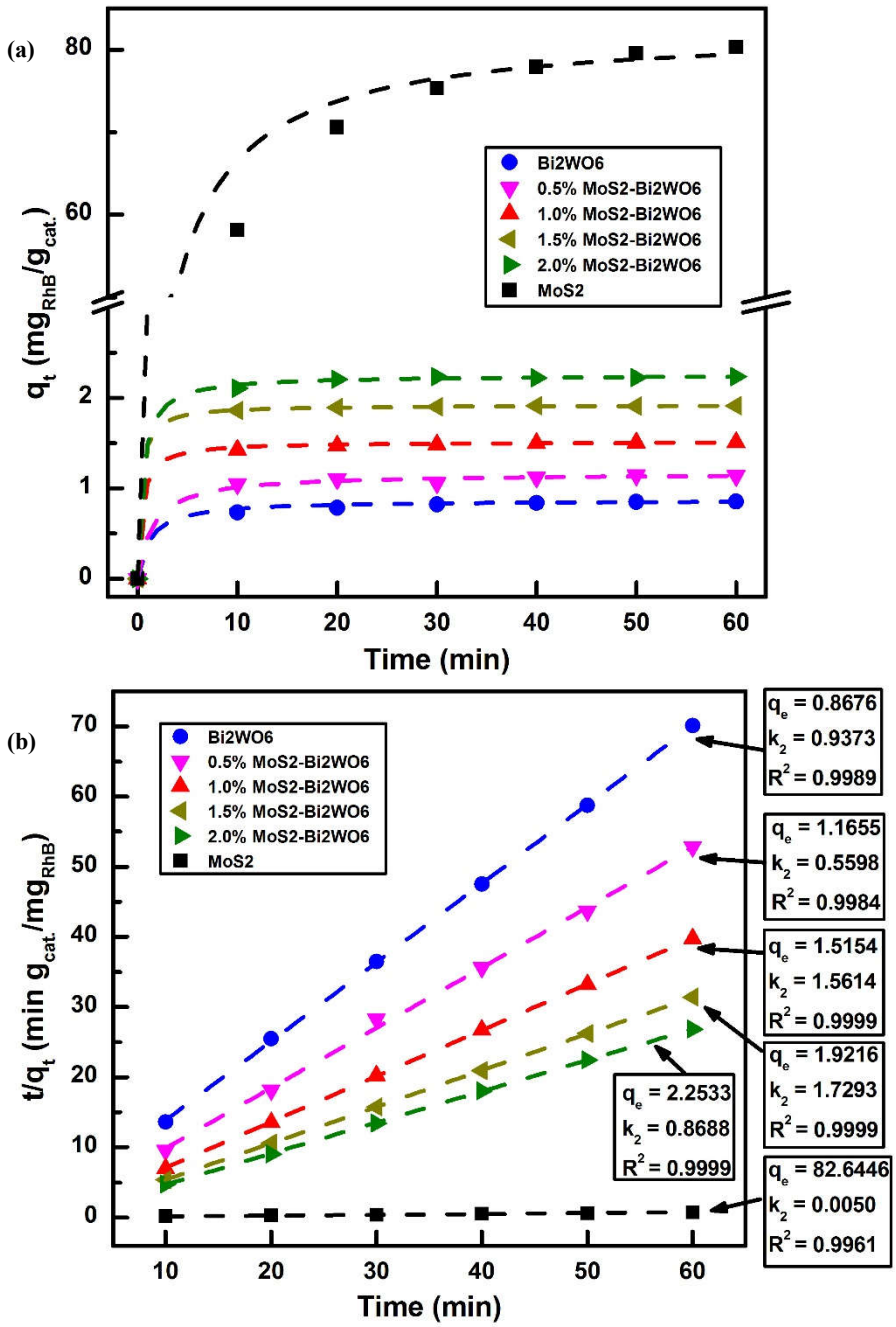


Figure 6.7 (a) RhB adsorption isotherms (b) Pseudo second-order modelling for pure Bi_2WO_6, MoS_2 and MoS_2-Bi_2WO_6 composites, where dash lines in (a) and (b) represent Pseudo second-order modelling results and fitting lines, respectively.

6.3.6 Photocatalytic activity test

6.3.6.1 Degradation of RhB

Activity screening for the prepared composites was performed by comparing the RhB removal observed using a photocatalysis process under visible light irradiation. The screening results are given in Fig. 6.8. Preliminary trials using pure MoS_2 indicated only 20% of RhB removal in 90 min under visible light irradiation, while a 99% RhB removal can be reached in 90 min when pure Bi_2WO_6 presented under visible light irradiation. A synergy effect is observed between MoS_2 and Bi_2WO_6 when they are coupled. With increase the content of MoS_2 from 0.5 - 1.0%, the RhB removal efficiency was significantly improved. Specifically, a complete RhB removal can be reached in 50 min in the presence of 1.0% MoS_2-Bi_2WO_6 under visible light. However, further increase the loading amount of MoS_2 to 1.5% and even 2.0%, the photocatalytic activity of RhB removal become worse, while it is still higher than that for using bare Bi_2WO_6. This phenomenon may be because the excessive MoS_2 QDs possibly blocked the irradiation reach the surface of Bi_2WO_6 so as to the decrease the production of strong oxidative species (*i.e.* h^+). To further explore the synergy effect, 1.0% of MoS_2 were mechanically mixed with Bi_2WO_6 and the photocatalytic removal result is shown in Fig. 6.8. It turns out the RhB removal efficiency in 90 min under visible light is lightly lower than that when using bare Bi_2WO_6. It confirmed that the MoS_2 QDs dispersed on the Bi_2WO_6 may form p-n heterojunctions. The establishment of heterojunction is benefit of photogenerated electrons/holes separation, and as a result, the photocatalytic activity may be improved [4, 13, 14].

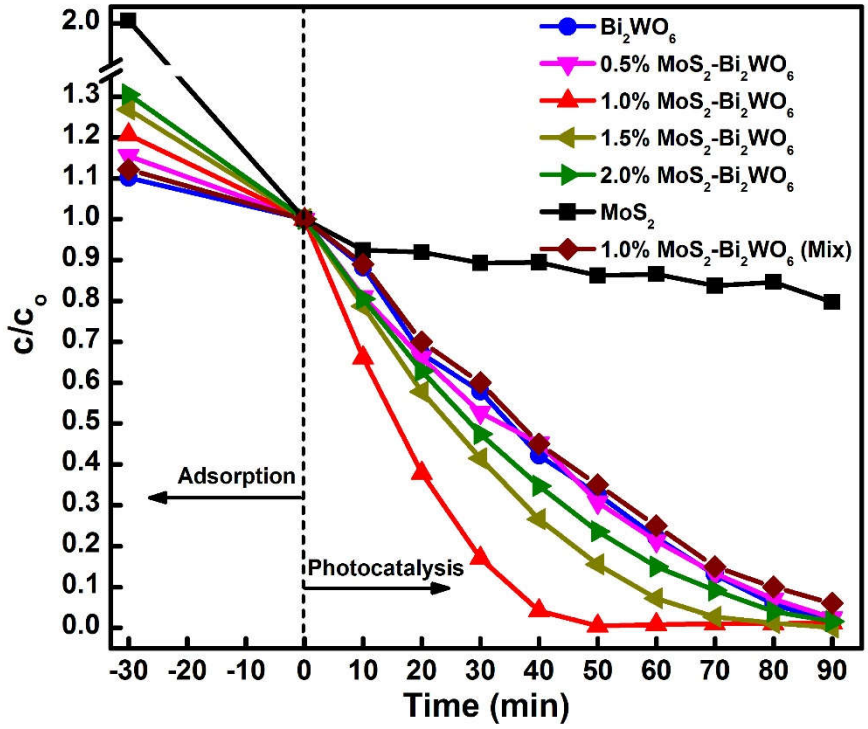


Figure 6.8 Photocatalytic degradation of RhB in the presence of prepared samples under visible light irradiation. (Catalyst dosages: 1g/L, initial concentration of RhB: 10 mg/L, Temperature: 20°C)

The photocatalytic kinetics of RhB degradation may be described using the Langmuir-Hinshelwood (L-H) model (Equation 4). The initial concentration of RhB in this work was set to approximately 10 mg/L (~2.1 × 10^{-5} mol/L), so (1+*Kc*) may be assumed to be equal to 1. Equation 5 may be expressed in the form of Equation 6, where *k'* is the pseudo first-order rate constant. Integration of Equation 6 then results in Equation 7.

$$r = -\frac{dc}{dt} = k\theta = \frac{kKc}{1+Kc} \qquad \textit{Equation 5}$$

$$-\frac{dc}{dt} = kKc = k'c \qquad \textit{Equation 6}$$

$$\ln\left(\frac{c_o}{c_t}\right) = k't \qquad \textit{Equation 7}$$

where r, c, t, k, θ, K, and k' represent reaction rate, concentration of RhB (c_o: initial concentration; c_t: concentration at time t), time, reaction rate constant, ratio of adsorbed RhB, adsorption constant apparent reaction constant respectively. The apparent constants (k') can be obtained by fitting the plots of $\ln(c_o/c)$ vs t, which are summarized in Table 6.3. For the processes with pure MoS_2 and Bi_2WO_6, the apparent reaction constant are 0.00421 and 0.01831 min^{-1} respectively. The introduction of MoS_2 greatly improved the reaction rate, and loading 1% of MoS_2 onto Bi_2WO_6 increased the constant up to 3 times that for bare Bi_2WO_6. However, excessive MoS_2 onto Bi_2WO_6 hinders further increase of reaction constant, while it still higher than bare Bi_2WO_6.

Table 6.3 Apparent reaction kinetic constants of photocatalytic processes with different samples.

Composites	**Bi_2WO_6**	**x% MoS_2-Bi_2WO_6**				**MoS_2**
		x = 0.5	**x = 1.0**	**x = 1.5**	**x = 2.0**	
k' (min^{-1})	0.01831	0.02114	0.05473	0.02841	0.02443	0.00421
$(k'- k'_{Bi2WO6})/k'_{Bi2WO6}$	0	0.15	2.00	0.55	0.33	-0.77
R^2	0.9876	0.9997	0.9845	0.9962	0.9982	0.9733

As for the step-by-step decomposition of RhB, it is explored by measuring the UV-Vis spectra for samples taken during the degradation process. As shown in Fig. 6.9, the degradation process may incorporate two competitive processes as reported, namely the de-ethylation process and destruction of the conjugated structure [9, 43]. Specifically, the blue-shift in wavelength from 554 to 498 nm for characteristic peaks may be attributed to the RhB were transformed into rhodamine with intermediate products such as *N, N, N'-Triethyl-Rhodamine* (TER); *N, N'-Diethyl-Rhodamine* (DER); *N-Ethyl-Rhodamine* (ER). In the first 40 min, the de-ethylation is the dominated process. After that, the destruction of aromatic ring becomes the dominated process. And rhodamine are degraded into small species such as CO_2, H_2O, which is corresponding the intensity decrease until to none of the characteristic peak for rhodamine. This indicates RhB may be completely degraded into small species in the presence of MoS_2-Bi_2WO_6 under visible light for 90 min. Further then, the total organic carbon concentration in the photodegradation of RhB by prepared samples was tested and illustrated in Fig. 6.10. It can be observed, the reduction rate of TOC is

much slower than that of the dye; only 6% and 1% of TOC was reduced in the presence of pure Bi_2WO_6 and MoS_2, respectively. It exhibited higher TOC reduction rate when MoS_2 loaded on Bi_2WO_6, and when the content of MoS_2 accounting for 1.0%, the mineralization yielded the maximum value of 42% in 90 min. This result keeps consistent with the decolorization result as shown in Fig. 6.9. Even though RhB were completely removed, it may be transformed into other organic compounds and longer time is required to achieve a complete photocatalytic mineralization of the dye.

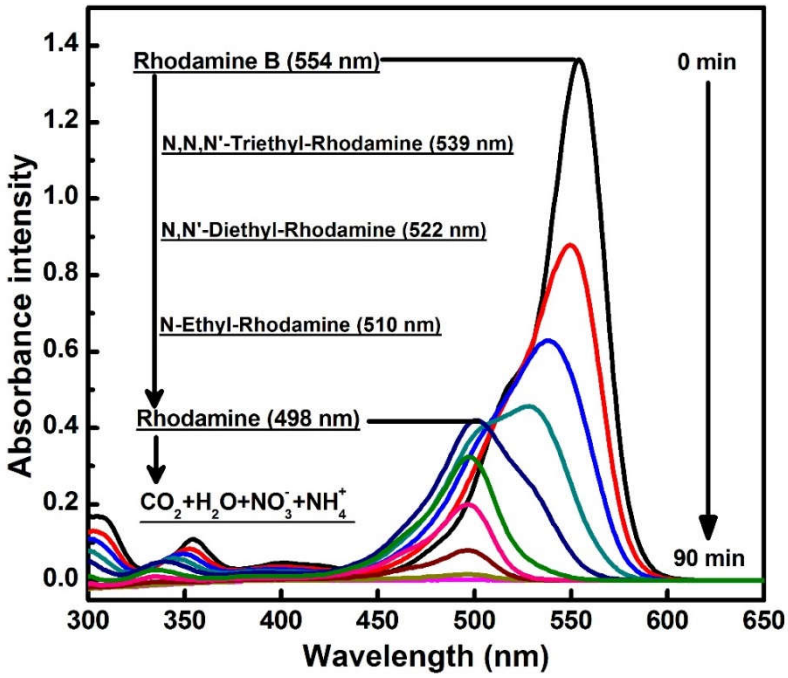


Figure 6.9 UV-Vis spectra of RhB samples taken during the photocatalytic process in the presence of 1.0% MoS_2-Bi_2WO_6.

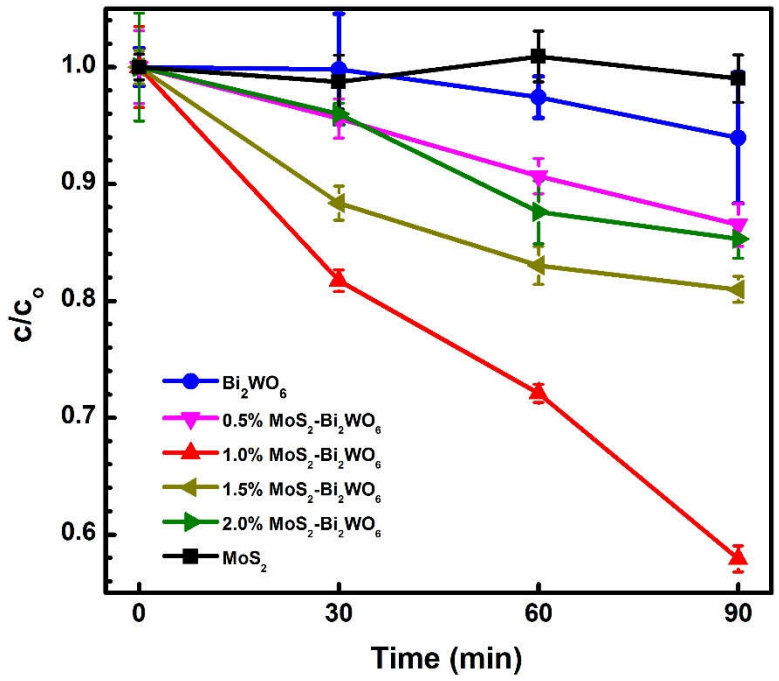


Figure 6.10 Changes in TOC concentration during the course of photocatalytic degradation of RhB in the presence of prepared samples under visible light irradiation. (Catalyst dosages: 1g/L, initial concentration of RhB: 10 mg/L, Temperature: 20°C)

The stability of MoS_2-Bi_2WO_6 composites in the degradation of RhB was investigated via recycling for four runs. The concentration profiles for each run are shown in Fig. 6.11. RhB were complete removed in 50 min for all runs, and a slight decrease was also observed in the initial degradation efficiency of RhB from the first run to fourth run. The decrease may be due to the catalysts loss in the processes of sampling and filtration. The negligible decrease in the photocatalytic performance with regard to RhB indicates the high stability of as-prepared MoS_2-Bi_2WO_6 composites.

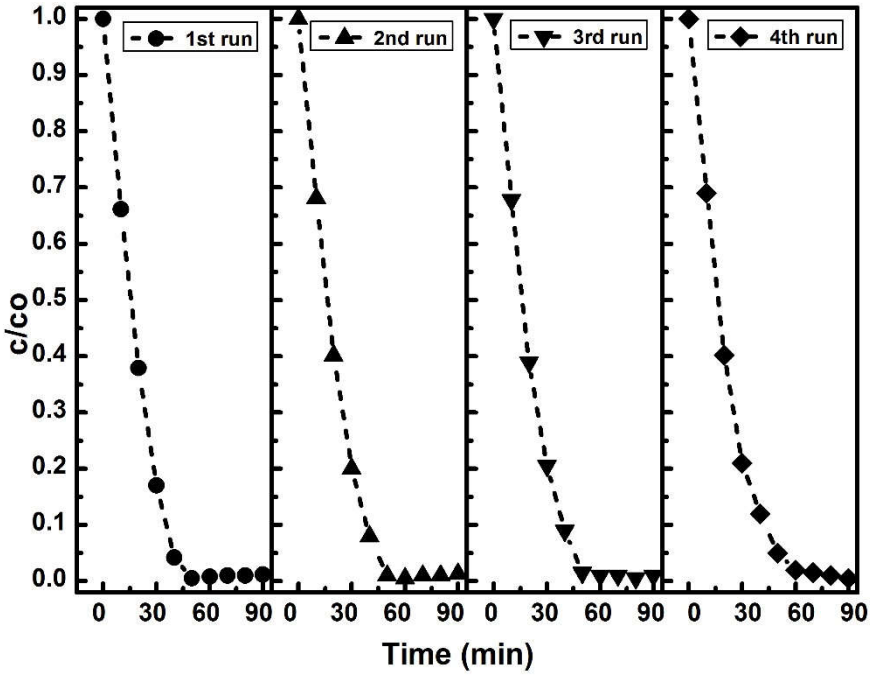
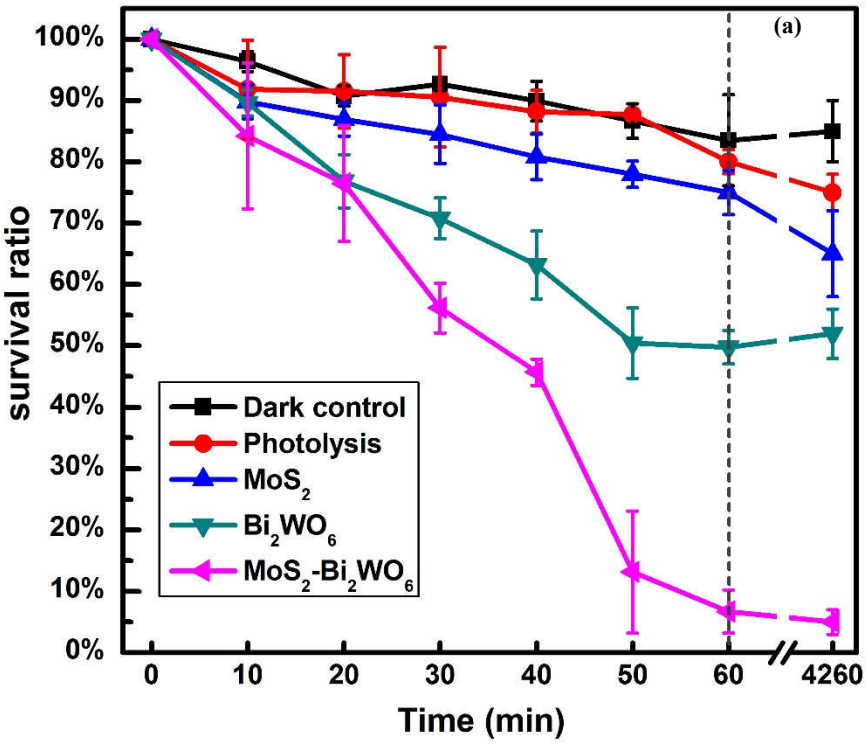


Figure 6.11 Recycling 1.0% MoS_2-Bi_2WO_6 composites for four runs in the degradation of RhB under visible light irradiation.

6.3.6.2 Temporal course of inactivation

The photocatalytic reactive oxidative species (ROS) interacting with the bacterial are able to result in the damage of the cell wall integrity, as the wall structural elements such as lipopolysaccharide, phosphatidylethanolcholine and peptidoglycan can be degraded by photocatalytic ROS [44, 45]. When the integrity of the cell wall is damaged, it will alter the outer membrane permeability to allow the penetration of deleterious substances. The loss of membrane structure and function can result in bacterial death. To evaluate the temporal course of inactivation due to photocatalysis, a standard plate count method was used to quantify viable and cultivable bacterial concentration changes with time upon exposure to various treatments. A comparison of survival curves for dark control, photolysis and the prepared samples are shown in Fig. 6.12. The final survival ratio of (80.0±1.96)% was observed for the photolysis run, which represent cell death without any antibacterial, adsorptive or photocatalysis. For the dark control process, about (83.5±7.41)% of *E.coli* are survived, and the inactivation may be attributed to the adsorptive of the photocatalysts, suggesting the photocatalysts itself is not toxic to *E.coli*. For pure MoS_2 and Bi_2WO_6 trials, final survival ratios of (75.0±3.59)% and (49.8±2.72)% respectively are

found. Via coupling MoS_2 with Bi_2WO_6, only (6.7±3.53)% of *E.coli* are survived owing for the enhanced photocatalytic effect. The significant decrease in population of *E.coli* in solution under visible light may be resulted from the improved separation efficiency of photogenerated electrical carriers after the formation of MoS_2-Bi_2WO_6 p-n heterojunction. The results are in good agreement with the photocatalytic degradation of RhB. The treated waters were stored for three days to investigate the bacterial regrowth. No apparent increase after 3-day storage suggests the bacteria were completely inactivated via the photocatalysis.



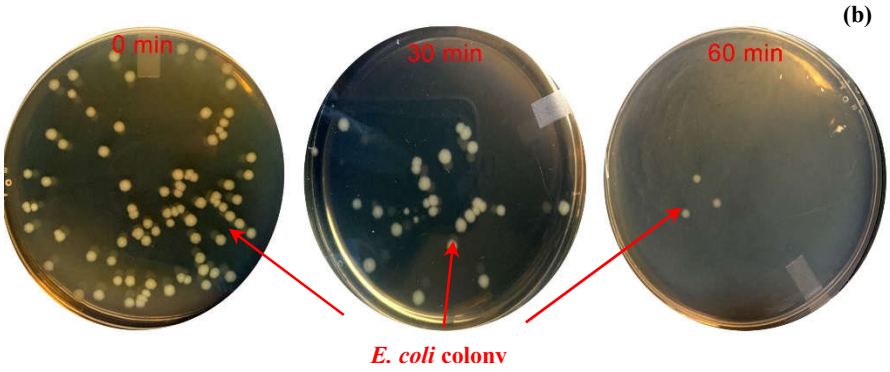


Figure 6.12 (a) Inactivation curves for dark control, photolysis and irradiated composite; (b) photos of E. coli colonies on an agar plate for samples taken and spread at different time during the photocatalytic disinfection in the presence of 1%MoS_2-Bi_2WO_6.

6.3.7 Electrochemical exploration

To explore the electrochemical property, especially the interface charge separation efficiency, electrochemical impedance spectroscopy (EIS) was measured and the EIS Nyquist plots of Bi_2WO_6 as well as MoS_2-Bi_2WO_6 composites under visible light irradiation are shown in Fig. 6.13. Only one semicircle is observed for each EIS Nyquist plot, indicates these photocatalysis process in the presence of prepared samples may be a simple electrode reaction. And the photogenerated electrical carriers transfer rate is able to be determined by their recombination rate [46, 47]. Based on plots shown in Fig. 6.13, the equivalent circuit and the fitted electrical parameters for each process are summarized in Table 6.4. Specifically, R_s is the resistance of the solution, R_{ct} is the resistance to electron transfer and CPE represents the constant phase element, which may be considered as a double-layered capacitor. The diameter of the arc in the EIS Nyquist plot determines the R_{ct}, where larger diameters resulting in higher values for R_{ct} and lower electrons transfer rate [48]. It can be observed, processes with MoS_2-Bi_2WO_6 exhibit smaller resistance compared to that of bare Bi_2WO_6 which is 328.5 kΩ. And when the introduction of MoS_2 with the quantity increase from 0.5% to 1%, the R_{ct} value is decreased from 30.4 to 18.1 kΩ. However, further increase the loading amount of MoS_2 higher than 1%, the R_{ct} is increase to 27.8 kΩ for 1.5%MoS_2-Bi_2WO_6 and 26.1 kΩ for 2.0% MoS_2-Bi_2WO_6. It suggests the introduction of MoS_2 QDs on Bi_2WO_6 can greatly improve the separation of photogenerated electron/hole pairs, and when the quantity of MoS_2 account for 1.0%, the

electron/hole separation efficiency is the highest. It is a crucial evidence to confirm that the introduction MoS_2 on Bi_2WO_6 can significantly improve the electron/hole separation efficiency and further enhanced the photocatalytic activity in the removal of organic pollutants as well as bacterial inactivation under visible light irradiation.

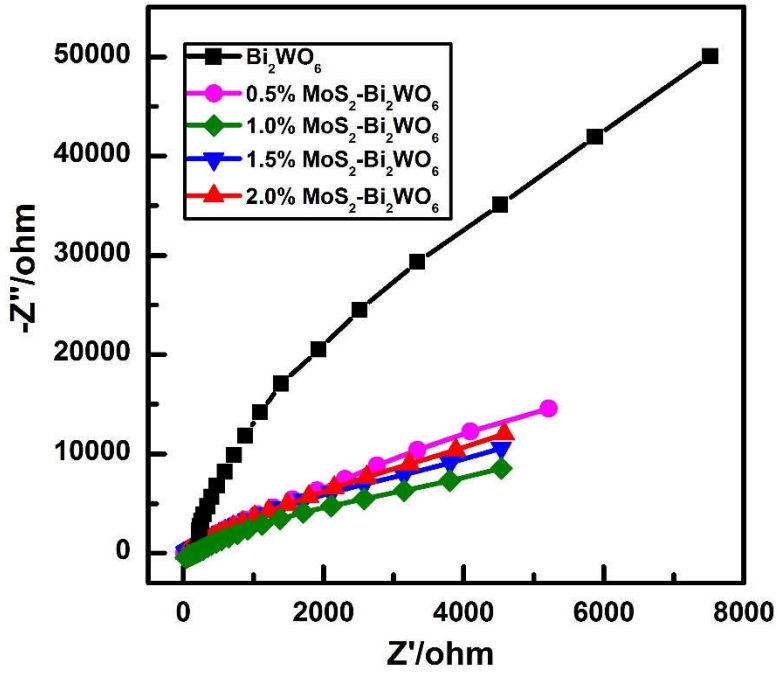
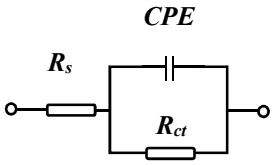


Figure 6.13 EIS Nyquist plots of the Bi_2WO_6 and MoS_2-Bi_2WO_6 photocatalysts.

Table 6.4 Fitting results for equivalent circuits of different prepared samples.

Samples	R_s (Ω)	R_{ct} (kΩ)	*CPE* (μf)	Equivalent circuits
Bi_2WO_6	165.8	328.5	41.6	
0.5%MoS_2-Bi_2WO_6	154.1	30.4	59.9	
1.0%MoS_2-Bi_2WO_6	125.5	18.1	83.1	
1.5%MoS_2-Bi_2WO_6	141.9	27.8	55.0	
2.0%MoS_2-Bi_2WO_6	167.4	26.1	36.1	

6.3.8 Energy band engineering analysis

Band structures and partial/total density of states (PDOS/TDOS) for Bi_2WO_6 and MoS_2 are simulated based on DFT method and illustrated in Fig. 6.14. The energy of top of valence band is fixed at zero. The band gap value (Fig. 6.14a and 6.14b) can be measured as about 1.91 eV for Bi_2WO_6 and 0.89 eV for MoS_2. The simulated band gap values are narrower than experimental results (2.70 eV for Bi_2WO_6 and 1.3 eV for bulk MoS_2 [49]), which may be resulted from the well-known limitation of GGA [50]. It can be found the Bi_2WO_6 is attributed to the direct band-gap semiconductor and MoS_2 is attributed to indirect band-gap semiconductor. It should also be noted the correlation between velocity of electron (v) and the energy of electron E can be expressed as in Equation 8.

$$v = \frac{\Delta_\kappa E(\kappa)}{} \qquad \textit{Equation 8}$$

It means that the more flat the energy band is, the more localized the charge carriers [51]. For Bi_2WO_6, the mobility of both electrons and holes are relatively low, which inevitably inhibit the separation efficiency of photogenerated electrical carriers. It indicates even for a 'perfect' bulk Bi_2WO_6, the photocatalytic activity can still be significantly improved in photocatalysis. From the PDOS/DOS shown in Fig. 6.14c and 6.14d, the valence band of Bi_2WO_6 is composed of O 2p, W 5d and a little Bi 6s. As reported the well-dispersed Bi 6s orbital facilitate the mobility of photogenerated carriers and narrows the band gap [3, 4]. The top valence band of MoS_2 mainly originated from the 4d orbital of Mo and 3p orbital of S, and the bottom of MoS_2 is mainly contributed to 4d orbitals of Mo.

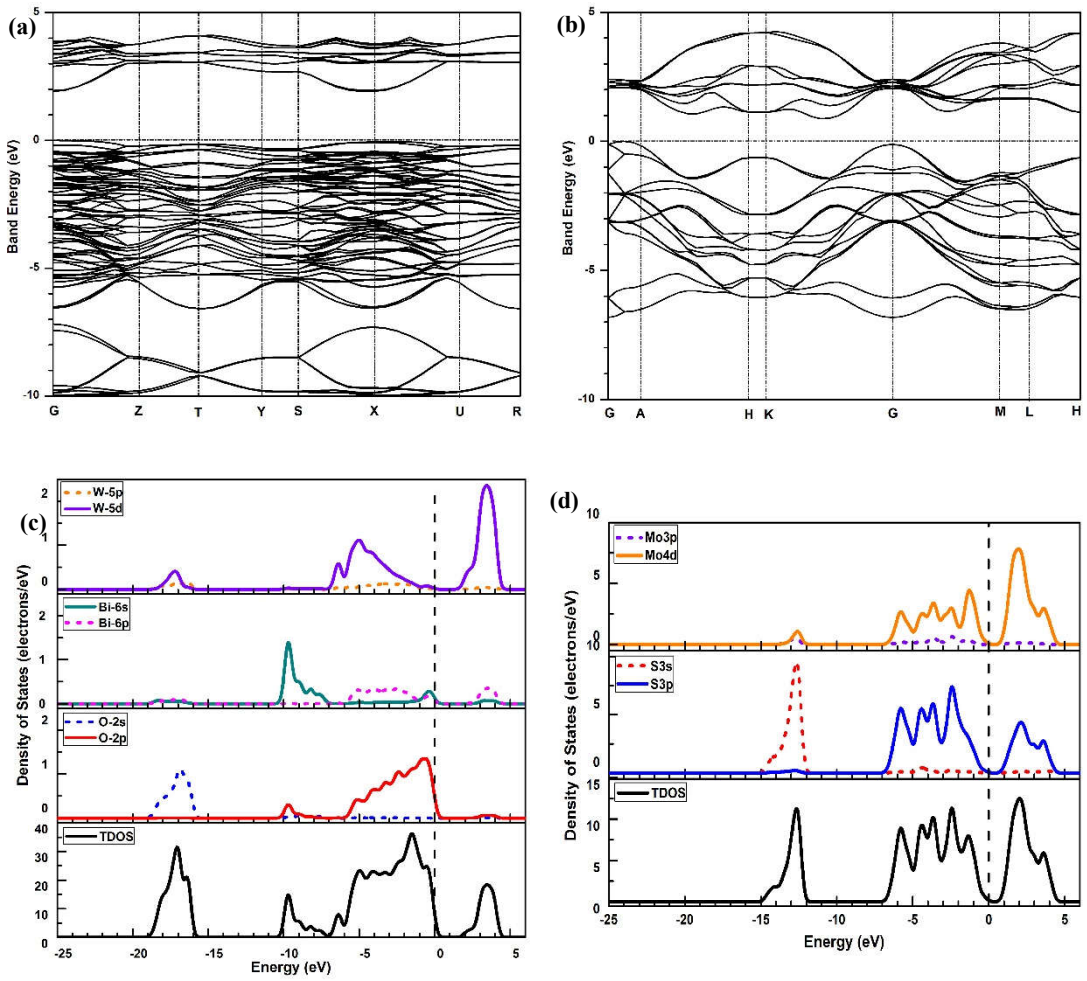


Figure 6.14 (a, b) Band structure for Bi_2WO_6 and MoS_2. (c, d) Partial and total density of states (PDOS and TDOS) for Bi_2WO_6 and MoS_2. (Simulated by Quantum Espresso [29])

To further study photogenerated electrons and holes transfer when MoS_2-Bi_2WO_6 composite applied in photocatalysis, The flat-band potentials of semiconductors can be calculated by applying the Mulliken electronegativity theory for atoms as follows (Equation 9 and 10) [1, 52],

$$E_{CB} = \chi_p - E^e - \frac{1}{2}E_g \qquad \textit{Equation 9}$$

$$E_{VB} = E_{CB} + E_g \qquad \textit{Equation 10}$$

where E_{CB} and E_{VB} are bottom position of conduction band and top position of valence band respectively; χ_p represents the electronegativity which can be estimated by the geometric mean of electronegativity of the constituent atoms [53-55]; E^e is the energy of free electrons on the hydrogen scale (~ 4.5eV) and E_g is the band gap value. The calculated results for Bi_2WO_6 and MoS_2 are summarized in Table 6.5, and the flat-band position for MoS_2-Bi_2WO_6 is schemed in Fig. 6.15. A staggered type II band alignment and a built-in electric field formed near the interface. The formation MoS_2-Bi_2WO_6 p-n heterojunction facilitate the separation of photogenerated electrons and holes. The built-in electric field may drive the mobility of electrons from conduction band of MoS_2 to that of Bi_2WO_6, while holes transferred from the valence band of Bi_2WO_6 to that of MoS_2. As a result, electrons and holes are accumulated on Bi_2WO_6 and MoS_2 separately. It is also reported that QDs combined on a photocatalysts may provide a convenient way to direct the flow of the photogenerated charge carriers [24, 25]. Fast electron transfer between MoS_2 QDs and Bi_2WO_6 may lead to higher quantum efficiency, providing more photogenerated electrons utilized in photocatalytic reactions. The surface –OH or H_2O capture the separated holes at the surface of the photocatalysts and produce hydroxyl free radicals (•OH). Besides, the dissolved O_2 can also react with the separated electrons to generated the superoxide free radicals ($\bullet O_2^-$) or hydroperoxyl radicals ($\bullet O_2H$). The generated free radicals as well as the photogenerated holes are oxidative enough to effectively decompose the organic pollutants and the damage the cell envelope integrity.

Table 6.5 Band gap and flat-band edge position of Bi_2WO_6 and MoS_2.

Composites	E_g/**eV**	χ_p/**eV**	E^e/**eV**	E_{CB} ***vs*** **NHE[a]/eV**	E_{VB} ***vs*** **NHE[a]/eV**
Bi_2WO_6	2.70	6.20	4.50	0.35	3.05
MoS_2	1.30[b]	5.33	4.50	0.18	1.48

a. NHE: Normal Hydrogen Electrode; b. For bulk MoS_2, band gap is 1.30 eV (adapted from [49])

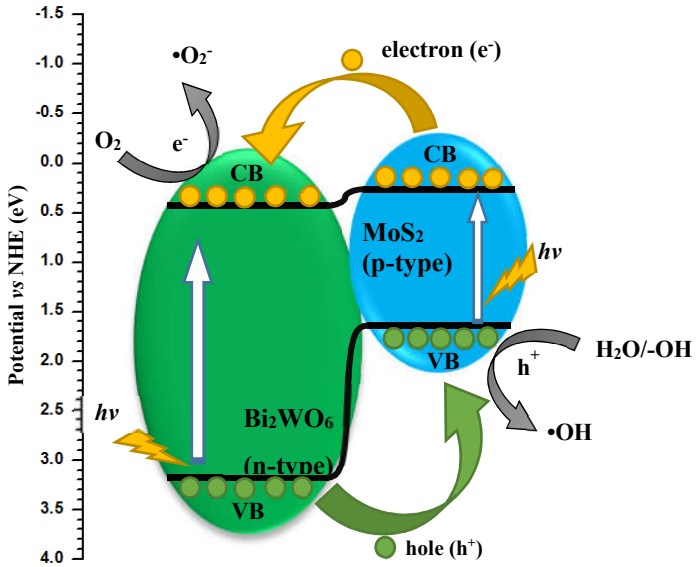


Figure 6.15 Proposed mechanism of photogenerated electrons and holes transfer for MoS_2-Bi_2WO_6 composite under visible light irradiation.

6.4 Conclusions

MoS_2 QDs interspersed-Bi_2WO_6 heterostructure was successfully prepared via a simple bath sonication method. Characterizations are performed and suggest hexagonal MoS_2 QDs with size of 1.8-5.6 nm are interspersed on Bi_2WO_6 nanoplates. The band gap of Bi_2WO_6 is 2.70 eV, and the band gap is narrowed after MoS_2 QDs loading on its surface. The adsorption capacity is significantly improved with introduction of MoS_2, compared to bare Bi_2WO_6. Moreover, in the photocatalytic RhB degradation and the temporal course of inactivation, MoS_2-Bi_2WO_6 exhibit enhanced photocatalytic activity compared to bare Bi_2WO_6 and MoS_2. The synergy effect on photocatalysis oxidization may be attributed to the p-n heterostructure between MoS_2 and Bi_2WO_6, as well as the MoS_2 QDs facilitate the charge carrier separation. This work is a crucial evidence to confirm MoS_2 QDs as a promising co-catalyst in preparation of an efficient photocatalyst.

References

1. Xiangchao Meng and Zisheng Zhang, "Bismuth-based Photocatalytic Semiconductors: Introduction, Challenges and Possible Approaches," *Journal of Molecular Catalysis A: Chemical*, vol. 423, pp. 533-549, 2016.

2. Rong'an He, Shaowen Cao, Peng Zhou and Jiaguo Yu, "Recent advances in visible light Bi-based photocatalysts," *Chinese Journal of Catalysis*, vol. 35, no. 7, pp. 989-1007, 2014.

3. Huizhong An, Yi Du, Tianmin Wang, Cong Wang, Weichang Hao and Junying Zhang, "Photocatalytic properties of BiOX (X = Cl, Br, and I)," *Rare Metals*, vol. 27, no. 3, pp. 243-250, 2008.

4. Xiangchao Meng and Zisheng Zhang, "Facile synthesis of BiOBr/Bi_2WO_6 heterojunction semiconductors with high visible-light-driven photocatalytic activity," *Journal of Photochemistry and Photobiology A: Chemistry*, vol. 310, no. 0, pp. 33-44, 2015.

5. Chuan Zhang and Yongfa Zhu, "Synthesis of Square Bi_2WO_6 Nanoplates as High-Activity Visible-Light-Driven Photocatalysts," *Chemistry of Materials*, vol. 17, no. 13, pp. 3537-3545, 2005.

6. Lisha Zhang, Wenzhong Wang, Lin Zhou and Haolan Xu, "Bi_2WO_6 Nano‐and Microstructures: Shape Control and Associated Visible‐Light‐Driven Photocatalytic Activities," *Small*, vol. 3, no. 9, pp. 1618-1625, 2007.

7. Yu Huang, Zhihui Ai, Wingkei Ho, Meijuan Chen and Shuncheng Lee, "Ultrasonic Spray Pyrolysis Synthesis of Porous Bi_2WO_6 Microspheres and Their Visible-Light-Induced Photocatalytic Removal of NO," *The Journal of Physical Chemistry C*, vol. 114, no. 14, pp. 6342-6349, 2010.

8. Xiaoyue Hu, Xiangchao Meng and Zisheng Zhang, "Synthesis and Characterization of Graphene Oxide-Modified Bi_2WO_6 and Its Use as Photocatalyst," *International Journal of Photoenergy*, vol. 2016, pp. 8, 2016.

9. Hongbo Fu, Shicheng Zhang, Tongguang Xu, Yongfa Zhu and Jianmin Chen, "Photocatalytic Degradation of RhB by Fluorinated Bi_2WO_6 and Distributions of the Intermediate Products," *Environmental Science & Technology*, vol. 42, no. 6, pp. 2085-2091, 2008.

10. Yu Fu, Chun Chang, Peng Chen, Xiaolong Chu and Lingyan Zhu, "Enhanced photocatalytic performance of boron doped Bi_2WO_6 nanosheets under simulated solar light irradiation," *Journal of Hazardous Materials*, vol. 254–255, no. 0, pp. 185-192, 2013.

11. Lei Ge, Changcun Han and Jing Liu, "Novel visible light-induced g-C_3N_4/Bi_2WO_6 composite photocatalysts for efficient degradation of methyl orange," *Applied Catalysis B: Environmental*, vol. 108–109, pp. 100-107, 2011.

12. Ming Ge, Yafei Li, Lu Liu, Zhen Zhou and Wei Chen, "Bi_2O_3−Bi_2WO_6 Composite Microspheres: Hydrothermal Synthesis and Photocatalytic Performances," *The Journal of Physical Chemistry C*, vol. 115, no. 13, pp. 5220-5225, 2011.

13. Xiangchao Meng, Lingyun Jiang, Weiwen Wang and Zisheng Zhang, "Enhanced Photocatalytic Activity of BiOBr/ZnO Heterojunction Semiconductors Prepared by Facile Hydrothermal Method," *International Journal of Photoenergy*, vol. 2015, pp. 9, 2015.

14. Xiangchao Meng and Zisheng Zhang, "Synthesis, Analysis, and Testing of BiOBr-Bi_2WO_6 Photocatalytic Heterojunction Semiconductors," *International Journal of Photoenergy*, vol. 2015, pp. 12, 2015.

15. Quanjun Xiang, Jiaguo Yu and Mietek Jaroniec, "Graphene-based semiconductor photocatalysts," *Chemical Society Reviews*, vol. 41, no. 2, pp. 782-796, 2012.

16. Shaowen Cao and Jiaguo Yu, "g-C_3N_4-Based Photocatalysts for Hydrogen Generation," *The Journal of Physical Chemistry Letters*, vol. 5, no. 12, pp. 2101-2107, 2014.

17. Qian Li, Ning Zhang, Yong Yang, Guozhong Wang and Dickon H. L. Ng, "High Efficiency Photocatalysis for Pollutant Degradation with MoS_2/C_3N_4 Heterostructures," *Langmuir*, vol. 30, no. 29, pp. 8965-8972, 2014.

18. Song Bai, Limin Wang, Xiaoyi Chen, Junteng Du and Yujie Xiong, "Chemically exfoliated metallic MoS_2 nanosheets: A promising supporting co-catalyst for enhancing the photocatalytic performance of TiO_2 nanocrystals," *Nano Research*, vol. 8, no. 1, pp. 175-183, 2015.

19. Thomas F. Jaramillo, Kristina P. Jørgensen, Jacob Bonde, Jane H. Nielsen, Sebastian Horch and Ib Chorkendorff, "Identification of Active Edge Sites for Electrochemical H_2 Evolution from MoS_2 Nanocatalysts," *Science*, vol. 317, no. 5834, pp. 100-102, 2007.

20. Junfeng Xie, Jiajia Zhang, Shuang Li, Fabian Grote, Xiaodong Zhang, Hao Zhang, Ruoxing Wang, Yong Lei, Bicai Pan and Yi Xie, "Controllable Disorder Engineering in Oxygen-Incorporated MoS_2 Ultrathin Nanosheets for Efficient Hydrogen Evolution,"

Journal of the American Chemical Society, vol. 135, no. 47, pp. 17881-17888, 2013.

21. Jun Zhang, Lihai Huang, Haoyun Jin, Yunlei Sun, Xinming Ma, Erpan Zhang, Hongbo Wang, Zhe Kong, Junhua Xi and Zhenguo Ji, "Constructing two-dimension MoS_2/Bi_2WO_6 core-shell heterostructure as carriers transfer channel for enhancing photocatalytic activity," *Materials Research Bulletin*, vol. 85, pp. 140-146, 2017.

22. Fangzhi Wang, Wenjun Li, Shaonan Gu, Hongda Li, Xue Wu, Chaojun Ren and Xintong Liu, "Facile fabrication of direct Z-scheme MoS_2/Bi_2WO_6 heterojunction photocatalyst with superior photocatalytic performance under visible light irradiation," *Journal of Photochemistry and Photobiology A: Chemistry*, vol. 335, pp. 140-148, 2017.

23. Deepesh Gopalakrishnan, Dijo Damien and Manikoth M. Shaijumon, "MoS_2 Quantum Dot-Interspersed Exfoliated MoS_2 Nanosheets," *ACS Nano*, vol. 8, no. 5, pp. 5297-5303, 2014.

24. Hengchao Zhang, Hui Huang, Hai Ming, Haitao Li, Lili Zhang, Yang Liu and Zhenhui Kang, "Carbon quantum dots/Ag_3PO_4 complex photocatalysts with enhanced photocatalytic activity and stability under visible light," *Journal of Materials Chemistry*, vol. 22, no. 21, pp. 10501-10506, 2012.

25. Gui-Sheng Li, Die-Qing Zhang and Jimmy C. Yu, "A New Visible-Light Photocatalyst: CdS Quantum Dots Embedded Mesoporous TiO_2," *Environmental Science & Technology*, vol. 43, no. 18, pp. 7079-7085, 2009.

26. Ying-Hua Tan, Ke Yu, Jin-Zhu Li, Hao Fu and Zi-Qiang Zhu, "MoS_2@ZnO nano-heterojunctions with enhanced photocatalysis and field emission properties," *Journal of Applied Physics*, vol. 116, no. 6, pp. 064305, 2014.

27. Joanne Gamage McEvoy, Didier Alexandre Bilodeau, Wenquan Cui and Zisheng Zhang, "Visible-light-driven inactivation of *Escherichia coli* K-12 using an Ag/AgCl–activated carbon composite photocatalyst," *Journal of Photochemistry and Photobiology A: Chemistry*, vol. 267, pp. 25-34, 2013.

28. Walter Kohn and Lu Jeu Sham, "Self-consistent equations including exchange and correlation effects," *Physical Review*, vol. 140, no. 4A, pp. A1133, 1965.

29. Giannozzi Paolo, Baroni Stefano, Bonini Nicola, Calandra Matteo, Car Roberto,

Cavazzoni Carlo, Ceresoli Davide, L. Chiarotti Guido, Cococcioni Matteo, Dabo Ismaila, Corso Andrea Dal, Gironcoli Stefano de, Fabris Stefano, Fratesi Guido, Gebauer Ralph, Gerstmann Uwe, Gougoussis Christos, Kokalj Anton, Lazzeri Michele, Martin-Samos Layla, Marzari Nicola, Mauri Francesco, Mazzarello Riccardo, Paolini Stefano, Pasquarello Alfredo, Paulatto Lorenzo, Sbraccia Carlo, Scandolo Sandro, Sclauzero Gabriele, P. Seitsonen Ari, Smogunov Alexander, Umari Paolo and M. Wentzcovitch Renata, "QUANTUM ESPRESSO: a modular and open-source software project for quantum simulations of materials," *Journal of Physics: Condensed Matter*, vol. 21, no. 39, pp. 395502, 2009.

30. Kevin S Knight, "The crystal structure of russellite; a re-determination using neutron powder diffraction of synthetic Bi_2WO_6," 1992.

31. Ting Xiong, Mengqing Wen, Fan Dong, Jiayan Yu, Lulin Han, Ben Lei, Yuxin Zhang, Xiaosheng Tang and Zhigang Zang, "Three dimensional Z-scheme $(BiO)_2CO_3/MoS_2$ with enhanced visible light photocatalytic NO removal," *Applied Catalysis B: Environmental*, vol. 199, no. Complete, pp. 87-95, 2016.

32. Yuanguo Xu, Hui Xu, Huaming Li, Jiexiang Xia, Chengtang Liu and Ling Liu, "Enhanced photocatalytic activity of new photocatalyst Ag/AgCl/ZnO," *Journal of Alloys and Compounds*, vol. 509, no. 7, pp. 3286-3292, 2011.

33. Zhuang Shuxian, W. Keith Hall, Gerhard Ertl and Helmut Knözinger, "X-ray photoemission study of oxygen and nitric oxide adsorption on MoS_2," *Journal of Catalysis*, vol. 100, no. 1, pp. 167-175, 1986.

34. H. W. Wang, P. Skeldon and G. E. Thompson, "XPS studies of MoS_2 formation from ammonium tetrathiomolybdate solutions," *Surface and Coatings Technology*, vol. 91, no. 3, pp. 200-207, 1997.

35. Thomas A. Patterson, James C. Carver, Donald E. Leyden and David M. Hercules, "A surface study of cobalt-molybdena-alumina catalysts using x-ray photoelectron spectroscopy," *The Journal of Physical Chemistry*, vol. 80, no. 15, pp. 1700-1708, 1976.

36. C. D. Wagner, "Sensitivity of detection of the elements by photoelectron spectrometry," *Analytical Chemistry*, vol. 44, no. 6, pp. 1050-1053, 1972.

37. Junqi Li, Zhanyun Guo, Yu Wang and Zhenfeng Zhu, "Three-dimensional TiO_2/Bi_2WO_6 hierarchical heterostructure with enhanced visible photocatalytic activity," *Micro & Nano Letters, IET*, vol. 9, no. 2, pp. 65-68, 2014.

38. KSW Sing, DH Everett, RAW Haul, L Moscou, RA Pierotti, J Rouquerol and T Siemieniewska, "Physical and biophysical chemistry division commission on colloid and surface chemistry including catalysis," *Pure Applied Chemistry*, vol. 57, no. 4, pp. 603-619, 1985.

39. Michal Kruk and Mietek Jaroniec, "Gas Adsorption Characterization of Ordered Organic−Inorganic Nanocomposite Materials," *Chemistry of Materials*, vol. 13, no. 10, pp. 3169-3183, 2001.

40. Xiangchao Meng and Zisheng Zhang, "Plasmonic ternary Ag–rGO–Bi_2MoO_6 composites with enhanced visible light-driven photocatalytic activity," *Journal of Catalysis*, vol. 344, pp. 616-630, 2016.

41. Ho Yuh-Shan, "Citation review of Lagergren kinetic rate equation on adsorption reactions," *Scientometrics*, vol. 59, no. 1, pp. 171-177, 2004.

42. Mahmut Özacar, "Equilibrium and Kinetic Modelling of Adsorption of Phosphorus on Calcined Alunite," *Adsorption*, vol. 9, no. 2, pp. 125-132, 2003.

43. Tadashi Watanabe, Takuo Takizawa and Kenichi Honda, "Photocatalysis through excitation of adsorbates. 1. Highly efficient N-deethylation of rhodamine B adsorbed to cadmium sulfide," *The Journal of Physical Chemistry*, vol. 81, no. 19, pp. 1845-1851, 1977.

44. J. Kiwi and V. Nadtochenko, "Evidence for the Mechanism of Photocatalytic Degradation of the Bacterial Wall Membrane at the TiO_2 Interface by ATR-FTIR and Laser Kinetic Spectroscopy," *Langmuir*, vol. 21, no. 10, pp. 4631-4641, 2005.

45. S. Pigeot-Rémy, F. Simonet, E. Errazuriz-Cerda, J. C. Lazzaroni, D. Atlan and C. Guillard, "Photocatalysis and disinfection of water: Identification of potential bacterial targets," *Applied Catalysis B: Environmental*, vol. 104, no. 3–4, pp. 390-398, 2011.

46. Janet M. Kesselman, Gary A. Shreve, Michael R. Hoffmann and Nathan S. Lewis, "Flux-Matching Conditions at TiO_2 Photoelectrodes: Is Interfacial Electron Transfer to O_2 Rate-Limiting in the TiO_2-Catalyzed Photochemical Degradation of Organics?," *The*

Journal of Physical Chemistry, vol. 98, no. 50, pp. 13385-13395, 1994.

47. Baifu Xin, Zhiyu Ren, Haiyuan Hu, Xiangyu Zhang, Chunlei Dong, Keying Shi, Liqiang Jing and Honggang Fu, "Photocatalytic activity and interfacial carrier transfer of Ag–TiO_2 nanoparticle films," *Applied Surface Science*, vol. 252, no. 5, pp. 2050-2055, 2005.

48. Baifu Xin, Zhiyu Ren, Peng Wang, Jia Liu, Liqiang Jing and Honggang Fu, "Study on the mechanisms of photoinduced carriers separation and recombination for Fe^{3+}–TiO_2 photocatalysts," *Applied Surface Science*, vol. 253, no. 9, pp. 4390-4395, 2007.

49. Kin Fai Mak, Changgu Lee, James Hone, Jie Shan and Tony F. Heinz, "Atomically Thin MoS_2: A New Direct-Gap Semiconductor," *Physical Review Letters*, vol. 105, no. 13, pp. 136805, 2010.

50. Kangrong Lai, Wei Wei, Ying Dai, Ruiqin Zhang and Baibiao Huang, "DFT calculations on structural and electronic properties of Bi_2MO_6 (M = Cr, Mo, W)," *Rare Metals*, vol. 30, no. 1, pp. 166-172, 2011.

51. Honglin Li, Ke Yu, Xiang Lei, Bangjun Guo, Hao Fu and Ziqiang Zhu, "Hydrothermal Synthesis of Novel MoS_2/$BiVO_4$ Hetero-Nanoflowers with Enhanced Photocatalytic Activity and a Mechanism Investigation," *The Journal of Physical Chemistry C*, vol. 119, no. 39, pp. 22681-22689, 2015.

52. Yong Xu and Martin A.A. Schoonen, "The absolute energy positions of conduction and valence bands of selected semiconducting minerals," *American Mineralogist*, vol. 85, no. 3-4, pp. 543-556, 2000.

53. Robert Thomas Sanderson, *Chemical periodicity*, Reinhold, New York, US, 1961.

54. Robert S. Mulliken, "A New Electroaffinity Scale; Together with Data on Valence States and on Valence Ionization Potentials and Electron Affinities," *The Journal of Chemical Physics*, vol. 2, no. 11, pp. 782-793, 1934.

55. Robert S. Mulliken, "Electronic Structures of Molecules XI. Electroaffinity, Molecular Orbitals and Dipole Moments," *The Journal of Chemical Physics*, vol. 3, no. 9, pp. 573-585, 1935.

SECTION IV: TERNARY BISMUTH-BASED STRUCTURE WITH ENHANCED PHOTOCATALYTIC ACTIVITY

Chapter 7 Plasmonic Ternary Ag-rGO-Bi_2MoO_6 Composites with Enhanced Visible Light-driven Photocatalytic Activity

Xiangchao Meng and Zisheng Zhang

Journal of Catalysis 344 (2016), 616-630

Abstract

Bi_2MoO_6 photocatalysts were hybridized with reduced graphene oxide (rGO) and Ag via solvothermal chemical reduction processes and photoreduction for the first time. The prepared ternary composites exhibited enhanced photocatalytic activities with respect to the removal of organic pollutants in wastewater under visible light irradiation. The resistance to electron transfer in Ag-rGO-Bi_2MoO_6 was decreased to 1/16 that of pure Bi_2MoO_6, which confirms an excellent separation of photogenerated electron-hole pairs. The reduced rate of electron-hole recombination may be attributed to the synergetic effects among Ag nanoparticles, rGO and Bi_2MoO_6. Electrons accumulated on the conduction band of Bi_2MoO_6 may be either trapped by Ag or transferred to the rGO layer. Ag nanoparticles on the surface may harvest additional visible light photons via surface plasmonic resonance.

7.1 Introduction

Photocatalysis, one of the advanced oxidation processes (AOPs), has been increasingly studied and widely applied in the treatment of pollutants (removal of organics and disinfection), as well as the conversion of CO_2 and water to hydrocarbon fuels [1-6]. The benefits of this advanced technology applied to environmental protection are mainly attributed to the abundance of natural light as an energy source, the high rate of conversion

of light energy, and complete mineralization. However, some issues need to resolve before it is widely adopted in industry. For example, the high recombination rate of photogenerated electron-hole pairs and a low visible light-driven activity for traditional photocatalyst semiconductors should be accounted for.

Band energy configuration is crucial to most photocatalytic activities, such as the wavelength range at which irradiation is activated, the redox capacities of photogenerated holes and electrons, and the recombination rate of electron-hole pairs. Bismuth-based semiconductors are promising candidates for visible light-responsive photocatalysts because they usually have narrow band gaps (< 3.0 eV). The valence bands of bismuth-based compounds are composed of hybrid orbitals of O *2p* and Bi *6s*, while only O *2p* orbitals are found in the valence band of TiO_2 and other metal oxides. The well-dispersed band structure facilitates the mobility of photogenerated electrical carriers and narrows the band gap [7].

Bi_2MoO_6 has already been reported as a potential visible light-responsive photocatalyst applied to the area of environmental protection [8, 9]. What hinders its wide application is the high recombination rate of photogenerated carriers and a low visible light-driven activity. Approaches to compensate for these downfalls mainly include metal/non-metal doping [10, 11], fabrication of heterostructures with other semiconductors [12, 13] as well as combinations with other techniques (such as electrochemistry via applying external bias potential [6]). Among these methods, Bi_2MoO_6 doped with Ag/AgCl [14, 15] and reduced Graphene oxide (rGO) [16, 17] have been separately reported with enhanced effects towards the photocatalytic degradation of organic pollutants in wastewater. Specifically, Ag nanoparticles on the surface may be activated by visible light photons via the surface plasmon resonance (SPR) effect. Furthermore, AgCl with Bi_2MoO_6 can form a Z-scheme structure which may increase the separation efficiency of electron-hole pairs [18]. Graphene, a single layer of sp^2-bonded carbon atoms tightly packed into a two-dimensional honeycomb structure, has increasingly drawn the attention of researches owing to its excellent mechanical, thermal, optical, and electrical properties [19]. It was proven to be an effective and inexpensive material to produce graphene nanosheets by reducing graphene oxide (GO). It is also noteworthy that pure GO is electrically insulating due to the disrupted sp^2 bonding networks [20]. Therefore, the photogenerated electrons can

transfer to the widespread GO layer only when these oxygen functional groups are reduced. The rGO-doped Bi_2MoO_6 composites were also reported with enhanced photocatalytic activities under visible light irradiation [16, 17]. Bi et al. have recently reported on the preparation of ternary Au-rGO-Bi_2MoO_6 composites with enhanced photocatalytic activities under visible light irradiation [21]. There is currently no reported work describing the synthesis of a plasmonic Z-scheme ternary composite via the combination of Bi_2MoO_6, rGO, Ag nanoparticles and AgCl.

Herein, we report for the first time, the facile preparation of the Ag/AgCl-rGO-Bi_2MoO_6 composites by solvothermal methods followed by a photoreduction process. The ternary composites exhibited excellent photocatalytic degradation of phenol compared to pure Bi_2MoO_6, rGO-Bi_2MoO_6 and Ag/AgCl-Bi_2MoO_6. The synergetic effects of Ag, AgCl, rGO and Bi_2MoO_6 were comprehensively explored and discussed.

7.2 Experimental

7.2.1 Preparation of GO- and rGO-Bi_2MoO_6

The GO-Bi_2MoO_6 composites were prepared by a one-pot solvothermal method. Typically, 264 μL of graphene oxide (4 mg/mL dispersed in H_2O, Sigma-Aldrich) were first added to 20 mL of ethanol and ultrasonicated for 1 h, termed as solution A. Next, 1.68 g of $Bi(NO_3)_3$•$5H_2O$ (Fisher Scientific, Certified ACS) and 0.421 g of Na_2MoO_4•$2H_2O$ (Fisher Scientific, Certified ACS) were separately dissolved in 5 mL of ethylene glycol (EG, analytical purity, Fisher Scientific) under magnetic stirring, termed as solutions B and C respectively. Subsequently, solution B was mixed with solution A and stirred for 10 min. Solution C was then added to the mixture and stirred for another 20 min. The mixture was transferred to a 45-mL Teflon-lined stainless steel autoclave (Parr Instrument Company) and heated at 160°C for 20 h. After the autoclave was allowed to naturally cool to room temperature, the GO-Bi_2MoO_6 (with 0.1 wt% GO) precipitates were filtered out and washed once with ethanol then twice with distilled, deionized water (DDW). The washed samples were then dried at 60°C for 12 h and collected. To further reduce GO in the GO-Bi_2MoO_6 composites [22], 0.5 g of prepared composite was mixed with 50 mL of EG by ultrasonication for 30 min. The solution was then heated and stirred at 140°C for 2h. The

particle samples were separated and washed once with ethanol and twice with DDW. The resultant particles were dried at 60°C for 12 h and collected as rGO-Bi_2MoO_6 composites.

7.2.2 Preparation of Ag-rGO-Bi_2MoO_6

The Ag-rGO-Bi_2MoO_6 composite samples were synthesized by a photoreduction method [23]. In a typical procedure, 0.3 g of rGO-Bi_2MoO_6 were dispersed in 40 mL of DDW and sonicated for 30 min. Afterwards, 0.24 g of NaCl (Fisher Scientific, Certified ACS) (excess amount) were added to the suspension and magnetically stirred for 10 min. Meanwhile, 0.0376 g of $AgNO_3$ (Fisher Scientific, Certified ACS) were dissolved in 20 mL of DDW and then added dropwise to the above solution under vigorous stirring for 30 min. The mixtures were then illuminated under a 300-W halogen tungsten projector lamp (Ushio) for 30 min. The resultant products were separated via centrifugation, washed twice with DDW and dried at 60°C for 12 h. The sample was then collected and labelled as 8 wt% Ag-rGO-Bi_2MoO_6. Similarly, 1, 2, 4, and 16 wt% Ag-rGO-Bi_2MoO_6 samples were also prepared. For comparison, 8 wt% Ag-Bi_2MoO_6, Ag/AgCl and Ag/AgCl-3.2% rGO [24] was prepared by changing the substrate to Bi_2MoO_6 instead of rGO-Bi_2MoO_6.

7.2.3 Characterization

X-ray diffraction (XRD) analysis was performed on a Rigaku Ultima IV Diffractometer with Cu Kα radiation (λ = 0.15418 nm) at 40 kV and 44 mA. Elements and chemical states on the sample surface were measured using a XSAM-800 X-ray Photoelectron Spectroscope (XPS). A field-emission scanning electron microscope (FE-SEM, JEOL JSM-7500F) for energy dispersive X-ray spectroscopy (EDS) and a transmission electron microscope (TEM, JEM-2100F) were applied to study the morphologies of prepared samples. Optical properties (ultraviolet-visible diffuse reflectance spectra) of samples were investigated by using the Thermo Evolution 300 spectrophotometer. Fourier Transform Infrared Spectroscopy (FTIR) was performed on a Cary 630 (Agilent Technologies). Spectra were recorded at room temperature with wavenumbers ranging from 2000 to 600 cm^{-1}. The specific surface area, pore volume and average pore size were obtained from N_2 sorption isotherms at 77 K, using automatic adsorption apparatus and measurement systems (ASAP 2020, Micromeritics and Nova 4200E, Quantachrome). The Brunauer, Emmett and Teller (BET) surface area of the samples were calculated using multi-point

estimation; the pore volumes were calculated using the volumes of adsorbed N_2 at p/p_o = 0.977; and the Barrett-Joyner-Halenda (BJH) method was used for the desorption branch to calculate the pore size data. Electrochemical properties of prepared samples were performed on a CHI 604E electrochemical analyzer (CH Instruments Inc., USA) with a platinum wire as a counter electrode, a calomel reference electrode and a working electrode. The working electrode was composed of indium tin oxide (ITO, 75 × 25 × 1.1 mm, 15 - 25 Ω, Sigma-Aldrich Canada Co.), glass coated with the prepared samples. The electrochemical impedance spectroscopies (EIS) were recorded with frequencies in the range of 1 – 1000000 Hz and a sinusoidal wave of 5 mV. The electrolyte was Na_2SO_4 with a concentration of 0.5 mol/L.

7.2.4 Photocatalytic activity tests

The photocatalytic activities of prepared samples under visible light irradiation were investigated by degrading the colourless organic model compound, phenol. The geometry of the reacting system is shown in Fig. 7.1. A 500-mL beaker served as the reactor, and a cooling jacket was applied to maintain the temperature of the system at around 20°C. The light source was a 300-W halogen tungsten projector lamp (Ushio, wavelength mainly in the range of 310 – 800 nm) with a UV cut-off (Kenko Zeta, transmittance > 90%) to filter out irradiation with wavelength below 410 nm. The irradiation intensity on the surface of the solution was measured by a quantum meter (Biospherical QSL-2100, $400 < \lambda < 700$ nm) to be 1.1×10^{-2} Einsteins m^{-2} s^{-1}. In each test, 100 mL of phenol solution (10 mg/L) was mixed with 0.1 g of prepared photocatalyst composites. The suspensions were magnetically stirred for 60 min before turning on the light, the purpose of which was to reach adsorption-desorption equilibrium between the pollutant and the photocatalyst. The photocatalytic test was carried out for 6 h, and aliquots were drawn every 30 min. After centrifuging at 13,000 rpm for 5 min, the supernatant was analyzed by using a high-performance liquid chromatograph (HPLC, Agilent 1100 series) equipped with a UV-Vis detector. A ZORBAX Eclipse Plus C18 column (4.6 × 250 mm) was used at a temperature of 60°C. The detecting wavelength was fixed at 270 nm for the detection of phenol and possible intermediates. The flow phase was composed of methanol (55%, V/V) and water (45%, V/V) at a flow rate of 0.6 mL/min. The injection volume was set to 25 μL. The adsorption testing were performed with the same condition of photocatalysis except with light off.

In the quenching experiments, ethylenediaminetetraacetic acid disodium (EDTA-2Na) and t-butanol with a concentration of 1 mol/L were added to the reaction system as scavengers for holes and oxidative free radicals respectively.

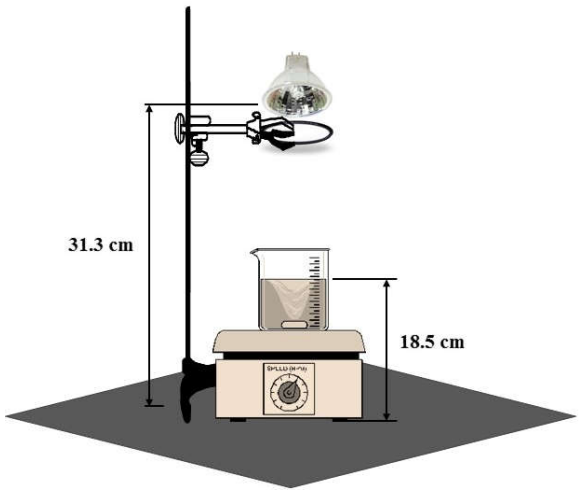


Figure 7.1 Photoreactor geometry and positioning.

7.3 Results and discussion

7.3.1 Crystal structure analysis

XRD patterns of prepared samples were recorded and are shown in Fig. 7.2a. For pure Bi_2MoO_6, major peaks at 2θ values of 28.3°, 32.6°, 47.1° and 55.6° were observed, which match well with the (1 3 1), (0 0 2), (2 0 2) and (1 3 3) crystal planes of orthorhombic Bi_2MoO_6 (space group: pbca (61), PDF card number: 72-1524 [25]), respectively. No impurity peaks were found, indicating a high purity of Bi_2MoO_6 in the prepared sample. Patterns of GO and rGO-modified Bi_2MoO_6 exhibited negligible differences with those of pure Bi_2MoO_6. It may be due to the low quantity (1 wt%) in the composites which is below the limit of detection for XRD. It also suggests that the main crystal structure of pure Bi_2MoO_6 was not destroyed after loading either GO or rGO. Furthermore, when Ag was introduced to the composites, numerous peaks emerged. Typically, peaks located at 2θ values of 27.8°, 32.2°, 46.2°, 54.8° and 57.5° corresponded to (1 1 1), (2 0 0), (2 2 0), (3 1 1) and (2 2 2) faces of cubic AgCl (space group: Fm-3m(225), PDF card no. 006-0480), respectively [23, 26]. In addition, two small peaks at 2θ = 36.7° and 44.3° were observed in the enlarged XRD patterns shown in Fig. 7.2b, corresponding to (1 1 1) and (2 0 0) faces

of metallic Ag (space group: Fm-3m (225), PDF card no.: 01-087-0597), respectively [27]. The lattice parameters of pure Bi_2MoO_6 were calculated as: a = 5.5219 Å, b = 16.0925 Å and c = 5.4918 Å. In regards to these parameters shown in Table 7.1, negligible differences between them were observed. This indicates that loading of Ag and (r)GO may not destroy the main crystal structure of Bi_2MoO_6, simply resting on the surface as opposed to covalently anchoring to the lattice [28]. In Fig. 7.2b, the peak at 2θ of 27.1° emerged when GO-Bi_2MoO_6 was reduced. This peak may be attributed to β-$Bi_2Mo_2O_9$ (JSPDS 33-209). It was reported that different phase of bismuth molybdate (α-$Bi_2Mo_3O_{12}$, β-$Bi_2Mo_2O_9$ and γ-Bi_2MoO_6) can be transferred with different performances in catalytic oxidative activity [29, 30]. The phase of β-$Bi_2Mo_2O_9$ in the rGO-Bi_2MoO_6 was calculated as ~13.6%. The presence of β-$Bi_2Mo_2O_9$ may be detrimental to photocatalytic activity of Bi_2MoO_6 within the visible light region [29, 30]. However, the synergistic result was that the photocatalytic activity of rGO modified Bi_2MoO_6 was improved (Fig. 7.11).

Table 7.1 Lattice parameters of Bi_2MoO_6 and Ag/AgCl-rGO-Bi_2MoO_6 composites

Samples	a	b	C
Bi_2MoO_6	5.52 (0%)	16.09 (0%)	5.49 (0%)
GO-Bi_2MoO_6	5.51 (-0.15%)	16.20 (+0.66%)	5.49 (+0.02%)
rGO-Bi_2MoO_6	5.51 (-0.21%)	16.23 (+0.88%)	5.49 (+0.01%)
1%Ag-rGO-Bi_2MoO_6	5.51 (-0.25%)	16.22 (+0.79%)	5.48 (-0.16%)
2%Ag-rGO-Bi_2MoO_6	5.50 (-0.32%)	16.33 (+1.46%)	5.48 (-0.23%)
4%Ag-rGO-Bi_2MoO_6	5.50 (-0.47%)	16.28 (+1.14%)	5.50 (+0.20%)
8%Ag-rGO-Bi_2MoO_6	5.48 (-0.78%)	16.41 (+1.99%)	5.52 (+0.43%)
16%Ag-rGO-Bi_2MoO_6	5.49 (-0.60%)	16.29 (+1.20%)	5.51 (+0.20%)

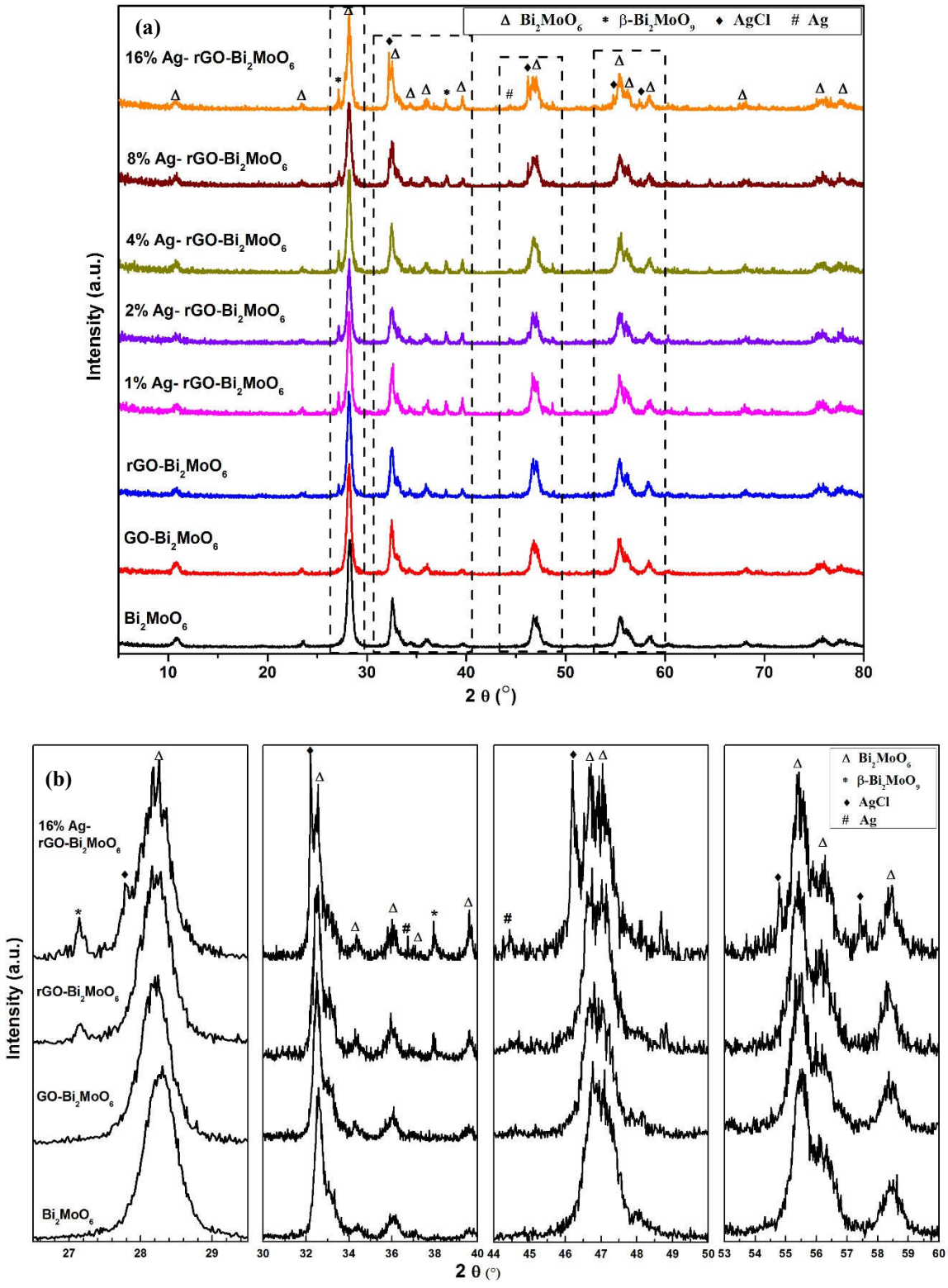


Figure 7.2 (a) XRD patterns of prepared samples; (b) fragments of enlarged XRD patterns for pure Bi_2MoO_6, GO-Bi_2MoO_6, rGO-Bi_2MoO_6 and 16% Ag-rGO-Bi_2MoO_6.

7.3.2 Spectroscopic analysis

Fig. 7.3 and Fig. 7.4 depict the XPS spectra of GO-Bi_2MoO_6 and Ag-rGO-Bi_2MoO_6 composites, including survey spectra and high-resolution orbit scans. All spectra were calibrated with C 1s, the binding energy of which is 284.6 eV. In the survey spectrum of GO-Bi_2MoO_6, all component elements (*i.e.* C, O, Bi, Mo) were detected and identified in Fig. 7.3. After loading silver on the rGO-Bi_2MoO_6 composites, small peaks of Ag as well as of Cl were detected in the survey spectrum of Ag-rGO-Bi_2MoO_6. All peaks in the survey spectra were identified, and peaks for impurities were not found. To further explore the chemical states of elements in the composites, high-resolution orbit scans were also employed, the results of which are illustrated in Fig. 7.4. The characteristic binding energy values of 158.5 and 163.8 eV for Bi $4f_{7/2}$ and Bi $4f_{5/2}$ of Bi_2MoO_6 (Fig. 7.4a) indicate a trivalent oxidation state of bismuth. And the binding energies of 231.8 and 235.0 eV for Mo $3d_{5/2}$ and Mo $3d_{3/2}$ of Bi_2MoO_6 (Fig. 7.4b) can be assigned to a Mo^{6+} oxidation state [31]. There is no peak shift of both Bi 4f and Mo 3d for GO modified Bi_2MoO_6. However, two sets of spin-orbit doublets were found in both Bi 4f and Mo 3d spectra after GO-Bi_2MoO_6 were reduced. Bi ($4f_{7/2}$, $4f_{5/2}$) and Mo ($3d_{5/2}$, $3d_{3/2}$) peaks located at binding energies of (158.8 eV, 164.1 eV) and (235.2 eV, 232.03 eV), as well as at (159.9 eV, 165.3 eV) and (235.8 eV, 233.1 eV) may be ascribed to Bi^{3+} and Mo^{6+} present in Bi_2MoO_6 and β-$Bi_2Mo_2O_9$ respectively. It can be calculated about 17.6% of Bi_2MoO_6 were transformed to β-$Bi_2Mo_2O_9$, which is similar to the result (~13.6%) obtained from XRD patterns. In Fig. 7.4c, three peaks located at binding energies of 284.6 285.5 and 288.3 eV for the C 1s spectrum of GO-Bi_2MoO_6 may be attributed to the C-C, C-O, and O-C=O groups, respectively [32, 33]. After the reduction process, the peaks at binding energies of 285.5 and 288.3 eV in the C 1s spectrum of Ag-rGO-Bi_2MoO_6 were significantly reduced in intensity, indicating that most of the functional groups had been removed. In the O 1s spectra in Fig. 7.4d, peaks located at binding energies of 529.8, 530.5, 531.3 and 533.2 eV may relate to oxygen in the forms of Bi-O, Mo-O, C-O and C=O, respectively [34]. Similar to the carbon spectra, functional group peak intensities were decreased by the reduction process, which can be observed in the O 1s spectrum of Ag-rGO-Bi_2MoO_6. In Fig. 7.4e, two sets of spin-orbit doublets were found in the Ag 3d spectrum. Accordingly, Ag ($3d_{3/2}$, $3d_{5/2}$) peaks located at binding energies of 373.6 and 367.6 eV, as well as at 372.7 and

366.7 eV may be ascribed to Ag^+ present in AgCl and metallic Ag^0 respectively [35, 36]. This indicates that both bivalent and metallic Ag may be present on the surface of rGO-Bi_2MoO_6. The relative concentrations of Ag^+ and Ag^0 may be calculated by the following equation [37]:

$$\frac{\eta_{Ag^0}}{\eta_{Ag^+}} = \frac{I_{Ag^0}}{I_{Ag^+}} \times \frac{\sigma_{Ag}\lambda_{Ag}D_E(Ag)}{\sigma_{Ag}\lambda_{Ag}D_E(Ag)} \qquad \textit{Equation 1}$$

where η, I, σ, λ, and D_E are the surface concentration, the intensity, the photoelectric cross-section, the electron free mean path, and the geometric factor respectively. The values of σ, λ, and D_E were calculated by Penn and Scofield, and may be obtained from literature [38, 39]. I_{Ag0} and I_{Ag+} may be calculated by integrating the intensities of the Ag^0 and Ag^+ peaks. The relative combined surface concentration ratio of Ag^0/Ag^+ is approximately 1/1. In addition, high-resolution Cl 2p orbit scans are depicted in Fig. 7.4f. Peaks located at binding energies of 197.9 and 199.5 eV for Cl $2p_{1/2}$ and Cl $2p_{3/2}$ respectively suggest the presence of Cl^-, which further indicates the presence of AgCl in the composite.

Surface elements ratios can also be semi-quantitatively indicated based on the survey spectra by accumulating the area under the characteristic peak of each element (i.e. C 1s, Bi 4f, Mo 3d, O 1s, Ag 3d and Cl 2p). Relative surface element ratios for pure Bi_2MoO_6, GO-Bi_2MoO_6 and Ag-rGO-Bi_2MoO_6 were summarized in Table 7.2. The atomic ratios of Bi:Mo:O were nearly the same at about 2:1:6 regardless of the GO or Ag-rGO-doped on Bi_2MoO_6. The Ag/Bi atomic ratio on the 8wt% Ag-rGO-Bi_2MoO_6 is about 0.086. The weight ratio of silver in the composite can be calculated as 3.3 wt%, instead of 8 wt%. As for the limitation of quantitative calculation via XPS spectra, the doping quantity of silver may only be used as reference for the estimation of its quantity.

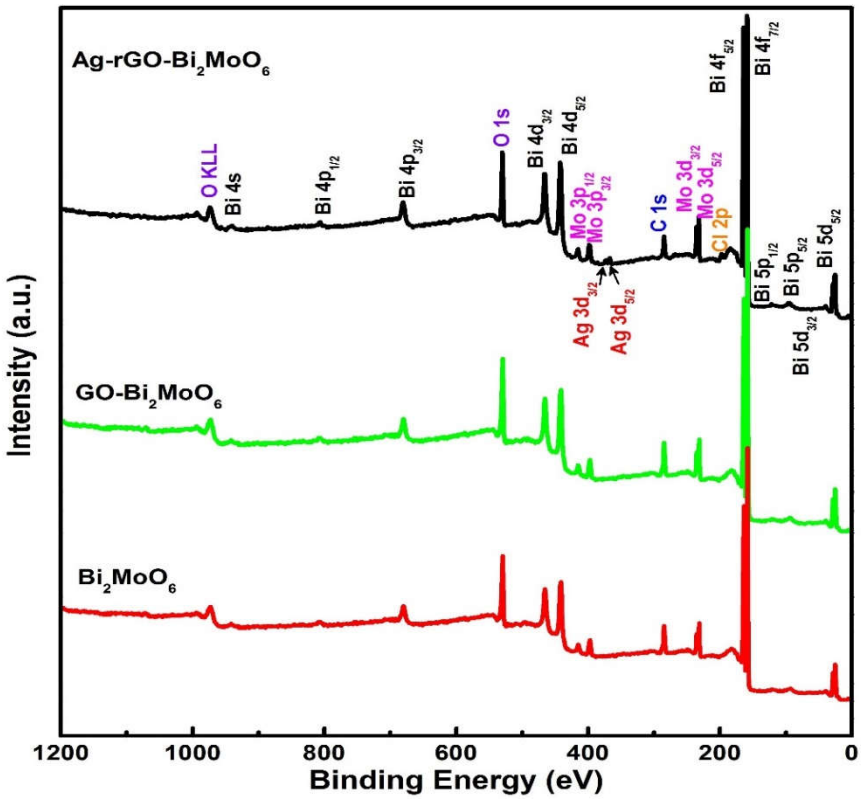
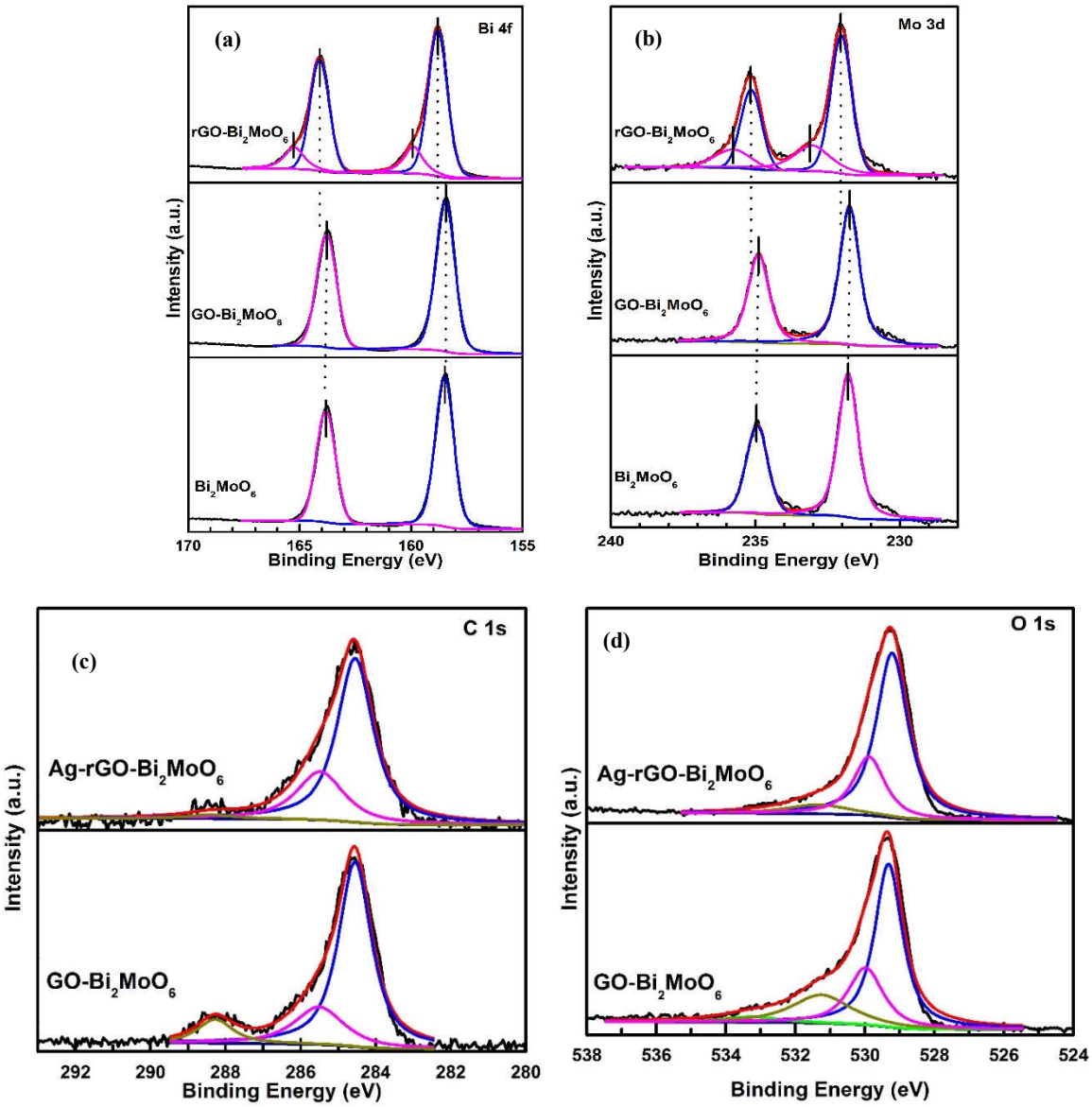


Figure 7.3 XPS survey spectra of pure Bi_2MoO_6, GO-Bi_2MoO_6 and Ag-rGO-Bi_2MoO_6.

Table 7.2 Surface composition of Bi_2MoO_6, GO-Bi_2MoO_6, and Ag-rGO-Bi_2MoO_6 composites according to XPS analysis.

Composites	Composition (at.%)					
	Bi	Mo	O	Ag	Cl	C
Bi_2MoO_6	12.99	6.86	36.96	-	-	43.19
GO-Bi_2MoO_6	11.88	5.80	39.36	-	-	42.96
Ag-rGO-Bi_2MoO_6	11.68	6.03	39.53	1.00	0.65	41.11


(a)
Bi 4f
rGO-Bi2MoO6
GO-Bi2MoO6
Bi2MoO6
Intensity (a.u.)
170
165
160
155
Binding Energy (eV)
(b)
Mo 3d
rGO-Bi2MoO6
GO-Bi2MoO6
Bi2MoO6
Intensity (a.u.)
240
235
230
Binding Energy (eV)
(c)
C 1s
Ag-rGO-Bi2MoO6
GO-Bi2MoO6
Intensity (a.u.)
292
290
288
286
284
282
280
Binding Energy (eV)
(d)
O 1s
Ag-rGO-Bi2MoO6
GO-Bi2MoO6
Intensity (a.u.)
538
536
534
532
530
528
526
524
Binding Energy (eV)

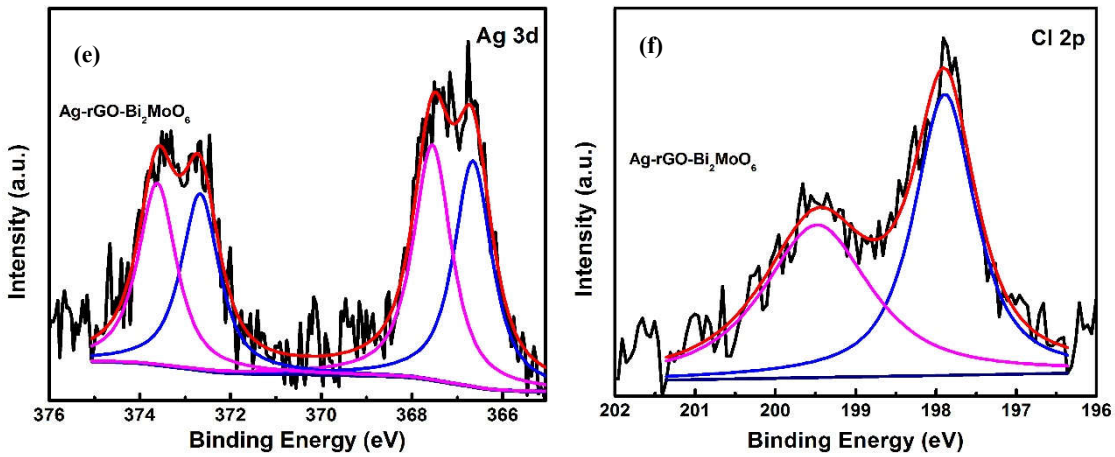


Figure 7.4 High-resolution orbits scan of (a) Bi 4f, (b) Mo 3d, (c) C 1s, (d) O 1s, (e) Ag 3d and (f) Cl 2p in prepared samples.

7.3.3 FT-IR

Fig. 7.5 shows the FT-IR spectra of Bi_2MoO_6, GO-Bi_2MoO_6, rGO-Bi_2MoO_6 and Ag-rGO-Bi_2MoO_6 samples. The main absorption bands at 600 - 1000 cm^{-1} are possibly due to Bi-O and Mo-O stretching modes as well as Mo-O-Mo bridging stretching modes [40]. Typically, the band located at approximately 690 cm^{-1} may be a result of the asymmetric stretching mode of MoO_6 involving vibrations of the equatorial oxygen atoms [41, 42]. Two peaks at wavenumbers of 795 and 845 cm^{-1} may be attributed to the asymmetric and symmetric stretching modes of MoO_6 involving vibrations of the apical oxygen atoms. Small peaks at approximately 1500 - 1600 cm^{-1} may be attributed to O-H vibrations [43]. Absorption peaks between 1000 and 1700 cm^{-1} can also be clearly observed, which may be attributed to impurities of C=O and C-O stretching in CO_2 or CH_3COOH [44-46]. These impurities may slightly block the surface of samples and deteriorate photocatalytic activity. In the spectrum of GO-modified Bi_2MoO_6 samples, it is clear that strong absorption peaks corresponding to various oxygen functional groups were found, such as -OH stretching (3306.0 cm^{-1}), -CH_2- stretching (2932.8 and 2874.1 cm^{-1}), C=O stretching (1624.4 cm^{-1}), C-O-C (or H) stretching (1336.4cm^{-1}) and C-O stretching (2085.7 cm^{-1}) [47]. Following the reduction treatment process, the intensities of all these peaks related to the oxygen functional groups (-OH, C=O, C-O-C and C-OH) were greatly decreased. This further confirms the effective reduction of GO to rGO by the reduction process, and agrees well

with the XPS results. Furthermore, after introducing Ag on the surface of rGO-Bi_2MoO_6, the main structures of both rGO and Bi_2MoO_6 were negligibly influenced. Therefore, the above results further confirm the successful preparation of chemical-coupling rGO-Bi_2MoO_6 composites.

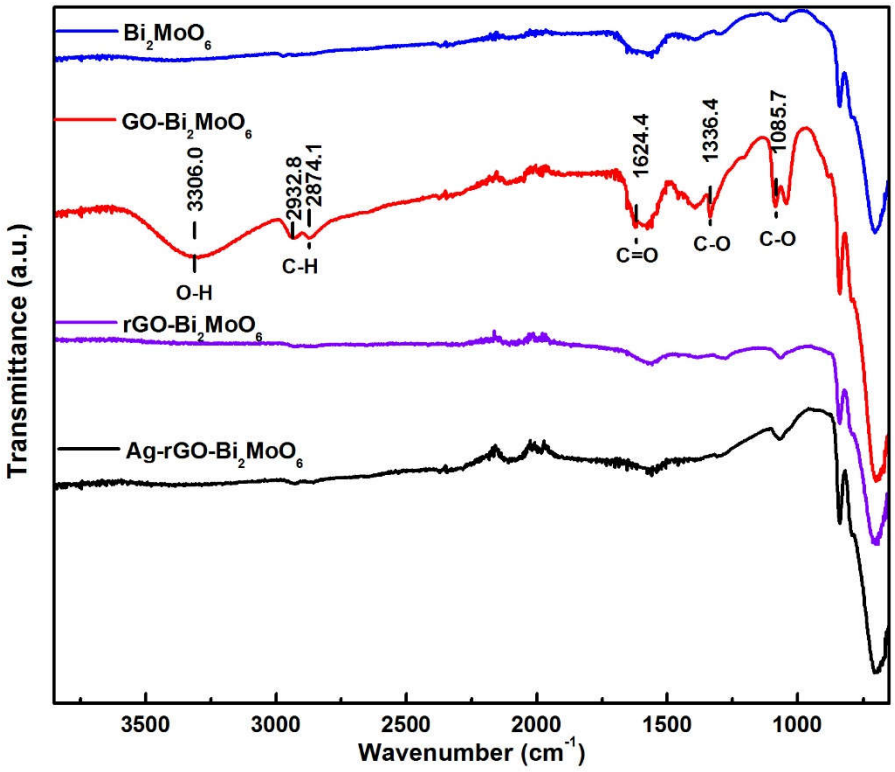


Figure 7.5 FT-IR of prepared samples: Bi_2MoO_6, GO-Bi_2MoO_6, rGO-Bi_2MoO_6 and Ag-rGO-Bi_2MoO_6.

7.3.4 Morphologies and possible formation processes

The morphologies of prepared powder samples of Bi_2MoO_6, rGO-Bi_2MoO_6 and Ag-rGO-Bi_2MoO_6 composites were investigated using SEM, STEM and TEM (Fig. 7.6). The solvothermally synthesized Bi_2MoO_6 sample exhibited a hierarchical microsphere morphology with diameters in the range of 1-3 μm (Fig. 7.6a). The sample synthesized solvothermally in the presence of GO shows a hierarchical microsphere morphology as well (Fig. 7.6b). No GO was observed however, which may be a result of SEM being unable to observe the relatively thin GO. For morphologies of Ag-rGO-Bi_2MoO_6, small particles were found on the surface (Fig. 7.6c and 7.6d). The plate-like particle on the surface of Bi_2MoO_6 in Fig. 6d may be the AgCl, and metallic Ag grown on the surfaces of

both AgCl and Bi_2MoO_6. Solid evidence of the presence of GO in the Ag-rGO-Bi_2MoO_6 composites was the layered structure which was observed (Fig. 7.6e). Small particles were also found on the layered GO, which may be the Ag/AgCl. At the edge of Bi_2MoO_6 particles, clusters of Ag/AgCl were also observed. In the high-resolution TEM image of the Ag-rGO-Bi_2MoO_6 composite, clear lattice fringes can be seen (Fig. 7.6f). The fringes of d = 0.31 nm match with those of the (1 3 1) crystal plane of Bi_2MoO_6, which is the strongest crystal plane. The fringes of d = 0.24 nm corresponded to the (1 1 1) crystal plane of Ag nanoparticles. EDS was also employed to measure the component elements on the surface, the results of which are shown in Fig. 7.7. The relative intensities of carbon and oxygen peaks were improved after introducing GO on the surface of Bi_2MoO_6. Peaks of Ag and Cl were also observed, which further confirms the presence of Ag and AgCl in the Ag-rGO-Bi_2MoO_6 composite.

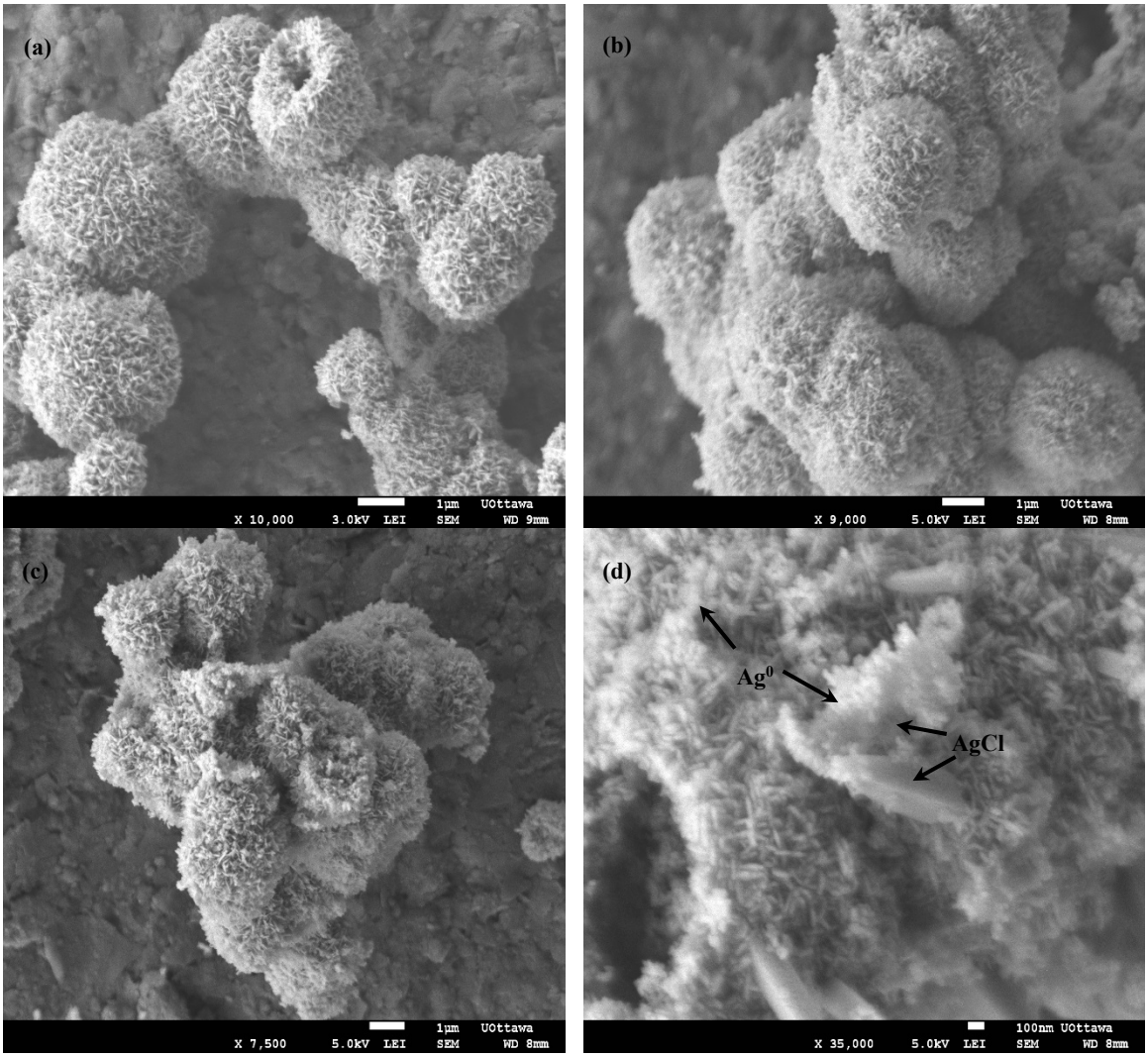
Based on the above discussion, a step-by-step formation process for Ag-rGO-Bi_2MoO_6 was proposed in Fig. 7.8. Specifically, precursors of Bi_2MoO_6 were well dispersed on the layered GO, and hierarchical Bi_2MoO_6 microspheres were first grown on the layered GO during the solvothermal treatment. Oxygen functional groups bonded with graphite were then reduced by the reduction process with the formation of rGO-Bi_2MoO_6 composite. Afterwards, Ag nanoparticles were photoreduced from AgCl on the surfaces of both Bi_2MoO_6 microspheres and rGO. The flat-band potential of the conduction band bottom of Bi_2MoO_6 can be obtained by applying the Mulliken electronegativity theory of atoms as follows (Equation 2):

$$E_{CB,Bi_2MoO_6} = X_{Bi_2MoO_6} - E^e - \frac{1}{2}E_g \qquad \textbf{\textit{Equation 2}}$$

where $E_{CB,Bi2MoO6}$, $X_{Bi2MoO6}$, E^e and E_g are the bottom potential of the conduction band, the electronegativity, the energy of free electrons on the hydrogen scale (≈ 4.5 eV) and the band gap energy of Bi_2MoO_6 (2.58 eV, tested by DRS shown in section 3.6), respectively. $E_{CB,Bi2MoO6}$ may be calculated as -0.34 eV, which is lower than the redox potential (0.80 eV) of Formula 2. In other words, electrons generated by visible light-activated Bi_2MoO_6 in Formula 1 have a reductive potential strong enough to reduce Ag^+ to metallic Ag.

$$Bi_2MoO_6 \xrightarrow{h\upsilon} e^-_{Bi_2MoO_6} + h^+_{Bi_2MoO_6}$$ ***Formula 3***

$$Ag^+_{adsorbed} + e^-_{Bi_2MoO_6} \longrightarrow Ag$$ ***Formula 4***



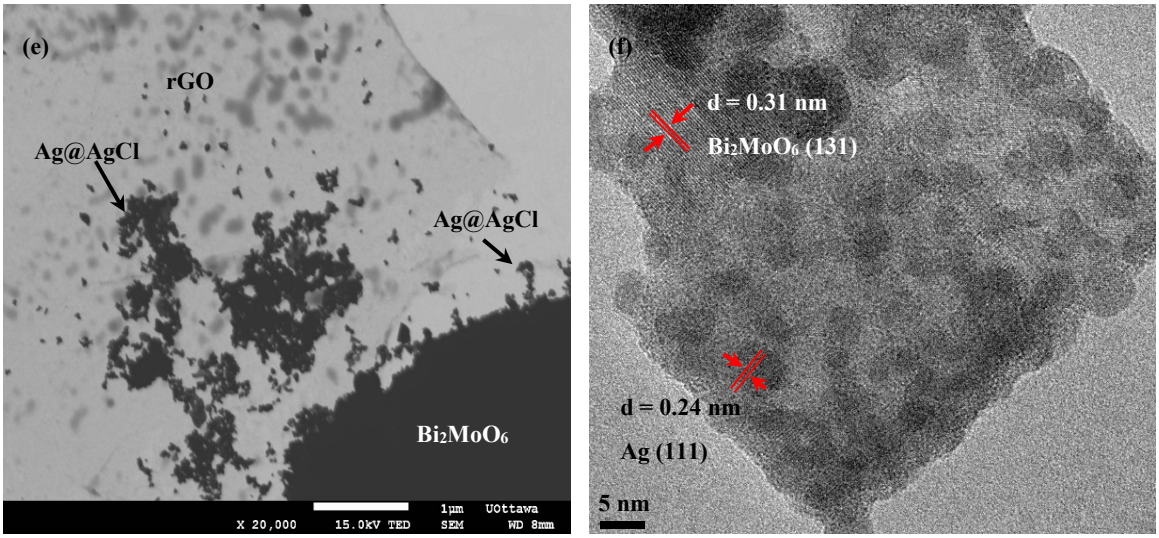


Figure 7.6 SEM images of (a) Bi_2MoO_6, (b) rGO-Bi_2MoO_6 and (c, d) Ag-rGO-Bi_2MoO_6 in low- and high-magnification, STEM images of (e) Ag-rGO-Bi_2MoO_6, and high-resolution TEM image of Ag-rGO-Bi_2MoO_6.

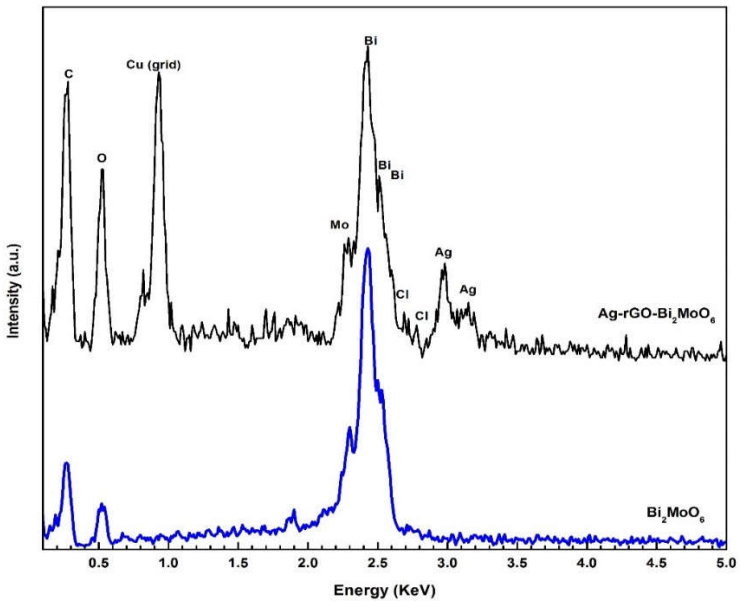


Figure 7.7 EDS of Bi_2MoO_6 and Ag-rGO-Bi_2MoO_6.

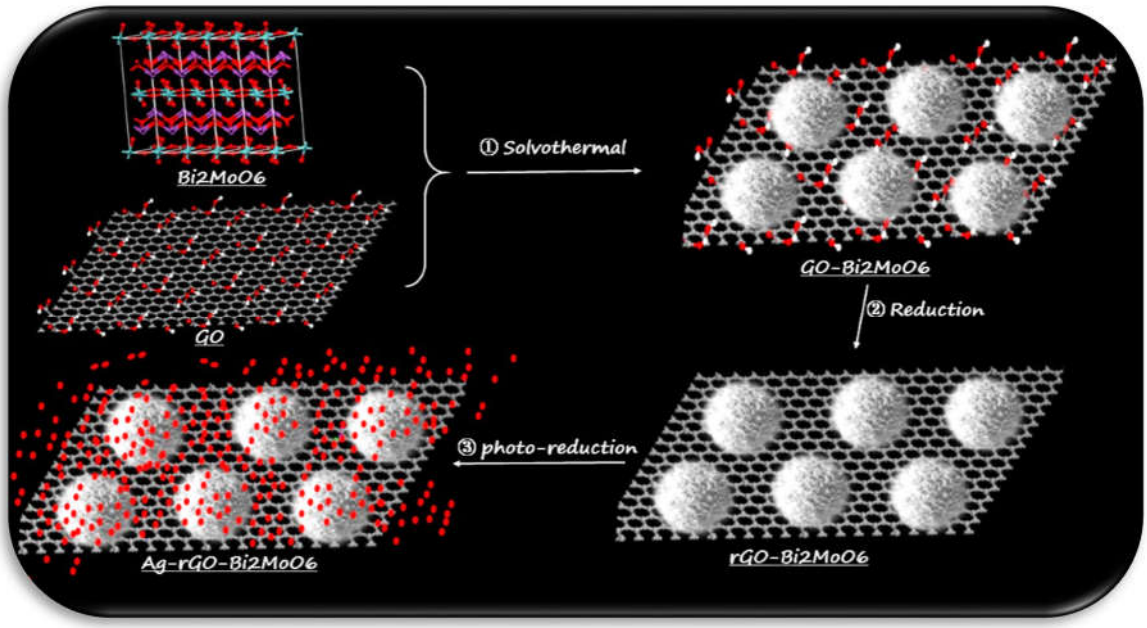


Figure 7.8 Proposed formation process for Ag (Ag^0 and AgCl)-, rGO-comodified Bi_2MoO_6.

7.3.5 BET surface areas

The N_2 adsorption/desorption isotherm of Bi_2MoO_6, GO-Bi_2MoO_6, rGO-Bi_2MoO_6 and Ag-rGO-Bi_2MoO_6 were obtained and are shown in Fig. 7.9. Each isotherm may be identified as a type IV physisorption isotherm [48]. However, different hysteresis loops between pure Bi_2MoO_6 and modified Bi_2MoO_6 composites were observed. Bi_2MoO_6 displays two hysteresis loops, while GO-, rGO- and Ag-rGO-Bi_2MoO_6 composites display only one hysteresis loop. Typically, for pure Bi_2MoO_6, the hysteresis loop at low relative pressures between 0.4 and 0.8 is of type H2, which indicates the existence of ink-bottle pores with narrow necks and wider bodies [48, 49]. The other hysteresis loop at a high relative pressure between 0.8 and 1.0 is of type H3, indicating the presence of aggregations of plate-like particles giving rise to slit-shaped pores [21, 48]. For Bi_2MoO_6 composites modified by GO, a hysteresis loop of type H2 was not observed, possibly due to the solvothermal treatment, in which GO may serve as a template to form more nanosheets and correspondingly results in a decrease of the finer intra-aggregated pores [16, 21]. The pore size distributions may be found in the insets of Fig. 7.9. The mesopores may correspond to the pores formed by Ostwald ripening [50] and the voids between crystals within the two-dimensional layers and interspaces between these stacked layers. The specific surface area,

pore volume, and average pore size are summarized in Table 7.3. As for the small quantity of GO in the composite, the differences in specific surface areas between the Bi_2MoO_6 and (r)GO-Bi_2MoO_6 composites were negligible. However, when silver was loaded onto the surface of the rGO-Bi_2MoO_6 composite, the specific surface area decreased. When the content of silver in the composites increased from 8 wt% to 16 wt%, the specific surface area was decreased from 27.2 to 26.8 m^2/g. The slight decrease in the surface area may result in the reduction of photocatalytic activity. The pore volume and average pore size decreased with loading Ag as well as (r)GO. This may decrease the photocatalytic activity as the adsorption capacity was reduced. However, this effect is negligible compared to the influence of doping silver and rGO in supressing electron/hole recombination to improve photocatalytic activity.

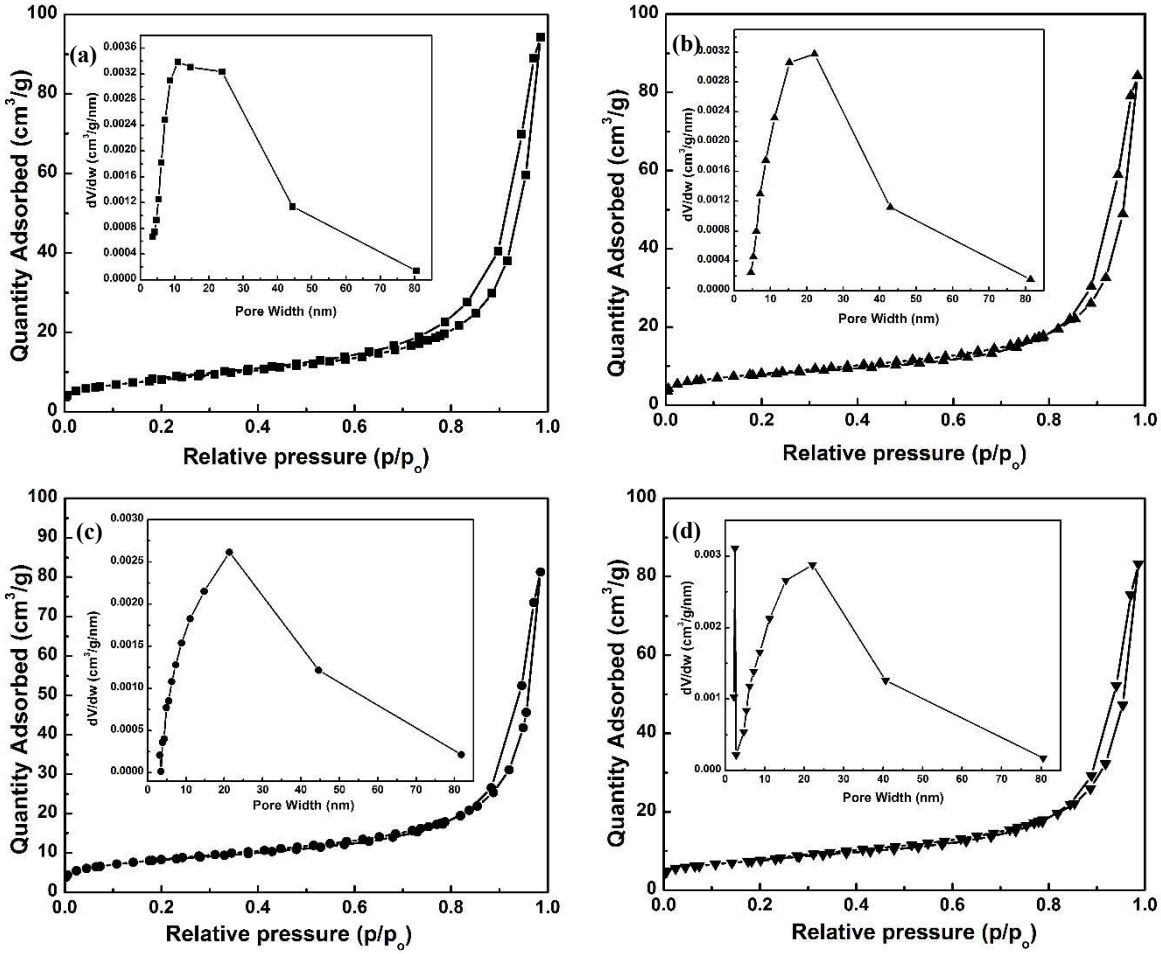


Figure 7.9 Nitrogen adsorption-desorption isotherms and the corresponding pore size distribution curves (insets) of (a) Bi_2MoO_6, (b) GO-Bi_2MoO_6, (c) rGO-Bi_2MoO_6, and (d) 8 wt%Ag-rGO-Bi_2MoO_6.

Table 7.3 Specific surface area, pore volume, and average pore size of Bi_2MoO_6, GO-Bi_2MoO_6, rGO-Bi_2MoO_6, and Ag-rGO-Bi_2MoO_6 composites.

Sample	S_{BET} (m^2/g)	Pore volume (cm^3/g)	Average pore size (nm)
Bi_2MoO_6	29.4	0.15	20.4
GO-Bi_2MoO_6	29.1	0.13	20.2
rGO-Bi_2MoO_6	30.2	0.13	18.8
8% Ag-rGO-Bi_2MoO_6	27.2	0.13	18.9
16% Ag-rGO-Bi_2MoO_6	26.8	0.12	18.8

7.3.6 Optical properties

Optical properties of prepared composite samples were investigated by UV-Vis diffuse reflectance spectroscopy and are shown in Fig. 7.10. It can be seen that the band gap absorption edge of Bi_2MoO_6 is around 480 nm. The band gap value can be calculated by the Kubelka-Munk function as approximately 2.58 eV [51]. When Bi_2MoO_6 was combined with GO and rGO, the band gap energies were negligibly influenced, although the ability to harvest visible light energy was improved. This enhancement in the visible light region may be attributed to the chemical bonding between Bi_2MoO_6 and (r)GO, similarly to what is seen in carbon-doped Bi_2MoO_6 composites [52]. With the reduction of oxygen functional groups, more carbon may bond with Bi_2MoO_6, and as a result the absorption intensity in the visible light region was further improved. It can be observed there was a strong absorbance signal for Ag/AgCl in the spectrum from 300 - 700 nm. As previously reported, the band gap edge of AgCl is approximately 420 nm (2.95 eV) [53]. The strong absorbance in the visible region may due to the strong surface plasmon resonance (SPR) absorption of Ag nanoparticles on the surface [18]. Correspondingly, the presence of Ag/AgCl on the surface of the rGO-Bi_2MoO_6 composite significantly improves its absorption capacity in the visible light region. Specifically, with increase to the content of silver from 1% to 16% in Ag-rGO-Bi_2MoO_6 composites, the adsorption in the visible region was strengthened. This improvement is supposed to enhance the visible-light driven photocatalytic activity.

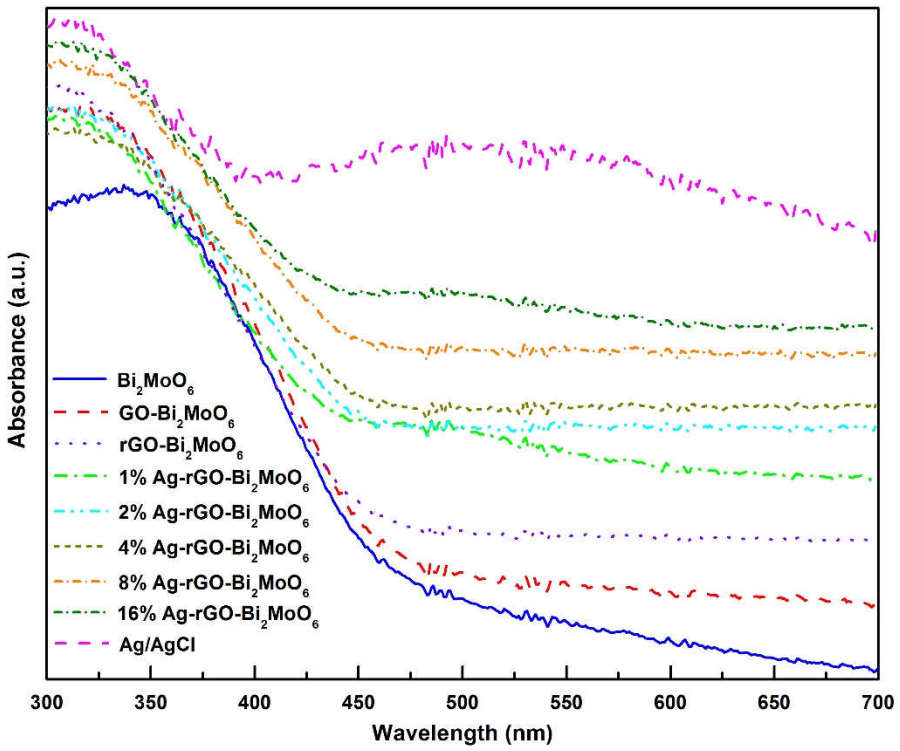


Figure 7.10 DRS of prepared samples: Bi_2MoO_6, Ag/AgCl, GO-Bi_2MoO_6, rGO-Bi_2MoO_6 and Ag-rGO-Bi_2MoO_6 composites.

7.3.7 Photocatalytic activity test

The photocatalytic oxidation properties of prepared samples were investigated by degrading phenol under visible light irradiation, the results of which are shown in Fig. 7.11. In Fig. 7.11a, it can be seen that approximately 10% of the phenol was removed in the presence of Bi_2MoO_6 under visible light irradiation over 300 min. For the GO-modified Bi_2MoO_6 composite, a relatively high removal efficiency was observed (26.5% over 300 min) for the visible light-driven photocatalytic degradation of phenol. When GO was reduced, the capacity of rGO-Bi_2MoO_6 to photocatalytically remove phenol was further improved. This phenomenon may occur due in part to the adsorption ability of phenol as well as the mobilities of photogenerated electrical carriers on GO, which were improved when most of the oxygen functional groups were reduced. Furthermore, when Ag was introduced to the rGO-Bi_2MoO_6 composites, the photocatalytic degradation efficiencies were significantly improved. When the quantity of Ag in the composite was increased from 1% to 8%, the removal efficiency of phenol was shown to increase from 52.0% to 97.5% under visible light irradiation over 300 min. This may be a result of the recombination rate

of photogenerated electrons and holes gradually reducing and the harvesting efficiency of visible light gradually improving with increasing Ag content. However, when the Ag content was above 8%, a decrease in the photocatalytic activity of Ag-rGO-Bi_2MoO_6 was observed, primarily because the effective decrease in available surface area resulted in a decrease in the number of reactive sites. In addition, excessive quantities of Ag on the surface may serve as recombination sites for photogenerated electrical pairs As a result, rGO-Bi_2MoO_6 doped with 8% Ag exhibited the best performance with regards to the photocatalytic degradation of phenol under visible light irradiation.

Separate component testing (GO, rGO, Ag-rGO, Ag/AgCl and Ag-Bi_2MoO_6) was investigated to ascertain the active site of this system (Fig. 7.11b). For pure GO, only about 10% of phenol were removed over 300 min. And there were about 15% of phenol were removed in the presence of rGO, which possibly resulted from mobility of photogenerated electrons was improved when functional groups on GO were reduced. It is clear that the Ag/AgCl photocatalyst shows an obvious photocatalytic activity with removal efficiency of 63.8% in 300 min, owing to its well-known visible light photocatalytic performance. After Ag/AgCl is coupled with rGO, the resultant Ag-rGO composites (Fig. 7.11b) show slightly enhanced photocatalytic activity. Additionally, when 8% Ag is directly deposited on the surface of Bi_2MoO_6, 62.4% of phenol was destroyed over 300 min, which is still 36% lower than that of the system with 8% Ag-rGO-Bi_2MoO_6. It can be concluded the synergy effect of Ag, rGO and Bi_2MoO_6 were observed with remarkably enhanced visible-light driven photocatalytic activity in the removal of colorless phenol.

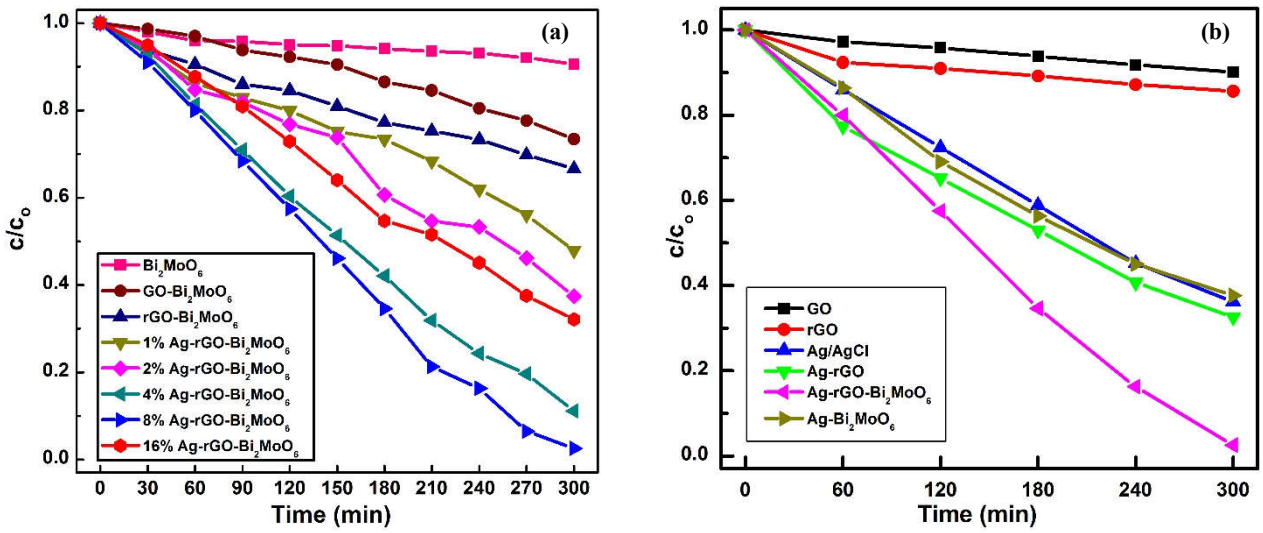


Figure 7.11 Concentration profiles of phenol during the photocatalytic degradation tests in the presence of different photocatalyst composites under visible light irradiation.

The photocatalytic kinetics of phenol degradation may be described by the Langmuir-Hinshelwood (L-H) model. As for the low initial concentration of phenol (~1 × 10^{-4} mol/L), the model can be simplified as (Equation 3):

$$\ln(\frac{c_o}{c_t}) = k't \qquad \textit{Equation 3}$$

where c_o, c_t, k' and t respectively represent the initial concentration of phenol, the concentration of phenol at time t, the reaction rate constant, and time. Kinetic results are summarized in Table 7.4. The high R^2 and low standard error (SE) indicate that the photocatalytic degradation of phenol under visible light irradiation in the presences of the prepared samples follows Pseudo-first-order kinetics. It can also be seen that the system with pure Bi_2MoO_6 exhibited the lowest rate constant. When GO in the composites was reduced to rGO, the reaction rate constant almost doubled. After loading Ag onto the rGO-Bi_2MoO_6 composite, the reaction rates were remarkably increased. The 8% Ag sample was found to exhibit the largest reaction rate constant, which was over ten times greater than that of pure Bi_2MoO_6 and about 57% higher than that of the 8% Ag-Bi_2MoO_6 composite. This further confirms the synergetic effects of Ag and rGO in the ternary composites accounting for the enhancement of the photocatalytic oxidation activity.

Table 7.4 Photocatalytic kinetics constants for systems with various photocatalyst composites.

Composite	k (x10^{-3})	R^2	SE (x10^{-5})	$k/k_{Bi2MoO6}$
Bi_2MoO_6	0.455	0.957	0.391	1
GO	0.354	0.997	0.781	0.778
rGO	0.587	0.948	0.560	1.29
Ag/AgCl	3.22	0.994	1.06	7.08
Ag/AgCl-rGO	3.70	0.999	0.510	8.13
Ag-Bi_2MoO_6	2.98	0.991	1.17	6.55
GO-Bi_2MoO_6	0.689	0.986	0.330	1.51
rGO-Bi_2MoO_6	1.46	0.988	0.658	3.21
1% Ag-rGO-Bi_2MoO_6	1.97	0.992	0.731	4.33
2% Ag-rGO-Bi_2MoO_6	2.16	0.991	0.848	4.75
4% Ag-rGO-Bi_2MoO_6	4.16	0.990	1.71	9.14
8% Ag-rGO-Bi_2MoO_6	4.70	0.987	2.24	10.3
16% Ag-rGO-Bi_2MoO_6	2.69	0.985	1.36	5.91

7.3.8 Possible mechanisms

7.3.8.1 Adsorption capacity

It has been reported aromatic organics can be easily adsorbed on graphene because of the presence of π-π interaction [19]. In Fig. 7.12, about 25% and 38% of phenol were adsorbed on GO and rGO respectively. It indicates phenol were much easier to adsorb on GO when functional groups were reduced. The adsorption capacity of Bi_2MoO_6 was slightly increased when GO and rGO doped. As photocatalysis occurs at the interface of the catalyst and adsorbed organics (phenol), the adsorption capacity is significant and directly determine the photocatalytic removal efficiency.

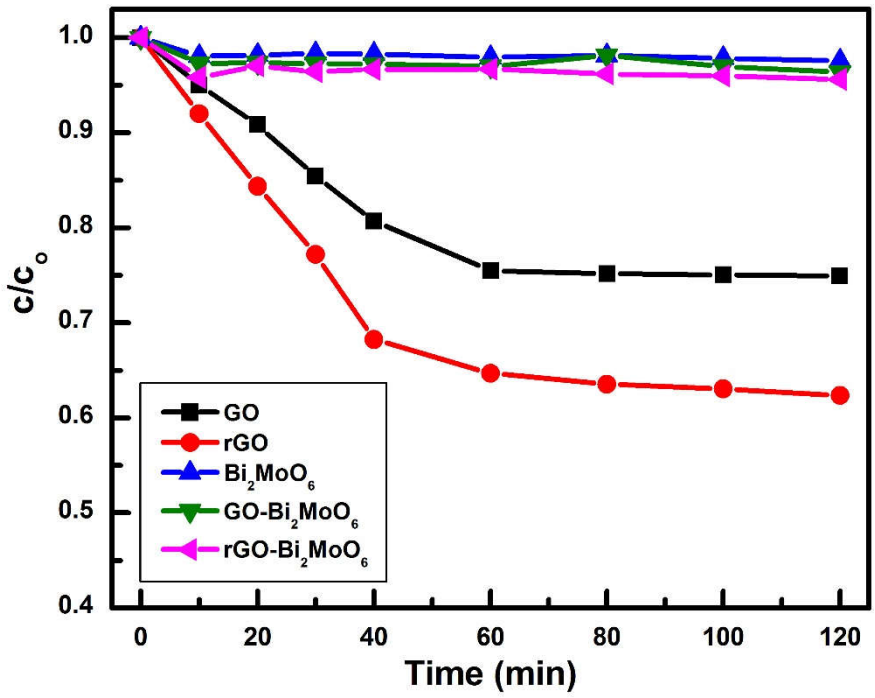


Figure 7.12 Adsorption profiles of phenol on samples: GO, rGO, Bi_2MoO_6, GO-Bi_2MoO_6 and rGO-Bi_2MoO_6.

7.3.8.2 Electrochemical property

To study the electrochemical properties, especially the interface charge separation efficiency of prepared samples, electrochemical impedance spectroscopy (EIS) was employed, and the EIS Nyquist plots of Bi_2MoO_6 as well as Ag-, rGO-, and Ag-rGO- doped Bi_2MoO_6 composites under visible light irradiation are shown in Fig. 7.13. It can be seen that only one semicircle is present for the EIS Nyquist plots of all prepared samples, indicating that the photocatalytic degradation process may be a simple electrode reaction and that the photogenerated electron transfer and the rate may be determined by the recombination of photogenerated electron/hole pairs [54, 55]. The equivalent circuits of these processes and the fitted electrical parameters are shown in Table 7.5. R_s is the resistance of the solution, R_{ct} is the resistance to electron transfer and CPE represents the constant phase element, which may be considered as a double-layered capacitor. The diameter of the arc in the EIS Nyquist plot determines the R_{ct}, where larger diameters resulting in higher values for R_{ct} [56]. It can be seen that the semicircle of Bi_2MoO_6 with the largest diameter and the highest resistance of 21630 Ω, when Ag and rGO are separately

doped on its surface, the diameters of their semicircles were decreased, resulting in R_{ct} values of 12760 and 3880 Ω respectively. This suggests that Ag or rGO doped in the composites may increase the amount of electron transfer and may decrease the recombination of electron/hole pairs. When both Ag and rGO are present in the Bi_2MoO_6 composites, the R_{ct} values were further decreased to 1280 which is 1/16 that of pure Bi_2MoO_6. The lowest resistance to electron transfer is crucial evidence to confirm that it can significantly improve the separation of photogenerated electron/hole pairs by introducing Ag and rGO to the composite. The highest electron/hole separation efficiency may also be a result of the enhanced photocatalytic activity in the removal of organic pollutants under visible light irradiation.

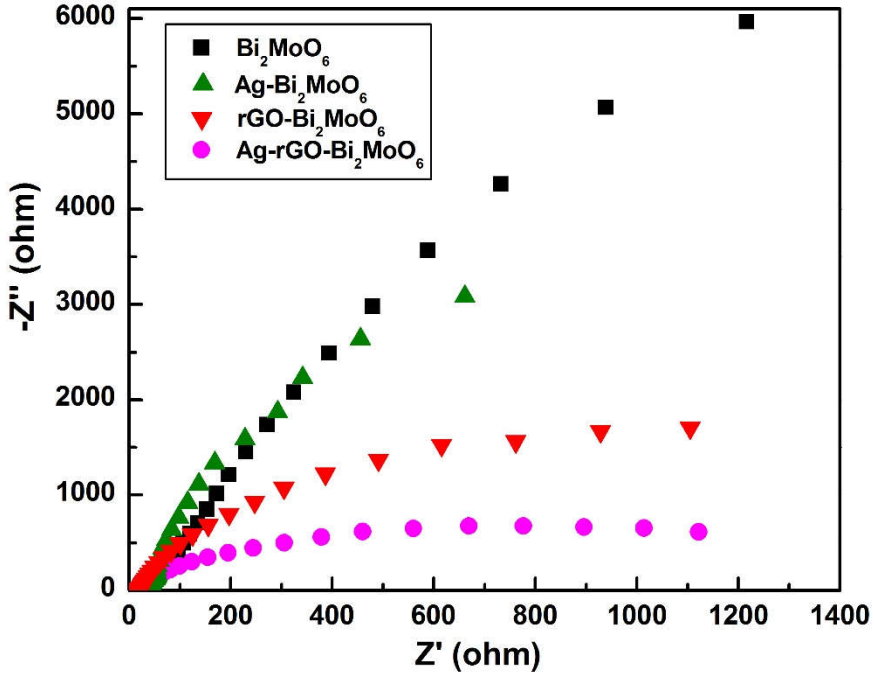
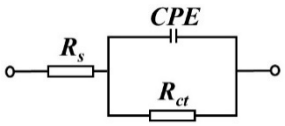


Figure 7.13 EIS Nyquist plots of the Bi_2MoO_6, Ag-Bi_2MoO_6, rGO-Bi_2MoO_6, and Ag-rGO-Bi_2MoO_6 photocatalysts.

Table 7.5 Fitting results for equivalent circuits of different prepared samples.

Samples	R_s (Ω)	R_{ct} (Ω)	*CPE* (μf)	Equivalent circuits
Bi_2MoO_6	35.21	21630	21.52	
Ag-Bi_2MoO_6	29.76	12760	41.60	
rGO-Bi_2MoO_6	40.79	3880	40.27	
Ag-rGO-Bi_2MoO_6	23.59	1280	46.64	

7.3.8.3 Proposed oxidation processes

In the photocatalytic oxidation process, photogenerated holes and oxidative free radicals were reported as the most important species with regards to the removal of organic pollutants from wastewater. In this work, EDTA-2Na and t-butanol were selected as scavengers for holes and oxidative free radicals, and the phenol relative concentration profiles of these tests are shown in Fig. 7.14a. It can be seen that about 23.0% and 85.9% of phenol was removed under visible light irradiation over 300 min in the presence of EDTA-2Na and t-butanol respectively. This suggests that both holes and oxidative free radicals contribute to the photocatalytic degradation of organics, and that photogenerated holes play the dominant role owing for their strong oxidative capacities in the system.

The reaction pathways for the photocatalytic degradation of phenol were also studied. Possible intermediates including hydroquinone, catechol and benzoquinone were also detected, the results of which are shown in Fig. 7.14b. It was found that the concentration of phenol decreased from 11.8 to 0.5 mg/L over 300 min, with the generation of hydroquinone, catechol and benzoquinone at low concentrations. This indicates that the rate-determining step to completely destroy phenol is the phenol hydroxylation. The proceeding intermediates are then more easily and rapidly degraded, the products of which may be carboxylic acids then finally CO_2 and H_2O under the influence of photogenerated oxidants [57, 58].

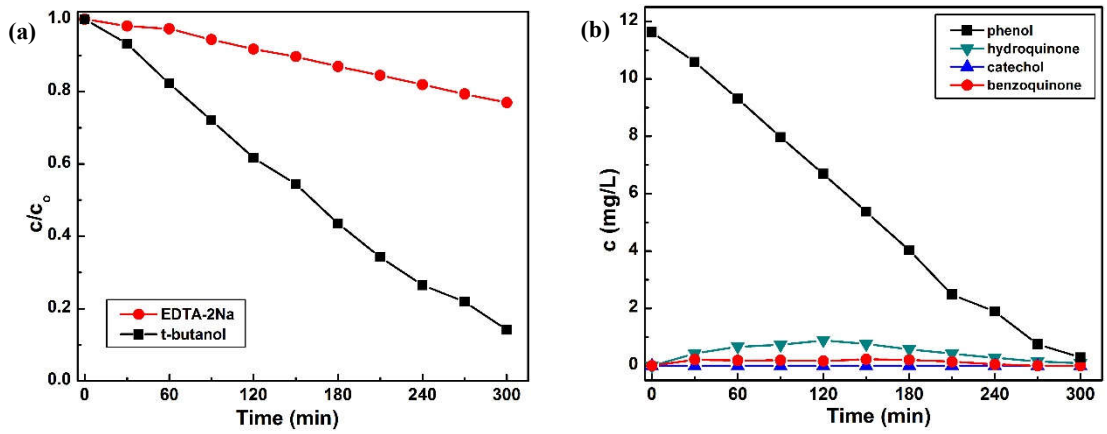


Figure 7.14 (a) Relative concentration of phenol with different scavengers added, and (b) concentrations of phenol and possible intermediates (hydroquinone, catechol and benzoquinone) in the presence of Ag-rGO-Bi_2MoO_6 composites under visible light irradiation.

Based on the above analysis, a possible mechanism for the enhanced photocatalytic activity of Ag- and GO-modified Bi_2MoO_6 Z-scheme composites is proposed (as shown in Fig. 7.15). Bi_2MoO_6, with a band gap of 2.58 eV may be activated by visible light photons with electrons jump from the valence band (VB) to the conduction band (CB). Silver nanoparticles on the surface of the composite can also absorb visible light photons with energies between 1.0 and 4.0 eV as a result of the SPR effect and their dipolar character [18, 59]. Therefore, the generated electrons have enough energy to transfer to the CB of either Bi_2MoO_6 or AgCl. The band gap of AgCl is 3.25 eV, and the CB potentials of AgCl and Bi_2MoO_6 are -0.09 and -0.34 eV, respectively, both of which are more negative than the one-electron reduction potential of $E(O_2/\bullet O_2^-)$ (-0.046 eV vs NHE) [14, 60]. This suggests that $\bullet O_2^-$ may be generated via oxygen being reduced by electrons on the CB of both Bi_2MoO_6 and AgCl. Photogenerated holes left on the VB of AgCl with strong oxidative capacities may react with adsorbed H_2O and -OH to produce hydroxyl free radicals (•OH). Comparatively, holes accumulated on the VB of Bi_2MoO_6 cannot generate •OH, as the potential of its VB (2.24 eV) is more negative than the redox potential of •OH/-OH (2.80 eV). This agrees well with the results obtained in the quenching experiments. Adsorbed Cl^- may also be oxidized to Cl•, which is capable of oxidizing phenol and returning to its reduced, anionic state (Cl^-) [35]. Electrons on the CB of Bi_2MoO_6 can be captured by Ag^+ via recombination with holes generated by the SPR absorption of Ag

nanoparticles. This may significantly decrease the recombination rate of electrons and holes generated in Bi_2MoO_6. Furthermore, the Z-scheme structure between Bi_2MoO_6 and AgCl was also found to be beneficial for the separation of photogenerated electron-hole pairs [61]. In addition, using reduced GO as the substrate may contribute to the suppression of charge recombination by accepting and transporting electrons. Phenol may also be much easier to adsorb onto the surface of rGO via strong π-π interactions compared to Bi_2MoO_6 [62]. In conclusion, the improved separation efficiency of photogenerated electron-hole pairs via capture of Ag nanoparticles; Z-scheme structure and transportation through rGO; increased harvesting intensity of visible light photons due to the SPR effect; and strong adsorption of phenol on rGO layers contributed to an enhanced photocatalytic activity towards the degradation of phenol under visible light irradiation.

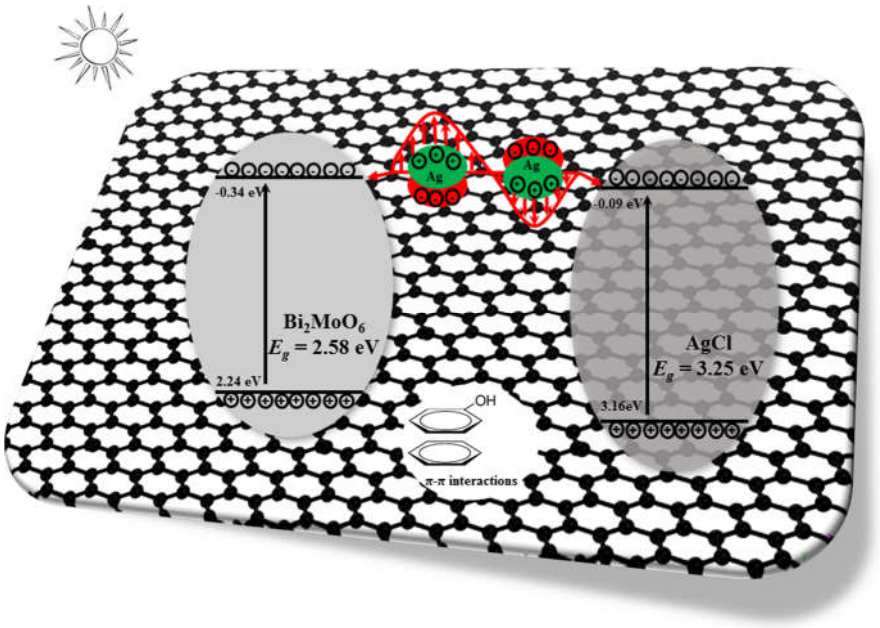


Figure 7.15 Proposed photocatalytic degradation of organics in the presence of Ag-rGO-Bi_2MoO_6 composites under visible light irradiation.

7.4 Conclusions

A plasmonic ternary Ag-rGO-Bi_2MoO_6 composite was prepared and studied. It exhibited an excellent photocatalytic degradation for the removal of organic pollutants in wastewater. The enhanced effect may be interpreted as a high separation efficiency of photogenerated electron/hole pairs as the electrons are trapped by Ag nanoparticle and rGO. The

electrochemical properties further confirmed that the electrons can be easier to transfer when Ag and rGO are introduced to the composites. Additionally, the Ag nanoparticles may harvest visible light photons due to the surface plasmon resonance effect, and the construction of a Z-scheme band structure between the AgCl and Bi_2MoO_6 may also contribute to the reduction of the photogenerated electron/hole pair recombination rate. The excellent visible light-driven photocatalytic degradation activity make this ternary composite a promising and competitive candidate in the area of photocatalytic wastewater treatment.

References

1. Meng Nan Chong, Bo Jin, Christopher WK Chow and Chris Saint, "Recent developments in photocatalytic water treatment technology: a review," *Water research*, vol. 44, no. 10, pp. 2997-3027, 2010.

2. Dhananjay S Bhatkhande, Vishwas G Pangarkar and Anthony A Beenackers, "Photocatalytic degradation for environmental applications–a review," *Journal of Chemical Technology and Biotechnology*, vol. 77, no. 1, pp. 102-116, 2002.

3. Giovanni Palmisano, Vincenzo Augugliaro, Mario Pagliaro and Leonardo Palmisano, "Photocatalysis: a promising route for 21st century organic chemistry," *Chemical Communications*, no. 33, pp. 3425-3437, 2007.

4. Oomman K. Varghese, Maggie Paulose, Thomas J. LaTempa and Craig A. Grimes, "High-Rate Solar Photocatalytic Conversion of CO2 and Water Vapor to Hydrocarbon Fuels," *Nano Letters*, vol. 9, no. 2, pp. 731-737, 2009.

5. Joanne Gamage and Zisheng Zhang, "Applications of Photocatalytic Disinfection," *International Journal of Photoenergy*, vol. 2010, pp. 1-11, 2010.

6. Xiangchao Meng, Zisheng Zhang and Xingang Li, "Synergetic photoelectrocatalytic reactors for environmental remediation: A review," *Journal of Photochemistry and Photobiology C: Photochemistry Reviews*, vol. 24, pp. 83-101, 2015.

7. Xiangchao Meng and Zisheng Zhang, "Facile synthesis of BiOBr/Bi_2WO_6 heterojunction semiconductors with high visible-light-driven photocatalytic activity," *Journal of Photochemistry and Photobiology A: Chemistry*, vol. 310, no. 0, pp. 33-44, 2015.

8. HongHua Li, ChaoYu Liu, KunWei Li and Hao Wang, "Preparation, characterization and photocatalytic properties of nanoplate Bi2MoO6 catalysts," *Journal of Materials Science*, vol. 43, no. 22, pp. 7026-7034, 2008.

9. Kangrong Lai, Wei Wei, Ying Dai, Ruiqin Zhang and Baibiao Huang, "DFT calculations on structural and electronic properties of Bi_2MO_6 (M = Cr, Mo, W)," *Rare Metals*, vol. 30, no. 1, pp. 166-172, 2011.

10. Xu Zhao, Jiuhui Qu, Huijuan Liu, Zhimin Qiang, Ruiping Liu and Chengzhi Hu, "Photoelectrochemical degradation of anti-inflammatory pharmaceuticals at Bi2MoO6–boron-doped diamond hybrid electrode under visible light irradiation," *Applied Catalysis B: Environmental*, vol. 91, no. 1–2, pp. 539-545, 2009.

11. Tengfei Zhou, Juncheng Hu and Jinlin Li, "Er3+ doped bismuth molybdate nanosheets with exposed {0 1 0} facets and enhanced photocatalytic performance," *Applied Catalysis B: Environmental*, vol. 110, pp. 221-230, 2011.

12. Haiping Li, Jingyi Liu, Wanguo Hou, Na Du, Renjie Zhang and Xutang Tao, "Synthesis and characterization of g-C3N4/Bi2MoO6 heterojunctions with enhanced visible light photocatalytic activity," *Applied Catalysis B: Environmental*, vol. 160–161, pp. 89-97, 2014.

13. Mingyi Zhang, Changlu Shao, Jingbo Mu, Zhenyi Zhang, Zengcai Guo, Peng Zhang and Yichun Liu, "One-dimensional Bi2MoO6/TiO2 hierarchical heterostructures with enhanced photocatalytic activity," *CrystEngComm*, vol. 14, no. 2, pp. 605-612, 2012.

14. Xiaoxuan Li, Siman Fang, Lei Ge, Changcun Han, Ping Qiu and Weilong Liu, "Synthesis of flower-like Ag/AgCl-Bi2MoO6 plasmonic photocatalysts with enhanced visible-light photocatalytic performance," *Applied Catalysis B: Environmental*, vol. 176–177, pp. 62-69, 2015.

15. Jing Zhang, Chenggang Niu, Ji Ke, Laifeng Zhou and Guangming Zeng, "Ag/AgCl/Bi2MoO6 composite nanosheets: A plasmonic Z-scheme visible light photocatalyst," *Catalysis Communications*, vol. 59, pp. 30-34, 2015.

16. Yan Zhang, Yukun Zhu, Jianqiang Yu, Dongjiang Yang, Tsz Wai Ng, Po Keung Wong and Jimmy C. Yu, "Enhanced photocatalytic water disinfection properties of Bi2MoO6-

RGO nanocomposites under visible light irradiation," *Nanoscale*, vol. 5, no. 14, pp. 6307-6310, 2013.

17. Peifang Wang, Yanhui Ao, Chao Wang, Jun Hou and Jin Qian, "A one-pot method for the preparation of graphene–Bi2MoO6 hybrid photocatalysts that are responsive to visible-light and have excellent photocatalytic activity in the degradation of organic pollutants," *Carbon*, vol. 50, no. 14, pp. 5256-5264, 2012.

18. Peng Wang, Baibiao Huang, Xiaoyan Qin, Xiaoyang Zhang, Ying Dai, Jiyong Wei and Myung-Hwan Whangbo, "Ag@AgCl: A Highly Efficient and Stable Photocatalyst Active under Visible Light," *Angewandte Chemie International Edition*, vol. 47, no. 41, pp. 7931-7933, 2008.

19. Quanjun Xiang, Jiaguo Yu and Mietek Jaroniec, "Graphene-based semiconductor photocatalysts," *Chemical Society Reviews*, vol. 41, no. 2, pp. 782-796, 2012.

20. Daniel R. Dreyer, Sungjin Park, Christopher W. Bielawski and Rodney S. Ruoff, "The chemistry of graphene oxide," *Chemical Society Reviews*, vol. 39, no. 1, pp. 228-240, 2010.

21. Jinhong Bi, Wei Fang, Li Li, Xiaofen Li, Minghua Liu, Shijing Liang, Zizhong Zhang, Yunhui He, Huaxiang Lin, Ling Wu, Shengwei Liu and Po Keung Wong, "Ternary reduced-graphene-oxide/Bi_2MoO_6/Au nanocomposites with enhanced photocatalytic activity under visible light," *Journal of Alloys and Compounds*, vol. 649, pp. 28-34, 2015.

22. Yan Liu, Yao Zhang, Guoheng Ma, Zan Wang, Kaiyu Liu and Hongtao Liu, "Ethylene glycol reduced graphene oxide/polypyrrole composite for supercapacitor," *Electrochimica Acta*, vol. 88, pp. 519-525, 2013.

23. Xiangchao Meng and Zisheng Zhang, "Ag/AgCl Loaded Bi_2WO_6 Composite: A Plasmonic Z-Scheme Visible Light-Responsive Photocatalyst," *International Journal of Photoenergy*, vol. 2016, pp. 11, 2016.

24. Guoqiang Luo, Xiaojuan Jiang, Meijuan Li, Qiang Shen, Lianmeng Zhang and Huogen Yu, "Facile fabrication and enhanced photocatalytic performance of Ag/AgCl/rGO heterostructure photocatalyst," *ACS applied materials & interfaces*, vol. 5, no. 6, pp. 2161-2168, 2013.

25. F Pertlik and J Zemann, "Neubestimmung der Kristallstruktur des Köchlinits," *Fortschr.*

Miner. Beih, vol. 60, pp. 162-163, 1982.

26. J. P. Tiwari and Chepuri R. K. Rao, "Template synthesized high conducting silver chloride nanoplates," *Solid State Ionics*, vol. 179, no. 9–10, pp. 299-304, 2008.

27. A. Smakula and J. Kalnajs, "Precision Determination of Lattice Constants with a Geiger-Counter X-Ray Diffractometer," *Physical Review*, vol. 99, no. 6, pp. 1737-1743, 1955.

28. Yuanguo Xu, Hui Xu, Huaming Li, Jiexiang Xia, Chengtang Liu and Ling Liu, "Enhanced photocatalytic activity of new photocatalyst Ag/AgCl/ZnO," *Journal of Alloys and Compounds*, vol. 509, no. 7, pp. 3286-3292, 2011.

29. Minh Thang Le, Luong Huu Bac, Isabel Van Driessche, Serge Hoste and Willy J. M. Van Well, "The synergy effect between gamma and beta phase of bismuth molybdate catalysts: Is there any relation between conductivity and catalytic activity?," *Catalysis Today*, vol. 131, no. 1–4, pp. 566-571, 2008.

30. HongHua Li, KunWei Li and Hao Wang, "Hydrothermal synthesis and photocatalytic properties of bismuth molybdate materials," *Materials Chemistry and Physics*, vol. 116, no. 1, pp. 134-142, 2009.

31. Jinhong Bi, Ling Wu, Jie Li, Zhaohui Li, Xuxu Wang and Xianzhi Fu, "Simple solvothermal routes to synthesize nanocrystalline Bi_2MoO_6 photocatalysts with different morphologies," *Acta Materialia*, vol. 55, no. 14, pp. 4699-4705, 2007.

32. CH Bichler, M Bischoff, HC Langowski and U Moosheimer, "39th Annual Technical Conference of the Society of Vacuum Coaters," *Philadelphia, USA, May*, vol. 5, 1996.

33. Peng Zeng, Qinggang Zhang, Tianyou Peng and Xiaohu Zhang, "One-pot synthesis of reduced graphene oxide-cadmium sulfide nanocomposite and its photocatalytic hydrogen production," *Physical Chemistry Chemical Physics*, vol. 13, no. 48, pp. 21496-21502, 2011.

34. Yang-Sen Xu and Wei-De Zhang, "Monodispersed Ag3PO4 nanocrystals loaded on the surface of spherical Bi_2MoO_6 with enhanced photocatalytic performance," *Dalton Transactions*, vol. 42, no. 4, pp. 1094-1101, 2013.

35. Joanne Gamage McEvoy, Wenquan Cui and Zisheng Zhang, "Synthesis and

characterization of Ag/AgCl–activated carbon composites for enhanced visible light photocatalysis," *Applied Catalysis B: Environmental*, vol. 144, no. 0, pp. 702-712, 2014.

36. D Briggs and MP Seah, "John Willey & Sons," Ed., 1993.

37. CD Wagner and GE Muilenberg, *Handbook of X-ray photoelectron spectroscopy*, Perkin-Elmer, 1979.

38. J. H. Scofield, "Hartree-Slater subshell photoionization cross-sections at 1254 and 1487 eV," *Journal of Electron Spectroscopy and Related Phenomena*, vol. 8, no. 2, pp. 129-137, 1976.

39. David R. Penn, "Quantitative chemical analysis by ESCA," *Journal of Electron Spectroscopy and Related Phenomena*, vol. 9, no. 1, pp. 29-40, 1976.

40. Liwu Zhang, Tongguang Xu, Xu Zhao and Yongfa Zhu, "Controllable synthesis of Bi2MoO6 and effect of morphology and variation in local structure on photocatalytic activities," *Applied Catalysis B: Environmental*, vol. 98, no. 3–4, pp. 138-146, 2010.

41. S. R. G. Carrazán, C. Martin, V. Rives and R. Vidal, "An FT-IR spectroscopy study of the adsorption and oxidation of propene on multiphase Bi, Mo and Co catalysts," *Spectrochimica Acta Part A: Molecular and Biomolecular Spectroscopy*, vol. 52, no. 9, pp. 1107-1118, 1996.

42. F. Trifirò, H. Hoser and R. D. Scarle, "Relationship between structure and activity of mixed oxides as oxidation catalysts: I. Preparation and solid state reactions of Bi-molybdates," *Journal of Catalysis*, vol. 25, no. 1, pp. 12-24, 1972.

43. J. M. Fernández, C. Barriga, M. A. Ulibarri, F. M. Labajos and V. Rives, "New Hydrotalcite-like Compounds Containing Yttrium," *Chemistry of Materials*, vol. 9, no. 1, pp. 312-318, 1997.

44. Michael R. Prairie, Albert Renken, James G. Highfield, K. Ravindranathan Thampi and Michael Grätzel, "A fourier transform infrared spectroscopic study of CO_2 methanation on supported ruthenium," *Journal of Catalysis*, vol. 129, no. 1, pp. 130-144, 1991.

45. M. A. Hasan, M. I. Zaki and L. Pasupulety, "Oxide-catalyzed conversion of acetic acid into acetone: an FTIR spectroscopic investigation," *Applied Catalysis A: General*, vol. 243,

no. 1, pp. 81-92, 2003.

46. Li-Fen Liao, Chen-Fu Lien and Jong-Liang Lin, "FTIR study of adsorption and photoreactions of acetic acid on TiO_2," *Physical Chemistry Chemical Physics*, vol. 3, no. 17, pp. 3831-3837, 2001.

47. Ping Wang, Jin Wang, Xuefei Wang, Huogen Yu, Jiaguo Yu, Ming Lei and Yonggang Wang, "One-step synthesis of easy-recycling TiO_2-rGO nanocomposite photocatalysts with enhanced photocatalytic activity," *Applied Catalysis B: Environmental*, vol. 132–133, pp. 452-459, 2013.

48. KSW Sing, DH Everett, RAW Haul, L Moscou, RA Pierotti, J Rouquerol and T Siemieniewska, "Physical and biophysical chemistry division commission on colloid and surface chemistry including catalysis," *Pure Applied Chemistry*, vol. 57, no. 4, pp. 603-619, 1985.

49. Jiaguo Yu and Lifang Qi, "Template-free fabrication of hierarchically flower-like tungsten trioxide assemblies with enhanced visible-light-driven photocatalytic activity," *Journal of Hazardous Materials*, vol. 169, no. 1-3, pp. 221-227, 2009.

50. Peter W Voorhees, "The theory of Ostwald ripening," *Journal of Statistical Physics*, vol. 38, no. 1-2, pp. 231-252, 1985.

51. Gaozu Liao, Shuo Chen, Xie Quan, Hongtao Yu and Huimin Zhao, "Graphene oxide modified g-C_3N_4 hybrid with enhanced photocatalytic capability under visible light irradiation," *Journal of Materials Chemistry*, vol. 22, no. 6, pp. 2721-2726, 2012.

52. Hao Zhang, Xiaojun Lv, Yueming Li, Ying Wang and Jinghong Li, "P25-Graphene Composite as a High Performance Photocatalyst," *ACS Nano*, vol. 4, no. 1, pp. 380-386, 2010.

53. Hui Zhang, Xinfei Fan, Xie Quan, Shuo Chen and Hongtao Yu, "Graphene Sheets Grafted Ag@AgCl Hybrid with Enhanced Plasmonic Photocatalytic Activity under Visible Light," *Environmental Science & Technology*, vol. 45, no. 13, pp. 5731-5736, 2011.

54. Janet M. Kesselman, Gary A. Shreve, Michael R. Hoffmann and Nathan S. Lewis, "Flux-Matching Conditions at TiO_2 Photoelectrodes: Is Interfacial Electron Transfer to O_2 Rate-Limiting in the TiO_2-Catalyzed Photochemical Degradation of Organics?," *The*

Journal of Physical Chemistry, vol. 98, no. 50, pp. 13385-13395, 1994.

55. Baifu Xin, Zhiyu Ren, Haiyuan Hu, Xiangyu Zhang, Chunlei Dong, Keying Shi, Liqiang Jing and Honggang Fu, "Photocatalytic activity and interfacial carrier transfer of Ag–TiO_2 nanoparticle films," *Applied Surface Science*, vol. 252, no. 5, pp. 2050-2055, 2005.

56. Baifu Xin, Zhiyu Ren, Peng Wang, Jia Liu, Liqiang Jing and Honggang Fu, "Study on the mechanisms of photoinduced carriers separation and recombination for Fe^{3+}–TiO_2 photocatalysts," *Applied Surface Science*, vol. 253, no. 9, pp. 4390-4395, 2007.

57. Xiao-yan Li, Yu-hong Cui, Yu-jie Feng, Zhao-ming Xie and Ji-Dong Gu, "Reaction pathways and mechanisms of the electrochemical degradation of phenol on different electrodes," *Water Research*, vol. 39, no. 10, pp. 1972-1981, 2005.

58. Chunde Wu, Xinhui Liu, Dongbin Wei, Jinchu Fan and Liansheng Wang, "Photosonochemical degradation of Phenol in water," *Water Research*, vol. 35, no. 16, pp. 3927-3933, 2001.

59. Suljo Linic, Phillip Christopher and David B. Ingram, "Plasmonic-metal nanostructures for efficient conversion of solar to chemical energy," *Nature Materials*, vol. 10, no. 12, pp. 911-921, 2011.

60. Taixing Wu, Guangming Liu, Jincai Zhao, Hisao Hidaka and Nick Serpone, "Photoassisted Degradation of Dye Pollutants. V. Self-Photosensitized Oxidative Transformation of Rhodamine B under Visible Light Irradiation in Aqueous TiO2 Dispersions," *The Journal of Physical Chemistry B*, vol. 102, no. 30, pp. 5845-5851, 1998.

61. Yasuyoshi Sasaki, Hiroaki Nemoto, Kenji Saito and Akihiko Kudo, "Solar Water Splitting Using Powdered Photocatalysts Driven by Z-Schematic Interparticle Electron Transfer without an Electron Mediator," *The Journal of Physical Chemistry C*, vol. 113, no. 40, pp. 17536-17542, 2009.

62. Yanyuan Wen, Hanming Ding and Yongkui Shan, "Preparation and visible light photocatalytic activity of Ag/TiO_2/graphene nanocomposite," *Nanoscale*, vol. 3, no. 10, pp. 4411-4417, 2011.

SECTION V: MAGNETICALLY SEPARABLE BISMUTH-BASED PHOTOCATALYST

Chapter 8 Synthesis and Characterization of Plasmonic and Magnetically Separable Ag/AgCl-Bi_2WO_6@ Fe_3O_4@SiO_2 Core-shell Composites for Visible Light-Induced Water Detoxification

Xiangchao Meng and Zisheng Zhang

Journal of Colloid and Interface Science 485 (2017), 296-307

Abstract

A magnetic photocatalyst composite (Ag/AgCl-Bi_2WO_6) was proposed and investigated. Magnetic Bi_2WO_6 was hydrothermally loaded onto silica-coated Fe_3O_4 which was synthesized by coprecipitation in addition to a modified Stöber process. Ag nanoparticles were then photoreduced on the surface of Bi_2WO_6. The prepared samples were characterized by X-ray diffraction, transmission electron microscopy, X-ray photoelectron spectroscopy, Fourier transform infrared spectroscopy, and ultraviolet-visible light diffuse reflectance spectroscopy. Magnetic properties were investigated using a superconducting quantum interface magnetometer, with samples exhibiting quasi-superparamagnetic behaviour. The visible light-induced photocatalytic activities were evaluated by degrading a model dye, RhB, as well as a colourless aromatic organic compound, phenol. Samples found to possess an excellent performance in terms of detoxification. Pathways and mechanisms for the photocatalytic degradation of organic compounds in the presence of Ag/AgCl-(M) Bi_2WO_6 were also investigated and proposed.

8.1 Introduction

Semiconductor photocatalysts have been widely applied to the treatment of wastewater and air [1, 2]. Undeniably, the most widely used photocatalyst is TiO_2, which is activated by

UV light [3]. Aiming to broaden the range of wavelengths of the irradiation to incorporate visible light, a variety of novel materials have been investigated. Suitably, bismuth-based materials such as Bi_2MO_6 (M = W, Mo) or BiOX (X = Cl, Br, I) [4-7] exhibit visible light-induced photocatalytic activity with regards to the degradation of most organic pollutants.

As the simplest member of the Aurivillius family, Bi_2WO_6 is increasingly attracting the attention of researchers due to its promising activity in the degradation of organic contaminants. The major challenge in applying Bi_2WO_6 as a photocatalyst however is the high recombination rate of photogenerated electrons and holes. Approaches to overcome this obstacle mainly include adjustment of the morphologies of photocatalysts [8-10], formation of heterostructures [11, 12], and doping [13-15]. Recently, Ag/AgCl has been found to be a highly efficient and stable photocatalyst under visible light irradiation, primarily due to the surface plasmon resonance (SPR) effect [16, 17]. In addition, loading of Ag/AgCl onto other photocatalysts to form a heterostructure has been experimentally proven as an effective way to improve the separation rate of electron/hole pairs, so as to enhance the visible light-induced photocatalytic activity of the photocatalyst [18].

Implementation of the photocatalyst in the reactor require that particle samples are used so as to improve mass transfer between pollutants and the catalyst. However, this generally leads to a complicated operation process and increases the operating cost, especially for nanoscale catalysts. To mitigate this issue, magnetic separation provides an effective way to separate and recycle magnetic photocatalysts by use of an external magnet. This technique has recently been accomplished by many researchers [19-22]. Aiming to combine Bi_2WO_6 and Fe_3O_4, SiO_2 was applied as a binding material due to its flexibility and adhesiveness [23]. By coating Fe_3O_4 with SiO_2, acid corrosion and oxidation of Fe_3O_4 is minimized. To the best of our knowledge, Ag/AgCl-modified magnetic Bi_2WO_6 has yet to be reported in literature.

In this work, the successful preparation of Ag/AgCl-magnetic Bi_2WO_6 is reported. The composites were prepared by five steps. The prepared composites were characterized by various techniques to explore their properties. Photocatalytic activities of the prepared materials were also measured by degrading an organic pollutant dye (RhB) as well as a colourless aromatic organic pollutant (phenol) under visible light irradiation ($\lambda > 410$ nm).

8.2 Experimental

8.2.1 Preparation of magnetic Bi_2WO_6 ((M) Bi_2WO_6)

All chemicals were purchased from Fisher Scientific at analytical purities or higher and were used as received. Magnetic Bi_2WO_6 was synthesized under the following three steps: 1) preparation of Fe_3O_4 nanoparticles, 2) coating of prepared Fe_3O_4 nanoparticles with silica, and 3) hydrothermal preparation of Bi_2WO_6 on silica-coated Fe_3O_4 nanoparticles.

Magnetic Fe_3O_4 nanoparticles were prepared by co-precipitation of $FeCl_3$•$6H_2O$ and $FeSO_4$•$7H_2O$ at a molar ratio of 2.6:1 [24, 25]. Iron salts (7.17 g $FeCl_3$•$6H_2O$ and 2.83 g $FeSO_4$•$7H_2O$) were first mixed in 100 mL of distilled, deionized water (DDW) at 70°C under vigorous stirring. A solution of 2 M NaOH was added dropwise to the iron salt solution until the pH was approximately 11. The black suspension was maintained at 70°C for 1 h under magnetic stirring, after which the mixture was allowed to cool naturally to room temperature (22°C) before the separation of particles. The precipitates were washed with DDW several times until their pH was neutral. The Fe_3O_4 particles were then dried at 60°C overnight and collected.

SiO_2 could be regarded as a "bonding material", primarily due to its adhesiveness. When SiO_2 is coated onto Fe_3O_4, oxidation and corrosion of the latter may be minimized [23]. In this work, Fe_3O_4/SiO_2 core-shells were prepared using a modified Stöber process [26, 27]. Typically in this process, 2 g of as-prepared Fe_3O_4 particles were dispersed in 40 mL of a 0.1 M sodium dodecyl sulphate solution under sonication for 10 min, after which the solution was stirred vigorously for 30 min. Next, 40 mL of absolute ethanol, 12 mL of ammonia and 10 mL of tetraethyl orthosilicate were added successively to the suspension, which was maintained at 50°C for 5 h. The grey silica-coated Fe_3O_4 particles were then magnetically separated from the solution, washed three times with DDW, dried at 60°C overnight, and collected.

Bi_2WO_6 was loaded hydrothermally onto the silica-coated Fe_3O_4 particles to form magnetic Bi_2WO_6 ((M) Bi_2WO_6). To prepare these samples, 1.39 g of $Bi(NO_3)_3$•$5H_2O$ were dissolved in 10 mL of acetic acid and stirred magnetically for 10 min, followed by the addition of 0.1 g of Fe_3O_4/SiO_2 and sonication for 10 min. Next, a Na_2WO_4•$2H_2O$ solution

(0.47 g of Na_2WO_4•$2H_2O$ dissolved in 20 mL of DDW) was added dropwise to the previous mixture and stirred magnetically for 20 min. The resultant mixture was then transferred to a 45-mL Teflon-lined stainless steel autoclave (Parr Instrument Company), and heated at 180°C for 20 h. After the autoclave was allowed to naturally cool to room temperature, the precipitates were magnetically separated from solution then washed twice with DDW and once with absolute ethanol. After drying overnight at 60°C, the precipitates were collected and labelled as (M) Bi_2WO_6. For comparison, Bi_2WO_6 was also prepared under the same hydrothermal conditions, albeit without the addition of silica-coated Fe_3O_4.

8.2.2 Preparation of Ag/AgCl-(M) Bi_2WO_6

Ag/AgCl-(M) Bi_2WO_6 composites were prepared by a precipitation–photoreduction method. In this method, 0.55 g of (M) Bi_2WO_6 were dissolved in 40 mL of DDW using ultrasonication for 30 min. Next, 0.24 g of NaCl (excess) were added to the suspension. After 10 min of magnetic stirring, an $AgNO_3$ solution (0.0593 g of $AgNO_3$ dissolved in 20 mL of DDW) was added dropwise to the mixture under magnetic stirring over 20 min. Precipitates were then separated from the solution by centrifugation, and dispersed in 40 mL of DDW. The suspension was then illuminated under a 300-W halogen tungsten projector lamp (Ushio) while it was stirred magnetically for 30 min. The precipitates were then magnetically separated from solution, rinsed twice with DDW then once with absolute ethanol, and dried at 60°C overnight before being collected and labelled as Ag/AgCl-(M) Bi_2WO_6. For comparison, Ag/AgCl-Bi_2WO_6 was also prepared under similar conditions [28], except (M) Bi_2WO_6 was substituted with Bi_2WO_6. The theoretical compositions of the composites are listed in Table 8.1.

Table 8.1 Compositions of the prepared photocatalysts

Composites	**Weight ratios**	**Equivalent weight percentage**		
	Ag/AgCl:Bi_2WO_6:SiO_2@Fe_3O_4	Ag/AgCl	Bi_2WO_6	SiO_2@Fe_3O_4
Ag/AgCl-Bi_2WO_6	1 : 10 : 0	9.09%	90.91%	0%
Ag/AgCl-(M) Bi_2WO_6	1 : 10 : 1	8.33%	83.33%	8.34%

8.2.3 Characterization

X-ray diffraction (XRD) analysis was performed by using a Rigaku Ultima IV Diffractometer with Cu Kα radiation (λ = 0.15418 nm) at 40 kV and 44 mA. XRD patterns were recorded at 2θ ranging from 20° to 70°. XSAM-800 X-ray photoelectron spectroscopy (XPS) was employed to detect the surface atomic composition and chemical states. Fourier transform infrared spectroscopy (FTIR) was also performed with a wave number ranging from 4000 to 650 cm^{-1} at room temperature on a Cary 630 (Agilent Technologies). Morphologies of prepared samples were analyzed by transmission electron microscopy (TEM) with a JEM-2100F FE-TEM (JEOL), the acceleration voltage of which was 200 kV. Optical properties of the composites were measured on a Thermo Evolution 300 spectrophotometer by testing the ultraviolet-visible diffuse reflectance spectra (DRS) in the range of 300-700 nm. Isothermal magnetization data was collected in the field range from -4×10^4 to 4×10^4 Oe at 300 K using a Quantum Design magnetic properties measurement system (MPMS) superconducting quantum interference device (SQUID).

8.2.4 Photocatalytic activity test

8.2.4.1 Photocatalytic reactor

A schematic of the photocatalytic reactor employed in this work is shown in Fig. 8.1. A 500-mL beaker fitted with a cooling jacket served as the reactor. The temperature of the reactor was maintained at 20°C. The visible light source was a 300-W halogen tungsten projector bulb (Ushio) with a UV cut-off (Kenko Zeta, transmittance > 90%) to filter out irradiation with a wavelength below 410 nm. The distance between the cut-off filter and the top of the beaker was 10 cm, and the light intensity was 1.1×10^{-2} Einsteins m^{-2} s^{-1}, measured by a quantum meter (Biospherical QSL-2100, 400 nm< λ < 700 nm).

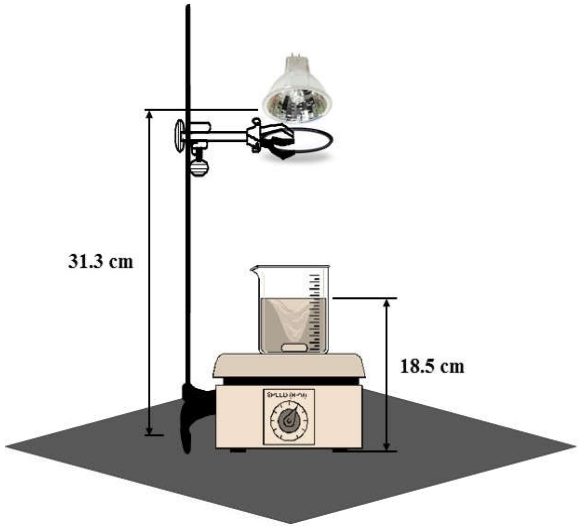


Figure 8.1 Schematic of photocatalytic reactor

8.2.4.2 Photocatalytic degradation of Rhodamine B (RhB)

Prior to each photocatalysis test, 100 mL of 10 mg/L RhB solution was allowed to reach equilibrium in the absence of light with 1 g/L (0.1 g of photocatalyst in 100 mL solution) of photocatalyst under magnetic stirring at 300 rpm for 30 min. The volume thickness of the contaminant in the beaker was 2.6 cm. Photocatalytic degradation was then performed for 90 min under visible light irradiation. In all experiments, a 1-mL aliquot was drawn every 10 min from the reactor and centrifuged, the supernatant of which was analyzed by a UV-Vis spectrometer (Genesys 10 UV, Thermo Scientific). The UV-Vis spectra of the supernatant samples ranging from 300 to 700 nm were also recorded by the UV-Vis spectrometer (Biochrom Ultrospec 60). The characteristic absorbance peak of RhB was found at 554 nm. Initial concentration of RhB is fixed at 10 mg/L. The change in concentration of RhB may be calculated based on the Beer-Lambert law (Equation 1):

$$\frac{c_t}{c_0} = \frac{\frac{A_t}{\varepsilon \times l}}{\frac{A_0}{\varepsilon \times l}} = \frac{A_t}{A_0} \qquad \textit{Equation 1}$$

where c, A, ε, and l are the concentration of RhB, the absorbance intensity at $\lambda = 554$ nm, the molar attenuation coefficient, and the path length of the light beam respectively.

Subscripts, namely *t* and *0*, represent parameters at the time of sampling and initial conditions respectively.

8.2.4.3 Photocatalytic degradation of phenol

To explore the photocatalytic activity with regards to the degradation of colourless organic pollutants, phenol was employed as a target pollutant. For all tests, 100-mL solution of phenol (20 mg/L) was stirred magnetically with 0.1 g (1 g/L) of photocatalyst for 1 h in the absence of light in order to obtain adsorption-desorption equilibrium. The photocatalytic activity test was then performed over 300 min in the presence of prepared samples under visible light irradiation. During the process, 1-mL aliquots of the mixture were drawn from the reactor every 30 min. After centrifugation, the supernatant samples were monitored using a high performance liquid chromatograph (HPLC, Agilent 1100 series) equipped with a UV-Vis detector. A ZORBAX Eclipse Plus C18 (4.6 × 250 mm) was used below 60°C and the detection wavelength was fixed at 270 nm for detection of phenol, hydroquinone, catechol and benzoquinone. The eluent was composed of 55% (V/V) methanol and 45% DDW at a flow rate of 0.6 mL/min. The injection volume was 25 μL.

8.3 Results and discussions

8.3.1 XRD and XPS analysis

XRD patterns of prepared samples are shown in Fig. 8.2. The diffraction patterns obtained for pure Fe_3O_4 are in good agreement with the cubic spinel structure of magnetite (space group: Fd-3m (227), PDF card no.: 00-085-1436) [29]. Characteristic peaks located at 2θ = 30.1°, 35.4°, 43.1°, 53.4°, 57.0° and 62.6° correspond with the (2 2 0), (3 1 1), (4 0 0), (4 2 2), (5 1 1) and (4 4 0) planes of Fe_3O_4, respectively. After silica coating, the XRD patterns of the samples were observed with all the characteristic peaks of Fe_3O_4 present. However, these peaks were noticeably less intense and broader. In addition, a small, broad amorphous halo was observed in the range of 2θ = 20° - 30°, which may be due to the silica coating. Diffraction patterns of pure Bi_2WO_6 agreed well with the orthorhombic structure (space group: Pbca (61), PDF card no.: 00-039-0256) [30]. Specifically, peaks at 2θ = 28.3°, 32.7°, 47.1°, 55.8° and 58.5° were assigned to faces of (1 3 1), (0 6 0)/(2 0 0)/(0 0 2), (2 6 0)/(2 0 2), (1 9 1)/(3 3 1)/(1 3 3) and (2 6 2) for Bi_2WO_6, respectively. Diffraction patterns of Ag/AgCl showed peaks at 2θ = 27.8°, 32.2°, 46.2°, 54.8°, 57.5° and 67.5°,

corresponding to (1 1 1), (2 0 0), (2 2 0), (3 1 1), (2 2 2) and (4 0 0) faces of cubic AgCl, respectively (space group: Fm-3m (225), PDF card no.: 00-006-0480) [31]. A small peak at 38.2° was attributed to the (1 1 1) crystal plane of metallic silver (Ag^0) (space group: Fm-3m (225), PDF card no.: 01-087-0597) [32]. In patterns of magnetic Bi_2WO_6 and Ag/AgCl-loaded Bi_2WO_6, phases of magnetite and Bi_2WO_6, as well as AgCl and Bi_2WO_6 are respectively observed. Furthermore, in the diffraction patterns of Ag/AgCl-(M) Bi_2WO_6, it could be observed that the phase of Bi_2WO_6 with the strongest diffraction intensity, specifically at 2θ = 30.1° and 35.4°, which may be attributed to magnetite. Signals located at 2θ = 27.8°, 32.2°, 46.2°, 54.8° and 57.5° are due to silver chloride. As for the small amount of metallic Ag, no peak for Ag^0 were detected, owing to the relatively high limit of detection for XRD.

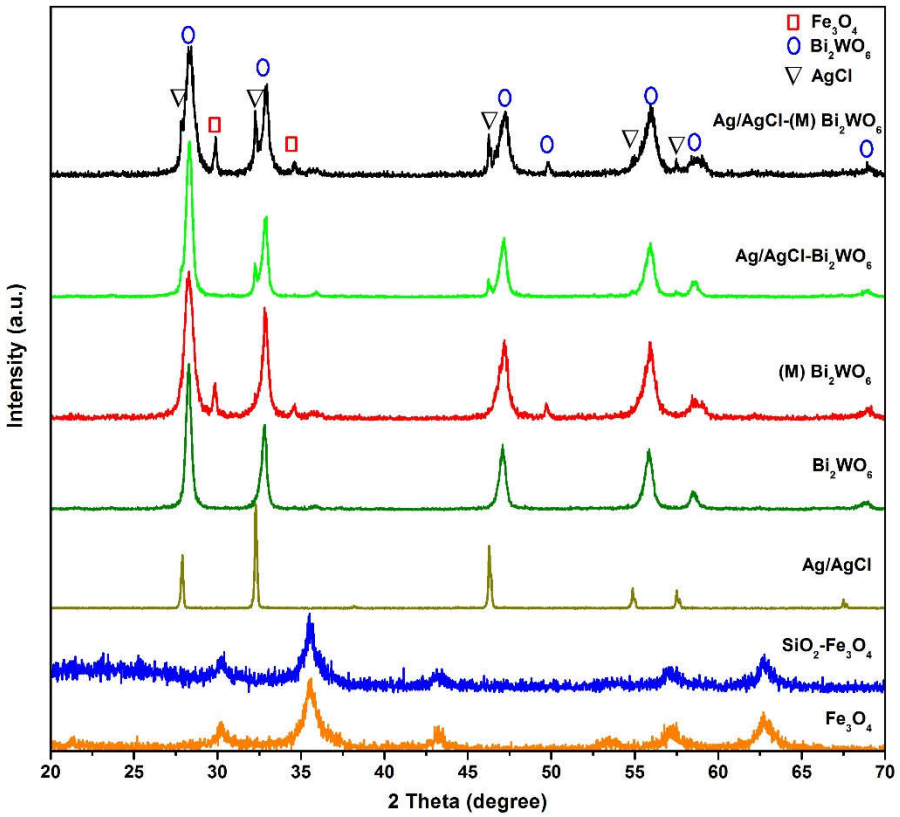


Figure 8.2 XRD patterns of prepared samples.

Surface elemental compositions and chemical states were analyzed by XPS. After calibration with C 1s (binding energy = 284.6 eV), the survey spectrum of Ag/AgCl-(M) Bi_2WO_6 was determined and is illustrated in Fig. 8.3. Elements including Fe, Si, O, Bi, W,

Ag and Cl were observed and labelled appropriately. No peaks of impurities were found, indicating a high sample purity. Peaks for iron and silicon were found to be fairly weak, which may be due to the (SiO_2@Fe_3O_4)-(Ag/AgCl@Bi_2WO_6) core-shell structure. XPS may only measure exposed surface elements, resulting in weak peaks for elements located in the core (i.e. SiO_2@Fe_3O_4) and sharp peaks for elements in the outer shell (Bi_2WO_6). A high-resolution orbital scan of Ag 3d was performed to determine the chemical states for silver, the results of which are shown in Fig. 8.4. The peaks located at approximately 366.8 eV and 372.8 eV were assigned to Ag $3d_{5/2}$ and Ag $3d_{3/2}$ respectively, and describe Ag^+ present in AgCl [33]. Furthermore, smaller peaks located at 368.0 eV and 374.3 eV were ascribed to Ag $3d_{5/2}$ and Ag $3d_{3/2}$ respectively, and describe metallic Ag^0 [34]. The relative concentrations of Ag^+ and Ag^0 may be calculated by the following equation [35]:

$$\frac{\eta_{Ag^0}}{\eta_{Ag^+}} = \frac{I_{Ag^0}}{I_{Ag^+}} \times \frac{\sigma_{Ag}\lambda_{Ag}D_E(Ag)}{\sigma_{Ag}\lambda_{Ag}D_E(Ag)} \qquad \textbf{\textit{Equation 2}}$$

where η, I, σ, λ, and D_E are the surface concentration, the intensity, the photoelectric cross-section, the electron free mean path, and the geometric factor respectively. The values of σ, λ, and D_E were calculated by Penn and Scofield, and may be obtained from literature [36, 37]. I_{Ag0} and I_{Ag+} may be calculated by integrating the intensities of the Ag^0 and Ag^+ peaks. The relative surface concentration of Ag^0/Ag^+ is approximately 13.18%. As a result, the amount of metallic silver (Ag^0) in the sample was theoretically 0.01318 g (~ 1.1% in the Ag/AgCl-(M) Bi_2WO_6 composite). The XPS results confirmed the presence of both Ag^+ and metallic Ag^0 in the prepared composites.

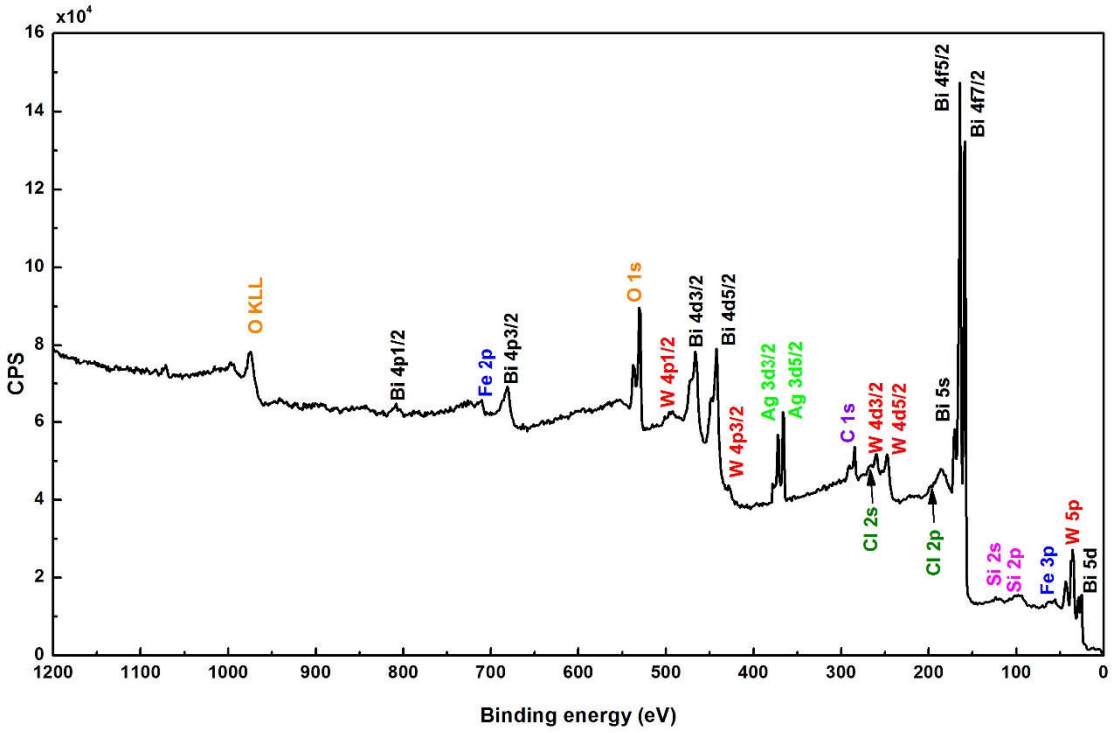


Figure 8.3 XPS survey spectrum of Ag/AgCl-(M) Bi_2WO_6.

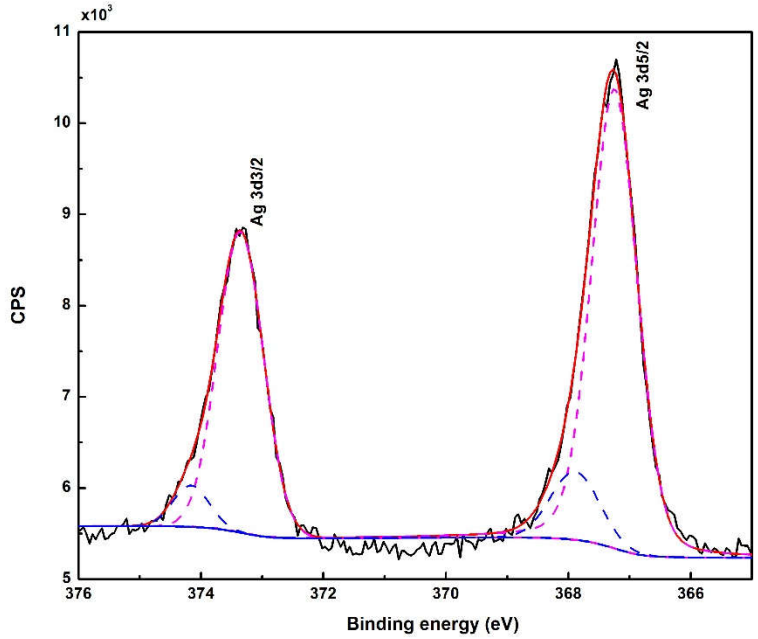


Figure 8.4 High-resolution orbital scan of Ag 3d in Ag/AgCl-(M) Bi_2WO_6 composite.

8.3.2 FT-IR

FT-IR spectra of prepared samples are shown in Fig. 8.5. For pure Bi_2WO_6, the main absorption bands at wavenumbers in the range of 600-1000 cm^{-1} may be ascribed to Bi-O and W-O stretching as well as W-O-W bridging stretching modes [38, 39]. Small peaks located at wavenumbers in the range of 1300-1600 cm^{-1} may be attributed to adsorbed CH_3COOH from the preparation process, where the signals are primarily caused by δCH vibrations of the $CH_3C=O$ moiety and coupled ν C-O and δ OH vibrations [40]. For spectra of pure Fe_3O_4 nanoparticles, absorption peaks with wavenumbers lower than 650 cm^{-1} (at the edge) may be attributed to Fe^{2+}-O^{2-} vibrations [41]. An absorption peak appeared at a wavenumber of 1094 cm^{-1} following silica coating. This peak appeared due to vibrations along the Si-O-Si bonds [42]. No peaks of either Ag or AgCl were found due to their low loading quantities.

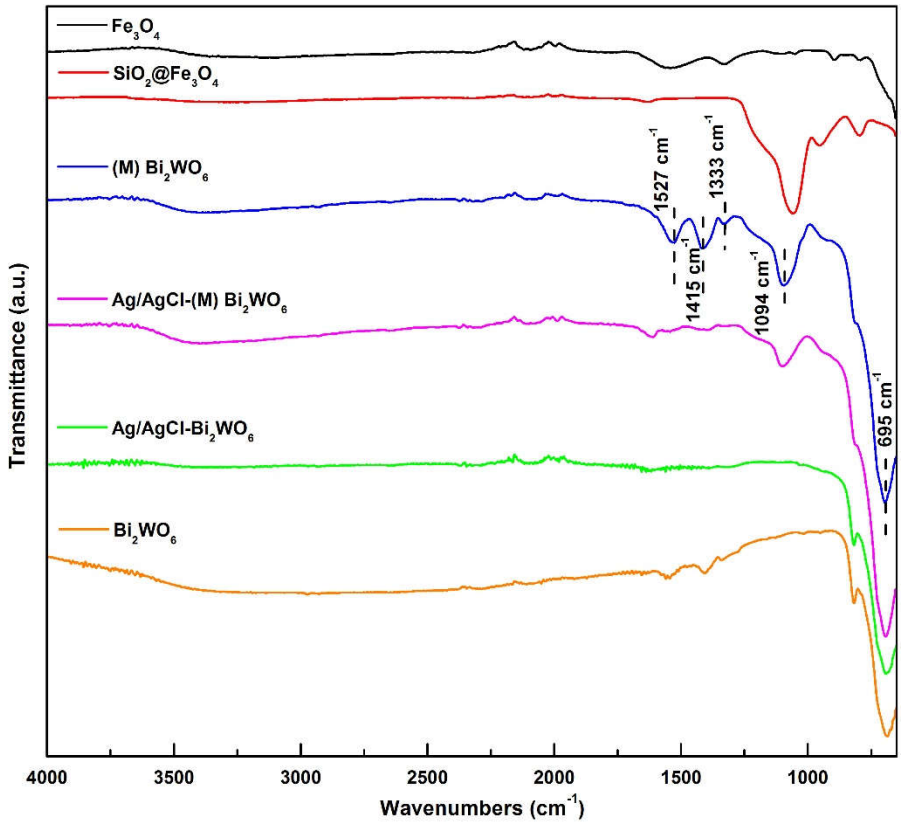


Figure 8.5 FTIR of prepared samples.

8.3.3 Morphologies and proposed formation process

Morphologies of prepared samples were characterized by TEM, the results of which are shown in Fig. 8.6. For pure Bi_2WO_6 (Fig. 8.6a), stacked rectangle plates of various sizes may be seen. After Ag was loaded on the surface, quantum dots with diameters of 1-2 nm were observed in Fig. 8.6b. Particles with sizes ranging from 5-15 nm were found to be stacked together in images of Fe_3O_4 (Fig. 8.6c). By introducing the silica coating, the particle size of silica-coated Fe_3O_4 increased to approximately 100 nm. In each silica-coated magnetite particle, several individual magnetite particles may be found in the core, while the shell is composed of silica. Fig. 8.6e shows Bi_2WO_6 loaded on the silica-coated magnetite particles, resulting in even larger particles with sizes of approximately 300-400 nm. Ag/AgCl loading resulted in quantum dots (Fig. 8.6f) on the Ag/AgCl-(M) Bi_2WO_6 composite.

A possible step-by-step formation process for these particles is proposed in Fig. 8.7. Specifically, magnetite nanoparticles were prepared first. Coating these particles with silica, resulted in the formation of Fe_3O_4/SiO_2 core/shell particles. Nanoplate-like Bi_2WO_6 was then linked around the SiO_2 shell, forming large particles of Bi_2WO_6 with magnetic properties. Finally, Ag/AgCl quantum dots were loaded on the particle surface producing Ag/AgCl-(M) Bi_2WO_6. Theoretically, the redox potential for the reduction of Ag^+ to Ag^0 is 0.7991 eV. The reducing capacity of photogenerated electrons depends on the edge of the conduction band for Bi_2WO_6, which may be calculated by the Mulliken electronegativity theory of atoms [12] as follows (Equation 3):

$$E_{CB,Bi2WO6} = X_{Bi2WO6} - E^e - \frac{1}{2}E_g \qquad \textbf{\textit{Equation 3}}$$

where X_{Bi2WO6} (6.455 eV), E^e and E_g are the electronegativity, the energy of free electrons on the hydrogen scale (≈ 4.5eV), and the band gap of Bi_2WO_6 (2.89 eV, obtained from DRS results) [43, 44]. The bottom potential of the conduction band for Bi_2WO_6 was calculated to be 0.51 eV, which is lower than the redox potential for the reduction of Ag^+ to Ag^0. In other words, Ag^+ may be reduced by electrons generated from Bi_2WO_6 in the presence of visible light irradiation. It also indicates the possible presence of metallic Ag^0 in the Ag/AgCl-(M) Bi_2WO_6 composites.

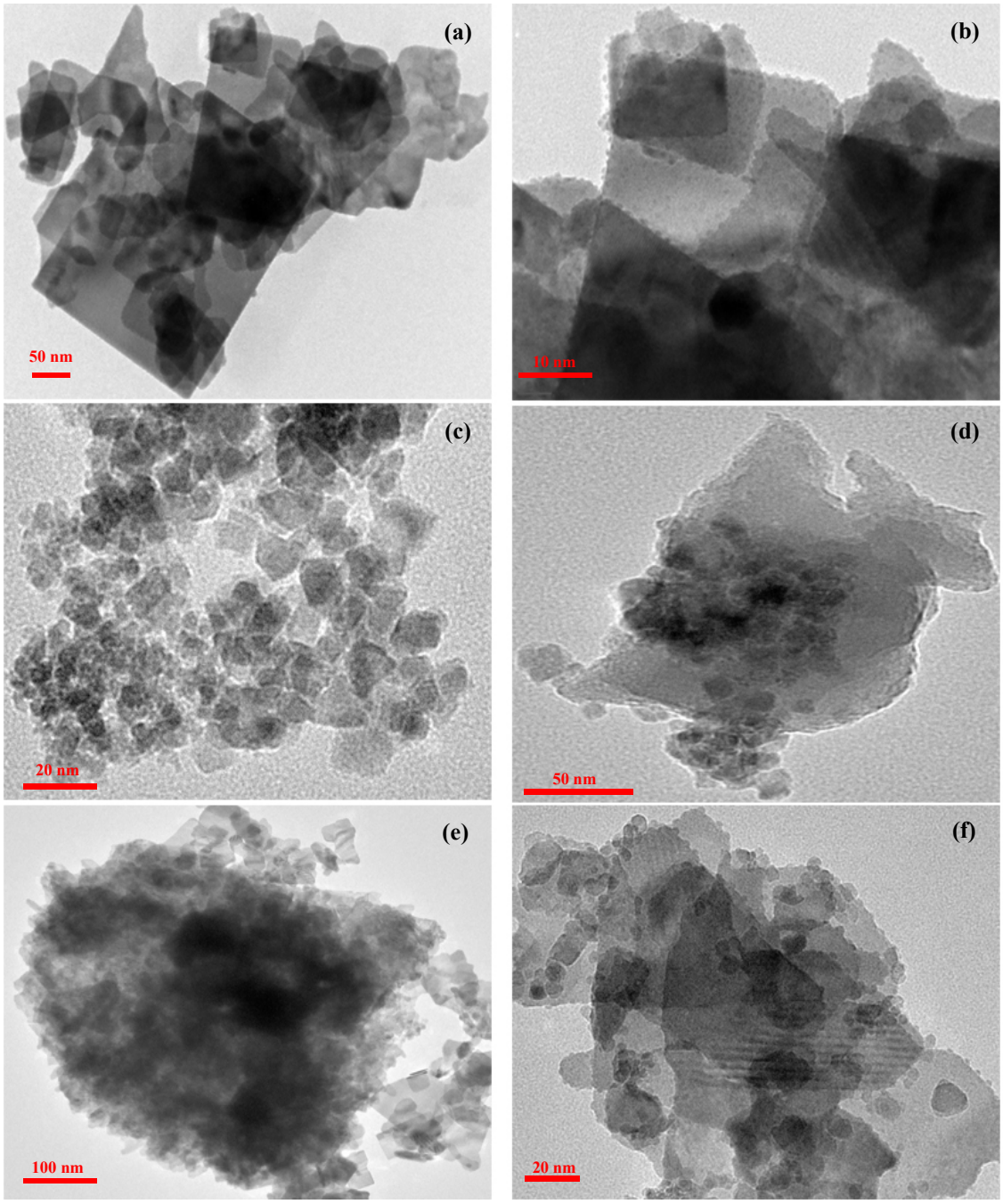


Figure 8.6 TEM photos of (a) Bi_2WO_6, (b) Ag/AgCl-Bi_2WO_6, (c) Fe_3O_4, (d) SiO_2-Fe_3O_4, (e) magnetic Bi_2WO_6, and (f) Ag/AgCl-(M) Bi_2WO_6.

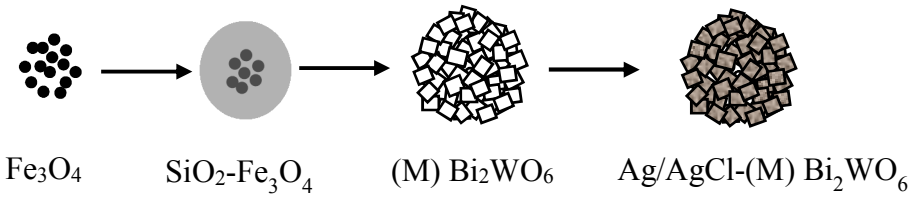


Figure 8.7 Possible process for formation of Ag/AgCl-(M) Bi_2WO_6.

8.3.4 Optical properties

The optical properties of the prepared samples were measured by detecting the UV-Vis diffuse reflectance spectra, as shown in Fig. 8.8. For pure Bi_2WO_6, it was found that the absorption edge was located at approximately 430 nm. The band gap for Bi_2WO_6 may be calculated as approximately 2.89 eV ($E_g = 1240/\lambda$). By loading Ag/AgCl onto Bi_2WO_6, a broad absorption spectrum could be seen from 300–700 nm. This may be attributed to the surface plasmon resonance of metallic Ag^0 nanoparticles, resulting in a response to visible light in the Ag nanoparticles [17]. When Bi_2WO_6 was linked with Fe_3O_4/SiO_2, the absorption intensity in the visible light range was also enhanced, which is most likely due to the narrow band gap of Fe_3O_4 (1.92 eV in [45]). By reduction of silver on (M) Bi_2WO_6, the absorption band was further broadened due to the plasmon resonance of silver nanoparticles on its surface. All results suggest that Ag/AgCl-(M) Bi_2WO_6 is an effective candidate for a visible light-induced photocatalytic material.

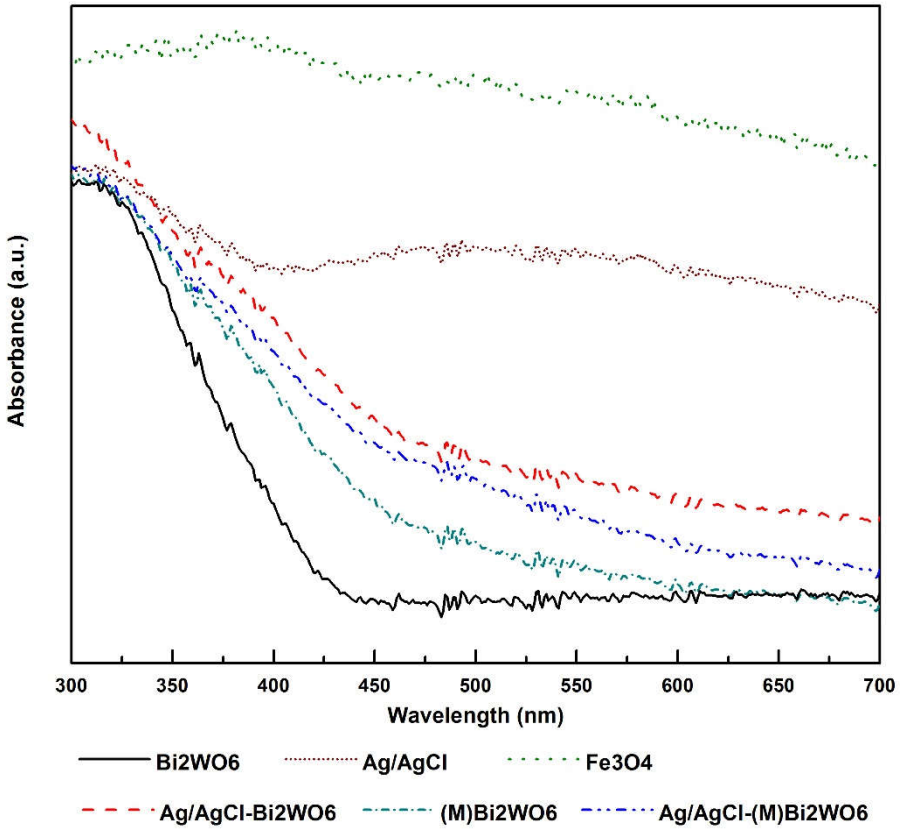


Figure 8.8 DRS of prepared samples.

8.3.5 SQUID magnetometry and magnetic separation

Magnetic properties of the synthesized materials were investigated by SQUID magnetometry. The magnetization hysteresis loop of (M) Bi_2WO_6 and Ag/AgCl-(M) Bi_2WO_6 at room temperature is shown in Fig. 8.9. Magnetic properties including saturation magnetization (Ms), coercive field (Hc) remnant magnetization (Mr) and Mr/Ms are shown in Table 8.2. Typically, both materials exhibit quasi-superparamagnetic behaviours, as demonstrated by their low remnant magnetizations and squareness ratios ($|Mr/Ms| < 1\%$). The saturation magnetization was found to decrease slightly when Ag/AgCl was loaded on (M) Bi_2WO_6, which may be attributed to the effects of non-magnetic contents (Ag/AgCl) on the surface weakening the magnetism of (M) Bi_2WO_6. The remnant magnetizations (Mr) of both materials are close to zero. In addition, the coercive fields for (M) Bi_2WO_6 and Ag/AgCl-(M) Bi_2WO_6 are 1.38 and 3.12 Oe respectively. These low remnant magnetizations and coercivities imply that aggregation of catalyst may be reduced, allowing for easy redispersion of the catalyst in a suspended system for reuse [46].

Furthermore, the acceptable saturation magnetization (Ms) suggests that the prepared materials are suited to magnetic removal strategies [24, 47, 48]. As shown in the inset of Fig. 8.9, Ag/AgCl-(M) Bi_2WO_6 exposed to two 12.5 mm cubic NdFeB magnets with a total surface field strength of 1.15×10^4 Gauss for five minutes, resulted in the separation of photocatalyst from the original reaction system.

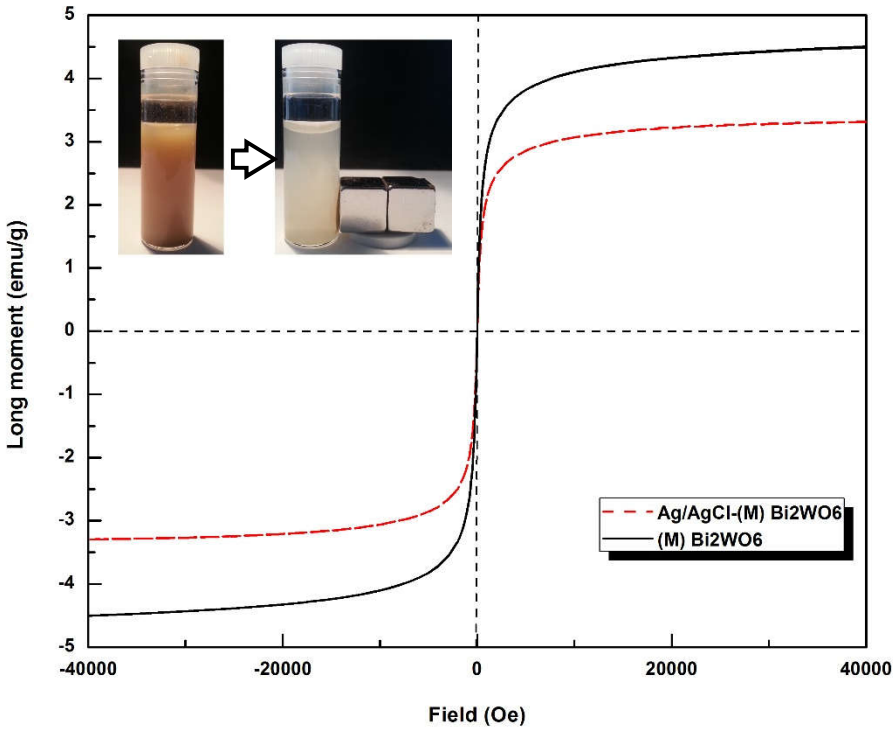


Figure 8.9 Room temperature magnetization hysteresis loops of (M) Bi_2WO_6 and Ag/AgCl-(M) Bi_2WO_6. (Inset: magnetic separation using Ag/AgCl-(M) Bi_2WO_6 exposed to cubic NdFeB magnets)

Table 8.2 Magnetic properties of (M) Bi_2WO_6 and Ag/AgCl-(M) Bi_2WO_6.

Sample	Ms (emu/g)	Hc (Oe)	Mr (emu/g)	|Mr/Ms| (%)
(M) Bi_2WO_6	4.49	1.38	-0.02	0.4
Ag/AgCl-(M) Bi_2WO_6	3.31	3.12	-0.01	0.3

8.3.6 Photocatalytic activity test

8.3.6.1 Degradation of RhB

One of the dye pollutants, Rhodamine B (RhB), was chosen as a model to evaluate the photocatalytic activities of prepared samples, including Bi_2WO_6, (M) Bi_2WO_6, Ag/AgCl-Bi_2WO_6 and Ag/AgCl-(M) Bi_2WO_6, the results of which are shown in Fig. 8.10. It can be found the adsorption-desorption equilibrium of RhB between liquid and solid was reached in 30 minutes. After turning on the light, RhB removal may only be attributed to photocatalytic degradation. For pure Bi_2WO_6, the removal efficiency was found to be approximately 70.2% (c/c_o) after 90 min of visible light irradiation. For magnetic Bi_2WO_6, the removal efficiency decreased to approximately 61.7% after photocatalytic degradation over 90 min. This may be because only 90% of the composites are Bi_2WO_6 (about 0.9 g/L). This decreased effective catalyst dosage may therefore result in a decrease in the removal of RhB. By modification with Ag/AgCl, the photocatalytic activity of Bi_2WO_6 was significantly improved to a 100% removal efficiency in the presence of Ag/AgCl-Bi_2WO_6 under visible light irradiation after only 60 min. This enhancement effect may be attributed to heterostructures formed between Ag, AgCl and Bi_2WO_6. It has been reported that these types of heterojunctions are beneficial to the separation of photogenerated electron/hole pairs, thereby improving the photocatalytic activity [49-51]. The surface plasmon effect of silver nanoparticles also plays an important role in improving the visible light-induced photocatalytic activity of the Ag/AgCl-Bi_2WO_6 composites [17]. When the composite was changed from Bi_2WO_6 to magnetic Bi_2WO_6, a slight decrease in the removal of RhB was observed. However, the removal efficiency of Ag/AgCl-(M) Bi_2WO_6 can reach 100% after 90 min. This may be due to the fact that in the effective photocatalyst structure, Bi_2WO_6 accounts for 83.33% of the magnetic composite, compared to 90.91% in the non-magnetic composite. In addition, a portion of the loaded Ag/AgCl may be found on the exposed SiO_2 instead of the Bi_2WO_6. Each of these explanations would contribute to a reduction in the degradation of RhB by using Ag/AgCl-(M) Bi_2WO_6 under visible light irradiation.

A pseudo first-order reaction model (Equation 4) may be used to best describe the kinetics of the photocatalytic process for these samples under visible light irradiation. By plotting $\ln(c_o/c)$ *vs* t, the rate constant may be obtained from the slope of the fitted line, which is

shown in Fig. 8.11. The high degree of linearity of these fitted lines suggests the feasibility of applying this model to this process. The rate constants for processes with Bi_2WO_6 and (M) Bi_2WO_6 modified by Ag/AgCl were found to be approximately 5.6 and 3.6 times larger than those for processes with Bi_2WO_6 and (M) Bi_2WO_6 without modification, respectively. The rate constant in systems with Bi_2WO_6 is larger than that in systems with (M) Bi_2WO_6, which may be influenced by the difference in effective catalyst dosage.

$$\ln(\frac{C_o}{C}) = kt \qquad \textbf{\textit{Equation 4}}$$

The pathway for the degradation of RhB comprise two main steps, namely the deethylation and destruction of aromatic ring [11]. From Fig. 8.12, differences between processes in the presence of Ag/AgCl doped- (M) Bi_2WO_6 and Bi_2WO_6 can be observed. Specifically, RhB was degraded stepwise to N,N,N'-Triethyl-Rhodamine, N,N'-Triethyl-Rhodamine, N-Ethyl-Rhodamine and Rhodamine via deethylation, indicated by the blue-shift of the characteristic absorption peak from 554 to 498 nm. Furthermore, the aromatic ring of Rhodamine may then be further destroyed, producing smaller species such as CO_2 and H_2O, which is supported by a reduction in absorbance intensity at 498 nm. It is easier of the de-ethylation process compared to the destruction of aromatic ring. Only after RhB was completely decomposed to Rhodamine, the destruction process of Rhodamine was triggered.

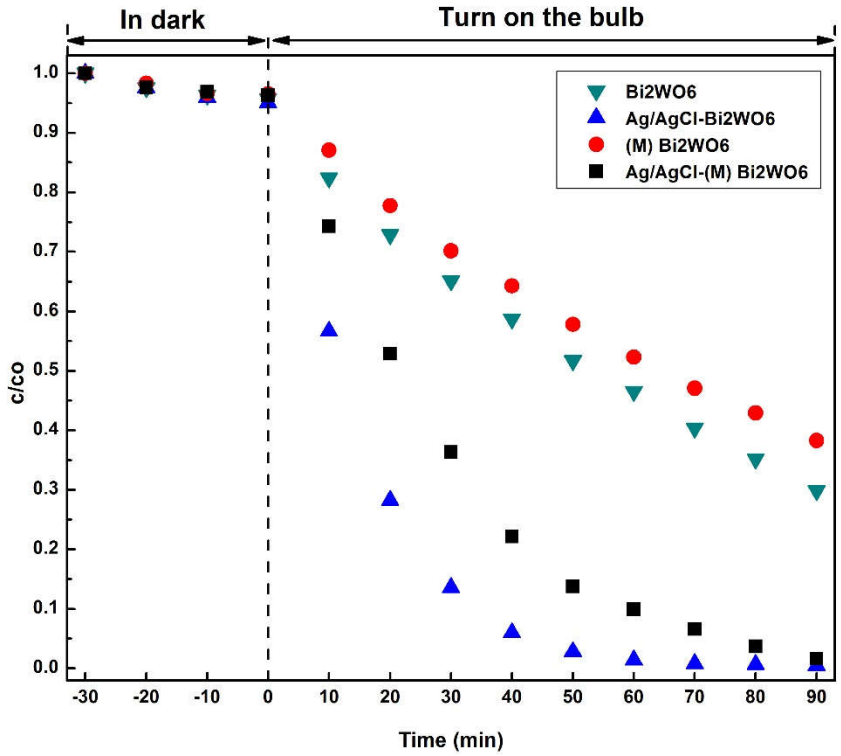


Figure 8.10 Photocatalytic degradation of RhB in the presence of prepared samples under visible light irradiation. (c_o = 10 mg/L, catalyst dosage = 1 g/L, T = 20°C)

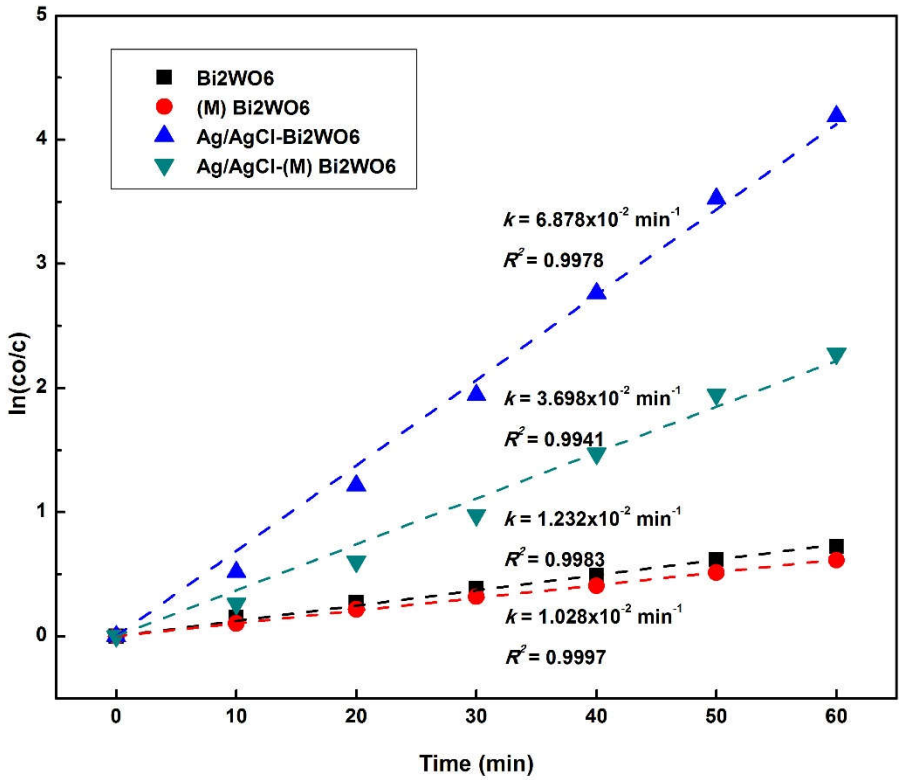


Figure 8.11 Photocatalytic kinetics of each process in the degradation of RhB under visible light irradiation.

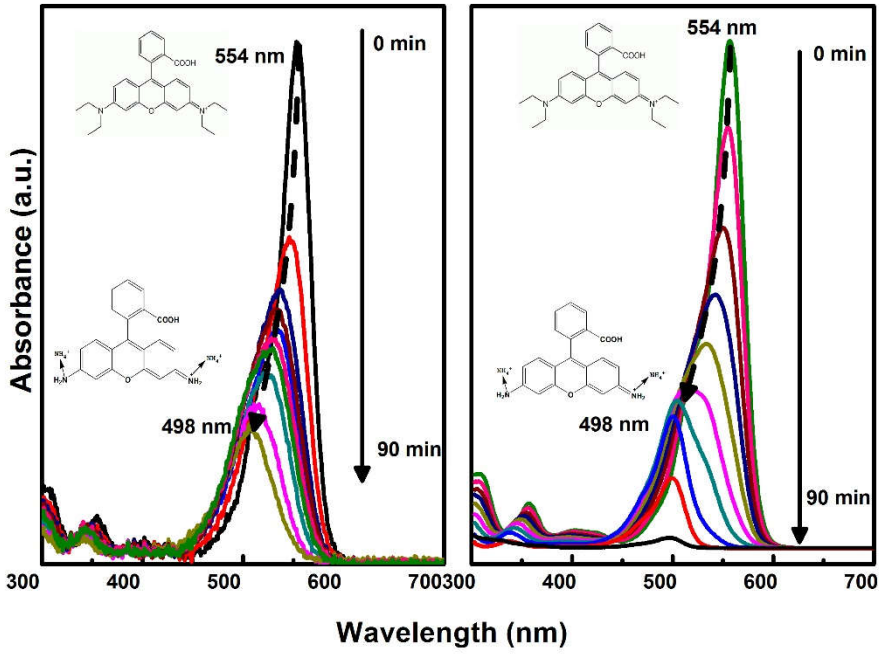


Figure 8.12 UV-Vis spectra of samples taken from reactor in the presence of Ag/AgCl-(M) Bi_2WO_6 (left) and Ag/AgCl-Bi_2WO_6 (right) with regards to RhB.

8.3.6.2 Degradation of phenol

For dye pollutants, the effect of photosensitization can produce extra electrons and accelerate the photocatalytic process [52]. Other colourless organic pollutants should also be examined so as to indicate the high photocatalytic activities of the prepared samples [53]. Colourless phenol was employed in this work to explore the photocatalytic activities of the prepared composites. Concentrations of phenol over time using different photocatalysts under visible light irradiation are shown in Fig. 8.13. It can be found that adsorption-desorption equilibrium of phenol between the liquid and solid was reached in 60 min for systems with all these four prepared photocatalysts. After turning on the light, phenol removal may only be attributed to photocatalysis. For systems with pure Bi_2WO_6, approximately 13.51 mg/L of phenol was decomposed under visible light irradiation after 300 min. Comparatively, approximately 12.82 mg/L of phenol was removed in the presence of magnetic Bi_2WO_6 under visible light irradiation after 300 min. After loading Ag/AgCl on both Bi_2WO_6 and (M) Bi_2WO_6 composites, approximately 16.15 mg/L and 15.65 mg/L of phenol were removed in systems with Ag/AgCl-Bi_2WO_6 and Ag/AgCl-(M) Bi_2WO_6 respectively, under visible light irradiation after 300 min. The same relationship for the photocatalytic activities of the prepared photocatalysts with regards to the degradation of both RhB and phenol was observed as follows: Ag/AgCl-Bi_2WO_6 > Ag/AgCl-(M) Bi_2WO_6 > Bi_2WO_6 > (M) Bi_2WO_6.

The pseudo first-order model was also applied to the kinetics for phenol degradation, attributed to the low concentration of solutes (~ 2.3×10^{-4} M < 10^{-3} M). By plotting $\ln(c_o/c)$ vs t (Fig. 8.14), the slopes of the fitted lines were calculated as the rate constants, which were 2.87×10^{-3} min^{-1}, 3.24×10^{-3} min^{-1}, 4.29×10^{-3} min^{-1}, and 4.77×10^{-3} min^{-1}, for systems in the presence of Bi_2WO_6, (M) Bi_2WO_6, Ag/AgCl-Bi_2WO_6 and Ag/AgCl-(M) Bi_2WO_6 respectively. Compared to rate constants in RhB systems, the rate constants for phenol systems were approximately 10 times smaller. This outlines the difficulty that comes with the destruction of aromatic rings. However, the photocatalytic activities were improved after loading of Ag/AgCl, and all of the Bi_2WO_6-based materials were capable of breaking the bonds of aromatic rings.

The pathways for the degradation of phenol were investigated. In previous reported work, when hydroxyl radicals are present in the phenol solution, possible oxidized intermediates mainly include hydroquinone, catechol and benzoquinone [54, 55]. Concentrations of phenol as well as possible intermediates were detected and illustrated in Fig. 8.15 in the presence of Ag/AgCl-(M) Bi_2WO_6 under visible light irradiation over 300 min. It can be seen that with a decrease in the concentration of phenol, hydroquinone accumulated to approximately 4 mg/L over 300 min. In addition, catechol and benzoquinone were also detected. The possible pathways for the degradation of phenol are illustrated in Fig. 8.16. Typically, photogenerated hydroxyl radicals first react with phenol to produce dihydroxyl cyclohexadienyl radicals. In the presence of dissolved O_2, intermediates include hydroquinone, benzoquinone and catechol which may be formed by different reactions. Furthermore, the aromatic rings of these compounds can be destroyed, producing carboxylic acids. Finally, these acids may further decompose to CO_2 and H_2O under the effects of photogenerated oxidants. These results suggest the prepared composites are active in the degradation of both dye pollutants and colourless aromatic organic pollutants under visible light irradiation.

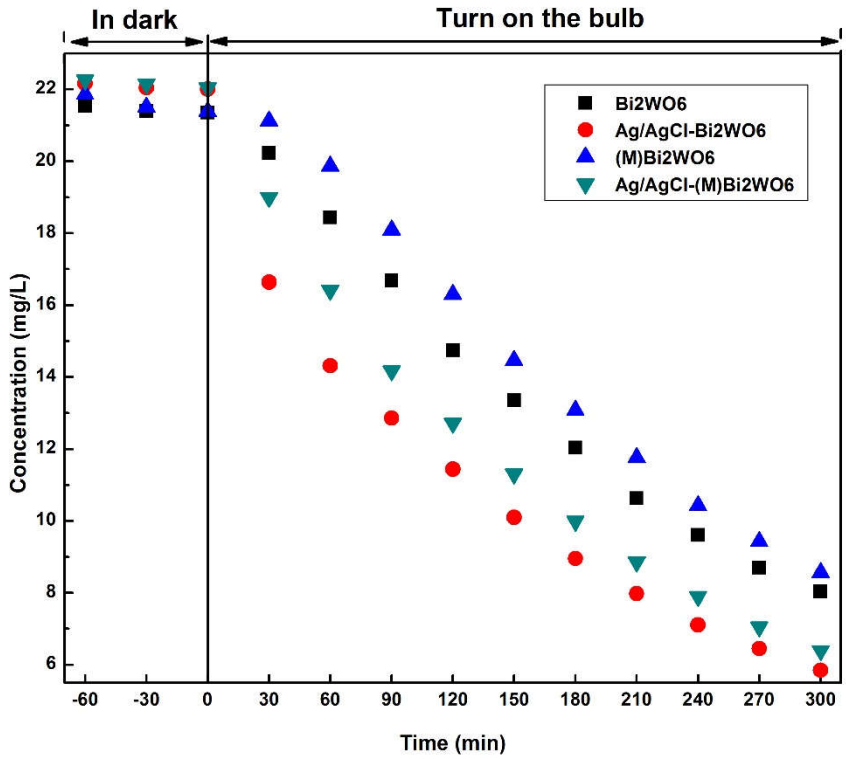


Figure 8.13 Concentration of phenol in the solution with prepared samples under visible light

irradiation. (Catalysts dosage = 1 g/L, T = 20 °C)

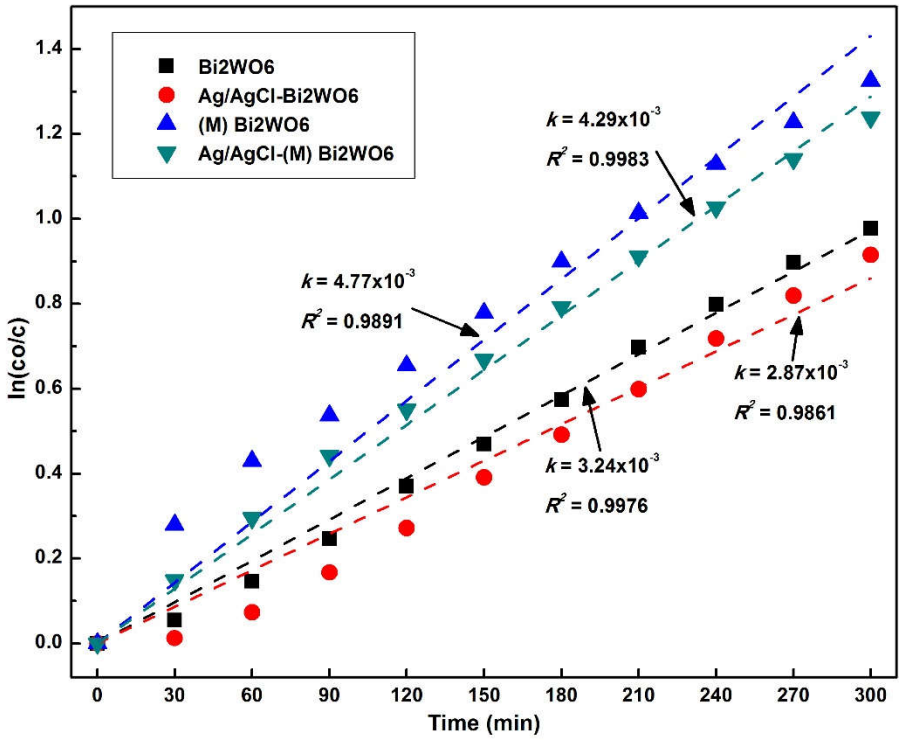


Figure 8.14 Photocatalytic kinetics of each process in the degradation of phenol under visible light irradiation.

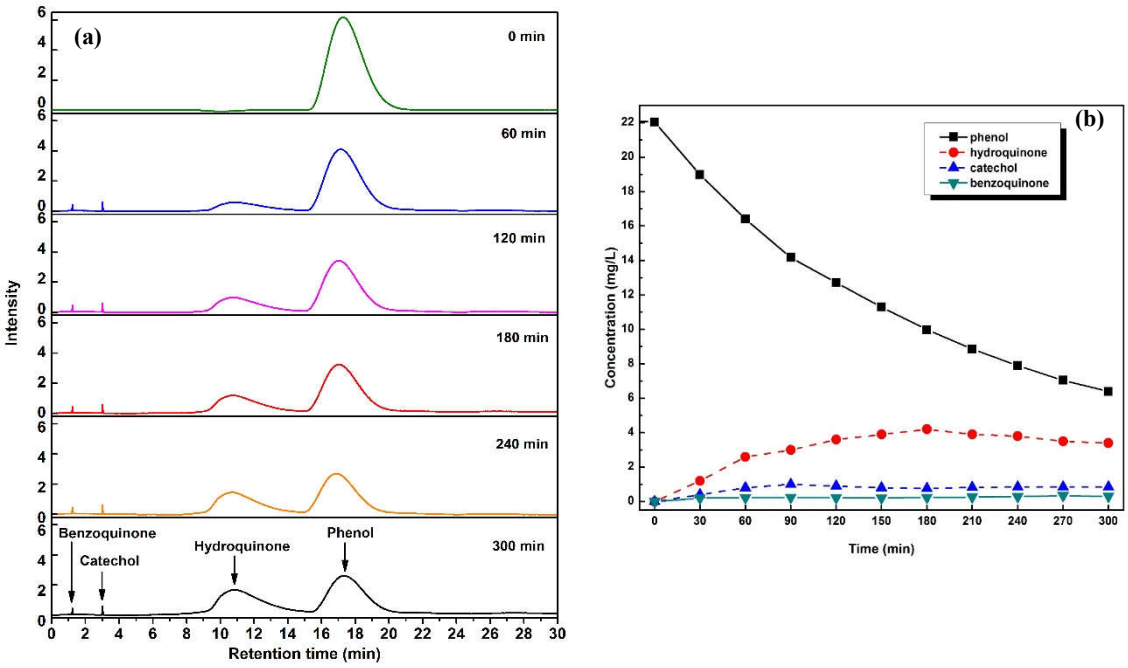


Figure 8.15 (a) Chromatograms of samples taken at different time and (b) calculated

concentration profiles of phenol and possible intermediates (hydroquinone, catechol and benzoquinone) in the presence of Ag/AgCl-(M) Bi_2WO_6 under visible light irradiation.

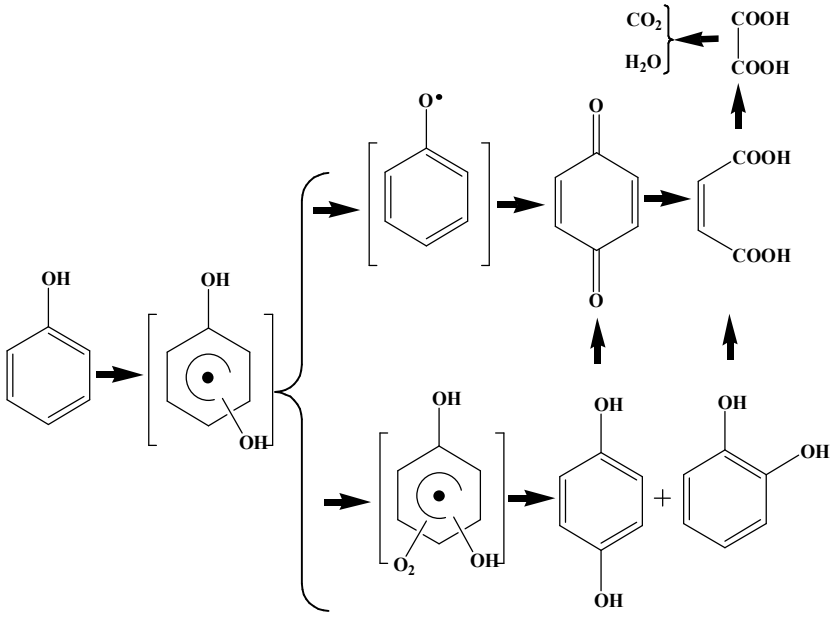


Figure 8.16 Possible pathways for the photocatalytic degradation of phenol.

8.3.7 Proposed mechanism for photocatalytic degradation of organic compounds

The band structure of Ag/AgCl-(M) Bi_2WO_6 is illustrated in Fig. 8.17. Typically, Bi_2WO_6 with a band gap of 2.89 eV may be activated by irradiation with a wavelength less than 430 nm, generating electrons and holes. In addition, silver nanoparticles may be induced by surface plasmon resonance under visible light irradiation, producing electron and hole (e^-/h^+) pairs. Therefore, electrons could rapidly transfer to the conduction bands of either Bi_2WO_6 or AgCl. The AgCl/Bi_2WO_6 heterostructure may also benefit the separation of e^-/h^+ pairs, as electrons move from the conduction band of AgCl to that of Bi_2WO_6 while holes move countercurrently [56]. This movement significantly improves the separation efficiency of electrons and holes, preventing recombination. Electrons may react with dissolved O_2, and produce superoxide radicals, while holes may either directly oxidize most organic compounds or react with adsorbed H_2O to generate hydroxyl radicals which subsequently oxidize the pollutants. It was also reported that Cl^- may be oxidized to a Cl• radical, which can also remove some organic pollutants [17, 51]. As a result, the integrated

effect leads to an enhanced photocatalytic activity, effectively degrading organic pollutants in the presence of Ag/AgCl-(M) Bi_2WO_6 composites.

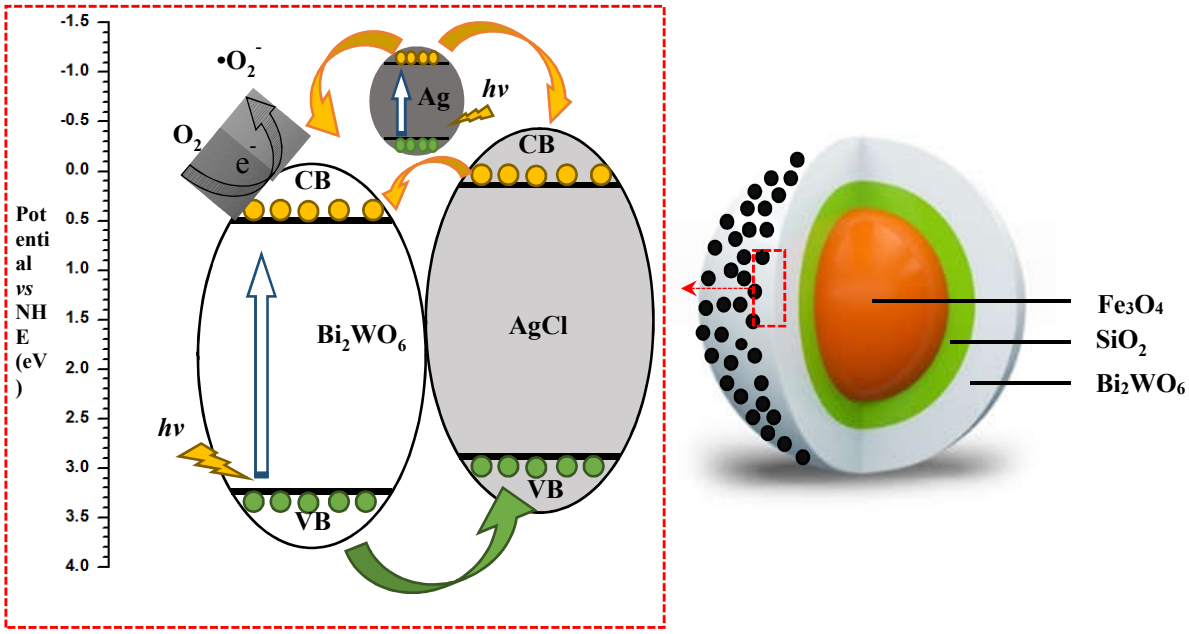


Figure 8.17 Proposed mechanism for the photocatalytic degradation of organic compounds in the presence of Ag/AgCl-(M) Bi_2WO_6.

8.4 Conclusions

In this work, novel magnetic photocatalytic composites were successfully synthesized by the preparation of magnetic Bi_2WO_6, incorporating silica-coated Fe_3O_4 nanoparticles and Ag/AgCl-magnetic Bi_2WO_6 by a photoreduction method. The prepared samples were tested with quasi-superparamagnetic behaviour and exhibited excellent visible light-driven photocatalytic activities with regards to the degradation of a model dye, RhB, as well as a colourless aromatic compound, phenol. The pathways for the degradation of RhB and phenol in the presence of prepared samples under visible light irradiation were explored. A mechanism for the photocatalytic degradation of organic compounds in the presence of prepared samples as also proposed.

References

1. Meng Nan Chong, Bo Jin, Christopher WK Chow and Chris Saint, "Recent

developments in photocatalytic water treatment technology: a review," *Water research*, vol. 44, no. 10, pp. 2997-3027, 2010.

2. Masao Kaneko and Ichiro Okura, "Photocatalysis science and technology," *Kodansha Springer*, 2002.

3. David F Ollis and Hussain Al-Ekabi, *TiO_2 Photocatalytic Purification and Treatment of Water and Air*, Elsevier Science Ltd, Photocatalytic purification and treatment of water and air: proceedings of the 1st International Conference, 1993.

4. Liqun Ye, Yurong Su, Xiaoli Jin, Haiquan Xie and Can Zhang, "Recent advances in BiOX (X = Cl, Br and I) photocatalysts: synthesis, modification, facet effects and mechanisms," *Environmental Science: Nano*, vol. 1, no. 2, pp. 90-112, 2014.

5. Huizhong An, Yi Du, Tianmin Wang, Cong Wang, Weichang Hao and Junying Zhang, "Photocatalytic properties of BiOX (X = Cl, Br, and I)," *Rare Metals*, vol. 27, no. 3, pp. 243-250, 2008.

6. Kangrong Lai, Wei Wei, Ying Dai, Ruiqin Zhang and Baibiao Huang, "DFT calculations on structural and electronic properties of Bi_2MO_6 (M = Cr, Mo, W)," *Rare Metals*, vol. 30, no. 1, pp. 166-172, 2011.

7. Xiangchao Meng and Zisheng Zhang, "Bismuth-based Photocatalytic Semiconductors: Introduction, Challenges and Possible Approaches," *Journal of Molecular Catalysis A: Chemical*, vol. 423, pp. 533-549, 2016.

8. Nan Zhang, Rosaria Ciriminna, Mario Pagliaro and Yi-Jun Xu, "Nanochemistry-derived Bi_2WO_6 nanostructures: towards production of sustainable chemicals and fuels induced by visible light," *Chemical Society Reviews*, vol. 43, no. 15, pp. 5276-5287, 2014.

9. Lisha Zhang, Wenzhong Wang, Zhigang Chen, Lin Zhou, Haolan Xu and Wei Zhu, "Fabrication of flower-like Bi_2WO_6 superstructures as high performance visible-light driven photocatalysts," *Journal of Materials Chemistry*, vol. 17, no. 24, pp. 2526-2532, 2007.

10. Meng Shang, Wenzhong Wang, Songmei Sun, Lin Zhou and Ling Zhang, "Bi_2WO_6 Nanocrystals with High Photocatalytic Activities under Visible Light," *The Journal of Physical Chemistry C*, vol. 112, no. 28, pp. 10407-10411, 2008.

11. Xiangchao Meng and Zisheng Zhang, "Synthesis, Analysis, and Testing of BiOBr-Bi_2WO_6 Photocatalytic Heterojunction Semiconductors," *International Journal of Photoenergy*, vol. 2015, pp. 12, 2015.

12. Xiangchao Meng and Zisheng Zhang, "Facile synthesis of BiOBr/Bi_2WO_6 heterojunction semiconductors with high visible-light-driven photocatalytic activity," *Journal of Photochemistry and Photobiology A: Chemistry*, vol. 310, no. 0, pp. 33-44, 2015.

13. Meng Shang, Wenzhong Wang, Ling Zhang and Haolan Xu, "Bi2WO6 with significantly enhanced photocatalytic activities by nitrogen doping," *Materials Chemistry and Physics*, vol. 120, no. 1, pp. 155-159, 2010.

14. Ying Zhou, Qian Zhang, YuanHua Lin, Elena Antonova, Wolfgang Bensch and GretaR Patzke, "One-step hydrothermal synthesis of hierarchical Ag/Bi2WO6 composites: In situ growth monitoring and photocatalytic activity studies," *Science China Chemistry*, vol. 56, no. 4, pp. 435-442, 2013.

15. Xiangchao Meng and Zisheng Zhang, "Pd-doped Bi_2MoO_6 Plasmonic Photocatalysts with Enhanced Visible Light Photocatalytic Performance," *Applied Surface Science*, vol. 392, pp. 169-180, 2016.

16. Suljo Linic, Phillip Christopher and David B. Ingram, "Plasmonic-metal nanostructures for efficient conversion of solar to chemical energy," *Nature Materials*, vol. 10, no. 12, pp. 911-921, 2011.

17. Peng Wang, Baibiao Huang, Xiaoyan Qin, Xiaoyang Zhang, Ying Dai, Jiyong Wei and Myung-Hwan Whangbo, "Ag@AgCl: A Highly Efficient and Stable Photocatalyst Active under Visible Light," *Angewandte Chemie International Edition*, vol. 47, no. 41, pp. 7931-7933, 2008.

18. Joanne Gamage McEvoy and Zisheng Zhang, "Antimicrobial and photocatalytic disinfection mechanisms in silver-modified photocatalysts under dark and light conditions," *Journal of Photochemistry and Photobiology C: Photochemistry Reviews*, vol. 19, pp. 62-75, 2014.

19. Shouhu Xuan, Wanquan Jiang, Xinglong Gong, Yuan Hu and Zuyao Chen, "Magnetically Separable Fe3O4/TiO2 Hollow Spheres: Fabrication and Photocatalytic

Activity," *The Journal of Physical Chemistry C*, vol. 113, no. 2, pp. 553-558, 2009.

20. Santosh Kumar, Surendar T, Bharat Kumar, Arabinda Baruah and Vishnu Shanker, "Synthesis of Magnetically Separable and Recyclable g-C3N4–Fe3O4 Hybrid Nanocomposites with Enhanced Photocatalytic Performance under Visible-Light Irradiation," *The Journal of Physical Chemistry C*, vol. 117, no. 49, pp. 26135-26143, 2013.

21. Ling Zhang, Wenzhong Wang, Lin Zhou, Meng Shang and Songmei Sun, "Fe3O4 coupled BiOCl: A highly efficient magnetic photocatalyst," *Applied Catalysis B: Environmental*, vol. 90, no. 3–4, pp. 458-462, 2009.

22. S. Watson, J. Scott, D. Beydoun and R. Amal, "Studies on the Preparation of Magnetic Photocatalysts," *Journal of Nanoparticle Research*, vol. 7, no. 6, pp. 691-705, 2005.

23. Su-Hua Chen, Zhen Yin, Sheng-Lian Luo, Chak-Tong Au and Xue-Jun Li, "Preparation of magnetic Fe3O4/SiO2/Bi2WO6 microspheres and their application in photocatalysis," *Materials Research Bulletin*, vol. 48, no. 2, pp. 725-729, 2013.

24. Joanne Gamage McEvoy and Zisheng Zhang, "Synthesis and characterization of magnetically separable Ag/AgCl–magnetic activated carbon composites for visible light induced photocatalytic detoxification and disinfection," *Applied Catalysis B: Environmental*, vol. 160–161, pp. 267-278, 2014.

25. J. Meng, G. Yang, L. Yan and X. Wang, "Synthesis and characterization of magnetic nanometer pigment Fe3O4," *Dyes and Pigments*, vol. 66, no. 2, pp. 109-113, 2005.

26. Werner Stöber, Arthur Fink and Ernst Bohn, "Controlled growth of monodisperse silica spheres in the micron size range," *Journal of Colloid and Interface Science*, vol. 26, no. 1, pp. 62-69, 1968.

27. Changhua An, Xijuan Ming, Jizhuang Wang and Shutao Wang, "Construction of magnetic visible-light-driven plasmonic Fe3O4@SiO2@AgCl : Ag nanophotocatalyst," *Journal of Materials Chemistry*, vol. 22, no. 11, pp. 5171-5176, 2012.

28. Xiangchao Meng and Zisheng Zhang, "Ag/AgCl Loaded Bi_2WO_6 Composite: A Plasmonic Z-Scheme Visible Light-Responsive Photocatalyst," *International Journal of Photoenergy*, vol. 2016, pp. 11, 2016.

29. Michael E. Fleet, "The structure of magnetite: Symmetry of cubic spinels," *Journal of Solid State Chemistry*, vol. 62, no. 1, pp. 75-82, 1986.

30. Kevin S Knight, "The crystal structure of russellite; a re-determination using neutron powder diffraction of synthetic Bi_2WO_6," 1992.

31. J. P. Tiwari and Chepuri R. K. Rao, "Template synthesized high conducting silver chloride nanoplates," *Solid State Ionics*, vol. 179, no. 9–10, pp. 299-304, 2008.

32. A. Smakula and J. Kalnajs, "Precision Determination of Lattice Constants with a Geiger-Counter X-Ray Diffractometer," *Physical Review*, vol. 99, no. 6, pp. 1737-1743, 1955.

33. Joanne Gamage McEvoy, Wenquan Cui and Zisheng Zhang, "Synthesis and characterization of Ag/AgCl–activated carbon composites for enhanced visible light photocatalysis," *Applied Catalysis B: Environmental*, vol. 144, no. 0, pp. 702-712, 2014.

34. D Briggs and MP Seah, "John Willey & Sons," Ed., 1993.

35. CD Wagner and GE Muilenberg, *Handbook of X-ray photoelectron spectroscopy*, Perkin-Elmer, 1979.

36. J. H. Scofield, "Hartree-Slater subshell photoionization cross-sections at 1254 and 1487 eV," *Journal of Electron Spectroscopy and Related Phenomena*, vol. 8, no. 2, pp. 129-137, 1976.

37. David R. Penn, "Quantitative chemical analysis by ESCA," *Journal of Electron Spectroscopy and Related Phenomena*, vol. 9, no. 1, pp. 29-40, 1976.

38. M. Lourdes Calzada, Rafael Sirera, Francisco Carmona and Basilio Jiménez, "Investigations of a Diol-based Sol-Gel Process for the Preparation of Lead Titanate Materials," *Journal of the American Ceramic Society*, vol. 78, no. 7, pp. 1802-1808, 1995.

39. M. F. Daniel, B. Desbat, J. C. Lassegues and R. Garie, "Infrared and Raman spectroscopies of rf sputtered tungsten oxide films," *Journal of Solid State Chemistry*, vol. 73, no. 1, pp. 127-139, 1988.

40. M. A. Hasan, M. I. Zaki and L. Pasupulety, "Oxide-catalyzed conversion of acetic acid into acetone: an FTIR spectroscopic investigation," *Applied Catalysis A: General*, vol. 243,

no. 1, pp. 81-92, 2003.

41. Sharif Ahmad, Ufana Riaz, Ajeet Kaushik and Javed Alam, "Soft Template Synthesis of Super Paramagnetic Fe3O4 Nanoparticles a Novel Technique," *Journal of Inorganic and Organometallic Polymers and Materials*, vol. 19, no. 3, pp. 355-360, 2009.

42. F. H. Chen, Q. Gao and J. Z. Ni, "The grafting and release behavior of doxorubincin from Fe 3 O 4 @ SiO 2 core–shell structure nanoparticles via an acid cleaving amide bond: the potential for magnetic targeting drug delivery," *Nanotechnology*, vol. 19, no. 16, pp. 165103, 2008.

43. M. A. Butler and D. S. Ginley, "Prediction of Flatband Potentials at Semiconductor - Electrolyte Interfaces from Atomic Electronegativities," *Journal of The Electrochemical Society*, vol. 125, no. 2, pp. 228-232, 1978.

44. Arthur H. Nethercot, "Prediction of Fermi Energies and Photoelectric Thresholds Based on Electronegativity Concepts," *Physical Review Letters*, vol. 33, no. 18, pp. 1088-1091, 1974.

45. H El Ghandoor, HM Zidan, Mostafa MH Khalil and MIM Ismail, "Synthesis and some physical properties of magnetite (Fe3O4) nanoparticles," *Int. J. Electrochem. Sci*, vol. 7, no. 6, pp. 5734-5745, 2012.

46. Zhiqiao He, Tianmi Hong, Jianmeng Chen and Shuang Song, "A magnetic TiO2 photocatalyst doped with iodine for organic pollutant degradation," *Separation and Purification Technology*, vol. 96, pp. 50-57, 2012.

47. M. Villani, T. Rimoldi, D. Calestani, L. Lazzarini, V. Chiesi, F. Casoli, F. Albertini and A. Zappettini, "Composite multifunctional nanostructures based on ZnO tetrapods and superparamagnetic Fe 3 O 4 nanoparticles," *Nanotechnology*, vol. 24, no. 13, pp. 135601, 2013.

48. Te-Li Su, Chyow-San Chiou and Hua-Wei Chen, "Preparation, Photocatalytic Activity, and Recovery of Magnetic Photocatalyst for Decomposition of Benzoic Acid," *International Journal of Photoenergy*, vol. 2012, pp. 8, 2012.

49. Yuanguo Xu, Hui Xu, Huaming Li, Jiexiang Xia, Chengtang Liu and Ling Liu,

"Enhanced photocatalytic activity of new photocatalyst Ag/AgCl/ZnO," *Journal of Alloys and Compounds*, vol. 509, no. 7, pp. 3286-3292, 2011.

50. Wei Xiong, Qidong Zhao, Xinyong Li and Dongke Zhang, "One-step synthesis of flower-like Ag/AgCl/BiOCl composite with enhanced visible-light photocatalytic activity," *Catalysis Communications*, vol. 16, no. 1, pp. 229-233, 2011.

51. Liqun Ye, Jinyan Liu, Chuqing Gong, Lihong Tian, Tianyou Peng and Ling Zan, "Two Different Roles of Metallic Ag on Ag/AgX/BiOX (X = Cl, Br) Visible Light Photocatalysts: Surface Plasmon Resonance and Z-Scheme Bridge," *ACS Catalysis*, vol. 2, no. 8, pp. 1677-1683, 2012.

52. George J. Kavarnos and Nicholas J. Turro, "Photosensitization by reversible electron transfer: theories, experimental evidence, and examples," *Chemical Reviews*, vol. 86, no. 2, pp. 401-449, 1986.

53. Xiaoli Yan, Teruhisa Ohno, Kazumoto Nishijima, Ryu Abe and Bunsho Ohtani, "Is methylene blue an appropriate substrate for a photocatalytic activity test? A study with visible-light responsive titania," *Chemical Physics Letters*, vol. 429, no. 4–6, pp. 606-610, 2006.

54. Xiao-yan Li, Yu-hong Cui, Yu-jie Feng, Zhao-ming Xie and Ji-Dong Gu, "Reaction pathways and mechanisms of the electrochemical degradation of phenol on different electrodes," *Water Research*, vol. 39, no. 10, pp. 1972-1981, 2005.

55. Chunde Wu, Xinhui Liu, Dongbin Wei, Jinchu Fan and Liansheng Wang, "Photosonochemical degradation of Phenol in water," *Water Research*, vol. 35, no. 16, pp. 3927-3933, 2001.

56. Edward T. Yu, James O. McCaldin and Thomas C. McGill, "Band Offsets in Semiconductor Heterojunctions," in *Solid State Physics*, E. Henry and T. David, Ed., pp. 1-146, Academic Press, 1992.

SECTION VI: PHOTOREACTOR DESIGN

Chapter 9 Experimental analysis of a photoreactor packed with Pd-$BiVO_4$-coated glass beads

Xiangchao Meng and Zisheng Zhang

AIChE Journal, 2018

Abstract

A photoreactor packed with glass beads coated by palladium nanoparticles-modified $BiVO_4$ was tested and analysed in phenol degradation under UV-Visible light. The photocatalytic activity of Pd-$BiVO_4$ under visible light is higher than TiO_2 under UV light, as we previously reported. In this work, we try to utilize the Pd-$BiVO_4$ in a large scale by coating the glass beads with it, a potentially industrial-scale use. For comparison, a flat-plate reactor and a slurry reactor were also examined. The photocatalytic activity of Pd-$BiVO_4$ in phenol degradation was found to be higher than that of TiO_2 in all systems (slurry, flat-plate and PBR). Furthermore, PBR exhibited higher energy efficiency compared to the flat-plate reactor in phenol oxidation. The superior performance of this reactor is due primarily to the highly exposed catalyst surface area, high mass transfer coefficient, and effective delivery of both photons and reactants to the catalyst surfaces.

Nomenclature

A	Coated area (m^2)
a	Length of reactive area (m)
b	Width of reactive area (m)

c	Concentration (mg/L)
c^*	Concentration at the solid-liquid interface (mg/L)
c_f	Final concentration (mg/L)
D	Diameter of beads (mm)
EEO	Electricity energy per order (kW h/m^3)
f	Flowrate (mL/min)
I	Intensity of irradiation (W/m^2)
k_L	Average mass transfer coefficient (m/s)
N	Number of beads layer
P	Lamp power (W)
t	Time (h)
T	Temperature (°C)
$t_{1/2}$	Half-life of reaction (h)
V	Volume (m^3)
α	Degree (°)
ε	Attenuation factor

9.1 Introduction

Over the last four decades, photocatalysis has been extensively studied and developed [1]. This advanced technique can potentially be applied in various areas such as water splitting to evolve hydrogen and oxygen, decomposition of pollutants in waste water and polluted air, disinfection, recently developed CO_2 reduction and N_2 fixation [2-9]. . Aiming to sufficiently utilize sunlight as the energy source for a photocatalytic process, it is significant to develop a material with high both ultraviolet and visible light-driven photoactivity. When a semiconductor respond to visible light, this semiconductor is

generally with a narrow band gap, which may lead to a high possibility of photogenerated charge carriers' recombination. In this context, two primary approaches were developed to resolve the contradictory between band gap distances and recombination of photogenerated charge carriers, *i.e.* modifications of TiO_2 (the most widely applied photocatalyst) and development and design of novel materials/ composites with visible light-responsivity [10, 11].

Among these visible light-responsive novel materials, bismuth based semiconductors (BBS) exhibited superior qualities such as easy-to-prepare, adjustable morphology and suitable band gaps [12]. However, the activity for BBS was still not very high as for the high recombination rate of photogenerated charge carriers. We have recently reported on plasmonic photocatalysis via loading noble metal nanoparticles on the surface of BBS, with the purpose of improving their photoactivity [5, 13-21]. Palladium nanoparticles were found to be capable of effectively boosting the photocatalytic activity of BBS. Palladium nanoparticles on catalyst surfaces possess two merits: enhanced capturing of visible light photons and decrease in the recombination rate of photogenerated charge carriers (palladium served as a charge acceptor). In our recent reported work [20], it was found that palladium nanoparticles loaded on the surface of peanut-shaped $BiVO_4$ (Pd-$BiVO_4$) exhibited excellent activity in phenol degradation under visible light, which is even higher than TiO_2 under ultraviolet (UV) light.

In practice, a photocatalytic water treatment system has not yet been widely accepted in practice due to its high cost, relatively low overall rate and low energy efficiency caused by, among other factors, the low-order dependency (0.5–1) of reaction rates on radiation intensity and limited capacity to deliver photons and reactants to catalyst surfaces [22-24]. A novel photoreactor system needs to be developed to practically implement Pd-$BiVO_4$. The development of a photoreactor with photocatalysts immobilized has become an active research field of research to address practical issues related to separation of suspended photocatalysts from slurry. . It should also be noted that a slurry system is widely accepted for the activity test for a new photocatalyst. The effect of the total surface area/ specific surface area was negligibly addressed, however, which significantly determines the total amount of reactive sites. For example, TiO_2 powder with a diameter of 25 nm was commercially available and widely applied in photocatalysis. Compared with the catalyst

particles as prepared in this work (*i.e.* Pd-$BiVO_4$), the specific surface area for TiO_2 powder is about 60 times higher than that for as-prepared Pd-$BiVO_4$. It may be not rigorous for the comparison of photoactivity using a slurry system without consideration of the particle size. And this query is avoided when an immobilized photoreactor was applied, as the available surface area for photocatalyst with different particle size is maintained as the same.

Various immobilized photoreactors were designed. Apart from advantages of no downstream processing restrictions and appropriateness for both batch and continuous flow phase, the restrictions for an immobilized photoreactor are also obvious, such as low surface area and limited mass transfer between both pollutant and light photons to the catalyst surface. Providing these restrictions were overcome, the efficiency of an immobilized photoreactor would be comparable with that of a slurry/ fluidized photoreactor. A packed beads photoreactor has been developed in the course of this research. Studies on glass beads coated with TiO_2 and applied under UV light have also been reported [25-27]. As for the intrinsic property of TiO_2, its band gap is too wide to be visible light-responsive. A UV lamp is usually utilized as a light source and a tube light reactor has also been used. As for the exhibited higher activity of Pd-$BiVO_4$ under visible light, it is possible to design a photoreactor under solar light in a large scale. The objective of this work was to experimentally examine the performance of a Pd-$BiVO_4$-coated glass beads photoreactor, which theoretically has advantages in terms of high visible light-driven photoactivity, high catalyst surface area per unit volume and photon capture and distribution on the catalyst surface. It should be noted that a scaled-up version can be designed by employing multiple chambers and illuminating it on both sides.

9.2 Experimental methods and materials

9.2.1 Chemical and catalyst

All chemicals were of reagent-grade or higher purity and purchased from Fisher Scientific (Canada) unless otherwise mentioned. Glass beads with different diameters (3, 4, and 5 mm) were also purchased from Fisher Scientific (Walter Stern Economical Solid Glass Beads, soda-lime glass, chemical resistant, Canada). Palladium modified $BiVO_4$ (Pd-$BiVO_4$) was prepared, as we reported previously [20], and used as the photocatalyst.

9.2.2 Coating procedures

A procedure to coat the surface of glass beads with the catalysts was developed. Typically, a silica sol was prepared and used to bind the catalyst particles onto the surface of the glass beads. The sol was prepared by mixing tetraethyl orthosilicate (TEOS), deionized distilled water (DDW), ethanol and hydrochloric acid with a molecular ratio of 1:2:4:0.0007 [25]. After that, the mixture was vigorously stirred at 60°C for 2 h, and then aged for 24h at room temperature before further use. A designate amount of photocatalyst was dispersed in 50 mL DDW, and 1.3 mL of silica sol were added in the suspension. Then, this suspension was ultrasonicated for 30 min. After that, 100-mL glass beads were poured into the suspension, and transferred to a flask. The flask was then rotated at a speed of 50 rpm for 24h using a rotary evaporator (IKA, RV 10 digital V, USA) to completely evaporate the solvent. The temperature was maintained at 120°C, using an oil bath (IKA, HB 10, USA). The coated beads were then calcined at a temperature of 450°C for 1h in air. After they were allowed to naturally cool down to room temperature, the coated glass beads were rinsed with DDW to remove loosely attached catalyst particles. The thickness of the coated particles was measured using a field-emission scanning electron microscope (FE-SEM, JEOL JSM-7500F). For comparison, catalysts were also coated onto stainless steel (SS) plates (13 cm by 13 cm, SS-304, 3/64-inch thickness, Metal Supermarkets, Ottawa, Canada). The procedure of coating onto SS plates were the same as we previously reported [23]. Specifically, the SS plates were cleaned with HCl (20%), and dried at 200°C for 2h. A catalysts suspension (180 g/L, dispersed in 25% aqueous methanol) was prepared and painted onto the plate surface using a brush. Then, the coated plates were calcined at 300°C for 5h in air. After they are cooled down to room temperature, the coated plates were washed several times using DDW to remove the loosely attached catalyst particles.

9.2.3 Photoreactor and system setup

A schematic with dimensions of the packed beads reactor (PBR) is shown in Figure 9.1. The light source was a 300 W halogen tungsten projector lamp (Ushio, USA). The chamber was made of Plexiglas acrylic plastic (Canus Plastics Inc., Ottawa, Canada) and a distributer composed of 3 mm bare glass beads was applied. The experimental system setup is detailed in Figure 9.2. Two peristaltic pumps were used for system circulation and a flow

rate meter was equipped to detect the flow rate of the inlet stream. All water-contacting parts, including tubing and connecters, were tested without adsorption of phenol. The temperature of the reservoir was maintained at 25°C with a water bath.

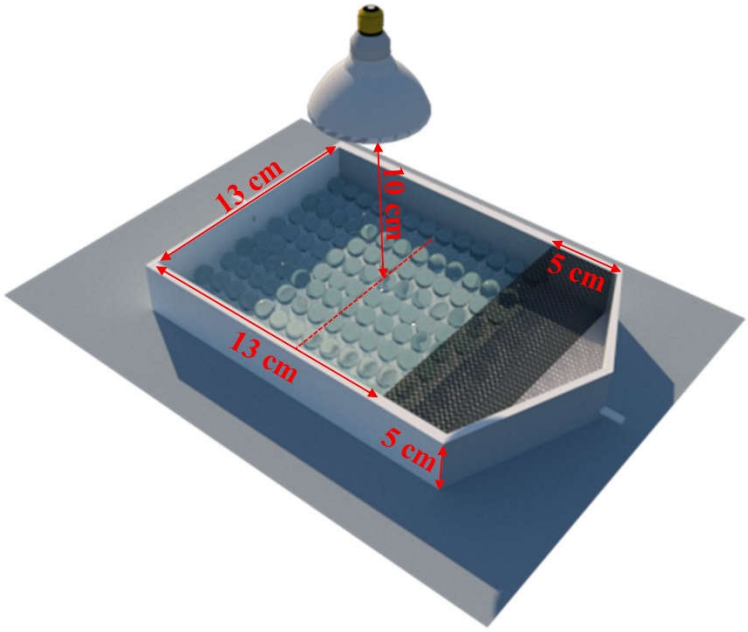


Figure 9.1 Schematic of the experimental packed beads reactor with dimensions.

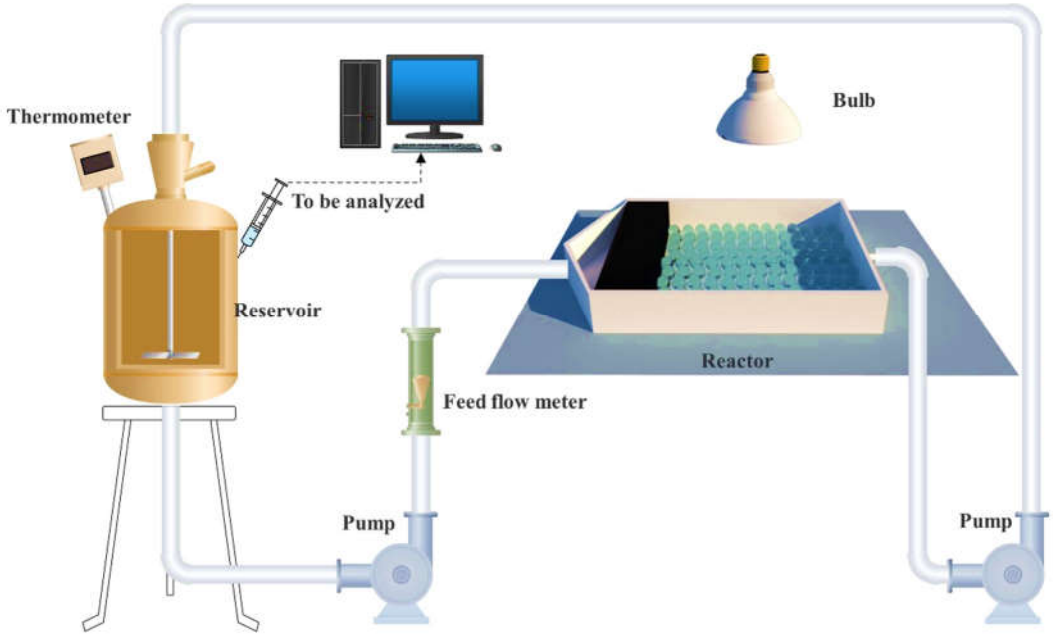


Figure 9.2. Schematic of the experimental system setup.

9.2.4 Testing procedure and analysis methods

Prior to each test, the system was cleaned by pumping DDW through it for 30 min. For the experimental tests of PBR, a designate amount of coated glass beads was packed in the chamber. And a 1 L phenol solution with an initial concentration of 5 mg/L was prepared and pumped to the reactor system. The flowrate was controlled at 5 GPH (315.45 mL/min). After circulation for 30 min, the bulb was switched on to start the photocatalytic process. Samples were drawn from the reservoir and analyzed using a high-performance liquid chromatograph (HPLC, Agilent 1100 series) equipped with a UV-Vis detector. A ZORBAX Eclipse Plus C18 column (4.6 × 250 mm) was used at a temperature of 60°C. The detecting wavelength was fixed at 270 nm for the detection of phenol and possible intermediates. The flow phase was composed of methanol (55%, V/V) and water (45%, V/V) at a flow rate of 0.6 mL/min. The injection volume was set to 25 μL. For comparison, the coated SS plate was also embedded in the chamber with the same testing procedures as PBR.

9.2.5 Mass transfer measurement

The benzoic acid dissolution method was adopted to estimate the mass transfer coefficient [23, 28, 29]. Typically, benzoic acid (BA, ACS reagent, Fisher Scientific, Canada) melts at a temperature of 140°C. Then, molten BA was coated on a SS sheet of with a dimension of 13 cm * 13 cm *2 mm. Glass beads were mixed with molten BA at 140°C to adhere to their surfaces before solidifying. After coating, the sheet and glass beads were allowed to cool down to room temperature and rinsed with DDW prior to the tests. The tests were performed using a reservoir with a volume of 2 L, the flow rate was kept at 5 GPH (315.45 mL/min), and the temperature was maintained at 20°C. The concentration of BA in the reservoir was measured using a UV-Visible spectrometer (Genysys 10-UV, Geneq Inc., Quebec, Canada) at a fixed wavelength of 228 nm. To determine the mass transfer coefficient (k_L), the following equation (Eq. 1) was applied:

$$V\frac{dc}{dt} = k_L A\left(c^* - c\right) \qquad \textit{Eq. 1}$$

where V represents volume of the solution (m^3), A is the area coated with BA (m^2), c (mg/L) is a concentration of BA in the bulk at the time of t (s), and c^* is a concentration of BA at the liquid side near the solid-liquid interface (mg/L). Due to the low solubility of BA at 20°C, c^* is a constant and equal to 2900 mg/L. By integrating Eq. 1,

$$\ln\frac{c^*}{c^* - c} = k_L\frac{A}{V}t \qquad \textit{Eq. 2}$$

From Eq. 2, it can be found via plotting $\ln(c^*/(c^*-c))$ *vs* t, k_L can be determined via the slope of the fitted line.

9.3 Results and discussion

9.3.1 System validation

Typical properties of the photocatalysts Pd-$BiVO_4$ were tested and summarized in Table 9.1. It should be noted that the content of palladium accounted for 8 wt% in the composites,

at which ratio the photocatalytic activity performs the highest [20]. Degussa TiO_2 was used for comparison.

Table 9.1. Properties of Pd-$BiVO_4$ used in the work.

Property	**Details**
Crystal structure	monoclinic phase, space group: I41/a (88)
Composition	8 wt% Pd/$BiVO_4$
Morphology	$BiVO_4$: Peanut-shape particle with a dimension of (3~4) μm by ~1 μm; Palladium particles with a diameter of 3~11 nm
Density	3.283×10^6 g/m^3
Band gap	$BiVO_4$: 2.36 eV

The average weight of coated catalysts per surface area of glass beads was calculated by weighing the glass beads before and after coating. To eliminate the influence of silica on the calculation, glass beads were also coated with silica sol without adding Pd-$BiVO_4$. The average weight of the coated catalysts was found to be about 0.528 g/m^2 (0.247 mg/g-glass beads). Photos of bare and coated beads as well as coated SS plates were taken and shown in Figure 9.3. To investigate the thickness of coated catalyst particles, SEM images of coated glass beads are shown in Figure 9.4a. The thickness is measured as about 3.9 μm. Figure 9.4b shows the peanut-shaped morphology of Pd-$BiVO_4$ that was prepared. Also, as shown in Figure 9.4c, palladium particles were successfully loaded on the surface of $BiVO_4$. A size distribution of palladium particles on the surface is shown in the inset of Figure 9.4c. The thickness of catalyst particles on the SS plate was estimated as about 10μm.

Before the start of degradation tests, the effects of photolysis and adsorption of phenol on coated glass beads were measured and found to be negligible.

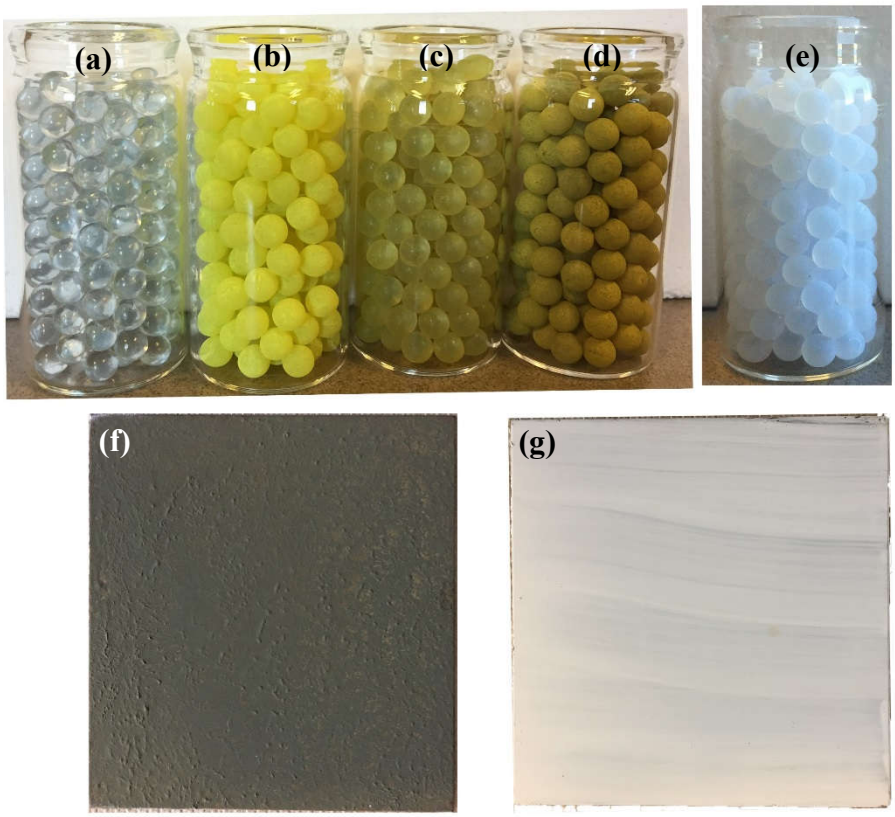


Figure 9.3. Photos of coated beads and stainless steel plates: (a) bare glass beads (d = 5 mm); (b) $BiVO_4$, (c) Pd-$BiVO_4$ (0.1 g/ 100 mL glass beads), (d) Pd-$BiVO_4$ (0.5 g/ 100 mL glass beads), and (e) TiO_2 (0.5 g/ 100 mL glass beads) coated glass beads (d = 5 mm); (f) Pd-$BiVO_4$ and (g) TiO_2 coated stainless steel plates.

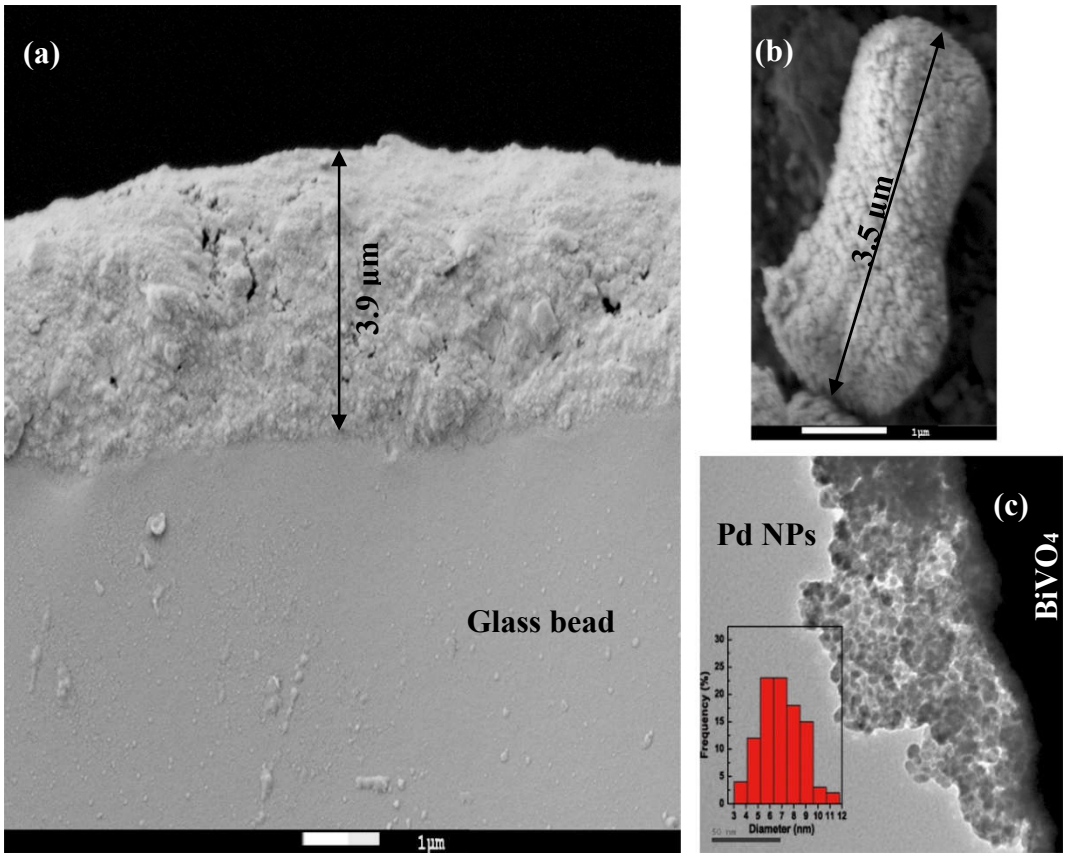


Figure 9.4. SEM images of (a) Pd-$BiVO_4$ coated glass beads and (b) Pd-$BiVO_4$, and TEM image of Pd-$BiVO_4$ (size distribution of palladium nanoparticles).

9.3.2 Experimental results

9.3.2.1 Effect of packed beads volume

The packed beads volume determines the thickness of the packed bed in the reactor. It can be calculated for glass beads with a diameter of 5 mm; the volume is about 85 mL for one-layer glass beads in the chamber. If the irradiation is unable to penetrate the beads, the effective area would be only the top surfaces of the beads, and photocatalytic activity should be influenced only by the photocatalysts coated on the beads at the top. However, as shown in Figure 9.5, irradiation is capable of penetrating the glass beads to some extent. For bare beads, ~20% of the light energy was reserved on the 10th-layer beads. After coating the glass beads with silica, ~20% of the light energy was reserved on the fifth-layer beads. Greater irradiation was blocked after further coating with photocatalysts; the extent of blocking was related to the thickness of coated particles. The relation between the light

intensity and the number of glass bead layers was assumed according to first-order attenuation (Eq. 3). By finding the integral of Eq. 3 using boundary conditions (when $N = 0$, $I = I_0$, and when $N = N$, $I = I$) as shown in Eq. 4, Eq. 5 can be obtained as follow:

$$\frac{dI}{dN} = \varepsilon I \qquad \textit{Eq. 3}$$

$$\int_{I_0}^{I} \frac{dI}{I} = \int_{0}^{N} \varepsilon dN \qquad \textit{Eq. 4}$$

$$I = I_0 e^{\varepsilon N} \qquad \textit{Eq. 5}$$

where N is the number of layers and ε is a attenuation factor. The equation solution fitted well with the experimental results at $I/I_0 > 5\%$. The fitted attenuation factors for glass beads coated with different materials are shown in Table 9.2. After coating with silica, the attenuation in the light intensity became twice faster. After coating with Pd-$BiVO_4$, the attenuation became 5–7 times faster compared to that for bare beads.

To study the effect of the thickness of packed beads on photocatalytic activity, three different thicknesses, namely 1, 2 and 3-layer Pd-$BiVO_4$ coated glass beads were tested. The results are shown in Figure 9.6. With an increase in thickness, photocatalytic activity in the degradation phenol improved. The difference between systems with 2-layer and 3-layer beads is negligible. It indicates that even though more light energy was absorbed with an increase in the number of layers from two to three, the improvement in the activity is negligible. For the following tests, 2-layer Pd-$BiVO_4$ coated beads were applied.

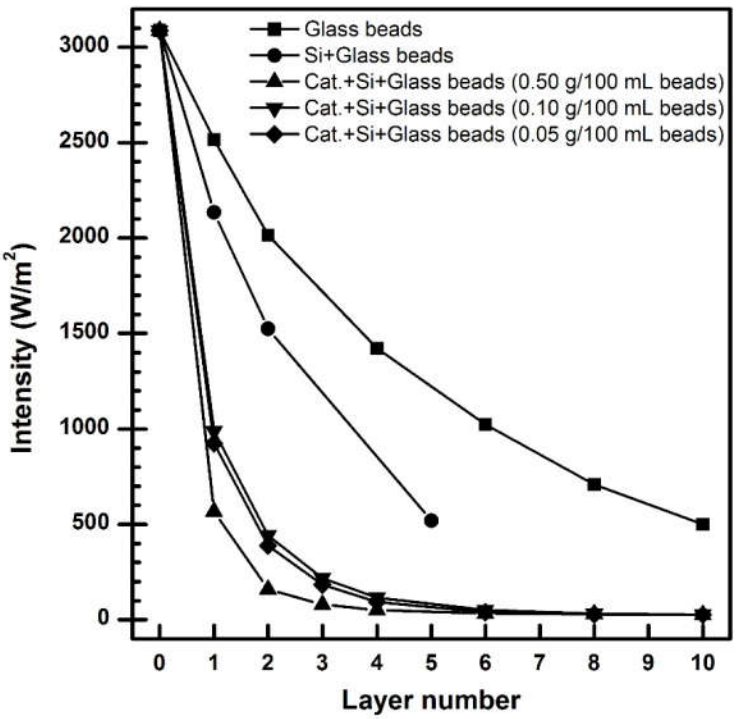


Figure 9.5. Light distribution at different thickness of beads (diameter: 5 mm)

Table 9.2. Attenuation factor for glass beads without and with coating.

Glass beads		**ε (W/m^2-N)**	***$\varepsilon/\varepsilon_{bare\ beads}$***
Bare		0.185	1
Silica coated		0.356	1.92
Pd-$BiVO_4$ coated (g/100-mL beads)	0.05	0.928	5.02
	0.10	0.987	5.34
	0.50	1.329	7.18

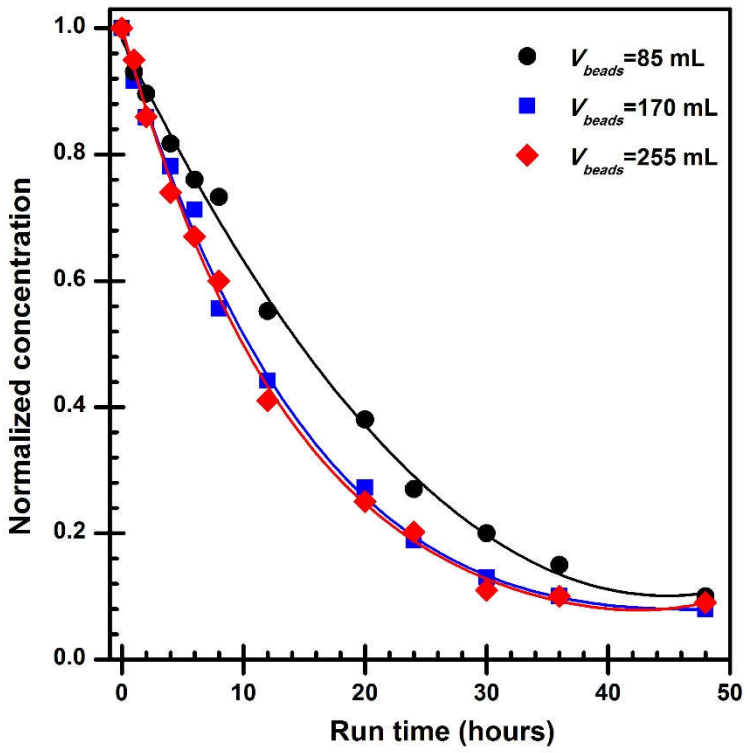


Figure 9.6. Effect of volume of coated beads on degradation kinetics (c_o = 5 mg/L; f = 5 GPH; T = 25°C, lines: fittings).

9.3.2.2 Effect of bead size

To explore the effect of bead size on photocatalytic activity, glass beads with three different diameters were used, tested and compared with flat plates. Theoretically, the exposed surface areas determine the amount of reactive sites. For flat plates, the area can be estimated using Eq. 6, where *a* is the length and *b* is the width of the flat plate. For a single bead, as only the upper semicircle is exposed to irradiation, the illuminated area can be calculated using Eq. 7, where *D* is the diameter of the bead. In the chamber, the total exposed area for glass beads with a diameter of *D* can be determined by Eq. 8. The result suggests that the exposed area for glass beads at the top layer is about π/2 times larger than that of flat plates. As glass beads under the top layer are also illuminated by penetrated irradiation, the exposed area for glass beads is much larger than is calculated in Eq. 8. The illumination on the second and third layer beads with weak intensity was not considered for the calculation, which simplified the simulation. The result indicates the exposed area for glass beads is independent on the bead diameter. The exact exposed areas for flat plates

and glass beads with different diameters are estimated and summarized in Table 9.3. The differences in areas for glass beads with different diameters occur because only intact beads are embedded in the chamber.

$$A_{flat\ plate} = a \times b \qquad \textit{Eq. 6}$$

$$A_{bead} = \frac{1}{2}\pi D^2 \qquad \textit{Eq. 7}$$

$$A_{beads} = \frac{1}{2}\pi D^2 \times \frac{a}{D} \times \frac{b}{D}$$

$$= \frac{\pi}{2} \times a \times b \qquad \textit{Eq. 8}$$

$$= \frac{\pi}{2} \times A_{flat\ plate}$$

Table 9.3. Exposed area for flat plat and glass beads with different diameters.

Reactor configuration		**Film area (illuminated) (cm^2)**
Flat plate		169
Beads with different diameter	3 mm	261.3
	4 mm	257.2
	5 mm	265.3

The irradiation energy irradiated on the top layer of glass beads can be determined using geometry as shown in Figure 9.7. Specifically, for these positions with an angle of α, the irradiation intensity can be determined using Eq. 9.

$$I_\alpha = I_0 \cos\alpha \qquad \textit{Eq. 9}$$

The area for the location with the energy of I_α can be estimated using Eq. 10.

$$
\begin{aligned}
A_\alpha &= length \times width \\
&= \left(2 \times \pi \times R \times \sin\alpha\right) \times \left(\pi \times D \times \frac{d\alpha}{2\pi}\right) \\
&= \pi \times D^2 \times \sin\alpha \times d\alpha
\end{aligned}
\qquad \textit{Eq. 10}
$$

For a single bead, the intensity of the illumination can be calculated using Eq. 11. The energy distribution on a glass bead is calculated and depicted in Figure 9.8.

$$
\begin{aligned}
I &= \int_{\alpha=0}^{\alpha=\frac{\pi}{2}} I_\alpha \times A_\alpha \\
&= \int_{\alpha=0}^{\alpha=\frac{\pi}{2}} I_0 \cos\alpha \times \pi \times D^2 \times \sin\alpha \times d\alpha \\
&= I_0 \pi D^2 \int_{\alpha=0}^{\alpha=\frac{\pi}{2}} \sin\alpha \cos\alpha d\alpha \quad \text{(assume: u=sin}\alpha\text{)} \\
&= I_0 \pi D^2 \int_0^1 u du \\
&= \frac{I_0 \pi D^2}{2}
\end{aligned}
\qquad \textit{Eq. 11}
$$

Equation 12 can be used for the calculation of the total energy of glass beads embedded in the reactor. The results suggest that the total energy of glass beads is also independent on the diameter and is about π/2 higher than that for a flat plate.

$$I_{\text{beads}} = \frac{I_0 \pi D^2}{2} \times \frac{a}{D} \times \frac{b}{D}$$

$$= \frac{\pi}{2} I_0 ab \qquad \textit{Eq. 12}$$

$$= \frac{\pi}{2} I_{\textit{Flat plate}}$$

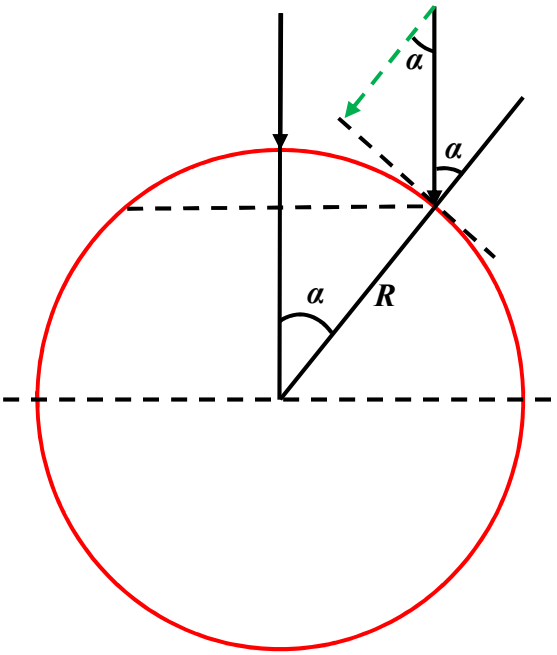


Figure 9.7. Geometry of the cross-section of a bead.

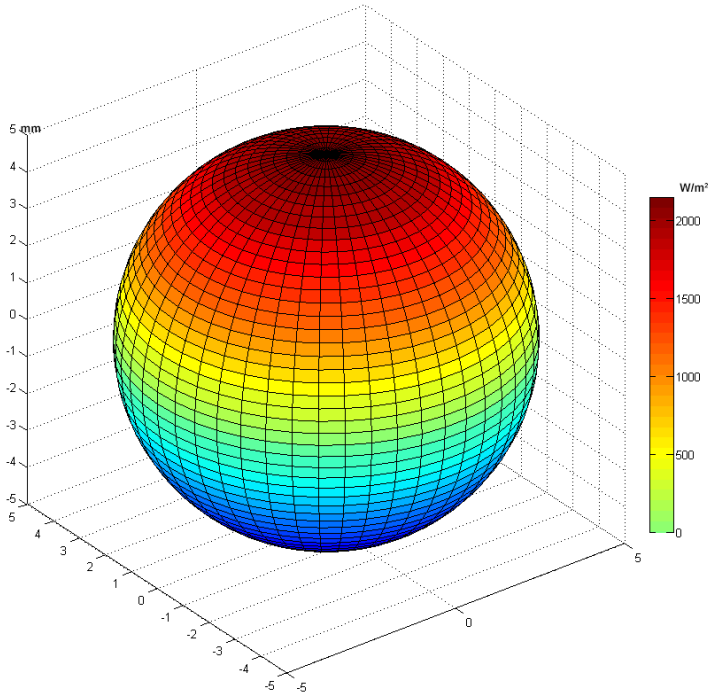


Figure 9.8. Energy distribution for a glass bead.

Photocatalytic activities of Pd-$BiVO_4$ coated glass beads with different diameters were tested, and the results are shown in Figure 9.9. The photocatalytic activities in the degradation of phenol for the systems with beads with different diameters were found to be close. The system with 5 mm glass beads had the highest activity, which might be due to the slightly larger surface area as shown in Table 9.3. This result agreed with the theoretical analysis, i.e., the influence of the diameter of glass beads is negligible as the exposed area and total irradiation energy are independent on the diameter of the beads.

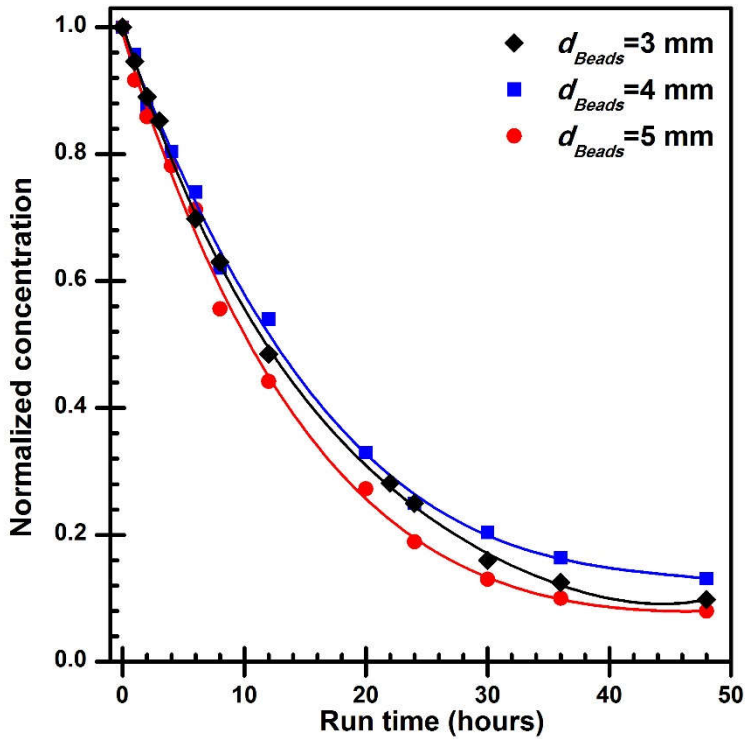


Figure 9.9. Effect of diameter of coated beads on degradation kinetics (c_o = 5 mg/L; f = 5 GPH; T = 25°C, lines: fittings).

9.3.2.3 Effect of coating amount

The concentration of the Pd-$BiVO_4$ suspension in the coating process was adjusted from 0.05 to 0.5 g per 100 mL glass beads (diameter: 5 mm). Photocatalytic activity was studied with regard to the degradation of phenol, the results of which are shown in Figure 9.10. Specifically, with an increase in concentration from 0.05 to 0.10, the photocatalytic activity was improved. A further increase in the concentration had a negligible influence on the photocatalytic activity. This phenomenon can be interpreted as follows. First, there might be an optimum amount of the actual coated catalyst, meaning even though the concentration of the coating suspension was increased, the actual coated amount of the catalyst was kept the same. Second, as shown in Figure 9.1c, 9.1d, and 9.5, an increase in the coating amount meant that a lot more irradiation energy was blocked. An increase in the concentration of the coating suspension may result in creating more reactive sites and blocking more energy. The synergy result is a suitable concentration of the coating

suspension that existed after obtaining the highest photocatalytic activity in the decomposition of phenol.

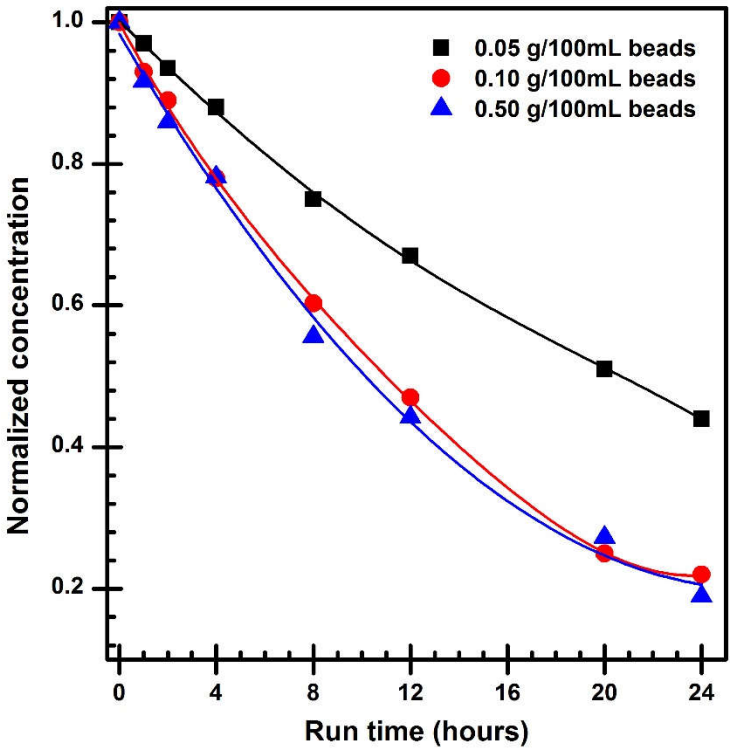


Figure 9.10. Effect of concentration of photocatalysts on coated beads (diameter: 5 mm) on degradation kinetics (c_o = 5 mg/L; f = 5 GPH; T = 25°C, lines: fittings).

9.3.2.4 Comparison with other systems

The performances of the packed beads reactor, slurry and flat-plate reactors in phenol degradation are summarized in Figure 9.11. To evaluate the activity of each system, the half-life of the reaction ($t_{1/2}$), when c/c_o = 1/2 is estimated in Table 9.4. The slurry system exhibited the highest activity and a complete removal of phenol was obtained over 3 h. For flat-plate systems, the photocatalytic activity in phenol degradation is the lowest. Photocatalytic activity for a flat-plate reactor is higher than that of a flat-plat reactor, but lower than that of a slurry reactor. The superiority of PBR, compared to a flat-plate reactor, is due to the larger exposed areas and higher illumination energy. In addition, mass transfer in PBR may be higher than in a flat-plate reactor. The average mass transfer coefficients for these two systems, which are 8.28×10^{-7} and 3.02×10^{-6} m/s for flat-plate reactor and PBR, respectively, are estimated using Eq. 2 in section 2.4. The high mass transfer

coefficient facilitates the adsorption of organics and phenol onto the film surface so as to improve the photocatalytic activity. The electricity energy per order (*EEO,* kW h/m^3) was used to evaluate the energy efficiency for a photocatalytic process, which can be calculated using Eq. 13 [30].

$$EEO = \frac{P \times t}{V \times \log \frac{c_0}{c_f}} \qquad \textbf{Eq. 13}$$

where P is the lamp power (W), t is time (h), V is the volume of treated water (m^3), and c_o and c_f represent the concentration of phenol at start and end, respectively (mg/L). Calculated results for *EEO* values are shown in Table 9.4. Based on these results, it can be concluded that: 1) a PBR system has higher energy efficiency than a flat-plate reactor, but lower than that of a slurry system; 2) Pd-$BiVO_4$ has higher energy efficiency in all systems (slurry, PBR and flat-plate reactor) than TiO_2 in photocatalytic phenol degradation in the same conditions.

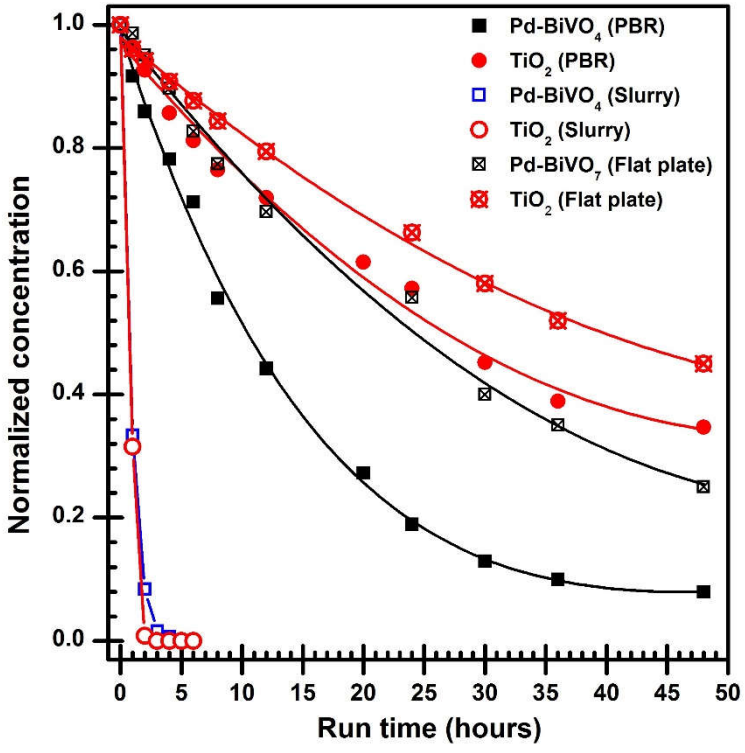


Figure 9.11. Photocatalytic degradation of phenol in different systems (For the systems with

flat plate and glass beads: c_o = 5 mg/L; f = 5 GPH; T = 25°C, lines: fittings).

Table 9.4. Calculated $t_{1/2}$ and EEO for slurry, PBR and flat-plate reactor systems.

System	$t_{1/2}$ (h)	*EEO* （kW h/m^3）
TiO_2 (slurry)	0.8	288.9
Pd-$BiVO_4$ (slurry)	0.8	558.5
TiO_2 (PBR)	26.6	29733.8
Pd-$BiVO_4$ (PBR)	10.4	9951.1
TiO_2 (Flat plate)	39.5	40343.6
Pd-$BiVO_4$ (Flat-plate)	24.1	28333.8

9.4 Conclusion

The packed beads (coated by Pd-$BiVO_4$) reactor was found to be 132% faster and more energy-efficient for photocatalytic phenol degradation than the flat-plate reactor. Its EEO was estimated to be 9951.1 kW h/m^3 for Pd-$BiVO_4$ (PBR), which increased by ~65% compared to that for Pd-$BiVO_4$ (flat plate), and by ~67% compared to TiO_2 (PBR). The superior performance of PBR is due primarily to its large illuminated catalyst surface area, high mass transfer coefficient, and efficient capture of photons on the catalyst surfaces. As for the smaller particle size, TiO_2 exhibited higher photoactivity in a slurry system, but lower photoactivity in an immobilized photoreactor, compared to Pd-$BiVO_4$. This is a solid evidence to support that using a slurry system to compare photoactivity of materials with different particle size may be not rigorous, and specific surface should be taken into the account for this kind of comparison.

This work has successfully scaled up the application of a promising photocatalytic material, Pd-$BiVO_4$ through a packed beads photoreactor. The method for coating catalyst particles on the surface of beads can be extended to all solid catalyst systems. As for the cost of applying this photocatalytic system, an unescapable question is about the high cost of the catalyst with several noble metals included, compared to TiO_2. This will increase the

capital cost beyond doubt. However, as the Pd-$BiVO_4$ catalysts are recyclable and negligibly dissolved into the solution, and solar energy can be efficiently applied as the energy source, it will reduce the operation cost when this system was applied. This is still a promising system from the point of economy in a long term. And a further scaled-up version can be designed by employing multiple chambers in series/ parallel and illuminating it on both sides.

References

1. Akira Fujishima and Kenichi Honda, "Electrochemical photolysis of water at a semiconductor electrode," *nature*, vol. 238, pp. 37-38, 1972.

2. Xiangchao Meng, Zisheng Zhang and Xingang Li, "Synergetic photoelectrocatalytic reactors for environmental remediation: A review," *Journal of Photochemistry and Photobiology C: Photochemistry Reviews*, vol. 24, pp. 83-101, 2015.

3. Ayla Ahmad, Xiangchao Meng, Nan Yun and Zisheng Zhang, "Preparation of Hierarchical BiOBr Microspheres for Visible Light-Induced Photocatalytic Detoxification and Disinfection," *Journal of Nanomaterials*, vol. 2016, pp. 10, 2016.

4. Zizhen Li, Xiangchao Meng and Zisheng Zhang, "Recent Development on MoS_2-based Photocatalysis: a Review," *Journal of Photochemistry and Photobiology C: Photochemistry Reviews*, 2017.

5. Xiangchao Meng, Hanna Qin and Zisheng Zhang, "New insight into the enhanced visible light-driven photocatalytic activity of Pd/$PdCl_2$-doped Bi_2WO_6 photocatalysts," *Journal of Colloid and Interface Science*, vol. 513, pp. 877-890, 2018.

6. Xiangchao Meng and Zhang Zisheng, "Two Dimensional Graphitic Materials for Photoelectrocatalysis: A Short Review," *Catalysis Today*, 2018.

7. Joanne Gamage and Zisheng Zhang, "Applications of Photocatalytic Disinfection," *International Journal of Photoenergy*, vol. 2010, pp. 1-11, 2010.

8. Kan Li, Bosi Peng and Tianyou Peng, "Recent Advances in Heterogeneous Photocatalytic CO2 Conversion to Solar Fuels," *ACS Catalysis*, vol. 6, no. 11, pp. 7485-

7527, 2016.

9. Chunyang Dong, Cheng Lian, Songchang Hu, Zesheng Deng, Jianqiu Gong, Mingde Li, Honglai Liu, Mingyang Xing and Jinlong Zhang, "Size-dependent activity and selectivity of carbon dioxide photocatalytic reduction over platinum nanoparticles," *Nature Communications*, vol. 9, no. 1, pp. 1252, 2018.

10. Shahed U. M. Khan, Mofareh Al-Shahry and William B. Ingler, "Efficient Photochemical Water Splitting by a Chemically Modified n-TiO_2," *Science*, vol. 297, no. 5590, pp. 2243-2245, 2002.

11. Miguel Pelaez, Nicholas T Nolan, Suresh C Pillai, Michael K Seery, Polycarpos Falaras, Athanassios G Kontos, Patrick SM Dunlop, Jeremy WJ Hamilton, J Anthony Byrne and Kevin O'Shea, "A review on the visible light active titanium dioxide photocatalysts for environmental applications," *Applied Catalysis B: Environmental*, vol. 125, pp. 331-349, 2012.

12. Xiangchao Meng and Zisheng Zhang, "Bismuth-based Photocatalytic Semiconductors: Introduction, Challenges and Possible Approaches," *Journal of Molecular Catalysis A: Chemical*, vol. 423, pp. 533-549, 2016.

13. Xiangchao Meng and Zisheng Zhang, "Ag/AgCl Loaded Bi_2WO_6 Composite: A Plasmonic Z-Scheme Visible Light-Responsive Photocatalyst," *International Journal of Photoenergy*, vol. 2016, pp. 11, 2016.

14. Xiangchao Meng and Zisheng Zhang, "Bi_2MoO_6 co-modified by reduced graphene oxide and palladium (Pd^{2+} and Pd^0) with enhanced photocatalytic decomposition of phenol," *Applied Catalysis B: Environmental*, vol. 209, pp. 383-393, 2017.

15. Xiangchao Meng, Zizhen Li, Nan Yun and Zisheng Zhang, "A Comparison of Pd^0 Nanoparticles and Pd^{2+} Modified $Bi_2O_2CO_3$ for Visible Light-Driven Photocatalysis," *Journal of Nanomaterials*, vol. 2018, pp. 9, 2018.

16. Xiangchao Meng, Zizhen Li, Jie Chen, Hongwei Xie and Zisheng Zhang, "Enhanced visible light-induced photocatalytic activity of surface-modified BiOBr with Pd nanoparticles," *Applied Surface Science*, vol. 433, no. Supplement C, pp. 76-87, 2018.

17. Xiangchao Meng, Zizhen Li and Zisheng Zhang, "Highly efficient degradation of

phenol over a Pd-BiOBr Mott–Schottky plasmonic photocatalyst," *Materials Research Bulletin*, vol. 99, pp. 471-478, 2018.

18. Xiangchao Meng, Zizhen Li and Zisheng Zhang, "Palladium nanoparticles and rGO co-modified $BiVO_4$ with greatly improved visible light-induced photocatalytic activity," *Chemosphere*, vol. 198, pp. 1-12, 2018.

19. Xiangchao Meng and Zisheng Zhang, "Pd-doped Bi_2MoO_6 Plasmonic Photocatalysts with Enhanced Visible Light Photocatalytic Performance," *Applied Surface Science*, vol. 392, pp. 169-180, 2016.

20. Xiangchao Meng, Zizhen Li and Zisheng Zhang, "Pd-nanoparticle-decorated peanut-shaped $BiVO_4$ with improved visible light-driven photocatalytic activity comparable to that of TiO_2 under UV light," *Journal of Catalysis*, vol. 356, pp. 53-64, 2017.

21. Xiangchao Meng and Zisheng Zhang, "Plasmonic ternary Ag–rGO–Bi_2MoO_6 composites with enhanced visible light-driven photocatalytic activity," *Journal of Catalysis*, vol. 344, pp. 616-630, 2016.

22. Yves Parent, Daniel Blake, Kim Magrini-Bair, Carol Lyons, Craig Turchi, Andy Watt, Edward Wolfrum and Michael Prairie, "Solar photocatalytic processes for the purification of water: state of development and barriers to commercialization," *Solar Energy*, vol. 56, no. 5, pp. 429-437, 1996.

23. Z. Zhang, W. Anderson and M. Mooyoung, "Experimental analysis of a corrugated plate photocatalytic reactor," *Chemical Engineering Journal*, vol. 99, no. 2, pp. 145-152, 2004.

24. Adam A. Donaldson, Alice Ye, Joanne Gamage McEvoy and Zisheng Zhang, "Rotating corrugated photoreactor design: Experimental and computational analysis of TiO2-based photocatalysis," *AIChE Journal*, vol. 59, no. 2, pp. 560-570, 2013.

25. Frans Denny, Jason Scott, Vishnu Pareek, Gang Ding Peng and Rose Amal, "CFD modelling for a TiO_2-coated glass-bead photoreactor irradiated by optical fibres: Photocatalytic degradation of oxalic acid," *Chemical Engineering Science*, vol. 64, no. 8, pp. 1695-1706, 2009.

26. Chyow-San Chiou, Je-Lueng Shie, Ching-Yuan Chang, Cheng-Chung Liu and Chang-

Tang Chang, "Degradation of di-n-butyl phthalate using photoreactor packed with TiO_2 immobilized on glass beads," *Journal of Hazardous Materials*, vol. 137, no. 2, pp. 1123-1129, 2006.

27. Hajar Khalilian, Mohsen Behpour, Vajiheh Atouf and Seyed Nezam Hosseini, "Immobilization of S, N-codoped TiO_2 nanoparticles on glass beads for photocatalytic degradation of methyl orange by fixed bed photoreactor under visible and sunlight irradiation," *Solar Energy*, vol. 112, pp. 239-245, 2015.

28. T. A. McMurray, J. A. Byrne, P. S. M. Dunlop, J. G. M. Winkelman, B. R. Eggins and E. T. McAdams, "Intrinsic kinetics of photocatalytic oxidation of formic and oxalic acid on immobilised TiO_2 films," *Applied Catalysis A: General*, vol. 262, no. 1, pp. 105-110, 2004.

29. Hamid Amiri, Bita Ayati and Hossein Ganjidoust, "Mass transfer phenomenon in photocatalytic cascade disc reactor: Effects of artificial roughness and flow rate," *Chemical Engineering and Processing: Process Intensification*, vol. 116, pp. 48-59, 2017.

30. A. R. Khataee, "Photocatalytic removal of C.I. Basic Red 46 on immobilized TiO_2 nanoparticles: Artificial neural network modelling," *Environmental Technology*, vol. 30, no. 11, pp. 1155-1168, 2009.

SECTION VII: CONCLUSIONS

Chapter 10 General Discussion and Conclusions

In this thesis, a number of bismuth-based semiconductors were prepared based on various design strategies, and their activities were examined with regards to the degradation of organic compounds and the inactivation of bacteria in water under visible light irradiation. The high recombination rate of photogenerated charge carriers was found to result in a low activity. It was shown that strategies including the formations of binary / ternary heterostructures as well as of plasmonic systems are very effective in promoting photocatalytic oxidation activity. Specifically, heterostructures, especially p-n heterojunctions, facilitate the separation the photogenerated electrons and holes for the internal as-formed electric field. Noble metal nanoparticles, such as Ag, Pd, Au, and Pt, on the catalyst surface are capable of absorbing visible light photons when the frequency of the light photon matches the frequency of the oscillating electrons on the metal nanoparticle surfaces, as for the surface plasmon resonance effect. In addition, metal nanoparticles on the surface can serve as electrons acceptors, which promotes the separation of charge carriers. It was found that palladium nanoparticles may be more stable and effective compared to silver nanoparticles in a photocatalytic oxidation process. With the introduction of two-dimensional graphene layers between the metal nanoparticles and bismuth-based semiconductors, the photocatalytic activities of bismuth-based semiconductors were further improved, using the high conductivity of graphene and increased adsorption capacity of the π-π introduction. It should be noted that as-prepared materials with high repeatability.

Some of the as-prepared materials (Pd-$BiVO_4$ and Pd-Bi_2WO_6) exhibited higher visible light-driven activities than TiO_2. These new catalysts carry the potential to be implemented at a larger scale. To address the practical issues when using catalyst particles in a slurry system, the difficulty in separating out catalyst particles, especially those on the nanoscale

may increase operating costs and make industrial application infeasible. Preparation of magnetically separable composites is an effective approach to address this issue. In addition, immobilization of catalyst particles on a substrate may make commercialization easier.

Recommendations for future work are made below:

- Modifications of bismuth-based semiconductors with wide band gaps, such as $BiPO_4$ and $Bi_2O_2CO_3$ can be explored via doping with metal / nonmetal ions;
- Stability of bismuth-based materials under UV light should be studied, as UV accounts for 5% of sunlight;
- Tests with more photoreactor designs under real / simulated solar radiation are required;
- Integrating with other techniques such as electrochemistry, membrane techniques and biotechnology, can widen the applications area and promote further development;
- Applications in photoreduction using bismuth-based materials, such CO_2 reduction, should be extended to produce valuable hydrocarbons, and N_2 fixation to form ammonia / nitrates, and
- It is necessary to develop an evaluation system for the comparison of different photocatalysts.

Even though many bismuth-based semiconductors with high photocatalytic performances under visible light irradiation have been reported, they are still in the early stages of implementation for the commercialization of this advanced material. The excellent and promising properties of Bi-based compounds suggests a bright future.

SECTION VIII: APPENDICES

Appendix A Ag/AgCl Loaded Bi_2WO_6 Composite: A Plasmonic Z-Scheme Visible Light-Responsive Photocatalyst

Xiangchao Meng and Zisheng Zhang

International Journal of Photoenergy, (2016), Article ID 4054351

Abstract

Hierarchical flower-like Bi_2WO_6 was successfully synthesized by facile hydrothermal method at low pH. And Ag/AgCl was loaded by photo-reduction on its surface. As-prepared photocatalysts were characterized by various techniques. Bi_2WO_6 was successfully synthesized at a size of 2-3 μm. Depositing Ag/AgCl did not destroy the crystal structure, and both Ag^+ as well as metallic Ag^0 were found. The band gap of the composite was 2.57 eV, which indicates that visible light could be the activating irradiation. In the photocatalytic activity test, the composite with 10 wt% Ag/AgCl boasted the highest removal efficiency (almost 100%) in 45 min. The significant enhancement can be attributed to the surface plasmon resonance (SPR) effect and the establishment of heterostructures between Ag/AgCl and Bi_2WO_6. A possible mechanism of photocatalytic oxidation in the presence of Ag/AgCl-Bi_2WO_6 was proposed. This work sheds light on the potential applications of plasmonic metals in photocatalysis to enhance their activities.

A.1 Introduction

Surface plasmon resonance (SPR) has been widely applied in the conversion of solar to chemical energy. It may be described as the resonant photon-induced collective oscillation of valence electrons when the frequency of photons matches the natural frequency of surface electrons oscillating against the restoring force of positive nuclei [1]. The

wavelength of a resonant photon depends on the type of metal. For silver nanoparticles, surface electrons may be activated by ultraviolet (UV) and visible (vis) photons.

Ag/AgCl was first reported by Huang *et. al.* to exhibit an excellent photocatalytic activity due to the SPR effect [2]. This study shed light on the potential implementation of Ag/AgCl for the photocatalytic oxidation of organic pollutants. To date, researchers have designed composites by depositing Ag/AgCl on photocatalysts, such as Ag/AgCl-TiO_2 [3, 4], Ag/AgCl-BiOX (X=Cl, Br) [5], aiming to enhance their performances. Meanwhile, numerous novel photocatalytic materials have also been reported. Among these materials, Bi_2WO_6, with a band gap of 2.70 eV, has been found to exhibit a high visible-light-driven photocatalytic activity with regards to the degradation of organic contaminants [6]. This is due to the valence band of bismuth-based photocatalysts consisting of not only O 2p orbits but also Bi 6s orbits. It has been confirmed that moderately well-dispersed orbits are able to accelerate the mobilities of photo-generated carriers and narrower the band gap [7]. However, one of the main problems surrounding Bi_2WO_6 implemented in the degradation of organic pollutants in wastewater is the high recombination rate of photo-generated carriers. One of the most effective approaches to deal with this issue is to establish heterostructures such as BiOBr-Bi_2WO_6 [8, 9], WO_3/Bi_2WO_6 [10, 11] and Bi_2O_3/Bi_2WO_6 [10]. At present, there is still no published work establishing the Ag/AgCl-Bi_2WO_6 heterostructure applied in the degradation of organic pollutants.

Based on the above analysis, depositing Ag/AgCl on Bi_2WO_6 should enhance its photocatalytic activity due to the SPR effect and the heterostructure. The depositing method (the photo-reduction method) can be implemented as reported [12]. In this work, a facile method of preparing an Ag/AgCl-Bi_2WO_6 composite was developed. As-synthesized photocatalysts were investigated in terms of their crystal structures, morphologies, optical properties and visible-light-induced photocatalytic activities with regards to the degradation of the organic contaminant Rhodamine B (RhB). A possible mechanism of the photocatalytic oxidation process in the presence of the Ag/AgCl-Bi_2WO_6 composite was also explored and proposed. The enhanced photocatalytic activity may be regarded as solid evidence of the potential application of Ag/AgCl in photocatalytic oxidation processes.

A.2 Experimental

A.2.1 Preparation of Bi_2WO_6 and Ag/AgCl-Bi_2WO_6 composites

All of the reagents were purchased from the Sigma-Aldrich Company at analytical purities and used as received. Bi_2WO_6 was synthesized by a hydrothermal method. In a typical process, 0.9702 g $Bi(NO_3)_3$•$5H_2O$ were dissolved in 20 mL Acetic acid, termed solution A, which was magnetically stirred for 10 min. Next, 0.3298 g Na_2WO_4•$2H_2O$ were dissolved in 40 mL Distilled De-ionized water (DDW), termed solution B. Solution B was added dropwise into solution A and stirred magnetically for 30 min. The suspension was then transferred to a 100 mL Teflon-lined stainless steel autoclave (approximately 60% of its maximum volume) and heated at 180°C for 20 h. After the autoclave was allowed to cool to room temperature, the precipitate was separated by centrifugation, washed once with ethanol then twice with DDW. The precipitate was then dried at 60°C for 12 h.

The Ag/AgCl-Bi_2WO_6 composite was prepared by the photo-reduction method. Typically, 0.32 g Bi_2WO_6 were dispersed in 40 mL DDW and sonicated for 30 min. Next, 0.24 g NaCl (excess amount) was added to the suspension, which was termed solution C. Meanwhile, 0.0421 g $AgNO_3$ were added to 20 mL DDW, termed solution D. Solution D was added dropwise to solution C with vigorous stirring for 30 min. Products were separated by centrifugation and dispersed in 40 mL DDW, then illuminated under a 300 W halogen tungsten projector lamp (Ushio) for 30 min. Final products were separated via centrifugation, washed twice with DDW and dried at 60°C for 12 h. The sample was then collected and labelled as Ag/AgCl (10 wt%)-Bi_2WO_6. Similarly, Ag/AgCl (1 wt%)-Bi_2WO_6, Ag/AgCl (2 wt%)-Bi_2WO_6, Ag/AgCl (4 wt%)-Bi_2WO_6, Ag/AgCl (8 wt%)-Bi_2WO_6 and Ag/AgCl (20 wt%)-Bi_2WO_6 were also prepared.

A.2.2 Characterization

X-ray diffraction (XRD) analysis was performed using a Rigaku Ultima IV Diffractometer with Cu Kα radiation (λ = 0.15418 nm) at 40 kV and 44 mA. Surface elements and the chemical states of samples were tested using a XSAM-800 X-ray Photoelectron Spectroscope (XPS). A field-emission scanning electron microscope (FE-SEM, JEOL JSM-7500F) using energy dispersive X-ray spectroscopy (EDS) as well as transmission electron microscopy (TEM, JEM-2100F) were applied to explore the morphologies of

samples. Acceleration voltages of the SEM and TEM were 3.00 kV and 200 kV, respectively. The Thermo Evolution 300 spectrophotometer was used to evaluate the ultraviolet-visible (UV-Vis) diffuse reflectance spectra (DRS) of the photocatalysts.

A.2.3 Photocatalytic activity test

The target organic pollutant was Rhodamine B (RhB). The characteristic peak in UV-Vis spectroscopy of RhB is found at a wavelength of 554 nm, which was used to calculate its concentration based on the Beer-Lambert law. A 500 mL beaker with a cooling jacket maintaining the system at 20°C served as the photocatalytic reactor. The visible light source was a 300 W halogen tungsten projector lamp (Ushio) with a cut-off (Kenko Zeta, transmittance>90%) to filter out irradiation with a wavelength below 400 nm. The distance between the irradiation source and the top of the beaker was 10 cm, and the irradiation intensity was measured by a quantum meter (Biospherical QSL-2100, 400 nm<λ<700 nm) to be 1.1×10^{-2} Einsteins m^{-2} s^{-1}. In each batch, 100 mL fresh solution with a concentration of RhB at 10 mg/L (10 ppm) was added to the reactor and mixed with as-prepared photocatalysts in the absence of light for 30 min to ensure that adsorption-desorption equilibrium was achieved. The quantity of photocatalyst added was 0.5 g/L. After mixing, the light was turned on to begin the photocatalytic process. An aliquot of 1 mL suspension was taken every 3 min for 45 min and tested using a Genysys 10-UV spectrophotometer (Geneq Lnc.). To explore the roles of radical species, EDTA-2Na and 2-Butanol with concentrations of 0.01 mol/L were added to the reactor.

To study the degradation of phenol, 100 mL phenol solution with a concentration of 10 mg/L (ppm) were mixed with an Ag/AgCl-Bi_2WO_6 composite. Samples taken during the photocatalytic process were tested using UV-Vis spectroscopy with the peak absorption at a wavelength of 270 nm. Other procedures used the same with process as that of the degradation of RhB.

To recycle the photocatalysts, photocatalysts were separated by centrifugation between experiments and then used in the following experiment without a wash. The final used products were separated via centrifugation and dried at 60°C for 12h. Products were collected and tested using XRD to measure their crystal stabilities.

A.3 Results and discussions

A.3.1 XRD and XPS

The X-ray diffraction (XRD) patterns of as-prepared Ag/AgCl-Bi_2WO_6 composites, pure Bi_2WO_6 and Ag/AgCl are shown in Fig. A.1. The diffraction peaks of pure Bi_2WO_6 agreed well with the orthorhombic structure (space group: Pbca(61), PDF card no. 00-039-0256) [13]. Specifically, peaks at 2θ = 28.3°, 32.7°, 47.1°, 55.8° and 58.54°, were assigned to the (131), (060)/(200)/(002), (260)/(202), (191)/(331)/(133) and (262) planes of Bi_2WO_6, respectively. Samples with deposit amounts of Ag/AgCl larger than and including 4 wt% showed characteristic peaks of Ag and AgCl. As for the small amount of Ag^0, the peak was weak. In Fig. A.2, the XRD pattern of Ag/AgCl (10 wt%)-Bi_2WO_6 was enlarged and each species in the composite was identified. Excluding peaks from Bi_2WO_6, peaks at 2θ = 27.8° (Fig. A.2a), 32.2°, 46.2°, 54.8° and 57.5° (Fig. A.2c) were found, indicating the existence of AgCl (Cubic structure, space group Fm-3m (225), PDF card no. 00-006-0480). Meanwhile, the peak at 2θ = 38.2° (Fig. A.2b) was attributed to the (111) crystal plane of Ag (PDF card no. 01-087-0719). The lattice parameters of Bi_2WO_6 are a = 5.4513 Å, b = 16.4192 Å and c = 5.4587 Å. In regards to these parameters shown in Table A.1, negligible differences between them were observed. This indicates that loading of Ag/AgCl may not destroy the main structure of Bi_2WO_6, and merely laid upon its surface as opposed to covalently anchoring to its lattice [14].

Table A.1 Lattice parameters of Bi_2WO_6 and Ag/AgCl-Bi_2WO_6 composites

Amount of Ag/AgCl (wt%)	**a**	**b**	**c**
0 (pure Bi_2WO_6)	5.45 (±0%)	16.42 (±0%)	5.46 (±0%)
1	5.44 (-0.2%)	16.44 (+0.1%)	5.44 (-0.3%)
2	5.43 (-0.4%)	16.44 (+0.1%)	5.45 (-0.2%)
4	5.44 (-0.2%)	16.42 (+0.01%)	5.44 (-0.3%)
8	5.44 (-0.2%)	16.44 (+0.1%)	5.45 (-0.1%)
10	5.44 (-0.2%)	16.45 (+0.2%)	5.46 (-0.05%)
20	5.44 (-0.3%)	16.44 (+0.1%)	5.46 (+0.02%)

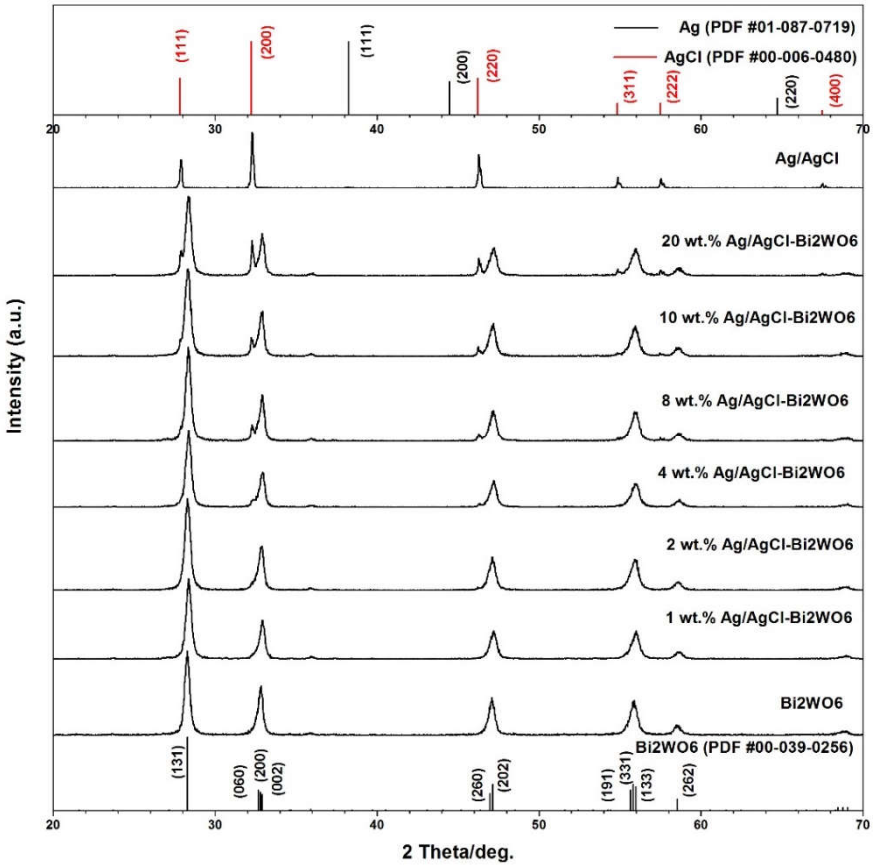


Figure A.1 XRD patterns of as-prepared samples: pure Bi_2WO_6, Ag/AgCl and Ag/AgCl-Bi_2WO_6 composites.

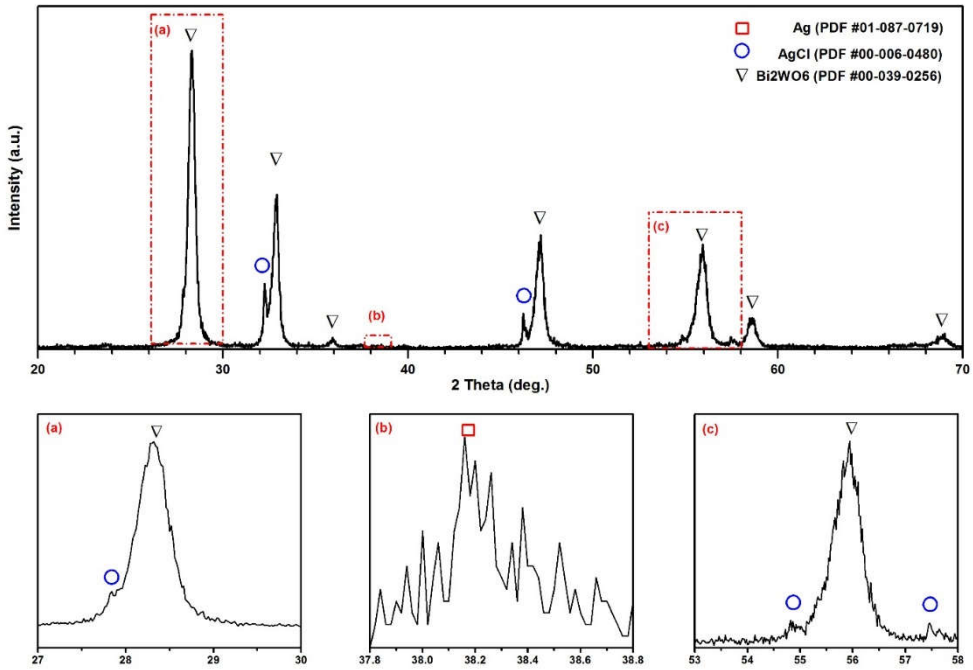
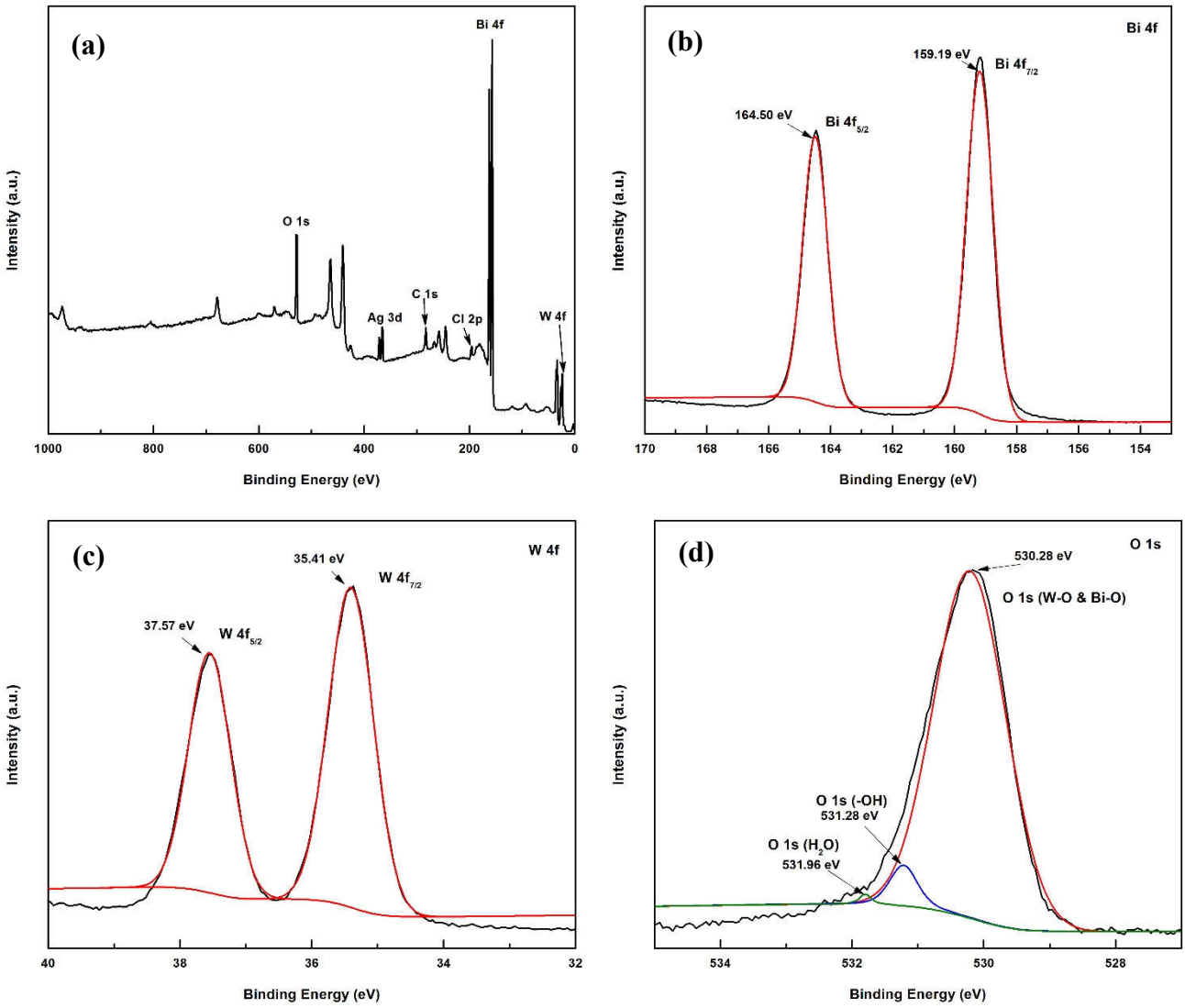


Figure A.2 XRD pattern of Ag/AgCl (10 wt%)-Bi_2WO_6

The elemental compositions and chemical states of Ag/AgCl-Bi_2WO_6 composites were determined by x-ray photoelectron spectroscopy. In Fig. A.3a, survey spectra and high-resolution scans of typical orbits in Ag/AgCl (10 wt%)-Bi_2WO_6 are illustrated. Specifically in the survey spectra, all elements of the composite (Bi, W, O, Ag, and Cl) were demonstrated. The spectra were calibrated using C 1s, the binding energy of which was 284.6 eV. As for high-resolution XPS spectra in Fig. A.3b, two strong peaks centered at 164.50 eV and 159.19 eV indicate that the valence of Bi in the composite was +2 [15]. Furthermore, it was found that binding energies of 37.57 eV and 35.41 eV for W $4f_{5/2}$ and W $4f_{7/2}$ respectively in Fig. A.3c, which were confirmed W in the composite with valence of +6 [15, 16]. The largest peak in Fig. A.3d could be separated into 3 smaller peaks which are in correspond well with O in the composite with forms of Bi_2WO_6 at 530.28 eV, -OH at 531.28 eV and H_2O at 531.96 eV. The existence of a negligible fraction of hydroxyl anion and H_2O in the composite may be attributed to the reaction of atmospheric water with the oxide surface and the chemisorbed water vapor on top of the oxide surface [17]. Silver peaks at 373.39 eV and 367.30 eV in Fig. A.3e were ascribed to binding energies of Ag $3d_{3/2}$ and Ag $3d_{5/2}$, respectively, in the presence of Ag^+ in AgCl [18]. Smaller peaks

located at 374.39 eV and 368.32 eV for binding energies of Ag $3d_{3/2}$ and Ag $3d_{5/2}$ were assigned to that of metallic Ag^0 [18]. This may suggest that metallic Ag^0 can be found in the composite.



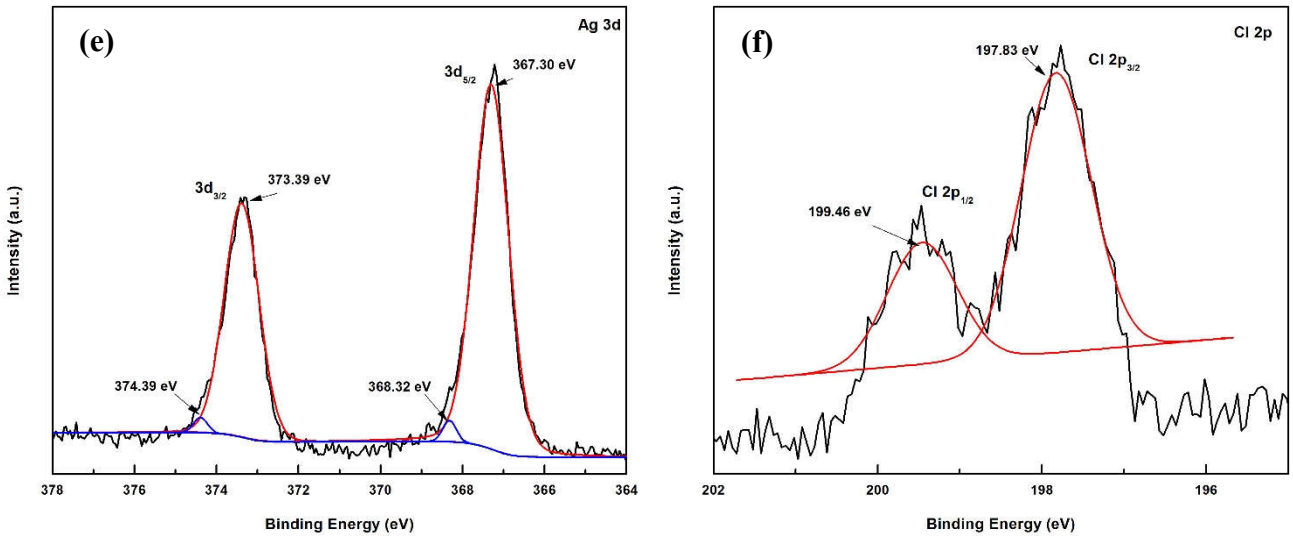
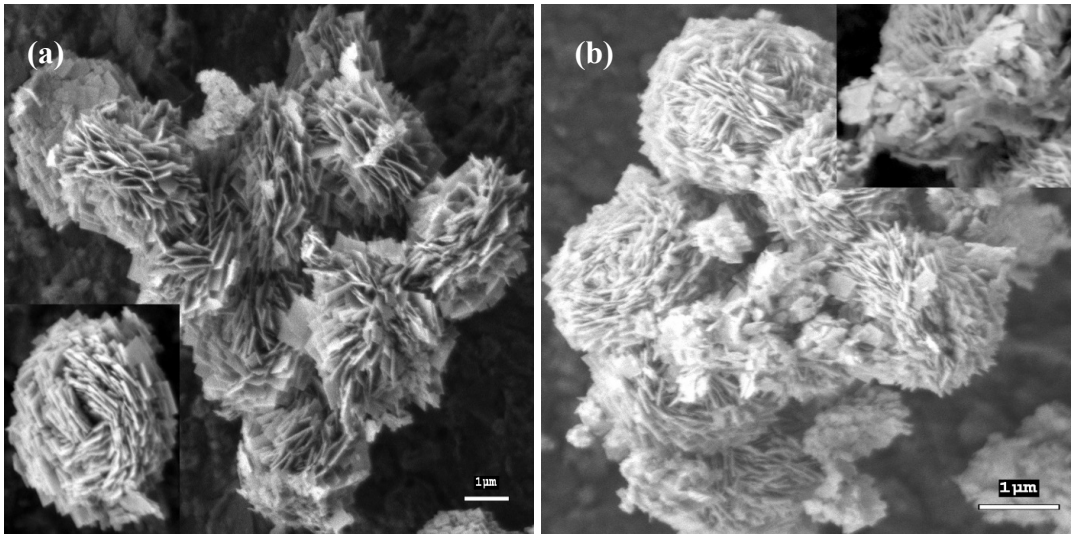


Figure A.3 XPS spectra of Ag/AgCl (10 wt%)-Bi_2WO_6 composite: (a) survey spectra, and high-resolution orbits scan of (b) Bi 4f, (c) W4f, (d) O 1s, (e) Ag 3d and (f) Cl 2p.

A.3.2 SEM, EDS and TEM



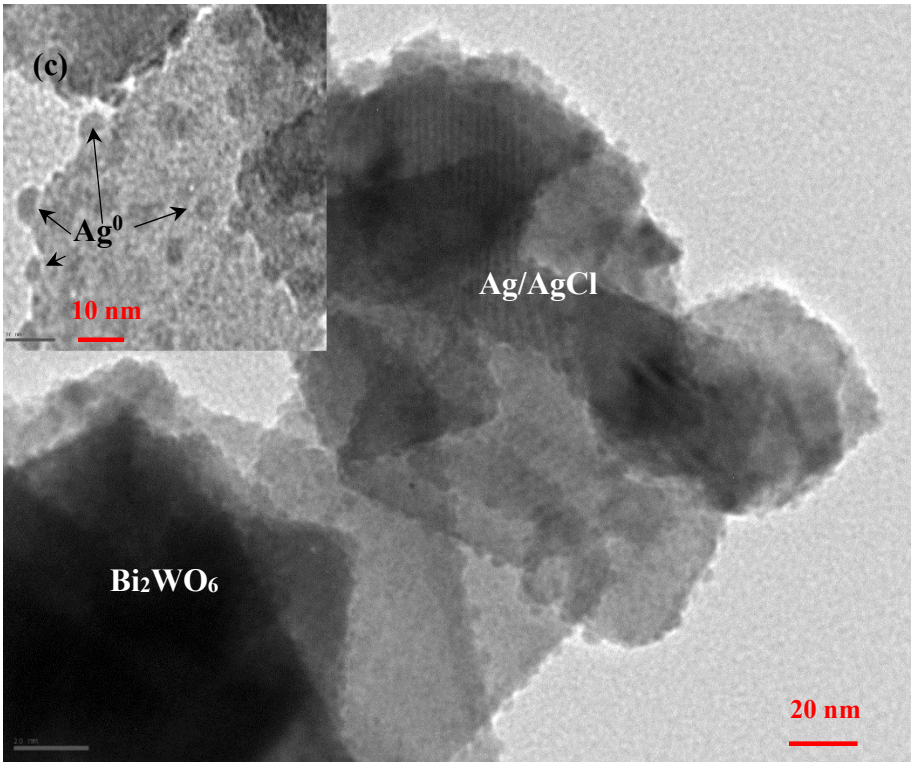


Figure A.4 SEM images of pure Bi_2WO_6 (a) and Ag/AgCl (10 wt%)-Bi_2WO_6 composite (b), and TEM images of Ag/AgCl (10 wt%)-Bi_2WO_6 composite (c).

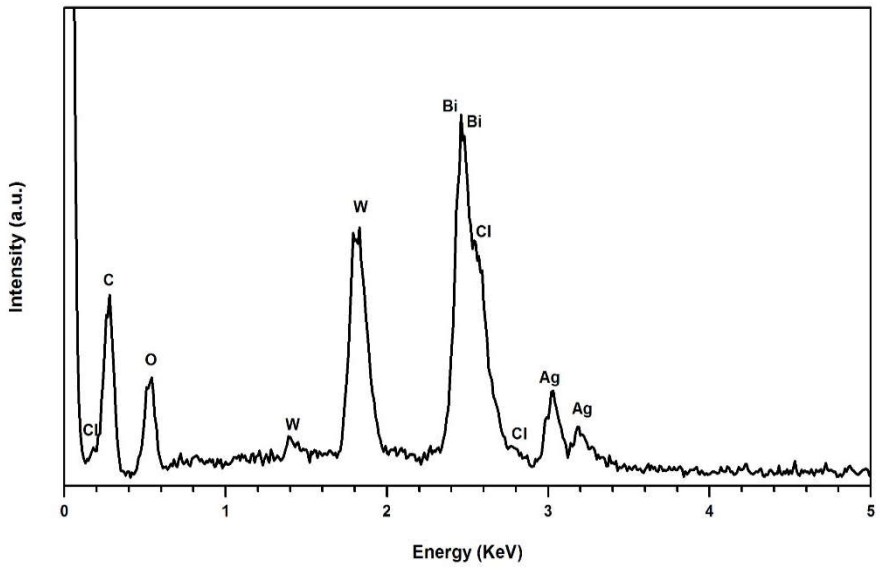


Figure A.5 EDS of Ag/AgCl (10 wt%)-Bi_2WO_6 composite.

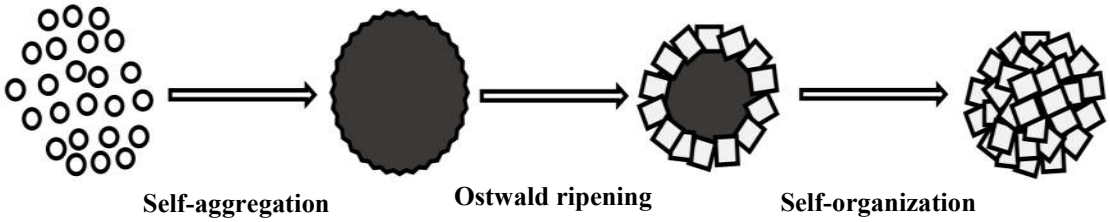


Figure A.6 Potential mechanism of forming the hierarchical flower-like superstructure of Bi_2WO_6.

Morphologies of as-prepared samples were measured by SEM and TEM, the results of which are shown in Fig. A.4. Bi_2WO_6 synthesized by the hydrothermal method described in this work exhibited a nanoplate-built hierarchical flower-like structure (Fig. A.4a). Similar structures were also reported in literatures [19, 20]. A potential mechanism for the formation of this superstructure is shown in Fig. A.6. The scheme shows that an irregular structure is formed through self-aggregation at the first step. As for the low pH (<1), $Bi_2O_2^{2+}$and WO_4^{2-} ions are generated in solution, and may be nucleate onto protuberances on the surface of solid spheres. This dissolution-recrystallization process is called Ostwald ripening. The plate-like structure is owed to the intrinsic anisotropic growth habits of Bi_2WO_6 [21]. According to the Gibbs-Thomson law, larger particles grow at the cost of small particles as for the energy difference in solubility. Flower-like superstructures eventually self-organize after sufficient duration of hydrothermal treatment. The size of each hierarchical microsphere was around 2-3 μm. Ag/AgCl growing on the surface of Bi_2WO_6 is shown in Fig. A.4b. Smaller plate-like AgCl could be observed as randomly loaded on its surface and metallic silver (Ag^0) was not observed. However, Ag^0 was shown to be present in the composite based on TEM imaging results (Fig. A.4c). In the inset of Fig. A.4c, nanoparticles with a size of no more than 5 nm could possibly be identified as metallic silver (Ag^0). Furthermore, EDS was performed on the composite and is illustrated in Fig. A.5. Characteristic peaks of all elements in the composite were found, which further confirms the successful synthesis of Ag/AgCl-Bi_2WO_6 in this work.

A.3.3 UV-Vis diffused reflectance spectra (DRS)

The optical absorbant properties of the Ag/AgCl-Bi_2WO_6 composite were measured using UV-Vis diffused reflectance spectroscopy. Spectra of pure Bi_2WO_6, Ag/AgCl, and Ag/AgCl (10 wt%)-Bi_2WO_6 are illustrated in Fig. A.7a. After loading Ag/AgCl onto Bi_2WO_6, The absorbent ability of the photocatalyst in the visible-light range was enhanced. This is mainly due to the plasmon resonance of photo-reduced silver (Ag^0) from AgCl [2], which could also be evidence for the existence of Ag^0 in the composite. To further explore the band gap (E_g) of samples, the classical Tauc equation (*Equation 1&2*) was employed as follows:

$$\alpha E_{photon} = K(E_{photon} - E_g)^{\frac{n}{2}} \qquad (Equation\ 1)$$

$$E_{photon} = h\nu \qquad (Equation\ 2)$$

Where α, h, ν and K are the absorption coefficient, the Planck constant, the irradiation frequency, and the constant for semiconductors (usually equal to 1) respectively. The constant n depends on the type of band gap, where $n = 1$ is for direct transition and $n = 4$ is for indirect transition. The band gap of the as-prepared Bi_2WO_6 in this work is characteristic of a direct transition (Fig. A.8), so n is equal to 4. By plotting $(\alpha E_{photon})^{1/2}$ vs E_{photon} as illustrated in Fig. A.7b, the intercept at the horizontal axis is the band gap value. This indicates that Ag/AgCl in composites narrowed the band gap from 2.70 eV to 2.57 eV compared to pure Bi_2WO_6, which could widen the edge wavelength of incidence from 459.3 nm to 482.5 nm. This indicates that Ag/AgCl-Bi_2WO_6 composites could be effectively activated under visible light irradiation.

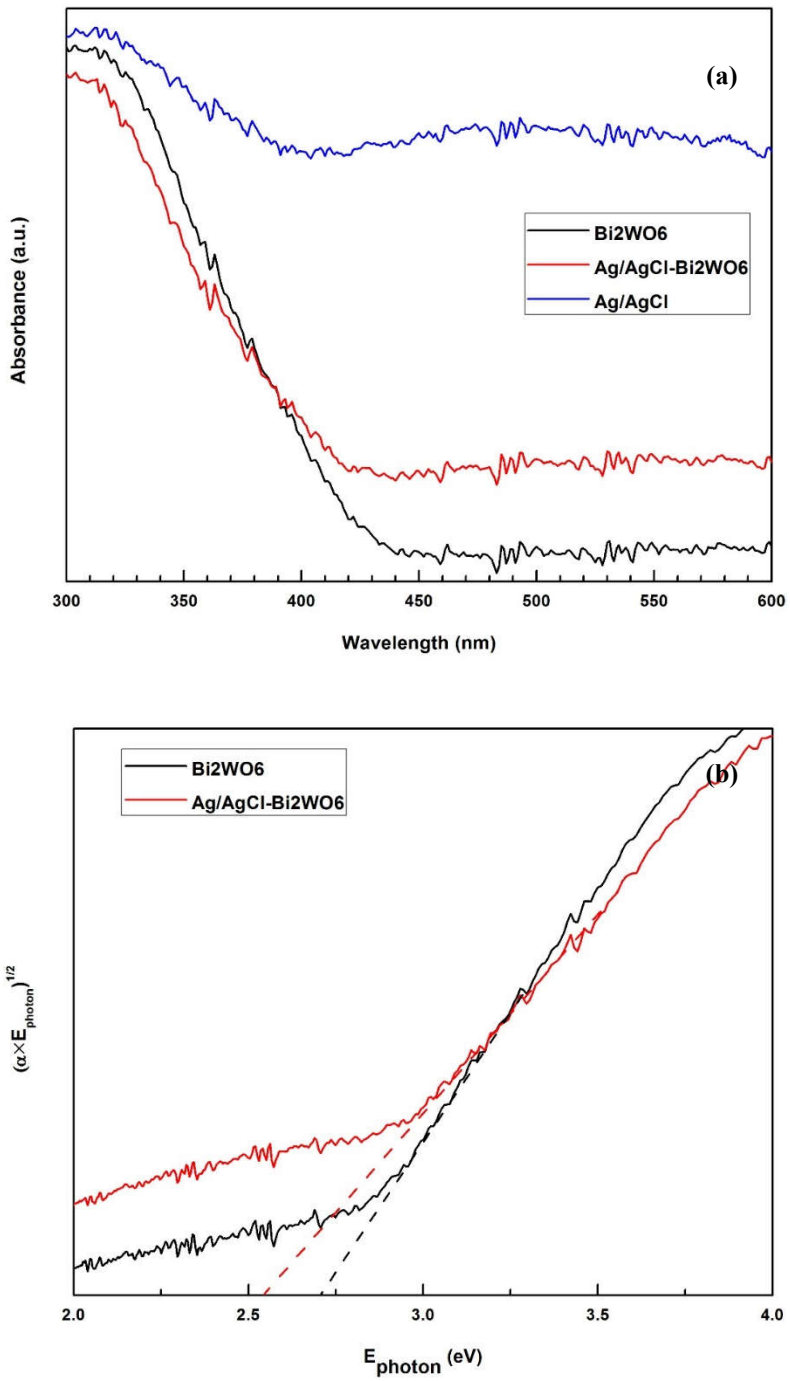


Figure A.7 (a) UV-Vis diffused reflectance spectra and (b) $(\alpha E_{photon})^{1/2}$-$E_{photon}$ curves of as-prepared pure Bi_2WO_6, Ag/AgCl and Ag/AgCl (10 wt%)-Bi_2WO_6.

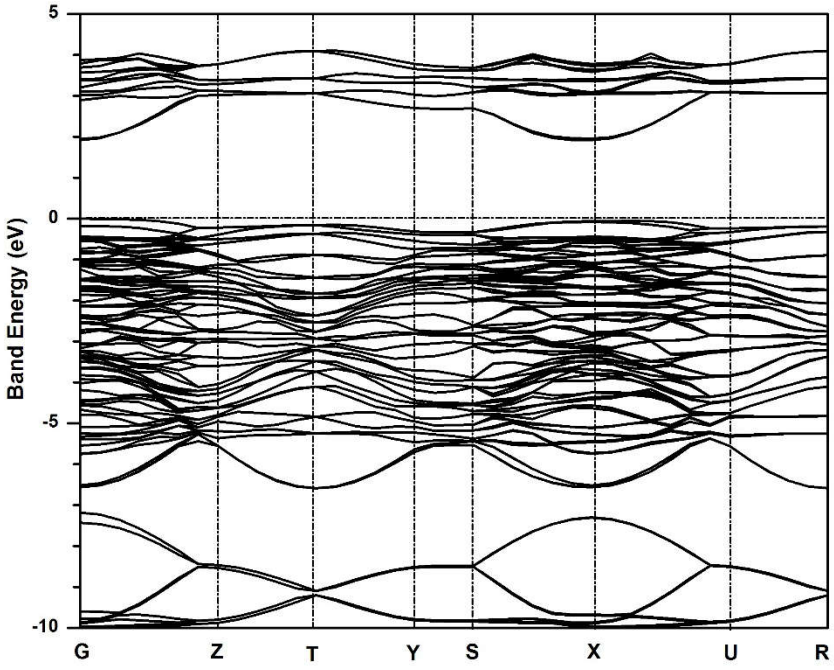


Figure A.8 Band gap of Bi_2WO_6. (Simulated by Quantum Espresso [22])

A.3.4 Photocatalytic activity test under visible light

Photocatalytic activities of as-prepared samples were tested by degrading *RhB* (10 mg/L). All of the screening test results are plotted in Fig. A.9. The removal efficiencies for pure Bi_2WO_6 and Ag/AgCl were 38.8% and 65.3% in 45 min, respectively. By increasing the loading amount of Ag/AgCl in the composites from 1 wt% to 10 wt%, removal efficiencies of the composites were increased up to 100% after 45 min under visible light. This enhancement effect may be attributed to the establishment of a heterojunction between Ag/AgCl and Bi_2WO_6 [3, 14, 23]. However, further increasing the amount of Ag/AgCl in the composites deteriorates the photocatalytic degradation performances. This may be interpreted as larger nanoparticles which are loaded onto Bi_2WO_6 possibly weakening the anchoring forces between them and destroying the hetero-structure.

Langmuir-Hinshelwood kinetic analysis was applied to RhB degradation in the presence of as-prepared photocatalysts. Trials performed with diluted concentrations of RhB ($c_o < 10^{-3}$ mol/L), showed that the Langmuir-Hinshelwood model could be simplified to a pseudo-first-order reaction model [24], expressed as follows (*Equation 3*):

$$\ln(\frac{c_o}{c}) = k_r \times K \times t = k't \qquad \textit{(Equation 3)}$$

Where *t, c_o* and *c* are the time, the initial concentration and concentration at each specific reaction time *t* of *RhB*, k_r is the reaction rate constant, *K* is the adsorption coefficient of the pollutant on the photocatalyst, and *k'* is pseudo-first-order reaction kinetics constant used as the parameter to evaluate the performances of as-prepared photocatalysts in degrading pollutants. A plot of $\ln(c_o/c)$ as a function t is found in Fig. A.10, where the slope of the line of best fit is the pseudo-first-order kinetics constant, the results of which are summarized in Table A.2. The excellent linearity of each line of best fit indicates that the photocatalytic degradation of RhB under visible light irradiation in the presence of Ag/AgCl-Bi_2WO_6 follows first order kinetics. The process carried out with pure Bi_2WO_6 as the photocatalyst exhibited the lowest reaction constant, while loading of Ag/AgCl onto Bi_2WO_6 increased the constant up to 5.4 times than that of pure Bi_2WO_6 at 10 wt% Ag/AgCl. These results confirm that the presence of Ag/AgCl in the composites significantly increases photocatalytic activity with regards to the degradation of organic pollutants.

The step-wise mechanism for the degradation of RhB was observed by taking UV-Vis spectra, which are illustrated in Fig. A.11. In the inset table, the positions of characteristic peaks for each intermediate species are summarized [25]. It can be concluded that two processes of RhB degradation exist, namely de-ethylation and destruction of the aromatic ring. In the de-ethylation process, RhB is decomposed into N,N,N'-Triethyl-rhodamine (TER), N,N'-Triethyl-rhodamine (DER), N-Ethyl-rhodamine (MER) and Rhodamine, the UV-Vis characteristic peaks of which are located at wavelengths of 539 nm, 522 nm, 510nm and 498 nm respectively. In the first 33 min, peak positions blue-shifted from 554 nm to 498 nm, indicating that RhB degraded into Rhodamine. After that, peak positions stabilized at 498 nm and gradually reduced in intensity. This may be attributed to the degradation of Rhodamine into smaller species such H_2O and CO_2.

The photocatalytic activity with respect to the degradation of the colourless organic compound, phenol, was investigated and is illustrated in Fig. A.12. These results aimed to confirm the increased photocatalytic activity in the presence of the Ag/AgCl-Bi_2WO_6 composite under visible light attributed to the surface plasmon resonance effect instead of

photosensitization of the dye (RhB in this work) [26]. The composite performed well in the degradation of Phenol (approximately 30% of phenol was converted in 45 min), which was a better performance than that exhibited by pure Bi_2WO_6 (only about 5% of phenol was converted in 45 min). This confirmed the enhancement effect of loading Ag/AgCl onto Bi_2WO_6 exists under visible light irradiation.

Table A.2 Pseudo-first order reaction rate constants for various processes.

	Bi_2WO_6	1 wt%	2 wt%	4 wt%	8 wt%	10 wt%	20 wt%	Ag/AgCl
Pseudo-first order:								
k ($10^{-2}min^{-1}$)	1.047	2.733	3.371	3.930	4.576	5.688	4.508	2.037
R^2	0.9999	0.9961	0.9989	0.9979	0.9989	0.9993	0.9987	0.9939

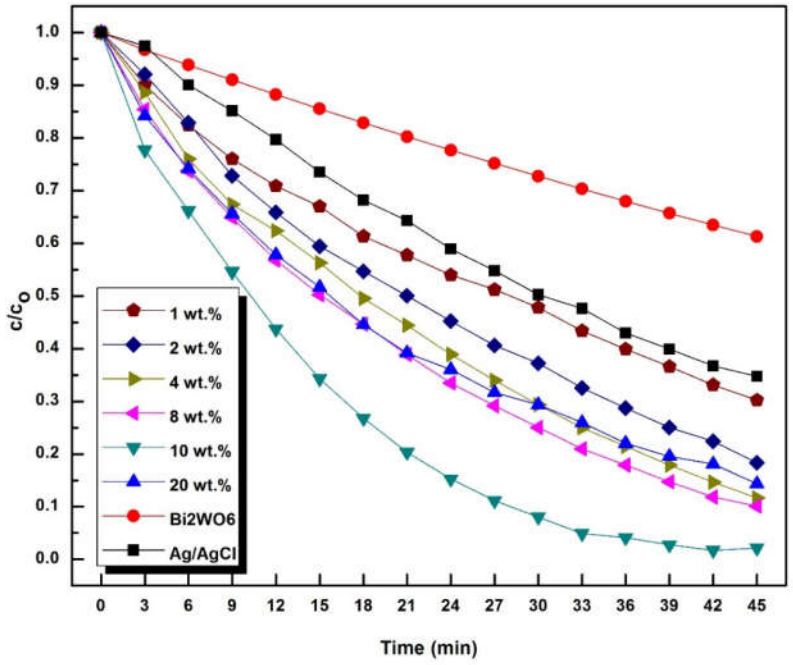


Figure A.9 Photocatalytic degradation of RhB (10 mg/L) under visible light with as-prepared pure Bi_2WO_6, Ag/AgCl and Ag/AgCl-Bi_2WO_6 composites.

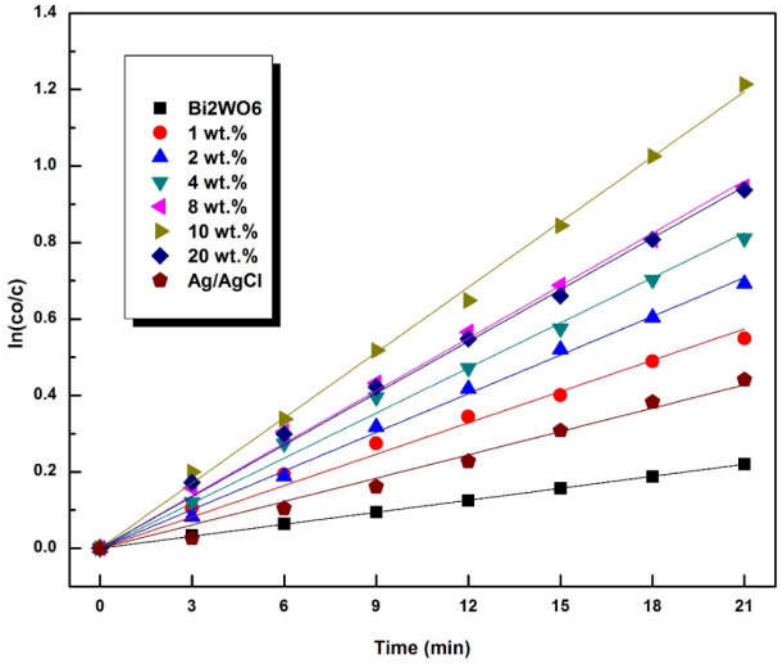


Figure A.10 Photocatalytic kinetics of each process.

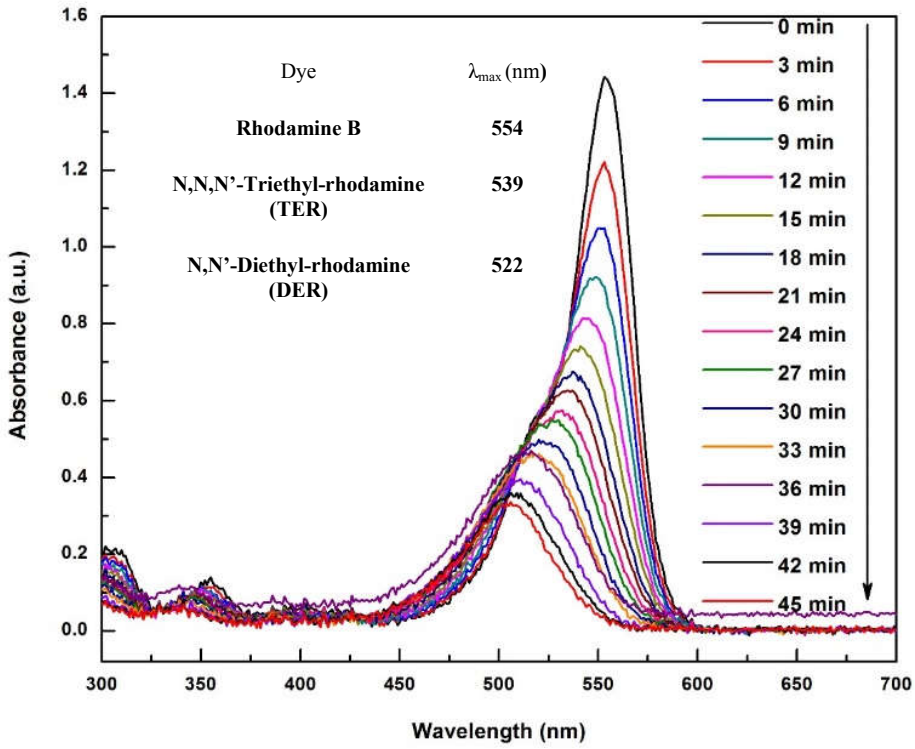


Figure A.11 UV-Vis spectra of solutions taken during the photocatalytic process in the presence of Ag/AgCl (10 wt%)-Bi_2WO_6 (inset table shows characteristic wavelength for each intermediate species in water [25]).

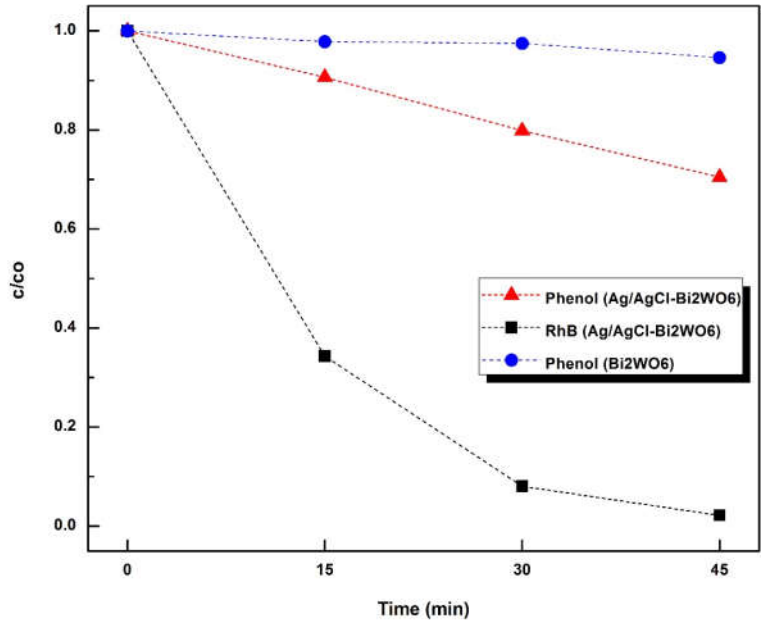


Figure A.12 Degradation of Phenol (10 mg/L) by using Ag/AgCl-Bi_2WO_6 composite.

A.3.5 Roles of radical species

Holes (h+) and free radicals, especially •OH, are regarded as the main oxidative species in photocatalytic degradation of organic pollutants [27]. In this study, EDTA-2Na and 2-Butanol were chosen as the hole and hydroxyl radical scavengers respectively [28]. When holes were quenched, only 15% of RhB was removed (Fig. A.13). Comparatively, there was little influence when 2-Butanol was added to quench hydroxyl radicals. This suggests that the hydroxyl radical is not the main oxidative species in the degradation of RhB, and that holes govern the photocatalytic process. Similar results were also reported in literature [9, 29]. This phenomenon may be explained knowing that the standard redox potential of Bi_2O_4/BiO^+ (Bi^V/Bi^{III}) (+1.59 eV) is much more negative than that of •OH/-OH (+2.30 eV) [9, 29]. This suggests that "non-selective" •OH could not be produced in this photocatalytic oxidation process.

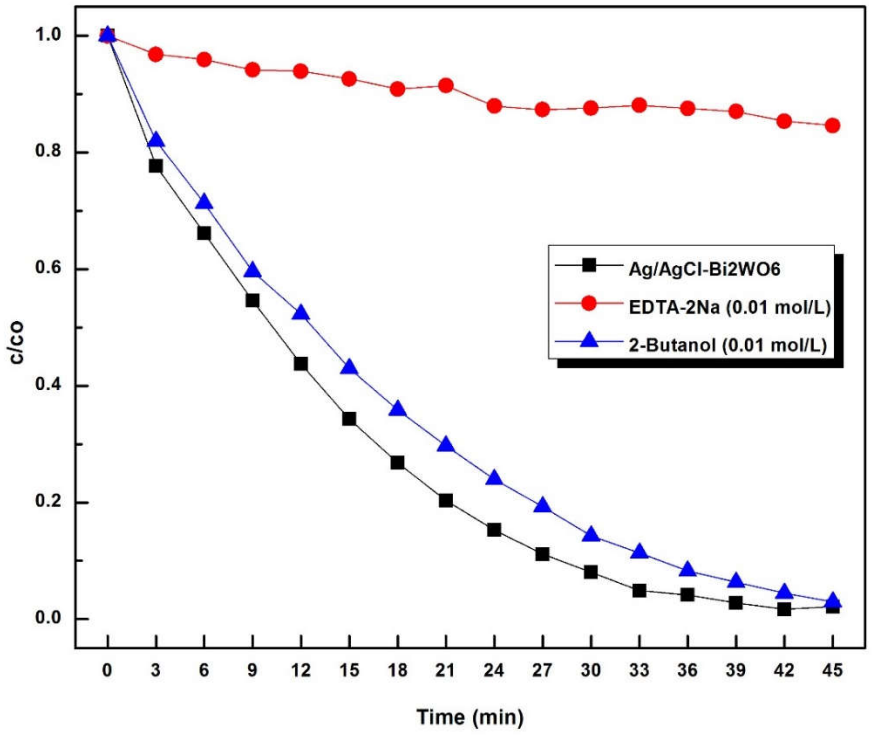


Figure A.13 Photocatalytic activity in presences of Ag/AgCl/-Bi_2WO_6 and quenchers.

A.3.6 Reusability

Reusability is a significant parameter used to evaluate photocatalysts implemented in practical applications. As-prepared composites were investigated by taking 4 runs where RhB was degraded. Removal efficiencies after 45 min were plotted in Fig. A.14. After 4 runs, the removal efficiency decreased slightly from 97.8% to 91.5%, but this relatively high removal efficiency still implies the high stability of the Ag/AgCl-Bi_2WO_6 composite. Furthermore, used photocatalysts were observed by XRD, the patterns of which are shown in Fig. A.15. Lattice parameters of Bi_2WO_6 after four runs were a = 5.4577 Å, b = 16.3970 Å and c = 5.4505 Å. All the characteristic peaks of Bi_2WO_6 were found with high intensities, indicating that the main crystal structure of Bi_2WO_6 was stable and was not destroyed during the recycle. However, the characteristic peaks of AgCl were observed with reduced intensities. On the other hand, intensities of other peaks, especially the peak at $2\theta = 38.2°$ (Fig. A.15b), for metallic Ag^0, became stronger. This may be attributed to the reduction of AgCl to metallic Ag^0 in the photocatalytic process under visible light irradiation, as photo-generated electrons are produced and easily react with Ag^+. This may be an explanation for

the decreased removal efficiency of RhB. Another possible explanation is that the intermediate species of RhB were adsorbed on the composite and refractory to be degraded.

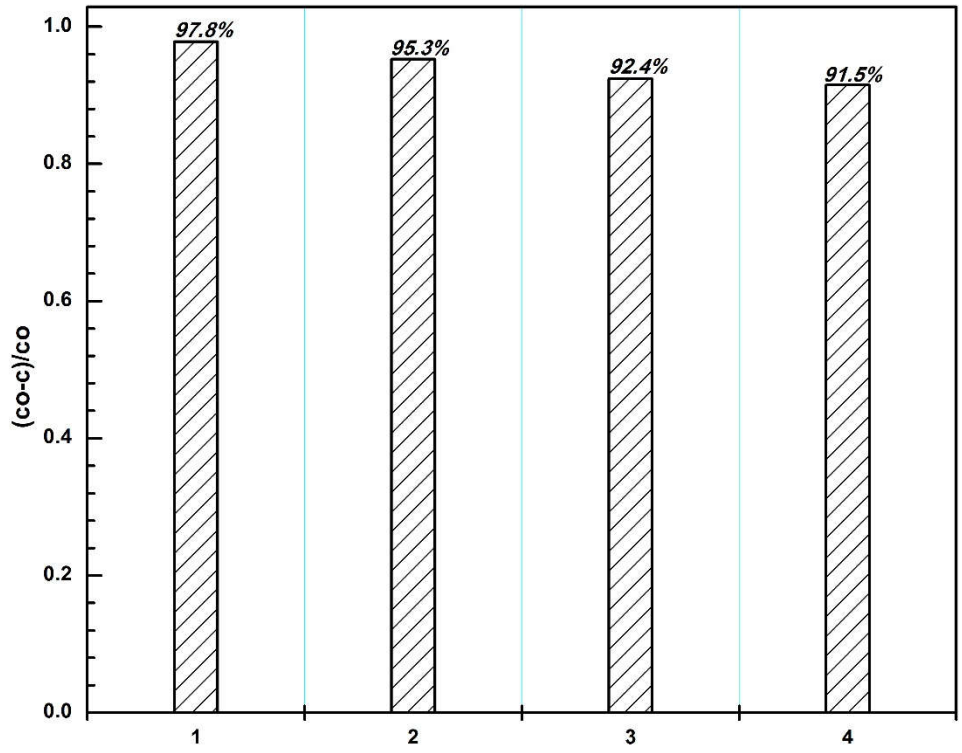


Figure A.14 Removal efficiencies for 4 runs of 45 min.

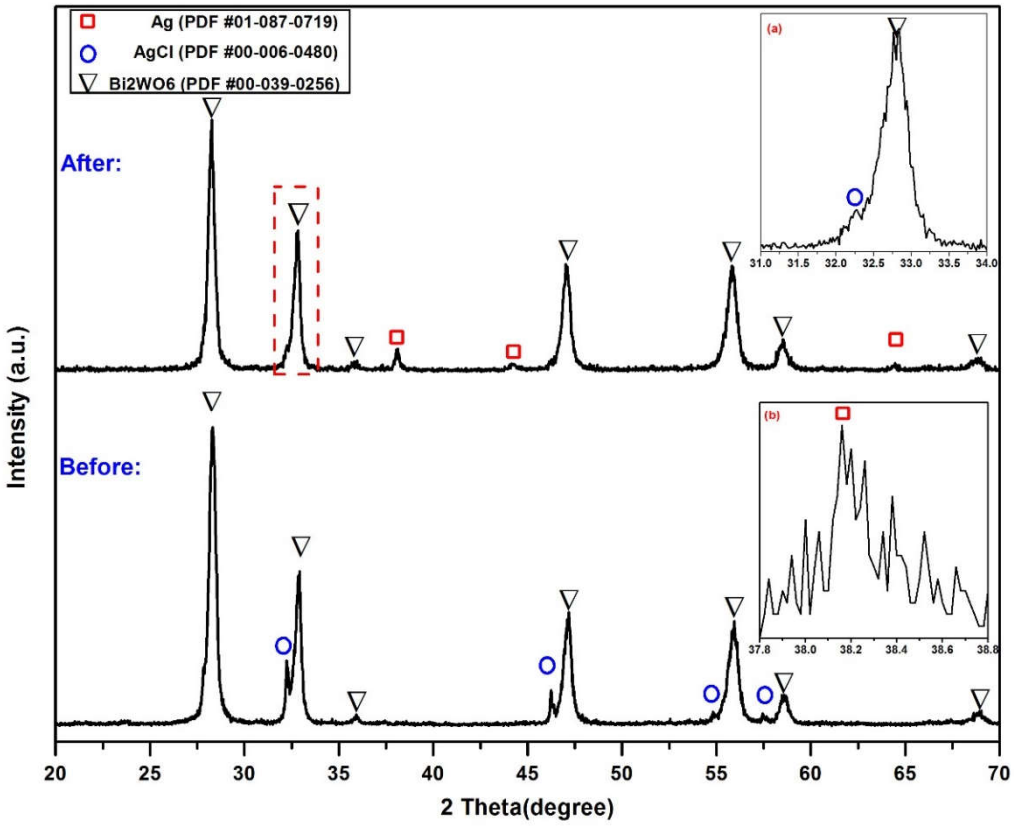


Figure A.15 XRD patterns of Ag/AgCl (10 wt%)-Bi_2WO_6 before and after 4 runs.

A.3.7 Proposed mechanism of photocatalytic degradation

The Band structure of the Ag/AgCl-Bi_2WO_6 composite is illustrated in Fig. A.16. The proposed mechanism of using the composite to degrade RhB could be summarized as: (1) Bi_2WO_6 with a band gap of 2.70 eV is activated by visible light irradiation, generating electrons and holes; (2) Ag^0 nanoparticles induced by surface plasmon resonance under visible light could produce electrons and leave holes on the valence band [1], and electrons could rapidly transfer to Bi_2WO_6 or AgCl; (3) RhB could be activated by photons (photosensitization) and generate electrons which could transfer to the conduction band of either Bi_2WO_6 or AgCl; (4) Cl^- could be oxidized into a Cl• radical which is supposed to oxidize organic pollutants. Holes on the valence band of Bi_2WO_6 would transfer to that of AgCl, and the separation efficiency of photo-generated electrons and holes would improve [30]. Meanwhile, electrons induced by the surface plasmon resonance and photosensitization effects would be beneficial to produce more oxidative species. The integrated effect results in an enhanced photocatalytic activity to degrade organic pollutants.

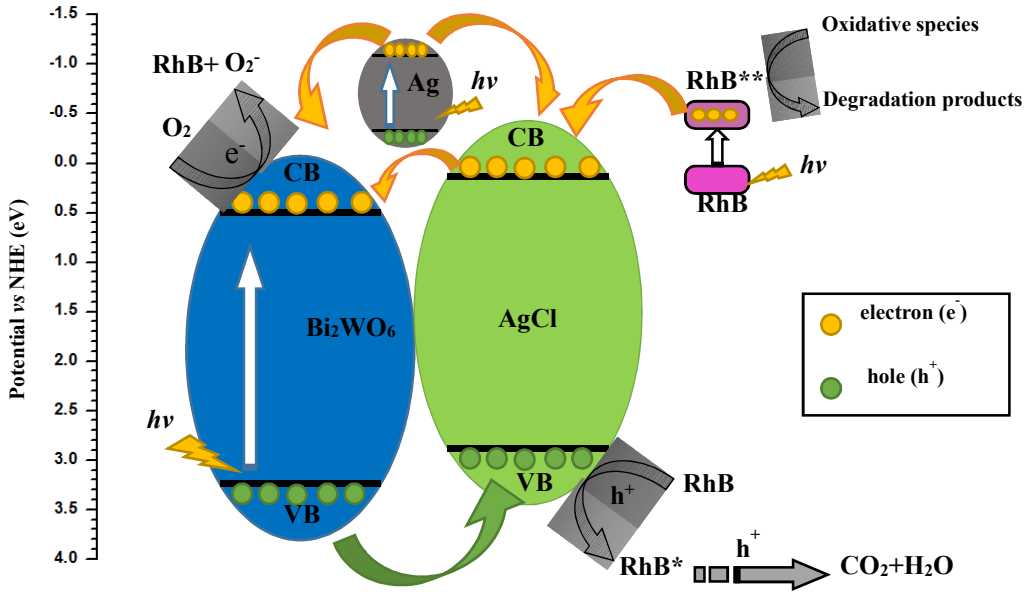


Figure A.16 Schematic of possible mechanism of degrading RhB in the presence of Ag/AgCl-Bi_2WO_6.

A.4 Conclusion

An Ag/AgCl-Bi_2WO_6 composite was successfully synthesized using a hydrothermal and photo-reduced method. Its morphology was hierarchical and flower-like with a size of 2-3 μm. As-prepared photocatalysts performed with increased photocatalytic activities and high stabilities when degrading RhB under visible light irradiation. The 10 wt% Ag/AgCl sample exhibited the best performance. A mechanism of photocatalytic oxidation was proposed, and it was deduced that the enhancement effect is mainly due to the establishment of a heterostructure, as well as the surface plasmon resonance and photosensitization effects. This work is evidence for the potential application of plasmonic metals in photocatalytic oxidation processes with enhancement effects.

References

1. Suljo Linic, Phillip Christopher and David B. Ingram, "Plasmonic-metal nanostructures for efficient conversion of solar to chemical energy," *Nature Materials*, vol. 10, no. 12, pp. 911-921, 2011.

2. Peng Wang, Baibiao Huang, Xiaoyan Qin, Xiaoyang Zhang, Ying Dai, Jiyong Wei and Myung-Hwan Whangbo, "Ag@AgCl: A Highly Efficient and Stable Photocatalyst Active under Visible Light," *Angewandte Chemie International Edition*, vol. 47, no. 41, pp. 7931-7933, 2008.

3. Jiaguo Yu, Gaopeng Dai and Baibiao Huang, "Fabrication and Characterization of Visible-Light-Driven Plasmonic Photocatalyst Ag/AgCl/TiO_2 Nanotube Arrays," *The Journal of Physical Chemistry C*, vol. 113, no. 37, pp. 16394-16401, 2009.

4. Jiabin Zhou, Ya Cheng and Jiaguo Yu, "Preparation and characterization of visible-light-driven plasmonic photocatalyst Ag/AgCl/TiO2 nanocomposite thin films," *Journal of Photochemistry and Photobiology A: Chemistry*, vol. 223, no. 2–3, pp. 82-87, 2011.

5. Liqun Ye, Jinyan Liu, Chuqing Gong, Lihong Tian, Tianyou Peng and Ling Zan, "Two Different Roles of Metallic Ag on Ag/AgX/BiOX (X = Cl, Br) Visible Light Photocatalysts: Surface Plasmon Resonance and Z-Scheme Bridge," *ACS Catalysis*, vol. 2, no. 8, pp. 1677-1683, 2012.

6. Hongbo Fu, Chengshi Pan, Wenqing Yao and Yongfa Zhu, "Visible-Light-Induced Degradation of Rhodamine B by Nanosized Bi2WO6," *The Journal of Physical Chemistry B*, vol. 109, no. 47, pp. 22432-22439, 2005.

7. Huizhong An, Yi Du, Tianmin Wang, Cong Wang, Weichang Hao and Junying Zhang, "Photocatalytic properties of BiOX (X = Cl, Br, and I)," *Rare Metals*, vol. 27, no. 3, pp. 243-250, 2008.

8. Xiangchao Meng and Zisheng Zhang, "Synthesis, Analysis, and Testing of BiOBr-Bi_2WO_6 Photocatalytic Heterojunction Semiconductors," *International Journal of Photoenergy*, vol. 2015, pp. 12, 2015.

9. Xiangchao Meng and Zisheng Zhang, "Facile synthesis of BiOBr/Bi_2WO_6 heterojunction semiconductors with high visible-light-driven photocatalytic activity," *Journal of Photochemistry and Photobiology A: Chemistry*, vol. 310, no. 0, pp. 33-44, 2015.

10. Xiaona Li, Renkun Huang, Yanhua Hu, Yongjuan Chen, Wenjun Liu, Rusheng Yuan and Zhaohui Li, "A Templated Method to Bi2WO6 Hollow Microspheres and Their Conversion to Double-Shell Bi2O3/Bi2WO6 Hollow Microspheres with Improved

Photocatalytic Performance," *Inorganic Chemistry*, vol. 51, no. 11, pp. 6245-6250, 2012.

11. Ming-Sheng Gui, Wei-De Zhang, Ya-Qi Chang and Yu-Xiang Yu, "One-step hydrothermal preparation strategy for nanostructured WO3/Bi2WO6 heterojunction with high visible light photocatalytic activity," *Chemical Engineering Journal*, vol. 197, pp. 283-288, 2012.

12. Lilia Coronato Courrol, Flávia Rodrigues de Oliveira Silva and Laércio Gomes, "A simple method to synthesize silver nanoparticles by photo-reduction," *Colloids and Surfaces A: Physicochemical and Engineering Aspects*, vol. 305, no. 1–3, pp. 54-57, 2007.

13. Kevin S Knight, "The crystal structure of russellite; a re-determination using neutron powder diffraction of synthetic Bi_2WO_6," 1992.

14. Yuanguo Xu, Hui Xu, Huaming Li, Jiexiang Xia, Chengtang Liu and Ling Liu, "Enhanced photocatalytic activity of new photocatalyst Ag/AgCl/ZnO," *Journal of Alloys and Compounds*, vol. 509, no. 7, pp. 3286-3292, 2011.

15. Guo-Hua He, Gang-Ling He, An-Jie Li, Xin Li, Xian-Ju Wang, Yue-Ping Fang and Yue-Hua Xu, "Synthesis and visible light photocatalytic behavior of WO3 (core)/Bi2WO6 (shell)," *Journal of Molecular Catalysis A: Chemical*, vol. 385, pp. 106-111, 2014.

16. Ming Ge, Yafei Li, Lu Liu, Zhen Zhou and Wei Chen, "Bi2O3−Bi2WO6 Composite Microspheres: Hydrothermal Synthesis and Photocatalytic Performances," *The Journal of Physical Chemistry C*, vol. 115, no. 13, pp. 5220-5225, 2011.

17. Jan Wielant, Tom Hauffman, Orlin Blajiev, René Hausbrand and Herman Terryn, "Influence of the Iron Oxide Acid−Base Properties on the Chemisorption of Model Epoxy Compounds Studied by XPS," *The Journal of Physical Chemistry C*, vol. 111, no. 35, pp. 13177-13184, 2007.

18. Joanne Gamage McEvoy, Wenquan Cui and Zisheng Zhang, "Synthesis and characterization of Ag/AgCl–activated carbon composites for enhanced visible light photocatalysis," *Applied Catalysis B: Environmental*, vol. 144, no. 0, pp. 702-712, 2014.

19. Lisha Zhang, Wenzhong Wang, Zhigang Chen, Lin Zhou, Haolan Xu and Wei Zhu, "Fabrication of flower-like Bi2WO6 superstructures as high performance visible-light driven photocatalysts," *Journal of Materials Chemistry*, vol. 17, no. 24, pp. 2526-2532,

2007.

20. Ju Wu, Fang Duan, Yan Zheng and Yi Xie, "Synthesis of Bi2WO6 Nanoplate-Built Hierarchical Nest-like Structures with Visible-Light-Induced Photocatalytic Activity," *The Journal of Physical Chemistry C*, vol. 111, no. 34, pp. 12866-12871, 2007.

21. Liwu Zhang and Yongfa Zhu, "A review of controllable synthesis and enhancement of performances of bismuth tungstate visible-light-driven photocatalysts," *Catalysis Science & Technology*, vol. 2, no. 4, pp. 694-706, 2012.

22. Giannozzi Paolo, Baroni Stefano, Bonini Nicola, Calandra Matteo, Car Roberto, Cavazzoni Carlo, Ceresoli Davide, L. Chiarotti Guido, Cococcioni Matteo, Dabo Ismaila, Corso Andrea Dal, Gironcoli Stefano de, Fabris Stefano, Fratesi Guido, Gebauer Ralph, Gerstmann Uwe, Gougoussis Christos, Kokalj Anton, Lazzeri Michele, Martin-Samos Layla, Marzari Nicola, Mauri Francesco, Mazzarello Riccardo, Paolini Stefano, Pasquarello Alfredo, Paulatto Lorenzo, Sbraccia Carlo, Scandolo Sandro, Sclauzero Gabriele, P. Seitsonen Ari, Smogunov Alexander, Umari Paolo and M. Wentzcovitch Renata, "QUANTUM ESPRESSO: a modular and open-source software project for quantum simulations of materials," *Journal of Physics: Condensed Matter*, vol. 21, no. 39, pp. 395502, 2009.

23. Wei Xiong, Qidong Zhao, Xinyong Li and Dongke Zhang, "One-step synthesis of flower-like Ag/AgCl/BiOCl composite with enhanced visible-light photocatalytic activity," *Catalysis Communications*, vol. 16, no. 1, pp. 229-233, 2011.

24. Jean-Marie Herrmann, "Heterogeneous photocatalysis: fundamentals and applications to the removal of various types of aqueous pollutants," *Catalysis Today*, vol. 53, no. 1, pp. 115-129, 1999.

25. Tadashi Watanabe, Takuo Takizawa and Kenichi Honda, "Photocatalysis through excitation of adsorbates. 1. Highly efficient N-deethylation of rhodamine B adsorbed to cadmium sulfide," *The Journal of Physical Chemistry*, vol. 81, no. 19, pp. 1845-1851, 1977.

26. Taixing Wu, Guangming Liu, Jincai Zhao, Hisao Hidaka and Nick Serpone, "Photoassisted Degradation of Dye Pollutants. V. Self-Photosensitized Oxidative Transformation of Rhodamine B under Visible Light Irradiation in Aqueous TiO2

Dispersions," *The Journal of Physical Chemistry B*, vol. 102, no. 30, pp. 5845-5851, 1998.

27. Michael R. Hoffmann, Scot T. Martin, Wonyong Choi and Detlef W. Bahnemann, "Environmental Applications of Semiconductor Photocatalysis," *Chemical Reviews*, vol. 95, no. 1, pp. 69-96, 1995.

28. Tongguang Xu, Liwu Zhang, Hanyun Cheng and Yongfa Zhu, "Significantly enhanced photocatalytic performance of ZnO via graphene hybridization and the mechanism study," *Applied Catalysis B: Environmental*, vol. 101, no. 3–4, pp. 382-387, 2011.

29. Yanhui Zhang, Nan Zhang, Zi-Rong Tang and Yi-Jun Xu, "Identification of Bi2WO6 as a highly selective visible-light photocatalyst toward oxidation of glycerol to dihydroxyacetone in water," *Chemical Science*, vol. 4, no. 4, pp. 1820-1824, 2013.

30. Edward T. Yu, James O. McCaldin and Thomas C. McGill, "Band Offsets in Semiconductor Heterojunctions," in *Solid State Physics*, E. Henry and T. David, Ed., pp. 1-146, Academic Press, 1992.

Appendix B Pd-doped Bi_2MoO_6 Plasmonic Photocatalysts with Enhanced Visible Light Photocatalytic Performance

Xiangchao Meng and Zisheng Zhang

Applied Surface Science 392 (2017), 169-180

Abstract

Pd-doped Bi_2MoO_6 was prepared and investigated for the first time. The prepared samples were characterized by their crystal structures, chemical states, atomic compositions, optical properties and morphologies. The photocatalytic activities of prepared samples under visible light irradiation were determined by degradation of phenol, which is widely found in wastewater from many industrial processes and is difficult to destroy. The sample exhibiting the highest removal efficiency with respect to the degradation of phenol contained 2% Pd. The enhancement effect can be interpreted as the integrated effects of a reduction in the rate of electron-hole recombination, surface plasmon resonance, and production of Cl^0. This work sheds light on the potential applications of noble metal nanoparticles in visible light-driven photocatalysis.

B.1 Introduction

Semiconductor-based photocatalysis has attracted extensive interest since water splitting on TiO_2 electrodes was first reported [1]. One of the more recent applications of photocatalysis focuses on the degradation of organic compounds by photogenerated reactive oxidative species (free radicals and electron holes). The bottleneck issues inhibiting widely application mainly include low visible light responses and high recombination rates of electron-hole pairs [2-4]. Studies that explore narrow band gap semiconductors that are visible light-responsive has therefore become a hot topic.

Bismuth-based compounds including Bi_2WO_6 [5], Bi_2MoO_6 [6], BiOX (X = Cl, Br, I) [7, 8], were found to have suitable band structures which can be activated by visible light irradiation [9]. Furthermore, the valence band (VB) of a bismuth-based semiconductor consists of not only O 2p orbitals (generally the only orbital in a VB for metal oxides), but also Bi 6s orbitals. The hybrid orbitals of O 2p and Bi 6s are reported to be beneficial by increasing the mobilities of photogenerated carriers [10]. Bi_2MoO_6, as an important Aurivillius oxide, has increasingly drawn the attention of researchers, owing to its excellent intrinsic properties such as its dielectric nature, its catalytic behaviour and its luminescence [11]. The band gap of Bi_2MoO_6 was reported in the range of 2.5 - 2.8 eV [12, 13], indicating that Bi_2MoO_6 is capable of visible light-driven photocatalytic activity. It is generally known that narrower band gaps lead to higher recombination rates for electron-hole pairs, resulting in a reduction of photocatalytic activity. For the purpose of decreasing this recombination rate, approaches including the adjustment of morphology [14, 15], the fabrication of heterojunctions [16, 17], and doping [18, 19] were studied. Among them, doping may be considered to be the easiest and most efficient way to decrease the recombination rate, as doped metals may be regarded as electrons traps. Electrons accumulated on the dopant may also react with dissolved O_2 to produce oxidative free radicals ($\bullet O_2$).

It was reported that noble metal nanoparticles on a surface may be activated by photons in the visible light spectrum, which may be attributed to the surface plasmon resonance (SPR) effect [20]. Ag/AgCl has been reported as a highly efficient plamonic photocatalyst under visible light irradiation [21, 22]. Yuan et al. [23] have reported on the incorporation of Ag nanoparticles on the surface of Bi_2MoO_6 by means of an in situ reduction process. The prepared composite was found to exhibit an enhanced visible light-induced photocatalytic activity. Ag/AgCl- and Ag/AgBr-Bi_2MoO_6 were also reported to exhibit enhanced visible light-induced photocatalytic performances in the degradation of organic pollutants from wastewater [18, 24]. It was reported that the SPR peaks of Pd nanostructures can be tuned from 410 to 870 nm [25, 26]. And Pd nanoparticles on $(BiO)_2CO_3$ and C_3N_4 were reported with enhanced visible-light-driven photocatalytically activity, because of the SPR effect and up-lift of valence band of support [27, 28]. To the best knowledge of the authors, there is presently no research reported on Pd nanoparticles doped onto Bi_2MoO_6.

This work discusses the fabrication of Pd-doped Bi_2MoO_6 composites for the first time. Photocatalytic activities under visible light irradiation were evaluated by degrading phenol, which is widely found in wastewater from many industrial processes and is generally difficult to decompose. The effect of dopant quantity in the composites was also investigated. A mechanism describing the enhancement of photocatalytic activity after introducing Pd on the surface of Bi_2MoO_6 was also proposed. It is worth noting that Pd-Bi_2MoO_6 exhibited an excellent visible light-driven photocatalytic performance.

B.2 Experimental

B.2.1 Synthesis of Bi_2MoO_6

All reagents were purchased from Fisher Scientific in analytical purities. Bi_2MoO_6 was synthesized by solvothermal methods as reported in literature [11]. In a typical procedure, 1.6866 g of $Bi(NO_3)_3 \cdot 5H_2O$ and 0.4210 g of $Na_2MoO_4 \cdot 2H_2O$ were dissolved in separate volumes of 5 mL of ethylene glycol (EG) under magnetic stirring. These two solutions were then mixed together, followed by dropwise addition of 20 mL of ethanol. The mixture was then magnetically stirred for 10 min. The clear solution was transferred to a 45-mL Teflon-lined stainless steel autoclave (Parr Instrument Company) and heated at 160°C for 20 h. After the autoclave was allowed to naturally cool to room temperature, the Bi_2MoO_6 precipitates were filtered out and washed once with ethanol then twice with distilled deionized water (DDW). The washed Bi_2MoO_6 samples were dried at 60°C overnight and collected.

B.2.2 Synthesis of $Pd/PdCl_2$-Bi_2MoO_6

The $Pd/PdCl_2$-Bi_2MoO_6 was prepared via a photoreduction method. Typically, 0.0015 g of $PdCl_2$ were dispersed in 40 mL of DDW, followed by ultrasonication treatment for 30 min. A quantity of 0.3 g of Bi_2MoO_6 was then added to the suspension under magnetic stirring and the suspension was exposed to light. The light source was a 300-W halogen tungsten projector lamp (Ushio). After 1 h of irradiation, the samples were filtered and dried at 60°C overnight. The cooled sample was collected and labelled as 0.5wt% Pd-Bi_2MoO_6. Similarly, 1.0wt% Pd-Bi_2MoO_6, 2.0wt% Pd-Bi_2MoO_6, 4.0wt% Pd-Bi_2MoO_6, and 8.0wt% Pd-Bi_2MoO_6 samples were also prepared.

B.2.3 Characterization

The crystal structures of prepared samples were analyzed by X-ray diffraction (XRD), carried out using a Rigaku Ultima IV Diffractometer with Cu Kα radiation (λ = 0.15418 nm) at 44 kV and 44 mA. XRD patterns were tested at 2θ in the range of 5 - 80°. Surface atomic components and chemical states were measured by a XSAM-800 X-ray photoelectron spectrophotometer (XPS). The Fourier Transform Infrared Spectrometer (FTIR) was used via a Cary 630 (Agilent Technologies). Spectra were recorded at room temperature with wavenumbers in the range of 600 – 2000 cm^{-1}. Transmission electron microscopy (TEM) was carried out with a JEM-2100F FE-TEM (JEOL), operating at an acceleration voltage of 200 kV. Ultraviolet-visible diffuse reflectance spectra (DRS) were observed with a Thermo Evolution 300 spectrophotometer. Electrochemical properties of prepared samples were performed on a CHI 604E electrochemical analyzer (CH Instruments Inc., USA) with a platinum wire as counter electrode, a calomel reference electrode and a working electrode. The working electrode was an indium tin oxide (ITO, 75 × 25 × 1.1 mm, 15 - 25 Ω, Sigma-Aldrich Canada Co.) glass coated with the prepared samples. The electrochemical impedance spectroscopies (EIS) were recorded with frequency in the range of 0.01 - 1000000 Hz and the sinusoidal wave of 5 mV. The electrolyte was Na_2SO_4 with concentration of 0.25 mol/L.

B.2.4 Photocatalytic activity tests

Photocatalytic activities of prepared samples were evaluated by degrading the colourless organic model compound, phenol. The geometry of the reaction system is schemed in Fig. B.1. A 500-mL beaker fitted with a cooling jacket which maintained the temperature of the system at 20°C served as the photocatalytic reactor. The visible light source was a 300-W halogen tungsten projector lamp (Ushio, wavelength mainly in the range of 310 – 800 nm) with a UV cut-off (Kenko Zeta, transmittance > 90%) to filter out irradiation with a wavelength below 410 nm. The irradiation intensity on the surface of the solution was measured by a quantum meter (Biospherical QSL-2100, 400 nm < λ < 700 nm) to be 1.1 × 10^{-2} Einsteins m^{-2} s^{-1}. In each test, 100 mL of 10 mg/L phenol solution was added to the reactor. The quantity of catalyst that was subsequently added was 1 g/L of reactor solution (0.10 g in 100 mL of solution). The suspensions were magnetically stirred for 60 min before

turning on the lamp, so as to obtain an adsorption-desorption equilibrium between phenol and the catalyst. The photocatalytic test was carried out for 300 min, and aliquots were drawn every 30 min, each of which was centrifuged at a rate of 13,000 rpm for 5 min. The supernatant was then separated and analyzed using a high-performance liquid chromatograph (HPLC, Agilent 1100 series) equipped with a UV-Vis detector. A ZORBAX Elipse Plus C18 (4.6 × 250 mm) was used at 60°C. The wavelength of the detector was fixed at 270 nm for the detection of phenol, hydroquinone, catechol and benzoquinone. The flow phase was composed of methanol (55%, V/V) and water (45%, V/V) at a flow rate of 0.6 mL/min. The injection volume was set to 25 µL.

The reusability of the prepared sample (2% Pd-Bi_2MoO_6) was also studied by separating the photocatalysts from the suspension following a single run. Catalysts were then mixed with fresh wastewater to start another run. Four runs were performed in total for these tests.

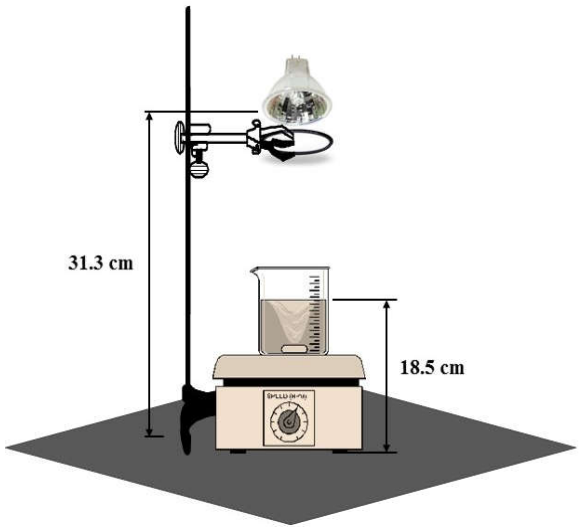


Figure B.1 Photoreactor geometry and positioning.

B.2.5 Electronic structure calculation

The quantum-mechanical calculations were performed on the basis of the density functional theory (DFT) [29]. The generalized gradient approximation (GGA) was applied to exchange-correlation effects. The open access software Quantum ESPRESSO was used, which utilizes pseudopotentials to describe electron-ion interactions and represents electronic wave functions using a plane-wave basis set [30]. The kinetic energy cut-off was set to 300 eV.

B.3 Results and discussions

B.3.1 XRD and XPS

XRD patterns of pure Bi_2MoO_6 and Bi_2MoO_6 composites doped with different quantities of Pd are shown in Fig. B.2. Pure Bi_2MoO_6 was found to have an orthorhombic crystal structure (space group: pbca (61), PDF card number: 00-72-1524 [31]). All peaks observed were identified, indicating that a well-crystalized Bi_2MoO_6 sample was synthesized. Loading of Pd on the surface of Bi_2MoO_6 was found to have a negligible influence on XRD patterns of Bi_2MoO_6. Peaks for $PdCl_2$ and metallic Pd were not found in composites with Pd contents less than or equal to 4%, possibly due to the limit of detection of XRD. However, peaks located at 12.0°, 24.7°, 48.7° and 55.0° were found in the 8% Pd sample, and may be attributed to the presence of $PdCl_2$ (space group: Pnmn (58), PDF card number: 01-075-0871) [32], and a peak located at 40.0° may suggest the presence of metallic Pd (space group: Fm-3m (225), PDF card number: 00-005-0681) [33].

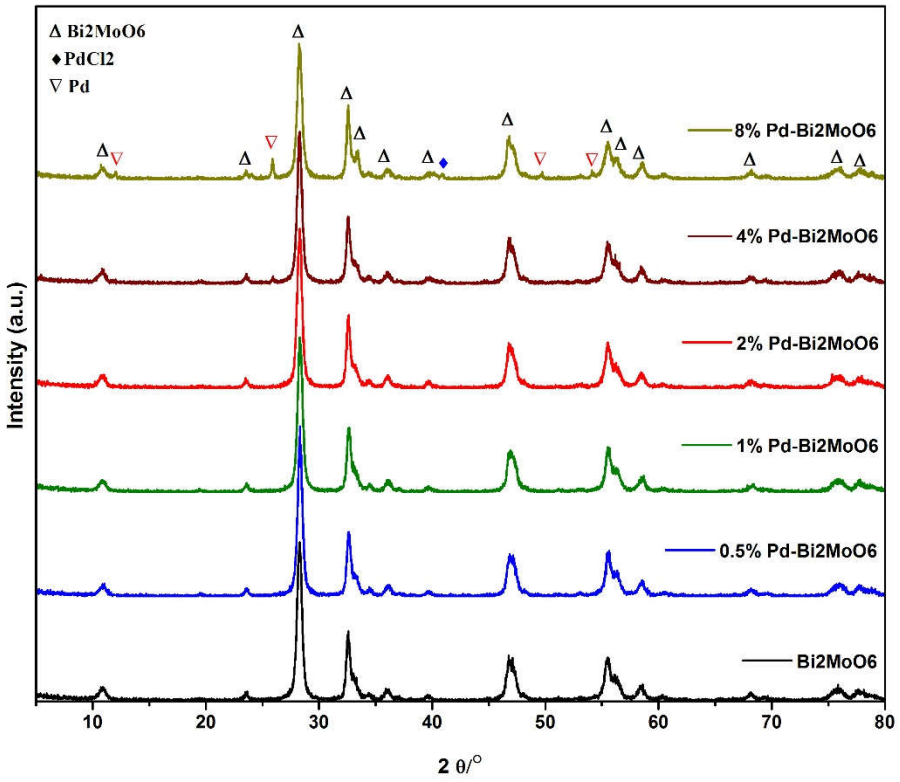


Figure B.2 XRD patterns of pure Bi_2MoO_6, and Bi_2MoO_6 composites with different quantities of doped Pd.

The chemical states and elemental compositions of Pd-Bi_2MoO_6 samples were investigated by XPS. The survey spectrum and high-resolution scan of O 1s, Pd 3d and Cl 2p orbitals for 2%Pd-Bi_2MoO_6 are illustrated in Fig. B.3. All spectra were calibrated with C 1s, the binding energy of which is 284.6 eV. In the survey spectrum (Fig. B.3a), all component elements (*i.e.* Bi, Mo, O, Pd, Cl) were found and identified, and no peaks for impurities were found. In Fig. B.3b, it can be seen that there are two single-spin orbitals. The peak located at a binding energy of 530.0 eV may correspond with oxygen atoms in the Bi_2MoO_6 in the form of W-O and Bi-O bonds. The other peak located at a binding energy of 531.8 eV may be attributed to the oxygen atoms in adsorbed H_2O [34, 35]. For the high-resolution Pd 3d orbital scan in Fig. B.3c, there were two sets of spin-orbit doublets found. Accordingly, Pd (3d5/2, 3/2) peaks located at 334.7 and 340.0 eV, as well as at 336.8 and 341.6 eV may be attributed to Pd^0 and Pd^{2+} respectively [36, 37]. This indicates that both bivalent and metallic Pd may be present on the surface of Bi_2MoO_6. The relative concentration of Pd^0/Pd^{2+} may be obtained by using the following equation (Equation 1) [38]:

$$\frac{\eta_{Pd^0}}{\eta_{Pd^{2+}}} = \frac{I_{Pd^0}}{I_{Pd^{2+}}} \times \frac{\sigma_{Pd}\lambda_{Pd}D_E(Pd)}{\sigma_{Pd}\lambda_{Pd}D_E(Pd)} \qquad \text{Equation 1}$$

where η, I, σ, λ, and D_E are the surface concentration, integrated intensity, photoelectric cross-section, electron free mean path, and geometric factor respectively. The values of σ, λ, and D_E have been calculated by Penn and Scofield, and were obtained from literature [39, 40]. Integration of Pd^0 and Pd^{2+} peaks was performed to estimate their concentrations. The relative combined surface concentration ratio of Pd^0 to Pd^{2+} was approximately 10/9. In addition, the high-resolution Cl 2p orbital scan shown in Fig. B.3d further suggests the presence of $PdCl_2$ on the surface of the Pd-Bi_2MoO_6 composites. Peaks located at binding energies of 197.5 and 199.1 eV for Cl $2p_{1/2}$ and Cl $2p_{3/2}$ respectively clearly indicate the presence of Cl^- [41]. It can be concluded that only a portion of Pd^{2+} was reduced to metallic Pd in the photoreduction process.

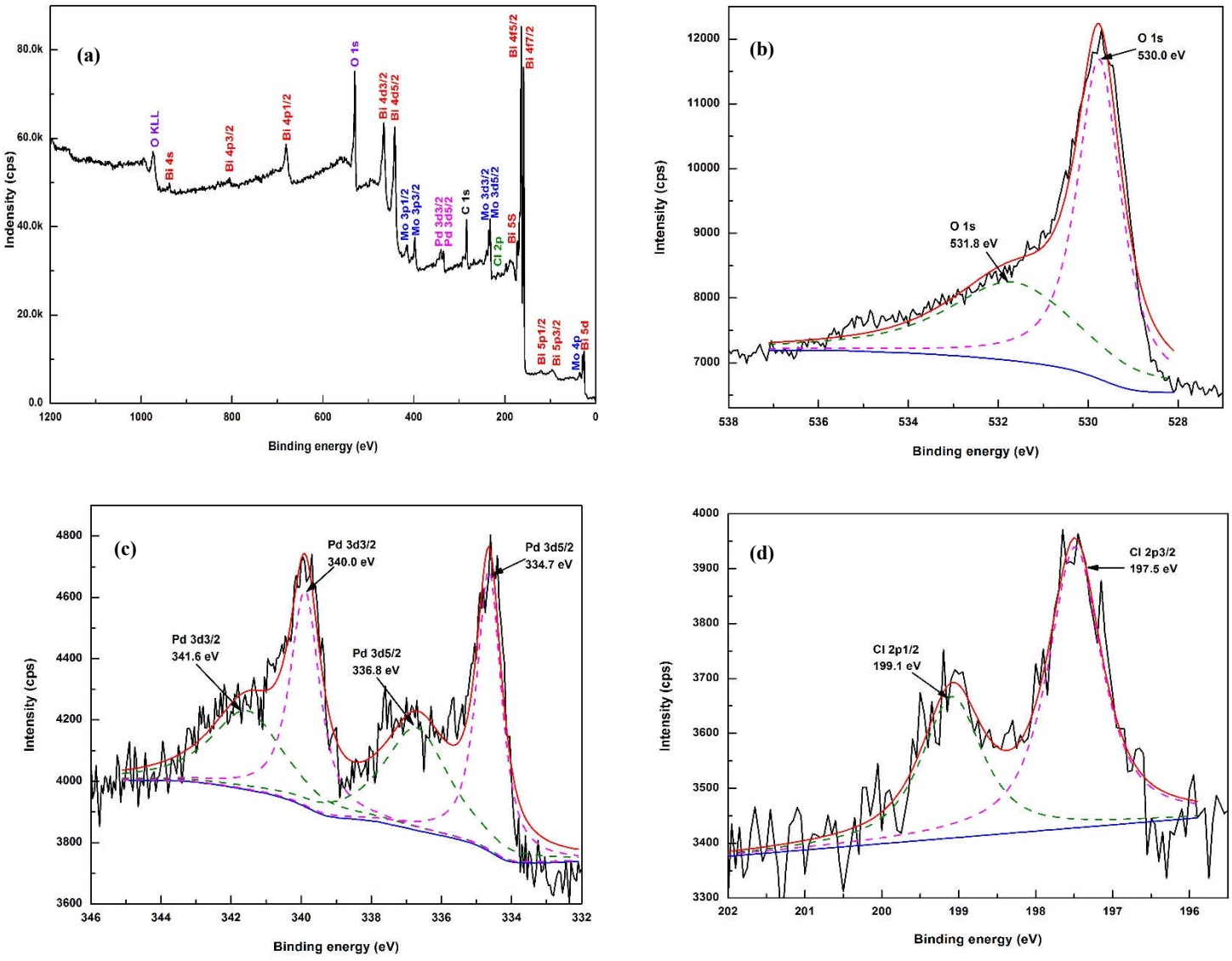


Figure B.3 XPS spectra of 2% Pd-Bi_2MoO_6 composite: (a) survey, and high-resolution orbital scan of (b) O 1s, (c) Pd 3d and (d) Cl 2p.

B.3.2 FT-IR

FT-IR spectra of prepared samples are shown in Fig. B.4. For pure Bi_2MoO_6, the regions of wavelength number ranging from 600 cm^{-1} to 1000 cm^{-1}, may be possibly attributed to Bi-O and Mo-O stretching as well as Mo-O-Mo bridging stretching modes, which can respond to the variation of crystal structure of Bi_2MoO_6 [12, 42]. The band located at 690 cm^{-1} may have therefore resulted from the asymmetric stretching mode of MoO_6 involving vibrations of the equatorial oxygen atoms [43, 44]. The absorption peaks at approximately

795 cm^{-1} and 841 cm^{-1} may be attributed to the asymmetric and symmetric stretching modes of MoO_6 involving vibrations of the apical oxygen atoms. The absorption bands at 937 cm^{-1} together with a small peak at 902 cm^{-1} may be attributed to Mo-O stretching modes. Small peaks located in the range of 1300-1600 cm^{-1} may have resulted from adsorbed CH_3COOH, specifically the δCH vibrations of the $CH_3C=O$ moiety as well as coupled νC-O and δOH vibrations [45, 46]. After loading Pd on the surface of Bi_2MoO_6, there was a negligible difference, independent of the amount of Pd. This indicates that the structure of Bi_2MoO_6 was not influenced during the modification process by Pd loading.

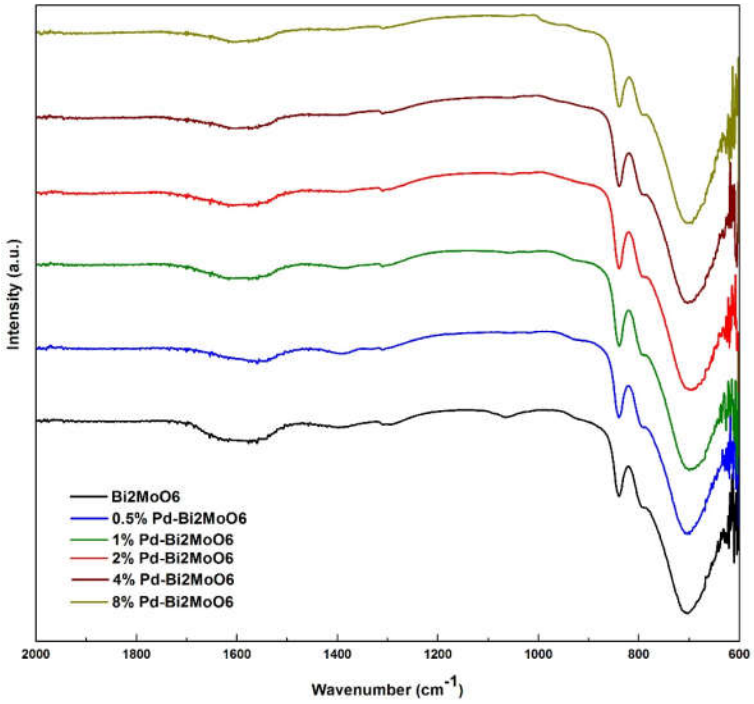


Figure B.4 FT-IR spectra of pure Bi_2MoO_6 and those of Pd-Bi_2MoO_6 composites with different quantities of Pd.

B.3.3 Morphologies

The morphologies of prepared samples including Bi_2MoO_6 and 2% Pd-Bi_2MoO_6 were observed by SEM and TEM, the results of which are shown in Fig. B.5. For pure Bi_2MoO_6, uniform, sphere-like structures ranging from 1 to 3 μm in diameter (Fig. B.5a) were observed. It can also be seen that the 3-D microspheres are composed of 2-D crystalline nanosheets. Hollow Bi_2MoO_6 was also observed (dashed circle in Fig. B.5a), the formation process of which may be interpreted by Ostwald Ripening [47, 48]. When the reaction time

is short, the Bi_2MoO_6 sphere has a solid core. With a longer reaction time however, the dissolution-recrystallization process occurs, and crystalline nanosheets form on the outer surface by dissolving crystallites located in the inner cores. This may be due to crystallites at the inner core possessing higher surface energies than those at the outer surface. After loading Pd on the surface of Bi_2MoO_6, no significant differences in the SEM images (Fig. B.5b) were found compared to pure Bi_2MoO_6. Furthermore, in the TEM image of Pd-Bi_2MoO_6, the solid core of Bi_2MoO_6 may be seen (Fig. B.5c). In the high-resolution TEM image (inset of Fig. B.5c), quantum dots were observed, which may be metallic Pd^0 as well as adsorbed $PdCl_2$. The lattice spacing of the nanospot was measured as 0.225nm which was assigned to the (1 1 1) plane of metallic palladium (Pd^0). The lattice of Bi_2MoO_6 was also observed in the HRTEM of Pd-Bi_2MoO_6 composite. And it can be seen Pd nanoparticles were intimately attached on the surface of Bi_2MoO_6. Theoretically, the redox potential of Pd^{2+} reduced to Pd^0 (Formula 2) is 0.915 eV. The feasibility of the process depends on the bottom potential of the conduction band of Bi_2MoO_6. The plate-band potential of Bi_2MoO_6 may be calculated by applying the Mulliken electronegativity theory of atoms (Equation 2):

$$E_{CB,Bi_2MoO_6} = X_{Bi_2MoO_6} - E^e - \frac{1}{2}E_g \qquad \textbf{\textit{Equation 2}}$$

where $E_{CB,Bi2MoO6}$, $X_{Bi2MoO6}$, E^e and E_g are the bottom potential of the conduction band, the electronegativity (6.13 eV), the energy of free electrons on the hydrogen scale (≈ 4.5 eV) and the band gap energy of Bi_2MoO_6 (2.64 eV, tested by DRS shown in section 3.4), respectively. $E_{CB,Bi2MoO6}$ may be calculated as 0.31 eV, which is lower than the redox potential of Formula 2. In other words, electrons generated by visible light-activated Bi_2MoO_6 in Formula 1 have a reductive potential strong enough to reduce Pd^{2+} to metallic Pd.

$$Bi_2MoO_6 \xrightarrow{h\upsilon} e^-_{Bi_2MoO_6} + h^+_{Bi_2MoO_6}$$ ***Formula 5***

$$Pd^{2+}_{adsorbed} + 2e^-_{Bi_2WO_6} \longrightarrow Pd$$ ***Formula 6***

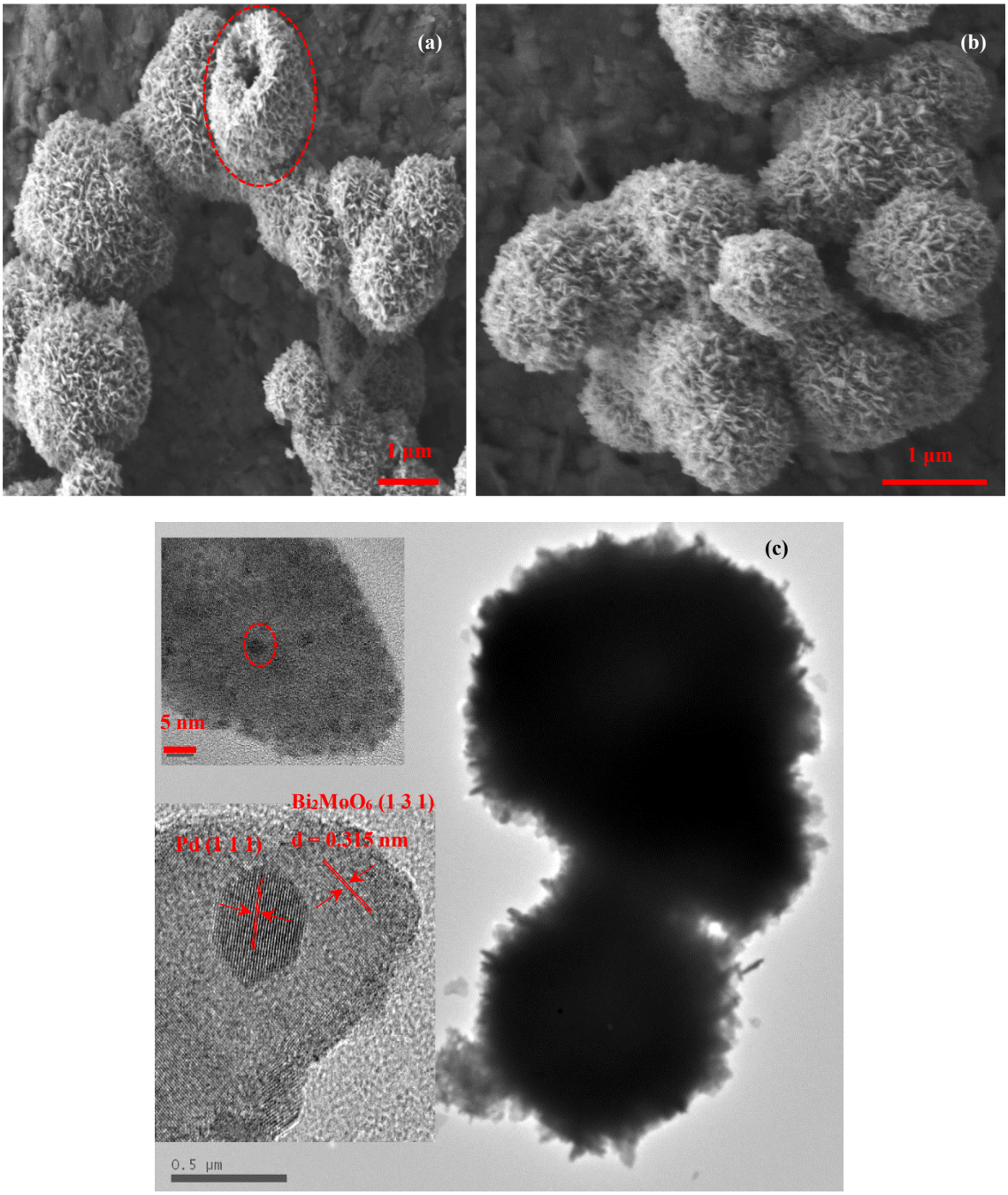


Figure B.5 SEM images of (a) pure Bi_2MoO_6 and (b) Pd-Bi_2MoO_6, and (c) TEM/HRTEM images of Pd-Bi_2MoO_6.

B.3.4 Optical properties

The optical properties of prepared photocatalytic materials were determined through UV-Vis diffuse reflectance spectroscopy, shown in Fig. B.6. Pure Bi_2MoO_6 exhibited excellent photoabsorptive properties in the UV-visible light spectrum. A steep increase in the spectrum of pure Bi_2MoO_6 was observed when the wavelength was below 470 nm, which may have resulted from the band gap transition. The band gap value may be calculated from the band edge ($E_g = 1240/\lambda$) to be 2.64 eV. The band structure and density of states (DOS) of pure Bi_2MoO_6 were also simulated based on the DFT method. The total and partial densities of states (TDOS and PDOS) of Bi_2MoO_6 are given in Fig. B.7, setting an energy of zero at the top of the valence band. For pure Bi_2MoO_6, O 2p and Bi 6s states contribute to the valence band, while Bi 6p, Mo 4d and O 2p states account for the conduction band. As reported, the well-dispersed Bi 6s orbital facilitates the mobilities of photogenerated carriers and narrows the bandgap [10, 49]. The band gap of pure Bi_2MoO_6 was calculated as approximately 1.91 eV. The simulated result (1.91 eV) is lower than the detected result (2.64 eV), which is due to the well-known limitation of GGA [50]. Both of these results suggest that pure Bi_2MoO_6 is visible light-responsive. When Pd^{2+} doped in the composites, a doped-band edge (Pd 4d) can be observed between the valence band and conduction band of Bi_2MoO_6. It resulted in the up-lift of valence band and narrow the band gap. Furthermore, after loading Pd on the surface of Bi_2MoO_6, a colour change from white to grey was observed, and photoabsorption in the visible light region was greatly improved. The red shift of absorption edge observed in Fig. B.6 with increasing Pd content may be attributed to the Pd^{2+} doping. Pd^{2+} in the Bi_2MoO_6 lattice possibly up-lifted the position of valence band [27]. The further improvement of absorption in the visible light range may be attributed to the surface plasmon resonance effect of Pd nanoparticles on the surface [20].

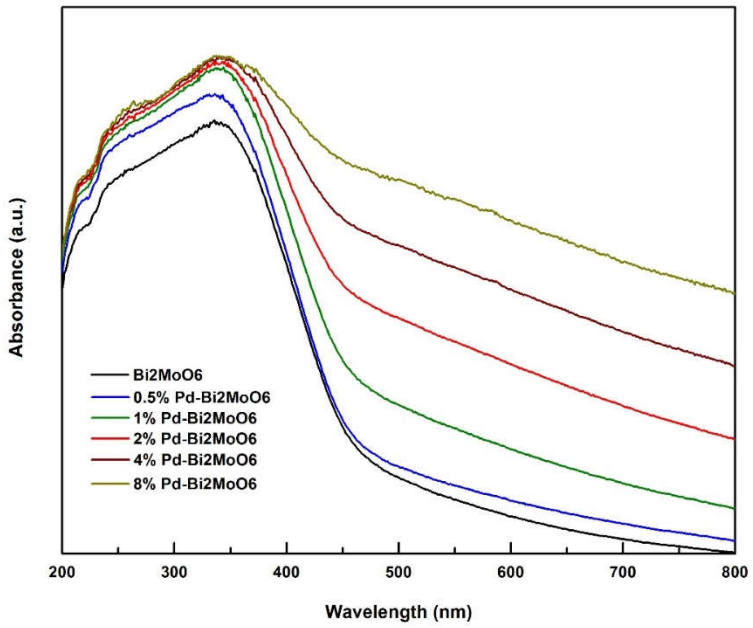


Figure B.6 DRS of pure Bi_2MoO_6 and Pd-Bi_2MoO_6 composites.

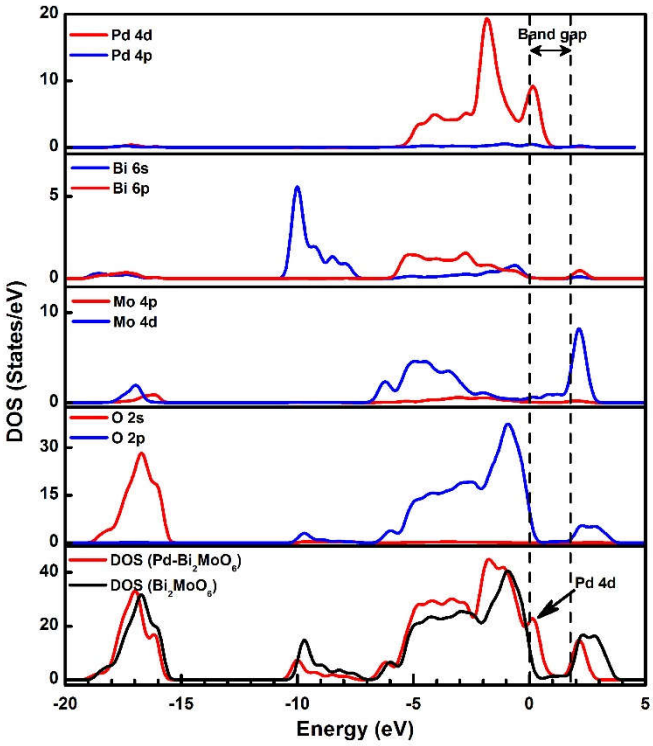


Figure B.7 Total and partial densities of states (DOS) of relaxed Bi_2MoO_6 and Pd-Bi_2MoO_6.

B.3.5 Photocatalytic activity test

Photocatalytic activity tests of prepared samples were performed by degrading the colourless organic model compound, phenol, under visible light irradiation. Relative concentrations of phenol as a function of time are plotted in Fig. B.8. It can be seen that no more than 10% of phenol was removed over 300 min in the presence of pure Bi_2MoO_6 under visible light irradiation. This may be due to the high recombination rate of photogenerated electrons and holes when pure Bi_2MoO_6 is implemented in the system. After doping the surface of Bi_2MoO_6 with Pd, a significant improvement was observed, dependent on the quantity of Pd. Specifically, the relative removal efficiencies (c/c_o) of systems with 0.5, 1.0, 2.0, 4.0, and 8.0% Pd-Bi_2MoO_6 were approximately 7.6%, 13.5%, 22.2%, 18.8%, and 12.5% respectively after 30 min of phenol degradation. The highest photocatalytic activity of the Pd-Bi_2MoO_6 composites under visible light irradiation was observed with 2.0% Pd-Bi_2MoO_6. An increase in Pd content from 0.5% to 2.0% resulted in the improvement of photocatalytic activity, primarily because the recombination rate of photogenerated electrons and holes gradually reduces and photoabsorption in the visible light region gradually improves with increasing Pd content. However, when the Pd content was above 2.0%, a decrease in the photocatalytic activities of composites could be observed. This is thought to be caused by an effective decrease in surface area, which results in a decrease in the number of reactive sites. Additionally, the presence of Pd on the surface of Bi_2MoO_6 may introduce new recombination sites for electrons and holes [51, 52], which would therefore contribute to a reduction in photocatalytic activity. As a result, Bi_2MoO_6 doped with 2.0% Pd exhibited the best performance with regards to the photocatalytic degradation of phenol under visible light irradiation.

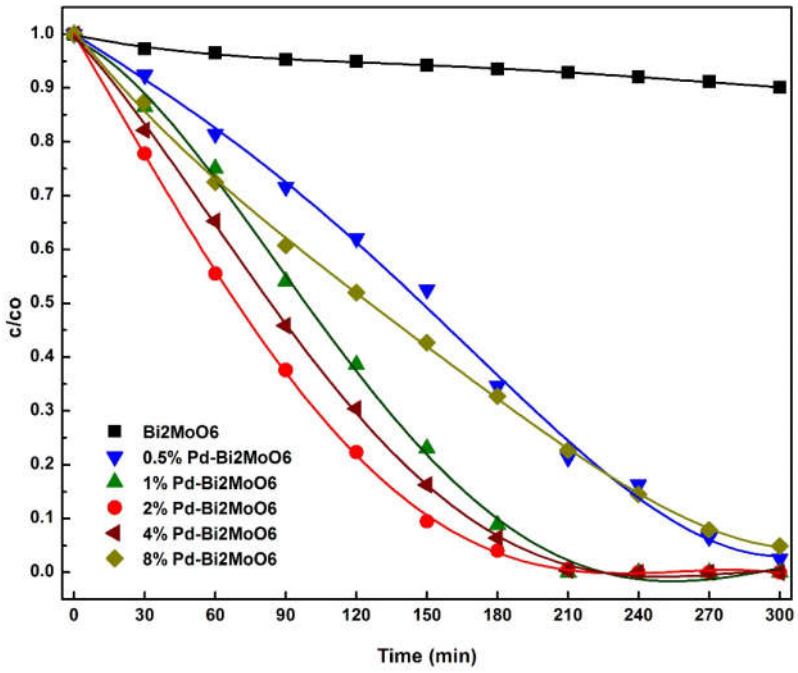


Figure B.8 Photocatalytic degradation of phenol in the presence of pure Bi_2MoO_6 and Pd-Bi_2MoO_6 composites.

The photocatalytic kinetics of phenol degradation may be analyzed using the Langmuir-Hinshelwood (L-H) model (Equation 2). The initial concentration of phenol in this work was set to approximately 10 mg/L (~1 × 10^{-4} mol/L), so (1+*Kc*) may be assumed to be equal to 1. Equation 2 may be expressed in the form of Equation 3, where k' is the pseudo first-order rate constant. Integration of Equation 3 then results in Equation 4.

$$r = -\frac{dc}{dt} = k\theta = \frac{kKc}{1+Kc} \qquad \text{Equation 2}$$

$$-\frac{dc}{dt} = kKc = k'c \qquad \text{Equation 3}$$

$$\ln(\frac{c_o}{c_t}) = k't \qquad \text{Equation 4}$$

where r, c, t, k, θ, K, and k' represent reaction rate, concentration of phenol (c_o: initial concentration; c_t: concentration at time t), time, reaction rate constant, ratio of adsorbed phenol, and adsorption constant respectively. By plotting $\ln(c_o/c_t)$ as a function of time (t),

the slope of the fitted line may be obtained, which is equal to the pseudo first-order rate constant (*k'*). The photocatalytic kinetic analysis of systems with pure Bi_2MoO_6 and Pd-Bi_2MoO_6 composites are illustrated in Fig. B.9. The slopes of fitted lines are summarized in Table B.1. The excellent linearity of each line of best fit indicates that the photocatalytic degradation of phenol under visible light irradiation in the presences of pure Bi_2MoO_6 as well as Pd-Bi_2MoO_6 composites follows Pseudo-first order kinetics. The process carried out with pure Bi_2MoO_6 as the photocatalyst exhibited the lowest rate constant, while loading of Pd onto Bi_2MoO_6 increased the constant up to 23.0 times that of pure Bi_2MoO_6 at 2% Pd. These results confirm that the presence of Pd in the composite significantly increases photocatalytic activity with regards to the degradation of organic pollutants.

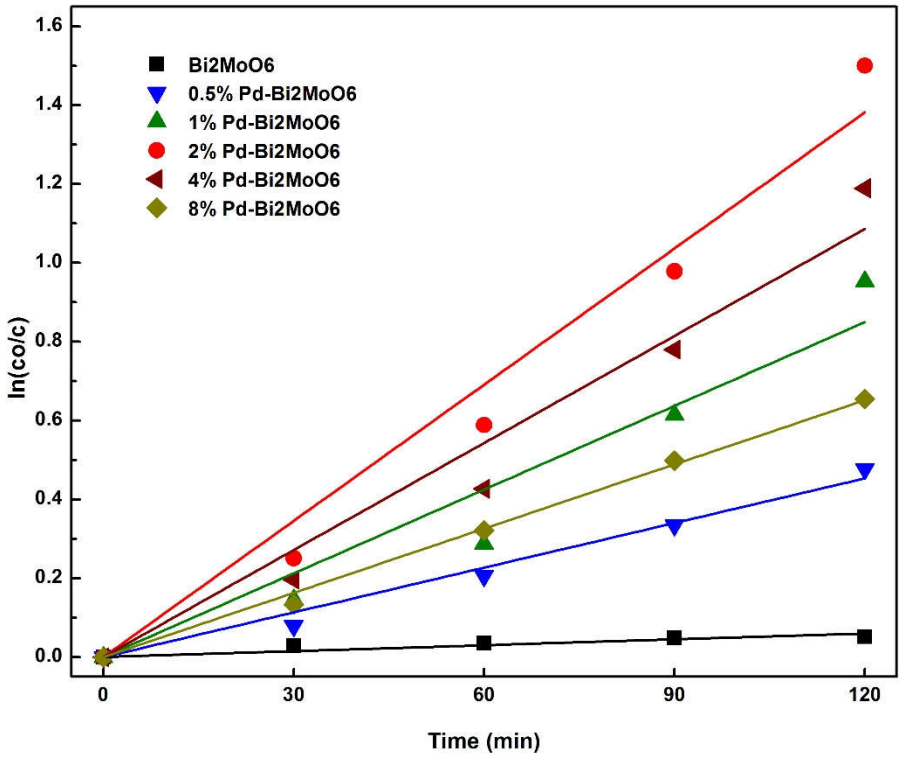


Figure B.9 Photocatalytic kinetic analysis of processes in the presence of pure Bi_2MoO_6 and Pd-Bi_2MoO_6 composites.

Table B.1 Pseudo first-order kinetic constants of systems with Bi_2MoO_6 doped with different quantities of Pd.

Pd doping quantity (%)	0	0.5%	1%	2%	4%	8%
k' (10^{-3} min^{-1})	0.50	3.78	7.08	11.52	9.05	5.43
R^2	0.953	0.993	0.969	0.987	0.982	0.998

B.3.6 Pathways for the photocatalytic degradation of phenol

To explore pathways for the photocatalytic degradation of phenol in the presence of Pd-Bi_2MoO_6 under visible light irradiation, possible intermediates [53, 54] including hydroquinone, catechol and benzoquinone were measured, and their concentrations during the degradation process are illustrated in Fig. B.10. It was found that phenol, with an initial concentration of 11.2 mg/L, was completely removed in 210 min. Intermediates including hydroquinone, catechol and benzoquinone were also detected at low concentrations. These smaller concentrations indicate that the direct consumption of phenol is the rate-determining step. Hydroquinone was found to have the highest concentration among these intermediates, followed by catechol and negligibly, benzoquinone. Almost all of the intermediates were removed over 300 min, and the final products of the overall reactions were assumedly CO_2 and H_2O. Possible pathways for the degradation of phenol in the presence of Pd-Bi_2MoO_6 under visible light irradiation were proposed in Fig. B.11. Phenol is first oxidized to a dihydroxyl cyclohexadienyl radical due to the effects of photogenerated oxidative species. Hydroquinone, catechol and benzoquinone were then possibly generated in the presence of dissolved O_2. As these compounds are more easily degraded than phenol, the aromatic rings may be destroyed to produce carboxylic acids, and ultimately, CO_2 and H_2O.

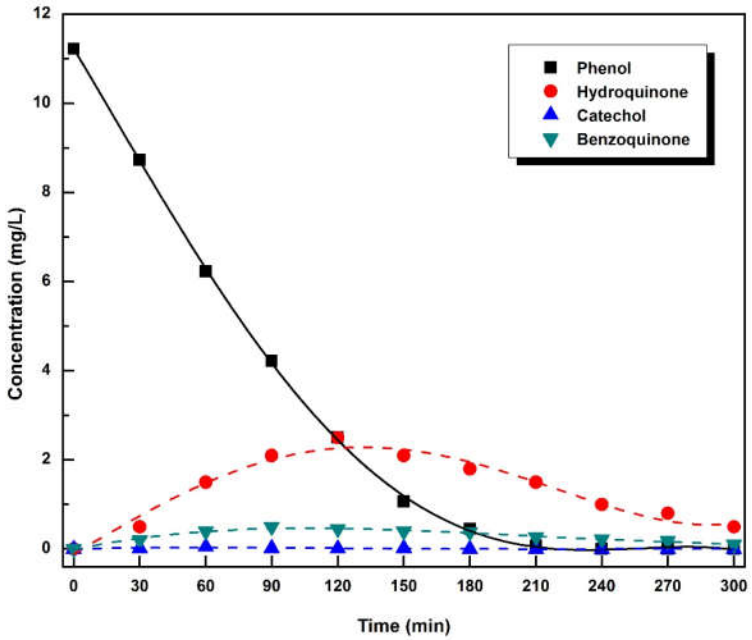


Figure B.10 Concentrations of phenol, hydroquinone, catechol and benzoquinone during the degradation process in the presence of 2% Pd-Bi_2MoO_6 under visible light irradiation.

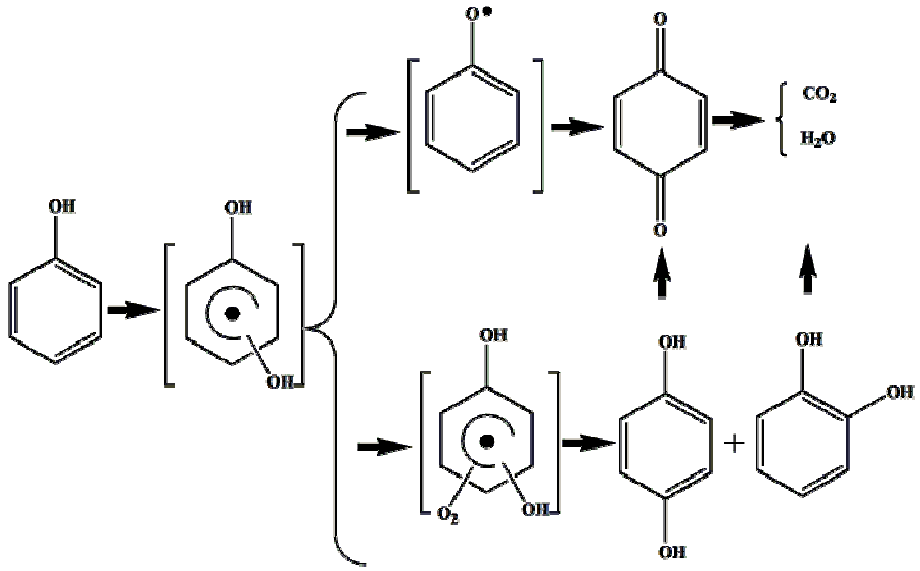


Figure B.11 Possible pathways for the photocatalytic degradation of phenol in the presence of Pd-Bi_2MoO_6 under visible light irradiation.

B.3.7 Reusability

Reusability is an important parameter to evaluate a photocatalyst from an economic perspective. The 2% Pd-Bi_2MoO_6 sample was investigated by recycling it for four runs,

and the removal efficiencies for phenol over each run are shown in Fig. B.12. After four runs, the photocatalyst still exhibited an excellent performance with regards to the degradation of phenol. A slight decrease was observed in the removal efficiency at the initial 30 min (23.2% in the first run and 17.2% in the fourth run), which may have resulted from the loss of catalyst mass between two runs. In addition, the adsorption of refractory intermediates such as organic acids on the surface of the photocatalyst decreases the number of exposed reactive sites, resulting in a reduction in the removal efficiency for phenol. Despite this slight decrease in removal efficiency, the prepared photocatalysts possess a high reusability and stability in the removal of organic pollutants from wastewater.

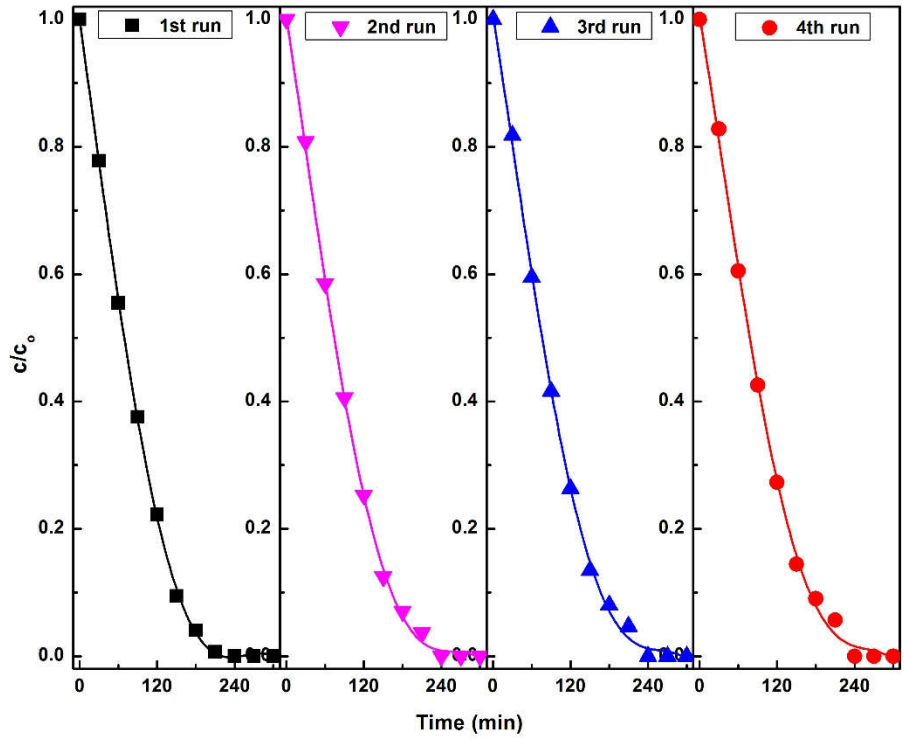


Figure B.12 Removal efficiencies of phenol with recycled 2% Pd-Bi_2MoO_6.

B.3.8 Mechanisms

To explore the recombination rate of photogenerated electrons and holes under visible light irradiation, electrochemical impedance spectroscopy (EIS) was employed, and the EIS Nyquist plots for pure Bi_2MoO_6 and 2%Pd-Bi_2MoO_6 were shown in Fig. B.13. Only one semicircle was found for each plot, indicating the photocatalytic process in the presence of

prepared sample was a simple electrode reaction and electrons transfer on the electrode, the rate may be determined by the recombination rate of photogenerated electron/hole pairs [55, 56]. The fitted values for the equivalent circuits were obtained and shown in Table B.2. It can found the resistance of electrons on the electrode (R_{ct}) was significantly decreased from 163.5 to 1.148 kΩ, which suggests the recombination rate of photogenerated electron and hole was greatly supressed. Therefore, the photocatalytic activity of Bi_2MoO_6 were significantly improved in the photocatalytic removal of organic pollutants after doping Pd.

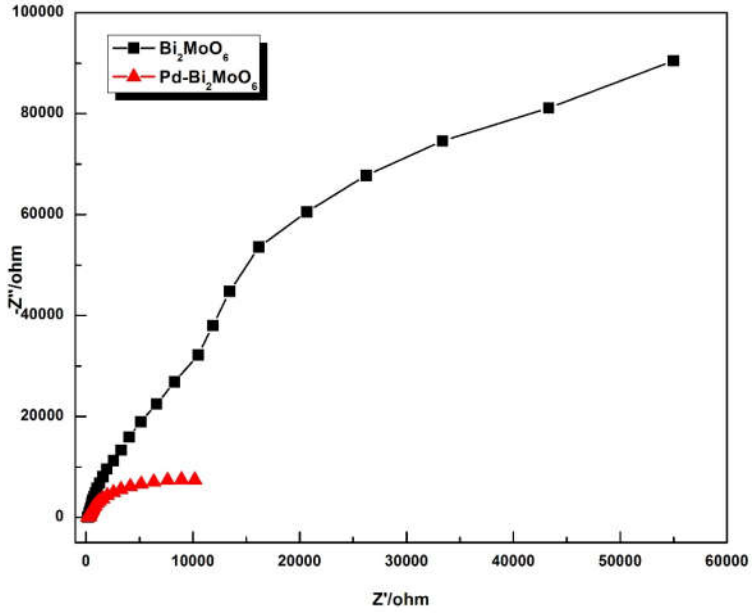
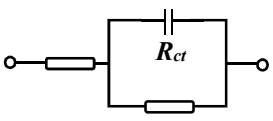


Figure B.13 EIS Nyquist plots of the Bi_2MoO_6 and 2% Pd-Bi_2MoO_6 photocatalysts.

Table B.2 Fitting results for equivalent circuits of different prepared samples.

Samples	R_s (Ω)	R_{ct} (kΩ)	*CPE* (μf)	Equivalent circuits
Bi_2MoO_6	172.2	163.5	34.51	
2%Pd-Bi_2MoO_6	191.1	1.148	30.51	

Note: R_s: resistance of solution; R_{ct}: resistance of electron transfer on the electrode; CPE: constant phase element which can be regarded as a capacity of double layer.

The mechanism of Pd-Bi_2MoO_6 applied in the photocatalysis was proposed in Fig. B.14. Bi_2MoO_6 is a visible light photocatalyst, absorbing wavelengths shorter than 470 nm.

Electrons on the valence band of Bi_2MoO_6 may be activated and transfer to the conduction band under visible light irradiation. Oxidative species including free radicals (•OH, $•O_2$) and holes may then form and decompose most organic compounds. The photogenerated electrons may also recombine with holes, which reduces the photocatalytic activity. By introducing Pd on the surface of Bi_2MoO_6, Pd nanoparticles can act as electron traps, improving the separation rate of electron-hole pairs. Additionally, by doping noble metal nanoparticles on the surface of a composite, these metals may also be activated by visible light owing to the surface plasmon resonance effect [20, 21, 57]. It was reported that SPR peaks of Pd nanostructures can be tuned from 410 to 870 nm [25, 26]. From this respect, doped Pd nanoparticles may also absorb visible light energy to produce electrons, which may transfer to the conduction band of Bi_2MoO_6 and further enhance the visible light-driven photocatalytic activity. Pd^{2+} doped band level within the band gap of Bi_2MoO_6 may narrow the band gap of the composites, resulting in the improvement in the utilization of visible light irradiation. Furthermore, Cl^- on the surface of Bi_2MoO_6 may be oxidized to Cl^0, which is itself a strong oxidizing agent that may be capable of oxidizing phenol and returning to its reduced, anionic state (Cl^-) [58]. The series of integrated effects results in an enhanced photocatalytic activity for the removal of phenol under visible light irradiation after the introduction of Pd on the surface of Bi_2MoO_6.

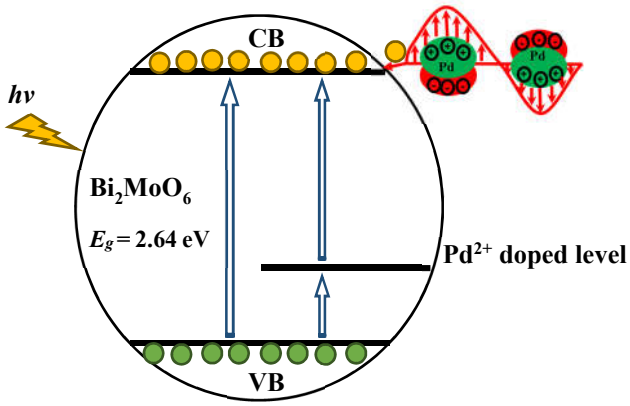


Figure B.14 Photocatalytic mechanism of Pd-Bi_2MoO_6 composite under visible light.

B.4 Conclusions

A Pd-doped Bi_2MoO_6 composite was successfully prepared and investigated in this work. It was found that palladium was present in the forms of metallic Pd^0 and Pd^{2+}. By

introducing Pd, the crystal structure of Bi_2MoO_6 was not influenced, and the photocatalytic activity in the removal of organic pollutants (phenol) was significantly promoted. Optimal performance in the degradation of phenol was observed when the quantity of Pd in the composite reached 2%. A pseudo first-order reaction model was also suitably applied. A mechanism for the degradation of phenol in a stepwise fashion was explored. A mechanism accounting for the significant enhancement by means of introducing Pd on the surface of Bi_2MoO_6 was also proposed, integrating the reduction of electron-hole recombination rate, the surface plamon resonance of Pd nanoparticles, and the generation of Cl^0.

References

1. Akira Fujishima and Kenichi Honda, "Electrochemical photolysis of water at a semiconductor electrode," *nature*, vol. 238, pp. 37-38, 1972.

2. Akihiko Kudo and Yugo Miseki, "Heterogeneous photocatalyst materials for water splitting," *Chemical Society Reviews*, vol. 38, no. 1, pp. 253-278, 2009.

3. Masao Kaneko and Ichiro Okura, "Photocatalysis science and technology," *Kodansha Springer*, 2002.

4. Cathy McCullagh, Nathan Skillen, Morgan Adams and Peter KJ Robertson, "Photocatalytic reactors for environmental remediation: a review," *Journal of Chemical Technology and Biotechnology*, vol. 86, no. 8, pp. 1002-1017, 2011.

5. Yanhui Shi, Shouhua Feng and Changsheng Cao, "Hydrothermal synthesis and characterization of Bi2MoO6 and Bi2WO6," *Materials Letters*, vol. 44, no. 3–4, pp. 215-218, 2000.

6. Mingyun Guan, Xianghong He, Tongming Shang, Jianhua Sun and Quanfa Zhou, "Hydrothermal synthesis of ultrathin Bi2MO6 (M=W, Mo) nanoplates as new host substances for red-emitting europium ion," *Progress in Natural Science: Materials International*, vol. 22, no. 4, pp. 334-340, 2012.

7. Wen Lai Huang and Qingshan Zhu, "Electronic structures of relaxed BiOX (X = F, Cl, Br, I) photocatalysts," *Computational Materials Science*, vol. 43, no. 4, pp. 1101-1108, 2008.

8. Hefeng Cheng, Baibiao Huang and Ying Dai, "Engineering BiOX (X = Cl, Br, I) nanostructures for highly efficient photocatalytic applications," *Nanoscale*, vol. 6, no. 4, pp. 2009-2026, 2014.

9. Xiangchao Meng and Zisheng Zhang, "Bismuth-based Photocatalytic Semiconductors: Introduction, Challenges and Possible Approaches," *Journal of Molecular Catalysis A: Chemical*, vol. 423, pp. 533-549, 2016.

10. Huizhong An, Yi Du, Tianmin Wang, Cong Wang, Weichang Hao and Junying Zhang, "Photocatalytic properties of BiOX (X = Cl, Br, and I)," *Rare Metals*, vol. 27, no. 3, pp. 243-250, 2008.

11. Guohui Tian, Yajie Chen, Wei Zhou, Kai Pan, Youzhen Dong, Chungui Tian and Honggang Fu, "Facile solvothermal synthesis of hierarchical flower-like Bi2MoO6 hollow spheres as high performance visible-light driven photocatalysts," *Journal of Materials Chemistry*, vol. 21, no. 3, pp. 887-892, 2011.

12. Liwu Zhang, Tongguang Xu, Xu Zhao and Yongfa Zhu, "Controllable synthesis of Bi2MoO6 and effect of morphology and variation in local structure on photocatalytic activities," *Applied Catalysis B: Environmental*, vol. 98, no. 3–4, pp. 138-146, 2010.

13. Jinhong Bi, Ling Wu, Jie Li, Zhaohui Li, Xuxu Wang and Xianzhi Fu, "Simple solvothermal routes to synthesize nanocrystalline Bi2MoO6 photocatalysts with different morphologies," *Acta Materialia*, vol. 55, no. 14, pp. 4699-4705, 2007.

14. Wenzong Yin, Wenzhong Wang and Songmei Sun, "Photocatalytic degradation of phenol over cage-like Bi2MoO6 hollow spheres under visible-light irradiation," *Catalysis Communications*, vol. 11, no. 7, pp. 647-650, 2010.

15. Mingyi Zhang, Changlu Shao, Peng Zhang, Chunyan Su, Xin Zhang, Pingping Liang, Yangyang Sun and Yichun Liu, "Bi2MoO6 microtubes: Controlled fabrication by using electrospun polyacrylonitrile microfibers as template and their enhanced visible light photocatalytic activity," *Journal of Hazardous Materials*, vol. 225–226, pp. 155-163, 2012.

16. Mingyi Zhang, Changlu Shao, Jingbo Mu, Zhenyi Zhang, Zengcai Guo, Peng Zhang and Yichun Liu, "One-dimensional Bi2MoO6/TiO2 hierarchical heterostructures with enhanced photocatalytic activity," *CrystEngComm*, vol. 14, no. 2, pp. 605-612, 2012.

17. Peifang Wang, Yanhui Ao, Chao Wang, Jun Hou and Jin Qian, "A one-pot method for the preparation of graphene–Bi2MoO6 hybrid photocatalysts that are responsive to visible-light and have excellent photocatalytic activity in the degradation of organic pollutants," *Carbon*, vol. 50, no. 14, pp. 5256-5264, 2012.

18. Guohui Tian, Yajie Chen, Xiangying Meng, Juan Zhou, Wei Zhou, Kai Pan, Chungui Tian, Zhiyu Ren and Honggang Fu, "Hierarchical Composite of Ag/AgBr Nanoparticles Supported on Bi2MoO6 Hollow Spheres for Enhanced Visible-Light Photocatalytic Performance," *ChemPlusChem*, vol. 78, no. 1, pp. 117-123, 2013.

19. Tengfei Zhou, Juncheng Hu and Jinlin Li, "Er3+ doped bismuth molybdate nanosheets with exposed {0 1 0} facets and enhanced photocatalytic performance," *Applied Catalysis B: Environmental*, vol. 110, pp. 221-230, 2011.

20. Suljo Linic, Phillip Christopher and David B. Ingram, "Plasmonic-metal nanostructures for efficient conversion of solar to chemical energy," *Nature Materials*, vol. 10, no. 12, pp. 911-921, 2011.

21. Peng Wang, Baibiao Huang, Xiaoyan Qin, Xiaoyang Zhang, Ying Dai, Jiyong Wei and Myung-Hwan Whangbo, "Ag@AgCl: A Highly Efficient and Stable Photocatalyst Active under Visible Light," *Angewandte Chemie International Edition*, vol. 47, no. 41, pp. 7931-7933, 2008.

22. Peng Wang, Baibiao Huang, Zaizhu Lou, Xiaoyang Zhang, Xiaoyan Qin, Ying Dai, Zhaoke Zheng and Xiaoning Wang, "Synthesis of highly efficient Ag@ AgCl plasmonic photocatalysts with various structures," *Chemistry-a European Journal*, vol. 16, no. 2, pp. 538-544, 2010.

23. Bo Yuan, Changhua Wang, Ying Qi, Xiaolong Song, Kai Mu, Peng Guo, Lingtao Meng and Hongmin Xi, "Decorating hierarchical Bi2MoO6 microspheres with uniformly dispersed ultrafine Ag nanoparticles by an in situ reduction process for enhanced visible light-induced photocatalysis," *Colloids and Surfaces A: Physicochemical and Engineering Aspects*, vol. 425, pp. 99-107, 2013.

24. Jing Zhang, Chenggang Niu, Ji Ke, Laifeng Zhou and Guangming Zeng, "Ag/AgCl/Bi_2MoO_6 composite nanosheets: A plasmonic Z-scheme visible light

photocatalyst," *Catalysis Communications*, vol. 59, pp. 30-34, 2015.

25. Yujie Xiong, Benjamin Wiley, Jingyi Chen, Zhi-Yuan Li, Yadong Yin and Younan Xia, "Corrosion-Based Synthesis of Single-Crystal Pd Nanoboxes and Nanocages and Their Surface Plasmon Properties," *Angewandte Chemie International Edition*, vol. 44, no. 48, pp. 7913-7917, 2005.

26. Yujie Xiong, Jingyi Chen, Benjamin Wiley, Younan Xia, Yadong Yin and Zhi-Yuan Li, "Size-Dependence of Surface Plasmon Resonance and Oxidation for Pd Nanocubes Synthesized via a Seed Etching Process," *Nano Letters*, vol. 5, no. 7, pp. 1237-1242, 2005.

27. Fan Dong, Peidong Li, Junbo Zhong, Xiaoying Liu, Yuxin Zhang, Wanglai Cen and Hongwei Huang, "Simultaneous Pd^{2+} doping and Pd metal deposition on $(BiO)_2CO_3$ microspheres for enhanced and stable visible light photocatalysis," *Applied Catalysis A: General*, vol. 510, pp. 161-170, 2016.

28. Zilin Ni, Fan Dong, Hongwei Huang and Yuxin Zhang, "New insights into how Pd nanoparticles influence the photocatalytic oxidation and reduction ability of g-C_3N_4 nanosheets," *Catalysis Science & Technology*, 2016.

29. Walter Kohn and Lu Jeu Sham, "Self-consistent equations including exchange and correlation effects," *Physical Review*, vol. 140, no. 4A, pp. A1133, 1965.

30. Giannozzi Paolo, Baroni Stefano, Bonini Nicola, Calandra Matteo, Car Roberto, Cavazzoni Carlo, Ceresoli Davide, L. Chiarotti Guido, Cococcioni Matteo, Dabo Ismaila, Corso Andrea Dal, Gironcoli Stefano de, Fabris Stefano, Fratesi Guido, Gebauer Ralph, Gerstmann Uwe, Gougoussis Christos, Kokalj Anton, Lazzeri Michele, Martin-Samos Layla, Marzari Nicola, Mauri Francesco, Mazzarello Riccardo, Paolini Stefano, Pasquarello Alfredo, Paulatto Lorenzo, Sbraccia Carlo, Scandolo Sandro, Sclauzero Gabriele, P. Seitsonen Ari, Smogunov Alexander, Umari Paolo and M. Wentzcovitch Renata, "QUANTUM ESPRESSO: a modular and open-source software project for quantum simulations of materials," *Journal of Physics: Condensed Matter*, vol. 21, no. 39, pp. 395502, 2009.

31. F Pertlik and J Zemann, "Neubestimmung der Kristallstruktur des Köchlinits," *Fortschr. Miner. Beih*, vol. 60, pp. 162-163, 1982.

32. Xiaolong Li, Tianmei Xuan, Guilin Yin, Zhenyuan Gao, Kunfeng Zhao, Peng Yan and Dannong He, "Highly sensitive amperometric CO sensor using nanocomposite C-loaded PdCl2–CuCl2 as sensing electrode materials," *Journal of Alloys and Compounds*, vol. 645, pp. 553-558, 2015.

33. HE Swanson, "US Natl Bur. Stand. 1," Ed., Circular, 1953.

34. Jessica Torres, C. C. Perry, Stephen J. Bransfield and D. Howard Fairbrother, "Low-Temperature Oxidation of Nitrided Iron Surfaces," *The Journal of Physical Chemistry B*, vol. 107, no. 23, pp. 5558-5567, 2003.

35. Jan Wielant, Tom Hauffman, Orlin Blajiev, René Hausbrand and Herman Terryn, "Influence of the Iron Oxide Acid−Base Properties on the Chemisorption of Model Epoxy Compounds Studied by XPS," *The Journal of Physical Chemistry C*, vol. 111, no. 35, pp. 13177-13184, 2007.

36. K. R. Priolkar, Parthasarathi Bera, P. R. Sarode, M. S. Hegde, S. Emura, R. Kumashiro and N. P. Lalla, "Formation of Ce1-xPdxO2-δ Solid Solution in Combustion-Synthesized Pd/CeO2 Catalyst: XRD, XPS, and EXAFS Investigation," *Chemistry of Materials*, vol. 14, no. 5, pp. 2120-2128, 2002.

37. Gobind Kumar, J. R. Blackburn, R. G. Albridge, W. E. Moddeman and M. M. Jones, "Photoelectron spectroscopy of coordination compounds. II. Palladium complexes," *Inorganic Chemistry*, vol. 11, no. 2, pp. 296-300, 1972.

38. CD Wagner and GE Muilenberg, *Handbook of X-ray photoelectron spectroscopy*, Perkin-Elmer, 1979.

39. J. H. Scofield, "Hartree-Slater subshell photoionization cross-sections at 1254 and 1487 eV," *Journal of Electron Spectroscopy and Related Phenomena*, vol. 8, no. 2, pp. 129-137, 1976.

40. David R. Penn, "Quantitative chemical analysis by ESCA," *Journal of Electron Spectroscopy and Related Phenomena*, vol. 9, no. 1, pp. 29-40, 1976.

41. R. D. Seals, Robert Alexander, Larry T. Taylor and John G. Dillard, "Core electron binding energy study of group IIb-VIIa compounds," *Inorganic Chemistry*, vol. 12, no. 10, pp. 2485-2487, 1973.

42. HongHua Li, ChaoYu Liu, KunWei Li and Hao Wang, "Preparation, characterization and photocatalytic properties of nanoplate Bi2MoO6 catalysts," *Journal of Materials Science*, vol. 43, no. 22, pp. 7026-7034, 2008.

43. S. R. G. Carrazán, C. Martin, V. Rives and R. Vidal, "An FT-IR spectroscopy study of the adsorption and oxidation of propene on multiphase Bi, Mo and Co catalysts," *Spectrochimica Acta Part A: Molecular and Biomolecular Spectroscopy*, vol. 52, no. 9, pp. 1107-1118, 1996.

44. F. Trifirò, H. Hoser and R. D. Scarle, "Relationship between structure and activity of mixed oxides as oxidation catalysts: I. Preparation and solid state reactions of Bi-molybdates," *Journal of Catalysis*, vol. 25, no. 1, pp. 12-24, 1972.

45. M. A. Hasan, M. I. Zaki and L. Pasupulety, "Oxide-catalyzed conversion of acetic acid into acetone: an FTIR spectroscopic investigation," *Applied Catalysis A: General*, vol. 243, no. 1, pp. 81-92, 2003.

46. Li-Fen Liao, Chen-Fu Lien and Jong-Liang Lin, "FTIR study of adsorption and photoreactions of acetic acid on TiO2," *Physical Chemistry Chemical Physics*, vol. 3, no. 17, pp. 3831-3837, 2001.

47. Peter W Voorhees, "The theory of Ostwald ripening," *Journal of Statistical Physics*, vol. 38, no. 1-2, pp. 231-252, 1985.

48. Hua Gui Yang and Hua Chun Zeng, "Preparation of Hollow Anatase TiO_2 Nanospheres via Ostwald Ripening," *The Journal of Physical Chemistry B*, vol. 108, no. 11, pp. 3492-3495, 2004.

49. Xiangchao Meng and Zisheng Zhang, "Facile synthesis of BiOBr/Bi_2WO_6 heterojunction semiconductors with high visible-light-driven photocatalytic activity," *Journal of Photochemistry and Photobiology A: Chemistry*, vol. 310, no. 0, pp. 33-44, 2015.

50. Kangrong Lai, Wei Wei, Ying Dai, Ruiqin Zhang and Baibiao Huang, "DFT calculations on structural and electronic properties of Bi_2MO_6 (M = Cr, Mo, W)," *Rare Metals*, vol. 30, no. 1, pp. 166-172, 2011.

51. Fang Duan, Yan Zheng and MingQing Chen, "Flowerlike PtCl4/Bi2WO6 composite photocatalyst with enhanced visible-light-induced photocatalytic activity," *Applied Surface*

Science, vol. 257, no. 6, pp. 1972-1978, 2011.

52. Changlin Yu, Fangfang Cao, Gao Li, Rongfu Wei, Jimmy C. Yu, Rongchao Jin, Qizhe Fan and Chunying Wang, "Novel noble metal (Rh, Pd, Pt)/BiOX(Cl, Br, I) composite photocatalysts with enhanced photocatalytic performance in dye degradation," *Separation and Purification Technology*, vol. 120, pp. 110-122, 2013.

53. Xiao-yan Li, Yu-hong Cui, Yu-jie Feng, Zhao-ming Xie and Ji-Dong Gu, "Reaction pathways and mechanisms of the electrochemical degradation of phenol on different electrodes," *Water Research*, vol. 39, no. 10, pp. 1972-1981, 2005.

54. Chunde Wu, Xinhui Liu, Dongbin Wei, Jinchu Fan and Liansheng Wang, "Photosonochemical degradation of Phenol in water," *Water Research*, vol. 35, no. 16, pp. 3927-3933, 2001.

55. Janet M. Kesselman, Gary A. Shreve, Michael R. Hoffmann and Nathan S. Lewis, "Flux-Matching Conditions at TiO_2 Photoelectrodes: Is Interfacial Electron Transfer to O_2 Rate-Limiting in the TiO_2-Catalyzed Photochemical Degradation of Organics?," *The Journal of Physical Chemistry*, vol. 98, no. 50, pp. 13385-13395, 1994.

56. Baifu Xin, Zhiyu Ren, Haiyuan Hu, Xiangyu Zhang, Chunlei Dong, Keying Shi, Liqiang Jing and Honggang Fu, "Photocatalytic activity and interfacial carrier transfer of Ag–TiO_2 nanoparticle films," *Applied Surface Science*, vol. 252, no. 5, pp. 2050-2055, 2005.

57. Jiabin Zhou, Ya Cheng and Jiaguo Yu, "Preparation and characterization of visible-light-driven plasmonic photocatalyst Ag/AgCl/TiO2 nanocomposite thin films," *Journal of Photochemistry and Photobiology A: Chemistry*, vol. 223, no. 2–3, pp. 82-87, 2011.

58. Joanne Gamage McEvoy, Wenquan Cui and Zisheng Zhang, "Synthesis and characterization of Ag/AgCl–activated carbon composites for enhanced visible light photocatalysis," *Applied Catalysis B: Environmental*, vol. 144, no. 0, pp. 702-712, 2014.

Appendix C Highly efficient degradation of phenol over a Pd-BiOBr Mott-Schottky plasmonic photocatalyst

Xiangchao Meng, Zizhen Li and Zisheng Zhang

Materials Research Bulletin 99 (2018), 471-478

Abstract

Surface plasmonic resonance effect has been widely applied to improve oxidation activity of a photocatalyst under visible light irradiation. Palladium particles were successfully prepared, and electrostatically assembled with BiOBr in this work. Due to the differences in work function between palladium and BiOBr, a Mott-Schottky junction may be established. This junction is in favor of the separation of photogenerated charge carriers. Also, Pd particles on the surface may absorb visible-light photons and produce extra electrons to participate in the photocatalysis. The great improvement in the photocatalytic oxidation of phenol confirms the synergetic effect (SPR and Mott-Schottky junction). This work may serve as a solid evidence to confirm that surface-loaded palladium particles are capable of improving photocatalytic activity, and that electrostatic assembly may be an effective approach to load metal particles onto a surface.

C.1 Introduction

Photocatalysis has been extensively studied and applied in various areas, primarily in H_2 evolution via water splitting and organics decomposition [1-4]. The photocatalytic oxidation process, as one of the advanced oxidation processes (AOPs), exhibited a significant promise in water treatment. The most widely used photocatalyst is TiO_2 [5]. However, some hindrances emerged despite its wide application. The intrinsic drawbacks

for TiO_2 is the band gap which is too wide to be visible light-responsive. Approaches to overcome this mainly include modification of TiO_2 and synthesis of novel materials with suitable band gaps.

Recently developed bismuth-based semiconductors have attracted researchers' attentions [6-13]. The electronic structure of bismuth-based semiconductors gives them a suitable band gap for visible-light response and a well-dispersed valence band composed of hybrid orbitals of Bi*6s* and O*2p*, making them a promising candidate when compared to other metal oxide semiconductors. Moreover, bismuth-based semiconductors are easy to prepare and their morphologies are adjustable by controlling the preparation conditions. BiOX (X = Cl, Br or I), as one of the bismuth-based semiconductors, exhibited outstanding optical properties and electrical properties [6, 14-16]. All BiOX compounds are crystallized in tetragonal matlockite with layered structures. The layered structures are composed of $[Bi_2O_2]$ slabs interleaved with double halogen atom slabs along the [001] direction. It should be noted band gaps among BiOX compounds are narrower with increasing atom number of halogen. More specifically, BiOCl with a band gap value of 3.2 - 3.4 eV [17] is visible light irresponsive; BiOBr and BiOI with narrower band gaps are visible light responsive. However, BiOI with a band gap of 1.8 eV exhibited high recombination of photogenerated charge carriers, resulting in weakened photocatalytic oxidation activity [18]. As a result, BiOBr with a suitable band gap has been extensively applied, and exhibited excellent visible light-induced photocatalytic activity. However, the high recombination rate of photogenerated charge carriers for BiOBr hinders its wide application. Application strategies mainly include metal loadings and establishment of heterostructures [6-8, 19]. Recently, the surface plasmonic resonance (SPR) effect was implemented to effectively improve the photocatalytic activity [20-25]. Because of the SPR effect, more visible-light photons may be absorbed and generate more hot electrons [26-28]. Silver nanoparticles were successfully loaded on the surface of BiOBr to also improve its photocatalytic oxidation activity [29-31]. Palladium-modified BiOBr was also reported via a facile one-pot process [32, 33]. The drawbacks of a one-pot process to prepare Pd-BiOBr are: 1) most of the palladium is located in the bulk and is difficult to activate by illumination, and 2) divalent palladium may not be completely reduced to Pd metallic particles. Palladium particles modified BiOBr were rarely reported.

In this work, an electrostatic assembly method was applied to load palladium particles on the surface of BiOBr. The activity of prepared samples was compared with reported works, and exhibited advances in the removal of organics from waste water. The difference in work functions between Pd and BiOBr indicates a Mott-Schottky junction may be established to facilitate the separation of photogenerated charge carriers. The synergetic effects (SPR and Mott-Schottky junction) contributed to the enhancement in photocatalytic activity of Pd-BiOBr with respect to the degradation of organics in water under visible light irradiation.

C.2 Experimental

C.2.1 Preparation of palladium particles

Pd particles were prepared using a modified method as reported previously [34, 35]. Typically, 105 mg of poly vinyl pyrrolidone (PVP), 60 mg of L-ascorbic acid (AA) and 500 mg of KBr were mixed in 8.0 mL distilled deionized water (DDW). The mixture was preheated at 80°C for 10 min under magnetic stirring. Then, 3 mL of aqueous solution containing Na_2PdCl_4 (57 mg) were rapidly injected into the mixture which was maintained at 80°C for 3h. After that, the reaction was quenched using an ice-eater bath for 30 min, and washed with n-hexane and DDW. Products were collected and dispersed in pure ethanol for further usage.

C.2.2 Preparation of BiOBr

BiOBr was synthesized using a hydrothermal method. Specifically, 2.00 g of $Bi(NO_3)_3 \cdot 5H_2O$ were dissolved in 10 mL of acetic acid. Next, 30 mL of distilled deionized water (DDW) containing 0.49 g of KBr were added dropwise to the bismuth precursor solution. After stirring magnetically for 30 min, the suspension was transferred to a 50-mL Teflon-lined stainless steel autoclave (Parr Instrument Company). The autoclave was heated at 120°C for 12 hours. After the autoclave was allowed to naturally cool to room temperature, the precipitates were filtered out and washed twice with DDW, then once with ethanol. The precipitates were dried at 60°C overnight before being collected for further use.

C.2.3 Preparation of Pd -BiOBr composites

Electrostatic assembly of Pd particles onto BiOBr was applied to prepare Pd-BiOBr composites. Typically, 300 mg of BiOBr and a designated amount of Pd particles were mixed in 100 mL DDW under ultrasonication for 1 h. After that, pH of the mixture was adjusted to 2.5 (zeta potentials of BiOBr and Pd suspensions at pH 2.5 are 10 mV and -0.232 mV, respectively) using HNO_3 (0.5 mol/L), and then magnetically stirred for 1h and sonicated for 2h. The products were washed with DDW and dried at 60°C for 12h. Multiple samples were prepared by varying the amount of Pd particles; 0.5, 1.0 and 1.5 mL of Pd solution was added, and products were labelled as 0.5, 1.0 and 1.5 Pd-Bi. For comparison, Pd nanoparticles loaded on BiOBr were also prepared using two reported methods, namely, photodeposition (A 300-W halogen tungsten projector lamp (Ushio, USA) served as the light source, illuminated for 1h) [23] and one-pot preparation [32, 33], and labelled as Pd-Bi-P and Pd-Bi-OP.

The reusability of the prepared sample (1.0 Pd-Bi) was studied by separating the photocatalysts from the suspension following a single run. Catalysts were then mixed with fresh waste water to start another run. Four runs were performed in total for these tests.

C.2.4 Characterization

Crystal structure was analyzed using X-ray diffraction (XRD) on a Rigaku Ultima IV Diffractometer with Cu Kα radiation ($\lambda = 0.15418$ nm) at 40 kV and 44 mA. XRD patterns were recorded at 2θ of 5 - 80°. Morphologies were investigated using a transmission electron microscopy (JEM-2100F). UV-Vis diffused reflectance spectroscopy (DRS) was applied to analyze the optical properties of prepared samples. Electrochemical properties of prepared samples were analyzed on a CHI 604E electrochemical analyzer (CH Instruments Inc., USA) with a platinum wire as a counter electrode, a calomel reference electrode and a working electrode. The working electrode composed of indium tin oxide (ITO, 75 × 25 × 1.1 mm, 15 - 25 Ω, Sigma-Aldrich Canada Co.), glass coated with the prepared samples. The electrolyte used was Na_2SO_4 with a concentration of 0.05 mol/L. A 300-W halogen tungsten projector lamp (Ushio, USA) served as the light source for all electrochemical tests.

C.2.5 Photocatalytic activity tests

Photocatalytic activity was evaluated via the degradation of phenol under visible light irradiation. The photocatalytic reactor was composed of a 500 mL beaker with a cooling jacket to maintain the temperature of the reactive suspension at 20°C. A 300-W halogen tungsten projector lamp (Ushio, USA) served as the light source, with a UV cut-off (Kenko Zeta, transmittance > 90%) to filter out irradiation with wavelength below 400 nm. The irradiation intensity at the surface of the reactive solution was measured with a quantum meter (Biospherical QSL-2100, $400 < \lambda < 700$ nm), which was measured to be approximately 1.1×10^{-2} Einsteins m^{-2} s^{-1}. To confirm the light source applied was in visible light region, the spectra of the lamp were measured using a Newport IQE-200 system over wavelengths of 350 to 1000 nm, and results were depicted in Fig. C.1. It can be observed the light with wavelength below 400 nm was almost completely eliminated when the UV cut-off was applied on the lamp. This result indicates the irradiation through the cut-off was attributed visible light and the UV light was completely filtered out.

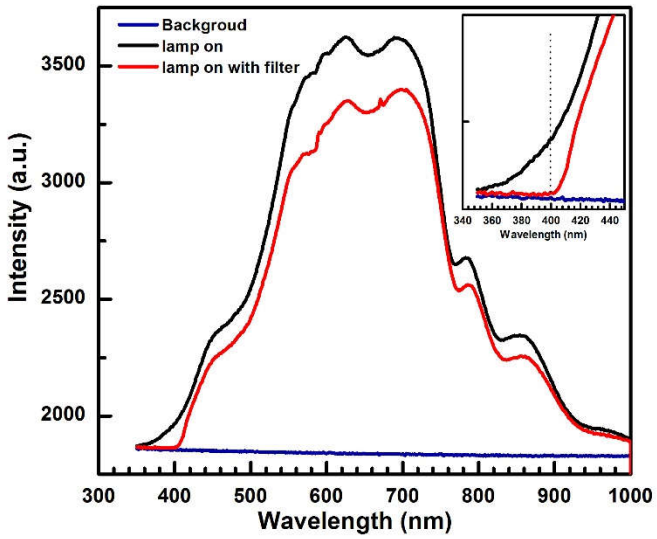


Figure C.1 Spectra for the lamp (Ushio, USA) with and without the UV cut-off.

In each test, 0.1 g of photocatalysts were added into 100 mL of phenol solution with a concentration of 10 mg/L. Before each test, the suspension was magnetically stirred in the dark for 60 min, so as to obtain an adsorption-desorption equilibrium between phenol and the photocatalyst. After that, the photocatalytic process was initiated by turning on the lamp, and the process lasted for 180 min. During this process, 1-mL aliquots was drawn every 30

min. These samples were centrifuged for 5 min at 13000 rpm, and the supernatant was separated and analyzed on a high-performance liquid chromatograph (HPLC, Agilent 1100 series). The HPLC was equipped with a UV detector and the detecting wavelength was fixed at 270 nm. A ZORBAX Eclipse Plus C18 column (4.6 × 250 mm, Agilent Technology) was used as well, at a temperature of 60°C. The flow phase was composed of 55% methanol and 45% water at a flow rate of 0.6 mL/min. The injection volume was 25 μL for each sample. The total organic carbon (TOC) was evaluated on an Appollo 9000 TOC analyzer equipped with a Non-Dispersive Infra-Red (NDIR) detector. The combustion temperature was fixed at 750°C.

C.3 Results and discussions

C.3.1 Crystal structures analysis

Crystal structures of prepared samples were investigated using XRD; patterns were depicted in Fig. C.2. Diffraction patterns for pure BiOBr agree well with the tetragonal BiOBr crystal structure (space group: P4/nmm (129), a = b = 3.92 Å, c = 8.11 Å, PDF card #: 85-0862 [36]). All peaks can be indexed, and no impurities were observed for pure BiOBr. With the introduction of Pd particles, no impurity peaks were found, possibly due to the loading quantity being too low to be detected by XRD. No peak shift and negligible influence on the lattice parameters of BiOBr after the Pd modification were found, as shown in Table C.1. This indicates the Pd particles may simply rest on the surface as opposed to covalently anchoring to the lattice. It should be noted that the relative intensity between the [001] plane and [102] plane gradually decreased with increasing Pd contents. This phenomenon may be attributed to the nanosheet morphology of BiOBr, and a large amount of [001] planes were exposed and Pd particles were mainly loaded on the [001] facets. The high exposure fraction of [001] facets was reported with an optimized band structure and in favor of facilitating the separation of photogenerated charge carriers [37, 38]. The cover of Pd particles on the [001] facets may deteriorate the photocatalytic activity of BiOBr. An optimal amount of loading quantity of Pd may exist.

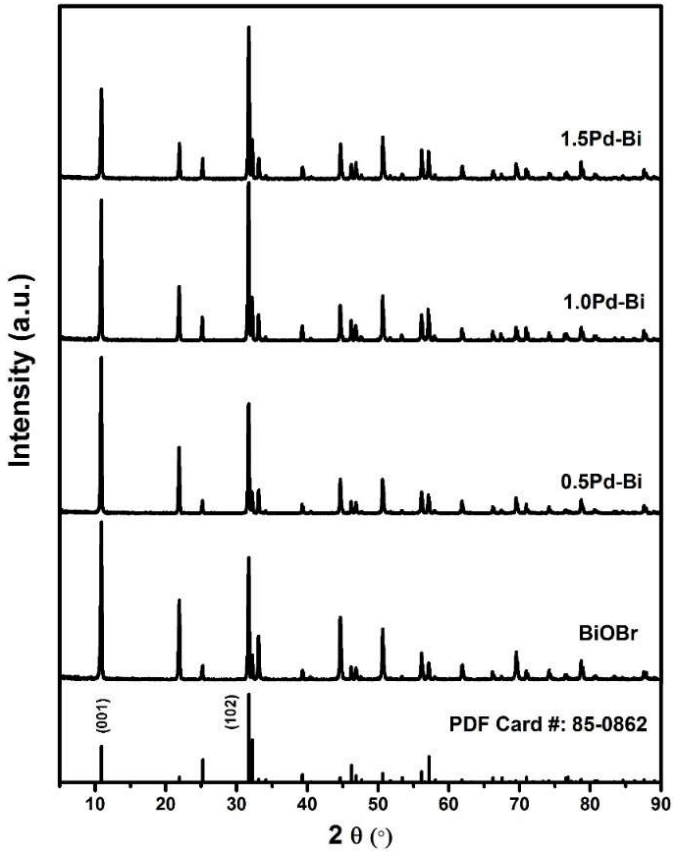


Figure C.2 XRD patterns of prepared samples.

Table C.1 Lattice parameters derived from the XRD patterns

Samples	Lattice constants				$\frac{I_{[001]}}{I_{[102]}}$
	a (Å)	b (Å)	c (Å)	V (Å^3)	
BiOBr	3.927	3.927	8.103	124.94	1.265
0.5Pd-Bi	3.923	3.923	8.097	124.62	1.258
1.0Pd-Bi	3.928	3.928	8.105	125.06	0.738
1.5Pd-Bi	3.926	3.926	8.103	124.89	0.624

C.3.2 Morphologies

For pure Pd particles (Fig. C3a), three forms of particles can be observed, namely cube with side length of ~9.8 nm, tetrahedrons with side length of ~14.5 nm, and cuboid with

side length of 9.8 nm × 40.8 nm. All of these forms of Pd as co-catalysts may be active in enhancing the photocatalytic activity of BiOBr [35]. Nanosheets of BiOBr as shown in Fig. C.3b were observed with a smooth surface. With the introduction of Pd particles, they can be observed in Fig. C.3c. The EDS as shown in Fig. C.3d further confirmed the presence of palladium on the surface of BiOBr after modification of Pd. It indicates the Pd co-catalysts were successfully deposited onto BiOBr via the electrostatic assembly.

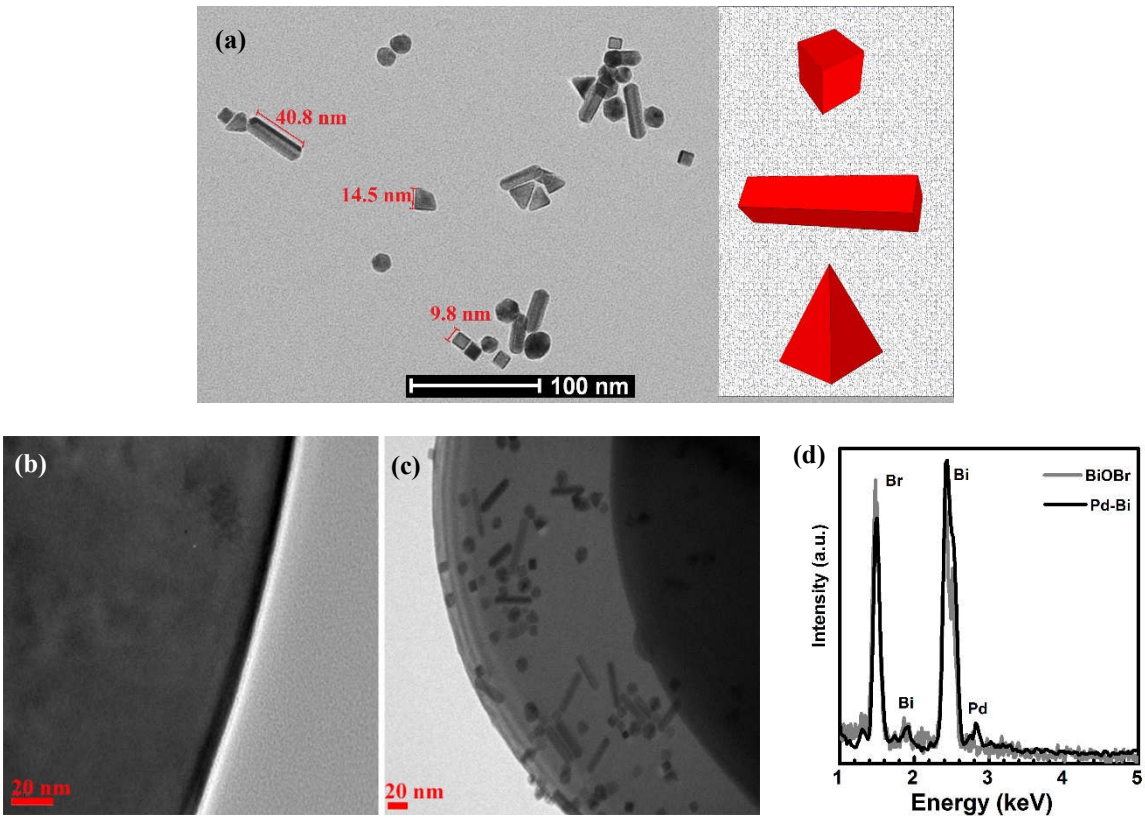


Figure C.3 TEM images of (a) Pd particles, (b) BiOBr, (c) Pd-Bi composites, and (d) EDS spectra of BiOBr and Pd-Bi composites.

C.3.3 Optical properties

Optical property of prepared Pd particles dispersed in ethanol was investigated, and the spectroscopy was illustrated in the inset of Fig. C.4. It can be observed that irradiation in the UV-Vis-NIR wavelength range can be absorbed by the Pd particles. This optical property is probably due to the excitation of resonant collective oscillations of the conduction band electrons by electromagnetic radiation, namely the localized surface plasmon resonance (LSPR) [39]. The frequency of the LSPR can be tuned by adjusting the

particle size, shape and the dielectric environmental of the particles. By combining the Pd particles with BiOBr, it can be observed in Fig. C.4 that the absorption intensity in the UV-Vis-NIR range increased gradually with increasing Pd content in the composites. This improvement may be attributed to the LSPR effect of palladium particles on the surface. A steep decrease in absorption intensity is observed when the irradiation wavelength is around 429 nm, which may be caused by the band gap transition of BiOBr; the band edge was at the wavelength of 429 nm, which corresponds with the band gap of 2.89 eV for BiOBr. No apparent red-shift in the band edge was observed, confirming that the Pd particles may simply rest on the surface instead of doped in the lattice of BiOBr.

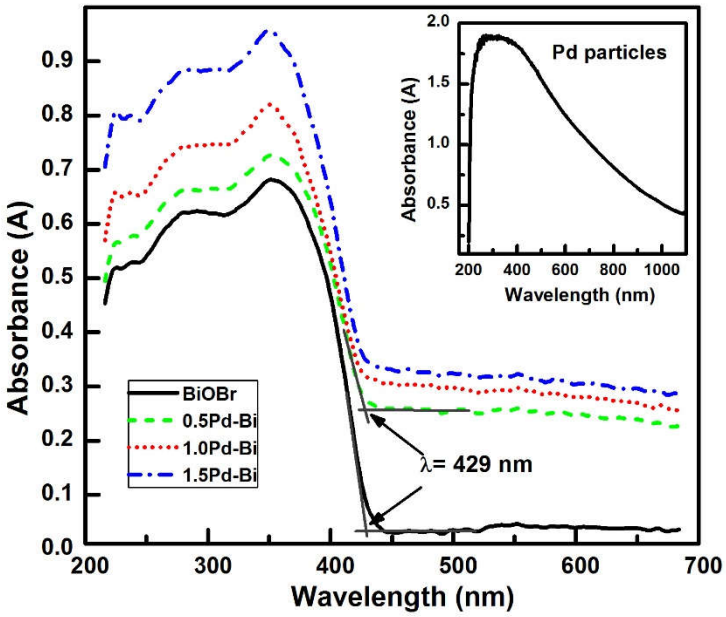


Figure C.4 DRS spectra of BiOBr as well as Pd-Bi composites. (Inset: UV-Vis-Infrared spectroscopy Pd particles dispersed in ethanol)

C.3.4 Photocatalytic activity evaluation

C.3.4.1 Degradation of phenol

Photocatalytic activity of prepared samples was evaluated via the degradation of phenol under visible light irradiation. The concentration profiles were illustrated in Fig. C.5a. The adsorption of phenol on prepared samples was as low as 6% in 60 min. By turning on the lamp, approximately 53.7% of phenol was removed in the presence of BiOBr over 180 min. The removal fraction of phenol also increased to 67.9, 95.1 and 76.1 % for systems with

0.5, 1.0 and 1.5 Pd-Bi, respectively. Because of the low concentration of phenol in the reactive solution, a pseudo first-order model using the Langmuir-Hinshelwood model as shown in Equation 1 may be applied to describe these photocatalytic processes. Integration of Equation 1 with respect to the concentration from c_o to c_t at time between zero and t, can then produce Equation 2.

$$r = -\frac{dc}{dt} = \left.\frac{kKc}{1+Kc}\right|_{Kc \ll 1} \approx kKc\big|_{kK=k'} = k'c \qquad \textbf{Equation 1}$$

$$\ln\left(\frac{c_o}{c_t}\right) = k't \qquad \textbf{Equation 2}$$

where k' represents the apparent reaction constant. By plotting $\ln(c_o/c_t)$ *vs* t, k' can be obtained as the slope from a linear regression with an intercept fixed at the origin. The kinetic constants were computed and plotted in Fig. C.5b. It can be found that k' was improved from 0.0043 to 0.016 min^{-1} for systems with pure BiOBr and 1.0 Pd-Bi composites, respectively. The kinetics reaction constants were increased 4 times higher for BiOBr modified by Pd particles. As reported, phenol can be decomposed into various intermediates including hydroquinone, benzoquinone, catechol and organic acids with the cleavage of benzene ring [11, 24]. It is important to explore whether phenol was mineralized by testing the TOC in the reactive solution. The testing results were shown in Fig. C.5b. About 20.2% of TOC was removed in 180 min for the system with pure BiOBr, and it increased to 50.7% for the system in the presence of Pd modified BiOBr composites. It further confirmed the loading of Pd particles is capable of enhancing the visible light-driven photocatalytic activity of BiOBr in the degradation of phenol.

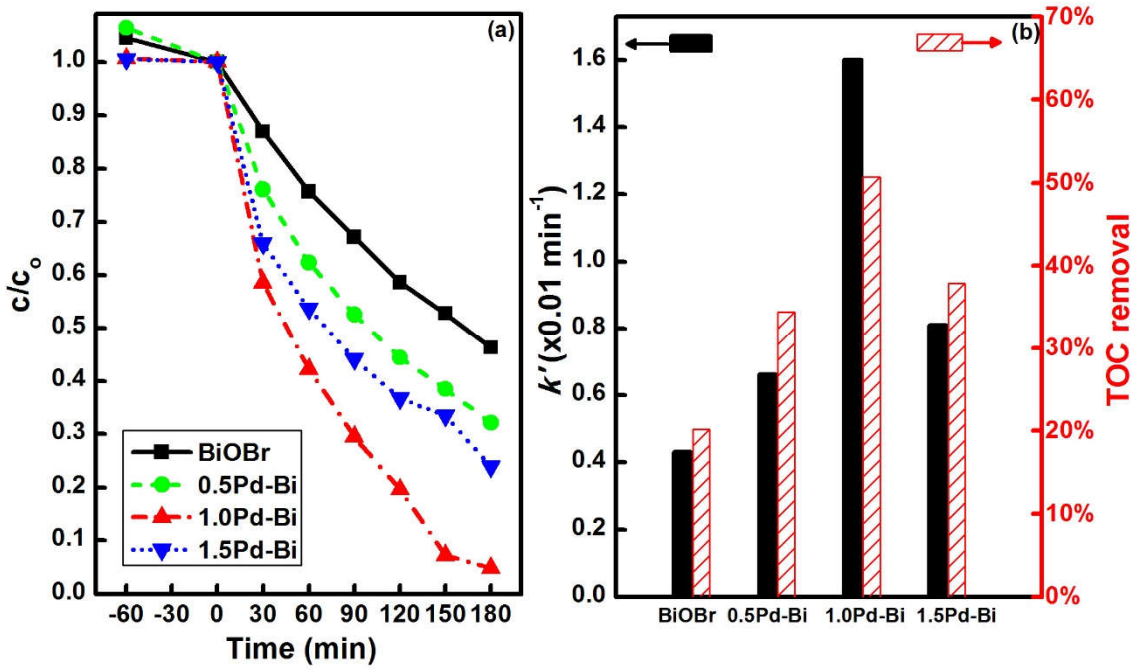


Figure C.5 (a) Phenol concentration profiles of systems in the presence of various prepared samples under visible light irradiation; (b) pseudo first-order reaction constants and TOC removal fraction of different systems.

C.3.4.2 Comparison with reported Pd-BiOBr composites

Photocatalytic activity of prepared Pd-BiOBr composites was compared in the degradation of phenol under visible light irradiation, results are shown in Fig. C.6a. Compared with pure BiOBr, removal efficiencies of phenol after illumination for 180 min, were improved by 13.0%, 49.1% and 89.4%, respectively, for Pd-Bi-OP, Pd-Bi-P and Pd-Bi composites. The smallest increase for Pd-Bi-OP may be due to the palladium may not only load on the surface but also present in the bulk, and even doped in the lattice of BiOBr. As photocatalysis is a process occurring at the interface, those palladium in the bulk insignificantly contribute to the enhancement of photocatalytic activity. And palladium possibly doped in the lattice of BiOBr, may add impure energy levels within the band gap of BiOBr, which may increase the possibility of photogenerated charge carriers' recombination [40]. As shown in Fig. C.6b, Palladium particles on the surface with size of 10-30 μm, are too large to exhibit surface plasmonic resonance (SPR) effect. Comparatively, photodeposition is an excellent method to prepared palladium nanoparticles on the surface [11, 13, 23, 24, 41]. As shown in Fig. C.6c, Pd particles with

size of 1 - 5 nm were successfully prepared on the surface of BiOBr. The enhancement for Pd nanoparticles deposited on BiOBr may be resulted from the SPR effect. Also, photogenerated charge carriers were easy to separate because of the metallic Pd loaded on the surface. However, palladium may also serve as an excellent recombination site for separated charge carriers, and the recombination may be much easier on Pd nanoparticles compared to Pd particles with larger size. That may lead to that the activity of Pd-Bi was better than that of Pd-Bi-P.

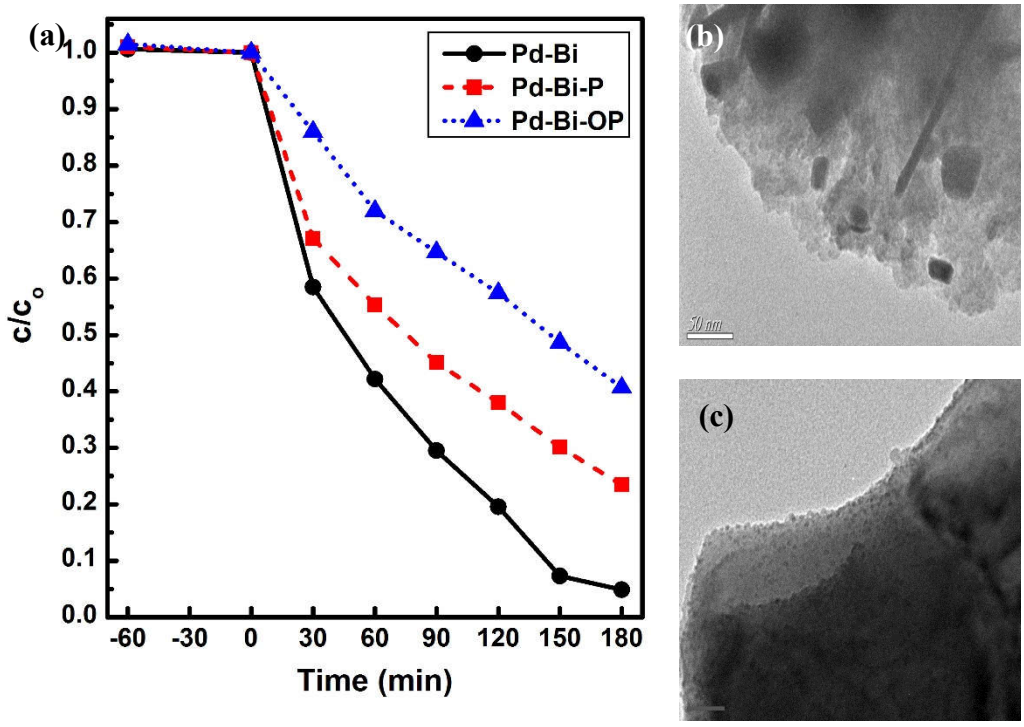


Figure C.6 (a) Photocatalytic degradation of phenol in the presence of Pd-BiOBr composites prepared with different methods; and TEM images for Pd-BiOBr prepared by one-pot (b, adapted from [32]) and photodeposition (c) methods, respectively.

C.3.4.3 Reusability

Reusability is an important parameter to evaluate a photocatalyst from an economic perspective. The sample, 1.0 Pd-Bi, was recycled for four runs, and the results were shown in Fig. C.7. After four runs, the photocatalyst still exhibit excellent activity in the removal of phenol. A slight decrease in phenol removal ratio was observed (95.1%, 92.0%, 88.9% and 86.7% at 180 min for the first, second, third and fourth run, respectively). This

phenomenon may be attributed to the following reasons: the loss of photocatalysts between two runs and the adsorption of refractory intermediates such as organic acids on the surface which may reduce the reactive sites. Despite this slight decrease in phenol removal efficiency, as-prepared samples exhibited a high reusability and stability in the removal of organics from waste water.

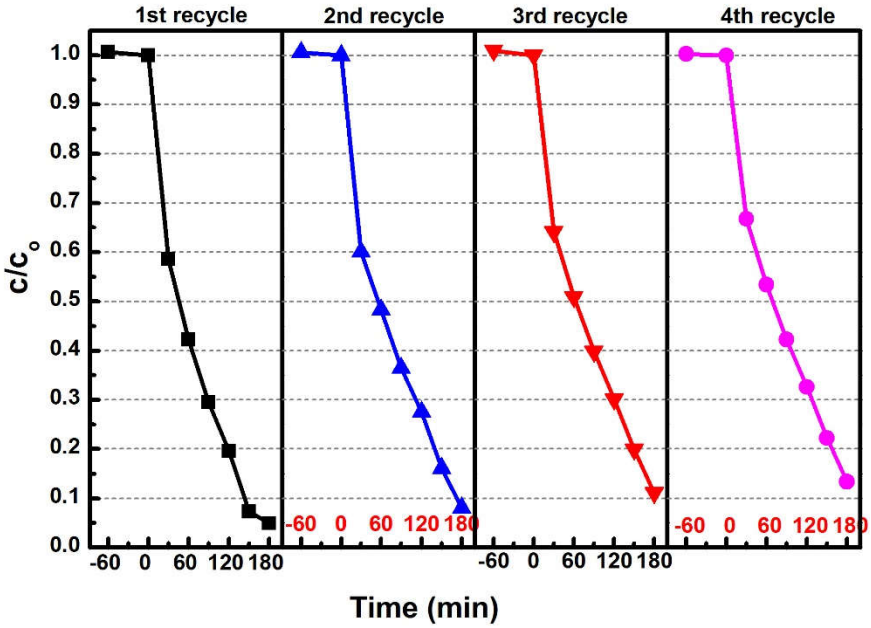


Figure C.7 Removal efficiencies of phenol with recycled 1.0 Pd-Bi composites.

C.3.5 Electrochemical properties

To further explore the photogenerated charge carriers on pure BiOBr and Pd modified BiOBr composite, electrochemical properties were investigated and depicted in Fig. C.8. The electrochemical impedance spectra (EIS) Nyquist and Bode plots were illustrated in Fig. C.8a and C.8b, respectively. Only one arc was observed for each EIS Nyquist plot for pure BiOBr and Pd-Bi electrode, indicating these two photocatalytic processes were just simple electrode reactions. The diameter of the arc can be fitted and is in proportion to the resistance value of electron transfer on the electrode. The equivalent circuit was shown in the inset of Fig. C.8a, and fitted values for resistances were summarized in Table C.2. The resistance for the solution (R_s) is similar between the BiOBr and Pd-Bi electrodes, and the resistance to electron transfer (R_{ct}) on BiOBr electrode was about twice of that on Pd-Bi electrode. This phenomenon suggests that more separated electrons were generated on the

Pd-Bi electrode. Furthermore, as shown in Fig. C.8b, the characteristic frequency peak of Pd-Bi electrode was shifted to a higher frequency, compared to pure BiOBr electrode. The relation between the frequency (f) and lifetime (τ) of the injected electrons follows Equation 3 as below [42]:

$$\tau = \frac{1}{2\pi f} \qquad \textit{Equation 3}$$

Lifetimes for BiOBr and Pd-Bi electrodes were calculated and shown in Table C.2. Lifetime of electrons on Pd-Bi electrode was over 2-fold longer than that of BiOBr electrode, indicating that the separation of photogenerated charge carriers is enhanced via loading Pd on the surface of BiOBr. Another property analyzed to confirm the separation extent of electron-hole pairs is the photocurrent intensity. As shown in Fig. C.8c, uniform and fast photocurrent responses were found for both electrodes, and the responses were reversible. Upon illumination, the photocurrent intensity on the Pd-Bi electrode is around 4-fold higher than that on the BiOBr electrode. The apparent improvement may further confirm that loading Pd supressed the recombination of electrons and holes, so as to improve the photocatalytic activity.

Mott-Schottky (MS) plots of BiOBr and Pd-Bi electrodes were shown in Fig. C.8d. It indicates that as-prepared BiOBr is an n-type semiconductor. The flat band potentials (V_{fb}) for BiOBr and Pd-Bi were about 0.11 and -0.40 V vs. SCE (0.35 and -0.16 V vs. NHE), respectively. A negative shift (~0.51 V) was observed after loading palladium particles on the surface of BiOBr. This may be attributed to the band bending occurring at the interface between palladium and BiOBr [43]. Specifically, the work function of palladium (Φ_{Pd}) is 5.12 V at vacuum (0.62 V vs. NHE) [44], which is larger than the work function of BiOBr (Φ_{BiOBr}, = V_{fb} = 0.11 V vs. NHE) [45]. Under this condition, a negative band bending for BiOBr occurs at the depletion layer. Because of the band bending, a barrier may be formed at the metal-semiconductor interface, which is called the Schottky barrier [46-49]. Thus, palladium served as an excellent acceptor of the generated electrons of BiOBr, and effectively suppressed the recombination of charge carriers.

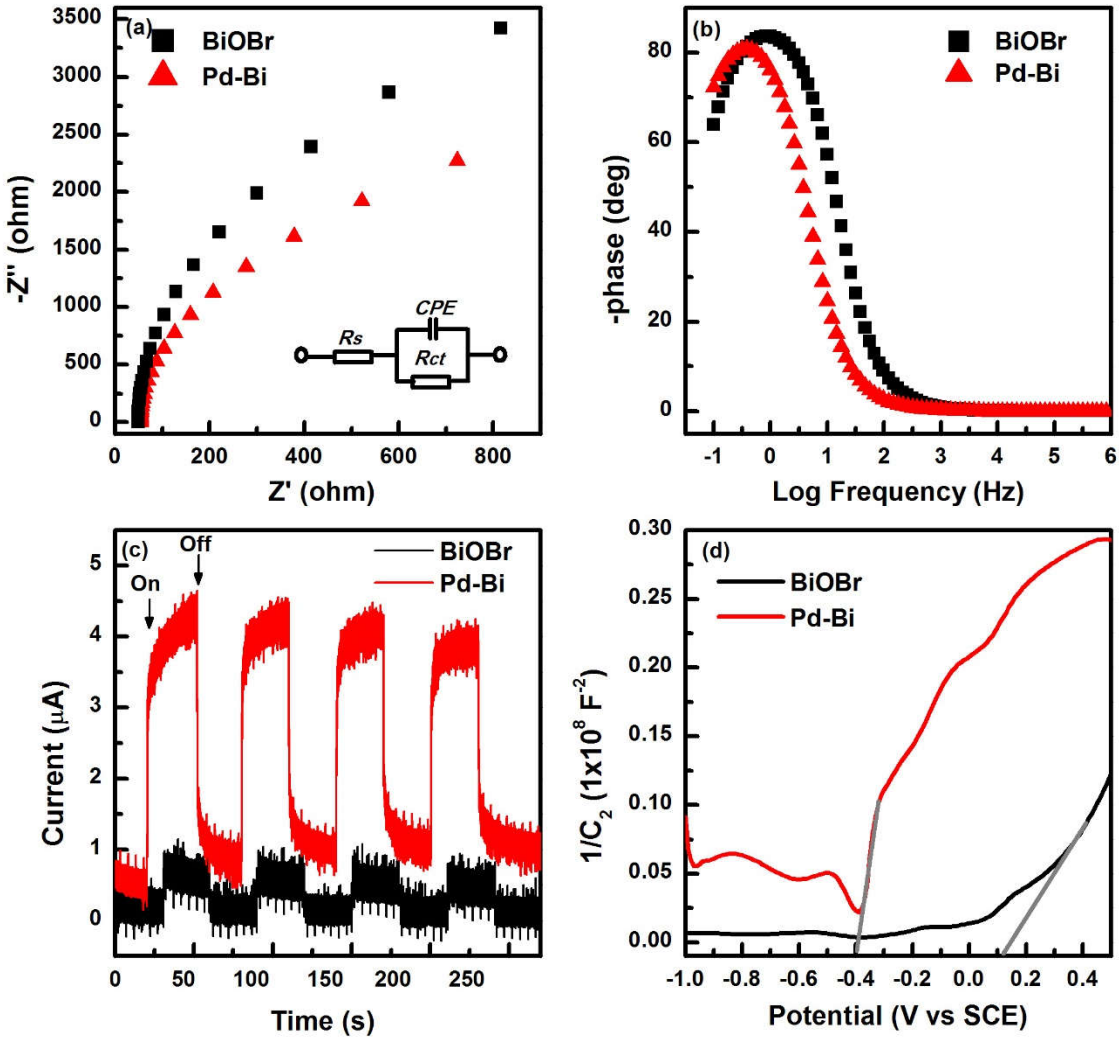


Figure C.8 (a) EIS Nyquist plots, (b) Bode plot curves, (c) transient photocurrent response and (d) Mott-Schottky plots of BiOBr and Pd-Bi electrodes.

Table C. 2 Electrochemical impedance results of $BiVO_4$, rGO-Bi, Pd(G)-Bi and Pd-Bi.

Samples	R_s (Ω)	R_{ct} (Ω)	f_{min} (Hz)	τ (ms)
BiOBr	53.91	16020	0.825	193
0.5 Pd-Bi	49.42	8354	0.383	416

C.3.6 Proposed mechanism

Mechanisms of enhancement by loading palladium particles on the surface of BiOBr can be divided into two parts (Fig. C.9):

(I) Plasmonic-metal-induced enhancements

Plasmonic nanostructures of noble metals exhibit significant promise in improving visible light-driven photocatalysis [21]. As shown in Fig. C.1, photons through the UV filter were totally in the visible light range. Activity reported in this work may be totally induced by visible light. Palladium particles, especially those in nanosize, are capable of capturing visible-light photons with the generation of hot electrons, because of the surface plasmon resonance (SPR) effect [22]. The generated electrons may be injected to the conduction band of BiOBr when their potential is more negative than the conduction-band potential of BiOBr. SPR enhanced visible light-induced photocatalytic activity contributed to the improved activity of Pd modified BiOBr.

(II) Metal-semiconductor contact induced band bending

When the metal and semiconductor are in contact, free electrons may transfer between each other due to the work function difference. As the work function for palladium is higher than that of BiOBr, electrons may transfer from BiOBr to palladium. The transfer will continue until an equilibrium is achieved when the Fermi levels of palladium and BiOBr are aligned. Accordingly, a Pd-BiOBr Schottky junction was established. As reported, Schottky contact facilitates the separation of photogenerated charge carriers, so as to improve the photocatalytic activity [50-52].

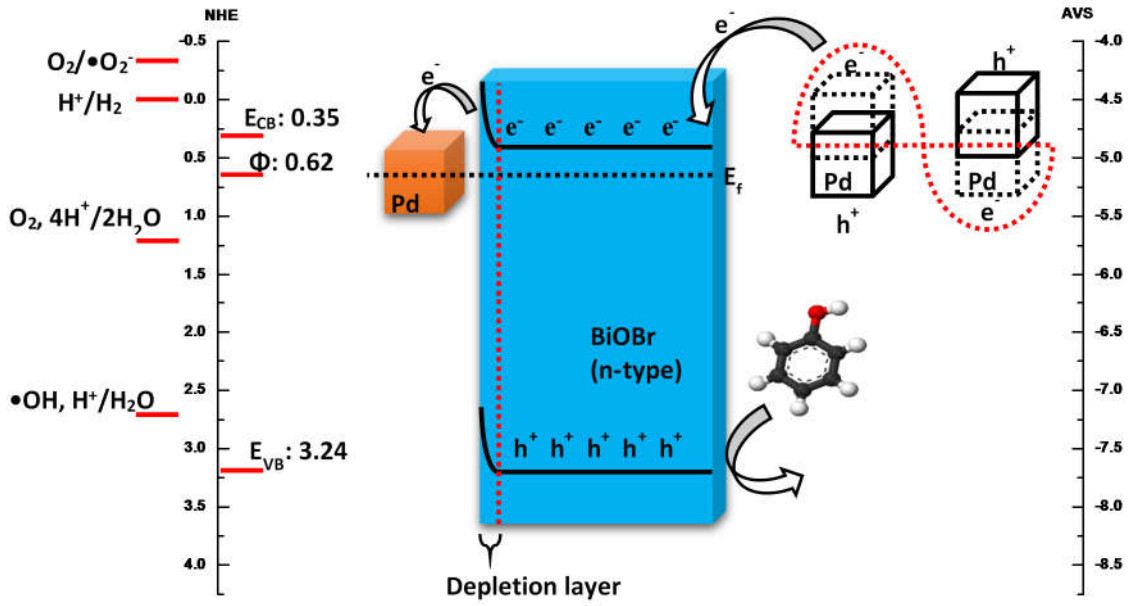


Figure C.9 Proposed mechanism of the enhancement in photocatalysis of loading palladium cubic on the surface of BiOBr.

C.4 Conclusions

Palladium particles were successfully prepared and electrostatically assembled on the surface of BiOBr by adjusting the pH of the reactive solution. Palladium particles in nanosize on the surface may contribute to absorb more visible-light photons so as to generate more hot electrons. Moreover, a Mott-Schottky junction between palladium and BiOBr may be established to facilitate the separation of photogenerated charge carriers. The synergetic effects result in the enhanced photocatalytic activity in the degradation of phenol under visible light irradiation. This work further confirms the significance of the SPR effect in improving activities of a photocatalyst.

References

1. Kazuhiko Maeda and Kazunari Domen, "Photocatalytic Water Splitting: Recent Progress and Future Challenges," *The Journal of Physical Chemistry Letters*, vol. 1, no. 18, pp. 2655-2661, 2010.

2. Akihiko Kudo and Yugo Miseki, "Heterogeneous photocatalyst materials for water splitting," *Chemical Society Reviews*, vol. 38, no. 1, pp. 253-278, 2009.

3. Wendong Wang, Philippe Serp, Philippe Kalck, Cláudia Gomes Silva and Joaquim Luís Faria, "Preparation and characterization of nanostructured MWCNT-TiO_2 composite materials for photocatalytic water treatment applications," *Materials Research Bulletin*, vol. 43, no. 4, pp. 958-967, 2008.

4. Lagnamayee Mohapatra and Kulamani Parida, "A review of solar and visible light active oxo-bridged materials for energy and environment," *Catalysis Science & Technology*, vol. 7, no. 11, pp. 2153-2164, 2017.

5. Rimeh Daghrir, Patrick Drogui and Didier Robert, "Modified TiO_2 For Environmental Photocatalytic Applications: A Review," *Industrial & Engineering Chemistry Research*, vol. 52, no. 10, pp. 3581-3599, 2013.

6. Xiangchao Meng, Lingyun Jiang, Weiwen Wang and Zisheng Zhang, "Enhanced Photocatalytic Activity of BiOBr/ZnO Heterojunction Semiconductors Prepared by Facile Hydrothermal Method," *International Journal of Photoenergy*, vol. 2015, pp. 9, 2015.

7. Xiangchao Meng and Zisheng Zhang, "Synthesis, Analysis, and Testing of BiOBr-Bi_2WO_6 Photocatalytic Heterojunction Semiconductors," *International Journal of Photoenergy*, vol. 2015, pp. 12, 2015.

8. Xiangchao Meng and Zisheng Zhang, "Facile synthesis of BiOBr/Bi_2WO_6 heterojunction semiconductors with high visible-light-driven photocatalytic activity," *Journal of Photochemistry and Photobiology A: Chemistry*, vol. 310, no. 0, pp. 33-44, 2015.

9. Xiangchao Meng and Zisheng Zhang, "Ag/AgCl Loaded Bi_2WO_6 Composite: A Plasmonic Z-Scheme Visible Light-Responsive Photocatalyst," *International Journal of Photoenergy*, vol. 2016, pp. 11, 2016.

10. Xiangchao Meng and Zisheng Zhang, "Bismuth-based Photocatalytic Semiconductors: Introduction, Challenges and Possible Approaches," *Journal of Molecular Catalysis A: Chemical*, vol. 423, pp. 533-549, 2016.

11. Xiangchao Meng and Zisheng Zhang, "Plasmonic ternary Ag–rGO–Bi_2MoO_6 composites with enhanced visible light-driven photocatalytic activity," *Journal of Catalysis*, vol. 344, pp. 616-630, 2016.

12. Xiangchao Meng, Zizhen Li, Haoming Zeng, Jie Chen and Zisheng Zhang, "MoS_2

quantum dots-interspersed Bi_2WO_6 heterostructures for visible light-induced detoxification and disinfection," *Applied Catalysis B: Environmental*, vol. 210, pp. 160-172, 2017.

13. Xiangchao Meng and Zisheng Zhang, "Bi_2MoO_6 co-modified by reduced graphene oxide and palladium (Pd^{2+} and Pd^0) with enhanced photocatalytic decomposition of phenol," *Applied Catalysis B: Environmental*, vol. 209, pp. 383-393, 2017.

14. Huizhong An, Yi Du, Tianmin Wang, Cong Wang, Weichang Hao and Junying Zhang, "Photocatalytic properties of BiOX (X = Cl, Br, and I)," *Rare Metals*, vol. 27, no. 3, pp. 243-250, 2008.

15. Hefeng Cheng, Baibiao Huang and Ying Dai, "Engineering BiOX (X = Cl, Br, I) nanostructures for highly efficient photocatalytic applications," *Nanoscale*, vol. 6, no. 4, pp. 2009-2026, 2014.

16. Ayla Ahmad, Xiangchao Meng, Nan Yun and Zisheng Zhang, "Preparation of Hierarchical BiOBr Microspheres for Visible Light-Induced Photocatalytic Detoxification and Disinfection," *Journal of Nanomaterials*, vol. 2016, pp. 10, 2016.

17. Ke-Lei Zhang, Cun-Ming Liu, Fu-Qiang Huang, Chong Zheng and Wen-Deng Wang, "Study of the electronic structure and photocatalytic activity of the BiOCl photocatalyst," *Applied Catalysis B: Environmental*, vol. 68, no. 3, pp. 125-129, 2006.

18. Xin Xiao and Wei-De Zhang, "Facile synthesis of nanostructured BiOI microspheres with high visible light-induced photocatalytic activity," *Journal of Materials Chemistry*, vol. 20, no. 28, pp. 5866-5870, 2010.

19. Xixia Zhao, Guijuan Wei, Junxue Liu, Zhaojie Wang, Changhua An and Jun Zhang, "Synthesis of heterostructured Pd@TiO_2/$TiOF_2$ nanohybrids with enhanced photocatalytic performance," *Materials Research Bulletin*, vol. 80, no. Supplement C, pp. 337-343, 2016.

20. Peng Wang, Baibiao Huang, Ying Dai and Myung-Hwan Whangbo, "Plasmonic photocatalysts: harvesting visible light with noble metal nanoparticles," *Physical Chemistry Chemical Physics*, vol. 14, no. 28, pp. 9813-9825, 2012.

21. Suljo Linic, Phillip Christopher and David B. Ingram, "Plasmonic-metal nanostructures for efficient conversion of solar to chemical energy," *Nature Materials*, vol. 10, no. 12, pp. 911-921, 2011.

22. Wenbo Hou and Stephen B. Cronin, "A Review of Surface Plasmon Resonance-Enhanced Photocatalysis," *Advanced Functional Materials*, vol. 23, no. 13, pp. 1612-1619, 2013.

23. Xiangchao Meng, Zizhen Li, Jie Chen, Hongwei Xie and Zisheng Zhang, "Enhanced visible light-induced photocatalytic activity of surface-modified BiOBr with Pd nanoparticles," *Applied Surface Science*, vol. 433, no. Supplement C, pp. 76-87, 2018.

24. Xiangchao Meng and Zisheng Zhang, "Pd-doped Bi_2MoO_6 Plasmonic Photocatalysts with Enhanced Visible Light Photocatalytic Performance," *Applied Surface Science*, vol. 392, pp. 169-180, 2016.

25. Xiangchao Meng, Zizhen Li and Zisheng Zhang, "Pd-nanoparticle-decorated peanut-shaped $BiVO_4$ with improved visible light-driven photocatalytic activity comparable to that of TiO_2 under UV light," *Journal of Catalysis*, vol. 356, pp. 53-64, 2017.

26. V. Kesava Rao and T. P. Radhakrishnan, "In situ fabricated Ag/AgCl—polymer nanocomposite thin film: An appraisal of the efficient and reusable photocatalyst," *Materials Research Bulletin*, vol. 87, no. Supplement C, pp. 193-201, 2017.

27. Yanjun Liu, Chunxiang Xu, Zhu Zhu, Junfeng Lu, A. Gowri Manohari and Zengliang Shi, "Self-assembled ZnO/Ag hollow spheres for effective photocatalysis and bacteriostasis," *Materials Research Bulletin*, vol. 98, no. Supplement C, pp. 64-69, 2018.

28. Xiaojuan Zhao, Hongda Cui and Tianhe Wang, "Novel synthesis of plasmonic $Bi_2Sn_2O_7$/Ag-AgCl nanocomposite with enhanced visible light photocatalytic property," *Materials Research Bulletin*, vol. 95, no. Supplement C, pp. 392-401, 2017.

29. Lufeng Lu, Liang Kong, Zheng Jiang, Henry H.-C. Lai, Tiancun Xiao and Peter P. Edwards, "Visible-Light-Driven Photodegradation of Rhodamine B on Ag-Modified BiOBr," *Catalysis Letters*, vol. 142, no. 6, pp. 771-778, 2012.

30. Changlin Yu, Caifeng Fan, Xiangjie Meng, Kai Yang, Fangfang Cao and Xin Li, "A novel Ag/BiOBr nanoplate catalyst with high photocatalytic activity in the decomposition of dyes," *Reaction Kinetics, Mechanisms and Catalysis*, vol. 103, no. 1, pp. 141-151, 2011.

31. Girish Gupta, Amandeep Kaur, A. S. K. Sinha and Sushil Kumar Kansal, "Photocatalytic degradation of levofloxacin in aqueous phase using Ag/AgBr/BiOBr

microplates under visible light," *Materials Research Bulletin*, vol. 88, no. Supplement C, pp. 148-155, 2017.

32. J. Di, J. X. Xia, S. Yin, H. Xu, L. Xu, Y. G. Xu, M. Q. He, H. M. Li and J. G. Wang, "Reactable ionic liquid assisted synthesis of Pd modified BiOBr flower-like microsphere with high dispersion and their enhanced photocatalytic performances," *Materials Technology*, vol. 30, no. 2, pp. 113-121, 2015.

33. Changlin Yu, Fangfang Cao, Gao Li, Rongfu Wei, Jimmy C. Yu, Rongchao Jin, Qizhe Fan and Chunying Wang, "Novel noble metal (Rh, Pd, Pt)/BiOX(Cl, Br, I) composite photocatalysts with enhanced photocatalytic performance in dye degradation," *Separation and Purification Technology*, vol. 120, pp. 110-122, 2013.

34. Sang-Il Choi, Jeffrey A. Herron, Jessica Scaranto, Hongwen Huang, Yi Wang, Xiaohu Xia, Tian Lv, Jinho Park, Hsin-Chieh Peng, Manos Mavrikakis and Younan Xia, "A Comprehensive Study of Formic Acid Oxidation on Palladium Nanocrystals with Different Types of Facets and Twin Defects," *ChemCatChem*, vol. 7, no. 14, pp. 2077-2084, 2015.

35. Shaowen Cao, Yao Li, Bicheng Zhu, Mietek Jaroniec and Jiaguo Yu, "Facet effect of Pd cocatalyst on photocatalytic CO_2 reduction over g-C_3N_4," *Journal of Catalysis*, vol. 349, pp. 208-217, 2017.

36. FA Bannister and MH Hey, "The crystal structure of the bismuth oxyhalides," *Mineral. Mag*, vol. 24, pp. 49-58, 1935.

37. Jing Chen, Meili Guan, Weizheng Cai, Jinju Guo, Chong Xiao and Gaoke Zhang, "The dominant {001} facet-dependent enhanced visible-light photoactivity of ultrathin BiOBr nanosheets," *Physical Chemistry Chemical Physics*, vol. 16, no. 38, pp. 20909-20914, 2014.

38. Da Zhang, Jing Li, Qigang Wang and Qingsheng Wu, "High {001} facets dominated BiOBr lamellas: facile hydrolysis preparation and selective visible-light photocatalytic activity," *Journal of Materials Chemistry A*, vol. 1, no. 30, pp. 8622-8629, 2013.

39. Christoph Langhammer, Zhe Yuan, Igor Zorić and Bengt Kasemo, "Plasmonic Properties of Supported Pt and Pd Nanostructures," *Nano Letters*, vol. 6, no. 4, pp. 833-838, 2006.

40. Zong-Yan Zhao and Wen-Wu Dai, "Structural, Electronic, and Optical Properties of

Eu-Doped BiOX (X = F, Cl, Br, I): A DFT+U Study," *Inorganic Chemistry*, vol. 53, no. 24, pp. 13001-13011, 2014.

41. Xiangchao; Meng, Zizhen; Li and Zisheng Zhang, "Pd NPs decorated peanut-like $BiVO_4$ with improved visible light-driven photocatalytic activity comparable with TiO_2 under UV light," *Journal of Catalysis*, 2017.

42. Paul A. DeSario, Jeremy J. Pietron, Dereje H. Taffa, Ryan Compton, Stefan Schünemann, Roland Marschall, Todd H. Brintlinger, Rhonda M. Stroud, Michael Wark, Jeffrey C. Owrutsky and Debra R. Rolison, "Correlating Changes in Electron Lifetime and Mobility on Photocatalytic Activity at Network-Modified TiO_2 Aerogels," *The Journal of Physical Chemistry C*, vol. 119, no. 31, pp. 17529-17538, 2015.

43. Zhen Zhang and John T. Yates, "Band Bending in Semiconductors: Chemical and Physical Consequences at Surfaces and Interfaces," *Chemical Reviews*, vol. 112, no. 10, pp. 5520-5551, 2012.

44. Herbert B. Michaelson, "The work function of the elements and its periodicity," *Journal of Applied Physics*, vol. 48, no. 11, pp. 4729-4733, 1977.

45. Erping Gao, Wenzhong Wang, Meng Shang and Jiehui Xu, "Synthesis and enhanced photocatalytic performance of graphene-Bi_2WO_6 composite," *Physical Chemistry Chemical Physics*, vol. 13, no. 7, pp. 2887-2893, 2011.

46. W. Schottky, "Zur Halbleitertheorie der Sperrschicht- und Spitzengleichrichter," *Zeitschrift für Physik*, vol. 113, no. 5, pp. 367-414, 1939.

47. W. Schottky, "Halbleitertheorie der Sperrschicht," *Naturwissenschaften*, vol. 26, no. 52, pp. 843-843, 1938.

48. "The theory of crystal rectifiers," *Proceedings of the Royal Society of London. Series A. Mathematical and Physical Sciences*, vol. 171, no. 944, pp. 27-38, 1939.

49. N. F. Mott, "Note on the contact between a metal and an insulator or semi-conductor," *Mathematical Proceedings of the Cambridge Philosophical Society*, vol. 34, no. 4, pp. 568-572, 2008.

50. Dawei Ding, Kai Liu, Shengnan He, Chuanbo Gao and Yadong Yin, "Ligand-Exchange

Assisted Formation of Au/TiO_2 Schottky Contact for Visible-Light Photocatalysis," *Nano Letters*, vol. 14, no. 11, pp. 6731-6736, 2014.

51. Yi-Yu Cai, Xin-Hao Li, Ya-Nan Zhang, Xiao Wei, Kai-Xue Wang and Jie-Sheng Chen, "Highly Efficient Dehydrogenation of Formic Acid over a Palladium-Nanoparticle-Based Mott–Schottky Photocatalyst," *Angewandte Chemie*, vol. 125, no. 45, pp. 12038-12041, 2013.

52. Huan Chen, Shuo Chen, Xie Quan and Yaobin Zhang, "Structuring a TiO_2-Based Photonic Crystal Photocatalyst with Schottky Junction for Efficient Photocatalysis," *Environmental Science & Technology*, vol. 44, no. 1, pp. 451-455, 2010.

Appendix D A comparison of Pd^0 nanoparticles and Pd^{2+} modified $Bi_2O_2CO_3$ for visible light-driven photocatalysis

Xiangchao Meng, Zizhen Li, Nan Yun and Zisheng Zhang

Journal of Nanomaterials (2018), Article ID 1234506

Abstract

As two effective approaches to increase the visible light-absorption capacities of photocatalysts, ion doping and metallic nanoparticles loading are compared in this work. Palladium was selected to modify $Bi_2O_2CO_3$. Compared to dispersing palladium nanoparticles on the photocatalyst surface, it was more effective for the method of doping with palladium to shift the energy level within the bandgap of $Bi_2O_2CO_3$ in improving its photocatalytic activity under visible light. This might be because doping with Pd^{2+} narrow the band gap of $Bi_2O_2CO_3$ so as to increase the absorption capacity of visible light photons. Pd nanoparticles on the other hand can absorb photons to produce electrons which are then utilized by $Bi_2O_2CO_3$ for photocatalytic reactions. Different mechanisms resulted in significant differences, and this work provides a solid evidence that ion doping may be a more effective method to improve the photocatalytic activity of $Bi_2O_2CO_3$.

D.1 Introduction

Photocatalysis is an advanced oxidation process, which has been extensively studied in various areas. Two of its primary applications are hydrogen evolution via water splitting and decomposition of organic pollutants [1, 2]. Bismuth-based semiconductors (BBS) have been widely studied and applied to photocatalysis [3]. Compared to TiO_2, which is a pioneer in the field of photocatalysis, and not to mention the most widely studied, BBS

(*e.g.* Bi_2WO_6, BiOBr, Bi_2MoO_6, $BiVO_4$ *etc.*) exhibits a greater visible-light response [4-7]. However, among various BBS, there are some semiconductors with wide band gaps that may only be activated by UV light, such as $Bi_2O_2CO_3$, $BiOIO_3$, BiOCl and $BiPO_4$ [8-11]. To improve their visible light-driven photocatalytic activities, approaches are adopted, mainly including doping and preparation of plasmonic photocatalyst [12, 13].

$Bi_2O_2CO_3$, which is a lamellar compound, has a crystal structure consisting of $(Bi_2O_2)^{2+}$ layers interleaved by slabs comprising CO_3^{2-} groups [8]. The band gap of $Bi_2O_2CO_3$ is approximately 3.46 eV, which is wider than that of TiO_2 (~ 3.2 eV). This indicates that only irradiation with a wavelength lower than 358 nm may be absorbed by pure $Bi_2O_2CO_3$. Modifications are therefore required to make $Bi_2O_2CO_3$ visible light-response. Doping with elemental N, S and Br have been reported with improves visible light-induced photocatalytic activity [14-16]. Heterojunctions such as Ag_2O-$Bi_2O_2CO_3$ have also implemented [17]. Another popular approach to improve the visible light-driven photoactivity is by surface deposition of noble metal nanoparticles on a photocatalyst. Wang *et al.* have reported on $Bi_2O_2CO_3$ modified with Ag and Au nanoparticles, showing an enhanced visible light-driven photocatalytic activity [18, 19]. Our group recently found that palladium nanoparticles were also promising candidates to improve the photocatalytic activities of semiconductors [20-23]. However, most of our reported work focused on using palladium to improve the photocatalytic activity of a semiconductor which is visible light-responsive without modification. As for the intrinsic properties of $Bi_2O_2CO_3$, its band gap is too wide to be visible light-responsive. Palladium nanoparticles may be introduced to the surface of $Bi_2O_2CO_3$, and due to the resultant surface plasmon resonance (SPR) effect, more visible light photons may be absorbed by $Bi_2O_2CO_3$ [24, 25]. Palladium may also be doped into the lattice of $Bi_2O_2CO_3$ with dopant levels within its band gap. The comparison between loading with Pd nanoparticles and doping with Pd to improve the visible light-driven photocatalytic activity of $Bi_2O_2CO_3$ may be interesting to guide the adoption of a modification method.

In this work, both palladium nanoparticles and palladium ions are deposited/doped onto/into $Bi_2O_2CO_3$, respectively. Activity was evaluated with regard to the degradation of Rhodamine B under visible light irradiation. Mechanisms were also proposed and discussed.

D.2 Experimental

D.2.1 Preparation

Pure $Bi_2O_2CO_3$ was prepared using a hydrothermal method. Typically, 8 mmol of $Bi(NO_3)_3 \cdot 5H_2O$ was first dissolved in 20 mL of HNO_3 solution (1 mol/L) to form a clear solution. Then, 60 mL of Na_2CO_3 solution (0.8 mol/L) was added dropwise to the aforementioned solution. After magnetically stirring for 30 min, the mixture was transferred to a 100-mL Teflon-lined autoclave (Parr Instrument Company) and heated at 180°C for 24 h. After the autoclave was allowed to naturally cool down to room temperature, the $Bi_2O_2CO_3$ precipitates were separated by filtration and washed once with ethanol then twice with distilled deionized water (DDW). The washed powder samples were then dried at 60°C for 12 h and collected.

Pd nanoparticles were photoreduced on the surface of $Bi_2O_2CO_3$. In a typical process, $Bi_2O_2CO_3$ and $PdCl_2$ were first dispersed in a solution containing 40 mL of DDW and 5 mL of ethanol under ultrasonication for 30 min. The mixture was then illuminated under ultraviolet-light (UV) (40 W Reflector Blacklights at 353 nm wavelength from Philips) for 1 h with magnetically stirring. The resultant powder samples were then dried, collected and labelled as Pd(0)-Bi. For preparation of Pd^{2+} doped $Bi_2O_2CO_3$ composites, $Bi_2O_2CO_3$ and $PdCl_2$ were first dispersed in 40 mL of DDW and magnetically stirred for 24h. Next, the mixture was dried at 100°C for 12 h. The dried powder samples were then annealed at 450°C for 1h in air. The resultant powder samples were collected and labelled as Pd(II)-Bi. The quantity of Pd^0 and Pd^{2+} in Pd(0)-Bi and Pd(II)-Bi was both at 1.0 *wt*%.

D.2.2 Characterization

X-ray diffraction (XRD) analysis was performed on a Rigaku Ultima IV Diffractometer with Cu Kα radiation (λ = 0.15418 nm) at 40 kV and 44 mA. Elemental composition and chemical states on the sample surface were measured using XSAM-800 X-ray Photoelectron Spectroscopy (XPS). Transmission electron microscopy (JEM-2100F, JEOL) was applied to study the morphologies of the prepared samples. The fitting results of XPS curves were analyzed with CASAXPS (version: 2.3.16PR1.6) and XPSPEAK (version: 4.1). Shirley backgrounds were applied for all curve fittings of the XPS peaks. The specific surface area, pore volume and average pore size were obtained from N_2 sorption isotherms

at 77 K, using automatic adsorption apparatus and measurement systems (ASAP 2020, Micromeritics and Nova 4200E, Quantachrome). The Brunauer, Emmett and Teller (BET) surface area of the samples were calculated using multi-point estimation. Optical properties of the samples were investigated using a Thermo Evolution 300 spectrophotometer. The Fourier Transform Infrared Spectroscopy (FTIR) was performed using a Cary 630 (Agilent Technologies). Electrochemical properties of prepared samples were performed on a CHI 604E electrochemical analyzer (CH Instruments Inc., USA) with a platinum wire as a counter electrode, a calomel reference electrode and a working electrode. The working electrode was composed of indium tin oxide (ITO, 75 × 25 × 1.1 mm, 15 - 25 Ω, Sigma-Aldrich Canada Co.) glass coated with the prepared samples. The electrochemical impedance spectroscopies (EIS) were recorded with frequencies in the range of 1 – 1000000 Hz and a sinusoidal wave of 5 mV. The electrolyte was Na_2SO_4 with a concentration of 0.05 mol/L. The quantum-mechanical calculations were performed on the basis of the density functional theory (DFT) [26]. The generalized gradient approximation (GGA) was applied to exchange-correlation effects [27]. The open access software Quantum ESPRESSO was used, which utilizes pseudopotentials to describe electron-ion interactions and represents electronic wave functions using a plane-wave basis set [28]. The kinetic energy cut-off was set to 300 eV.

D.2.3 Photocatalytic activity tests

The photocatalytic activities of prepared samples under visible light irradiation were investigated with regards to the degradation of Rhodamine B (RhB). A 500 mL beaker served as the reactor with a cooling jacket to maintain the temperature at approximately 20°C. The light source was a 300-W halogen tungsten projector lamp (Ushio) with a UV cut-off (Kenko Zeta, transmittance > 90%) to filter out irradiation with wavelengths below 410 nm. The irradiation intensity on the surface of the solution was measured by a quantum meter (Biospherical QSL-2100, $400 < \lambda < 700$ nm) and was found to be 1.1×10^{-2} Einsteins m^{-2} s^{-1}. In each test, 100 mL of RhB solution (10 mg/L) were mixed with 0.05 g of prepared photocatalyst composites. Photocatalytic tests were each performed for 60 min, and aliquots were drawn periodically. The supernatants were analyzed using a UV-Visible absorption spectrometer (Genesys 10 UV) for RhB. The total organic carbon (TOC) was

evaluated on an Appollo 9000 TOC analyzer equipped with a Non-Dispersive Infra-Red (NDIR) detector. The combustion temperature was fixed at 750 °C.

D.3 Results and discussions

D.3.1 Crystal structures and compositions analysis

Crystal structures were studied using XRD (Fig. D.1). All observed peaks may be identified, and it can be seen that an orthorhombic $Bi_2O_2CO_3$ crystal structure (Pna21(33), cell = 5.468 × 27.320 × 5.468 $Å^3$) [29] was successfully prepared. No apparent differences were observed after modification with either Pd^0 or Pd^{2+}, indicating that the crystal structure of $Bi_2O_2CO_3$, was negligibly influenced by the modification process. The chemical bonding of composites was observed by FTIR measurements (Fig. D.2). The peaks absorption at 2415, 1370, 1066 and 844 cm^{-1} may be derived from the vibrations of CO_3^{2-} group [8, 30]. The peak at 1735 cm^{-1} may be attributed to the stretching and deformation vibrations of the O-H groups in physisorbed/chemisorbed water molecules [20]. No other impurities were detected, confirming a high purity of $Bi_2O_2CO_3$. As for the low content of palladium in Pd(0) and Pd (II) modified $Bi_2O_2CO_3$, no characterization peak for palladium was observed.

To confirm the presence of palladium in the Pd-$Bi_2O_2CO_3$ composites, XPS was employed. The XPS high-resolution orbital scan of Pd 3d, shown in Fig. D.3a, highlights the differences between Pd(0)-Bi and Pd(II)-Bi. Specifically, two peaks at binding energies (BE) of 342.5 and 337.2 eV were each observed in both spectra, possibly derived from the palladium precursor, $PdCl_2$. The peaks located at 340.3 and 335.4 eV in the spectrum of Pd(0)-Bi may be assigned to metallic palladium nanoparticles (Pd^0), whereas peaks at 343.5 and 338.8 eV in the spectrum of Pd(II)-Bi may be assigned to an O-Pd-O structure [31]. This suggests that Pd^{2+} may be doped into the lattice of $Bi_2O_2CO_3$. In the XPS spectra of Cl 2p (Fig. D.3b), one set of doublet peaks in the spectrum of Pd(0)-Bi further confirms the presence of $PdCl_2$ on the surface. In addition to the peaks ascribed to $PdCl_2$, another set of doublet peaks were also observed, which was probably due to the presence of Cl doped in the lattice of $Bi_2O_2CO_3$. It should be noted that a BiOCl-$Bi_2O_2CO_3$ heterostructure may be formed in the Pd(II)-Bi composites [32].

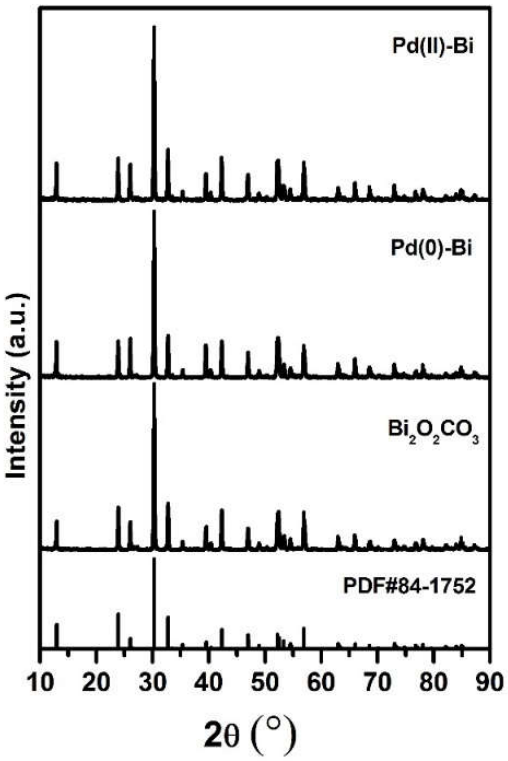


Figure D.1 XRD patterns for pure $Bi_2O_2CO_3$, Pd(0)-Bi and Pd(II)-Bi composites.

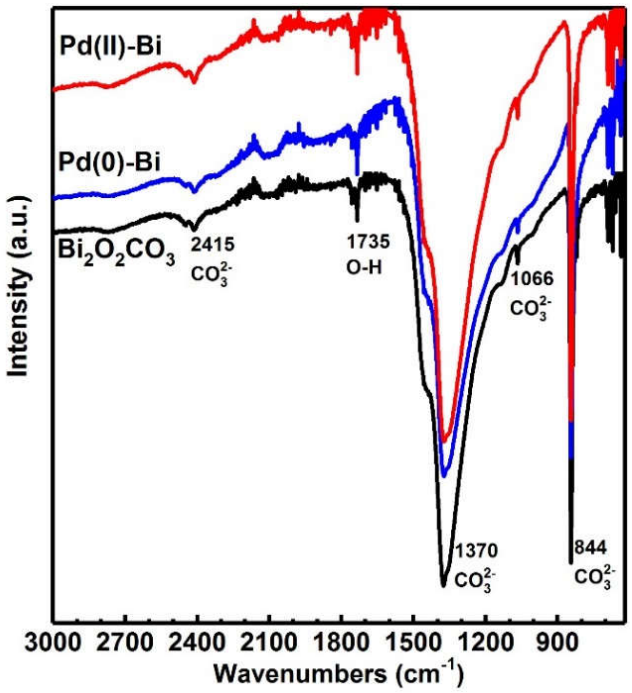


Figure D.2 FTIR for pure $Bi_2O_2CO_3$, Pd(0)-Bi and Pd(II)-Bi composites.

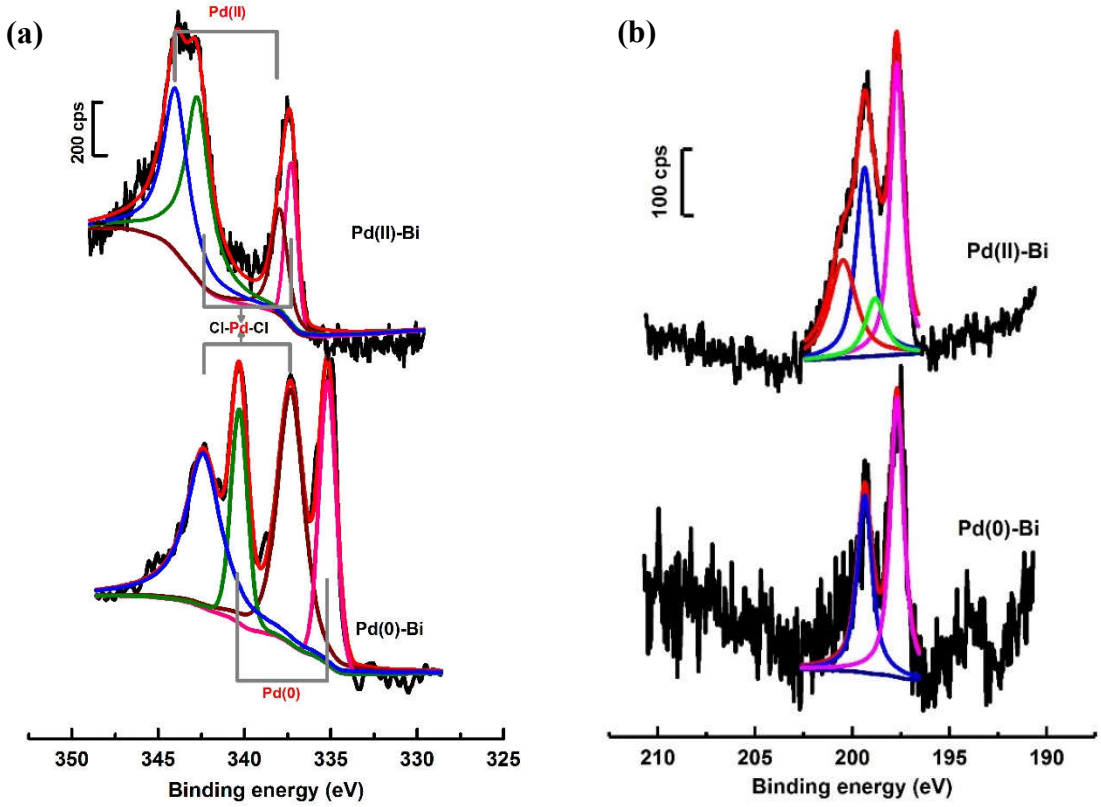


Figure D.3 High-resolution orbital scans of (a) Pd 3d and (b) Cl 2p for Pd(0)-Bi and Pd(II)-Bi composites.

D.3.2 Morphologies, optical properties and photocatalytic activity tests

The Morphology of Pd(0)-Bi was investigated using TEM imaging and shown in Fig. D.4. Palladium nanoparticles were successfully dispersed on the surface of the photocatalyst, and may be activated by visible light irradiation due to the local surface plasmon resonance effect (SPR), which was confirmed in the optical properties study (Fig. D.6). Nitrogen sorption isotherms were illustrated in Fig. D.5 for prepared samples. The specific surface areas for $Bi_2O_2CO_3$, Pd(II)-Bi and Pd(0)-Bi composites are calculated using multi-point estimation as 29.7, 29.3 and 27.2 m^2/g, respectively. It indicates the doping with Pd^{2+} negligibly influence on the specific surface area of $Bi_2O_2CO_3$. However, the loading of palladium nanoparticles on the surface may block the slit-shaped pores, which may lead to the reduction in photocatalytic activity of $Bi_2O_2CO_3$. In the diffused reflectance spectra

(DRS) as shown in Fig. D.6a, a steep increase was observed for pure $Bi_2O_2CO_3$, when the wavelength falls below 358 nm. This indicates that a band gap transition occurs at a wavelength of 358 nm. The corresponding band gap value calculated with the Kubelka-Munk function was about 3.46 eV. After modification with palladium nanoparticles, no red-shift was observed, and the band gap transition occurred at the same wavelength. A great increase in the visible light region was clearly observed after depositing palladium nanoparticles onto the surface, which may be a result of the SPR effect of palladium nanoparticles on the surface. As shown in Fig. D.6b, it confirms the palladium nanoparticles are capable of harvesting photons in visible-light region. For the spectrum of Pd(II)-Bi, a negligible red-shift occurred for the band transition, and the absorption capacity in the visible light region was improved, possibly due to the Pd^{2+} dopant which would add doping levels within the band gap of $Bi_2O_2CO_3$ [12]. Both Pd^0 and Pd^{2+} modifications result in $Bi_2O_2CO_3$ becoming visible-light responsive.

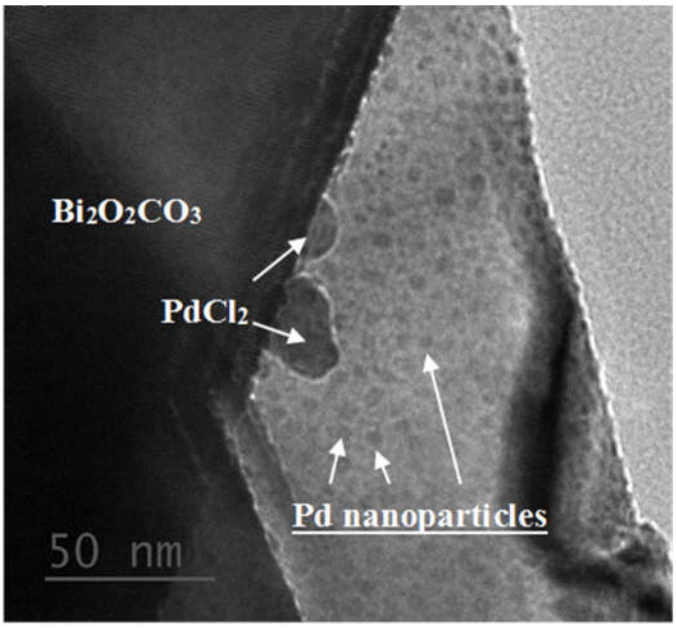


Figure D.4 TEM image of Pd(0)-Bi composite.

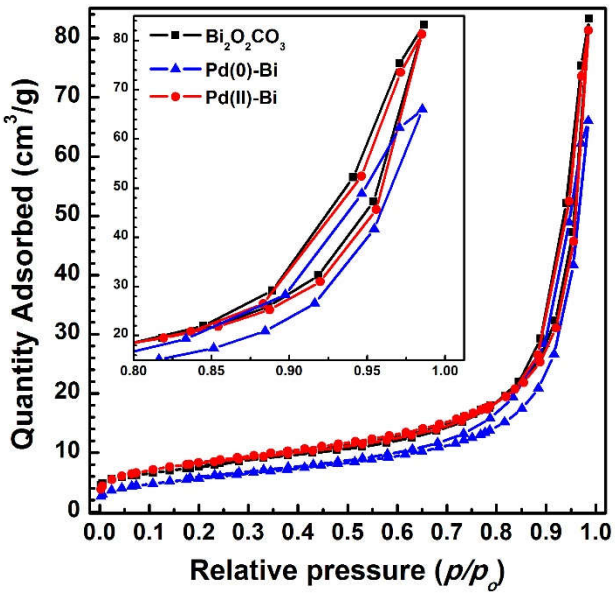
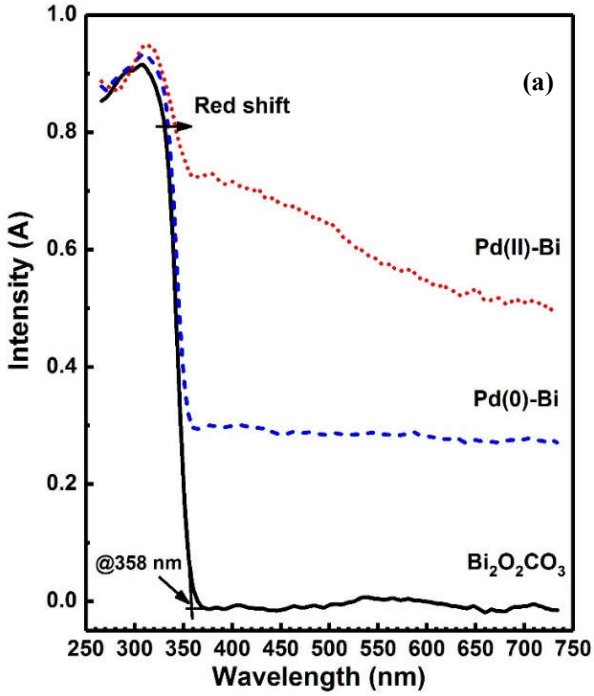


Figure D.5 N_2 adsorption-desorption isotherm of for pure $Bi_2O_2CO_3$, Pd(0)-Bi and Pd(II)-Bi composites (the inset shows the enlarged isotherm at p/p_0 = 0.80-1.00).



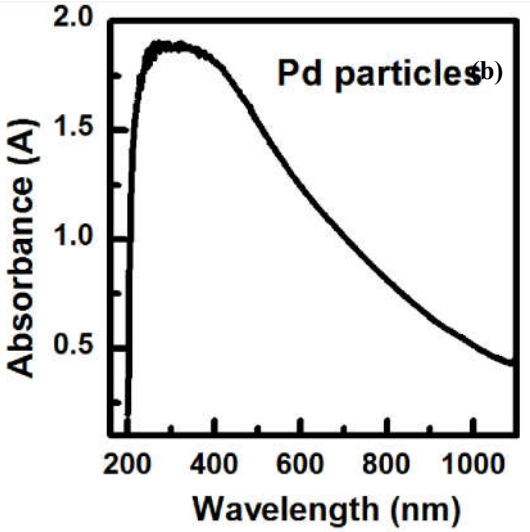


Figure D.6 (a) DRS for pure $Bi_2O_2CO_3$, Pd(0)-Bi and Pd(II)-Bi composites, and (b) UV-Visible spectrum for palladium nanoparticles.

The photocatalytic activity was evaluated with regards to the degradation of RhB, and the results of which are depicted in Fig. D.7. About 6.2% of initial RhB were removed by photolysis over 60 min. For the adsorption, about 8.8, 13.0 and 10.1% of RhB were adsorbed on pure $Bi_2O_2CO_3$, Pd(0)-Bi and Pd(II)-Bi composites over 30 min in the absence of light, respectively. With turning on the lamp to initialize the photocatalytic process, it can be found about 38.5% of initial RhB were removed over 60 min in the presence of pure $Bi_2O_2CO_3$ under visible light irradiation, as $Bi_2O_2CO_3$ is visible-light-irresponsive. The removal of RhB may be attributed to the photosensitization of RhB [33-35]. After deposition of palladium nanoparticles on the surface of $Bi_2O_2CO_3$, a slight increase in the photocatalytic removal of RhB was observed. The increase may be due to an improvement in the absorption of visible light photons by Pd nanoparticles on the surface [36, 37]. However, the intrinsic band gap of $Bi_2O_2CO_3$ is too wide to be visible light-responsive, and so the enhancement by palladium nanoparticles was limited. For Pd(II)-Bi composites, a significant increase in the photocatalytic removal of RhB was observed. Specifically, all RhB were completely removed over 60 min in the presence of Pd(II)-Bi composites under visible light irradiation. This greatly improvement may be attributed to the greatly increased visible light photons absorbing for Pd^{2+} modified $Bi_2O_2CO_3$. The dopant level within band gap of $Bi_2O_2CO_3$, not only confer it visible light-responsive, but also facilitate the separation of photogenerated charge carriers [38]. As for the TOC (Fig. D.8), about 3.8,

9.2 and 25.2 % of initial TOC were removed over 60 min for systems with pure $Bi_2O_2CO_3$, Pd(0)-Bi and Pd(II)-Bi composites, respectively. This further confirms that Pd doping may be more effective in improving the photocatalytic oxidation of organics in water by $Bi_2O_2CO_3$, with longer reaction time required to completely remove TOC [39].

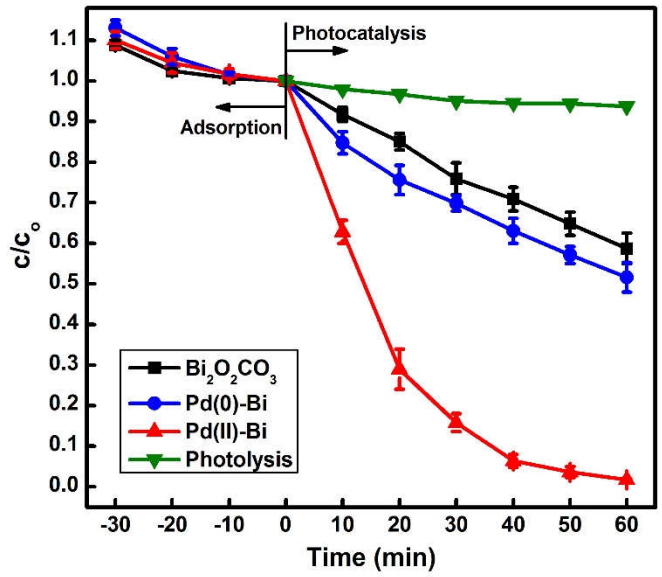


Figure D.7 Photocatalytic degradation of RhB in the presence of various prepared samples.

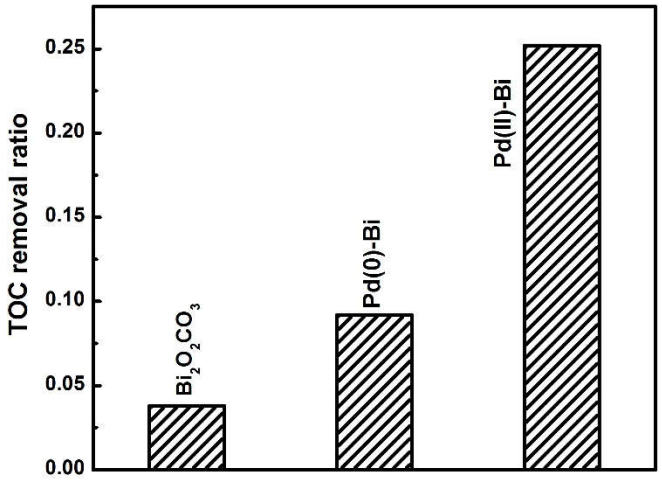


Figure D.8 TOC removal ratio for photocatalytic degradation of RhB in presence of various photocatalysts.

D.3.3 Mechanism exploration

The Electrochemical impedance spectra (EIS) Nyquist plots were illustrated in Fig. D.9. Only one arc was observed for all plots, indicating the photocatalytic process may be a simple electrode reaction. The diameter of the arc was in positive proportion to the resistance value of the electron transfer on the electrode. An equivalence circuit was also depicted in the inset of Fig. D.9, where R_s and R_{ct} represent resistance for the solution and resistance to the electron transfer on the electrode, respectively. R_s for all electrodes are similar, as all electrodes immersed in a same solution. R_{ct} for $Bi_2O_2CO_3$, Pd(0)-Bi and Pd(II)-Bi electrodes are estimated to be 65.32, 57.49 and 16.33 kΩ, respectively. This results suggest the recombination of photogenerated charge carriers was suppressed with Pd(0) and Pd(II) modification, and Pd(II) doping was more effective compared to Pd(0) loading.

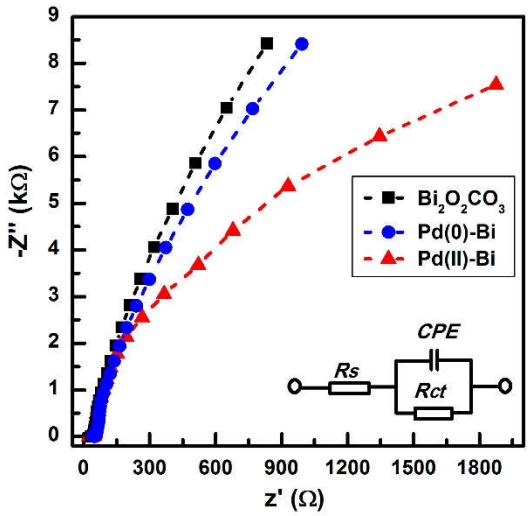


Figure D.9 EIS Nyquist plots of prepared samples (inset: equivalent circuit).

To study the mechanism for doping of Pd into $Bi_2O_2CO_3$, a palladium atom was added to the lattice of $Bi_2O_2CO_3$ as shown in Fig. D.10a. Simulated results for pure $Bi_2O_2CO_3$ and Pd(II)-Bi composites were plotted in Fig. D.10b. The calculated band gap for pure $Bi_2O_2CO_3$ was about 2.45 eV, which is lower than experimental result of 3.46 eV. This is a general phenomenon between the simulated and experimental results in the estimation of band gaps. With doping Pd^{2+} in the lattice of $Bi_2O_2CO_3$, several dopant energy levels were added within the band gap of $Bi_2O_2CO_3$. And these dopant levels are sufficiently

overlapped with the band states of $Bi_2O_2CO_3$, favoring the transfer of charge carriers [38]. This agrees well with DRS results, and the absorption of visible light photons was greatly improved due to these dopant levels.

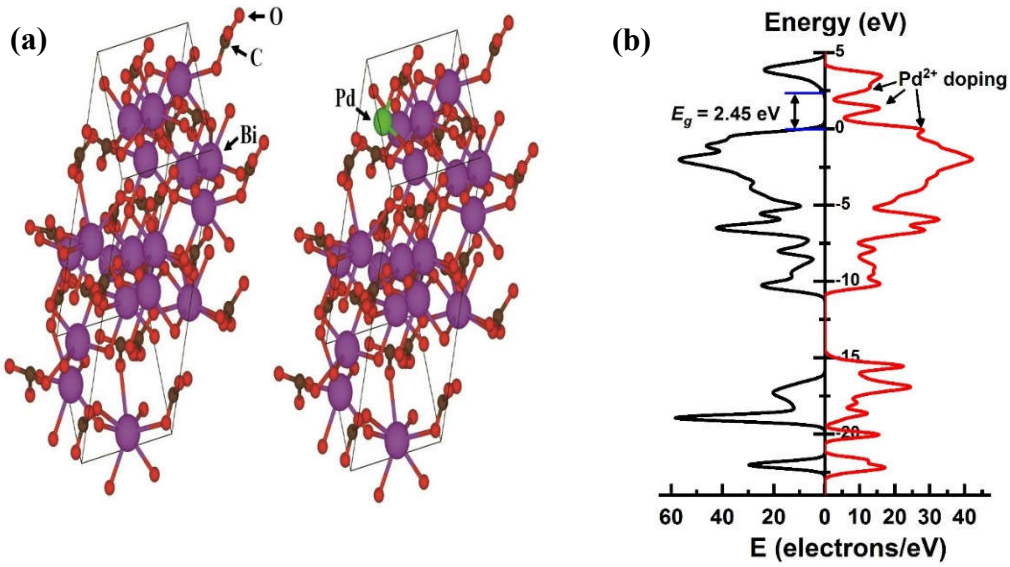


Figure D.10 (a) Crystal structures, and (b) total density of states of $Bi_2O_2CO_3$ with and without Pd(II) doping [28, 40];

Proposed mechanisms for an enhanced photocatalytic activity via deposition of palladium nanoparticles and doping of Pd^{2+} into $Bi_2O_2CO_3$ were illustrated in Fig. D.11a and D.11b, respectively. Typically, for Pd(0)-Bi composites, palladium nanoparticles on the surface may be capable of capturing visible-light photons, due to the SPR effect. However, the support, $Bi_2O_2CO_3$, was not in itself visible light-response. Comparatively, when palladium is doped into the lattice with dopant levels within band gaps of $Bi_2O_2CO_3$, visible light may be absorbed by the support to generate electrical charge carriers [38]. This is consistent with our experiments suggesting that doping is a more effective strategy to improve the activity of a photocatalyst that has a low visible light-responsivity.

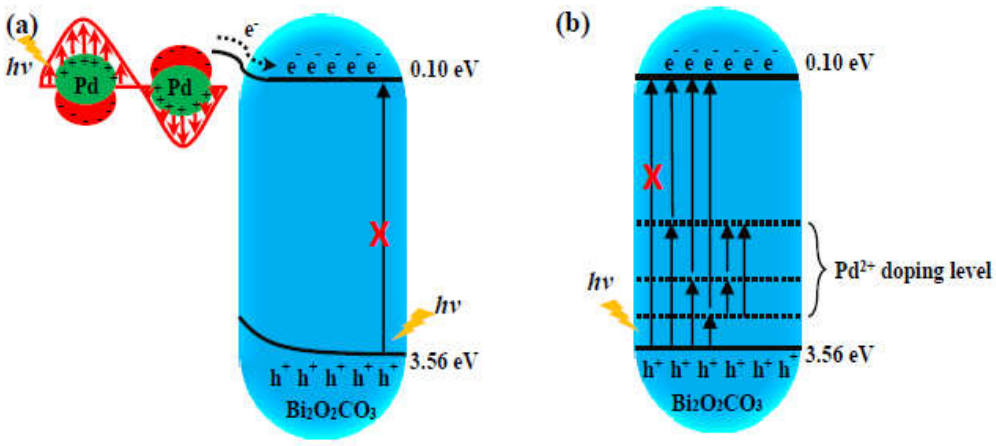


Figure D.11 Proposed mechanism for the photocatalytic degradation process in the presence of (a) Pd(0)-Bi and (b) Pd(II)-Bi.

D.4 Conclusions

Two main approaches to improve the visible light-driven photocatalytic activity, namely nanoparticle deposition and ion doping, have been extensively adopted in practice. A comparison of these two approaches in this work via combining palladium with $Bi_2O_2CO_3$ has been conducted. It can be concluded that both palladium nanoparticle deposition as well as palladium doping are capable of improving the absorption of visible light photons, although the extents of these improvements are drastically different. The band gap of $Bi_2O_2CO_3$ was negligibly influenced by the deposition of Pd nanoparticles, as visible light photons cannot be absorbed by $Bi_2O_2CO_3$, being absorbed solely by palladium nanoparticles at the photocatalyst surface. The activated electrons may inject into the conduction band of $Bi_2O_2CO_3$ due to the difference in work functions between palladium and $Bi_2O_2CO_3$; however, this improvement is limited. In contrast, palladium doping at several dopant levels within the band gap of $Bi_2O_2CO_3$ was capable of conferring visible-light responsivity to the support. This improvement appears to be significant.

This work infers that noble metal nanoparticles may be more effective in improving the photocatalytic activity of a semiconductor that is already visible light-responsive prior to modification. Improvements from the deposition of metallic nanoparticles on the surface

are limited by the intrinsic properties of the support. This work sheds a light on the importance of considering ion doping in the modification of a photocatalyst.

References

1. Dhananjay S Bhatkhande, Vishwas G Pangarkar and Anthony A Beenackers, "Photocatalytic degradation for environmental applications–a review," *Journal of Chemical Technology and Biotechnology*, vol. 77, no. 1, pp. 102-116, 2002.

2. Meng Ni, Michael KH Leung, Dennis YC Leung and K Sumathy, "A review and recent developments in photocatalytic water-splitting using TiO_2 for hydrogen production," *Renewable and Sustainable Energy Reviews*, vol. 11, no. 3, pp. 401-425, 2007.

3. Xiangchao Meng and Zisheng Zhang, "Bismuth-based Photocatalytic Semiconductors: Introduction, Challenges and Possible Approaches," *Journal of Molecular Catalysis A: Chemical*, vol. 423, pp. 533-549, 2016.

4. Meng Shang, Wenzhong Wang, Ling Zhang and Haolan Xu, "Bi_2WO_6 with significantly enhanced photocatalytic activities by nitrogen doping," *Materials Chemistry and Physics*, vol. 120, no. 1, pp. 155-159, 2010.

5. Haibin Li, Guocong Liu and Xuechen Duan, "Monoclinic BiVO4 with regular morphologies: Hydrothermal synthesis, characterization and photocatalytic properties," *Materials Chemistry and Physics*, vol. 115, no. 1, pp. 9-13, 2009.

6. Lijin Xie, Junfeng Ma and Gaojie Xu, "Preparation of a novel Bi_2MoO_6 flake-like nanophotocatalyst by molten salt method and evaluation for photocatalytic decomposition of rhodamine B," *Materials Chemistry and Physics*, vol. 110, no. 2–3, pp. 197-200, 2008.

7. HongHua Li, ChaoYu Liu, KunWei Li and Hao Wang, "Preparation, characterization and photocatalytic properties of nanoplate Bi2MoO6 catalysts," *Journal of Materials Science*, vol. 43, no. 22, pp. 7026-7034, 2008.

8. Hefeng Cheng, Baibiao Huang, Kesong Yang, Zeyan Wang, Xiaoyan Qin, Xiaoyang Zhang and Ying Dai, "Facile Template-Free Synthesis of $Bi_2O_2CO_3$ Hierarchical Microflowers and Their Associated Photocatalytic Activity," *ChemPhysChem*, vol. 11, no. 10, pp. 2167-2173, 2010.

9. Ke-Lei Zhang, Cun-Ming Liu, Fu-Qiang Huang, Chong Zheng and Wen-Deng Wang, "Study of the electronic structure and photocatalytic activity of the BiOCl photocatalyst," *Applied Catalysis B: Environmental*, vol. 68, no. 3, pp. 125-129, 2006.

10. Xue mei Qi, Miao li Gu, Xin yuan Zhu, Jiang Wu, Hui min Long, Kai He and Qiang Wu, "Fabrication of $BiOIO_3$ nanosheets with remarkable photocatalytic oxidation removal for gaseous elemental mercury," *Chemical Engineering Journal*, vol. 285, pp. 11-19, 2016.

11. Chengsi Pan and Yongfa Zhu, "New Type of $BiPO_4$ Oxy-Acid Salt Photocatalyst with High Photocatalytic Activity on Degradation of Dye," *Environmental Science & Technology*, vol. 44, no. 14, pp. 5570-5574, 2010.

12. Ying Zhou, Ziyan Zhao, Fang Wang, Kun Cao, Dmitry E. Doronkin, Fan Dong and Jan-Dierk Grunwaldt, "Facile synthesis of surface N-doped $Bi_2O_2CO_3$: Origin of visible light photocatalytic activity and in situ DRIFTS studies," *Journal of Hazardous Materials*, vol. 307, pp. 163-172, 2016.

13. Lei Jin, Gangqiang Zhu, Mirabbos Hojamberdiev, Xiancong Luo, Congwei Tan, Jianhong Peng, Xiumei Wei, Jinping Li and Peng Liu, "A Plasmonic Ag–AgBr/$Bi_2O_2CO_3$ Composite Photocatalyst with Enhanced Visible-Light Photocatalytic Activity," *Industrial & Engineering Chemistry Research*, vol. 53, no. 35, pp. 13718-13727, 2014.

14. Yang Liu, Shan Yu, Ziyan Zhao, Fan Dong, Xing An Dong and Ying Zhou, "N-Doped $Bi_2O_2CO_3$/Graphene Quantum Dot Composite Photocatalyst: Enhanced Visible-Light Photocatalytic NO Oxidation and In Situ DRIFTS Studies," *The Journal of Physical Chemistry C*, vol. 121, no. 22, pp. 12168-12177, 2017.

15. Hongwei Huang, Ke Xiao, Fan Dong, Jinjian Wang, Xin Du and Yihe Zhang, "Sulfur-doping synchronously ameliorating band energy structure and charge separation achieving decent visible-light photocatalysis of $Bi_2O_2CO_3$," *RSC Advances*, vol. 6, no. 97, pp. 94361-94364, 2016.

16. Jian Xu, Ke Ke Wang, Ting Liu, Yin Peng and Bin Gang Xu, "Br-Doped $Bi_2O_2CO_3$ exposed (001) crystal facets with enhanced photocatalytic activity," *CrystEngComm*, 2017.

17. Na Liang, Min Wang, Lun Jin, Shoushuang Huang, Wenlong Chen, Miao Xu, Qingquan He, Jiantao Zai, Nenghu Fang and Xuefeng Qian, "Highly Efficient $Ag_2O/Bi_2O_2CO_3$ p-n

Heterojunction Photocatalysts with Improved Visible-Light Responsive Activity," *ACS Applied Materials & Interfaces*, vol. 6, no. 14, pp. 11698-11705, 2014.

18. Shengjie Peng, Linlin Li, Huiteng Tan, Yongzhi Wu, Ren Cai, Hong Yu, Xin Huang, Peining Zhu, Seeram Ramakrishna, Madhavi Srinivasan and Qingyu Yan, "Monodispersed Ag nanoparticles loaded on the PVP-assisted synthetic $Bi_2O_2CO_3$ microspheres with enhanced photocatalytic and supercapacitive performances," *Journal of Materials Chemistry A*, vol. 1, no. 26, pp. 7630-7638, 2013.

19. Rui Wang, Xinwei Li, Wen Cui, Yuxin Zhang and Fan Dong, "In situ growth of Au nanoparticles on 3D $Bi_2O_2CO_3$ for surface plasmon enhanced visible light photocatalysis," *New Journal of Chemistry*, vol. 39, no. 11, pp. 8446-8453, 2015.

20. Xiangchao Meng and Zisheng Zhang, "Pd-doped Bi_2MoO_6 Plasmonic Photocatalysts with Enhanced Visible Light Photocatalytic Performance," *Applied Surface Science*, vol. 392, pp. 169-180, 2016.

21. Xiangchao Meng and Zisheng Zhang, "Bi_2MoO_6 co-modified by reduced graphene oxide and palladium (Pd^{2+} and Pd^0) with enhanced photocatalytic decomposition of phenol," *Applied Catalysis B: Environmental*, vol. 209, pp. 383-393, 2017.

22. Xiangchao Meng, Zizhen Li, Jie Chen, Hongwei Xie and Zisheng Zhang, "Enhanced visible light-induced photocatalytic activity of surface-modified BiOBr with Pd nanoparticles," *Applied Surface Science*, vol. 433, no. Supplement C, pp. 76-87, 2018.

23. Xiangchao Meng, Zizhen Li and Zisheng Zhang, "Pd-nanoparticle-decorated peanut-shaped $BiVO_4$ with improved visible light-driven photocatalytic activity comparable to that of TiO_2 under UV light," *Journal of Catalysis*, vol. 356, pp. 53-64, 2017.

24. Ping Yang, Cheng Lu, Nanping Hua and Yukou Du, "Titanium dioxide nanoparticles co-doped with Fe^{3+} and Eu^{3+} ions for photocatalysis," *Materials Letters*, vol. 57, no. 4, pp. 794-801, 2002.

25. Xiangchao Meng and Zisheng Zhang, "Plasmonic Z-scheme Ag_2O-Bi_2MoO_6 p-n heterojunction photocatalysts with greatly enhanced visible-light responsive activities," *Materials Letters*, vol. 189, pp. 267-270, 2017.

26. Walter Kohn and Lu Jeu Sham, "Self-consistent equations including exchange and

correlation effects," *Physical Review*, vol. 140, no. 4A, pp. A1133, 1965.

27. John P. Perdew, J. A. Chevary, S. H. Vosko, Koblar A. Jackson, Mark R. Pederson, D. J. Singh and Carlos Fiolhais, "Atoms, molecules, solids, and surfaces: Applications of the generalized gradient approximation for exchange and correlation," *Physical Review B*, vol. 46, no. 11, pp. 6671-6687, 1992.

28. Giannozzi Paolo, Baroni Stefano, Bonini Nicola, Calandra Matteo, Car Roberto, Cavazzoni Carlo, Ceresoli Davide, L. Chiarotti Guido, Cococcioni Matteo, Dabo Ismaila, Corso Andrea Dal, Gironcoli Stefano de, Fabris Stefano, Fratesi Guido, Gebauer Ralph, Gerstmann Uwe, Gougoussis Christos, Kokalj Anton, Lazzeri Michele, Martin-Samos Layla, Marzari Nicola, Mauri Francesco, Mazzarello Riccardo, Paolini Stefano, Pasquarello Alfredo, Paulatto Lorenzo, Sbraccia Carlo, Scandolo Sandro, Sclauzero Gabriele, P. Seitsonen Ari, Smogunov Alexander, Umari Paolo and M. Wentzcovitch Renata, "QUANTUM ESPRESSO: a modular and open-source software project for quantum simulations of materials," *Journal of Physics: Condensed Matter*, vol. 21, no. 39, pp. 395502, 2009.

29. C. Greaves and S. K. Blower, "Structural relationships between $Bi_2O_2CO_3$ and β-Bi_2O_3," *Materials Research Bulletin*, vol. 23, no. 7, pp. 1001-1008, 1988.

30. Xingfu Shang, Wencong Lu, Baohua Yue, Liangmiao Zhang, Jipeng Ni, Yong lv and Yongli Feng, "Synthesis of Three-Dimensional Hierarchical Dendrites of $NdOHCO_3$ via a Facile Hydrothermal Method," *Crystal Growth & Design*, vol. 9, no. 3, pp. 1415-1420, 2009.

31. Yanlong Yu, Tao He, Lingju Guo, Yajun Yang, Limei Guo, Yue Tang and Yaan Cao, "Efficient visible-light photocatalytic degradation system assisted by conventional Pd catalysis," *Scientific Reports*, vol. 5, pp. 9561, 2015.

32. Haijing Lu, Lingling Xu, Bo Wei, Mingyi Zhang, Hong Gao and Wenjun Sun, "Enhanced photosensitization process induced by the p–n junction of $Bi_2O_2CO_3$/BiOCl heterojunctions on the degradation of rhodamine B," *Applied Surface Science*, vol. 303, pp. 360-366, 2014.

33. Taixing Wu, Guangming Liu, Jincai Zhao, Hisao Hidaka and Nick Serpone,

"Photoassisted Degradation of Dye Pollutants. V. Self-Photosensitized Oxidative Transformation of Rhodamine B under Visible Light Irradiation in Aqueous TiO_2 Dispersions," *The Journal of Physical Chemistry B*, vol. 102, no. 30, pp. 5845-5851, 1998.

34. Tingting Li, Leihong Zhao, Yiming He, Jun Cai, Mengfei Luo and Jianjun Lin, "Synthesis of g-C_3N_4/$SmVO_4$ composite photocatalyst with improved visible light photocatalytic activities in RhB degradation," *Applied Catalysis B: Environmental*, vol. 129, pp. 255-263, 2013.

35. Guisheng Li, Bo Jiang, Shuning Xiao, Zichao Lian, Dieqing Zhang, Jimmy C. Yu and Hexing Li, "An efficient dye-sensitized BiOCl photocatalyst for air and water purification under visible light irradiation," *Environmental Science: Processes & Impacts*, vol. 16, no. 8, pp. 1975-1980, 2014.

36. Suljo Linic, Phillip Christopher and David B. Ingram, "Plasmonic-metal nanostructures for efficient conversion of solar to chemical energy," *Nature Materials*, vol. 10, no. 12, pp. 911-921, 2011.

37. Wenbo Hou and Stephen B. Cronin, "A Review of Surface Plasmon Resonance-Enhanced Photocatalysis," *Advanced Functional Materials*, vol. 23, no. 13, pp. 1612-1619, 2013.

38. R. Asahi, T. Morikawa, T. Ohwaki, K. Aoki and Y. Taga, "Visible-Light Photocatalysis in Nitrogen-Doped Titanium Oxides," *Science*, vol. 293, no. 5528, pp. 269-271, 2001.

39. Andrzej Sobczyński, Łukasz Duczmal and Wojciech Zmudziński, "Phenol destruction by photocatalysis on TiO_2: an attempt to solve the reaction mechanism," *Journal of Molecular Catalysis A: Chemical*, vol. 213, no. 2, pp. 225-230, 2004.

40. Koichi Momma and Fujio Izumi, "VESTA 3 for three-dimensional visualization of crystal, volumetric and morphology data," *Journal of Applied Crystallography*, vol. 44, no. 6, pp. 1272-1276, 2011.

Appendix E Enhanced Photocatalytic Activity of BiOBr/ZnO Heterojunction Semiconductors Prepared by Facile Hydrothermal Method

Xiangchao Meng, Lingyun Jiang, Weiwen Wang and Zisheng Zhang

International Journal of Photoenergy (2015), Article ID 747024

Abstract

In this study, hexagonal wurtzite pure ZnO and BiOBr-ZnO composites were synthesized by facile hydrothermal method. The amount of BiOBr as dopant was adjusted from 5 *wt.*% to 75 *wt.*%, and correspondingly the morphologies and crystal structures of the as-prepared composites were measured and discussed. Specifically, according to XRD patterns and SEM images, the main crystalline structure of ZnO was not destroyed after doping, but growth of ZnO crystals was inhibited by doping BiOBr. Meanwhile, the optical properties of the composites were measured by the Diffuse Reflectance Spectra (DRS). The band gap of composites was also calculated using the classical Tauc equation and it was found to be around 3.0 eV. In the test of photocatalytic activation, the ZnO-BiOBr photocatalysts exhibited high photocatalytic efficiencies in the degradation of *Rhodamine B* (RhB) under visible-light irradiation. It was ascribed to not only the small size of crystalline, but also the reduction in the recombination rate of the photo-generated carriers for the enhancement effect of p-n heterojunction. This work sheds light on improving the photocatalytic performance by establishing the heterojunction, and contribute to the development of a commercially competitive photocatalyst.

E.1 Introduction

Photocatalysis, one of the advanced oxidation processes (AOPs), has been vastly implemented in the remediation of environmental problems. In this promising technique, catalysts are stimulated by light with the generation of electron-hole pairs which would suffer from some secondary reactions to produce strong oxidative species such as $\bullet O_2^-$ and •OH. Organic pollutants in wastewater or polluted air could be completely mineralized by these species [1].

Since 1972, a variety of photocatalysts have been synthesized and implemented for environmental protection, such as TiO_2, CdS, ZnO *etc.* [2, 3]. Some critical drawbacks hinder their wide and commercial application in the industrial scale. Issues with the intrinsic properties of photocatalysts mainly include low visible-light-driven photocatalytic activity due to their wide band gaps and high recombination rates of photo-generated electron-hole pairs. Countermeasures were explored for these issues, including the modification of existing catalysts via noble metal deposition, doping *etc.* [4] and the fabrication of some novel materials with high visible-light photosensitivity [5].

In this work, BiOBr was chosen as the dopant and supported on ZnO to establish the p-n heterojunction which is supposed to possess an enhancement effect on the photocatalytic performance as reported in [6, 7]. Zinc oxide (ZnO), owing to its high stability, low cost, environmentally-friendly properties and easily-controlled structure, has gradually drawn researchers' attention [8]. As a direct n-type semiconductor, the band gap of ZnO is about 3.2 eV, similar to TiO_2. This means only irradiation with wavelengths lower than 400 nm, which attributes to the UV-light range, could stimulate the photocatalytic reactions. Recently, as a promising approach to improve the photocatalytic activity, p-n heterojunction has provoked a heated point of research. The naturally generated bias in the p-n heterojunction is able to drive the opposite movement of the electrons and holes so as to significantly improve the separation rate and enhance the photocatalytic performance. Herein, the p-type semiconductor BiOBr, which can be activated under visible light due to its relatively low band gap (2.7 eV), was doped onto ZnO in order to establish the Type II starred alignment heterojunction [9]. The facile hydrothermal method was applied in the synthesis of BiOBr-ZnO composites. Compared with the only reported solvothermal

method using CTAB as the solvent in reference [10], the operating procedures for the hydrothermal method were much easier and more environmentally-friendly, and showed a higher-yield and purity [11]. To the author's knowledge, this is the first time the hydrothermal method was used to fabricate the BiOBr-ZnO heterojunction.

E.2 Experiment

E.2.1 Synthesis

In this experiment, zinc nitrate hexahydrate ($Zn(NO_3)_2 \bullet 6H_2O$, Reagent grade) and sodium hydroxide (NaOH) were purchased from the Fisher Science Education, and potassium bromide (KBr, 99+% for spectroscopy, IR grade) and bismuth (III) nitrate pentahydrate ($Bi(NO_3)_3 \bullet 5H_2O$, 98% pure) were purchased from ACROS Company. All of the chemicals were of commercially available analytical grade and used without further purification.

BiOBr/ZnO heterojunctions were synthesized by the facile hydrothermal method. Typically, 1.485g of $Zn(NO_3)_2 \bullet 6H_2O$ and 0.4g of NaOH (Zn/OH^- molar ratio of 1:2) were dissolved in 20 mL deionized water in a flask. After stirring for 10 minutes, white precipitates were formed and the solution was regarded as the precursor of ZnO. Similarly, a stoichiometric amount of KBr and $Bi(NO_3)_3 \cdot 5H_2O$ (Bi/Br molar ratio of 1:1) were dissolved in 80mL deionized water. After stirring for 10 minutes, the precursor of BiOBr was synthesized. Then, these two precursors were mixed with continuous stirring for 20 minutes at room temperature. After that, the mixture was transferred into stainless steel Teflon-lined autoclaves and heated in the oven at 120 °C for 12 h. Finally, the precipitates were collected, washed thoroughly with deionized water, twice, and dried at 50°C for 12h. In this work, the doping amount of BiOBr was varied (5 *wt.*%, 10 *wt.*%, 15 *wt.*%, 25 *wt.*%, 50 *wt.*%, and 75 *wt.*%) to explore its effect on the photocatalytic performance of the composites.

E.2.2 Characterization

X-ray diffraction (XRD) patterns were recorded on Rigaku Ultima IV X-ray diffractometer using Cu-Kα radiation at 40 kV and 40 mA over the range of 2θ=5°-90°. The morphology of the samples was observed with scanning electron microscopy (SEM), using a JEOL JSM-7500F field emission scanning microscope. UV-Vis spectroscopy was recorded on an

Evolution 300 spectrophotometer equipped with a Labsphere diffuse reflectance accessory, with a reflectance spectra of range 200-800nm.

E.2.3 Photocatalytic Activity Test

The visible-light-driven photocatalytic activities of as-prepared pure ZnO and BiOBr/ZnO composites were measured by the degradation of *Rhodamine B* (RhB). As for the photocatalytic reactor, the light source was a 300W halogen tungsten projector lamp (Ushio) with a 410 nm UV cut-off filter (Kenko Zeta, transmittance > 90%) to ensure the wavelength attributed to the visible-light range. The distance between the irradiation source and the beaker was 10 cm, and the irradiation intensity was measured by a quantum meter (Biospherical QSL-2100, 400 nm<λ<700 nm) to be 1.1×10^{-2} Einsteins m^{-2} s^{-1}. In each batch, 0.1 g of the photocatalyst and 200 mL RhB aqueous solution with a concentration of 10 mg/m^3 were added into the beaker with a cooling jacket outside which could control the reaction temperature at around 25°C by a cooling/heating recirculating system. Before starting the photocatalytic reaction, the solution was magnetically stirred in the dark for 30 min to reach the adsorption-desorption equilibrium between the photocatalyst and dye RhB. Then, the solution was exposed to the visible light irradiation under constant magnetic stirring. 1 mL of solution was collected and centrifuged before and after the dark reaction process and at every 10 min interval, the concentration of which was tested by a Genysys 10-UV spectrophotometer (Geneq Lnc.) with the peak adsorption of RhB at 554 nm. A measured calibration curve was used to determine the RhB concentration from the absorbance shown in Fig. E.1.

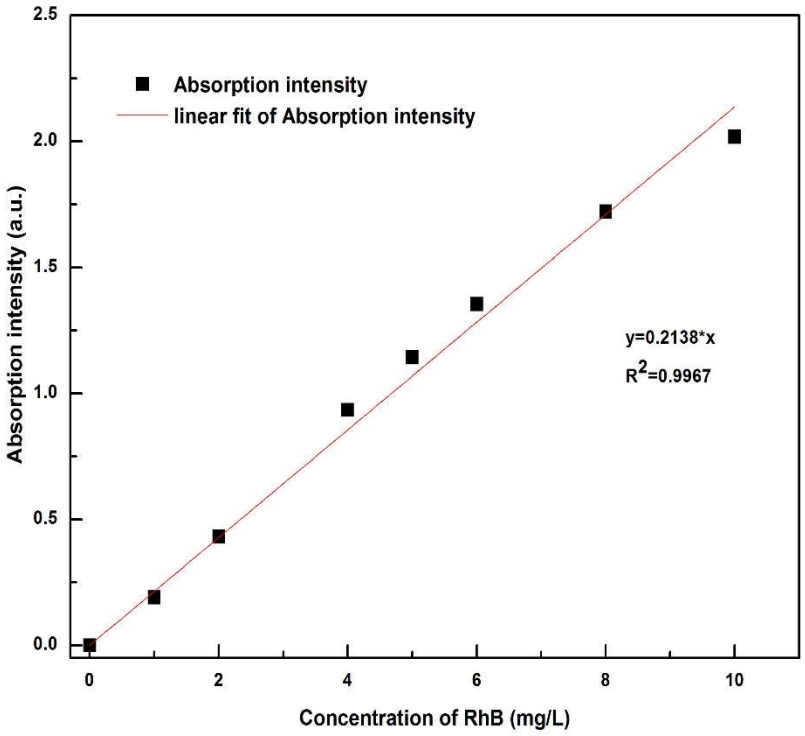


Figure E.1 Calibration curve of plotting absorption intensities at various concentration of RhB.

The linear relationship between the absorption intensity (A) and the concentration of RhB (c) could be expressed by *Eq. 1*:

$$A = 0.2138 \times c \quad (R^2=0.9967) \qquad \textbf{(Eq. 1)}$$

The linear relationship could be ascribed to the dilute solution which fulfills the conditions of the Beer-Lambert law, in which the absorption intensity is proportional to the concentration of the solution. Based on this theory (*Eq. 2*), the concentration of RhB could be determined by detecting the absorption intensity of the solution using a UV-Vis spectrometer.

$$\omega_{Degradation\ efficiency} = \frac{c_o - c_t}{c_o} \times 100\% = \frac{\frac{A_0}{0.2138} - \frac{A_t}{0.2138}}{\frac{A_0}{0.2138}} \times 100\% = \frac{A_o - A_t}{A_o} \times 100\% \qquad \textbf{(Eq. 2)}$$

E.3 Results and discussions

E.3.1 XRD analysis

The XRD patterns of pure ZnO, BiOBr, and 5 *wt.*% BiOBr-ZnO, 10 *wt.*%-ZnO, 15 *wt.*% BiOBr-ZnO, 25 *wt.*% BiOBr-ZnO, 50 *wt.*% BiOBr-ZnO and 75 *wt.*% BiOBr-ZnO composites synthesized by the hydrothermal method are shown in Fig. E.2. The characteristic peaks of both ZnO and BiOBr were in good agreement with the standard JCPDS cards (36-1451) and (09-0393) which suggested the crystal forms of hexagonal wurtzite ZnO and tetragonal crystal structure of BiOBr [12, 13]. No other impurity peaks were found, which indicated the high purity, and the sharp characteristic peaks proved high crystallinity of the samples. Meanwhile, with increasing amounts of BiOBr in the composites, the characteristic peaks of BiOBr came out gradually, especially the peaks at 10.9°, 25.2°, 31.7° and 32.2° in good accordance with the (001), (101), (102) and (110) facets. It should also be noted that the characteristic peaks of ZnO were not influenced, which indicated that the crystal structure of ZnO was not destroyed by the BiOBr dopant.

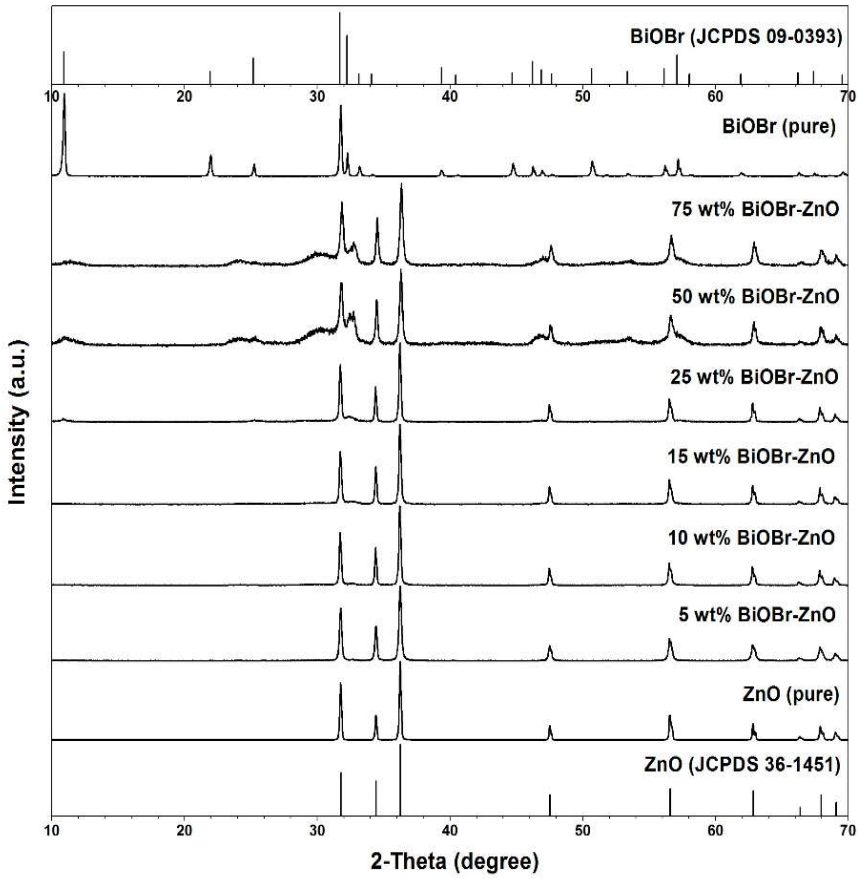
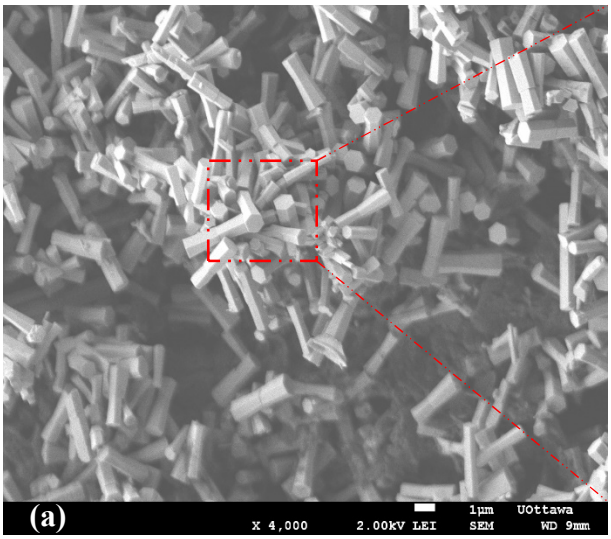


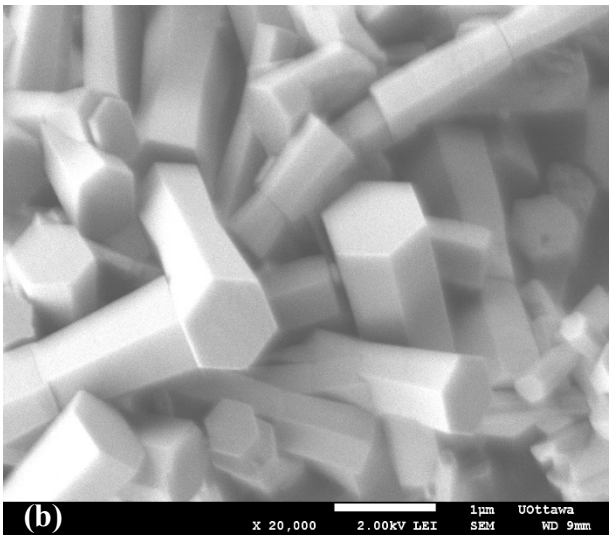
Figure E.2 XRD patterns of pure ZnO, BiOBr, and 5* wt.*% BiOBr-ZnO, 10* wt.*%-ZnO, 15* wt.*% BiOBr-ZnO, 25* wt.*% BiOBr-ZnO, 50* wt.*% BiOBr-ZnO and 75* wt.*% BiOBr-ZnO composites synthesized by hydrothermal method.

E.3.2 SEM analysis

SEM images of pure ZnO, BiOBr and 50 *wt.*% BiOBr-ZnO composites at low and high magnification are shown in Fig. E.3. The hourglass-like structure was found at about 3 μm in length and 0.5 μm in diameter for pure ZnO in Fig. E.3 (a) and (b), which was novel, and a similar structure was reported in [14-16]. As for the formation process, ZnO with wurtzite structure initially nucleates a truncated hexagonal pyramid, and another unit would gradually grow on the (001) plane of it. Finally, the coupled hourglass-like structures were formed as shown in Fig. E.4. Pure BiOBr synthesized by the hydrothermal method had the nano-plate structure as shown in Fig. E.3 (e) and (f). Meanwhile, by doping BiOBr in the composites, the regular structures were partially destroyed as shown in Fig. E.3 (c)

and (d). It exhibited many more defects in the polar planes on which some hollow sections were clearly observed. This kind of phenomenon could be caused by the Oswald ripening process [17-19], which could be expressed as aiming to minimize the total Gibbs energy of crystallites. The smaller particles with higher interfacial energy, which lead to larger total Gibbs energy, are much more soluble and could be redisposed to form larger particles. In this work, the inner crystallites with normally small particle sizes were formed early at the nucleation stage and started dissipating in the aqueous solution, leaving the interior space and forming the hollow structure. It is supposed to be the reason some cavities were found in Fig. E.3 (c) and (d). It should also be noted that the size of the crystallite was decreased to lower than 1 μm when doped by BiOBr compared with about 3 μm of the pure ZnO. When the amount of BiOBr in the composites increased to 50 wt.%, much more flake-like structures were found as shown in Fig. E.3 (c) and (d), especially in the SEM images at high magnifications (*i.e.* Fig. E.3d). Apparently, the flake-like BiOBr was closely contacted with hourglass-like ZnO. The length and diameter of the coupled truncated hexagonal pyramid and the microsphere were both around 1 μm. Meanwhile, the proposed formation process of BiOBr-ZnO composites were schemed in Fig. E.4.





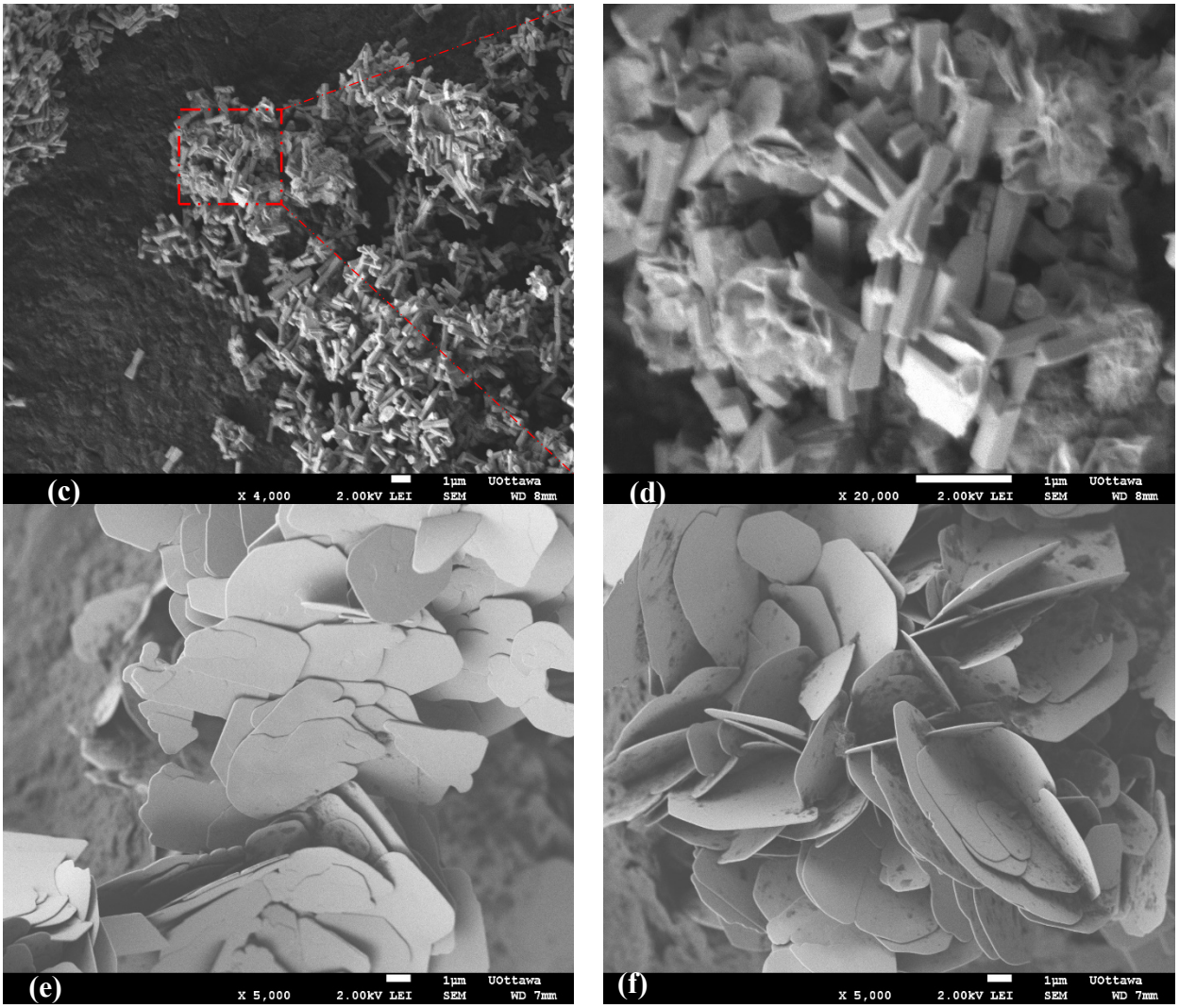


Figure E.3 SEM images of pure ZnO at low (a) and high (b) magnification, 50* wt. *% BiOBr-ZnO composites at low (c) and high (d) magnification, and pure BiOBr from different direction (e, f).

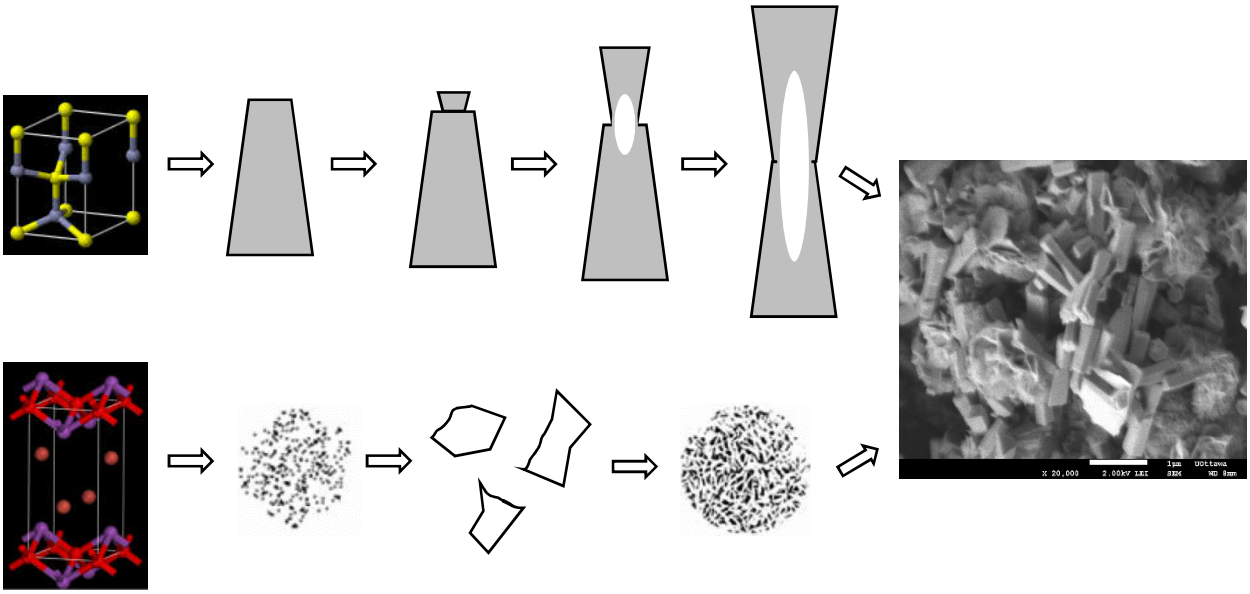
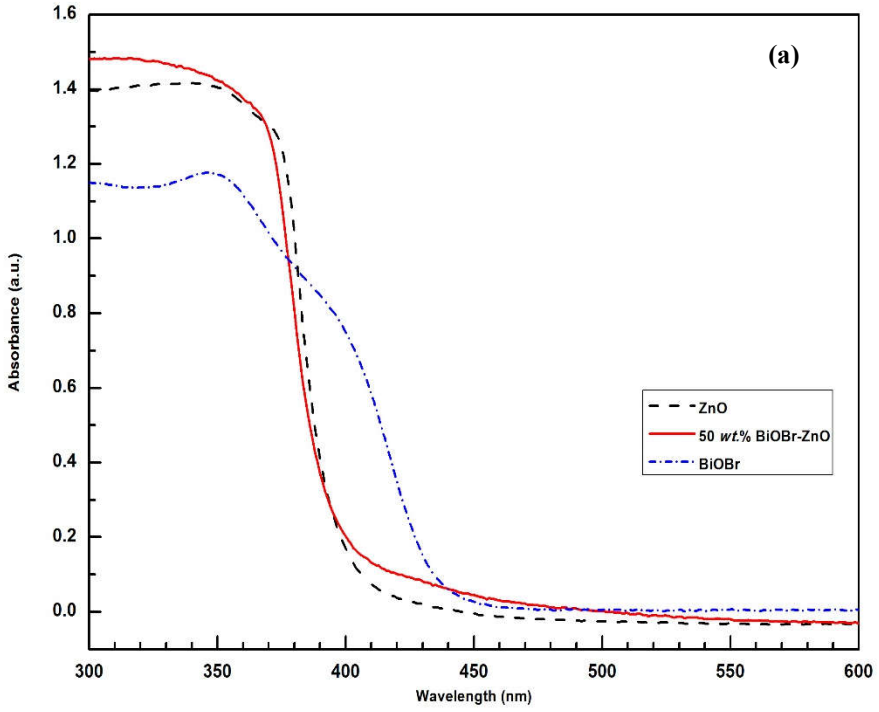


Figure E.4 Possible formation processes of hourglass-like ZnO (adapted from [14]), flake-like microspheres (adapted from [20]), and the SEM image of final BiOBr-ZnO composite.

E.3.3 UV-Vis diffuse reflection spectra (DRS)



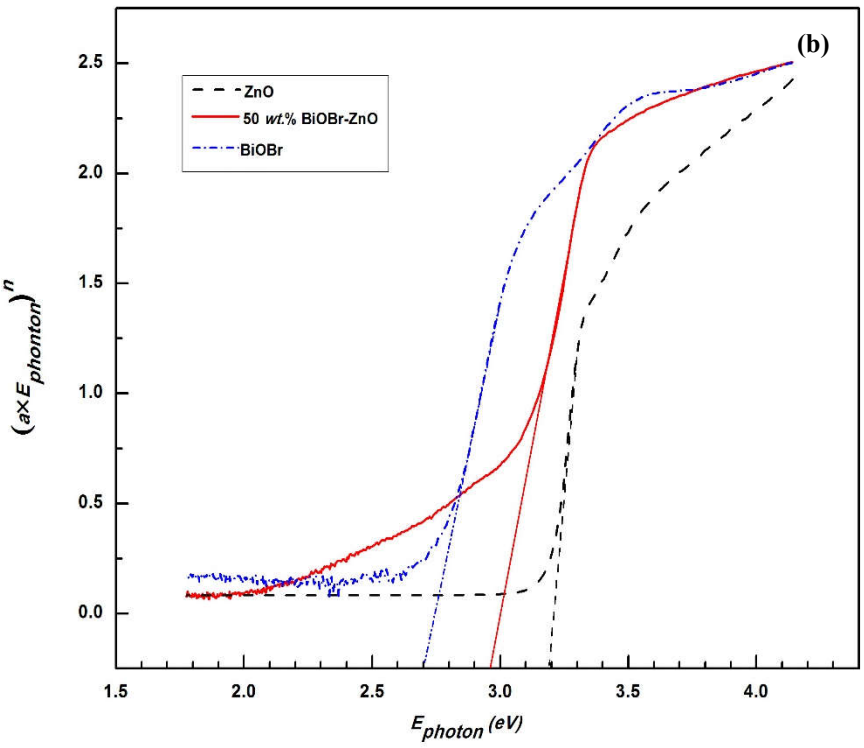


Figure E.5 (a) Diffused reflectance spectra (DRS) and (b) (α*E_{photon})^n-E_{photon} curves of pure ZnO and 50 wt.% BiOBr-ZnO composites.

The optical properties of pure ZnO and BiOBr-ZnO composites were performed by UV-Vis diffuse reflection spectra (DRS), which were shown in Fig. E.5. A sharp decrease existed with increasing irradiation wavelengths greater than a specific value in both of them, which resulted from the band-gap transition. The classical Tauc equation (*Eq. 3*) applies:

$$\alpha h\nu = A(h\nu - E_g)^n \qquad \textbf{(Eq. 3)}$$

It should be mentioned that α, A and n represent absorption coefficient, constant for semiconductors (equal to 1), and constant for type of semiconductor (n=2 for indirect band-gap semiconductor and n=1/2 for direct band-gap semiconductor, respectively) [21, 22]. It has been reported that ZnO attributed to the n-type direct band-gap semiconductor as shown in Fig. E.6 (left) [23], and BiOBr attributed to the p-type indirect band-gap semiconductor as simulated and shown in Fig. E.6 (right) [24]. So n=1/2 was definitely implemented in the calculation of the band-gap value of pure ZnO, and in this work n=2 was assumed to calculate the band gap of BiOBr-ZnO composites. The illustration in Fig. E.5 demonstrated the band gap values by plotting the tangent line. Band gap of the as-

prepared pure ZnO was estimated at about 3.2 eV, in good accordance with other reported works [3]. Via doping BiOBr (50 *wt*.%) on ZnO, the band gap was narrowed to about 2.95 eV, which means irradiation with wavelengths lower than 420 nm could induce the photocatalytic reaction.

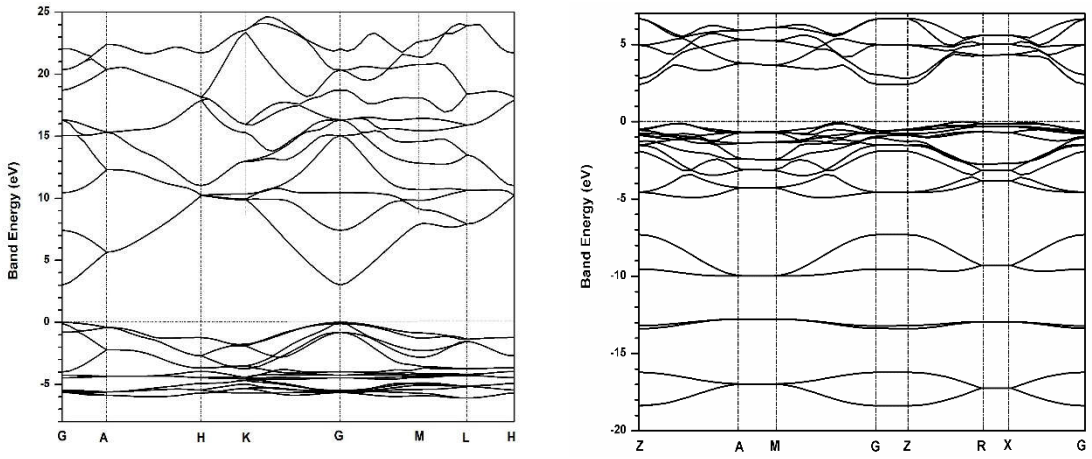


Figure E.6 Band structure of ZnO (left) and BiOBr (right). (simulated by using Quantum Espresso [25]).

E.3.4 Photocatalytic activity

The photocatalytic activities of pure ZnO and BiOBr-ZnO composites were evaluated by the degradation of *Rhodamine B* under visible light irradiation, results of which are shown in Fig. E.7. Two control tests were performed to account for the effects of photolysis and adsorption on the photocatalytic degradation of RhB. Results showed that 2.5% of the RhB reduction was caused by photolysis while 3.5 % by adsorption in the first 90 min of the control runs. An adsorption-desorption balance between the pollutants and the catalysts was obtained after 30 min. So, at the start of the photocatalytic process, pre-treatment of the reaction system for 30 min in the dark was needed to minimize the adsorption effect. As for the photocatalytic performance, the degradation efficiency for pure ZnO was just 6 % after 90 min. It might be due to the unsuitable band gap of ZnO under visible-light-induced conditions. In other words, ZnO was hard to stimulate by visible-light irradiation. By doping with BiOBr, the photocatalytic performances were significantly enhanced. Particularly, with increase of BiOBr in the composites from 5 *wt*.% to 50 *wt*.%, the degradation efficiency was improved from 6.5% to 97.0% in 90 min. The great

improvement when doping with BiOBr was ascribed to both the high activity of BiOBr and the enhancement effect of the heterojunction, as the degradation efficiency of 50 *wt.*% BiOBr-ZnO was higher than that of pure BiOBr. However, when the amount of BiOBr reached 75*wt.*% in composites, the degradation efficiency was reduced to 85.5% which was lower than that of 50 *wt.*% BiOBr-ZnO. It might because excess BiOBr cover on the heterojunction structure so as to deteriorate its enhancement effect. To further explore the reaction kinetics, pseudo-first order theory was applied in this system via plotting $ln(c_o/c)$ *vs t* shown Fig. E.8 [26]. The perfect linear relationship proved the feasibility of using this model [27]. The reaction rate constant in each system was shown in Table E.1. While BiOBr was below 50 wt% in the composites, increasing the amount of BiOBr resulted in a higher reaction rate in the system. It decreased when the amount of BiOBr reached 75 *wt.*%. This means the reaction rate was significantly enhanced with the BiOBr dopant compared with only implementing pure ZnO, and there exists an optimum value, in this work, at around 50 *wt.*% with the highest reactive activity.

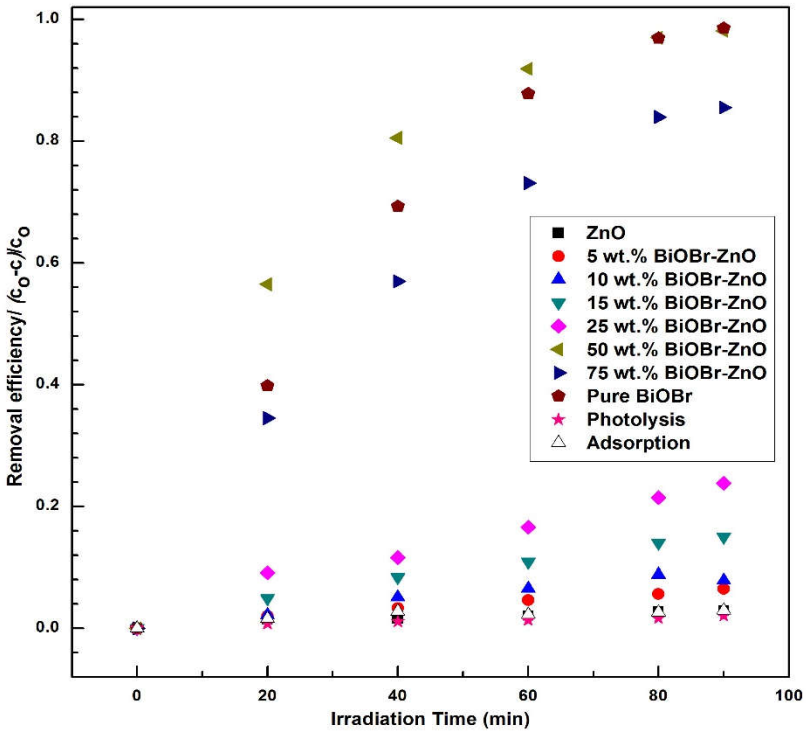


Figure E.7 Photocatalytic degradation efficiencies of RhB as a function of time by loading various photocatalysts. (Dosage amount of photocatalysts: 0.5 g/L, initial concentration of RhB: 10 mg/L and temperature of the system: 25 °C)

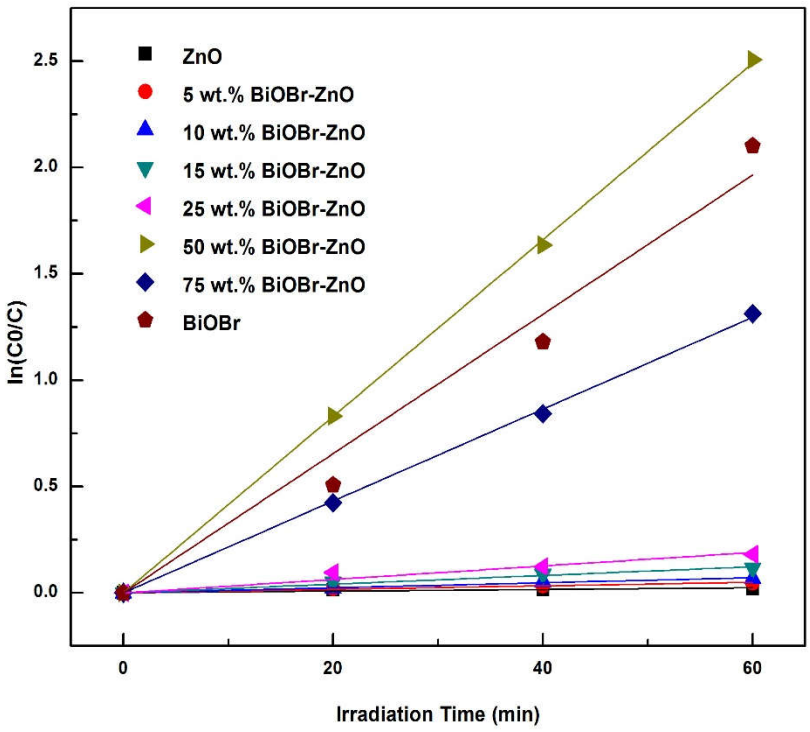


***Figure E.8 Kinetics for each photocatalytic process by plotting* ln(c_o/c) vs time.**

Table E.1 Pseudo-first order reaction rate constant (k) for various processes, respectively.

Composites	k (10^{-3}min^{-1})	R^2
ZnO	0.39	0.9288
5 *wt.*% BiOBr-ZnO	0.82	0.9935
10 *wt.*% BiOBr-ZnO	1.18	0.9933
15 *wt.*% BiOBr-ZnO	2.05	0.9903
25 *wt.*% BiOBr-ZnO	3.17	0.9739
50 *wt.*% BiOBr-ZnO	4.15	0.9999
75 *wt.*% BiOBr-ZnO	2.16	0.9996
BiOBr	3.28	0.9875

The cut-off has been used to ensure the wavelength of incident light was larger than 400 nm, so that only visible light contribute to the photocatalytic process. Fig. E.9 shows photocatalytic degradation efficiencies of the system with and without cut-off. After 20 min, the degradation efficiencies of RhB reached 56.5% and 68.1% in the system with and

without cut-off, respectively. The difference indicates that the additional reactions due to the short wavelength radiations were significant for the illumination source used.

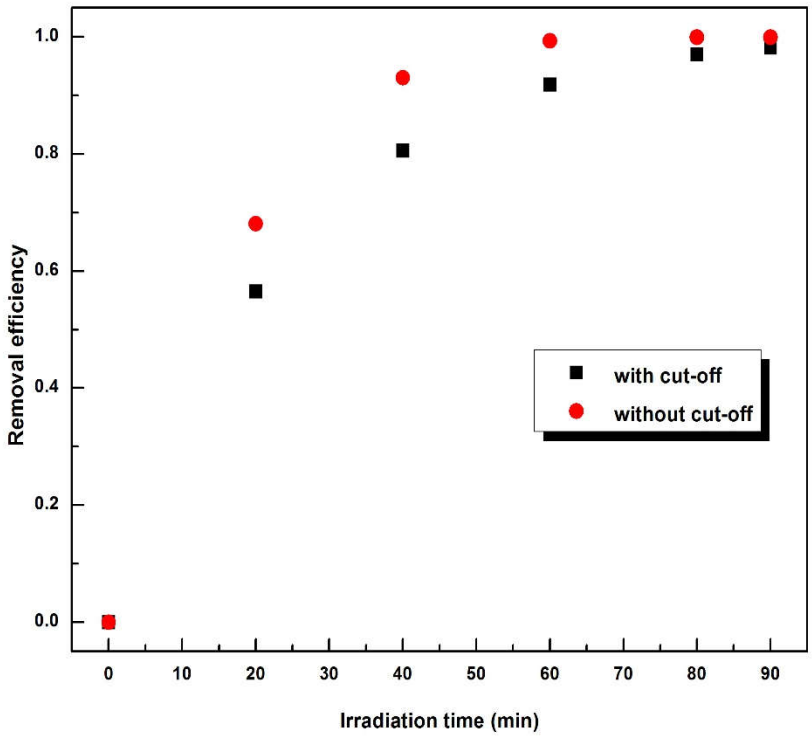


Figure E.9 Photocatalytic degradation efficiencies of RhB with or without cut-off. (Dosage amount of photocatalysts: 0.5 g/L, initial concentration of RhB: 10 mg/L and temperature of the system: 25 °C)

Furthermore, aiming to explore the effect of heterojunction, 50 wt% BiOBr-ZnO composites were synthesized by the hydrothermal method and also by mechanical mixing to compare their effect on the degradation efficiency of RhB. (Fig. E.10). It was clearly observed that the heterojunction enhanced the photocatalytic degradation process, with the degradation efficiency improving from 65.0% to 100% in 90 min. The degradation efficiency of mechanically mixed composites was just approximately the mathematical mean of that when using pure BiOBr and ZnO. This phenomenon proved that each of them reacted individually and without enhancement by heterojunction. It could also be regarded as solid evidence to prove the successful establishment of heterojunction in the BiOBr-ZnO composites synthesized in this work.

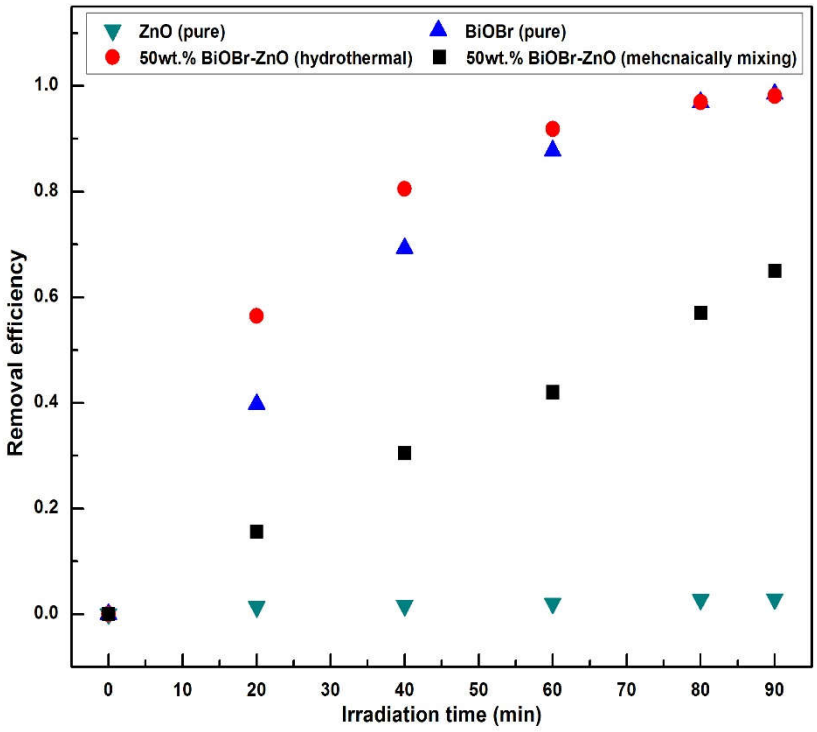


Figure E.10 Removal efficiencies in degrading RhB by using 50 **wt.%** *BiOBr-ZnO synthesized by hydrothermal method and mixed mechanically.*

E.4 Discussions and conclusions

E.4.1 Mechanism of the enhancement effect

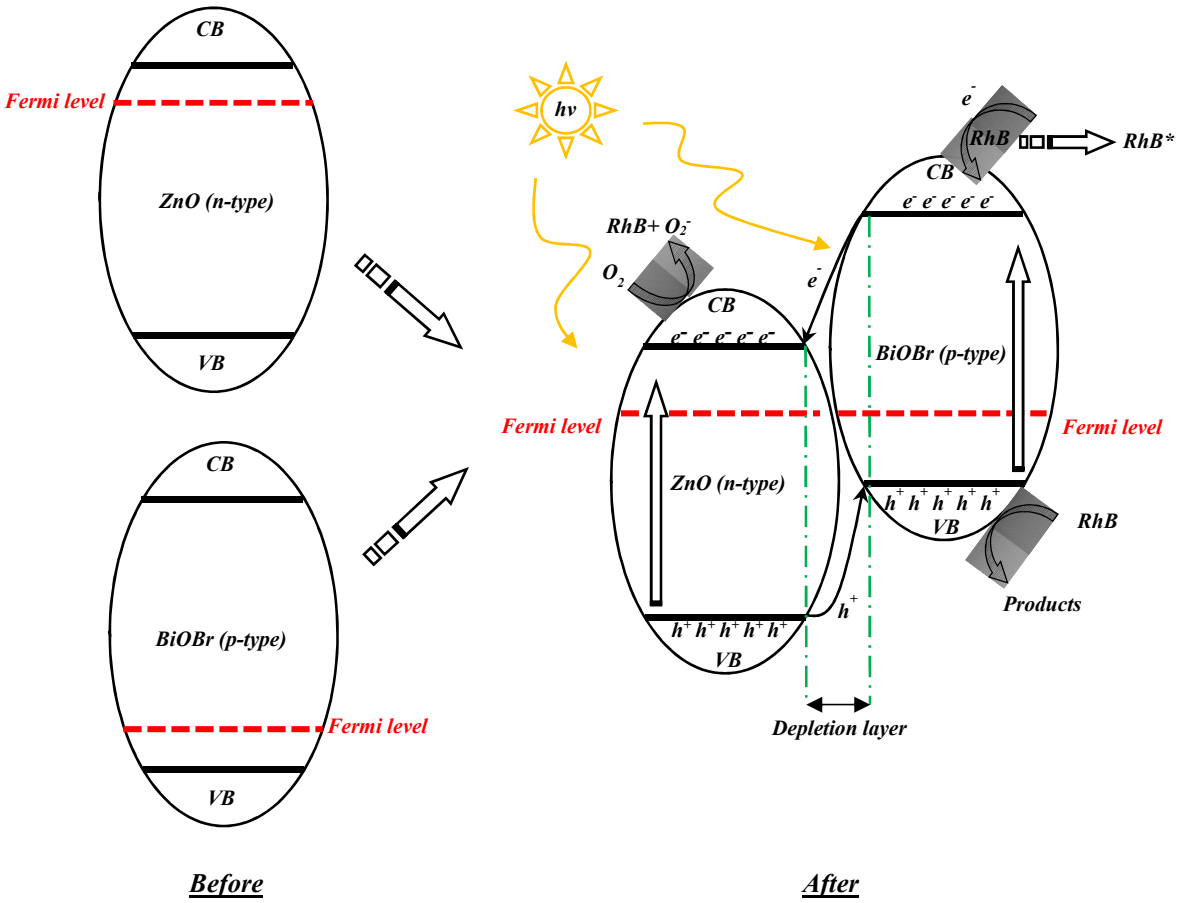


Figure E.11 Diagram of band structure for BiOBr/ZnO composite and the possible photocatalytic degradation process.

It has been reported that the E_{CB}, E_{VB} of p-type BiOBr and n-type ZnO were 0.8 eV, 0.85 eV and 3.5 eV, 3.9 eV, respectively, which has been depicted in Fig. E.11 [11]. The type of band alignments at the semiconductor interface attribute to type II-staggered [9]. Naturally, an energy bias was generated to drive the separation of photo-generated electron-holes pairs [28]. Specifically, after irradiation stimulation, electrons and holes were produced by the photocatalytic effect. Driven by the bias generated at the depletion layer, electrons on the valence band of BiOBr could transfer to the valence band of ZnO; correspondingly, holes are accumulated on the conduction band of BiOBr. That kind of transfer, induced by p-n heterojunction, significantly prolongs the lifetime of electron-hole carriers and prevents the recombination of the electrons and holes. As a result, the performance of the BiOBr-ZnO photocatalysts was evidently enhanced. Moreover, the

RhB was also probably excited by the irradiation due to the photosensitivity effect, and extra electrons were generated which could jump to the conduction band of either BiOBr or ZnO [29]. As for the photocatalytic degradation of RhB, the photo-generated electrons and holes suffer from some secondary reactions to produce some high oxidative radicals. To be more specific, electrons react with adsorbed O_2 to generate $\bullet O_2^-$, and holes could not only directly degrade RhB but also indirectly react with H_2O to produce the •OH which was regarded as the main species in the decomposition.

E.4.2 Conclusion

In summary, pure hexaganol wurtzite ZnO was successfully synthesized and doped with BiOBr to establish the p-n heterojunction by the facile hydrothermal method. Using the XRD and SEM analysis, the main crystal structure of ZnO was not destroyed and the hourglass-like structure was observed for the samples. As-prepared BiOBr-ZnO composites exhibited high photocatalytic activities in the degradation of RhB under visible-light irradiation. It has been significantly enhanced by the BiOBr dopant, and the possible mechanism of the enhancement effect by establishing p-n heterojunction was also explored and discussed. This work shed light on a feasible approach in improving the photocatalytic activity via p-n heterojunction.

References

1. Amy L. Linsebigler, Guangquan Lu and John T. Yates, "Photocatalysis on TiO_2 Surfaces: Principles, Mechanisms, and Selected Results," *Chemical Reviews*, vol. 95, no. 3, pp. 735-758, 1995.

2. Akira Fujishima and Kenichi Honda, "Electrochemical photolysis of water at a semiconductor electrode," *nature*, vol. 238, pp. 37-38, 1972.

3. Michael R. Hoffmann, Scot T. Martin, Wonyong Choi and Detlef W. Bahnemann, "Environmental Applications of Semiconductor Photocatalysis," *Chemical Reviews*, vol. 95, no. 1, pp. 69-96, 1995.

4. S. Girish Kumar and L. Gomathi Devi, "Review on Modified TiO_2 Photocatalysis under UV/Visible Light: Selected Results and Related Mechanisms on Interfacial Charge Carrier Transfer Dynamics," *The Journal of Physical Chemistry A*, vol. 115, no. 46, pp. 13211-

13241, 2011.

5. Issei Tsuji, Yoshiki Shimodaira, Hideki Kato, Hisayoshi Kobayashi and Akihiko Kudo, "Novel Stannite-type Complex Sulfide Photocatalysts A^{I2}-Zn-A^{IV}-S_4 (A^I = Cu and Ag; A^{IV} = Sn and Ge) for Hydrogen Evolution under Visible-Light Irradiation," *Chemistry of Materials*, vol. 22, no. 4, pp. 1402-1409, 2010.

6. J. Yu, S. Zhuang, X. Xu, W. Zhu, B. Feng and J. Hu, "Photogenerated electron reservoir in hetero-p-n CuO-ZnO nanocomposite device for visible-light-driven photocatalytic reduction of aqueous Cr(vi)," *Journal of Materials Chemistry A*, vol. 3, no. 3, pp. 1199-1207, 2015.

7. Y. Peng, M. Yan, Q. G. Chen, C. M. Fan, H. Y. Zhou and A. W. Xu, "Novel one-dimensional Bi_2O_3-Bi_2WO_6 p-n hierarchical heterojunction with enhanced photocatalytic activity," *Journal of Materials Chemistry A*, vol. 2, no. 22, pp. 8517-8524, 2014.

8. Dhananjay S. Bhatkhande, Vishwas G. Pangarkar and Anthony ACM Beenackers, "Photocatalytic degradation for environmental applications – a review," *Journal of Chemical Technology & Biotechnology*, vol. 77, no. 1, pp. 102-116, 2002.

9. Edward T. Yu, James O. McCaldin and Thomas C. McGill, "Band Offsets in Semiconductor Heterojunctions," in *Solid State Physics*, E. Henry and T. David, Ed., pp. 1-146, Academic Press, 1992.

10. Hefeng Cheng, Baibiao Huang, Zeyan Wang, Xiaoyan Qin, Xiaoyang Zhang and Ying Dai, "One-Pot Miniemulsion-Mediated Route to BiOBr Hollow Microspheres with Highly Efficient Photocatalytic Activity," *Chemistry – A European Journal*, vol. 17, no. 29, pp. 8039-8043, 2011.

11. Fangfang Duo, Yawen Wang, Xiaoming Mao, Caimei Fan and Hui Zhang, "Double Br sources fabrication and photocatalytic property of p-n junction BiOBr/ZnO composites for phenol removal," *Crystal Research and Technology*, vol. 49, no. 9, pp. 721-730, 2014.

12. Lang Chen, Rui Huang, Miao Xiong, Qing Yuan, Jie He, Jing Jia, Meng-Yuan Yao, Sheng-Lian Luo, Chak-Tong Au and Shuang-Feng Yin, "Room-Temperature Synthesis of Flower-Like BiOX (X ═ Cl, Br, I) Hierarchical Structures and Their Visible-Light Photocatalytic Activity," *Inorganic Chemistry*, vol. 52, no. 19, pp. 11118-11125, 2013.

13. Baruah Sunandan and Dutta Joydeep, "Hydrothermal growth of ZnO nanostructures," *Science and Technology of Advanced Materials*, vol. 10, no. 1, pp. 013001, 2009.

14. Da Zhang, Jing Li, Yun Chen, Qing-Sheng Wu and Ya-Ping Ding, "One-pot preparation and enhanced photocatalytic and electrocatalytic activities of ultralarge Ag/ZnO hollow coupled structures," *CrystEngComm*, vol. 14, no. 20, pp. 6738-6743, 2012.

15. Ke Xin Yao, Romilly Sinclair and Hua Chun Zeng, "Symmetric Linear Assembly of Hourglass-like ZnO Nanostructures," *The Journal of Physical Chemistry C*, vol. 111, no. 5, pp. 2032-2039, 2007.

16. Deliang Li, Jing Wang, Xu Wu, Caixia Feng and Xiaohong Li, "Ultraviolet-assisted synthesis of hourglass-like ZnO microstructure through an ultrasonic and microwave combined technology," *Ultrasonics Sonochemistry*, vol. 20, no. 1, pp. 133-136, 2013.

17. Bin Liu and Hua Chun Zeng, "Symmetric and Asymmetric Ostwald Ripening in the Fabrication of Homogeneous Core–Shell Semiconductors," *Small*, vol. 1, no. 5, pp. 566-571, 2005.

18. Hua Chun Zeng, "Synthesis and self-assembly of complex hollow materials," *Journal of Materials Chemistry*, vol. 21, no. 21, pp. 7511-7526, 2011.

19. Christopher C. Yec and Hua Chun Zeng, "Synthesis of complex nanomaterials via Ostwald ripening," *Journal of Materials Chemistry A*, vol. 2, no. 14, pp. 4843-4851, 2014.

20. Xi Zhang, Zhihui Ai, Falong Jia and Lizhi Zhang, "Generalized One-Pot Synthesis, Characterization, and Photocatalytic Activity of Hierarchical BiOX (X = Cl, Br, I) Nanoplate Microspheres," *The Journal of Physical Chemistry C*, vol. 112, no. 3, pp. 747-753, 2008.

21. Chien-Yie Tsay, Kai-Shiung Fan, Sih-Han Chen and Chia-Hao Tsai, "Preparation and characterization of ZnO transparent semiconductor thin films by sol–gel method," *Journal of Alloys and Compounds*, vol. 495, no. 1, pp. 126-130, 2010.

22. D. C. Reynolds, D. C. Look and B. Jogai, "Optically pumped ultraviolet lasing from ZnO," *Solid State Communications*, vol. 99, no. 12, pp. 873-875, 1996.

23. Janotti Anderson and G. Van de Walle Chris, "Fundamentals of zinc oxide as a

semiconductor," *Reports on Progress in Physics*, vol. 72, no. 12, pp. 126501, 2009.

24. Jiexiang Xia, Jun Di, Sheng Yin, Huaming Li, Hui Xu, Li Xu, Huoming Shu and Minqing He, "Solvothermal synthesis and enhanced visible-light photocatalytic decontamination of bisphenol A (BPA) by g-C_3N_4/BiOBr heterojunctions," *Materials Science in Semiconductor Processing*, vol. 24, no. 0, pp. 96-103, 2014.

25. Giannozzi Paolo, Baroni Stefano, Bonini Nicola, Calandra Matteo, Car Roberto, Cavazzoni Carlo, Ceresoli Davide, L. Chiarotti Guido, Cococcioni Matteo, Dabo Ismaila, Corso Andrea Dal, Gironcoli Stefano de, Fabris Stefano, Fratesi Guido, Gebauer Ralph, Gerstmann Uwe, Gougoussis Christos, Kokalj Anton, Lazzeri Michele, Martin-Samos Layla, Marzari Nicola, Mauri Francesco, Mazzarello Riccardo, Paolini Stefano, Pasquarello Alfredo, Paulatto Lorenzo, Sbraccia Carlo, Scandolo Sandro, Sclauzero Gabriele, P. Seitsonen Ari, Smogunov Alexander, Umari Paolo and M. Wentzcovitch Renata, "QUANTUM ESPRESSO: a modular and open-source software project for quantum simulations of materials," *Journal of Physics: Condensed Matter*, vol. 21, no. 39, pp. 395502, 2009.

26. Xiangchao Meng and Zisheng Zhang, "Synthesis, Analysis, and Testing of BiOBr-Bi_2WO_6 Photocatalytic Heterojunction Semiconductors," *International Journal of Photoenergy*, vol. 2015, pp. 12, 2015.

27. W. S. Kuo and P. H. Ho, "Solar photocatalytic decolorization of methylene blue in water," *Chemosphere*, vol. 45, no. 1, pp. 77-83, 2001.

28. Liang Kong, Zheng Jiang, Henry H. Lai, Rebecca J. Nicholls, Tiancun Xiao, Martin O. Jones and Peter P. Edwards, "Unusual reactivity of visible-light-responsive AgBr–BiOBr heterojunction photocatalysts," *Journal of Catalysis*, vol. 293, no. 0, pp. 116-125, 2012.

29. Jiandong Zhuang, Wenxin Dai, Qinfen Tian, Zhaohui Li, Liyan Xie, Jixin Wang, Ping Liu, Xicheng Shi and Donghui Wang, "Photocatalytic Degradation of RhB over TiO_2 Bilayer Films: Effect of Defects and Their Location," *Langmuir*, vol. 26, no. 12, pp. 9686-9694, 2010.

Appendix F Plasmonic Z-Scheme Ag_2O-Bi_2MoO_6 p-n Heterojunction Photocatalysts with Greatly Enhanced Visible-light Responsive Activities

Xiangchao Meng and Zisheng Zhang

Materials Letters 189 (2017), 267-270

Abstract

Ag_2O-Bi_2MoO_6 p-n heterojunction photocatalysts were prepared via simple precipitation and photosynthesis processes. The prepared composites exhibited excellent photocatalytic activity in the removal of organic pollutants (Rhodamine B and phenol) from wastewater. The improved visible-light driven photocatalytic activity can be attributed to the existence of silver nanoparticles on the surface and to the establishment of p-n heterojunctions between Ag_2O (p-type semiconductor) and Bi_2MoO_6 (n-type semiconductor). This work sheds light on the importance of considering the semiconductor type (p/n- type) when forming composite photocatalysts and utilization of the SPR effect of nanoparticles on the photocatalysts surface.

F.1 Introduction

Photocatalysis is an advanced oxidative processes that has been widely applied in polluted air purification and wastewater treatment [1, 2]. How to efficiently utilize the photons in the visible light range has become an important issue. Recently, bismuth-based semiconductors have drawn people's attention due to their suitable band structure and controllable morphologies [3, 4]. The relatively high rate of photo-generated electron/hole recombination hinders their further application. Metal doping and heterojunction establishment have become two of the most effective methods for reducing this rate of

recombination [5, 6]. Ag_2O (p-type semiconductor) has been studied as a dopant (co-catalyst) in photocatalysis owing for its narrow band gap (1.3 eV). Z-scheme Ag_2O-$Bi_2O_2CO_3$ p-n heterojunctions were successfully synthesized with improved visible-light responsive activity [7, 8]. Through the surface plasmonic resonance effect, silver nanoparticles on the surface may further improve the visible-light harvesting capacity and photogenerated electrons/holes separation efficiency [9]. To the best of our knowledge, reports on the preparation of Ag_2O/Bi_2MoO_6 photocatalytic composites remain rare [10].

F.2 Experimental

F.2.1 Preparation of Bi_2MoO_6 and Ag_2O-Bi_2MoO_6

All chemicals were purchased from Fisher Scientific and used as received. Pure Bi_2MoO_6 was prepared by a hydrothermal method. Typically, 0.485 g of $Bi(NO_3)_3 \cdot 5H_2O$ were first dissolved in 5 mL acetic acid with magnetic stirring for 10 min, defined as solution A. 0.121g of $Na_2MoO_4 \cdot 2H_2O$ were separately dissolved in 30 mL distilled deionized water (DDW), defined as solution B. Solution B was then added dropwise into solution A and stirred for another 20 min. The mixture was transferred to a 45-mL Teflon-lined stainless steel autoclave (Parr Instrument Company) and heated at 120°C for 24h. After the autoclave was allowed to naturally cool down to room temperature, the Bi_2MoO_6 precipitates were filtered out and washed once with ethanol and twice with DDW. The washed powder samples were then dried at 60°C for 12h and collected.

Ag_2O-Bi_2MoO_6 composites were prepared by a precipitation and photosynthesis method. In a typical process, 0.30 g of the as-prepared Bi_2MoO_6 were added into 40 mL DDW. The pH of the suspension was adjusted to 11 by adding $NH_3 \cdot H_2O$. A designate amount of $AgNO_3$ was then dissolved in 10 mL DDW and added dropwise into the suspension. The solution was then magnetically stirred for 2h at room temperature. After stirring, the mixed suspension was irradiated for 30 min under a 300-W halogen tungsten projector lamp (Ushio). The resulting products were filtered out, washed three times with DDW, and dried at 60°C for 12h. The sample was then collected and labelled as x%Ag_2O-Bi_2MoO_6 (x = 5, 10, 15 and 20, weight ratio).

F.2.2 Characterization

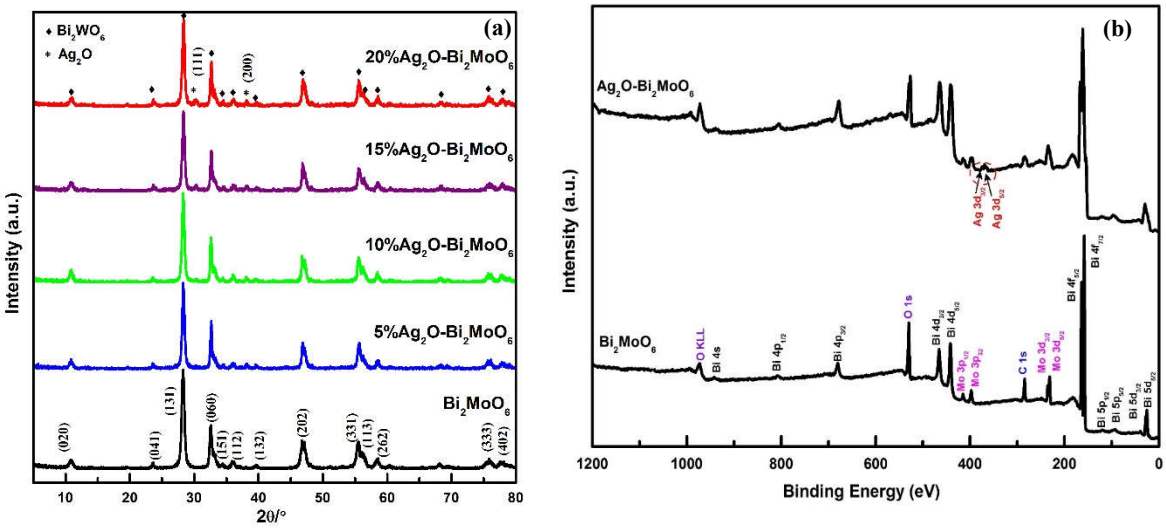
X-ray diffraction (XRD) analysis was performed on a Rigaku Ultima IV Diffractometer with Cu Kα radiation (λ = 0.15418 nm) at 40 kV and 44 mA. Elements and chemical states on the sample surface were measured using XSAM-800 X-ray Photoelectron Spectroscopy (XPS). Transmission electron microscopy (JEM-2100F, JEOL) was applied to study the morphologies of prepared samples. Optical properties of samples were investigated using the Thermo Evolution 300 spectrophotometer. Electrochemical properties of prepared samples were analyzed on a CHI 604E electrochemical analyzer (CH Instruments Inc., USA) with a platinum wire counter electrode, a calomel reference electrode, and a working electrode. The working electrode was an indium tin oxide (Sigma-Aldrich Canada Co.) glass coated with the prepared samples. Electrochemical impedance spectra (EIS) were recorded with frequency in the range of 1 - 1000000 Hz and a sinusoidal wave of 5 mV. The electrolyte was K_2SO_4 solution (0.5 mol/L).

F.2.3 Photocatalytic activity tests

The photocatalytic activity of prepared samples under visible light irradiation was investigated with regards to Rhodamine B (RhB) and phenol. A 500 mL beaker served as the reactor, and a cooling jacket was applied to maintain the temperature at around 20°C. The light source was a 300-W halogen tungsten projector lamp (Ushio) with a UV cut-off (Kenko Zeta, transmittance > 90%) to filter out irradiation with wavelengths below 410 nm. The irradiation intensity on the surface of the solution was measured by a quantum meter (Biospherical QSL-2100, $400 < \lambda < 700$ nm) and was found to be 1.1×10^{-2} Einsteins m^{-2} s^{-1}. In each test, 100 mL of RhB/phenol solution (10 mg/L) was mixed with 0.1 g prepared photocatalyst composites. The photocatalytic test was carried out for 90min for RhB and 5h for phenol, and aliquots were drawn. Supernatants were analyzed using a spectrometer (Genesys 10 UV) for RhB and a high-performance liquid chromatograph (HPLC, Agilent 1100 series) equipped with a UV-Vis detector for phenol. Scavengers including isopropanol for •OH, EDTA for h^+ and N_2 for $•O_2^-$ were used to analyze the roles of each species in the 15% Ag_2O-Bi_2MoO_6 photocatalysis system with regard to RhB.

F.3 Results and discussions

Fig. F.1a shows XRD patterns of prepared samples. All observed peaks were identified, indicating a well-crystalized structure of prepared samples. When Ag_2O was loaded on Bi_2MoO_6, peaks of Ag_2O with weak intensity were also observed. This suggests that Ag_2O was successfully combined with Bi_2MoO_6. The surface composites and chemical states of the prepared samples were also studied by XPS (Fig. F.1b, c and d). In the survey spectra, apparent differences between Bi_2MoO_6 and Ag_2O-Bi_2MoO_6 were found at the binding energy of 365~375 eV, which can be attributed to Ag. Ag 3d orbits were also scanned in order to further explore its chemical states (Fig. F.1d). Two sets of spin-orbit doublets were found, indicating that both metallic Ag (373.5 and 367.4 eV) and Ag^+ (374.5 and 368.4 eV) loaded onto the surface of Bi_2MoO_6 [11]. Additionally, in the O 1s orbits scan (Fig. F.1c), the peak located at binding energy of 533.1 eV may be assigned to the O in Ag_2O, which was not detected in pure Bi_2MoO_6.



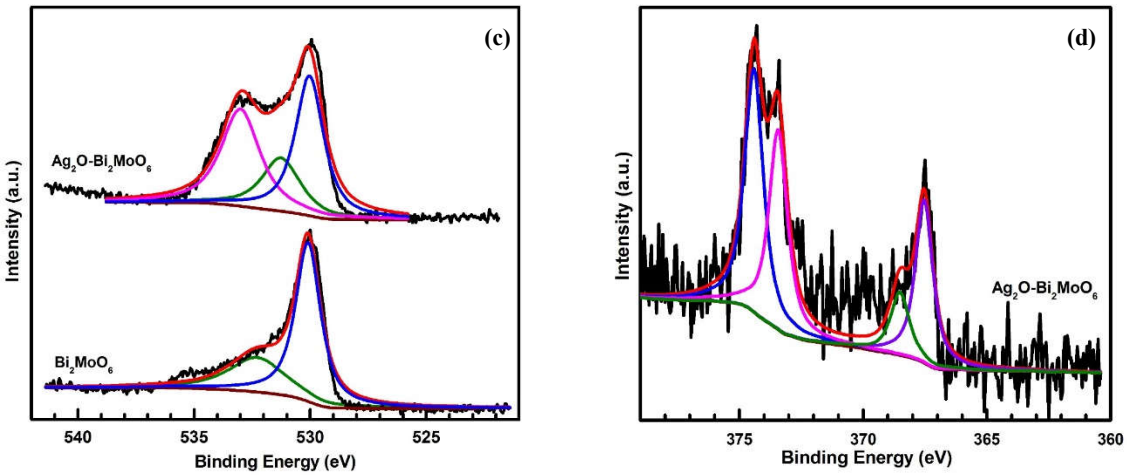


Figure F.1 (a) XRD patterns, (b) XPS survey spectrum, (c) O 1s orbits scan and (d) Ag 3d orbits scan of prepared samples.

The optical properties of prepared samples were measured by diffused reflectance spectrometry (Fig. F.2a). With the quantity of Ag_2O in the composites increased, the energy harvesting capacity in the visible-light range also increased. This may be due to the narrow band gap of Ag_2O (1.3 eV) and the surface plasmon resonance (SPR) of Ag nanoparticles loaded on the surface. The photocatalytic removal efficiency of RhB was greatly improved (Fig. F.2b) by adding Ag_2O. The highest photocatalytic activity occurred when the Ag_2O was doped at 15%. RhB was degraded step-by-step to rhodamine and possibly further to small species such as CO_2 and H_2O (Fig. F.2c) [12]. A great enhancement in degrading colorless phenol was also observed with the addition of Ag_2O (Fig. F.2d).

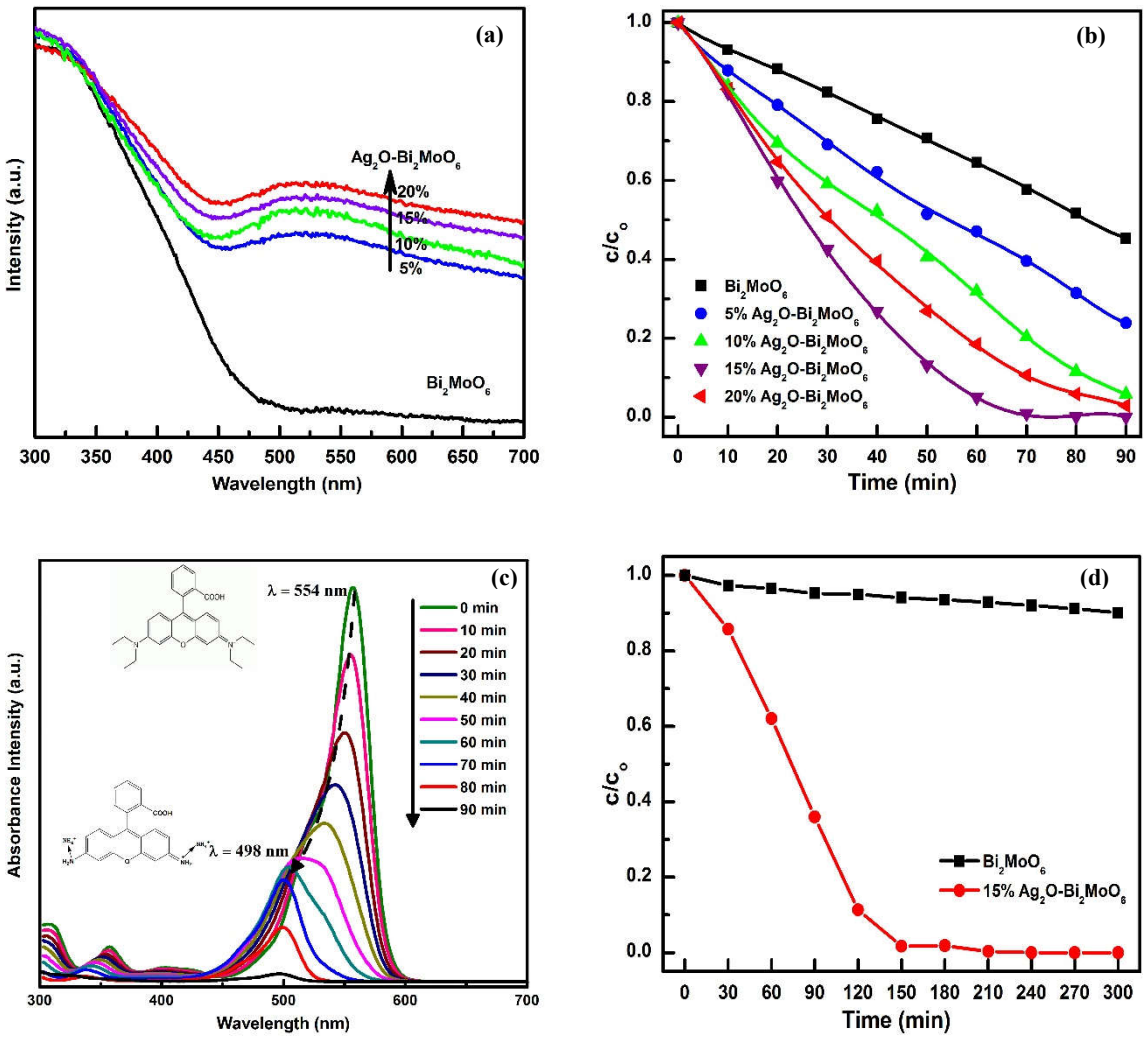


Figure F.2 (a) DRS of prepared samples, (b) RhB and (d) phenol removal profiles during photocatalytic degradation process, and (c) UV-Vis spectra of RhB samples taken during the degradation process.

The morphology of Ag_2O is shown in Fig. F.3a. Ag_2O with a size of about 10-15 nm were loaded onto plate-like Bi_2MoO_6 and silver nanoparticles were distributed on their surfaces. The interface charge separation efficiency was measured by EIS. The EIS Nyquist plots (Fig. F.3b) suggest that the photocatalytic degradation process may be a simple electrode reaction and photogenerated electron transfer, and the electron/hole separation efficiency of Bi_2MoO_6 was greatly improved with introduction of Ag_2O. This may be a result of p-n heterojunctions being successfully established between Ag_2O (p type) and Bi_2MoO_6 (n type) (Fig. F.3d). Specifically, photo-generated electrons accumulated on the conduction band

of Bi_2MoO_6 while holes gathered on the valence band of Ag_2O. Electrons may react with adsorbed oxygen to produce $\bullet O_2$. The free radicals as well as the holes on the valence band, the main active species for Ag_2O-Bi_2MoO_6 photocatalysis system (Fig. F.3c), are strong enough oxidants to oxidize organics in the solution.

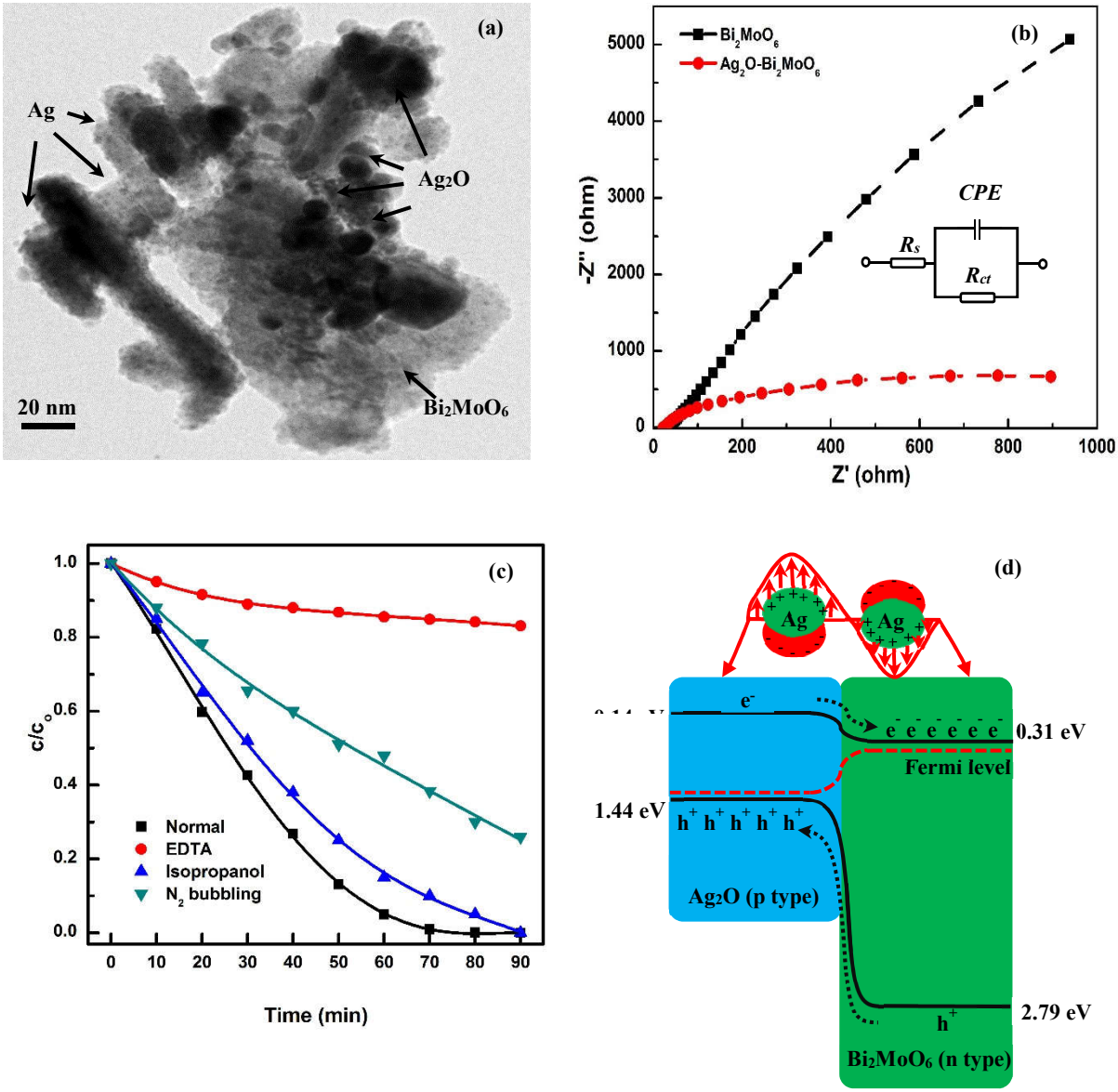


Figure F.3 (a) SEM image of 15%Ag_2O-Bi_2MoO_6, (b) EIS Nyquist plot of pure Bi_2MoO_6 and 15%Ag_2O-Bi_2MoO_6, (c) study of active species for 15% Ag_2O-Bi_2MoO_6 in photocatalysis and (d) proposed mechanism of the enhancement.

F.4 Conclusions

This work has described the successful preparation of Ag/Ag_2O doped Bi_2MoO_6 composites with greatly improved visible-light responsive activity. The enhancement may be a result of (1) silver nanoparticles on the surface with SPR effect improving the visible-light harvesting capacity, (2) p-n heterojunctions between Ag_2O and Bi_2MoO_6 increasing the separation efficiency of photogenerated charge carriers, and (3) metallic silver accelerating the charge separation. This work sheds light on the importance of considering the semiconductor type when forming composite photocatalysts and utilizing the SPR effect of nanoparticles on the photocatalysts surface.

References

1. Miguel Pelaez, Nicholas T Nolan, Suresh C Pillai, Michael K Seery, Polycarpos Falaras, Athanassios G Kontos, Patrick SM Dunlop, Jeremy WJ Hamilton, J Anthony Byrne and Kevin O'Shea, "A review on the visible light active titanium dioxide photocatalysts for environmental applications," *Applied Catalysis B: Environmental*, vol. 125, pp. 331-349, 2012.

2. Xiangchao Meng, Zisheng Zhang and Xingang Li, "Synergetic photoelectrocatalytic reactors for environmental remediation: A review," *Journal of Photochemistry and Photobiology C: Photochemistry Reviews*, vol. 24, pp. 83-101, 2015.

3. Xiangchao Meng and Zisheng Zhang, "Bismuth-based Photocatalytic Semiconductors: Introduction, Challenges and Possible Approaches," *Journal of Molecular Catalysis A: Chemical*, vol. 423, pp. 533-549, 2016.

4. Wei Chen, Guo-Rong Duan, Tian-Yu Liu, Shen-Ming Chen and Xiao-Heng Liu, "Fabrication of Bi_2MoO_6 nanoplates hybridized with g-C_3N_4 nanosheets as highly efficient visible light responsive heterojunction photocatalysts for Rhodamine B degradation," *Materials Science in Semiconductor Processing*, vol. 35, pp. 45-54, 2015.

5. Sittikorn Jonjana, Anukorn Phuruangrat, Titipun Thongtem and Somchai Thongtem, "Synthesis, analysis and photocatalysis of $AgBr/Bi_2MoO_6$ nanocomposites," *Materials Letters*, vol. 172, pp. 11-14, 2016.

6. Dingning Ke, Huajun Liu, Tianyou Peng, Xun Liu and Ke Dai, "Preparation and photocatalytic activity of WO_3/TiO_2 nanocomposite particles," *Materials Letters*, vol. 62, no. 3, pp. 447-450, 2008.

7. Na Liang, Min Wang, Lun Jin, Shoushuang Huang, Wenlong Chen, Miao Xu, Qingquan He, Jiantao Zai, Nenghu Fang and Xuefeng Qian, "Highly Efficient $Ag_2O/Bi_2O_2CO_3$ p-n Heterojunction Photocatalysts with Improved Visible-Light Responsive Activity," *ACS Applied Materials & Interfaces*, vol. 6, no. 14, pp. 11698-11705, 2014.

8. Miao Xu, Lei Han and Shaojun Dong, "Facile Fabrication of Highly Efficient g-C_3N_4/Ag_2O Heterostructured Photocatalysts with Enhanced Visible-Light Photocatalytic Activity," *ACS Applied Materials & Interfaces*, vol. 5, no. 23, pp. 12533-12540, 2013.

9. Yiqiong Yang, Hongxin Li, Fulin Hou, Jingyi Hu, Xiaodong Zhang and Yuxin Wang, "Facile synthesis of ZnO/Ag nanocomposites with enhanced photocatalytic properties under visible light," *Materials Letters*, vol. 180, pp. 97-100, 2016.

10. Junlei Zhang, Huan Liu and Zhen Ma, "Flower-like Ag_2O/Bi_2MoO_6 p-n heterojunction with enhanced photocatalytic activity under visible light irradiation," *Journal of Molecular Catalysis A: Chemical*, vol. 424, pp. 37-44, 2016.

11. Xiangchao Meng and Zisheng Zhang, "Ag/AgCl Loaded Bi_2WO_6 Composite: A Plasmonic Z-Scheme Visible Light-Responsive Photocatalyst," *International Journal of Photoenergy*, vol. 2016, pp. 11, 2016.

12. Xiangchao Meng and Zisheng Zhang, "Facile synthesis of $BiOBr/Bi_2WO_6$ heterojunction semiconductors with high visible-light-driven photocatalytic activity," *Journal of Photochemistry and Photobiology A: Chemistry*, vol. 310, no. 0, pp. 33-44, 2015.

Appendix G Bi_2MoO_6 Co-modified by Reduced Graphene Oxide and Palladium (Pd^{2+} and Pd^0) with Enhanced Photocatalytic Decomposition of Phenol

Xiangchao Meng and Zisheng Zhang

Applied Catalysis B: Environmental 209 (2017), 383-393

Abstract

A ternary Bi_2MoO_6 photocatalyst composite was hybridized for the first time, with reduced graphene oxide (rGO) and palladium (Pd) nanoparticles decorated on the surface. As-prepared composites exhibited excellent photocatalytic activity in the degradation of organic pollutants (phenol) in wastewater under visible light irradiation. The enhanced photocatalytic performance when rGO and Pd nanoparticles combined with Bi_2MoO_6 may be attributed to the reduction of the recombination rate of photogenerated electrons/holes. Specifically, the rGO layer may serve as the electron accepter, which means photogenerated electrons can rapidly transfer to its surface instead of jumping back to the valence band and combining with positive holes. Additionally, the black-body property of graphite-like material contribute the increased harvesting capacity of visible-light photons. Furthermore, palladium nanoparticles distributed on the surface can also be stimulated by visible light photons due to the surface plasmon resonance effect, which further increased the utilization efficiency of visible light irradiation. This work opens a new possibility for efficient removal of phenolic compounds in wastewater via visible light-driven photocatalysis in the presence of a Pd-rGO- Bi_2MoO_6 ternary composite.

G.1 Introduction

Bismuth-based visible light-driven photocatalysts have attracted extensive interests of researchers, and have exhibited strong potential for industrialization from an economic stand-point compared to the most widely studied UV-driven photocatalysts, such as TiO_2 [1-4]. Two main application areas of photocatalysis can be summarized as water-splitting to generate H_2 and degradation of organic pollutants in wastewater [5, 6]. When choosing a semiconductor for water splitting to generate both H_2 and O_2, two crucial factors must be considered: the availability of electrons on the conduction band for stronger capacity to reduce H^+ to H_2, and the maximum potential of a valence band being higher than the redox potential of O_2/H_2O. For bismuth-based photocatalyst semiconductors, the conduction bands are rarely suitable for the production of H_2 without modulation of the energy band as reported in [4]. Instead, photogenerated holes on the valence bands of bismuth-based semiconductors are usually oxidative enough to decompose most of the organic pollutants in wastewater.

Bi_2MoO_6, as a member of Aurivillius family, was originally considered because of their ferroelectric properties [7]. Recent results revealed that Bi_2MoO_6 may be a potential candidate as a visible light-driven photocatalyst applied in oxidizing organics in wastewater [8]. However, the relatively high recombination rate of photogenerated electrons/holes pairs for pure Bi_2MoO_6, when illuminated under visible light irradiation, hinders its widely application. Approaches such as doping [9, 10] and heterojunction formation [11] have been adopted to suppress the recombination of photo-generated e^-/h^+ pairs. Among them, reduced graphene oxide (rGO) integrated Bi_2MoO_6 hybrid photocatalysts were reported with enhanced photocatalytic activity and opened new possibilities in environmental remediation using solar energy [12-15]. Graphene, which is a single layer of sp^2-bonded carbon atoms tightly packed into a two-dimensional honeycomb structure, has been extensively studied due to its excellent physiochemical properties [16]. It is proven to be an effective and inexpensive way to produce graphene nanosheets by reducing graphene oxide (GO). Graphene is regarded as an excellent electrons accepter. As a result, electrons photogenerated by Bi_2MoO_6 activated by light irradiation may be easily transferred to the wide graphene layer, so as to reduce their

recombination rate and improve the photocatalytic activity. It was reported that silver nanoparticles decorated on the surface of Bi_2MoO_6 can greatly improve its performance in photocatalysis, which can also be activated by visible light photons via surface plasmon resonance (SPR) effect [10, 17]. The SPR peaks of Palladium nanoparticles, as reported, can be tuned from 410 nm to 870 nm [18, 19]. Also, 2D rGO sheets decorated with palladium nanoparticles were reported for efficient degradation of organic dyes [20, 21]. We recently have prepared Pd nanoparticle decorated Bi_2MoO_6 hybrid photocatalysts, Pd-Bi_2MoO_6, and they exhibited enhanced visible-light-driven photocatalytic activity in the degradation of organic pollutants in wastewater [22]. Compared with the chemical deposition method to doping metal ions [23-25], the photoreduction approach to load metallic nanoparticles on the surface is more facile. Moreover, metallic nanoparticles promote the effective separation of the photogenerated charge carriers and also improve the visible light-responsivity because of the SPR effect. It is reported the metallic nanoparticles are more stable when they present in the forms of both metallic and ionic valence states [26], suggesting the structure of Pd^0/Pd^{2+} is supposed to be more stable compared to bare Pd^0. Recently, Bi *et al.* have reported on the preparation of ternary Au-rGO-Bi_2MoO_6 composites with enhanced photocatalytic activities under visible light irradiation [27]. Based on above reported work, a ternary (metallic nanoparticles)-rGO-Bi_2MoO_6 composite is supposed to be a promising photocatalyst and need to be further developed [28]. Palladium may be one of the promising candidates, owing for its electrophilicity for facilitating the uptake of photogenerated electrons [29].

This work reports the preparation of a ternary composite composed of Pd, rGO and Bi_2MoO_6. The visible light-driven photocatalytic activities of prepared samples were measured by degrading a colorless organic model, phenol which is widely found in wastewater from many industrial processes and generally difficult to decompose by traditional methods due to its high chemical stability [30, 31]. This work has shed light on the possibility of using photocatalysis for treating phenolic compounds in wastewater under visible light irradiation.

G.2 Experimental

G.2.1 Preparation of rGO-Bi_2MoO_6

The GO-Bi_2MoO_6 composites were first prepared by the one-pot solvothermal method, as shown in Fig. G.1. In a typical process, 264 μL of graphene oxide (GO, dissolved in H_2O with concentration of 4 mg/mL, Sigma-Aldrich Canada) were dissolved in 20 mL ethanol and the suspension was sonicated for 1 h. Next, 1.68 g of $Bi(NO_3)_3 \cdot 5H_2O$ (Fisher Scientific Canada, Certified ACS) was dissolved in 5 mL of ethylene glycol (EG, analytical purity, Fisher Scientific Canada) and 0.42 g of $Na_2MoO_4 \cdot 2H_2O$ (Fisher Scientific Canada, Certified ACS) was also dissolved in another 5 mL of EG. These three mixtures were then mixed together via magnetic stirring for 30 min. The mixture was then transferred to a 45-mL Teflon-lined stainless steel autoclave (Parr Instrument Company, USA) and heated at 160°C for 20 h. The autoclave was then allowed to naturally cool down to room temperature. The precipitates were then filtered out and washed once with ethanol and twice with distilled deionized water (DD Water). The washed samples were then dried at 60°C overnight before being collected. As-prepared GO-Bi_2MoO_6 composites were further reduced as reported in [32]. Typically, 0.50 g of GO-Bi_2MoO_6 composites were added in 50 mL EG and ultrasonicated for 30 min. The mixture was then heated and stirred at 140°C for 2h. The particle sample was then separated out, washed by ethanol and dried at 60°C overnight before being collected. For comparison, pure Bi_2MoO_6 was also prepared using the solvothermal method without adding GO in the precursor solution.

G.2.2 Preparation of Pd-rGO-Bi_2MoO_6

Pd-rGO-Bi_2MoO_6 composite samples were synthesized by a photoreduction method, as shown in Fig. G.1. In a typical procedure, 0.30 g of as-prepared rGO-Bi_2MoO_6 composites were suspended in 40 mL DD Water and sonicated for 30 min before adding a designated amount of $PdCl_2$ (Fisher Scientific Canada, ACS certified). The mixture was then magnetically stirred for 10 min, and illuminated under a 300-W halogen tungsten projector lamp (wavelength: 310 – 800 nm, Ushio, USA) for 1 h. After that, the resultant products were separated out via centrifugation, washed twice with DDW and dried at 60°C overnight. Samples of 0.5, 1, 2 and 4 wt% Pd-rGO-Bi_2MoO_6 were prepared following the above procedures. For comparison, 2 wt% Pd-Bi_2MoO_6 were also prepared by changing the

substrate to Bi_2MoO_6 instead of rGO-Bi_2MoO_6. Also, 2wt % Pd-rGO composites were prepared by using $NaBH_4$ (Fisher Scientific Canada, 98%) as the reducing agent [20].

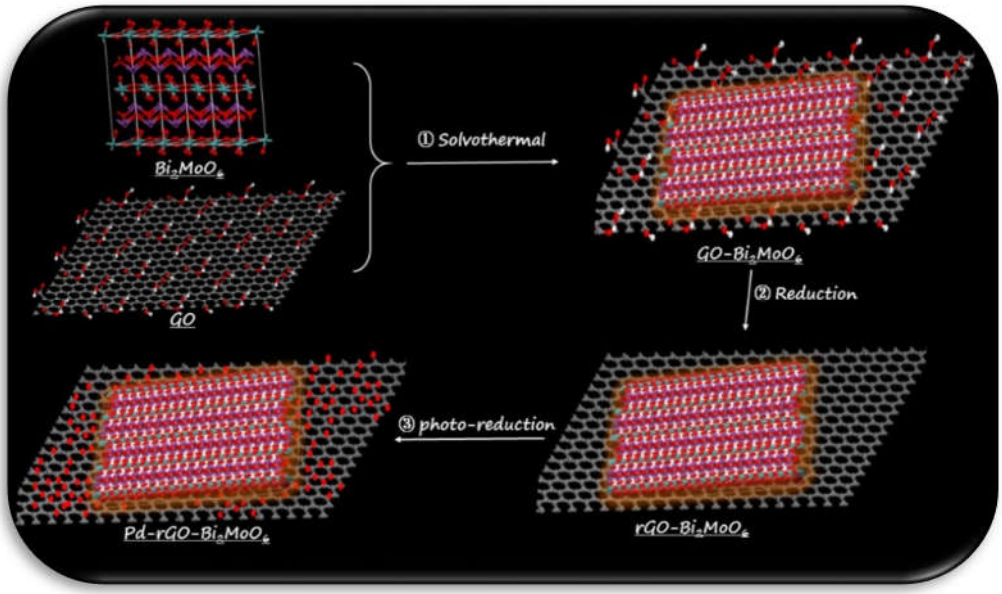


Figure G.1 Scheme of preparation processes of Pd-rGO-Bi_2MoO_6.

G.2.3 Characterization

Crystal structures of prepared samples were investigated by X-ray diffraction (XRD) on a Rigaku Ultima IV Diffractometer with Cu Kα radiation (λ = 0.15418 nm) at 40 kV and 44 mA. XRD patterns were recorded at 2θ of 5 - 80°. Surface composition and chemical states of the samples were analyzed using a XSAM-800 X-ray Photoelectron Spectroscope (XPS). The morphologies of prepared samples were investigated via scanning electron microscopy (SEM, model: JEOL JSM-7500F) equipped with energy dispersive X-ray spectroscopy (EDS) and transmission electron microscopy (TEM, model: JEM-2100F). The specific surface area, pore volume and average pore size were obtained from N_2 sorption isotherms at 77 K, using automatic adsorption apparatus and measurement systems (ASAP 2020, Micromeritics and Nova 4200E, Quantachrome). The Brunauer, Emmett and Teller (BET) surface area of the samples were calculated using multi-point estimation. The pore volumes were calculated using the volumes of adsorbed N_2 at p/p_o = 0.977. Pore volume distributions are calculated using N_2 desorption branch, and the Barrett-Joyner-Halenda

(BJH) method was used for the desorption branch to calculate the pore size data (d_p) using Equation 1 (where V/A_s is a ratio of volume to surface area of pores) as follows,

$$d_p = 4\left(\frac{V}{A_s}\right)_{BJH} \qquad \textbf{\textit{Equation 1}}$$

A thermos Evolution 300 spectrophotometer was applied to measure the optical properties of samples through ultraviolet-visible diffuse reflectance spectra (DRS). Fourier Transform Infrared Spectroscopy (FTIR) was performed on a Cary 630 (Agilent Technologies). The spectra were recorded at room temperature with wavenumbers ranging from 2000 to 600 cm^{-1}. Electrochemical properties of prepared samples were analyzed on a CHI 604E electrochemical analyzer (CH Instruments Inc., USA) with a platinum wire as a counter electrode, a calomel reference electrode and a working electrode. The working electrode composed of indium tin oxide (ITO, 75 × 25 × 1.1 mm, 15 - 25 Ω, Sigma-Aldrich Canada Co.), glass coated with the prepared samples. The electrochemical impedance spectroscopies (EIS) were recorded with frequencies in the range of 1 – 1,000,000 Hz and a sinusoidal wave of 5 mV. The electrolyte was Na_2SO_4 with a concentration of 0.5 mol/L.

G.2.4 Photocatalytic activity tests

Photocatalytic activities of prepared samples were measured with regard to degrading the colorless organic pollutant model compound (phenol) under visible light irradiation. Specifically, a 500-mL beaker with a cooling jacket served as the reactor. The temperature of the reacting solution was kept at ~20°C for all tests. The light source composed of a 300-W halogen tungsten projector lamp (Ushio, USA) with wavelengths mainly in the range of 310 – 800 nm. A cut-off (Kenko Zeta, transmittance > 90%) was used to filter out wavelengths below 410 nm to ensure the irradiation occurred within visible light range. The irradiation intensity on the surface of the solution was measured on a quantum meter (Biospherical QSL-2100, $400 < \lambda < 700$ nm) to be, on average, 1.1×10^{-2} Einsteins m^{-2} s^{-1}. In each test, 100 mL of phenol with a concentration of 10 ppm (mg/L) was mixed with 0.1 g (1.0 $g_{cat}/L_{solution}$) of as-prepared photocatalyst composites. This suspension was first magnetically stirred for 60 min in the dark before turning on the lamp, aiming to reach an adsorption-desorption equilibrium between the organic pollutants and the photocatalysts.

The photocatalytic tests last for 6 h, and aliquots were drawn every 30 min. After centrifuging at 13,000 rpm for 5 min, the supernatant was analyzed using a high-performance liquid chromatograph (HPLC, Agilent 1100 series) equipped with a UV-Vis detector. A ZORBAX Eclipse Plus C18 column (4.6 × 250 mm) was used at a temperature of 60°C. The detecting wavelength was fixed at 270 nm for the detection of phenol and possible intermediates. The flow phase was composed of methanol (55%, V/V) and water (45%, V/V) at a flow rate of 0.6 mL/min. The injection volume was set to 25 μL.

To measure the reusability of prepared photocatalysts, 2 wt% Pd-rGO-Bi_2MoO_6 composites were recycled for four times in total. Photocatalysts were separated out from the suspension following a single run, and then mixed with fresh wastewater to start another run.

G.2.5 Electronic structure calculation

The quantum-mechanical calculations were performed on the basis of the density functional theory (DFT) [33]. The generalized gradient approximation (GGA) was applied to exchange-correlation effects. The open access software Quantum ESPRESSO was used, which utilizes pseudo potentials to describe electron-ion interactions and represents electronic wave functions using a plane-wave basis set [34]. The kinetic energy cut-off was set to 300 eV.

G.3 Results and discussions

G.3.1 XRD and XPS

The crystal structures of as-prepared pure Bi_2MoO_6 and modified Bi_2MoO_6 composites were studied by XRD, patterns of which were shown in Fig. G.2. As for patterns of pure Bi_2MoO_6, all identifiable peaks agree well with an orthorhombic crystal structure (space group: pbca (61), PDF card number:00-72-1524) [35]. Impurity peaks were not found, indicating that a well-crystallized Bi_2MoO_6 sample was prepared by the solvothermal method. Patterns of GO, rGO, and Pd-rGO-modified Bi_2MoO_6 composites exhibit negligible differences with those of pure Bi_2MoO_6, most likely due to the small quantity of these dopants. Specifically, the loading quantity of (r)GO (0.1 wt%) and Pd (4 wt%) in the composites were too small to be detected by XRD. The lattice parameters of pure Bi_2MoO_6

were refined and calculated as: a = 5.5219 Å, b = 16.0925 Å, and c = 5.4918 Å. The lattice parameters of Bi_2MoO_6 in the GO-, rGO- and Pd-rGO- Bi_2MoO_6 composites were also calculated and shown in Fig. G.2. It can be found that these dopants have negligible influence on Bi_2MoO_6 crystal parameters.

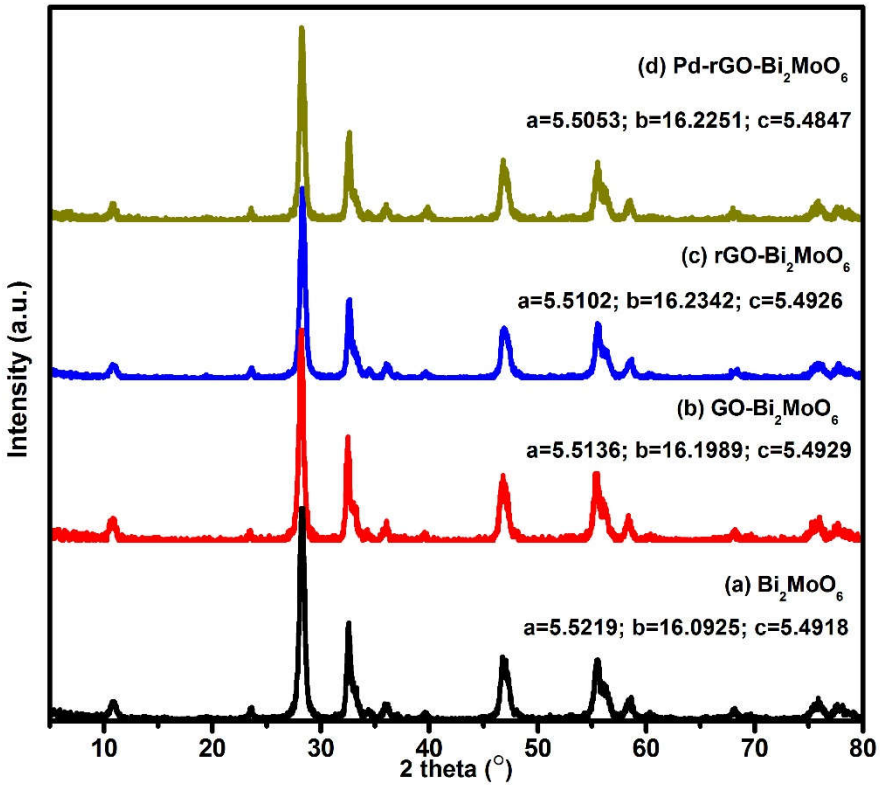


Figure G.2 XRD patterns of as-prepared composites: (a) pure Bi_2MoO_6, (b) GO-Bi_2MoO_6, (c) rGO-Bi_2MoO_6 and (d) Pd-rGO-Bi_2MoO_6.

To further explore the surface elements and chemical states of prepared composites, XPS survey spectra and high-resolution orbits scan for GO- and Pd-rGO-Bi_2MoO_6 composites were depicted in Fig. G.3. All spectra were calibrated with C *1s*, the binding energy of which was fixed at 284.6 eV. In the survey spectra for GO-Bi_2MoO_6 (Fig. G.3a), all elements, namely C, O, Bi and Mo, were detected with strong characteristic peaks; no impurities were detected. When Pd were introduced in the composites, characteristic peaks for Pd were detected. For the C *1s* orbits scan in Fig. G.3b, three peaks located at 284.6, 285.5 and 288.3 eV were found in the spectra for both GO- and Pd-rGO-Bi_2MoO_6 composites, which can be attributed to the C-C, C-O, and O-C=O groups in the GO and rGO. The intensity of the peak for O-C=O was slightly reduced when the GO was reduced,

indicating some of the oxygen functional groups were removed during the reduction process [36, 37]. Furthermore, in the O *1s* XPS spectra shown in Fig. G.3c, four small peaks were detected for GO-Bi_2MoO_6 composites, located at 529.8, 530.5, 531.3 and 533.2 eV, which may be attributed to Bi-O, Mo-O, C-O and C=O, respectively [38]. However, when GO was reduced, only three peaks were detected in the O *1s* XPS spectrum for Pd-rGO-Bi_2MoO_6 composites. Here, the intensities of peaks for C-O and C=O were reduced, which suggests the oxygen functional groups were greatly removed by the reduction process. Meanwhile, two sets of spin-orbit doublets for Pd *3d* were detected in the Pd-rGO-Bi_2MoO_6 composites (Fig. G.3d). Accordingly, Pd ($3d_{3/2}$, $3d_{5/2}$) located at binding energies of 334.7 and 340.0 eV, as well as at 337.0 and 342.3 eV may be attributed to the metallic Pd^0 and Pd^{2+}, respectively. The relative concentration of bivalent to metallic Pd can be calculated using Equation 2 [39]:

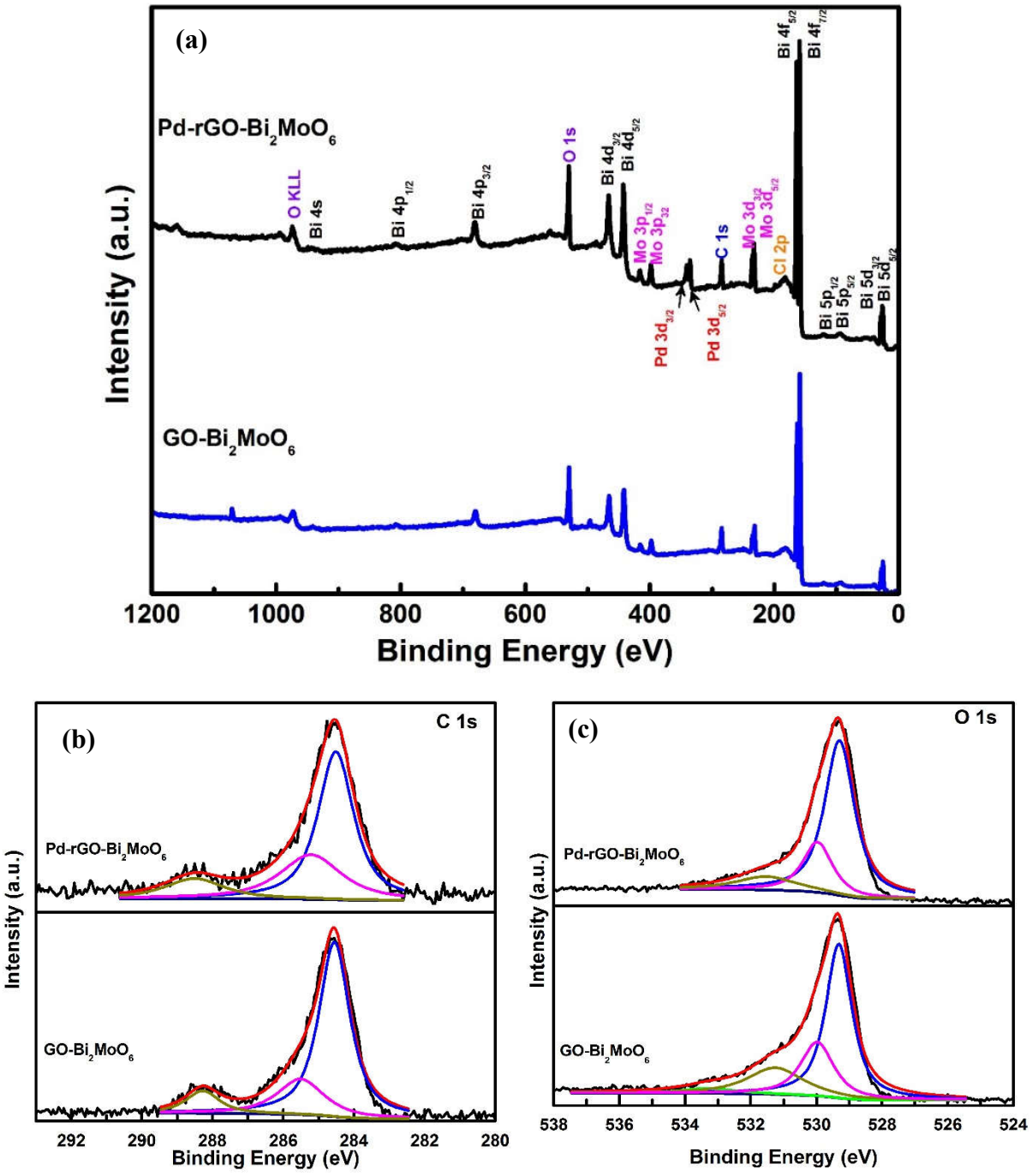
$$\frac{\eta_{Pd^0}}{\eta_{Pd^{2+}}} = \frac{I_{Pd^0}}{I_{Pd^{2+}}} \times \frac{\sigma_{Pd}\lambda_{Pd}D_E(Pd)}{\sigma_{Pd}\lambda_{Pd}D_E(Pd)} = \frac{I_{Pd^0}}{I_{Pd^{2+}}} \qquad \textbf{\textit{Equation 2}}$$

where η, I, σ, λ, and D_E are the surface concentration, integrated intensity, photoelectric cross-section, electron free mean path, and geometric factor, respectively. The values of σ, λ, and D_E have been calculated and summarized by Penn and Scofield, and can be obtained from literature [40, 41]. Integration areas of Pd^0 and Pd^{2+} peaks were performed to estimate their concentrations. The relative combined surface concentration ratio of Pd^0 to Pd^{2+} was approximately 3.7:1. Theoretically, the redox potential of Pd^{2+}/Pd was 0.987 V. The bottom potential of the conduction band of Bi_2MoO_6 can be calculated as 0.34 eV using Equation 3:

$$E_{CB,Bi_2MoO_6} = X_{Bi_2MoO_6} - E^e - \frac{1}{2}E_g \qquad \textbf{\textit{Equation 3}}$$

where $X_{Bi2MoO6}$ (6.13 eV), E^e and E_g are the electronegativity, the energy of free electrons on the hydrogen scale (≈ 4.5eV), and the band gap of Bi_2MoO_6 (2.58 eV, from section 3.4) [42, 43]. It means electrons on the conduction band of Bi_2MoO_6 are reductive enough to reduce Pd^{2+} to Pd. In addition, the high-resolution Cl *2p* orbital scan shown in Fig. G.3e further suggests the presence of $PdCl_2$ on the surface of the Pd-Bi_2MoO_6 composites. Peaks located at binding energies of 197.5 and 199.1 eV for Cl $2p_{1/2}$ and Cl $2p_{3/2}$, respectively,

clearly indicates the presence of Cl^- [44]. It can be concluded that only a portion of Pd^{2+} was reduced to metallic Pd in the photoreduction process.



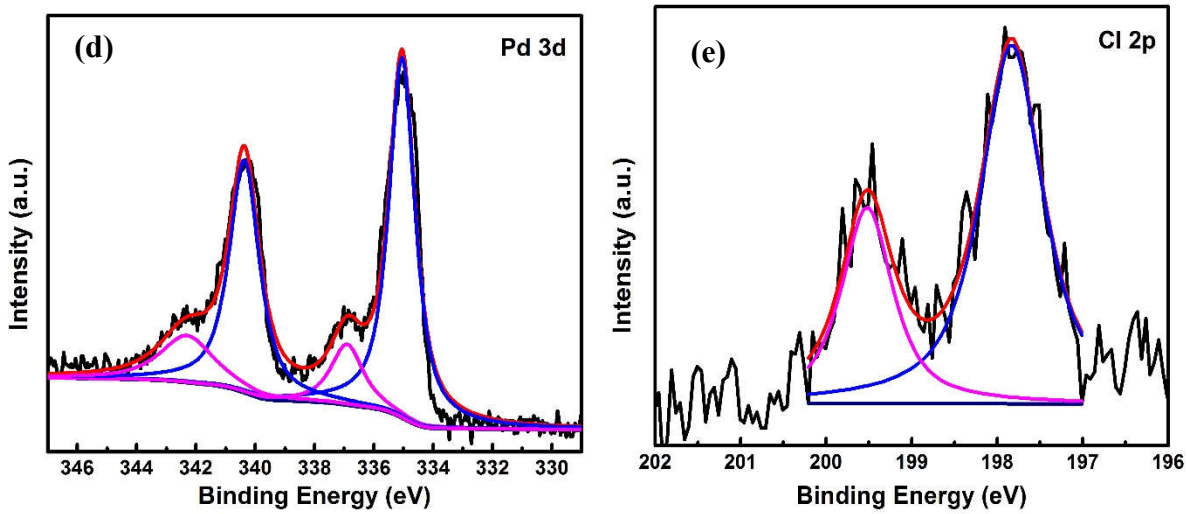


Figure G.3 (a) XPS survey spectra, and high –resolution orbits scan of (b) C 1s, (c) O 1s, (d) Pd 3d and (e) Cl 2p for GO- and Pd-rGO-Bi_2MoO_6 composites, respectively.

G.3.2 FT-IR

FTIR spectra for as-prepared samples were shown in Fig. G.4. For the spectrum of pure Bi_2MoO_6, the main absorbance bands at wavenumbers in the range of 1000 - 600 cm^{-1} may be attributed to Bi-O, Mo-O stretching and Mo-O bridging stretching modes [8]. The strongest absorbance peak at 690 cm^{-1} may have resulted from the asymmetric stretching mode of MoO_6 involving vibrations of the equatorial oxygen atoms. Two peaks at wavenumbers of 795 and 845 cm^{-1} may be attributed to the asymmetric and symmetric stretching modes of MoO_6 involving vibrations of the apical oxygen atoms [45, 46]. When GO was added in the composites, small absorbance peaks at wavenumbers between 3500 - 1000 cm^{-1} were found. Specifically, peaks at 3306, 2933, 2874, 2086, 1624, and 1336 cm^{-1} can be related to -OH, $-CH_2-$, C-O, C=O, C-O-C (or H) stretching, respectively [47]. After the reduction process, it can be found that these absorbance peaks for these oxygen functional groups in the spectrum for rGO-Bi_2MoO_6 were weakened or removed. The O=C-OH may be completely reduced to C, as for the –OH peak disappears [32, 48]. When Pd was loaded on the surface of rGO-Bi_2MoO_6, the differences in the spectra were negligible.

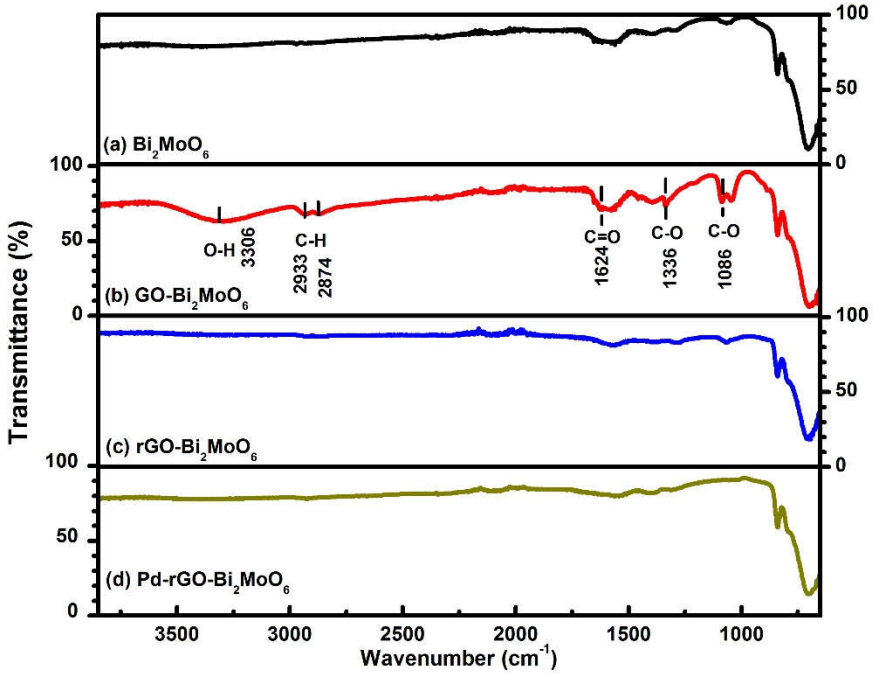


Figure G.4 FTIR spectra for (a) pure Bi_2MoO_6 and (b) GO-, (c) rGO-, (d) Pd-rGO-Bi_2MoO_6 composites.

G.3.3 Morphologies and possible formation processes

The morphologies of prepared pure Bi_2MoO_6 and Pd-rGO-Bi_2MoO_6 were observed by SEM, STEM and TEM, and illustrated in Fig. G.5. For pure Bi_2MoO_6 in Fig. G.5a, uniform hierarchical micro-spheres with a diameter of about 2 μm were observed, and were composed of crystalline nanosheets. Hollow microspheres were also observed in Fig. G.5a, which can be ascribed to the Ostawald ripening formation process [49, 50]. When the reaction time is short, the Bi_2MoO_6 sphere has a solid core. With a longer reaction time however, the dissolution-recrystallization process occurs, and crystalline nanosheets form on the outer surface by dissolving crystallites located in the inner cores. This may be due to crystallites at the inner core possessing higher surface energies than those at the outer surface. When the modifiers, namely Pd and rGO, were introduced on the surface of Bi_2MoO_6, flake-like particles were formed on the microspheres which can be seen from the SEM image in Fig. G.5b. STEM was applied to explore the morphologies of GO; in Fig. 5c, the curly GO sheets were observed. In the high-resolution TEM image of Pd-rGO-Bi_2MoO_6 shown in Fig. G.5d, nanoparticles with diameters of about 2-3 nm were observed. To confirm these nanoparticles are metallic palladium, EDS was applied and shown in Fig.

G.6. Peaks of Pd were found, which provided solid evidence that Pd nanoparticles were successfully formed on the surface. Meanwhile, the intensities of peaks for C and O in the EDS spectrum of Pd-rGO-Bi_2MoO_6 were greatly improved compared to those in the spectrum of Bi_2MoO_6. It also suggests GO was successfully combined in the composites.

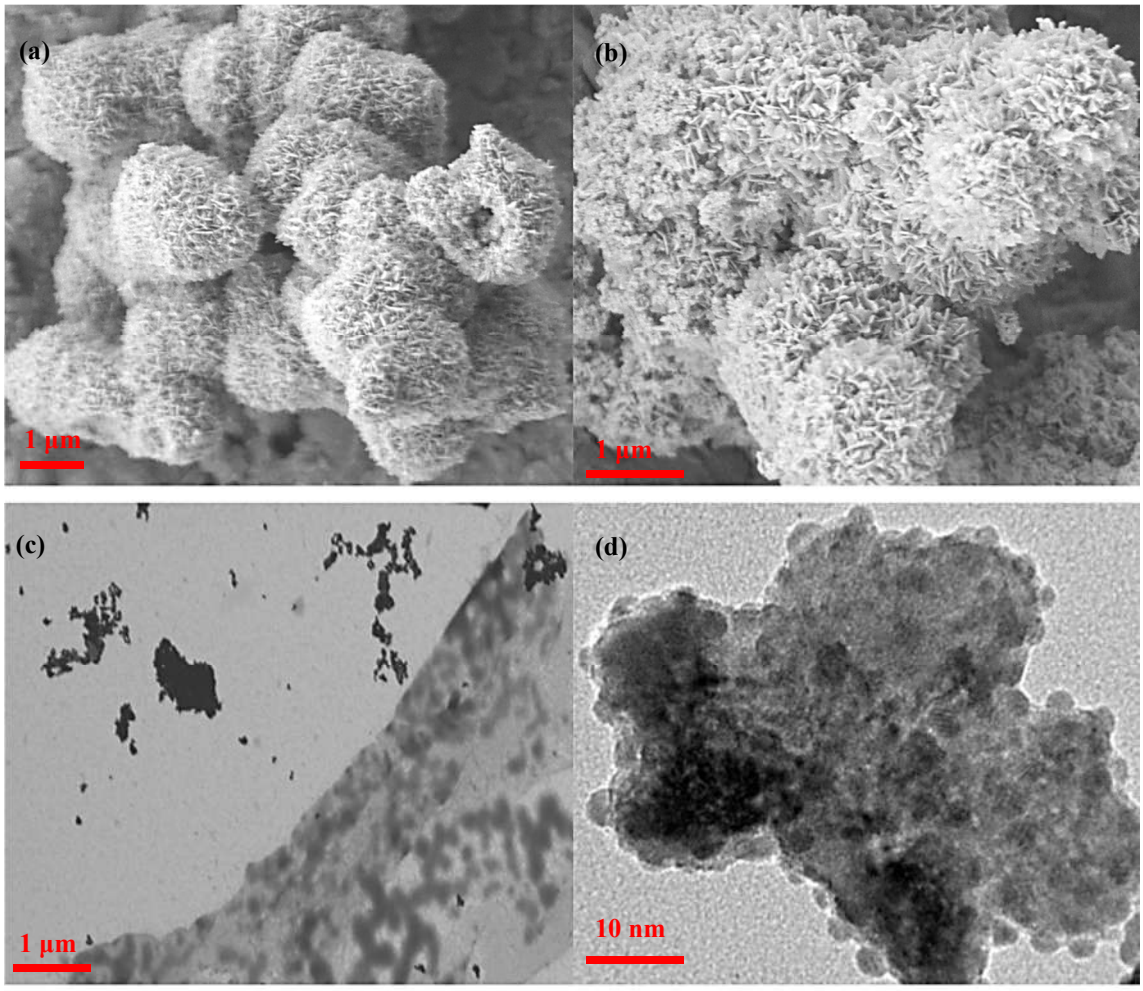


Figure G.5 SEM images for (a) pure Bi_2MoO_6 and (b) Pd-rGO-Bi_2MoO_6 composites, STEM image for Pd-rGO-Bi_2MoO_6 composites, and TEM image for Pd-rGO-Bi_2MoO_6 composites.

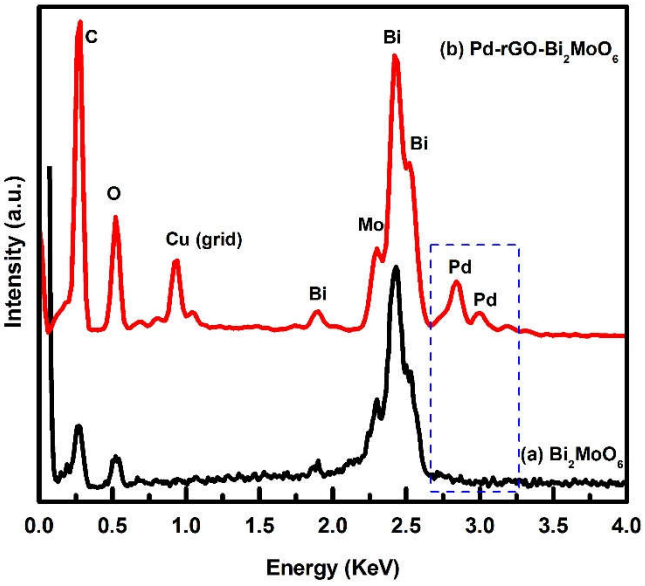


Figure G.6 EDS spectra for (a) pure Bi_2MoO_6 and (b) Pd-rGO-Bi_2MoO_6 composites.

G.3.4 N_2 sorption isotherms

Nitrogen sorption isotherms were obtained and shown in Fig. G.7 for pure Bi_2MoO_6, GO-Bi_2MoO_6, rGO-Bi_2MoO_6 and Pd-rGO-Bi_2MoO_6. All isotherms are attributed to a recombination of Type II and IV physisorption isotherms [51, 52]. The type IV isotherm is typical for mesoporous material. An adsorbate monolayer is firstly formed at low pressures, followed by the multilayer adsorption at high pressures. However, the typical feature for type IV sorption isotherm, which is a final saturation plateau, is not observed for each isotherm in Fig. G.7 [53]. This phenomenon may be caused by the capillary condensation does not occur in adsorption on the surface of macropores, resulting in a rapid increase in isotherm as type II isotherms. A hysteresis loop for each isotherm in Fig. G.7 is observed, which is attributed to H3 type. The onset of the hysteresis loop indicates the beginning of the capillary condensation in the mesopores. At upper closure point, the mesopores are fully filled with liquid. The H3-type hysteresis loop may be attributed to the presence of aggregations of plate-like particles giving rise to slit-shaped pores, which agrees well with the morphologies observed in the SEM images [27, 51]. Also, the pore size distributions for each sample are also plotted in the insets of Fig. G.7. The mesopores may correspond to the pores formed by Ostwald ripening [49] and the voids between crystals within the two-dimensional layers and interspaces between these stacked layers. The specific surface

area, pore volume and average pore size are summarized in Table G.1. Similar specific surface areas are obtained for (r)GO-Bi_2MoO_6 and bare Bi_2MoO_6, owing for the small quantity of (r)GO in the composite. A slight decrease in the specific surface area is observed when Palladium loaded on the surface. This phenomenon may be resulted from the palladium nanoparticles are blocked the slit-shaped pores. The pores volume for Pd modified rGO-Bi_2MoO_6 is also decreased. The decrease in specific surface area may lead to the reduction in photocatalytic activity via deterioration of the adsorption capacity of pollutants in the wastewater. However, compared to the improvement of photogenerated charge carriers' separation efficiency by loading Pd on the surface, the influence of reduction in specific surface area is negligible for the overall photocatalytic activity.

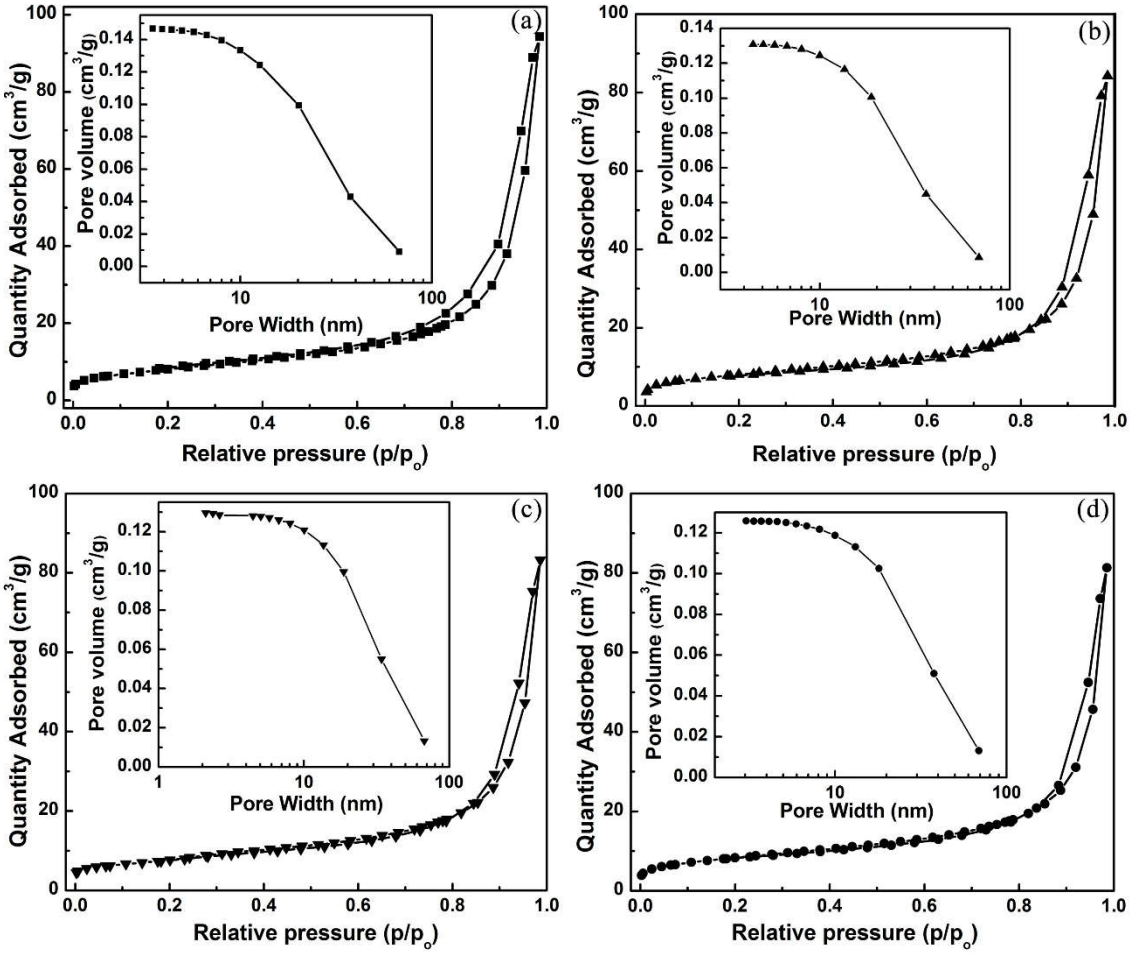


Figure G.7 N_2 sorption isotherms and pore size distributions for (a) Bi_2MoO_6, (b) GO-Bi_2MoO_6, (c) rGO-Bi_2MoO_6, and (d) Pd-rGO-Bi_2MoO_6, respectively.

Table G.1 Specific surface area, pore volume, and average pore size of Bi_2MoO_6, GO-Bi_2MoO_6,

rGO-Bi_2MoO_6, and Pd-rGO-Bi_2MoO_6 composites.

Sample	S_{BET} (m^2/g)	Pore volume (cm^3/g)	Average pore size (nm)
Bi_2MoO_6	29	0.15	20.4
GO-Bi_2MoO_6	29	0.13	20.2
rGO-Bi_2MoO_6	30	0.13	18.8
Pd-rGO-Bi_2MoO_6	29	0.12	18.5

G.3.5 Optical properties

The optical properties of prepared samples including pure Bi_2MoO_6 and Bi_2MoO_6 composites modified by GO, rGO and Pd-rGO were investigated by UV-Vis DRS, and the results were depicted in Fig. G.8. For the spectrum of pure Bi_2MoO_6, a steep increase in the absorbance intensity was observed when the wavelength was below 470 nm, which may have resulted from the band gap transition. The band gap energy can be calculated from the band edge with the Kubelka-Munk function as about 2.58 eV [54]. When GO combined with Bi_2MoO_6, the band gap transition was negligibly influenced; however, the visible light energy harvesting (VLEH) was improved. When GO was reduced, the VLEH capacity was further improved. The increase of absorption in the visible light region after (r)GO introduced on Bi_2MoO_6 may be due to the introduction of black body properties typical of graphite-like materials [23, 55]. When Pd nanoparticles were decorated on the surface of rGO-Bi_2MoO_6, the VLEH capacities were significantly enhanced, improving with increasing quantities of palladium in the composites. The strong absorbance in the visible light region when Pd nanoparticles formed on the surface of composites may be due to the surface plasmon resonance (SPR) effect [56]. For pure Bi_2MoO_6, O *2p* and Bi *6s* states mainly contribute to the valence band, while Bi *6p*, Mo *4d* and O *2p* states account for the conduction band (Fig. G.9). The band gap value can be estimated as about 1.91 eV which is smaller than that of the experimental result (2.58 eV) measured in Fig. G.8. This phenomenon possibly resulted from the well-known limitation of GGA [57]. In conclusion, the synergetic effect of rGO and palladium Pd^0 nanoparticles significantly improved absorption capacity of Bi_2MoO_6 in the visible light region of the spectrum, and lead it to become a potential candidate in visible light-driven photocatalysts.

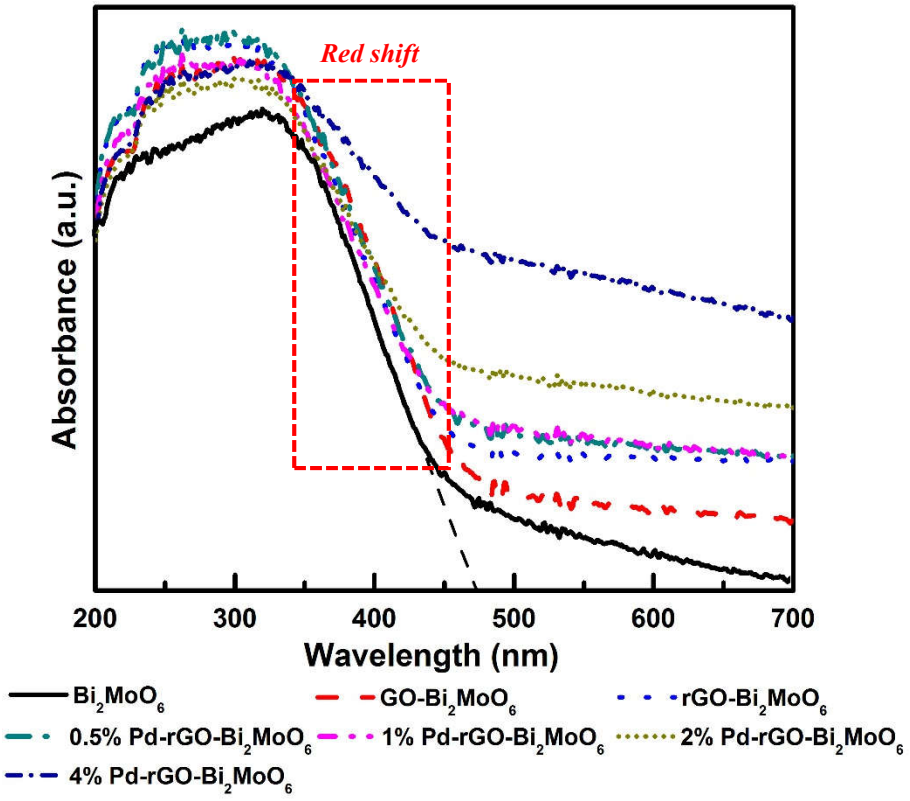


Figure G.8 UV-Vis spectra for as-prepared samples.

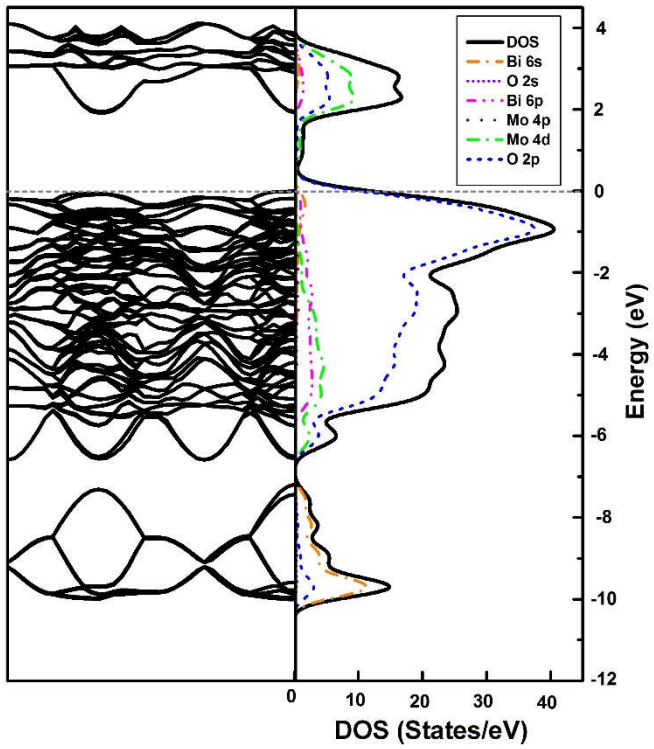


Figure G.9 Calculated band structure, and Density of states (DOS) and partial density of states

(PDOS) for pure Bi_2MoO_6 (Fermi level fixed at band energy of 0 eV).

G.3.6 Photocatalytic activity test

The photocatalytic activities of prepared photocatalysts were evaluated by degrading phenol under visible light irradiation. The relative concentration profiles of phenol as a function of irradiation time were illustrated in Fig. G.10. In the presence of pure Bi_2MoO_6, there were about 10% of phenol photocatalytically decomposed at 300 min. For GO combined with Bi_2MoO_6, the photocatalytic conversion of phenol was improved from 10% to 27% at 300 min. After the reduction process of GO, the conversion was further improved to 35% at 300 min. The improvement may be caused by the electrons photogenerated by Bi_2MoO_6 under visible light getting transferred to the GO layer, and when the oxygen groups of GO are reduced, the mobility of electrons on the graphene-like layer would be further improved. As a result, the recombination rate of photogenerated electrons and holes was significantly reduced and the photocatalytic activity of Bi_2MoO_6 was greatly improved. Even though the Pd-rGO exhibited highly efficient degradation of organic dyes, it only lead to no more than 5% of phenol degraded over 300 min [20]. The poor activity of employing the Pd-rGO in degradation of phenol may be due to the oxidative species in the system is not strong enough to destruct the aromatic ring and no photosensitivity occurs for phenol [58]. For Pd content loaded on rGO-Bi_2MoO_6 composites, the ternary photocatalysts performed better in the decomposition of phenol under visible light irradiation. Specifically, when the quantity of Pd increased from 0.5% to 2% in the composites, photocatalytic activity in phenol removal was greatly improved. However, when the quantity of Pd was further increased to 4%, the photocatalytic activity of the composites became worse. It might have occurred because Pd nanoparticles on the surface were also good recombination sites for photogenerated electrons and holes, resulting in the low electron/hole separation efficiency.

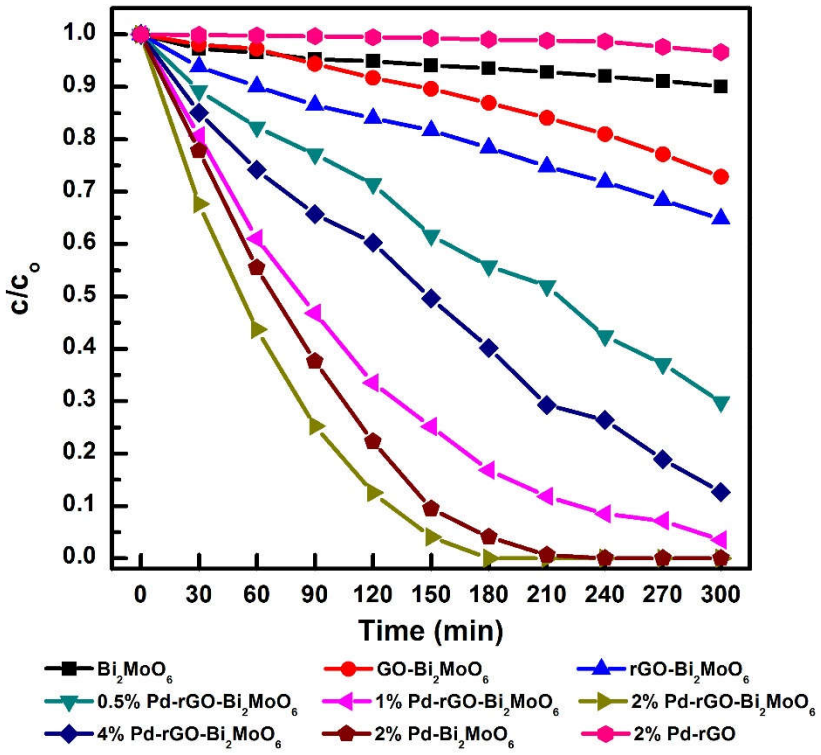


Figure G.10 Concentration profiles of phenol during the photocatalytic degradation tests in the presence different as-prepared photocatalysts under visible light irradiation.

To further quantitatively compare the photocatalytic activity, the Pseudo first-order model was used to derive the photocatalytic kinetics. For low concentrations of organics in the solution (< 1×10^{-4} M), the model can be simplified as Equation 4:

$$\ln(\frac{c_o}{c_t}) = k't \qquad \textit{Equation 4}$$

where c_o, c_t, k' and t represent initial concentration of phenol, concentration of phenol at time t, reaction rate constant and time. Simulated results of k' for each process in the presence of different photocatalysts with regard to phenol were summarized in Table G.2. Based on the values for R^2 and Standard Error (SE), it appears this model is highly suitable to simulate these photocatalytic processes in the presence of different as-prepared composites. Kinetics constants (k') may be employed to quantitatively evaluate the reaction rates for each process. It can be found that the kinetic constant increased to approximately three times when rGO combined with Bi_2MoO_6. It also greatly improved when Pd was loaded on rGO-Bi_2MoO_6. The maximum of k' was observed for the process in the presence

of 2% Pd-rGO-Bi_2MoO_6; ~32 times higher than in the presence of pure Bi_2MoO_6, ~10 times higher than in the presence of rGO-Bi_2MoO_6 and ~1.4 times higher than in the presence of 2% Pd-Bi_2MoO_6. This impressive enhancement in the photocatalytic degradation of phenol further confirmed the synergetic effect of palladium and rGO in these ternary composites.

Table G.2 Photocatalytic kinetic constants for the photocatalytic process of degradation of phenol with various photocatalysts under visible light irradiation.

Composite	k (x10^{-3} min^{-1})	R^2	SE (x10^{-4})	$k/k_{Bi_2MoO_6}$
Bi_2MoO_6	0.499	0.953	0.493	1
Pd-Bi_2MoO_6	11.5	0.987	5.84	23.1
Pd-rGO	0.0412	0.975	0.0266	0.0826
GO-Bi_2MoO_6	0.657	0.978	0.437	1.32
rGO-Bi_2MoO_6	1.56	0.990	0.715	3.13
0.5% Pd-rGO-Bi_2MoO_6	2.92	0.993	1.07	5.85
1% Pd-rGO-Bi_2MoO_6	8.72	0.996	2.36	17.5
2% Pd-rGO-Bi_2MoO_6	16.1	0.990	7.13	32.3
4% Pd-rGO-Bi_2MoO_6	4.49	0.994	1.62	9.00

G.3.7 Reusability

Reusability is an important parameter for evaluating a photocatalyst in terms of stability. Four runs were performed by recycling 2% Pd-rGO-Bi_2MoO_6 for the degradation of phenol in wastewater under visible light irradiation. The concentration profiles of phenol in the solution during the degradation process were shown in Fig. G.11. Complete removal of phenol can be obtained in 210 min for these four runs. A negligible difference among these four profiles can be observed, indicating the high stability of Pd-rGO-Bi_2MoO_6 composites in the photocatalytic organic degradation process. The slight decrease in the phenol conversion may be resulted from some refractory intermediates adsorbed on the surface of the photocatalysts which reduces the reactive sites in the following run. The high reusability of Pd-rGO-Bi_2MoO_6 composites make them an attractive candidate for use as visible light-driven photocatalysts.

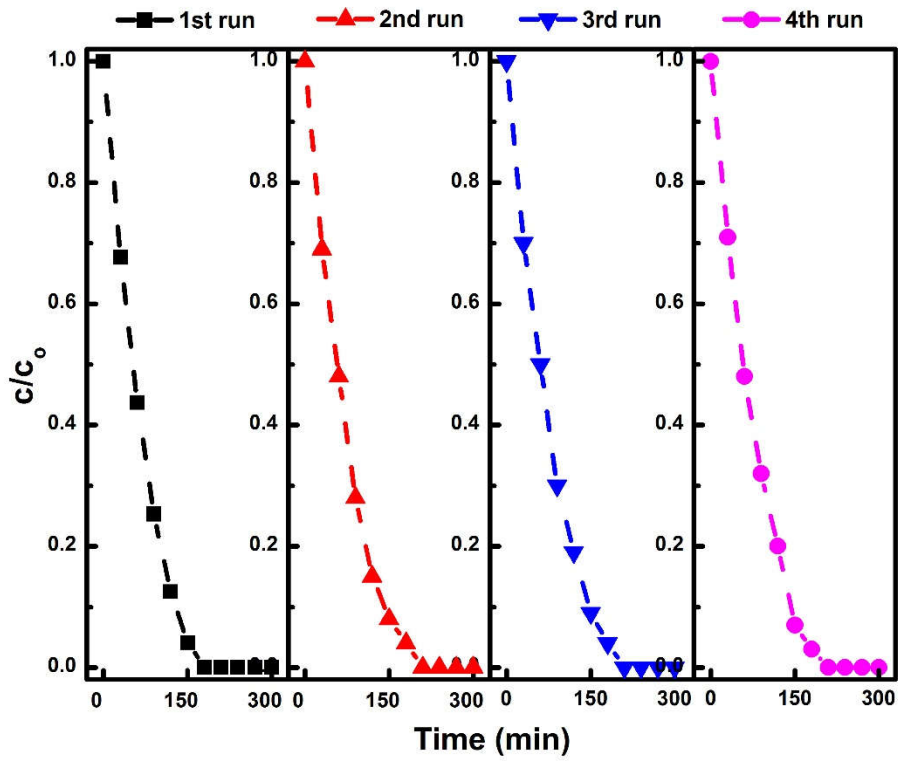


Figure G.11 Reusability of 2% Pd-rGO-Bi_2MoO_6 composites with regard to phenol under visible light irradiation.

G.3.8 Mechanism exploration

To explore the enhancement mechanism in the photocatalytic activity of Pd and rGO combined with Bi_2MoO_6, electrochemical impedance spectroscopy (EIS) was employed to measure the separation efficiency of photogenerated electrons and holes. The EIS Nyquist plots of Bi_2MoO_6, rGO-Bi_2MoO_6 and Pd-rGO-Bi_2MoO_6 under visible light irradiation are shown in Fig. G.12. Only one semicircle for each plot of all prepared samples suggest that the photocatalytic degradation process in the presence of these composites may be a simple electrode reaction and photogenerated electron transfer, and the rate may be determined by the recombination of photogenerated electron/hole pairs [59, 60]. The equivalent circuits of these three processes can be simulated as shown in Table G.3, where R_s is the resistance of the solution, R_{ct} represents the resistance to the electrons transfer and *CPE* represents the constant phase element which may be considered as a double-layered capacity. These values can be determined by the software equipped with an electrochemical analyzer (model CHI604E). R_{ct} can be calculated by the diameter of the arc in the EIS Nyquist plot;

a larger arc diameter gives a higher R_{ct} value, lower electron mobility and higher recombination of electrons and holes on the electrode. In the EIS Nyquist plot for pure Bi_2MoO_6 with the largest diameter and highest resistance of 21630 Ω, when rGO was coupled in the composites the diameter of the semicircle decreased and the R_{ct} value greatly reduced to 3880 Ω (~ 18% compared to that for pure Bi_2MoO_6). After Pd was further loaded on the surface of rGO-Bi_2MoO_6, mobility of electrons on the electrode was significantly improved with an R_{ct} value as small as 1470 Ω (~ 7% compared to that for pure Bi_2MoO_6 and ~ 38% compared to that for rGO-Bi_2MoO_6 composite). It suggests that the electrons/holes separation efficiency was greatly improved when rGO and Pd were loaded on Bi_2MoO_6, which directly resulted in the enhanced visible light-driven photocatalytic activity.

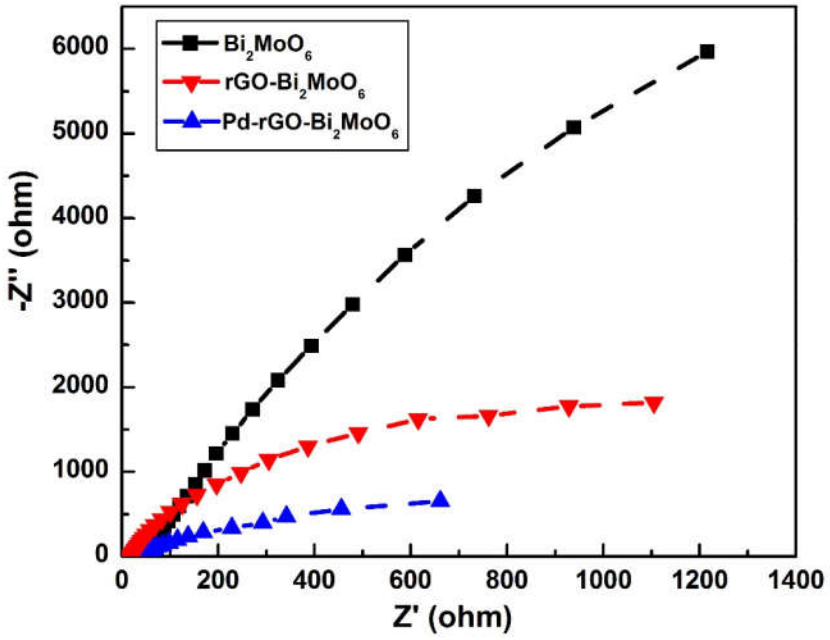
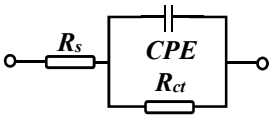


Figure G.12 EIS Nyquist plots of the Bi_2MoO_6, rGO-Bi_2MoO_6 and Pd-rGO-Bi_2MoO_6 samples.

Table G. 3 Fitting results for equivalent circuits of different prepared samples.

Samples	R_s (Ω)	R_{ct} (Ω)	*CPE* (μf)	Equivalent circuits
Bi_2MoO_6	35.21	21630	21.52	
rGO-Bi_2MoO_6	40.79	3880	40.27	
Pd-rGO-Bi_2MoO_6	21.19	1470	45.54	

The proposed mechanism was summarized in Fig. G.13 on the basis of results obtained and discussed above. Specifically, when rGO combined with Bi_2MoO_6, the rGO layer may perform as an electron acceptor, which means photogenerated electrons on the conduction band of Bi_2MoO_6 may transfer to the rGO layer so as to supress their recombination with holes on the valence band of Bi_2MoO_6 [12, 27, 61]. When Pd content was loaded on the surface of rGO-Bi_2MoO_6 composites, Pd nanoparticles distributed on both rGO and Bi_2MoO_6 may have absorbed visible light energy to produce electrons due to the SPR effect (the SPR peaks of Pd nanostructure can be tuned from 410 nm to 870 nm [18, 19]). Furthermore, Cl^- was also found in the composites (Fig. G.3e). The anion may be oxidized to Cl^0, which is itself a strong oxidizing agent that may be capable of oxidizing phenol to return to its reduced, anionic state (Cl^-) [62]. In addition, because of the strong π-π interaction between aromatic rings of phenol and rGO, phenol may also be much easier to adsorb onto the surface of rGO-Bi_2MoO_6 composite compared to pure Bi_2MoO_6 [63]. In conclusion, the improved separation efficiency of photogenerated electron-hole pairs via capture of palladium nanoparticles, transportation through the rGO, increased harvesting intensity of visible light photons due to the SPR effect and a narrowed band gap, and strong adsorption of phenol on rGO layers contributed to an enhanced photocatalytic activity towards the degradation of phenol under visible light irradiation.

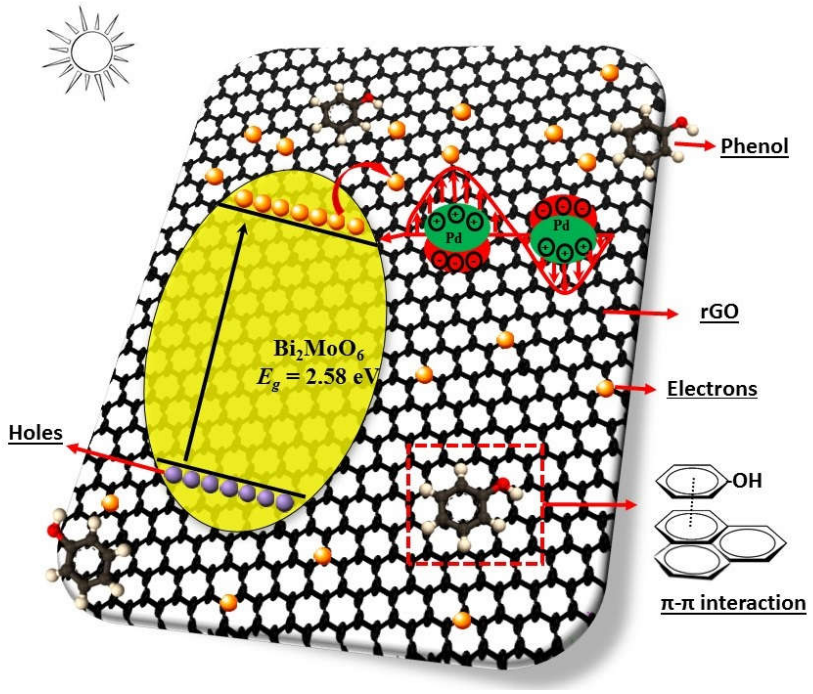


Figure G.13 Proposed mechanism of photocatalytic degradation of phenol in the presence of Pd-rGO-Bi_2MoO_6 composites.

G.4 Conclusions

A ternary Pd-rGO-Bi_2MoO_6 photocatalyst composite was first prepared via solvothermal-photoreduction method. It was found to provide enhanced visible light-driven photocatalytic activity in the removal of phenol in wastewater. The enhanced performance may be attributed to the high separation efficiency of photogenerated electrons and holes. Electrons may be transferred to either the rGO layer or the palladium nanoparticles on the surface. In addition, palladium nanoparticles on the surface can also produce electrons due to the SPR effect. This synergetic effect lead to the excellent visible light-driven photocatalytic degradation of phenol in the wastewater. At last, we believe this work will provide a new idea for the rGO based ternary composites in the area of visible light-driven photocatalysis and shed light on the significances of applying palladium nanoparticles to improve the visible light-induced photocatalytic activity.

References

1. David F Ollis and Hussain Al-Ekabi, *TiO_2 Photocatalytic Purification and Treatment of*

Water and Air, Elsevier Science Ltd, Photocatalytic purification and treatment of water and air: proceedings of the 1st International Conference, 1993.

2. Akihiko Kudo, "Recent progress in the development of visible light-driven powdered photocatalysts for water splitting," *International Journal of Hydrogen Energy*, vol. 32, no. 14, pp. 2673-2678, 2007.

3. Yajun Wang, Qisheng Wang, Xueying Zhan, Fengmei Wang, Muhammad Safdar and Jun He, "Visible light driven type II heterostructures and their enhanced photocatalysis properties: a review," *Nanoscale*, vol. 5, no. 18, pp. 8326-8339, 2013.

4. Xiangchao Meng and Zisheng Zhang, "Bismuth-based Photocatalytic Semiconductors: Introduction, Challenges and Possible Approaches," *Journal of Molecular Catalysis A: Chemical*, vol. 423, pp. 533-549, 2016.

5. Xiangchao Meng and Zisheng Zhang, "Facile synthesis of $BiOBr/Bi_2WO_6$ heterojunction semiconductors with high visible-light-driven photocatalytic activity," *Journal of Photochemistry and Photobiology A: Chemistry*, vol. 310, no. 0, pp. 33-44, 2015.

6. Meng Ni, Michael KH Leung, Dennis YC Leung and K Sumathy, "A review and recent developments in photocatalytic water-splitting using TiO_2 for hydrogen production," *Renewable and Sustainable Energy Reviews*, vol. 11, no. 3, pp. 401-425, 2007.

7. Yanhui Shi, Shouhua Feng and Changsheng Cao, "Hydrothermal synthesis and characterization of Bi2MoO6 and Bi2WO6," *Materials Letters*, vol. 44, no. 3–4, pp. 215-218, 2000.

8. Liwu Zhang, Tongguang Xu, Xu Zhao and Yongfa Zhu, "Controllable synthesis of Bi2MoO6 and effect of morphology and variation in local structure on photocatalytic activities," *Applied Catalysis B: Environmental*, vol. 98, no. 3–4, pp. 138-146, 2010.

9. Xu Zhao, Jiuhui Qu, Huijuan Liu, Zhimin Qiang, Ruiping Liu and Chengzhi Hu, "Photoelectrochemical degradation of anti-inflammatory pharmaceuticals at Bi2MoO6–boron-doped diamond hybrid electrode under visible light irradiation," *Applied Catalysis B: Environmental*, vol. 91, no. 1–2, pp. 539-545, 2009.

10. Bo Yuan, Changhua Wang, Ying Qi, Xiaolong Song, Kai Mu, Peng Guo, Lingtao Meng and Hongmin Xi, "Decorating hierarchical Bi2MoO6 microspheres with uniformly

dispersed ultrafine Ag nanoparticles by an in situ reduction process for enhanced visible light-induced photocatalysis," *Colloids and Surfaces A: Physicochemical and Engineering Aspects*, vol. 425, pp. 99-107, 2013.

11. Shengyao Wang, Xianglong Yang, Xuehao Zhang, Xing Ding, Zixin Yang, Ke Dai and Hao Chen, "A plate-on-plate sandwiched Z-scheme heterojunction photocatalyst: BiOBr-Bi_2MoO_6 with enhanced photocatalytic performance," *Applied Surface Science*.

12. Peifang Wang, Yanhui Ao, Chao Wang, Jun Hou and Jin Qian, "A one-pot method for the preparation of graphene–Bi2MoO6 hybrid photocatalysts that are responsive to visible-light and have excellent photocatalytic activity in the degradation of organic pollutants," *Carbon*, vol. 50, no. 14, pp. 5256-5264, 2012.

13. Guohui Tian, Yajie Chen, Juan Zhou, Chungui Tian, Rong Li, Chujun Wang and Honggang Fu, "In situ growth of Bi_2MoO_6 on reduced graphene oxide nanosheets for improved visible-light photocatalytic activity," *CrystEngComm*, vol. 16, no. 5, pp. 842-849, 2014.

14. Yan Zhang, Yukun Zhu, Jianqiang Yu, Dongjiang Yang, Tsz Wai Ng, Po Keung Wong and Jimmy C. Yu, "Enhanced photocatalytic water disinfection properties of Bi_2MoO_6-RGO nanocomposites under visible light irradiation," *Nanoscale*, vol. 5, no. 14, pp. 6307-6310, 2013.

15. Yuchen Hao, Xiaoli Dong, Xiuying Wang, Shangru Zhai, Hongchao Ma and Xiufang Zhang, "Controllable electrostatic self-assembly of sub-3 nm graphene quantum dots incorporated into mesoporous Bi_2MoO_6 frameworks: efficient physical and chemical simultaneous co-catalysis for photocatalytic oxidation," *Journal of Materials Chemistry A*, vol. 4, no. 21, pp. 8298-8307, 2016.

16. Quanjun Xiang, Jiaguo Yu and Mietek Jaroniec, "Graphene-based semiconductor photocatalysts," *Chemical Society Reviews*, vol. 41, no. 2, pp. 782-796, 2012.

17. Jing Zhang, Chenggang Niu, Ji Ke, Laifeng Zhou and Guangming Zeng, "Ag/AgCl/Bi_2MoO_6 composite nanosheets: A plasmonic Z-scheme visible light photocatalyst," *Catalysis Communications*, vol. 59, pp. 30-34, 2015.

18. Yujie Xiong, Benjamin Wiley, Jingyi Chen, Zhi-Yuan Li, Yadong Yin and Younan Xia,

"Corrosion-Based Synthesis of Single-Crystal Pd Nanoboxes and Nanocages and Their Surface Plasmon Properties," *Angewandte Chemie International Edition*, vol. 44, no. 48, pp. 7913-7917, 2005.

19. Yujie Xiong, Jingyi Chen, Benjamin Wiley, Younan Xia, Yadong Yin and Zhi-Yuan Li, "Size-Dependence of Surface Plasmon Resonance and Oxidation for Pd Nanocubes Synthesized via a Seed Etching Process," *Nano Letters*, vol. 5, no. 7, pp. 1237-1242, 2005.

20. Siliang Li, Hua Li, Jian Liu, Haoli Zhang, Yanmei Yang, Zhengyin Yang, Linyun Wang and Baodui Wang, "Highly efficient degradation of organic dyes by palladium nanoparticles decorated on 2D magnetic reduced graphene oxide nanosheets," *Dalton Transactions*, vol. 44, no. 19, pp. 9193-9199, 2015.

21. Jian Liu, Xing Huo, Tianrong Li, Zhengyin Yang, Pinxian Xi, Zhiyi Wang and Baodui Wang, "Palladium Nanoparticles Bonded to Two-Dimensional Iron Oxide Graphene Nanosheets: A Synergistic and Highly Reusable Catalyst for the Tsuji–Trost Reaction in Water and Air," *Chemistry – A European Journal*, vol. 20, no. 36, pp. 11549-11555, 2014.

22. Xiangchao Meng and Zisheng Zhang, "Pd-doped Bi_2MoO_6 Plasmonic Photocatalysts with Enhanced Visible Light Photocatalytic Performance," *Applied Surface Science*, vol. 392, pp. 169-180, 2016.

23. Satyajit Gupta and Vaidyanathan Subramanian, "Encapsulating $Bi_2Ti_2O_7$ (BTO) with Reduced Graphene Oxide (RGO): An Effective Strategy to Enhance Photocatalytic and Photoelectrocatalytic activity of BTO," *ACS Applied Materials & Interfaces*, vol. 6, no. 21, pp. 18597-18608, 2014.

24. Bradley Allured, Steven DelaCruz, Timothy Darling, Muhammad N. Huda and Vaidyanathan Subramanian, "Enhancing the visible light absorbance of $Bi_2Ti_2O_7$ through Fe-substitution and its effects on photocatalytic hydrogen evolution," *Applied Catalysis B: Environmental*, vol. 144, pp. 261-268, 2014.

25. W. Feng Yao, Hong Wang, X. Hong Xu, X. Na Yang, Yin Zhang, S. Xia Shang and Min Wang, "Preparation and photocatalytic property of La (Fe)-doped bismuth titanate," *Applied Catalysis A: General*, vol. 251, no. 2, pp. 235-239, 2003.

26. Rui Liu, Ping Wang, Xuefei Wang, Huogen Yu and Jiaguo Yu, "UV- and Visible-Light

Photocatalytic Activity of Simultaneously Deposited and Doped Ag/Ag(I)-TiO_2 Photocatalyst," *The Journal of Physical Chemistry C*, vol. 116, no. 33, pp. 17721-17728, 2012.

27. Jinhong Bi, Wei Fang, Li Li, Xiaofen Li, Minghua Liu, Shijing Liang, Zizhong Zhang, Yunhui He, Huaxiang Lin, Ling Wu, Shengwei Liu and Po Keung Wong, "Ternary reduced-graphene-oxide/Bi_2MoO_6/Au nanocomposites with enhanced photocatalytic activity under visible light," *Journal of Alloys and Compounds*, vol. 649, pp. 28-34, 2015.

28. Xiangchao Meng and Zisheng Zhang, "Plasmonic ternary Ag–rGO–Bi_2MoO_6 composites with enhanced visible light-driven photocatalytic activity," *Journal of Catalysis*, vol. 344, pp. 616-630, 2016.

29. Gengtao Fu, Lin Tao, Min Zhang, Yu Chen, Yawen Tang, Jun Lin and Tianhong Lu, "One-pot, water-based and high-yield synthesis of tetrahedral palladium nanocrystal decorated graphene," *Nanoscale*, vol. 5, no. 17, pp. 8007-8014, 2013.

30. I. Oller, S. Malato and J. A. Sánchez-Pérez, "Combination of Advanced Oxidation Processes and biological treatments for wastewater decontamination—A review," *Science of The Total Environment*, vol. 409, no. 20, pp. 4141-4166, 2011.

31. Parag R. Gogate, "Treatment of wastewater streams containing phenolic compounds using hybrid techniques based on cavitation: A review of the current status and the way forward," *Ultrasonics Sonochemistry*, vol. 15, no. 1, pp. 1-15, 2008.

32. Yan Liu, Yao Zhang, Guoheng Ma, Zan Wang, Kaiyu Liu and Hongtao Liu, "Ethylene glycol reduced graphene oxide/polypyrrole composite for supercapacitor," *Electrochimica Acta*, vol. 88, pp. 519-525, 2013.

33. Walter Kohn and Lu Jeu Sham, "Self-consistent equations including exchange and correlation effects," *Physical Review*, vol. 140, no. 4A, pp. A1133, 1965.

34. Giannozzi Paolo, Baroni Stefano, Bonini Nicola, Calandra Matteo, Car Roberto, Cavazzoni Carlo, Ceresoli Davide, L. Chiarotti Guido, Cococcioni Matteo, Dabo Ismaila, Corso Andrea Dal, Gironcoli Stefano de, Fabris Stefano, Fratesi Guido, Gebauer Ralph, Gerstmann Uwe, Gougoussis Christos, Kokalj Anton, Lazzeri Michele, Martin-Samos Layla, Marzari Nicola, Mauri Francesco, Mazzarello Riccardo, Paolini Stefano,

Pasquarello Alfredo, Paulatto Lorenzo, Sbraccia Carlo, Scandolo Sandro, Sclauzero Gabriele, P. Seitsonen Ari, Smogunov Alexander, Umari Paolo and M. Wentzcovitch Renata, "QUANTUM ESPRESSO: a modular and open-source software project for quantum simulations of materials," *Journal of Physics: Condensed Matter*, vol. 21, no. 39, pp. 395502, 2009.

35. F Pertlik and J Zemann, "Neubestimmung der Kristallstruktur des Köchlinits," *Fortschr. Miner. Beih*, vol. 60, pp. 162-163, 1982.

36. CH Bichler, M Bischoff, HC Langowski and U Moosheimer, "39th Annual Technical Conference of the Society of Vacuum Coaters," *Philadelphia, USA, May*, vol. 5, 1996.

37. Peng Zeng, Qinggang Zhang, Tianyou Peng and Xiaohu Zhang, "One-pot synthesis of reduced graphene oxide-cadmium sulfide nanocomposite and its photocatalytic hydrogen production," *Physical Chemistry Chemical Physics*, vol. 13, no. 48, pp. 21496-21502, 2011.

38. Yang-Sen Xu and Wei-De Zhang, "Monodispersed Ag3PO4 nanocrystals loaded on the surface of spherical Bi_2MoO_6 with enhanced photocatalytic performance," *Dalton Transactions*, vol. 42, no. 4, pp. 1094-1101, 2013.

39. CD Wagner and GE Muilenberg, *Handbook of X-ray photoelectron spectroscopy*, Perkin-Elmer, 1979.

40. J. H. Scofield, "Hartree-Slater subshell photoionization cross-sections at 1254 and 1487 eV," *Journal of Electron Spectroscopy and Related Phenomena*, vol. 8, no. 2, pp. 129-137, 1976.

41. David R. Penn, "Quantitative chemical analysis by ESCA," *Journal of Electron Spectroscopy and Related Phenomena*, vol. 9, no. 1, pp. 29-40, 1976.

42. M. A. Butler and D. S. Ginley, "Prediction of Flatband Potentials at Semiconductor - Electrolyte Interfaces from Atomic Electronegativities," *Journal of The Electrochemical Society*, vol. 125, no. 2, pp. 228-232, 1978.

43. Arthur H. Nethercot, "Prediction of Fermi Energies and Photoelectric Thresholds Based on Electronegativity Concepts," *Physical Review Letters*, vol. 33, no. 18, pp. 1088-1091, 1974.

44. R. D. Seals, Robert Alexander, Larry T. Taylor and John G. Dillard, "Core electron binding energy study of group IIb-VIIa compounds," *Inorganic Chemistry*, vol. 12, no. 10, pp. 2485-2487, 1973.

45. S. R. G. Carrazán, C. Martin, V. Rives and R. Vidal, "An FT-IR spectroscopy study of the adsorption and oxidation of propene on multiphase Bi, Mo and Co catalysts," *Spectrochimica Acta Part A: Molecular and Biomolecular Spectroscopy*, vol. 52, no. 9, pp. 1107-1118, 1996.

46. F. Trifirò, H. Hoser and R. D. Scarle, "Relationship between structure and activity of mixed oxides as oxidation catalysts: I. Preparation and solid state reactions of Bi-molybdates," *Journal of Catalysis*, vol. 25, no. 1, pp. 12-24, 1972.

47. Ping Wang, Jin Wang, Xuefei Wang, Huogen Yu, Jiaguo Yu, Ming Lei and Yonggang Wang, "One-step synthesis of easy-recycling TiO_2-rGO nanocomposite photocatalysts with enhanced photocatalytic activity," *Applied Catalysis B: Environmental*, vol. 132–133, pp. 452-459, 2013.

48. Haruna Adamu, Prashant Dubey and James A. Anderson, "Probing the role of thermally reduced graphene oxide in enhancing performance of TiO_2 in photocatalytic phenol removal from aqueous environments," *Chemical Engineering Journal*, vol. 284, pp. 380-388, 2016.

49. Peter W Voorhees, "The theory of Ostwald ripening," *Journal of Statistical Physics*, vol. 38, no. 1-2, pp. 231-252, 1985.

50. Hua Gui Yang and Hua Chun Zeng, "Preparation of Hollow Anatase TiO_2 Nanospheres via Ostwald Ripening," *The Journal of Physical Chemistry B*, vol. 108, no. 11, pp. 3492-3495, 2004.

51. KSW Sing, DH Everett, RAW Haul, L Moscou, RA Pierotti, J Rouquerol and T Siemieniewska, "Physical and biophysical chemistry division commission on colloid and surface chemistry including catalysis," *Pure Applied Chemistry*, vol. 57, no. 4, pp. 603-619, 1985.

52. Michal Kruk and Mietek Jaroniec, "Gas Adsorption Characterization of Ordered Organic−Inorganic Nanocomposite Materials," *Chemistry of Materials*, vol. 13, no. 10, pp.

3169-3183, 2001.

53. Matthias Thommes, Katsumi Kaneko, V. Neimark Alexander, P. Olivier James, Francisco Rodriguez-Reinoso, Jean Rouquerol and S. W. Sing Kenneth, "Physisorption of gases, with special reference to the evaluation of surface area and pore size distribution (IUPAC Technical Report)," in *Pure and Applied Chemistry*, Ed., pp. 1051, 2015.

54. Gaozu Liao, Shuo Chen, Xie Quan, Hongtao Yu and Huimin Zhao, "Graphene oxide modified g-C_3N_4 hybrid with enhanced photocatalytic capability under visible light irradiation," *Journal of Materials Chemistry*, vol. 22, no. 6, pp. 2721-2726, 2012.

55. Erping Gao, Wenzhong Wang, Meng Shang and Jiehui Xu, "Synthesis and enhanced photocatalytic performance of graphene-Bi_2WO_6 composite," *Physical Chemistry Chemical Physics*, vol. 13, no. 7, pp. 2887-2893, 2011.

56. Suljo Linic, Phillip Christopher and David B. Ingram, "Plasmonic-metal nanostructures for efficient conversion of solar to chemical energy," *Nature Materials*, vol. 10, no. 12, pp. 911-921, 2011.

57. Kangrong Lai, Wei Wei, Ying Dai, Ruiqin Zhang and Baibiao Huang, "DFT calculations on structural and electronic properties of Bi_2MO_6 (M = Cr, Mo, W)," *Rare Metals*, vol. 30, no. 1, pp. 166-172, 2011.

58. Manon Vautier, Chantal Guillard and Jean-Marie Herrmann, "Photocatalytic Degradation of Dyes in Water: Case Study of Indigo and of Indigo Carmine," *Journal of Catalysis*, vol. 201, no. 1, pp. 46-59, 2001.

59. Janet M. Kesselman, Gary A. Shreve, Michael R. Hoffmann and Nathan S. Lewis, "Flux-Matching Conditions at TiO_2 Photoelectrodes: Is Interfacial Electron Transfer to O_2 Rate-Limiting in the TiO_2-Catalyzed Photochemical Degradation of Organics?," *The Journal of Physical Chemistry*, vol. 98, no. 50, pp. 13385-13395, 1994.

60. Baifu Xin, Zhiyu Ren, Haiyuan Hu, Xiangyu Zhang, Chunlei Dong, Keying Shi, Liqiang Jing and Honggang Fu, "Photocatalytic activity and interfacial carrier transfer of Ag–TiO_2 nanoparticle films," *Applied Surface Science*, vol. 252, no. 5, pp. 2050-2055, 2005.

61. Hao Zhang, Xiaojun Lv, Yueming Li, Ying Wang and Jinghong Li, "P25-Graphene

Composite as a High Performance Photocatalyst," *ACS Nano*, vol. 4, no. 1, pp. 380-386, 2010.

62. Joanne Gamage McEvoy, Wenquan Cui and Zisheng Zhang, "Synthesis and characterization of Ag/AgCl–activated carbon composites for enhanced visible light photocatalysis," *Applied Catalysis B: Environmental*, vol. 144, no. 0, pp. 702-712, 2014.

63. Yanyuan Wen, Hanming Ding and Yongkui Shan, "Preparation and visible light photocatalytic activity of Ag/TiO_2/graphene nanocomposite," *Nanoscale*, vol. 3, no. 10, pp. 4411-4417, 2011.

Appendix H Palladium nanoparticles and rGO co-modified $BiVO_4$ with greatly improved visible light-induced photocatalytic activity

Xiangchao Meng, Zizhen Li and Zisheng Zhang

Chemosphere 198 (2018), 1-12

Abstract

A ternary composite, Pd-rGO-$BiVO_4$, was fabricated with reduced graphene oxide (rGO) and palladium nanoparticles decorated on the surface of $BiVO_4$. As-prepared samples were tested for the photocatalytic degradation of phenol under visible light irradiation. Enhancement was observed for the ternary structure, merits of which may be as follows: 1) rGO wrapped $BiVO_4$ facilitated the photogenerated electrons transfer, 2) palladium nanoparticles served as electron acceptors, 3) palladium nanoparticles on the surface were capable of absorbing visible light photons. The uptake of photogenerated charge carriers would improve their separation and more oxidative species may be produced that can participate in the degradation of organics. Due to the SPR effect of palladium nanoparticles on the surface, the harvesting capacity of the photocatalyst to absorb visible light photons was increased, and thus its photocatalytic activity was improved. It should be noted that phenol was more easily adsorbed by rGO due to the π-π interaction between rGO and phenol, which also contributed to the enhancement in the photocatalytic activity. This work provides new evidence to confirm the advances of ternary structures applied in the photocatalytic removal of phenolic compounds in water under visible light irradiation.

H.1 Introduction

$BiVO_4$ as a ferroelastic and ion conductive material has attracted extensive attentions [1-4]. The properties of $BiVO_4$ significantly depend on the crystal form. There are three primary crystal forms: zircon structure with tetragonal system (ZT), scheelite structure with monoclinic system (SM), and scheelite structure with tetragonal (ST) system. Generally, it was reported that $BiVO_4$ with monoclinic crystal structure exhibited higher photocatalytic activity than that with tetragonal crystal structure [5, 6]. This phenomenon was probably attributed to the narrower band gap (ca. 2.4 eV) for monoclinic $BiVO_4$ compared with that (ca. 2.9 eV) for tetragonal $BiVO_4$ [7]. As a result, monoclinic $BiVO_4$ with the suitable band gap has been comprehensively studied and implemented in visible light-driven photocatalysis.

One of the hindrances for photocatalysis with $BiVO_4$, to date, is the low photoconversion efficiency, mainly due to the high recombination rate of photogenerated charge carriers. Aiming to deal with this hindrance for $BiVO_4$ based systems, various approaches were employed, mainly including metal/nonmetal doping [8-12] and the formation of heterojunctions [4, 13-20]. Li et al. deposited Au, Pt and Ag nanoparticles on the surface of $BiVO_4$ polyhedrons [21]. It was found metals and metal oxides were facet-selectively photo-deposited on the surface of $BiVO_4$. This phenomenon may occur because the photogenerated electrons tend to transfer to the 010 facets and holes accumulate on the 110 facets. This mechanism can be applied in designing efficient photocatalysts. Moreover, well-dispersed metallic nanoparticles on the surface are capable of facilitating the separation of photogenerated charge carriers and absorbing visible light photons via the surface plasmon resonance (SPR) effect [22]. Ag, Au and Pt nanoparticles loaded on $BiVO_4$ have been reported with enhanced visible light-driven photocatalytic activity in the oxidation of organics in water [23-25]. Recently, we reported palladium nanoparticles can also be photoreduced onto a support to improve its photocatalytic activity [26-28]. The SPR peaks for palladium nanoparticles can be tuned from 410 to 870 nm [29, 30].

Graphene, a single layer of sp^2-bonded carbon atoms tightly packed into a two-dimensional honey bomb structure, has been extensively studied and implemented in various areas including photocatalysis. The excellent conductivity of graphene suggests it may be a

promising candidate in facilitating the separation of photogenerated charge carriers. Graphene wrapped $BiVO_4$ were reported with greatly improved photocatalytic activity in the organics degradation [31]. It should also be noted that graphene may be prepared by reducing graphene oxide (GO), which is an effective an inexpensive approach. Ng et al. reported on oxygen-functional groups on GO may be reduced through hydrothermal treatment [32]. Since rGO can be regarded as an electron acceptor, an rGO layer may be introduced between the metallic nanoparticles and $BiVO_4$ to further facilitate the separation of photogenerated charge carriers [33]. We recently successfully prepared ternary structures of Ag/Pd and rGO co-modified Bi_2MoO_6 with synergetic effects in enhancing the photocatalytic activity of the support [34, 35].

In this work, GO wrapped $BiVO_4$ polyhedrons would be fabricated and further hydrothermally reduced to rGO-$BiVO_4$ composites. Palladium nanoparticles would then be photo-dispersed on rGO-$BiVO_4$ composites to fabricate the ternary structure. As-prepared composites were applied in photocatalytic degradation of a colorless organics model, phenol, which is widely found in wastewater from many industrial processes and is generally difficult to decompose [36, 37]. This work would shed a light on the possibility of using ternary photocatalysts for treating phenolic compounds in water under visible light irradiation.

H.2 Experimental

H.2.1 Preparation of $BiVO_4$, rGO-$BiVO_4$ and Pd-rGO-$BiVO_4$

$BiVO_4$ polyhedrons were prepared using a hydrothermal method. Typically, 36 mmol NH_4VO_3 (Fisher Scientific, Certified ACS) and 36 mmol of $Bi(NO_3)_3 \cdot 5H_2O$ (Fisher Scientific, Certified ACS) were first dissolved in 300 mL of nitric acid solution (2.0 M). The pH was then adjusted to 2 using an ammonia solution. Orange precipitates were immediately formed and the suspension was then magnetically stirred for 30 min. After a 2 h aging period, the orange precipitates at the bottom were transferred to a 100-mL Teflon-lined autoclave (Parr Instrument Company, USA) and heated up to 200 °C for 24 h. After the autoclave naturally cooled down to room temperature, the yellow precipitates were filtered out and washed twice with distilled deionized water (DDW) and one time with

absolute ethanol. The precipitates were then dried at 60 °C for 12 h before getting collected for further use.

The rGO-$BiVO_4$ composites were synthesized through an evaporation-induced self-assembly process to form GO-$BiVO_4$ composites followed with a photo-reduction process [38]. Firstly, 1.0 g of as-prepared $BiVO_4$ polyhedrons dispersed in 50 mL ethanol and 3.75 mL of graphene oxide (GO, 4 mg/mL, Sigma-Aldrich Canada) dispersed in 50 mL DDW, respectively, were ultrasonicated for 1 h. Then, GO precursor suspension was dropwise added into the $BiVO_4$ suspension and magnetically stirred for 8 h without sealing. After that, the mixture was heated up to 60 °C and maintained using a water bath, and continuously magnetically stirred until the solvent evaporated completely. The formed precipitates were dried at 60 °C for 12 h before they were collected and labelled as GO-Bi for further use. The formed GO-Bi samples were further reduced using a photo-reduction method. Specifically, 1.0 g of GO-Bi were dispersed in a solution containing 100 mL DDW and 20 mL ethanol. After magnetically stirring for 30 min, the suspension was purged using pure N_2 for 30 min. After that, the suspension was illuminated for 3h using a 300-W halogen tungsten projector lamp (Ushio, USA). Prepared particles in the suspension were filtered out, dried at 60°C for 12h and labelled as rGO-Bi.

Palladium nanoparticles are dispersed on the rGO-Bi composites through a photo-reduction process [26, 35]. Typically, 0.30 g of rGO-Bi composites were dispersed in 40 mL DDW under ultrasonication for 30 min. A designate amount of $PdCl_2$ (Fisher Scientific Canada, ACS certified) suspension was then added into the suspension with magnetic stirring for 10 min. After that, the suspension was illuminated under a 300-W halogen tungsten projector lamp (Ushio, USA) for 1 h. The resultant products were filtered out, washed twice with DDW and dried at 60 °C for 12 h. Composites of 0.5, 1.0 and 2.0 wt% Pd-rGO-$BiVO_4$ were prepared following the above procedures and labelled as 0.5, 1.0 and 2.0 Pd(G)-Bi. For comparison, composites of 1.0 wt% Pd-$BiVO_4$ were also prepared following the above procedures except with pure $BiVO_4$ instead of rGO-Bi, and labelled as 1.0 Pd-Bi.

H.2.2 Characterization

Crystal structures of prepared samples were measured using a Rigaku Ultima IV diffractometer with Cu Kα radiation (λ = 0.15418 nm) at 40 kV and 44 mA for the X-ray

diffraction analysis (XRD). Surface composition and chemical states were studied using a XSAM-800 X-ray Photoelectron Spectroscope (XPS). Morphologies of prepared samples are investigated using a field-emission scanning electron microscope (FE-SEM, JEOL JSM-7500F) and a transmission electron microscope (TEM, JEM-2100F). An Energy-dispersive X-ray spectroscopy (EDS) was also equipped in the FE-SEM for the elemental analysis of prepared samples. Optical properties were explored on an ultraviolet-visible diffuse reflectance spectroscopy (UV-Vis DRS). Electrochemical properties of prepared samples were performed on a CHI 604E electrochemical analyzer (CH Instruments Inc., USA) with a platinum wire as a counter electrode, a calomel reference electrode and a working electrode. The working electrode was composed of indium tin oxide (ITO, 75 × 25 × 1.1 mm, 15 - 25 Ω, Sigma-Aldrich Canada Co.) glass coated with the prepared samples. The electrolyte was Na_2SO_4 with a concentration of 0.1 M.

H.2.3 Photocatalytic activity tests

Photocatalytic activity of as-prepared samples was evaluated by degradation of a colorless organic pollutant, phenol, in water under visible light irradiation. For each test, 100 mL of phenol solution with an initial concentration of 10 mg/L was placed in a 500 mL-beaker, and the temperature was maintained at 20°C using a cooling jacket. A 300-W halogen tungsten projector lamp was used with a UV cut-off (Kenko Zeta, transmittance > 90%) to filter out irradiation with wavelengths below 410 nm. The irradiation intensity at the surface of the reacting solution was measured using a quantum meter (Biospherical QSL-2100, $400 < \lambda < 700$ nm) to be 1.1×10^{-2} Einsteins m^{-2} s^{-1}. In each test, 0.10 g of samples were first mixed in the phenol solution by magnetically stirring for 60 min. This was performed in the dark so as to reach an adsorption-desorption equilibrium. The photocatalytic degradation of phenol was performed for 6 h, and aliquots were drawn and filtered using 0.2-μm filters. The filtered solvent was analyzed on a high-performance liquid chromatograph (HPLC, Agilent 1100 series) equipped with a UV-Vis detector. A ZORBAX Eclipse Plus C18 column (4.6 × 250 mm) was used at a temperature of 60°C. The detecting wavelength was fixed at 270 nm for the detection of phenol and possible intermediates. The flow phase was composed of methanol (55%, V/V) and water (45%, V/V) at a flow rate of 0.6 mL/min. The injection volume was set to 25 μL. The total organic

carbon (TOC) was evaluated on an Appollo 9000 TOC analyzer equipped with a Non-Dispersive Infra-Red (NDIR) detector. The combustion temperature was fixed at 750 °C.

In the quenching experiments, ethylenediaminetetraacetic acid disodium (EDTA-2Na) and isopropanol (IPA) with a concentration of 1 M were added to the reaction system as scavengers for holes and hydroxyl free radicals, respectively. Also, N_2 bubbling was applied to purge dissolved oxygen so as to explore the effect of superoxide free radicals on the photocatalytic degradation of phenol. Photocatalysts in all quenching tests were 1.0 Pd(G)-Bi composites.

To explore the reusability of as-prepared photocatalysts, five degradation cycles were tested for the degradation of phenol under visible light. The testing conditions for all cycles were kept consistent with the photocatalytic activity tests, except recycling use of the photocatalysts without regeneration. The composite of 1.0 Pd(G)-Bi was used for the recycling tests.

A *p*-chlorobenzoic acid (pCBA, Fisher Scientific Canada, ACS certified) was used to probe the concentration of OH radicals produced during the photocatalysis [39-41]. The initial concentration of pCBA was at 10 μM, catalysts ($BiVO_4$ and 1.0 Pd(G)-Bi) dosage amount was equal to 1.0 g/L and the solution volume was 100 mL. Photocatalytic degradation of pCBA was carried out for 90 min under visible light irradiation. Aliquots were taken and centrifuged. The supernatant was analyzed using an HPLC with the detecting wavelength at 254 nm. All other parameters were kept the same with the detection of phenol. For comparison, TiO_2 (anatase powder, Fisher Scientific Canada, ACS certified) was also tested under UV light.

H.2.4 Electronic structure calculation

The quantum-mechanical calculations were performed on the basis of the density functional theory (DFT) [42]. The Perdew-Burke-Ernzerhof generalized gradient approximation (GGA) was applied to exchange-correlation effects. The open access software Quantum ESPRESSO was used, which utilizes pseudopotentials to describe electron-ion interactions and represents electronic wave functions using a plane-wave basis set [43]. The kinetic energy cut-off was set to 25 Ry (340 eV).

H.3 Results and discussions

H.3.1 Crystal structure and surface components analysis

XRD patterns (Fig. H.1) indicates the as-prepared $BiVO_4$ has a monoclinic scheelite phase (space group: I2/b(15), PDF card #: 75-1866). All peaks can be indexed and no impurities were found. It suggests a high crystallinity of $BiVO_4$ was prepared using the hydrothermal method. For XRD patterns for GO, rGO, and Pd-rGO modified $BiVO_4$ composites, negligible influence on the $BiVO_4$ support was observed, suggesting the crystal structure of $BiVO_4$ was not destructed during the modification processes. The quantity of GO, rGO and Pd was too low to be detected by the XRD technique. Furthermore, lattice parameters were also calculated and shown in Fig. H.1. No apparent differences were found, which further confirmed these modifiers may not be doped in the lattice of $BiVO_4$ and possibly just rest on the surface as opposed to covalently anchoring to the lattice of $BiVO_4$.

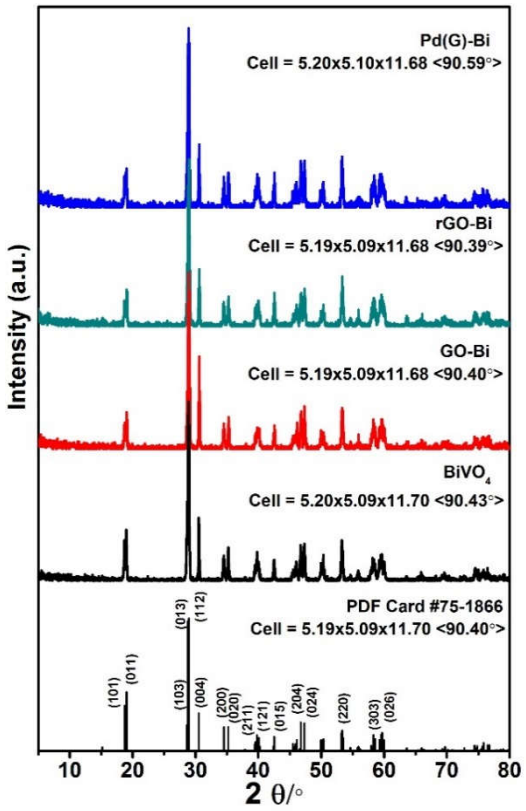


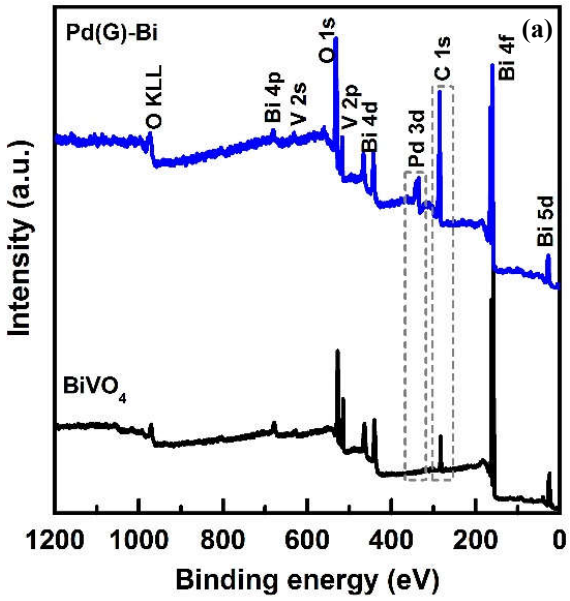
Figure H.1 XRD patterns of as-prepared samples.

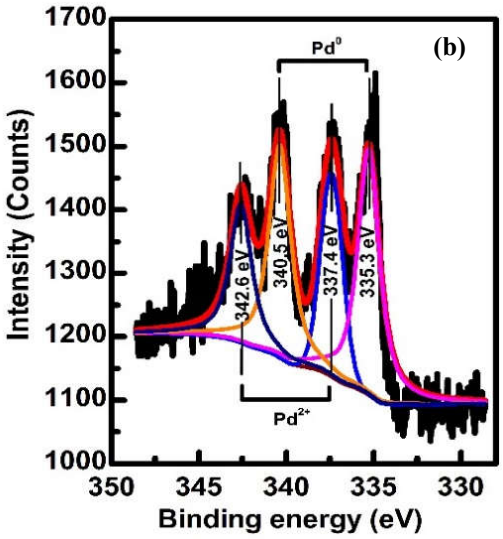
To further probe the surface composition as well as its chemical states, XPS was employed and the results are shown in Fig. H.2. All spectra were calibrated with C 1s, the binding

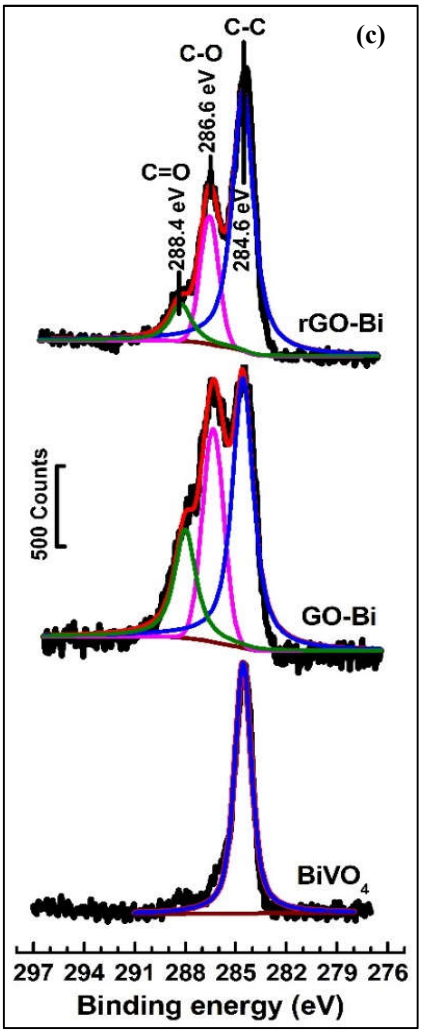
energy of which was fixed at 284.6 eV. In the survey spectra (Fig. H.2a), for pure $BiVO_4$, all components namely Bi, V and O are identified; for Pd(G)-Bi, peaks for palladium were also detected and peaks for C 1s orbits became stronger. Furthermore, high-resolution orbital scan for C 1s was measured (Fig. H.2c). XPS C1s spectrum for GO-Bi clearly shows three peaks located at binding energies of 284.6, 286.6 and 288.4 eV, corresponding to nonoxygenated ring C bonds, the C-O and the carbonyl C in C=O, respectively [34, 35, 44, 45]. After the photo-reduction process, the peak intensities for C-O and C=O were decreased, indicating GO was partially converted to rGO. To quantitively evaluate the reduction degree, the surface concentration for a component can be calculated using Equation 1 as below,

$$c_i = \frac{\frac{A_i}{q_i}}{\left[\sum_{i=1}^{n} \frac{A_i}{q_i}\right]} \qquad \textbf{\textit{Equation 1}}$$

where c_i are concentrations of specie i, A_i are XPS peak areas and q_i are experimental photoionization cross sections as given by Wagner [46] for various elements present in the surface. As a result, there were 35.0% and 65.1% reduction of C=O and C-O. In Fig. H.2d, two peaks at 159.1 and 164.5 eV are attributed to Bi $4f_{7/2}$ and Bi $4f_{5/2}$ of $BiVO_4$, respectively, and the other two peaks at 161.0 and 166.2 eV may be ascribed to the formation of Bi-O-C bonds that formed between the $BiVO_4$ and rGO [47]. This strong bonding is in favor of the uptake of charge carriers between $BiVO_4$ and rGO. With further loading of palladium on the surface of rGO-Bi composites, negligible influence on the Bi4f orbits was observed. This indicates palladium may not doped in the lattice of $BiVO_4$ and merely rest on the surface. A set of spin-orbit doublets were observed in the XPS Pd 3d spectrum (Fig. H.2b) for Pd(G)-Bi composites. Specifically, peaks at 342.6 and 337.4 eV may be accorded to Pd $3d_{3/2}$ and $3d_{5/2}$ binding energies, respectively, being indicative of Pd^{2+} in the form of $PdCl_2$. Moreover, smaller peaks at binding energies of 340.5 and 335.3 eV may be attributed to the metallic Pd (Pd^0) [26]. The relative concentration ratio of bivalent to metallic palladium (c_{Pd2+}/c_{Pd0}) can be calculated through Equation 1, as approximately 1:1.6. It suggests Pd^{2+} was partially reduced to metallic Pd during the photoreduction process.


Pd(G)-Bi
(a)
O KLL
Bi 4p
V 2s
O 1s
V 2p
Bi 4d
Pd 3d
C 1s
Bi 4f
Bi 5d
BiVO4
Intensity (a.u.)
1200 1000 800 600 400 200 0
Binding energy (eV)


(b)
Pd0
342.6 eV
340.5 eV
337.4 eV
335.3 eV
Pd2+
Intensity (Counts)
1700 1600 1500 1400 1300 1200 1100 1000
350 345 340 335 330
Binding energy (eV)


(c)
C-C
C-O
286.6 eV
C=O
288.4 eV
284.6 eV
rGO-Bi
500 Counts
GO-Bi
BiVO4
297 294 291 288 285 282 279 276
Binding energy (eV)

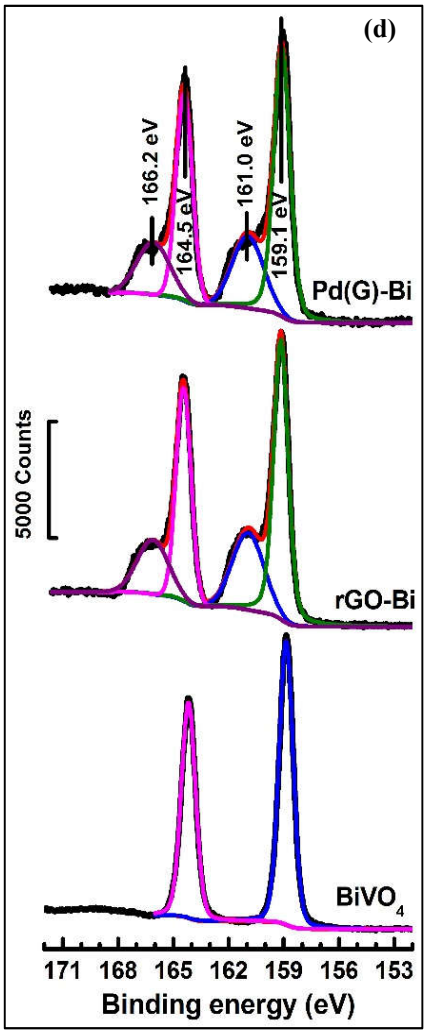

(d)
166.2 eV
164.5 eV
161.0 eV
159.1 eV
Pd(G)-Bi
5000 Counts
rGO-Bi
BiVO4
171 168 165 162 159 156 153
Binding energy (eV)

Figure H.2 (a) XPS survey spectra for $BiVO_4$ and Pd(G)-Bi, and high-resolution orbital scans of (b) Pd 3d for Pd(G)-Bi, (c) C 1s for $BiVO_4$, GO-Bi and rGO-Bi and (d)Bi 4f for $BiVO_4$, rGO-Bi and Pd(G)-Bi.

H.3.2 Morphologies and possible formation processes

Morphologies of prepared samples are investigated through SEM and TEM as shown in Fig. H.3 and H.4. Pure $BiVO_4$ polyhedrons show a well-defined truncated bipyramid shape with highly active (040) facets exposed, and the surfaces are smooth (Fig. H.3a). For rGO-Bi composites as shown in Fig. H.3b, rGO sheets are completely covered on $BiVO_4$ surfaces. Moreover, nanoparticles as well as wrinkled rGO sheets at the edges can be observed in Fig. H.3c for Pd(G)-Bi composites. The existence of Pd in the Pd(G)-Bi was further confirmed in the EDS spectra as shown in Fig. H.3d. Wrinkled GO sheets can be observed in Fig. H.4a. For pure $BiVO_4$, no impurities can be found on the surface which agrees well with the SEM result (Fig. H.4b). In Fig. H.4c, rGO sheets were perfectly wrapped on $BiVO_4$, and $BiVO_4$ fragments can also be found on the rGO sheets. In Fig. H.4d, since the $BiVO_4$ was too thick, nanoparticles on $BiVO_4$ as shown in Fig. H.3c were not observed, but palladium nanoparticles were well dispersed on the rGO sheets. In Fig. H.5, palladium nanoparticles were also found present on the surface of $BiVO_4$. It indicates photogenerated electrons, during the photoreduction process, may be reacted with Pd^{2+} on the surface of $BiVO_4$, and may transferred to graphene sheets and then reduced Pd^{2+} on graphene. As a result, palladium nanoparticles were prepared on both graphene sheets and surface of $BiVO_4$. The size distribution is shown in the inset of Fig. H.4d; all particles were with diameters in the range of 2 - 6 nm which is a solid evidence to prove the successful formation palladium nanoparticles on the surface of Pd(G)-Bi.

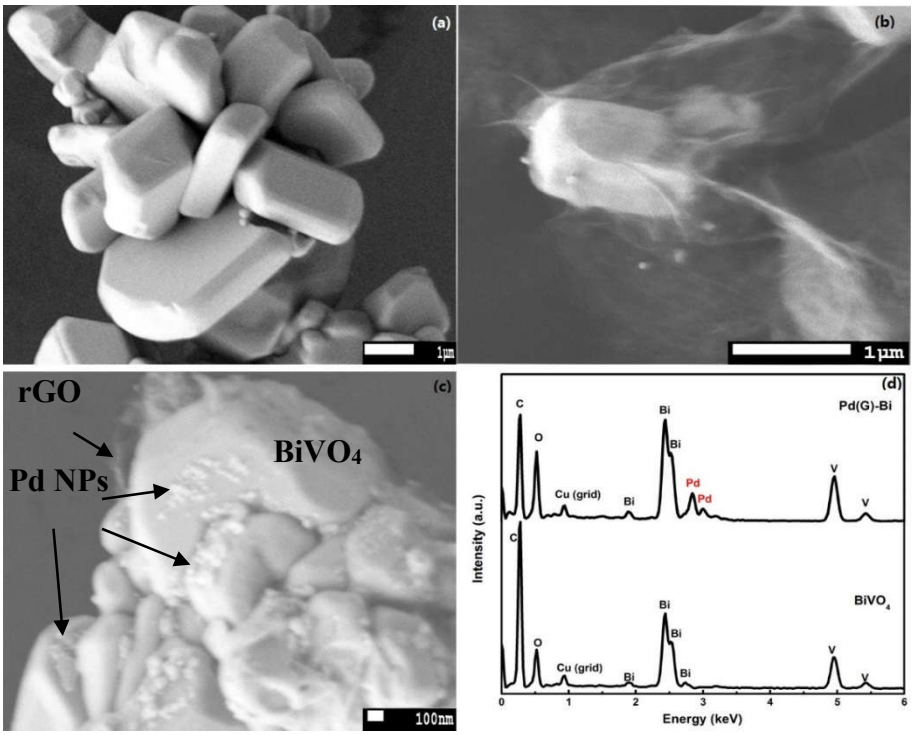


Figure H.3 SEM images of (a) $BiVO_4$, (b) rGO-Bi and (c) Pd(G)-Bi, and (d) EDS spectra for pure $BiVO_4$ and Pd(G)-Bi.

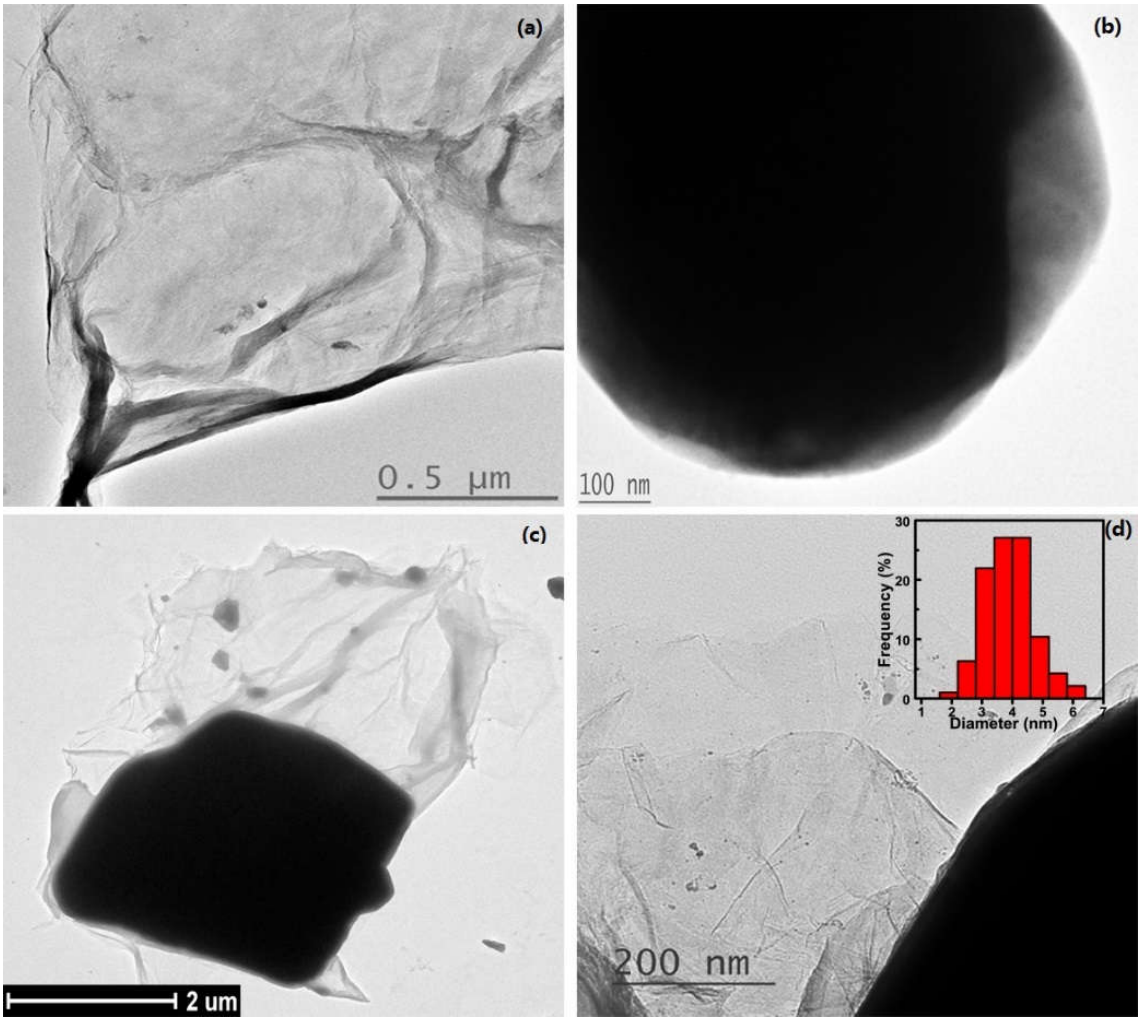


Figure H.4 TEM images of (a) GO, (b) $BiVO_4$, (c) rGO-Bi and (d) Pd(G)-Bi (inset: particle sizes distribution).

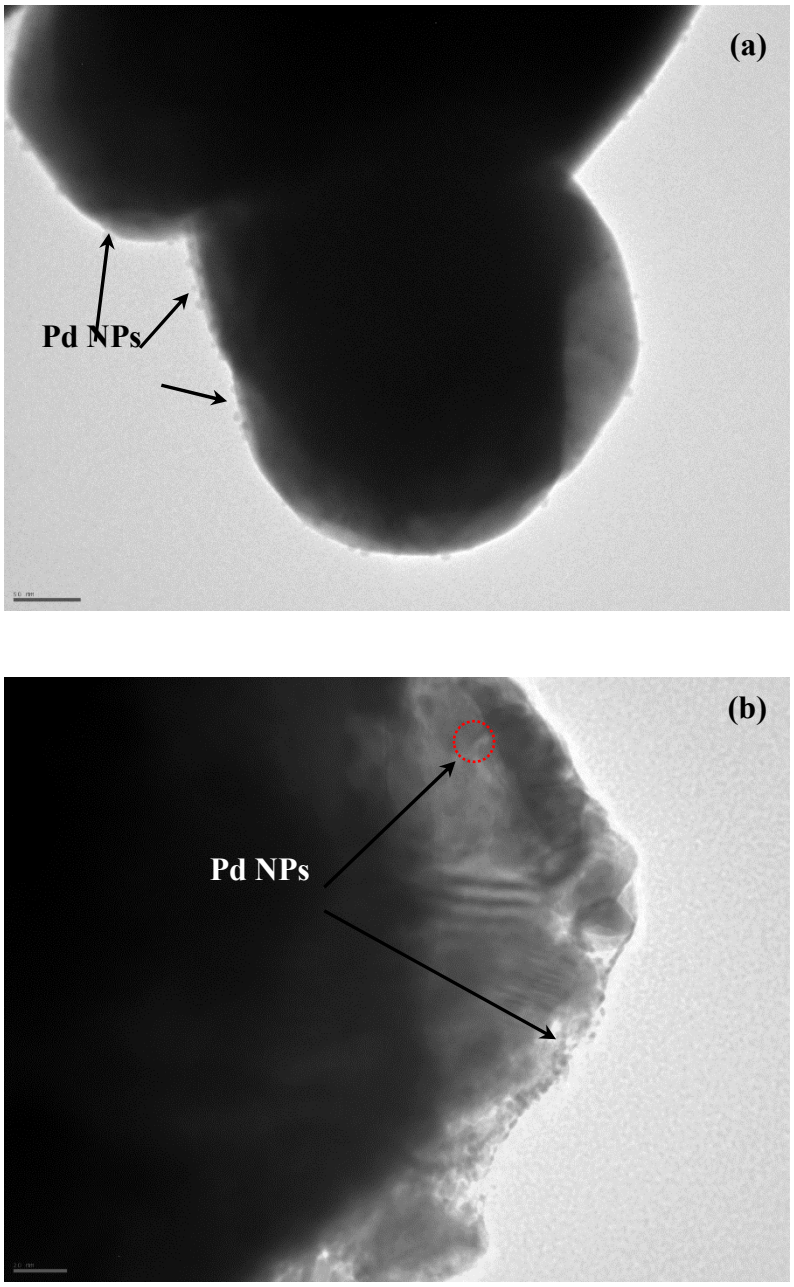


Figure H.5 TEM images of Pd(G)-Bi composites.

Based on the discussions above, a possible step-by-step process for synthesizing Pd(G)-Bi composites were proposed in Fig. H.6. Specifically, when the yellow suspension of $BiVO_4$ and the black suspension mixed together, their self-assembly formed the GO-Bi composites with the suspension color of light green. In the photo-reduction process, the color of the GO-Bi suspension was changed to dark brown, which was possibly attributed to the partial

restoration of the π-network within the graphitic carbon structure [48]. This color change was also an indication of the successful reduction of GO. As indicated from the XPS results, GO was successfully reduced, especially the oxygen-functional groups. The reduction process facilitated the transfer of photogenerated charge carriers from $BiVO_4$ to the rGO sheets. As for the photo-reduction process when loading palladium nanoparticles, the color of the suspension was changed to black. Theoretically, the redox potential of Pd^{2+}/Pd^0 was 0.987 V (*vs* NHE). The bottom potential of the conduction band of $BiVO_4$ can be calculated as 0.395 eV using Equation 2 and the top potential of the valence band of $BiVO_4$ can be obtained as 2.685 eV through Equation 3 as follows:

$$E_{\mathrm{CB,\,BiVO_4}} = \chi_{\mathrm{BiVO_4}} - E^e - \frac{1}{2}E_g \qquad \textbf{\textit{Equation 2}}$$

$$E_{\mathrm{VB,\,BiVO_4}} = E_{\mathrm{CB,\,BiVO_4}} + E_g \qquad \textbf{\textit{Equation 3}}$$

where χ_{BiVO_4}, E^e and E_g are the electronegativity (6.04 eV for $BiVO_4$) [49], the energy of free electrons on the hydrogen scale ($\approx$ 4.5eV), and the band gap of $BiVO_4$ (2.29 eV, from section 3.3) [50, 51]. This means the photogenerated electrons on the conduction band of $BiVO_4$ can reduce Pd^{2+} to Pd^0 during the photo-reduction process. The color change to black, shown in Fig. H.6, revealed that the Pd^{2+} was successfully reduced to metallic Pd^0 on the rGO-Bi composites.

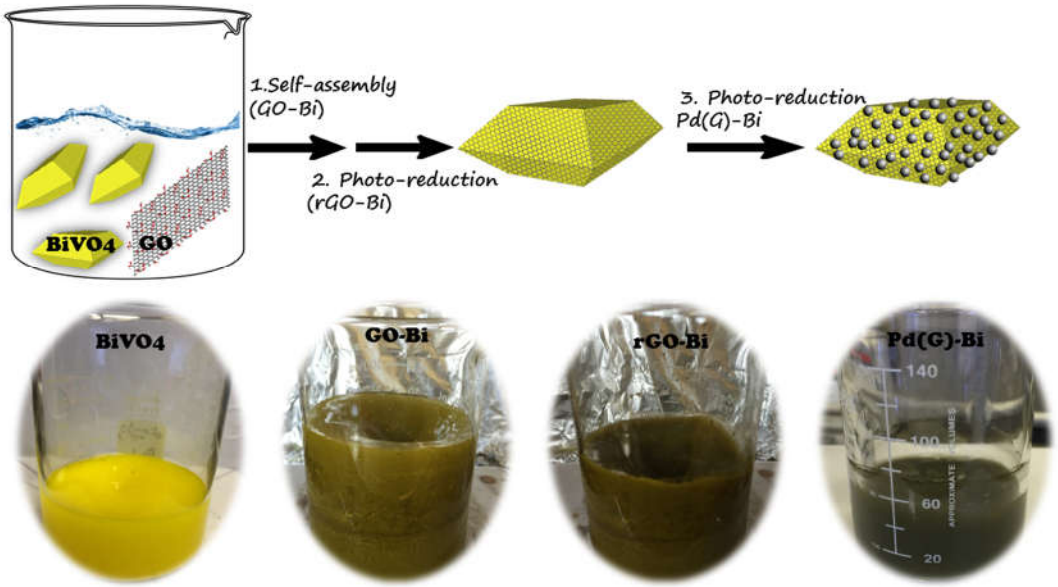


Figure H.6 Schematic illustration of preparation of Pd(G)-Bi composites and photos for prepared samples.

H.3.3 Band structure analysis and optical properties

The band configuration of $BiVO_4$ based on the obtained crystal structures and lattice parameters was simulated and shown in Fig. H.7. The band gap value can be calculated as about 2.46 eV. The band-gap transition for $BiVO_4$ attributed to the indirect type. In an indirect band gap, activated electrons on the conduction band may return to the valence band to recombine with the holes. However, it cannot directly transfer from the bottom of conduction band to the top of valence band. Instead, assistance by additional photons is required for the transfer within the indirect band gap as shown in Fig. H.7 [52]. Thus, the lifetimes of photogenerated charge carriers were prolonged, thereby increasing the photocatalytic activity. The tendency of recombination between photogenerated electrons and holes may be evaluated via comparison of their effective mass [53, 54]. The effective mass (m^*) of electrons and holes can be obtained through Equation 4, and the relative ratio of effective mass of electrons (m_e^*) to that of holes (m_h^*) can be expressed through Equation 5 as follows,

$$m^* = \frac{\hbar^2}{\frac{d^2 E_\kappa}{d\kappa^2}} \qquad \textit{Equation 4}$$

$$\frac{m_e^*}{m_h^*} = \left| \frac{\left.\frac{d^2 E_\kappa}{d\kappa^2}\right|_h}{\left.\frac{d^2 E_\kappa}{d\kappa^2}\right|_e} \right| \qquad \textit{Equation 5}$$

where κ is the wave vector, and $E\kappa$ is the energy corresponding to the wave vector κ. It should be noted that charge carriers with higher effective mass with lower mobility. Using parabolic fitting, values of the second-order term of $E\kappa$ for electrons on the conduction band minimum (CBM) and holes on the valence band maximum (VBM) are computed and shown in Table H.1 [55]. It reveals that the mobility of the electrons is similar to that of the holes. It indicates the photo-generated charge carriers' separation is difficult for a perfect $BiVO_4$ and approaches to facilitate the separation are required to increase the photocatalytic activity.

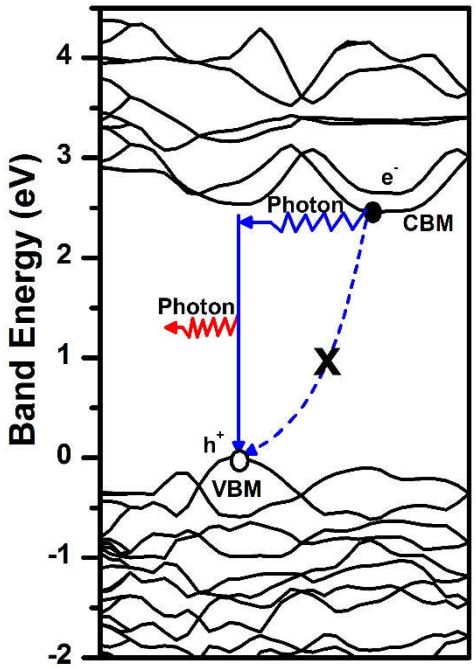


Figure H.7 Band configuration of $BiVO_4$ simulated using the Quantum Espresso code [43], and pathways of electrons recombined with holes.

Table H.1 Parameter values for Equation 4 and 5.

Parameter	$\left.\frac{d^2E_\kappa}{d\kappa^2}\right\|_h$	$\left.\frac{d^2E_\kappa}{d\kappa^2}\right\|_e$	$\frac{m_e^*}{m_h^*}$
Value	-27.78	27.22	1.02

Optical properties of prepared samples were investigated through the UV-Vis DRS as shown in Fig. H.8. Pure $BiVO_4$ clearly shows an absorption edge at around 540 nm. The steep increase with wavelength below 540 nm was resulted from the band-gap transition. With the introduction of GO and rGO, the absorption intensity in the range of 540 – 700 nm was improved, possibly attributed to the broad contribution from the absorbance of GO and rGO [56, 57]. Upon introduction of palladium nanoparticles on the surface of rGO-Bi composites, the absorption intensity in the visible light range was greatly improved and the enhancement was increased with increase of the palladium content. This improvement may be caused by the local surface plasmonic resonance effect of palladium nanoparticles [10, 26, 30, 58]. To further quantitively explore the band gap value for prepared samples, classic Tauc relation as shown in Equations 6 and 7 were applied [59] as follows,

$$\alpha E_{photon} = K(E_{photon} - E_g)^{\frac{n}{2}} \qquad \textbf{Equation 6}$$

$$E_{photon} = h\nu \qquad \textbf{Equation 7}$$

Where α, E_{photon}, K, E_g n, h and ν, respectively, represent the absorption coefficient, energy of irradiated photon, constant (usually equal to 1 for semiconductors), band gap value, constant depending on the type of band-gap transition (specifically, n = 1 for direct transition and n = 4 for indirect transition). E_g can be obtained by plotting αE_{photon} *vs* E_{photon} (Fig. H.9). For $BiVO_4$, a band gap of 2.29 eV was obtained, and with the introduction of GO, rGO, and palladium, no apparent red shift was observed. This phenomenon suggests no elements were doped in the lattice of the support $BiVO_4$.

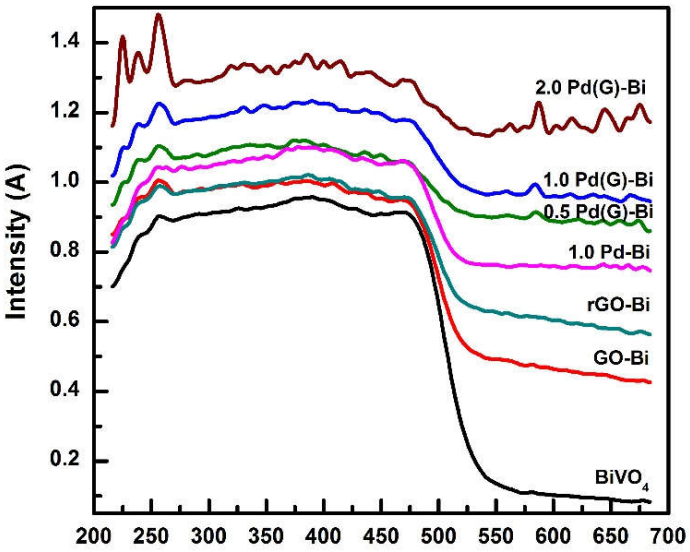


Figure H.8 UV-Vis diffused reflectance spectra (DRS) for prepared samples.

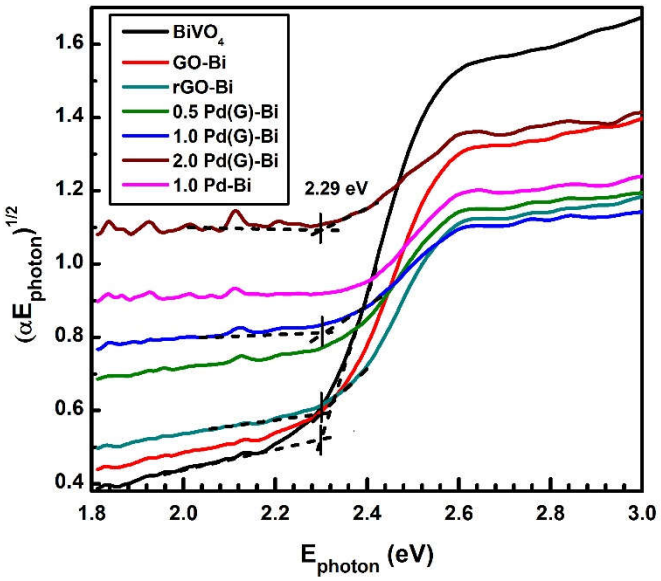


Figure H.9 Plots of $(\alpha E_{photon})^{1/2}$ vs E_{photon} for prepared samples.

H.3.4 Photocatalytic activity tests

Photocatalytic activities of prepared samples were evaluated by degrading a colorless organic, phenol, in water under visible light irradiation. As shown in Fig. H.10, the adsorption of phenol on $BiVO_4$-based samples was low with less than 2% of phenol adsorbed. The adsorption capacity of phenol on Pd-rGO is 5%, which is the highest. After turning on the lamp, apparent differences were observed among these systems with

different samples. Specifically, about 13.0% of phenol were removed over pure $BiVO_4$ in 360 min. With the introduction of rGO on the surface of $BiVO_4$ polyhedrons, the removal amount was increased to about 30.9%. The improvement may be caused by the photogenerated electrons transferred to the surface of rGO sheets by an interfacial transfer along the π-π graphite carbon network [60]. Upon dispersion of palladium nanoparticles on the surface of rGO-Bi, the photocatalytic degradation of phenol was greatly enhanced, and the enhancement varied with the loading content of palladium. Based on the phenol removal amount over 360 min, the photocatalytic activity of the Pd(G)-Bi composites had the following order of significance: 1.0 Pd(G)-Bi (91.3%) > 2.0 Pd(G)-Bi (83.7%) > 0.5Pd(G)-Bi (82.2%). The significant improvement in the removal may be resulted from i) the surface plasmonic resonance effect by the palladium nanoparticles on the surface, and ii) the palladium acting as an excellent charge acceptor (Reaction 1) to facilitate the photogenerated charge carriers' separation. The separated electrons may react with the adsorbed O_2 to produce superoxide free radicals (Reaction 2). However, excess palladium nanoparticles may decrease the charge carrier space distance (CCSD) and thereby increase the recombination between electrons and holes (Reaction 3) [61, 62]. The competition between Reactions 2 and 3 implies that an optimum loading amount of palladium on the surface exists for achieving the highest photocatalytic activity. For comparison, the binary composites, Pd-Bi and Pd-rGO, were also prepared and tested. Only 5% of phenol were removed in the presence of Pd-rGO over 360 min, and about 75.5% of phenol were removed in the system with Pd-Bi, which is still lower than the system with the ternary composites, Pd(G)-Bi (91.3%). It further confirmed that the synergetic effect among $BiVO_4$, rGO and Pd nanoparticles was obtained with enhanced visible light-driven photocatalytic activity in the removal of phenol in water. Compared with reported work related to improve photocatalytic activity of $BiVO_4$, it is still promising for Pd(G)-Bi prepared in this work with higher photocatalytic activity. For example, Wang et al. reported on Cu_2O-$BiVO_4$ heterostructures, and about 50% of phenol were removed in 360 min after modification [63]. Si-doped $BiVO_4$ were also reported to be applied in degradation of phenol, it took 9 hours to completely removal phenol [64]. It should also be noted, Long et al. reported on Au nanoparticles modified $BiVO_4$ with higher activity, compared with we herein reported [65]. It suggests Au and graphene commodified $BiVO_4$ may exhibit higher photocatalytic

activity in the photocatalytic oxidation of phenol, and will be a promising future work. All in all, photocatalytic activity of Pd(G)-Bi is competitive in the removal of phenol under visible light, compared with reported works. Moreover, the stability of as-prepared Pd(G)-Bi composites was studied via recycling tests. Results were should in Fig. H.11. It can be found that about 82% of phenol were removed over 360 min in the 5th run, which is still very high. The reduction in the photocatalytic activity may be resulted from the refractory intermediates adsorbed on the surface which may blocking the reactive sites. Another possible reason is the loss of photocatalysts between two cycles. It indicates the high stability and reusability of as-prepared samples in photocatalytic degradation of phenol under visible light.

$$e^- + Pd_n \rightarrow Pd_n^- \qquad \textbf{Reaction 1}$$

$$Pd_n^- + O_2 \rightarrow O_2^{\bullet -} + Pd_n \qquad \textbf{Reaction 2}$$

$$Pd_n^- + h^+ \rightarrow Pd_n \qquad \textbf{Reaction 3}$$

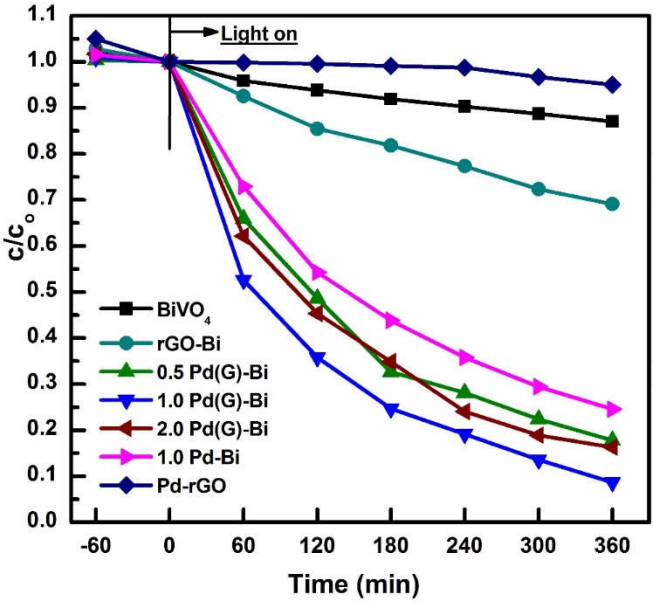


Figure H.10 Photocatalytic degradation of phenol in the presences of prepared samples under visible light irradiation.

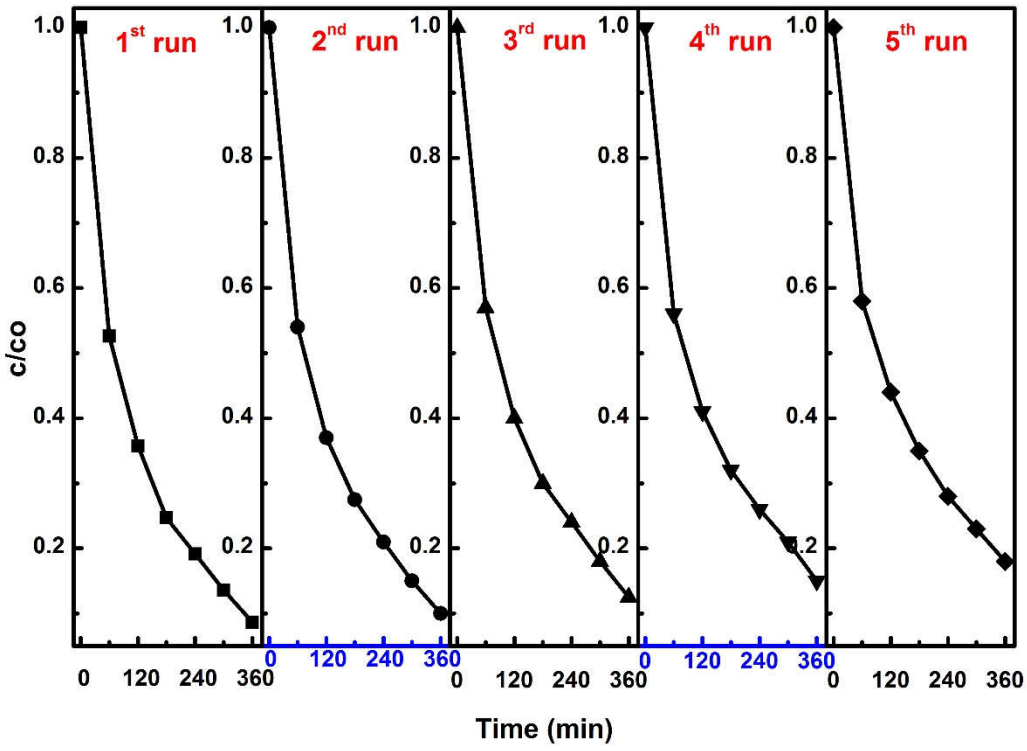


Figure H.11 Five cycles for degradation of phenol over 1.0 Pd(G)-Bi photocatalysts.

For the kinetic study, the Langmuir-Hinshelwood (L-H) model (Equation 8) may be applied to describe the photocatalytic degradation of phenol,

$$r = -\frac{dc}{dt} = k\theta = \frac{kKc}{1+Kc} \qquad \textit{Equation 8}$$

Where r, c, t, k, θ and K represent reaction rate, concentration of phenol, time, reaction rate constant, ratio of adsorbed phenol and adsorption constant, respectively. The initial concentration of phenol for all the tests was 10 mg/L (~ 1×10^{-4} M) and no obvious adsorption of phenol was observed, indicating a low adsorption constant (k) for phenol adsorbed on $BiVO_4$ as well as on other prepared composites. Thus, $1 + Kc$ may be assumed to be equal to 1 and Equation 8 can be then converted to Equation 9,

$$-\frac{dc}{dt} = kKc = k'c \qquad \textit{Equation 9}$$

$$\ln(\frac{c_o}{c_t}) = k't \qquad \textbf{Equation 10}$$

where *k'* is the pseudo first-order reaction constant. To integrate Equation 9 with the boundary conditions (c_o at time of 0 min and c_t at time of t), Equation 10 can be obtained for the calculation of the value of *k'*. By plotting $\ln(c_o/c_t)$ *vs* t, *k'* may be determined through the slope of the fitting line. Moreover, the photonic efficiency (ζ) for photocatalysis may be evaluated using Equation 11 [66] as follows,

$$\zeta = \frac{V \times \Delta c}{J \times A \times \Delta t} \qquad \textbf{Equation 11}$$

where V, J, A, Δc and Δt represent volume of solution (100 mL), flux of incoming photons (2.39 kW/m^2), illuminated area (0.0050 m^2), change in concentration and change in time, respectively. Following the above discussions, calculated results are summarized in Table H.2. For all fitting lines, the R^2 values were close to 1, and the standard errors (*SE*) were in the 10^{-4} order of magnitude. The high linearity of fitting lines confirmed the high suitability of L-H model in describing these photocatalytic processes in the presence of prepared samples. As for values of *k'*, it is increased more than twice for rGO-Bi compared to pure $BiVO_4$. The reaction constants were significantly higher when loading palladium nanoparticles on the surface of rGO-Bi composites. Specifically, the values of k' are 12.4, 16.8 and 13.3 times higher for 0.5, 1.0 and 2.0 Pd(G)-Bi composites respectively, than that of $BiVO_4$. Also, a synergetic effect was observed when comparing the ternary composites (Pd(G)-Bi) with the binary composites (rGO-Bi, Pd-Bi and Pd-rGO), which further validated the preparation of ternary structures to reach a high photocatalytic activity for the removal of phenol. The photonic efficiencies and kinetic reaction constants for processes with prepared samples were similar in order, as shown in Table H.2. The highest photonic efficiency was found for the photocatalytic process in the presence of 1.0 Pd(G)-Bi composites, which is 21.8 μg W^{-1} h^{-1}. All results regarding the photocatalytic degradation of phenol suggest that the ternary structure provides a superior enhancement of activity.

Table H.2 Photocatalytic kinetic constants and average photonic efficiencies for the photocatalytic process of degradation of phenol with various photocatalysts under visible light irradiation.

Composite	k' (x10^{-3} min^{-1})	R^2	SE (x10^{-4})	k/k_{BiVO_4}	ζ ($\mu g\ W^{-1}\ h^{-1}$)	ζ/ζ_{BiVO_4}
$BiVO_4$	0.415	0.985	0.193	1	2.33	1
rGO-Bi	1.07	0.996	0.258	2.58	5.15	2.21
Pd-rGO	0.104	0.855	0.160	0.251	0.353	0.152
1.0 Pd-Bi	4.15	0.993	1.29	10.0	15.5	6.65
0.5 Pd(G)-Bi	5.15	0.990	1.99	12.4	18.0	7.73
1.0 Pd(G)-Bi	6.99	0.991	2.48	16.8	21.8	9.36
2.0 Pd(G)-Bi	5.52	0.991	2.03	13.3	18.8	8.07

H.3.5 Mechanism exploration

H.3.5.1 Pathways of decomposition of phenol

Generally, pathways of phenol degradation include the formation of hydroquinone (HQ), benzoquinone (BQ) and catechol (CA), ring cleavage, formation of organic acids and complete mineralization with formation of CO_2 and H_2O (Fig. H.12) [34, 35, 67, 68]. More specifically, under the effect of produced oxidants in photocatalysis, phenol may be transformed into phenoxy radicals which may further be oxidized into three major intermediates, namely HQ, BQ, and CA. If the aromatic ring was attacked, organic acids such as maleic acid, oxalic acid, succinic acid and malonic acid may be generated. Finally, these organic acids may be further oxidized until completely mineralized. The hypothesized intermediates were monitored and shown in Fig. H.13. There were about 0.53, 0.44 and 0.13 mg/L of BQ, HQ and CA accumulated over 360 min in the photocatalytic degradation of phenol. To further explore the mineralization of the photocatalytic system, TOC before and after the treatment over 360 min was detected and shown in the inset of Fig. H.13. Quantitively, only about 28.4% of TOC were removed even though 91.3% of phenol removal was reached. It indicates some phenol was completely mineralized, and a large amount of intermediates were left in the reactive system. It reveals that the prepared samples were capable of photocatalytically mineralizing phenol under visible light irradiation.

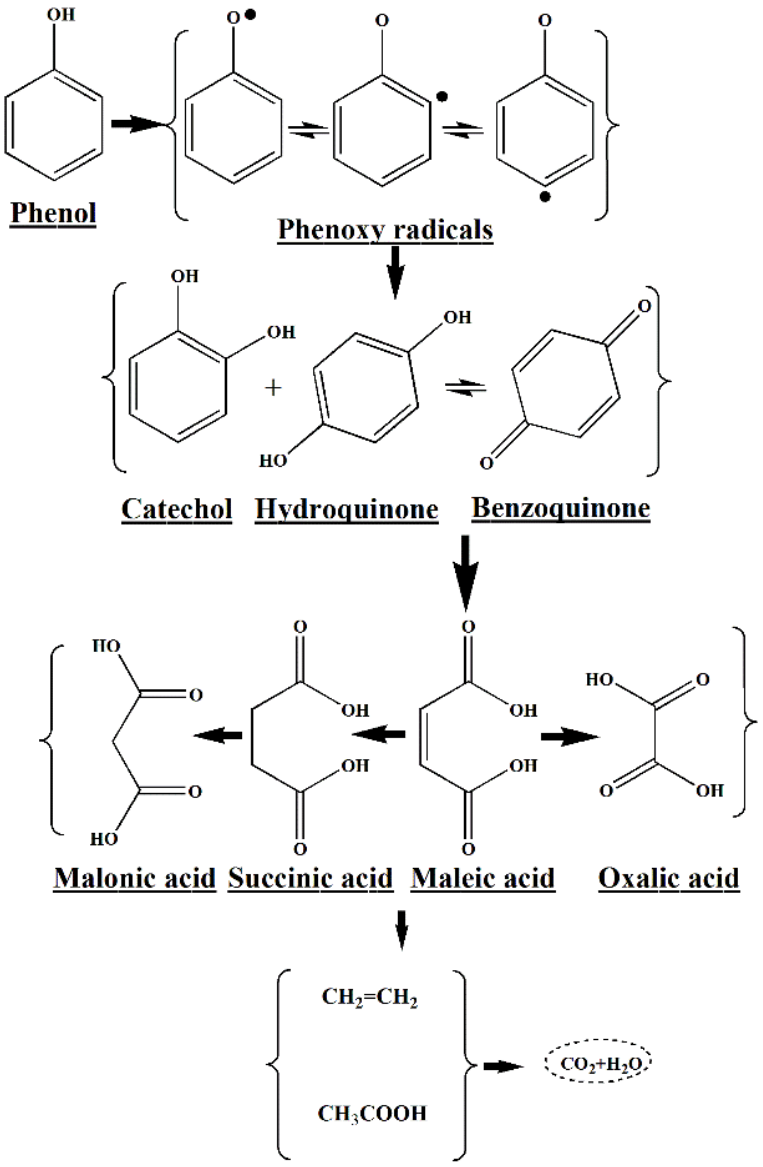


Figure H.12 Possible pathways of phenol in the photocatalytic degradation process in the presence of 1.0 Pd(G)-Bi composites.

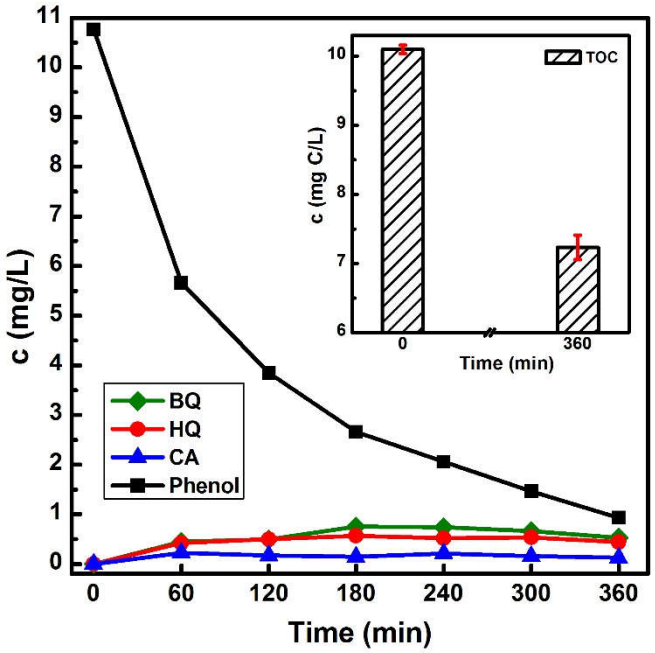


Figure H.13 Concentrations of phenol as well as produced intermediates: benzoquinone (BQ), hydroquinone (HQ) and catechol (CA) along with the photocatalytic process in the presence of 1.0 Pd(G)-Bi composites under visible light irradiation (Inset: TOC change before and after the photocatalysis).

H.3.5.2 Effective species

The well-known oxidative species in photocatalysis are photogenerated holes and free radicals including $\bullet O_2^-$ and •OH. To study the effective oxidants for the Pd(G)-Bi based photocatalytic system, quench tests were carried out by adding scavengers. IPA, EDTA-2Na and N_2 are scavengers for free radicals, holes and $\bullet O_2^-$, respectively. Reaction kinetic constants for processes with and without adding scavengers was calculated and shown in Fig. H.14a. It is obvious with adding scavengers, the reaction kinetic constant was decreased, indicating both free radicals and holes contributed to the photocatalytic oxidation of phenol. Specifically, the decrease in phenol removal was greatest when quenching the holes. This phenomenon indicates that separated holes may be the major oxidants in the oxidation process. It should be noted that OH radicals play the most important role in the TiO_2 based photocatalytic degradation of organics [69, 70]. However, it exhibited negligible influence in the Pd(G)-Bi system. To further confirm the effect of OH radicals in this system, the concentration of OH radicals was probed through the

compound *p*-chlorobenzoic acid (pCBA) [39, 71]. pCBA can selectively react with OH radicals (Reaction 4) with a reaction constant ($k_{\bullet OH\text{-}pCBA}$) as high as 5×10^9 M^{-1} s^{-1} (3.12×10^{11} M^{-1} min^{-1}) (Equation 12). By integrating Equation 12, Equation 13 can be obtained and used for the calculation of the concentration of produced OH radicals in the system. The concentrations of pCBA along with time in different photocatalytic processes were depicted in Fig. H.14b. Apparently, OH radicals were promptly produced at the start of the photocatalysis, and there were about 9.7 x 10^{-14} M of OH radicals generated. However, negligible changes in the concentration of pCBA were found for systems in the presences of $BiVO_4$ and Pd(G)-Bi composites. This is solid evidence to confirm the absence of OH radicals in the oxidation processes for as-prepared samples as photocatalysts, and the photogenerated holes may directly react with adsorbed oxidants. The oxidative capacity of photogenerated holes depends on the potential of the valence band top position. As calculated using Equation 3, the valence band top position is estimated at about 2.685 eV, which is higher than the redox potential of 2.27 V at pH 7 (vs SHE) [72]. This suggests the separated holes are more capable of oxidizing adsorbed organics (phenol).

$$p-CBA+\bullet OH \rightarrow p-CBA^{*} \qquad \textbf{Reaction 4}$$

$$\frac{dc_{p-CBA}}{dt} = -k_{\bullet OH-pCBA} \times c_{p-CBA} \times c_{\bullet OH} \qquad \textbf{Equation 12}$$

$$\int_0^t c_{\bullet OH} dt = \frac{1}{k_{\bullet OH-pCBA}} \times \ln \frac{c^o_{p-CBA}}{c^t_{p-CBA}} = \frac{1}{3.12\times10^{11}} \times \ln \frac{c^o_{p-CBA}}{c^t_{p-CBA}} \qquad \textbf{Equation 13}$$

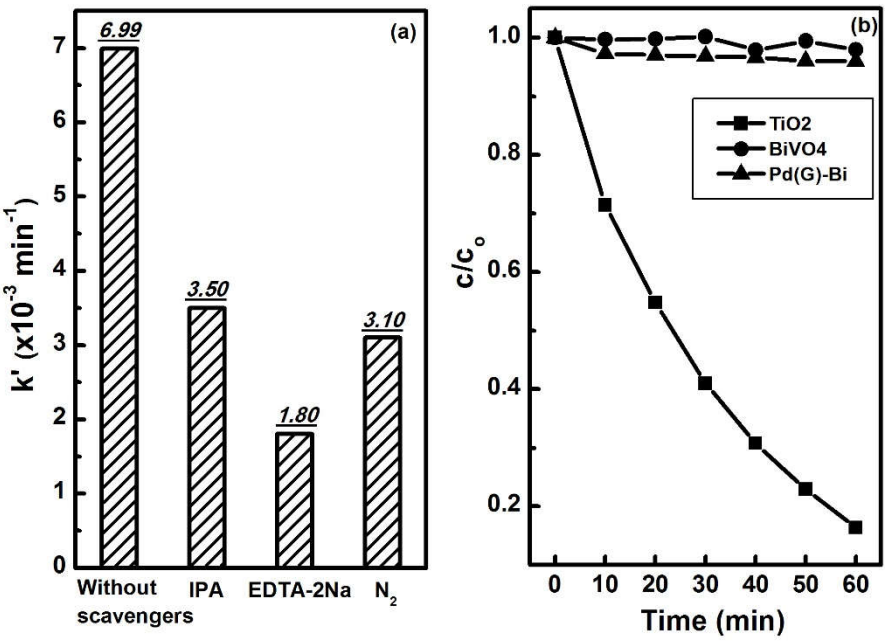


Figure H.14 (a) Photocatalytic degradation phenol in the presence of 1.0 Pd(G)-Bi composites with or without adding scavengers; (b) Photocatalytic degradation of p-CBA in the presence of TiO_2 under UV light as well as $BiVO_4$ and 1.0 Pd(G)-Bi under visible light irradiation.

H.3.5.3 Recombination of electrons and holes

To reveal that the recombination of photogenerated holes and electrons was suppressed through the modifications in this work, electrochemical impedance spectroscopy (EIS) was employed. EIS Nyquist as well as Bode plots were illustrated in Fig. H.15. In Fig. H.15a, only one semicircle was observed, indicating these photocatalytic processes were just a simple electrode reaction. The diameter of the arc can be fitted and is in direct proportion to the resistance value of the electron transfer on the electrode (R_{ct}) [73]. It should be noted a wider diameter corresponds with a higher recombination of photogenerated charge carriers. The simulated circuit was shown in Fig. H.15a, where R_s and *CPE* respectively represents the resistance of solution and the constant phase element which can be regarded as a capacity of double layer. The fitted values were shown in Table H.3. Specifically, when $BiVO_4$ was covered by GO, R_{ct} was decreased from 12240 to 1047 Ω. After the photoreduction process, reducing the oxygen-functional groups for GO, R_{ct} was further decreased to 331.6 Ω. The significantly decrease may be caused by the excellent conductivity of graphene, and the photogenerated electrons were easily transferred from

$BiVO_4$ to the contacted graphene sheets. When palladium was dispersed on the surface of rGO-Bi, the recombination of electrons and holes pair was further supressed, possibly attributed to the electrons transferring to the palladium nanoparticles. Also, the R_{ct} for Pd-Bi electrode was also lower than that for pure $BiVO_4$ electrode, but higher than that for Pd(G)-Bi electrode, confirming the synergetic effect of the ternary structure in the suppression of photogenerated charge carriers. Observing from Fig. H.15b, the characteristic frequency peaks of GO-Bi, rGO-Bi, and Pd(G)-Bi electrodes were gradually shifted to lower frequencies compared with pure $BiVO_4$ electrode (Table H.3). The shift from high frequency to low frequency reveals a more rapid electron transport process, as the frequency (f) is related to the life time (τ) of the injected electrons as shown in Equation 14 below [74, 75].

$$\tau = \frac{1}{2\pi f} \qquad \textbf{\textit{Equation 14}}$$

From this equation, the lifetime of electrons for different systems were computed and shown in Table H.3. The electron lifetime of GO-Bi, rGO-Bi and Pd(G)-Bi composites are about 5, 10 and 32 times higher than that of the $BiVO_4$ sample. The electron lifetime of Pd-Bi is about 18 times higher than that of $BiVO_4$. It further confirms the advance of the ternary structure in suppressing the charge recombination, thereby enhancing the photoconversion efficiency.

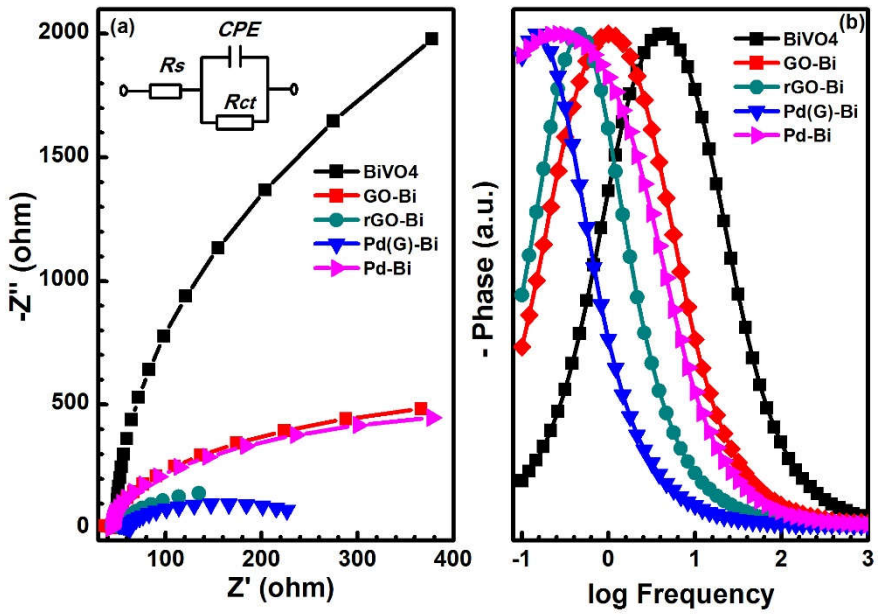


Figure H.15 (a) EIS Nyquist plots and (b) the Bode plot curves of $BiVO_4$, rGO-Bi, Pd(G)-Bi and Pd-Bi.

Table H.3 Electrochemical impedance results of $BiVO_4$, rGO-Bi, Pd(G)-Bi and Pd-Bi.

Samples	R_s (Ω)	R_{ct} (Ω)	*CPE* (μf)	f_{min} *(Hz)*	τ *(ms)*
$BiVO_4$	49.06	12240	782.6	4.64	34.3
GO-Bi	46.01	1047	723.5	1.00	159
rGO-Bi	45.28	331.6	850.6	0.464	343
Pd(G)-Bi	53.9	194.8	846.6	0.147	1083
Pd-Bi	43.5	930.9	688.5	0.261	610

H.3.5.4 Proposed photocatalytic processes

Based on the above discussion, proposed processes for the photocatalytic degradation of phenol were illustrated in Fig. H.16. Specifically, when irradiation occurs with energy greater than the band gap energy of $BiVO_4$ (2.29 eV), electrons on the valence band may jump to the conduction band. The activated electrons may either return to the valence band,

or transfer to the contacted rGO sheets and palladium nanoparticles. Also, as for the SPR effect, palladium nanoparticles on the surface may also be activated by the irradiation and generate extra electrons. The separated electrons may react with the adsorbed oxygen to produce superoxide free radicals; the holes may directly react with the adsorbed organics. In addition, because of the strong π-π interaction between aromatic rings of phenol and rGO, phenol may also adsorb onto the surface of rGO-Bi composite much more easily compared to pure Bi_2MoO_6 [76]. The improved separation efficiency of photogenerated charge carriers through the capture of palladium nanoparticles and transportation by rGO, and the increased harvesting capacity of visible light photons due to the SPR effect as well as the strong adsorption of phenol on rGO sheets contributed to an enhanced photocatalytic activity towards the oxidation of phenol under visible light irradiation.

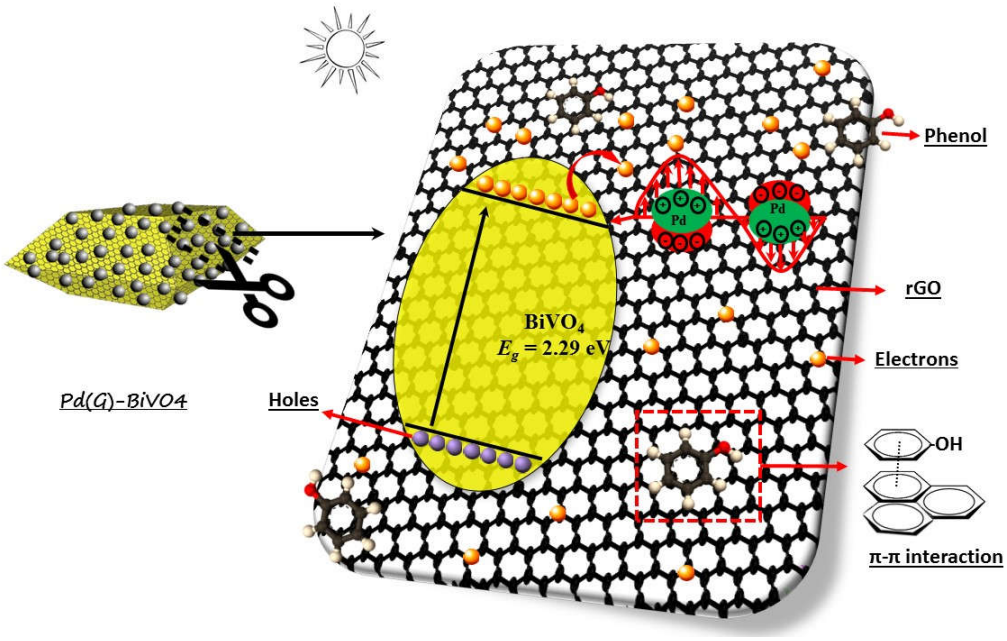


Figure H.16 Proposed processes of photocatalytic degradation of phenol in the presence of Pd(G)-Bi composites.

H.4 Conclusions

Pd-rGO-$BiVO_4$ composites were successfully prepared with enhanced visible light-driven photocatalytic activity in the degradation of phenol. As-prepared samples were comprehensively characterized. Moreover, the mechanisms including pathways of phenol, effective oxidants and recombination of photogenerated charge carriers were explored and

discussed. In this system, the lifetime of holes was prolonged and the separated holes were more inclined to react with organics directly, instead of reacting with adsorbed water to produce OH radicals. Photocatalytic processes of decomposing phenol were also proposed. At last, we believe this work will provide a new idea for the rGO based ternary composites in the field of visible light-driven photocatalysis and shed light on the significances of applying palladium nanoparticles to improve the visible light-induced photocatalytic activity.

References

1. Saimi Tokunaga, Hideki Kato and Akihiko Kudo, "Selective Preparation of Monoclinic and Tetragonal $BiVO_4$ with Scheelite Structure and Their Photocatalytic Properties," *Chemistry of Materials*, vol. 13, no. 12, pp. 4624-4628, 2001.

2. Conrado Martinez Suarez, Simelys Hernández and Nunzio Russo, "$BiVO_4$ as photocatalyst for solar fuels production through water splitting: A short review," *Applied Catalysis A: General*, vol. 504, pp. 158-170, 2015.

3. Zhen-Feng Huang, Lun Pan, Ji-Jun Zou, Xiangwen Zhang and Li Wang, "Nanostructured bismuth vanadate-based materials for solar-energy-driven water oxidation: a review on recent progress," *Nanoscale*, vol. 6, no. 23, pp. 14044-14063, 2014.

4. Puttaswamy Madhusudan, Jingrun Ran, Jun Zhang, Jiaguo Yu and Gang Liu, "Novel urea assisted hydrothermal synthesis of hierarchical $BiVO_4/Bi_2O_2CO_3$ nanocomposites with enhanced visible-light photocatalytic activity," *Applied Catalysis B: Environmental*, vol. 110, pp. 286-295, 2011.

5. Xi Zhang, Zhihui Ai, Falong Jia, Lizhi Zhang, Xiaoxing Fan and Zhigang Zou, "Selective synthesis and visible-light photocatalytic activities of $BiVO_4$ with different crystalline phases," *Materials Chemistry and Physics*, vol. 103, no. 1, pp. 162-167, 2007.

6. Li Zhang, Dairong Chen and Xiuling Jiao, "Monoclinic Structured $BiVO_4$ Nanosheets: Hydrothermal Preparation, Formation Mechanism, and Coloristic and Photocatalytic Properties," *The Journal of Physical Chemistry B*, vol. 110, no. 6, pp. 2668-2673, 2006.

7. Sergio Obregon, Soo W. Lee and Gerardo Colon, "Exalted photocatalytic activity of tetragonal $BiVO_4$ by Er^{3+} doping through a luminescence cooperative mechanism," *Dalton*

Transactions, vol. 43, no. 1, pp. 311-316, 2014.

8. Aiping Zhang and Jinzhi Zhang, "Effects of europium doping on the photocatalytic behavior of $BiVO_4$," *Journal of Hazardous Materials*, vol. 173, no. 1–3, pp. 265-272, 2010.

9. Xiufang Zhang, Yaobin Zhang, Xie Quan and Shuo Chen, "Preparation of Ag doped $BiVO_4$ film and its enhanced photoelectrocatalytic (PEC) ability of phenol degradation under visible light," *Journal of Hazardous Materials*, vol. 167, no. 1–3, pp. 911-914, 2009.

10. Xiangchao Meng and Zisheng Zhang, "Ag/AgCl Loaded Bi_2WO_6 Composite: A Plasmonic Z-Scheme Visible Light-Responsive Photocatalyst," *International Journal of Photoenergy*, vol. 2016, pp. 11, 2016.

11. Xiangchao Meng and Zisheng Zhang, "Synthesis and characterization of plasmonic and magnetically separable Ag/AgCl-Bi_2WO_6@ Fe_3O_4@SiO_2 core-shell composites for visible light-induced water detoxification," *Journal of Colloid and Interface Science*, vol. 485, pp. 296-307, 2017.

12. Chhabilal Regmi, Yuwaraj K. Kshetri, Schindra Kumar Ray, Ramesh Prasad Pandey and Soo Wohn Lee, "Utilization of visible to NIR light energy by Yb^{+3}, Er^{+3} and Tm^{+3} doped $BiVO_4$ for the photocatalytic degradation of methylene blue," *Applied Surface Science*, vol. 392, no. Supplement C, pp. 61-70, 2017.

13. Mingce Long, Weimin Cai, Jun Cai, Baoxue Zhou, Xinye Chai and Yahui Wu, "Efficient Photocatalytic Degradation of Phenol over Co_3O_4/$BiVO_4$ Composite under Visible Light Irradiation," *The Journal of Physical Chemistry B*, vol. 110, no. 41, pp. 20211-20216, 2006.

14. Weirong Zhao, Yan Wang, Yong Yang, Jing Tang and Yanan Yang, "Carbon spheres supported visible-light-driven CuO-$BiVO_4$ heterojunction: Preparation, characterization, and photocatalytic properties," *Applied Catalysis B: Environmental*, vol. 115–116, pp. 90-99, 2012.

15. Xiangchao Meng, Zizhen Li, Haoming Zeng, Jie Chen and Zisheng Zhang, "MoS_2 quantum dots-interspersed Bi_2WO_6 heterostructures for visible light-induced detoxification and disinfection," *Applied Catalysis B: Environmental*, vol. 210, pp. 160-172, 2017.

16. Xiangchao Meng, Lingyun Jiang, Weiwen Wang and Zisheng Zhang, "Enhanced

Photocatalytic Activity of BiOBr/ZnO Heterojunction Semiconductors Prepared by Facile Hydrothermal Method," *International Journal of Photoenergy*, vol. 2015, pp. 9, 2015.

17. Xiangchao Meng and Zisheng Zhang, "Synthesis, Analysis, and Testing of BiOBr-Bi_2WO_6 Photocatalytic Heterojunction Semiconductors," *International Journal of Photoenergy*, vol. 2015, pp. 12, 2015.

18. Xiangchao Meng and Zisheng Zhang, "Facile synthesis of BiOBr/Bi_2WO_6 heterojunction semiconductors with high visible-light-driven photocatalytic activity," *Journal of Photochemistry and Photobiology A: Chemistry*, vol. 310, no. 0, pp. 33-44, 2015.

19. Sonal Singh, Rishabh Sharma and Bodh Raj Mehta, "Enhanced surface area, high Zn interstitial defects and band gap reduction in N-doped ZnO nanosheets coupled with $BiVO_4$ leads to improved photocatalytic performance," *Applied Surface Science*, vol. 411, no. Supplement C, pp. 321-330, 2017.

20. Jin Zhang, Hao Cui, Bing Wang, Chuang Li, Jianping Zhai and Qin Li, "Preparation and characterization of fly ash cenospheres supported CuO–$BiVO_4$ heterojunction composite," *Applied Surface Science*, vol. 300, no. Supplement C, pp. 51-57, 2014.

21. Rengui Li, Fuxiang Zhang, Donge Wang, Jingxiu Yang, Mingrun Li, Jian Zhu, Xin Zhou, Hongxian Han and Can Li, "Spatial separation of photogenerated electrons and holes among {010} and {110} crystal facets of $BiVO_4$," *Nature Communications*, vol. 4, pp. 1432, 2013.

22. Wenbo Hou and Stephen B. Cronin, "A Review of Surface Plasmon Resonance-Enhanced Photocatalysis," *Advanced Functional Materials*, vol. 23, no. 13, pp. 1612-1619, 2013.

23. Shigeru Kohtani, Misa Tomohiro, Kunihiro Tokumura and Ryoichi Nakagaki, "Photooxidation reactions of polycyclic aromatic hydrocarbons over pure and Ag-loaded $BiVO_4$ photocatalysts," *Applied Catalysis B: Environmental*, vol. 58, no. 3–4, pp. 265-272, 2005.

24. Lei Ge, "Novel visible-light-driven Pt/$BiVO_4$ photocatalyst for efficient degradation of methyl orange," *Journal of Molecular Catalysis A: Chemical*, vol. 282, no. 1–2, pp. 62-66, 2008.

25. Shao-Wen Cao, Zhen Yin, James Barber, Freddy Y. C. Boey, Say Chye Joachim Loo and Can Xue, "Preparation of Au-$BiVO_4$ Heterogeneous Nanostructures as Highly Efficient Visible-Light Photocatalysts," *ACS Applied Materials & Interfaces*, vol. 4, no. 1, pp. 418-423, 2012.

26. Xiangchao Meng and Zisheng Zhang, "Pd-doped Bi_2MoO_6 Plasmonic Photocatalysts with Enhanced Visible Light Photocatalytic Performance," *Applied Surface Science*, vol. 392, pp. 169-180, 2016.

27. Xiangchao Meng, Zizhen Li and Zisheng Zhang, "Pd-nanoparticle-decorated peanut-shaped $BiVO_4$ with improved visible light-driven photocatalytic activity comparable to that of TiO_2 under UV light," *Journal of Catalysis*, vol. 356, pp. 53-64, 2017.

28. Xiangchao Meng, Zizhen Li, Jie Chen, Hongwei Xie and Zisheng Zhang, "Enhanced visible light-induced photocatalytic activity of surface-modified BiOBr with Pd nanoparticles," *Applied Surface Science*, vol. 433, no. Supplement C, pp. 76-87, 2018.

29. Yujie Xiong, Benjamin Wiley, Jingyi Chen, Zhi-Yuan Li, Yadong Yin and Younan Xia, "Corrosion-Based Synthesis of Single-Crystal Pd Nanoboxes and Nanocages and Their Surface Plasmon Properties," *Angewandte Chemie International Edition*, vol. 44, no. 48, pp. 7913-7917, 2005.

30. Yujie Xiong, Jingyi Chen, Benjamin Wiley, Younan Xia, Yadong Yin and Zhi-Yuan Li, "Size-Dependence of Surface Plasmon Resonance and Oxidation for Pd Nanocubes Synthesized via a Seed Etching Process," *Nano Letters*, vol. 5, no. 7, pp. 1237-1242, 2005.

31. Yongsheng Fu, Xiaoqiang Sun and Xin Wang, "$BiVO_4$–graphene catalyst and its high photocatalytic performance under visible light irradiation," *Materials Chemistry and Physics*, vol. 131, no. 1–2, pp. 325-330, 2011.

32. Yun Hau Ng, Akihide Iwase, Akihiko Kudo and Rose Amal, "Reducing Graphene Oxide on a Visible-Light $BiVO_4$ Photocatalyst for an Enhanced Photoelectrochemical Water Splitting," *The Journal of Physical Chemistry Letters*, vol. 1, no. 17, pp. 2607-2612, 2010.

33. Quanjun Xiang, Jiaguo Yu and Mietek Jaroniec, "Graphene-based semiconductor photocatalysts," *Chemical Society Reviews*, vol. 41, no. 2, pp. 782-796, 2012.

34. Xiangchao Meng and Zisheng Zhang, "Plasmonic ternary Ag–rGO–Bi_2MoO_6 composites with enhanced visible light-driven photocatalytic activity," *Journal of Catalysis*, vol. 344, pp. 616-630, 2016.

35. Xiangchao Meng and Zisheng Zhang, "Bi_2MoO_6 co-modified by reduced graphene oxide and palladium (Pd^{2+} and Pd^0) with enhanced photocatalytic decomposition of phenol," *Applied Catalysis B: Environmental*, vol. 209, pp. 383-393, 2017.

36. I. Oller, S. Malato and J. A. Sánchez-Pérez, "Combination of Advanced Oxidation Processes and biological treatments for wastewater decontamination—A review," *Science of The Total Environment*, vol. 409, no. 20, pp. 4141-4166, 2011.

37. Parag R. Gogate, "Treatment of wastewater streams containing phenolic compounds using hybrid techniques based on cavitation: A review of the current status and the way forward," *Ultrasonics Sonochemistry*, vol. 15, no. 1, pp. 1-15, 2008.

38. Tuo Wang, Changjiang Li, Junyi Ji, Yijia Wei, Peng Zhang, Shengping Wang, Xiaobin Fan and Jinlong Gong, "Reduced Graphene Oxide (rGO)/$BiVO_4$ Composites with Maximized Interfacial Coupling for Visible Lght Photocatalysis," *ACS Sustainable Chemistry & Engineering*, vol. 2, no. 10, pp. 2253-2258, 2014.

39. S.-K. Han, S.-N. Nam and J.-W. Kang, "OH radical monitoring technologies for AOP advanced oxidation process," *Water Science and Technology*, vol. 46, no. 11-12, pp. 7-12, 2002.

40. Yoshio Nosaka, Shigeki Komori, Kenta Yawata, Tsutomu Hirakawa and Atsuko Y. Nosaka, "Photocatalytic OH radical formation in TiO_2 aqueous suspension studied by several detection methods," *Physical Chemistry Chemical Physics*, vol. 5, no. 20, pp. 4731-4735, 2003.

41. Yunzheng Pi, Jochen Schumacher and Martin Jekel, "The Use of para-Chlorobenzoic Acid (pCBA) as an Ozone/Hydroxyl Radical Probe Compound," *Ozone: Science & Engineering*, vol. 27, no. 6, pp. 431-436, 2005.

42. Walter Kohn and Lu Jeu Sham, "Self-consistent equations including exchange and correlation effects," *Physical Review*, vol. 140, no. 4A, pp. A1133, 1965.

43. Giannozzi Paolo, Baroni Stefano, Bonini Nicola, Calandra Matteo, Car Roberto,

Cavazzoni Carlo, Ceresoli Davide, L. Chiarotti Guido, Cococcioni Matteo, Dabo Ismaila, Corso Andrea Dal, Gironcoli Stefano de, Fabris Stefano, Fratesi Guido, Gebauer Ralph, Gerstmann Uwe, Gougoussis Christos, Kokalj Anton, Lazzeri Michele, Martin-Samos Layla, Marzari Nicola, Mauri Francesco, Mazzarello Riccardo, Paolini Stefano, Pasquarello Alfredo, Paulatto Lorenzo, Sbraccia Carlo, Scandolo Sandro, Sclauzero Gabriele, P. Seitsonen Ari, Smogunov Alexander, Umari Paolo and M. Wentzcovitch Renata, "QUANTUM ESPRESSO: a modular and open-source software project for quantum simulations of materials," *Journal of Physics: Condensed Matter*, vol. 21, no. 39, pp. 395502, 2009.

44. CH Bichler, M Bischoff, HC Langowski and U Moosheimer, "39th Annual Technical Conference of the Society of Vacuum Coaters," *Philadelphia, USA, May*, vol. 5, 1996.

45. Peng Zeng, Qinggang Zhang, Tianyou Peng and Xiaohu Zhang, "One-pot synthesis of reduced graphene oxide-cadmium sulfide nanocomposite and its photocatalytic hydrogen production," *Physical Chemistry Chemical Physics*, vol. 13, no. 48, pp. 21496-21502, 2011.

46. C. D. Wagner, "Sensitivity of detection of the elements by photoelectron spectrometry," *Analytical Chemistry*, vol. 44, no. 6, pp. 1050-1053, 1972.

47. Tianjin Ma, Juan Wu, Yidong Mi, Qinghua Chen, Dong Ma and Chao Chai, "Novel Z-Scheme g-C_3N_4/C@Bi_2MoO_6 composite with enhanced visible-light photocatalytic activity for β-naphthol degradation," *Separation and Purification Technology*, vol. 183, pp. 54-65, 2017.

48. Graeme Williams, Brian Seger and Prashant V. Kamat, "TiO_2-Graphene Nanocomposites. UV-Assisted Photocatalytic Reduction of Graphene Oxide," *ACS Nano*, vol. 2, no. 7, pp. 1487-1491, 2008.

49. Xiangchao Meng and Zisheng Zhang, "Bismuth-based Photocatalytic Semiconductors: Introduction, Challenges and Possible Approaches," *Journal of Molecular Catalysis A: Chemical*, vol. 423, pp. 533-549, 2016.

50. M. A. Butler and D. S. Ginley, "Prediction of Flatband Potentials at Semiconductor - Electrolyte Interfaces from Atomic Electronegativities," *Journal of The Electrochemical Society*, vol. 125, no. 2, pp. 228-232, 1978.

51. Arthur H. Nethercot, "Prediction of Fermi Energies and Photoelectric Thresholds Based on Electronegativity Concepts," *Physical Review Letters*, vol. 33, no. 18, pp. 1088-1091, 1974.

52. Jinfeng Zhang, Peng Zhou, Jianjun Liu and Jiaguo Yu, "New understanding of the difference of photocatalytic activity among anatase, rutile and brookite TiO_2," *Physical Chemistry Chemical Physics*, vol. 16, no. 38, pp. 20382-20386, 2014.

53. Haijun Zhang, Lu Liu and Zhen Zhou, "Towards better photocatalysts: first-principles studies of the alloying effects on the photocatalytic activities of bismuth oxyhalides under visible light," *Physical Chemistry Chemical Physics*, vol. 14, no. 3, pp. 1286-1292, 2012.

54. Xiangchao Ma, Ying Dai, Meng Guo and Baibiao Huang, "The Role of Effective Mass of Carrier in the Photocatalytic Behavior of Silver Halide-Based Ag@AgX (X=Cl, Br, I): A Theoretical Study," *ChemPhysChem*, vol. 13, no. 9, pp. 2304-2309, 2012.

55. Naoto Umezawa, Ouyang Shuxin and Jinhua Ye, "Theoretical study of high photocatalytic performance of Ag_3PO_4," *Physical Review B*, vol. 83, no. 3, pp. 035202, 2011.

56. Ting Xiong, Fan Dong, Ying Zhou, Min Fu and Wing-Kei Ho, "New insights into how RGO influences the photocatalytic performance of $BiOIO_3$/RGO nanocomposites under visible and UV irradiation," *Journal of Colloid and Interface Science*, vol. 447, pp. 16-24, 2015.

57. Xiaojuan Bai, Li Wang, Ruilong Zong, Yanhui Lv, Yiqing Sun and Yongfa Zhu, "Performance Enhancement of ZnO Photocatalyst via Synergic Effect of Surface Oxygen Defect and Graphene Hybridization," *Langmuir*, vol. 29, no. 9, pp. 3097-3105, 2013.

58. Peng Wang, Baibiao Huang, Ying Dai and Myung-Hwan Whangbo, "Plasmonic photocatalysts: harvesting visible light with noble metal nanoparticles," *Physical Chemistry Chemical Physics*, vol. 14, no. 28, pp. 9813-9825, 2012.

59. J. Tauc, "Absorption edge and internal electric fields in amorphous semiconductors," *Materials Research Bulletin*, vol. 5, no. 8, pp. 721-729, 1970.

60. Ian V. Lightcap, Thomas H. Kosel and Prashant V. Kamat, "Anchoring Semiconductor and Metal Nanoparticles on a Two-Dimensional Catalyst Mat. Storing and Shuttling

Electrons with Reduced Graphene Oxide," *Nano Letters*, vol. 10, no. 2, pp. 577-583, 2010.

61. M. Sadeghi, W. Liu, T. G. Zhang, P. Stavropoulos and B. Levy, "Role of Photoinduced Charge Carrier Separation Distance in Heterogeneous Photocatalysis: Oxidative Degradation of CH_3OH Vapor in Contact with Pt/TiO_2 and Cofumed $TiO_2{-}Fe_2O_3$," *The Journal of Physical Chemistry*, vol. 100, no. 50, pp. 19466-19474, 1996.

62. S. Sakthivel, M. V. Shankar, M. Palanichamy, Banumathi Arabindoo, D. W. Bahnemann and V. Murugesan, "Enhancement of photocatalytic activity by metal deposition: characterisation and photonic efficiency of Pt, Au and Pd deposited on TiO_2 catalyst," *Water Research*, vol. 38, no. 13, pp. 3001-3008, 2004.

63. Wenzhong Wang, Xiangwei Huang, Shuang Wu, Yixi Zhou, Lijuan Wang, Honglong Shi, Yujie Liang and Bin Zou, "Preparation of p–n junction $Cu_2O/BiVO_4$ heterogeneous nanostructures with enhanced visible-light photocatalytic activity," *Applied Catalysis B: Environmental*, vol. 134-135, no. Supplement C, pp. 293-301, 2013.

64. Xiufang Zhang, Xie Quan, Shuo Chen and Yaobin Zhang, "Effect of Si doping on photoelectrocatalytic decomposition of phenol of $BiVO_4$ film under visible light," *Journal of Hazardous Materials*, vol. 177, no. 1, pp. 914-917, 2010.

65. Mingce Long, Jingjing Jiang, Yan Li, Ruqiong Cao, Liying Zhang and Weimin Cai, "Effect of Gold Nanoparticles on the Photocatalytic and Photoelectrochemical Performance of Au Modified $BiVO_4$," *Nano-Micro Letters*, vol. 3, no. 3, pp. 171-177, 2011.

66. Clarissa Baumanis and Detlef W. Bahnemann, "TiO_2 Thin Film Electrodes: Correlation between Photocatalytic Activity and Electrochemical Properties," *The Journal of Physical Chemistry C*, vol. 112, no. 48, pp. 19097-19101, 2008.

67. Xiao-yan Li, Yu-hong Cui, Yu-jie Feng, Zhao-ming Xie and Ji-Dong Gu, "Reaction pathways and mechanisms of the electrochemical degradation of phenol on different electrodes," *Water Research*, vol. 39, no. 10, pp. 1972-1981, 2005.

68. W. F. L. M. Hoeben, E. M. van Veldhuizen, W. R. Rutgers, C. A. M. G. Cramers and G. M. W. Kroesen, "The degradation of aqueous phenol solutions by pulsed positive corona discharges," *Plasma Sources Science and Technology*, vol. 9, no. 3, pp. 361, 2000.

69. Craig S. Turchi and David F. Ollis, "Photocatalytic degradation of organic water

contaminants: Mechanisms involving hydroxyl radical attack," *Journal of Catalysis*, vol. 122, no. 1, pp. 178-192, 1990.

70. Soonhyun Kim and Wonyong Choi, "Kinetics and Mechanisms of Photocatalytic Degradation of $(CH_3)_nNH_{4-n}^+$ ($0 \leqslant n \leqslant 4$) in TiO_2 Suspension: The Role of OH Radicals," *Environmental Science & Technology*, vol. 36, no. 9, pp. 2019-2025, 2002.

71. Michael S. Elovitz and Urs von Gunten, "Hydroxyl Radical/Ozone Ratios During Ozonation Processes. I. The Rct Concept," *Ozone: Science & Engineering*, vol. 21, no. 3, pp. 239-260, 1999.

72. Akira Fujishima, Tata N. Rao and Donald A. Tryk, "Titanium dioxide photocatalysis," *Journal of Photochemistry and Photobiology C: Photochemistry Reviews*, vol. 1, no. 1, pp. 1-21, 2000.

73. Baifu Xin, Zhiyu Ren, Peng Wang, Jia Liu, Liqiang Jing and Honggang Fu, "Study on the mechanisms of photoinduced carriers separation and recombination for Fe^{3+}–TiO_2 photocatalysts," *Applied Surface Science*, vol. 253, no. 9, pp. 4390-4395, 2007.

74. R. Kern, R. Sastrawan, J. Ferber, R. Stangl and J. Luther, "Modeling and interpretation of electrical impedance spectra of dye solar cells operated under open-circuit conditions," *Electrochimica Acta*, vol. 47, no. 26, pp. 4213-4225, 2002.

75. Songmei Sun, Wenzhong Wang and Ling Zhang, "Bi_2WO_6 Quantum Dots Decorated Reduced Graphene Oxide: Improved Charge Separation and Enhanced Photoconversion Efficiency," *The Journal of Physical Chemistry C*, vol. 117, no. 18, pp. 9113-9120, 2013.

76. Yanyuan Wen, Hanming Ding and Yongkui Shan, "Preparation and visible light photocatalytic activity of Ag/TiO_2/graphene nanocomposite," *Nanoscale*, vol. 3, no. 10, pp. 4411-4417, 2011.

Appendix I Synergetic Photoelectrocatalytic Reactors for Environmental Remediation: a Review

Xiangchao Meng, Zisheng Zhang and Xingang Li

Journal of Photochemistry & Photobiology C: Reviews 24 (2015), 83-101

Abstract

Integrating electrochemistry with photocatalytic technology, photoelectrocatalysis has been identified as a superior candidate to debottleneck photocatalytic processes. Photoelectrocatalysis involves a photocatalytic system to which an external positive bias is applied, which can significantly increase the rates of photocatalytic reactions by driving the photo-generated electron-hole pairs in opposite directions, reducing their recombination rates. The design of a cost-efficient photoelectrocatalytic reactor plays a critical role in the ultimate acceptance of this promising technology in industry for environmental remediation as well as other applications. In this study, photoelectrocatalysis and associated novel reactor designs reported in recent years are reviewed and discussed. Some of the topics which are discussed in this study include various reactor configurations with different illumination sources, photocatalyst utilization modes, and electrodes as well as composite systems incorporating solar cells in addition to microbial and photocatalytic fuel cells. Future efforts are suggested to push the industrial application of photoelectrocatalysis out of its infancy.

I.1 Introduction

With the continuous and prosperous development of modern civilizations, environmental contamination has spread from pole to pole. Faced with this issue, mankind reached a consensus on environmental treatment and remediation. A photoelectrocatalytic system,

which utilizes photocatalysis enhanced by an external electric field, has been confirmed to be a valuable method in environmental remediation [1].

Photocatalysis, an advanced oxidation process (AOP), indirectly degrades most of the organic pollutants by producing strong oxidants (hydroxyl, •OH). This process has been widely applied in the field of environmental remediation [2-6]. Prominent advantages for photocatalytic processes include non-toxicity, low cost, high efficiency, no secondary-pollution and thorough mineralization. Comparatively, for some physical methods such as adsorption by active carbon and coagulation/flocculation process, even though they could lead to approximately 80%-90% reduction in COD value in treatment of dye water [7-9], phase transfer processes alone cannot achieve the final goal of thoroughly decomposing pollutants. For some other AOPs directly utilizing the strong oxidant, they could lead to the complete mineralization of the pollutants and convert them into environmental-friendly compounds such as CO_2 and H_2O [10]. It is still noteworthy that some drawbacks hinder its wide practical application such as the generation of carcinogenic by-products (chlorite and chlorate) when using chloride in drinking water disinfection [11, 12], and the high cost and harmful by-products (e.g. bromate) of the ozonation process [13].

In 1972, Fujishima and Honda introduced photocatalysis into water splitting and hydrogen and oxygen production in the electrochemical cell [14], which triggered the intensive concentration on photocatalytic science and engineering research. As a whole, two distinct areas have been studied on heterogeneous photocatalysis: the basic theoretical chemical investigation, including the photocatalytic mechanisms, the kinetic analysis, synthesis and modification of photocatalysts, etc. [15-22], and the industrial scale-up studies which are associated with the photocatalytic reactor design [23-25]. Even though much more attention was focused on the modification of as-prepared photocatalysts (*e.g.* TiO_2) and the synthesis of novel solar responded photocatalysts to overcome the photocatalysis barriers (such as high electron-hole pair recombination rates and low efficiency of light utilization) [26], there are still some researches focused on the photoelectrocatalytic (PEC) process, which uses an external positive bias potential across the photocatalyst to prevent the recombination of the photo-generated electron-hole pairs. Dated from 1982 by Ward *et al.* [27], photoelectrocatalysis, an efficient method to improve the photocatalytic activity, continues to drive the research [1, 5, 28]. In order to implement the photoelectrocatalytic

technology into practical application, the reactor design plays a significant role. It is important to balance the interdisciplinary studies to scheme out the high-efficiency, practical and energy-saving reactor configurations. The determinants of the reactor performance are some individual components related to the system, including the external potential, photocatalytic anode material and type, the conditions of the electrolyte (*e.g.* pH, temperature, dissolved oxygen, ionic liquid, *etc.*), counter cathode and wall material irradiated directly by incident illumination. The studies mostly focused on synthesizing novel efficient photocatalysts or photocatalytic electrodes, and research on PEC reactor configuration design has increasingly become an intractable issue in the photocatalytic domain. Based on the research on photocatalysis technology done for the review, a wide range of photocatalytic reactor designs have been reviewed [21, 22, 24, 27]. Comparatively, this review will summarize the recent development of the synergetic photoelectrocatalytic reactor designs divided into the slurry system and the immobilized system, and will include the comprehensive introduction and comparison between various photoelectrocatalytic reactor configurations. Finally, the current development and potential future work will be concluded and predicted across this area.

I.2 Mechanism of heterogeneous photoelectrocatalysis

Approximately 3×10^{24} J of solar energy irradiates on the earth's surface annually, which is over 10^4 times the global consumption of energy, based on the data from the U.S. Energy Information Administration (EIA). Effective restoration or transfer of solar energy drives extensive research and tremendous results continue to be obtained. The photocatalytic process, one of the most promising techniques in utilizing the solar energy, attracted growing interest in the past 4 decades. On one hand, photocatalysis could use solar energy to produce hydrogen, which has high chemical potential, and release oxygen via water splitting, analogous to natural photosynthesis [14, 29]. On the other hand, photocatalysis shows potential in the field of environmental remediation [1, 5, 29, 30]. Based on the photocatalytic technology, photoelectrocatalysis (PEC) has been carried out in environmental protection research since 1982 when Ward *et al.* synthesized the TiO_2 film as the anode [27]. The objective of combining the external electrical potential is to effectively prevent the exothermal recombination of photo-generated electron-hole pairs,

and also to improve the photocatalytic efficiency in the degradation of the pollutants. In this section, the mechanism and the affecting factors of synergetic photoelectrocatalysis will be introduced.

I.2.1 Photocatalysis

The use of semiconductors as photocatalysts is ascribed to its special electrical configuration. Band theory is usually explained by the top two energy bands (conduction band, CB and valence band, VB). Comparing the band configurations of the metal, semiconductor and insulator, the high conductivity of metals is ascribed to the partly filled conduction band which results in electrons being removed without engagement. Comparatively, the fully filled valence band and completely empty conduction band in insulator and semiconductor electrical configurations form a band gap which is a significant concept in photocatalysis. An important intrinsic property for semiconductors is their narrow band gaps (mostly lower than 3 eV) relative to that of insulators. It leads to electrons in the highest energy band (valence band) of a semiconductor to be easily motivated to jump to the adjacent band (conduction band). Every leap of the electron to the conduction band leaves a positive hole in the valence band. Since there is a discontinuity between the conduction band and valence band, the longevity of electron-hole pairs are extended. The band gaps of frequently-used semiconductors have been illustrated in Table I.1 [28, 31]. It should also be mentioned that the flatbands depend on the pH. Under conditions other than pH_{ZPC} (the pH at which the net adsorbed charge within the Helmholtz layer is zero, i.e. at the zero point of charge), the flatbands would be flat and band bending would exist. All of band gaps in Table I.1 were calculated or measured at pH_{ZPC} [31].

Table I.1 Band gaps (E_g), and measured or estimated pH_{ZPC} for semiconducting metal oxides. (adapted from [31])

Semiconductor	E_g/eV	pH_{ZPC}	Semiconductor	E_g/eV	pH_{ZPC}	Semiconductor	E_g/eV	pH_{ZPC}
Ag_2O	1.20	11.20	HgO	1.90	7.30	Sb_2O_3	3.00	5.98
Bi_2O_3	2.80	6.20	In_2O_3	2.80	8.64	SnO	4.20	7.59
CdO	2.20	11.60	La_2O_3	5.50	10.40	SnO_2	3.50	4.30
Ce_2O_3	2.40	8.85	MnO	3.60	8.61	Ta_2O_5	4.00	2.90
CoO	2.60	7.59	MnO_2	0.25	4.60	Tb_2O_3	3.80	8.50
Cr_2O_3	3.50	8.10	Nb_2O_5	3.40	6.06	TiO_2	3.20	5.80
CuO	1.70	9.50	Nd_2O_3	4.70	8.81	Tl_2O_3	1.60	8.47
Cu_2O	2.20	8.53	NiO	3.50	10.30	V_2O_5	2.80	6.54
FeO	2.40	8.00	PbO	2.80	8.29	WO_3	2.70	0.43
Fe_2O_3	2.20	8.60	PdO	1.00	7.34	Yb_2O_3	4.90	8.15
Fe_3O_4	0.10	6.50	Pr_2O_3	3.90	8.87	ZnO	3.20	8.80

The energy of the incident light is sufficient to activate the electron leap from the valence band to the conduction band when $hv > E_g$ (where h is Planck constant and v is the frequency). For instance, the band gap of the widely used photocatalyst TiO_2 is 3.2 eV. Only irradiation with wavelengths less than 387.5 nm could motivate the electron in the valence band. As a result, most of the research using TiO_2 as the photocatalyst utilize UV lamps as their incidence resource, which would increase the operating cost and correspondingly hinder the photocatalytic industrial scale-up [32]. Upon irradiation, the photo-generated electrons and holes could separately participate in various chemical reactions (Formula 1-5) [33]. The formation of the extremely powerful oxidant hydroxyl could trigger the complete degradation of the pollutants owing for its high oxidant property (Table I.2).

$$TiO_2 + hv \longrightarrow h^+_{VB} + e^-_{CB} \quad (1)$$

$$H_2O + h^+_{VB} \longrightarrow \bullet OH + H^+ \quad (2)$$

$$h^+ + \text{Pollutant} \longrightarrow \text{Pollutant}^+ \quad (3)$$

$$\bullet OH + \text{Pollutant} \longrightarrow CO_2 + H_2O \quad (4)$$

$$O_2 + e^-_{CB} \longrightarrow \bullet O_2^- \quad (5)$$

Table I.2 Standard electrode potential (E^o) of general oxidant. (* adapted from [4])

Oxidant	E^o (V)	Oxidant	E^o (V)
F_2	2.87	$HClO_4$	1.63
•OH	2.80*	ClO_2	1.50
O_3	2.07	Cl_2	1.36
H_2O_2	1.77	$Cl_2O_7^{2-}$	1.33
MnO_2	1.68	O_2	1.23

I.2.2 Photoelectrocatalysis

The photo-generated electron-hole pairs could either migrate to the surface of the photocatalyst to react with the adsorbed species, or recombine in both the bulk and the surface to release heat. The quantum yield of photons directly influences the performance of the degradation process. Even though TiO_2 is environmentally-friendly, chemically stable and has ideal photocatalytic properties, the high recombination rate of electron-hole pairs hinders its application. Avoiding the recombination of electron-hole pairs continues to drive research. Two main types of countermeasures from the point of the catalyst are focused on: modification of as-synthesized photocatalysts [34] and synthesis of novel photocatalysts [35, 36]. Meanwhile, from the point of the reacting system, the synergetic effect of photoelectrocatalysis has also been treated as a promising aspect to break the tough barrier as mentioned above. The process is illustrated in Fig. I.1 when combined with an external circuit.

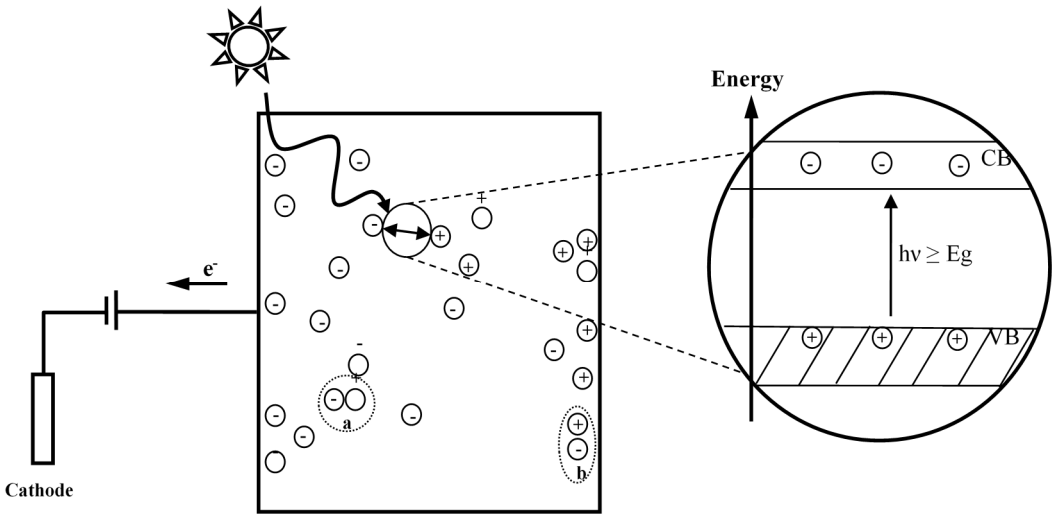


Figure I.1 Schematic processes of photocatalysis when combined with an external circuit (a) recombination in bulk (b) recombination on the surface.

External potential applied plays a significant role in improving the photocatalytic efficiency. Thereunto, photocatalysts that act as the anode and cathode are usually Cu [30], OTE [37], *etc.* Under the force of the electrical potential, the photo-generated electrons spontaneously move to the external circuit and concentrate in the cathode. The absence of the electrons results in the holes gathering in the anode. It correspondingly leads to the desired decrease of the recombination rate. The holes on the surface of the anode could either directly oxidize some organic species or react with the adsorbed water to produce hydroxyl radicals which are able to thoroughly decompose the refractory organics. It is reported that without water on the surface the strong oxidant could not be formed and thus unable to degrade the pollutants [38]. The electrons gathered in the cathode could also react with the dissolved oxygen (Equation 5) to form superoxide radicals [39]. Even though the oxidizing ability of superoxide radicals ($\bullet O_2/O^{2-}$, 1.77 V) is lower than hydroxide radicals ($\bullet OH/H_2O$, 2.80 V), partial organics could be additionally degraded on the cathode surface by the superoxide radicals [39, 40].

I.2.3 Affecting factors in designing PEC reactor

During the photoelectrocatalytic process, several factors directly influence the performance other than the external potential, including the substrate of the electrode, dissolved oxidants,

pH of the solvent, temperature, and electrolytes. These factors have been comprehensively studied and reviewed [1, 38, 41-43]. The integration of the optimal operating conditions into a device is actually the so-called design of a photoelectrocatalytic reactor. The reactor design, a multidisciplinary technique, demands comprehensive acknowledgement of variables ranging from the light intensity profiles in the reactor to the mechanism of the degradation process. Therefore, the design of the PEC reactor currently rests on the laboratorial scale. Nonetheless, a wide range of PEC reactor designs continue to be proposed, which lay the solid and promising foundation for pilot and even industrial applications of PEC reactors.

Daghrir *et al.* has particularly introduced the parameters affecting the photoelectrocatalytic process [1]. The work could be concluded as follows: (a) even a small applied external potential (e.g. 0.6 V) could significantly enhance the efficiency and an optimal value exists which varies with the various degradation processes [37, 43]; (b) an optimum range of pH and operating temperature could be detected, albeit varying from different operating conditions. Generally, pH value ranging from 3 to 10 [38] and temperature between 20 ˚C and 80 ˚C [44] of the electrolyte is in favor of the degradation process; (c) performing as the electron scavenger, the dissolved oxygen could be reduced into superoxide radical which subsequently forms the reactive oxidant species including HO_2• and H_2O_2 [45].

Additionally, the light intensity profiles ought to be considered in the photoelectrocatalytic reactor design since electron-hole pairs are generated only after excitation by photons, and so the profiles directly determine the light energy utilization efficiency. As early as 1970, the light intensity profiles in a perfectly mixed photoreactor has been depicted and a theoretical model is established as shown in equation (6) [46].

$$I_\lambda(r,z) = \frac{S_{L,\lambda}}{4\pi r}(\theta_1 + \theta_2) \tag{6}$$

Where $S_{L,\lambda}$ is the linear source strength per unit length, r; θ_1 and θ_2 are illustrated in Fig. I.2. It can be concluded that the relative position of the sample solution and the light source directly determines the reactor's performance. Specifically, reducing the light propagation path in the liquid could minimize the attenuation. Meanwhile, the emerging mass transfer

problem could be minimized by sparging the pressured gas to achieve turbulence, which has been discussed in [47, 48].

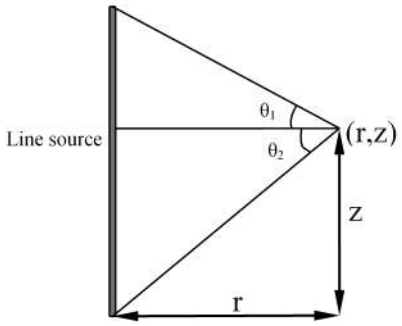


Figure I.2 Line source geometry.

Furthermore, from the point of the mechanism, the relationship between the yield of hydroxide radicals and the light intensity has been summarized by Chen *et al.* [49] as follows:

$$[\bullet OH] = \sqrt{\frac{(1-\alpha) I_a \phi}{k_D}} \tag{7}$$

Where I_a is the number of light quanta absorbed per second, Φ is the quantum yield, k_D is the diffusion-limited rate constant and α is the parameter depending on the pH. It is proven that more light irradiated on the semiconductor results in much higher generation of hydroxide radicals and correspondingly higher catalytic efficiency. An engineering approach to collecting the maximum photons is by the novel design of the reactor configuration. For example, using a concave mirror to collect as much reflected light as possible, the parabolic trough reactor (PTR) [50, 51] and compound parabolic collector (CPC) [52] (Fig. I.3) has been developed in the pilot scale. Zhang *et al.* [53, 54] has studied the corrugated plate photocatalytic reactor.

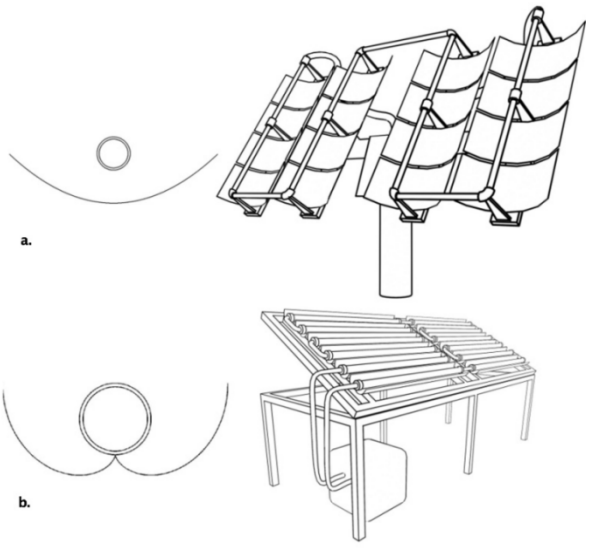


Figure I.3 Scheme of (a) parabolic trough reactor (PTR) and (b) compound parabolic collector (CPC). (adapted from reference [25])

In conclusion, a PEC reactor design is an integrated technique, concerning the synthesis of materials, reactor structure, light energy utilization, photocatalyst use and integration with other advanced techniques. Photoelectrocatalysis is also an integrated technique which includes photolysis, electrolysis, and photocatalysis. These complicated components directly determine the numerous affecting factors in designing a PEC reactor. In reality, various reactor types were reported with distinctive advantages and disadvantages. They are introduced and compared in next section and summarized in Table I.3.

I.3 Types of photoelectrocatalytic reactor configuration

I.3.1 Slurry photoelectocatalytic reactor with three-dimensional electrodes

Initially, three-dimensional electrodes have been widely used in electrochemistry as cathodes for heavy metal removal. Fluidized bed and circulating particulate-bed electrodes are the general reactor types, among which the fixed bed type is widely utilized as illustrated in Fig. I.4 [55]. Due to their high specific surface area relative to thin-film electrodes and their excellent mass transfer, which indirectly reduces the operational costs, three-dimensional electrode systems are favorable in some cases of heavy metal removal in dilute solutions. Since 2001, An *et al.* introduced the three-dimensional electrode into photoelectrochemistry and designed two types of PEC reactors, namely the three-

dimensional electrode-slurry reactor (Fig. I.5) [56, 57] and the three-dimensional electrode-packed bed reactor (Fig. I.6) [58-60].

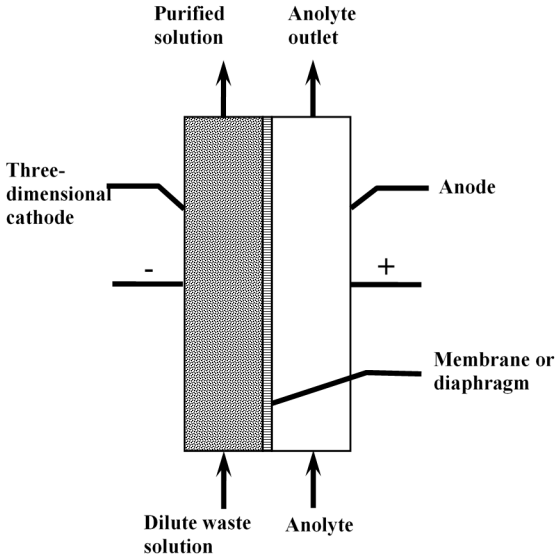


Figure I.4 Diagram of cell with three-dimensional. (adapted from reference [55])

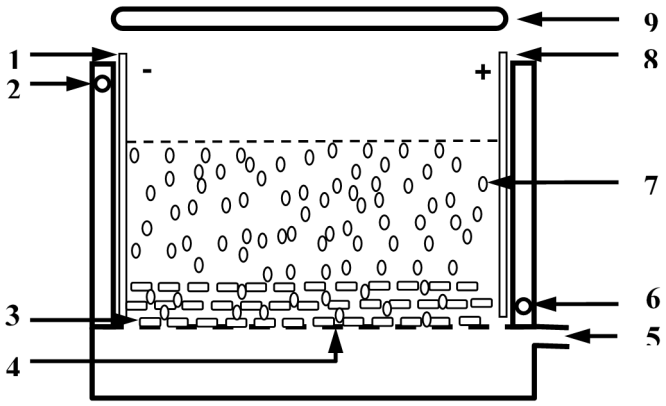


Figure I.5 Diagram of three-dimensional electrode slurry PEC reactor (1. Stainless steel cathode 2. Recycled water outlet 3. Granulated activated carbon layer 4. Microporous plate 5. Pressured air inlet 6. Recycled water inlet 7. TiO_2 particle layer 8. Stainless steel anode 9. UV lamp). (adapted from reference [56])

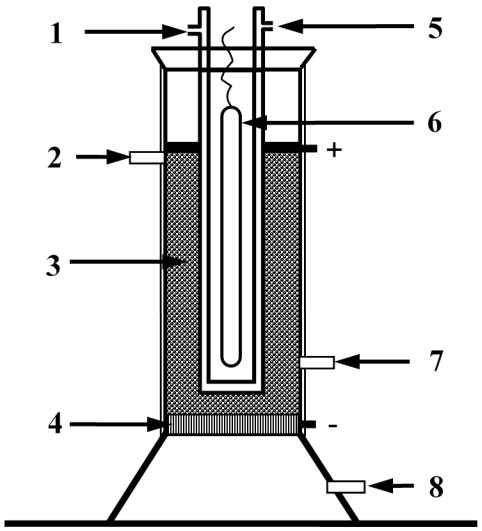


Figure I.6 Diagram of three-dimensional electrode packed bed PEC reactor (1, 5. Recycled water in/out 2. Purified solution 3. Packed TiO_2 particle 4. Microporous plate 6. UV lamp 7. Solution inlet 8. Pressured air inlet). (adapted from reference [58])

I.3.1.1 Description of the three-dimensional electrode PEC process

Upon degradation of the refractory contaminants methylene blue (MB) [57], RED X-3B [56], formic acid [58], reactive brilliant orange K-R [60] and quinoline [59], the 3D electrodes used in the photoelectrocatalytic system, which has a higher efficiency than the single application of electrochemical oxidation or photocatalytic degradation, showed promising prospects in creating a new orientation of PEC reactor design. In the slurry system, stainless steel as the anode and cathode material is immersed in the processing solution. The electrocatalyst is prepared by adding granite activated carbon, modified by 5% MnO_2, as the particle electrode to establish the three dimensional electrode system. Photocatalyst particles are well-distributed in the sample solution by sparging pressured air. Sparging air could strengthen mass transfer by increasing turbulence, thereby reducing the fouling effect at the macro level and the dissolved oxygen could easily capture the photo-generated electrons from the mechanism level, both of which could enhance the efficiency of degradation. The synergetic effect of photocatalysis and electrochemistry performs effectively, proven by the experimental results. Moreover, the high specific surface area relative to the thin-film reactor lowers the mass transfer barriers. By optimizing the

experimental conditions, the COD reduction could attain approximately 90% conversion and more than 80% of the pollutants have been completely mineralized into small compounds such as CO_2 and H_2O by performing Total Organic Carbon (TOC) reduction in 30 minutes [57]. By packing the TiO_2 particles in the reactor, the fixed bed reactor configuration has been constituted. Analogically, comparing the slurry system with the packed bed system is like the comparison of a fluidized bed reactor with the fixed bed reactor. As is well known, the advantages of applying fixed bed reactor include lower backmixing resulting in effective contact of the catalysts with the solution; lower collision rate of the catalysts with the vessel wall and more simple configuration. Meanwhile, disadvantages of fixed bed system exist in relatively poorer heat and mass transfer and the complicated process of changing the fixed catalyst. The relatively high degradation efficiency makes the easy to operate packed bed systems a promising choice in some specific applications, especially the mineralization of toxic organic pollutants to small inorganic materials such as CO_2 and H_2O [59].

I.3.1.2 Mechanism

As for the mechanism of the synergetic process, similar to the one mentioned in the previous section, the directly and indirectly generated strong oxidants including hydroxyl (•OH) and hydrogen peroxide (H_2O_2) are able to break the refractory organics into small intermediates and even completely mineralize them into CO_2 and H_2O. Furthermore, it has been confirmed that much more •OH could be obtained in the three dimensional electrode system than that in two dimensional systems when particle electrodes are absent from the cell (Fig. I.7) [61, 62]. Even more noteworthy is that the high potential (30 V in both systems) could lead to the side reaction-electrolytic process (Formula 8) [63-65]. Coincidently, the production of O_2 could scavenge photo-generated electrons and form $\bullet O_2$, a highly oxidative radical which could degrade partial organics. In other words, the electrolytic process predicts to improve the PEC efficiency.

$$H_2O \rightarrow \frac{1}{2}O_2 \uparrow + H_2 \uparrow \tag{8}$$

Additionally, a new-defined parameter, synergetic factor (SF), was used to evaluate the synergetic effect of the PEC process [58], which simplifies and unifies the evaluation

standard. It is defined as:

$$SF = R_{pe} - (R_p + R_e) \quad (9)$$

R_{pe}, R_p and R_e represent the efficiencies or kinetic constants of COD or organic pollutants removal for the photoelectrocatalytic, photocatalytic and electrolytic processes, respectively. The synergetic effect exists only when $SF > 0$.

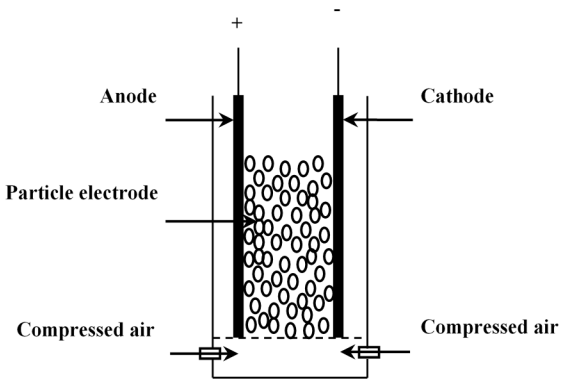


Figure I.7 Scheme of Three-dimensional reactor, and two-dimentional reactor when without the particle electrode. (adapted from [62])

I.3.1.3 Limitations

In the author's opinion, the laboratory set-up has some obstacles to overcome before scale-up. The general shortcomings of slurry reactors utilized in photocatalysis are the complicated separation process, the low re-usability of the catalyst and the high external potential. Smaller catalyst particles, although possessing higher specific surface areas, need a more complicated process to separate from the treated water. Catalysts with small particle sizes could suffer from sedimentation issues due to iron salts causing the flocculation effect [48]. In actual practice, it would be uneconomical due to the higher operational cost. Moreover, in the three-dimensional electrode reactor the side electrolytic reaction could simultaneously generate hydrogen instead of just oxygen. The increase in hydrogen would increase the pH of the solution [55]. This could directly lead to the shift of the valence band of semiconductors to a more positive potential, which means the photogenerated holes

would have slightly higher oxidizing abilities [31, 66]. When the pH is larger than the optimal data ($pH_{optimal}$ = 3.5), the efficiency would decrease with increasing pH [58]. Meanwhile, the high potential used in the reactors could increase the cost of the production process. More specifically, these two kinds of reactors demonstrate the effect of the simple superposition of electrochemistry and photocatalysis instead of the synergetic effect of an integral unit. However, the experimental results proved that the photoelectrocatalytic efficiency is even greater than the summation of these two individual efficiencies which proves that this type of reactor innovatively provides new countermeasures to improve the photocatalytic activity by PEC reactor design.

I.3.2 Immobilized photoelectrocatalytic reactor

To overcome the existing hindrances in the slurry system, especially the complex and pricy separation process, the photocatalyst can be immobilized on a solid substrate such as conductive glass, stainless steel, titanium foil and porous metal mesh. Since 1982, Ward *et al.* immobilized TiO_2 on titanium and applied positive bias to control the electrons and holes to move to opposite directions to improve the photocatalytic efficiency [67]. To prepare the film, anodization method [68, 69], chemical vapor deposition (CVD) [70], sol-gel method [48, 71], dip coating [41, 68, 72], brush-painting [68], spin-coating [73] and directly thermal method [41] are widely utilized.

It is noteworthy that the immobilized thin-film electrode is superior in the reduction of the recombination rate. The interpretation is ascribed that the distance of photo-generated holes moving freely to the surface is approximately 0.1 μm (l_p) for TiO_2 before recombination in the bulk [74], which means the thickness of the semiconductor film immobilized on the substrate should be comparable or smaller than l_p. Furthermore, the mirror effect when the film is thin enough could enhance the absorption of illumination. It could be ascribed that the incident light in the first pass has not been absorbed thoroughly and reflected by the support and has been reutilized by the photocatalyst. Hence, the effective thickness of the film is two-fold [27, 73].

The high controllability and simple operating process, which reasonably meet the necessities for practical application, have prompted the progress of concentrated research on immobilized PEC electrodes and also on reactor designs, which would be illustrated in

the sections below.

I.3.2.1 Single-compartment reactor with flat plate photoanode

Photoelectrocatalytic technology integrates the photocatalytic and electrochemical techniques. Derived from experimental devices applied in these two individual processes, the configuration of an electrolytic tank with an external light source has been constructed in photoelectrocatalytic experiments for basic research of this field [73, 75-80]. The general outline of this kind of reactor is depicted in Fig. I.8. The parallel anode (photocatalysts immobilized on the surface of rectangular substrate) and the conductive cathode are placed in a single compartment. External or internal stimulating light source pass through the effluent and finally get to the photoelectrical anode to trigger a series of photochemical reactions.

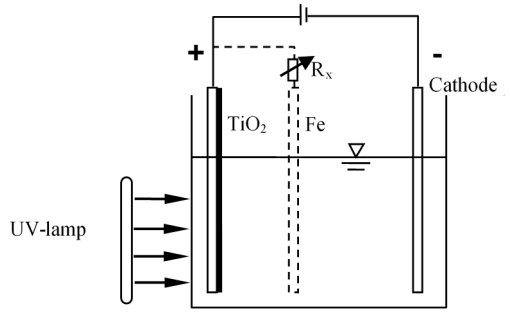


Figure I.8 Diagram of cylinder groove PEC reactor with the external light source.

The PEC system consists of a photocatalyst film (TiO_2, ZnO, CdS, etc.) coated on a conductive substrate (titanium, conductive glass, etc.) as the anode and another conductive electrode as the cathode (stainless steel, Graphite felt, etc.) in a closed circuit. By applying proper external potential, the holes accumulate on the surface of the anode and the electrons gather on the surface of the cathode. The •OH and $•O_2$ could then be produced separately. During the experimental disinfection process, nearly 95% of *E.coli* was killed after 150 min under 1.5 V external bias with ZnO film immobilized on transparent conducting substrate upon UV illumination [76]. When positive bias is applied, it not only enhances the production of reactive oxygen species (ROS), but it also induces the electrostatic attraction between the viral capsid and the photoelectrode [81]. Besides the disinfection application, other interesting trials of single compartment reactor are not only the removal

of the organic molecules by the hydroxyl radicals oxidation on the anode surface, but also the recovery of heavy and precious metals electrodeposited on the cathode surface [70, 77].

On the basis of a single compartment reactor, Zhao *et al.* [75] integrated another effective AOP: the E-Fenton oxidation process, together with the photoelectrocatalytic process by inserting an iron (Fe) electrode parallel to the photocatalytic electrode. The degradation of pollutants by Fenton effect could be ascribed to the hydrogen peroxide catalyzed by the Fe^{2+} to produce •OH with strong oxidizability. The iron electrode under positive bias could be oxidized into Fe^{2+} and the H_2O_2 could be produced around the cathode. Thus, the inserted iron electrode would enhance the degradation process theoretically and the synergetic effect has been confirmed experimentally.

Replacing TiO_2, a WO_3 thin film, immobilized on the conductive glasses, has been synthesized by the brush-painting and spin-coating methods [73]. WO_3, as an n-type semiconductor with narrow band gap energy (E_g = 2.7 eV), could extend the wavelength of the stimulating incident light up to visible light range (approximately 470 nm) which accounts for 12% of the solar energy (comparatively, only 5% of solar energy attribute to UV range). For industrial application, directly applying the solar energy is a potentially promising route.

Meanwhile, double-compartment, where the anode and the cathode are separated into individual compartments, was equipped in the degradation of pollutants [82-88]. The experimental results showed that the double-compartment has lower degradation efficiency than the single compartment [82]. It could be interpreted that the decrease of pH in the anodic compartment would lead to the lower production rate of •OH and the increase of pH in the cathodic compartment would influence the stability of generated H_2O_2. Conversely, the neutralization effect in the electrolyte of single compartment would be beneficial for the production of intermediates and the degradation process.

In the author's opinion, hindrances for commercial application of single compartment PEC reactor might include (a) energy loss during the irradiating process of incident by the absorption of the aqueous phase and (b) the lower mass transfer rate and smaller specific surface area compared to the suspension system. At any rate, as the basic design of the immobilized PEC reactor, the single compartment PEC reactor has been widely applied in

the evaluation and characterization of photocatalytic electrodes in laboratory-scale studies.

I.3.2.2 Cylindrical PEC reactor with annular electrodes

Annular parallel electrodes placed in a cylinder and exciting light from inside-out are the typical features of the Cylindrical PEC reactor, depicted in Fig. I.9. It could be placed either in horizontal [72, 89] or vertical forms [48, 90-92]. Particular advantages associated with the cylindrical configuration are the full utilization of irradiation from every direction and the reinforcement of mass transfer by using mesh electrodes and by sparging with pressured gas [48].

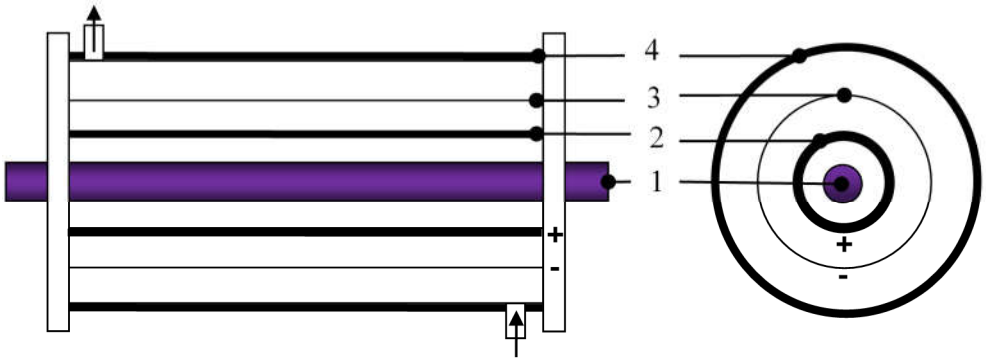


Figure I.9 Diagram of cylindrical PEC reactor (1. Lamp 2. Photoanode 3. Counter electrode 4. Outer glass tube). (adapted from reference [72])

Initially, influenced by the plate and bar electrode used in single-compartment reactors, Horikoshi *et al.* [71] set up a photoelectrocatalytic reactor by using six TiO_2/OTE plate electrodes surrounding the middle lamp (top view of the setup in Fig. I.10). Similarly, Palmisano *et al.* used six rod electrodes fixed by Teflon supports (Fig. I.11) [93]. If there were an infinite number of plate electrodes surrounding the lamp, then the plate electrodes would constitute a single cylindrical electrode. It could be regarded as the link between the plate electrode and the cylindrical electrode. Aiming to minimize the light scattering on the cracks and grooves of the surface, the hybrid immobilized method, pasted method, and sol-gel method have been applied on the fixation of the photocatalyst films. Not only did it enhance the photo-conversion effect, it also improved the affinity between the organic (Benzene sulfonate, BS) and the surface of the photoelectrodes. By optimizing the experimental conditions and the configuration of the setup, the results indicate that the

hybrid method anticipates a higher photo-degradation rate of BS than the individual method [71]. Meanwhile, the TiO_2 is immobilized on the graphite as the anode to produce electron and holes. This corresponds to the golden sheet as the cathode surrounding the inner surface of the outer wall, which improves the utilization of the irradiation on the one side and recovers precious metal ions in the effluent (recovery of silver in the [93]) on the other side. Both of these mentioned reactor configurations above lay the solid foundation for the development of the cylindrical PEC reactor design.

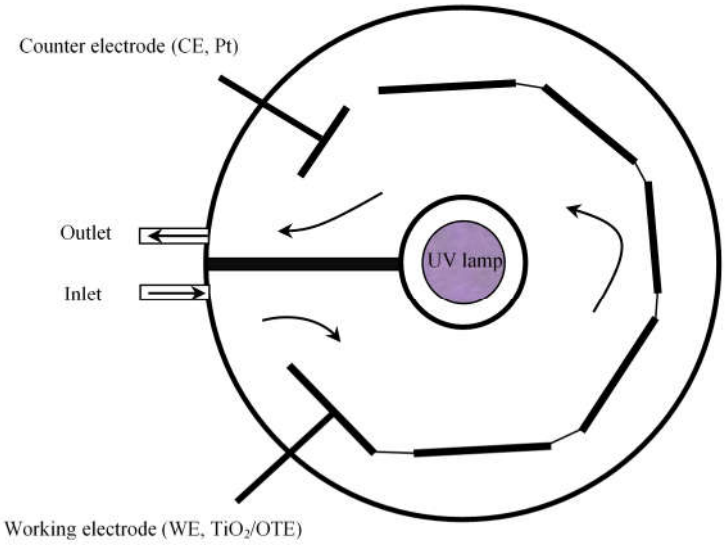


Figure I.10 Top view of the PEC reactor. (adapted from reference [71])

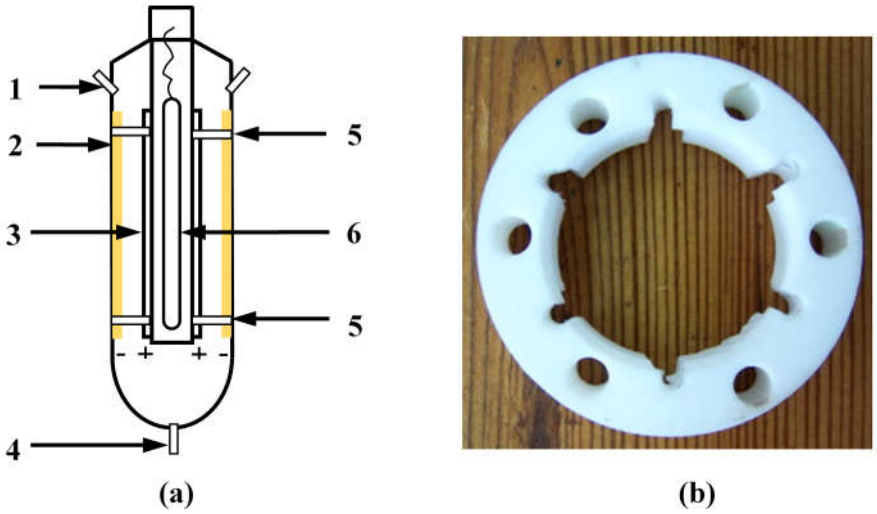


Figure I.11 Cylindrical PEC reactor with bar-type electrode fixed by Teflon support (a) 1.

Liquid outlet 2. Cathode 3. Anode 4. Liquid inlet 5. Telflon support 6. UV-vis lamp (b) Teflon support. (adapted from reference [93])

Since then, extensive research has been focused on the establishment of the cylindrical PEC reactor to date. One major application of the reactor is water purification. Marugán *et al.* [72] and Pablos *et al.*[89] designed the vertical cylindrical reactor and applied it in the degradation of methanol. The results indicate that particulate film electrodes, prepared by dip-coating in a suspension, seem to have notably higher photoelectrocatalytic activity than thermal electrodes prepared by annealing of metal (e.g. thermal TiO_2/Ti electrode prepared by annealing a titanium foil at 700 °C for 30 min [89]). Even though it could considerably improve the photocatalytic activity for the thermal electrodes when the charge carrier separation is forced by the external potential, the major barrier to hinder the oxidation of the pollutants by thermal electrodes has been related to the lower surface area compared to the particulate electrode. The TiO_2 self-organized nanotubes has also been synthesized by anodic oxidization on titanium and placed as the anode against graphite as the cathode [94]. Notwithstanding the high surface area of nanostructures, it takes about 24 hours to obtain approximately 90% decolorization owing to the long distance of the light propagation and poor mass transfer. To minimize irradiation attenuation and improve mass transfer, Christensen *et al.* [48, 90] decreased the distance between the lamp and the photoanode to approximately 2 mm and used mesh electrodes combined with sparging to ensure turbulent flow. The novel reactor named Bubble Column Reactor (BCR) has been applied in the mineralization of aqueous nitrophenol and disinfection of *E.coli* enhanced by electric fields. Similarly, the differences between the particulate and the thermal electrodes have also been compared by the BCR reactor. Conversely, the thermal electrodes could lead to entirely killing off the *E.coli* in 10 minutes compared to over 25 minutes for particulate electrodes [48]. It has been interpreted by the author that the size of the particles on the surface is comparably smaller than the thickness of the depletion layer so that the effectiveness of the electric field enhancement would be reduced. When external potential is applied, the charge carrier separation is much more considerable for thermal electrodes than particulate electrodes.

Even though most of the studies focused on the conversion of the holes generated on the

anode to oxidize the contaminants, Zhao and co-workers still utilize electrons gathered on the cathode for the recovery of metal ions (*e.g.* $Cu^{2+} + 2e^- = Cu$) [91]. Theoretically, it is infallible to reduce metal ions along with the degradation of the pollutants on individual electrode surfaces operated at the appropriate conditions. However, comparing the photoelectrocatalytic process with the electrochemical process in terms of energy cost, it is approximately 10-fold higher for the PEC process with 1.2 kWh/ (g metal recovery) than for the process without UV lamps and simply applying external potential. In pilot scale experiments, work needs to be focused on finding alternative methods in reducing the energy cost on the UV lamp.

It can be concluded that PEC reactors with cylindrical configuration electrodes are much more adaptable in practice with the following adjustments: (a) decrease the distance between the lamp and the photoanode to avoid light attenuation; (b) reinforce the turbulence by sparging pressured gas or by direct mechanical agitation to reduce the mass transfer barriers; (c) suggest alternative methods to decrease the energy cost of UV lamp or replace it with solar energy by modifying or synthesizing novel photocatalysts. Meanwhile, the difficulty of the catalyst regeneration in the cylindrical reactor and the preparation of the cylindrical electrodes should also be considered in future studies.

I.3.2.3 Thin-layer PEC reactor with double-faced Titania Nanotube Arrays (TNAs) electrode

The energy lost in the pathway from the lamp to the electrode directly influences the photon utilization and the maximum concentration of the effluent. It would be infallible to decrease the thickness of the liquid layer on the electrode in order to reduce light energy consumption, based on Beer's Law. Gan *et al.* synthesized the TiO_2 thin film electrodes by the evaporation-induced self-assembly technique as the anode in the thin-layer photoelectrocatalytic system [95]. Aiming to improve the performance of the thin-layer system, the photoelectrode TNAs were synthesized by the anodization method and treated as the working electrode (Fig. I.12) [96]. It has been confirmed that TiO_2 nanotubes could enhance the photocatalysis reaction owing to the lower photo-generated electron-hole pair recombination rate, higher photoefficiency without light-scattering effects and excellent electron transfer velocity for the special one dimensional structure [97-101]. In the novel

photoelectrocatalytic thin-layer reactor [96], the thickness of the aqueous layer is approximately 0.2 mm, which not only reduces the loss of the irradiation energy, but also provides efficient mass transfer from the bulk to the reaction sites. Meanwhile, the double-faced TNAs could improve the catalyst surface area. The combination of all these factors result in the removal rate of 76.8% for degrading tetracycline by PEC effect, compared to 45.3% for PC process and 28.8% for photolytic process after 90 minutes; the maximum concentration of the treating solution has been improved. Another trial of the thin-layer PEC reactor was also utilized in the disinfection by decomposition of *E.coli* [69]. The experimental results show that the disinfection efficiency is more than 10-folds faster by the photoelectrocatalytic process than the photocatalytic process, and over 3-folds faster by using TiO_2 nanotube arrays than that by using TiO_2 nanoparticles. These works confirm that the PEC process combined with the thin-layer reactor configuration is an effective method for not only the removal of the organic pollutants but also the disinfection of water-borne pathogens.

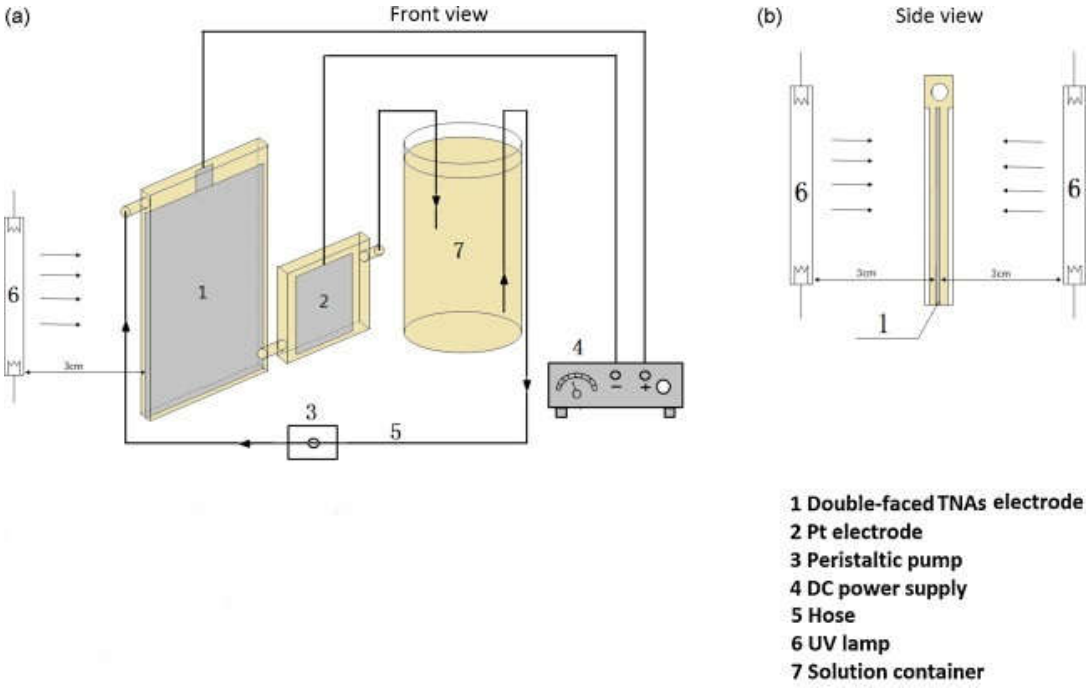


Figure I.12 Schematic diagram of the TNAs based thin-layer PEC reactor (a) front view and (b) side view. (adapted from reference [96])

In conclusion, this reactor configuration provides new ideas to improve the photon utilization by decreasing the distance of the pathway of the irradiation. It is noteworthy that

the close packed system is in favor of degradation of toxic pollutants, but the complicated maintenance procedure and fouling influence must be addressed. Other visible light-response nanotubes need to be synthesized and detected for their photocatalytic performance. Some focus should be placed on parallel multi-thin-layers PEC reactor establishment to improve the process capacity and accelerate its industrialization.

I.3.2.4 Slant-placed electrodes thin-film PEC reactor

Initially, the Thin-film Fixed Bed Reactor (TFFBR) has been introduced in the photocatalytic process [102, 103]. It is noteworthy that the design of TFFBR could implement a continuous process instead of a batch process and there is no need for separation of the photocatalyst compared to the suspension system. Meanwhile, the enlarged treatment capacity is much more suitable for the practical application. Based on the TFFBR, Xu and co-workers designed the slant-placed electrodes thin film PEC reactor (Fig. I.13) [39, 40]. Firstly, the photoanode was immersed in the aqueous sample and an external cathode was applied like the area in the dotted line in Fig. I.13 [104]. In order to decrease the energy consumption and improve the photocatalytic activation, the cathode was also slant-placed and immersed in the electrolyte. Recently, the slant-placed TiO_2 nanotubes electrode was also introduced in the thin-film PEC reactor as an attempt to improve the surface area [105]. However, the results were unsatisfactory as the solution and the air are easily sealed in the nano-level tube, which is detrimental to the mass transfer.

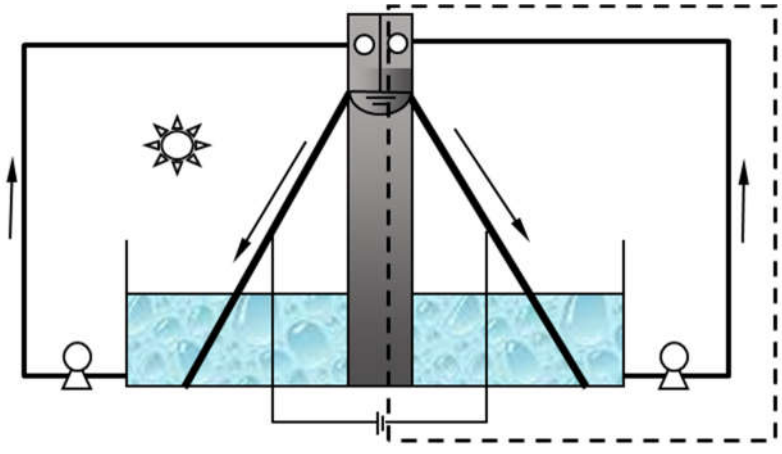


Figure I.13 Diagram of dual slant-placed electrodes thin-film PEC reactor. (adapted from reference [39])

The features of the slant-placed PEC reactor could be concluded as follows: (a) Based on the Beer's Law ($A = \varepsilon bc$, where A is the absorbance, ε is the absorption coefficient, b is the path length and c is the concentration), the thinner the solution film on the electrode, the less the absorbance of the incidence. So, the irradiation consumed by the absorption of the solution would be comparatively reduced. (b) Circulation of the solution could guarantee the saturated dissolved oxygen and overcome the mass transfer barrier. (c) It has been confirmed that the H_2O_2 generated on the anode could improve the photocatalytic oxidation ability; specifically, the efficiency of decolorization on the cathode accounts for approximately 1/3 of the whole effect. (d) With the establishment of Schottky barrier between the semiconductor and some relatively inactive metals such as Cu, the external potential could be replaced by the self-generated electric field so that the external bias energy consumed could be avoided. Even applying a bias as low as 0.0 V, the photocatalytic efficiency could be enhanced.

It proves that by the reactor design, the mass transfer issue has been relieved to some extent and the saving-energy target could be obtained. Even though the pilot device of the slanted-placed photocatalytic reactor has been introduced in [102, 103], as a growing area of study, the slant-placed PEC reactor is still in the laboratorial scale resulting from some influencing factors where the scale-up still needs to be optimized. This includes the potential applied, the flux of the circulation solution, the angle of the electrodes and the economic feasibility. Nevertheless, as a potentially promising route, the slant-placed PEC reactor would become a noteworthy configuration.

I.3.2.5 Vortex PEC reactor

Aiming to alleviate the detrimental effect of the low incident utilization rate caused by the high recombination of the photo-induced photon-electron pairs, Butterfield *et al.* introduced the large-scale vortex reactor as early as 1997 [106]. As seen in the reactor configuration depicted in Fig. I.14, the TiO_2 film, regarded as the anode, was immobilized on the titanium by the thermal method and a nickel mesh counter electrode was placed above the photoelectrode. During the degradation process, the effluent injects into the vortex reactor through tangential ports pushed by a pump and the flow velocity directly determines the thickness of the solution covered on the work electrode. The solution rotates

upward in the vortex configuration until reaching the outlet in the center and then flows back to the reservoir. By decomposing the phenol, the degradation efficiency is increased by 27% in the presence of positive potential bias than the photocatalytic effect alone.

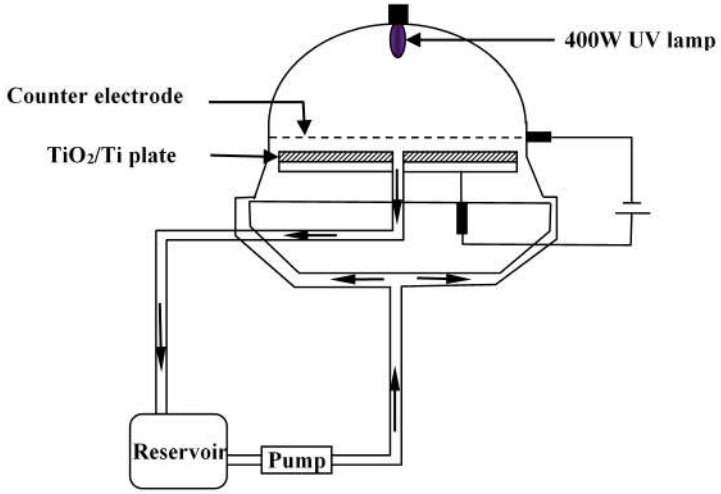


Figure I.14 Diagram of vortex reactor. (adapted from reference [106])

Clearly, the results of the research prove that the electric field enhancement (EFE) could be applied in large scale PEC reactors. However, the mechanism of the organic degradation process and the flow characteristics in the vortex reactor has not yet been explored, which significantly affects the structural optimization of the reactor. Meanwhile, based on the research for this report, the thickness of immobilized film in the large-scale reactor is approximately 1.0 cm which is a relatively thick layer [107] and the photo-generated electron-hole pairs could be recombined in the bulk before reaching the surface which reduces the photoelectrocatalytic effect to some extent. The sophisticated structure of the vortex reactor might also hinder the forward step. Nonetheless, the vortex reactor configuration triggered some novel ideas in PEC reactor design.

I.3.2.6 Rotating disk PEC reactor

Early in the last decade, the Rotating Disk Photocatalytic Reactor (RDPC) has been particularly introduced in mixing studies, light intensity on the rotating disk, liquid carrying capacity of the rotating disk and degradation of 4-chlorobenzoic acid [108]. It has been proven that the mixing process in the RDPC is close to that in the ideal CSTR, which means

mass transfer in the immobilized system has been enhanced. In 2008, Xu *et al.* introduced the identical technique into establishing the photoelectrocatalytic system by adding an external positive bias and an external cathode [30, 109].

The system could be translated into the combination of the thin-film photocatalysis on the upper half of the disk and the conventional bulk-phase photocatalysis on the lower half of the disk. Therefore, the bottleneck problem, which is the loss of the irradiation light absorbed by the aqueous solution, becomes negligible and correspondingly the photocatalytic activity would be enhanced. Meanwhile, the external potential forces the separation of the carriers and electrons resulting in improved light utilizing efficiency. It could not only improve the photocatalytic activity, but also break the restriction on the concentration of the substrate [30, 110]. Furthermore, the parallel cathode was also half immersed in the solution to degrade organic pollutants shown in Fig. I.15 [42]. The reaction on the cathode could be either the pollutants reduced by electrons or pollutants indirectly oxidized by the H_2O_2. In the experimental degradation of Rhodamine B, approximately two-thirds of the treatment efficiency was owed to the cathode effect. Another trial focuses on using a stack of disks associated to the biological contactor by using two electrolytic cells to make sure the sides of the multidiscs could be irradiated [109, 111]. This makes the RDPEC reactor much more feasible for industrialization. As for the low surface area of the flat electrode, the mass transfer has been restricted and, even worse, about 30% of the incidence are reflected and lost. Combined with the corrugated plate used in photocatalytic reactor, Li *et al.* has set up a photoelectrocatalytic reactor with a pyramid-surface electrode [54, 110, 112, 113]. Either the light utilization or the surface area is enlarged. The experimental results show the decolorization efficiency increases by 53%, of which 25% is owed to improving the light utilization and 28% to enlarging the surface area [110]. Aiming to increase the surface area and enhance the photo-generated carriers and holes, the TiO_2 nanotube (TNT) was immobilized on the disk surface using the anodization method [114, 115]. The application of 1D nanotubular photocatalysts could directly accelerate the diffusive transport of the holes to the surface and oxidize the surface adsorbed species so that the photocatalytic efficiency could be improved. Meanwhile, to modify the photocatalyst to extend the absorption wavelength into the visible light range, the β-Bi_2O_3/Ti photoelectrode has been applied in the rotating disk reactor [116]. It has

been reported that Cl^- conversely enhances the photocatalytic degradation since Cl^- could react with the •OH and holes (h^+), especially in the acid solution [117]. It could be accredited to the formation of BiOCl on the surface which could be easily negative charged; even though the BiOCl could hardly be excited by the visible light [118], the cationic dye Rhodamine B could be easily adsorbed on the BiOCl surface and degraded under the visible irradiation by the effect of dye self-photosensitization [119].

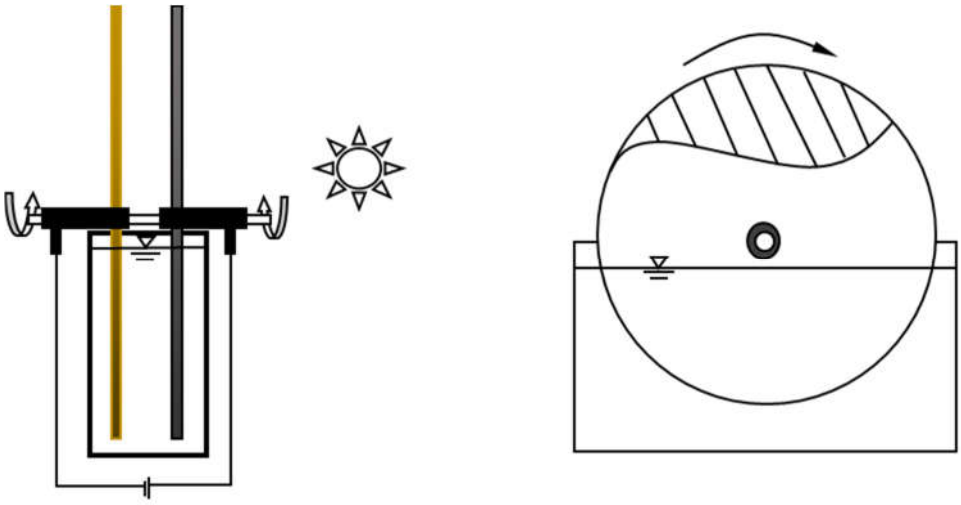


Figure I.15 Diagram of rotating disk PEC reactor. (adapted from reference [42])

In summation, the rotating disk PEC reactor owns the following features: (a) With the rotating of the disk, a thin aqueous film is formed and irradiated by the UV light, the energy consumption for absorption by the solution could be reduced based on Beer's Law; (b) in addition to the PEC process on the upper half of the disk, the lower half of the disk could also occur by the conventional PEC process. The combination of these two processes comparatively improves the photoelectrocatalytic activity; (c) The refreshment effect via disk rotating could guarantee the high driving force and keep the process kinetically favorable. Attention has been focused on the modification of photocatalysts to widen the absorbing wavelength, and on the improvement of the surface area to enhance the mass transfer.

I.3.2.7 Compound parabolic (CPC) or parabolic trough reactor (PTR)

Since the last century, the parabolic trough reactor (PTR, Helioman) and compound parabolic photocatalytic reactor (CPC) have completed the outdoor field test and developed

in engineering-scale and revealed promising prospects[50-52, 120-122] (Fig. I.3). Even though the PTR type possesses advantages including high optical efficiency and simple and inexpensive operating cost, it can only use direct irradiation and need high fabrication costs. This hastens the development of the CPC photoreactor which has high irradiation utilizing efficiency from every direction and intrinsic simplicity with cost-effective and simple use features [32]. However, the photocatalyst is usually suspended in the system which means a post-separation step is needed. Additionally, both the lower solar light response of the photocatalyst and the inevitable high recombination rate of the electron-hole pairs results in lower photocatalytic activity.

In 1999, Fernandez-Ibañez *et al.* merged the photoelectrocatalytic technique together with the PTR and CPC reactor configuration and set up the pilot-scale reactor and performed outdoor field tests (Fig. I.17) [123]. Instead of the slurry system, the photocatalyst (TiO_2) was immobilized on a substrate (Ti) as the anode and Pt/SnO_2 worked as the counter electrode in the immobilized system. Two types of the reactor has been established and compared: photoreactors with single-compartment formed by commercial glass with the anode and counter electrode immobilized in the same compartment (Fig. I.16a); and double-compartment separating the cylindrical photoanodes and the cathodes placed in the inner compartment (Fig. I.16b). The outdoor experimental results of degrading Cl-phenol show that the double-compartment photoelectrocatalytic reactor decreases the filtering effect from the cathodes and the commercial glass substrate with decreasing photocurrent (15% and 35%, respectively). However, extending the distance between the electrodes in the double-compartment system would reduce the electrolyte transfer compared with the single-compartment system. Meanwhile, the experimental results showed the photo-oxidation rate of the immobilized system are higher than the slurry system. In terms of the type of collector, the CPC uses only 43.2% of the area of the Helioman system to obtain 70% of its photocurrent.

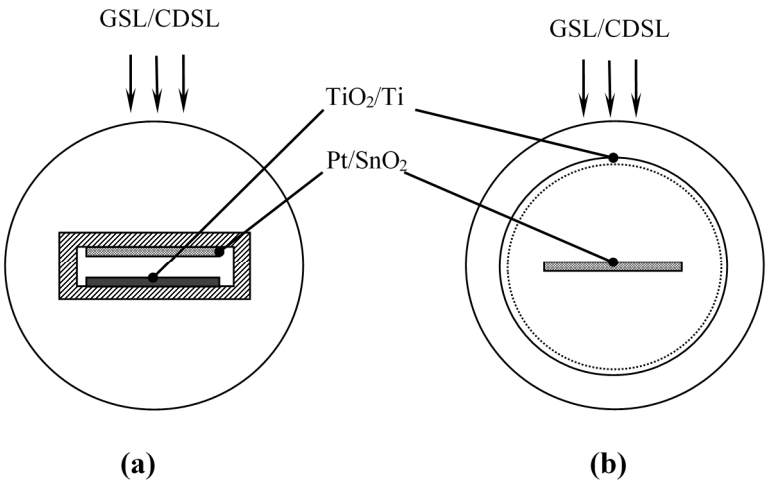


Figure I.16 Schematic cross section of cylindrical PEC reactor. (adapted from reference [123])

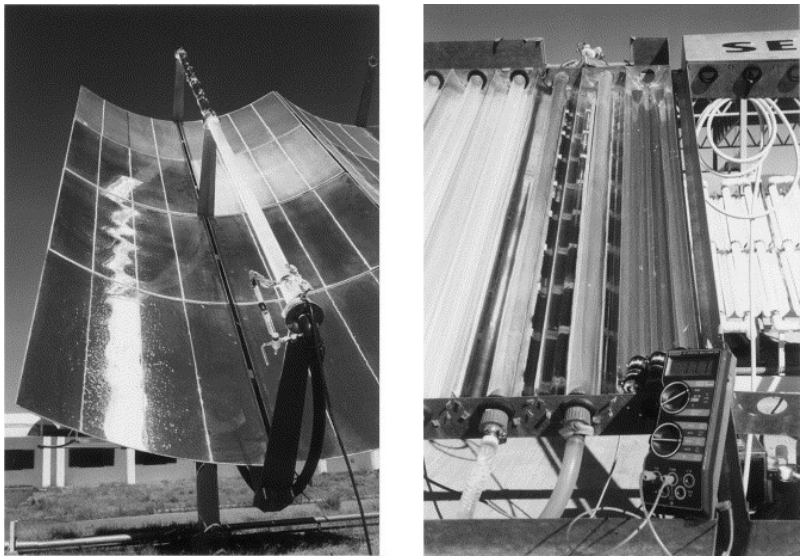


Figure I.17 PEC reactors in operation: (a) left, Helioman module (b) right, CPCs. (adapted from reference [123])

As a whole, the immobilized PEC, CPC or Helioman reactor solves the complicated photocatalyst separation process in the slurry system without decreasing the photocatalytic activity. The utilization of CPC could harvest light with low concentration ratios. Additionally, the double-compartment is suitable for simultaneously dealing with two different electrolytes separately, under their optimal experimental conditions. However, before its practical application, numerous barriers still need to be overcome, which include

the low mass transfer due to the low flow rate, low visible light responded photocatalysts and high investment for its practical application.

I.3.2.8 Determination of chemical oxygen demand (COD)

Chemical Oxygen Demand (COD), one of the most significant parameters to evaluate the quality of water, indirectly represents the quantity of organic compounds in the surface water or wastewater. The conversional methods for detecting the COD include the dichromate method and the permanganate method. Regardless of the widespread use of the standard methods, several drawbacks are present. It takes a long time (2-4 h) to completely oxidize organics in the sample and expensive and toxic reagents such as Ag_2SO_4, Hg^{2+}, and Cr^{6+} are consumed during the analysis process, which raises the risk of secondary-pollution. Based on the above background, enhanced methods such as electrochemical and photocatalytic methods to detect the COD in the effluent were established in the laboratory scale [124-127]. However, they are still unfeasible for practical application, mainly because the electrochemical process is unable to oxidize indiscriminate organics. Recently, the photocatalytic method showed promising prospects in this field in spite of several drawbacks, such as the solubility of oxygen in water and the low degradation efficiency which directly impacts the accuracy of this method [128].

Photoelectrochemical oxidative degradation process (PECOD), which integrates both the photocatalytic and electrochemical processes and exhibits the advantages of both. Other than the improvement of the photocatalytic activity via reduction of the recombination rate of the electron-hole pairs, the quantity of the organics consumed could be directly measured by the electron transfer at the photoelectrode. In 2004, Zhao and his co-workers designed the thin-layer reactor using the TiO_2 nanoparticle film immobilized on the ITO as the electrode shown in Fig. I.18 [128]. The COD value could be calculated by the following equation:

$$COD\ \left(mg/L, O_2\right) = \frac{Q}{4FV} \times 3200 \qquad (10)$$

Where Q is the total electrons transferred during the process which can be measured by the experiment, F is the Faraday constant and V is the volume of the sample which is a constant. By this equation, the detection of the COD parameter is transferred into the measurement

of the electrons which simplifies the operation. Through the optimization of the analytical conditions, it only takes 1-5 minutes to complete the analysis, which is much lower compared to 2-4 hours for the conventional method. The concentration of COD, that could be accurately detected, could be decreased as low as 0.2 mg/L which makes it much more suitable for the practical application. Moreover, it is an environmentally friendly and economical method since it does not use any additional toxic or expensive reagents [128, 129].

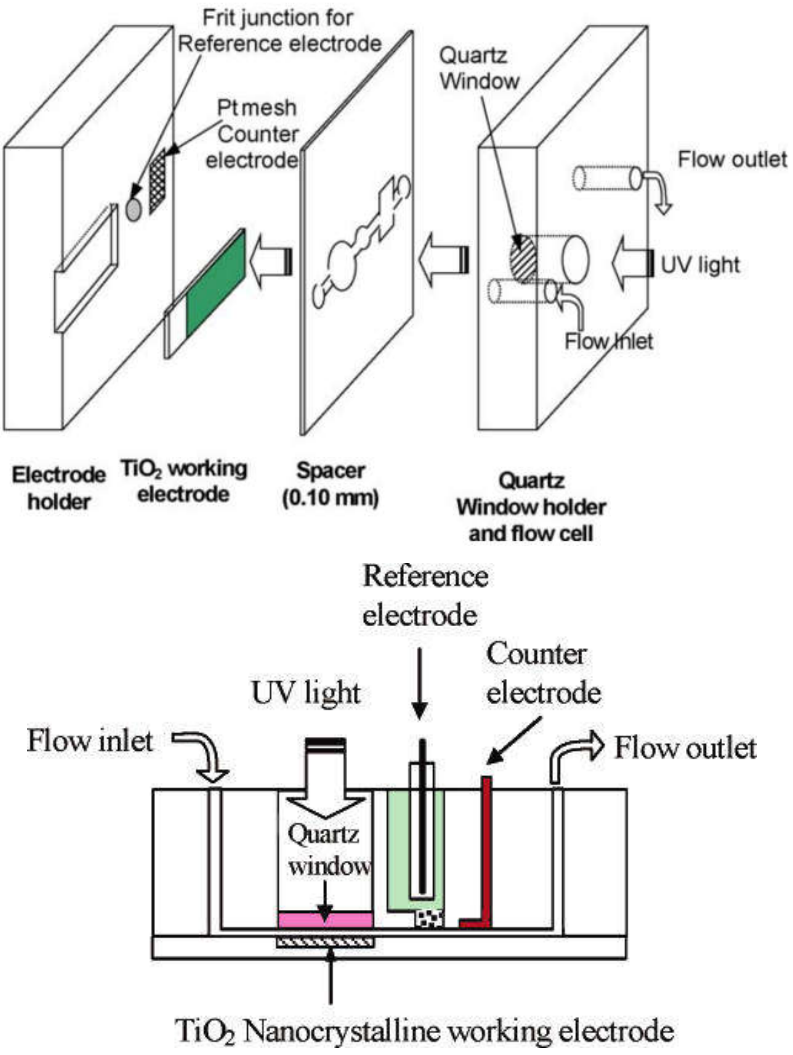


Figure I.18 Thin-layer reactor used in PECOD analysis. (adapted from [129])

Recently, boron-doped diamond (BDD) thin film electrodes have been intensively studied and applied, especially in electrochemical decomposition of organic pollutants [130-132]. It was reported that using BDD electrodes could achieve high current efficiency and high

coversion of the organic carbon into carbon dioxide. Ochiai *et al.* has developed a hybrid system with electrolysis (BDD electrode applied) and photocatalysis units to be implemented in wastewater treatement (Fig. I.19) [133, 134]. Priorities of this system include a fully solar-driven process and separate degradation of different wastewater levels, i.e. electrolysis unit for high-level wasterwater and photocatalysis for low-level wasterwater. However, the system can be simplified by developing PEC system. Correspondingly, TiO_2 immobilized on boron-doped diamond, instead of ITO to improve the acidoresistance, has been used in the COD measurements of the real wastewater samples [135, 136]. Experimental results show that the method is much more reliable, is highly reproducible, and has a wide application range, among other advantages. Meanwhile, owing to the specialty of this method, the on-line monitoring system has also been established with the electrons as the signal [137]. As the special features of the TiO_2 nanotubes have been well-documented, Zhou *et al.* introduced this nanomaterial into the PECOD detection [138-140]. As the TiO_2 nanotubes are perpendicular to the substrate (Ti), the Schottky-type contact has been naturally formed. So in their work, no external bias has been applied. The similar analytical features such as time-saving, high sensitivity, and high-accuracy are obtained.

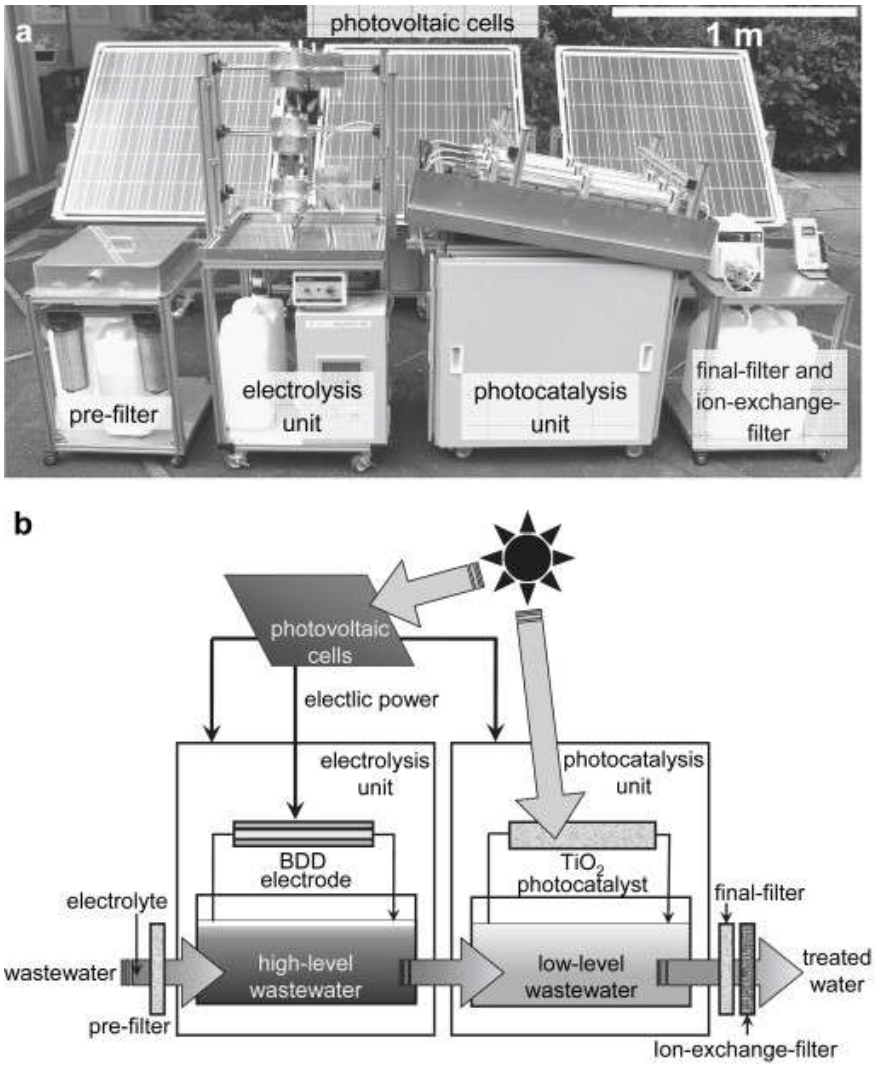


Figure I.19 (a) overview and (b) illustration of hybrid system (electrolysis and photocatalysis). (adapted from [134])

I.3.2.9 PEC reactor used in gas purification

Photocatalysis technology is appropriate for not only, as mentioned above, water treatment, disinfection and metal recovery in the liquid phase, but also for air purification and remediation [141-143]. Conventionally, filters and sorption materials such as active carbon are widely used to adsorb pollutants in the gas phase [144, 145]. These techniques, rather than thoroughly decomposing the pollutants, simply gather the pollutants through a physical process and additional disposal processes are still required. Comparatively, a heterogeneous photocatalytic process is able to completely mineralize the pollutants into small molecules such as CO_2 and H_2O and has promising prospects. Correspondingly,

photocatalytic reactors have been designed and reviewed such as the honeycomb monolith reactors [146], fluidized-bed reactors [147] and annular reactors [148]. Aiming to reduce the recombination probability of the electron hole pairs to improve the photocatalytic activity, the positive bias has been applied to the working electrode to establish the photoelectrocatalytic devices [149-152].

In 2007, Shang *et al.* immobilized the TiO_2 films on ITO for the solid-state planar PEC device and was evaluated by degrading gaseous formaldehyde (HCHO) [152]. The obviously positive synergetic effect could be interpreted as the electrons reacting with adsorbed oxygen to produce O_2^- radicals which could oxidize the HCHO. The accumulating holes, due to its poor conductivity, could be forced to move away by the external bias instead of recombining with the electrons. Another flat-plate type device was fabricated by the technique of screen printing to degrade acetone in the gas phase [150, 153]. The semiconductors used in the photoelectrodes were comprehensively studied in these references [154, 155]. Herein, the WO_3/TiO_2 photocatalyst was synthesized by a ball miller and then immobilized on the substrate (Alumina) (Fig. I.20c). By doping with WO_3, the electrons could move to the external circuit much more easily, which means lower bias is needed to promote the degradation performance [156]. Because the pollutant gas has no water vapor, the holes and the O_2^- produced from the adsorbed oxygen reduced by electrons directly oxidizes the acetone vapor into CO_2 and H_2O. In order to facilitate the photoelectrochemical process in the gas phase, the proton exchange membrane (PEM)-based reactor was fabricated to decompose the gaseous isopropanol [157, 158]. During this process, not only is the pollutant degraded on the photoanode, but hydrogen is also generated on the cathode.

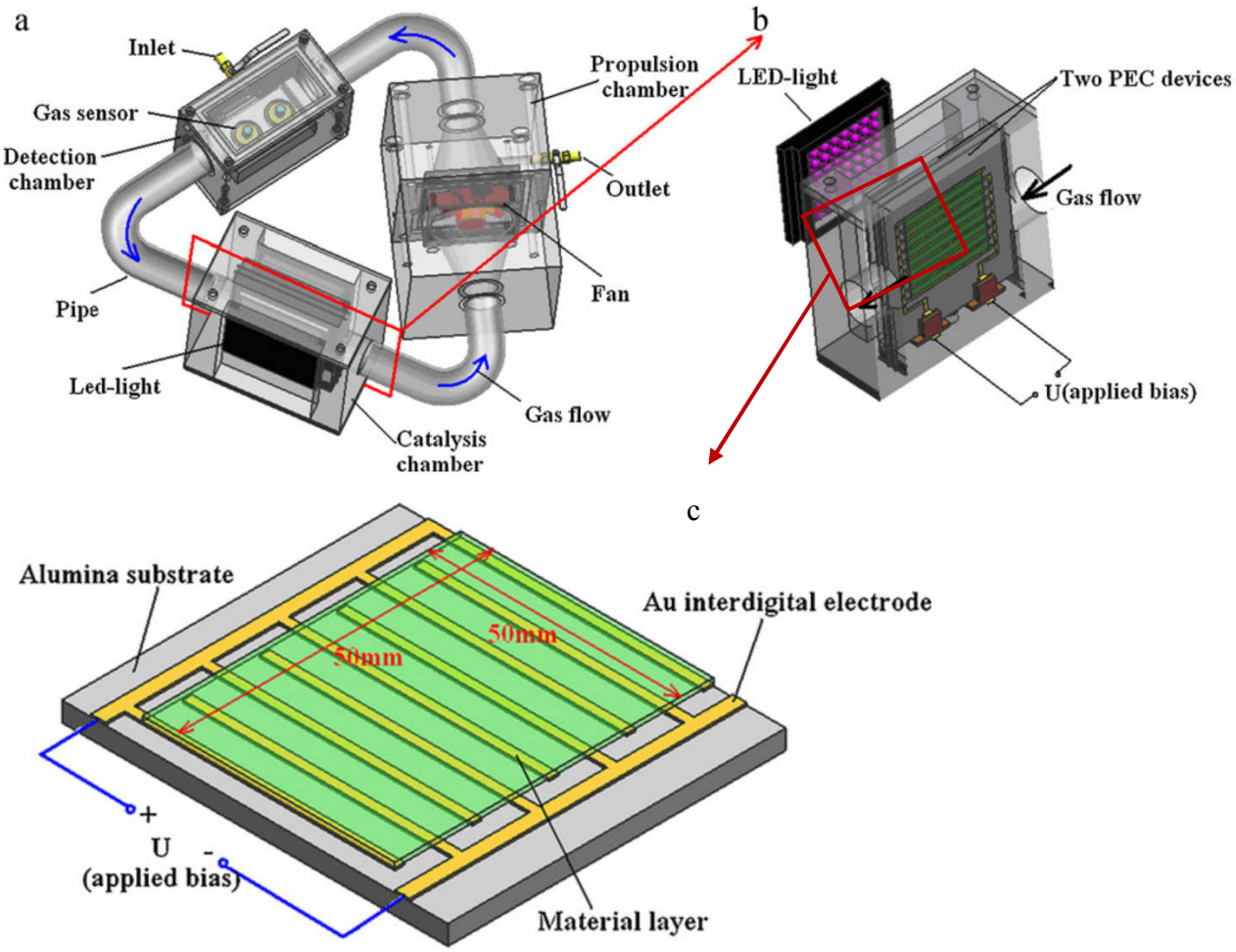


Figure I.20 (a) Schematic of the flat-plate PEC reactor (b) photoelectrocatalytic unit (c) photoelectrocatalytic electrodes. (adapted from [150])

Compared with other disposal methods when dealing with air pollution, the photocatalytic process is superior due to the complete mineralization of pollutants, low energy consumption, and no secondary pollution. Enhanced by the electric field with a positive bias, the quantum yield of the light energy is improved by reducing the recombination property of the electron-hole pairs. However, to the author's acknowledgement, the high cost of the light energy, the adaptability to only low pollutant concentration and the low air to surface ratio of the reactors restrict the photoelectrocatalytic technique for widely practical applications. The mechanism for the degradation process also needs to be comprehensively investigated in future work.

I.4 Cost-effective composite system

One significant factor for the photoelectrocatalytic process that needs to be considered is the cost of the external bias, which requires more energy compared to the photocatalytic process alone. Except for directly using a battery, some alternative methods have been introduced including the microbial fuel cells, photocatalytic fuel cells and solar cells. Each of them provides a cost-effective approach to solve the critical issue.

The microbial fuel cell (MFC), a device that oxidizes organic or inorganic matters catalyzed by bacteria to generate electricity, was once treated as the most suitable wastewater purification method for the synergetic effect of the degradation of pollutants with electricity generation [159-161]. Until 2010, Yuan *et al.* set up a photoelectrocatalytic system enhanced by the microbial fuel cell [162]. Carbon paper was widely utilized as the air-cathode and anode, and it also provided a place for microbial cultivation in the microbial fuel cell. The open circuit voltage could reach around 0.5 V, which increased the degradation rate over two times higher than the individual photocatalytic method. With the prominent performance of the composite system (MFC + PEC), there are still several drawbacks that need to be addressed before up-scale applications, such as the complicated mechanism of the cell system, the complex and lengthy operating process and the rigorous bacterial cultivation conditions.

Instead of the microbial fuel cell, the photocatalytic fuel cell (PFC), a device that converts chemical energy into electrical energy, has been introduced in photoelectrocatalysis and replaced the external bias supply in order to reduce costs for the practical application of photoelectrocatalytic technology (Fig. I.21) [163-165]. The recovery of the chemical energy not used by the wastewater treatment possesses the highest priority for energy-saving and environmental remediation. Therefore, highly ordered TiO_2 nanotube arrays were synthesized by the sonoelectrochemical anodization method and was treated as the photoanode. Pt-black/Pt was chosen as the counter electrode. In terms of the working theory of the PFC, similar to photoelectrocatalytic process, the induced holes left on the valence band after electrons jump to the conduction band by irradiation stimulation are able to oxidize the organic substrate with the production of hydrogen ions. With accumulation of the electrons in the photoanode, electrons could move to the cathode which could be

consumed by reacting with the hydrogen ions diffusing from the anode under aerobic or anaerobic conditions [166, 167]. The net effect indicates that the PFC system could sufficiently supply electrical energy for the PEC process. After optimizing the influencing factors including the electrolyte concentration, surface area of the photoelectrode, external resistor, experimental results of the degradation of tetracycline exhibit that the synergetic effect sharply improves the removal ratio from 16% for photolysis to 81% for photoelectrocatalysis after 3 h in specific experimental conditions. The rate constant of the PEC process is approximately double than that of the photocatalytic (PC) process, which inevitably proves not only that the external bias effectively suppresses the recombination of the photo-generated electron-hole pairs, but also the external electrical energy could be supplied by the PFC.

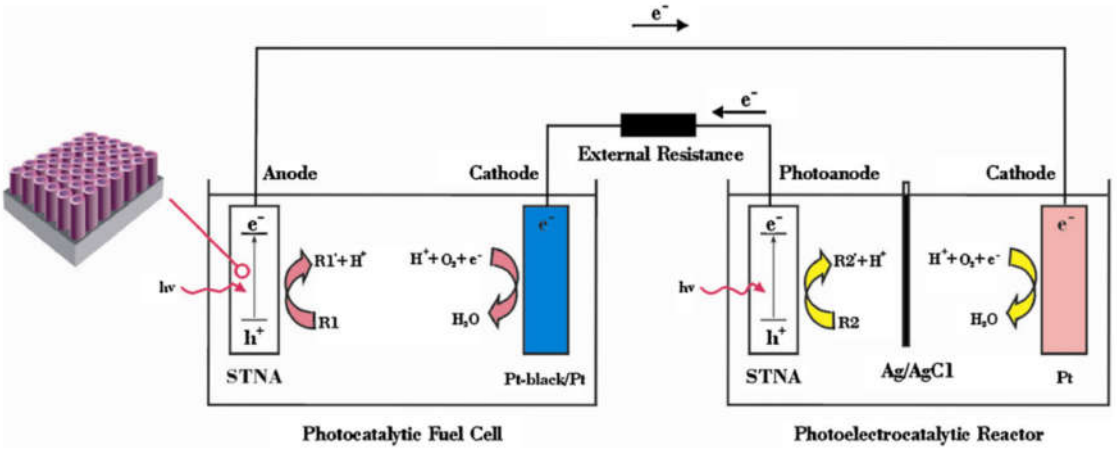


Figure I.21 Schematic diagram of the composite system. (adapted from reference [163])

Recently, Mohammad *et al.* introduced the feasibility of utilizing solar cells to produce direct current to supply electricity for the photoelectrocatalytic process [168, 169]. By optimizing the experimental conditions including photocatalyst dose, initial dye concentration, pH, bias potential and electrolyte types, the removal rate of the dye could reach approximately 95% in 30 minutes. The equation below is used to calculate the overall costs of the external electrical energy, the synthesis of the photocatalyst, the UV lamp and the additional electrolyte [170]. C_{energy} is the energy consumed on the UV lamp and the electrode, $C_{photocatalyst}$ is the amount of photocatalyst consumption and $C_{electrolyte}$ is the amount of the additional electrolyte. The letters *a*, *b* and *c* are the unit prices. In the specific

experiment [168], the overall operating cost is about 9.42 USD/m^3 effluent, and correlates to saving 17% of the overall cost for the electrode energy if it was supplied by solar cells. Sun *et al.* has also coated the graphite oxide on the solar cell to harvest the infrared light to generate electricity used in the photoelectrocatalytic process with similar results [171].

$$\text{Operating Cost} = a \times C_{energy} + b \times C_{photocatalyst} + c \times C_{electrolyte}$$

As modern combinations of the photoelectric technology and the photoelectrocatalytic decontamination method, the innovative design makes the utmost use of the solar energy and correspondingly conforms to the concept of green chemistry [172]. The hindrances for the technique's industrialization are the weak solar light response of the photocatalysts and the detrimental mass transfer of the reactor configuration. As for the PFC-assisted composite system, the cost of the establishment and the operating stability still need to be compared and studied in the future. Overall, these designs obtain the cost-effective goal and show a promising prospective in the development of PEC industrialization.

Table I.3 Overview of photoelectrocatalytic reactor types, application and electrode materials.

Reactor type	Reactor phase	Rector name	Experiment	Photocatalyst	Electrode material	Ref.
Three dimensional electrode	Liquid	Three-dimensional electrode-slurry photocatalytic reactor	Degradation of methylene blue and reactive brilliant Red X-3B	TiO_2 (Degussa P25)	**Anode:** Stainless steel **Cathode:** Stainless steel **Three-dimensional electrode:** Granulated activated carbon adding 5% MnO_2	[56, 57]
	Liquid	Three-dimensional electrode-packed bed photocatalyti	Degradation of quinoline, formic acid and reactive brilliant orange	TiO_2	**Anode:** Porous titanium plate **Cathode:** Cirque made of porous titanium plate **Three-dimensional electrode:** Quartz sand-supported TiO_2	[58-60]

		c reactor	K-R			
Immobilized film reactor	Liquid	Vortex reactor	Degradation salicylic acid, phenol and 4-chlorophenol, respectively	TiO_2	**Anode:** TiO_2/Ti plate **Cathode:** Nickel mesh	[106]
	Liquid	Single-compartment reactor	Against *E.coli* Davis	ZnO	**Anode:** ZnO/FTO/Glass **Cathode:** Stainless steel	[76]
	Liquid	Single-compartment reactor	Oxidative degradation of oxalic acid	WO_3	**Anode:** WO_3/(ITO/glass) **Cathode:** Stainless steel	[73]
	Liquid	Single-compartment reactor	Inactivation of MS-2 bacteriophage	TiO_2	**Anode:** TiO_2/ITO **Cathode:** Stainless metal	[81]
	Liquid	PEC/E-Fenton integrated reactor	Degradation of 2, 4-DCP	TiO_2	**Anode:** TiO_2/Ti **Cathode:** Graphite Felt	[75]
	Liquid	Single-compartment reactor	Oxidation of Cu^{II}-EDTA	TiO_2	**Anode:** TiO_2/Ti **Cathode:** Stainless steel	[77]
	Liquid	Cylindrical reactor with rod-type electrode	Recovery of Silver	TiO_2	**Anode:** TiO_2/graphite **Cathode:** Golden sheet	[70]

	Liquid	Cylindrical reactor	Oxidation of Methanol	TiO_2	**Anode:** TiO_2/Ti and TiO_2/ITO **Cathode:** Nickel mesh	[72, 89]
	Liquid	Cylindrical reactor	Treatment of landfill leachate	TiO_2	**Anode:** TiO_2/Ti **Cathode:** Stainless steel	[92]
	Liquid	Tubular PEC reactor	Cu-EDTA complex	TiO_2	**Anode:** TiO_2/Ti **Cathode:** Stainless steel	[91]
	Liquid	Nanotubular PEC reactor	Decolorization of an azo dye	TiO_2	**Anode:** TiO_2 nanotube **Cathode:** Graphite bar	[94]
	Liquid	Bubble column reactor (BCR)	Disinfection/degradation of 4-Nitrophenol	TiO_2	**Anode:** TiO_2/Ti mesh **Cathode:** Nickel mesh	[48, 90, 173]
	Liquid	Continuous flow reactor	Degradation of benzene sulfonate	TiO_2	**Anode:** TiO_2/OTE **Cathode:** Pt	[71]
	Liquid	Thin-layer PEC rector with double-faced titania nanotube arrays electrode	Degradation of tetracycline	TiO_2	**Anode:** Double-faced titania nanotube arrays **Cathode:** Platinum foil	[96]
	Liquid	Thin-layer	Decomposition	TiO_2	**Anode:** TiO_2 /Ti (nanotube array)	[69]

		PEC reactor	of *E.Coli*		**Cathode:** Auxilizry electrode	
	Liquid	Slant-placed PEC reactor	Degradation of Rhodamine B in dye wastewater	TiO_2	**Anode:** TiO_2/Ti **Cathode:** Cu	[104]
	Liquid	Dual slant-placed PEC reactor	Degradation of Carmine/Amaranth	TiO_2	**Anode:** TiO_2/Ti **Cathode:** Cu, Zn, Fe, C	[39, 40]
	Liquid	Rotating disk PEC reactor	Degradation of Rhodamine B/Allura Red and textile effluent	TiO_2	**Anode:** TiO_2/Ti **Cathode:** Cu	[30, 109]
	Liquid	Dual rotating disk reactor	Degradation of Rhodamine B	TiO_2	**Anode:** TiO_2/Ti **Cathode:** Cu	[42]
	Liquid	Rotating disk PEC reactor with pyramid-surface electrode	Degradation of Rhodamine B	TiO_2	**Anode:** TiO_2/Ti with pyramid surface **Cathode:** Cu	[110]
	Liquid	Rotating disk PEC reactor	Degradation of Methyl orange	TiO_2	**Anode:** TiO_2 nanotube/Ti **Cathode:** Cu	[114, 115]
	Liquid	Single-compartment reactor	Treatment of dyes	TiO_2	**Anode:** TiO_2/Ni **Cathode:** Ti	[168, 169]

	Liquid	PTR & CPC reactor	4 Cl-phenol	TiO_2	**Anode:** TiO_2/Ti **Cathode:** Pt/SnO_2	[123]
	Liquid	Thin-cell reactor	Detecting COD	TiO_2	**Anode:** TiO_2 nanotube **Cathode:** Pt	[140]
	Liquid	Thin layer PEC cell	Detecting COD	TiO_2	**Anode:** TiO_2/Substrate (ITO, boron-doped diamond) **Cathode:** Pt	[128, 135]
	Gas	Solid-state, planar PEC device	Formaldehyde (HCHO)	TiO_2	**Anode:** TiO_2/ITO/Glass **Cathode:** TiO_2/ITO/Glass	[152]
	Gas	Flat-plate PEC device	Acetone	TiO_2/WO_3	**Anode:** TiO_2/WO_3 **Cathode:** Au	[150]

I.5 Conclusions and future work for PEC reactor designs

Recent technological advances in photoelectrocatalysis are fueling its continued development as one of the most promising, versatile, and powerful environmental remediation processes. Given its potential for low recombination of electrical carriers and its high efficiency under visible light irradiation, it is not surprising that this technology is of considerable industrial interest.

Despite the fact that a few pilot-scale reactors have already been reported, development of the PEC reactor design is still in fact in the laboratory stage. Its industrialization is hindered by a multitude of factors, including a costly investment requirement as well as complex operating procedures [48, 89, 92]. Numerous kinetic parameters and models still need to be studied; however, these models are unsubstantial to date despite composing the most fundamental basis of the scale-up process in reactor engineering. Due to the limitations of the slurry system, the immobilized photoelectrode may still be the major direction for reactor design. In our opinion, the ideal reactor configuration should make use of a highly

active and visible-light-active photocatalyst, allow for the efficient aborption of photons by the photocatalyst, have a photoelectrode that effectively suppresses the recombination of photo-generated electron-hole pairs, boast a high mass transfer capacity, and be easy to scale up, fabricate, and operate. Thanks to the swift development of nanotechnologies [20, 174-177] in recent years, further research on new materials for visible-light-active and high-efficiency photocatalysts as well as on novel PEC electrodes is expected to significantly advance the development of photoelectrocatalytic technologies.

It is worth mentioning that most applications of the photoelectrocatalytic reactor place emphasis on the purification of water or disinfection, but rarely focus on the remediation of air quality, which has been widely studied in the field of photocatalytic reactor design[178-180]. Meanwhile, no work has been reported to date exploring the use of photoelectrocatalysis in the field of organic synthesis, which is another area of interest that employs photocatalysis [181, 182].

References

1. R Daghrir, P Drogui and D Robert, "Photoelectrocatalytic technologies for environmental applications," *Journal of Photochemistry and Photobiology A: Chemistry*, vol. 238, pp. 41-52, 2012.

2. Raquel Portela and María Dolores Hernández-Alonso, "Environmental Applications of Photocatalysis," in *Design of Advanced Photocatalytic Materials for Energy and Environmental Applications*, Ed., pp. 35-66, Springer, 2013.

3. Miguel Pelaez, Nicholas T Nolan, Suresh C Pillai, Michael K Seery, Polycarpos Falaras, Athanassios G Kontos, Patrick SM Dunlop, Jeremy WJ Hamilton, J Anthony Byrne and Kevin O'Shea, "A review on the visible light active titanium dioxide photocatalysts for environmental applications," *Applied Catalysis B: Environmental*, vol. 125, pp. 331-349, 2012.

4. Michael R Hoffmann, Scot T Martin, Wonyong Choi and Detlef W Bahnemann, "Environmental applications of semiconductor photocatalysis," *Chemical reviews*, vol. 95, no. 1, pp. 69-96, 1995.

5. Katsunori Yogo and Masamichi Ishikawa, "Recent progress in environmental catalytic

technology," *Catalysis surveys from Japan*, vol. 4, no. 1, pp. 83-90, 2000.

6. Roberto Andreozzi, Vincenzo Caprio, Amedeo Insola and Raffaele Marotta, "Advanced oxidation processes (AOP) for water purification and recovery," *Catalysis Today*, vol. 53, no. 1, pp. 51-59, 1999.

7. P. K. Malik, "Dye removal from wastewater using activated carbon developed from sawdust: adsorption equilibrium and kinetics," *Journal of Hazardous Materials*, vol. 113, no. 1–3, pp. 81-88, 2004.

8. Imen Khouni, Benoît Marrot, Philippe Moulin and Raja Ben Amar, "Decolourization of the reconstituted textile effluent by different process treatments: Enzymatic catalysis, coagulation/flocculation and nanofiltration processes," *Desalination*, vol. 268, no. 1–3, pp. 27-37, 2011.

9. Carmen S. D. Rodrigues, Rui A. R. Boaventura and Luis M. Madeira, "Technical and economic feasibility of polyester dyeing wastewater treatment by coagulation/flocculation and Fenton's oxidation," *Environmental Technology*, vol. 35, no. 10, pp. 1307-1319, 2014.

10. Anu Matilainen and Mika Sillanpää, "Removal of natural organic matter from drinking water by advanced oxidation processes," *Chemosphere*, vol. 80, no. 4, pp. 351-365, 2010.

11. Sabrina Sorlini, Francesca Gialdini, Michela Biasibetti and Carlo Collivignarelli, "Influence of drinking water treatments on chlorine dioxide consumption and chlorite/chlorate formation," *Water Research*, vol. 54, no. 0, pp. 44-52, 2014.

12. MohammedAbdELHamid Khairy, Marit Kolb, AlaaR Mostafa, Anwar El-Fiky and Müfit Bahadir, "Risk posed by chlorinated organic compounds in Abu Qir Bay, East Alexandria, Egypt," *Environmental Science and Pollution Research*, vol. 19, no. 3, pp. 794-811, 2012.

13. Sandip Sharma, Jimit Buddhdev, Manish Patel and Jayesh P. Ruparelia, "Studies on Degradation of Reactive Red 135 Dye in Wastewater using Ozone," *Procedia Engineering*, vol. 51, no. 0, pp. 451-455, 2013.

14. Akira Fujishima and Kenichi Honda, "Electrochemical photolysis of water at a semiconductor electrode," *nature*, vol. 238, pp. 37-38, 1972.

15. Hua Tong, Shuxin Ouyang, Yingpu Bi, Naoto Umezawa, Mitsutake Oshikiri and Jinhua Ye, "Nano - photocatalytic Materials: Possibilities and Challenges," *Advanced Materials*, vol. 24, no. 2, pp. 229-251, 2012.

16. Nick Serpone and Ezio Pelizzetti, *Photocatalysis: fundamentals and applications*, Wiley New York, 1989.

17. Chuan Fu, Tingzhen Li, Junsheng Qi, Jie Pan, Shuhong Chen and Cong Cheng, "Theoretical study on the electronic and optical properties of Ce^{3+}-doped TiO_2 photocatalysts," *Chemical Physics Letters*, vol. 494, no. 1, pp. 117-122, 2010.

18. Huili Yu, Kaili Zhang and Carole Rossi, "Theoretical study on photocatalytic oxidation of VOCs using nano-TiO_2 photocatalyst," *Journal of Photochemistry and Photobiology A: Chemistry*, vol. 188, no. 1, pp. 65-73, 2007.

19. Hongtao Gao, Jing Zhou, DONGMEI Dai and YADONG Qu, "Photocatalytic Activity and Electronic Structure Analysis of N - doped Anatase TiO_2: A Combined Experimental and Theoretical Study," *Chemical Engineering & Technology*, vol. 32, no. 6, pp. 867-872, 2009.

20. ChungHsuang Hung, KeeRong Wu, ChungWei Yeh, JuiChing Sun and ChuanJen Hsu, "Photoelectrocatalytic property of microporous Pt-TiO_2/Ti electrodes," *Thin Solid Films*, vol. 529, no. 0, pp. 19-24, 2013.

21. Xiangchao Meng and Zisheng Zhang, "Synthesis, Analysis, and Testing of BiOBr-Bi_2WO_6 Photocatalytic Heterojunction Semiconductors," *International Journal of Photoenergy*, vol. 2015, pp. 12, 2015.

22. Xiangchao Meng and Zisheng Zhang, "Facile synthesis of BiOBr/Bi_2WO_6 heterojunction semiconductors with high visible-light-driven photocatalytic activity," *Journal of Photochemistry and Photobiology A: Chemistry*, vol. 310, no. 0, pp. 33-44, 2015.

23. Alberto E Cassano, Carlos A Martin, Rodolfo J Brandi and Orlando M Alfano, "Photoreactor analysis and design: fundamentals and applications," *Industrial & engineering chemistry research*, vol. 34, no. 7, pp. 2155-2201, 1995.

24. Cathy McCullagh, Nathan Skillen, Morgan Adams and Peter KJ Robertson,

"Photocatalytic reactors for environmental remediation: a review," *Journal of Chemical Technology and Biotechnology*, vol. 86, no. 8, pp. 1002-1017, 2011.

25. Rowan J Braham and Andrew T Harris, "Review of major design and scale-up considerations for solar photocatalytic reactors," *Industrial & Engineering Chemistry Research*, vol. 48, no. 19, pp. 8890-8905, 2009.

26. Ramesh Thiruvenkatachari, Saravanamuthu Vigneswaran and Il Shik Moon, "A review on UV/TiO_2 photocatalytic oxidation process (Journal Review)," *Korean Journal of Chemical Engineering*, vol. 25, no. 1, pp. 64-72, 2008.

27. Roel van de Krol and Michael Grätzel, *Photoelectrochemical hydrogen production*, Springer, 2011.

28. Masao Kaneko and Ichiro Okura, "Photocatalysis science and technology," *Kodansha Springer*, 2002.

29. Kelei Zhang, Cunming Liu, Fuqiang Huang, Chong Zheng and Wendeng Wang, "Study of the electronic structure and photocatalytic activity of the BiOCl photocatalyst," *Applied Catalysis B: Environmental*, vol. 68, no. 3, pp. 125-129, 2006.

30. Yunlan Xu, Yi He, Xinde Cao, Dengjie Zhong and Jinping Jia, "TiO2/Ti rotating disk photoelectrocatalytic (PEC) reactor: a combination of highly effective thin-film PEC and conventional PEC processes on a single electrode," *Environmental science & technology*, vol. 42, no. 7, pp. 2612-2617, 2008.

31. Yong Xu and Martin AA Schoonen, "The absolute energy positions of conduction and valence bands of selected semiconducting minerals," *American Mineralogist*, vol. 85, no. 3-4, pp. 543-556, 2000.

32. Sixto Malato, Julián Blanco, Alfonso Vidal and Christoph Richter, "Photocatalysis with solar energy at a pilot-plant scale: an overview," *Applied Catalysis B: Environmental*, vol. 37, no. 1, pp. 1-15, 2002.

33. Soonchul Kwon, Maohong Fan, Adrienne T Cooper and Hongqun Yang, "Photocatalytic applications of micro-and nano-TiO_2 in environmental engineering," *Critical Reviews in Environmental Science and Technology*, vol. 38, no. 3, pp. 197-226, 2008.

34. Hyunwoong Park, Yiseul Park, Wooyul Kim and Wonyong Choi, "Surface modification of TiO_2 photocatalyst for environmental applications," *Journal of Photochemistry and Photobiology C: Photochemistry Reviews*, vol. 15, pp. 1-20, 2013.

35. Yves Parent, Daniel Blake, Kim Magrini-Bair, Carol Lyons, Craig Turchi, Andy Watt, Edward Wolfrum and Michael Prairie, "Solar photocatalytic processes for the purification of water: state of development and barriers to commercialization," *Solar Energy*, vol. 56, no. 5, pp. 429-437, 1996.

36. Joanne Gamage McEvoy, Didier Alexandre Bilodeau, Wenquan Cui and Zisheng Zhang, "Visible-light-driven inactivation of Escherichia coli K-12 using an Ag/AgCl–activated carbon composite photocatalyst," *Journal of Photochemistry and Photobiology A: Chemistry*, vol. 267, pp. 25-34, 2013.

37. K Vinodgopal, Surat Hotchandani and Prashant V Kamat, "Electrochemically assisted photocatalysis: titania particulate film electrodes for photocatalytic degradation of 4-chlorophenol," *The Journal of Physical Chemistry*, vol. 97, no. 35, pp. 9040-9044, 1993.

38. Meng Nan Chong, Bo Jin, Christopher WK Chow and Chris Saint, "Recent developments in photocatalytic water treatment technology: a review," *Water research*, vol. 44, no. 10, pp. 2997-3027, 2010.

39. Yunlan Xu, Dengjie Zhong, Jinping Jia, Kan Li, Juexiu Li and Xuejun Quan, "Dual slant-placed electrodes thin-film photocatalytic reactor: Enhanced dye degradation efficiency by self-generated electric field," *Chemical Engineering Journal*, vol. 225, pp. 138-143, 2013.

40. Yun L Xu, Jue X Li, Deng J Zhong and Jin P Jia, "Dual electrodes degradation of Amaranth using a thin-film photocatalytic reactor with dual slant-placed electrodes," *Journal of Environmental Science and Health, Part A*, vol. 48, no. 13, pp. 1700-1706, 2013.

41. C Pablos, R van Grieken, J Marugdán, C Adán, M Osuna and J Palma, "Photoelectrocatalytic study and scaling up of titanium dioxide electrodes for wastewater treatment," *Water Science & Technology*, vol. 68, no. 5, pp. 999-1003, 2013.

42. Yunlan Xu, Yi He, Jinping Jia, Dengjie Zhong and Yalin Wang, "Cu−TiO_2/Ti Dual Rotating Disk Photocatalytic (PC) Reactor: Dual Electrode Degradation Facilitated by

Spontaneous Electron Transfer," *Environmental science & technology*, vol. 43, no. 16, pp. 6289-6294, 2009.

43. Huseyin Selcuk, Jeosadaque J Sene and Marc A Anderson, "Photoelectrocatalytic humic acid degradation kinetics and effect of pH, applied potential and inorganic ions," *Journal of Chemical Technology and Biotechnology*, vol. 78, no. 9, pp. 979-984, 2003.

44. Sixto Malato, P Fernández-Ibáñez, MI Maldonado, J Blanco and W Gernjak, "Decontamination and disinfection of water by solar photocatalysis: recent overview and trends," *Catalysis Today*, vol. 147, no. 1, pp. 1-59, 2009.

45. Yongbing Wang and Chiaswee Hong, "Effect of hydrogen peroxide, periodate and persulfate on photocatalysis of 2-chlorobiphenyl in aqueous TiO_2 suspensions," *Water Research*, vol. 33, no. 9, pp. 2031-2036, 1999.

46. Solomon M Jacobm and Joshua S Dranoff, "Light intensity profiles in a perfectly mixed photoreactor," *AIChE Journal*, vol. 16, no. 3, pp. 359-363, 1970.

47. J. C. Harper, P. A. Christensen, T. A. Egerton and K. Scott, "Mass transport characterization of a novel gas sparged photoelectrochemical reactor," *Journal of Applied Electrochemistry*, vol. 31, no. 3, pp. 267-273, 2001.

48. PA Christensen, TP Curtis, TA Egerton, SAM Kosa and JR Tinlin, "Photoelectrocatalytic and photocatalytic disinfection of *E. coli* suspensions by titanium dioxide," *Applied Catalysis B: Environmental*, vol. 41, no. 4, pp. 371-386, 2003.

49. Fengna Chen, Xudong Yang, Henry K. C. Mak and Daniel W. T. Chan, "Photocatalytic oxidation for antimicrobial control in built environment: A brief literature overview," *Building and Environment*, vol. 45, no. 8, pp. 1747-1754, 2010.

50. Mark Mehos, C Turchi, Jim Pacheco, AJ Boegel, Tim Merrill and R Stanley, "Pilot-scale study of the solar detoxification of VOC-contaminated groundwater," Ed., National Renewable Energy Lab., Golden, CO (United States), 1992.

51. C. Minero, E. Pelizzetti, S. Malato and J. Blanco, "Large solar plant photocatalytic water decontamination: Degradation of pentachlorophenol," *Chemosphere*, vol. 26, no. 12, pp. 2103-2119, 1993.

52. Erick R Bandala, Camilo A Arancibia-Bulnes, Sayra L Orozco and Claudio A Estrada, "Solar photoreactors comparison based on oxalic acid photocatalytic degradation," *Solar energy*, vol. 77, no. 5, pp. 503-512, 2004.

53. Z Zhang, WA Anderson and M Moo‐Young, "Rigorous modeling of UV absorption by TiO_2 films in a photocatalytic reactor," *AIChE journal*, vol. 46, no. 7, pp. 1461-1470, 2000.

54. Zisheng Zhang, William A Anderson and Murray Moo-Young, "Experimental analysis of a corrugated plate photocatalytic reactor," *Chemical Engineering Journal*, vol. 99, no. 2, pp. 145-152, 2004.

55. Daniel Simonsson, "Electrochemistry for a cleaner environment," *Chemical Society Reviews*, vol. 26, no. 3, pp. 181-189, 1997.

56. TaiCheng An, XiHai Zhu and Ya Xiong, "Synergic degradation of reactive brilliant red X-3B using three dimension electrode-photocatalytic reactor," *Journal of Environmental Science and Health, Part A*, vol. 36, no. 10, pp. 2069-2082, 2001.

57. Taicheng An, Xihai Zhu and Ya Xiong, "Feasibility study of photoelectrochemical degradation of methylene blue with three-dimensional electrode-photocatalytic reactor," *Chemosphere*, vol. 46, no. 6, pp. 897-903, 2002.

58. Taicheng An, Ya Xiong, Guiying Li, Changhong Zha and Xihai Zhu, "Synergetic effect in degradation of formic acid using a new photoelectrochemical reactor," *Journal of Photochemistry and Photobiology A: Chemistry*, vol. 152, no. 1, pp. 155-165, 2002.

59. Taicheng An, Wenbing Zhang, Xianming Xiao, Guoying Sheng, Jiamo Fu and Xihai Zhu, "Photoelectrocatalytic degradation of quinoline with a novel three-dimensional electrode-packed bed photocatalytic reactor," *Journal of Photochemistry and Photobiology A: Chemistry*, vol. 161, no. 2, pp. 233-242, 2004.

60. Wenbing Zhang, Taicheng An, Xianming Xiao, Jiamo Fu, Guoying Sheng, Mingchao Cui and Guiying Li, "Photoelectrocatalytic degradation of reactive brilliant orange KR in a new continuous flow photoelectrocatalytic reactor," *Applied Catalysis A: General*, vol. 255, no. 2, pp. 221-229, 2003.

61. Huazhang Zhao, Yan Sun, Lina Xu and Jinren Ni, "Removal of Acid Orange 7 in simulated wastewater using a three-dimensional electrode reactor: Removal mechanisms and dye degradation pathway," *Chemosphere*, vol. 78, no. 1, pp. 46-51, 2010.

62. Lina Xu, Huazhang Zhao, Shaoyuan Shi, Guangzhi Zhang and Jinren Ni, "Electrolytic treatment of CI Acid Orange 7 in aqueous solution using a three-dimensional electrode reactor," *Dyes and Pigments*, vol. 77, no. 1, pp. 158-164, 2008.

63. Meng Ni, Michael KH Leung, Dennis YC Leung and K Sumathy, "A review and recent developments in photocatalytic water-splitting using TiO_2 for hydrogen production," *Renewable and Sustainable Energy Reviews*, vol. 11, no. 3, pp. 401-425, 2007.

64. Akihiko Kudo and Yugo Miseki, "Heterogeneous photocatalyst materials for water splitting," *Chemical Society Reviews*, vol. 38, no. 1, pp. 253-278, 2009.

65. Blaise A Pinaud, Jesse D Benck, Linsey C Seitz, Arnold J Forman, Zhebo Chen, Todd G Deutsch, Brian D James, Kevin N Baum, George N Baum and Shane Ardo, "Technical and economic feasibility of centralized facilities for solar hydrogen production via photocatalysis and photoelectrochemistry," *Energy & Environmental Science*, vol. 6, no. 7, pp. 1983-2002, 2013.

66. M. A. Butler and D. S. Ginley, "Prediction of Flatband Potentials at Semiconductor - Electrolyte Interfaces from Atomic Electronegativities," *Journal of The Electrochemical Society*, vol. 125, no. 2, pp. 228-232, 1978.

67. Michael D Ward and Allen J Bard, "Photocurrent enhancement via trapping of photogenerated electrons of titanium dioxide particles," *The Journal of Physical Chemistry*, vol. 86, no. 18, pp. 3599-3605, 1982.

68. NS Gaikwad, G Waldner, A Brüger, A Belaidi, SM Chaqour and M Neumann-Spallart, "Photoelectrochemical characterization of semitransparent WO_3 films," *Journal of The Electrochemical Society*, vol. 152, no. 5, pp. G411-G416, 2005.

69. Xiaolu Liu, Yanhe Han, Guiying Li, Haimin Zhang and Huijun Zhao, "Instant inactivation and rapid decomposition of Escherichia coli using a high efficiency TiO_2 nanotube array photoelectrode," *RSC Advances*, vol. 3, no. 43, pp. 20824-20828, 2013.

70. Chaolang Kao, Yunghsu Hsieh, Mingyi Chang, Chiahsin Li and Chinchuan Liu, "TiO_2/Ti thin-film electrode manufacturing equipment and combined external circuit photoelectrical catalytic process for reducing silver ions," *Separation and Purification Technology*, vol. 63, no. 3, pp. 546-551, 2008.

71. Satoshi Horikoshi, Youko Satou, Hisao Hidaka and Nick Serpone, "Enhanced photocurrent generation and photooxidation of benzene sulfonate in a continuous flow reactor using hybrid TiO_2 thin films immobilized on OTE electrodes," *Journal of Photochemistry and Photobiology A: Chemistry*, vol. 146, no. 1–2, pp. 109-119, 2001.

72. Javier Marugán, Rafael van Grieken, Cristina Pablos, Cristina Adán and Ruud Timmers, "Determination of Photochemical, Electrochemical and Photoelectrochemical Efficiencies in a Photoelectrocatalytic Reactor," *International Journal of Chemical Reactor Engineering*, vol. 11, no. 2, pp. 787-797, 2013.

73. G Waldner, A Brüger, NS Gaikwad and M Neumann-Spallart, "WO_3 thin films for photoelectrochemical purification of water," *Chemosphere*, vol. 67, no. 4, pp. 779-784, 2007.

74. H. Paul Maruska and Amal K. Ghosh, "Transition-metal dopants for extending the response of titanate photoelectrolysis anodes," *Solar Energy Materials*, vol. 1, no. 3–4, pp. 237-247, 1979.

75. B. X. Zhao, X. Z. Li and P. Wang, "2,4-Dichlorophenol degradation by an integrated process: Photoelectrocatalytic oxidation and E-Fenton oxidation," *Photochemistry and Photobiology*, vol. 83, no. 3, pp. 642-646, 2007.

76. R. T. Sapkal, S. S. Shinde, D. M. Sapkal, A. R. Babar, V. V. Shinde, C. B. Jalkute, A. V. Moholkar, K. Y. Rajpure, K. D. Sonawane, P. S. Patil and C. H. Bhosale, "Photoelectrocatalytic activity of spray deposited ZnO thin films against *E. coli* Davis," *Energy Materials: Materials Science and Engineering for Energy Systems*, vol. 7, no. 4, pp. 417-424, 2012.

77. Xu Zhao, Libao Guo, Baofeng Zhang, Huijuan Liu and Jiuhui Qu, "Photoelectrocatalytic Oxidation of CuII–EDTA at the TiO_2 Electrode and Simultaneous Recovery of CuII by Electrodeposition," *Environmental science & technology*, vol. 47, no.

9, pp. 4480-4488, 2013.

78. X. Z. Li and H. S. Liu, "Development of an E-H_2O_2/TiO_2 Photoelectrocatalytic Oxidation System for Water and Wastewater Treatment," *Environmental Science & Technology*, vol. 39, no. 12, pp. 4614-4620, 2005.

79. Tao Fang, Lixia Liao, Xiangju Xu, Jinsong Peng and Yingqi Jing, "Removal of COD and colour in real pharmaceutical wastewater by photoelectrocatalytic oxidation method," *Environmental Technology*, vol. 34, no. 6, pp. 779-786, 2013.

80. Baoshun Liu, Liping Wen and Xiujian Zhao, "Efficient degradation of aqueous methyl orange over TiO_2 and CdS electrodes using photoelectrocatalysis under UV and visible light irradiation," *Progress in Organic Coatings*, vol. 64, no. 2–3, pp. 120-123, 2009.

81. Min Cho, Ezra L. Cates and Jae-Hong Kim, "Inactivation and surface interactions of MS-2 bacteriophage in a TiO_2 photoelectrocatalytic reactor," *Water Research*, vol. 45, no. 5, pp. 2104-2110, 2011.

82. Wenhua Leng, Zhao Zhang, Shaoan Cheng, Jianqing Zhang and Chunan Cao, "Photoelectrocatalytic degradation of aniline-comparison of single compartment with double compartment reactor," *Journal of Environmental Science* vol. 22, no. 1, pp. 5, 2002.

83. W. H. Leng, Z. Zhang and J. Q. Zhang, "Photoelectrocatalytic degradation of aniline over rutile TiO_2/Ti electrode thermally formed at 600 °C," *Journal of Molecular Catalysis A: Chemical*, vol. 206, no. 1–2, pp. 239-252, 2003.

84. W. H. Leng, W. C. Zhu, J. Ni, Z. Zhang, J. Q. Zhang and C. N. Cao, "Photoelectrocatalytic destruction of organics using TiO_2 as photoanode with simultaneous production of H_2O_2 at the cathode," *Applied Catalysis A: General*, vol. 300, no. 1, pp. 24-35, 2006.

85. Fabiana Maria Monteiro Paschoal, Greg Pepping, Maria Valnice Boldrin Zanoni and Marc A. Anderson, "Photoelectrocatalytic Removal of Bromate Using Ti/TiO_2 Coated as a Photocathode," *Environmental Science & Technology*, vol. 43, no. 19, pp. 7496-7502, 2009.

86. Guohui Qin, Quanping Wu, Zhe Sun, Ying Wang, Jiangzhou Luo and Song Xue, "Enhanced photoelectrocatalytic degradation of phenols with bifunctionalized dye-sensitized TiO_2 film," *Journal of Hazardous Materials*, vol. 199–200, no. 0, pp. 226-232,

2012.

87. Mohammad Hossein Habibi, Nasrin Talebian and Jong-Ha Choi, "Characterization and photocatalytic activity of nanostructured indium tin oxide thin-film electrode for azo-dye degradation," *Thin Solid Films*, vol. 515, no. 4, pp. 1461-1469, 2006.

88. Maria Valnice B. Zanoni, Jeosadaque J. Sene, Huseyin Selcuk and Marc A. Anderson, "Photoelectrocatalytic Production of Active Chlorine on Nanocrystalline Titanium Dioxide Thin-Film Electrodes," *Environmental Science & Technology*, vol. 38, no. 11, pp. 3203-3208, 2004.

89. C. Pablos, J. Marugán, R. Van Grieken, C. Adán, A. Riquelme and J. Palma, "Correlation between photoelectrochemical behaviour and photoelectrocatalytic activity and scaling-up of P25-TiO_2 electrodes," *Electrochimica Acta*, vol. 130, pp. 261-270, 2014.

90. PA Christensen, TA Egerton, SAM Kosa, JR Tinlin and K Scott, "The photoelectrocatalytic oxidation of aqueous nitrophenol using a novel reactor," *Journal of applied electrochemistry*, vol. 35, no. 7-8, pp. 683-692, 2005.

91. Xu Zhao, Libao Guo and Jiuhui Qu, "Photoelectrocatalytic oxidation of Cu-EDTA complex and electrodeposition recovery of Cu in a continuous tubular photoelectrochemical reactor," *Chemical Engineering Journal*, vol. 239, pp. 53-59, 2014.

92. Xu Zhao, Jiuhui Qu, Huijuan Liu, Chunxia Wang, Shuhu Xiao, Ruiping Liu, Pengju Liu, Huachun Lan and Chengzhi Hu, "Photoelectrochemical treatment of landfill leachate in a continuous flow reactor," *Bioresource technology*, vol. 101, no. 3, pp. 865-869, 2010.

93. Giovanni Palmisano, Vittorio Loddo, Hossam Hamed El Nazer, Sedat Yurdakal, Vincenzo Augugliaro, Rosaria Ciriminna and Mario Pagliaro, "Graphite-supported TiO_2 for 4-nitrophenol degradation in a photoelectrocatalytic reactor," *Chemical Engineering Journal*, vol. 155, no. 1–2, pp. 339-346, 2009.

94. Andrea Turolla, Massimo Fumagalli, Massimiliano Bestetti and Manuela Antonelli, "Electrophotocatalytic decolorization of an azo dye on TiO_2 self-organized nanotubes in a laboratory scale reactor," *Desalination*, vol. 285, pp. 377-382, 2012.

95. Wee Yong Gan, Huijun Zhao and Rose Amal, "Photoelectrocatalytic activity of mesoporous TiO_2 thin film electrodes," *Applied Catalysis A: General*, vol. 354, no. 1–2,

pp. 8-16, 2009.

96. Jing Bai, Yanbiao Liu, Jinhua Li, Baoxue Zhou, Qing Zheng and Weimin Cai, "A novel thin-layer photoelectrocatalytic (PEC) reactor with double-faced titania nanotube arrays electrode for effective degradation of tetracycline," *Applied Catalysis B: Environmental*, vol. 98, no. 3–4, pp. 154-160, 2010.

97. Kai Zhu, Nathan R. Neale, Alexander Miedaner and Arthur J. Frank, "Enhanced Charge-Collection Efficiencies and Light Scattering in Dye-Sensitized Solar Cells Using Oriented TiO_2 Nanotubes Arrays," *Nano Letters*, vol. 7, no. 1, pp. 69-74, 2006.

98. Haimin Zhang, Huijun Zhao, Shanqing Zhang and Xie Quan, "Photoelectrochemical Manifestation of Photoelectron Transport Properties of Vertically Aligned Nanotubular TiO_2 Photoanodes," *ChemPhysChem*, vol. 9, no. 1, pp. 117-123, 2008.

99. Martin Zlamal, Jan M. Macak, Patrik Schmuki and Josef Krýsa, "Electrochemically assisted photocatalysis on self-organized TiO_2 nanotubes," *Electrochemistry Communications*, vol. 9, no. 12, pp. 2822-2826, 2007.

100. Huifang Zhuang, Changjian Lin, Yuekun Lai, Lan Sun and Jing Li, "Some Critical Structure Factors of Titanium Oxide Nanotube Array in Its Photocatalytic Activity," *Environmental Science & Technology*, vol. 41, no. 13, pp. 4735-4740, 2007.

101. Haimin Zhang, Xiaolu Liu, Yibing Li, Qingfeng Sun, Yun Wang, Barry J. Wood, Porun Liu, Dongjiang Yang and Huijun Zhao, "Vertically aligned nanorod-like rutile TiO_2 single crystal nanowire bundles with superior electron transport and photoelectrocatalytic properties," *Journal of Materials Chemistry*, vol. 22, no. 6, pp. 2465-2472, 2012.

102. M. Noorjahan, M. Pratap Reddy, V. Durga Kumari, B. Lavédrine, P. Boule and M. Subrahmanyam, "Photocatalytic degradation of H-acid over a novel TiO_2 thin film fixed bed reactor and in aqueous suspensions," *Journal of Photochemistry and Photobiology A: Chemistry*, vol. 156, no. 1–3, pp. 179-187, 2003.

103. Muthukonda Venkatakrishnan Shankar, Srinivasan Anandan, Nallusamy Venkatachalam, Banumathi Arabindoo and Velayutham Murugesan, "Novel thin-film reactor for photocatalytic degradation of pesticides in an aqueous solution," *Journal of Chemical Technology & Biotechnology*, vol. 79, no. 11, pp. 1279-1285, 2004.

104. Yunlan Xu, Jinping Jia, Dengjie Zhong and Yalin Wang, "Degradation of dye wastewater in a thin-film photoelectrocatalytic (PEC) reactor with slant-placed TiO_2 /Ti anode," *Chemical Engineering Journal*, vol. 150, no. 2–3, pp. 302-307, 2009.

105. Ye Yao, Kan Li, Si Chen, Jinping Jia, Yalin Wang and Haowei Wang, "Decolorization of Rhodamine B in a thin-film photoelectrocatalytic (PEC) reactor with slant-placed TiO_2 nanotubes electrode," *Chemical Engineering Journal*, vol. 187, no. 0, pp. 29-35, 2012.

106. IM Butterfield, PA Christensen, A Hamnett, KE Shaw, GM Walker, SA Walker and CR Howarth, "Applied studies on immobilized titanium dioxide films ascatalysts for the photoelectrochemical detoxification of water," *Journal of applied electrochemistry*, vol. 27, no. 4, pp. 385-395, 1997.

107. Jaques Gautron, Philippe Lemasson and Jean-Francis Marucco, "Correlation between the non-stoichiometry of titanium dioxide and its photoelectrochemical behaviour," *Faraday Discussions of the Chemical Society*, vol. 70, pp. 81-91, 1980.

108. Dionysios D. Dionysiou, Ganesh Balasubramanian, Makram T. Suidan, Amid P. Khodadoust, Isabelle Baudin and Jean-Michel Laîné, "Rotating disk photocatalytic reactor: development, characterization, and evaluation for the destruction of organic pollutants in water," *Water Research*, vol. 34, no. 11, pp. 2927-2940, 2000.

109. Yun L. Xu, Deng J. Zhong and Jin P. Jia, "Electrochemical-assisted photodegradation of Allura Red and textile effluent using a half-exposed rotating TiO_2 /Ti disc electrode," *Journal of Environmental Science and Health, Part A*, vol. 43, no. 5, pp. 503-510, 2008.

110. Kan Li, Chen Yang, YaLin Wang, JinPing Jia, YunLan Xu and Yi He, "A high-efficient rotating disk photoelectrocatalytic (PEC) reactor with macro light harvesting pyramid-surface electrode," *AIChE Journal*, vol. 58, no. 8, pp. 2448-2455, 2012.

111. F. Visscher, J. van der Schaaf, T. A. Nijhuis and J. C. Schouten, "Rotating reactors – A review," *Chemical Engineering Research and Design*, vol. 91, no. 10, pp. 1923-1940, 2013.

112. Z Zhang, William A Anderson and Murray Moo-Young, "An engineering model for the scale-up and design of photocatalytic reactors," *Int J Chem Reactor Eng*, vol. 1, no. 1, pp. 1-8, 2003.

113. Kan Li, Yi He, Yunlan Xu, Yalin Wang and Jinping Jia, "Degradation of Rhodamine B using an unconventional graded photoelectrode with wedge structure," *Environmental Science & Technology*, vol. 45, no. 17, pp. 7401-7407, 2011.

114. Aiyong Zhang, Minghua Zhou, Liang Liu, Wei Wang, Yongli Jiao and Qixing Zhou, "A novel photoelectrocatalytic system for organic contaminant degradation on a TiO_2 nanotube (TNT)/Ti electrode," *Electrochimica Acta*, vol. 55, no. 18, pp. 5091-5099, 2010.

115. Aiyong Zhang, Minghua Zhou, Lu Han and Qixing Zhou, "The combination of rotating disk photocatalytic reactor and TiO_2 nanotube arrays for environmental pollutants removal," *Journal of Hazardous Materials*, vol. 186, no. 2–3, pp. 1374-1383, 2011.

116. Kan Li, Chen Yang, Yunlan Xu, Diwen Ying, Yalin Wang and Jinping Jia, "Effect of inorganic anions on Rhodamine B removal under visible light irradiation using Bi_2O_3/Ti rotating disk reactor," *Chemical Engineering Journal*, vol. 211–212, no. 0, pp. 208-215, 2012.

117. Chantal Guillard, Eric Puzenat, Hinda Lachheb, Ammar Houas and Jean-Marie Herrmann, "Why inorganic salts decrease the TiO_2 photocatalytic efficiency," *International Journal of Photoenergy*, vol. 7, no. 1, pp. 1-9, 2005.

118. Huizhong An, Yi Du, Tianmin Wang, Cong Wang, Weichang Hao and Junying Zhang, "Photocatalytic properties of BiOX (X= Cl, Br, and I)," *Rare Metals*, vol. 27, no. 3, pp. 243-250, 2008.

119. Taixing Wu, Guangming Liu, Jincai Zhao, Hisao Hidaka and Nick Serpone, "Photoassisted Degradation of Dye Pollutants. V. Self-Photosensitized Oxidative Transformation of Rhodamine B under Visible Light Irradiation in Aqueous TiO_2 Dispersions," *The Journal of Physical Chemistry B*, vol. 102, no. 30, pp. 5845-5851, 1998.

120. J. E. Pacheco, M. R. Prairie and L. Yellowhorse, "Photocatalytic Destruction of Chlorinated Solvents in Water With Solar Energy," *Journal of Solar Energy Engineering*, vol. 115, no. 3, pp. 123-129, 1993.

121. Mark S. Mehos and Craig S. Turchi, "Field testing solar photocatalytic detoxification on TCE-contaminated groundwater," *Environmental Progress*, vol. 12, no. 3, pp. 194-199, 1993.

122. S. Malato, J. Blanco, C. Richter, D. Curcó and J. Gimenez, "Low-concentrating CPC collectors for photocatalytic water detoxification: Comparison with a medium concentrating solar collector," *Water Science and Technology*, vol. 35, no. 4, pp. 157-164, 1997.

123. Pilar Fernandez-Ibañez, Sixto Malato and Octav Enea, "Photoelectrochemical reactors for the solar decontamination of water," *Catalysis Today*, vol. 54, no. 2, pp. 329-339, 1999.

124. Yoonchang Kim, Satoshi Sasaki, Kazuyoshi Yano, Kazunori Ikebukuro, Kazuhito Hashimoto and Isao Karube, "Photocatalytic sensor for the determination of chemical oxygen demand using flow injection analysis," *Analytica Chimica Acta*, vol. 432, no. 1, pp. 59-66, 2001.

125. Yoonchang Kim, Kyonghoon Lee, Satoshi Sasaki, Kazuhito Hashimoto, Kazunori Ikebukuro and Isao Karube, "Photocatalytic Sensor for Chemical Oxygen Demand Determination Based on Oxygen Electrode," *Analytical Chemistry*, vol. 72, no. 14, pp. 3379-3382, 2000.

126. Junshui Chen, Jidong Zhang, Yuezhong Xian, Xiangyang Ying, Meichuan Liu and Litong Jin, "Preparation and application of TiO2 photocatalytic sensor for chemical oxygen demand determination in water research," *Water Research*, vol. 39, no. 7, pp. 1340-1346, 2005.

127. Kyonghoon Lee, Tomoko Ishikawa, Scott McNiven, Yoko Nomura, Satoshi Sasaki, Yoshiko Arikawa and Isao Karube, "Chemical oxygen demand sensor employing a thin layer electrochemical cell," *Analytica Chimica Acta*, vol. 386, no. 3, pp. 211-220, 1999.

128. Huijun Zhao, Dianlu Jiang, Shanqing Zhang, Kylie Catterall and Richard John, "Development of a Direct Photoelectrochemical Method for Determination of Chemical Oxygen Demand," *Analytical Chemistry*, vol. 76, no. 1, pp. 155-160, 2003.

129. Shanqing Zhang, Huijun Zhao, Dianlu Jiang and Richard John, "Photoelectrochemical determination of chemical oxygen demand based on an exhaustive degradation model in a thin-layer cell," *Analytica Chimica Acta*, vol. 514, no. 1, pp. 89-97, 2004.

130. T. Yano, D. A. Tryk, K. Hashimoto and A. Fujishima, "Electrochemical Behavior of Highly Conductive Boron‐Doped Diamond Electrodes for Oxygen Reduction in Alkaline

Solution," *Journal of The Electrochemical Society*, vol. 145, no. 6, pp. 1870-1876, 1998.

131. P. Cañizares, J. Lobato, R. Paz, M. A. Rodrigo and C. Sáez, "Electrochemical oxidation of phenolic wastes with boron-doped diamond anodes," *Water Research*, vol. 39, no. 12, pp. 2687-2703, 2005.

132. Bensalah, Gadri, Pablo Cañizares, Cristina Sáez, Justo Lobato and Manuel A. Rodrigo, "Electrochemical Oxidation of Hydroquinone, Resorcinol, and Catechol on Boron-Doped Diamond Anodes," *Environmental Science & Technology*, vol. 39, no. 18, pp. 7234-7239, 2005.

133. Tsuyoshi Ochiai, Hirofumi Moriyama, Kazuya Nakata, Taketoshi Murakami, Yoshihiro Koide and Akira Fujishima, "Electrochemical and Photocatalytic Decomposition of Perfluorooctanoic Acid with a Hybrid Reactor Using a Boron-doped Diamond Electrode and TiO2 Photocatalyst," *Chemistry Letters*, vol. 40, no. 7, pp. 682-683, 2011.

134. Tsuyoshi Ochiai, Kazuya Nakata, Taketoshi Murakami, Akira Fujishima, Yanyan Yao, Donald A. Tryk and Yoshinobu Kubota, "Development of solar-driven electrochemical and photocatalytic water treatment system using a boron-doped diamond electrode and TiO2 photocatalyst," *Water Research*, vol. 44, no. 3, pp. 904-910, 2010.

135. Yanhe Han, Jingxia Qiu, Yuqing Miao, Jisheng Han, Shanqing Zhang, Haimin Zhang and Huijun Zhao, "Robust TiO_2/BDD heterojunction photoanodes for determination of chemical oxygen demand in wastewaters," *Analytical Methods*, vol. 3, no. 9, pp. 2003-2009, 2011.

136. Jvjun Yuan, Hongdong Li, Shiyong Gao, Yanhong Lin and Haiyan Li, "A facile route to n-type TiO2-nanotube/p-type boron-doped-diamond heterojunction for highly efficient photocatalysts," *Chemical Communications*, vol. 46, no. 18, pp. 3119-3121, 2010.

137. Shanqing Zhang, Dianlu Jiang and Huijun Zhao, "Development of Chemical Oxygen Demand On-Line Monitoring System Based on a Photoelectrochemical Degradation Principle," *Environmental Science & Technology*, vol. 40, no. 7, pp. 2363-2368, 2006.

138. Hongchong Chen, Jialing Zhang, Quanpeng Chen, Jinhua Li, Di Li, Chaoping Dong, Yanbiao Liu, Baoxue Zhou, Shuchuan Shang and Weimin Cai, "Assessment of a COD analytical method based on the photoelectrocatalysis of a TiO_2 nanotube array sensor,"

Analytical Methods, vol. 4, no. 6, pp. 1790-1796, 2012.

139. Jialing Zhang, Baoxue Zhou, Qing Zheng, Jinhua Li, Jing Bai, Yanbiao Liu and Weimin Cai, "Photoelectrocatalytic COD determination method using highly ordered TiO_2 nanotube array," *Water Research*, vol. 43, no. 7, pp. 1986-1992, 2009.

140. Q. Zheng, B. Zhou, J. Bai, L. Li, Z. Jin, J. Zhang, J. Li, Y. Liu, W. Cai and X. Zhu, "Self-Organized TiO_2 Nanotube Array Sensor for the Determination of Chemical Oxygen Demand," *Advanced Materials*, vol. 20, no. 5, pp. 1044-1049, 2008.

141. Juan Zhao and Xudong Yang, "Photocatalytic oxidation for indoor air purification: a literature review," *Building and Environment*, vol. 38, no. 5, pp. 645-654, 2003.

142. C. H. Ao, S. C. Lee, C. L. Mak and L. Y. Chan, "Photodegradation of volatile organic compounds (VOCs) and NO for indoor air purification using TiO_2: promotion versus inhibition effect of NO," *Applied Catalysis B: Environmental*, vol. 42, no. 2, pp. 119-129, 2003.

143. David F. Ollis, "Photocatalytic purification and remediation of contaminated air and water," *Comptes Rendus de l'Académie des Sciences - Series IIC - Chemistry*, vol. 3, no. 6, pp. 405-411, 2000.

144. Motoyuki Suzuki, "Activated carbon fiber: Fundamentals and applications," *Carbon*, vol. 32, no. 4, pp. 577-586, 1994.

145. Amos Turk, Khizar Mahmood and Jahangir Mozaffari, "Activated carbon for air purification in New York City's sewage treatment plants," *Water Science & Technology*, vol. 27, no. 7-8, pp. 121-126, 1993.

146. Md Moazzem Hossain, Gregory B. Raupp, Steven O. Hay and Timothy N. Obee, "Three-dimensional developing flow model for photocatalytic monolith reactors," *AIChE Journal*, vol. 45, no. 6, pp. 1309-1321, 1999.

147. Lynette A. Dibble and Gregory B. Raupp, "Fluidized-bed photocatalytic oxidation of trichloroethylene in contaminated air streams," *Environmental Science & Technology*, vol. 26, no. 3, pp. 492-495, 1992.

148. S. A. Larson, J. A. Widegren and J. L. Falconer, "Transient Studies of 2-Propanol

Photocatalytic Oxidation on Titania," *Journal of Catalysis*, vol. 157, no. 2, pp. 611-625, 1995.

149. Satoshi Kaneco, Hideyuki Katsumata, Tohru Suzuki and Kiyohisa Ohta, "Photoelectrocatalytic reduction of CO_2 in LiOH/methanol at metal-modified p-InP electrodes," *Applied Catalysis B: Environmental*, vol. 64, no. 1–2, pp. 139-145, 2006.

150. Yuan Liu, Changsheng Xie, Huayao Li, Hao Chen, Yichuan Liao and Dawen Zeng, "Low bias photoelectrocatalytic (PEC) performance for organic vapour degradation using TiO_2/WO_3 nanocomposite," *Applied Catalysis B: Environmental*, vol. 102, no. 1–2, pp. 157-162, 2011.

151. Shengying Ye, Qingmei Tian, Xianliang Song and Shucan Luo, "Photoelectrocatalytic degradation of ethylene by a combination of TiO_2 and activated carbon felts," *Journal of Photochemistry and Photobiology A: Chemistry*, vol. 208, no. 1, pp. 27-35, 2009.

152. Jing Shang, Shaodong Xie, Tong Zhu and Jia Li, "Solid-State, Planar Photoelectrocatalytic Devices Using a Nanosized TiO_2 Layer," *Environmental Science & Technology*, vol. 41, no. 22, pp. 7876-7880, 2007.

153. Yuan Liu, Changsheng Xie, Huayao Li, Hao Chen, Tao Zou and Dawen Zeng, "Improvement of gaseous pollutant photocatalysis with WO_3/TiO_2 heterojunctional-electrical layered system," *Journal of Hazardous Materials*, vol. 196, no. 0, pp. 52-58, 2011.

154. Yichuan Liao, Huayao Li, Yuan Liu, Zhijun Zou, Dawen Zeng and Changsheng Xie, "Characterization of Photoelectric Properties and Composition Effect of $TiO_2/ZnO/Fe_2O_3$ Composite by Combinatorial Methodology," *Journal of Combinatorial Chemistry*, vol. 12, no. 6, pp. 883-889, 2010.

155. Zhijun Zou, Yuan Liu, Huayao Li, Yichuan Liao and Changsheng Xie, "Synthesis of $TiO_2/WO_3/MnO_2$ Composites and High-Throughput Screening for Their Photoelectrical Properties," *Journal of Combinatorial Chemistry*, vol. 12, no. 3, pp. 363-369, 2010.

156. Y. Muraoka, N. Takubo and Z. Hiroi, "Photoinduced conductivity in tin dioxide thin films," *Journal of Applied Physics*, vol. 105, no. 103702, pp. 1-7, 2009.

157. Weiming Hou and Young Ku, "Photoelectrocatalytic decomposition of gaseous isopropanol in a polymer electrolyte photoreactor," *Journal of Solid State Electrochemistry*,

vol. 17, no. 3, pp. 737-741, 2013.

158. Weiming Hou and Young Ku, "Enhanced Photocatalytic Decomposition of Gaseous Isopropyl Alcohol in a Polymer Electrolyte Cell," *Aerosol and Air Quality Research*, vol. 13, no. 5, pp. 1570-1581, 2013.

159. Bruce E. Logan, Bert Hamelers, René Rozendal, Uwe Schröder, Jürg Keller, Stefano Freguia, Peter Aelterman, Willy Verstraete and Korneel Rabaey, "Microbial Fuel Cells: Methodology and Technology," *Environmental Science & Technology*, vol. 40, no. 17, pp. 5181-5192, 2006.

160. Xin Wang, Shaoan Cheng, Yujie Feng, Matthew D. Merrill, Tomonori Saito and Bruce E. Logan, "Use of Carbon Mesh Anodes and the Effect of Different Pretreatment Methods on Power Production in Microbial Fuel Cells," *Environmental Science & Technology*, vol. 43, no. 17, pp. 6870-6874, 2009.

161. Fang Qian, Gongming Wang and Yat Li, "Solar-Driven Microbial Photoelectrochemical Cells with a Nanowire Photocathode," *Nano Letters*, vol. 10, no. 11, pp. 4686-4691, 2010.

162. Shijie Yuan, Guoping Sheng, Wenwei Li, Zhiqi Lin, Raymond J. Zeng, Zhonghua Tong and Hanqing Yu, "Degradation of Organic Pollutants in a Photoelectrocatalytic System Enhanced by a Microbial Fuel Cell," *Environmental Science & Technology*, vol. 44, no. 14, pp. 5575-5580, 2010.

163. Yanbiao Liu, Jinhua Li, Baoxue Zhou, Shubin Lv, Xuejin Li, Hongchong Chen, Quanpeng Chen and Weimin Cai, "Photoelectrocatalytic degradation of refractory organic compounds enhanced by a photocatalytic fuel cell," *Applied Catalysis B: Environmental*, vol. 111–112, no. 0, pp. 485-491, 2012.

164. Donald Macphee, Richard Wells, Angela Kruth, Malcolm Todd, Taha Elmorsi, Cairns Smith, Dubravka Pokrajac, Norval Strachan, Mwiny Mwinyhija, Efe Scott-Emuakpor, Silke Nissen and Ken Killham, "A visible light driven photoelectrocatalytic fuel cell for clean-up of contaminated water supplies," *Desalination*, vol. 248, no. 1–3, pp. 132-137, 2009.

165. Claudio Ampelli, Gabriele Centi, Rosalba Passalacqua and Siglinda Perathoner,

"Synthesis of solar fuels by a novel photoelectrocatalytic approach," *Energy & Environmental Science*, vol. 3, no. 3, pp. 292-301, 2010.

166. Yanbiao Liu, Jinhua Li, Baoxue Zhou, Xuejin Li, Hongchong Chen, Quanpeng Chen, Zhongsheng Wang, Lei Li, Jiulin Wang and Weimin Cai, "Efficient electricity production and simultaneously wastewater treatment via a high-performance photocatalytic fuel cell," *Water Research*, vol. 45, no. 13, pp. 3991-3998, 2011.

167. Yanbiao Liu, Jinhua Li, Baoxue Zhou, Hongchong Chen, Zhongsheng Wang and Weimin Cai, "A TiO_2-nanotube-array-based photocatalytic fuel cell using refractory organic compounds as substrates for electricity generation," *Chemical Communications*, vol. 47, no. 37, pp. 10314-10316, 2011.

168. Mohammad Ebrahim Olya and Azam Pirkarami, "Cost-effective photoelectrocatalytic treatment of dyes in a batch reactor equipped with solar cells," *Separation and Purification Technology*, vol. 118, no. 0, pp. 557-566, 2013.

169. Mohammad Ebrahim Olya, Azam Pirkarami, Majid Soleimani and Manochehr Bahmaei, "Photoelectrocatalytic degradation of acid dye using Ni–TiO_2 with the energy supplied by solar cell: Mechanism and economical studies," *Journal of Environmental Management*, vol. 121, no. 0, pp. 210-219, 2013.

170. M. Kobya and S. Delipinar, "Treatment of the baker's yeast wastewater by electrocoagulation," *Journal of Hazardous Materials*, vol. 154, no. 1–3, pp. 1133-1140, 2008.

171. Songmei Sun, Wenzhong Wang, Dong Jiang, Ling Zhang and Jing Zhou, "Infrared light induced photoelectrocatalytic application via graphene oxide coated thermoelectric device," *Applied Catalysis B: Environmental*, vol. 158–159, no. 0, pp. 136-139, 2014.

172. James H. Clark, "Green chemistry: challenges and opportunities," *Green Chemistry*, vol. 1, no. 1, pp. 1-8, 1999.

173. IM Butterfield, PA Christensen, TP Curtis and J Gunlazuardi, "Water disinfection using an immobilised titanium dioxide film in a photochemical reactor with electric field enhancement," *Water Research*, vol. 31, no. 3, pp. 675-677, 1997.

174. Zheng Xie, Yongbin Zhang, Xiangxuan Liu, Weipeng Wang, Peng Zhan, Zhengcao Li

and Zhengjun Zhang, "Visible Light Photoelectrochemical Properties of N-Doped TiO_2 Nanorod Arrays from TiN," *Journal of Nanomaterials*, vol. 2013, pp. 9, 2013.

175. Qing Wang, Jing Shang, Han Song, Tong Zhu, Junhui Ye, Fengwei Zhao, Jing Li and Songjie He, "Visible-light photoelectrocatalytic degradation of rhodamine B over planar devices using a multi-walled carbon Nanotube-TiO_2 composite," *Materials Science in Semiconductor Processing*, vol. 16, no. 2, pp. 480-484, 2013.

176. Liaochuan Jiang and Weide Zhang, "Charge transfer properties and photoelectrocatalytic activity of TiO_2/MWCNT hybrid," *Electrochimica Acta*, vol. 56, no. 1, pp. 406-411, 2010.

177. Juan Wang and Weide Zhang, "Modification of TiO_2 nanorod arrays by graphite-like C_3N_4 with high visible light photoelectrochemical activity," *Electrochimica Acta*, vol. 71, no. 0, pp. 10-16, 2012.

178. Peng Du, Joana T. Carneiro, Jacob A. Moulijn and Guido Mul, "A novel photocatalytic monolith reactor for multiphase heterogeneous photocatalysis," *Applied Catalysis A: General*, vol. 334, no. 1–2, pp. 119-128, 2008.

179. Gustavo E. Imoberdorf, Alberto E. Cassano, Horacio A. Irazoqui and Orlando M. Alfano, "Optimal design and modeling of annular photocatalytic wall reactors," *Catalysis Today*, vol. 129, no. 1–2, pp. 118-126, 2007.

180. Choching Lo, Chunghsuang Hung, Chungshin Yuan and Jenfong Wu, "Photoreduction of carbon dioxide with H_2 and H_2O over TiO_2 and ZrO_2 in a circulated photocatalytic reactor," *Solar Energy Materials and Solar Cells*, vol. 91, no. 19, pp. 1765-1774, 2007.

181. Horst Kisch, "Semiconductor Photocatalysis for Organic Synthesis," in *Advances in Photochemistry*, Ed., pp. 93-143, John Wiley & Sons, Inc., 2007.

182. Giovanni Palmisano, Vincenzo Augugliaro, Mario Pagliaro and Leonardo Palmisano, "Photocatalysis: a promising route for 21st century organic chemistry," *Chemical Communications*, no. 33, pp. 3425-3437, 2007.

Appendix J Acetic Acid Assisted to Prepare Bi_2MoO_6 with Visible-light-induced Activity

Xiangchao Meng and Zisheng Zhang

General Chemistry 3 (2017), 159-163

Abstract

Photocatalysis has been extensively studied and developed. To overcome the visible-light irresponsive hindrance, developing novel materials has become a significant promise. Bismuth-based semiconductors were promising candidates with suitable band gaps, and various bismuth-based semiconductors can be prepared via facile methods. Herein, we report a modified hydrothermal method assisted by adding acetic acid in the precursor to prepare Bi_2MoO_6 with enhanced photocatalytic activity in the degradation of RhB under visible light irradiation. This work provides a new approach to improve photocatalytic activity via adding chemicals in the precursors during the preparation.

J.1 Introduction

Photocatalysis, as one of the advanced oxidation processes, has been extensively studied since 1972 [1]. This technology has been applied in various areas, mainly including hydrogen evolution via water splitting and organic pollutants degradation [2-9]. As a pioneer photocatalysis material, TiO_2 exhibited various superiorities [10]. However, its drawbacks are also apparent, especially the visible light-irresponsiveness. Approaches to overcome these hindrances primarily include modification of TiO_2 and development of novel visible light-responsive photocatalysts.

Among these visible light-responsive photocatalysts, bismuth based semiconductor exhibits priorities [11-26]. Bi-based materials with suitable band gaps, can be prepared via

facile method, and their morphologies can be adjusted by changing the preparation conditions. Furthermore, the valence band (VB) of a bismuth-based semiconductor consists of not only O 2p orbitals (generally the only orbital in a VB for metal oxides), but also Bi 6s orbitals. The hybrid orbitals of O 2p and Bi 6s are reported to be beneficial by increasing the mobility of photogenerated carriers [27]. As one of the Bi-based semiconductors, Bi_2MoO_6 has increasingly drawn the attentions of researchers, owing to its excellent intrinsic properties such as its dielectric nature, its catalytic behavior, and its luminescence [28]. The band gap of Bi_2MoO_6 was reported in the range of 2.5 - 2.8 eV [29, 30], indicating that Bi_2MoO_6 is capable of visible light-driven photocatalytic activity.

Generally, Bi_2MoO_6 was prepared by hydrothermal and solvothermal methods. In this work, we report a new method to prepare Bi_2MoO_6 via a hydrothermal method assisted with acetic acid. It exhibited excellent photocatalytic activity in decomposition of RhB. And preparation conditions including hydrothermal temperature and treatment duration were optimized.

J.2 Experimental

J.2.1 Preparation of Bi_2MoO_6

Bi_2MoO_6 was prepared via an acetic acid assisted hydrothermal method. Typically, 1 mmol of $Bi(NO_3)_3 \cdot 5H_2O$ were dissolved in 5 mL acetic acid, and 0.5 mmol of $Na_2MoO_4 \cdot 2H_2O$ were dissolved in 30 mL deionized distilled water (DDW). Then, $Na_2MoO_4 \cdot 2H_2O$ solution was dropwise added into the $Bi(NO_3)_3 \cdot 5H_2O$ solution. After stirring for 30 min, the mixture was transferred into a 50 mL autoclave, heated and maintained for designate time. After the autoclave was naturally cooled down to room temperature, the precipitates were filtered out and washed with DDW and ethanol. The precipitates were dried at 60°C overnight before being collected for further use. The hydrothermal temperatures of 60, 90, 12, 150, 180 and 210°C and durations of 6, 12, 18, 24, 36, 48 h were selected to optimize the preparation condition. For comparison, Bi_2MoO_6 was also prepared without adding acetic acid.

J.2.2 Characterizations

A scanning electron microscopy (FE-SEM, JEOL JSM-7500F) was used to investigate the morphology of prepared samples. Crystal structures were studied by X-ray diffraction (XRD) on a Rigaku Ultima IV Diffractometer with Cu Kα radiation (λ = 0.15418 nm) at 40 kV and 44 mA. XRD patterns were recorded at 2θ of 5 - 80°. The Fourier Transform Infrared Spectrometer (FTIR) was used via a Cary 630 (Agilent Technologies). Ultraviolet-visible diffuse reflectance spectra (DRS) was observed with a Thermo Evolution 300 spectrophotometer.

J.2.3 Photocatalytic activity testing

Photocatalytic activity of prepared samples was tested through degradation of RhB under visible light irradiation. Specifically, a 500-mL beaker served as the reactor, and the temperature was maintained at 20°C using a water bath. The visible light irradiation was a 300-W halogen tungsten projector lamp Ushio, wavelength mainly in the range of 310 – 800 nm) with a UV cut-off (Kenko Zeta, transmittance > 90%) to filter out irradiation with a wavelength below 410 nm. The irradiation intensity on the surface of the solution was measured using a quantum meter (Biospherical QSL-2100, 400 nm < λ < 700 nm) being equal to 1.1×10^{-2} Einsteins m^{-2} s^{-1}. In each test, 100 mL of 10 mg/L RhB solution was added to the reactor. The quantity of catalyst that was subsequently added was 1 g/L of reactor solution (0.10 g in 100 mL of solution). The suspensions were magnetically stirred for 30 min before turning on the lamp, in order to obtain an adsorption-desorption equilibrium between RhB and the catalyst. The photocatalytic test was carried out for 60 min, and aliquots were drawn every 10 min, each of which were centrifuged at a rate of 13,000 rpm for 5 min. The supernatant was then separated and analyzed using a spectrometer at the wavelength of 554 nm. Photocatalytic degradation of phenol with initial concentration of 10 mg/L was also measured. The concentration of phenol was analyzed using a high-performance liquid chromatograph (HPLC, Agilent 1100 series) equipped with a UV-Vis detector. A ZORBAX Eclipse Plus C18 column (4.6 × 250 mm) was used at a temperature of 60°C. The detecting wavelength was fixed at 270 nm for the detection of phenol and possible intermediates. The flow phase was composed of methanol (55%,

V/V) and water (45%, V/V) at a flow rate of 0.6 mL/min. The injection volume was set to 25 μL.

J.2.4 Electronic structure calculation

The quantum-mechanical calculations were performed on the basis of the density functional theory (DFT) [31]. The generalized gradient approximation (GGA) was applied to exchange-correlation effects. The open access software Quantum ESPRESSO was used, which utilizes pseudopotentials to describe electron-ion interactions and to represent electronic wave functions using a plane-wave basis set [32]. The kinetic energy cut-off was set to 300 eV.

J.3 Results and Discussion

J.3.1 Morphology

Morphologies of prepared Bi_2MoO_6 were investigated using SEM as shown in Figure J.1. It can be observed plate-like morphology was prepared. And with increase of the hydrothermal treatment duration, the size of plate became slightly larger and thicker. It should be noted the thicker the plate is, the longer lifetime required for the separated charge carriers. It means the plate with thicker size may be with lower photocatalytic activity.

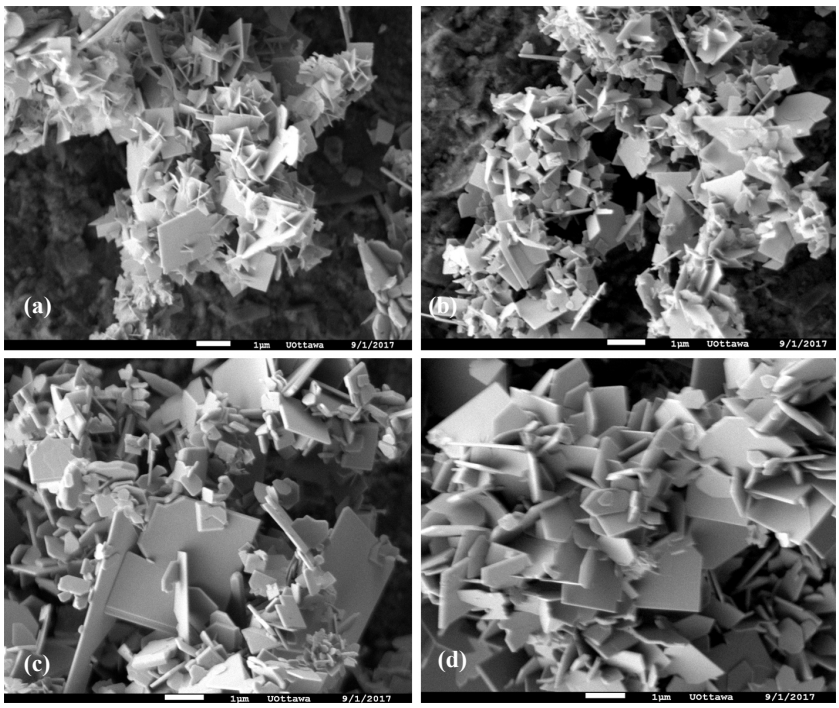


Figure J.1 SEM images of Bi_2MoO_6 prepared at 120°C for (a) 6h, (b) 12h, (c) 24h and (d) 48h.

J.3.2 XRD analysis

Crystal structures of Bi_2MoO_6 samples prepared at different temperature for 24h and at 120°C for different duration time, were investigated by XRD. As shown in Figure J.2, only when hydrothermal temperature increased above or equal to 120°C, Bi_2MoO_6 with orthorhombic crystal structure (space group: pbca (61), PDF card number 72-1524 [33]) can be observed. Meanwhile, with hydrothermal temperature improvement, impurity peaks were increasingly diminished. Relative intensity of characteristic peaks is also orderly changed, especially peaks at $2\theta = 33.1°$ and 47.2° which are in correspondence with plane (060) and (062), respectively. Specifically, the increase of relative intensity of these peaks with increase of hydrothermal temperature from 120°C to 210°C, indicated that the crystal tends to grow in the directions of corresponding planes, mainly including plane (060) and (062) (Figure J.4). It is beneficial to form thin nano-plates. As for the effect of hydrothermal duration on the crystal structures of Bi_2MoO_6, XRD patterns of samples prepared at 120°C for different time ranging from 6h to 48h were performed and shown in Figure J.3. Compared to precipitation directly separated out before hydrothermal treatment, Bi_2MoO_6 samples exhibit high crystallinity with sharp and narrow characteristic peaks. It should be

noticed that with extension of hydrothermal time, impurity peaks were gradually diminished and completely disappeared for samples hydrothermally treated longer than 18h. Specifically, improvement of hydrothermal treatment duration is also in favor of orientated growth of the crystal, and forming nano-plates.

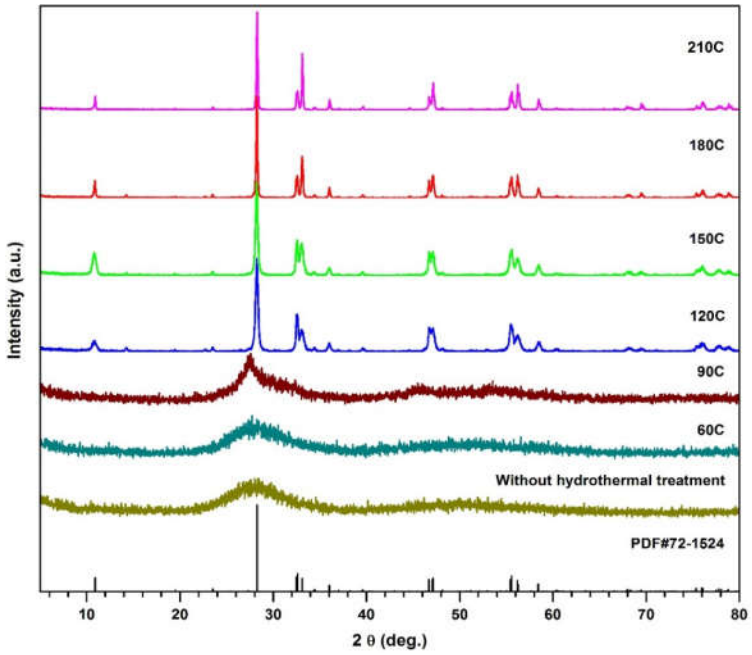


Figure J.2 XRD patterns of Bi_2MoO_6 synthesized under different hydrothermal temperature for 24 hours.

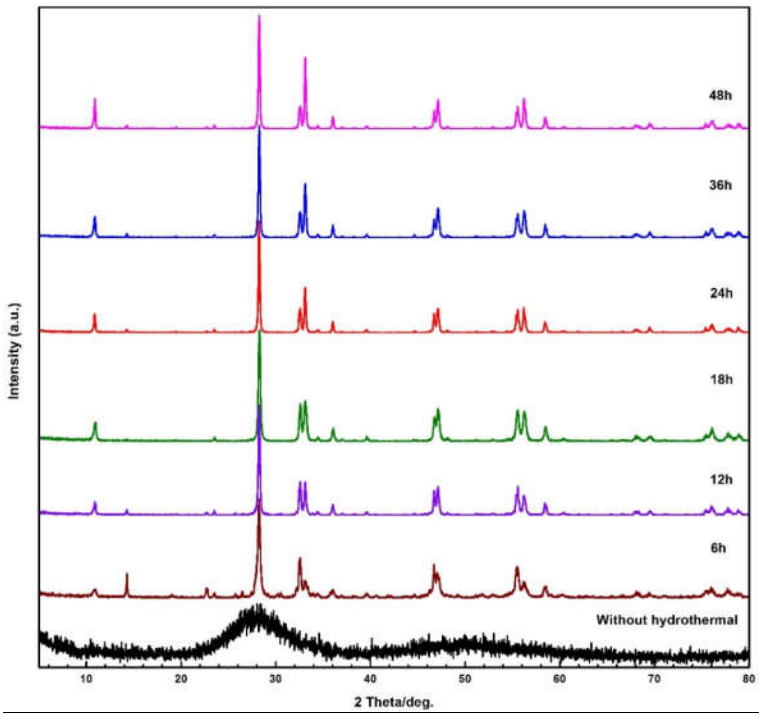


Figure J.3 XRD patterns of Bi_2MoO_6 synthesized at 120 °C for different duration.

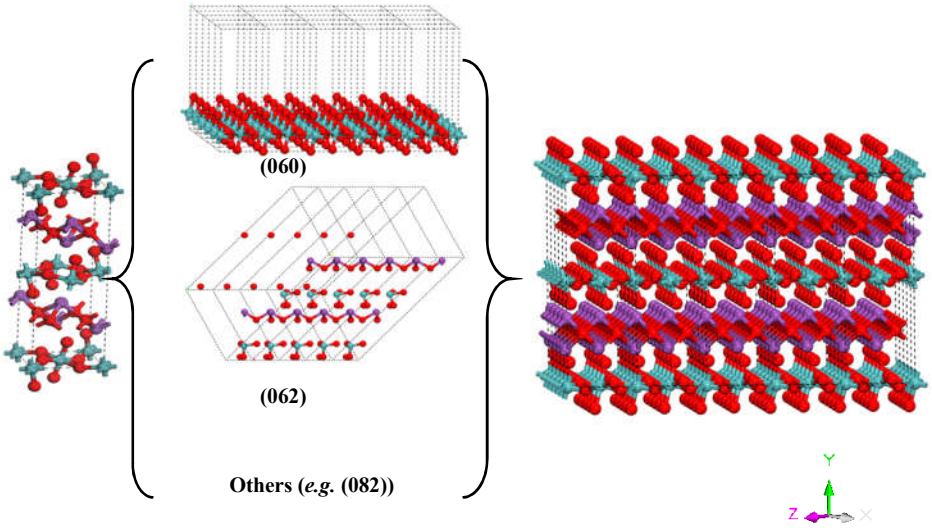
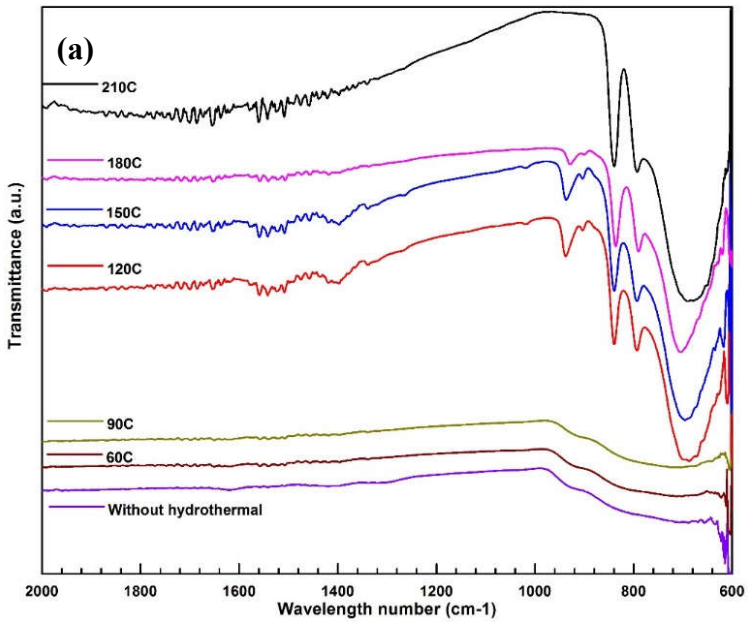


Figure J.4 Proposed crystal growth in the directions of plane (060) and (062).

J.3.3 FT-IR

Figure J.5 shows FT-IR spectra of Bi_2MoO_6 samples prepared by hydrothermal method with different experimental conditions. The regions of wavelength number ranging from 600 cm^{-1} to 1000 cm^{-1}, are possibly attributed to Bi-O, Mo-O stretching and Mo-O-Mo bridging stretching modes, which can respond to the variation of crystal structure of

Bi_2MoO_6 [29, 34]. Specifically, the band at 690 cm^{-1} resulted from the asymmetric stretching mode of MoO_6 involving vibrations of the equatorial oxygen atoms [35]. The absorption peak at around 795 cm^{-1} and 841 cm^{-1} can be attributed to the asymmetric and symmetric stretching mode of MoO_6 involving vibrations of the apical oxygen atoms, separately. The absorption bands at 937 cm^{-1} together with a small peak at 902 cm^{-1} may be due to Mo-O stretching modes. Small peaks at the wavelength number range of 1300-1600 cm^{-1} may result from the adsorbed CH_3COOH, specifically, the δCH vibrations of the $CH_3C{=}O$ moiety and coupled νC-O and δOH vibrations [36, 37]. In Figure J.5a and J.5b, a minor peak shift of wavelength number at 690 cm^{-1} is observed, indicating the structure variation for MoO_6 octahedra occurred with increase of temperature and duration time. Furthermore, when the hydrothermal temperature improved to 210°C, peaks at 937 cm^{-1} and 902 cm^{-1} disappeared; further confirming the changes of Bi_2MoO_6 crystal structure. Based on above analysis, it can be concluded that crystal structure of Bi_2MoO_6 samples may be influenced by changing hydrothermal temperature and duration time.



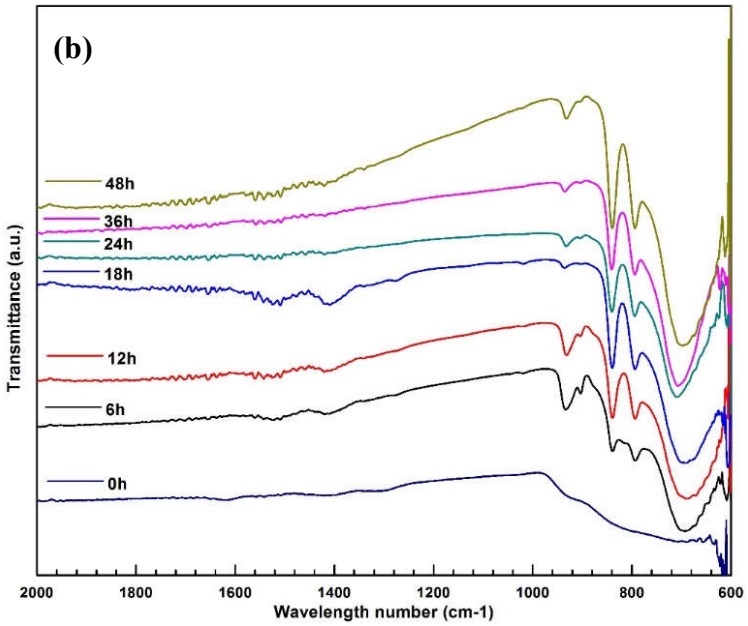


Figure J. 5 FT-IR spectra of Bi_2MoO_6 samples prepared (a) at different temperature for 24h and (b) at 120°C for different hydrothermal duration time.

J.3.4 Optical properties

The electrical band structure of the relaxed Bi_2MoO_6 is illustrated in Figure J.6. The energy zero was set at the top of valence band. The bandgap width (E_g) can be calculated as around 1.910 eV. Moreover, the valence-band and conduction-band width (W_{vb} and W_{cb}) are 6.65 eV and 2.20 eV, respectively. The band edges are situated at the X point for Bi_2MoO_6, indicating the direct bandgap feature. The total and partial density of states (TDOS and PDOS) of Bi_2MoO_6 is given in Figure J.7, with setting energy zero at top of valence band. O 2p and Bi 6s states contribute to the valence band. Meanwhile, Bi 6p, Mo 4d and O 2p state account for the conduction band. As reported, the well-dispersed Bi 6s orbital facilitates the mobility of photo-generated carriers and narrow the bandgap [13, 27].

Diffused reflectance spectrometer (DRS) is performed to detect the optical properties of Bi_2MoO_6 samples which were prepared at 120°C for 24 h (Figure J.8). The photoabsorption occur in the region of UV light and visible –light with wavelength lower than about 490 nm. The steep decrease in the spectrum attributes to the bandgap transition. The UV-Vis photoabsorption property was also simulated and shown in Figure J.8. It suggests that much more visible light could be used to activate the photocatalysis. As for the experimental bandgap value, it can be calculated using classical Tauc equation (Equation 1)

$$\alpha E_{photon} = K\left(E_{photon} - E_g\right)^{\frac{n}{2}} \qquad \textbf{Equation 1}$$

Where α, h, v and K are the absorption coefficient, the Planck constant, the irradiation frequency, and the constant for semiconductors (usually equal to 1), respectively. Constant n depends on the bandgap feature; it is suggested in the electrical structure that Bi_2MoO_6 attributes to direct-transition band gap, so n = 4. Inset in Figure J.8 is plot of $(\alpha E_{photon})^{1/2}$ vs E_{photon}. The intercept at the horizontal axis of the tangent line is rightly the bandgap value, which is about 2.5 eV. The difference between the theoretical and experimental bandgap value is 0.59 eV, which is due to the well-known limitation of GGA. A similar result was also reported [38]. Although calculated bandgap value could underdetermine the real value, it is still reliable and reasonable to qualitatively analyze the characteristics of the band structure.

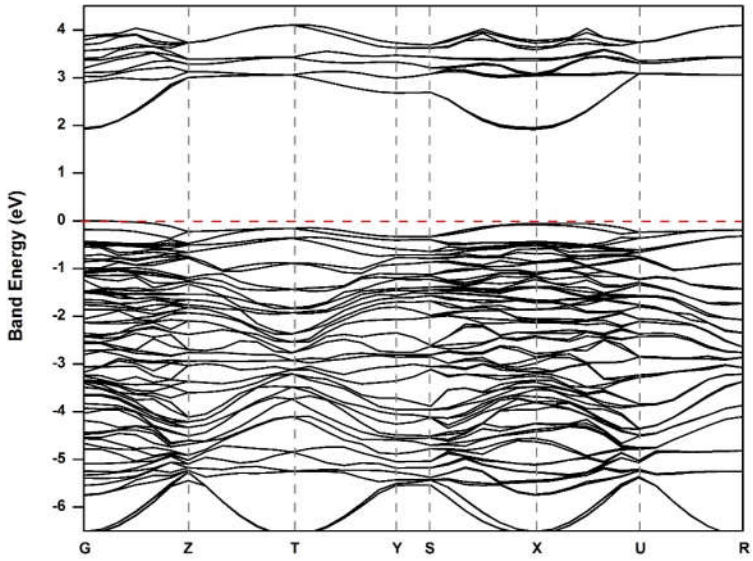


Figure J.6 Band structure of Bi_2MoO_6. (The red dash line represents the Fermi level)

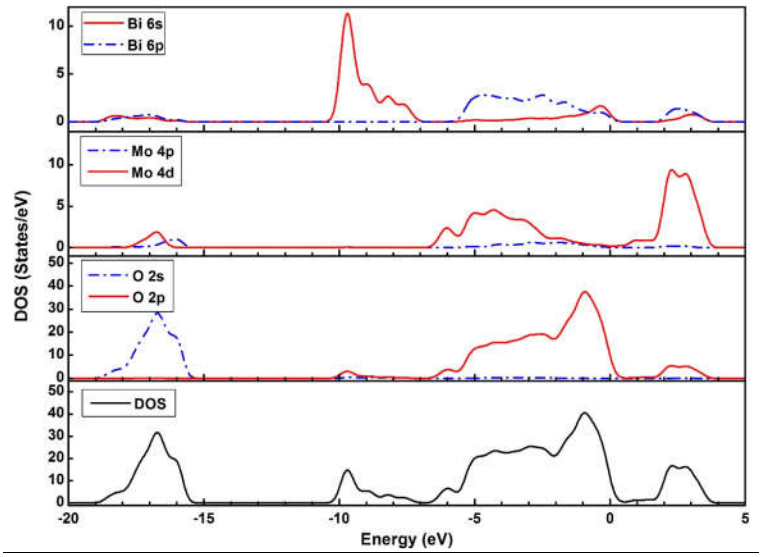


Figure J.7 Total and partial DOS of relaxed Bi_2MoO_6.

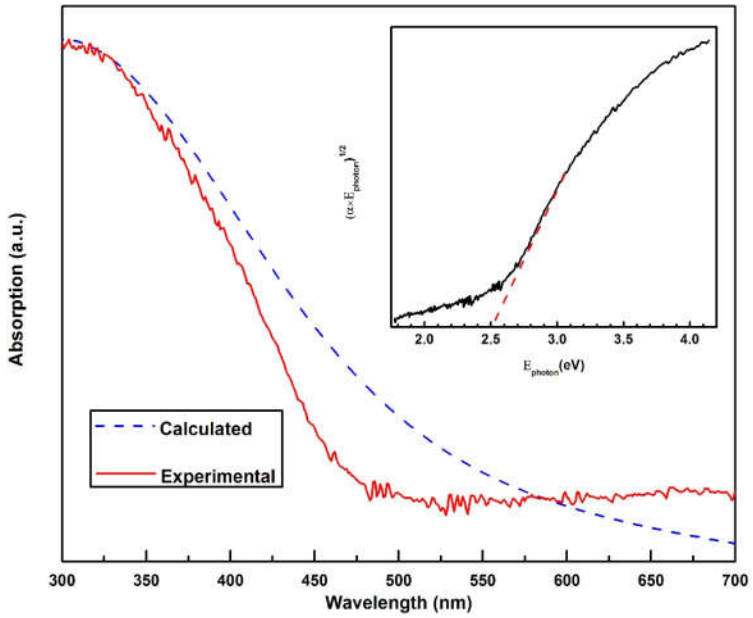


Figure J.8 DRS of as-prepared Bi_2MoO_6 (red line) with corresponding $(\alpha E_{photon})^{1/2}$ vs E_{photon} curves shown in inset, and simulated UV-Vis absorption properties of relaxed Bi_2MoO_6 (blue dash line).

J.3.5 Photocatalytic activity test

Photocatalytic activity of prepared Bi_2MoO_6 under different conditions was investigated through degradation of RhB under visible light irradiation. As shown in Figure J.9, Bi_2MoO_6 prepared at 60 and 90 °C, exhibited negligible activity in the degradation of RhB

over 60 min. With increase of the treatment temperature, the photocatalytic activity was greatly improved. And when the thermal treatment temperature at 120°C, RhB were completely removed over 60. And further increase the temperature, the activity in the removal of RhB was deteriorate. Similarly, the treatment duration was another significant factor as shown in Figure J.10. It is clear when the hydrothermal treatment lasted for 24 hours, the prepared sample exhibited the best activity in the removal of RhB under visible light irradiation. This phenomenon indicates the optimum hydrothermal treatment temperature and duration existed to prepare a Bi_2MoO_6 sample with excellent photocatalytic activity in the degradation of RhB under visible light irradiation.

To explore the effect of acetic acid, the photocatalytic activity of Bi_2MoO_6 samples prepared with and without acetic acid added in the precursor was measured and shown in Figure J.11. It can be found the photocatalytic activity of Bi_2MoO_6 assisted by acetic exhibited higher activity in the degradation of RhB. Compared to reported work, the photocatalytic activity of Bi_2MoO_6 prepared in this work is higher than that prepared by solvothermal method [28] and hydrothermal method [39]. It confirms acetic acid assisted preparation of Bi_2MoO_6 enhance its photocatalytic activity of degradation of RhB. To further explore the activity of as-prepared Bi_2MoO_6, photocatalytic degradation of a colorless organic, phenol was also measured, and results were illustrated in inset of Figure J.11. It can be found about 10% of phenol were removed over 5h under visible light irradiation. It further confirms the photocatalytic activity of as-prepared Bi_2MoO_6.

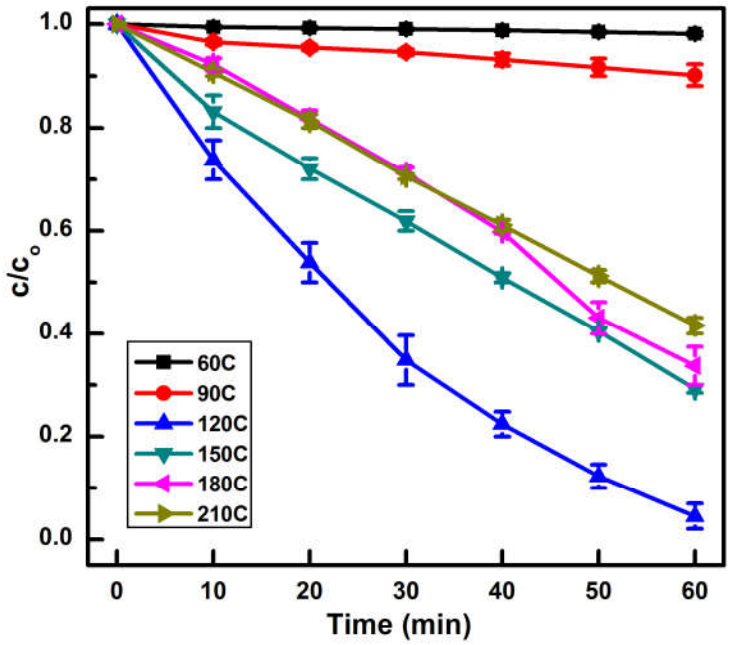


Figure J.9 Photocatalytic degradation RhB in the presences of Bi_2MoO_6 prepared at different temperature for 24 h under visible light irradiation.

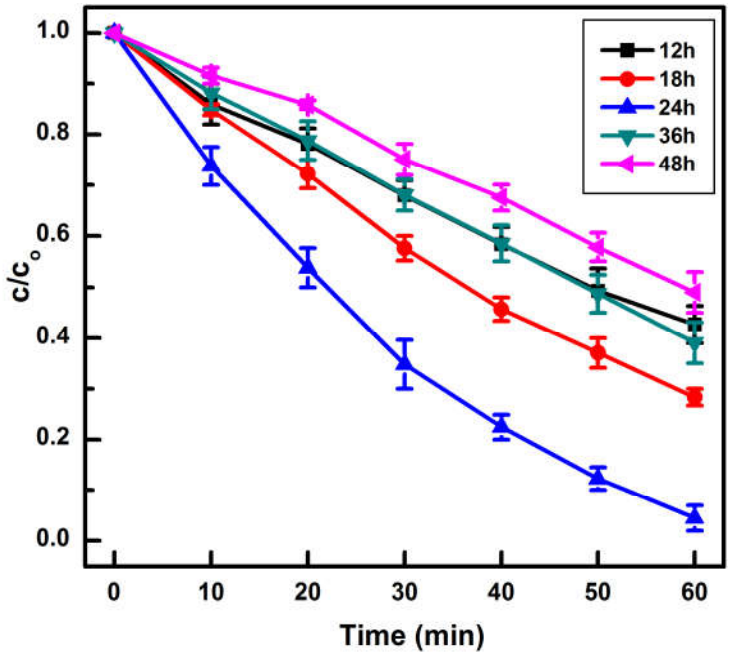


Figure J.10 Photocatalytic degradation RhB in the presences of Bi_2MoO_6 prepared at 120°C for different time under visible light irradiation.

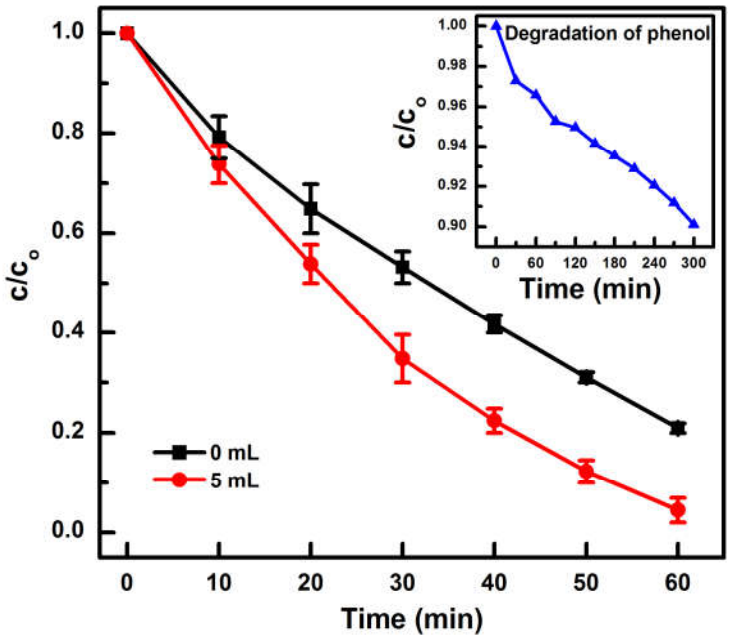


Figure J.11 Photocatalytic degradation of RhB in the presence of Bi_2MoO_6 samples prepared with and without acetic acid in the precursor (inset: photocatalytic degradation of phenol in the presence of Bi_2MoO_6 prepared assisted with acetic acid).

J.4 Conclusions

Bi_2MoO_6 were successfully prepared using a hydrothermal method assisted by acetic acid. The preparation conditions, including hydrothermal temperature and treatment duration were optimized. It was found when the temperature of 120°C and the duration of 24h, prepared Bi_2MoO_6 exhibited the highest activity in the degradation of RhB under visible light irradiation. This work provides a new approach to the improvement of photocatalytic activity via adding chemicals in the precursors during the preparation.

References

1. Akira Fujishima and Kenichi Honda, "Electrochemical photolysis of water at a semiconductor electrode," *nature*, vol. 238, pp. 37-38, 1972.

2. Marye Anne Fox and Maria T. Dulay, "Heterogeneous photocatalysis," *Chemical Reviews*, vol. 93, no. 1, pp. 341-357, 1993.

3. Michael R. Hoffmann, Scot T. Martin, Wonyong Choi and Detlef W. Bahnemann,

"Environmental Applications of Semiconductor Photocatalysis," *Chemical Reviews*, vol. 95, no. 1, pp. 69-96, 1995.

4. Masao Kaneko and Ichiro Okura, "Photocatalysis science and technology," *Kodansha Springer*, 2002.

5. I. M. Kobasa and G. P. Tarasenko, "Photocatalysis of Reduction of the Dye Methylene Blue by Bi2S3/CdS Nanocomposites," *Theoretical and Experimental Chemistry*, vol. 38, no. 4, pp. 255-258, 2002.

6. Didier Robert and Sixto Malato, "Solar photocatalysis: a clean process for water detoxification," *Science of The Total Environment*, vol. 291, no. 1–3, pp. 85-97, 2002.

7. Kan Zhang, Luyang Wang, Jung Kyu Kim, Ming Ma, Ganapathy Veerappan, Chang-Lyoul Lee, Ki-jeong Kong, Hyoyoung Lee and Jong Hyeok Park, "An order/disorder/water junction system for highly efficient co-catalyst-free photocatalytic hydrogen generation," *Energy & Environmental Science*, vol. 9, no. 2, pp. 499-503, 2016.

8. Kan Zhang, Nansra Heo, Xinjian Shi and Jong Hyeok Park, "Chemically Modified Graphene Oxide-Wrapped Quasi-Micro Ag Decorated Silver Trimolybdate Nanowires for Photocatalytic Applications," *The Journal of Physical Chemistry C*, vol. 117, no. 45, pp. 24023-24032, 2013.

9. Yongchao Huang, Bei Long, Minni Tang, Zebao Rui, Muhammad-Sadeeq Balogun, Yexiang Tong and Hongbing Ji, "Bifunctional catalytic material: An ultrastable and high-performance surface defect CeO2 nanosheets for formaldehyde thermal oxidation and photocatalytic oxidation," *Applied Catalysis B: Environmental*, vol. 181, pp. 779-787, 2016.

10. Akira Fujishima, Tata N. Rao and Donald A. Tryk, "Titanium dioxide photocatalysis," *Journal of Photochemistry and Photobiology C: Photochemistry Reviews*, vol. 1, no. 1, pp. 1-21, 2000.

11. Xiangchao Meng, Lingyun Jiang, Weiwen Wang and Zisheng Zhang, "Enhanced Photocatalytic Activity of BiOBr/ZnO Heterojunction Semiconductors Prepared by Facile Hydrothermal Method," *International Journal of Photoenergy*, vol. 2015, pp. 9, 2015.

12. Xiangchao Meng and Zisheng Zhang, "Synthesis, Analysis, and Testing of BiOBr-Bi_2WO_6 Photocatalytic Heterojunction Semiconductors," *International Journal of*

Photoenergy, vol. 2015, pp. 12, 2015.

13. Xiangchao Meng and Zisheng Zhang, "Facile synthesis of BiOBr/Bi_2WO_6 heterojunction semiconductors with high visible-light-driven photocatalytic activity," *Journal of Photochemistry and Photobiology A: Chemistry*, vol. 310, no. 0, pp. 33-44, 2015.

14. Ayla Ahmad, Xiangchao Meng, Nan Yun and Zisheng Zhang, "Preparation of Hierarchical BiOBr Microspheres for Visible Light-Induced Photocatalytic Detoxification and Disinfection," *Journal of Nanomaterials*, vol. 2016, pp. 10, 2016.

15. Xiaoyue Hu, Xiangchao Meng and Zisheng Zhang, "Synthesis and Characterization of Graphene Oxide-Modified Bi_2WO_6 and Its Use as Photocatalyst," *International Journal of Photoenergy*, vol. 2016, pp. 8, 2016.

16. Xiangchao Meng and Zisheng Zhang, "Ag/AgCl Loaded Bi_2WO_6 Composite: A Plasmonic Z-Scheme Visible Light-Responsive Photocatalyst," *International Journal of Photoenergy*, vol. 2016, pp. 11, 2016.

17. Xiangchao Meng and Zisheng Zhang, "Bismuth-based Photocatalytic Semiconductors: Introduction, Challenges and Possible Approaches," *Journal of Molecular Catalysis A: Chemical*, vol. 423, pp. 533-549, 2016.

18. Xiangchao Meng and Zisheng Zhang, "Pd-doped Bi_2MoO_6 Plasmonic Photocatalysts with Enhanced Visible Light Photocatalytic Performance," *Applied Surface Science*, vol. 392, pp. 169-180, 2016.

19. Xiangchao Meng and Zisheng Zhang, "Plasmonic ternary Ag–rGO–Bi_2MoO_6 composites with enhanced visible light-driven photocatalytic activity," *Journal of Catalysis*, vol. 344, pp. 616-630, 2016.

20. Xiangchao Meng, Zizhen Li, Haoming Zeng, Jie Chen and Zisheng Zhang, "MoS_2 quantum dots-interspersed Bi_2WO_6 heterostructures for visible light-induced detoxification and disinfection," *Applied Catalysis B: Environmental*, vol. 210, pp. 160-172, 2017.

21. Xiangchao Meng and Zisheng Zhang, "Plasmonic Z-scheme Ag_2O-Bi_2MoO_6 p-n heterojunction photocatalysts with greatly enhanced visible-light responsive activities," *Materials Letters*, vol. 189, pp. 267-270, 2017.

22. Xiangchao Meng and Zisheng Zhang, "Bi_2MoO_6 co-modified by reduced graphene oxide and palladium (Pd^{2+} and Pd^0) with enhanced photocatalytic decomposition of phenol," *Applied Catalysis B: Environmental*, vol. 209, pp. 383-393, 2017.

23. Yongchao Huang, Haibo Li, Muhammad-Sadeeq Balogun, Wenyue Liu, Yexiang Tong, Xihong Lu and Hongbing Ji, "Oxygen Vacancy Induced Bismuth Oxyiodide with Remarkably Increased Visible-Light Absorption and Superior Photocatalytic Performance," *ACS Applied Materials & Interfaces*, vol. 6, no. 24, pp. 22920-22927, 2014.

24. Yongchao Huang, Haibo Li, Wenjie Fan, Fengyi Zhao, Weitao Qiu, Hongbing Ji and Yexiang Tong, "Defect Engineering of Bismuth Oxyiodide by IO_3^- Doping for Increasing Charge Transport in Photocatalysis," *ACS Applied Materials & Interfaces*, vol. 8, no. 41, pp. 27859-27867, 2016.

25. Yongchao Huang, Wenjie Fan, Bei Long, Haibo Li, Fengyi Zhao, Zili Liu, Yexiang Tong and Hongbing Ji, "Visible light $Bi_2S_3/Bi_2O_3/Bi_2O_2CO_3$ photocatalyst for effective degradation of organic pollutions," *Applied Catalysis B: Environmental*, vol. 185, pp. 68-76, 2016.

26. Yongchao Huang, Hanxi Hu, Shuxian Wang, Muhammad-Sadeeq Balogun, Hongbing Ji and Yexiang Tong, "Low concentration nitric acid facilitate rapid electron–hole separation in vacancy-rich bismuth oxyiodide for photo-thermo-synergistic oxidation of formaldehyde," *Applied Catalysis B: Environmental*, vol. 218, pp. 700-708, 2017.

27. Huizhong An, Yi Du, Tianmin Wang, Cong Wang, Weichang Hao and Junying Zhang, "Photocatalytic properties of BiOX (X = Cl, Br, and I)," *Rare Metals*, vol. 27, no. 3, pp. 243-250, 2008.

28. Guohui Tian, Yajie Chen, Wei Zhou, Kai Pan, Youzhen Dong, Chungui Tian and Honggang Fu, "Facile solvothermal synthesis of hierarchical flower-like Bi2MoO6 hollow spheres as high performance visible-light driven photocatalysts," *Journal of Materials Chemistry*, vol. 21, no. 3, pp. 887-892, 2011.

29. Liwu Zhang, Tongguang Xu, Xu Zhao and Yongfa Zhu, "Controllable synthesis of Bi2MoO6 and effect of morphology and variation in local structure on photocatalytic activities," *Applied Catalysis B: Environmental*, vol. 98, no. 3–4, pp. 138-146, 2010.

30. Jinhong Bi, Ling Wu, Jie Li, Zhaohui Li, Xuxu Wang and Xianzhi Fu, "Simple solvothermal routes to synthesize nanocrystalline Bi2MoO6 photocatalysts with different morphologies," *Acta Materialia*, vol. 55, no. 14, pp. 4699-4705, 2007.

31. Walter Kohn and Lu Jeu Sham, "Self-consistent equations including exchange and correlation effects," *Physical Review*, vol. 140, no. 4A, pp. A1133, 1965.

32. Giannozzi Paolo, Baroni Stefano, Bonini Nicola, Calandra Matteo, Car Roberto, Cavazzoni Carlo, Ceresoli Davide, L. Chiarotti Guido, Cococcioni Matteo, Dabo Ismaila, Corso Andrea Dal, Gironcoli Stefano de, Fabris Stefano, Fratesi Guido, Gebauer Ralph, Gerstmann Uwe, Gougoussis Christos, Kokalj Anton, Lazzeri Michele, Martin-Samos Layla, Marzari Nicola, Mauri Francesco, Mazzarello Riccardo, Paolini Stefano, Pasquarello Alfredo, Paulatto Lorenzo, Sbraccia Carlo, Scandolo Sandro, Sclauzero Gabriele, P. Seitsonen Ari, Smogunov Alexander, Umari Paolo and M. Wentzcovitch Renata, "QUANTUM ESPRESSO: a modular and open-source software project for quantum simulations of materials," *Journal of Physics: Condensed Matter*, vol. 21, no. 39, pp. 395502, 2009.

33. F Pertlik and J Zemann, "Neubestimmung der Kristallstruktur des Köchlinits," *Fortschr. Miner. Beih*, vol. 60, pp. 162-163, 1982.

34. HongHua Li, ChaoYu Liu, KunWei Li and Hao Wang, "Preparation, characterization and photocatalytic properties of nanoplate Bi2MoO6 catalysts," *Journal of Materials Science*, vol. 43, no. 22, pp. 7026-7034, 2008.

35. Carrazán, S. R. G.; Martin, C.; Rives, V.; Vidal, R. *Spectrochimica Acta Part A: Molecular and Biomolecular Spectroscopy 52*, 1107. 1996.

36. M. A. Hasan, M. I. Zaki and L. Pasupulety, "Oxide-catalyzed conversion of acetic acid into acetone: an FTIR spectroscopic investigation," *Applied Catalysis A: General*, vol. 243, no. 1, pp. 81-92, 2003.

37. Li-Fen Liao, Chen-Fu Lien and Jong-Liang Lin, "FTIR study of adsorption and photoreactions of acetic acid on TiO2," *Physical Chemistry Chemical Physics*, vol. 3, no. 17, pp. 3831-3837, 2001.

38. Kangrong Lai, Wei Wei, Ying Dai, Ruiqin Zhang and Baibiao Huang, "DFT

calculations on structural and electronic properties of Bi_2MO_6 (M = Cr, Mo, W)," *Rare Metals*, vol. 30, no. 1, pp. 166-172, 2011.

39. HongHua Li, KunWei Li and Hao Wang, "Hydrothermal synthesis and photocatalytic properties of bismuth molybdate materials," *Materials Chemistry and Physics*, vol. 116, no. 1, pp. 134-142, 2009.

Appendix K Two Dimensional Graphitic Materials for Photoelectrocatalysis: A Short Review

Xiangchao Meng and Zisheng Zhang

Catalysis Today

Abstract:

Combining photocatalysis with electrochemistry, photoelectrocatalysis with an external circuit has been regarded as an effective approach for suppressing the recombination of photogenerated charge carriers in order to improve the photocatalytic activity. Two-dimensional graphitic materials have started being applied in photoelectrocatalysis in the past five years; it will be a popular research area in the near future. To date, the two-dimensional graphitic materials applied in photoelectrocatalysis are mainly graphene, layered transition metal dichalcogenides and g-C_3N_4. The reported works in this area have been reviewed and discussed. Even though the number of publications is still very few, it would be an attractive research area for effectively improving the photocatalytic activity for direct conversion of solar energy to chemical energy or solar fuels.

K.1 Introduction

Photocatalysis, as an efficient and cost-effective method for direct conversion of solar energy to chemical energy and solar fuels, has been extensively studied and exhibited the potential to solve the environmental and energy issues in the near future [1-4]. Since 1972, TiO_2 had successfully been implemented in photoelectrochemical water splitting to generate H_2 under UV light [5]. A massive amount of work has been done on improving the performance of photocatalysts. As shown in Fig. K.1a, in the past 10 years, the number of yearly publications was significantly increased, which indicates the significance of

photocatalysis. However, hindrances for large-scale application of photocatalysis are still obvious, mainly including the relatively low activity under visible/solar light. This low activity is generally considered as the high recombination of photogenerated charge carriers. As a result, the primary method to improve photocatalytic activity is to reduce the recombination possibility of photogenerated charge carriers.

Approaches to improve photocatalytic activity via suppressing recombination of photogenerated charge carriers are numerous, one of which is modification/combination with graphitic materials. Graphitic materials exhibited excellent electrical conductivity and are considered a promising group of materials to be applied in photocatalysis [6]. As shown in Fig. K.1b, graphene-based photocatalysis has been massively implemented and reported in the past 5 years.

Studies have been reported on the combination of photocatalysis with other techniques in order to further improve the photocatalytic activity. One of these combinatory techniques is photoelectrocatalysis, which is an effective approach to suppressing the recombination of photogenerated charge carriers. The mechanism for photoelectrocatalysis was schemed in Fig. K.2 [7]. Specifically, under an external bias, photogenerated charge carriers are driven to different directions; electrons accumulated in the external cathode and holes accumulated on the photocatalyst. As shown Fig. K.1c, photoelectrocatalysis has been gradually developed, and graphene applied in photoelectrocatalysis has also seen increased interest. However, compared with photocatalysis and graphene-based photocatalysis, the number of yearly publications on photoelectrocatalysis is still very few.

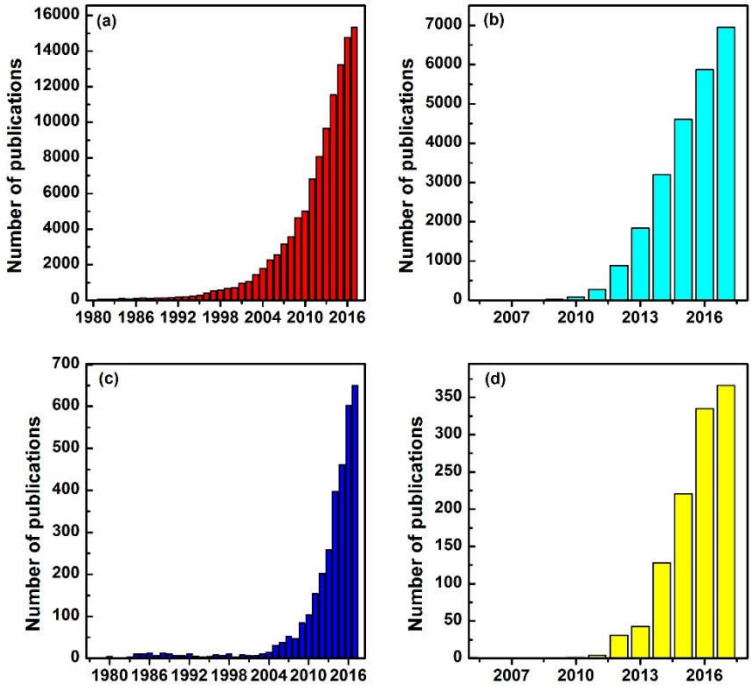


Figure K.1 Number of yearly publications with topic keywords of (a) 'photocatalysis', (b) 'photocatalysis' + 'graphene', (c) 'photoelectrocatalysis' and (d) 'photoelectrocatalysis' + 'graphene'. (Searched on November 19, 2017, using the SCOPUS database)

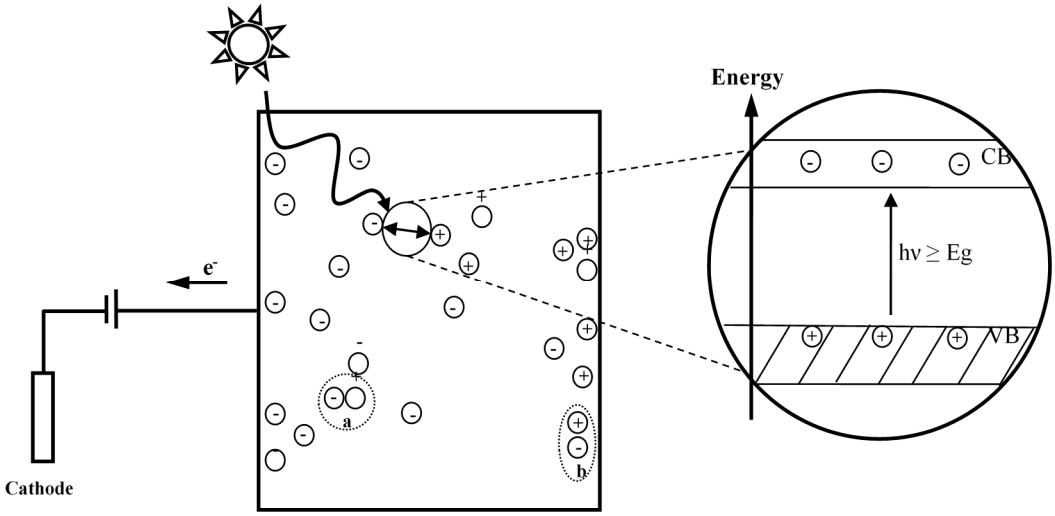


Figure K.2 Schematic processes of photoelectrocatalysis when combined with an external circuit.

Electrodes applied in photoelectrocatalysis are generally composed of photocatalyst(s) and co-catalyst(s) deposited on a conductive glass or metal mesh. In this case, various photocatalytic materials have been extended into the application of photoelectrocatalysis. TiO_2, as one of the most popular photocatalysts, has been extensively studied as a materials on photoelectrocatalysis as the photoanode [8-10]. Other visible light-responsive materials such as bismuth based semiconductors were also implemented in photoelectrocatalysis [11, 12]. However, one-component photoanode was generally with high recombination rate of photogenerated charge carriers, and modifications are aided to improve the photoelectrocatalytic activities. One of the approaches is to combine with a co-catalyst. Graphitic materials can be promising candidates as co-catalysts to improve the photoelectrocatalytic activity, with superiorities compared with other materials. Graphitic materials with two dimensional (2D) structures exhibited excellent electrical conductivity and may be served as an electron transporter to improve the separation of photogenerated charge carriers and in turn improve the photoelectrocatalytic activity. Some 2D graphitic materials applied in photocatalysis are graphene, monolayer *h*-BN, monolayer MS_2 (M = Mo, W), monolayer MoT_2 (T = Se, Te) and g-C_3N_4. However, among them, those applied in photoelectrocatalysis are limited. In this review, the 2D graphitic materials implemented in photoelectrocatalysis aiming to improve the photocatalytic activity are introduced and discussed.

K.2 Graphitic materials implemented in photoelectrocatalysis

K.2.1 Graphene/reduced graphene oxide

Graphene is defined by the International Union for Pure and Applied Chemistry (IUPAC) as 'a single carbon layer of graphite structure, describing its nature by analogy to a polycyclic aromatic hydrocarbon of quasi-infinite size' [13]. Graphene is considered to be the first two-dimensional crystal. For the lattice cell of graphene, each unit cell is composed of two carbon atoms. Of the four valence states, three sp^2 orbitals form a σ state with three neighboring carbon atoms, and one p orbital develops into delocalized π and π^* states that form the highest occupied valence band (VB) and the lowest unoccupied conduction band (CB). The π and π^* states of graphene are degenerate at the corner (K point) of the hexagonal Brillouin zone (BZ) (Fig. K.3) [14]. Graphene with a band gap of zero exhibits

excellent electron mobility, and even outperforms metals and metal composites [15]. This property can be applied in photo(electro)catalysis to enhance the photocatalytic activity. As for the preparation of graphene, various synthetic routes have been reported, and can be primarily divided into two distinct approaches, namely top-down and bottom-up. The top-down approach includes exfoliation from graphite via mechanical, chemical, or electrochemical methods, aiming to weaken the Van der Waals forces between layers. The top-down approach is to fabricate graphene from graphene nanoribbons via thermal or chemical processes [16]. It should be noted that graphene oxide, GO, is an attractive material, and graphene may be directly produced from GO using a simple reduction process, products of which is named reduced graphene oxide (rGO). Isolated GO sheets can be obtained in a solution form and exhibits a great potential for the large-scale production of graphene [17].

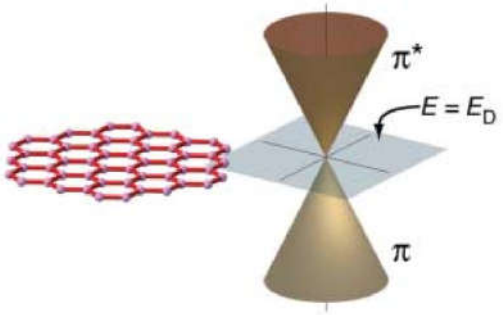


Figure K.3 Electronic structure of a single layer of graphene (Adapted from [14], Copyright 2006, American Association for the Advancement of Science).

Graphene has been implemented in photocatalysis and photoelectrocatalysis as an additive [6, 18-20]. Graphene is applied in photo(electro)catalysis due to its strong adsorption of organic pollutants, enhanced visible light-photon absorption and improved separation efficiency of photogenerated charge carriers. Specifically, it has been reported that graphene exhibits superior adsorption capacity for organic pollutants with an aromatic structure, due to the strong π-π interactions [21-25]. Zhang et al. reported on TiO_2-graphene applied in photoelectrocatalytic decomposition of bisphenol A [26]. The composite exhibited an adsorption capacity of 476.2 mg/g, which is 4 times higher than that for TiO_2 loaded on activated carbon. Graphene nanosheets are also capable of improving the absorption of visible light-photons. As reported in [11, 27, 28], when graphene/rGO was

introduced on a support, the absorbance intensity in the visible light region was greatly enhanced, which is typical for graphene-based composites. The most important property for graphene implemented in photo(electro)catalysis is the high conductivity of electrons on its surface, which is in favor of suppressing the recombination photogenerated charge carriers. Zhou et al. has reported on Er^{3+}:$YAlO_3$/rGO/TiO_2 (ERT) applied in photoelectrocatalytic degradation of methylene Blue under visible light [29]. The proposed mechanism is illustrated in Fig. K.4. The photocurrent was improved from 2.5 μA/cm^2 on TiO_2 electrode to 16.8 μA/cm^2 on ERT electrode. The enhancement may be due to the high conductivity of graphene and the outside bias voltage, which allowed the transfer of photogenerated charge carriers to the counter-electrode (Pt foil) via the outside circuit. This transfer of electrons can suppress the recombination of electrons and holes, and lead to the enhanced catalytic activity in the oxidation of organic pollutants. Similar results about graphene-based photoelectrocatalysis applied in organic pollutant decomposition were also reported [12, 30-33].

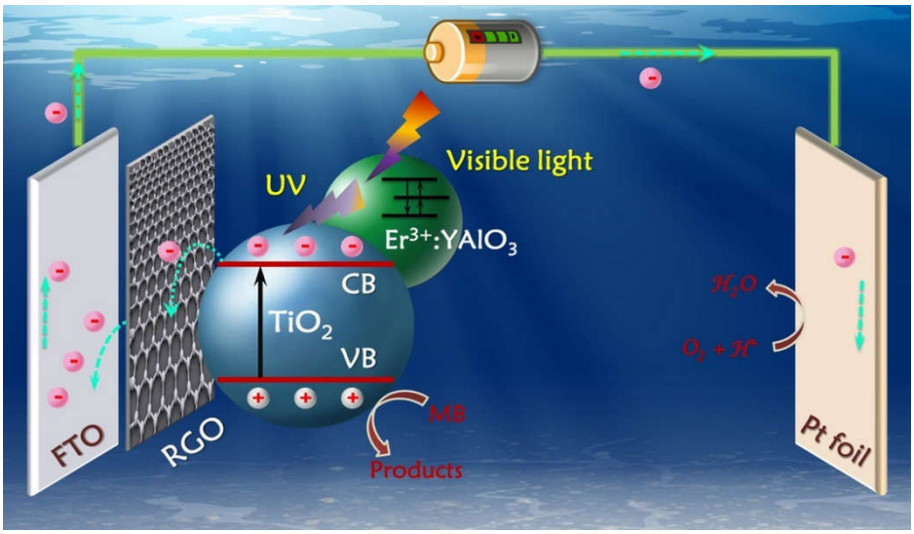


Figure K.4 Photoelectrocatalytic mechanism for Er^{3+}:$YAlO_3$/rGO/TiO_2 electrode under visible light. (Adapted from [29], Copyright 2017 The American Society of Photobiology)

Another important application of photoelectrocatalysis is hydrogen (H_2) evolution via water splitting. Graphene has also been applied as a charge transporter on the electrode in photoelectrocatalysis. Wang et al. reported on an umbrella-shaped Bi_2S_3/rGO-modified TiO_2 electrode applied in photoelectrocatalytic water splitting to produce hydrogen (Fig.

K.5) [34]. It was found that the photocurrent was greatly increased to ~2.0 mA/cm^{-2} with the introduction of rGO. Similar structures were also reported [35, 36]. The fabrication process was illustrated in Fig. K.6 [28]. Specifically, the main photocatalyst grow on a substrate, and graphene/rGO nanosheets were then coated on the photocatalyst. Modifications may be required to further improve the photocatalytic activity of the photocatalyst. Cheng et al. reported on the preparation of an electrode with 3 dimensional graphene flowers applied in photoelectrocatalytic hydrogen evolution [37]. It was found that this structure is beneficial in providing an electrode with a large surface area for the redox reaction which greatly facilitated the electron/hole separation, and further enhanced the activity for water splitting.

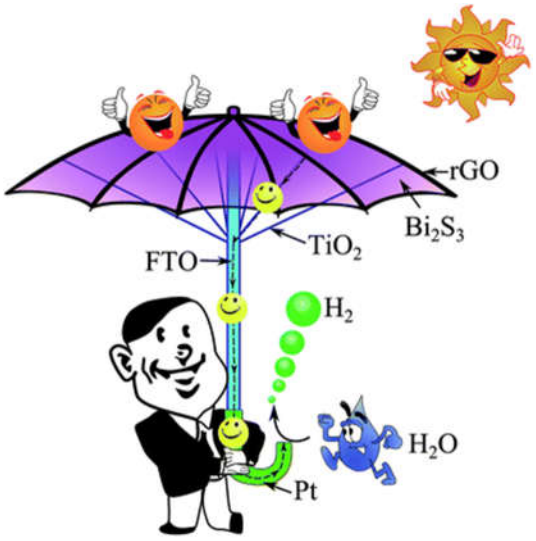


Figure K.5 Schematic diagram of Schematic diagram of the smart "umbrella" Bi_2S_3/rGO-modified TiO_2 NRs structure. The Bi_2S_3 nanostructures act as the "canopy" and can efficiently harvest sunlight. The rGO sheet layers and 1D TiO_2 NRs act as the "ribs" and "stretchers", respectively, and can quickly transport electrons. The FTO conductive layer acts as the "shaft". The Pt counter electrode serves as the "handle". (Adapted from [34], Copyright 2014, Royal Society of Chemistry)

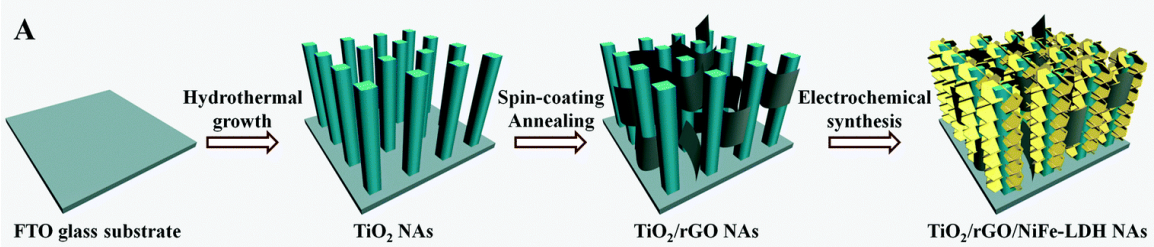


Figure K.6 Schematic illustration for the fabrication of the electrode in photoelectrocatalysis. (Adapted from [28], Copyright 2016, Royal Society of Chemistry)

Application of graphene-assisted photoelectrocatalysis was also extended to the area of CO_2 reduction to produce high-value hydrocarbons. Photocatalysis has been regarded as a promising way to reduce CO_2, as it is an artificial model for photosynthesis when solar energy can be directly utilized. However, the extremely low quantum efficiency of the conversion hinders its widely application. Photoelectrocatalysis with external bias can be regarded as a potential approach to increase the quantum efficiency [38]. Cheng et al. reported on an electrode composed of Pt-modified rGO combined with Pt-modified TiO_2 nanotubes, which was implemented for the photoelectrocatalytic reduction of CO_2 [39]. It was found that HCOOH and CH_3OH may be produced, and the introduction of rGO greatly improved the production yield. Hasan et al. reported on Ga doped rGO-TiO_2 on ITO as the electrode for the photoelectrocatalytic reduction of CO_2 to produce formic acid [40]. It was found that with the assistance of rGO, about 178 ppm of formic acid was recovered for a 2-h reaction period.

K.2.2 Layered Transition Metal Dichalcogenides (TMDs)

TMDs with a general formula of MX_2, are semiconductors that have attracted an extensive amount of attention due to their superior properties, such as super conductivity and half-metal magnetism. This class of materials have been applied in various areas, including catalysis, super capacitor, lubrication, and rechargeable battery systems [41-43]. There are two types of crystal structures of TMDs, namely, 2H (trigonal prismatic with a D_{3h} points group symmetry) and 1T (octahedral with a C_{3v} symmetry) [44]. Properties and stabilities of MX_2 are dependent on the crystal structure, and a summary was shown in Fig. K.7. Unlike graphene, some layered TMDs exhibit semiconducting properties with band gaps not equal to zero (such as MoS_2 and WS_2). The band gap values depend on the number of

layers of the nanosheets. Kuc et al. reported on the electronic band structures of MS_2 (M = Mo and W) using the first-principle theory (Fig. K.8) [45]. It was found that the band gap for Bulk MoS_2 is 1.2 eV, and it increased to 1.9 eV for a monolayer MoS_2. Moreover, the band gap transition was changed from indirect to direct transition. A similar verdict was obtained for WS_2. It suggested that the monolayer structure, namely the graphene-shaped form, can be applied in photocatalysis under visible light. TMDs have also been applied in photoelectrocatalysis with external bias, aiming to further improve its photocatalytic activity.

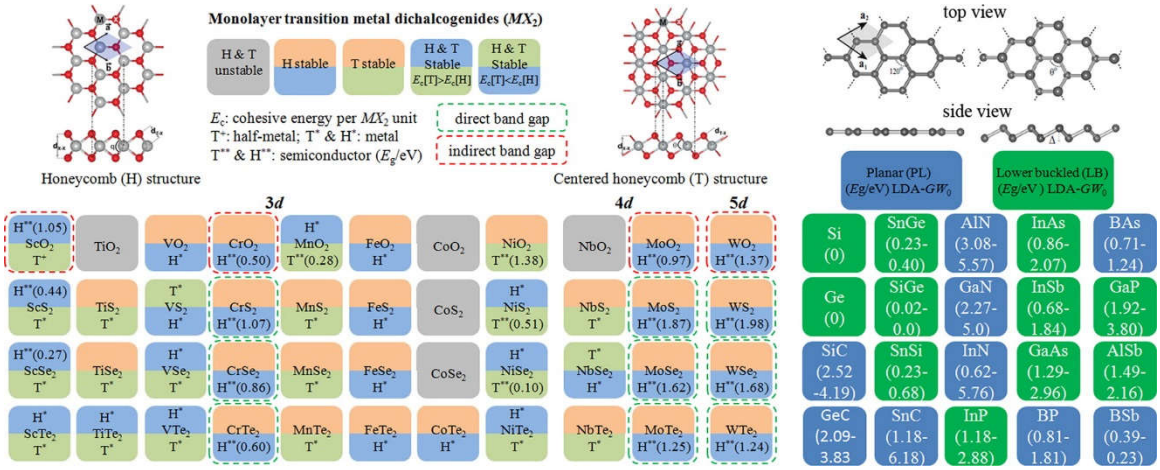


Figure K.7 Summary of stability analysis and semiconducting properties of 44 different MX_2 compounds and binary compounds of group-IV elements and group III–V. (Adapted from [46], Copyright 2013, American Chemical Society)

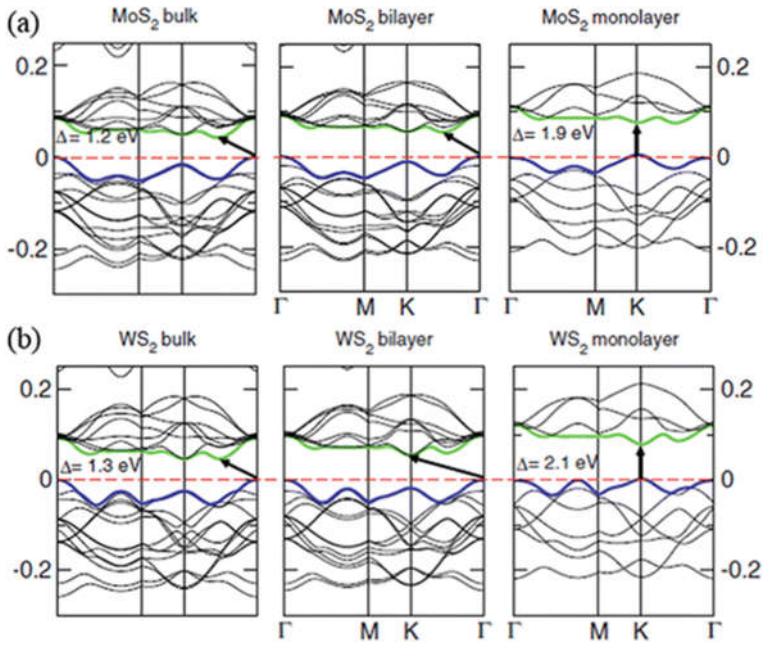


Figure K.8 Band structure of MoS_2 and WS_2 with the form of bulk, bilayer and mono layer (Adapted from [45], Copyright 2011 American Physical Society)

Layered MoS_2, which is a promising non-metal catalyst, has two phases: 2H and 1T. It should be noted that 1T-MoS_2 exhibited metallic properties, and 2H-MoS_2 is semiconducting. As reported [47], combining 1T with 2H-MoS_2 to form a heterojunction was capable of facilitating the separation of photogenerated charge carriers. Qi et al. has reported on an electrode which was composed of 1T-2H MoS_2 heterojunctions, applied in photoelectrocatalysis [48]. It was found that a phase change from 2H to 1T can be induced by supercritical carbon dioxide (SC CO_2). Using this modification, a heterojunction between 1T and 2H MoS_2 was fabricated. The photocurrent was improved from 400 $\mu A/cm^2$ to 1400 $\mu A/cm^2$ with the phase change. Zhu et al. has also reported on an electrode fabricated with h-MoO_3 and 1T-MoS_2 and tested its photoelectrocatalytic performance [49]. The electrode treated with SC CO_2 exhibited enhanced photoelectrocatalytic activity. Molybdenum diselenide ($MoSe_2$) with a graphene-like structure has also attracted attention and applied in various areas, such as energy storage, electrocatalysis and photo(electro)catalysis [50]. Compared with MoS_2, $MoSe_2$ exhibited higher electrical conductivity and showed more potential in the same range of applications. Jia et al. has reported a novel $MoSe_2$-rGO/polyimide composite for application in photoelectrocatalytic hydrogen evolution [51]. It was found that the cathode current was improved from 10.9

mA/cm^2 to 14.5 mA/cm^2 for -0.6V with a 400-W illumination. Park et al. has also reported on an $MoSe_2$ embedded CNT (carbon nanotubes)-rGO composite applied in photoelectrocatalytic H_2 evolution [52]. An improvement in the photoelectrocatalytic activity was observed with the addition of $MoSe_2$. These results suggest that $MoSe_2$ may be promising in photoelectrocatalysis. Other TMDs have rarely been reported in the area of photoelectrocatalysis.

K.2.3 Graphite-like carbon nitride (g-C_3N_4)

As a metal-free polymer n-type semiconductor, g-C_3N_4 possesses unique electric, optical, structural and physiochemical properties [53]. This material has been implemented in various areas, such as electronic, catalysis and energy storage [54]. It was first applied by Wang and his coworkers as a photocatalyst for H_2 evolution in 2009 [55]. It was found that g-C_3N_4 possesses a stacked 2D layered structure, which is composed of single-layer nitrogen heteroatom-substituted graphite nanosheets, formed through sp^2 hybridization of C and N atoms bounded by van der Waals force between layers. It was reported with excellent optical properties, as its band gap is about 2.7 eV. As shown in Fig. K.9, the potential of the conduction band and valence band for g-C_3N_4 was estimated as about -1.30 and 2.29 eV (vs. NHE at pH 7), respectively. This indicates that g-C_3N_4 may be a promising material in photocatalysis. Advantages as well as challenges about g-C_3N_4 applied in photocatalysis were also listed in Fig. K.9. It should be noted that the main hindrances for g-C_3N_4 applied in photocatalysis is the high recombination of photogenerated charge carriers and low charge carrier mobility. To overcome these hindrances and improve the catalytic activity, photoelectrocatalysis could be applied with an external bias to drive the mobility direction of photogenerated charge carriers. Liu et al. has reported a novel GQDs (graphene quantum dots)/PANI/g-C_3N_4 as an electrode applied in photoelectrocatalysis [56]. It was found that the recombination of photogenerated charge carriers was greatly suppressed. Liang et al. has also reported on the photoelectrocatalysis of g-C_3N_4 film in the decomposition of phenol under visible light [57]. It was found that the mineralization ability of phenol was enhanced via the synergetic effect. This material has also been applied in the photoelectrocatalytic oxidation of methanol with modified Pt [58]. This result showed that the 2D ultrathin g-C_3N_4 nanosheets can be used as a promising photoactive support in the fields of solar and chemical energy conversion and provided more insights

into developing novel visible light photoactive electrodes in direct methanol fuel cells. Zhang and his coworkers have reported the photoelectrocatalytic reduction of Cr(VI) on g-C_3N_4/TiO_2 nanotubes electrodes with enhanced activity [59].

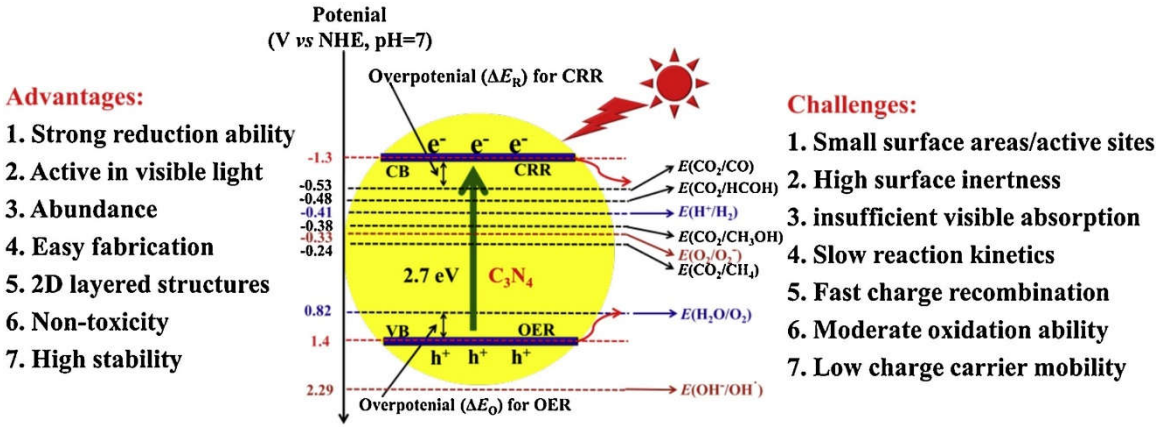


Figure K.9 The redox potentials of the relevant reactions with respect to the estimated position of the g-C_3N_4 band edges at pH 7. (Adapted from [53], copyright 2016 Elsevier)

K.3 Concluding remarks and prospects

In this review, we have summarized the 2D graphitic materials applied in photoelectrocatalysis. Even though as-reported work in this area is still rare, we believe it will be extremely developed in the near future, due to its superiorities. These superiorities are the high electrical conductivity of 2D graphitic materials, which can make them an excellent electron transporter, so as to reduce the recombination of photogenerated charge carriers. Following prospects are suggested as references for future work in this area:

(i) So far, most of the work focused on graphene based photoelectrocatalysis; exploration on other 2D graphitic materials may be also promising.

(ii) Photoreactors applied in photoelectrocatalysis were generally composed of a photocatalyst film electrode and a metal cathode, which is a conventional two/three-electrode system. Photoreactors design is extremely required to apply photoelectrocatalysis from exploratory phase to an industrial scale.

(iii) Fundamental studies are required specifically for photoelectrocatalysis, may be not suitable for directly applying theories from photocatalysis. For example, Langmuir-Hinshelwood (L-H) model was widely applied to describe kinetics of a photocatalytic

process. This model may be modified for the photoelectrocatalysis, as more parameters are required to be considered, such as bias potential and additional electrolytes.

(iv) Moreover, their applications can be widened and implemented in photocatalytic organic synthesis, disinfection, CO_2 reduction and N_2 reduction. The diverse possibilities for forming the graphitic photoelectrode, discovering exotic properties and implementing in various areas make this field a fertile one for future investigation and emerging technological applications with precisely tailored properties.

References

1. Masao Kaneko and Ichiro Okura, "Photocatalysis science and technology," *Kodansha Springer*, 2002.

2. Sixto Malato, Julián Blanco, Alfonso Vidal and Christoph Richter, "Photocatalysis with solar energy at a pilot-plant scale: an overview," *Applied Catalysis B: Environmental*, vol. 37, no. 1, pp. 1-15, 2002.

3. Giovanni Palmisano, Vincenzo Augugliaro, Mario Pagliaro and Leonardo Palmisano, "Photocatalysis: a promising route for 21st century organic chemistry," *Chemical Communications*, no. 33, pp. 3425-3437, 2007.

4. Xiangchao Meng and Zisheng Zhang, "Synthesis and characterization of plasmonic and magnetically separable Ag/AgCl-Bi_2WO_6@ Fe_3O_4@SiO_2 core-shell composites for visible light-induced water detoxification," *Journal of Colloid and Interface Science*, vol. 485, pp. 296-307, 2017.

5. Akira Fujishima and Kenichi Honda, "Electrochemical photolysis of water at a semiconductor electrode," *nature*, vol. 238, pp. 37-38, 1972.

6. Xin Li, Jiaguo Yu, S. Wageh, Ahmed A. Al-Ghamdi and Jun Xie, "Graphene in Photocatalysis: A Review," *Small*, vol. 12, no. 48, pp. 6640-6696, 2016.

7. Xiangchao Meng, Zisheng Zhang and Xingang Li, "Synergetic photoelectrocatalytic reactors for environmental remediation: A review," *Journal of Photochemistry and Photobiology C: Photochemistry Reviews*, vol. 24, pp. 83-101, 2015.

8. J. Georgieva, E. Valova, S. Armyanov, N. Philippidis, I. Poulios and S. Sotiropoulos,

"Bi-component semiconductor oxide photoanodes for the photoelectrocatalytic oxidation of organic solutes and vapours: A short review with emphasis to TiO_2–WO_3 photoanodes," *Journal of Hazardous Materials*, vol. 211-212, pp. 30-46, 2012.

9. Ming-Zheng Ge, Chun-Yan Cao, Jian-Ying Huang, Shu-Hui Li, Song-Nan Zhang, Shu Deng, Qing-Song Li, Ke-Qin Zhang and Yue-Kun Lai, "Synthesis, modification, and photo/photoelectrocatalytic degradation applications of TiO_2 nanotube arrays: a review," in *Nanotechnology Reviews*, Ed., pp. 75, 2016.

10. Yanzong Zhang, Xiaoyan Xiong, Yue Han, Xiaohong Zhang, Fei Shen, Shihuai Deng, Hong Xiao, Xinyao Yang, Gang Yang and Hong Peng, "Photoelectrocatalytic degradation of recalcitrant organic pollutants using TiO_2 film electrodes: An overview," *Chemosphere*, vol. 88, no. 2, pp. 145-154, 2012.

11. Huan Wang, Yinghua Liang, Li Liu, Jinshan Hu and Wenquan Cui, "Reduced graphene oxide wrapped Bi2WO6 hybrid with ultrafast charge separation and improved photoelectrocatalytic performance," *Applied Surface Science*, vol. 392, no. Supplement C, pp. 51-60, 2017.

12. Huan Wang, Yinghua Liang, Li Liu, Jinshan Hu, Ping Wu and Wenquan Cui, "Enriched photoelectrocatalytic degradation and photoelectric performance of BiOI photoelectrode by coupling rGO," *Applied Catalysis B: Environmental*, vol. 208, no. Supplement C, pp. 22-34, 2017.

13. E. Fitzer, K. H. Kochling, H. P. Boehm and H. Marsh, "Recommended terminology for the description of carbon as a solid (IUPAC Recommendations 1995)," in *Pure and Applied Chemistry*, Ed., pp. 473, 1995.

14. Taisuke Ohta, Aaron Bostwick, Thomas Seyller, Karsten Horn and Eli Rotenberg, "Controlling the Electronic Structure of Bilayer Graphene," *Science*, vol. 313, no. 5789, pp. 951-954, 2006.

15. Vasilios Georgakilas, Jitendra N. Tiwari, K. Christian Kemp, Jason A. Perman, Athanasios B. Bourlinos, Kwang S. Kim and Radek Zboril, "Noncovalent Functionalization of Graphene and Graphene Oxide for Energy Materials, Biosensing, Catalytic, and Biomedical Applications," *Chemical Reviews*, vol. 116, no. 9, pp. 5464-5519,

2016.

16. Adriano Ambrosi, Chun Kiang Chua, Alessandra Bonanni and Martin Pumera, "Electrochemistry of Graphene and Related Materials," *Chemical Reviews*, vol. 114, no. 14, pp. 7150-7188, 2014.

17. Yanwu Zhu, Shanthi Murali, Weiwei Cai, Xuesong Li, Ji Won Suk, Jeffrey R. Potts and Rodney S. Ruoff, "Graphene and Graphene Oxide: Synthesis, Properties, and Applications," *Advanced Materials*, vol. 22, no. 35, pp. 3906-3924, 2010.

18. Nan Zhang, Min-Quan Yang, Siqi Liu, Yugang Sun and Yi-Jun Xu, "Waltzing with the Versatile Platform of Graphene to Synthesize Composite Photocatalysts," *Chemical Reviews*, vol. 115, no. 18, pp. 10307-10377, 2015.

19. Lütfiye Yıldız Ozer, Corrado Garlisi, Habeebllah Oladipo, Mario Pagliaro, Saad Asadullah Sharief, Ahmed Yusuf, Saif Almheiri and Giovanni Palmisano, "Inorganic semiconductors-graphene composites in photo(electro)catalysis: Synthetic strategies, interaction mechanisms and applications," *Journal of Photochemistry and Photobiology C: Photochemistry Reviews*, 2017.

20. Alejandra Garcia, Cristina Fernandez-Blanco, Jose R. Herance, Josep Albero and Hermenegildo Garcia, "Graphenes as additives in photoelectrocatalysis," *Journal of Materials Chemistry A*, vol. 5, no. 32, pp. 16522-16536, 2017.

21. Jun Wang and Baoliang Chen, "Adsorption and coadsorption of organic pollutants and a heavy metal by graphene oxide and reduced graphene materials," *Chemical Engineering Journal*, vol. 281, no. Supplement C, pp. 379-388, 2015.

22. Xiangchao Meng and Zisheng Zhang, "Bi_2MoO_6 co-modified by reduced graphene oxide and palladium (Pd^{2+} and Pd^0) with enhanced photocatalytic decomposition of phenol," *Applied Catalysis B: Environmental*, vol. 209, pp. 383-393, 2017.

23. Xiangchao Meng and Zisheng Zhang, "Plasmonic ternary Ag–rGO–Bi_2MoO_6 composites with enhanced visible light-driven photocatalytic activity," *Journal of Catalysis*, vol. 344, pp. 616-630, 2016.

24. Xiaoyue Hu, Xiangchao Meng and Zisheng Zhang, "Synthesis and Characterization of Graphene Oxide-Modified Bi_2WO_6 and Its Use as Photocatalyst," *International Journal of*

Photoenergy, vol. 2016, pp. 8, 2016.

25. Jun Wang, Zaiming Chen and Baoliang Chen, "Adsorption of Polycyclic Aromatic Hydrocarbons by Graphene and Graphene Oxide Nanosheets," *Environmental Science & Technology*, vol. 48, no. 9, pp. 4817-4825, 2014.

26. Yu Zhang, Wenquan Cui, Weijia An, Li Liu, Yinghua Liang and Yongfa Zhu, "Combination of photoelectrocatalysis and adsorption for removal of bisphenol A over TiO_2-graphene hydrogel with 3D network structure," *Applied Catalysis B: Environmental*, vol. 221, no. Complete, pp. 36-46, 2018.

27. Su Zhan, Feng Zhou, Naibao Huang, Qiuchen He and Yongfa Zhu, "Deactivating harmful marine microorganisms through photoelectrocatalysis by GO/ZnWO4 electrodes," *Chemical Engineering Journal*, vol. 330, no. Supplement C, pp. 635-643, 2017.

28. Fanyu Ning, Mingfei Shao, Simin Xu, Yi Fu, Ruikang Zhang, Min Wei, David G. Evans and Xue Duan, "TiO2/graphene/NiFe-layered double hydroxide nanorod array photoanodes for efficient photoelectrochemical water splitting," *Energy & Environmental Science*, vol. 9, no. 8, pp. 2633-2643, 2016.

29. Xian Zhou, Jun Zhang, Yue Ma, Hanqing Cheng, Shaozhu Fu, Dandan Zhou and Shuangshi Dong, "Construction of Er^{3+}:$YAlO_3$/RGO/TiO_2 Hybrid Electrode with Enhanced Photoelectrocatalytic Performance in Methylene Blue Degradation Under Visible Light," *Photochemistry and Photobiology*, vol. 93, no. 5, pp. 1170-1177, 2017.

30. Zhijun Li, Yang Qu, Kang Hu, Muhammad Humayun, Shuangying Chen and Liqiang Jing, "Improved photoelectrocatalytic activities of BiOCl with high stability for water oxidation and MO degradation by coupling RGO and modifying phosphate groups to prolong carrier lifetime," *Applied Catalysis B: Environmental*, vol. 203, no. Supplement C, pp. 355-362, 2017.

31. Meng Wang, Xinke Shang, Xuelian Yu, Rongji Liu, Yongbing Xie, He Zhao, Hongbin Cao and Guangjin Zhang, "Graphene-CdS quantum dots-polyoxometalate composite films for efficient photoelectrochemical water splitting and pollutant degradation," *Physical Chemistry Chemical Physics*, vol. 16, no. 47, pp. 26016-26023, 2014.

32. Lili Wei, Juan Yang, Joanna Borowiec and Jingdong Zhang, "A Metal-Free Approach

Based on Graphene Oxide-Modified Electrode for Monitoring the Photoelectrocatalytic Degradation of EDTA," *Electroanalysis*, vol. 23, no. 10, pp. 2373-2378, 2011.

33. Xianjie Chen, Qian Chen, Wenjun Jiang, Zhen Wei and Yongfa Zhu, "Separation-free TiO2-graphene hydrogel with 3D network structure for efficient photoelectrocatalytic mineralization," *Applied Catalysis B: Environmental*, vol. 211, no. Supplement C, pp. 106-113, 2017.

34. Xiaodeng Wang, Jiale Xie and Chang Ming Li, "Architecting smart "umbrella" Bi_2S_3/rGO-modified TiO_2 nanorod array structures at the nanoscale for efficient photoelectrocatalysis under visible light," *Journal of Materials Chemistry A*, vol. 3, no. 3, pp. 1235-1242, 2015.

35. Yang Hou, Fan Zuo, Alex Dagg and Pingyun Feng, "Visible Light-Driven α-Fe_2O_3 Nanorod/Graphene/$BiV_{1-x}Mo_xO_4$ Core/Shell Heterojunction Array for Efficient Photoelectrochemical Water Splitting," *Nano Letters*, vol. 12, no. 12, pp. 6464-6473, 2012.

36. Zhipeng Huang, Peng Zhong, Chifang Wang, Xuanxiong Zhang and Chi Zhang, "Silicon Nanowires/Reduced Graphene Oxide Composites for Enhanced Photoelectrochemical Properties," *ACS Applied Materials & Interfaces*, vol. 5, no. 6, pp. 1961-1966, 2013.

37. Qifa Cheng, Jing Xu, Tao Wang, Ling Fan, Ruifang Ma, Xinzhi Yu, Jian Zhu, Zhi Xu and Bingan Lu, "Double quantum dots decorated 3D graphene flowers for highly efficient photoelectrocatalytic hydrogen production," *Applied Surface Science*, vol. 422, no. Supplement C, pp. 528-535, 2017.

38. Quan Quan, Xie Shun-Ji, Wag Ye and Xu Yi-Jun, "Photoelectrochemical Reduction of CO_2 Over Graphene-Based Composites:Basic Principle, Recent Progress, and Future Perspective," *Acta Physico-Chimica Sinica*, vol. 33, no. 12, pp. 2404-2423, 2017.

39. Jun Cheng, Meng Zhang, Gai Wu, Xin Wang, Junhu Zhou and Kefa Cen, "Photoelectrocatalytic Reduction of CO_2 into Chemicals Using Pt-Modified Reduced Graphene Oxide Combined with Pt-Modified TiO_2 Nanotubes," *Environmental Science & Technology*, vol. 48, no. 12, pp. 7076-7084, 2014.

40. Md Rakibul Hasan, Sharifah Bee Abd Hamid, Wan Jeffrey Basirun, Zaira Zaman

Chowdhury, Ahmad Esmaielzadeh Kandjani and Suresh K. Bhargava, "Ga doped RGO-TiO_2 composite on an ITO surface electrode for investigation of photoelectrocatalytic activity under visible light irradiation," *New Journal of Chemistry*, vol. 39, no. 1, pp. 369-376, 2015.

41. Gianluca Fiori, Francesco Bonaccorso, Giuseppe Iannaccone, Tomás Palacios, Daniel Neumaier, Alan Seabaugh, Sanjay K. Banerjee and Luigi Colombo, "Electronics based on two-dimensional materials," *Nature Nanotechnology*, vol. 9, pp. 768, 2014.

42. Oriol Lopez-Sanchez, Dominik Lembke, Metin Kayci, Aleksandra Radenovic and Andras Kis, "Ultrasensitive photodetectors based on monolayer MoS_2," *Nature Nanotechnology*, vol. 8, pp. 497, 2013.

43. Zizhen Li, Xiangchao Meng and Zisheng Zhang, "Recent Development on MoS_2-based Photocatalysis: a Review," *Journal of Photochemistry and Photobiology C: Photochemistry Reviews*, 2017.

44. N. V. Podberezskaya, S. A. Magarill, N. V. Pervukhina and S. V. Borisov, "Crystal Chemistry of Dichalcogenides MX_2," *Journal of Structural Chemistry*, vol. 42, no. 4, pp. 654-681, 2001.

45. A. Kuc, N. Zibouche and T. Heine, "Influence of quantum confinement on the electronic structure of the transition metal sulfide TS_2," *Physical Review B*, vol. 83, no. 24, pp. 245213, 2011.

46. Mingsheng Xu, Tao Liang, Minmin Shi and Hongzheng Chen, "Graphene-Like Two-Dimensional Materials," *Chemical Reviews*, vol. 113, no. 5, pp. 3766-3798, 2013.

47. Urmimala Maitra, Uttam Gupta, Mrinmoy De, Ranjan Datta, A. Govindaraj and C. N. R. Rao, "Highly Effective Visible-Light-Induced H_2 Generation by Single-Layer 1T-MoS_2 and a Nanocomposite of Few-Layer 2H-MoS_2 with Heavily Nitrogenated Graphene," *Angewandte Chemie International Edition*, vol. 52, no. 49, pp. 13057-13061, 2013.

48. Yuhang Qi, Qun Xu, Yun Wang, Bo Yan, Yumei Ren and Zhimin Chen, "CO_2-Induced Phase Engineering: Protocol for Enhanced Photoelectrocatalytic Performance of 2D MoS_2 Nanosheets," *ACS Nano*, vol. 10, no. 2, pp. 2903-2909, 2016.

49. Chuanhui Zhu, Qun Xu, Wei Liu and Yumei Ren, "CO_2-assisted fabrication of novel

heterostructures of h-MoO_3/1T-MoS_2 for enhanced photoelectrocatalytic performance," *Applied Surface Science*, vol. 425, no. Supplement C, pp. 56-62, 2017.

50. Ali Eftekhari, "Molybdenum diselenide ($MoSe_2$) for energy storage, catalysis, and optoelectronics," *Applied Materials Today*, vol. 8, no. Supplement C, pp. 1-17, 2017.

51. Lingpu Jia, Xiao Sun, Yimin Jiang, Shenjiao Yu and Chunming Wang, "A Novel MoSe2–Reduced Graphene Oxide/Polyimide Composite Film for Applications in Electrocatalysis and Photoelectrocatalysis Hydrogen Evolution," *Advanced Functional Materials*, vol. 25, no. 12, pp. 1814-1820, 2015.

52. Gi Dae Park, Jung Hyun Kim, Seung-Keun Park and Yun Chan Kang, "$MoSe_2$ Embedded CNT-Reduced Graphene Oxide Composite Microsphere with Superior Sodium Ion Storage and Electrocatalytic Hydrogen Evolution Performances," *ACS Applied Materials & Interfaces*, vol. 9, no. 12, pp. 10673-10683, 2017.

53. Jiuqing Wen, Jun Xie, Xiaobo Chen and Xin Li, "A review on g-C_3N_4-based photocatalysts," *Applied Surface Science*, vol. 391, no. Part B, pp. 72-123, 2017.

54. Wenjun Jiang, Wenjiao Luo, Jun Wang, Mo Zhang and Yongfa Zhu, "Enhancement of catalytic activity and oxidative ability for graphitic carbon nitride," *Journal of Photochemistry and Photobiology C: Photochemistry Reviews*, vol. 28, no. Supplement C, pp. 87-115, 2016.

55. Xinchen Wang, Kazuhiko Maeda, Arne Thomas, Kazuhiro Takanabe, Gang Xin, Johan M. Carlsson, Kazunari Domen and Markus Antonietti, "A metal-free polymeric photocatalyst for hydrogen production from water under visible light," *Nature Materials*, vol. 8, pp. 76, 2008.

56. Xian Liu, Huimin Yang, Xuan Jian, Hongyan Dai, Xiuli Song and Zhenhai Liang, "Constructing a novel GQDs/PANI/g-C_3N_4 ternary heterostructure with enhanced photoelectrocatalytic performance," *Materials Letters*, vol. 209, no. Supplement C, pp. 247-250, 2017.

57. Fenfen Liang and Yongfa Zhu, "Enhancement of mineralization ability for phenol via synergetic effect of photoelectrocatalysis of g-C3N4 film," *Applied Catalysis B: Environmental*, vol. 180, no. Supplement C, pp. 324-329, 2016.

58. Mingshan Zhu, Chunyang Zhai, Mingjuan Sun, Yufang Hu, Bo Yan and Yukou Du, "Ultrathin graphitic C_3N_4 nanosheet as a promising visible-light-activated support for boosting photoelectrocatalytic methanol oxidation," *Applied Catalysis B: Environmental*, vol. 203, no. Supplement C, pp. 108-115, 2017.

59. Yi Zhang, Qiang Wang, Jiani Lu, Qi Wang and Yanqing Cong, "Synergistic photoelectrochemical reduction of Cr(VI) and oxidation of organic pollutants by g-C_3N_4/TiO_2-NTs electrodes," *Chemosphere*, vol. 162, no. Supplement C, pp. 55-63, 2016.

Appendix L New insight into BiOX (X = Cl, Br, and I) hierarchical microspheres in photocatalysis

Xiangchao Meng and Zisheng Zhang

Materials Letters, 225, 152-156, 2018

Abstract:

BiOX (X = Cl, Br and I) hierarchical microspheres were prepared using a solvothermal method. As a popular group of photocatalysts, adsorption capacity of BiOX with the special morphology was rarely reported. Its adsorption capacity was greatly improved with a specific surface area of as high as ~23 mg/g. Also, from the crystal structure analysis, the exposed 102 facets are primary for BiOX microspheres (001 facets for BiOX nanosheets), which is in favor of enhancing photocatalytic activity. In this work, we have also addressed the importance to consider the color change of BiOX when applied in photocatalysis, as oxygen/ halogen vacancies may be generated. This work sheds a light on reconsidering the role of adsorption as well as the stability (reusability) of BiOX in photocatalysis is significant.

L.1 Introduction

Bismuth based photocatalysis has extensively reported and studied [1]. BiOX (X = Cl, Br and I) hierarchical architectures were reported as promising photocatalysts in oxidizing organics in water [2-5]. The layered structure of BiOX was composed of $[Bi_2O_2]^{2+}$ slabs embedded in double slabs of X^+. For this special structure, the related atoms and orbitals possess enough space to polarize. Subsequently, the formation of induced dipole could contribute to the effective separation of photon-generated electrons and holes. Also, BiOX can be easily prepared using hydrothermal or solvothermal methods with different

morphologies [6, 7]. For the advanced three dimensional hierarchical architectures with high specific surface area, however, the high adsorption capacity was neglected for most reported works. The hierarchical microspheres is also in favor of enhancing the adsorption capacity of the illuminated irradiation.

In this work, we have fabricated BiOX hierarchical microspheres, tested their adsorption capacity of organics in water. Also, the light harvesting capacity was also investigated. It should be noted that the low bond energy and long bond length of Bi-O in the $[Bi_2O_2]^{2+}$ slabs [8], lead to the production of oxygen vacancies. This results suggest the stability of pure BiOX may be a significant issue when they are applied in photocatalysis. The production of vacancies may perform dual character. We suggest the stability of BiOX in photocatalysis should be addressed and considered in future works.

L.2 Experimental

L.2.1 Preparation of BiOX microspheres

BiOX microspheres were prepared using a solvothermal method. In a typical procedure, 2 mmol of $Bi(NO_3)_3 \cdot 5H_2O$ and 2 mmol of KX (X = Cl, Br and I) were separately dispersed in 15 mL ethylene glycol (EG). After that, the two suspensions were mixed together with magnetically stirring for 30 min. The mixture was then transferred into a 50-mL Teflon-line autoclave, heated at 120°C for 12 h. After the autoclave cooled down to room temperature, the precipitates were filtered out, washed with ethanol and DDW, and dried at 60°C for 12 before collected. As prepared samples were labelled as BiOCl-S, BiOBr-S and BiOI-S. For comparison, BiOX nanoplates were also prepared using a hydrothermal method with pure water as solvent instead. As prepared samples were labelled as BiOCl-H, BiOBr-H and BiOI-H.

L.2.2 Characterizations

XRD tests were performed on a Rigaku Ultima IV Diffractometer. Morphologies were investigated using a scanning electron microscopy (SEM). The specific surface area, pore volume and average pore size were obtained from N_2 sorption isotherms at 77 K, using automatic adsorption apparatus and measurement systems (ASAP 2020, Micromeritics and Nova 4200E, Quantachrome). A thermos Evolution 300 spectrophotometer was applied to

measure the optical properties of samples through ultraviolet-visible diffuse reflectance spectra (DRS).

L.2.3 Adsorption tests

Adsorption capacity was tested by adsorbing RhB in dark. The temperature was maintained at 20°C. In each test, 0.01 g of catalysts were added in 100 mL RhB solution with an initial concentration of 10 mg/L. The suspension was magnetically stirred, and 1 mL solution was drawn and separation using a centrifuge, the supernate was analyzed using a UV-Vis spectrometer.

L.3 Results and discussions

L.3.1 Morphologies and crystal structures

Morphologies of prepared samples were investigated using SEM, as shown in Figure L.1. Hierarchical microspheres with different sizes were successfully fabricated using the solvothermal method for all BiOX samples. The sizes of the microspheres vary from 1μm to 10 μm. The microspheres were composed of flakes, and slit-like pores were formed. In comparison, the BiOX samples were also prepared using the hydrothermal method, and can be observed with plate-like sheets with width of 1 - 5μm and thickness of less than 100 nm. This phenomenon may be resulted from the different growth direction. To explore the crystal structure of prepared samples, XRD patterns were recorded and depicted in Fig. L.2. All BiOX samples were with a tetragonal structure and attributed to the space group of P4/nmm(129). Lattice parameters were calculated and shown in Table L.1. It can be found lattice parameters for hydrothermally and solvothermally treated BiOX samples were similar. However, the relative intensity between different peaks in the XRD patterns was different, especially the relative intensity of peaks for 001 and 102 facets which has been calculated and shown in Table L.1. It can be found relative intensity ($I_{[001]}/I_{[102]}$) was higher for hydrothermally prepared BiOX, compared to solvothermally prepared samples. The higher ratio of exposed facets of 102 has following merits: narrower band gap (~2.22 eV for 001 facets and ~1.44 eV for 102 facets), higher separation rate of photogenerated charge carriers and stronger oxidizability as for the lower potential position of the valence band for 102 facets [9]. All of these advantages suggest BiOX prepared with solvothermal method may be with higher photocatalytic activity in oxidizing organics in water.

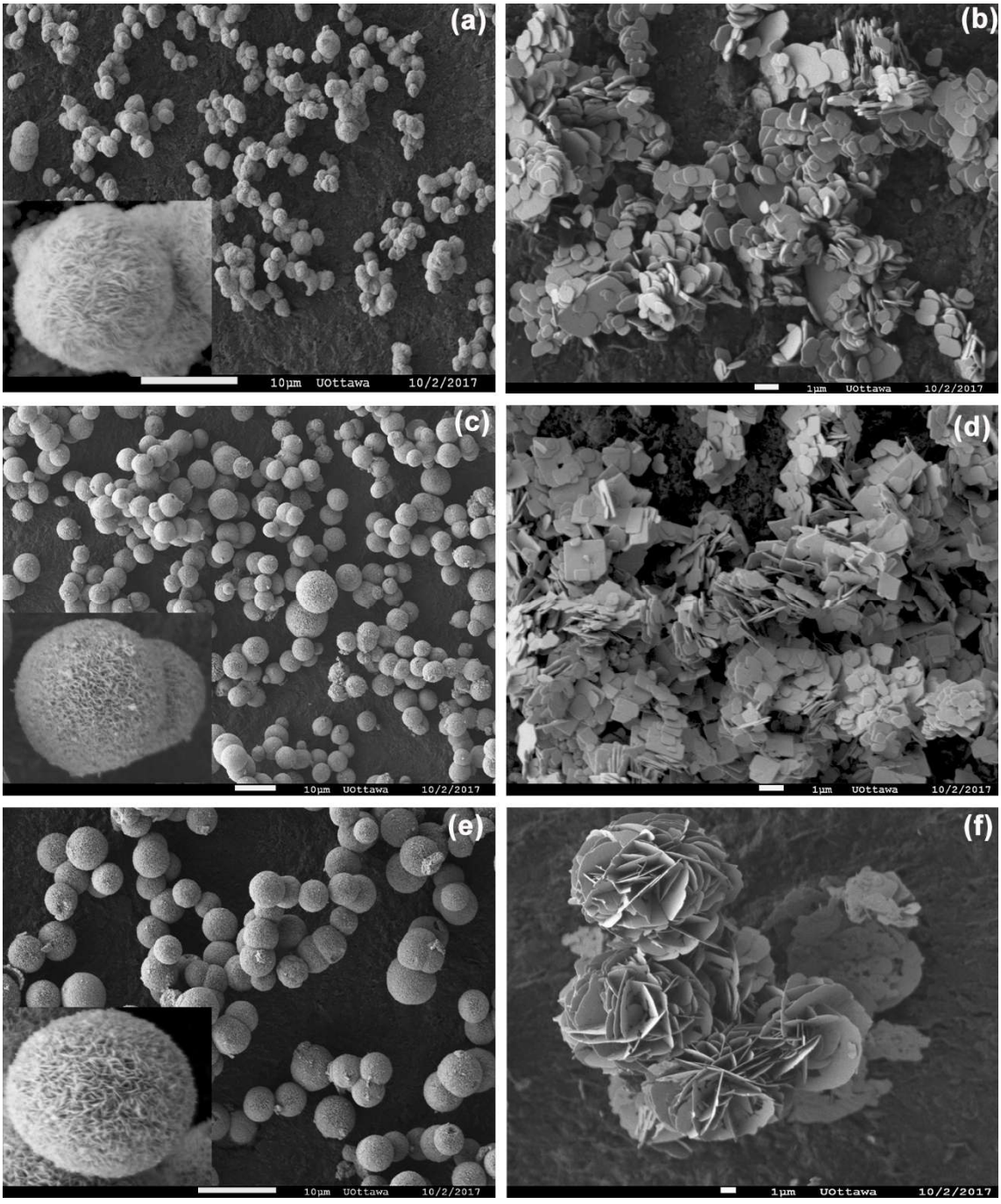


Figure L.1 SEM images of (a) BiOCl-S, (b) BiOCl-H, (c) BiOBr-S, (d) BiOBr-H, (e) BiOI-S and (f) BiOI-H.

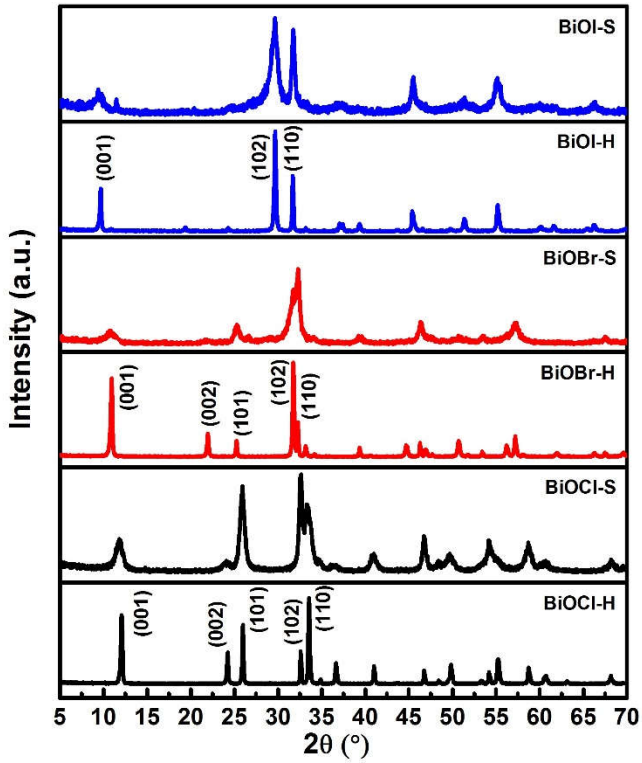
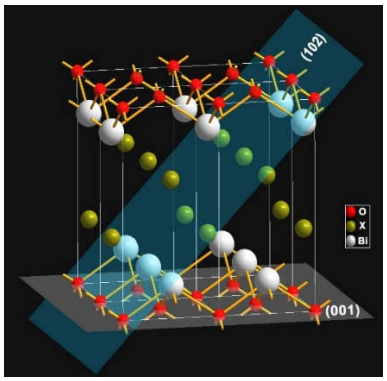


Figure L.2 XRD patterns of prepared samples.

Table L.1 Crystal parameters calculated from XRD patterns and specific surface area for prepared samples.

Composites	Lattice parameters (Å)			$\frac{I001}{I102}$	$\frac{X_{c,BiOX-H}}{X_{c,BiOX-S}}$	Unit cell (2X2X1)	S_{BET} (m^2/g)
	a	*b*	*c*				
BiOCl-H	3.89	3.89	7.35	2.10	1.20		11.99
BiOCl-S	3.85	3.85	7.36	0.34			29.87
BiOBr-H	3.92	3.92	8.10	0.83	1.30		21.18
BiOBr-S	3.91	3.91	7.97	0.26			26.15
BiOI-H	3.99	3.99	9.16	0.43	1.50		29.75
BiOI-S	4.00	4.00	9.10	0.27			54.91

L.3.2 Adsorption

The adsorption capacity of BiOX samples was measured, and N_2 sorption isotherms were obtained and shown in Fig. 3.2a. It can be found the quantity of adsorbed N_2 is higher for solvothermally prepared BiOX, compared to hydrothermally prepared ones. All isotherms are attributed to Type II physisorption isotherms, and a hysteresis loop was observed for each BiOX-S samples which is attributed to a H3 type [10]. It should be noted the H3-type hysteresis loop may be due to the aggregations of the plate-like particles giving rising to slit-like shaped pores. This phenomenon agrees well with the morphology observed in Fig. L.1. The pore size distributions were shown in Fig. L.4, as no obvious pore was observed for BiOX-H samples, and mesopores and macropores were observed for BiOX-S samples, which also agree well with the morphology as shown in Fig. L.1. To quantitively investigate the specific surface area, Brunauer, Emmett and Teller (BET) surface area was estimated and shown in Tables L.1 and L.2. It can be found the specific surface area of BiOX-S is higher than that of BiOX-H. Same results were obtained for both the pore volumes and pore sizes. In fact, no pore was formed for hydrothermally prepared BiOX. All discussions above indicate solvothermally prepared BiOX samples with higher specific surface area and higher adsorption capacity, compared to hydrothermally prepared BiOX samples. To quantitively measure the adsorption capacity of BiOX microspheres (BiOX-S samples), the adsorption of RhB was tested, and adsorption isotherms were shown in Fig. L.3b-d. The equilibrium adsorption capacity for BiOCl, BiOBr and BiOI, was calculated as 13.53, 12.82 and 22.99 $mg_{RhB}/g_{catalyst}$, respectively. This result indicates the adsorption capacity of BiOX microspheres is directly dependent on their specific surface areas. Three isotherm models were applied to simulate the adsorption process. The parameters and correlation coefficients calculated for the models were shown in Table L.3. It can be found Langmuir isotherm fitted the best. It should be noted the adsorption capacity of organics on BiOX microspheres is impressive, and rival the photocatalytic activity of BiOX sheets. As reported [11], O atoms on the surface are in favor of absorbing positive dyes (*e.g.* RhB). As shown in Table L.1, 001 plane is composed of five O atoms, and 102 plane is composed of two O atoms. It further suggests the increased adsorption capacity of RhB on BiOX microspheres may be primarily resulted from the increased specific surface area.

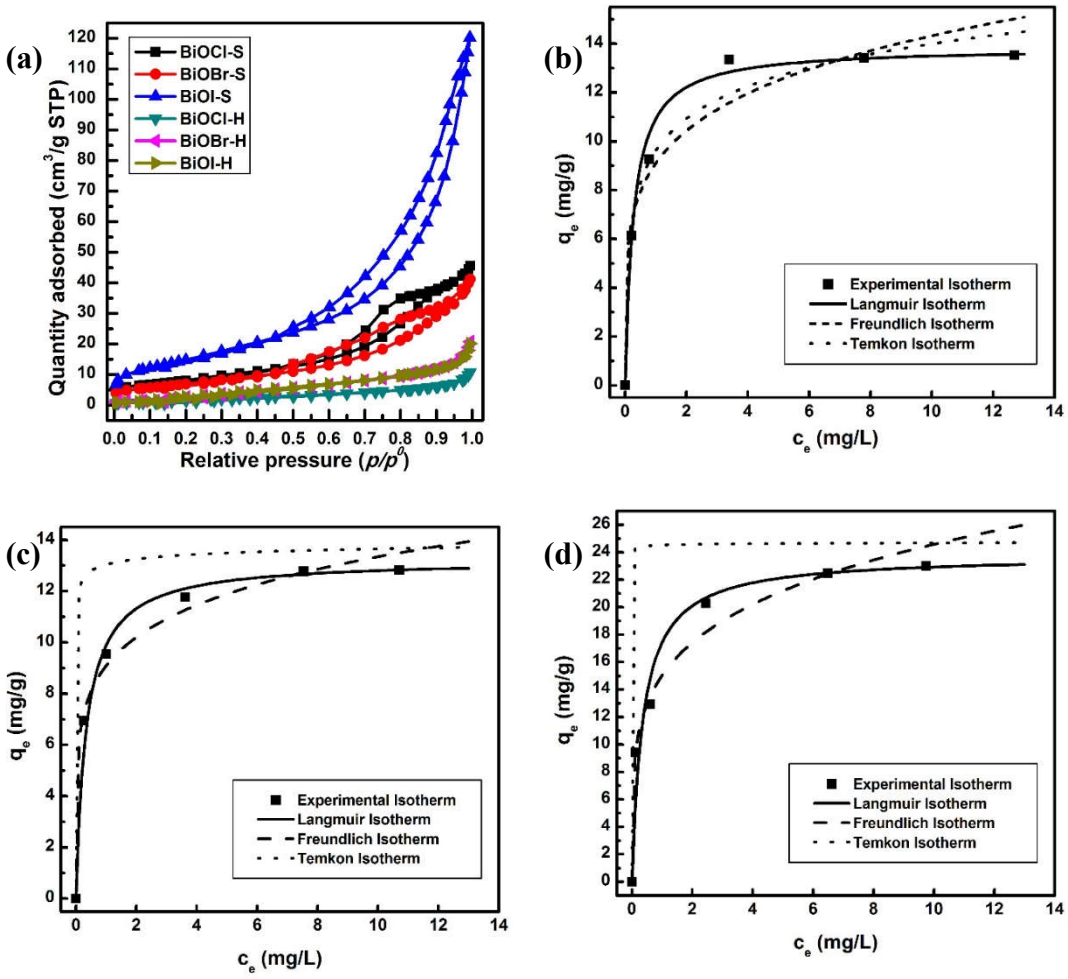


Figure L.3 N_2 sorption isotherms (a), and adsorption isotherms for RhB adsorption over BiOCl-S (b), BiOBr-S (c) and BiOI-S (d).

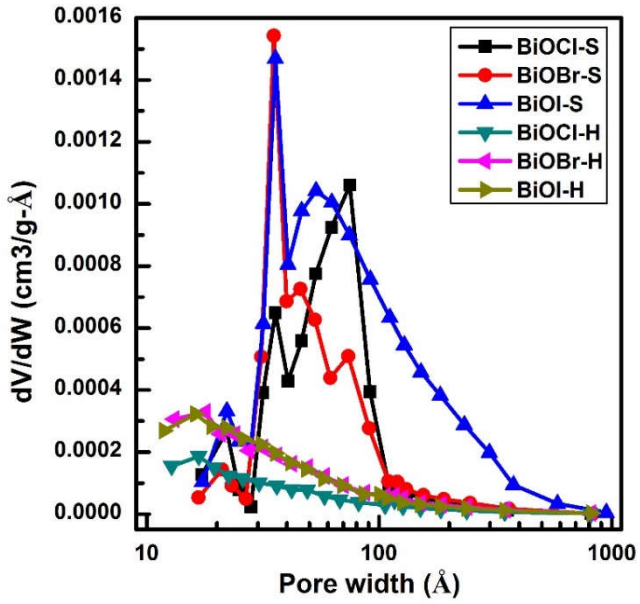


Figure L.4 Pore size distribution of BiOX samples

Table L.2 Pore volume, and average pore size of BiOX samples.

Adsorbents	Pore volume (cm^3/g)	Average pore size (nm)
BiOCl-H	0.017	6.48
BiOCl-S	0.071	7.33
BiOBr-H	0.032	6.47
BiOBr-S	0.064	7.17
BiOI-H	0.031	6.08
BiOI-S	0.187	10.32

Table L.3 Fitting results for adsorption isotherms of RhB over BiOX samples.

Adsorbent	Langmuir model			Freundlich model			Temkon model		
	K_L	a_L	R^2	K_F	n	R^2	A	B	R^2
BiOCl-S	51.813	3.741	0.9997	9.105	5.081	0.9100	157.788	1.900	0.9288
BiOBr-S	39.216	2.965	0.9996	9.091	6.006	0.9685	318.244	1.625	0.9866
BiOI-S	63.359	2.752	0.9991	15.024	4.679	0.9714	127.925	3.305	0.9698

L.3.3 Optical properties

The microsphere morphology is not only in favor of improving the adsorption capacity of organics in water, but also of potential to increase the absorbance capacity of illuminated photons. As shown in Fig. L.5a, red-shifts in band gap transition were found for BiOCl and BiOBr, which may be due to more 102 facets were exposed as shown in Fig. L.2. The light harvesting capacity was greatly improved for all BiOX samples with microsphere morphologies. This phenomenon may be interpreted by using the scheme as shown in Fig. L.5b. The hierarchical microspheres with slits formed by sheets. When the light illuminated on the plate, the reflected light was totally left for sheets, and may be further absorbed in slits. Hierarchical structure is of interest in fully use the irradiations. It would be beneficial in improving photocatalytic activity of BiOX. However, for BiOX-S samples after illumination for 1h, color of BiOCl and BiOBr samples was changed from white to grey and the color of BiOI was negatively changed (Fig. L.5d). As for the change in color, the light absorbance capacity was improved as shown in Fig. L.5c. This phenomenon may be due to the bond between Bi and O, and force between $[Bi_2O_2]$ slabs and halogen atoms were weak, and oxygen and halogen vacancies may be generated under light irradiation [12, 13]. This interesting phenomenon suggests: 1) pure BiOX may be unstable under light when implemented in photocatalysis, and 2) the production of vacancies may be in favor of narrowing the band gaps with impurity energy added within band gap [14]. As for the band gap of BiOCl is wide, with the formation of vacancies, the band gap may be suitable for visible light-driven photocatalysis. However, for BiOBr, when the band gap become

narrower, the separation efficiency of photogenerated charge carriers may be decreased, as the impurity band may also become recombination site for photogenerated charge carriers. And for BiOI, the band gap for pure BiOI is too narrow, and the photocatalytic activity may be further reduced with the production of vacancies. As BiOBr has been extensively studies and regarded as a promising candidate for visible light-driven photocatalysis, the change in the structure under light irradiation should be addressed, as it may be unstable and cannot the reused.

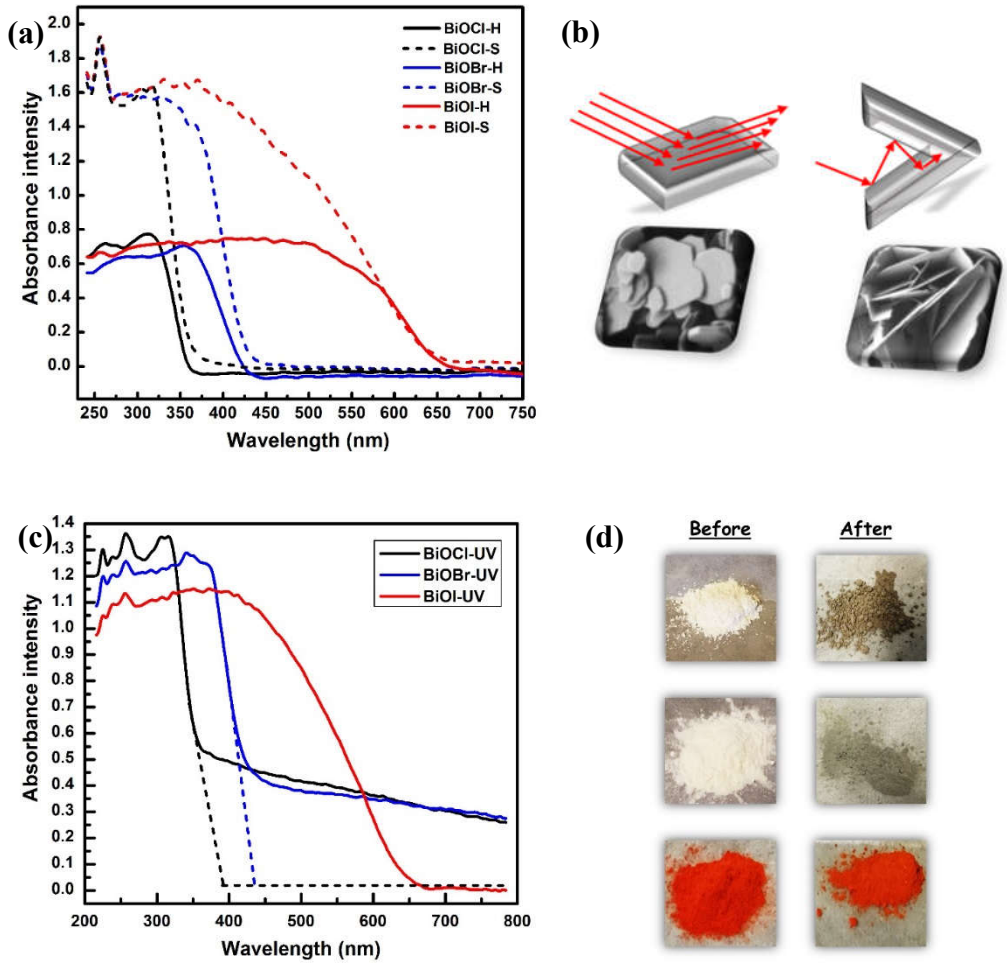


Figure L.5 (a) DRS spectra for BiOX samples, (b) scheme for the light propagation on plate and slit-like morphologies, (c) DRS spectra for BiOX after illumination under visible light (a 300-W halide tungsten projector bulb) for 1h, and (d) color of BiOX-S samples before and after illumination.

L.4 Conclusion

BiOX hierarchal microspheres were prepared with high specific surface area. The adsorption capacity of organics and the absorbance capacity of irradiation were greatly improved, both of which are in favor of increasing photocatalytic activity. Oxygen/ halogens vacancies may be generated under light on BiOX surfaces, it should be considered and addressed for future works.

References

1. Xiangchao Meng and Zisheng Zhang, "Bismuth-based Photocatalytic Semiconductors: Introduction, Challenges and Possible Approaches," *Journal of Molecular Catalysis A: Chemical*, vol. 423, pp. 533-549, 2016.

2. Xiaoyan Qin, Hefeng Cheng, Wenjun Wang, Baibiao Huang, Xiaoyang Zhang and Ying Dai, "Three dimensional BiOX (X=Cl, Br and I) hierarchical architectures: facile ionic liquid-assisted solvothermal synthesis and photocatalysis towards organic dye degradation," *Materials Letters*, vol. 100, no. Supplement C, pp. 285-288, 2013.

3. Yang Zhao, Xin Tan, Tao Yu and Shucong Wang, "SDS-assisted solvothermal synthesis of BiOBr microspheres with highly visible-light photocatalytic activity," *Materials Letters*, vol. 164, no. Supplement C, pp. 243-247, 2016.

4. Chao Xue, Jiale Xia, Ting Wang, Shishun Zhao, Guidong Yang, Bolun Yang, Yanzhu Dai and Guang Yang, "A facile and efficient solvothermal fabrication of three-dimensionally hierarchical BiOBr microspheres with exceptional photocatalytic activity," *Materials Letters*, vol. 133, no. Supplement C, pp. 274-277, 2014.

5. Hongwei Huang, Ke Xiao, Tierui Zhang, Fan Dong and Yihe Zhang, "Rational design on 3D hierarchical bismuth oxyiodides via in situ self-template phase transformation and phase-junction construction for optimizing photocatalysis against diverse contaminants," *Applied Catalysis B: Environmental*, vol. 203, pp. 879-888, 2017.

6. Xiangchao Meng, Zizhen Li, Jie Chen, Hongwei Xie and Zisheng Zhang, "Enhanced visible light-induced photocatalytic activity of surface-modified BiOBr with Pd nanoparticles," *Applied Surface Science*, vol. 433, no. Supplement C, pp. 76-87, 2018.

7. Ayla Ahmad, Xiangchao Meng, Nan Yun and Zisheng Zhang, "Preparation of Hierarchical BiOBr Microspheres for Visible Light-Induced Photocatalytic Detoxification and Disinfection," *Journal of Nanomaterials*, vol. 2016, pp. 10, 2016.

8. Wen Lai Huang, "Electronic structures and optical properties of BiOX (X = F, Cl, Br, I) via DFT calculations," *Journal of Computational Chemistry*, vol. 30, no. 12, pp. 1882-1891, 2009.

9. Haijun Zhang, Yuxiao Yang, Zhen Zhou, Yaping Zhao and Lu Liu, "Enhanced Photocatalytic Properties in BiOBr Nanosheets with Dominantly Exposed (102) Facets," *The Journal of Physical Chemistry C*, vol. 118, no. 26, pp. 14662-14669, 2014.

10. Xiangchao Meng and Zisheng Zhang, "Bi_2MoO_6 co-modified by reduced graphene oxide and palladium (Pd^{2+} and Pd^0) with enhanced photocatalytic decomposition of phenol," *Applied Catalysis B: Environmental*, vol. 209, pp. 383-393, 2017.

11. Hongwei Huang, Ranran Cao, Shixin Yu, Kang Xu, Weichang Hao, Yonggang Wang, Fan Dong, Tierui Zhang and Yihe Zhang, "Single-unit-cell layer established Bi_2WO_6 3D hierarchical architectures: Efficient adsorption, photocatalysis and dye-sensitized photoelectrochemical performance," *Applied Catalysis B: Environmental*, vol. 219, pp. 526-537, 2017.

12. Min Li, Yihe Zhang, Xiaowei Li, Yonggang Wang, Fan Dong, Liqun Ye, Shixin Yu and Hongwei Huang, "Nature-Derived Approach to Oxygen and Chlorine Dual-Vacancies for Efficient Photocatalysis and Photoelectrochemistry," *ACS Sustainable Chemistry & Engineering*, vol. 6, no. 2, pp. 2395-2406, 2018.

13. Jiushan Cheng, Cong Wang, Yinfang Cui, Ying Sun, Ying Zuo and Tianming Wang, "Large improvement of visible-light-driven photocatalytic property in AgCl nanoparticles modified black BiOCl microsphere," *Materials Letters*, vol. 127, no. Supplement C, pp. 28-31, 2014.

14. Hao Li, Jian Shang, Zhihui Ai and Lizhi Zhang, "Efficient Visible Light Nitrogen Fixation with BiOBr Nanosheets of Oxygen Vacancies on the Exposed {001} Facets," *Journal of the American Chemical Society*, vol. 137, no. 19, pp. 6393-6399, 2015.

Appendix M Recent advances of computational photocatalysis: a review

Xiangchao Meng, Nan Yun and Zisheng Zhang

Abstract

Photocatalysis has been extensively developed in recent years. Along with the development of computational software and hardware technology, the idea of designing a novel material (such as photocatalytic materials) starting from computation methods has been becoming more and more popular. The combination of computational methods and material design is known as material simulation. The aforetime hindrance of material simulation is to solve the Schrödinger equation. Aiming to overcome it, a large variety of approaches have been implemented and a fundamental package has been developed. Based on the simulated results, most of critical parameters in photocatalysis such as band gap, optical property, recombination of photogenerated charge carriers, as well as the adsorption and its mechanism can be investigated. Moreover, other computation methods relevant to photocatalysis were also herein introduced, primarily including the light absorption intensity distribution in a photoreactor, mass transfer, adsorption, desorption and evaluation of photocatalytic activity. Computation methods applied to photocatalysis using various fundamental and equations are reviewed, with an emphasis on the materials simulation.

M.1 Introduction

Photocatalysis, as one of the advanced oxidation processes (AOPs), has been extensively developed since 1972 [1]. Applications of this advanced technique have been implemented into various areas such as water splitting [2], wastewater/water treatment [3, 4], air purification [5] and bacteria inactivation [6]. Among reported works related to

photocatalysis, it can be divided into the following aspects: fundamental studies on photocatalysis, developments of novel photocatalysts, preparations of visible light-response photocatalysts, photoreactor design and scaling up.

The mechanism of photocatalysis is initiated when irradiations with suitable energy are absorbed by a photocatalyst. The electrons on the valence band (VB) of a material are activated by the irradiation and jump to the conduction band (CB) with positive holes left behind. The photogenerated charge carriers then travel to the surface from the bulk and can react with either adsorbed water, dissolved oxygen or organics. In turn, strong oxidative species, mainly free radicals, are produced, which can react with these adsorbed species [7]. A photocatalytic process, from an engineering point of view, is composed of irradiation transfer, mass transfer, adsorption, desorption and photocatalytic reactions. The embedded calculation can be summarized as follows:

i) Irradiation: irradiation density distribution
ii) Media: mass transfer of the organics or dissolved oxygen from the bulk to the photocatalyst surface; adsorption/desorption of water, organics, intermediates or dissolved oxygen on the surface of a photocatalyst.
iii) Photocatalysts: material simulation via solving Schrödinger equation and exploration of various physiochemical properties based on the calculated results
iv) Photocatalytic activity evaluation.

In this review, the above-mentioned calculations will be concluded and introduced in detail based on reported works.

M.2 Modelling of light absorption in photoreactors

The radiation transport equation (RTE) was well established and has been widely applied since 1960 [8]. This formulation was used in the design of a furnace and the characterization of solar irradiation. It also has been used for modelling the light intensity distribution in a photoreactor [9, 10]. The RTE, after making a radiation balance across a thin slab and substituting appropriate constitutive relations [11], can be expressed as follows (Equation 1):

$$\frac{dI_v(s,\Omega)}{ds} = \overbrace{-\kappa_v I_v(s,\Omega)}^{\text{Absorption}} - \overbrace{\sigma_v I_v(s,\Omega)}^{\text{Out-scattering}} + \overbrace{\frac{1}{4\pi}\sigma_v \int_{4\pi} p(\Omega' \to \Omega) I_v(s,\Omega') d\Omega'}^{\text{In-scattering}} \qquad \textbf{Equation 11}$$

where $I_v(s, \Omega)$ represents the monochromatic radiation intensity in the direction Ω along the path s, κ_v and σ_v represent coefficients of absorption and out-scattering, respectively, and $p(\Omega' \rightarrow \Omega)$ is a phase function of the in-scattering of incident radiation to an element from other directions (Ω'). Equation 1 can be interpreted as the change in the radiation intensity during travelling, primarily caused by three ways: loss by absorption, loss by out scattering and contribution by in-scattering from fluxes in all other directions.

The incident intensity at any point from all directions can be expressed as follows (Equation 2):

$$G_v(s) = \int_{\Omega=0}^{\Omega=4\pi} I_v(s,\Omega)\, d\Omega \qquad \textbf{Equation 12}$$

And the local volumetric rate of energy absorption (LVREA) at any point is given by (Equation 3):

$$E_{l,v}(s) = \kappa_v G_v(s) \qquad \textbf{Equation 13}$$

For the calculation of absorption and scattering coefficients, it is difficult to conceive a theoretical approach. Alternatively, experimental measurements may be adopted. However, for a slurry system, absorption and scattering are concomitant phenomena, and only the extinction coefficient ($\beta_v = \kappa_v + \sigma_v$) can be measured using a conventional spectrometer [12]. Cassano *et al.* reported on the measurement of scattering coefficient using a integrating sphere as shown in Fig. M.1 [13]. The results for TiO_2 (Anatase, Aldrich) were experimentally tested and shown in Table M.1. They have also addressed that the scattering coefficient is always a very significant part of the extinction coefficient, which cannot be neglected under normal conditions in a photocatalytic system [12].

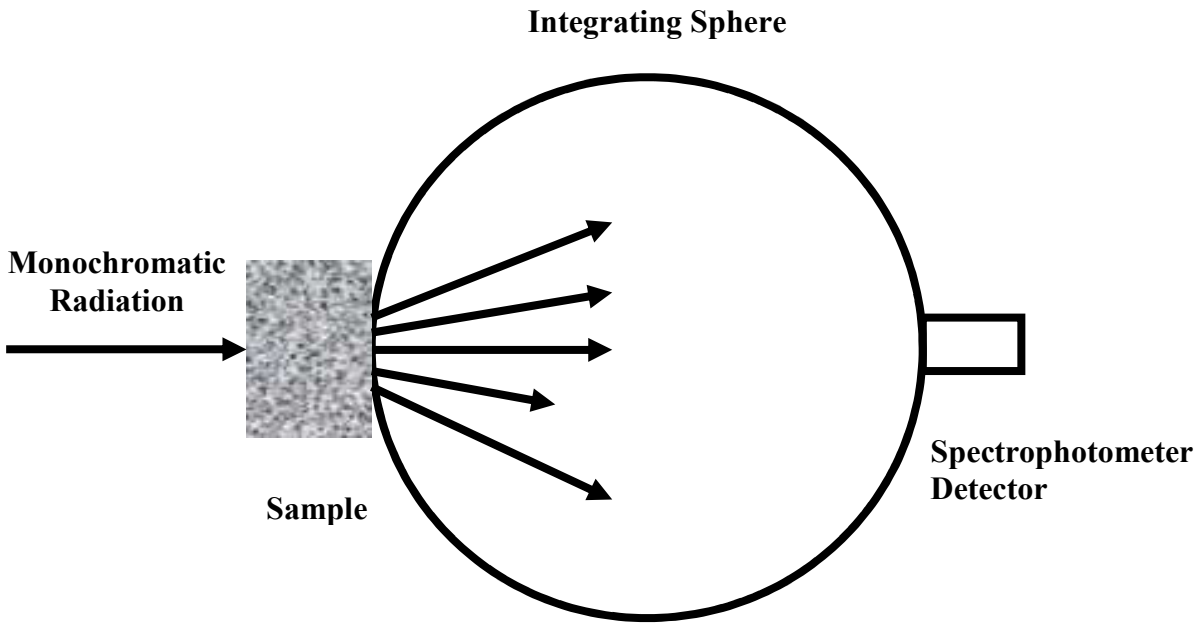


Figure M.1 Sample detector system for measurement of the absorption coefficient (Adapted from [13], copyright 1995, Elsevier).

Table M.1 Absorption and Scattering coefficients of TiO_2

λ (nm)	κ_v (cm^2/g)	σ_v (cm^2/g)
295	4206	33795
305	4224	34152
315	4543	33952
325	4570	34377
335	4524	35386
345	4283	36414
355	3432	38409
365	1469	41895
375	182	43380
390	0	44782
405	0	45784

To solve the phase function, the type of the scattering is supposed to be considered. Specifically, for isotropic scattering the phase function parameter was equal to a value of

unity. For anisotropic scattering, the phase function depended on the specific photocatalytic system. The widest use was given by Fiveland [14] as follows:

$$p\left(\Omega \to \Omega'\right) = 1 + a\cos\varphi \qquad \textit{Equation 14}$$

where a is equal to -1 when scattering is 100% backward, +1 when scattering is 100% forward and 0 when scattering is isotropic; φ represents the scattering angle.

The RTE may be used to simulate light distribution in a photoreactor. The light energy distribution in a photoreactor depends on various factors, namely, i) lamp type, ii) geometry between lamp and photoreactor, iii) optical properties of medium, and iv) property of reactor materials. The light distribution in an annular heterogeneous photocatalytic reactor, which is a widely used photoreactor, has been simulated and reported [11, 15-18]. As shown in Fig. M.2, it can be found for a system with a relatively low catalyst dosage amount (< 0.05 g/L), the light energy distribution was significantly influenced by the wall reflectivity, while the wall reflectivity negligibly influenced the light energy distribution in the system with high catalyst loading amount. Also, the LVREA was greatly increased with increasing catalyst loading amount, until a point was reached after which it remains invariant with further increase. At this point, it will yield a highest radiation absorption intensity. It should be noted that the photocatalytic activity depends on not only the optical properties but also properties such as the adsorption capacity of target organic models and solution pH. As such, the optimal amount of catalyst loading may not be predicted only based on radiation absorption. Light intensity distribution in photoreactors with multi-lamps was also simulated and reported [19, 20]. Rigorous modelling of the radiation energy distribution in a flat-plate photoreactor (Fig. M.3) was carried out by Brandi *et al.* [21, 22]. Two UV lamps with parabolic reflectors were used to irradiate the suspension. The idealized boundary conditions in solving RTE were not used, as these two reactor surface may be considered from the following aspects: i) absorption, reflection and refraction properties of the front glass walls, and ii) the fouling of photocatalysts on the surface of interior side of the glass. For simplifying the computation in this rigorous modelling, net-radiation method with the assumption of absorption and multipole reflections was applied [23]. Results showed that with an increase of the loading amount of photocatalysts in the

flat-plate reactor, both the radiation flux leaving the reactor and backward flux were significantly decreased; when the catalysts loading amount increased to a specific amount (depending on the type of the catalysts), the radiation flux leaving the reactor was almost equal to zero and the reflection effects by the back wall have no significance; and fouling should be considered for the reactive system with high catalysts loading. Other approaches to model radiation energy distribution in other types of photoreactors such as rotating disc reactor [24], corrugated-plate reactor [25, 26], flat fluidized reactor [10, 27] and thin-film reactor [28] were also reported. For a photoreactor under artificial light or solar radiation (the most attractive application from the economical viewpoint), Alfano *et al.* had comprehensively reviewed [29]. It should be noted when a photoreactor applied under solar light, a light concentrating system may be employed. In Fig. M.4, a parabolic trough reactor (PTR) has been widely applied, and a PTR concentrates the direct rays of the photocatalytically active UV part of solar spectrum by a factor of 20-50 [29]. It is essential to model the radiation distribution in a photocatalytic reactor, especially for the design and optimization of a reactor, as the photocatalytic activity is significantly influenced by the local volumetric rate of photon absorption.

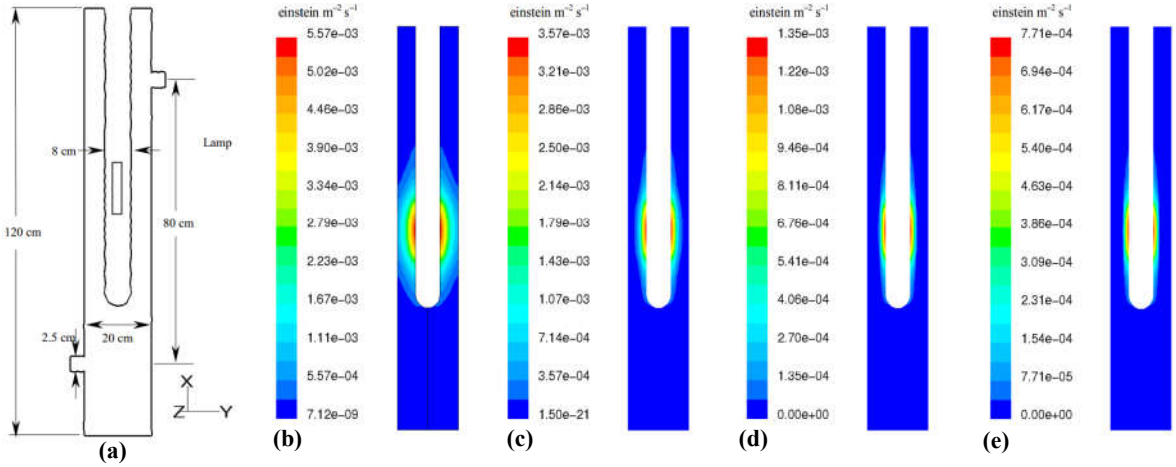


Figure M.2 (a) Geometry of the annular photoreactor, and simulated profiles of incident radiation with high optical density: (a) diactinic medium ($\kappa = \sigma = 0\ m^{-1}$), and catalysts dosage amount = 0.10 ($\kappa = 28\ m^{-1}$, $\sigma = 360\ m^{-1}$), 0.50 ($\kappa = 140\ m^{-1}$, $\sigma = 1800\ m^{-1}$), and 1.0 ($\kappa = 280\ m^{-1}$, $\sigma = 3600\ m^{-1}$) g/L in (b), (c) and (d), respectively. (Adapted from [11], Copyright 2014 AIChE journal)

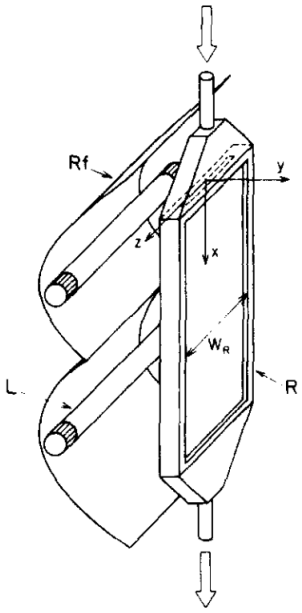


Figure M.3 Geometry of the flat plate photocatalytic reactor. (Adapted from [21, 22], copyright 1996, 1999, Elsevier)

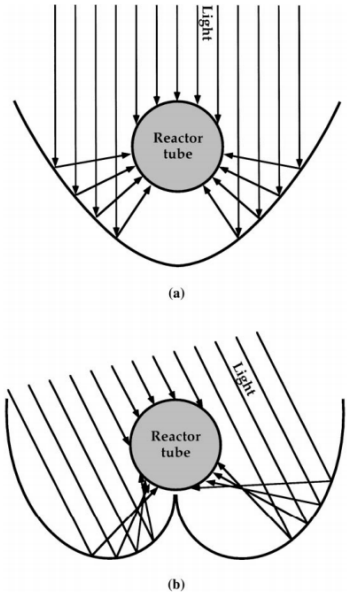


Figure M.4 Geometric profile of (a)a parabolic trough reactor (PTR) and (b) a compound parabolic collecting reactor (Adapted from [29], copyright 2000, Elsevier).

M.3 Mass transfer and reaction kinetics

A photocatalytic process is conducted with diverse mass transfer options, mainly including: i) target organics and photocatalytically produced intermediates adsorbed on the surface and internal pores of a photocatalyst, ii) oxygen dissolved in the solution and further transferred to the surface and internal pores of a photocatalyst, iii) oxidation products (i.e. intermediates and final degraded products) desorbed from the surface to the bulk solution and iv) photo-generated oxidative species such as H_2O_2 [30] desorbed from the surface of a photocatalyst (Fig. M.5). These mass transfer processes can be classified into two categories based on where they take place, namely internal and external mass transfer.

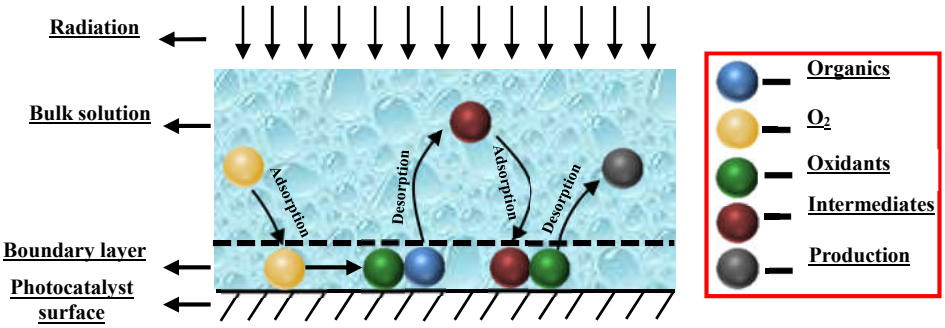


Figure M.5 Mass transfer of a photocatalytic process.

For external mass transfer, the rate ($r_{external}$) can be expressed by Equation 5 based on the two-film model [31]:

$$r_{external} = k_{external}\left(c_{bulk} - c_{surface}\right) \qquad \textit{Equation 15}$$

where $k_{external}$, c_{bulk} and c_s represent external mass transfer coefficient, concentration in the bulk and concentration on the surface of a catalyst, respectively. In Equation 5, the coefficient can be experimentally determined, which is related to the Reynolds number [32, 33] as shown in Equation 6:

$$k_{external}\left(\text{in m/s}\right) = 3.49\times10^{-7}\times\text{Re}^{0.77} \qquad \textit{Equation 16}$$

It can be deduced that the coefficient increases with the turbulence of the reactive solution. A well-stirred system generally has a high rate of external mass transfer. In a suspended system, i.e. for small catalyst particles with a high specific surface area, it facilitates the external mass transfer [34]. However, the apparent drawback for a suspended reactor is catalyst separation; small particles and catalysts in nano-size cannot be separated easily via conventional methods. This phenomenon may increase the operating expenses for using this technique. It should also be mentioned that a photoreactor may use air or O_2 bubbling to maintain the dissolved O_2 saturated in the system and enhance the turbulence of the reactive system, and the photocatalytic degradation of phenol was improved by 10.6% and 18.1% with air and O_2 bubbling, respectively [35-37]. In a bubbling photocatalytic reactor, external mass transfer of O_2 from the bubble to the bulk solution and further to the surface of a catalyst should be taken into consideration [38]. And mass transfer coefficient (k_L) between the O_2 bubbles and water is significantly influenced by the bubble diameter. Specifically, when bubbles with diameters smaller than 2 mm, the k_L value decreases with decreasing the bubble size. The value of k_L is also influenced by other factors, such as bubbling velocity, reactor geometry and bubble spargers, which have been comprehensively reviewed [38].

For internal mass transfer (diffusion) in photocatalysis, it is more significant in an immobilized reactor compared to a suspended system, and mainly depends on the porosity of a photocatalyst. Since internal diffusion is composed of a variety of parameters such as the pore dimensions and the molecular diffusion coefficient, it cannot be directly calculated. Instead, an indirect approach was proposed via the surface reaction rate using Weisz-Prater modulus (φ') as follows [39],

$$\varphi' = \frac{r' d_L^2 \tau}{D \varepsilon c^*} \qquad \textbf{Equation 17}$$

where r' is the reaction rate per unit of catalyst, d_L is the characteristic dimension of the deposit, τ is the tortuosity of the catalyst, D is the diffusion coefficient, ε is the porosity of the catalysts, and c^* is the concentration at the interface [40]. It should be noted the internal mass transfer should be considered only when $\varphi' > 1$.

For a well-stirred reactor, both external and internal mass transfer may be assumed to be negligible. Photocatalysis is a first-order reaction for a dilute solution system and zero-order reaction for a concentrated solution system. Redox reactions in a photocatalytic process occur primarily at the catalyst surface. Also, trapping of electrons as well as holes also requires the adsorption of oxygen and water. Therefore, adsorption is one of the critical processes to determine the photocatalytic reaction rate. On the basis of Langmuir adsorption-desorption isotherm, the kinetics of a single-component photocatalytic process may be described using the Langmuir-Hinshelwood (L-H) model (Equation 8) [41].

$$r = -\frac{dc}{dt} = k\theta = \frac{kKc}{1+Kc} \qquad \textbf{Equation 18}$$

where r, c, t, k, θ and K represent reaction rate, concentration of phenol, time, reaction rate constant, ratio of adsorbed phenol and adsorption constant, respectively. $1 + Kc$ may be assumed to equal to 1 for dilute solutions. Equation 8 can be then converted to Equation 9 as shown below,

$$-\frac{dc}{dt} = kKc = k'c \qquad \textbf{Equation 19}$$

where k' is the pseudo first-order reaction constant. By integrating Equation 9 from c_o at time 0 min to c_t at time t, Equation 10 can be obtained. To calculate the k' for each photocatalysis process, it may be applied via plotting $\ln(c_o/c_t)$ vs t, and the slope of the fitting line is the value of k' which is a significant parameter to evaluate the rate of a photocatalytic process.

$$\ln(\frac{c_o}{c_t}) = k't \qquad \textbf{Equation 20}$$

For applying L-H model to describe a photocatalytic process, influence of the radiation was neglected, which should be considered for the expression of the reaction kinetics tailoring for a photoreactor. Cassano *et al.* reported on developing reaction rate kinetics expression considering the radiation absorption by the catalytic particles, and also provide reaction kinetics expression for a flat photoreactor [42]. Cassano, Alfano *et al.* further explored the

reaction kinetics in gas phase [43]. They obtained the following results: 1) first-order kinetics with respect to the organic pollutants in water, 2) linear dependence with respect to the irradiation level, and 3) site-competitive kinetics for the dependence on the relative humidity. Li *et al.* have reported on photocatalytic oxidation kinetics of indoor air pollutants using CFD modeling with consideration of the radiation intensity at the catalyst surface (TiO_2 film was used for experimental tests) [44]. Marugán *et al.* have reported on the kinetics of the photocatalytic disinfection of *E. Coli* suspensions [45]. They found the efficiency of the disinfection process is significantly influenced by the chemical composition and concentration of the inorganic ions in the solution, except the adsorption property of the catalyst. Bahnemann *et al.* have comprehensively reviewed the parameters affecting the kinetics for a TiO_2-based photocatalytic process applied in water treatment [46]. Numerous kinetic studies were carried out for a photocatalytic process, however, only a few have considered to evaluate the kinetic parameters with the influence of the radiation intensity at the catalyst surface. To evaluate the affecting parameters for photocatalytic kinetics is necessary to efficiently improve a photocatalytic process and scale-up of photocatalytic reactors.

M.4 Computational methods for photocatalyst design

M.4.1 Principles

M.4.1.1 Development of approaches to solve Schrödinger equation

Based on the quantum mechanics description of the interaction between electrons and atomic nuclei, computational simulation applied in material science has been extensively explored not only in the fundamental study but also in advanced photocatalyst design [47]. The fundamental goal of material simulation is to solve the Schrödinger equation [48]. The time-independent Schrödinger equation is shown in Equation 11 when there are N electrons and M nuclei in the system, and the Hamiltonian operator, $\hat{H}$ can be expressed as shown in Equation 12 as follows:

$$\hat{H}\psi\left(x_1, x_2, ..., x_N, R_1, R_2, ..., R_M\right) = E\psi\left(x_1, x_2, ..., x_N, R_1, R_2, ..., R_M\right) \qquad \textit{Equation 21}$$

$$\hat{H} = \underbrace{-\frac{1}{2}\sum_{i=1}^{N}\nabla_i^2}_{\text{Momentum of electron}} \underbrace{-\frac{1}{2}\sum_{A=1}^{M}\frac{1}{M_A}\nabla_A^2}_{\text{Momentum of nuclei}} \underbrace{-\sum_{i=1}^{N}\sum_{A=1}^{M}\frac{Z_A}{r_{iA}}}_{\text{Coulomb potential between electrons}} \underbrace{+\sum_{i=1}^{N}\sum_{i<j}^{N}\frac{1}{r_{ij}}}_{\text{Repelling potential between electrons}} \underbrace{+\sum_{A=1}^{M}\sum_{A<B}^{M}\frac{Z_A Z_B}{R_{AB}}}_{\text{Repelling potential between nucleis}} \qquad \textbf{Equation 22}$$

where Ψ is a wave function where Hamiltonian operator acts, E is the energy state of the wave function, and x and R represent the coordinate of electron and nuclei. In the expression of Hamilton operator, five potentials are listed in the five terms on the right of Equation 12. It is difficult to directly solve the Schrödinger equation and assumptions are required. As the nuclear motion is much slower than electrons and can be considered to be fixed, Born-Oppenheimer (BO) approximation [49] is applied to separate the motion of atomic nuclei and electrons, and only the motion of electrons is taken into account in the calculation of the Hamilton operator as shown in Equation 13. Substituting $\hat{H}_{electron}$ in Equation 14 which is the electronic Eigen function, the ground-state energy of electron ($E_{electron}$) can be computed. Also, the total energy can be obtained through Equation 15.

$$\hat{H}_{\text{electron}} = -\frac{1}{2}\sum_{i=1}^{N}\nabla_i^2 - \sum_{i=1}^{N}\sum_{A=1}^{M}\frac{Z_A}{r_{iA}} + \sum_{i=1}^{N}\sum_{i<j}^{N}\frac{1}{r_{ij}} \qquad \textbf{Equation 23}$$

$$\hat{H}_{\text{electron}}\psi_{\text{electron}} = E_{\text{electron}}\psi_{\text{electron}} \qquad \textbf{Equation 24}$$

$$E_{\text{total}} = E_{\text{electron}} + E_{\text{nuclei}} = E_{\text{electron}} + \sum_{A=1}^{M}\sum_{A<B}^{M}\frac{Z_A Z_B}{R_{AB}} \qquad \textbf{Equation 25}$$

As for the interactions between electrons, for a system with more electrons it is still difficult to solve the Schrödinger equation with the assumption of BO approximation. Further simplifications are required. A very coarse assumption is to have no interactions between electrons. Then, the Hamilton operator can be simplified as shown in Equation 16 for a system with a single electron (Single-electron approximation). The calculated wave function (φ_i) from Equation 17 is a molecular orbit, and the calculated energy (ε_i) is an energy state. The next target is to compute the multi-electron function through the single-electron function.

$$\hat{H}_{\text{electron}} = -\frac{1}{2}\sum_{i=1}^{N}\nabla_i^2 - \sum_{i=1}^{N}\sum_{A=1}^{M}\frac{Z_A}{r_{iA}} \qquad \textit{Equation 26}$$

$$\hat{H}_{\text{electron}}\varphi_i = \varepsilon_i\varphi_i \qquad \textit{Equation 27}$$

Hartree method (HP) was used to calculate the multi-body wave function as shown in Equation 18. The total energy is equal to a sum of energy for every single electron (Equation 19). For a system with N electrons, Slater Determinant (SD), as shown in Equation 20, may be used to determine the wave function. It should be noted if there were two wave functions equal to each other, Ψ_{SD} would be equal to zero, which is impossible. And this result follows the Pauli Exclusion Principle.

$$\begin{cases} \psi_{HP} = \varphi_1 \times \varphi_2 \times ... \times \varphi_N & \textit{Equation 28} \\ E = \sum_{i=1}^{N}\varepsilon_i & \textit{Equation 29} \end{cases}$$

$$\psi_{SD} = \frac{1}{\sqrt{N!}}\begin{vmatrix} \varphi_1(x_1)\ \varphi_2(x_1)\ ...\ \varphi_N(x_1) \\ \varphi_1(x_2)\ \varphi_2(x_2)\ ...\ \varphi_N(x_2) \\ \\ \varphi_1(x_N)\ \varphi_2(x_N)\ ...\ \varphi_N(x_N) \end{vmatrix} = \left|\varphi_1,\ \varphi_2,\ ...\ \varphi_N\right\rangle \qquad \textit{Equation 30}$$

Hartree method assumes no interactions between electrons, which is feasible when considering a single electron while all the other electrons are considered as a mean field. In this case, the self-consistent field method (SCF) may be used for the calculation of Ψ_{SD} which is suggested by Fock; thus it is called Hartree-Fock (HF) approximation. The Hartree-Fock method is the fundamental method of quantum chemistry and significantly simplified the computation of the multi-body Schrödinger equation. However, the rigorous solution cannot be obtained by HF method, as the repelling potential between spin

antiparallel electrons as well as the relativity effect have not been taken into consideration. Approaches such as Configuration Interaction (CI) [50], Coupled-Cluster method (CC) [51], Møller-Plesset perturbation theory (MPx) [52, 53] based on the HF method have been developed, which are called post-HF methods. HF as well as post-HF methods significantly simplify the calculation of the Schrödinger equation. However, for large systems, the computation is still too complicated to implement in practice. Under this background, the density function theory has been developed to pursue high accuracy and quick computation speed.

M.4.1.2 Development of Density Function Theory (DFT)

Compared with HP method to solve the Schrödinger equation, the fundamental of DFT is that basic physical properties in a system is merely a function of electron density. The electron density can be defined as the probability of an electron occupying an infinitesimal element of space surrounding any given point. And the electron density of a system with N electrons can be expressed as follows (Equation 21):

$$\rho\left(r\right) = N\int \quad \int\left|\psi\left(x_1, x_2, \quad x_N\right)\right|^2 d\,x_1 d\,x_2 \quad x_N \qquad \textit{Equation 31}$$
$$x \equiv r, s$$

where r and s represent spatial and spin coordinates. The following properties for electron density should be noted: i) when the distance is infinity, the electron density is equal to zero and ii) the integration of electron density on all positions is equal to the number of the electrons in the system (N) (Equation 22). Also the electron density can be experimentally detected using X-ray diffraction technique.

$$\begin{cases} \rho\left(r \to \infty\right) = 0 \\ \int \rho\left(r\right) dr = N \end{cases} \qquad \textit{Equation 32}$$

As the rudiment of DFT, Thoms-Fermi (TF) model was developed in 1927 just after the introduction of the Schrödinger equation [54, 55]. Dirac further modified the TF model through adding a term about the exchange energy which was not considered in the TF

model, the developed model is named Thomas-Fermi-Dirac (TFD) theory. However, the TFD model remained inaccurate for most applications. The error mainly came from the representation of the kinetic energy as well as the exchange energy due to the neglect of the electron correlation. Until 1964 [56, 57], the Hohenberg-Kohn (HK) theorems were mathematically proven, which lay the foundation of the modern DFT. In the first HK theorem, for every system, parameters including the number of electrons as well as all ground-state properties such as kinetic energy ($T[\rho]$), potential energy ($V[\rho]$) and total energy ($E[\rho]$) can be determined merely by electronic density (ρ), and the total energy can be expressed as follows (Equation 23):

$$E[\rho] = E_{N\leftrightarrow e}[\rho] + T[\rho] + E_{e\leftrightarrow e}[\rho] = \int \rho(r) V_{N\leftrightarrow e}(r)\, dr + F_{HK}[\rho] \qquad \textbf{Equation 33}$$

where $F_{HK}[\rho]$ is a universal function which is suitable to every system and independent of its size. If $F_{HK}[\rho]$ is known, the solution to the Schrödinger equation can be obtained. The expressions of $T[\rho]$ and $E_{e\leftrightarrow e}[\rho]$ have become the largest hindrances for computation. In 1965, the Kohn-Sham (KS) equation was derived based on the variational principle to express the function of $F_{HK}[\rho]$ as shown in Equation 24 [58]. A new term, the exchange-correlation energy ($E_{xc}[\rho]$), is applied, which can be obtained using Equation 25. However, all variables in Equation 25 are unknown. Therefore, the accuracy of the solution to the Schrödinger equation greatly depends on the expression of exchange-correlation energy ($E_{xc}[\rho]$). It should be noted that the KS equations simplify the simulation of a multi-body system to that of a single-electron system. However, the rigorous expression of the exchange-correlation energy was not determined in the KS equation. Recently developed approaches to estimate the exchange-correlation energy are listed in Table M.2.

$$F_{HK}[\rho] = T_s[\rho] + J[\rho] + E_{xc}[\rho] \qquad \textbf{Equation 34}$$

$$E_{xc}[\rho] \equiv \left(T[\rho] - T_s[\rho]\right) + \left(E_{e\leftrightarrow e}[\rho] - J[\rho]\right) \qquad \textbf{Equation 35}$$

Table M.2 Approaches to estimate the exchange-correlation energy in KS equation.

Approximation	Expression	Descriptions
Local Density Approximation (LDA)	$E_{xc}^{LDA}[\rho]=\int \rho(r)\varepsilon_{xc}\left(\rho(r)\right)dr$ $\varepsilon_{xc}\left(\rho(r)\right)=\varepsilon_x\left(\rho(r)\right)+\varepsilon_c\left(\rho(r)\right)$	LDA [58] is extensively employed in solid state physical simulations, especially for the electronic and magnetic interactions in semiconductors. However, an overestimation of binding energy as well as underestimation of band gaps result in false predictions.
Generalized Gradient Approximation (GGA)	$E_{xc}^{GGA}\left[\rho_\alpha,\rho_\beta\right]=\int f\left(\rho_\alpha,\rho_\beta,\nabla\rho_\alpha,\nabla\rho_\beta\right)dr$	LDA was derived via assuming the electron density is an ideal form. GGA was developed based on LDA (generally named LAD+GGA). The widely used expressions for exchange-correlation energy in GGA are PBE [59], PW91 [60], and BLYP [61, 62]. It can improve the simulation accuracy of binding energy but still under estimates the band gap value.
Hybrid Functional	$E_{xc}^{HSE}=\frac{1}{4}E_X^{SR}(\mu)+\frac{3}{4}E_X^{PBE,SR}(\mu)+E_X^{PBE,LR}(\mu$	Hybrids are composed of the DFT and HF model [63]. The hybrids most used are Heyd-Scuseria-Ernzerhof (HSE) [64] (as shown on the left), B3LYP [65], PBE0 [66], and Meta hybrid GGA [67]. The calculation, especially for band gap, is more accurate using the hybrid functions.
DFT+U	$E^{DFT+U}=E^{DFT}+U^{EFF}\sum_\sigma\left(\sum_{m_i}n_{m_im_i}^\sigma-\sum_{m_1m_2}n_{m_1m_2}^\sigma\right.$	For a system with a strong on-site Coulomb interaction of localized electrons, especially for localized d and f electrons as well as p orbitals, LDA and GGA cannot be correctly described. In this case, an additional Hubbard-like term [68] can be used to revise the simulated results.

M.4.2 Applications

M.4.2.1 Band structure

Band structure for a photocatalyst, especially the band gap value, determines its optical properties. Experimentally, band gap values can be determined by employing a UV-Vis diffused reflectance spectrometer (DRS) [69-73], and calculated by the classical Tauc equation as shown in Equation 26:

$$\alpha E_{photon} = k\left(E_{photon} - E_g\right)^{\frac{n}{2}} \qquad \textbf{Equation 36}$$

$$E_{photon} = h\nu \qquad \textbf{Equation 37}$$

where E_{photon}, the energy of photons can be calculated by Equation 27; α, k, E_g, h and v respectively represent the absorption coefficient, constant for a semiconductor (usually equal to 1), band gap value, Planck constant and the frequency of irradiation; and the value of n depends on the band-gap transition: $n = 1$ for direct transition and $n = 4$ for indirect transition. The band-gap transition can be explored in resonant inelastic X-ray scattering (RIXS). RIXS is one type of normal x-ray emission spectroscopy (NXES) when incident-photon energy is not equal to the emitted-photo energy. This technique is a powerful tool to explore the states of electrons in solids including semiconductors by an energy-band model [74, 75]. Indirect band-gap transition is capable of prolonging the lifetime of photogenerated carriers [76]. By plotting αE_{photon} vs E_{photon}, the band gap (E_g) can be determined as the intercept on the abscissa. Furthermore, the valence and conduction band edge can be calculated by substituting the band-gap value obtained via Equation 26 into Equations 28 and 29 [77-81] as follows:

$$E_{CB} = \chi_p - E^e - \frac{1}{2}E_g \qquad \textbf{Equation 38}$$

$$E_{VB} = E_{CB} + E_g \qquad \textbf{Equation 39}$$

$$\chi_{A_aB_bC_c} = \left(\chi_A^a \times \chi_B^b \times \chi_C^c\right)^{\frac{1}{a+b+c}} \quad \textit{Equation 40}$$

where E_{CB} is the bottom position of the conduction band, E_{VB} is the top position of the valence band, E_g is the band gap value of a semiconductor, χ_p is the electronegativity of the semiconductor, and E^e is the energy of free electrons on the hydrogen scale (~ 4.5 eV). The electronegativity of the semiconductor, χ_p, can be estimated by the geometric mean of electro negativities of the constituent atoms through Equation 30 [82]. The above-mentioned method is a typical experimental approach to determine band structure of a photocatalyst and it is valid for prepared photocatalyst. However, for designing a novel photocatalyst, electronic structure simulation would be more effective.

The electronic band structure can be described by calculating the wave function for each electron in the Schrödinger equation. A large majority of electronic band structures are simulated based on DFT and agree well with the experimentally measured bands. As mentioned in Table M.2, exchange-correlation energy is important to obtain accurate band gap values. Specifically, calculations using LDA or LDA+GGA may underestimate the band gap values due to the delocalization error [83]. Band gaps of TiO_2 calculated using DFT methods with different exchange-correlation energy functional and Hartree-Fock equation compared with experimental result are shown in Table M.3. It can be found that the DFT method is much more accurate compared to the HF method. Among results calculated using DFT with different functionals, B3LYP has advantages in the prediction of band gaps which is more close to the detected value. A typical configuration of a simulated band electronic structure is depicted in Fig. M.6. The following information may be obtained through a band electronic structure diagram: i) band gap value, ii) band-gap transition type and iii) possibility of photogenerated charge carriers' recombination (discussed in section 4.2.3). In Fig. M.6, the band gap value for BiOBr is calculated as about 2.41 eV and an indirect band-gap transition is observed.

Comparison of processes of photogenerated carriers' recombination can be interpreted by Fig. M.7. Specifically, activated electrons on the conduction band may return to the valence band to recombine with the holes. The difference in energy between electron on the conduction band and valence band will be released as photons. This process takes place

only when it follows the transition selection rule of momentum conservation, as illustrated in Equation 31,

$$k_e^{'} - k_e = \pm q_{photon} \qquad \textbf{Equation 41}$$

where $\hbar$ is the reduced Planck constant, $k_e^{'}$ and k_e are electron wave vectors at the top of the valence band and bottom of the conduction band, respectively, and q_{photon} is the wave vector of the assisted photon [84]. For direct band-gap transition, $k_e^{'} = k_e$, whereas $k_e^{'} \neq k_e$ for indirect band-gap transition. It can be interpreted as the activated electrons on the conduction band cannot directly come back to the valence band as shown in Fig. M.7a. Instead, assistance by additional photons is needed for the transfer within an indirect band gap. As a result, the lifetime of photogenerated electrons and holes within an indirect band gap is longer than that within a direct band gap, thus increasing the diffusion length and reaction time of the photogenerated charge carriers. Correspondingly, the photocatalytic activity of materials with indirect band-gap transitions exhibited higher photocatalytic activity compared to those with direct band-gap transitions [85].

Table M.3 Band gaps for TiO_2 (anatase) using different DFT methods and Hartree-Fock calculation compared with experimental result (Adapted from [86], Copyright 2010, American Chemical Society).

Approaches	Band gap/eV	Difference
Experimental	3.3	--
Simulation with different Functional		
LDA	2.31	-30.0%
PBE	2.39	-27.6%
PW	2.40	-27.3%
PBE0	4.58	+38.8%
B3LYP	3.98	+20.6%
Hartree-Fock	12.79	+288%

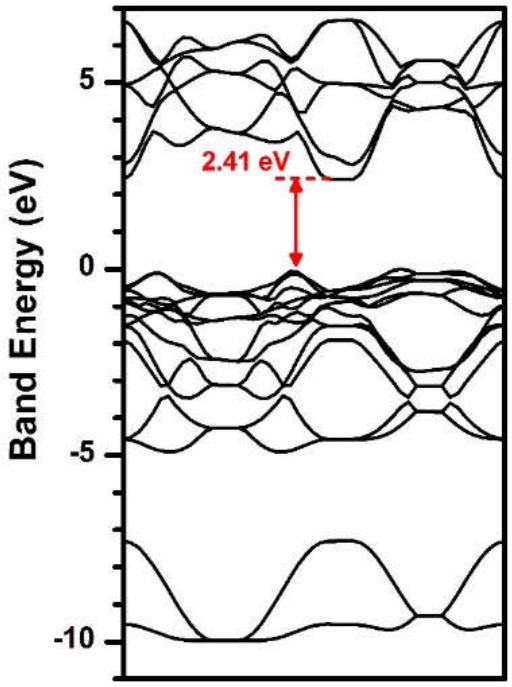


Figure M.6 Band electronic structure of BiOBr, simulated using a DFT method with LDA+GGA as implemented in the Quantum Espresso code [87].

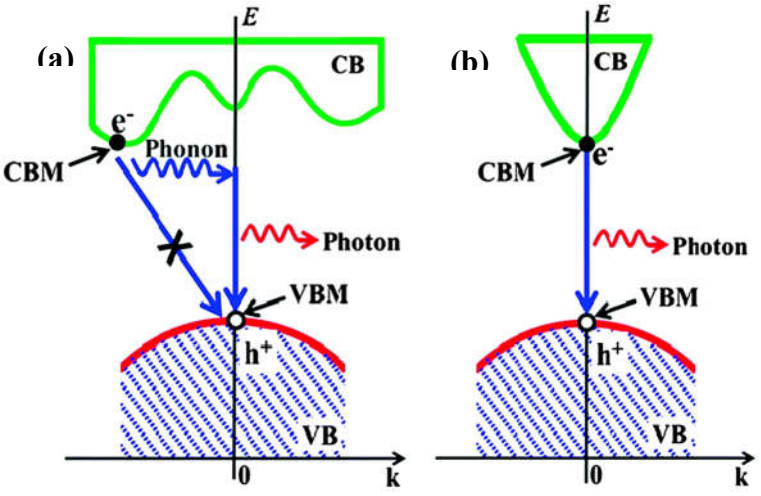


Figure M.7 Comparison of recombination processes of photogenerated charge carriers within (a) indirect and (b) direct band gaps. (Adapted from [84], Copyright 2014, Royal Society of Chemistry)

M.4.2.2 Density of states (DOS)

The density of states (DOS) is defined as the number of electronic states per unit volume, per unit energy at each energy level that are available to be occupied. The higher DOS at a

specific energy level, the more states available for occupation. When the value of DOS equal to zero, it means no states are available for occupation at that energy level. In a DOS diagram obtained from the DFT calculation, not only can the band gap be calculated, but the orbits distribution in the band structure can also be described. Asahi *et al.* reported on visible-light photocatalysis in non-metal-doped TiO_2, and DOS simulation of doped TiO_2 was first carried out to explore the dopant level between the band gaps as shown in Fig. M.8 [88]. For a doped TiO_2 with effective visible light-driven photocatalytic activity, the following requirements should be taken into account: i) additional state in the band gap of TiO_2 as the dopant level to absorb visible light, ii) the conduction band bottom of doped TiO_2 should be as high as the one of TiO_2 or higher than the H_2/H_2O to ensure its photoreduction activity and iii) the states in the gap should overlap sufficiently with the band states of TiO_2 for transferring photogenerated carriers to reactive sites at the catalysts surface within their lifetime [88]. As only the N-doped states closely interact with the band states of TiO_2 and follow well with the other conditions (condition i and ii), it indicates the effectiveness of N-TiO_2 in photocatalysis under visible light irradiation, which was confirmed by experimental results. This work provides a new approach to prepare an effective photocatalyst by using the electronic structure to predict its photocatalytic activity.

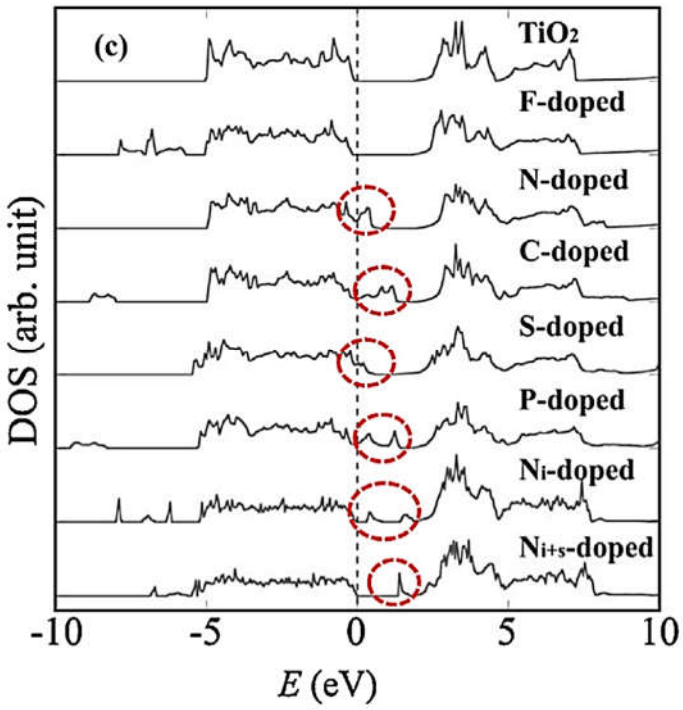


Figure M.8 Total DOSs of TiO_2 as well as doped TiO_2. (Adapted from [88], Copyright 2001, The American Association for the Advancement Science)

M.4.2.3 Evaluation of recombination of photogenerated carriers

Photocatalytic activity is influenced by various factors including the recombination of photogenerated charge carriers as well as the surface properties (especially the surface potential barrier). If the particle size of a photocatalyst is as in the nanometric scale, the band bending on the surface is negligible and the photocatalytic activity is solely determined by the recombination of photogenerated charge carriers [89]. The recombination rate can be evaluated by the transfer rate of photogenerated electrons and holes. The transfer rate of charge carriers can be indirectly determined using the effective mass of electrons and holes [85, 90-92]. The effective mass (m^*) can be expressed as shown in Equation 32,

$$m^* = \frac{\hbar^2}{\frac{d^2 E_\kappa}{d\kappa^2}} \qquad \textit{Equation 42}$$

$$D=\frac{m_h^*}{m_e^*}=\left|\frac{\left.\frac{d^2\mathrm{E}_\kappa}{d\kappa^2}\right|_e}{\left.\frac{d^2\mathrm{E}_\kappa}{d\kappa^2}\right|_h}\right| \qquad \textit{Equation 43}$$

where κ is a wave vector and E_κ is the energy corresponding to the wave vector κ. As $\hbar$ is a constant, the relative effective mass (D) of electrons and holes can be expressed as shown in Equation 33. The value of D determines the separation efficiency of photogenerated electrons and holes. The significance of solving Equation 33 is to calculate the value of the second derivative of energy on the wave vector. The second-order term can be determined via a quadratic fit in the band structure. For example [93], in Fig. M.9a, two bands of BiOI containing the bottom of the conduction band and top of the valence band are plotted. The second-term can be determined by the fitted line (red dash line in Fig. M.9a) separately for electrons on the conduction band and holes on the valence band. For different bismuth oxyhalides, variation of D are calculated and illustrated in Fig. M.9b. It can be found in BiOXs, with increasing content of heavy halogens, the separation of photogenerated charge carriers is greatly improved as with the increase in the value of D. It provides a simple approach via estimation of D for the evaluation of the separation effectiveness of charge carriers in photocatalysis.

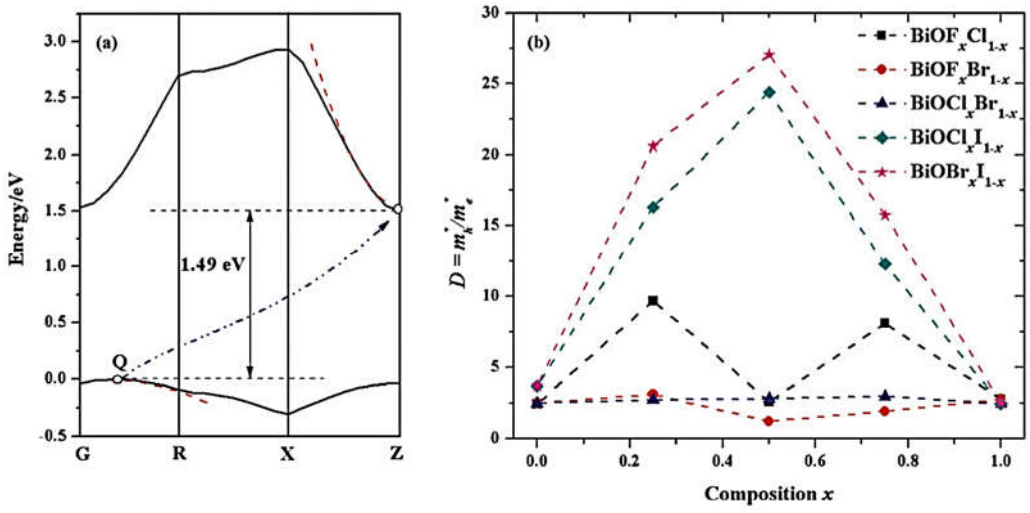


Figure M.9 (a) Bands of BiOI including the bottom of conduction band and top of valence band; (b) Calculated D for different bismuth oxyhalides (x: composition fraction) (Adapted from [93], Copyright 2012, Royal Society of Chemistry).

M.4.2.4 Optical property

According to the simulated electronic band structure (Section 4.2.1), the optical property for a material can be computed with the complex dielectric function as shown in Equation 34 [94, 95]. Calculated real part (ε_1) and imaginary part (ε_2) can be applied in Equation 35 as follows,

$$\varepsilon = \varepsilon_1 + i\varepsilon_2 \qquad \textit{Equation 44}$$

$$I(\omega) = 2\omega \left[\frac{\left(\varepsilon_1^2(\omega) + \varepsilon_2^2(\omega)\right)^{\frac{1}{2}} - \varepsilon_1(\omega)}{2} \right]^{\frac{1}{2}} \qquad \textit{Equation 45}$$

where $I(\omega)$ is the optical absorption intensity at the angular frequency (ω). Lin *et al.* reported on optical absorption of Si, Fe co-doped TiO_2 and application in water splitting with hydrogen production [96]. Optical absorption intensities simulated based on DFT calculations for pure TiO_2 as well as doped TiO_2 are depicted in Fig. M.10. For comparison, these samples are also prepared and detected for their optical absorption capacities. Difference in the spectra obtained by simulation and experiment can be found, especially in the visible light range. However, this tendency kept consistent between the simulated and experimentally detected results. Differences may be resulted from the simulation considering the material at an ideal condition without any influence by the surrounding conditions, which is almost impossible in practice, along with existing inaccuracies in the DFT. More specifically, in Si-doped TiO_2, the valence band of TiO_2 broadens with mixing Si 3p states, and the conduction band bottom has a decline of about 0.15 eV, resulting in a band gap narrowing. And the absorption in visible light region was not improved. Comparatively, for Fe doped TiO_2, Fe 3d states were located between the band gap of TiO_2, which decrease the band gap and increase the absorption of visible light photons. Recently, the optical spectra can be also simulated via time-dependent DFT (TDDFT) and Green's function methods (*e.g.* GW approximation and Bethe-Salpeter equation), which were found to be more accurate [97, 98]. Despite these differences between the simulated and

experimental results, simulation is an effective approach to study the optical absorption intensity, especially for a new material design [99, 100].

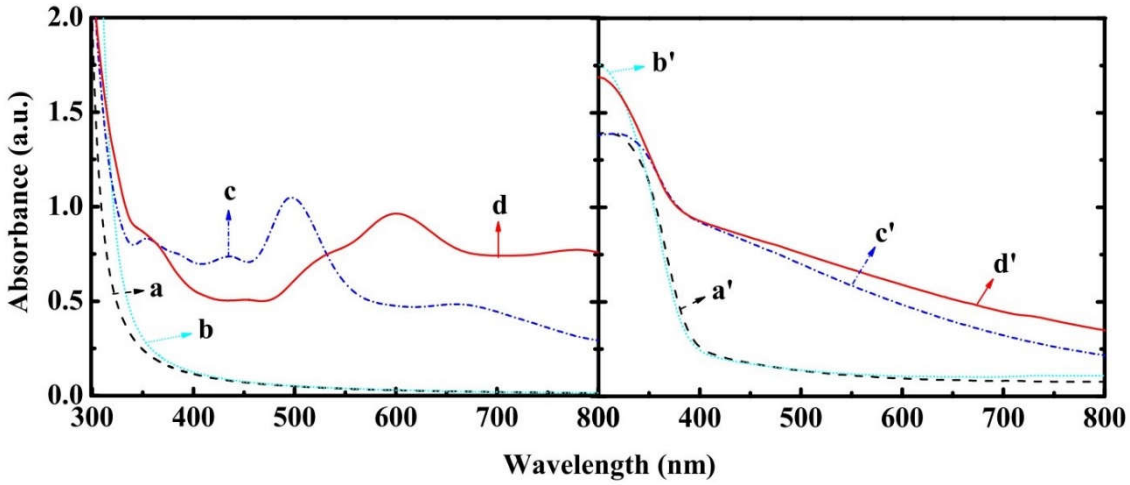


Figure M.10 Optical absorption curves of pure (a, a'), Si-doped (b, b'), Fe-doped (c, c') and Si, Fe-codoped (d, d') TiO_2 (Left: obtained by simulation; Right: obtained by experiments) (Adapted from [96], Copyright 2013, Elsevier)

M.4.2.5 Understanding of heterostructures

Heterojunction construction has been proven to be an effective approach to improve the separation efficiency of photogenerated charge carriers in photocatalysis [101, 102]. Three main band alignments in junctions are shown in Fig. M.11. For type I, where the CB of component B is lower than that of component A, and the VB of component B is higher than that of component A, photogenerated electrons and holes are both transferred from A to B. For Type II and III, both CB and VB of component B are higher than those of component A, it is also named Z-scheme junctions, and electrons on the CB of component B tend to be transferred to the CB of component A while holes are transferred in the opposite direction. The charge transfers in Type II and III junctions are in favor of supressing their recombination, as they are accumulated on different components [69, 72]. For a deep understanding of the mechanism of heterojunction in the enhancement for photocatalysis, material simulation based on DFT is an excellent approach from the aspect of the electronic structure. Liu *et al.* have reported on the understanding of Z-scheme g-C_3N_4/TiO_2 heterostructure in photocatalysis by using a hybrid DFT method [103]. The results indicate the heterostructure narrowed the band gap compared to pure TiO_2 and g-

C_3N_4, which is in favor of harvesting visible light irradiation. Moreover, the charge redistribution mainly takes place at the interface, and a negligible difference was found in the bulk of TiO_2 (Fig. M.12a), and the electrons mainly transfer from the g-C_3N_4 side to the TiO_2 side. When an equilibrium state is reached, net charge accumulation forms a built-in electric field at the interface, and the electric field motivates the electron transfer from the g-C_3N_4 to the surface of TiO_2, which facilitates the separation photogenerated charge carriers and improves its photocatalytic activity. Similar simulated results were also reported [104, 105]. Three-dimensional charge density difference, calculated using DFT, provided a visual and direct way to understand the mechanism of heterostructures in the enhancement of photocatalysis.

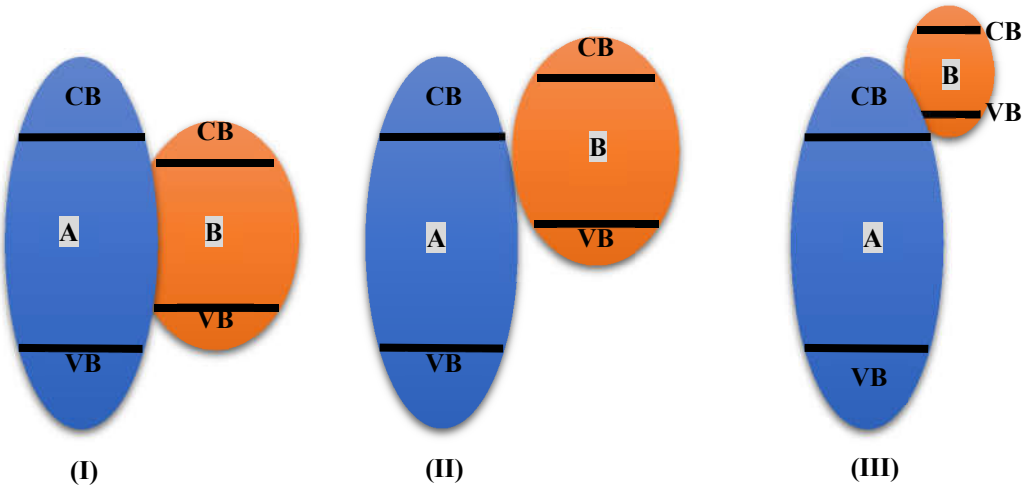


Figure M.11 Band alignment with three types.

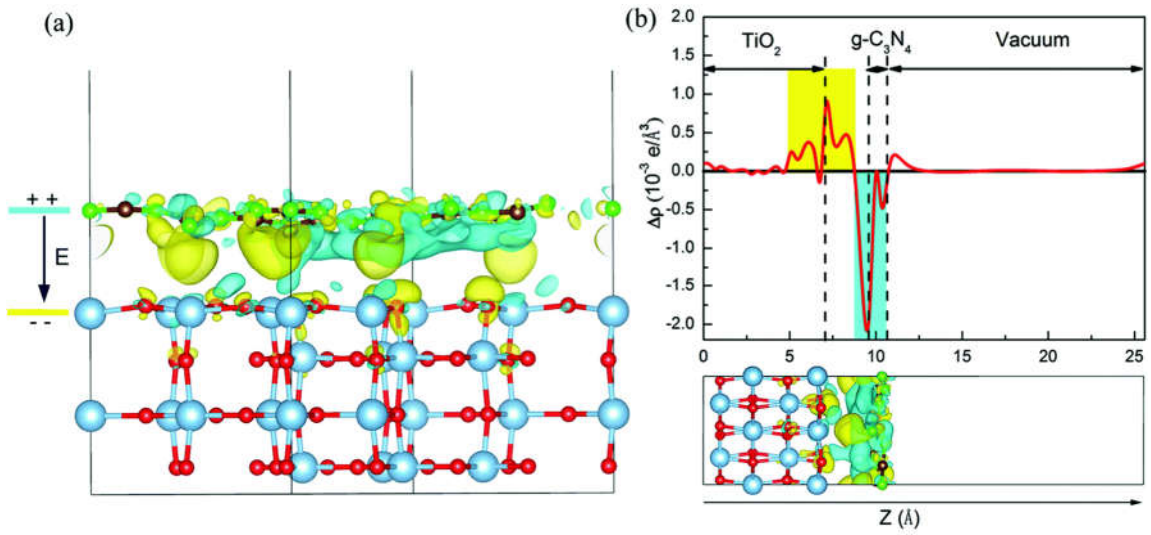


Figure M.12 (a) The charge density difference (0.0004 eÅ-3) for g-C_3N_4/TiO_2; (b) Planar-averaged electron density difference Δρ(Z) for g-C_3N_4/TiO_2. (The yellow and cyan areas represent the electron accumulation and depletion, respectively). (Adapted from [103], Copyright 2016, Royal Society of Chemistry))

M.4.2.6 Adsorption

The adsorption energy can be determined by comparing the difference in energy between the adsorbed complex and the sum of adsorbate and adsorbent as shown in Equation 36. Also, desorption energy is equated to the negative adsorption energy as shown in Equation 37. The total energy of each component can be obtained using DFT calculations. Pipornpong *et al.* have reported on the adsorption and photocatalytic conversion of CO_2 to CO on the surface of TiO_2 [106]. The adsorption mechanism of CO_2 on the surface of TiO_2 were explored and simulated results are shown in Fig. M.13. The adsorption process is composed of one step of physisorption and one step of non-dissociative chemisorption (primary chemisorption and two steps of dissociative chemisorption). The activation energy for the transition from physisorption state to chemisorption state is 1.3 kcal/mol. It suggests the dissociative chemisorption easily takes place from the physisorption at its low transition energy. However, these two dissociative chemisorptions are unstable and cannot occur. Furthermore, the photocatalytic conversion of CO_2 to CO on the surface of TiO_2 was also studied, and transition states as well as the energies for each step were also described. Similarly, phosphonic acid and formic acid adsorbed on the surface of TiO_2 were also

separately studied [107, 108]. It should be noted photocatalytic reduction of CO_2 in the aqueous phase, the competitive adsorption between CO_2 and H_2O is supposed to be taken into account. It was reported that the water may be more strongly bonded with the photocatalytic surface, compared to CO_2, and CO_2 need to diffuse through the water layer to be adsorbed [109, 110]. Computation on the adsorption in photocatalysis provides an approach to understand its mechanisms from the aspect of the potential of each state.

$$\Delta E_{ads}^{adsorbate} = E_{adsorbate-adsorbent} - \left(E_{adsorbate} + E_{adsorbent}\right) \quad \textit{Equation 46}$$

$$\Delta E_{des}^{adsorbate} = \left(E_{adsorbate} + E_{adsorbent}\right) - E_{adsorbate-adsorbent} \quad \textit{Equation 47}$$

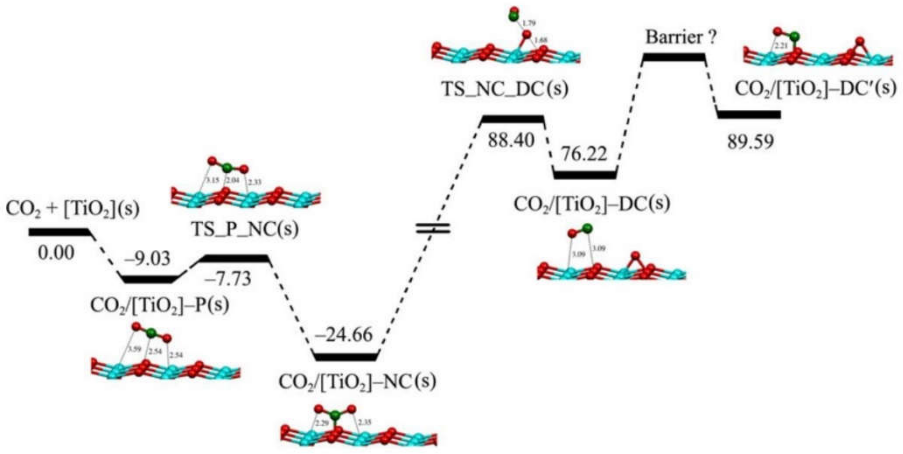


Figure M.13 Potential energy profiles for adsorption mechanism of CO_2 on TiO_2 surface (CO_2/[TiO_2]-P: physical adsorption, CO_2/[TiO_2]-NC: non-dissociative chemical adsorption, CO_2/[TiO_2]-DC and CO_2/[TiO_2]-DC': two dissociative chemical adsorptions). (Adapted from [106], Copyright 2011, Elsevier)

M.4.2.7 Surface properties investigation

The particle morphologies as well as surface properties can be experimentally investigated via scanning tunneling microscopy (STM), atomic force microscopy (AFM), low-energy electron diffraction (LEED), and surface X-ray diffraction (SXRD). Recently, *ab initio* modelling accompanied with experimentally characterized techniques were applied to explain the surface properties [111]. The computational study eases the understanding of

the most probably exposed surfaces. CO, as a probe molecule, is used the most[112]. The stretching frequency of the adsorbed CO, obtained from FTIR, is related to the electrophilicity and polarizing power of the surface Lewis acid sites, and the stretching frequency can be calculated from the simulation results. Another advantage of the use of CO probe is the well-establishment of first principle calculations of CO adsorbed on a surface[113]. Mino *et al.* [114] successfully investigated the surface properties of the rutile through FTIR combined with the DFT using CO as a probe. It would be of interest to explore the active sites of a photocatalyst and so as to purposefully enhance its activity.

M.4.3 Limitations

Material simulations provide an effective approach to explore the mechanism and design of advanced materials in photocatalysis. Its applications can be implemented in various areas. However, the limitations are obvious:

i) Inaccuracy of the simulation. The development of correlation-exchange functions is still required to improve the simulation accuracy. The emphasis can be placed on specific applications, such as developing a package of equations as well as fundamentals to be implemented specifically in photocatalysis.

ii) Limitations of the software and hardware. Development of software and hardware can improve the calculation speed as well as allow some fascinating problems to be tackled.

iii) Isolated with experiments. Material simulations should be combined or compared with experimental results. It will be more convictive and in favor of accelerating the development for both of them.

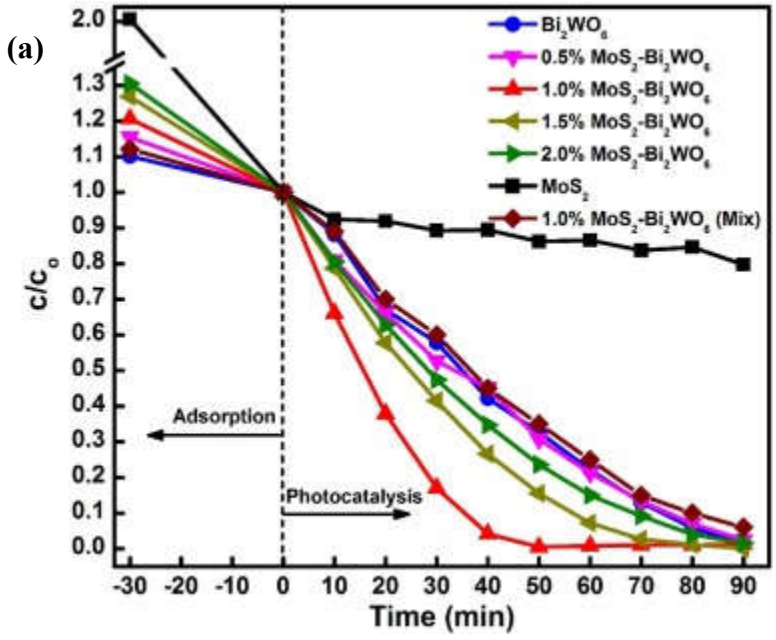
iv) Restricted to TiO_2. The simulations should be extended to every potential photocatalyst, instead of only the well-developed material such as TiO_2. It is beneficial for the development of photocatalysis.

M.5 Evaluation of photocatalytic activity

Photocatalytic activity can be evaluated using various approaches which are summarized as follows,

i) Time course

For photocatalytic water splitting, it can be described as the amounts of H_2 and O_2 evolved with increase of irradiation time. For photocatalytic degradation of organics in water after an adsorption-desorption equilibrium was obtained in dark, it can be described as the decrease in concentration of the organic with increase of irradiation time. For photocatalytic inactivation, the survival ratio as a function of irradiation time may be applied [115]. Time is certainly important, which directly exhibits the reaction rate. Finally, repeated experiments can be informative. Our group reported on MoS_2-Bi_2WO_6 applied to photocatalytically degrade RhB and inactivation of bacteria in water. Profiles of concentrations of organic pollutants and survival ratio of bacteria in water along with time were shown in Fig. M.14, which is easy-to-compare for the comparison of photocatalytic activity of each substrate.



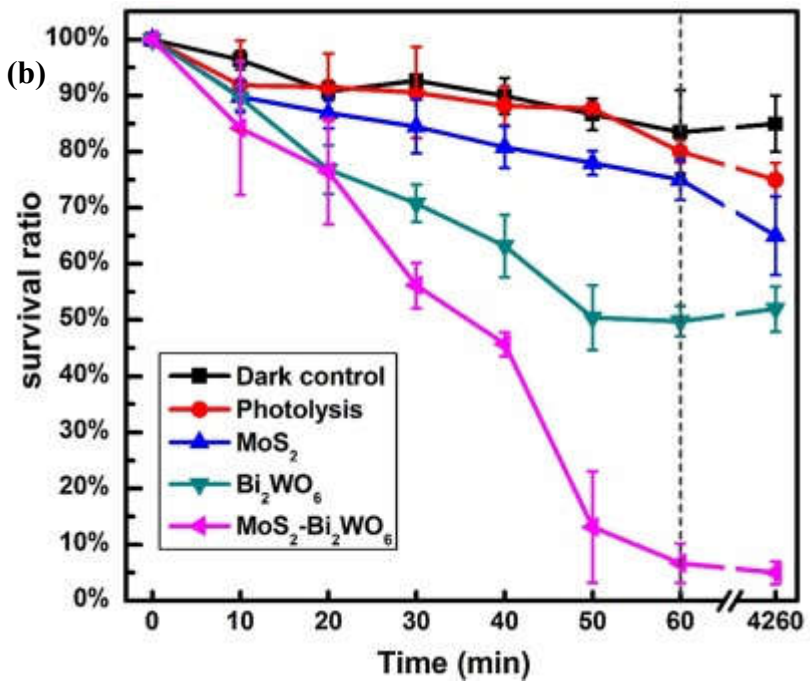


Figure M.14 (a) Photocatalytic degradation of RhB, and (b) Inactivation curves for dark control, photolysis and irradiated composite (Adapted from [116], Copyright 2017, Elsevier).

ii) Kinetic rate constant

As described in Section 4, it can be applied to evaluate the photocatalytic reaction rate for a photocatalysis process.

iii) Quantum yield

Photocatalytic activity can be influenced by a variety of experimental conditions for different systems. These factors may include the light source (types, irradiation intensity, etc.), reactive volume, initial concentration of the reactive solution, catalyst dosage amounts and temperature. The quantum yield is an effective parameter for comparing results obtained from different systems. The apparent quantum yield can be estimated through the number of reacted electrons divided by the number of incident photons as shown in Equation 38. For quantum yields in heterogeneous photocatalysis, the testing protocols as well as experimental determination have been suggested by Serpone and Sakinaro [117, 118]. For a solar cell, the solar energy conversion can be calculated via Equation 39. The energy conversion efficiency can be used to evaluate

the process of photocatalytic water splitting. For photocatalytic degradation of organic pollutants, the photonic efficiency as shown in Equation 40 may be applied to evaluate the removal efficiency [119]. In this equation, V, J, A, Δc and Δt represent volume of solution, flux of photons, illuminated area, change in concentration and change in time, respectively.

$$\eta_{Quantum\ yield}(\%) = \frac{N_{reacted\ electrons}}{N_{incident\ \text{photons}}} \times 100 \qquad \textbf{Equation 48}$$

$$\zeta(\%) = \frac{E_{H_2}}{E_{incident\ \text{photons}}} \times 100 \qquad \textbf{Equation 49}$$

$$\zeta = \frac{V \times \Delta c}{J \times A \times \Delta t} \qquad \textbf{Equation 50}$$

iv) Photoresponse

The irradiation with energy higher than the band gap of a material can activate a photocatalysis process. Photoresponse is important when evaluating a photocatalyst. It can be measured by the detection of its band gap. The relationship between the irradiation in nm and the band gap in eV is expressed in Equation 41. For example, N-TiO_2 with a band gap energy of 3.0 eV, which corresponds to the band transition at about 414 nm [120]. As a photocatalyst may absorb visible light photons, it may not exhibit a photocatalytic activity under visible light irradiation. A UV cut-off filter is generally used to evaluate the visible light-induced photocatalytic activity under visible light irradiation [2].

$$\lambda[nm] = \frac{1240}{E[eV]} \qquad \textbf{Equation 51}$$

M.6 Concluding remarks

Critical calculations in photocatalysis are reviewed from the aspect of engineering. For a photocatalytic process, the energy source is the light, whose absorption intensity

distribution can be derived from the radiation transport equations. The mass transfer occurs in the reaction media between the solution and the photocatalyst. The most significant of photocatalysis is a material preparation and design. Material simulations has become more and more popular, due to its visualized, multifunctional and easy-to-operate characteristics. Also, it can tackle some fascinating problems which are difficult to be detected or solved via experiments. Finally, photocatalytic activity of a material can be evaluated by various parameters. Future work may be addressed in the field of material simulations, and fundamentally understanding of a photocatalytic process; improvement of accuracy of the DFT calculations is also required. The simulations and modelling in the field of scaling-up a photocatalytic reactor may also be considered. The inaccuracy of computations and the limitation of scale-up models may be the hindrances before the wide applications of photocatalysis. Overall, typical calculations related to photocatalysis are summarized and emphasized in this review.

Nomenclature

AFM	Atomic force microscopy
AOPs	Advanced oxidation processes
CB	Conduction band
CC	Coupled-Cluster
CI	Configuration Interaction
DFT	Density Function Theory
DOS	Density of states
DRS	Diffused reflectance spectrometer
GGA	Generalized Gradient Approximation
HF	Hartree-Fock
HK	Hohenberg-Kohn
KS	Kohn-Sham

LDA	Local Density Approximation
LEED	Low-energy electron diffraction
L-H	Langmuir-Hinshelwood
LVREA	Local volumetric rate of energy absorption
MPx	Møller-Plesset perturbation theory
NXES	Normal x-ray emission spectroscopy
RTE	Radiation transport equation
SCF	Self-consistent field
STM	Scanning tunneling microscopy
SXRD	Surface X-ray diffraction
TF	Thoms-Fermi
TFD	Thomas-Fermi-Dirac
VB	Valence band

c^*	Concentration at the interface (mol L^{-1})
c_{bulk}	Concentration in the bulk (mol L^{-1})
c_o	Initial concentration (mol L^{-1})
c_s	Concentration on the surface (mol L^{-1})
c_t	Concentration at time of t (mol L^{-1})
D	Diffusion coefficient (m^2 s^{-1})
d_L	Characteristic dimension of the deposit (m)
E	Energy state of the wave function (eV)
$E[\rho]$	Total energy (eV)
E_g	Band gap value (eV)

E_{photon}	Energy of photons (eV)
$E_{xc}[\rho]$	Exchange-correlation energy (eV)
$\hat{H}$	Hamiltonian operator
$\hbar$	Reduced Planck constant (eV-s)
$I(\omega)$	Optical absorption intensity at the angular frequency (ω)
I_v	Monochromatic radiation intensity (einsteins m^{-2} s^{-1} sr^{-1})
k	Reaction rate constant
K	Adsorption constant
k'	Pseudo first-order reaction constant (s^{-1})
$k_{external}$	External mass transfer coefficient (m s^{-1})
m^*	Effective mass
p	Phase function of the in-scattering of incident radiation to an element (dimensionless)
q_{photon}	Wave vector of the assisted photon
R	Coordinate of nuclei (m)
r'	Reaction rate per unit of catalyst (mol L^{-1} s^{-1} g^{-1})
$r_{external}$	Rate of external mass transfer (mol m^{-2} s^{-1})
s	Spin coordinates (m)
t	Time (s, min, h)
$T[\rho]$	Kinetic energy (eV)
$V[\rho]$	Potential energy (eV)
x	Coordinate of electron (m)
α	Absorption coefficient
ε	Porosity of the catalysts
E_κ	Energy corresponding to the wave vector κ

η	Quantum yield (%)
θ	Ratio of adsorbed molecules
κ	Wave vector (m^{-1})
κ_v	Coefficient of absorption (m^{-1})
λ	Wavelength (nm)
ρ	Density ($g\ m^{-3}$)
σ_v	Coefficient of out-scattering (m^{-1})
τ	Tortuosity of the catalyst (dimensionless)
φ	Scattering angle (°)
χ_p	Electronegativity of the semiconductor (eV)
Ψ	A wave function where Hamiltonian operator acts ($m^{-3/2}$)

References:

1. Akira Fujishima and Kenichi Honda, "Electrochemical photolysis of water at a semiconductor electrode," *nature*, vol. 238, pp. 37-38, 1972.

2. Akihiko Kudo and Yugo Miseki, "Heterogeneous photocatalyst materials for water splitting," *Chemical Society Reviews*, vol. 38, no. 1, pp. 253-278, 2009.

3. Kavita Kabra, Rubina Chaudhary and Rameshwar L. Sawhney, "Treatment of Hazardous Organic and Inorganic Compounds through Aqueous-Phase Photocatalysis: A Review," *Industrial & Engineering Chemistry Research*, vol. 43, no. 24, pp. 7683-7696, 2004.

4. Xiangchao Meng, Zizhen Li and Zisheng Zhang, "Palladium nanoparticles and rGO co-modified $BiVO_4$ with greatly improved visible light-induced photocatalytic activity," *Chemosphere*, vol. 198, pp. 1-12, 2018.

5. Juan Zhao and Xudong Yang, "Photocatalytic oxidation for indoor air purification: a literature review," *Building and Environment*, vol. 38, no. 5, pp. 645-654, 2003.

6. Joanne Gamage and Zisheng Zhang, "Applications of Photocatalytic Disinfection,"

International Journal of Photoenergy, vol. 2010, 2010.

7. Xiangchao Meng, Zisheng Zhang and Xingang Li, "Synergetic photoelectrocatalytic reactors for environmental remediation: A review," *Journal of Photochemistry and Photobiology C: Photochemistry Reviews*, vol. 24, pp. 83-101, 2015.

8. Subrahmanyan Chandrasekhar, *Radiative transfer*, Courier Corporation, 2013.

9. Maurice Roger and Jacques Villermaux, "Modelling of light absorption in photoreactors Part I. General formulation based on the laws of photometry," *The Chemical Engineering Journal*, vol. 17, no. 3, pp. 219-226, 1979.

10. D. Iatridis, P. L. Yue, L. Rizzuti and A. Brucato, "The absorption of light energy in flat fluidized photoreactors," *The Chemical Engineering Journal*, vol. 45, no. 1, pp. 1-8, 1990.

11. Vishnu K. Pareek and Adesoji A. Adesina, "Light intensity distribution in a photocatalytic reactor using finite volume," *AIChE Journal*, vol. 50, no. 6, pp. 1273-1288, 2004.

12. María I. Cabrera, Orlando M. Alfano and Alberto E. Cassano, "Absorption and Scattering Coefficients of Titanium Dioxide Particulate Suspensions in Water," *The Journal of Physical Chemistry*, vol. 100, no. 51, pp. 20043-20050, 1996.

13. Orlando M. Alfano, Mari´a I. Cabrera and Alberto E. Cassano, "Modeling of light scattering in photochemical reactors," *Chemical Engineering Science*, vol. 49, no. 24, Part 2, pp. 5327-5346, 1994.

14. WA Fiveland, "Discrete-ordinates solutions of the radiative transport equation for rectangular enclosures," *ASME, Transactions, Journal of Heat Transfer(ISSN 0022-1481)*, vol. 106, pp. 699-706, 1984.

15. Roberto L. Romero, Orlando M. Alfano and Alberto E. Cassano, "Cylindrical Photocatalytic Reactors. Radiation Absorption and Scattering Effects Produced by Suspended Fine Particles in an Annular Space," *Industrial & Engineering Chemistry Research*, vol. 36, no. 8, pp. 3094-3109, 1997.

16. Quan Yang, Pei Ling Ang, Madhumita B. Ray and Simo O. Pehkonen, "Light distribution field in catalyst suspensions within an annular photoreactor," *Chemical*

Engineering Science, vol. 60, no. 19, pp. 5255-5268, 2005.

17. Vishnu K Pareek, S Cox and Adesoji A Adesina, "Light intensity distribution in photocatalytic reactors using finite volume method," in *Third international conference on CFD in the minerals and process industries. CSIRO, Melbourne*, Ed., pp. 10-12, 2003.

18. Roberto L. Romero, Orlando M. Alfano and Alberto E. Cassano, "Radiation Field in an Annular, Slurry Photocatalytic Reactor. 2. Model and Experiments," *Industrial & Engineering Chemistry Research*, vol. 42, no. 12, pp. 2479-2488, 2003.

19. Yash Boyjoo, Ming Ang and Vishnu Pareek, "Light intensity distribution in multi-lamp photocatalytic reactors," *Chemical Engineering Science*, vol. 93, pp. 11-21, 2013.

20. Vishnu Pareek, Siewhui Chong, Moses Tadé and Adesoji A. Adesina, "Light intensity distribution in heterogenous photocatalytic reactors," *Asia-Pacific Journal of Chemical Engineering*, vol. 3, no. 2, pp. 171-201, 2008.

21. Rodolfo J. Brandi, Orlando M. Alfano and Alberto E. Cassano, "Modeling of radiation absorption in a flat plate photocatalytic reactor," *Chemical Engineering Science*, vol. 51, no. 11, pp. 3169-3174, 1996.

22. R. J. Brandi, O. M. Alfano and A. E. Cassano, "Rigorous model and experimental verification of the radiation field in a flat-plate solar collector simulator employed for photocatalytic reactions," *Chemical Engineering Science*, vol. 54, no. 13, pp. 2817-2827, 1999.

23. John R Howell, M Pinar Menguc and Robert Siegel, *Thermal radiation heat transfer*, CRC press, 2010.

24. Lianfeng Zhang, William A. Anderson and Zisheng Zhang, "Development and modeling of a rotating disc photocatalytic reactor for wastewater treatment," *Chemical Engineering Journal*, vol. 121, no. 2–3, pp. 125-134, 2006.

25. Z. Zhang, W. A. Anderson and M. Moo-Young, "Rigorous modeling of UV absorption by TiO_2 films in a photocatalytic reactor," *AIChE Journal*, vol. 46, no. 7, pp. 1461-1470, 2000.

26. Zisheng Zhang, William A. Anderson and Murray Moo-Young, "Modeling of

corrugated plate photocatalytic reactors and experimental validation," *Chemical Engineering Science*, vol. 58, no. 3–6, pp. 911-914, 2003.

27. Gustavo E. Imoberdorf, Fariborz Taghipour, Mehrdad Keshmiri and Madjid Mohseni, "Predictive radiation field modeling for fluidized bed photocatalytic reactors," *Chemical Engineering Science*, vol. 63, no. 16, pp. 4228-4238, 2008.

28. Gianluca Li Puma, "Modeling of Thin-Film Slurry Photocatalytic Reactors Affected by Radiation Scattering," *Environmental Science & Technology*, vol. 37, no. 24, pp. 5783-5791, 2003.

29. O. M. Alfano, D. Bahnemann, A. E. Cassano, R. Dillert and R. Goslich, "Photocatalysis in water environments using artificial and solar light," *Catalysis Today*, vol. 58, no. 2, pp. 199-230, 2000.

30. Michael R. Hoffmann, Scot T. Martin, Wonyong Choi and Detlef W. Bahnemann, "Environmental Applications of Semiconductor Photocatalysis," *Chemical Reviews*, vol. 95, no. 1, pp. 69-96, 1995.

31. Gordon McKay, "The adsorption of dyestuffs from aqueous solution using activated carbon: Analytical solution for batch adsorption based on external mass transfer and," *The Chemical Engineering Journal*, vol. 27, no. 3, pp. 187-196, 1983.

32. Dingwang Chen, Fengmei Li and Ajay K. Ray, "External and internal mass transfer effect on photocatalytic degradation," *Catalysis Today*, vol. 66, no. 2–4, pp. 475-485, 2001.

33. Dingwang Chen, Fengmei Li and Ajay K. Ray, "Effect of mass transfer and catalyst layer thickness on photocatalytic reaction," *AIChE Journal*, vol. 46, no. 5, pp. 1034-1045, 2000.

34. Ganesh Balasubramanian, Dionysios D. Dionysiou, Makram T. Suidan, Isabelle Baudin and Jean-Michel Laîné, "Evaluating the activities of immobilized TiO2 powder films for the photocatalytic degradation of organic contaminants in water," *Applied Catalysis B: Environmental*, vol. 47, no. 2, pp. 73-84, 2004.

35. Huijuan Wang, Jie Li, Xie Quan, Yan Wu, Guofeng Li and Fangzheng Wang, "Formation of hydrogen peroxide and degradation of phenol in synergistic system of pulsed corona discharge combined with TiO_2 photocatalysis," *Journal of Hazardous Materials*,

vol. 141, no. 1, pp. 336-343, 2007.

36. Hui-juan Wang and Xiao-yang Chen, "Kinetic analysis and energy efficiency of phenol degradation in a plasma-photocatalysis system," *Journal of Hazardous Materials*, vol. 186, no. 2–3, pp. 1888-1892, 2011.

37. Qijin Geng and Wenwen Cui, "Adsorption and Photocatalytic Degradation of Reactive Brilliant Red K-2BP by TiO_2/AC in Bubbling Fluidized Bed Photocatalytic Reactor," *Industrial & Engineering Chemistry Research*, vol. 49, no. 22, pp. 11321-11330, 2010.

38. J. J. Heijnen and K. Van't Riet, "Mass transfer, mixing and heat transfer phenomena in low viscosity bubble column reactors," *The Chemical Engineering Journal*, vol. 28, no. 2, pp. B21-B42, 1984.

39. P. B. Weisz and C. D. Prater, "Interpretation of Measurements in Experimental Catalysis," in *Advances in Catalysis*, V. I. K. W.G. Frankenburg and E. K. Rideal, Ed., pp. 143-196, Academic Press, 1954.

40. Benoit Boulinguiez, Abdelkrim Bouzaza, Smail Merabet and Dominique Wolbert, "Photocatalytic degradation of ammonia and butyric acid in plug-flow reactor: Degradation kinetic modeling with contribution of mass transfer," *Journal of Photochemistry and Photobiology A: Chemistry*, vol. 200, no. 2–3, pp. 254-261, 2008.

41. Erdeng Du, Yu Xian Zhang and Lu Zheng, "Photocatalytic degradation of dimethyl phthalate in aqueous TiO_2 suspension: a modified Langmuir–Hinshelwood model," *Reaction Kinetics and Catalysis Letters*, vol. 97, no. 1, pp. 83-90, 2009.

42. Alberto E. Cassano and Orlando M. Alfano, "Reaction engineering of suspended solid heterogeneous photocatalytic reactors," *Catalysis Today*, vol. 58, no. 2, pp. 167-197, 2000.

43. Gustavo E. Imoberdorf, Horacio A. Irazoqui, Alberto E. Cassano and Orlando M. Alfano, "Photocatalytic Degradation of Tetrachloroethylene in Gas Phase on TiO_2 Films: A Kinetic Study," *Industrial & Engineering Chemistry Research*, vol. 44, no. 16, pp. 6075-6085, 2005.

44. Ignasi Salvadó-Estivill, David M. Hargreaves and Gianluca Li Puma, "Evaluation of the Intrinsic Photocatalytic Oxidation Kinetics of Indoor Air Pollutants," *Environmental Science & Technology*, vol. 41, no. 6, pp. 2028-2035, 2007.

45. Javier Marugán, Rafael van Grieken, Carlos Sordo and Cristina Cruz, "Kinetics of the photocatalytic disinfection of *Escherichia coli* suspensions," *Applied Catalysis B: Environmental*, vol. 82, no. 1, pp. 27-36, 2008.

46. Donia Friedmann, Cecilia Mendive and Detlef Bahnemann, "TiO2 for water treatment: Parameters affecting the kinetics and mechanisms of photocatalysis," *Applied Catalysis B: Environmental*, vol. 99, no. 3, pp. 398-406, 2010.

47. Eberhard Engel and Reiner M Dreizler, *Density functional theory: an advanced course*, Springer Science & Business Media, 2011.

48. E. Schrödinger, "An Undulatory Theory of the Mechanics of Atoms and Molecules," *Physical Review*, vol. 28, no. 6, pp. 1049-1070, 1926.

49. M. Born and R. Oppenheimer, "Zur Quantentheorie der Molekeln," *Annalen der Physik*, vol. 389, no. 20, pp. 457-484, 1927.

50. U. Fano, "Effects of Configuration Interaction on Intensities and Phase Shifts," *Physical Review*, vol. 124, no. 6, pp. 1866-1878, 1961.

51. Hendrik J. Monkhorst, "Calculation of properties with the coupled-cluster method," *International Journal of Quantum Chemistry*, vol. 12, no. S11, pp. 421-432, 1977.

52. Rodney J. Bartlett and David M. Silver, "Many‐body perturbation theory applied to electron pair correlation energies. I. Closed‐shell first‐row diatomic hydrides," *The Journal of Chemical Physics*, vol. 62, no. 8, pp. 3258-3268, 1975.

53. John A. Pople, J. Stephen Binkley and Rolf Seeger, "Theoretical models incorporating electron correlation," *International Journal of Quantum Chemistry*, vol. 10, no. S10, pp. 1-19, 1976.

54. Enrico Fermi, "Un metodo statistico per la determinazione di alcune priorieta dell'atome," *Rend. Accad. Naz. Lincei*, vol. 6, no. 602-607, pp. 32, 1927.

55. L. H. Thomas, "The calculation of atomic fields," *Mathematical Proceedings of the Cambridge Philosophical Society*, vol. 23, no. 5, pp. 542-548, 1927.

56. Eugene S. Kryachko, "Hohenberg-Kohn theorem," *International Journal of Quantum Chemistry*, vol. 18, no. 4, pp. 1029-1035, 1980.

57. T. L. Gilbert, "Hohenberg-Kohn theorem for nonlocal external potentials," *Physical Review B*, vol. 12, no. 6, pp. 2111-2120, 1975.

58. W. Kohn and L. J. Sham, "Self-Consistent Equations Including Exchange and Correlation Effects," *Physical Review*, vol. 140, no. 4A, pp. A1133-A1138, 1965.

59. John P. Perdew, J. A. Chevary, S. H. Vosko, Koblar A. Jackson, Mark R. Pederson, D. J. Singh and Carlos Fiolhais, "Atoms, molecules, solids, and surfaces: Applications of the generalized gradient approximation for exchange and correlation," *Physical Review B*, vol. 46, no. 11, pp. 6671-6687, 1992.

60. John P. Perdew, Kieron Burke and Matthias Ernzerhof, "Generalized Gradient Approximation Made Simple," *Physical Review Letters*, vol. 77, no. 18, pp. 3865-3868, 1996.

61. A. D. Becke, "Density-functional exchange-energy approximation with correct asymptotic behavior," *Physical Review A*, vol. 38, no. 6, pp. 3098-3100, 1988.

62. Chengteh Lee, Weitao Yang and Robert G. Parr, "Development of the Colle-Salvetti correlation-energy formula into a functional of the electron density," *Physical Review B*, vol. 37, no. 2, pp. 785-789, 1988.

63. Axel D. Becke, "A new mixing of Hartree–Fock and local density‐functional theories," *The Journal of Chemical Physics*, vol. 98, no. 2, pp. 1372-1377, 1993.

64. Jochen Heyd, Gustavo E. Scuseria and Matthias Ernzerhof, "Hybrid functionals based on a screened Coulomb potential," *The Journal of Chemical Physics*, vol. 118, no. 18, pp. 8207-8215, 2003.

65. K. Kim and K. D. Jordan, "Comparison of Density Functional and MP2 Calculations on the Water Monomer and Dimer," *The Journal of Physical Chemistry*, vol. 98, no. 40, pp. 10089-10094, 1994.

66. Carlo Adamo and Vincenzo Barone, "Toward reliable density functional methods without adjustable parameters: The PBE0 model," *The Journal of Chemical Physics*, vol. 110, no. 13, pp. 6158-6170, 1999.

67. Yan Zhao and Donald G. Truhlar, "The M06 suite of density functionals for main group

thermochemistry, thermochemical kinetics, noncovalent interactions, excited states, and transition elements: two new functionals and systematic testing of four M06-class functionals and 12 other functionals," *Theoretical Chemistry Accounts*, vol. 120, no. 1, pp. 215-241, 2008.

68. A. I. Liechtenstein, V. I. Anisimov and J. Zaanen, "Density-functional theory and strong interactions: Orbital ordering in Mott-Hubbard insulators," *Physical Review B*, vol. 52, no. 8, pp. R5467-R5470, 1995.

69. Xiangchao Meng and Zisheng Zhang, "Ag/AgCl Loaded Bi_2WO_6 Composite: A Plasmonic Z-Scheme Visible Light-Responsive Photocatalyst," *International Journal of Photoenergy*, vol. 2016, pp. 11, 2016.

70. Xiangchao Meng and Zisheng Zhang, "Pd-doped Bi_2MoO_6 Plasmonic Photocatalysts with Enhanced Visible Light Photocatalytic Performance," *Applied Surface Science*, vol. 392, pp. 169-180, 2016.

71. Xiangchao Meng and Zisheng Zhang, "Plasmonic ternary Ag–rGO–Bi_2MoO_6 composites with enhanced visible light-driven photocatalytic activity," *Journal of Catalysis*, vol. 344, pp. 616-630, 2016.

72. Xiangchao Meng and Zisheng Zhang, "Plasmonic Z-scheme Ag_2O-Bi_2MoO_6 p-n heterojunction photocatalysts with greatly enhanced visible-light responsive activities," *Materials Letters*, vol. 189, pp. 267-270, 2017.

73. Xiangchao Meng and Zisheng Zhang, "Bi_2MoO_6 Co-modified by Reduced Graphene Oxide and Palladium (Pd^{2+} and Pd^0) with Enhanced Photocatalytic Decomposition of Phenol," *Applied Catalysis B: Environmental*.

74. Mino Lorenzo, Agostini Giovanni, Borfecchia Elisa, Gianolio Diego, Piovano Andrea, Gallo Erik and Lamberti Carlo, "Low-dimensional systems investigated by x-ray absorption spectroscopy: a selection of 2D, 1D and 0D cases," *Journal of Physics D: Applied Physics*, vol. 46, no. 42, pp. 423001, 2013.

75. Akio Kotani and Shik Shin, "Resonant inelastic x-ray scattering spectra for electrons in solids," *Reviews of Modern Physics*, vol. 73, no. 1, pp. 203-246, 2001.

76. Jason K. Cooper, Sheraz Gul, Francesca M. Toma, Le Chen, Yi-Sheng Liu, Jinghua

Guo, Joel W. Ager, Junko Yano and Ian D. Sharp, "Indirect Bandgap and Optical Properties of Monoclinic Bismuth Vanadate," *The Journal of Physical Chemistry C*, vol. 119, no. 6, pp. 2969-2974, 2015.

77. Yong Xu and Martin A.A. Schoonen, "The absolute energy positions of conduction and valence bands of selected semiconducting minerals," *American Mineralogist*, vol. 85, no. 3-4, pp. 543-556, 2000.

78. Xiangchao Meng and Zisheng Zhang, "Synthesis, Analysis, and Testing of BiOBr-Bi_2WO_6 Photocatalytic Heterojunction Semiconductors," *International Journal of Photoenergy*, vol. 2015, pp. 12, 2015.

79. Xiangchao Meng, Lingyun Jiang, Weiwen Wang and Zisheng Zhang, "Enhanced Photocatalytic Activity of BiOBr/ZnO Heterojunction Semiconductors Prepared by Facile Hydrothermal Method," *International Journal of Photoenergy*, vol. 2015, pp. 9, 2015.

80. Xiangchao Meng and Zisheng Zhang, "Facile synthesis of BiOBr/Bi_2WO_6 heterojunction semiconductors with high visible-light-driven photocatalytic activity," *Journal of Photochemistry and Photobiology A: Chemistry*, vol. 310, no. 0, pp. 33-44, 2015.

81. Xiangchao Meng and Zisheng Zhang, "Synthesis and characterization of plasmonic and magnetically separable Ag/AgCl-Bi_2WO_6@ Fe_3O_4@SiO_2 core-shell composites for visible light-induced water detoxification," *Journal of Colloid and Interface Science*, vol. 485, pp. 296-307, 2017.

82. Robert Thomas Sanderson, *Chemical periodicity*, Reinhold, New York, US, 1961.

83. Paula Mori-Sánchez, Aron J. Cohen and Weitao Yang, "Localization and Delocalization Errors in Density Functional Theory and Implications for Band-Gap Prediction," *Physical Review Letters*, vol. 100, no. 14, pp. 146401, 2008.

84. Jinfeng Zhang, Peng Zhou, Jianjun Liu and Jiaguo Yu, "New understanding of the difference of photocatalytic activity among anatase, rutile and brookite TiO_2," *Physical Chemistry Chemical Physics*, vol. 16, no. 38, pp. 20382-20386, 2014.

85. Rosendo López and Ricardo Gómez, "Band-gap energy estimation from diffuse reflectance measurements on sol–gel and commercial TiO2: a comparative study," *Journal of Sol-Gel Science and Technology*, vol. 61, no. 1, pp. 1-7, 2012.

86. Natalia Martsinovich, Daniel R. Jones and Alessandro Troisi, "Electronic Structure of TiO_2 Surfaces and Effect of Molecular Adsorbates Using Different DFT Implementations," *The Journal of Physical Chemistry C*, vol. 114, no. 51, pp. 22659-22670, 2010.

87. Giannozzi Paolo, Baroni Stefano, Bonini Nicola, Calandra Matteo, Car Roberto, Cavazzoni Carlo, Ceresoli Davide, L. Chiarotti Guido, Cococcioni Matteo, Dabo Ismaila, Corso Andrea Dal, Gironcoli Stefano de, Fabris Stefano, Fratesi Guido, Gebauer Ralph, Gerstmann Uwe, Gougoussis Christos, Kokalj Anton, Lazzeri Michele, Martin-Samos Layla, Marzari Nicola, Mauri Francesco, Mazzarello Riccardo, Paolini Stefano, Pasquarello Alfredo, Paulatto Lorenzo, Sbraccia Carlo, Scandolo Sandro, Sclauzero Gabriele, P. Seitsonen Ari, Smogunov Alexander, Umari Paolo and M. Wentzcovitch Renata, "QUANTUM ESPRESSO: a modular and open-source software project for quantum simulations of materials," *Journal of Physics: Condensed Matter*, vol. 21, no. 39, pp. 395502, 2009.

88. R. Asahi, T. Morikawa, T. Ohwaki, K. Aoki and Y. Taga, "Visible-Light Photocatalysis in Nitrogen-Doped Titanium Oxides," *Science*, vol. 293, no. 5528, pp. 269-271, 2001.

89. Kenichi Ozawa, Masato Emori, Susumu Yamamoto, Ryu Yukawa, Shingo Yamamoto, Rei Hobara, Kazushi Fujikawa, Hiroshi Sakama and Iwao Matsuda, "Electron–Hole Recombination Time at TiO_2 Single-Crystal Surfaces: Influence of Surface Band Bending," *The Journal of Physical Chemistry Letters*, vol. 5, no. 11, pp. 1953-1957, 2014.

90. Peng Zhou, Jiaguo Yu and Yuanxu Wang, "The new understanding on photocatalytic mechanism of visible-light response NS codoped anatase TiO_2 by first-principles," *Applied Catalysis B: Environmental*, vol. 142–143, pp. 45-53, 2013.

91. Jiaguo Yu, Peng Zhou and Qin Li, "New insight into the enhanced visible-light photocatalytic activities of B-, C- and B/C-doped anatase TiO_2 by first-principles," *Physical Chemistry Chemical Physics*, vol. 15, no. 29, pp. 12040-12047, 2013.

92. Xiangchao Ma, Ying Dai, Meng Guo and Baibiao Huang, "The Role of Effective Mass of Carrier in the Photocatalytic Behavior of Silver Halide-Based Ag@AgX (X=Cl, Br, I): A Theoretical Study," *ChemPhysChem*, vol. 13, no. 9, pp. 2304-2309, 2012.

93. Haijun Zhang, Lu Liu and Zhen Zhou, "Towards better photocatalysts: first-principles

studies of the alloying effects on the photocatalytic activities of bismuth oxyhalides under visible light," *Physical Chemistry Chemical Physics*, vol. 14, no. 3, pp. 1286-1292, 2012.

94. Ling Cao, Dongxiao Wang, Lichun Xu and Xiuyan Li, "First-principles study on the synergistic effects of Mo–C codoped anatase TiO_2," *Solid State Communications*, vol. 185, no. Complete, pp. 5-9, 2014.

95. Ling Cao, Rong Wang, Dongxiao Wang, Lichun Xu and Xiuyan Li, "Enhanced visible light photocatalytic activity for the hybrid MoS_2/anatase TiO_2(0 0 1) nanocomposite: A first-principles study," *Chemical Physics Letters*, vol. 612, pp. 285-288, 2014.

96. Yanming Lin, Zhenyi Jiang, Chaoyuan Zhu, Xiaoyun Hu, Haiyan Zhu, Xiaodong Zhang, Jun Fan and Sheng Hsien Lin, "The optical absorption and hydrogen production by water splitting of (Si,Fe)-codoped anatase TiO_2 photocatalyst," *International Journal of Hydrogen Energy*, vol. 38, no. 13, pp. 5209-5214, 2013.

97. Linda Hung, Kopinjol Baishya and Serdar Öğüt, "First-principles real-space study of electronic and optical excitations in rutile TiO_2 nanocrystals," *Physical Review B*, vol. 90, no. 16, pp. 165424, 2014.

98. Mariachiara Pastore, "First Principle Modelling of Materials and Processes in Dye-Sensitized Photoanodes for Solar Energy and Solar Fuels," *Computation*, vol. 5, no. 1, pp. 5, 2017.

99. Jianjun Liu, Shifu Chen, Qinzhuang Liu, Yongfa Zhu and Yanfeng Lu, "Density functional theory study on electronic and photocatalytic properties of orthorhombic $AgInS_2$," *Computational Materials Science*, vol. 91, pp. 159-164, 2014.

100. Zongyan Zhao, Zhaosheng Li and Zhigang Zou, "Electronic structure and optical properties of monoclinic clinobisvanite $BiVO_4$," *Physical Chemistry Chemical Physics*, vol. 13, no. 10, pp. 4746-4753, 2011.

101. Huanli Wang, Lisha Zhang, Zhigang Chen, Junqing Hu, Shijie Li, Zhaohui Wang, Jianshe Liu and Xinchen Wang, "Semiconductor heterojunction photocatalysts: design, construction, and photocatalytic performances," *Chemical Society Reviews*, vol. 43, no. 15, pp. 5234-5244, 2014.

102. Savio J. A. Moniz, Stephen A. Shevlin, David James Martin, Zheng-Xiao Guo and

Junwang Tang, "Visible-light driven heterojunction photocatalysts for water splitting - a critical review," *Energy & Environmental Science*, vol. 8, no. 3, pp. 731-759, 2015.

103. Jianjun Liu, Bei Cheng and Jiaguo Yu, "A new understanding of the photocatalytic mechanism of the direct Z-scheme g-C_3N_4/TiO_2 heterostructure," *Physical Chemistry Chemical Physics*, vol. 18, no. 45, pp. 31175-31183, 2016.

104. Mang Niu, Daojian Cheng and Dapeng Cao, "Understanding the Mechanism of Photocatalysis Enhancements in the Graphene-like Semiconductor Sheet/TiO2 Composites," *The Journal of Physical Chemistry C*, vol. 118, no. 11, pp. 5954-5960, 2014.

105. Mang Niu, Daojian Cheng and Dapeng Cao, "SiH/TiO_2 and GeH/TiO_2 Heterojunctions: Promising TiO_2-based Photocatalysts under Visible Light," *Scientific Reports*, vol. 4, pp. 4810, 2014.

106. Waranyu Pipornpong, Raina Wanbayor and Vithaya Ruangpornvisuti, "Adsorption CO_2 on the perfect and oxygen vacancy defect surfaces of anatase TiO_2 and its photocatalytic mechanism of conversion to CO," *Applied Surface Science*, vol. 257, no. 24, pp. 10322-10328, 2011.

107. Mattias Nilsing, Sten Lunell, Petter Persson and Lars Ojamäe, "Phosphonic acid adsorption at the TiO2 anatase (1 0 1) surface investigated by periodic hybrid HF-DFT computations," *Surface Science*, vol. 582, no. 1–3, pp. 49-60, 2005.

108. A. Vittadini, A. Selloni, F. P. Rotzinger and M. Grätzel, "Formic Acid Adsorption on Dry and Hydrated TiO2 Anatase (101) Surfaces by DFT Calculations," *The Journal of Physical Chemistry B*, vol. 104, no. 6, pp. 1300-1306, 2000.

109. Dan C. Sorescu, Junseok Lee, Wissam A. Al-Saidi and Kenneth D. Jordan, "Coadsorption properties of CO_2 and H_2O on TiO_2 rutile (110): A dispersion-corrected DFT study," *The Journal of Chemical Physics*, vol. 137, no. 7, pp. 074704, 2012.

110. Lorenzo Mino, Giuseppe Spoto and Anna Maria Ferrari, "CO_2 Capture by TiO_2 Anatase Surfaces: A Combined DFT and FTIR Study," *The Journal of Physical Chemistry C*, vol. 118, no. 43, pp. 25016-25026, 2014.

111. Lorenzo Mino, Giuseppe Spoto, Silvia Bordiga and Adriano Zecchina, "Particles Morphology and Surface Properties As Investigated by HRTEM, FTIR, and Periodic DFT

Calculations: From Pyrogenic TiO2 (P25) to Nanoanatase," *The Journal of Physical Chemistry C*, vol. 116, no. 32, pp. 17008-17018, 2012.

112. Lorenzo Mino, Anna Maria Ferrari, Valentina Lacivita, Giuseppe Spoto, Silvia Bordiga and Adriano Zecchina, "CO Adsorption on Anatase Nanocrystals: A Combined Experimental and Periodic DFT Study," *The Journal of Physical Chemistry C*, vol. 115, no. 15, pp. 7694-7700, 2011.

113. Jessica Scaranto and Santi Giorgianni, "A DFT study of CO adsorbed on clean and hydroxylated anatase TiO_2 (001) surfaces," *Molecular Physics*, vol. 107, no. 19, pp. 1997-2003, 2009.

114. Lorenzo Mino, Giuseppe Spoto, Silvia Bordiga and Adriano Zecchina, "Rutile Surface Properties Beyond the Single Crystal Approach: New Insights from the Experimental Investigation of Different Polycrystalline Samples and Periodic DFT Calculations," *The Journal of Physical Chemistry C*, vol. 117, no. 21, pp. 11186-11196, 2013.

115. Joanne Gamage McEvoy, Didier Alexandre Bilodeau, Wenquan Cui and Zisheng Zhang, "Visible-light-driven inactivation of *Escherichia coli* K-12 using an Ag/AgCl–activated carbon composite photocatalyst," *Journal of Photochemistry and Photobiology A: Chemistry*, vol. 267, pp. 25-34, 2013.

116. Xiangchao Meng, Zizhen Li, Haoming Zeng, Jie Chen and Zisheng Zhang, "MoS_2 quantum dots-interspersed Bi_2WO_6 heterostructures for visible light-induced detoxification and disinfection," *Applied Catalysis B: Environmental*, vol. 210, pp. 160-172, 2017.

117. Nick Serpone and Angela Salinaro, "Terminology, relative photonic efficiencies and quantum yields in heterogeneous photocatalysis. Part I: Suggested protocol," in *Pure and Applied Chemistry*, Ed., pp. 303, 1999.

118. Angela Salinaro, V. Emeline Alexei, Jincai Zhao, Hisao Hidaka, K. Ryabchuk Vladimir and Nick Serpone, "Terminology, relative photonic efficiencies and quantum yields in heterogeneous photocatalysis. Part II: Experimental determination of quantum yields," in *Pure and Applied Chemistry*, Ed., pp. 321, 1999.

119. Clarissa Baumanis and Detlef W. Bahnemann, "TiO_2 Thin Film Electrodes: Correlation between Photocatalytic Activity and Electrochemical Properties," *The Journal*

of Physical Chemistry C, vol. 112, no. 48, pp. 19097-19101, 2008.

120. Shahed U. M. Khan, Mofareh Al-Shahry and William B. Ingler, "Efficient Photochemical Water Splitting by a Chemically Modified n-TiO_2," *Science*, vol. 297, no. 5590, pp. 2243-2245, 2002.

Appendix N Resume

Education

Ph.D., Chemical & Biological Engineering, University of Ottawa, Canada, 2018

M.A.Sc., Chemical & Biological Engineering, University of Ottawa, Canada, 2015

B.E.Sc., Chemical Engineering, Ocean University of China, China, 2013

Research interest

Catalytic reaction engineering applied into green processes

Functional materials preparation for green processes

Energy storage technology development

Chemical reactor design

Publications

30 papers were accepted for publication in referred journals (total impact factor: 149.539, citations: 442, h-index: 12 and ESI: 2). Four manuscripts are under review, and 12 publications were published on conference proceedings. Typical publications are listed below:

1. **X. Meng** and Z. Zhang, ***AIChE Journal*** (2018)
2. **X. Meng** and Z. Zhang, ***Progress in Petrochemical Science*** 1, 4, 1-4 (2018).
3. **X. Meng** and Z. Zhang, ***Materials Letters*** 225, 152-156 (2018)
4. **X. Meng** and Z. Zhang, ***Catalysis Today***, 315， 2-8 (2018)
5. Z. Li, **X. Meng** and Z. Zhang, ***Catalysis Today***, 315 67-78 (2018)
6. **X. Meng**, Z. Li and Z. Zhang, ***Chemosphere*** 198, 1-12 (2018)
7. Z. Li, **X. Meng** and Z. Zhang, ***J. of photochem. & photobio. C*** 35, 39-55, (2018)
8. **X. Meng**, H. Qin and Z. Zhang, ***J. of Colloid & Interface Sci.***, 513, 877-890, (2018)
9. **X. Meng**, Z. Li and Z. Zhang, ***Material Research Bulletin***, 99, 471-478 (2018)
10. **X. Meng**, Z. Li, N. Yun and Z. Zhang, ***Journal of Nanomaterials*** 1234506 (2018)

11. **X. Meng**, et al., ***Applied Surface Science***, 433, 76-87 (2018)
12. **X. Meng**, Z. Li and Z. Zhang, ***Journal of Catalysis***, 356, 53 – 64 (2017)
13. **X. Meng** and Z. Zhang, ***General Chemistry***, 3, 3, 159-163 (2017)
14. **X. Meng**, et al., ***Applied Catalysis B: Environmental***, 210, 160-172 (2017)
15. **X. Meng** and Z. Zhang, ***Materials Letters***, 189, 267-270 (2017)
16. **X. Meng** and Z. Zhang, ***Applied Catalysis B: Environmental***, 209, 383-393 (2017)
17. **X. Meng** and Z. Zhang, ***Applied Surface Science***, 392, 169-180 (2017).
18. **X. Meng** and Z. Zhang, ***J. of Colloid and Interface Science***, 485, 296-307 (2017)
19. **X. Meng** and Z. Zhang, ***Journal of Catalysis*** 344, 616-630 (2016)
20. A. Ahmad, **X. Meng**, et al., ***Journal of Nanomaterials***, 1373725 (2016)
21. X. Hu, **X. Meng** and Z. Zhang, ***International J. of Photoenergy*** 8730806, (2016)
22. **X. Meng** and Z. Zhang, ***J. of Molecular Catalysis A***, 423, 533-549 (2016).
23. R. Ran, **X. Meng** and Z. Zhang, ***Applied Catalysis B***, 196, 1-15 (2016)
24. Y. Zheng, C. Li, **X. Meng** and Z. Zhang, ***J. of Molecul. Cata. A***, 421, 16-28 (2016)
25. **X. Meng** and Z. Zhang, ***International Journal of Photoenergy***, 4054351, (2016)
26. **X. Meng**, Z. Zhang and X. Li, ***J. of photochem. & photobio. C***, 24, 83-101 (2015)
27. **X. Meng** and Z. Zhang, ***J. of Photochemistry & Photobiology A***, 310, 33-44 (2015)
28. **X. Meng**, et al., ***International Journal of Photoenergy***, 747024, (2015)
29. **X. Meng** and Z. Zhang, ***International Journal of Photoenergy***, 630476 (2015)
30. **X. Meng**, N. Yun and Z. Zhang, ***Can. J of Chem. Eng.*** (2018). (under review)
31. Z. Li, **X. Meng** and Z. Zhang, ***J. Colloid Interface Sci.*** (2018). (under review)
32. H. Luo, **X. Meng et al.**, ***Colloids and Surfaces A*** (2018) (under review)
33. Z. Li, **X. Meng** and Z. Zhang, ***Materials Research Bulletin*** (2018). (under review)
34. **X. Meng** and Z. Zhang, ***Catalysts*** (2018) (Under revision)

Scholarly and professional activities

2018- Committee member, European Advanced Materials Congress, Sweden

2017- Assistant Editor, Journal of Chemical Compounds & Biochemistry

2017- Editorial board member, General Chemistry Journal

2017- Editorial board member, Journal of Molecular Nanotechnology & Nanomedicine

2017- Invited Editor, Micro & Nanotechnology Books, Elsevier

2015- Journal Referee: Journal of Alloys and Compounds, Chemosphere, Canadian Journal of Chemical Engineering, Materials Letters, Journal of Photochemistry and Photobiology A Chemistry, Chemical Engineering Journal, Applied Catalysis B: Environmental, Journal of hazardous materials, Journal of Molecular Liquids, RSC Advances, etc.

2014- Member, Canadian Society for Chemical Engineering (CSChE)

2014- Member, Chemical Institute of Canada (CIC)

Academic honours and awards

2018- Part-time Assistant Professor, University of Ottawa

2018- Student Travel Award, Canadian Symposium on Catalysis (CSC), the Catalysis Division of the Chemical Institute of Canada

2017- Kokes Award, North American Catalysis Society (NACS)

2017- The Best TA of 2017 (nominated), University of Ottawa

2017- International Experience Scholarship, University of Ottawa

2016- Student Travel Award, Canadian Symposium on Catalysis (CSC), the Catalysis Division of the Chemical Institute of Canada

2016- Innovation & Entrepreneurship Competition Award, China Ministry of Education

2015- Excellence of Graduate Studies, University of Ottawa

2015- Chinese Government Scholarship, China Ministry of Education

2013- International Admission Scholarship, University of Ottawa

Contact information

Website: https://uniweb.uottawa.ca/#!uottawa/members/2885/profile

Google Scholar: https://scholar.google.ca/citations?user=or7gRnQAAAAJ&hl=en